

ADA022379

MAR 30 1976

LIBRARY

A

10th Symposium on

NAVAL HYDRODYNAMICS (10th)

HYDRODYNAMICS FOR SAFETY
FUNDAMENTAL HYDRODYNAMICS

sponsored by the

OFFICE OF NAVAL RESEARCH

the

MASSACHUSETTS INSTITUTE OF TECHNOLOGY

and the

UNITED STATES COAST GUARD

June 24-28, 1974

Cambridge, Massachusetts

RALPH D. COOPER
STANLEY W. DOROFF
Editors

ONR - ACR-204

OFFICE OF NAVAL RESEARCH - DEPARTMENT OF THE NAVY
Arlington, Va.

DDC
RECEIVED
MAR 30 1976
A

2

12 787p.

11

10

14

27

db

26-250

PREVIOUS BOOKS IN THE NAVAL HYDRODYNAMICS SERIES

"First Symposium on Naval Hydrodynamics," National Academy of Sciences—National Research Council, Publication 515, 1957, Washington, D.C.; PB138732, paper copy \$11.25, 16-mm microfilm \$2.25.

"Second Symposium on Naval Hydrodynamics: Hydrodynamic Noise and Cavity Flow," Office of Naval Research, Department of the Navy, ACR-58, 1958; PB157668, paper copy \$13.25, 16-mm microfilm \$2.25.

"Third Symposium on Naval Hydrodynamics: High-Performance Ships," Office of Naval Research, Department of the Navy, ACR-65, 1960; AD430729, paper copy \$15.25, 16-mm microfilm \$2.25.

"Fourth Symposium on Naval Hydrodynamics: Propulsion and Hydroelasticity," Office of Naval Research, Department of the Navy, ACR-92, 1962; AD447732, paper copy \$29.25, 16-mm microfilm \$2.25.

"The Collected Papers of Sir Thomas Havelock on Hydrodynamics," Office of Naval Research, Department of the Navy, ACR-103, 1963; AD623589, paper copy \$15.25, microfiche \$2.25.

"Fifth Symposium on Naval Hydrodynamics: Ship Motions and Drag Reduction," Office of Naval Research, Department of the Navy, ACR-112, 1964; AD640539, paper copy \$29.25, microfiche \$2.25.

"Sixth Symposium on Naval Hydrodynamics: Physics of Fluids, Maneuverability and Ocean Platforms, Ocean Waves, and Ship-Generated Waves and Wave Resistance," Office of Naval Research, Department of the Navy, ACR-136, 1966; AD676079, paper copy \$17.25, microfiche \$2.25.

"Seventh Symposium on Naval Hydrodynamics: Unsteady Propeller Forces, Fundamental Hydrodynamics, Unconventional Propulsion," Office of Naval Research, Department of the Navy, DR-148, 1968; AD721180 paper copy \$49.25, microfiche \$2.25.

"Eighth Symposium on Naval Hydrodynamics: Hydrodynamics in the Ocean Environment," Office of Naval Research, Department of the Navy, ACR-179, 1970; AD748721; Available from Superintendent of Documents, U.S. Government Printing Office, Washington, D.C., 20404, Clothbound, 1185 pages, illustrated (Catalog No. D 210.15: ACR-179; Stock No. 0851-0056), \$11.75, microfiche \$2.25.

"Ninth Symposium on Naval Hydrodynamics: Unconventional Ships, Ocean Engineering, Frontier Problems," Office of Naval Research, Department of the Navy, ACR-203, 1974; Two Volumes; Vol. 1, ADA010505; Vol. 2, ADA010506; Available from Superintendent of Documents, U.S. Government Printing Office, Washington, D.C., 20404, Clothbound, 1108 pages, Vol. 1, 903 pages, Vol. 2, illustrated (Catalog Nos. D210.15:ACR-203/V1; D210.15:ACR-203/V2; Stock Nos. 0851-00062, 0851-00063); Vol. 1, \$15.55, Vol. 2, \$13.55; microfiche \$2.25.

NOTE: The above books are available on microfilm and microfiche from the National Technical Information Service, U.S. Department of Commerce, Springfield, Virginia 22151. The first six books are also available from NTIS in paper copies. The catalog numbers and the prices for paper, clothbound, and microform copies are shown for each book.

ACCESSION for NTIS DEC 1974	<div style="border: 1px solid black; padding: 5px;"> Statements and opinions contained herein are those of the authors and do not to be construed as official or reflecting the views of the Navy Department or of the naval service at large. </div>
<div style="font-size: 2em; font-family: cursive;">A 12-4</div>	For sale by the Superintendent of Documents, U.S. Government Printing Office Washington, D.C. 20402 - Price \$15 Stock Number 008-051-00065-8

PREFACE

The Tenth Symposium on Naval Hydrodynamics, which was held in Cambridge, Massachusetts, on 24-28 June 1974 under the joint sponsorship of the Office of Naval Research, the United States Coast Guard, and the Massachusetts Institute of Technology, continued the traditional pattern which has been established for this series of meetings. The two organizations which joined with the Office of Naval Research in sponsoring this Symposium are deeply and actively engaged in research on hydrodynamic problems of critical interest to the naval and maritime community, and several such hydrodynamic problem areas were selected as the principal themes of the Symposium.

The United States Coast Guard has in recent years significantly expanded its activity in ship-oriented hydrodynamic research, and it was a great honor to have its cooperation and assistance in sponsoring the Tenth Symposium. The Massachusetts Institute of Technology has a long history of interaction with the United States Navy in general and with the Office of Naval Research in particular. The lion's share contribution of the Massachusetts Institute of Technology to the organization and management of the Tenth Symposium adds to the long list of distinguished and invaluable services which it has rendered.

The two major technical themes of the Tenth Symposium are Hydrodynamics for Safety and Fundamental Hydrodynamics. The former addresses in some detail critical problems of growing concern in naval and maritime circles—the related problems of collision avoidance and maneuvering in confined waters. The latter presents results from a wide variety of fundamental hydrodynamic research areas which bear rather directly on various ship-oriented problems.

In such an undertaking as the organization and management of a large meeting, the list of persons making valuable contributions must necessarily be long indeed. In the case of the Tenth Symposium on Naval Hydrodynamics, such a list must without question be headed by Professor Philip Mandel of the Massachusetts Institute of Technology Department of Ocean Engineering, who served as chairman of the Symposium. The success of this meeting is due in large part to Professor Mandel's careful, dedicated, and detailed attention to every aspect of the Symposium arrangements. He was capably assisted by many members of the staff of the Department of Ocean Engineering, including: Professor J. N. Newman, who played a major role in organizing the technical program, Professor J. E. Kerwin, who organized and managed the tour of the Massachusetts Institute of Technology which preceded the Woods Hole visit, Professor Martin Abkowitz who made the arrangements for the reception and banquet, Mr. Keatinge Keays, Administrative Officer, and Ms. Gwen Johnson, Administrative Assistant, who discharged a wide variety of managerial tasks with great expertise, and Ms. Jinny Nathans and Ms. Chris Simony who provided invaluable secretarial assistance. In addition, we are indebted to Mrs. Davette Abkowitz, Mrs. Betty Dyer and Mrs. Marge Chrysostomidis for their assistance in planning and executing the social events which were held in connection with the Symposium and which provided a very welcomed and very enjoyable respite from the long and crowded technical calendar. It is also a pleasure to express our gratitude to the Woods Hole Oceanographic Institute for the very delightful visit to the Institute and to Mr. Charles Innis of the Woods Hole staff who made the arrangements for the visit. The Office of Naval Research extends its heartfelt appreciation to all of these, and to the many more who remain unnamed, whose unselfish efforts made the Tenth Symposium on Naval Hydrodynamics possible.

Finally, it would be greatly remiss of me not to mention Dr. Albert Wood of the Boston Branch Office of the Office of Naval Research and Mr. Stanley Doroff of the Fluid Dynamics Program of ONR, who provided continual support and assistance in the planning of the Symposium from its inception.

Ralph D. Cooper

RALPH D. COOPER
Fluid Dynamics Program
Office of Naval Research

CONTENTS

	Page
Preface	iii
Introductory Remarks	x
Dr. Alfred H. Keil, Dean of Engineering, Massachusetts Institute of Technology	
Welcoming Address	xi
Dr. Jerome B. Wiesner, President, Massachusetts Institute of Technology	
Welcoming Address	xiii
Rear Admiral M. D. Van Orden, USN, Chief of Naval Research	
Welcoming Address	xv
Rear Admiral A. P. Siemens, Chief of Research and Development, United States Coast Guard	
A Tribute to Georg Weinblum	xvi
Dr. J. V. Wehausen, Professor of Engineering Science, University of California, Berkeley	
Dr. T. Y. Wu, Professor of Applied Mechanics, California Institute of Technology	
A Catalogue of Published Papers of by Georg P. Weinblum	xix
HYDRODYNAMICS FOR SAFETY - MANEUVERING SESSION I	
THE EFFECTS OF BEAM ON THE HYDRODYNAMIC CHARACTERISTICS OF SHIP HULLS	3
J. Gerritsma, W. Beukelman, and C. C. Glandsdorp, University of Technology, Delft, The Netherlands	
DISCUSSION	30
W. R. Jacobs, Stevens Institute of Technology, U.S.A.	
DISCUSSION	30
K. Nomoto, University of Hiroshima, Japan	
DISCUSSION	30
E. V. Lewis, Webb Institute of Naval Architecture, U.S.A.	
DISCUSSION	30
C. M. Lee, Naval Ship Research and Development Center, U.S.A.	
DISCUSSION	31
M. Honkanen, Finland	
DISCUSSION	31
N. H. Norrbin, Swedish State Shipbuilding Experimental Tank, Sweden	
AUTHOR'S REPLY	33
J. Gerritsma, University of Technology, The Netherlands	
HYDRODYNAMIC INTERACTIONS BETWEEN SHIPS	35
E. O. Tuck, University of Adelaide, Australia and J. N. Newman, M.I.T., Cambridge, Massachusetts	
DISCUSSION	59
M. Schmiechen, Versuchsanstalt für Wasserbau und Schiffbau, Germany	
DISCUSSION	59
I. W. Dand, National Physical Laboratory, England	
DISCUSSION	59
L. L. Martin, Admiralty Experimental Works, England	
DISCUSSION	62
S. Wang, Tetra Tech, Inc., U.S.A.	
AUTHOR'S REPLY	70
E. O. Tuck, University of Adelaide, Australia	

Effects of bank on the hydrodynamic characteristics of ship hulls

BANK EFFECTS ON A SHIP MOVING THROUGH A SHORT DREDGED CHANNEL,	71
N. H. Norrbin, Swedish State Shipbuilding Experimental Tank, Sweden	
DISCUSSION	83
C. T. Earnest, Panama Canal Co., Panama	
DISCUSSION	83
L. L. Martin, Admiralty Experimental Works, England	
DISCUSSION	83
E. Müller, Versuchsanstalt für Binnenschiffbau, Germany	
AUTHOR'S REPLY	88
N. H. Norrbin, Swedish State Shipbuilding Experimental Tank, Sweden	
DOUBLE-BODY FLOW THEORY, A NEW LOOK AT THE CLASSICAL PROBLEM	89
T. Y. Wu and A. T. Chwang, California Institute of Technology, Pasadena, California	
DISCUSSION	102
L. Landweber, University of Iowa, U.S.A.	
DISCUSSION	103
T. Miloh, University of Iowa, U.S.A.	
AUTHOR'S REPLY	105
T. Y. Wu, California Institute of Technology, U.S.A.	
SESSION II	
OSCILLATORY TESTING FOR THE ASSESSMENT OF SHIP MANEUVERABILITY,	109
R. E. D. Bishop and A. G. Parkinson, University College, London, England	
R. K. Burcher and W. G. Price, RCNC, England	
DISCUSSION	122
L. L. Martin, Admiralty Experimental Works, England	
DISCUSSION	123
M. Schmichen, Versuchsanstalt für Wasserbau und Schiffbau, Germany	
DISCUSSION	126
A. Goodman, Hydronautics, Inc., U.S.A.	
DISCUSSION	128
T. F. Ogilvie, University of Michigan, U.S.A.	
AUTHOR'S REPLY	129
R. E. D. Bishop, University College, England	
LARGE AMPLITUDE PMM TESTS AND MANEUVERING PREDICTIONS FOR A MARINER CLASS VESSEL,	131
L. W. Smitt and M. S. Chislett, Skibsteknisk Laboratorium, Lyngby, Denmark	
DISCUSSION	152
A. Goodman, Hydronautics, Inc., U.S.A.	
DISCUSSION	152
R. C. Uhlin, Exxon International Co., U.S.A.	
DISCUSSION	153
C. C. Glansdorff, Technical University of Delft, The Netherlands	
DISCUSSION	153
S. A. R. Thulin	
AUTHOR'S REPLY	157
L. W. Smitt, Skibsteknisk Laboratorium, Denmark	
ON A STUDY OF SHIP-CONTROLLABILITY OF A WIDE-BEAM TANKER USING LARGE SCALE MODEL,	159
S. Sato, M. Takagi and T. Takai, Hitachi Shipbuilding & Engineering Co., Ltd. Osaka, Japan	
DISCUSSION	178
H. W. W. Thieme, Institut für Schiffbau der Universität Hamburg, Germany	
AUTHOR'S REPLY	179
S. Sato, Hitachi Shipbuilding and Engineering Co., Ltd., Japan	
DIGITAL SIMULATION ANALYSIS OF MANEUVERING PERFORMANCE,	181
H. Eda, Davidson Laboratory, Stevens Institute of Technology, Hoboken, New Jersey	
DISCUSSION	204
A. Goodman, Hydronautics, Inc., U.S.A.	
AUTHOR'S REPLY	205
H. Eda, Davidson Laboratory, Stevens Institute of Technology, U.S.A.	

SESSION III

HYBRID COMPUTATION FOR THE SIMULATION OF THE MANEUVERING SHIPS,	209
G. Mak and G.M. van der Bend, Netherlands Ship Model Basin, Wageningen, The Netherlands	
SIMULATION OF VESSEL ENCOUNTERS IN CONFINED WATERS,	221
J.W. Devanney III, N. Szasz, M.I.T., Cambridge, MA, J. Patell, Carnegie-Mellon University, Pittsburgh, PA and N. Norrbin, Swedish State Shipbuilding Experimental Tank, Goteborg, Sweden	
THE ANALYSIS OF SAFETY MARGINS IN THE MANEUVERING OF LARGE SHIPS IN CONFINED WATERS	245
I. Oldenkamp, Royal Institution of Engineers, Netherlands and P.J. Paymans, Ergonomics Society, Netherlands	
SOME ASPECTS OF MANEUVERING IN COLLISION SITUATIONS IN SHALLOW WATER,	281
I.W. Dand, National Physical Laboratory, Feltham, Middlesex, England	
DISCUSSION	273
E.O. Tuck, University of Adelaide, Australia	
DISCUSSION	273
P. Oltmann, Institut für Schiffbau der Universität Hamburg, Germany	
DISCUSSION	273
M. Schmiedchen, Versuchsanstalt für Schiffbau der Universität Hamburg, Germany	
DISCUSSION	274
G.E. Gadd, National Physical Laboratory, England	
AUTHOR'S REPLY	275
I.W. Dand, National Physical Laboratory, England	
WHEN IS COLLISION UNAVOIDABLE?	277
W.C. Webster, University of California, Berkeley, California	
DISCUSSION	291
J.C. Card, U.S. Coast Guard, U.S.A.	
DISCUSSION	292
S.D. Sharma, Institut für Schiffbau der Universität Hamburg, Germany	
AUTHOR'S REPLY	293
W.C. Webster, University of California, U.S.A.	

HYDRODYNAMICS FOR SAFETY - OTHER SESSION IV

SHIP MOTIONS AND CAPSIZING IN ASTERN SEAS,	297
O.H. Oakley, Jr., J.R. Paulling, and P.D. Wood, University of California, Berkeley, California	
DISCUSSION	349
C.M. Lee, Naval Ship Research and Development Center, U.S.A.	
DISCUSSION	349
L.L. Martin, Admiralty Experimental Works, England	
AUTHOR'S REPLY	350
O.H. Oakley, University of California, U.S.A.	
DESIGN ACCELERATION AND SHIP MOTIONS FOR LNG CARGO TANKS,	351
A.E. Baitir, S.L. Bales, and W.G. Meyers, NSRDC Bethesda, Maryland	
DISCUSSION	368
E.V. Lewis, Webb Institute of Naval Architecture, U.S.A.	
DISCUSSION	369
D.L. Folsom, U.S. Coast Guard, U.S.A.	
AUTHOR'S REPLY	370
A.E. Baitir, Naval Ship Research and Development Center, U.S.A.	
LIQUID SLOSH IN LNG CARRIERS,	371
H.N. Abramson and R.L. Bass, Southwest Research Institute San Antonio, Texas and O. Faltinsen and H.A. Olsen, Det Norske Veritas, Oslo, Norway	
THE HYDRODYNAMIC INFLUENCE ON THE NON-LINEAR MOTION OF AN ACV OVER WAVES,	389
L.J. Doctors, University of New South Wales, Sydney, Australia	

DISCUSSION	408
N. King, Naval Ship Research and Development Center, U.S.A.	
DISCUSSION	408
A. Magnuson, Naval Ship Research and Development Center, U.S.A.	
DISCUSSION	415
T.T. Huang, Naval Ship Research and Development Center, U.S.A.	
DISCUSSION	415
D.D. Moran, Naval Ship Research and Development Center, U.S.A.	
DISCUSSION	417
R.A. Barr, Hydronautics, Inc., U.S.A.	
DISCUSSION	417
P. Kaplan, Oceanics, Inc., U.S.A.	
AUTHOR'S REPLY	419
L.J. Doctors, University of New South Wales, Australia	
➤ SEMI-SUBMERGED AIR CUSHION VEHICLE (SSACV)	421
T.K.S. Murthy, Portsmouth, U.K.	
DISCUSSION	431
P. Kaplan, Oceanics, Inc., U.S.A.	
DISCUSSION	432
R.A. Barr, Hydronautics, Inc., U.S.A.	
DISCUSSION	433
L.J. Doctors, University of New South Wales, Australia	
AUTHOR'S REPLY	434
T.K.S. Murthy, England	
➤ FUNDAMENTAL HYDRODYNAMICS - SESSION V	
SMALL PARAMETER EXPANSIVES IN SHIP HYDRODYNAMICS	439
R. Timman, Delft University of Technology, Delft, The Netherlands	
EXTENSION, ANALYSIS, AND IMPROVEMENT OF PERTURBATION SERIES	449
M. Van Dyke, Stanford University, Stanford, California	
DISCUSSION	458
J.M. Witting, Naval Research Laboratory, U.S.A.	
DISCUSSION	458
M.S. Longuet-Higgins, University of Cambridge, England	
AUTHOR'S REPLY	461
M. Van Dyke, Stanford University, U.S.A.	
CALCULATION OF VORTEX SHEETS IN UNSTEADY FLOW AND APPLICATIONS IN SHIP HYDRODYNAMICS	463
P.T. Fink and W.K. Soh, University of New South Wales, Sydney, Australia	
DISCUSSION	488
L. Landweber, University of Iowa, U.S.A.	
DISCUSSION	488
K. Wieghardt, Institut für Schiffbau der Universität Hamburg, Germany	
DISCUSSION	489
L.J. Doctors, University of New South Wales, Australia	
DISCUSSION	489
G.F. Gadd, National Physical Laboratory, England	
AUTHOR'S REPLY	490
P.T. Fink, University of New South Wales, Australia	
2 and THE FORCE AND MOMENT ON A TWIN-HULL SHIP IN A STEADY POTENTIAL FLOW	493
Wen-Chin Lin, Naval Ship Research and Development Center, Bethesda, Maryland	
SECOND-ORDER HYDRODYNAMIC FORCES DUE TO STOCHASTIC EXCITATION	517
Eddie Neal, Naval Ship Research and Development Center, Bethesda, Maryland	
SESSION VI	
WAVE PATTERNS OF NON-THIN OR FULL-BODIED SHIP	543
Joseph B. Keller, Courant Institute of Mathematical Sciences New York University, New York, New York	

DISCUSSION	546
T.F. Ogilvie, University of Michigan, U.S.A.	
AUTHOR'S REPLY	547
J.B. Keller, New York University, U.S.A.	
VELOCITY FIELD MEASUREMENTS APPLIED FOR ANALYSIS OF SHIP'S WAVE-MAKING SINGULARITIES	549
T. Kitazawa, Hitachi Shipbuilding & Engineering Co., Ltd. Osaka, Japan	
and T. Inui and H. Kajitani, The University of Tokyo, Tokyo, Japan	
DISCUSSION	562
G.E. Gadd, National Physical Laboratory, U.S.A.	
DISCUSSION	562
K.W.H. Eggers, Institut für Schiffbau der Universität Hamburg, Germany	
AUTHOR'S REPLY	563
T. Kitazawa, Hitachi Shipbuilding and Engineering Co., Ltd., Japan	
NOTE ON THE REFRACTION OF HEAD SEAS BY LONG SHIPS	565
F. Ursell, University of Manchester, England	
DISCUSSION	569
T.F. Ogilvie, University of Michigan, U.S.A.	
AUTHOR'S REPLY	571
F. Ursell, University of Manchester, England	
OSCILLATIONS AND WAVE FORCES IN A MAN-MADE HARBOR IN THE OPEN SEA	573
H.S. Chen and C.C. Mei, MIT, Cambridge, Massachusetts	
DISCUSSION	595
R.T. Ho and H. Bornze, Frederick R. Harris Inc., U.S.A.	
BREAKING WAVES — IN DEEP OR SHALLOW WATER	597
M.S. Longuet-Higgins, Department of Applied Mathematics and Theoretical Physics, Silver Street, Cambridge, England and Institute of Oceanographic Sciences, Wormley, Surrey, England	
SESSION VII	
NUMERICAL SOLUTIONS TO FREE-SURFACE FLOW PROBLEMS	609
K.J. Bai and R.W. Yeung, MIT, Cambridge, Massachusetts	
DISCUSSION	634
N. Salvesen, Naval Ship Research and Development Center, U.S.A.	
DISCUSSION	634
H. Keil, Massachusetts Institute of Technology, U.S.A.	
DISCUSSION	635
Y.K. Chung, H. Bornze, and M. Coleman, Frederick R. Harris, Inc., U.S.A.	
DISCUSSION	642
F. Ursell, University of Manchester, England	
DISCUSSION	642
C.J. Garrison, Naval Post Graduate School, U.S.A.	
DISCUSSION	644
D.C. Tolefson, Newport News Shipbuilding and Drydock Co., U.S.A.	
DISCUSSION	644
E.O. Tuck, University of Adelaide, Australia	
AUTHOR'S REPLY	646
K.J. Bai, Massachusetts Institute of Technology, U.S.A.	
NUMERICAL SOLUTIONS OF TWO-DIMENSIONAL NONLINEAR WAVE PROBLEMS	649
C.H. vonKerczek and N. Salvesen, NSRDC, Bethesda, Maryland	
DISCUSSION	664
H.J. Hausling, Naval Ship Research and Development Center, U.S.A.	
DISCUSSION	665
C.M. Lee, Naval Ship Research and Development Center, U.S.A.	
AUTHOR'S REPLY	666
C.H. vonKerczek, Naval Ship Research and Development Center, U.S.A.	
TWO-DIMENSIONAL CALCULATIONS OF THE MOTION OF FLOATING BODIES	667
R.K.C. Chan and C.W. Hirt, Science Applications, Inc., La Jolla, California	

DISCUSSION	682
N. Salveser, Naval Ship Research and Development Center, U.S.A.	
AUTHOR'S REPLY	683
R.K.C. Chan, Science Applications, Inc., U.S.A.	
THREE-DIMENSIONAL TURBULENT BOUNDARY LAYERS	685
J. Kux, Institut für Schiffbau der Universität Hamburg, Hamburg, Germany	
DISCUSSION	697
V.C. Patel, University of Iowa, U.S.A.	
DISCUSSION	699
T.T. Huang, Naval Ship Research and Development Center, U.S.A.	
DISCUSSION	699
I. Tanaka, Osaka University, Japan	
DISCUSSION	700
G.E. Gadd, National Physical Laboratory, England	
AUTHOR'S REPLY	702
J. Kux, Institut für Schiffbau der Universität Hamburg, Germany	
THE PREDICTION OF TRANSITION FROM LAMINAR TO TURBULENT FLOW IN BOUNDARY LAYERS ON BODIES OF REVOLUTION	705
P.S. Granville, NSRDC, Bethesda, Maryland	
DISCUSSION	722
A.M.O. Smith and K. Kaups, Douglas Aircraft Co., U.S.A.	
DISCUSSION	722
C.S. Wells, Jr., Advanced Technology Center L.T.V., U.S.A.	
DISCUSSION	722
F.R. Goldschmied, Westinghouse Electric Corp., U.S.A.	
AUTHOR'S REPLY	729
P.S. Granville, Naval Ship Research and Development Center, U.S.A.	
SESSION VIII	
RAYLEIGH-TAYLOR INSTABILITY OF SURFACE LAYERS AS THE MECHANISM FOR BIOCONVECTION	733
Milton S. Plesset, Christopher G. Whipple, and Howard Winet, California Institute of Technology, Pasadena, California	
HYDRODYNAMICS OF THE CONTAINMENT OF OIL SLICKS	743
J.H. Milgram and R.J. VanHouten, M.I.T., Cambridge, Massachusetts	
THE MANEUVERABILITY OF FISH, WITH POSSIBLE IMPLICATIONS FOR MAN-MADE VESSELS	763
D. Weihs, Technion-Israel Institute of Technology, Haifa, Israel	
LASER-DOPPLER MEASUREMENTS OF TRAILING VORTICES IN A WATER TUNNEL	771
S.J. Barker, California Institute of Technology, Pasadena, California	
THE INFLUENCE OF FENCES ON SURFACE PIERCING STRUTS AND FOILS	779
R.C. McGregor, J.L. Foster, R.S. Rothblum, and P.D. Swales, The University, Leeds, England	
DISCUSSION	791
E.A. Jones and R.T. Schmitke, Defense Research Establishment, England	
DISCUSSION	791
A. Barr, Hydronautics, Inc., U.S.A.	
DISCUSSION	791
B. Morgan and E.P. Rood, Naval Ship Research and Development Center, U.S.A.	
AUTHOR'S REPLY	792
R.C. McGregor, The University, Leeds, England	

INTRODUCTORY REMARKS

Dr. Alfred H. Keil

*Dean of Engineering
Massachusetts Institute of Technology*

Ladies and Gentlemen, may I call the meeting to order. It is a great privilege for me to be asked to chair the first session of the Tenth Symposium on Naval Hydrodynamics. I consider it a personal privilege for two reasons. I have worked for nearly twenty years on ship research for the Navy, and though I did not do any research in ship hydrodynamics, I must say I was very closely associated with it. And the second reason is that we have the honor of accommodating you here at the MIT. I would like to call now on our President, Dr. Jerome Wiesner, for his remarks.

WELCOMING ADDRESS

Dr. Jerome B. Wiesner

President

Massachusetts Institute of Technology

Thank you, Dean Keil. If the Dean has to protest that he knows nothing about ship hydrodynamics, what do you suppose I should say, although I should confess that last year I designed a 30-foot boat that somebody built for me. It did float, and it did move through the water, but I wouldn't go beyond that in bragging about its hydrodynamics.

I take great pleasure in welcoming this, the Tenth Biennial Symposium on Naval Hydrodynamics, here to MIT. I'm particularly pleased to be here because I feel a special bond to our sponsors, and particularly to the Office of Naval Research. Any American scientist who has the privilege of working under federal sponsorship, whether he knows it or not, owes a great deal to the Office of Naval Research. Following World War II, in a vacuum of research interests and support, the Office of Naval Research was set up under the inspired leadership of some people who had witnessed the contribution that science could make to naval warfare and naval matters during the war. They held wartime basic research activities together and established a very farsighted program under the Office of Naval Research that set the pattern which ultimately led to the National Science Foundation. The Office of Naval Research has continued to be an important sponsor of basic and applied research in this country. It has provided an important link between scientists and engineers in American universities and our armed services. We have always found that ONR provided a degree of understanding present in very few other sponsoring agencies, probably because of the direct involvement of so many of the people in ONR in the ongoing activities of the Navy.

When I was a working scientist-engineer, involved with military electronics, particularly radar, I always found it a special pleasure to work with the Navy, partially because of the severe technical demands that a seaborne environment placed on equipment, and partially because of the deep understanding I found among the people I had to work with. I always got a special pleasure out of being aboard ship. I used to suspect that I hadn't grown up, because all the gadgets and devices I found on submarines and ships gave me a thrill. Later in life, just a few years ago, I discovered in talking to Buckminster Fuller that the Navy had been his inspiration that led to such things, he claimed, as the geodesic dome and a variety of other things. He put it very simply that, while most of us spend our engineering hours learning how to do more with more, in the shipborne environment you had to learn how to do more with less. This was the lesson that he had learned as a young Navy officer aboard a submarine, and it never left him.

In any event, we are very pleased to be joint sponsors with the Office of Naval Research and the Coast Guard, and I would like particularly to welcome our cosponsors, RADM M.D. Van Orden, Chief of Naval Research; RADM A.H. Siemens, Chief of Research and Development of the United States Coast Guard; Dr. C.C. Bates, Science Advisor to the Commandant of the United States Coast Guard; and Mr. P. Eisenberg, President of the Society of Naval Architects and Marine Engineers of the United States.

This is the tenth of these symposia, and they have alternated between the United States and a country overseas. I understand that about half of you are from overseas, and I would like particularly to welcome you to the MIT campus and hope that you have an opportunity to see something besides this hall while you are here. If any of you would like to have a tour of a part of the MIT campus which isn't already offered, see me and I will arrange it for you. We would welcome an opportunity to show you MIT. The school is a small university by American, and I suppose even European, standards. We have a total of 7500 students, about 4200 of whom are what we call undergraduates, and the remainder are graduate students. We have a faculty of about 900 professors, an additional research staff of about 1500 people, and a postdoctorate student body of about 600. We have a very heavy emphasis on applied science in engineering, and a good deal of basic research as well. In recent years, as the concern about the social consequences of science and technology has grown around the world, our political science, economics, and other social sciences have grown and have become an important part of our curriculum. Some of you might welcome an opportunity to see these activities as well. In any event, I welcome you here; I hope you have a very productive meeting; and, if there is anything any of us from MIT can do to make your stay in the Boston area more delightful, please let us know. Thank you.

WELCOMING ADDRESS

Rear Admiral M.D. Van Orden, USN
Chief of Naval Research

I am pleased to welcome you to the Tenth Symposium on Naval Hydrodynamics. This biennial symposium is sponsored by the Office of Naval Research to stimulate research in hydrodynamics by providing a forum for world leaders in this field to meet and discuss their latest ideas and discoveries.

This is one of several international symposia held by ONR that helps to fulfill a principal ONR objective, which is to conduct a continual survey of worldwide findings, trends, potentialities, and achievements in research and development of interest to the Navy. Another major function of ONR is to support research at universities and laboratories. And we also provide the bridge between basic research and practical naval applications.

We are gratified that we can count as many as nine different countries in addition to the U.S. who will have representatives presenting papers at this symposium. I understand we also have visitors from the Soviet Union and Bulgaria, as well as Spain, Finland, and Brazil.

I should stress that ONR considers it important that the information we gain not be hoarded, but that it be exchanged between the U.S. and the rest of the world. In addition to symposia such as this, another major instrument for achieving this is our branch office in London, which has operated as long as ONR has been in existence, that is, since 1946. Scientists on the staff of our London office visit various research establishments throughout Europe to learn about the newest ideas and theories that are evolving there. In return, the U.S. scientists help to distribute to their colleagues in those countries copies of technical reports prepared by scientific investigators in this country supported by ONR as well as by other U.S. government research agencies. The Navy also conducts data exchange agreements with 16 countries.

In that connection, it seems fitting that this symposium should be dedicated to the late Professor Georg N. Weinblum of Germany, who served for a time as special consultant to the U.S. Navy at its David Taylor Model Basin, now renamed the Naval Ship Research and Development Center. The contributions of this creative investigator are perhaps best epitomized by Captain Harold R. Saunders, a leading naval architect, in his book *Hydrodynamics in Ship Design*. Writing about Professor Weinblum in 1957, he said: "He, in the opinion of many, is blessed with the most amazing combination of theoretical, analytical, and practical intelligence and ability to be found

in any naval architect today. What is still more wonderful, he is able to give this information to others in *their* language."

Captain Saunders was undoubtedly referring to the fact that hydrodynamics research must draw its material from a variety of scientific disciplines. Consequently, hydrodynamicists must be able to discuss their problems with mathematicians, chemists, marine architects, and oceanographers, for example, with mutual understanding and respect. The very nature of hydrodynamics forbids parochialism. It is essential that people in this field interact effectively with other scientists engaged in basic research, as well as with design engineers.

For the Navy, progress in hydrodynamics research has become increasingly urgent. Traditionally our goal has been to design new and improved types of ships that not only make use of advanced technology but also operate efficiently, reliably, and safely. Now we face a new challenge in the construction of ships to sail on or beneath the unforgiving sea.

The Navy must find ways to discover and correct the problems that a new design may run into before reaching the point of full-scale sea trials. Congress and the public are more cost-conscious than ever before in regard to the expenditure of public funds. No longer are excuses accepted for the failure or sputtering operation of a new, expensive ship because it has encountered problems we had not anticipated.

Since the sea is the Navy's business and we have been involved in it a long time, we are expected to know it well. Only investigators like yourselves are aware of how limited is our knowledge of the forces that impact on a buoyant body propelled through the water. As much as our understanding has increased, we know we have much more to learn. This information can be obtained only through the arduous bit-by-bit process of basic research, such as you gentlemen pursue.

Today our nation is faced with the dilemma that we must make do with a much smaller navy, but still retain our global responsibility. This means we must plan types of ships that are radically different in design from anything in the past in order to meet this requirement. At the same time, these ships must be inexpensive to operate and maintain in addition to satisfying our traditional standards.

The results of the research that will be reported at this symposium should help us move toward that formidable goal. It is clear that all of you here today are dedicated scientists, so I do not need to urge you to keep pressing forward in your search for solutions to the frustrating problems in hydrodynamics. I would like to stress, however, that you maintain strong lines of communication so that as many people as possible can benefit when you inevitably succeed in your endeavors.

WELCOMING ADDRESS

Rear Admiral A.H. Siemens
Chief of Research and Development
United States Coast Guard

On behalf of the U.S. Coast Guard, I am pleased to welcome you to the Tenth Symposium on Naval Hydrodynamics. I would like to thank Dr. Wiesner and Admiral Van Orden for the opportunity to co-sponsor this symposium. I am sure it will be a technically enlightening and a personally satisfying experience for all participants. I am delighted that a major portion of this symposium has been devoted to hydrodynamics for safety.

The Coast Guard's interest in hydrodynamic research is mainly for technical support of its regulatory responsibility. Our traditional interests have been in the areas of vessel survivability, such as the development of impact and damaged stability criteria, the use of seakeeping research to help in establishing vessel loadline criteria, and structural strength criteria. With recent legislation which the Congress has passed, the Ports and Waterways Act of 1972, we have received new areas of responsibility. The Coast Guard must now establish standards for vessel maneuverability and must also promulgate as necessary the operational controls to minimize collisions, ramming, and grounding incidents. Our present research program in hydrodynamics consists of investigations of vessel stability in a seaway, being done for us at the University of California; the analysis of towing and fishing-vessel stability criteria, being conducted at Hydronautics Incorporated; the prediction of extreme acceleration of vessels, which is being done at the Naval Ship Research and Development Center; and investigations of springing stresses in Great Lakes ore ships, being conducted by Webb Institute of Naval Architecture. Our research efforts in 1975 and 1976 will concentrate on the vessel maneuvering problem, with special emphasis on measuring maneuvering performance in restricted waters. Stevens Institute of technology is already working on some initial tasks of this program. A review of the papers for this symposium indicated to me that many of the subjects to be discussed relate directly to the Hydrodynamics Research needs of the Coast Guard. I encourage all of you to continue these important research efforts, so that we may continue to improve the safety of maritime transportation. Thank you.

A TRIBUTE TO GEORG WEINBLUM

J. V. Wehausen and T. Y. -T. Wu



On April 4 of this year we lost Georg Weinblum. It seems especially appropriate that this symposium be dedicated to his memory, for the complexion of the symposium would have pleased him. He would have liked the broad spectrum of topics ranging from "Ship Theory" in its most immediate sense to hydrodynamical problems on its fringes. He would have been pleased by the diverse origins, both nationally and professionally, of the contributors. For it was characteristic of Georg Weinblum to see his favorite subject in a broader context and to know that an advance in a related field often entails an advance in ship theory itself. He realized that researchers from other disciplines, with their different backgrounds and

experience, might provide fruitful insights overlooked by those too close to the problems of ship theory, and he welcomed their help. Although he himself was single-minded in his pursuit of ship theory, he was always on the alert for these possible contributions from other fields, and he was remarkably acute in recognizing them.

Georg Weinblum was interested not only in the scientific discoveries that might advance ship theory but also in the persons who made them. He took a warm personal interest in their lives as well as their work. He was unstinting in his encouragement, in seeing to it that their work was recognized and in arranging financial support when possible. He was especially zealous in trying to attract young people into the field and in seeing that they had adequate opportunities. Moreover, his support always included an intelligent and enthusiastic interest in the progress of their work and a generous input of ideas.

His presence at a meeting relating to ships was a guarantee of its liveliness and interest because of his quick grasp of the significance of the papers or of the issues under discussion. At international meetings his warmth and knowledge of languages were important aids in establishing a feeling of amity among all participants. In many respects he was really a citizen of the World, belonging to each of us and to no special country.

Georg Weinblum's interests were by no means limited to ship theory, or engineering and science in general. He was an attentive student of political, social and educational developments and an acute observer of contemporary events. In view of his background, this was perhaps not surprising. He had lived in several countries and had experienced two of the cataclysmic events of the 20th century and dislocations associated with them. Moreover, Georg Weinblum was the product of an educational system and philosophy that hardly exists nowadays and that even in his youth was perhaps not for everyone. However, he seemed to thrive on it. Whereas for some the study of the Roman and Greek classics was only a hurdle to be passed, for him they were an introduction into the cultures underlying European civilization. As an adult he could still read Latin. His reading in literature was wide; in German and Russian, of course, for he was educated in these languages, but also in English and French. Apt quotations from the great poets, but especially Goethe and Rilke, always seemed to be on the tip of his tongue. His interest in music, ballet and graphic arts was also intense and informed.

There is much more to be said about Georg Weinblum than can be touched upon here. On the occasion of his 60th birthday a short biography was given by F. Horn in *Schiffstechnik*, Vol. 4 (1957), pp. 47-48. In more

recent years he received honorary doctorates from the Technical Universities in Berlin and Vienna and the University of Michigan. He had recently become a Corresponding Member of the Académie des Sciences of Paris. His own research has been briefly described in the Journal of Ship Research, Vol. 16 (1972), pp. 1-2. However, as an aid to those interested in further study of his work we append a list of published papers that we hope is complete.

Georg Weinblum will be sorely missed by those who knew him, but his spirit has affected all of us who did, and through us, we hope even those who were not so fortunate as to have known him personally.

A CATALOGUE OF PUBLISHED PAPERS BY GEORG P. WEINBLUM

The following list does not include all of Georg Weinblum's publications. It does not include discussions of papers by other authors nor the many notes written on the occasion of some anniversary of a colleague, or of his death. Neither does it include unpublished manuscripts nor material appearing only informally as a report. On the other hand, we believe that all research papers have been included, all expository articles and most of the short notes written to bring to the attention of naval architects and others progress in ship theory. Wherever possible we have tried to check the bibliographical data. When this has not been possible, we have relied upon the accuracy of a list prepared at the Institut für Schiffbau several years ago. Papers are listed approximately in chronological order.

- Reibungsfestigkeit von Nietverbindungen. Schiffbau 30 (1929), 590-593.
- Beiträge zur Theorie der Schiffsoberfläche. Werft, Reederei, Hafen 10 (1929), 462-466, 489-493; 11 (1930), 12-14.
- Anwendungen der Michellschen Widerstandstheorie. Jahrb. Schiffbautech. Ges. 31 (1930), 39-436; disc. 436-440.
- Schiffe geringsten Widerstandes. Proc. 3rd Internat. Congr. Appl. Mech., Stockholm, 1930, pp. 449-458.
- Beitrag zur Systematik der Schiffslinien. Werft, Reederei, Hafen 11 (1930), 469-473.
- Über die Berechnung des wellenbildenden Widerstandes von Schiffen, insbesondere die Hognersche Formel. Z. angew. Math. Mech. 10 (1930), 453-466.
- Schiffe geringsten Widerstandes. Schiffbau 31 (1930), 579-582.
- Die Bewegungsgleichungen des Schiffes im Seegang. Schiffbau 32 (1931), 488-495, 509-511, 525-529.
- Schiffsform und Wellenwiderstand. Jahrb. Schiffbautech. Ges. 33 (1932), 419-451; disc. 456-460.
- Die Theorie des Wellenwiderstandes und ihre praktischen Anwendungen. VDI 76 (1932), 127-131.
- Der Luftwiderstand von Schiffen mit verschieden geformten und verteilten Aufbauten. VDI 76 (1932), 621-622.
- Beitrag zur Ausbildung von Schiffsformen. VDI 76 (1932), 1149-1154.
- Hohle oder gerade Wasserlinien? Hydromechanische Probleme des Schiffsantriebs, Hamburg, 1932, pp. 115-131, 417-419.

- Hohle oder gerade Wasserlinien (Spantflächenkurven)? Werft, Reederei, Hafen 13 (1932), 223-225.
- Die Konferenz über hydromechanische Probleme des Schiffsantriebs in Hamburg. Schiffbau 33 (1932), 168-170, 210-211.
- Über den Einfluss der Schiffsform auf die Bewegungen eines Schiffes im Seegang. Werft, Reederei, Hafen 14 (1933), 269-275, 289-292.
- Ausländische Forschung auf dem Gebiet des Schiffbaus und ihre Auswertung für deutsche Verhältnisse. VDI 77 (1933), 1065-1069.
- Die analytische Ausbildung von Schnelldampferformen. Z. angew. Math. Mech. 13 (1933), 447.
- Quelques observations au sujet du tracé des plans des formes de navires. Bull. Tech. du Bureau Veritas 15 (1933), 232-234.
- Theoretische Untersuchungen der Strömungsbeeinflussung zweier Schiffe auf einander beim gegenseitigen Begegnen und Überholen auf tiefem und beschränktem Wasser. Schiffbau 34 (1933), 113-117.
- Einige Bemerkungen über den Entwurf von Schiffsformen. Schiffbau 34 (1933), 242-245.
- Die Verlängerung der Schlingerperiode eines Frachtschiffes infolge der mitschwingenden Wassermasse. (With W. Bock) Schiffbau 34 (1933), 285-286.
- Untersuchungen über den Wellenwiderstand völliger Schiffsformen. Jahrb. Schiffbautechn. Ges. 35 (1934), 164-192.
- Formelzeichen der Stabilitäts- und Schwingungslehre. (With F. Horn) Schiffbau 35 (1934), 7 8.
- Einfluss der endlichen Querschnittsabmessungen einer Schlepprinne auf den Modellwiderstand. Schiffbau 35 (1934), 83-85.
- Exakte Wasserlinien und Spantflächenkurven. Schiffbau 35 (1934), 120-121, 135-142.
- Über einige Ansätze zur Ausbildung von Stabilitätsnormen. Werft, Reederei, Hafen 15 (1934), 201-202.
- Schwingungen von Schiffen im Seegang. VDI 78 (1934), 1373-1379.
- Les mouvements de navires sur mer houleuse. Bull. Tech. du Bureau Veritas 17 (1935), 84-86.
- Die analytische Ausbildung von Schiffsformen. Z. angew. Math. Mech. 15 (1935), 205-219.
- Widerstandsuntersuchungen an Schiffen. Z. angew. Math. Mech. 15 (1935), 382-384.
- Über einige neuere Arbeiten auf dem Gebiete des Wellenwiderstandes von Schiffen. Schiffbau 36 (1935), 200-202.
- Widerstandsuntersuchungen an scharfen Schiffsformen. Schiffbau 36 (1935), 355-359, 408-413.
- Die Theorie der Wulstschiffe. Schiffbau 37 (1936), 55-65.

- Stereophotogrammetrische Wellenaufnahmen. (With W. Block) Jahrb. Schiffbautech. Ges. 37 (1936), 214-250; disc. 259-276. Translated as: Stereophotogrammetric Wave Photographs, David Taylor Model Basin Translation 204 (1949), i + 76 pp.
- Beitrag zur Ausbildung völligerer Schiffsformen. Schiffbau 37 (1936), 285-289.
- Theorie der aktiven Schlingertanks. Z. angew. Math. Mech. 16 (1936), 375-376.
- Stabilisierung mit aktiven Tanks. Schiffahrtstechnische Forschungshefte, Heft 7, 6-8. Schiffbautechnische Gesellschaft, Berlin, 1936.
- Rotationskörper geringsten Wellenwiderstandes. Ing.-Arch. 7 (1936), 104-117.
- Versuche über den Wellenwiderstand geauchter Rotationskörper. (With H. Amtsberg, W. Bock) Schiffbau 37 (1936), 411-419. Translated as: Tests on Wave Resistance of Immersed Bodies of Revolution, David Taylor Model Basin Translation 234 (1950), + 22 pp.
- Beitrag zur Theorie der Kursstabilität und der Steuerfahrt. Schiffbau 38 (1937), 51-59.
- Seegang und Schiffe. Deutsche Technik 9 (1937), 174-176.
- Überblick über die Wellenmessungen auf dem M.S., "San Francisco". Jahrb. 1936 d. Lilienthal-Ges. f. Luftfahrtforschung, 248-254 (1937).
- Abmessungen der Meereswellen. Forschungen und Fortschritte 13 (1937), 224.
- Seegangsforschung und Schiffbau. Umschau 41 (1937), 873-877.
- Wellenwiderstand von Körpern. Umschau 42 (1938), 34-36.
- Rechnerische Entwicklung von Schiffsformen. Schiffbau 39 (1938), 129-133, 151-155, 170-173.
- Wellenwiderstand auf beschränktem Wasser. Jahrb. Schiffbautech. Ges. 39 (1938), 286-289; disc. 289-291.
- Seegangsforschung. Naturwiss. 26 (1938), 193-198.
- Zur Theorie der aktiven Schlingertanks. Z. angew. Math. Mech. 18 (1938), 122-127.
- Fortschritte auf dem Gebiete der Berechnung des Wellenwiderstandes. Schiffbau 39 (1938), 43-45.
- Über die Kursstabilität von Schiffen. (With H. Künzel) Schiffbau 39 (1938), 181-184.
- Schiffsform und Widerstand. Schiffbau 40 (1939), 27-33, 46-51, 66-70.
- Analysis of wave resistance. The David W. Taylor Model Basin, Washington, D.C., Rep. no. 710 (1950), 102pp.
- On the motions of ships at sea. (With M. St. Denis) Trans. Soc. Naval Arch. Marine Engrs. 58 (1950), 184-231; discussion 232-248.

- The wave resistance of bodies of revolution. (Appendix II by J. Blum).
The David Taylor Model Basin, Washington, D.C., Rep. 758 (1951),
58pp.
- On the directional stability of ships in calm water and in a regular seaway.
Proc. 1st U.S. Nat. Congr. Appl. Mech., Chicago, 1951, pp. 43-47.
- Über hydromechanische Massen. Schiff und Hafen 3 (1951), 422-427.
- The thrust deduction. J. Soc. Naval Eng. 63 (1951), 363-379.
- Die künftige Entwicklung des Schiffes im Lichte der Schiffstheorie.
Hansa 89 (1952), 1541-1545, 1683-1686.
- Investigation of wave effects produced by a thin body — TMB Model
4125. (With J.J. Kendrick, M.A. Todd) The David Taylor Model
Basin, Washington, D.C., Rep. 840 (1952), 14 pp.
- On hydrodynamic masses. The David Taylor Model Basin, Washington,
D.C., Rep. 809 (1952), ii + 15 pp.
- Kräfte bei Bewegungen von Körpern in oder nahe der freien Oberfläche.
Schiffstechnik 1, 21-31 (1952).
- Schiffbauforschung im Ausland: Bestimmung der notwendigen Maschinen-
leistung aus Modellversuchen. Hansa 89 (1952), 1027.
- Organisation der Schiffbauforschung in England und in den Vereinigten
Staaten von Amerika. Hansa 89 (1952), 1149-1. 1.
- Der David-Taylor-Tank in Washington, D.C. Schiff und Hafen 4 (1952),
212-213.
- The present state of the theory of the ship. Appl. Mech. Rev. 6 (1953),
217-219.
- Systematische Entwicklung von Schiffsförmern. Jahrb. Schiffbautech.
Ges. 47 (1953), 186-210; disc. 210-215.
- Schiffe mit Tragflügeln. Umschau 53 (1953), 449-451.
- Probleme der Schiffbauforschung und ihre Behandlung im Ausland.
Schriftenreihe des Seeverkehrsbeirates 1953, Heft 5, 19-34.
- Entwicklung und Stand der Schiffbauforschung. Jahrbuch der Tech-
nischen Hochschule Hannover, 1953-1954, pp. 124-130.
- Über die Entwicklung und den heutigen Stand der Schiffbauforschung.
Schiff und Hafen 5 (1953), 44-46.
- Die neuen amerikanischen "Mariner" Schiffe: Untersuchungen über
Widerstand und Antrieb. Hansa 90 (1953), 1151-1153.
- Approximate theory of heaving and pitching of hydrofoils in regular
shallow waves. The David Taylor Model Basin, Washington, D.C.,
Rep. C-479 (1954), 31 pp.
- Die Bewertung von Tragflügelfahrzeugen. Hansa 91 (1954), 491-492.
- Recent progress in theoretical studies on the behaviour of ships in a sea-
way. 7th Internat. Conf. on Ship Hydrodynamics, Oslo, 1954,
26 pp.

- Die Frühjahrstagung der Institution of Naval Architects in London. Hansa 91 (1954), 1364-1370.
- Progress of theoretical investigations on ship motions in a seaway. Proc. 1st Conf. on Ships and Waves, Hoboken, N.J., 1954, pp. 129-159.
- Die Ergebnisse der Standardserienversuche von D.W. Taylor in einem neuen Gewand. Hansa 92 (1955), 412-414.
- Propulsionsversuche mit Einschraubenmodellen der Serie 60. Hansa 92 (1955), 565-568.
- A systematic evaluation of Michell's integral. The David Taylor Model Basin, Washington, D.C., Rep. 886 (1955), 59 pp.
- Ein Verfahren zur Auswertung des Wellenwiderstandes vereinfachter Schiffsförmlichkeiten. Schiffstechnik 3 278-287 (1956).
- Neuere Untersuchungen über die das Schiff im Seegang beanspruchenden Kräfte. Hansa 93 (1956), 352-358.
- Über die Förderung der deutschen Schiffbau Forschung. Schiff und Hafen 8 (1956), 381-382.
- Contribution of ship theory to the seaworthiness problem. Symposium on Naval Hydrodynamics, Washington, D.C., 1956, pp. 61-98; disc. 98-107.
- Schiffe geringsten Widerstandes. (With D. Wustrau, G. Vossers) Jahrb. Schiffbautech. Ges. 51 (1957), 175-204; disc. 205-214.
- Über eine angenäherte Behandlung des Tauchens und Stampfens von Tragflächensystemen in regelmässigem Seegang. Schiffstechnik 5 (1958), 2-5.
- Wellenwiderstand von Rotationskörpern. Schiffstechnik 5 (1958), 43-54.
- Gemeinsame Tagung der Association Technique Maritime und der Institution of Naval Architects in Paris von 30. Juni bis zum 4. Juli 1958. Schiff und Hafen 10 (1958), 635-636.
- Über Schiffsförmlichkeiten. VDI-Zeitschrift 100 (1958), 1513-1522.
- Applications of wave resistance theory to problems of ship design. Trans. Inst. Engrs. Shipbldrs. Scotland 102 (1959), 119-152; disc. 153-163.
- Experimental investigations of the inertia and damping coefficients of a spheroid and surface ship in free heave. (With S. Brooks, P. Golovato) Internat. Shipbldg. Progr. 6 (1959), 45-62.
- Eröffnung des Neubaus des Instituts für Schiffbau in Hamburg. Schiffstechnik 7 (1960), 131-132.
- Entwicklungsmöglichkeiten des Schiffes. In: Vom geistigen Fortleben der Technischen Hochschule Danzig. Verlag Brausdruck, Heidelberg, 1961.
- Untersuchungen über den Widerstand einer systematisch entwickelten Modellfamilie. (With S. Schuster, Chr. Boes, R. Bhattacharyya) Jahrb. Schiffbautech. Ges. 56 (1962), 296-319; disc. 320-324.

- On problems of wave resistance research. Internat. Sem. Theoret. Wave Resistance, Ann Arbor, 1963, pp. 1-44; disc. 45-49.
- Das Internationale Seminar über die Theorie des Wellenwiderstandes von Schiffen an der University of Michigan, Ann Arbor, vom 19. bis 23. August 1963. Schiff und Hafen 16 (1964), 291-296.
- Zuschrift zu: Die Entwicklung von Tragflügelbooten in den USA, von H. Klawe. Schiff und Hafen 16 (1964), 625.
- Some extensions of D. W. Taylor's Standard Series. (With W. Graff, A. Kracht) Trans. Soc. Nav. Arch. Marine Engrs. 72 (1964), 374-396; disc. 396-403.
- Die Abteilung für Schiffstechnik an der Universität Hamburg. VDI-Zeitschrift 106 (1964), 694-695.
- Über neue Verfahren und neue Ergebnisse bei der Entwicklung von Schiffsformen. VDI-Zeitschrift 106 (1964), 1603-1610.
- Forschungsschiff "Meteor" — Entstehung und Zweck. (With O. Krapinger) Jahrb. Schiffbautech. Ges. 59 (1965), 362-367.
- Probleme des Schiffbaus. Bild der Wissenschaft 2 (1965), 1003-1011.
Translated as: Problems of naval architecture, Univ. of Michigan, College of Engineering, Rep. No. 107 (1971).
- Schiffe geringsten Wellenwiderstandes. Schiffstechnik 12 (1965), 131-136.
- Schiffbau und seine Förderung durch die Deutsche Forschungsgemeinschaft (DFG). Hansa 102 (1965), 2053-2055.
- Über die Unterteilung des Schiffswiderstandes. Schiff und Hafen 22 (1970), 807-812.
- Beitrag der Schiffstheorie zur Entwicklung des Schiffes. Hansa 107 (1970), Sondernummer: Das Schiff von Morgen, 37-45.
- Remarks on ships and ship speed. Proc. 13th Internat. Towing Tank Conf., Berlin-Hamburg, 1972, vol. 1, pp. 6-13.
- Note: A complete list of all of Georg Weinblum's publications is planned by the Institut für Schiffbau for some time in the future.

HYDRODYNAMICS FOR SAFETY — MANEUVERING

SESSION I

Monday, June 24, 1974
9:00 A.M. — 12:35 P.M.

Chairman: Dr. Alfred H. Keil
Dean of Engineering
Massachusetts Institute of Technology
United States

The Effects of Beam On the Hydrodynamic Characteristics of Ship Hulls	3
J. Gerritsma, W. Beukelman, and C.C. Glansdorp, University of Technology, Delft, The Netherlands	
Hydrodynamic Interactions Between Ships	35
E.O. Tuck, University of Adelaide, Australia and J.N. Newman, M.I.T., Cambridge, Massachusetts	
Bank Effects On a Ship Moving Through a Short Dredged Channel	71
N.H. Norrbin, Swedish State Shipbuilding Experimental Tank, Sweden	
Double-Body Flow Theory — A New Look at the Classical Problem	89
T.Y. Wu and A.T. Chwang, California Institute of Technology, Pasadena, California	

THE EFFECTS OF BEAM ON THE HYDRODYNAMIC CHARACTERISTICS OF SHIP HULLS

J. Gerritsma
University of Technology
Mekelweg 2, Delft
The Netherlands

W. Beukelman
University of Technology
Mekelweg 2, Delft
The Netherlands

C. C. Glansdorp
University of Technology
Mekelweg 2, Delft
The Netherlands

ABSTRACT

Forced oscillation experiments have been carried out with a systematic ship model family of which the length-beam ratio was ranging from 4 to 20. The experiments also included a thin plate to simulate the case of an infinite length-beam ratio. Vertical and horizontal harmonic motions in calm water have been considered and the corresponding hydrodynamic coefficients have been determined. Moreover the vertical motions and added resistance in waves have been measured. The results are presented in graphical form and are compared with some existing calculation methods.

NOMENCLATURE

A, B, C, D, E, G } hydrodynamic coefficients of the
a, b, c, d, e, g } equations of pitch and heave
respectively

B ship's beam
 C_B block coefficient
 C_P prismatic coefficient
 C_s horizontal sectional added mass coefficient
c wave celerity
F total vertical wave force
F' sectional hydromechanic force
 F_n Froude number
g acceleration owing to gravity
 I_{yy} vertical longitudinal moment of inertia
 I_{zz} dimensionless horizontal moment of inertia
 K' coefficient of accession to moment of inertia
K empirical coefficient in the low aspect ratio lift formula
 $K_{1,2}$ coefficients of accession (long., lat.)
k wave number
 k_{yy} vertical longitudinal radius of inertia of ship
 k_{zz} horizontal longitudinal radius of inertia of ship
L ship's length
M total vertical wave moment; mass of ship
 M' dimensionless mass of ship
 m' vertical sectional added mass
 N' vertical sectional damping coefficient
 N'_v, N'_r, N'_y, N'_z hydrodynamic coefficients of the
 Y'_v, Y'_r, Y'_y, Y'_z equations of yaw and sway
respectively
 r' dimensionless yaw velocity
 \ddot{r}' dimensionless yaw acceleration
T ship's draught
 T^* effective draught
 T_e period of encounter
V forward velocity of ship
 V_z vertical relative velocity with respect to the water
 v' dimensionless sway velocity
 \ddot{v}' dimensionless sway acceleration
 X'_{11} dimensionless longitudinal added mass

x' dimensionless length coordinate in a right hand body fixed coordinate system with centre of gravity in the origin and the starboard side positive
 x_b, y_b, z_b righthand coordinate system fixed to ship with the origin situated in the ship's waterline and the portside positive
 x'_1 dimensionless centre connected with the first moment of viscous force distribution
 x'_2 dimensionless centre connected with the second moment of viscous force distribution
 x'_3 point of application of total yaw force
 x'_4 point of application of total sway force
 Y' dimensionless hydrodynamic lateral force
 y'_0 dimensionless motion amplitude
 y'_w half width of waterline ($\eta=0$)
z heave displacement
 ϵ phase angle
 λ wave length
V volume of ship's displacement
 ω circular wave frequency
 ω' dimensionless PMM frequency
 ω_e circular frequency of encounter
 ρ density of water
 σ'_1 dimensionless stability root
 σ'_2 dimensionless stability root
 θ pitch angle
 ζ instantaneous wave elevation

Subscripts :

a amplitude of denoted parameter
 F_ζ wave force with respect to wave elevation
 M_ζ wave moment with respect to wave elevation

Superscripts :

' sectional values or dimensionless values according to SNAME-nomenclature

1. INTRODUCTION

The calculation of the vertical hydrodynamic forces and moments acting on a ship in seaway, according to the strip theory, has proved to be a valuable tool. This is also true to a limited extent for horizontal motions, but the experimental verification for low frequency motions, which are of interest for manoeuvring and steering problems, is rather scarce. The detailed comparisons of calculation and experiment for pitch and heave are for the greater part restricted to more or less average hull dimensions, for instance a length-beam ratio of approximately 6 to 8 and block coefficients around .70. Although predictions of vertical motions of extreme ship forms have been quite successful, it has not been known to what extent the strip theory is valid when more extreme hull dimensions are considered. Intuitively one may imagine, that the thinner the ship form, the more the application of the strip method is justified. For manoeuvring and steering purposes the hydrodynamic coefficients of the equations of motion depend to a larger extent on viscous effects introducing lift phenomena, when compared with vertical motions of a ship in waves. Existing methods to approximate these hydrodynamic forces have a more empirical character. Apart from the length-draught ratio in both cases the length-beam ratio may be regarded as a useful parameter in a comparison of theory and experiment. The main objective of this paper is to provide extensive experimental data respecting the influence of the length-beam ratio of a systematic ship model family on the hydrodynamic forces on the hull for vertical oscillatory motions in the wave frequency range, as well as for low frequency horizontal motions of interest for steering and manoeuvring. The experiments cover a large range of length-beam ratios which includes a very thick ship-form ($L/B=4$) and a very thin ship with $L/B=20$. In addition a thin plate has been tested in horizontal motion to simulate an infinitely large length-beam ratio. All of the models have been derived from the standard Sixty Series hull form with $L/B=7$ and $C_B=.70$ [1], by multiplying the width by constant factors, to arrive at $L/B=4, 5.5, 7, 10$ and 20 . All models have been made from glass reinforced polyester and have a length of 10 feet. For main particulars see table 1.

2. EXPERIMENTAL PROGRAM AND RESULTS

With a vertical Planar Motion Mechanism (PMM) the hydrodynamic coefficients of the heave and pitch equations according to equations (1) of appendix 1 have been measured for Froude numbers $F_n=.20$ and $F_n=.30$. The latter speed is high for all models and large wave making has been observed during the experiments. Excellent linearity has been found for the considered heave amplitudes which go to 1% of the model length and pitch amplitudes up to 3.5 degrees. For the wave tests wave heights of 2.5 % of the model length have been considered.

The linearity has been proved to be good with $L/B=4$.

The non-dimensional mass and damping coefficients as well as the mass and damping cross coupling coefficients are given in figures 1 to 8 in non-dimensional form as a function of the Froude number, the frequency of oscillation and the length-beam ratio.

Figures 9 and 10 give the dimensionless motion amplitudes of heave and pitch and figure 11 gives the added resistance in regular waves. The motions and the added resistance in waves could not be measured for the $L/B=20$ model owing to experimental difficulties.

The hydrodynamic coefficients for yaw and sway according to equations (13) of appendix 3 have been measured for three velocities: $F_n=.15, .20$ and $.30$.

A large amplitude PMM has been used; the model frequency range has been between $\omega=.2(1) 1.0$. Strut amplitudes for both modes of motion were respectively 5, 10, 15, 20 and 25 cm, the horizontal distance between the struts being 1 m. A relatively small wave making was observed for the lowest of the three velocities considered, and therefore the experimental results for $F_n=.15$ have been used for comparing with some calculation methods. Figure 12, 13 and 14 show the coefficients, derived from the force and moment measurements as a function of L/B -ratio for the three considered forward speeds. Table 2 gives the numerical values of the various hydrodynamic coefficients.

In figure 15 and 16 the results of the swaying force and swaying moment are presented as a function of speed, frequency, L/B -ratio and amplitude.

3. DISCUSSION OF THE RESULTS

3.1. Vertical Motions

First of all the heaving and pitching motions have been calculated with as a basis a formulation of the strip theory as given in appendix 1 and [2]. This formulation has been derived using earlier work by Shintani [3], Söding [4], Semenov-Tjan-Tsanský et al [5], Tasai [6] and affords the same results as given by Salvesen et al [7]. Afterwards the method has been used, which has been formulated principally by Korvin-Kroukovsky and Jacobs [8] and modified by the authors [9]. The results of both methods have been compared with the experimental results.

The added resistance in waves owing to the pitching and heaving motions has been calculated by the method described in appendix 2. The added resistance is determined by calculating the work done by the radiated damping waves, which result from the vertical motions of the ship relative to the water. In [10] this method has been confirmed by experimental results derived from model tests with a fast cargo ship hull form. Further experience included blunt tanker forms, although in some of these cases the agreement has been somewhat less satisfactory at high frequency of encounter.

In the figures 1 to 11 the experimental values are compared with corresponding calculations according to the modified Korvin-Kroukovsky formulation [9] and according to equations (6) and (7). For convenience we will call these the old and the new method respectively. With regard to the coefficients of the equations of motion for heave and pitch the two calculation methods give almost identical results, except for the pitch damping coefficient at low frequencies and for the added mass cross coupling coefficient D for pitch. The differences between the measured added mass and the calculated value are small, even for the very low L/B ratio's. For the added moment of inertia the correlation is still satisfactory, with only few differences for the highest speed and the lowest L/B ratio. The heave damping coefficient is reasonably predicted except for high frequencies where viscous effects, for instance separation of flow, may be important. Both the new and the old method predict the pitch damping rather poorly, particularly at low frequencies. The experimental data do not show a clear preference for one of the two methods. For practical purposes the over-estimation of the pitch damping at low frequencies, according to the new method is not too important in the motion prediction. Considering the absolute magnitude of the damping cross coupling terms the coefficients e and E are very well predicted by both theories for the two considered forward speeds, as well as for all length-beam ratio's. Also the added mass cross coupling coefficient d for heave is reasonably well predicted by both methods, but in the case of the mass cross coupling coefficient D for pitch the experimental points for low frequencies lie between the two predicted curves. For low frequencies the experimental values favour the prediction according to the new method. Heave amplitudes in waves are somewhat over-estimated by the new method. Earlier experience with both methods has shown us a slight preference for the modified Korvin-Kroukovsky and Jacobs method although a desired symmetry in the mass cross coupling coefficients is not fulfilled in their presentation. Moreover added resistance is overestimated by the new method and in this respect it should be remembered that added resistance varies as the squared motion amplitudes. For $F_n=0.20$ the predicted added resistance agrees very well with the measured values, with only minor differences at high frequencies. Even for the very low length-beam ratio's the agreement is satisfactory, considering the more or less extreme hull form and the relatively high forward speed in those cases. For $F_n=0.30$ the correlation between theory and experiment is less. However for all length-beam ratio's, except for L/B=7 this speed is very high, with corresponding high ship waves. Especially for L/B=4 the added resistance at high frequencies is under estimated by the theory.

3.2. Horizontal Motions

The coefficients have been determined in a standard graphical way from the in phase and quadrature components of forces and moments measured with the PMM. The accuracy of the coefficients which are displayed in fig. 12, 13 and 14, is probably not high since the relevant forces and moments are small in magnitude. The coefficients indicate a trend in the results and do not pretend to be highly accurate. In table 2 the numerical values of the coefficients are summarized using the dynamic modes of motions. The figures 12, 13 and 14 clearly show the effect of beam, which is not very pronounced for a low Froude number. As could be expected the forward speed affects the results to a certain extent: the thicker the model the more the model generated wave system plays a decisive role in the creation of the resulting hydrodynamic forces and moments. Hu [11] predicted the effect of speed upon the hydrodynamic coefficients, applying sources and doublets in the ship's centerplane and wake and taking into account the boundary conditions on the surface. Comparing the trend of the experimental results and the predicted values with regard to the forward velocity according to Hu, it can be said, that his prediction gives a more pronounced effect of speed. It is interesting to note, that Van Leeuwen's results of his PMM tests [12] with an 8 feet model of the L/B=7 are practically the same as the results presented in this paper, taking a reasonable margin of accuracy into account. In figures 12, 13 and 14 some evidence is produced, that the values of the static and dynamic sway coefficients are approaching each other closely. The condition for straight line stability (this word is used rather than controls fixed stability, since no rudder, propeller nor other hull appendices have been fitted) yields:

$$\frac{x'_v}{x'_r} < 1$$

When x'_v and x'_r both are positive this condition postulates, that the point of application of the total yaw force is located before the point of application of the sway force. In figure 12, 13 and 14 it may be observed, that for a L/B-ratio exceeding 8 this condition is fulfilled. Since at a L/B-ratio of approximately 20 Y'_r equals the mass M' , x'_r will change sign and becomes extremely negative. In this case the aforementioned criterion is still satisfied, since it is obvious that x'_v remains positive. In table 2 the stability roots are calculated; the smaller roots are positive for the smaller L/B-ratio's and they are becoming negative for the larger L/B-ratio's. Noteworthy is the difference between the two last columns indicating, that the actually used plate for the experiments has a stable behaviour, but that an imaginary massless plate has an oscillatory stable behaviour. This fact is also found in stability analysis of ships which have large fins or deep keels, like sailing yachts and is caused by the small inertia forces relative to the lift forces [13].

Jacobs [14,15] published a brief account of a simple theory for the calculation of the linear coefficients of the horizontal motion based upon simple hydrodynamic concepts. Apart from an ideal fluid treatment of a wing shaped body in an unbounded flow, resulting in hydrodynamic added masses and added moments of inertia with cross coupling coefficients, a viscous part is included representing the generation of a lift. Therefore, as an example the Jones' low aspect ratio lift formula has been applied. Lift generation depends upon the flow conditions near the trailing edge. As these conditions vary, it seems appropriate to introduce an empirical constant K to take these variations into account, as was suggested by Inoue [16]. This K -constant turns out to be nearly .75 as an average. In appendix 3 a brief account is given of Jacobs' method, which has been chosen for a comparison with the measured results. The total lift, as a result of an inertia distribution and a viscous distribution along the ship length is generated for the greater part in the forebody, which means that the viscous part counter-balances nearly the inertia part in the afterbody [15,17]. The centre of the viscous force distribution therefore lies well aft of the centre of gravity (x'_{p1}). The second moment of the viscous force distribution is characterized by x'_{p2} and obviously this quantity is negative. From the measurements of the relevant quantities the values of K , x'_{p1} and x'_{p2} are calculated and they are displayed in Figure 17. They coincide remarkably well with empirical values presented by Inoue and Albring [18]. The coefficient Y'_L can also be used to check the validity of the empirical constants K_1, x'_{p1} . In figure 12 it may be seen, that there is a satisfactory agreement for the lower Froude number. Apart from considerations regarding the damping coefficients it is obvious, that the added mass, added moment of inertia and the mass cross coupling coefficients are accurately predicted by the simple stripwise integration of sectional values of added mass depending on local fullness and local B/T -values. So called three dimensional corrections have been applied as indicated by Jacobs and others. In order to compare the measured results with other methods available in literature, it has been decided to use the results of Inoue which are principally based upon Bollay's low aspect ratio theory and a number of empirical allowances. Appendix 3 gives a brief account of the used formulae according to Inoue. As can be seen in figure 12 the calculation agrees with the measured results with the exception of Y'_L . Norrbin [19] analysed statistical material and derived regression formulae on the basis of the so called "bis" system of reference. In appendix 3 these regression formulae are "translated" into the nomenclature adopted in this paper. Inspecting the formulae a small effect of the L/B -ratio can be demonstrated, while generally speaking the calculated results, using these regression formulae are in close agreement in the normal range of L/B -ratio's, as shown in figure 12. Since lift generation is of primary importance in manoeuvring problems and since experimental material about this subject is not extensively published in literature, it has been decided

to give the transverse force and moment in the sway motion for two speeds: $F_n=.15$ and $F_n=.30$, as a function of reduced frequency and amplitude in figures 15 and 16. In a very restricted range full linearity in frequency and amplitude exists. For the higher frequencies linearity is lost to some extent especially in the transverse force and to a smaller extent in the moment. A number of effects are obscuring the results, for instance nonlinearity owing to the cross flow. Also frequency- and amplitude effects are interfering when one tries to interpret the experimental results.

4. REFERENCES

- [1] Todd, F.H.,
"Some further experiments on single screw merchant ship forms Series 60"
Transactions of the Society of Naval Architects and Marine Engineers Vol. 61, 1953.
- [2] Gerritsma, J.
"Some recent advances in the prediction of ship motions and ship resistance in waves"
International Jubilee Meeting on the occasion of the 40th Anniversary of the Netherlands Ship Model Basin, 1973, Wageningen, The Netherlands.
- [3] Shintani, A.,
"The New formulae of calculating Pitch and Heave of Ships by the Strip Method"
Transactions Japan Society of Naval Architects Vol. 124, 1968.
- [4] Söding, H.,
"Eine Modifikation der Streifenmethode"
Schiffstechnik Bd.16, Heft 80, 1969, pp 15-18
Book
- [5] Semcnof-Tjan-Tsansky, W.W.,
Blagowetsjenski, S.N., Golodolin, A.N.,
"Motions of Ships" (in Russian language)
Publishing Office Shipbuilding, Leningrad 1969.
- [6] Tasai, F.,
"Improvements in the theory of ship motions in longitudinal waves"
Transactions International Towing Tank Conference Rome, 1969, pp. 677.
- [7] Salvesen, N., Tuck, E.O., and Faltinsen, O.
"Ship motions and Sea Loads"
Transactions of the Society of Naval Architects and Marine Engineers, Vol. 78, 1970.
- [8] Korvin-Kroukovsky, B.V., and Jacobs, W.R.,
"Pitching and Heaving Motions of a Ship in Waves"
Transactions of the Society of Naval Architects and Marine Engineers, Vol. 65, 1957
- [9] Gerritsma, J., and Beukelman, W.,
"Analysis of the modified Strip Theory for the Calculation of Ship Motions and Wave Bending Moments"
International Shipbuilding Progress, Vol. 14, No. 156, 1967.
- [10] Gerritsma, J. and Beukelman, W.,
"Analysis of the Resistance Increase in Waves of a fast Cargo Ship"
International Shipbuilding Progress, Vol. 19, No. 217, 1972.
- [11] Hu, P.N.,
"Forward Speed Effects on Lateral Stability Derivatives of a Ship"
DL Report 829, August 1961.

[12] Van Leeuwen, G.,
"The lateral Damping and Added Mass of an
Oscillating Shipmodel"
Shipbuilding Laboratory - University of
Technology, Delft, July 1964, Publication no.23.

[13] Gerritsma, J., Glansdorp, C.C.,
Moeyes, G.,
"Still water, Seakeeping and Steering
Performance of "Columbia" and "Valiant"
Shipbuilding Laboratory, University of
Technology, Delft, The Netherlands, report no.
391, March 1974.

[14] Jacobs, W.R.,
"Methods of Predicting Course Stability and
turning Qualities of Ships"
DL Report 945, March 1963.

[15] Jacobs, W.R.,
"Estimation of Stability Derivatives and
Indices of various Ship Forms and Comparison
with Experimental Results".
Journal of Ship Research, September 1966, pp.
135-162.

[16] Inoue, S.,
"The Determination of Transverse Hydrodynamic
Nonlinear Forces by Means of Steady Turning"
11th International Towing Tank Conference,
Tokyo 1966, pp. 542.

[17] Norrbin, N.H.,
"Forces in oblique Turning of a Model of a
Cargo-Liner and a Divided Double-Body Geosim"
The Swedish State Shipbuilding Experimental
Tank, Göteborg, Publication 57.

[18] Albring, W.,
"Summary Report of Experimental and Mathematical
Methods for the Determination of Coefficients
of Turning of Bodies of Revolution"
CONLAN 2

[19] Norrbin, N.H.,
"Theory and Observations on the use of a
Mathematical Model for Ship Manoeuvring in deep
and confined Waters"
The Swedish State Shipbuilding Experimental
Tank, Göteborg, 1971, Publication 68.

[20] Joosen, W.P.A.,
"Added Resistance of Ships in Waves"
Proceedings of the 6th Symposium on Naval
Hydrodynamics, Washington, D.C., 1966 pp. 637.

[21] Resistance in Waves
60th Anniversary Series, The Society of Naval
Architects of Japan, 1963, Vol. 8 Chapter 5.

[22] Havelock, T.H.,
"Notes on the Theory of Heaving and Pitching"
Transactions of the Institution of Naval
Architects, London 1945.

[23] Clarke, D.,
"A Two-Dimensional Strip Method for Surface Ship
Hull Derivatives : Comparison of Theory with
Experiments on a Segmented Tanker Model"
The International Symposium on Directional
Stability and Control of Bodies Moving in
Water, 17-21 April 1972, London, Paper 8.

5. APPENDIX 1

The equations of motion of heave and pitch

The equations of motion of heave and pitch and
their solution are given by :

$$\left. \begin{aligned} (\rho V + a)\ddot{z} + b\dot{z} + cz - d\dot{\theta} - c\dot{\theta} - g\theta &= F & (\text{heave}) \\ (I_{yy} + A)\ddot{\theta} + B\dot{\theta} + C\theta - D\dot{z} - E\dot{z} - Gz &= M & (\text{pitch}) \\ z = z_a \cos(\omega_e t + \epsilon_{z\epsilon}) &, \theta = \theta_a \cos(\omega_e t + \epsilon_{\theta\epsilon}) \end{aligned} \right\} (1)$$

The various coefficients a-g and A-G are
derived from :

$$\rho V \ddot{z} = \int_L F' dx_b \quad (2)$$

$$I_{yy} \ddot{\theta} = - \int_L F' x_b dx_b$$

where F' is the hydromechanical force acting
on a cross-section of the ship.

It can be found that :

$$F' = -2\rho g y_w (z - x_b \theta) - \left(\frac{\partial}{\partial t} - V \frac{\partial}{\partial x} \right) (\dot{z} - x_b \dot{\theta} + V\theta - \zeta^*) \left(m' \frac{iN'}{\omega_e} \right) \quad (3)$$

The effective wave elevation ζ^* is defined as :

$$\zeta^* = \zeta e^{-kT^*}, \text{ where :}$$

$$T^* = -\frac{1}{k} \ln \left(1 - \frac{k}{y_w} \int_{-T}^0 y_w e^{kz_b} dz_b \right) \quad (4)$$

This expression follows from the integration of
the vertical component of the undisturbed
incident wave pressure on a cross section
contour. The time derivatives of ζ^* are used in
the calculation of the damping and added mass
correction to the "Froude-Kriloff" wave force
and moment.

Because harmonic motions only are considered,
equation (3) can be written as :

$$\begin{aligned} F' = & -2\rho g y_w (z - x_b \theta - \zeta^*) - m' (\dot{z} - x_b \dot{\theta} + 2V\theta - \dot{\zeta}^*) + \\ & + V \frac{dm'}{dx_b} (\dot{z} - x_b \dot{\theta} + V\theta - \dot{\zeta}^*) - N' (\dot{z} - x_b \dot{\theta} + 2V\theta - \frac{\omega}{\omega_e} \dot{\zeta}^*) + \\ & + V \frac{dN'}{dx_b} (z - x_b \theta - \frac{V\dot{\theta}}{\omega_e^2} - \frac{\omega}{\omega_e} \zeta^*) \end{aligned} \quad (5)$$

Combining equations (2) and (5) one finds :

$$a = \int_L m' dx_b + \left[\frac{V}{\omega_e^2} \int \frac{dN'}{dx_b} dx_b \right]$$

$$b = \int_L (N' - V \frac{dm'}{dx_b}) dx_b$$

$$c = 2\rho g \int_L y_w dx_b$$

$$\begin{aligned} d = & \int_L m' x_b dx_b + 2 \frac{V}{\omega_e^2} \int_L (N' dx_b - \frac{V^2}{\omega_e^2} \int \frac{dm'}{dx_b} dx_b + \\ & + \left[\frac{V}{\omega_e^2} \int \frac{dN'}{dx_b} x_b dx_b \right] \end{aligned}$$

$$\begin{aligned} e = & \int_L N' x_b dx_b - 2V \int_L m' dx_b - V \int_L \frac{dm'}{dx_b} x_b dx_b + \\ & - \left[\frac{V^2}{\omega_e^2} \int \frac{dN'}{dx_b} dx_b \right] \end{aligned}$$

$$g = 2\rho g \int_L y_w x_b dx_b \quad (6a)$$

$$\begin{aligned}
A &= \int_L m' x_b^2 dx_b + 2 \frac{V}{\omega_e^2} \int_L N' x_b dx_b - \frac{V^2}{\omega_e^2} \int_L \frac{dm'}{dx_b} x_b dx_b + \\
&+ \left[\frac{V}{\omega_e^2} \int_L \frac{dN'}{dx_b} x_b^2 dx_b \right] \\
B &= \int_L N' x_b^2 dx_b - 2V \int_L m' x_b dx_b - V \int_L \frac{dm'}{dx_b} x_b^2 dx_b + \\
&- \left[\frac{V^2}{\omega_e^2} \int_L \frac{dN'}{dx_b} x_b dx_b \right] \\
C &= 2\rho g \int_L y_w x_b^2 dx_b \\
D &= \int_L m' x_b dx_b + \left[\frac{V}{\omega_e^2} \int_L \frac{dN'}{dx_b} x_b dx_b \right] \\
E &= \int_L N' x_b dx_b - V \int_L \frac{dm'}{dx_b} x_b dx_b \\
G &= 2\rho g \int_L y_w x_b dx_b \quad (6b)
\end{aligned}$$

If $F = F_a \cos(\omega_e t + \epsilon_{F\zeta})$ and $M = M_a \cos(\omega_e t + \epsilon_{M\zeta})$ then:

$$\begin{aligned}
\frac{F_a}{\zeta_a} \cos \epsilon_{F\zeta} &= 2\rho g \int_L y_w e^{-kT^*} \cos kx_b dx_b + \\
&+ \int_L \left(\frac{\omega}{\omega_e} N' - V \frac{dm'}{dx_b} \right) e^{-kT^*} \sin kx_b dx_b + \\
&- \omega^2 \int_L \left(m' + \left[\frac{V}{\omega_e} \frac{dN'}{dx_b} \right] \right) e^{-kT^*} \cos kx_b dx_b \quad (7a)
\end{aligned}$$

$$\begin{aligned}
\frac{M_a}{\zeta_a} \cos \epsilon_{M\zeta} &= -2\rho g \int_L y_w x_b e^{-kT^*} \cos kx_b dx_b + \\
&+ \omega \int_L \left(\frac{\omega}{\omega_e} N' - V \frac{dm'}{dx_b} \right) x_b e^{-kT^*} \sin kx_b dx_b + \\
&+ \omega^2 \int_L \left(m' + \left[\frac{V}{\omega_e} \frac{dN'}{dx_b} \right] \right) x_b e^{-kT^*} \cos kx_b dx_b \quad (7b)
\end{aligned}$$

For ships where N' and m' are zero at the stem and stern the expressions (6) and (7) can be simplified, but this has not been carried through in the corresponding computer program.

When the terms between the brackets are left out from equations (6) and (7) and when $\frac{\omega}{\omega_e} = 1$ in the coefficients of N' in (7) the resulting equations of motion are equal to those derived by the modified Korvin-Kroukovsky and Jacobs' results [9].

APPENDIX 2

The Added Resistance in Waves

The added resistance of a ship in waves is a result of the radiated damping waves created by the motions of the ship relative to the water. Joosen [20] showed that for the mean added resistance can be written:

$$R_{AW} = \frac{3}{2g} (bz_a^2 + B\theta_a^2) \quad (8)$$

This expression was derived by expanding Maruo's expression [21] into an asymptotic series with respect to a slenderness parameter and taking into account only first order terms. His simplified treatment results in an added resistance which is independent of the forward speed. This latter fact is roughly confirmed by experiments [10].

Equation (8) is equivalent to Havelock's equation [22]. Although not consistent with the theory, the frequency of encounter is used by Joosen in (8) when a ship with forward speed is considered. In equation (8) uncoupled motions are considered. In the present work the following procedure is adopted for the calculation of the radiated damping energy P of the oscillating ship during one period of encounter:

$$P = \int_0^T \int_L b' V_z^2 dt dx_b \quad (9)$$

where $b' = N' - V \frac{dm'}{dx_b}$, the sectional damping coefficient for ship at speed and:

$V_z = \dot{z} - x_b \dot{\theta} + V\theta - \dot{\zeta}^*$, the vertical relative water velocity at a cross section of the ship. As \dot{z} is a harmonic function with amplitude V_{za} and a frequency equal to the frequency of encounter ω_e we find:

$$P = \frac{\pi}{\omega_e} \int_L b' V_{za}^2 dx_b \quad (10)$$

Following the reasoning given by Maruo in [21] the work being done by the towing force R_{AW} is given by:

$$P = R_{AW} (V+c) T_e = R_{AW} \lambda \quad (11)$$

From (10) and (11) it follows that:

$$R_{AW} = \frac{k}{2\omega_e} \int_L b' V_{za}^2 dx_b \quad (12)$$

This expression is almost equal to (8) when the wave elevation ζ is small compared with the vertical motions of the ship in addition to a very low forward speed and fore and aft symmetry.

APPENDIX 3

The Equations of Motion of Yaw and Sway

Principally the following account is based upon work by Jacobs [14,15]. The equations of motion for the bare hull condition are given by:

$$M'(\dot{\psi} + r') = Y_V' \dot{\psi} + Y_V' v' + Y_F' \dot{\psi} + Y_F' r' \quad (\text{sway}) \quad (13)$$

$$I_{zz}' \dot{\psi} = N_V' \dot{\psi} + N_V' v' + N_F' \dot{\psi} + N_F' r' \quad (\text{yaw})$$

The hydrodynamic coefficients in (13) can be calculated by assuming a division between an inertia force distribution and a viscous force distribution along the ship's hull. The distribution of the hydrodynamic inertia forces can be found by well-known methods in hydrodynamics of which brief accounts can be found, among others in [19, 23]. Confining ourselves to horizontal motions at a constant forward velocity in an ideal fluid the following expressions for the right-hand sides of (13) are derived:

$$Y_{id}' = Y_V' \dot{\psi} + X_U' r' + Y_F' \dot{\psi} \quad (14)$$

$$N_{id}' = N_V' \dot{\psi} + (Y_V' - X_U') v' + Y_F' (\dot{\psi} + r')$$

The coefficients appearing in (14) are calculated by the following expressions, assuming that the strip method is applicable together with Lamb's correction coefficients of accension:

$$Y_V' = -\frac{\pi K_2 T^2}{L^2} \int_{-1/2}^{1/2} C_s dx' \quad (15)$$

$$N_V' = -\frac{\pi K_2 T^2}{L^2} \int_{-1/2}^{1/2} C_s x' dx'$$

$$Y_F' = -\frac{\pi K_1 T^2}{L^2} \int_{-1/2}^{1/2} C_s x' dx' = \frac{K_1}{K_2} N_V'$$

$$N_F' = -\frac{\pi K_1 T^2}{L^2} \int_{-1/2}^{1/2} C_s x'^2 dx'$$

$$X_U' = K_1 M'$$

From (14) it is obvious, that for the damping coefficients the following expressions exist in an inviscid fluid:

$$Y_{id}' = 0$$

$$Y_r' id = X_U'$$

$$N_{id}' = Y_V' - X_U'$$

$$N_r' id = Y_F'$$
(16)

A ship-shaped low aspect ratio wing in a real fluid develops a circulation around the profile generating a lift owing to the viscosity. This lift can be approximated for moderate speeds by the corrected Jones' low aspect ratio formula, taking into account the action of the water surface by doubling the draught. This formula can also be considered as the integral of the viscous force distribution along the hull. The first and second moments of this distribution yields the remaining damping derivatives:

$$Y_v' \text{ visc} = -K_1 \frac{2T}{L} \frac{T}{L}$$

$$N_v' \text{ visc} = Y_r' \text{ visc} = -x_p'^2 \frac{2\pi K_1 T^2}{L^2} \quad (17)$$

$$N_r' \text{ visc} = -x_p'^2 \frac{2\pi K_1 T^2}{L^2}$$

Numerical values of the empirical constants K_1 , x_p' and x_r' are displayed in figure 17. Combining equations (15, 17) the total damping coefficients can be listed as follows, assuming that mutual interference between inertia and viscous forces can be neglected:

$$Y_v' = -2K_1 \frac{T^2}{L^2}$$

$$N_v' = Y_V' - X_U' - x_p'^2 \frac{2K_1 T^2}{L^2} \quad (18)$$

$$Y_r' = X_U' - x_p'^2 \frac{2K_1 T^2}{L^2}$$

$$N_r' = -x_r'^2 \frac{2K_1 T^2}{L^2}$$

For the purpose of comparing the results of the experimental coefficients with some existing formulae concerning damping coefficients, the following expressions are appropriate for the even keel condition, following Inoue [16]:

$$Y_v' = -2K_1 \frac{T^2}{L^2}$$

$$N_v' = -2 \frac{T^2}{L^2} \quad (19)$$

$$Y_r' = 2K_1 \frac{T^2}{L^2} (.367 + .42 \frac{T}{L})$$

$$N_r' = -1.08 \frac{T^2}{L^2}$$

Norrbin [19] published data respecting the damping derivatives. His results are given in the form of regression formulae in his non dimensional so called 'bis' system. In the nomenclature adopted in this paper the expressions are given preceded by the corresponding formulae in the 'bis' system.

$$Y_{uv}'' = -1.69 \frac{\pi}{2} \frac{LT^2}{V} - 0.04; Y_v' = -1.69 \frac{\pi}{2} \frac{T^2}{L} - 0.08 \frac{B}{L} \frac{C_B T}{L}$$

$$N_{uv}'' = -1.28 \frac{\pi}{4} \frac{LT^2}{V} + 0.02; N_v' = -1.28 \frac{\pi}{2} \frac{T^2}{L^2} + 0.04 \frac{B}{L} \frac{C_B T}{L}$$

$$Y_{ur}'' = 1.29 \frac{\pi}{4} \frac{LT^2}{V} - 0.18; Y_r' = 1.29 \frac{\pi}{2} \frac{T^2}{L^2} - 0.36 \frac{B}{L} \frac{C_B T}{L}$$

$$N_{ur}'' = -1.88 \frac{\pi}{8} \frac{LT^2}{V} + 0.09; N_r' = -1.88 \frac{\pi}{4} \frac{T^2}{L^2} + 0.18 \frac{B}{L} \frac{C_B T}{L} \quad (20)$$

TABLE 1

		L/B=4.0	L/B=5.5	L/B=7.0	L/B=10.0	L/B=20.0	L/B= ∞
I_{PP}	m	3.048	.3.048	3.048	3.048	3.048	3.048
LWL	m	3.099	3.099	3.099	3.099	3.099	3.099
B	m	.7620	.5542	.4354	.3048	.1524	.006
T	m	.1742	.1742	.1742	.1742	.1742	.1742
V	m ³	.2832	.2060	.1618	.1133	.0566	.0032
A_w	m ²	1.8267	1.3342	1.0435	.7331	.3652	-
I_L	m ⁴	.9737	.7117	.5566	.3909	.1947	-
C_B		.70	.70	.70	.70	.70	-
C_P		.71	.71	.71	.71	.71	-
LCB before $L_{PP}/2$.014	.014	.014	.014	.014	-
LCF before $L_{PP}/2$		-.063	-.063	-.063	-.063	-.063	-
k_{yy}/L_{PP}		.25	.25	.25	.25	.25	-
M	kgf sec ² /m	28.859	20.988	16.491	11.544	5.772	7.513
k_{zz}/L_{PP}		.267	.268	.230	.229	.229	.275

TABLE 2

		$F_n = .15$					
L/B		4	5.5	7	10	20	∞
M'		1978	1433	1122	779	379	521
I'_{zz}		142	103	59	41	20	39
Y'_v		-1800	-1700	-1600	-1450	-1400	-1500
N'_v		- 610	- 670	- 730	-780	- 700	- 500
-M'	$\cdot 10^5$	-3198	-2703	-2352	-1899	-1559	-1601
		- 120	- 50	- 40	0	0	+ 20
-M'		-1858	-1243	- 872	- 479	0	0
		- 265	- 295	- 290	- 280	- 240	- 260
Y'_f		- 110	- 90	- 60	0	0	0
$N'_f - I'_v$		- 190	- 165	- 125	- 105	- 88	- 95
σ'_1		.538	.304	.200	-.048	-.901	-.935
σ'_2		-2.051	-2.468	-2.955	-3.382	-2.724	-2.739
							Re=-2.930
							Im=+1.471

Table 2 to be continued

$F_n = .20$

L/B	4	5.5	7	10	20	∞	∞^M
Y_v^I	-1850	-1760	-1750	-1500	-1400	-1600	-1600
N_v^I	- 650	- 720	- 790	- 850	- 700	- 450	- 450
$Y_v^I - M^I$	-3198	-2543	-2442	-1919	-1559	-1601	-1080
N_v^I	- 180	- 70	- 50	0	0	0	0
$Y_r^I - M^I$	-1748	-1283	- 892	- 499	0	0	- 521
N_r^I	- 270	- 300	- 310	- 310	- 250	- 240	- 240
Y_r^I	- 120	- 60	- 60	0	- 50	0	0
$N_r^I - I_{zz}^I$	- 195	- 165	- 135	- 112	- 97	- 120	- 81
σ_1^I	.548	.369	.170	-.088	-1.064	-.997	Re=-2.222
σ_2^I	-1.929	-2.584	-2.928	-3.461	-2.180	-2.002	Im=+1.458

 $F_n = .30$

L/B	4	5.5	7	10	20	∞	∞^M
Y_v^I	-2450	-2300	-2070	-1760	-1450	-1600	-1600
N_v^I	- 700	- 840	- 900	- 980	- 860	- 500	- 500
$Y_v^I - M^I$	-3078	-2603	-2652	-2189	-1599	-1621	-1100
N_v^I	- 160	- 100	- 20	0	- 50	0	0
$Y_r^I - M^I$	-1878	-1303	-1042	- 559	- 29	0	+ 521
N_r^I	- 330	- 360	- 400	- 340	- 310	- 230	- 230
Y_r^I	- 180	- 100	- 100	0	- 50	0	0
$N_r^I - I_{zz}^I$	- 200	- 160	- 120	- 115	- 95	- 90	- 51
σ_1^I	.387	.225	.090	-.054	-.955	-.985	Re=-2.982
σ_2^I	-2.227	-2.909	-3.879	-3.706	-2.878	-2.558	Im=+1.517

 ∞^M plate without mass

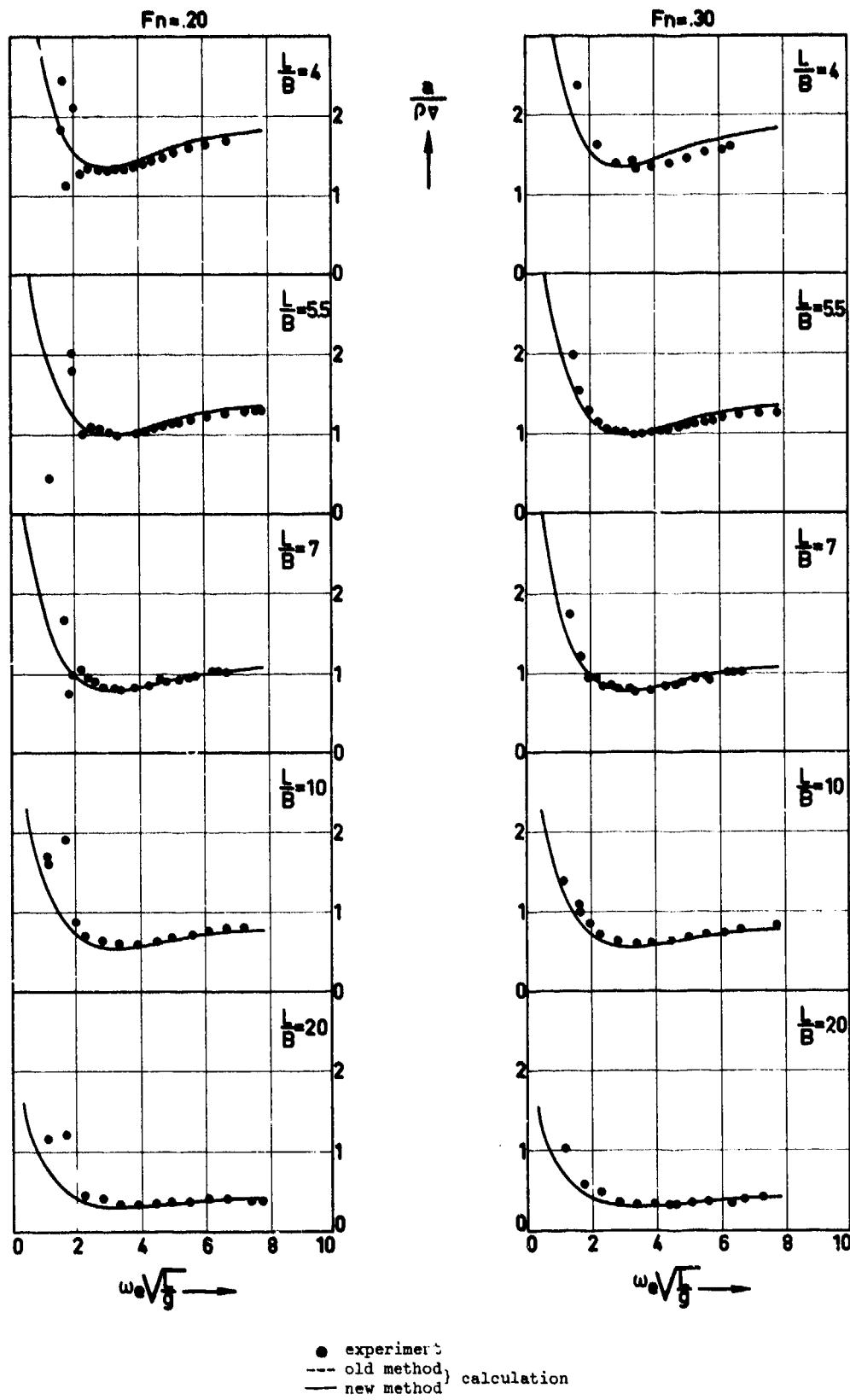


Figure 1: Added mass coefficient for heave

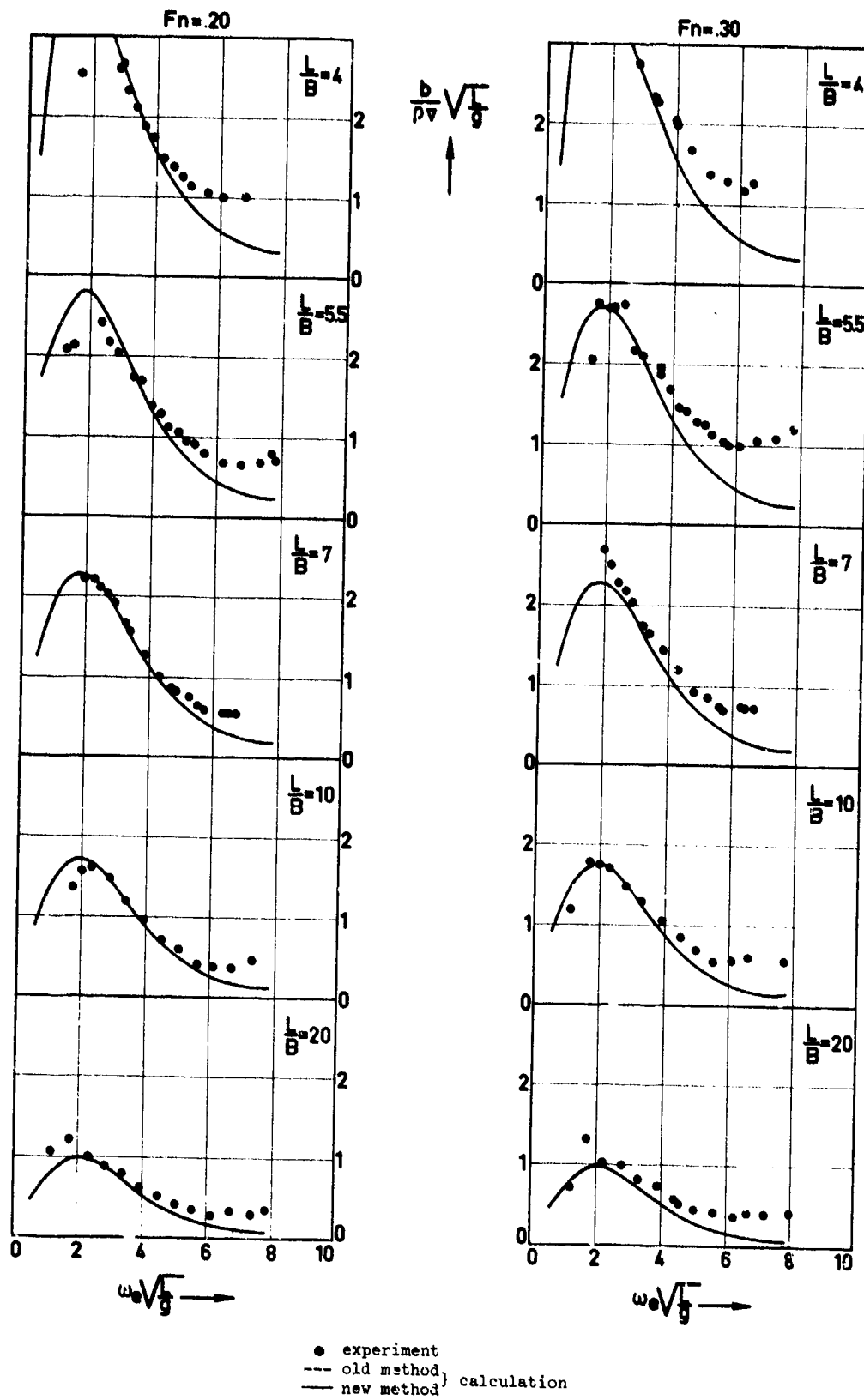


Figure 2 : Heave damping coefficient

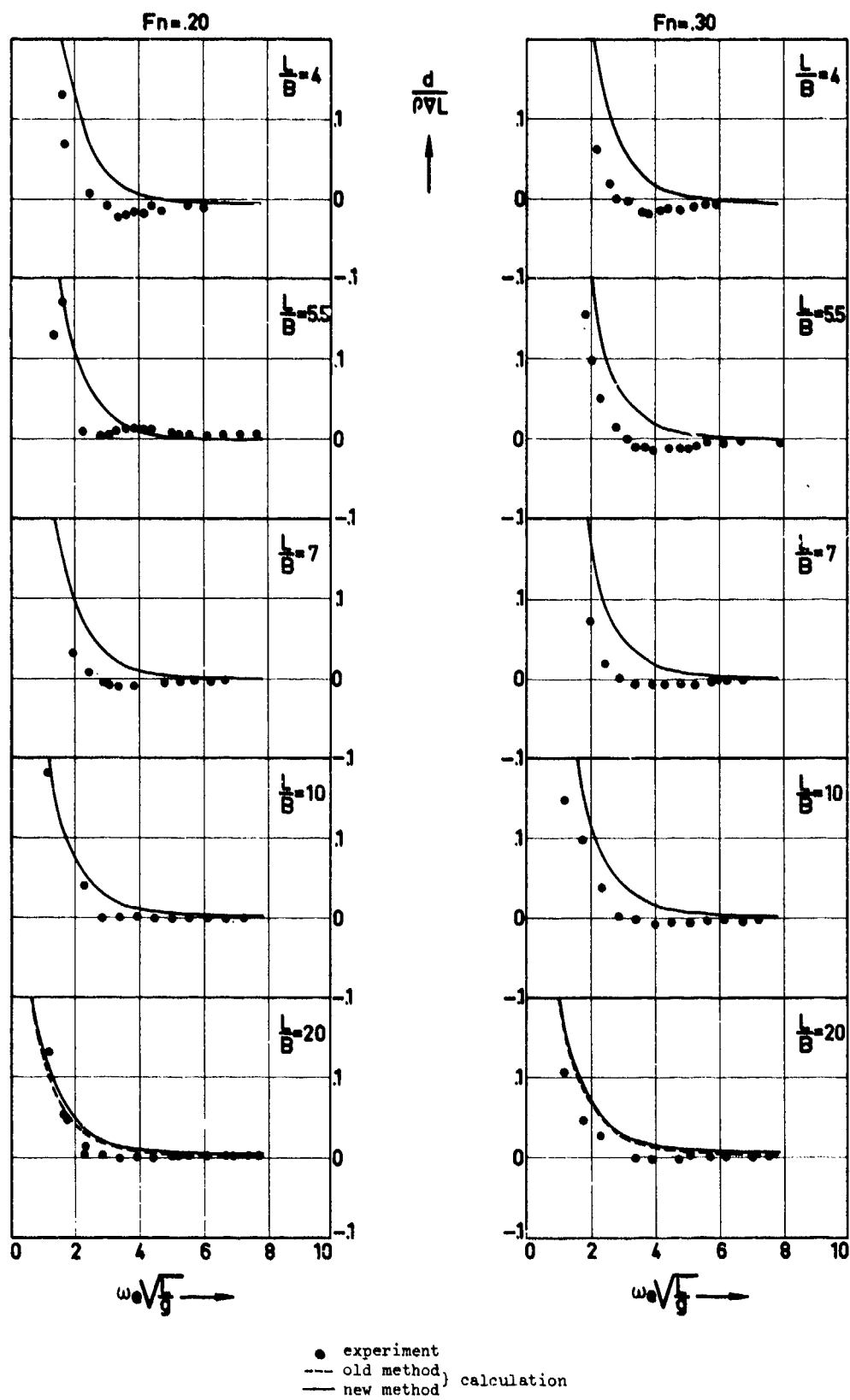


Figure 3 : Added mass cross coupling coefficient for heave

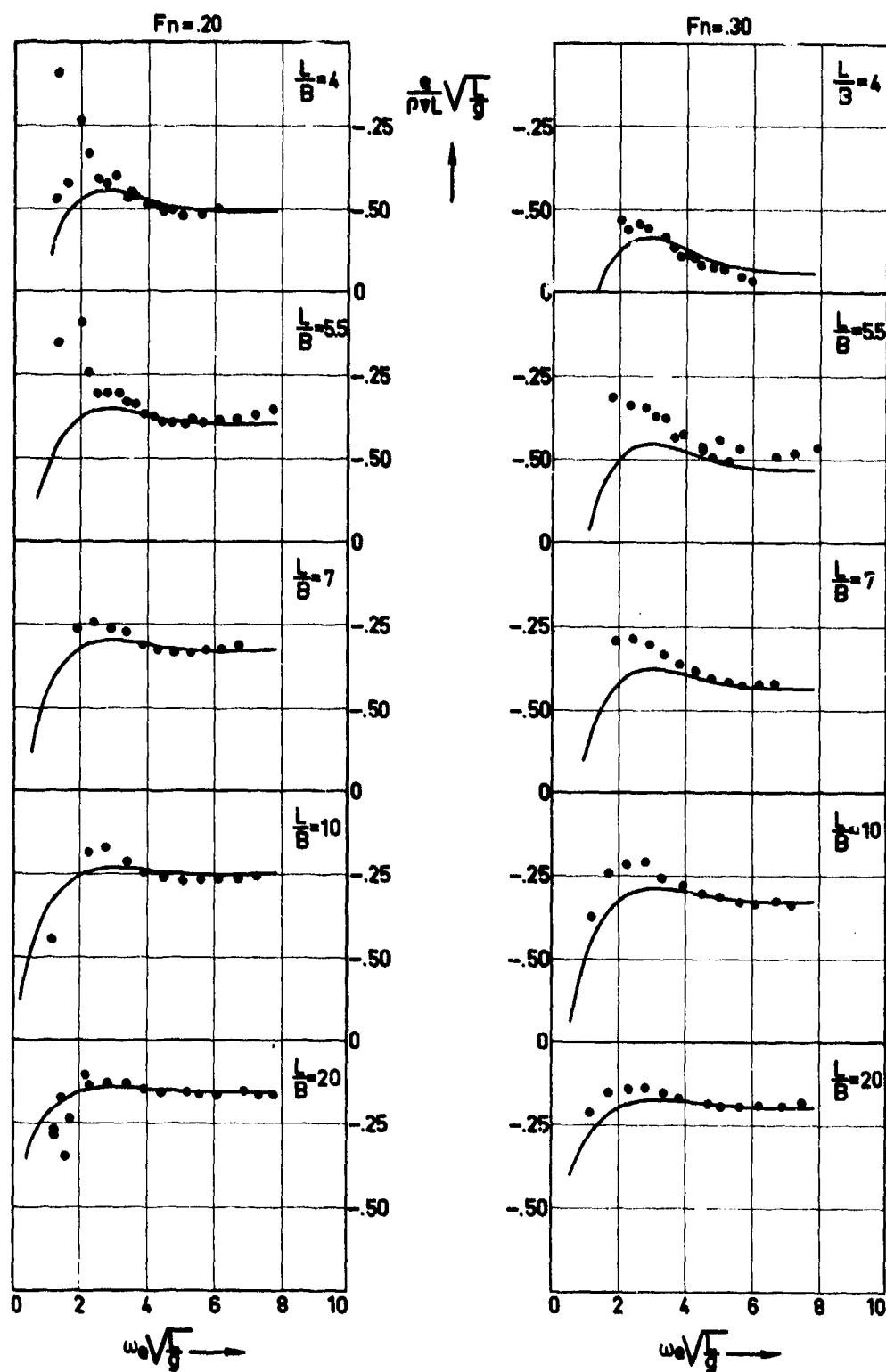


Figure 4 : Damping cross coupling coefficient for heave

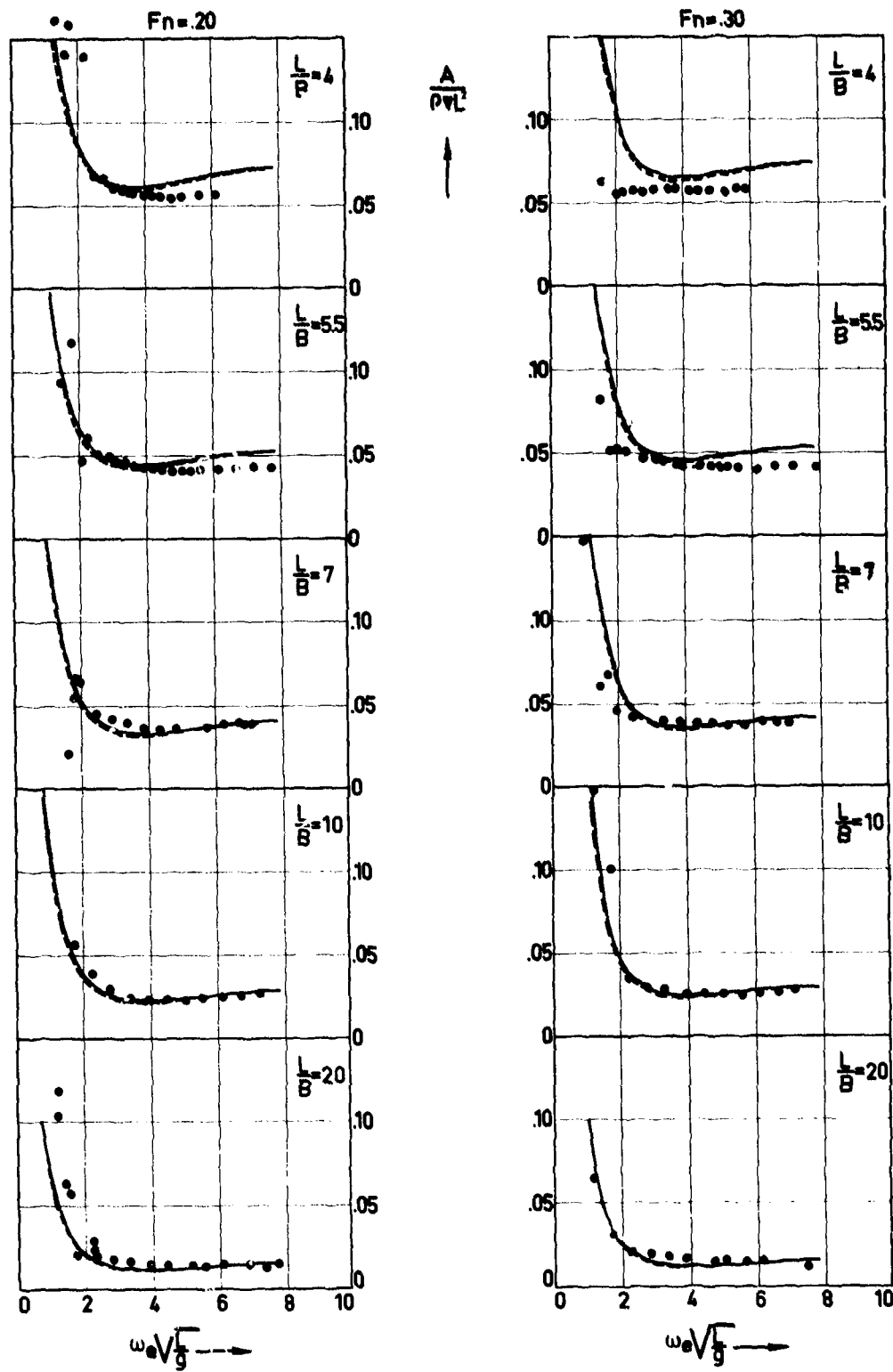


Figure 5 : Coefficient of added mass moment of inertia for pitch

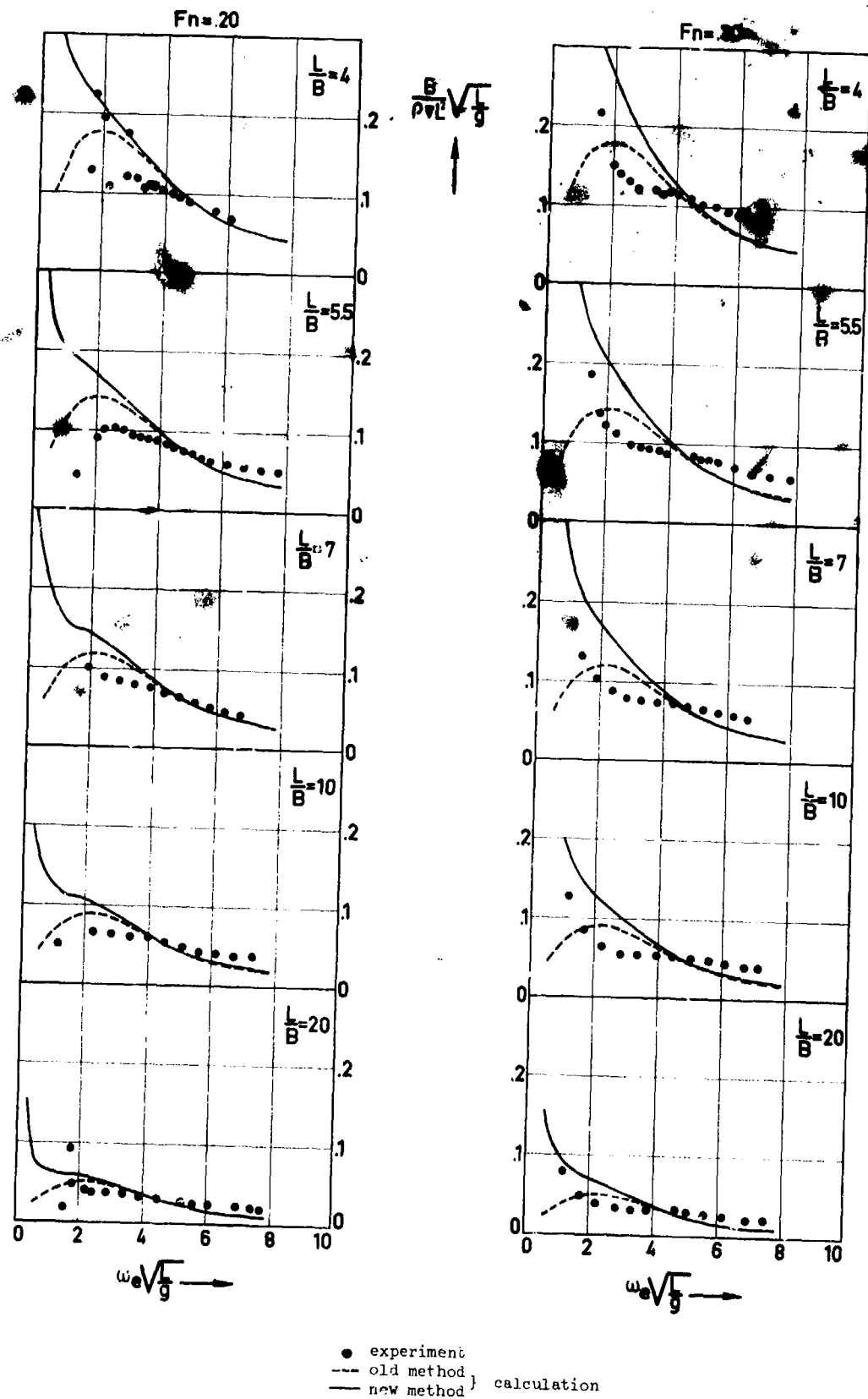


Figure 6 : Pitch damping coefficient

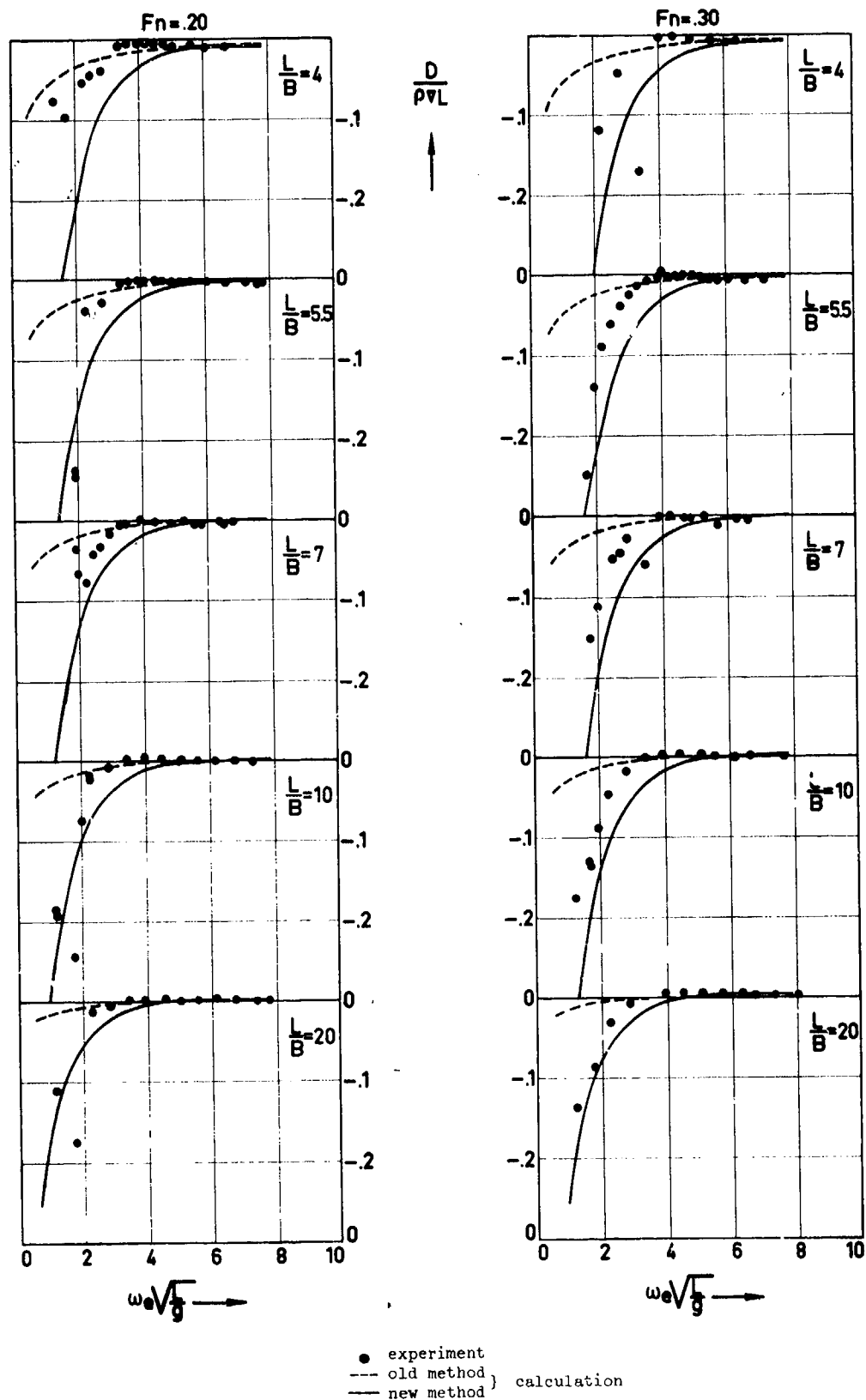


Figure 7 : Added mass cross coupling coefficient for pitch

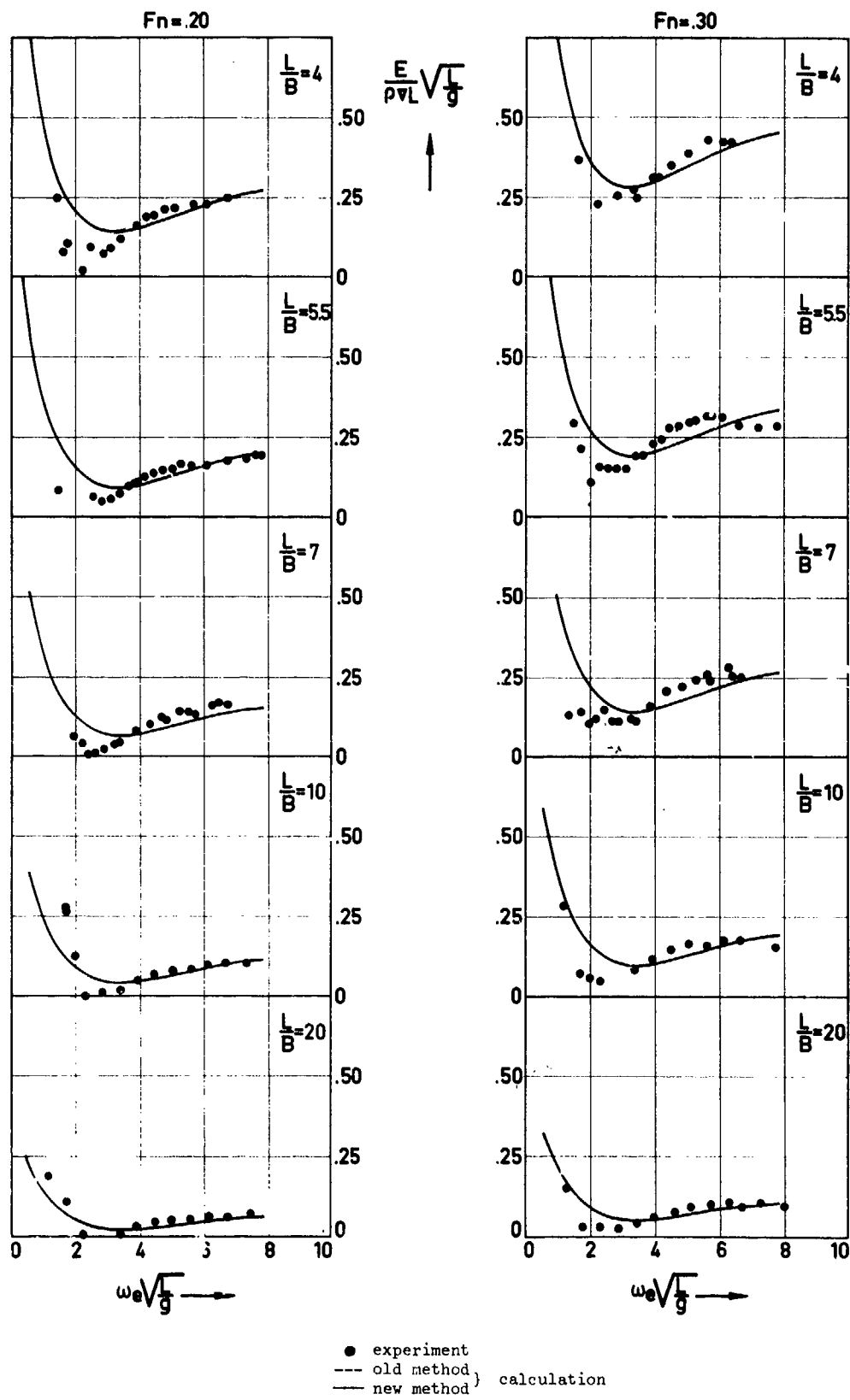


Figure 8 : Pitch damping cross coupling coefficient

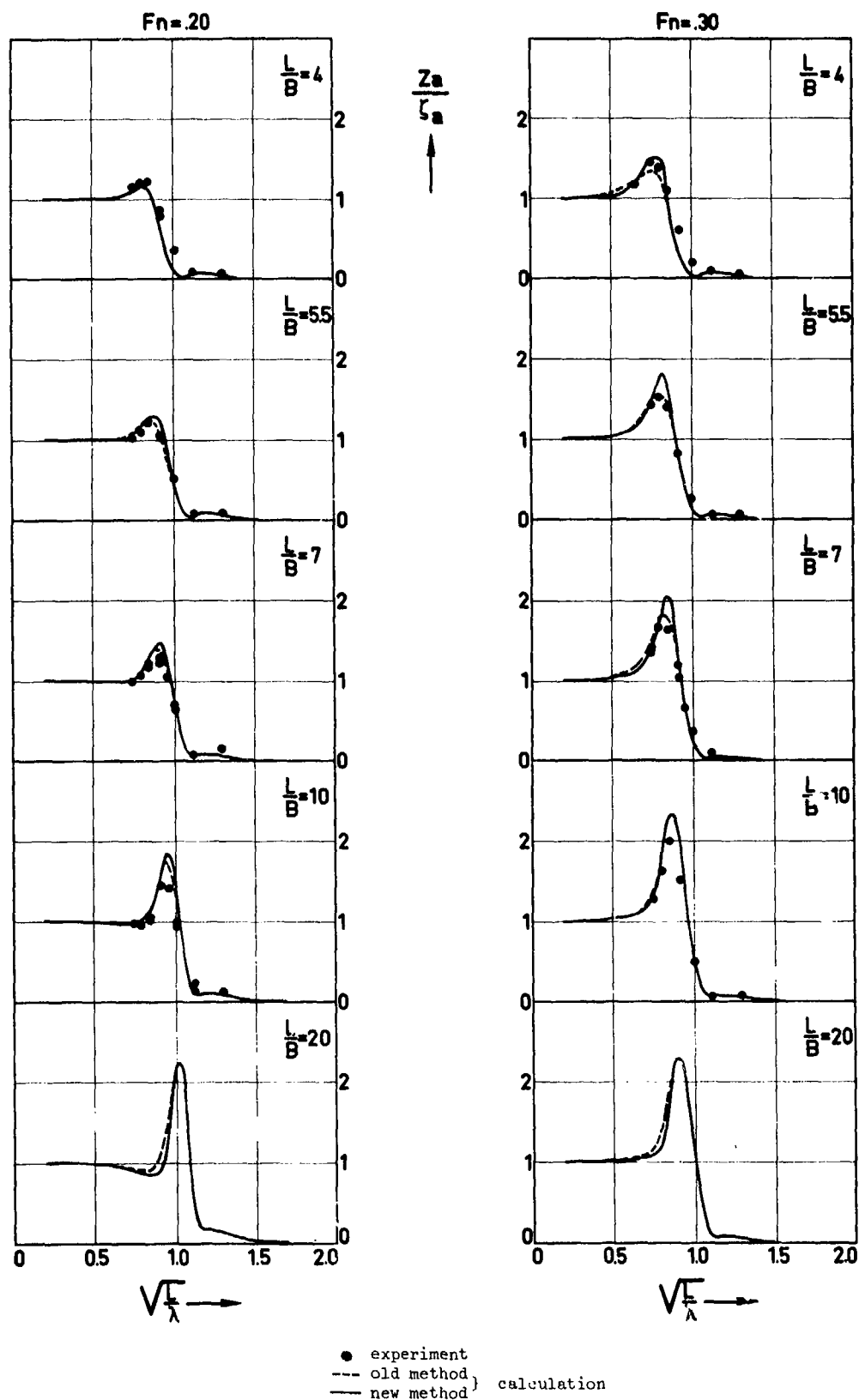


Figure 9 : Heave amplitude in waves

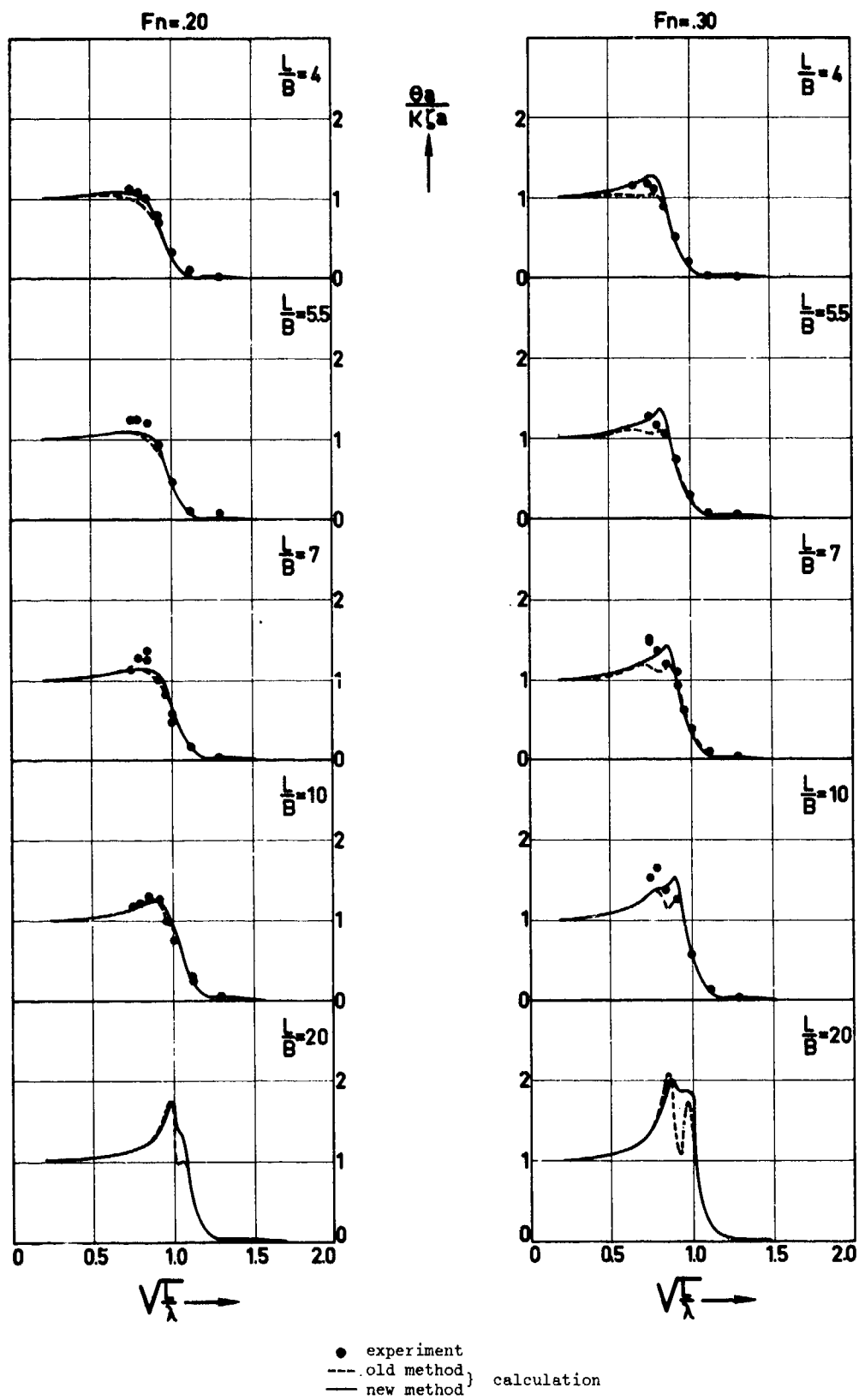


Figure 10 : Pitch amplitude in waves

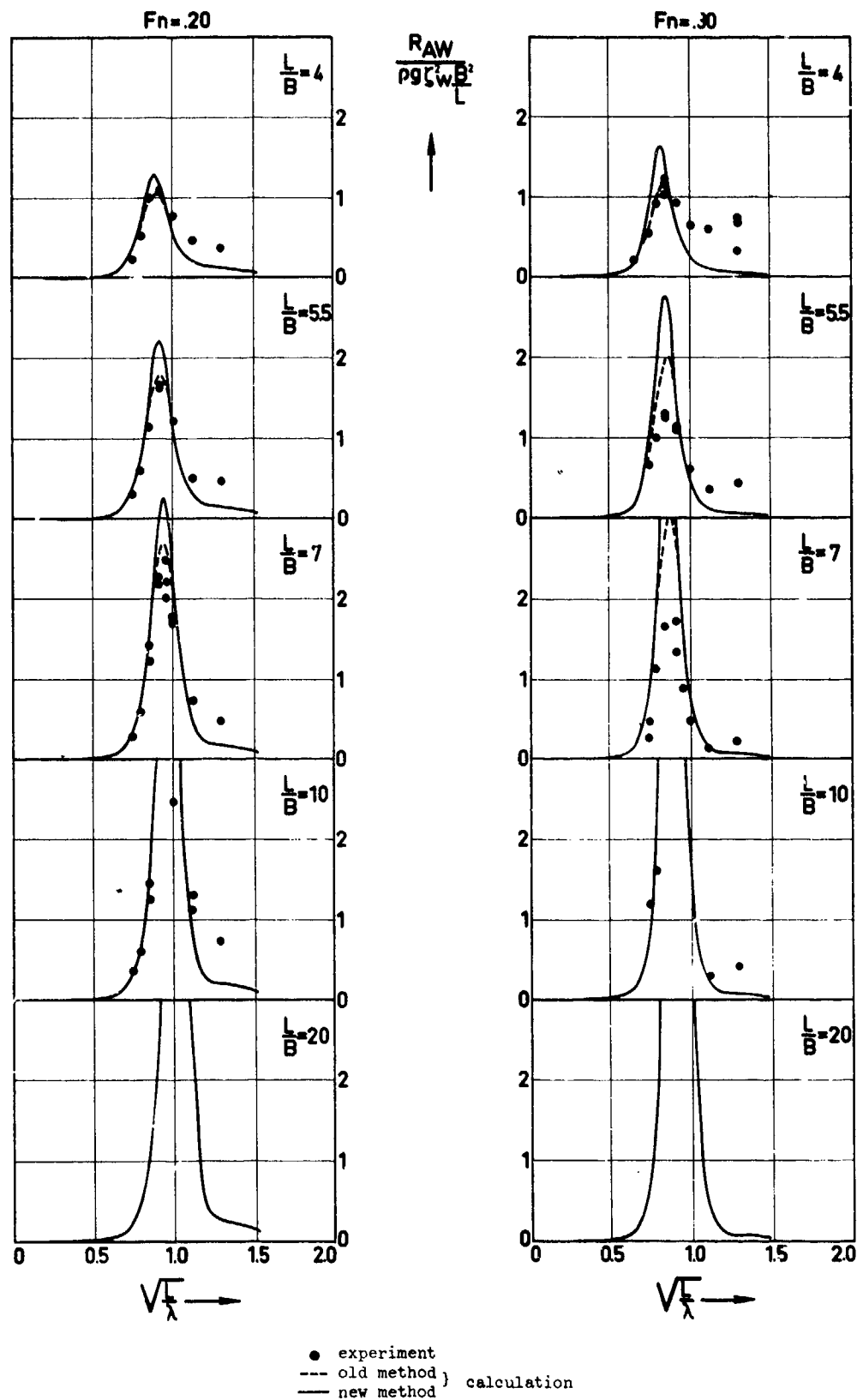


Figure 11 : Added resistance in waves

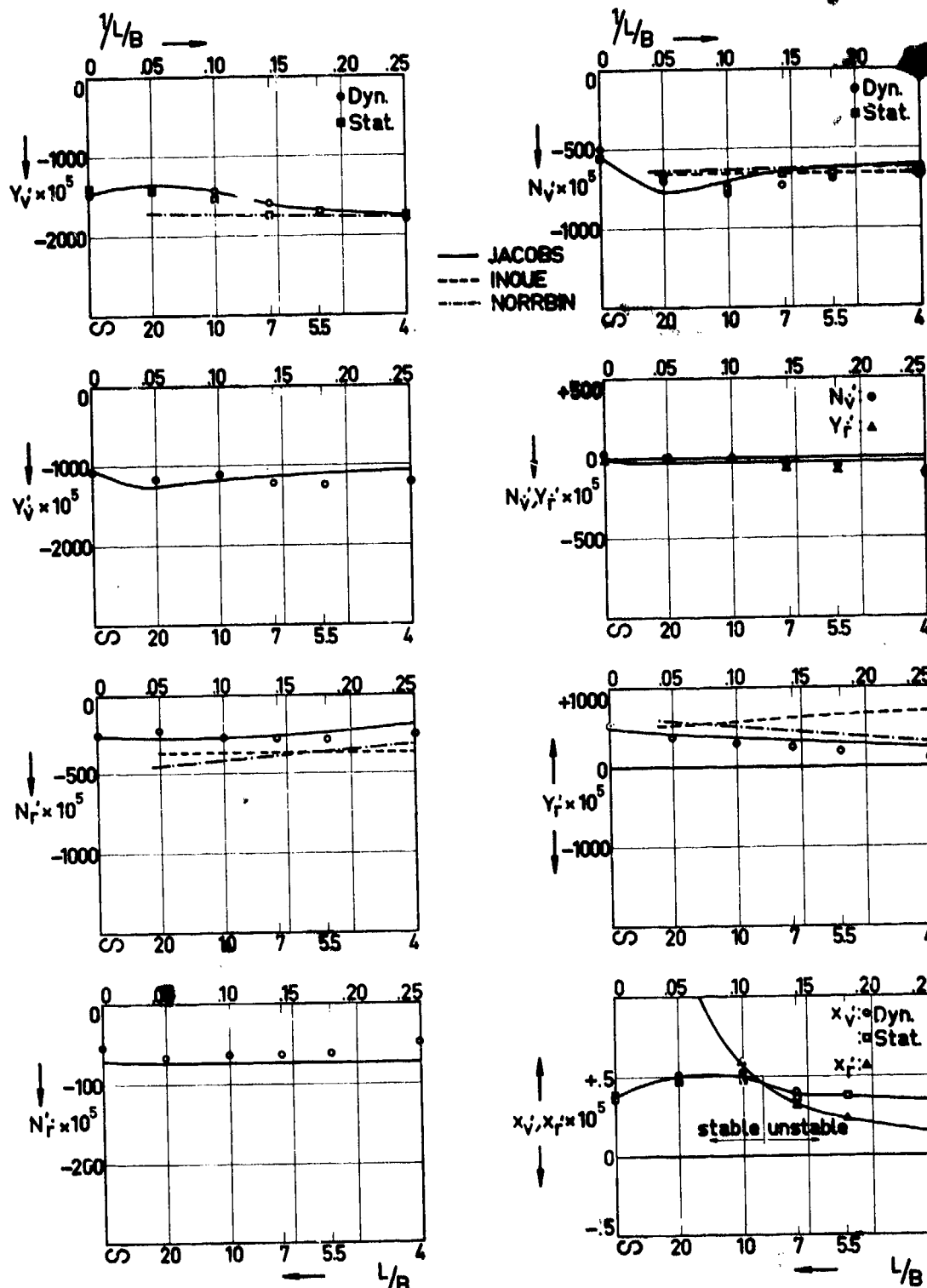


Figure 12 : Hydrodynamic coefficients for $F_n = 0.15$

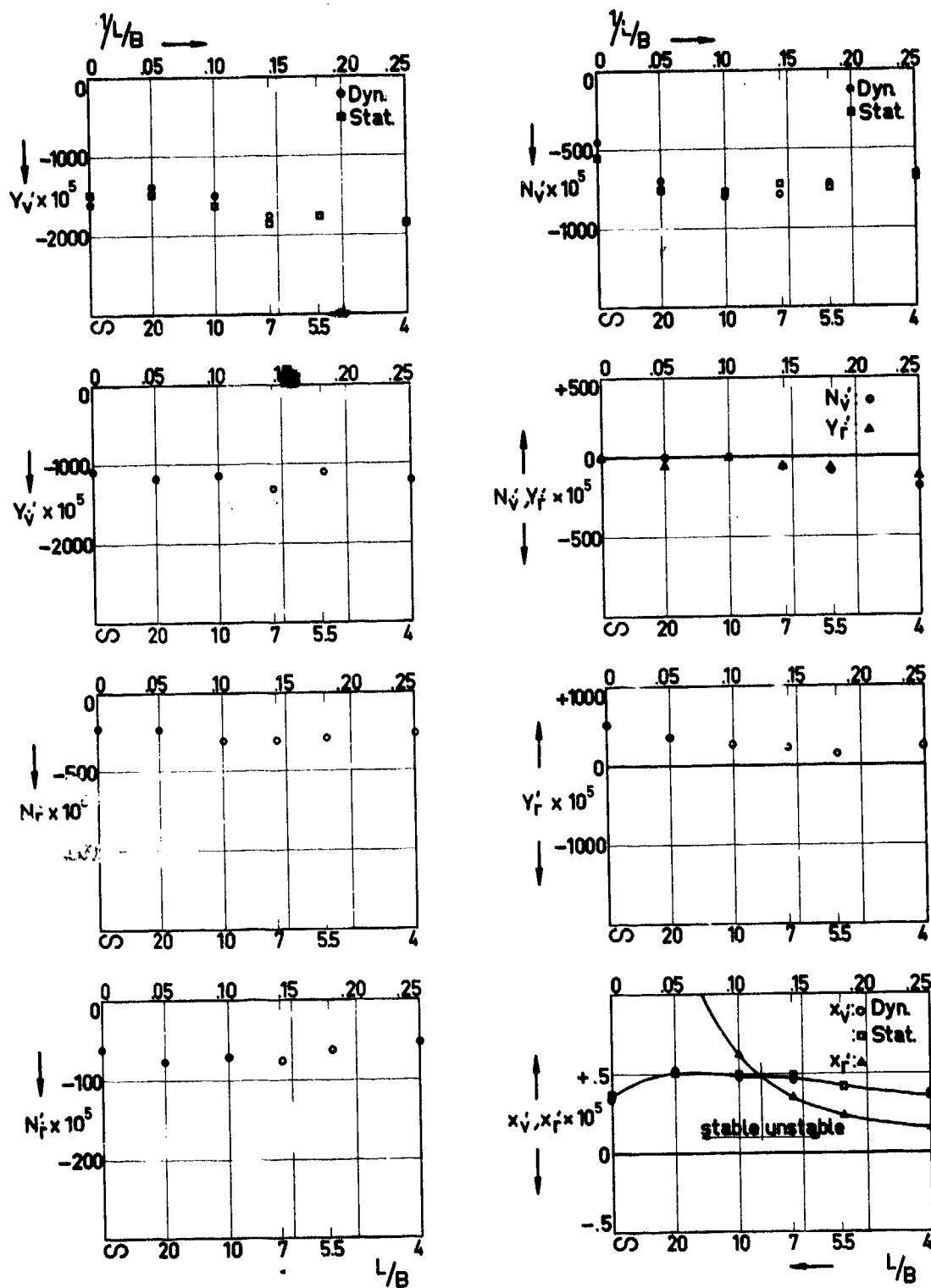


Figure 13 : Hydrodynamic coefficients for $F_n = 0.20$

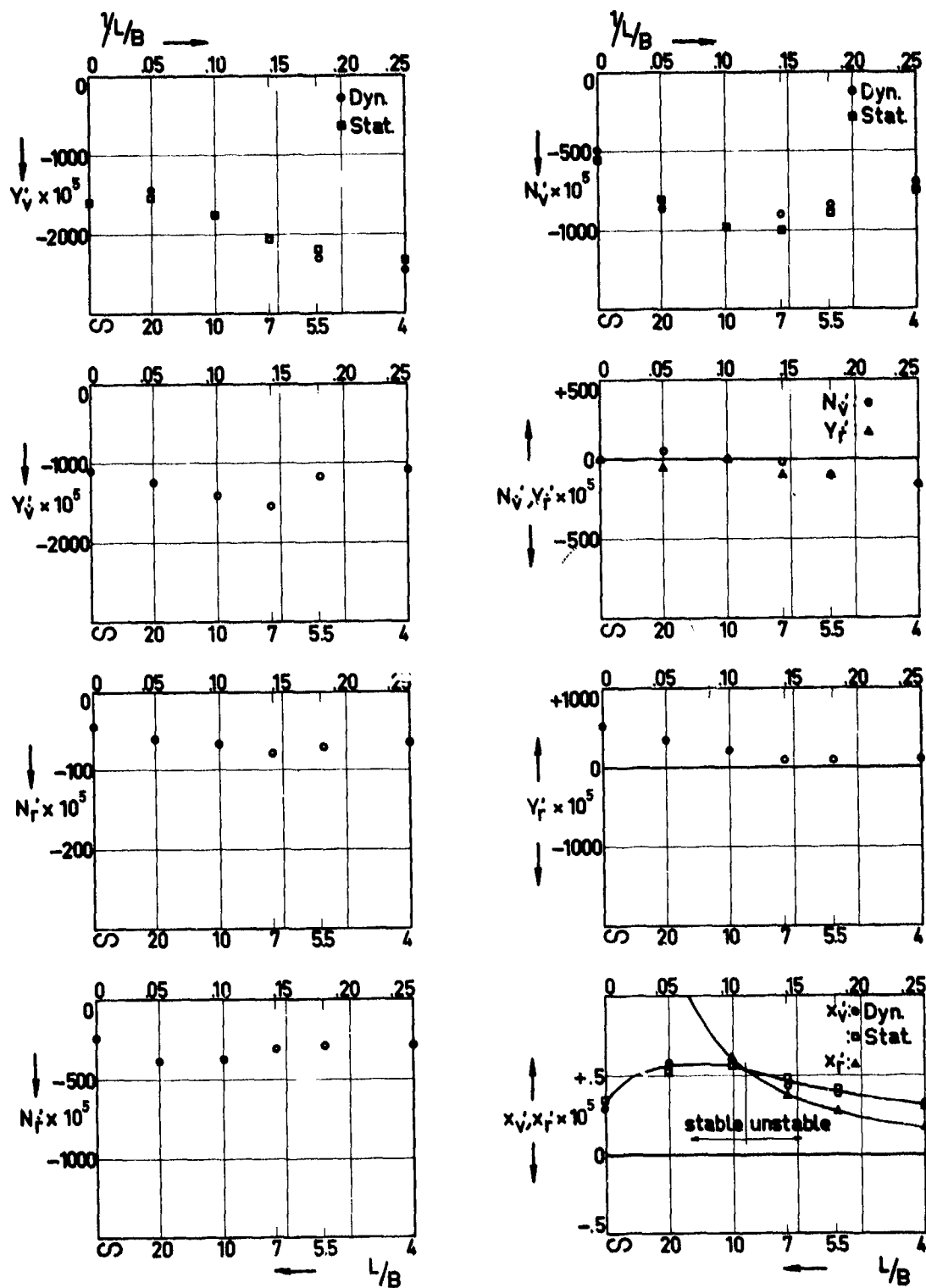


Figure 14 : Hydrodynamic coefficients for $F_n = 0.30$

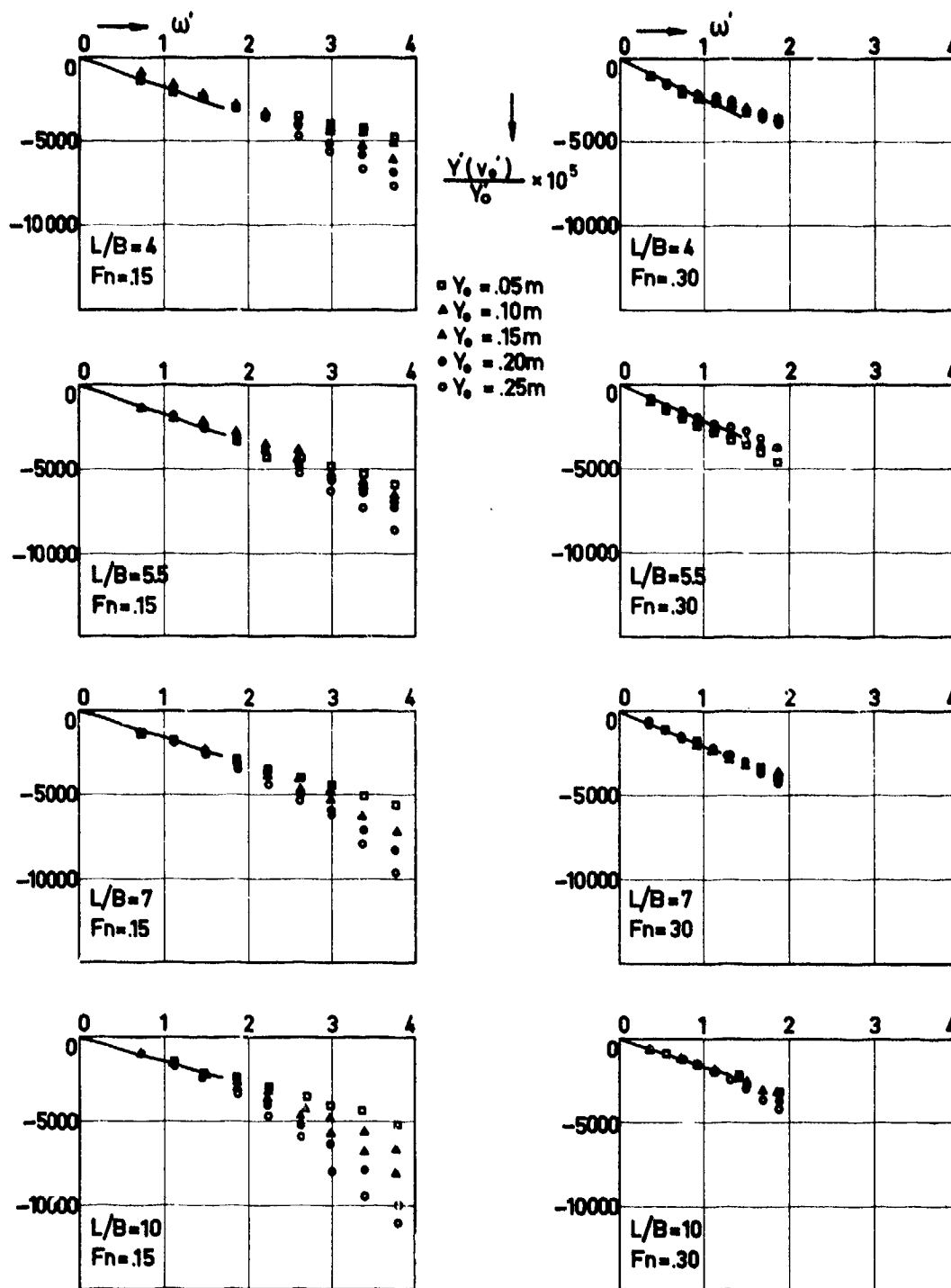


Figure 15 : to be continued

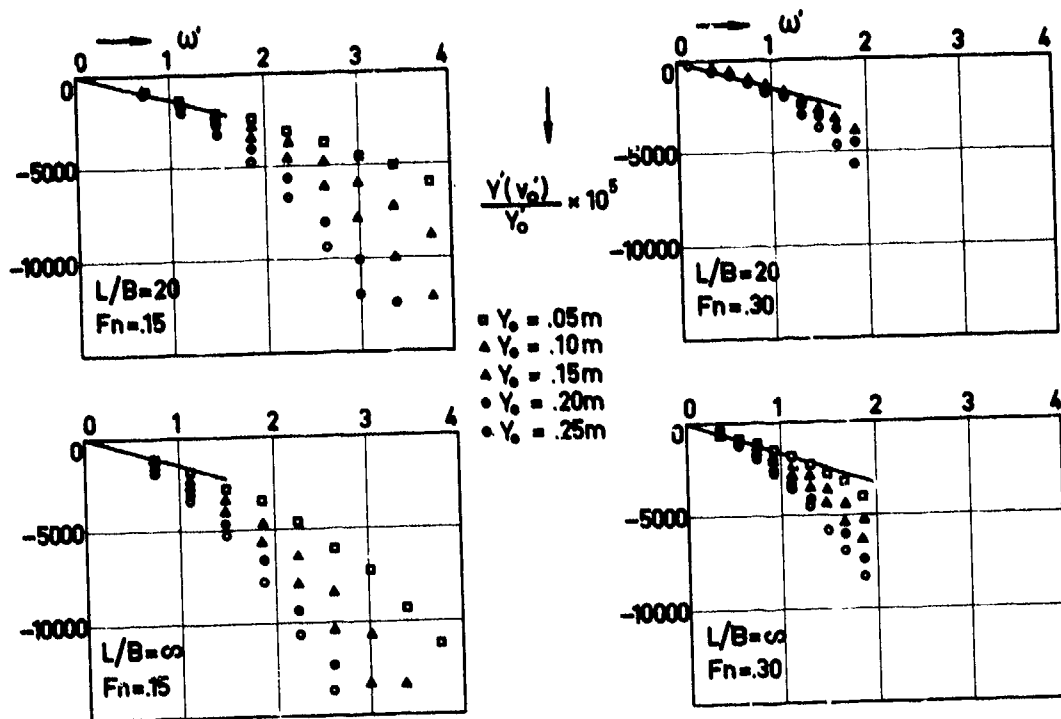


Figure 15 : Sway force for two Froude numbers as function of L/B -ratio

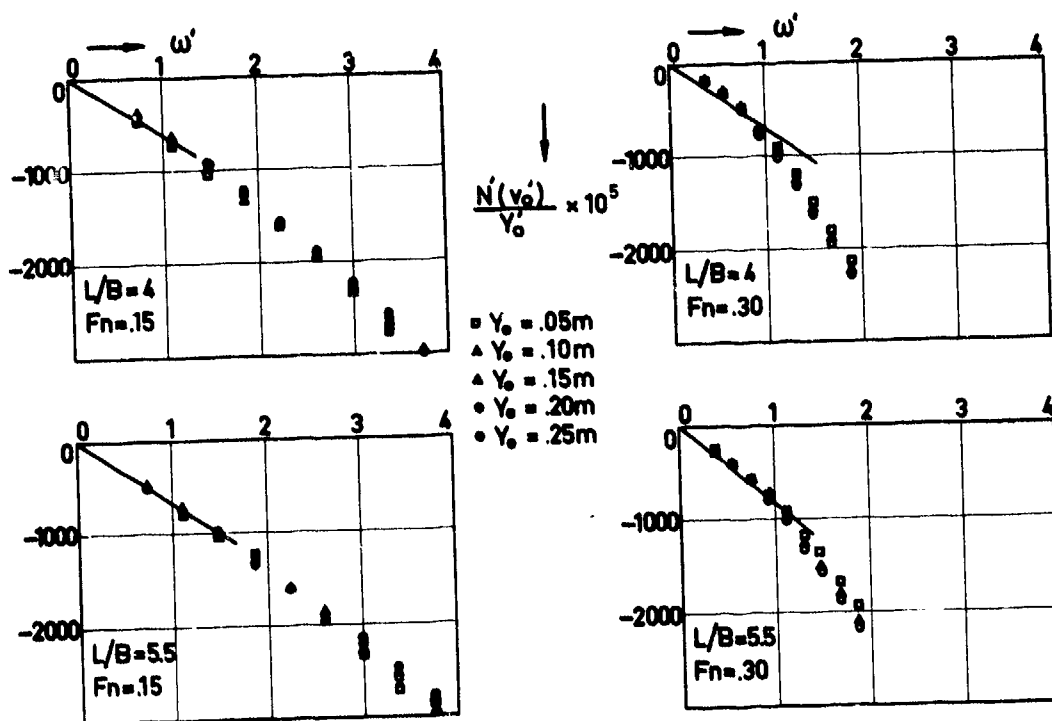


Figure 16 : to be continued

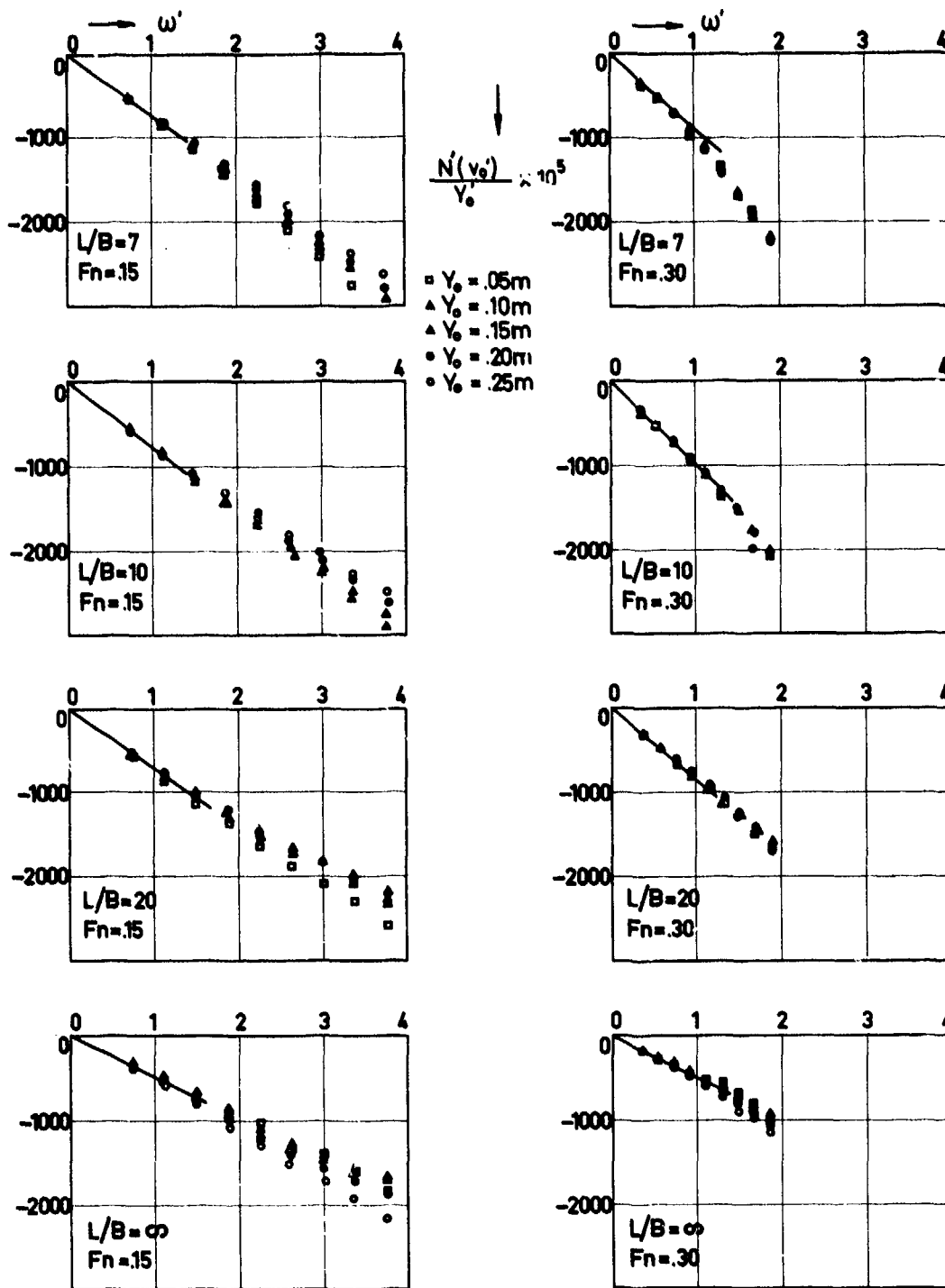


Figure 16 : Sway moment for two Froude numbers as function of L/B -ratio

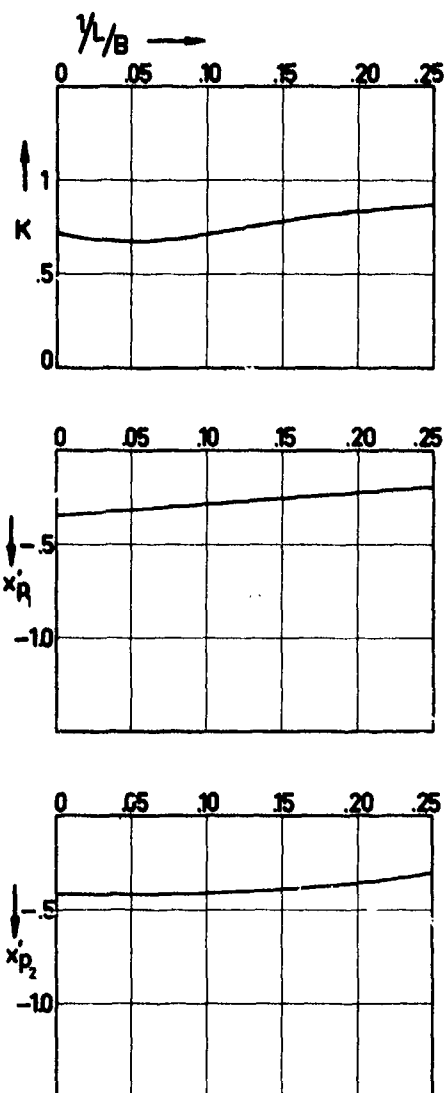


Figure 17 : Empirical coefficients derived from the experiments

DISCUSSION

W.R. JACOBS

I appreciate greatly your asking for my comments on your well-reasoned and informative paper. I am gratified, moreover, to see that the Korvin-Kroukovsky and Jacobs method for predicting heaving and pitching motions in regular head seas and the Jacobs method for estimating the linear hydrodynamic coefficients of the horizontal motions still hold up so well at Froude numbers no greater than 0.20. At such speeds, of course, the effects of wave-making can be neglected. (The experimental values in Fig. 13 for $F_n \approx 0.20$ are almost identical with those of Fig. 12 for $F_n = 0.15$ and therefore agreement between calculation and experiment should be as good.)

In your introduction, you state that, in the case of horizontal motions, "apart from the length-draft ratio.... the length-beam ratio may be regarded as a useful parameter in a comparison of theory and experiment." The length-beam ratio does not appear explicitly in my calculation method (Appendix 3). I wish to make clear that length-beam ratio is implicit in the ship mass coefficient M' which is identically equal to $2 C_B B/L$.

K. NOMOTO

It is a great pleasure to take part in the discussion on this interesting paper. Certainly the effect of length-beam ratio on the hydrodynamic damping in directional control of a ship is of great interest with special reference to the ease of control of giant tankers of the present day, whose length-beam ratio is lessening as low as 5.

In this connexion a look into Table 2 is highly suggestive. The damping in yaw and sway, and consequently the directional stability is governed by

$$Y'_v N'_r - (Y'_r - M') N'_v$$

Among these derivatives, what is most sensitive to the length-beam ratio is definitely $(Y'_r - M')$, and this comes largely from the drastic decrease in the nondimensional mass M' with increasing length-beam ratio. Compared with this, the purely hydrodynamic derivatives Y'_v , N'_v and N'_r are much less sensitive.

Since M' represents the contribution of the centrifugal force upon directional stability, this result suggests that the effect of length-beam ratio upon directional stability is more of the matter of mechanics rather than of hydrodynamics. This might sound a bit reluctant to hydrodynamicists, yet one thing worth noting.

Incidentally one can guess the effect of the block coefficient on the directional stability along the same line; the change in M' largely governs the fact.

As another remark, the frequency in PMM experiments should be adequately low so that $(WL/V) < 2 \sim 2.5$ in order to obtain the derivatives that are free from the frequency effect, in the discussor's view. That means in the present case $W < 0.7$ for $F_n = 0.15$ and < 1.4 for $F_n = 0.3$ and accordingly most of these experiments are apparently within this limit.

EDWARD V. LEWIS

This paper represents the type of well conceived and well executed experimental research that we expect from Delft University of Technology.

My brief comments refer only to the first part of the paper dealing with vertical motions. The experimental determination of coefficients for pitch and heave for an unusually wide range of L/B ratios shows encouraging results. Even at such extreme proportions as $L/B = 4$, the agreement between experiment and theory (Figures 1-8) is as good, or almost as good, as for narrower hulls. The so-called "new" theoretical method appears to give better agreement in some cases but not in others.

It is not surprising then that excellent agreement is obtained in Figures 9 and 10 between calculated and experimental motions over this wide range of L/B . In general the "new method" shows somewhat better results. Of particular interest is the excellent agreement shown in Figure 11 for added resistance in waves. All in all, the paper shows clearly the tremendous value of the "vigorous", though perhaps not entirely "rigorous", strip theory approach to ship motions. The high degree of practical usefulness of the method is due in large part to work such as reported in this paper, covering both refinements in the theory and experimental verification of various aspects.

C.M. LEE

Prof. Gerritsma and his co-authors, as always, have shown us again a valuable work which will greatly contribute to the advancement of knowledge in ship hydrodynamics.

The following is my opinion on a minor point which I would like to take this occasion to present to the authors for their comments.

The equations of motion for ships in waves which are derived under an assumption of linear frequency response, are usually given in the form of the second order differential equations with frequency-dependent coefficients. As Dr. Cummins* rightly pointed out, the physical meaning of these coefficients can be often misleading depending on how one arranges the coefficients in the equations. To be more specific, there is always a possibility of interchanging the coefficients between the inertia terms and restoring terms with only change in the factor $(-W^2)$. For instance, the coefficient A and C are given in Equation (6b) as

$$A = \int m' x_0^2 dx_0 + 2 \frac{V}{\omega^2} \int N' x_0 dx_0 - \frac{V}{\omega^2} \int \frac{dN'}{dx_0} x_0^2 dx_0, \quad C = 2 \rho g \int x_0^2 dx_0$$

We can transfer the terms containing $1/W^2$ in A to C by multiplying the terms by $(-W^2)$ without impairing the solutions of the equations. If this is done for a ship without abrupt ends, we have

*Cummins, W.E., "The Impulse Response Function and Ship Motions," Schiffstechnik, Vol. 9, 1962

$$A' = \int m' x_0^2 dx_0$$

$$C' = 2\rho g \int y_w x_0^2 dx_0 - V^2 a$$

The second term, $-V^2 a$, in C' is often called "Munk's Moment" and it is always a destabilizing moment due to its negative sign. A difference resulting from interchanging this Munk's moment term is in the determination of natural frequencies, especially for pitch. The natural frequency for uncoupled pitch mode can be estimated by

$$\omega_p = [C/A]^{1/2}$$

If we use A' and C' instead, then we have

$$\omega_p' = [C'/A']^{1/2}$$

The difference between W_p and W_p' is usually small for conventional ships for low speeds. However, the difference can be large for high speeds and particularly, for small waterplane area ships with a high cruising speed.

For a ship with very small waterplane area the vertical-plane stability can become a problem for high speeds. Depending on where the Munk moment term is placed, the estimation of vertical-plane stability can significantly change. There is no question that for a stability study the Munk moment should be placed in the restoring term.

For determining the natural frequencies and the vertical-plane stability, it appears physically more adequate to use A' and C' than to use A and C . I would like to know if the authors have some comments on this point.

MAX HONKANEN

At first I would like to express my gratitude for this very useful paper presented here as the first one today. I was very pleased to read it, because the first part, of which some details were published at ITTC in 1972, has already been used by me in checking the validity of my own calculations. There is one question regarding the lateral motions and forces associated with them that is bothering me and I would appreciate if the authors could throw some light on it.

As we all know, the theoretical treatment of the rotative modes of motions is based on the assumption of fixed axes of rotation. This, however, needs not necessarily be the truth, and in fact, there exists an apparent center of rotation, which usually differs slightly from the intersection point of the waterline and the symmetry plane of the ship. I have formulated a strip theory that makes allowance for

an arbitrary center of rotation, and preliminary calculations show that the location of this virtual center of rotation may have a significant effect on the hydrodynamic coefficients of the lateral motions. It should be understood that the PMM test results may very well be in a perfect agreement with the theoretical results, since the tests are actually run on the same assumption of a fixed center of rotation as the theory has been derived.

I would simply like to ask the authors if they have any experience on the effect of the virtual center of rotation on the hydrodynamic coefficients of the lateral motions and what order of magnitude they think that such an effect would be.

NILS H. NORRBIN

In this summary of my oral discussion I will once more bear witness to the benefit the reader may derive from results of careful systematic studies of this kind. I will restrict my comments to the analysis of the dynamic stability in the horizontal plane. Within the particular bare hull Series 60 family tested dynamic stability is inherent for L/B ratios above 8. With stern appendices stability will be realized for wider forms.

The analytical stability criterion compares the magnitude of two force levers, in the authors' notation x_v' and x_y' . In particular, $x_v' = 1_v/L$ is the relative center-of-pressure-in-sideslip, or the quotient N_v'/Y_v' . For a model family this quotient will be given by the slope of the radius vector to the locus $N_v'(Y_v')$. In Fig. 1 this locus is shown by the arc shape to the right. In the same diagram but to another scale the corresponding locus is also drawn as given in the "bis" system $N_{uv}''(Y_{uv}'')$: the locus now illustrates a moment and a force, which both uniquely increase with increasing L/B . The radius vector slope is shown for $L/B = 7$, for the bare hull as well as for a configuration with screw and rudder. (The finite increments of Y_{uv}'' and N_{uv}'' have been taken from model test results by van Leeuwen in authors' ref. [12].)

The diagram may be completed by adding the locus of $x'' - N_{uv}''$ to a base of $1 - Y_{uv}''$. (Again the use of the "bis" system will arrange the test data in a unique form.) The stability criterion and the way it is affected by modifications to the stern is easily appreciated from a comparison of vector slopes.

It would be of great value if, in the future, the authors could find an opportunity to include some results for hulls with screw and rudder, say for the cases of $L/B = 5.5, 7$ and 10.

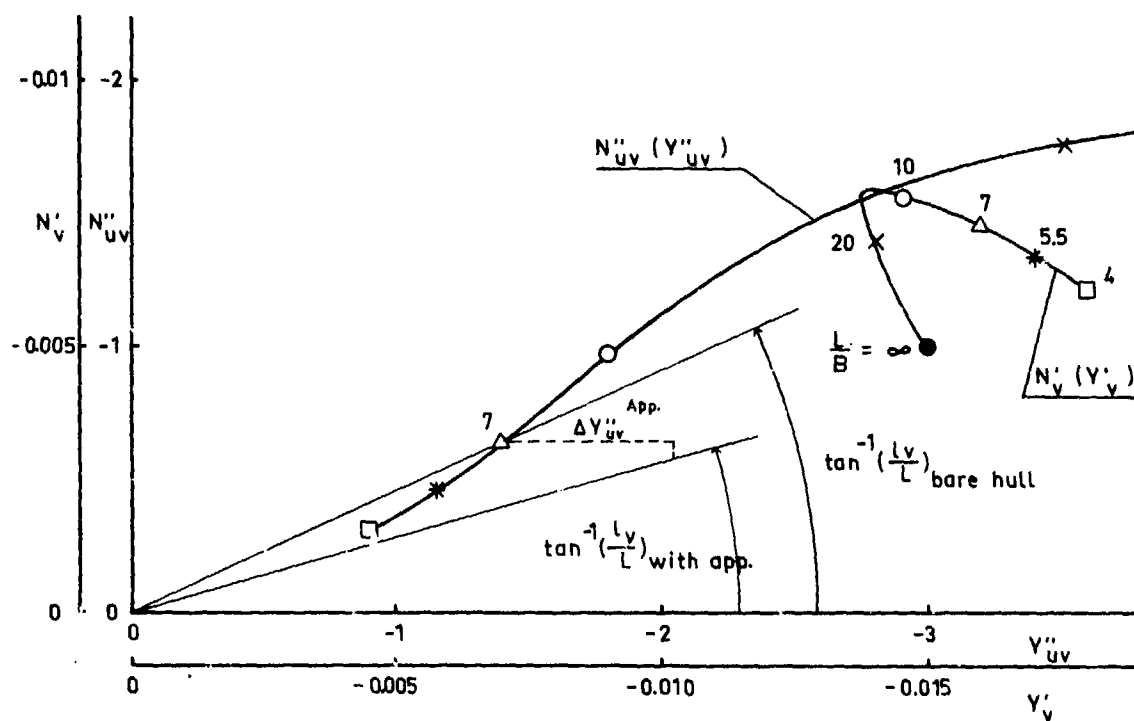


Figure 1: Loci of drift force derivatives for model family, also illustrating initial force c.p. position

AUTHOR'S REPLY

Referring to the kind remarks of Miss Jacobs, we agree that the differences in the experimental results for the Froude numbers .15 and .20 are so small that the effect of wave making in the development of simple theories can safely be ignored. Since the wing analogy, primarily represented by the length-draught ratio, is playing an important role in these theories for assessing the lateral maneuvering derivatives, it was thought that the length-beam ratio would provide some correction factors respecting the distribution of viscous forces along the length.

Prof. Nomoto points out that the derivative $Y'_r - N'$ is the most sensitive one, since the dimensionless mass appeared, which shows the largest changes with varying length-beam ratio's, see table 2. He concludes that the straight-line stability is more a matter of mechanics than of hydrodynamics. We agree with this conclusion. However we want to put emphasis upon the fact that the experiments were executed with a model series having a block coefficient $C_B = .70$ and a length-beam ratio $L/B = 7$ as a parent hull. It is therefore dangerous to extrapolate the information contained in this paper to blunt tanker forms with different block coefficients and different length-beam ratios. Furthermore one should bear in mind that the models tested were bare hulls. A rudder and propeller fitted to the models will improve straight line stability. Since changes in the form of the body and the distribution of displacement along the length sometimes might induce drastic changes in the hydrodynamic coefficients, we do not fully agree with Prof. Nomoto's remark respecting the effect of block coefficient. The last remark refers to the maximum permissible frequency in horizontal PMM-tests to avoid frequency effects. In the in this paper presented results there seems to be some evidence, Figs. 15 and 16, to conclude that the dimensionless frequency W' should be lower than 1 or at the most 1.5. Nevertheless not in all cases higher frequencies could be avoided in order to obtain measurable results.

Prof. Lewis confirms our point of view with regard to the usefulness of strip theory calculations. From the practical point of view we do not favor one of the two theories for the calculation of vertical motions. This is also based on further incidental comparisons for theory and experiment for slender ship hull forms at high speeds of advance. Of particular interest is the agreement between the two theories with regard to phase angles and the more or less overestimation of the heave amplitudes at resonance by the new theory. Up to now we use the old method for the prediction of heave, pitch and resistance increase in waves for design purposes.

Mr. Lee makes some valuable remarks about the determination of the natural frequency. In our formulation of the strip theory the restoring term is considered to be speed-independent and consequently the speed dependent part has been transferred to the added mass term. For the solution of the motion equations it is irrelevant where the speed dependent parts are situated. However for the determination of the natural frequency this may be important especially for high forward speeds. It is probably not correct to keep the restoring term speed-independent and the "Munk's moment" might be one significant addition for high speeds. However, there is another influence of the speed on the restoring term and this is due to the change

of trim and the wave formation. This effect should also be taken into account for the determination of the natural frequency. Experimentally we did not investigate the influence of "Munk's moment" but we will certainly take into account Mr. Lee's remarks in this respect.

According to Mr. Honkanen the situation of the centre of rotation may influence the hydrodynamic coefficients of the lateral motions. Unfortunately no experimental values of this influence are available. To the opinion of the authors the effect will not be so rigorous as suggested by the discussor. This effect can be determined by means of PMM test considering different positions of the rotation axis. However, up to now these tests have not been carried out by the authors.

Dr. Norrbin points out that the representation according to the "bis" system of reference is much more illustrative respecting the straight line stability as can be seen in Fig. 1 of his discussion. Nevertheless the SNAME-nomenclature is very widespread and used in a number of countries and the authors prefer to stick to this nomenclature. The authors agree with Dr. Norrbin's remark respecting the availability of results including propeller and rudder. Some results, however, have been published in [1] in case of full tanker models and probably it is possible to extrapolate some information of these tests to the length-beam series.

- [1] Glansdorp, C.C. Pijfers, J.G.L.
"Effect of Design Modifications on the natural course stability of full tanker models"
The Institution of Mechanical Engineers
17-21 April 1972; London.

HYDRODYNAMIC INTERACTIONS BETWEEN SHIPS

E. O. Tuck
University of Adelaide
Australia

J. N. Newman
M. T. T.
Cambridge, Massachusetts

ABSTRACT

Two theories are developed for predicting the hydrodynamic sway force and yaw moment acting on each of two ships while they are moving along parallel paths. In the first case, the two ship hulls are assumed slender, and moving with constant velocities which may differ. This case therefore includes examples such as steady parallel motion in a re-fuelling maneuver, passing of a slow vessel by a faster-moving vessel, passing in opposite directions, and passing of a moored vessel by a moving vessel. In the second case, the effects of shallow water are considered, but now with the restriction that the two vessels must be moving at the same velocity, so that the resulting hydrodynamic interaction is analogous to a two-dimensional bi-plane problem. In both theories the fluid is assumed to be ideal, and free-surface effects are ignored. Numerical examples are developed for both cases, and encouraging comparisons with existing experiments are noted.

NOMENCLATURE

A_j	Stripwise lateral added-mass per unit fluid density, of j th body
D	$\partial/\partial t - U_1 \partial/\partial x_1$
$r_j^\pm(x)$	Coordinates of upper (lower) surfaces of thin body
h	Fluid depth
j	Index denoting body 1 or 2
L_j	Length of j th body
m_j	Source strength
$N(t)$	Vertical (yaw) moment acting on body 1
n	Unit normal vector positive out of fluid domain
r_j	Polar radius from x_j -axis

S_j	Sectional-area function of j th (double) body
T_j	Draft of j th body
t	Time
U_j	Velocity of j th body
V	Lateral velocity field
x	Dummy variable
(x_0, y_0, z_0)	Cartesian coordinates fixed in space
(x_j, y_j, z_j)	Cartesian coordinates fixed with respect to the j th body ($j=1,2$)
$Y(t)$	Lateral (sway) force acting on body 1
$Y'(x, t)$	Stripwise lateral force on body 1
$\gamma_j(x)$	Vortex strength
ϵ	Slenderness parameter
η	Lateral separation between body centerplanes
ξ	Stagger
ϕ_j	Velocity potential of j th body alone
ϕ_{12}	Interaction potential

INTRODUCTION

Ship-to-ship interactions involving significant hydrodynamic forces and moments will occur when two vessels are moving in close proximity, or when a moving vessel passes a moored vessel. A particular case of special interest is the steady-state situation of two vessels moving in tandem, as in a re-fuelling maneuver, or of a single vessel moving parallel to a canal wall or channel bank. The "bank-suction" problem is related by the method of images, to the re-fuelling problem for two identical ships directly

abeam of each other, if the bank is a vertical wall. In each of these various problems, hydrodynamic interaction forces and moments may lead to collision, breakage of mooring lines, or grounding.

There have been only a few theoretical analyses or experimental investigations of the above problems in the past. For the steady-state bank-suction problem, or the equivalent re-fuelling problem, slender-body results have been developed by Newman (1,2) for axisymmetric bodies and for slender pointed bodies of arbitrary cross-section. For bodies moving at the same or different velocities, a two-dimensional theory for elliptical cylinders has been developed by Collatz (3). Newton (4) has reported experimental data for the re-fuelling problem, including measurements of the sway force and yaw moment on two ship hulls moving in tandem, and Oltmann (5) has performed experiments to compare with Collatz' (3) two-dimensional elliptic-cylinder theory. For the bank-suction problem other theories and experiments are surveyed by Norrbin (6).

In this paper we shall extend both the slender-body theory and the two-dimensional approach. In the former case, to be treated in Section 2, we allow the two vessels to be of arbitrary different slender forms, moving with constant velocities which may differ, and we relax the pointed-end condition to allow specifically for a low-aspect-ratio trailing-edge effect at the stern. The fluid depth may be infinite or finite, but must be large compared to the ships' beams and drafts. Similarly, the lateral separation between the two ships is assumed to be comparable to their lengths, and large compared to their beams. Subject to these restrictions it is then possible to develop a first-order theory for the interaction force and moment in which the two separate bodies are superposed, and each one is subject to the "exciting force and moment" due to the non-uniform field generated by the other hull.

The force and moment are analysed by developing a very general formula for the stripwise lateral force exerted on a slender body moving in the longitudinal direction through a lateral non-uniform flow field. The resulting expression is a generalization of classical slender-body theory, analogous to the use of G.I. Taylor's theorem (7) for the force on a body in an accelerating uniform field. This result appears to be of some interest in its own right, and possible applications to seakeeping theory will be noted.

By applying this formula to the ship-to-ship interaction problem, specific results are obtained for the

sway force and yaw moment acting on one body, due to the passage of a second, and calculations are presented for two ship hulls with parabolic sectional-area distributions and constant draft. Comparison is shown between these calculations and the experiments reported by Newton (4) for the re-fuelling problem, and qualitative agreement is found, but the experimental force and moment generally exceed those of the theory. Also illustrated in the computations are the effects of varying the two ships' speeds, it being noted that the force and moment acting on one ship depend linearly on the ratio of its speed to that of the passing ship. The force and moment are greater for ships moving in opposite directions, and, similarly, the force is greater on the slower of two vessels moving with unequal velocities. As a special case, it is noted that the force on a moored ship will exceed that acting on the same vessel while it is underway and moving in the same direction as the passing ship. Finally, the effects of finite depth are illustrated, and it is noted that the interaction force and moment are increased by finite-depth effects.

In order to pass to the important case of very shallow water, an entirely different approach must be made. Here, as noted by Tuck (8) for longitudinal motions, the flow is quasi-two-dimensional in horizontal planes, independent of the vertical coordinate except perhaps locally near the two bodies. Indeed, in the limit where the fluid depth equals the ships' drafts, and if the ships' sides are vertical, the flow is strictly two-dimensional everywhere, and this greatly simplifies the analysis. In this case, however, the interactions between the two bodies are more complex than for the deep water theory. The analysis is quite analogous to the two-dimensional symmetrical biplane problem, or the ground-effect problem of aerodynamics. This problem is solved here in Section 3 by an extension of classical thin-wing theory, using a distribution of sources to represent the thickness effects of the two bodies, and vortices to represent the interaction of the bodies with the lateral flow. A pair of coupled integral equations results, the solutions of which are unique if Kutta conditions are imposed at the "sterns", or trailing edges of the two bodies. Here we assume that the two bodies move in tandem with equal velocity, so the flow is steady-state; this avoids the well known complications of unsteady vortex shedding from the two trailing edges.

An efficient approach is outlined for the numerical solution of the coupled singular integral equations,

applied to bodies of rectangular thickness distribution, and compared with the experiments of Oltmann (5). Oltmann's experiments (5) were motivated by the theory of Collatz (3), which differs from the present thin-wing approach in that the two bodies are bluff ellipses, and there is no circulation or Kutta condition imposed. The present results seem in this respect to be an improvement on Collatz' theory, and this statement is confirmed by the improved qualitative agreement between the present theory and Oltmann's measurements. In fact, there is good quantitative agreement between the present calculations and Oltmann's experiments in the case of the side force, but for the yaw moment the agreement is not significantly better than that resulting from Collatz' theory.

Common to both the slender-body theory of Section 2 and the two-dimensional theory of Section 3 are the assumptions that the fluid is inviscid and incompressible, and that the Froude number is sufficiently small that free-surface effects can be ignored. It is also assumed that the lateral separation distance between the two bodies is comparable to their lengths, and large compared to their beams. In view of the rigid free-surface assumption a double-body model can be analysed in Section 2, and the two-dimensional assumption is valid in Section 3. The neglect of free-surface effects may be questioned, especially by ship hydrodynamicists who plow the more cultivated fields of wave resistance and seakeeping. However it is significant that in those cases the problem vanishes if there is no free surface, whereas here and more generally in the field of ship maneuvering, a non-trivial problem remains when the free surface is replaced by a rigid horizontal plane. Moreover, for conventional ships it may be more useful to concern ourselves in the future with overcoming the neglect of viscous effects, notably cross-flow separation forces, which are likely to be of more importance than the effects of the free surface.

Within the ideal-fluid, rigid-free-surface model utilized here, further generalizations are notable, and we shall outline in Section 4 the specific possibilities for considering the effects of a "gap" beneath the ship's bottom in shallow water, which requires modifications of the otherwise two-dimensional theory for shallow water, and the complications which result if the two bodies are in close proximity to each other, the present theories assuming on the contrary that the separation distances are comparable to the body lengths.

Before embarking upon the separate analyses of Sections 2 and 3, we first develop a consistent notation and reference system. In general the problem to be considered is that of two streamlined bodies, moving through an ideal fluid with constant velocities U_1, U_2 , along parallel paths separated by a constant distance η . It is convenient to use a separate moving coordinate system for each body, writing (x_j, y_j, z_j) as a set of Cartesian coordinates fixed in the j th body ($j=1,2$), such that x_j is the center-plane of symmetry and $x_j=0$ the mid-body station, with x_j measured forward and y_j to starboard. In accordance with the right-handed convention and the usual notation of ship maneuvering, the vertical z -coordinate is directed positive downward in Section 2, whereas in Section 3 the vertical coordinate is superfluous. It is conceptually convenient to relate these two moving reference frames to a fixed (x_0, y_0, z_0) system such that the later coincides with (x_1, y_1, z_1) at time $t=0$. Then it follows that

$$x_0 = x_1 + U_1 t = x_2 + U_2 t - \xi(0), \quad (1)$$

$$y_0 = y_1 = y_2 + \eta, \quad (2)$$

$$z_0 = z_1 = z_2, \quad (3)$$

where initially at time $t=0$, body 1 is $\xi(0)$ units ahead of body 2. At a general time t , body 1 is $\xi(t)$ units ahead of body 2, where

$$\xi(t) = x_2 - x_1 = (U_1 - U_2)t + \xi(0). \quad (4)$$

We shall call $\xi(t)$ the "stagger" of the bodies. Ultimately we shall be concerned with the lateral sway forces Y_j and yaw moments N_j , defined to be positive to starboard and for the bow turning to starboard respectively. These conventions and notations are illustrated in Figure 1, which is

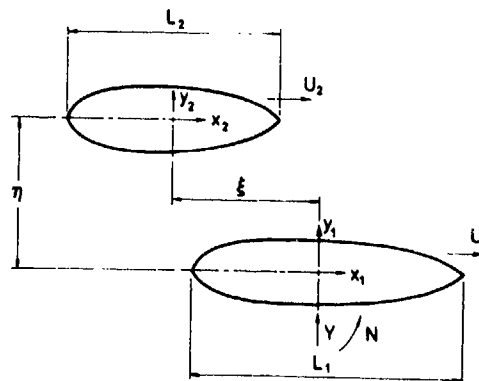


Figure 1 "Fish-eye" view of the two bodies and coordinate systems.

presented as a "fish-eye" view from below the vessels, in order that the coordinates (x_j, y_j) retain their usual orientation in the horizontal plane. The lengths of the two bodies are denoted by L_j and it is assumed throughout our analyses that the lateral dimensions of the bodies are of order ϵL_j , where ϵ is a slenderness parameter which is small compared to unity. We also assume that the separation distance η is $O(L_j)$, and hence is large compared to the lateral dimensions of the bodies.

2. INTERACTION BETWEEN TWO SLENDER BODIES

The problem to be considered here is that of two slender bodies, moving in a fluid of infinite depth or of depth comparable to the length of the bodies and large compared to their lateral dimensions. Initially we confine our attention to the infinite-depth case. Noting that the rigid-free-surface assumption leads to a "double-body" solution, i.e. the original ship hull beneath the plane of the free surface and an image hull above this plane, we shall consistently refer to the double body throughout this Section. The results are therefore applicable to other problems involving the motion of slender bodies through unbounded fluids, as well as to the aerodynamic problem of two passing automobiles or trains. In view of the original rigid-free-surface assumption, we assume that the plane $z=0$ is a plane of symmetry of the flow, and thus the double body has two planes of symmetry, but may be of arbitrary form in the longitudinal direction.

Since the lateral separation between the two bodies is large compared to their lateral dimensions (beam and draft) each body is in the other's far field, and to leading order in ϵ , the flow fields produced by each body can be computed as if the other were absent. This means that, in the j th co-ordinate system, the flow about the j th body is asymptotically steady, and can be estimated by standard methods of slender-body theory for steady motion of a single body in an infinite fluid. In particular, the perturbation velocity potential for flow past the j th body can be written

$$\phi_j(x_j, y_j, z_j) = \frac{U_j}{4\pi} \int_{L_j} \frac{S_j(x) dx}{[(x_j - x)^2 + r_j^2]^{\frac{3}{2}}} + O(\epsilon^4), \quad (5)$$

where $r_j = [y_j^2 + z_j^2]^{\frac{1}{2}}$ and $S_j(x)$ is the cross-section area curve of the j th body. Note that there is no

explicit time dependence in (5), the unsteadiness coming in only through the fact that the coordinate systems are moving in space. This expression is valid for $r_j = O(L_j)$ only. An estimate of ϕ_j for small r_j is

$$\phi_j(x_j, y_j, z_j) = -\frac{U_j}{2\pi} S_j(x_j) \log r_j + f_j(x_j) + O(\epsilon^4/r_j^2), \quad (6)$$

where $f_j(x_j)$ is a known function, dependent on $S_j(x_j)$. The "error" terms represented by $O(\epsilon^4/r_j^2)$ are due to local multipoles, etc. Note that these terms are not small at distances from the body comparable with its lateral dimensions, i.e. $r_j = O(\epsilon L_j)$. The formula (6) is in fact useful only in the intermediate region $\epsilon L_j \ll r_j \ll L_j$, where the error term is indeed small. In the true inner region $r_j = O(\epsilon L_j)$ we must in principle determine ϕ_j numerically for the given cross-section. Significant non-axisymmetric effects are present in the inner region, in contrast to the intermediate and far-field results (5,6) which are axisymmetric irrespective of the geometrical form of the bodies.

In the remainder of the analysis, we shall be considering the flow in the (x_1, y_1, z_1) co-ordinate system fixed in body 1. The complete solution in this co-ordinate system must be representable as the sum of an apparent uniform stream of magnitude U_1 in the $-x_1$ direction, the self-potential ϕ_1 , the other-body potential ϕ_2 , and an interaction potential measuring the (small) interaction effects. Thus we write

$$\phi(x_1, y_1, z_1, t) = -U_1 x_1 + \phi_1(x_1, y_1, z_1) + \phi_2(x_2, y_2, z_2) + \phi_{12}(x_1, y_1, z_1, t). \quad (7)$$

We note that the potentials ϕ_1 are $O(\epsilon^2)$, and shall find that $\phi_{12} = O(\epsilon^3)$.

The exact boundary condition on body 1 is simply $\partial\phi/\partial n = 0$, since body 1 appears fixed in the present co-ordinate system. Since the portion $-U_1 x_1 + \phi_1$ by definition already satisfies this condition, we must choose the correction term ϕ_{12} so as to cancel out the unwanted normal velocity induced by the potential ϕ_2 near body 1, i.e.

$$\frac{\partial\phi_{12}}{\partial n} = -\frac{\partial\phi_2}{\partial n} \text{ on body 1.} \quad (8)$$

Note that the particular interaction potential ϕ_{12} so determined is valid only in the neighbourhood of body 1, since the boundary condition on body 2 is still only satisfied to $O(\epsilon^4)$.

In order to satisfy (8), we need

the form of the potential ϕ_2 near $r_1 = 0$ i.e. near the axis of body 1, which (using (2) and a Taylor series expansion for small $y_1 = O(\epsilon)$) is given by

$$\phi_2(x_2, y_2, z_2) = \phi_2(x_2, -\eta, 0) + \frac{1}{2} \phi_{2yy}(x_2, -\eta, 0) + O(\epsilon^4). \quad (9)$$

The first term of (9) is simply the potential ϕ_2 evaluated on the axis $r_1 = 0$ of body 1, while the second term represents a uniform stream of magnitude

$$V(x_2) = \phi_{2y_2}(x_2, -\eta, 0) = \frac{U_2 \eta}{4\pi} \int_{L_2} \frac{S_2'(x) dx}{[(x_2 - x)^2 + \eta^2]^{\frac{3}{2}}}, \quad (10)$$

equal to the cross-flow velocity due to the presence of body 2, evaluated on the axis of body 1. Note that the term $\frac{1}{2} \phi_{2yy}$ of the Taylor expansion vanishes, because of the assumed symmetry of the flow about the plane $z_2 = 0$.

The boundary condition (8) does not involve the first term of (9) since $\phi_2(x_2, -\eta, 0)$ is a constant in each cross section $x_1 = \text{constant}$, so that (8) and (9) together imply

$$\frac{\partial \phi_{12}}{\partial \eta} = -V \frac{\partial y_1}{\partial \eta}, \quad \text{on body 1.} \quad (11)$$

This means physically that ϕ_{12} is the velocity potential for a lateral translation of velocity $-V$ of each section $x_1 = \text{constant}$ of body 1. Slenderness guarantees that ϕ_{12} is a two-dimensional potential in the (y, z) plane. Thus we can write

$$\phi_{12} = -V(x_2) \phi(x_1, y_1, z_1), \quad (12)$$

where

$$\frac{\partial \phi}{\partial \eta} = \frac{\partial y_1}{\partial \eta} \quad \text{on body 1.} \quad (13)$$

The canonical potential ϕ can only be determined numerically, for a general cross section. For bodies of revolution $r_1 = r_0(x_1)$ however, it clearly takes the value

$$\phi = r_0^2 \left(\frac{y_1}{r_1^2} \right), \quad (14)$$

and for general bodies we have (c.f. Batchelor (8)) the far-field result

$$\phi \rightarrow - \left(\frac{S_1 + A_1}{2\pi} \right) \left[\frac{y_1}{r_1^2} + O(r_1^{-3}) \right], \quad (15)$$

where S_1 is the cross-section area, as before, and ρA_1 the added mass per

unit length. Equations (14) (15) are in agreement for bodies of revolution, since $A_1 \equiv S_1 = \pi r_0^2$.

In summary, near body 1 we have

$$\phi = -U_1 x_1 + \phi_1(x_1, y_1, z_1) + \phi_2(x_2, -\eta, 0) + V(x_2)[y_1 - \phi(x_1, y_1, z_1)]. \quad (16)$$

Computation of Force and Moment

Once a suitable potential is obtained, the pressure on body 1 can be evaluated and hence the force distribution can be obtained by integration. On substitution of (16) into the unsteady Bernoulli equation

$$p = -\rho[\phi_t + \frac{1}{2}(\nabla\phi)^2 - \frac{1}{2}U_1^2], \quad (17)$$

we obtain the result

$$p = p_1 + p_2 + p_{12} + O(\epsilon^4), \quad (18)$$

where

$$p_1 = -\rho(U_1 \phi_{1x_1} + \frac{1}{2} \phi_{1y_1}^2 + \frac{1}{2} \phi_{1z_1}^2) = O(\epsilon^2) \quad (19)$$

is the pressure due to body 1 alone,

$$p_2 = -\rho D \phi_2(x_2, -\eta, 0) = O(\epsilon^2) \quad (20)$$

is the pressure due to body 2 alone, evaluated on the axis of body 1, and

$$p_{12} = -\rho[(y_1 - \phi)DV + U_1 V \phi_{x_1} + V \phi_{1y_1} - V(\phi_{1y_1} \phi_{y_1} + \phi_{1z_1} \phi_{z_1})] \quad (21)$$

is the $O(\epsilon^3)$ interaction pressure. Here

$$D = \frac{\partial}{\partial t} - U_1 \frac{\partial}{\partial x_1}$$

denotes the time derivative in the moving reference frame of body 1.

From symmetry considerations neither p_1 nor p_2 can induce lateral forces on body 1¹. Thus we shall concern ourselves only with p_{12} , which supplies a force dY on each section dx of the body where

$$Y'(x_1) \equiv \frac{dY}{dx_1} = \int_C p_{12} n_y dl. \quad (22)$$

¹ Note, however, that p_2 will cause a longitudinal or surging force on body 1, which is not considered in the present paper. In the special case where body 1 is fixed and axisymmetric, both the longitudinal and lateral forces have been computed in an unpublished work by S. Wang using Lagally's theorem. Wang's lateral-force formula agrees with that to be presented here.

Substitution of (21) in (22) results in a pressure integral on the contour C which would be complicated to work out directly, and which moreover requires the knowledge of the local multipole effects on the potentials ϕ_1 and ϕ_{12} which are not included in (6) and (15). It is possible to proceed by an indirect path, however, using conservation of momentum arguments or Green's theorem; the mathematical steps are essentially identical to those carried out by Lighthill (10) and reproduced by Newman and Wu (11), and an alternative three-dimensional derivation has been presented by Newman (12). These derivations are valid for a single slender body which undergoes lateral oscillations $V_b(x,t)$ in a fluid which is at rest at infinity except for a uniform longitudinal stream, and thus one must now include the inhomogeneous lateral flow at infinity which corresponds to the lateral stream potential $V(x_2, y_1)$. However the mathematical steps are sufficiently straightforward that it is not thought to merit a derivation here, and instead we present a physical argument for the final result.

We note first that if $V=0$, but instead the body moves with lateral displacement $y=y_b(x,t)$, and corresponding lateral velocity $V_b = Dy_b$, then the differential lateral force acting on the body is (10,11,12)

$$Y'(x,t) = -\rho D(V_b A), \quad (23)$$

where $\rho A(x)$ is the added-mass per unit length. Now if the inhomogeneous lateral flow $V(x,t)$ is superposed, two additional force components will result. First there will be a contribution due to the hydrodynamic disturbance of the incident flow by the body, which must vanish when $V=V_b$, and this implies

$$-\rho D[(V_b - V)A].$$

In addition we note that the non-uniform incident flow field results in a lateral pressure gradient

$$\partial p / \partial y = -\rho D(V),$$

and a corresponding "buoyancy force" equal to the negative product of this pressure gradient with the displaced volume of fluid. Thus, adding these two force components, the general expression for the differential lateral force acting on a body which moves with lateral velocity $V_b(x,t)$ in a non-uniform lateral stream of velocity $V(x,t)$ is

$$Y'(x,t) = \rho S D(V) - \rho D[(V_b - V)A] \quad (24)$$

Finally, for the present situation where body 1 is fixed, with $V_b=0$, and $S=S_1$, $A=A_1$, it follows that

$$Y' = \rho S_1 D(V) + \rho D(V A_1) \quad (25)$$

Equation (25) is the desired result for the differential lateral force acting on a slender body which is fixed in an incident flow of constant longitudinal velocity and non-uniform lateral velocity.

Before using the result (25) to find the interaction force and moment due to a second passing vessel, it may be appropriate to discuss some general aspects of equations (24) and (25). First we note that these formulae require that the body be geometrically slender, and pointed at the upstream end or bow, but it is not necessary for the tail or stern to be pointed and, as in the analogous formulae of slender lifting surfaces, (24) and (25) can be applied to bodies with finned trailing edges at the downstream end, from which vortex sheets trail downstream in the fluid. There is a wellknown analogy between the lateral oscillations of a ship hull in the horizontal plane, and the corresponding motions of a low-aspect-ratio double body, the trailing edge of the latter effectively being replaced by the rudder and deadwood of the ship and its image. This lifting effect is significant in general, and must be retained in the present analysis of lateral interaction forces and moments.

Equations (24) and (25) can also be applied to other problems involving nonuniform external fields, the most obvious example being the seakeeping problem where V_b represents the rigid-body motions of the vessel, and V represents the velocity field of the incident wave system. Thus (24) and (25) may be used to solve the seakeeping problem for submerged slender bodies, including the effects of tail-fin lifting surfaces.

For bodies with pointed sterns and no shed vorticity downstream, Lagally's theorem may also be applied to find the force and moment on the body, as in Wang's study of the ship-to-ship interaction forces, and Cummins' (13) analysis of wave forces on submerged bodies. However Lagally's theorem will give incorrect results if the tail span is non-zero. This point is emphasized because in recent years it has become somewhat common in seakeeping theory to extend formal strip-theory analyses to include transom-stern configurations, and such procedures are inherently dangerous unless one is sufficiently shrewd or lucky to integrate by parts and retain the correct end effects at the stern. A preferable approach to this problem would be to extend (24) to the case of a floating body, where S depends on time and the body can no longer be surrounded by a closed control volume, without careful

consideration of the free surface; however this analysis is obviously beyond the scope of the present paper.

Now let us use (25) to evaluate the ship-to-ship interaction force on body 1. Integrating over L_1 gives the total force

$$Y = \rho \int_{L_1} \{D(VA_1) + S_1 D(V)\} dx_1. \quad (26)$$

Noting that

$$D[V(x_2)] = -U_2 V'(x_2), \quad (27)$$

it follows that

$$\begin{aligned} Y &= -\rho \int_{L_1} [U_2 V'(x_1 + \xi)(S_1 + A_1) \\ &\quad - U_1 V(x_1 + \xi)A_1'] dx_1 \\ &= \rho \int_{L_1} [U_2 S_1' + (U_2 - U_1)A_1'] V(x_1 + \xi) dx_1 \\ &\quad + \rho U_2 V(-\frac{1}{2}L + \xi)A_1(-\frac{1}{2}L), \end{aligned} \quad (28)$$

where we assume that $S_1(\pm \frac{1}{2}L) = 0$ and $A_1(\pm \frac{1}{2}L) = 0$, whereas (to allow for finite trailing-edge span) $A_1(-\frac{1}{2}L)$ may be non-zero.

Using (10) to evaluate V , we obtain the final expression for the interaction force,

$$\begin{aligned} Y &= \frac{\rho U_2 \eta}{4\pi} \int_{L_1} [U_2 S_1'(x_1) + (U_2 - U_1)A_1'(x_1)] \\ &\quad \cdot \int_{L_2} \frac{S_2'(x_2) dx_2}{[(x_2 - x_1 - \xi)^2 + \eta^2]^{\frac{3}{2}}} \\ &\quad + \frac{\rho U_2 \eta}{4\pi} A_1(-\frac{1}{2}L) \int_{L_2} \frac{S_2'(x_2) dx_2}{[(x_2 + \frac{1}{2}L - \xi)^2 + \eta^2]^{\frac{3}{2}}}, \end{aligned} \quad (29)$$

and similarly, for the yawing moment,

$$\begin{aligned} N &= \frac{\rho U_2 \eta}{4\pi} \int_{L_1} [x_1 U_2 S_1'(x_1) + x_1 (U_2 - U_1)A_1'(x_1) \\ &\quad + U_2 S_1(x_1) + U_2 A_1(x_1)] \end{aligned}$$

$$\begin{aligned} &\cdot \int_{L_2} \frac{S_2'(x_2) dx_2}{[(x_2 - x_1 - \xi)^2 + \eta^2]^{\frac{3}{2}}} \\ &- \frac{\rho U_2 \eta}{8\pi} LA_1(-\frac{1}{2}L) \int_{L_2} \frac{S_2'(x_2) dx_2}{[(x_2 + \frac{1}{2}L - \xi)^2 + \eta^2]^{\frac{3}{2}}}. \end{aligned} \quad (30)$$

Both the force (29) and moment (30) are of the form $aU_1 U_2 + bU_2^2$, where a and b depend on the body geometries and separation distances. Thus the force and moment acting on body 1 will vanish if $U_2 = 0$, and also if $U_1/U_2 = -a/b$.

In the first case, there is no force on body one if body two is stationary, or no force on a passing vessel due to its interaction with a stationary vessel. This result appears to be unreasonable, on physical grounds, but may be reconciled with our slender-body analysis by concluding that the correct force in this case would be of higher order in ϵ . Indeed, the present results indicate for $U_2 \neq 0$ a force and moment of order ϵ^4 , whereas it is not difficult to establish that the corresponding results for $U_2 = 0$ would be $O(\epsilon^6)$.

The vanishing of the force and moment at a second speed, dependent on the ratio a/b , is more easily accepted in general, since the ratio a/b will depend on the separation distance and stagger, and vanishing of the force or moment for specific combinations of the speeds and geometrical configuration corresponds only to cross-over points between positive and negative values of the force or moment. However one special case where the force vanishes irrespective of the separation and stagger is that of a body of revolution, without tail fins, where $A_1 = S_1$, and thus from (29) it follows that the lateral force vanishes for all values of the stagger and separation distances, provided that $U_1/U_2 = 2$. In other words, the lateral interaction force on a body of revolution will always be zero if it passes a second body of arbitrary slender form at precisely twice the second body's speed! Again this result may appear to be surprising on physical grounds, and from the mathematical viewpoint higher-order terms will again become significant when the leading-order force vanishes. Moreover, this particular result is restricted to axisymmetric bodies, but we anticipate that for more general slender bodies the lateral interaction force may be relatively small in the vicinity of the point where $U_1 = 2U_2$.

Approximation for small lateral separation

Asymptotic approximations of the force (29) and moment (30) can be derived if the lateral separation η is small or large compared to the body lengths. The case of large separation is of limited interest from the practical standpoint. (It is easily shown that Y and N are $O(\eta^{-4})$ as $\eta \rightarrow \infty$.) The case of small separation is more interesting, since this is the situation of practical importance, and also because it is interesting to study the relationship (and possible matching) between the present results valid for $\eta = O(L)$, and the complementary results of Newman (1) where η is taken to be small, of order ϵ , from the very beginning.

It is clear, from (29) and (30) that, as $\eta \rightarrow 0$, the kernel function reduces to a delta function, i.e.,

$$\eta[x^2 + \eta^2]^{-\frac{3}{2}} \approx \frac{2}{\eta} \delta(x),$$

as can be confirmed by integration. Thus it follows that

$$Y \approx \frac{\rho U_2}{2\pi\eta} \int_L [U_2 S_1'(x_1) + (U_2 - U_1) A_1'(x_1)] \cdot S_2(x_1 + \xi) dx_1 + \frac{\rho U_2^2}{2\pi\eta} A_1(-\frac{1}{2}L) S_2'(-\frac{1}{2}L + \xi), \quad (31)$$

with a similar expression for the moment. It will be noted that, in this approximation, the interaction force and moment are inversely proportional to the separation distance η . Note also that in this case where η is small, the interaction force and moment vanish if there is no overlap between the two vessels.

The complementary theory, valid for $\eta = O(\epsilon)$, will generally require a numerical solution for the two-dimensional flow in the inner region occupied simultaneously by the two vessels. However a special case where simple closed-form results are obtained is that of a pair of identical axisymmetric bodies, moving in tandem with equal velocities and zero stagger or, equivalently, one axisymmetric body moving parallel to a wall. This problem has been solved by Newman (1) for the case where $\eta = O(\epsilon)$, and in the present notation the force and moment are given by

$$\left. \begin{matrix} Y \\ N \end{matrix} \right\} = \frac{\rho U^2}{2\pi} \int_L [S'(x)]^2 \left[\eta^2 - \frac{4}{\pi} S(x) \right]^{-\frac{1}{2}} \left(\frac{1}{x} \right) dx. \quad (32)$$

For $\eta \rightarrow \infty$ in this "inner" theory, the second term in the inverse square root is neglected and thus (32) reduces precisely to the appropriate special case of (31) where the speeds and bodies are identical and stagger is zero. A similar matching is readily demonstrated for the "inner limit of the outer moment".

Thus, for the special case noted above, we have explicit inner and outer theories which overlap. Unfortunately there is no simple way to generalize the inner result (32) for non-axisymmetric bodies, although the bi-polar coordinate system used in Reference (1) might still be applied to extend (32) to the unsteady passing problem for two axisymmetric bodies.

Finite Depth Effects

If the fluid domain is bounded by horizontal planes at $z = \pm h$, and h is $O(1)$ with respect to the slenderness parameter ϵ , the method of images can be used to generalize the above infinite-depth theory, simply by adding to the original source and dipole potentials in (25) and (15) an infinite system of image singularities at $z = \pm 2nh$, $n = 1, 2, \dots, \infty$. It is unnecessary to repeat the subsequent analysis, if one notes simply that (10) should be replaced by

$$V(x_2) = \frac{U_2 \eta}{4\pi} \sum_{n=-\infty}^{\infty} \int_{L_2} \frac{S_1'(x) dx}{[(x_2 - x)^2 + \eta^2 + 4n^2 h^2]^{\frac{3}{2}}}. \quad (33)$$

Thus, in general, if $Y(\eta, h)$ denotes the interaction force in depth h with lateral separation distance η , it is clear from (29) that

$$Y(\eta, h) = \eta \sum_{n=-\infty}^{\infty} \left[\frac{Y(u_n, \infty)}{u_n} \right]_{u_n = (\eta^2 + 4n^2 h^2)^{\frac{1}{2}}}, \quad (34)$$

with a similar expression for the moment N . This provides a convenient computational scheme for evaluation of the finite-depth effects on Y and N , for fluid depths which are large compared to the beam and draft of the vessels.

Numerical results

To simplify the evaluation of Y and N we assume that the two bodies have parabolic distributions of sectional area S_j , and constant values of their added-mass coefficients A_j . (For a ship the latter assumption is roughly equivalent to assuming constant draft along the length.) Thus we take

$$S_j(x_j) = S_j(0)(1-x_j^2/L_j^2), \quad (35)$$

where $S_j(0)$ is the mid-ship sectional area of the double body, and

$$A_j(x_j) = \pi T_j^2, \quad (36)$$

where T_j is the semi-span of the double body, or draft of the ship hull, at the tail $x_j = -L_j$. The derivative of S_j is elementary:

$$S_j' = -8S_j(x_j/L_j^2), \quad (37)$$

but the derivative of A_j must be evaluated with caution. In the spirit of slender lifting-surface theory, it is appropriate to impose a weak Kutta condition at the trailing edge, by regarding A_j as a continuous function at $x = -L$ (c.f. Newman and Wu, 1973). Thus, in an analogous manner to a low-aspect-ratio rectangular lifting surface, $A_j' = 0$ except at the nose or leading edge, where A_j must jump between the finite value πT_j^2 on the body and zero ahead of the body. Hence it follows that

$$A_j'(x_j) = -\pi T_j^2 \delta(x_j - L_j/2), \quad (38)$$

where δ denotes the Dirac delta-function.

Substitution of equations (35-38) in (29-30) gives expressions for the sway force and yaw moment in terms of elementary integrals. Evaluation of these integrals yields complicated but straightforward algebraic expressions for the force and moment, which have been evaluated on a digital computer. Results based on this computer program are shown in Figures 2-6, for the two ships (A and B) for which Newton (4) has reported experimental results. Ship A is the battleship KING GEORGE V, of length 740 feet, beam 103 feet, draft 29.3 feet, and displacement 36,890 tons. Ship B is the R.F.A. OLNA, of length 567 feet, beam 70 feet, draft 30 feet, and displacement 23,570 tons. These two vessels' midship section areas are 3050 and 2075 square feet, respectively. Their sectional area distributions depart only slightly from parabolic curves, and it is notable that Ship A is slightly fuller, so that these departures should tend to cancel out.

Figures 2 and 3 show the comparison between theory and experiments for the sway force and yaw moment respectively, in the steady case $U_1 = U_2$ and for a full-scale lateral separation of 136 feet (fifty feet clearance between the two ships when abeam). Generally speaking, the peak values of the force

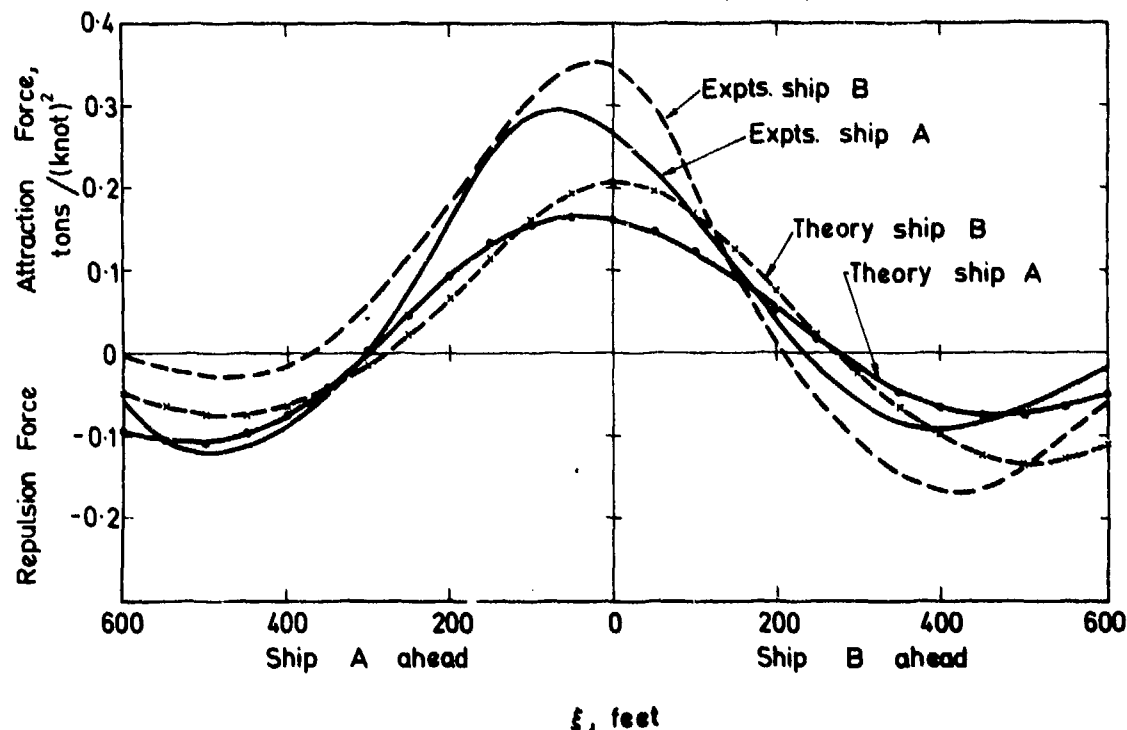


Fig. 2. Sway forces on two ships, and corresponding experimental results of Newton (4).

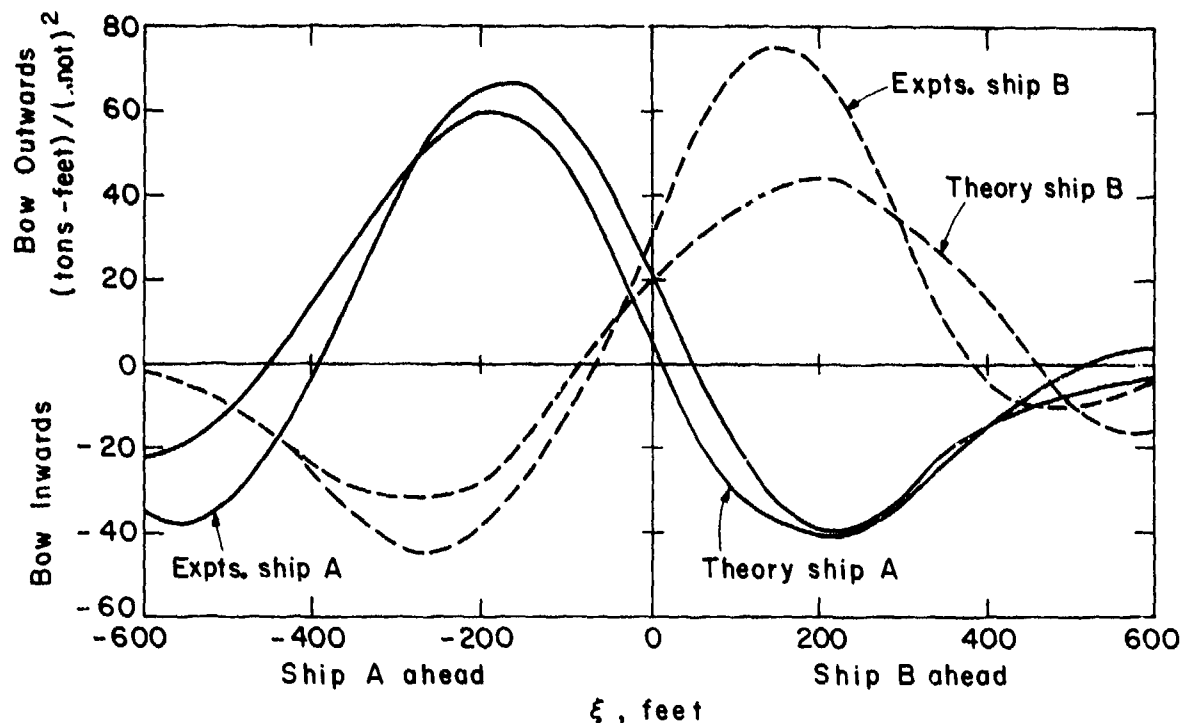


Fig. 3. Yaw moments on two ships, and corresponding experimental results of Newton (4).
Note: The theoretical portion of this figure has been revised as noted in the discussion.

occur virtually when the two vessels are abeam, the force then being one of attraction between the two vessels. It is disappointing to note that at this peak value the theory underpredicts the experimental measurements by a factor of approximately 40%. However the curves are qualitatively similar, and the agreement of the repulsion forces which occur when the ships are clear of each other, or only slightly overlapped, is more satisfactory.

The comparison of the moments shown in Figure 3 is less satisfactory*, although it will be noted that good agreement exists for the moment on the aft ship when the stagger or longitudinal separation exceeds about one-third of the ship length. This suggests the possible hypothesis that viscous separation forces are significant, since these would be expected only on the afterbody of the two ships, whereas the turning moment on the aft ship will arise primarily from lateral forces exerted on its forebody and so should be less sensitive to the effects of separation.

Figure 4 shows the effects of varying lateral separation or clearance on the sway force when the two vessels are abeam ($\xi=0$). Once again the qualitative agreement with experiments is very good, but the theoretical results are less satisfactory. See discussion.

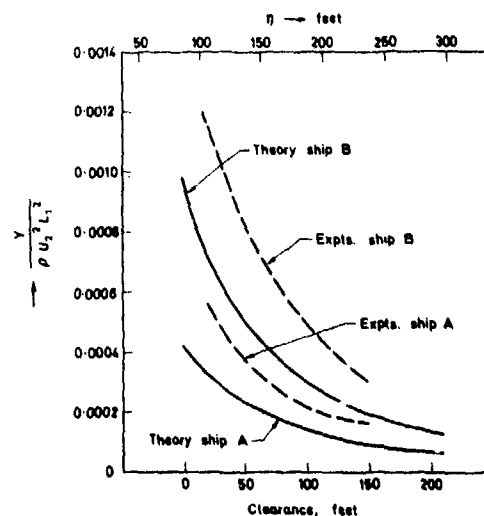


Fig. 4. Peak sway force as a function of separation distance. The lower abscissa shows actual clearance between hulls.

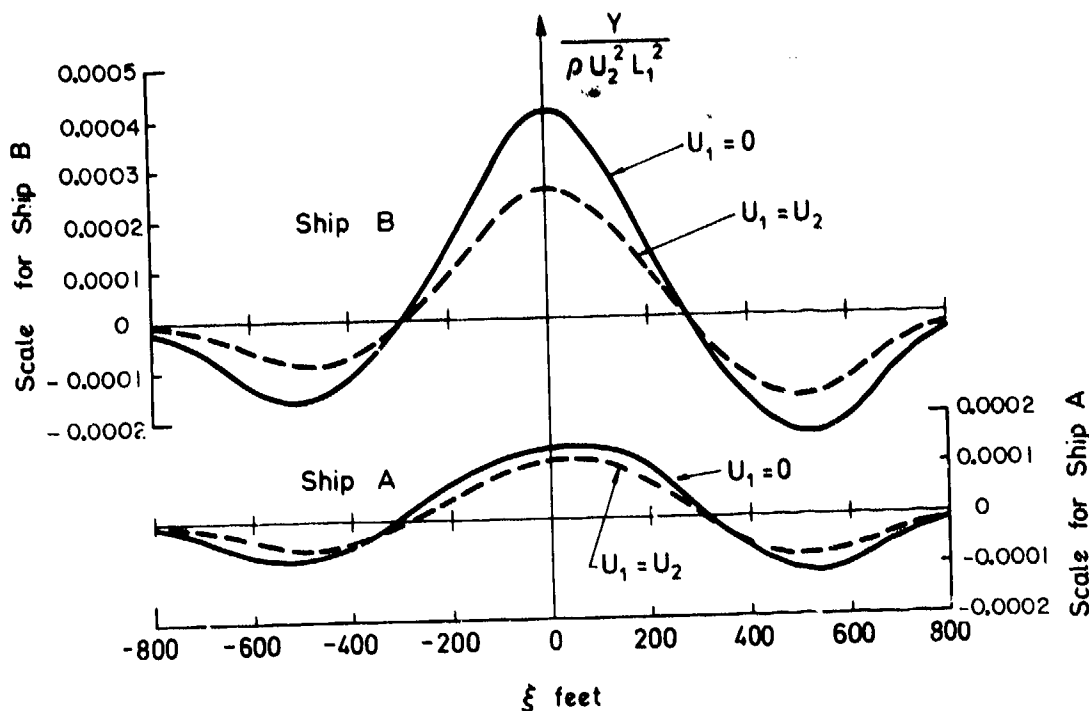


Fig. 5. Theoretical sway forces on two ships moving at the same or different speeds. Note that U_1 denotes the speed of the ship on which the force is measured.

sults are 30-40% lower than the experiments. Figure 5 shows the effect on the sway force of different velocities for the two ships, under the same conditions as in Figure 2. It is noteworthy that the force on the smaller vessel, Ship B, is increased by about 50% if it is moored ($U_1 = 0$) rather than moving at the same speed as Ship A, but in the converse case of the larger vessel, ship B, the effect of its own speed is less important. Recalling that the force on each ship is a linear function of its own velocity, more general results can be derived by linear extrapolation or interpolation in Figure 5. In particular it is obvious that the force on each ship will be greater if they pass in opposite directions, as compared to moving in the same direction. Also it is noted that the force on Ship B will be minimized if it moves at a speed slightly greater than twice the speed of ship A. In this connection we recall that if ship B was a body of revolution, the force on it would vanish precisely when its speed was two times that of the second ship.

Finally, in Figure 6, we show the effects of finite depth of water, by plotting the ratio of the sway force to its value in infinite depth. The curves in this figure are essentially universal, in that they are identical, to within graphical accuracy, for ships

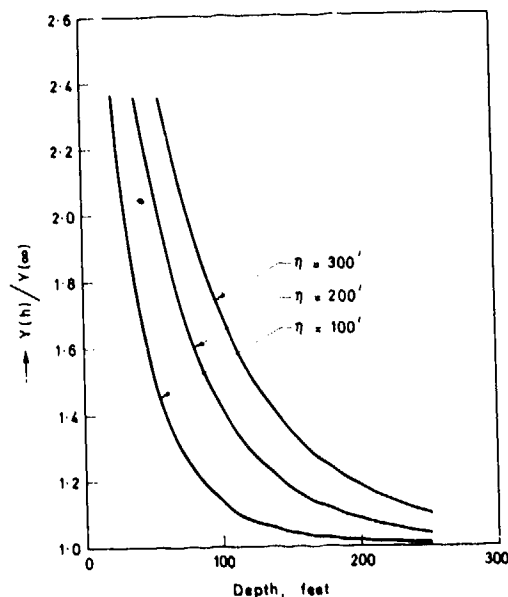


Fig. 6. Finite-depth effects on peak force.

A and B, and do not depend significantly on the ratio between the two ships' speeds. In general the effects of finite depth are to increase the sway force but this increase is less than 5% unless the fluid depth is less than the lateral separation distance between the two ships' centerlines.

3. INTERACTION BETWEEN THIN BODIES IN STEADY TWO-DIMENSIONAL FLOW

Derivation of Integral Equations

We now consider steady two-dimensional flow about a pair of thin bodies which are separated laterally by a fixed distance $y = \eta$ and longitudinally by a fixed distance ξ . Steadiness demands that the velocities of the two bodies be the same. With this restriction (i.e. $U_1 = U_2 = U$), Figure 1 still describes the flow situation, but now in two dimensions. For convenience, a stream of velocity U is superposed in the $-x$ direction to bring the two bodies to rest. We shall retain where convenient the (x_1, y_1) and (x_2, y_2) co-ordinates as in Figure 1.

We allow at first a degree of lateral asymmetry of the separate body surfaces, writing as the equation of body "j", $j=1,2$,

$$y_j = f_j^\pm(x_j), \quad -\frac{1}{2}L_j < x_j < \frac{1}{2}L_j, \quad (39)$$

with a + sign for the upper surface and a - sign for the lower surface. However the two bodies are assumed to be thin, i.e. all f_j^\pm are small compared with L_j and η . The requirement on η means that each body is in the far field of the other, as in the previous section.

However, because of the reduced freedom of flow in two dimensions relative to three dimensions, it is no longer true that the influence of body 2 on body 1 can be calculated using the singularity distribution which generates body 2 in the absence of body 1. In fact in the limit as $f_j^\pm \rightarrow 0$, the bodies shrink to zero-thickness cuts in the $(x-y)$ plane, which are formally representable as distributions of sources and vortices (or lateral dipoles) of strength determined by the boundary conditions. The source strength is related as in conventional thin-wing theory to the local slope of the thickness distribution curve, and no interaction occurs between body 1 and body 2 in its determination. On the other hand, the vortex strength at any particular point on a body is related to the effective local angle of attack at that point. This in turn depends on the sum of lateral velocities

induced by the vortices at all points on the same body, by the source distribution modelling thickness of the second body (as in Section 2 in three dimensions), and also (in contrast to Section 2) by the vortex distribution of the second body, which itself only exists because of the presence of the first body. Mathematically, this complex inter-relation implies that the vortex strengths satisfy coupled integral equations, and must be determined simultaneously.

The disturbance velocity potential due to the two bodies can be written

$$\phi = \frac{1}{2\pi} \sum_{j=1}^2 \int_{-\frac{1}{2}L_j}^{\frac{1}{2}L_j} dx \{ m_j(x) \log \sqrt{(x_j-x)^2 + y_j^2} + \gamma_j(x) \arctan \frac{y_j}{x_j-x} \}, \quad (40)$$

where $m_j(x)$ is the source strength and $\gamma_j(x)$ the vortex strength generating body j. The linearized boundary condition to be satisfied on the (+) surface of body 1 is

$$\lim_{y_1 \rightarrow 0} \phi_{y_1} = -U f_1^{+\prime}(x_1), \quad (41)$$

and that on body 2 is

$$\lim_{y_2 \rightarrow 0} \phi_{y_2} = -U f_2^{+\prime}(x_2). \quad (42)$$

On substitution of (40) into (41) we obtain

$$-U f_1^{+\prime}(x_1) = \frac{1}{2\pi} \int_{-\frac{1}{2}L_1}^{\frac{1}{2}L_1} dx \frac{\gamma_1(x)}{x_1-x} + \frac{1}{2\pi} \int_{-\frac{1}{2}L_2}^{\frac{1}{2}L_2} dx \left[m_2(x) \frac{-\eta}{(x_2-x)^2 + \eta^2} + \gamma_2(x) \frac{x_2-x}{(x_2-x)^2 + \eta^2} \right], \quad (43)$$

and (42) gives

$$-U f_2^{+\prime}(x_2) = \frac{1}{2\pi} \int_{-\frac{1}{2}L_2}^{\frac{1}{2}L_2} dx \frac{\gamma_2(x)}{x_2-x} + \frac{1}{2\pi} \int_{-\frac{1}{2}L_1}^{\frac{1}{2}L_1} dx \left[m_1(x) \frac{\eta}{(x_1-x)^2 + \eta^2} + \gamma_1(x) \frac{x_1-x}{(x_1-x)^2 + \eta^2} \right]. \quad (44)$$

Subtracting the + and - parts of (43) and (44) implies that

$$m_j(x_j) = -U \frac{d}{dx_j} [f_j^+(x_j) - f_j^-(x_j)] \quad (45)$$

which is the usual prescription for the source strength in terms of the local slope of the thickness $f_j^+ - f_j^-$ of the separate bodies. Thus the source strengths are entirely determined. On the other hand, on adding the + and - parts, we obtain:

$$\frac{1}{\pi} \int_{-\frac{1}{2}L_1}^{\frac{1}{2}L_1} \frac{dx \gamma_1(x)}{x_1 - x} + \frac{1}{\pi} \int_{-\frac{1}{2}L_2}^{\frac{1}{2}L_2} \frac{dx \gamma_2(x)}{(x_2 - x)^2 + \eta^2} = g_1'(x_1) \quad (46)$$

and

$$\frac{1}{\pi} \int_{-\frac{1}{2}L_1}^{\frac{1}{2}L_1} \frac{dx \gamma_1(x)(x_1 - x)}{(x_1 - x)^2 + \eta^2} + \frac{1}{\pi} \int_{-\frac{1}{2}L_2}^{\frac{1}{2}L_2} \frac{dx \gamma_2(x)}{x_2 - x} = g_2'(x_2), \quad (47)$$

where

$$g_1'(x_1) = -U \frac{d}{dx_1} [f_1^+(x_1) + f_1^-(x_1)] + \frac{\eta}{\pi} \int_{-\frac{1}{2}L_2}^{\frac{1}{2}L_2} \frac{dx m_2(x)}{(x_2 - x)^2 + \eta^2} \quad (48)$$

and

$$g_2'(x_2) = -U \frac{d}{dx_2} [f_2^+(x_2) + f_2^-(x_2)] - \frac{\eta}{\pi} \int_{-\frac{1}{2}L_1}^{\frac{1}{2}L_1} \frac{dx m_1(x)}{(x_1 - x)^2 + \eta^2}. \quad (49)$$

In interpreting the above equations, we must always keep in mind the relation $x_2 - x_1 = \xi$.

Since the source strengths $m_j(x)$ are known quantities, the functions $g_j'(x_j)$ appearing on the right of (46) and (47) are entirely known. Each of these functions, as defined in (48) and (49) consists of the sum of two terms. The first contribution is proportional to the camber $\frac{1}{2}(f_j^+ + f_j^-)$ of the individual bodies and is independent of their thickness. For example, this enables computation of the lift on a bi-plane wing, consisting of two zero-thickness plates at an angle of attack.

Of more interest in the present context is the contribution to $g_j'(x_j)$ from thickness effects, as represented by the integrals involving $m_j(x)$. If the separate bodies possess lateral symmetry and have parallel center planes, the camber vanishes, but

nevertheless there is still a non-zero net lateral force and moment in general, due to thickness-induced interaction effects. This effect may be studied by setting the camber portions of $g_j(x_j)$ to zero; any additional camber or angle of attack may be computed separately and added to the thickness effect subsequently. An alternative interpretation is that the thickness of body 2 induces an effective camber or angle of attack on body 1 (measured by the term of g_1 in m_2), even if body 1 is itself uncambered.²

In any case, whatever is the cause for existence of non-zero forcing terms, equations (46), (47) are mathematically a pair of coupled singular integral equations. The kernels possess a Cauchy or simple-pole type of singularity and hence their solution is not uniquely specified without further end conditions. The degree of non-uniqueness is equivalent to two arbitrary constants, associated with two linearly-independent solutions of the homogeneous problem with $g_1 = g_2 = 0$, and physically analogous to the circulation around each body.

These arbitrary constants are to be determined by supplying Kutta conditions at each trailing edge, of the form

$$\gamma_j(-\frac{1}{2}L_j) = 0, \quad j = 1, 2. \quad (50)$$

Physically, this arises from the fact that $\gamma_j(x_j)$ is proportional to the loading or pressure jump across the body center plane, which must vanish at the trailing edge. For example, from (40), the jump in the tangential disturbance velocity across body 1 is given by

$$\Delta u = \phi_{x_1}(x_1, 0_+) - \phi_{x_1}(x_1, 0_-) = -\gamma_1(x_1), \quad (51)$$

and hence the jump in pressure is

$$\Delta p = \rho U \Delta u = -\rho U \gamma_1(x_1), \quad (52)$$

as stated above. The net y_1 -directed force on body 1 is

$$Y = - \int_{-\frac{1}{2}L_1}^{\frac{1}{2}L_1} \Delta p dx_1 = \rho U \int_{-\frac{1}{2}L_1}^{\frac{1}{2}L_1} \gamma_1(x_1) dx_1, \quad (53)$$

² A further consequence, exploited by Lin in work to be presented at this Symposium on unstaggered ($\xi=0$) catamarans, is that for given thickness distributions m_j , there always exist camber distributions $f_j^+ + f_j^-$ which make $g_j' = 0$, and hence allow solutions with $\gamma_j = 0$.

and the net moment about the z -axis is

$$N = \rho U \int_{-\frac{1}{2}L_1}^{\frac{1}{2}L_1} x_1 \gamma_1(x_1) dx_1. \quad (54)$$

A particular case of interest is that of identical bodies, in which $L_1=L_2=L$ and $m_1(x)=m_2(x)=m(x)$. If we consider only the uncambered case, then

$$g_1'(x_1) = g'(x_2) = g'(x_1 + \frac{1}{2}), \quad (55)$$

and

$$g_2'(x_2) = -g'(x_1) = -g'(x_2 - \frac{1}{2}), \quad (56)$$

where

$$\begin{aligned} g'(x_j) &= \frac{n}{\pi} \int_{-\frac{1}{2}L}^{\frac{1}{2}L} dx \frac{m(x)}{(x_j - x)^2 + \eta^2} \\ &= -\frac{2U\eta}{\pi} \int_{-\frac{1}{2}L}^{\frac{1}{2}L} \frac{dx f'(x)}{(x_j - x)^2 + \eta^2}, \quad (57) \end{aligned}$$

and $f(x)$ is the half-thickness of the identical bodies. The coupled integral equations (46), (47) can now be written in the form

$$\begin{aligned} \frac{1}{\pi} \int_{-\frac{1}{2}L}^{\frac{1}{2}L} \frac{dx \gamma_1(x)}{x_0 - x} + \frac{1}{\pi} \int_{-\frac{1}{2}L}^{\frac{1}{2}L} \frac{dx \gamma_2(x)(x_0 + \xi - x)}{(x_0 + \xi - x)^2 + \eta^2} \\ = g'(x_0 + \xi) \\ \frac{1}{\pi} \int_{-\frac{1}{2}L}^{\frac{1}{2}L} \frac{dx \gamma_1(x)(x_0 - \xi - x)}{(x_0 - \xi - x)^2 + \eta^2} + \frac{1}{\pi} \int_{-\frac{1}{2}L}^{\frac{1}{2}L} \frac{dx \gamma_2(x)}{x_0 - x} \\ = -g'(x_0 - \xi), \quad (58) \end{aligned}$$

where x_0 is now used in place of x_1 in the first equation, and of x_2 in the second. We proceed to solve (58) numerically; the procedure for the case of non-identical bodies is only slightly more complicated.

Numerical Procedure

Our procedure for solving the integral equations (58) is a quite direct one, involving replacement of integration by summation, and inversion of a matrix. However, it is necessary to be a little careful about this process, and in particular one cannot expect it to succeed if applied to equations (58) as they stand. This is because of the non-uniqueness of the solutions to (58) in the absence of the Kutta condition. The fact that the homogeneous equations with $g'(x_0) \equiv 0$

possess two linearly independent eigen-solutions implies that any matrix obtained by approximation of the integrals will be singular, indeed having a rank 2 less than its order. Although one can still make progress using "pseudo-inverses", a simpler procedure is to perform first an indefinite integration of the singular integral equations, giving the only-logarithmically-singular pair

$$\begin{aligned} \frac{1}{\pi} \int_{-\frac{1}{2}L}^{\frac{1}{2}L} dx \gamma_1(x) \log|x_0 - x| + \frac{1}{\pi} \int_{-\frac{1}{2}L}^{\frac{1}{2}L} dx \gamma_2(x) \\ \cdot \log\sqrt{(x_0 + \xi - x)^2 + \eta^2} = g(x_0 + \xi) + C_1, \quad (59) \\ \frac{1}{\pi} \int_{-\frac{1}{2}L}^{\frac{1}{2}L} dx \gamma_1(x) \log\sqrt{(x_0 - \xi - x)^2 + \eta^2} \\ + \frac{1}{\pi} \int_{-\frac{1}{2}L}^{\frac{1}{2}L} dx \gamma_2(x) \log|x_0 - x| = -g(x_0 - \xi) + C_2, \quad (60) \end{aligned}$$

where $g(x_0)$ is any indefinite integral of $g'(x_0)$ and C_1, C_2 are arbitrary constants of integration. A suitable integral of (57) is

$$g(x_0) = \frac{2U}{\pi} \int_{-\frac{1}{2}L}^{\frac{1}{2}L} dx f'(x) \arctan\left(\frac{\eta}{x_0 - x}\right). \quad (61)$$

Integral equations with logarithmic kernels possess unique solutions, so that a numerical treatment of (59), (60) presents no difficulties. The non-uniqueness of the original problem (58) re-asserts itself in the form of the arbitrary constants C_1, C_2 , which are ultimately determined by the Kutta condition.

To set up a numerical solution, we suppose that the unknowns $\gamma_1(x), \gamma_2(x)$ can be represented by step functions on the interval $(-\frac{1}{2}L, \frac{1}{2}L)$, the values on the j th interval $x_{j-1} < x < x_j$ being γ_{1j}, γ_{2j} respectively. The mesh of end points $\{x_j\}$ can be arbitrary, but in anticipation of a square-root singularity at the ends $|x| = \frac{1}{2}L$, we set

$$x_j = -\frac{1}{2}L \cos\left(j \frac{\pi}{N}\right), \quad j=0, 1, 2, \dots, N, \quad (62)$$

which provides exactly the right increase in density of points near the ends to counter this singularity. Thus if $\gamma_{1,2}$ are replaced by step functions we have

$$\begin{aligned} & \frac{1}{\pi} \sum_{j=1}^N \gamma_{1j} \int_{x_{j-1}}^{x_j} dx \log|x_0-x| \\ & + \frac{1}{\pi} \sum_{j=1}^N \gamma_{2j} \int_{x_{j-1}}^{x_j} dx \log\sqrt{(x_0+\xi-x)^2+\eta^2} \\ & = g(x_0+\xi)+C_1, \end{aligned} \quad (63)$$

and

$$\begin{aligned} & \frac{1}{\pi} \sum_{j=1}^N \gamma_{1j} \int_{x_{j-1}}^{x_j} dx \log\sqrt{(x_0-\xi-x)^2+\eta^2} \\ & + \frac{1}{\pi} \sum_{j=1}^N \gamma_{2j} \int_{x_{j-1}}^{x_j} dx \log|x_0-x| \\ & = -g(x_0-\xi)+C_2. \end{aligned} \quad (64)$$

The integrals in (63), (64) may be carried out analytically, and on setting $x_0=\bar{x}_1$ where \bar{x}_1 is a point near the center of the i th interval, specifically

$$\bar{x}_1 = -\frac{1}{2}L \cos[(1-\frac{1}{2})\pi/N]. \quad (65)$$

we have

$$\sum_{j=1}^N (A_{1j}\gamma_{1j}+B_{1j}^+\gamma_{2j}) = g_{11}+C_1$$

$$\text{and } \sum_{j=1}^N (B_{1j}^-\gamma_{1j}+A_{1j}\gamma_{2j}) = g_{21}+C_2, \quad (66)$$

where

$$A_{1j} = \frac{1}{\pi} \left[-(\bar{x}_1-x) \log|\bar{x}_1-x| - x \right]_{x_{j-1}}^{x_j}, \quad (67)$$

$$\begin{aligned} B_{1j}^{\pm} &= \frac{1}{\pi} \left[-(\bar{x}_1 \pm \xi - x) \log\sqrt{(\bar{x}_1 \pm \xi - x)^2 + \eta^2} \right. \\ & \left. + \eta \arctan \frac{\eta}{\bar{x}_1 \pm \xi - x} - x \right]_{x_{j-1}}^{x_j}, \end{aligned} \quad (68)$$

$$g_{11} = g(\bar{x}_1+\xi), \quad (69)$$

$$g_{21} = -g(\bar{x}_1-\xi). \quad (70)$$

This set of equations can be written in terms of a $(2N \times 2N)$ composite matrix

$$\tilde{A} = \begin{bmatrix} A_{1j} & B_{1j}^+ \\ B_{1j}^- & A_{1j} \end{bmatrix}, \quad (71)$$

and $2N$ -vectors

$$\tilde{\gamma} = \begin{bmatrix} \gamma_{1j} \\ \gamma_{2j} \end{bmatrix}, \quad (72)$$

$$\tilde{g} = \begin{bmatrix} g_{11} \\ g_{21} \end{bmatrix}, \quad (73)$$

$$\tilde{e}^{(1)} = \begin{bmatrix} 1 \\ 0 \end{bmatrix}, \quad (74)$$

$$\tilde{e}^{(2)} = \begin{bmatrix} 0 \\ 1 \end{bmatrix}, \quad (75)$$

as

$$\tilde{A}\tilde{\gamma} = \tilde{g} + C_1\tilde{e}^{(1)} + C_2\tilde{e}^{(2)}. \quad (76)$$

Equation (74) is intended to imply that the first N elements of $\tilde{e}^{(1)}$ are unity, and the last N are zero.

The solution of (76) is obtained using a standard matrix-inversion subroutine, with the three right-hand sides \tilde{g} , $\tilde{e}^{(1)}$, $\tilde{e}^{(2)}$, and can be written

$$\tilde{\gamma} = \tilde{\gamma}^{(0)} + C_1\tilde{\gamma}^{(1)} + C_2\tilde{\gamma}^{(2)}, \quad (77)$$

where $\tilde{\gamma}^{(0)} = \tilde{A}^{-1}\tilde{g}$ is the solution with \tilde{g} as right-hand side, and $\tilde{\gamma}^{(k)} = \tilde{A}^{-1}\tilde{e}^{(k)}$ with $\tilde{e}^{(k)}$ on the right, $k=1,2$. In this manner we have determined a numerical approximation to the general solution to the pair of singular integral equations (58), with C_1, C_2 as arbitrary constants.

The constants C_1, C_2 are now determined by the Kutta conditions (50). A crude but effective numerical procedure is simply to force $\gamma_1(x)$ and $\gamma_2(x)$ to vanish on the trailing element $j=1$. This requires therefore that

$$(\gamma)_1 = (\gamma)_{N+1} = 0, \quad (78)$$

or

$$C_1(\gamma^{(1)})_1 + C_2(\gamma^{(2)})_1 = -(\gamma^{(0)})_1 \quad (79)$$

and

$$C_1(\gamma^{(1)})_{N+1} + C_2(\gamma^{(2)})_{N+1} = -(\gamma^{(0)})_{N+1}, \quad (80)$$

since the 1st element of the composite vector γ is the trailing-edge value of γ_1 and the $(N+1)$ th element of γ is the trailing-edge value of γ_2 . The pair of simultaneous equations (79,80) are readily solved for C_1, C_2 , and the solution (77) for γ is now complete. In fact the values of all 6 computed numbers in (79,80) are large, ("approximations of infinity") because of the square-root singularity in the general solution at both ends of both bodies. Nevertheless, satisfaction of the equations (79,80) serves to cancel out the trailing-edge singularity in the final particular solution, leaving a vanishing loading, as required.

Computed Results and Discussion

The above numerical procedure can now be used for identical bodies of arbitrary thickness $2f(x)$. However, to simplify the present preliminary computation we have used an extremely idealized "rectangular-box" representation of the thickness, namely

$$f(x) = \begin{cases} b, & |x| < \frac{1}{2}L, \\ 0, & |x| > \frac{1}{2}L, \end{cases} \quad (81)$$

where b is the half-beam. Thus $f'(x)$ in (61) is a sum of δ -functions at the ends $x = \pm \frac{1}{2}L$, and we have

$$g(x) = \frac{2Ub}{\pi} \left[\arctan \frac{\eta}{\frac{L}{2} + x} + \arctan \frac{\eta}{\frac{L}{2} - x} \right] \quad (82)$$

Although for most purposes (81) is a quite unrealistic model of a ship or wing profile, the only effect of thickness in the present problem is to induce an effective camber $g(x)$, which then influences the loading $\gamma(x)$ via the integral equation (58). The test then is not whether (81) is a realistic thickness model, but rather whether (82) is a realistic effective-camber model, and this seems to be the case.

Experimental results were in fact obtained by Oltmann (5) for elliptic-sectioned bodies with beam/length = 0.125. In Figures 7,8 we compare our computed results for the net force and moment (equations (53,54)) with Oltmann's experiments. We have no right to expect close agreement, since the two body shapes are not the same.

Nevertheless, our theory does appear to give excellent qualitative

and fair quantitative agreement with the experimental points. It is most likely that the agreement would be improved by a more accurate representation than (81) of the elliptic section shape, and this is left for future work. An indication that this might be so is that the negative (i.e. repulsive) peak on the force curve (Figure 7) occurs experimentally at a lower value (1.5) of the stagger $\xi/\frac{1}{2}L$ than on the theoretical curve ($\xi/\frac{1}{2}L = 1.8$). This is consistent with the observation that such repulsive forces are due to interactions between the ends of the bodies, and are therefore likely to occur nearer to the "bow-to-stem" configuration ($\xi/\frac{1}{2}L = 2.0$) for a very blunt body such as given by (81) than for a less-blunt body such as that tested by Oltmann.

A very significant qualitative aspect to these results is that there is very much less force and moment on the following body than on the leading body, in staggered configurations with $|\xi/\frac{1}{2}L| > 1$. The physical reason for this phenomenon is that the following body obtains the benefit of moving in the smooth flow field detaching from the trailing end of the body in front of it. On the other hand, the leader has to contend with large streamline curvatures induced near its trailing-edge by the leading edge of the following body. There is of course some doubt about the smoothness of the trailing-edge flow in the experimental situation with elliptic sections, but nevertheless the experimental points do seem to support the above conclusion.

This asymmetry is the feature of the present theory which contrasts it most dramatically with the numerical computation of Collatz (3), in which circulation about the bodies is ignored, and the Kutta condition at the trailing edges is not imposed. Inevitably, this leads to a prediction for the force which is symmetric with respect to stagger, and the moment is anti-symmetric. Thus the leading and following bodies are predicted by Collatz to be subject to the same magnitude of force and moment.

In addition, of course, Figure 7 indicates that the Collatz approach grossly underestimates the force, whereas the present theory is in fair agreement with experiment. This is not surprising, since the net circulation is a substantial contributor to the net force on the body. In our thin-wing approach it is the only such contributor; however, Collatz's computations are for thick elliptic sections, and he does obtain a non-zero, though small, force even without taking account of

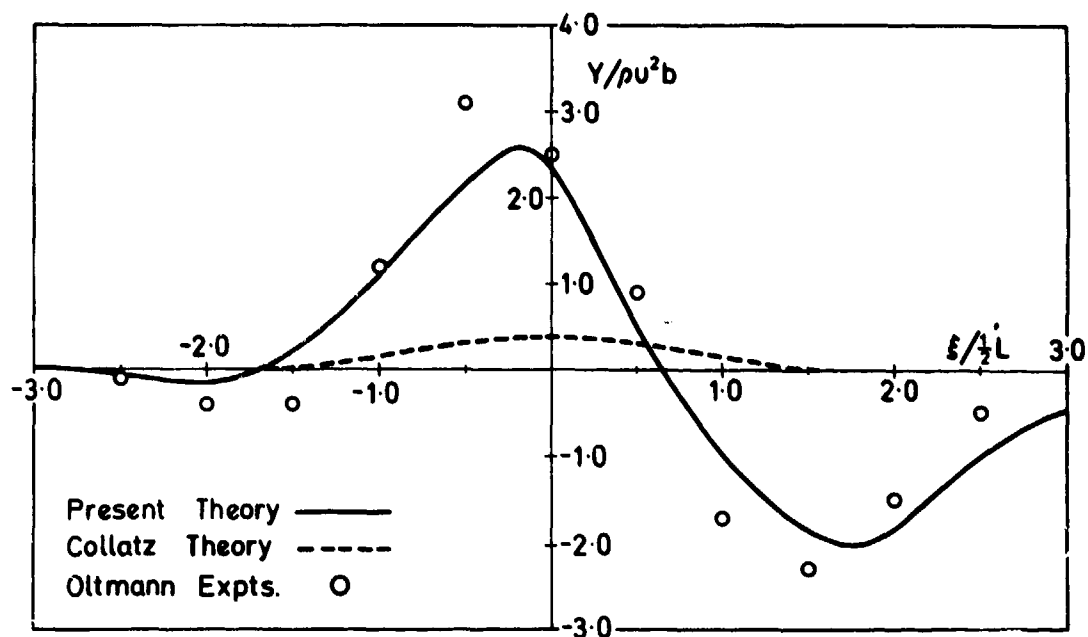


Fig. 7. Theoretical and experimental sway force on each of two identical two-dimensional bodies in steady motion, at a separation distance $\eta=0.625(\frac{1}{2}L)$.

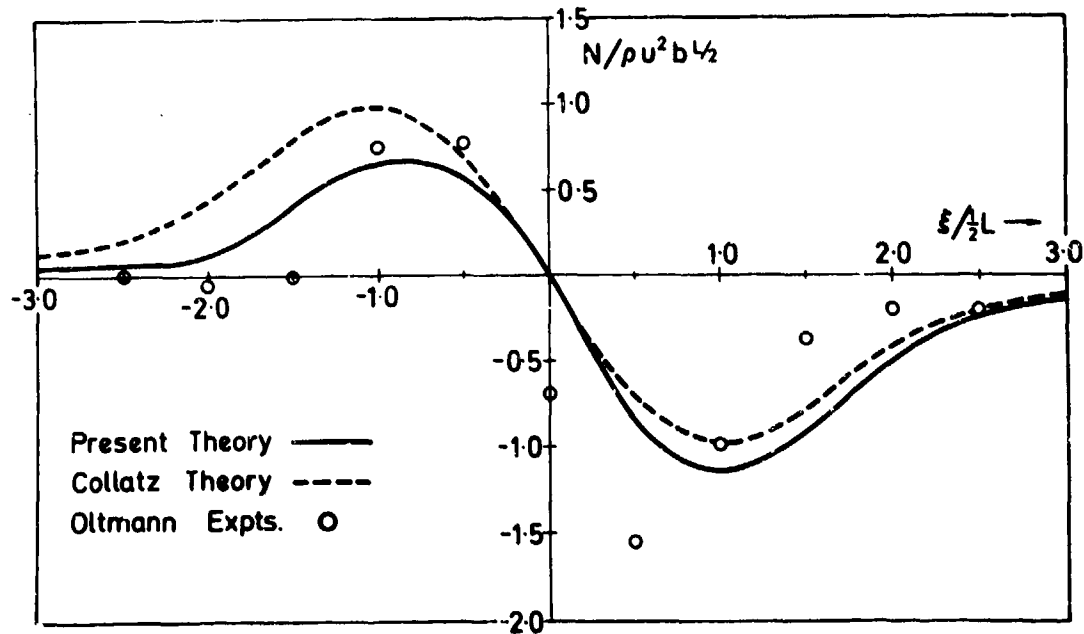


Fig. 8. Theoretical and experimental yaw moment on each of two identical two-dimensional bodies in steady motion, at a separation distance $\eta=0.625(\frac{1}{2}L)$.

circulation. On the other hand, Collatz obtains a reasonable prediction of the moment in Figure 8, presumably because net circulation is of less significance for the moment than for the force.

The effect of varying the lateral separation η is illustrated in Figures 9 and 10. It is to be noted that for large separation the force is asymptotically antisymmetrical about the point $\xi = \frac{1}{2}L$, or the point where the three-quarter-chord position of body 1 is abeam of the mid-station of body 2. This result can be explained by noting that if η is large compared to the chord length and stagger, the leading-order lateral flow at body 1 is due to the vortex distribution of body 1, and the source distribution of body 2, the effect of the body-2 vortices being negligible. Moreover, for η large compared to the chord, the thickness-induced streamlines from body 2, as measured at body 1, can be approximated locally by parabolic arcs, and thus the loading on body 1 is equivalent to that on a parabolic-cambered foil. But the lift on a parabolic-cambered foil is proportional to the local angle of attack at the three-quarter-chord point, and thus in the present case to the lateral flow induced by body 2 at the three-quarter-chord point of body 1. From the longitudinal symmetry of body 2, this vanishes when $x_2 = 0$, and hence for large separations there is no lateral force on either body when its three-quarter-chord position is abeam of the other body's mid-chord position.

Interaction between two-dimensional thin bodies in each other's near field

As in the analogous development of Section 2, the theory developed above for two-dimensional flows may be complemented by one in which the lateral separation η is $O(\epsilon)$, or comparable to the body thickness. For the two-dimensional flows considered in this Section, the complementary theory is almost trivial.

We begin with the assumption that body 1 is ahead, that there is some overlap, i.e. $\xi < \frac{1}{2}(L_1 + L_2)$, and that the width of the overlap region separating the two bodies is small compared to its length. Indeed, from Figure 1 it is obvious that the local clearance between the two bodies is

$$\eta - f_1^+(x_1) + f_2^-(x_2) = O(\epsilon), \quad (83)$$

whereas the length $\frac{1}{2}L_1 + \frac{1}{2}L_2 - \xi$ of this overlap region is $O(1)$. In such a thin region the flow will be one-dimensional, to leading order in ϵ , with a velocity

$$\phi_{x_1} = -Q/[\eta - f_1^+(x_1) + f_2^-(x_2)] \quad (84)$$

where Q is the total flux passing through this region. Note that in this inner region the variation of width is of the same order as the width itself, and thus the change in velocity along the region is a first-order quantity.

The remainder of the fluid domain is treated as an outer region, to be matched to the inner region at the two openings $x_1 = -\frac{1}{2}L_1$, $x_2 = \frac{1}{2}L_2$. In the outer region, the flow past the two thin bodies is simply the free stream velocity $-U$, together with a small $O(\epsilon)$ perturbation. Thus, to leading order, the matching of the inner and outer solutions can be carried out simply by equating the free-stream velocity to the inner-region flow, at the two entrances, without solving for the $O(\epsilon)$ outer perturbation.

In general, however, simultaneous matching at both entrances to the inner region is impossible, since (84) will take different values at these two ends. The appropriate end at which to carry out the matching process is the trailing edge of body 1, where the Kutta condition implies continuity of pressure and hence of the inner and outer velocities. At the leading edge, in general, there will be a source-like singularity the strength of which is $O(\epsilon)$, and which need not be considered in this leading-order analysis. Thus, matching (84) to the free stream at the trailing edge, it follows that

$$Q = U[\eta + f_2^-(\xi - \frac{1}{2}L_1)] \quad (85)$$

and hence the inner flow is determined. The corresponding pressure in the inner region is

$$p = -\frac{1}{2}\rho(\phi_{x_1}^2 - U^2) \\ = \frac{1}{2}\rho U^2 \left\{ 1 - \left[\frac{\eta + f_2^-(\xi - \frac{1}{2}L_1)}{\eta - f_1^+(x_1) + f_2^-(x_1 + \xi)} \right]^2 \right\} \quad (86)$$

and this may be integrated to find the interaction force Y and moment N .

Of particular interest, for comparison with the "outer theory" developed earlier in this section, is the "outer approximation of the inner theory", or the limiting form of Y and N as the separation distance increases (to infinity, by comparison to ϵ , but nevertheless small compared to L). The appropriate limits are

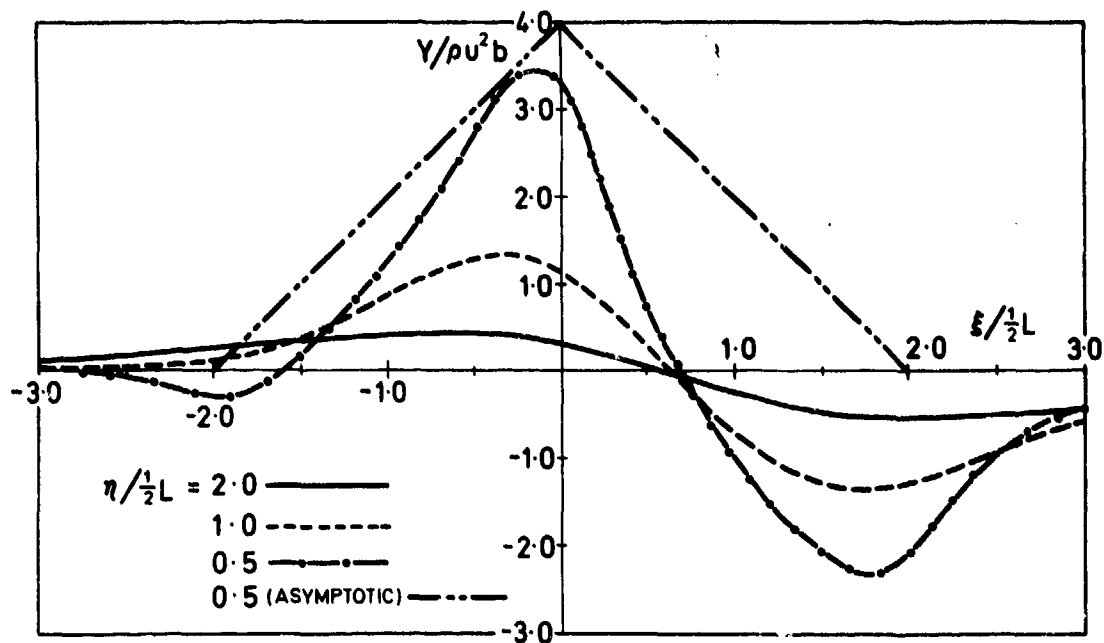


Fig. 9. Theoretical sway force on two-dimensional bodies for various separation distances. Dotted curve shows small-separation asymptote, evaluated at $\eta=0.5(\frac{1}{2}L)$.

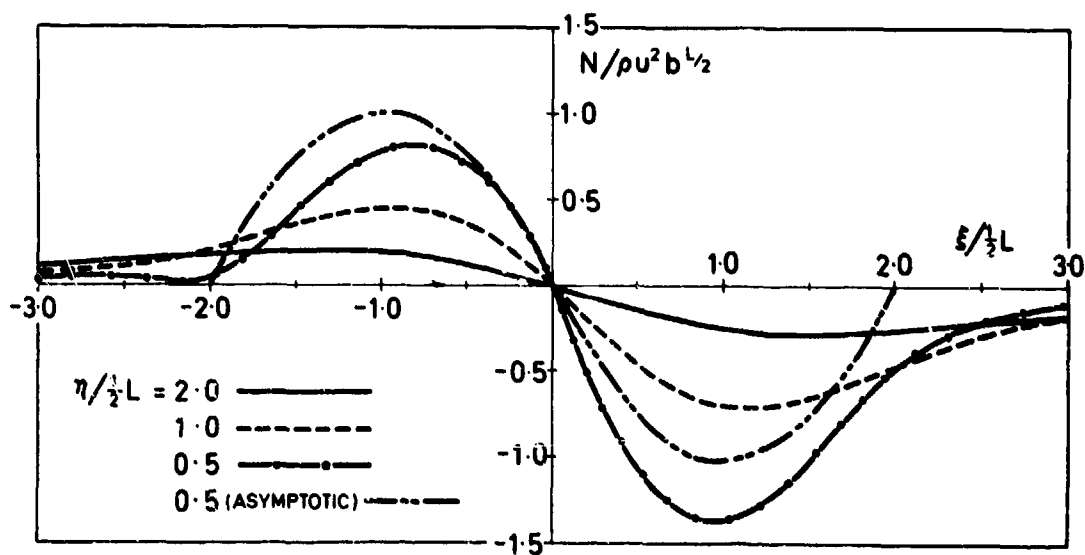


Fig. 10. Theoretical yaw moment on two-dimensional bodies for various separation distances. Dotted curve shows small-separation asymptote, evaluated at $\eta=0.5(\frac{1}{2}L)$.

$$Y_N = \frac{\rho U^2}{\eta} \int_{-\frac{1}{2}L_1}^{\frac{1}{2}L_2 - \xi} (f_1^+(x_1) - f_2^-(x_1 + \xi) + f_2^-(\xi - \frac{1}{2}L_1)) \left(\frac{1}{x_1} \right) dx_1. \quad (87)$$

Thus, for $\epsilon \ll \eta \ll L$, the force and moment are inversely proportional to η . Equation (87) can also be obtained by an asymptotic solution as $\eta \rightarrow 0$ of the integral equation (46), (47). Thus the large- η approximation of the $\eta=0(\epsilon)$ theory matches with the small- η approximation of the $\eta=0(1)$ theory, and these two complementary theories are consistent.

Equation (87) above is closely related to the study carried out by Widnall and Barrows (14), of a thin cambered wing in ground-effect. Those authors also used a matching procedure, and considered the effects of camber, but not of thickness, and assumed that the camber was small compared to the clearance parameter.

Computations based on the present results are particularly easy to carry out, especially the last result (87) which states in effect that the local interaction force is proportional to the sum of the local widths of the two bodies, minus the width of body 2 at the position opposite the trailing edge of body 1. This force is obviously an increasing function of body fullness, and is a maximum if the two bodies have the rectangular thickness distributions (81). Indeed, it is interesting to compare this theory, for that body shape, with the computations shown in Figures 7-10, in spite of the fact that a rectangular thickness distribution is particularly severe for the present inner theory. One obtains in this case for the force a diamond-shaped curve, symmetrical about $\xi=0$, having a peak value of $Y/\rho U^2 b = L/\eta$ at $\xi=0$, and vanishing when the overlap ceases at $\xi=\pm L$. For $\eta \approx L$ this is shown by the dotted line in Figure 9, and even for this relatively-large spacing, and extreme body form, the results agree fairly well with the outer theory for negative values of ξ , but rather poorly for positive values of the stagger distance. On the other hand the moment will be a pair of anti-symmetrical parabolas, which are shown in Figure 10 for the same separation, and the agreement here is better. While a similar comparison should be carried out for streamlined bodies, it seems likely that the agreement will be improved in this case and thus that the very simple formula (87) can be used

in practice to compute the interaction force and moment for the separation distances of practical importance, in problems where the two-dimensional assumptions of this Section are valid.

4. INTERACTIONS BETWEEN SHIPS IN SHALLOW WATER

Ships in each other's far field

The only case for which the two-dimensional analysis of Section 3 can be applied directly to ships is when the ships are wall-sided and are moving in water so shallow that the clearance between the ships' bottom and the bottom of the water can be neglected. In this case, providing free surface effects are negligible, i.e. for sufficiently small Froude numbers based on water depth h , the flow is truly two-dimensional everywhere.

However, it is well known (e.g. Tuck (8)) that in shallow water the flow is asymptotically two-dimensional, even when the clearance is not negligible compared to h , providing we are not too close to the ship. The general effect of a single ship with section area $S_1(x_1)$ moving with speed U_1 in shallow water is to push the water aside symmetrically, the apparent velocity in the y , -direction at which this pushing-aside takes place being of magnitude $U_1 S_1(x_1)/4h$. Note that $S_1(x_1)$ is the double-body section area, the double body being situated in a "double-body" of water of total depth $2h$.

If there is any disturbing influence which is unsymmetrical with respect to the center plane of ship 1, such as another ship, and the clearance is not zero, there is a possibility of a laterally-unsymmetric component to the flow near the first ship, and the resulting inner flow near this ship is quite complicated. What concerns us here, however, is only the "intermediate" approximation to the flow, i.e. the flow at a lateral distance η which is large compared with the beam but still small compared with the length of ship 1.

In the intermediate region, it is clear that we can write for the lateral velocity

$$\frac{\partial \phi}{\partial y_1} = - \frac{U_1}{4h} S_1'(x_1) \operatorname{sgn} y_1 + V(x_1, t), \quad (88)$$

where the first term measures the laterally-symmetric flow due to body 1's thickness, and V is the (unknown) apparent cross-flow velocity. On integrating (88) with respect to y_1 we can write

$$\phi = -\frac{U_1}{4h} S'_1(x_1) |y_1| + \phi_0(x_1, t) + V(x_1, t) \cdot (y_1 \pm C_1(x_1)), \quad (89)$$

where $\phi_0(x_1, t)$ is an unknown "constant" of integration, and $C_1(x_1)$ a (known) blockage coefficient (cf. Tuck and Taylor (15)).

The above discussion applies only to the case when any disturbing influence is far from ship 1, so that the blockage coefficient C_1 is that for ship 1 alone. A similar intermediate expansion applies near ship 2, if that disturbing influence is indeed another ship. The above is the intermediate approximation for the general unsteady case. We now use it as an effective boundary condition for the outer problem, but confine attention to the steady case, to avoid the complication of an unsteady wake.

We shall attempt to use the same source-vortex representation (40) for the disturbance potential in the far field, as we did when the clearance was zero. But now, instead of simply satisfying a boundary condition such as (41) on the center plane of the thin two-dimensional bodies, we must determine the source and vortex strengths by matching with the near field in the intermediate region where (89) is valid.

Now from (40), as $y_1 \rightarrow 0$, we have

$$\phi \rightarrow (\phi_0 \pm \phi_1) + y_1(V \pm V_1) + O(y_1^2), \quad (90)$$

where $V \pm V_1$ is given by the right-hand-side of (43) and

$$\phi_1 = \frac{1}{2} \int_{-\frac{1}{2}L_1}^{x_1} \gamma_1(x) dx. \quad (91)$$

We have no need for the symmetric part ϕ_0 of the value of ϕ at $y_1=0$, which does, however, match with the corresponding term in (89).

Thus equation (90) matches with (89) if

$$V_1 = \frac{U_1}{4h} S'_1(x_1) \quad (92)$$

and

$$\phi_1 = V C_1. \quad (93)$$

Thus (92) and (43) imply immediately that the source strength is given by

$$m_1(x_1) = -\frac{U_1}{2h} S'_1(x_1), \quad (94)$$

a straight-forward generalization of (45). Similarly, using (43) for V , equation (93) implies

$$\begin{aligned} \frac{1}{2C_1(x_1)} \int_{-\frac{1}{2}L_1}^{x_1} \gamma_1(x) dx &= \frac{1}{2\pi} \int_{-\frac{1}{2}L_1}^{\frac{1}{2}L_1} dx \frac{\gamma_1(x)}{x_1 - x} \\ &+ \frac{1}{2\pi} \int_{-\frac{1}{2}L_2}^{\frac{1}{2}L_2} dx \left[m_2(x) \left(\frac{-\eta}{(x_2 - x)^2 + \eta^2} \right) \right. \\ &\quad \left. + \gamma_2(x) \left(\frac{x_2 - x}{(x_2 - x)^2 + \eta^2} \right) \right]. \end{aligned} \quad (95)$$

A similar analysis of the behavior of ϕ for small y_2 leads to a corresponding expression to (94) for $m_2(x_2)$ and a relationship analogous to (95) involving on the left the blockage coefficient $C_2(x_2)$ of ship 2 and an indefinite integral of $\gamma_2(x_2)$. Finally, substituting the now-known source distributions $m_1(x_1)$, $m_2(x_2)$ into the relations of type (95), we obtain the coupled singular integral equations:

$$\begin{aligned} \frac{1}{\pi} \int_{-\frac{1}{2}L_1}^{\frac{1}{2}L_1} dx \gamma_1(x) \left[\frac{1}{x_1 - x} - \frac{H(x_1 - x)}{C_1(x_1)} \right] \\ + \frac{1}{\pi} \int_{-\frac{1}{2}L_2}^{\frac{1}{2}L_2} dx \gamma_2(x) \left[\frac{x_2 - x}{(x_2 - x)^2 + \eta^2} \right] &= g'_1(x_1) \end{aligned} \quad (96)$$

and

$$\begin{aligned} \frac{1}{\pi} \int_{-\frac{1}{2}L_1}^{\frac{1}{2}L_1} dx \gamma_1(x) \left[\frac{x_1 - x}{(x_1 - x)^2 + \eta^2} \right] \\ + \frac{1}{\pi} \int_{-\frac{1}{2}L_2}^{\frac{1}{2}L_2} dx \gamma_2(x) \left[\frac{1}{x_2 - x} - \frac{H(x_2 - x)}{C_2(x_2)} \right] &= g'_2(x_2) \end{aligned} \quad (97)$$

where $g'_1(x_1)$, $g'_2(x_2)$ are still given by (48), but without the camber terms, and with m_1 given by (94), etc. $H(x)$ is the Heaviside step-function, equal to zero for negative argument and one for positive argument.

The only difference between the pair of equations (96), (97) and the pair (47), (48) is the presence of the terms in C_1 , C_2 . There should be little additional numerical difficulty in including these extra terms in the kernel of the integral equations, although this is left for

future work. We merely note that the limit $C_1, C_2 \rightarrow \infty$ corresponds to the fully-blocked case, or zero clearance, and the two-dimensional results are retrieved.

Ships in Each Other's Near Field

If the two ships are sufficiently close to each other, the previous analysis breaks down, since the appropriate inner expansion is one which includes both ships. At any section the flow picture is as in Figure 11, in which there is a total flux

$$m = -U_1 S_1'(x_1) - U_2 S_2'(x_2) \quad (98)$$

produced by the changing sectional areas of the two ships, and (in contrast to the situation of the previous subsection) this flux need not split evenly as it is pushed to $y_0/\epsilon \rightarrow \pm\infty$. However, the extent to which the flux does not split evenly can be described in terms of a lateral flow past both ship sections, as if held fixed.

If ϕ_0 denotes the velocity potential for a cross flow of unit magnitude in the y_0 direction about the two fixed sections, we have

$$\phi_0 \rightarrow y_0 + C \operatorname{sgn} y_0 \quad (99)$$

as $y_0/\epsilon \rightarrow \pm\infty$. The blockage coefficient C may be taken as known, or

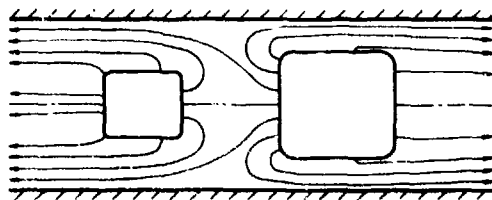


Fig.11. Sketch of inner flow near two closely-spaced moving body sections in shallow water.

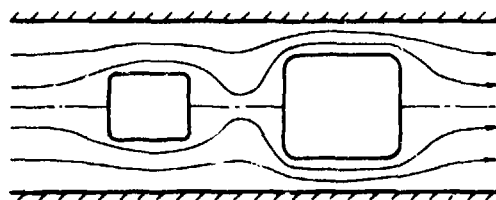


Fig.12. Sketch of inner flow for streaming motion past two closely-spaced body sections in shallow water.

numerically computable, for every given relative position of the two ship sections. The flow associated with ϕ_0 is sketched in Figure 12.

In order to specify a unique inner problem, let us suppose that we compute first a particular potential ϕ_1 due to the moving ships, in which the net flux m does split evenly at infinity, so that as $y_0/\epsilon \rightarrow \pm\infty$,

$$\phi_1 \rightarrow \frac{m}{4h} [|y_0| + D \operatorname{sgn} y_0]. \quad (100)$$

This particular solution satisfies the appropriate inhomogeneous boundary condition on the two hull sections, giving the net flux m as in (98). The quantity D is, like the blockage coefficient C , a unique numerically-computable number for every geometrical configuration of the two ship sections. Unfortunately, unlike C , it does also require information about the longitudinal rate of change of the shape of the bodies, which enters via the body boundary conditions.

The "general solution" for the complete inner potential ϕ must be a combination of the "symmetric" particular solution ϕ_1 and an arbitrary multiple of the "antisymmetric" potential ϕ_0 , together with an additive "constant" independent of the lateral coordinates, i.e.

$$\phi = \phi_1 + V(x_0, t)\phi_0 + f(x_0, t) \quad (101)$$

where V is, as in the previous subsection, the apparent lateral velocity in the intermediate region, and f is an arbitrary constant in the cross-flow plane, related to the longitudinal velocity. Both V and f are at the present stage arbitrary and must be determined by matching with the far field. Note that, since $\partial\phi_0/\partial n = 0$ on the body sections, ϕ satisfies the same body boundary condition as ϕ_1 .

The intermediate expansion of (101) gives, as $y/\epsilon \rightarrow \pm\infty$,

$$\phi \rightarrow \frac{m}{4h} (|y_0| + D \operatorname{sgn} y_0) + V(y_0 + C \operatorname{sgn} y_0) + f, \quad (102)$$

which can be split into an even part

$$\phi_{\text{even}} = \frac{m}{4h} |y_0| + f \quad (103)$$

and an odd part

$$\phi_{\text{odd}} = Vy_0 + \frac{1}{2}\Delta\phi \operatorname{sgn} y_0, \quad (104)$$

where

$$\Delta\phi = 2VC + mD/2h. \quad (105)$$

When we turn to the outer expansion, in which the region occupied by both ships has shrunk to the plane $y_0=0$, we

find that we are faced with solution of a pair of classical two-dimensional thin-airfoil problems. The even part ϕ_{even} of the intermediate potential provides the inner boundary condition for a non-lifting thickness problem, the combined effect of the two ships being equivalent to that of a single airfoil of thickness proportional to m , and hence to a linear combination of the section-area slopes of the two ships.

On the other hand, the odd portion ϕ_{odd} generates a lifting-surface or camber problem, in which V is proportional to the effective camber. But the potential jump, or loading must be given by (105), a formula which also includes V as its only unknown. If one evaluates the loading using standard (unsteady) thin airfoil theory, one therefore obtains an integral equation for V , the solution of which completes the problem. For the steady case, this integral equation is similar to that given by Newman (16).

This sub-section has provided a very brief and incomplete outline of a procedure for solving a very difficult problem. The complete problem has been reduced to a number of separate canonical, but still difficult tasks. In the first place one must solve (separately for every value of x_0 and time t) a pair of two-dimensional boundary-value problems in the (y_0, z_0) plane to determine the coefficients C, D , which are characteristic properties of the combined geometry of the two ship sections. Then one must use these coefficients, which vary from section to section, as inputs to a singular integral equation which results from application of unsteady airfoil theory in the (x_0, y_0) plane. Clearly, much more work needs to be done before one could have any hope of a practical solution to this problem.

ACKNOWLEDGEMENT

One of us (J.N.N.) acknowledges the support of the Australian-American Educational Foundation and the John Simon Guggenheim Memorial Foundation, and the hospitality provided by the Applied Mathematics Department of the University of Adelaide, and the Department of Mechanical and Industrial Engineering of the University of New South Wales. Acknowledgement is also made to the Australian Research Grants Committee for computing assistance.

REFERENCES

1. Newman, J.N. "The force and moment on a slender body of revolution moving near a wall." David Taylor Model Basin Report 2127, 1965.
2. Newman, J.N. "Some theories for ship maneuvering." Proc. International Symposium on Directional Stability and Control of Bodies Moving in Water, London, Inst. of Mech. Engs., 1972, pp. 34-42.
3. Collatz, G. "Potentialtheoretische Untersuchung der hydrodynamischen Wechselwirkung zweier Schiffskörper." Jahrbuch Schiffbautechnischen Gesellschaft, 57, 1963, pp. 281-329.
4. Newton, R.N. "Some notes on interaction effects between ships close aboard in deep water." Proc. First Symposium on Ship Maneuverability, David Taylor Model Basin Report 1461, 1960.
5. Oltmann, P. "Experimentelle Untersuchung der hydrodynamischen Wechselwirkung schiffsähnlicher Körper." Schiff und Hafen, 22, 1970, 701-709.
6. Norrbin, N.H. "Theory and observation on the use of a mathematical model for ship maneuvering in deep and confined waters." Proc. Eighth Symposium on Naval Hydrodynamics, 1968, pp. 807-904.
7. Taylor, G.I. "The force acting on a body placed in a curved and converging stream of fluid," A.R.C. R&M No. 116, 1928.
8. Tuck, E.O., "Shallow water flows past slender bodies." J. Fluid Mech., 26, 1966, pp. 81-95.
9. Batchelor, G.K. An Introduction to Fluid Mechanics. Cambridge Univ. Press, 1967.
10. Lighthill, M.J. "Note on the swimming of slender fish." J. Fluid Mech. 2, 1960, pp. 305-317.
11. Newman, J.N., and Wu, T.Y. "A generalized slender-body theory for fish-like forms." J. Fluid Mech. 57, 1973, pp. 673-693.
12. Newman, J.N. "The force on a slender fish-like body." J. Fluid Mech. 58, 1973, pp. 689-702.
13. Cummins, W.E. "Hydrodynamic forces and moments acting on a slender body of revolution moving under a regular train of waves." David Taylor Model Basin Report 910, 1954.

14. Widnall, S.E. and Barrows, T.M.
"An analytic solution for two- and
three-dimensional wings in ground
effect." J. Fluid Mech. 42, 1970,
pp. 769-792.

15. Tuck, E.O. and Taylor, P.J.
"Shallow-water problems in ship
hydrodynamics", Proc. Eighth Symposium
on Naval Hydrodynamics, 1968, pp. 627-
659.

16. Newman, J.N. "Lateral motion of
a slender body between two parallel
walls," J. Fluid Mech. 29, 1969
pp. 97-115.

DISCUSSION

M. SCHMIECHEN

The fact that forces due to circulation are omitted in Dr. Collatz's theory (1) may be deduced from very simple relative motion considerations. This has been discussed together with the consequences for passing and overtaking ships in my contribution (2) to Dr. Collatz's paper. As far as I remember consequently in the final title of his thesis Dr. Collatz did no longer refer to ships but rather to elliptical cylinders. Some more references to the relative motion concept may be found in the contribution to Dr. Dand's paper presented later at this Symposium.

- (1) Collatz, G.: Potentialtheoretische Untersuchung der hydrodynamischen Wechselwirkungen zweier Schiffkörper. STG 57(1963) S. 281/329.
- (2) Schmiechen, M.: Contribution to (1) STG 57 (1963) S. 368.

I.W. DAND

In this important paper the authors have tackled, and apparently largely solved, the difficult problem of interaction between ships in deep and shallow water. Agreement between theory and experiment has been significantly improved and the authors have shown the importance of including circulation in the final shallow water forces and moments. The insight gained by the authors' approach is valuable for the general practitioner.

It is unfortunate that so little published experimental data exists on two-ship interaction. However the writer notes that the authors do not refer to some shallow water interaction and bank effect data given in NSRDC report 1705 (August 1964) by C. G. Moody. It is perhaps to be regretted that for the case of shallow water interaction, the hull shape which has received the most theoretical and experimental attention should have been the ellipse with possibly separated flow near the stem. It would therefore be of some interest to see how the authors computed shallow water forces and moments compare with measurements on ship-shaped hull forms in shallow water.

Regarding the authors' deep water results, qualitative agreement between theory and experiment for the sway force is good, but the same cannot be said for the yaw moments shown in Fig. 3. A feature, important from the point of view of ship safety, is the 'bow inwards' moment measured on ship B when it is between 400 and 600 feet ahead of ship A. This indicates that ship B tends to cut across the bows of ship A — a particularly hazardous tendency which could give rise to a collision. Such behavior has also been observed when one model was made to overtake another in some experiments made recently at NPL. It appears that the authors' calculations do not predict this behavior and neither do they predict the strong 'bow outwards' moment at zero stagger indicated by the model measurements. Can the authors explain these discrepancies?

Finally an important type of interaction exists where one ship is much larger than the other and is operating in comparatively shallow water whereas the smaller ship

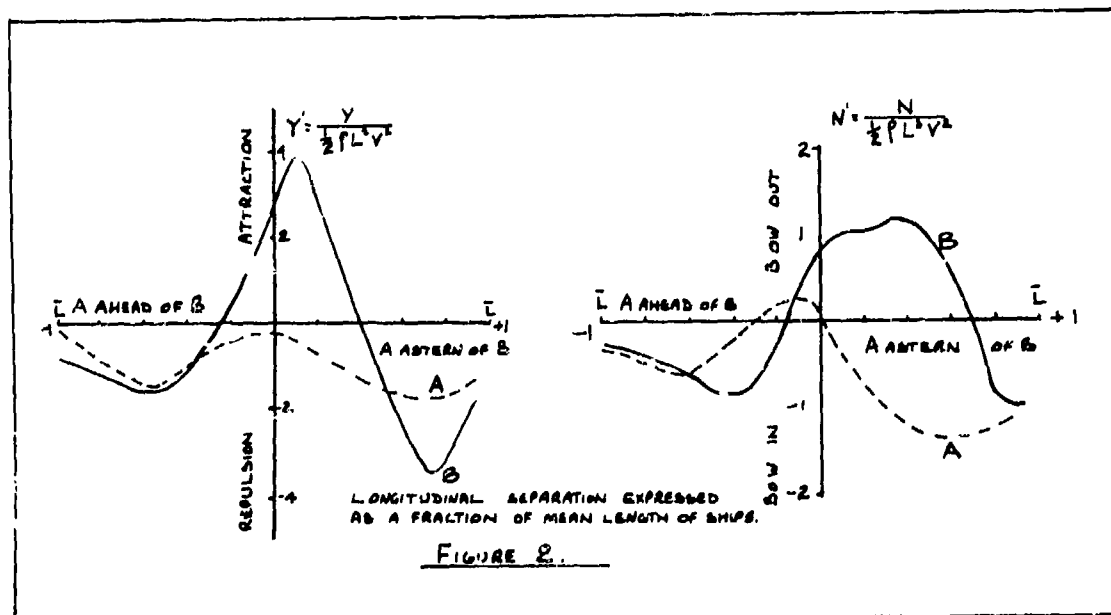
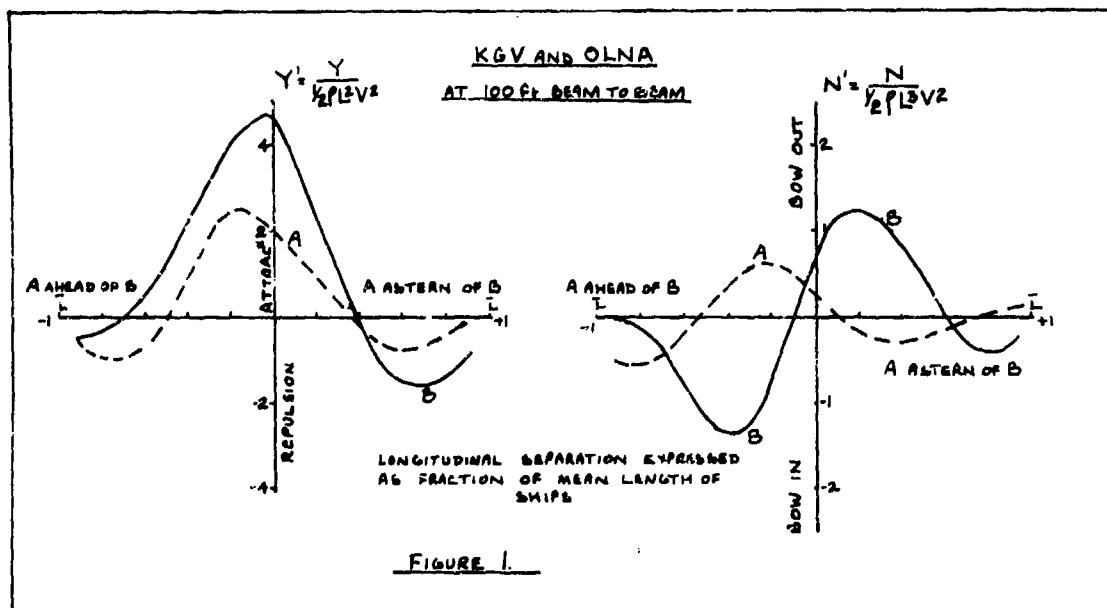
approaching it is in comparatively deep water. Can the authors theory encompass such a situation?

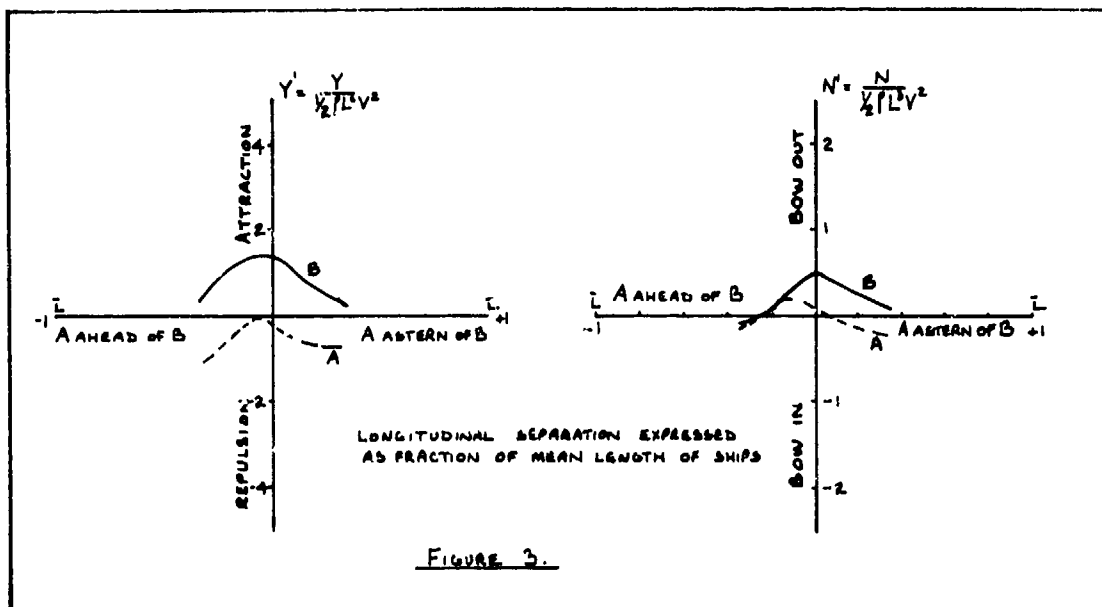
L.L. MARTIN

The authors have stressed that this is basically a potential flow problem and have neglected wavemaking effects. Newtons data for KGV and OLNA used by the authors was the average of a large number of experiments over a range of speeds and wave effects, so far as possible, have been smoothed out. Such measurements have not been made very frequently at AEW but I would like to show two other similar sets of unpublished data, Figures 2 and 3. These also have been smoothed out to eliminate as far as possible wave effects. (As it is necessary to publish this data in non-dimensional form, Figure 1 is a repeat of the KGV & OLNA data non-dimensionalized in the same way for ease of comparison). Whilst in general the shapes of the force and moment curves are similar to KGV and OLNA they both have a curious feature — the force on the larger vessel (vessel A in each case) is always repulsive, even when abreast. Except for a small range of separation near the abreast position the moment is also always bow inwards. This has naturally been ascribed to wave effects in the gap between the two ships, but it affects only the larger ship and if it is a wave effect must be of a similar magnitude to the forces considered by the authors. Apart from the large ratio of displacements in one case, the proportions of the ships as shown by the various geometric ratios in the table are not too far removed from KGV and OLNA. I would be pleased to hear comments on these additional data and suggestions as to why similar results were not obtained for KGV and OLNA.

Table of Geometric Ratios
of the Ships

Figure Number	1	2	3
Length of Ship A	1.31	1.54	1.18
Length of Ship B			
Displacement of Ship A	1.87	8.61	1.65
Displacement of Ship B			
Separation, M to M	0.285	0.255	0.29
Separation, M to M	1.87	1.94	1.65
Separation, beam to beam			
F node number based on mean length	0.15	0.24	0.29





SHEN WANG

FOREWORD

The work referred to in the paper was a part of my contribution dealing with the hydrodynamic interactions induced by passing ships on a moored tanker, prepared for the Port of Long Beach, Long Beach, California, October 1972. In that study, the surge force as well as the sway force and the yaw movement was examined. The results should be of interest to harbor engineers and can be useful for mooring line loading estimations. Presented in the following is a brief discussion of our approach as well as the computed results, which we feel should be complimentary to the present paper (referred as (I) in the discussion following).

FORMULATION

We are concerned with the interaction forces and moment induced by a passing ship on a moored vessel. The passing ship is assumed to move at a constant speed along a path parallel to the centerline of the moored vessel. Both ships are assumed slender but may be of different forms. The body slenderness is implied by that both beam and draft are small as compared to the ship's length. The lateral separation of the two ships, however, is assumed large as compared to their beams.

Only deep fluid is considered in this analysis. The fluid is assumed incompressible and inviscid, the flow being irrotational. It is also assumed that the Froude number of the moving ship is so small that the fluid surface may be treated as a rigid boundary and the free surface effect can be ignored. This assumption is justified for the case of passing moored ships as the passing speed is generally very low especially inside a harbor near the berthing area. As a result of this assumption, the method of image may be applied so that the problem may be considered as that of two double ships, the two slender ship hulls plus their images in the free surface, in an unbounded fluid.

In order to be consistent with the coordinate systems defined in (I), the body coordinate (x_1, y_1, z_1) is fixed in the moored ship, and (x_2, y_2, z_2) is fixed in the passing ship moving with a constant speed U_2 . Since we are interested in the induced exciting forces on the moored ship, we assume the body axes 1 to be stationary so that $U_1 = 0$. The two ships are separated by a lateral distance η , which is a constant, and a fore-and-aft distance ξ , which is a function of time t . As shown in

Figure A (same as Figure 1 of (I)), the fore-and-aft distance $\xi(t)$ is positive when body 2 is astern of body 1. In the following we shall use ship 1 and ship 2 to refer to the moored ship and the passing ship, respectively, and use body 1 and body 2 to refer to the two double-body forms.

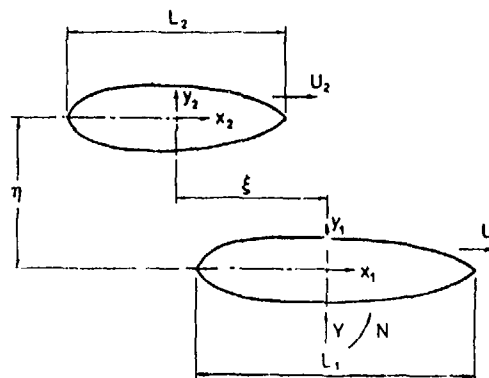


Figure A - Coordinate Systems

In ideal fluid, there exists a velocity potential ϕ which satisfies the following boundary conditions:

$$\frac{\partial \phi}{\partial n_1} = 0 \quad \text{on body 1} \quad (1)$$

$$\frac{\partial \phi}{\partial n_2} = U_2 \frac{\partial x_2}{\partial n_2} \quad \text{on body 2} \quad (2)$$

where n_1 and n_2 are the unit normal vectors on the body surfaces 1 and 2, respectively. In determining the total velocity potential ϕ , we shall first consider that due to the moving body 2. Let $S_2(x_2)$ be the cross sectional area curve of the moving ship. ($2 S_2(x_2)$ for the double-body form. A factor of 2 should be realized if comparing with the definition of $S_2(x_2)$ in (I).) For a slender body in a uniform axial stream velocity $-U_2$ relative to the body axes, a distribution of doublets oriented parallel to the longitudinal axis can be approximated by:

$$\mu_2(x_2) = -\frac{1}{2\pi} S_2(x_2) U_2 \quad (3)$$

To the leading order approximation of slender body theory the boundary condition (2) is satisfied with the above distribution. The velocity potential written in the fixed reference frame (x, y, z) , which is identical to (x_1, y_1, z_1) , is therefore:

$$\phi_2(x, y, z, \xi) = -\frac{U_2}{2\pi} \int_{L_2} \frac{S_2(x_2)(x - x_2 + \xi) dx_2}{[(x - x_2 + \xi)^2 + (y - \eta)^2 + z^2]^{3/2}} \quad (4)$$

On the body axis $y_1 = z_1 = 0$ there exists a stream field induced by ϕ_2 ; assuming $S_2(x_2) = 0$ at the body ends, the velocity components of the induced stream are obtained:

$$U(x_1, \xi) = \frac{\partial \phi_2}{\partial x}(x_1, 0, 0, \xi) = \frac{U_2}{2\pi} \int_{L_2} \frac{S_2'(x_2)(x_2 - x_1 - \xi) dx_2}{[(x_2 - x_1 - \xi)^2 + \eta^2]^{3/2}} \quad (5)$$

$$V(x_1, \xi) = \frac{\partial \phi_2}{\partial y}(x_1, 0, 0, \xi) = \frac{U_2 \eta}{2\pi} \int_{L_2} \frac{S_2'(x_2) dx_2}{[(x_2 - x_1 - \xi)^2 + \eta^2]^{3/2}} \quad (6)$$

where U represents an axial velocity component and V a cross-flow velocity component brought about due to the presence of the passing ship 2, and $S_2'(x_2)$ stands for $\partial S(x_2)/\partial x_2$. Equation (6) agrees with Equation (10) of (I), in which V is written in the moving reference frame of body 2, however.

Because of the existence of the induced stream on body axis 1, there must be an interaction potential ϕ_{12} such that the boundary condition (1) is satisfied. We shall assume the double-body form of ship 1 axisymmetrical; nevertheless, we should note that the results which we shall show may virtually apply for arbitrary slender ships. Since the stream velocity components U and V have been determined as given in (5) and (6), the singularity distribution on the centerline of body 1 can again be approximated from slender body theory; they are:

$$\mu_{1x}(x_1, \xi) = \frac{1}{2\pi} S_1(x_1) U(x_1, \xi) \quad (7)$$

$$\mu_{1y}(x_1, \xi) = \frac{1}{\pi} S_1(x_1) V(x_1, \xi) \quad (8)$$

distributions of doublets parallel to x_1 - and y_1 - axes, respectively.

At this point one may straightforwardly determine the velocity potential ϕ_{12} and substitute it with ϕ_2 into the unsteady Bernoulli equation to obtain pressure distributions and then the acting forces can be calculated by carrying integration of the pressure over the surface as outlined in Section 2 of (I). As the authors of (I) indicated, however, this pressure integral would be complicated to work out directly, so they instead followed the approach of Lighthill (1960) to obtain the lateral force without considering the detail geometry of the surface contour other than the sectional area curve and the added mass distribution. In the following we shall show that this problem can be solved directly by the application of Lagally's theorem. While the authors of (I) are highly critical of the use of Lagally's theorem and the approach in general to ignore end effects, we shall show that for our problem the approach is appropriate. We shall also show the application of the Lagally theorem to bodies of arbitrary cross section. If the body cross section form is properly considered, the application of the Lagally theorem will result in the same formula as that derived in (I) by using the momentum theorem.

FORCES AND MOMENT ON A MOORED VESSEL

The induced singularity distributions in body 1 have been determined and given in (7) and (8). The forces and moment can then be evaluated by application of the Lagally theorem for unsteady flow as shown by Cummins (1954). Accordingly, the differential forces on the moored ship can be written:

$$dX(x_1, \xi) = 2\pi\rho[\mu_{1x}\frac{\partial U}{\partial x_1} + \frac{\partial \mu_{1x}}{\partial t}]dx_1 \quad (9)$$

$$dY(x_1, \xi) = 2\pi\rho[\mu_{1x}\frac{\partial V}{\partial x_1} + \frac{\partial \mu_{1y}}{\partial t}]dx_1 \quad (10)$$

where ρ is the fluid density. The first term on the righthand side of the above equations is the Lagally forces in a steady flow. The second term is the contribution due to the flow unsteadiness, and corresponds to the rate of change of momentum arising from the singularities induced inside the body. In a fixed reference frame, the time derivative in the second term can be written:

$$\frac{\partial}{\partial t} = -U_2 \frac{\partial}{\partial \xi}$$

By definition, the velocity components U and V of the induced stream field are both small as compared with U_2 , so that the steady Lagally force term in (9) and (10) may be neglected as compared with the time varying term. Substituting (7) and (8) into (9) and (10) and integrating over the body length L_1 , we obtain the leading order approximation of the total surge and sway forces on the moored ship.

$$X(\xi) = -\rho U_2 \int_{L_1} S_1(x_1) \frac{\partial}{\partial \xi} [U(x_1, \xi)] dx_1 \quad (11)$$

$$Y(\xi) = -2\rho U_2 \int_{L_1} S_1(x_1) \frac{\partial}{\partial \xi} [V(x_1, \xi)] dx_1 \quad (12)$$

Substituting U and V from (5) and (6), integrating by parts, and assuming $S_1(x_1) = 0$ at the body ends, we obtain the final expressions for these forces:

$$X(\xi) = \frac{\rho U_2^2}{2\pi} \int_{L_1} S_1'(x_1) \int_{L_2} \frac{S_2'(x_2)(x_2 - x_1 - \xi) dx_2}{[(x_2 - x_1 - \xi)^2 + \eta^2]^{3/2}} dx_1 \quad (13)$$

$$Y(\xi) = \frac{\rho U_2^2 \eta}{\pi} \int_{L_1} S_1'(x_1) \int_{L_2} \frac{S_2'(x_2) dx_2}{[(x_2 - x_1 - \xi)^2 + \eta^2]^{3/2}} dx_1 \quad (14)$$

Tuck and Newman's expression for side force given in equation (29) of (I) agrees with (14) if their double-ship form 1 is axisymmetrical and $U_1 = 0$. (Note that their formula is given for the double body and their definition of $S(x)$ is twice as large as ours.)

Similarly, the yaw moment to leading order approximation is just the unsteady Lagally moment. For a slender body, it has been shown by Cummins that this moment can also be expressed by an integral over the ship length. The final expression for yaw moment is:

$$N(\xi) = \frac{\rho U_2^2 \eta}{\pi} \int_{L_1} [S_1'(x_1)x_1 + S_1(x_1)] \int_{L_2} \frac{S_2'(x_2) dx_2}{[(x_2 - x_1 - \xi)^2 + \eta^2]^{3/2}} dx_1 \quad (15)$$

Again, (15) agrees with (30) of (I).

Equations (13), (14), and (15) complete our results for the surge force, side force and yaw moment acting on a moored vessel as a result of the passing of another ship. These forces and moment are shown depending upon the two ships' separation distances and their sectional area distributions. In the derivation of these equations, the moored ship together with its image is represented by an axisymmetrical body; no such restriction on the passing ship is imposed, however.

NUMERICAL RESULTS

We assume the two ships both having a simple sectional-area distribution of parabolic form as follows:

$$S_j(x_j) = S_j (1 - 4x_j^2/L_j^2) \quad (16)$$

where S_j is the midship sectional area and j is the index denoting ship 1 or 2. In order to describe the general sequential phenomena on a moored ship as another ship passes alongside, we consider a special case that two ships of identical length L have a separation distance $\eta = L/4$. The calculated results are shown in Figure B. The resulting forces and moment are either an even or an odd function of the stagger distance ξ , as both ships are assumed fore-and-aft symmetric. According to the schematic drawing shown in Figure A, the moving ship passes from the stern of the moored ship to the direction of its bow. As shown in Figure B, the interactions begin well before the two ships actually start to overlap. Generally there is a small repulsion force acting on the stern of the moored ship in both longitudinal and lateral directions. As a result, the moored ship experiences a small surge force toward the bow, and a small lateral force tending to swing its stern toward the dock. As the passing ship proceeds to overlap, the moored ship begins to experience a suction force from the passing ship and the surge force changes its sign; the lateral force gradually reaches its secondary peak and the resulting tendency is to pull the stern of the moored ship back toward the passing ship. As the passing ship continues to pull up, the aftward surge force becomes stronger; so does the lateral attractive force at the stern of the moored ship. The longitudinal attraction soon reaches its maximum and eases off. The lateral attractive force continues to grow but more effect of bow picks up and the contribution of stern falls off. As the two ships come abreast, the lateral attraction reaches its primary peak; and meantime, there is a rapid change in surge force, which shifts from aftward to foreward, as well as there

is a change in yaw moment such that the attraction at the bow becomes stronger than that at the stern. As the passing vessel draws ahead, the above sequence is reversed as shown in Figure B.

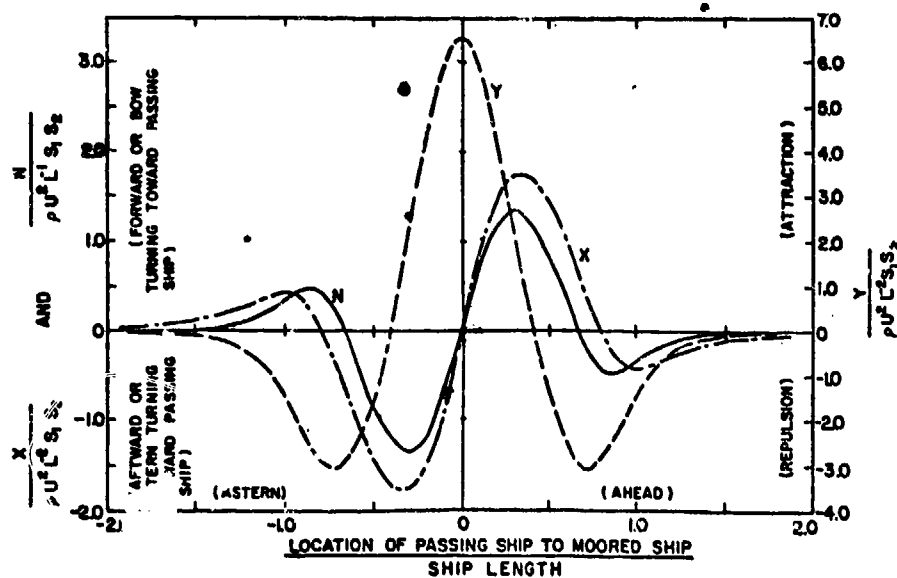


Figure B - Surge Force, Sway Force, and Yaw Moment on a Moored Ship (Two Ships of Equal Length with a Centerline Distance $\eta = 0.25L$)

In a general case, substituting the geometry information (16) into (13-15), one may evaluate the integrals and obtain the surge force, sway force and yaw moment as a function of the separation distance η , the stagger distance ξ , and the relative length ratio of the two ships L_2/L_1 . For given values of L_2/L_1 and η a similar result as shown in Figure B can be obtained. From the mooring design calculation point of view, however, only the peak values of these forces and moment are of interest. Figures C - E summarize the calculated results of the non-dimensional peak surge force, sway force, and yaw moment, respectively, plotted as a function of separation distance for a range of various length ratios from $L_2/L_1 = 0.5$ to 2.0. Noting from these figures, the strong dependence of the forces and moment on the separation distance is evident. This is especially true if $L_2/L_1 < 1$. The effect becomes slightly weaker when $L_2/L_1 > 1$, as the fore-and-aft interaction due to the passing ship is more effective when the separation is sufficiently large if the passing ship is much longer than the moored ship. By the same token, if the passing ship is much longer, the effects on the moored vessel are generally significant even when the separation distance is large.

This feature is rather clearly demonstrated in the plot of the maximum side force as shown in Figure D.

The calculations given above are based upon the assumption that the ship hull and its image constitute a double-body form which has an axisymmetry and its sectional area distribution is a parabolic curve as given by (16). While it is anticipated that this distribution of sectional area should provide a good representation for a wide range of regular surface ships, it is still interesting to examine the validity for application of the calculated results to ships of arbitrary cross section including the possible stern effects due to vortex shedding from the trailing edges of rudder and deadwood.

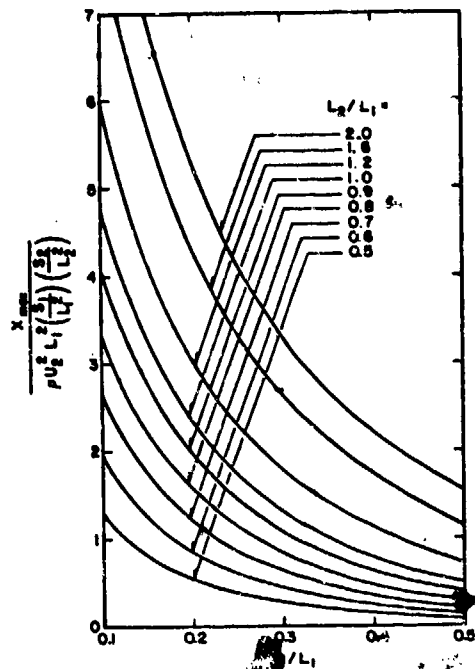


Figure C - Nondimensional Peak Surge Force on a Moored Ship as a Function of its Lateral Separation from a Passing Ship (Subscript 1 denotes for moored ship, 2 for passing ship)

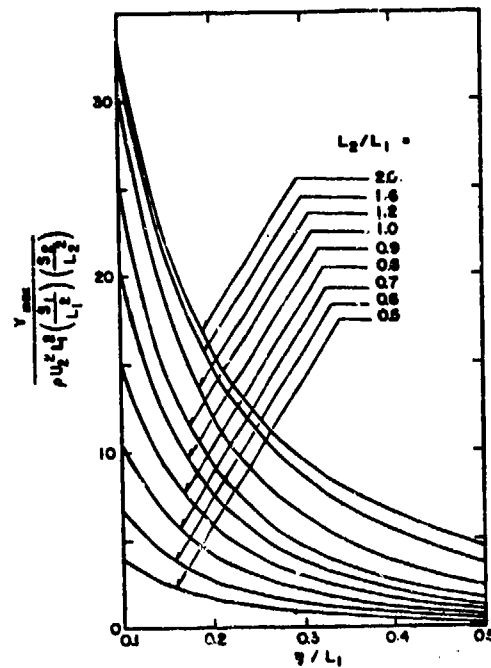


Figure D - Nondimensional Peak Sway Force on a Moored Ship as a Function of its Lateral Separation from a Passing Ship (Subscript 1 denotes for moored ship, 2 for passing ship)

To leading order of slender body approximation, the representation for bodies of arbitrary cross section departs from which for axisymmetric bodies by the refinement to include correct added mass effects. As is well known according to slender body theory, the kinetic energy of the fluid is zero due to the body's longitudinal movement, and there is no added mass effect in surge motion. Consequently, the present calculation of surge force makes no difference for ships of an arbitrary slender form. In lateral motion, the above analysis has assumed $A_1(x_1) = S_1(x_1)$, where A is the added mass per unit length, divided by the fluid density. For a ship having a conventional beam-draft ratio, the integrated effect of the added mass is generally smaller than the displaced mass. As a result, the present expressions for the side force and yaw moment virtually provide a conservative estimate, which is appropriate in dealing with peak loading design calculations. Figure 5 of (I) shows the side force on a moored ship when a moving ship passes by, in which the calculation considers a constant added mass coefficient and assumes a Kutta condition at the stern. The principal particulars of these two ships are given in (I) and included in the following for con-

venience of reference. Ship A is the battleship KING GEORGE V, of length 740 ft., beam 103 ft., draft 29.3 ft., and displacement 36890 tons. Ship B is the R.F.A. OLNA, of length 567 ft., beam 70 ft., draft 30 ft., and displacement 23570 tons. Their midship section areas are 3050 and 2075 sq. ft., respectively. The calculated result of side force on Ship A by the present formulation, assuming axisymmetrical double-body form and considering no stern effect, is compared with that of (I) as shown in Figure F. (The nondimensional force scale is wrongly labeled by a factor of two in Figure 5 of (I).) The axisymmetrical double-body model yields a larger peak force as expected. The difference is mainly due to the deviation in the added masses between the two models and can be roughly estimated from the midship information by the ratio $(S_1 - A_1)/2S_1$ or $\frac{1}{2} - \frac{1}{2} (T/R)^2$, where T is the mean draft and R is an equivalent radius of the midship section, $R = (2S_1/\pi)^{1/2}$. It accordingly yields a difference of 28% for the present case. The actual calculation reveals a difference of about 30% as shown in Figure F. For ships of smaller beam-draft ratio, this difference tends to be small. The stern effect is generally small; it slightly shifts the phase

and yields a small asymmetry but affects little on the magnitude of the peak forces. Therefore, for applications in mooring calculations in which the peak loadings are of primary interest, the end effects may be ignored.

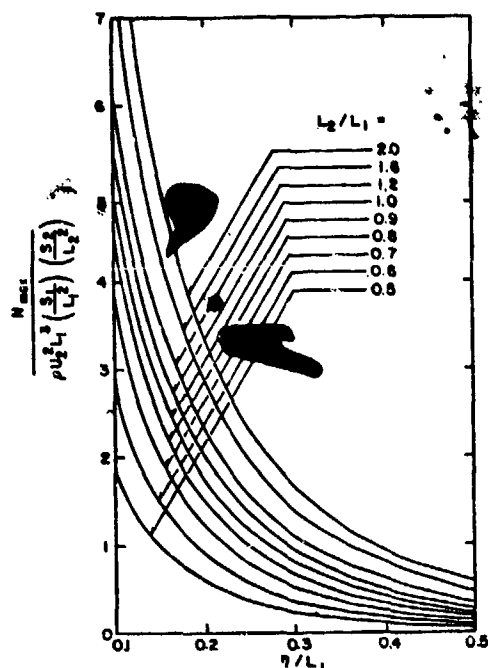


Figure E - Nondimensional Peak Yaw Moment on a Moored Ship as a Function of its Lateral Separation from a Passing Ship (Subscript 1 denotes for moored ship, 2 for passing ship)

APPLICATION OF LAGALLY'S THEOREM TO BODIES OF ARBITRARY SLENDER FORM

As was discussed in the previous section, the body cross section form does not affect the surge force. Only the lateral mode, therefore, is discussed in this section.

We consider a general case that $U_1 \neq U_2 \neq 0$. In a uniform flow field having velocity components U and V , body 1 has approximately an effective distribution of doublets as follows:

$$\mu_{1x}(x_1, \xi) = \frac{1}{2\pi} S_1(x_1) [U(x_1, \xi) - U_1] \quad (17)$$

$$\mu_{1y}(x_1, \xi) = \frac{1}{2\pi} [S_1(x_1) + A_1(x_1)] V(x_1, \xi) \quad (18)$$

U_1 is the constant speed of body 1. When $U_1 = 0$, (17) is identical to (7). $A_1(x_1)$ is proportional to the added mass distribution of ship 1. For an axisymmetrical body $A_1(x_1) = S_1(x_1)$, (18) is in agreement with (8). U and V are the velocity components of the flow field induced by body 2; they have been given in (5) and (6).

Disregarding the detailed distribution of $A_1(x_1)$, one may simply regard it as regular as $S_1(x_1)$ at the moment so that the differential side force may be obtained through application of Lagally's theorem using equation (10). The first term gives the Lagally force in a steady flow. Following (1), we write V in the moving reference frame of body 2:

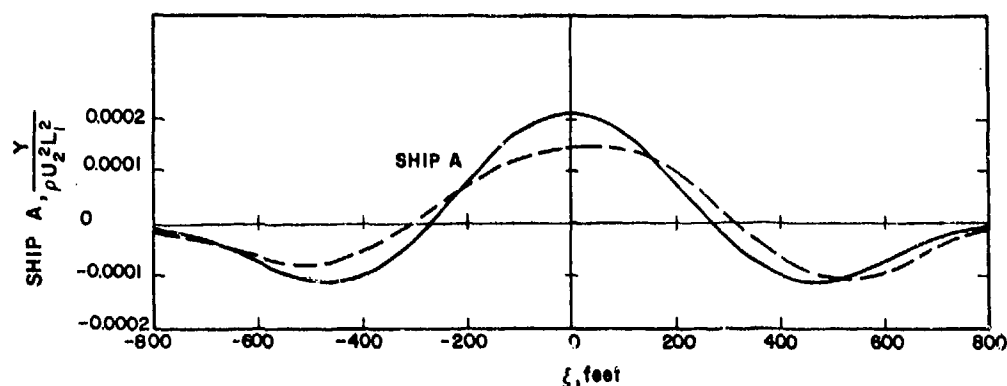


Figure F - Theoretical Sway Forces on Ship A ($U_1 = 0$) due to Ship B Passing at Speed U_2 . Solid line for symmetric model calculated according to Eq. (14), broken line for model of constant draft calculated by Tuck and Newman (1974)

$$V(x_2) = \frac{U_2 \eta}{2\tau} \int_{L_2} \frac{S_2'(x) dx}{[(x_2 - x)^2 + \eta^2]^{3/2}} \quad (15)$$

Substituting (17) in the first term of (10), making use of (19) for V , and noting that

$$\frac{\partial}{\partial x_1} = \frac{\partial}{\partial x_2} = \frac{\partial}{\partial x}, \text{ to leading order we obtain:}$$

$$dY_t = -\rho U_1 S_1(x_1) V'(x_2) \quad (20)$$

Similarly, after substitution of (18), the time varying term in (10) gives:

$$dY_t = \rho D \{ [S_1(x_1) + A_1(x_1)] V(x_2) \} \quad (21)$$

$$\text{where } D = \frac{\partial}{\partial t} - U_1 \frac{\partial}{\partial x_1}$$

in reference frame 1,

$$\text{and } D = \frac{\partial}{\partial t} - U_2 \frac{\partial}{\partial x_2}$$

in reference frame 2.

Separating $S_1(x_1)$ from $A_1(x_1)$, it follows that:

$$\begin{aligned} dY_t &= \rho S_1(x_1) D[V(x_2)] \\ &+ \rho D[A_1(x_1) V(x_2)] \\ &- \rho U_1 S_1'(x_1) V(x_2) \end{aligned} \quad (22)$$

Since that $S_1'(x_1) = 0$ has been assumed at the body ends, the integrations over the ship length of the last term in (22) and the steady Lagally force given in (20) exactly cancel out each other. The net result of the differential force is therefore simply:

$$\begin{aligned} dY &= \rho S_1(x_1) D[V(x_2)] \\ &+ \rho D[A_1(x_1) V(x_2)] \end{aligned} \quad (23)$$

which is in agreement with equation (25) derived in (1) using conservation of momentum arguments.

Up to this point, no detailed distribution of $A_1(x_1)$ has been considered. Now following the assumption of (1) that A_1 is allowed to be non-zero but is regarded as a continuous function at the stern in order to satisfy the Kutta condition, the final expressions of side force and yaw moment (29-30) given in (1) can be exactly reproduced. The major difference of these expressions from those for an axisymmetrical body is the trailing edge term, which corresponds to the rate of shedding of downward momentum at the

rear. Calculations have been conducted by evaluating these integrals for two ships moving parallelly at an equal speed, but various stagger distances. The experimental results of the interaction effects between the two ships has been reported by Newton (1960). Taking the same assumption as in (1) that the drafts of the two ships are constant along the length, we have obtained numerical results of interactions between the two ships. While the results of side force agree with that obtained by Tuck and Newman as shown in Figure 2 of (1), our results of yaw moment show better agreement with the experiments. The comparison between theory and experiments is given in Figure G.

CONCLUDING REMARKS

In concluding our discussion, the following remarks are made with regard to the induced loading on a moored vessel.

1. Theoretically, Figures C, D, and E provide a conservative estimate for the peak forces and moment on a moored vessel, resulting from hydrodynamic interactions induced by the passing of another ship.
2. The small hull asymmetry in the underwater profile, introduced by rudder deadwood, etc., may slightly shift the phase of interaction but insignificantly affects the magnitude of the peak loadings.
3. For ships of large beam-draft ratio, the overestimate on side force by using Figure D can be approximated by $\frac{1}{2} - \frac{1}{2} \left(\frac{T}{R} \right)^2$, where T is the mean draft of the moored vessel and R is an equivalent radius defined by $R = (2S_1'/\pi)^{1/2}$, S_1' being the midship section area of the moored vessel. For ships of relative small beam-draft ratio, say 2, the error should be small.
4. The peak loadings are strongly dependent on the lateral separation distance. If the passing ship is shorter than the moored ship, the interactions are noticeable only when the lateral distance is small. If the passing ship is much longer than the moored ship, the effects are generally significant even at a large lateral separation.

REFERENCES

- Cummins, W. E., "Hydrodynamic Forces and Moments Acting on a Slender Body of Revolution Moving Under a Regular Train of Waves," David Taylor Model Basin Report, 910, 1954.

Lighthill, M. J., "Note on the Swimming of Slender Fish," J. Fluid Mech. 9, 1960, pp. 305-317.

Newton, R. N., "Some Notes on Interaction Effects Between Ships Close Aboard in Deep Water," Proc. First Symposium on Ship Maneuverability, David Taylor Model Basin Report, 1461, 1960.

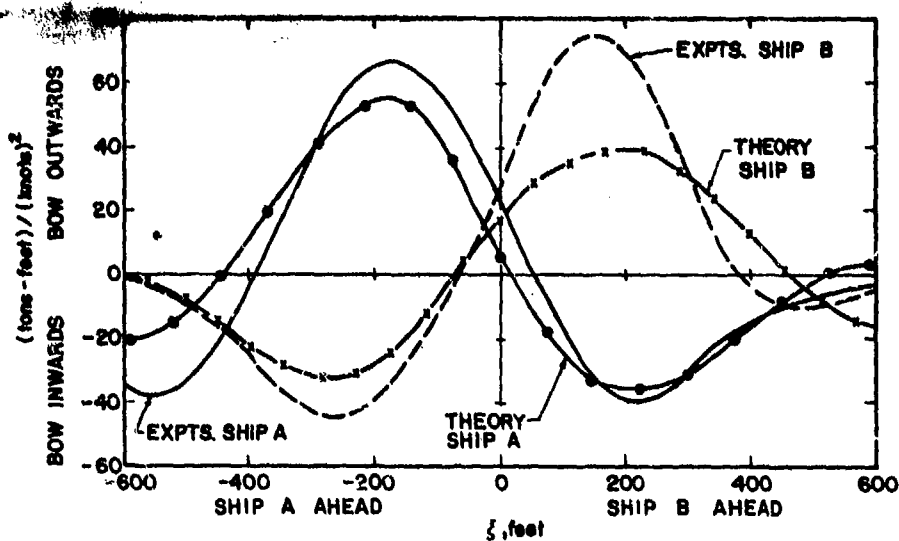


Figure G - Yaw Moments on Two Ships, and Corresponding Experimental Results of Newton (1960)

AUTHOR'S REPLY

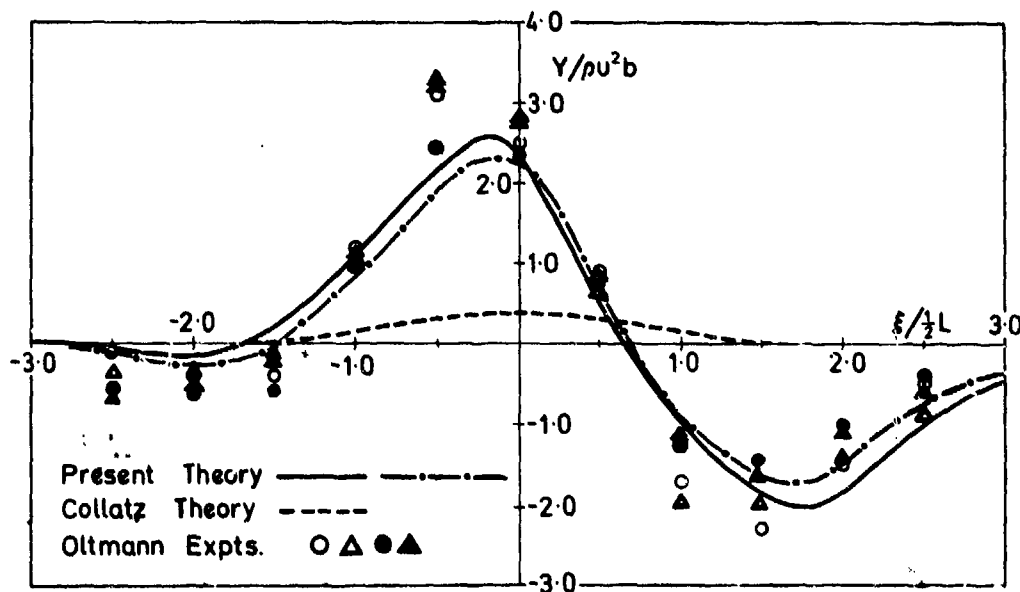
The authors thank Dr. Schmlechen for drawing attention to his own discussion of Collatz's paper, and for pointing out the modified final title of Collatz's thesis. The change in title from "ships" to "elliptical cylinders" nevertheless skirts the formidable problem of how to determine the circulation around a body with a blunt trailing edge. We should stress that, in spite of our criticism, we regard the paper of Collatz to be a significant contribution in its own right, since it presents an "exact" calculation in which no assumptions of thinness or slenderness have been made. Further comments on this matter are contained in the discussion by Professor Tuck of Dr. Dand's paper.

We share Dr. Dand's dismay at the paucity of experimental data, and thank him for noting the reference by Moody. Regarding the importance of hull shape in the shallow water case, the following new results may be of interest. The "Present Theory" curve of Figure 7 was computed by replacing the elliptical cross-section by a circumscribing rectangle. The corresponding results for a true ellipse have recently been computed by Mr. G. King, and are shown chain-dotted in Figure H. This figure is a reproduction of Figure 7, with the addition of the new theoretical curve and some additional experimental points taken from Oltmann (6). The two theoretical curves are quite close to each other. It would appear that the present theory is predicting the experimental results to within an order of error comparable to the variabilities in the experiments themselves due to effects of finite Froude number and of submergence depth. With respect to ship hulls in shallow water of realistic depths, it seems unlikely that satisfactory results will be obtained until the theory is extended to account for the gap effect beneath the keel, as

outlined in Section 4. Hopefully, while this theoretical extension is in progress, our towing-tank colleagues will carry out the corresponding experiments. The interaction between a small ship and a large ship, when the relative fluid depths based on each ship's draft are very different, is indeed an interesting problem, and one which could possibly be analysed by suitable extensions and combinations of our theories, but not without considerable additional work.

We are grateful to Mr. Martin for the new experimental data which he has shown. These results are quite striking, by comparison to the earlier published results for KGV and OLNA, but it is difficult to comment on these new results from the theoretical standpoint without performing computations for the ships in question.

Dr. Wang has elaborated on his own parallel work, and especially on the importance of the moored-ship interaction effects. He also has illustrated the point which we made regarding Lagally's Theorem; thus his equations (20) and (22) differ from our (25) or his (23) by a perfect differential in x , which affects the force distribution and yaw moment, but not the total force. Of more vital importance, Dr. Wang has brought to our attention errors in our original computation of the interaction moment, shown in Figure 3, as well as a factor of two error in labelling Figure 5. Both errors have been corrected in these Figures as they appear here. We are pleased to note that the corrected results for the interaction moment are in much better agreement with the experimental values, and hence the reservations made in the text below Figure 3 are less appropriate than had appeared previously.



BANK EFFECTS ON A SHIP MOVING THROUGH A SHORT DREDGED CHANNEL

N. H. Norrblin
Swedish State Shipbuilding Experimental Tank
Sweden

ABSTRACT

This paper presents a first description and analysis of a series of captive force measurements and "free-response" trajectory tests, which have been performed with a tanker model, moving along long and short side wall banks and platform shallows, and off-set from the centerline of a dredged channel. The results from the measurements of lateral force and yawing moment are displayed in various graphs, and they are compared with calculations according to known theories. The ultimate aim of the project is the formulation of an analytical model, which will simulate the "bank effects" experienced, and which, in a particular trial case, will make it possible to predict the free response of the model from the forces measured at the captive tests.

NOMENCLATURE

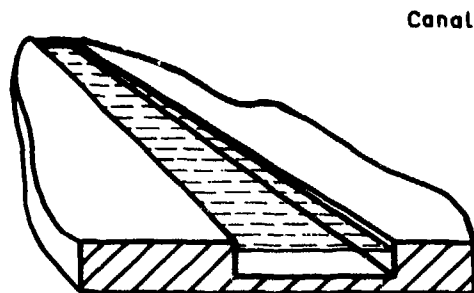
When applicable the symbols and abbreviations used here have been chosen in accordance with the SNAME and ITTC recommendations. Non-dimensional coefficients are given in the "b/s" system, in which the units for mass, length and time are m , $L = L_{pp}$, and L/g respectively, /1/.

Symbol	Definition	Physical Dimension
A	Section area of hull	L^2
A_m	Midship section area	L^2
A_r	Rudder area	L^2
B	Beam of hull	L
C_p	Pressure coefficient	-
D	Propeller diameter	L
F_n	Froude number (F_{nh} , $F_{nL} = V^n$)	-
H	Height of platform bank	L
L	Length of hull ($L = L_{pp}$)	L
M	Yawing moment about z axis	ML^2T^{-2}
P	Propeller pitch	L
S_n	Strouhal number	-
T	Draught of hull	L

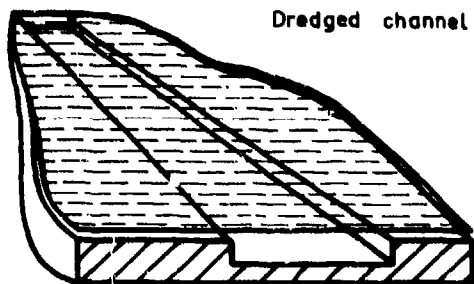
Symbol	Definition	Physical Dimension
V	Velocity of origin of body axes	LT^{-1}
W	Channel width	L
W_p, W_s	Distance from ref. line to port and stbd bank, resp.	L
X, Y, Z	Hydrodynamic forces along body axes	MLT^{-2}
b	Height of rudder	L
g	Acceleration of gravity	LT^{-2}
h	Depth of water in fairway	L
h_1	Depth of water above platform shallow	L
m	Mass of body	M
p	Pressure in general	$ML^{-1}T^{-2}$
q	Stagnation pressure	$ML^{-1}T^{-2}$
t	Time	T
u, v, w	Components of V along body axes	LT^{-1}
x, y, z	Co-ordinates in right-handed system of body axes	L
∇	Volume displacement	L^3
β	Angle of drift	$\tan \beta = \frac{v}{u}$
δ	Rudder angle	-
δ_{pp}	Block coefficient	-
$\}$	Under-keel clearance parameter, $\} = T/(h-T)$	-
η	Ship-to-bank distance parameter, $\eta = \eta_s + \eta_p$	-
η_p, η_s	Do, port and stbd resp.	-
$\bar{\eta}$	Bank spacing parameter, $\bar{\eta} = \eta_s - \eta_p$	-
ρ	Mass density of water	ML^{-3}
ϕ_{90}	Prismatic coefficient	-

INTRODUCTION

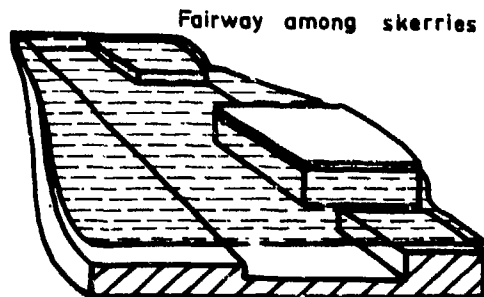
The problems associated with steering in a straight canal have been the subject of many classical experiments as well as of more recent studies of analytical nature, all pertaining to the case of long high side wall banks, protruding out of the water. The author is not aware of any paper related to the "short canal" or isolated bank segment, however, nor to the dredged channel configuration. The three diagrams in Fig. 1 may illustrate the schematic topography of a conventional (closed) canal, a dredged (open)



Canal



Dredged channel



Fairway among skerries

channel, and a fairway bounded by short side banks (walls) and shallows (platforms). The ultimate aim of the present project is an analytical model, which will simulate the "bank effects" experienced by a ship that moves in a fairway bounded by similar topographic elements.

We may also hope that the results will help to define the practical domains of channel and shallow water navigation. According to the International Oil Tanker Commission "channel navigation is not very different from the one over flat ground if bank height over depth < 0.4 , if not, it can be related to the navigation in a canal enclosed between two banks", /2/. We will see that our force measurements on a model in different channel sections do support the first part of this statement, but that even a moderate depth of water above the platform banks will reduce the bank effects well below those expected in a closed canal.

We may further hope to be able to better understand the meaning of a "long" or a "short" bank. In an earlier paper, and on the basis of an approximate calculation of the pressure distribution on a wall adjacent to a moving deep-draught oval cylinder, the present author concluded that "end effects from short banks will be felt at a longitudinal distance of $1.5 L$ forward of bow and aft of stern, and transient phenomena will dominate during the passage of a bank which is, say, of a length less than six times the length of the body", /1/. Again our force measurements on a model abreast banks of different lengths confirm this statement. Every finite bank element, long or short, will have an end, however, and the measurements also clearly indicate that a ship will experience yawing moments of appreciable magnitude during the passage of these ends.

The classical effect of bank suction on a ship that moves in a steady state off the centre-line of a long straight canal is illustrated in Fig. 2; to balance the suction force and the bow-away-from-wall moment it is necessary to find an equilibrium position with bow out and helm towards the near bank. (Typically, a drift angle of 1° may be associated with a rudder angle of, say 15° .)

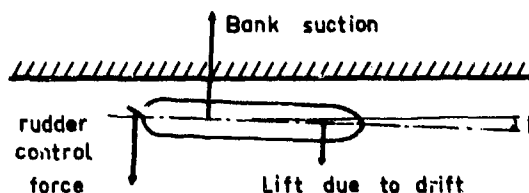


Fig. 1. Schematic classification of topographic environment

Fig. 2. Equilibrium conditions in motion along a long canal bank

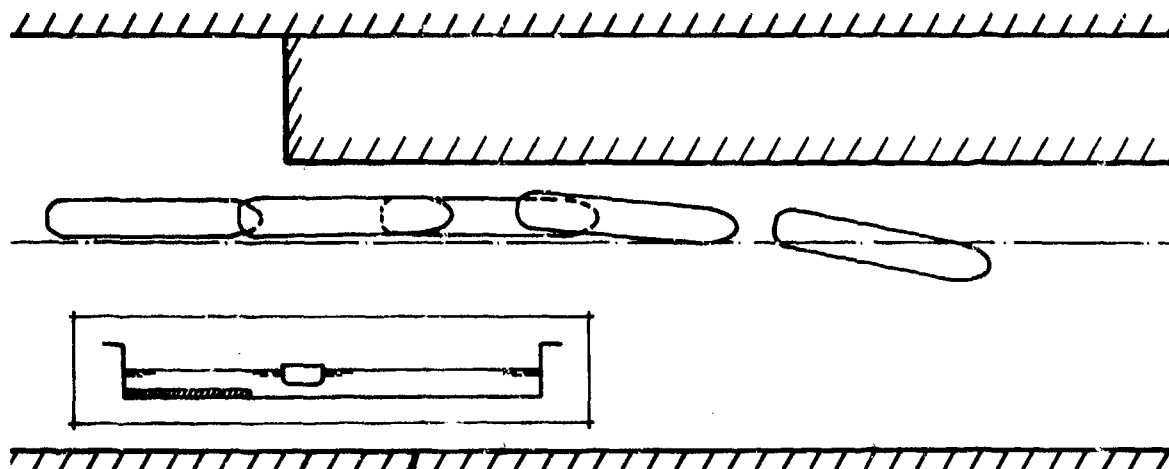


Fig. 3. Record of the movement of an uncontrolled model meeting a shallow bank

What will happen to a ship in a similar equilibrium position in a wide canal if it suddenly approaches the beginning of a side bank closer to one side, or if the long canal suddenly widens to one side? A typical result of one of the new free-running model experiments is reproduced in Fig. 3: soon before meeting the bank the model was let free to respond to the changing disturbances. The meeting phase is dominated by the effect of growing side-way suction, until, when its full length has passed past the edge of the bank, the model sheers away to the opposite side. There is every reason to study the details of the transient "bank effects" causing this behaviour.

MODEL EXPERIMENTS - SHIP MODEL AND PROTOTYPE

The ship model is a replica in the scale 1:64 of a 280 000 tdw ore/oil carrier prototype, for which delivery trial data and PMM model test results are available from previous studies of deep water manoeuvring, /3/. Body plan and contours are reproduced in Fig. 4, which shows a large protruding bulbous bow and a Mariner type half-spade rudder. At the experiments reported on here the model was propelled by a right-handed 4-bladed screw. The main characteristics of the hull form are given in Table 1, those of the rudder and screw in Table 3.

To encourage comparative calculations of hull hydrodynamics the ordinates of the sectional area curve are listed in Table 2. (Cf. Fig. 4.)

Table 1 Main Hull Characteristics (Loaded)

	Model	Ship	Non.-Dim. on L
L_{pp} (L)	5.024	321.56 m	1.0000
B	0.852	54.56 m	0.1696
T	0.339	21.67 m	0.0675*
∇	1.192	312 200 m ³	-
x_0/L	0.0292		
δ_{pp}	0.8213		
ϕ_{pp}	0.8231		
β	0.9978		

Table 2 Sectional Areas

Station	Co-ord. x/L	$A(x)/A_m$
-	-0.520	0
0	-0.500	0.043
1/2	-0.475	0.104
1	-0.450	0.255
1 1/2	-0.425	0.342
2	-0.400	0.457
3	-0.350	0.665
5	-0.250	0.925
7	-0.150	0.955
9	-0.050	1.000
10	0	1.000
11	0.050	1.000
13	0.150	1.000
15	0.250	1.000
17	0.350	0.954
18	0.400	0.816
18 1/2	0.425	0.753
19	0.450	0.503
19 1/2	0.475	0.276
19 3/4	0.4875	0.173
20	0.500	0.104
-	0.521	0.054
-	0.550	0

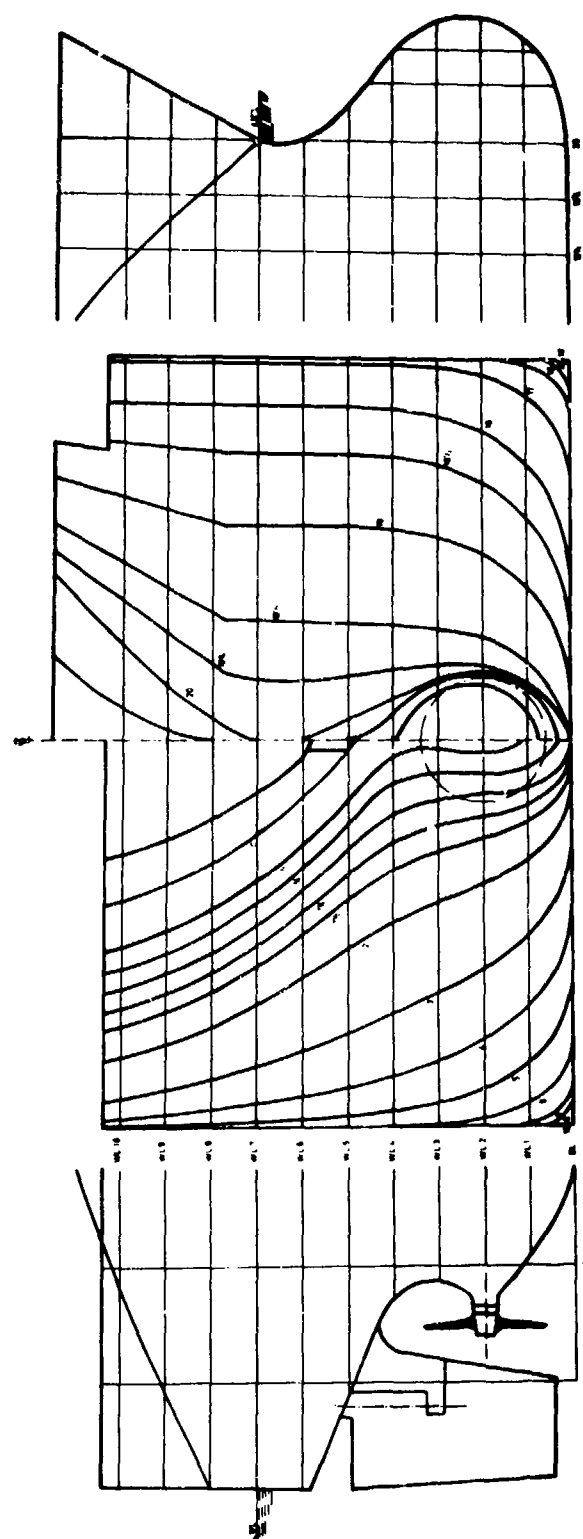


Fig. 4. Model 280 000 t_{dw} ore/oil carrier
Body plan and profiles

Table 3 Characteristics of rudder and screw

		Model	Ship	
Rudder area, total	A_r	0.0281	115.0	m ²
- " - movable	A_{rm}	0.0230	94.4	m ²
Rudder height	b	0.217	13.90	m
Rudder area ratio	A_r/LT	0.0165	-	-
Rudder aspect ratio		1.680	-	-
Propeller diameter	D	0.131	8.40	m
Pitch ratio	P/D	0.850	-	-
Blade area ratio	A_D/A_0	0.550	-	-

MODEL EXPERIMENTS - WATERWAY MODELS

The "waterway" was modelled in the Large Shallow Water Tank of Versuchsanstalt für Binnenschiffbau in Duisburg (VBD), where captive model tests also previously had been performed within SSPA research programs, /1/. The waterway was of necessity limited in width by the side walls of the basin, 9.800 m apart, and in depth by the maximum water height h allowed for, 1.020 m. The "fairway" is a more narrow lane within the waterway, bounded by the envelope of safe side bank and under-keel clearances. At the present tests side banks were represented by the basin walls and by platform solids of GRP panels built up to three different lengths (L_B) and three heights (H). To prevent pressure leakage between and into building blocks the platforms were covered by aluminium foils and joints and screw holes were sealed by plastic tape.

Fig. 5 (Below) Captive test program - Bank elements in the VBD Large Shallow Water Tank

Canal & bank configurations		Range of test parameters					
Section	Plan	Series No.	h mm	$W_p - \%$ mm	V m/s	RPS	δ
	 $L_B = \infty$	40	1020-442	730-1700	0.540	9.0-9.9	+2°
	 $L_B = 5L$	21	1020-850	660-1650	0.514	7.8	0°
		41	1020-646	590-1700	0.540	8.6-8.9	+2°
	 $6L$	22	850-510	660-1650	0.514	8.1-11.7	0°
		42	918-442	590-1700	0.540	8.9-9.0	+2°
	 $6L$	23	510-408	660-1650	0.514	10.1-10.5	0°
		43	646-408	590-1700	0.540	9.0-9.6	+2°
	 $6L$	44	646-442	590-1700	0.540	9.0-9.8	+2°
	 $3L \quad L$	25	510-408	660-1650	0.514	10.1-10.5	0°
		45	646-408	590-1700	0.540	8.5-10.2	+2°
	 $3L \quad L$	26	850-510	660-1650	0.514	8.0-9.3	0°
		46	918-442	590-1700	0.540	8.8-9.3	+2°
	 $3L \quad L$	27	1020-850	660-1650	0.514	7.8-7.9	0°

In all 11 different models of the waterway were investigated, using basin walls, and port and/or starboard platforms. (See schematic diagram in Fig. 5.) For each configuration tests were run at several depths of water. If $h \geq H$, water depth above side platform is denoted by h_1 , so that $(h - h_1)/h \leq 1$.

MODEL EXPERIMENTS - CAPTIVE TEST PROGRAM

The captive test program included two sequences of experiments, the first executed in 1972, the second in early 1974. The preliminary results of the 1972 "finite length platform" series suggested that these experiments be repeated and extended within a wider range of test parameters, using a new set of force gauges. (See below.) The 1974 series also included the long bank case - no platform in the basin - and they were finally completed by a set of free-running response tests as exemplified here in the Introduction.

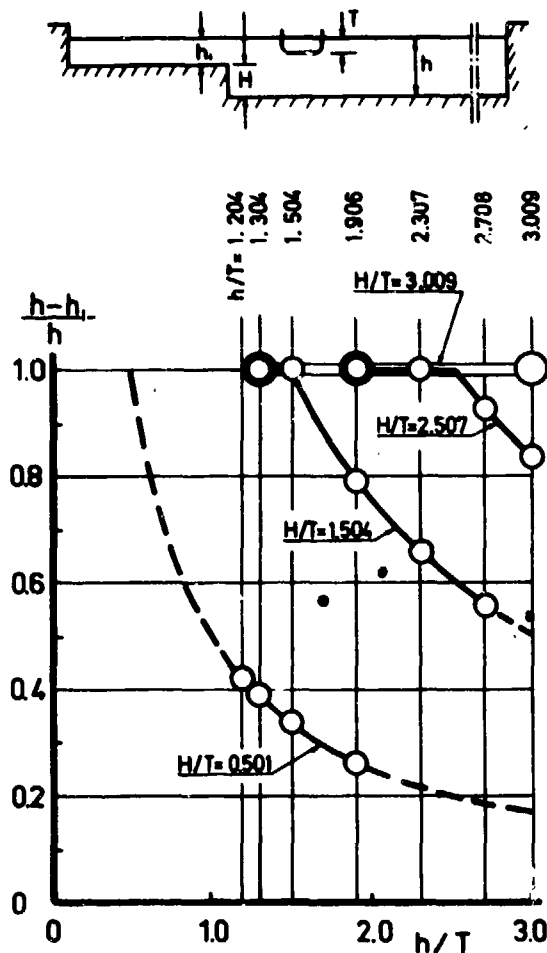


Fig. 6. Captive test program - Depth ratios in the 1974 (40 Series) tests

For the purpose of this first report the full range of test parameters was as given in Figs 5 and 6; additional runs covered variations of drift angle β , rudder angle δ , and screw RPM. (A rudder angle $\beta = 2^\circ$ - port rudder - proved to balance the asymmetrical effect of the single screws in free, deep water, and was selected as a basic setting in the 40 Series.) Model speed was equivalent to 8 - 8.4 knots for the 322 m ship. Froude number based on depth never exceeded $F_{nh} = 0.27$.

MODEL EXPERIMENTS - CAPTIVE TECHNIQUE

The model was free to heave and trim in a set of guiding linkages attached to the rigid frame of the carriage. The natural vertical frequency of the carriage was estimated to be of the order of 5 Hz. Special accelerometer measurements made on the carriage part members of the linkage system showed exciting frequencies of the order of 1 Hz, possibly due to wheel rotation, and isolated peaks at intervals; the latter only were refound in the force component records.

Aft and forward lateral force, and the small longitudinal force as difference between propulsive force and resistance, were all measured by resistance-wire-type strain gauges in full bridges. The analogue force records suffered from oscillations superimposed on the transient time histories, with a characteristic frequency of 0.25 - 0.35 Hz for lateral forces and twice as high for the longitudinal ones. (0.25 Hz corresponds to a Strouhal number based on beam equal to $St = 0.4$.) At the smallest bottom clearance ($h/T = 1.20$) there was a dominating disturbance in the forward gauge records, having a frequency of approximately 0.05 Hz or a period of 20 seconds, corresponding to the time in which the model travelled twice its length. This effect may be attributed to flow separation originated on the bulbous bow.

Zero readings were taken with model at rest before and after each run. These zero readings are the natural reference values to be used when evaluating the forces experienced when passing a long high wall, or a high isolated bank. In the course of a typical run down the basin and past an isolated shallow platform bank, such as illustrated in Fig. 7, the record contains one set of steady state forces during the approach, and another set of "steady state" or maximum forces abreast the platform. The assumption has then been made that the net effect of the presence of the shallow bank is given by the differences appearing between the two sets of values read.

The assumption just made may be inferred from the validity of the superposition principle as demonstrated in ref. /1/. In particular it was shown there that the asymmetrical forces on a ship in a canal could be obtained by adding the effects from port and starboard walls. (In very narrow canals there is also a coupling effect due to blockage.)

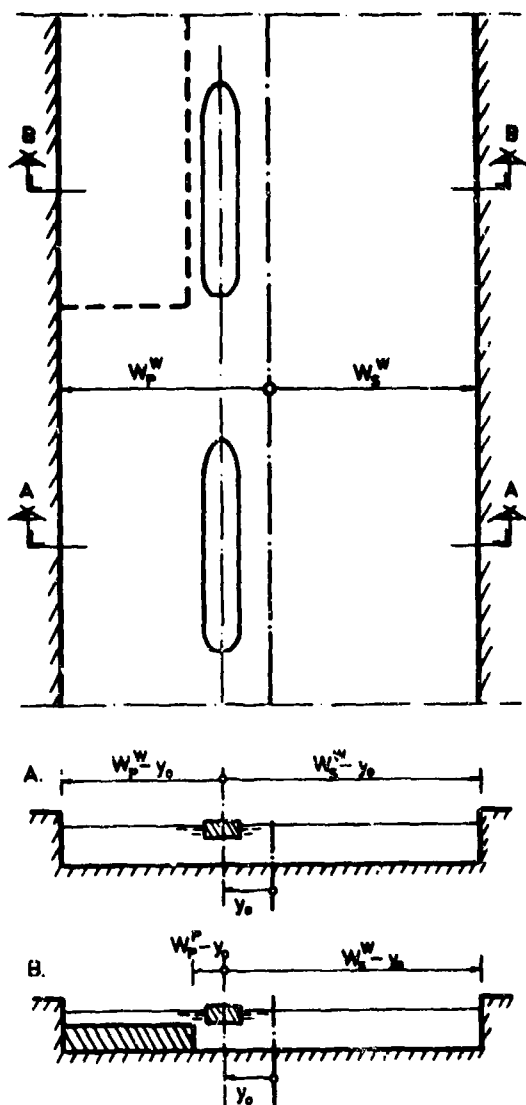


Fig. 7. Definition of bank off-sets and ship-to-bank distances in approaches and bank passages

MODEL EXPERIMENTS - RESULTS FOR FORCES ON MODEL MOVING PARALLEL TO A LONG HIGH WALL (SERIES 40)

The forces and moments measured on the model moving along the basin wall are presented in non-dimensional form in Figs 8 and 9, respectively, to a base of bank distance parameter $\eta = \eta_s + \eta_p$. With reference to Fig. 7 we observe that

$$\eta_s = \frac{B}{W_p - y_0} \quad (0 < \eta_s < 2)$$

$$\eta_p = \frac{B}{W_s - y_0} \quad (-2 < \eta_p < 0)$$

where B replaces the length L used in ref. /1/.

The ordinate of magnitude $Y^*/u^2 = -0.1$ corresponds to a suction force equal to 70 N on the model, or to 1 900 metric tonnes on a ship displacing 312 200 m³ and moving at a speed of 8.4 knots. At the captive model test about two thirds of the lateral force were carried by the aft gauge, indicating a clear bow-away-from-wall moment. Much larger transient moments, however, were experienced by the model when passing close to a finite bank extending into the fairway.

MODEL EXPERIMENTS - RESULTS FOR FORCES ON MODEL MOVING PAST HIGH BANKS OF FINITE LENGTH (SERIES 21, 27, 41, 42, 46)

As can be seen from Fig. 5 the test program included finite bank elements with a length equal to six, three and one unit of ship length L ; the two shorter banks, six unit lengths apart, were passed by in one single run down the basin. The distances covered from bow-meets-bank to stern-clears-bank are seven, four and two units respectively.

Fig. 10 presents a compilation of fore and aft lateral force transients recorded when meeting with the surface-piercing 6 L bank, all for three different depths of water and one lateral bank-passage distance.

In the analysis of these and similar records it was found necessary to "filter" the gauge signal values by use of a mean-of-envelopes technique. In Fig. 11 the dotted lines are time histories of total lateral force and total yawing moment obtained in that way for the passage of a surface-piercing 3 L bank at a water depth equal to 1.3 T. These dotted curves include the unbalanced bias due to the presence of the far port and starboard walls. The influence of the starboard wall remains constant (within the validity of the superposition principle) during the total run down the test basin, causing small shifts of the force to positive and the moment to negative values. At a sufficient distance before and after passing the finite protruding bank the influence of the far port wall will cause a shift of the force to negative and of the moment to positive values. The full curves of Fig. 11 have been corrected for this bias by use of the results of Figs. 8 and 9.

Note that the time histories shown relate to the instantaneous position of the bow of the model. Upon coming in line with the front edge of the bank the model experiences no net effect of the initial repulsion, which could have been expected in view of the pressure distribution on the bow known for the long bank case. (See below.) There appears to be a gradual build-up of

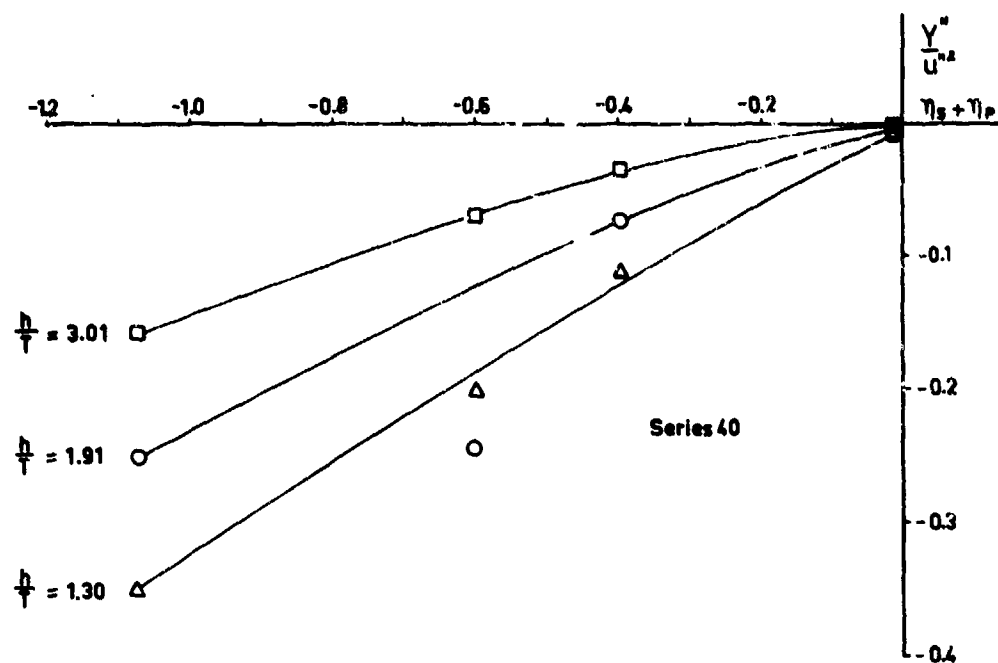


Fig. 8. Bank suction force coefficients in steady motion past long bank

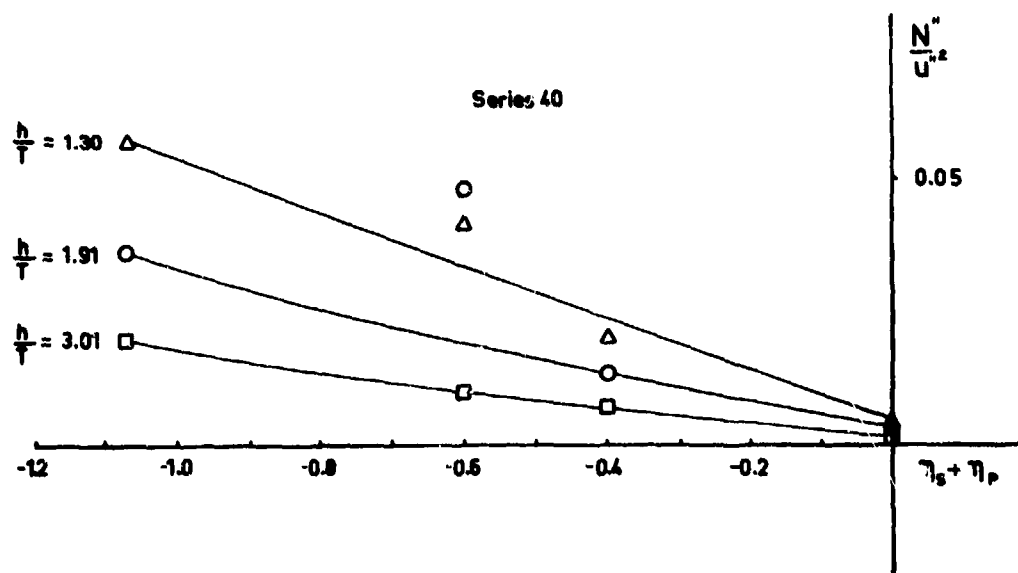


Fig. 9. Bow-away-from-wall moment coefficients in steady motion past long bank

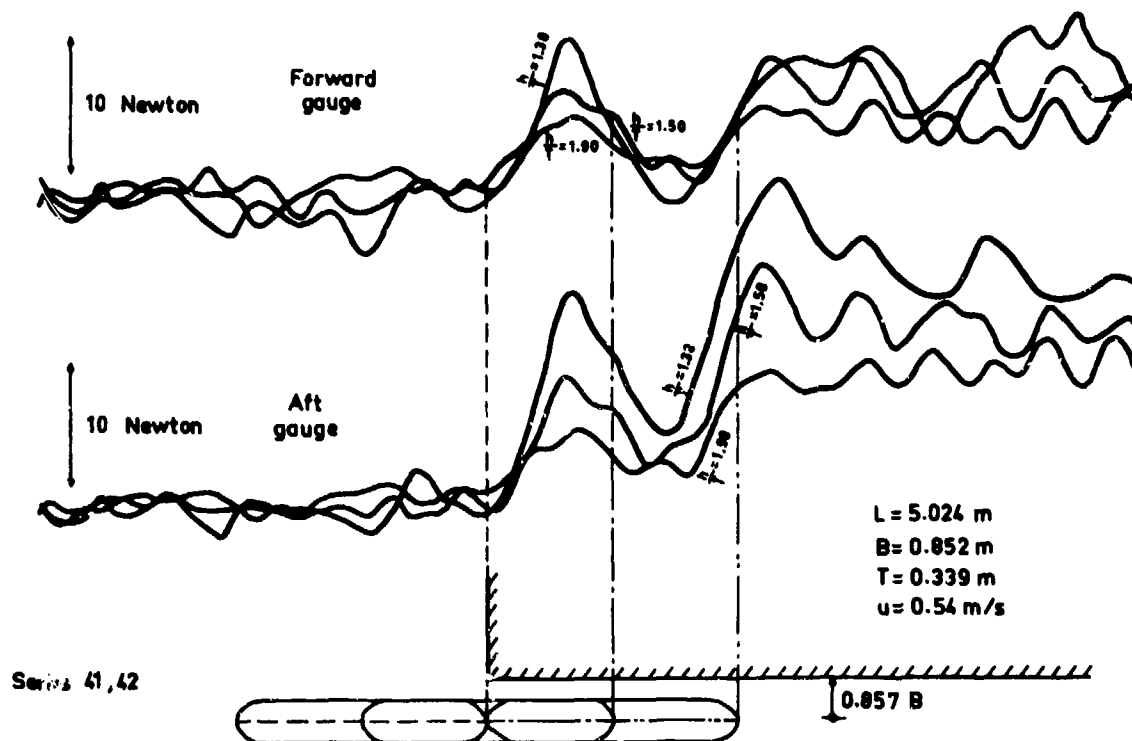


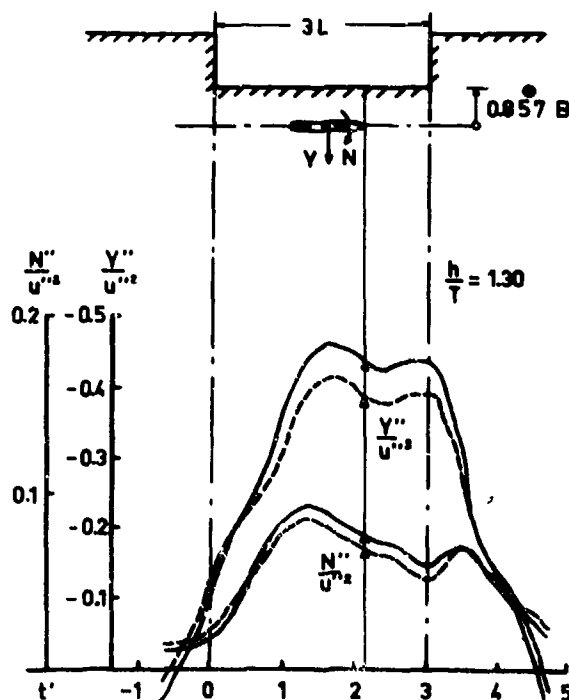
Fig. 10. Lateral force transients for model meeting surface-piercing finite bank

Fig. 11. (Right) Total net lateral force and moment transients as imposed by finite bank

suction force along the model as it proceeds towards the middle of the bank. Again, the accompanying moment as recorded has here a tendency always to turn the bow away from the bank, which suggests that the initial lift is produced on the after part of the hull. As the bow moves beyond the rear edge of the bank the moment shows a second maximum consistent with the simple two-dimensional theory.

A detailed evaluation of the finite bank transients is under way. Awaiting this analysis provisional results from the 1972 tests are given in Fig. 12, to show the relative magnitude of the maximum suction forces recorded on the model in a position midway along the bank.

Roughly, the long bank values may be reduced by 10 per cent to give values for a 4 L bank; and by 25 per cent for a 2 L bank. In the latter case, however, this force maximum is of very short duration, and the complete passage must be regarded as a transient phenomenon involving rapidly changing yawing moments.



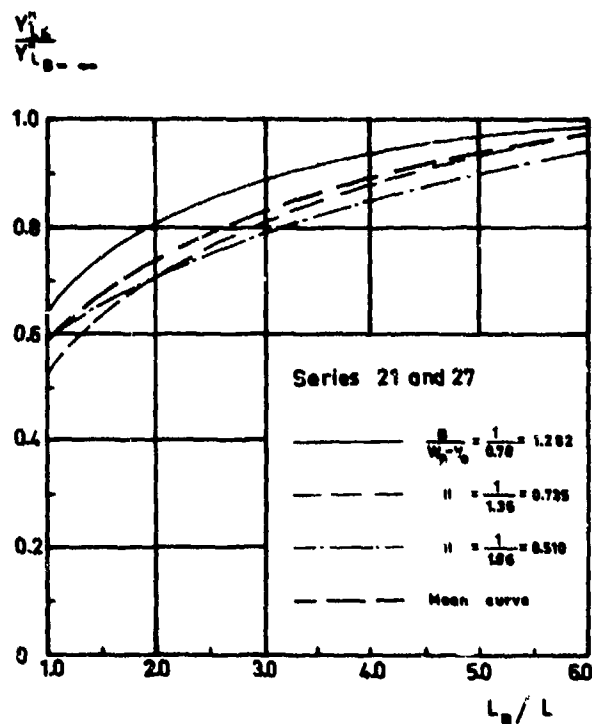


Fig. 12. Relative magnitude of maximum bank suction forces experienced during passages of banks of finite lengths

Such rapidly changing moments are particularly dangerous when they involve a change of sign as well. With reference to Fig. 11 on the previous page it should be pointed out that a preliminary evaluation of yawing moment transients in other test runs do indicate a small initial tendency to turn against the wall.

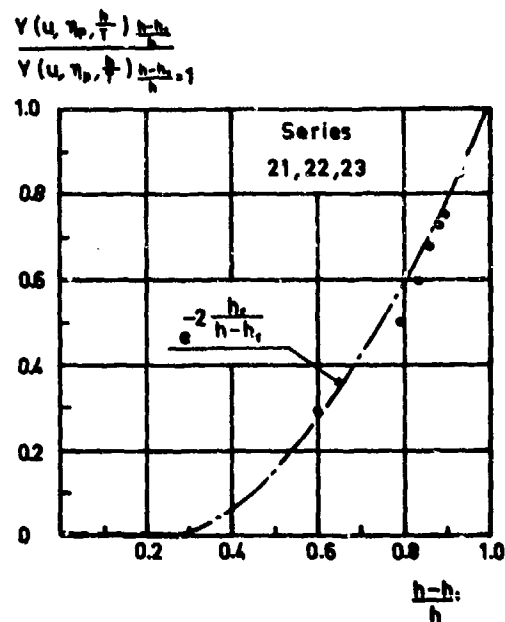
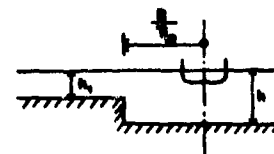


Fig. 13. Effect of platform submergence on maximum suction force in motion past 6 L platform bank

MODEL EXPERIMENTS - RESULTS FOR FORCES ON A MODEL PASSING SHALLOW PLATFORM BANKS (SERIES 21, 22, 23, 41, 42, 43)

Again, the analysis is not yet completed and provisional results will be given here based on the 1972 series of measurements during the passage of 6 L platform banks of different heights, Fig. 13. The new tests covered a range of lower platform-to-depth ratios, and the new results may or may not be in support of the simple quadratic dependence suggested in the diagram. From this diagram we note the rapid decrease of suction force with even a small height of water over the platform bank. Thus, we may benefit very much from having low side banks flooded at high tide. The presence of a platform type shallow with a height equal to up to 40 per cent of the depth will be of no great harm.

COMPARISONS WITH THEORY

Needless to say experimental results as those presented here will be more useful if they can be viewed against the background of a suitable theory. Again, theoretical results must often be held in doubt until they have been verified by careful experiments. Present theories for wall interference and asymmetrical forces are limited to the long wall case.

If we ignore the deformation of the free surface the problem of a ship - and then not necessarily a slender ship - offset to one side of a long canal or dredged channel may be handled by numerical methods for potential flow, /4/. The problem is equivalent to that of a stationary flow past the doublebody form close to a wall or blocking a tunnel with the appropriate vertically symmetric section.

At present this approach is still expensive, and when we come back to its application below, the solution is for just one position in the canal.

If the tunnel section is of a simple rectangular shape and if the ship is slender the asymmetric force may be found in explicit form by an elegant but approximate method of source images, /5/. (For the case of a slender body of revolution moving in deep water near a wall Newman has earlier devised a more accurate solution for the bank suction force, including a displacement of the axial source distribution to account for the deformation otherwise caused to the body, /6/.)

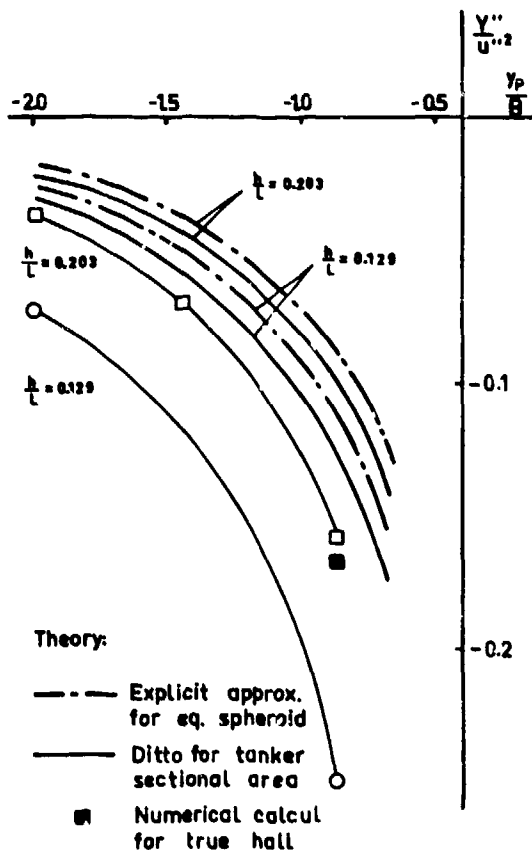
In view of the sufficiently large width of the test basin our experimental results for the model close to the port wall may safely be compared with calculations for the single wall case. The bias present in the experimental values of Y''/u^2 for $\eta_s + \eta_p = 0$ has been corrected for in this comparison shown in Fig. 14. (At a depth corresponding to $h = 0.203 L$ this bias value is -0.002 , so that the figure -0.158 will read -0.156 .)

The two thin curves connect experimental values at different distances from the wall, each one for the depth-to-length ratio given in the diagram. The thicker curves are calculated by Newman's approximate method /5/ for a body of revolution having the same distribution of sectional areas as the tanker form, and for an equivalent spheroid, defined as having the same length and the same midship section area as our ship model. The single black square, finally, is the value calculated according to the numerical method by Hess and Smith /4/.

The approximate method seems to underestimate the lateral force by some 40 per cent when the proper sectional area curve is used, and by some 50 per cent when applied to the equivalent spheroid. (These values will be somewhat lower at large depth figures, and even higher for small under-keel clearances.) The alternative numerical method gives a force within 6 per cent of the experimental value for the test case shown. (See again below.)

The numerical method defines a surface distribution of sources and sinks that makes the normal velocity equal to zero in a number of discrete points on the boundary. The capacity of the method when applied to the study of the potential flow past a combination of rigid surfaces is greatly increased by any symmetry present in the combination. Our present problem is basically asymmetrical, and we will not benefit from the port-and-starboard symmetry as far as minimum leakage through the hull itself is concerned. In order to produce a reliable result for comparison with experiments we chose to study the case of the model moving at zero Froude number close to one wall of a very wide canal, so that this (port) wall (as well as the water surface) could be considered a true plane of symmetry, which did not require any additional definition. Out of a total of 1 000 surface elements 700

Fig. 14 (Below) Bank suction force coefficients in motion past long high bank - Comparison of experiments and theory



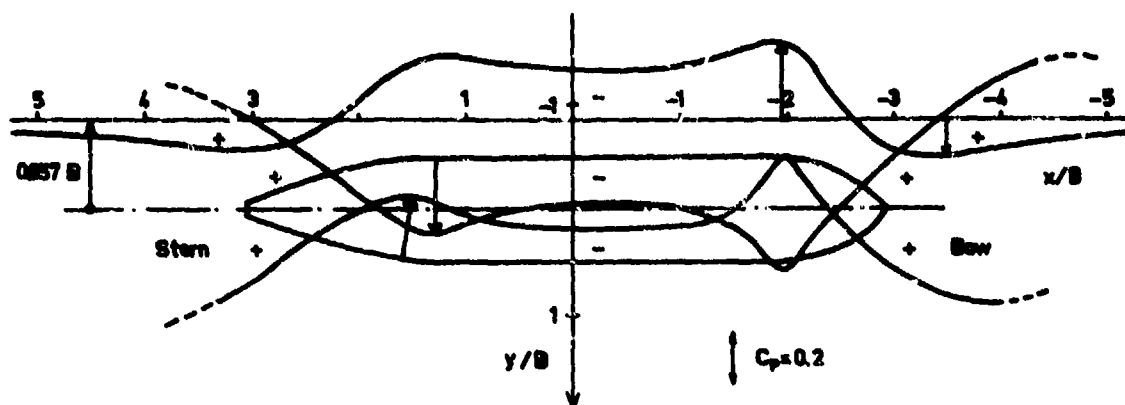


Fig. 15. Pressure distribution around ship hull form and along adjacent wall in plane close below water surface (Computed by method of Hess and Smith).

could therefore be distributed over the wetted surface of the hull and the remaining 300 over the wide bottom of the canal. (The bulbous bow alone required 100 elements.)

The final result of the calculation, $Y^*/u^2 = -0.168$, is entered as the black square plotted in Fig. 14, where it should be compared with the adjacent open square (at -0.156) from experiment series 40. The agreement is encouraging for calculation and comparisons will be pursued for the shallow platform case.

In the numerical calculation model beam B was taken as unity and the long canal was defined for $-14 B < x < 14 B$. The immediate result was obtained in terms of local velocity components and perturbation pressure coefficients (C_p) in points on the hull and canal walls. The diagram in Fig. 15 illustrates the pressure distribution on the two sides of the hull and on the near wall in a plane close below the water surface. It may be observed that the pressure distribution on the hull is more or less directly reflected on the wall. In the normal plane containing the midship section the local difference in C_p between a point on the hull side and an adjacent point on the canal wall, and between a point on the hull bottom and a point on the canal bottom below it do not exceed 4 and 8 per cent respectively.

The total asymmetrical force on the model is equal to the pressure force integrated over the full length of the plane, vertical, near wall. For the non-dimensional total-force coefficient Y^*/u^2 used throughout this paper we have simply

$$\frac{Y^*}{u^2} = \frac{1}{2} \cdot \frac{L^3}{B^3} \cdot \left(\frac{B}{L}\right)^2 \int_{-14}^{14} \int_{-1}^{1} C_p d\left(\frac{x}{B}\right) d\left(\frac{y}{B}\right)$$

ACKNOWLEDGEMENT

This study was made possible by a grant from the Swedish National Board for Technical Development (STU).

The author wishes to acknowledge the valuable assistance rendered by members of the staff of SSPA in the analysis of the experiments and numerical computations and in the preparation of the paper.

REFERENCES

1. Norrbin, N.H., "Theory and Observations on the Use of a Mathematical Model for Ship Manoeuvring in Deep and Confined Waters", SSPA Publ. No 68, 1971.
2. Bastard, P., Bohlin, A., Naumann and van der Burgt, "Optimal Dimensions and Lay-Outs of Approaches for Large Tankers", Report of Working Group No 2, International Oil Tanker Commission, PIANC Bulletin No 16, 1973.
3. van Berlekom, W.B., Trägrårdh, P. and Dellhag, A., "Large Tankers - Wind Coefficients and Speed Loss Due to Wind and Sea", Paper presented at the RINA 1974 Spring Meeting, London 1974.
4. Hess, J.L. and Smith, A.M.O., "Calculation of Non-Lifting Potential Flow about Arbitrary Three-Dimensional Bodies", Douglas Aircraft Co., Aircraft Division Report No E.S. 40622, Long Beach, Ca, March 1962.
5. Newman, J.N., "Some Theories for Ship Manoeuvring", Proc. International Symposium on Directional Stability and Control of Bodies Moving in Water, London 1972. J. Mech. Engng Sci., Vol. 14, No 7, Suppl. issue 1972.
6. Newman, J.N., "The Force and Moment on a Slender Body of Revolution Moving near a Wall", David Taylor Model Basin Report No 2127, 1965.

DISCUSSION

C. T. EARNEST

The author has prepared an interesting and timely paper. It is particularly pertinent to problems under study of the Panama Canal and certainly many other waterways. The volume of ocean traffic has been increasing and, even more dramatically, the size of ships has been increasing, yet channels remain the same until economics allow improvements to be funded. This can result in shift of traffic patterns, operation at reduced drafts, or eroded safety factors as larger ships use existing channels.

This study of the hydrodynamics of varying depths of water adjacent to channels and of isolated banks (islands or points of land adjacent to channels) is directly applicable to conditions in the submerged landscape of the man-made Gatun Lake which is the central portion of the Panama Canal. The transient hydraulic forces caused by these features are well known by pilots and can result in "shears" or uncontrolled yaws. As Figure 14 shows these forces can double and triple as the ship moves closer to the bank, and they increase significantly as the channel gets shallower. It also appears that the hull form is an important variable. As this work progresses, it will hopefully result in further refinements to the mathematical model of ship behavior in restricted waters.

This initial report covers full form ships moving in channels with a moderate amount of water under the hull ($h = 1.3$). The writer encourages extension of this work to include fine form ships with a block coefficient of perhaps .55 or .60 and lesser depths of water under the keel. Although existing channels may have been designed for more conservative usage, current practice in many world ports is to accept ships with five feet of water under keel or even less. This results in $T = 1.15$ as a routine occurrence. When working at a scale of 1:64 or 1:100 this small water layer would undoubtedly bring boundary effects into greater consideration, however there is a need to extend theory to cover this common condition.

With this evolving mathematical tool civil engineers, port authorities, pilots associations and ship owners will be able to afford to test hypothesis, examine potential future situations, search for optimum solutions to channel dimensions and establish criteria for minimum ship handling characteristics.

L. L. MARTIN

I wish to make just a small comment. At AEW we have occasionally measured pressure fields caused by various ships, with results generally corresponding very closely to Dr. Norrbin's Figure 15, for forces on the wall (though the ships had no bulk). It has been found that these can be computed with fair accuracy by assuming a continuous distribution of sources along the longitudinal axis of the ship, of strength $V \frac{dA}{dx}$, where V is ship speed and dA/dx is the gradient of the curve of areas.

E. MÜLLER

Systematic encountering and overtaking trials have been carried out by the Versuchsanstalt für Binnen-schiffbau, Duisburg, since 1960 with models of cargomotor-ships and pushing units on the Rhine, its tributary rivers

and channels. Depth of water, draught, lateral distance and speed of the models varied during the trials. On this occasion not only the occurring forces, but also the resulting dislocation of the vessels were measured. Our results are in general in conformity with Dr. Norrbin's results though there are some differences in the details. The reasons are due to the different conditions of the trials, shapes of the vessels and speeds. It is easy to understand that the pressure areas built-up about the vessel are stronger with fully shaped inland-water-way vessels with relatively higher model speed than with the vessel treated by Dr. Norrbin. On this understanding Figure 1 is to be contemplated. The coefficients of the changes of the longitudinal force

$$C_X = \frac{X}{\rho/2 V_A^2 \cdot L_{PP} \cdot T},$$

transversal force

$$C_Y = \frac{Y}{\rho/2 V_A^2 \cdot L_{PP} \cdot T},$$

yawing moment

$$C_N = \frac{N}{\rho/2 V_A^2 \cdot L_{PP} \cdot T}$$

V_A = speed of the adverse ship

and the changes of trimming and parallel lowering during an encounter of two cargo motorship models of the same size are indicated herein. The encountering phases, bow to bow, midship to midship and stern to stern have been drawn in the diagram for better guidance. The vessels passed each other in a lateral distance (board to board) of $2.7x$ ship's beam.—Increased pressure zones on bow and stern of the vessel (Fig. 2) are still clearly effective at this distance, as evidently shown by the resulting lateral force (repulsion) and moment in the beginning (turning outward) and end of the encounter (turning inward). If both ships lie side by side, at the same height, a maximum attraction is effective whereas the moment disappears.

The longitudinal force will be reduced in the first half of the encounter (reduction of the resistance) and will be increased in the second half (increase in resistance). Please compare in this connection also the course of trimming θ and lowering Z/L .

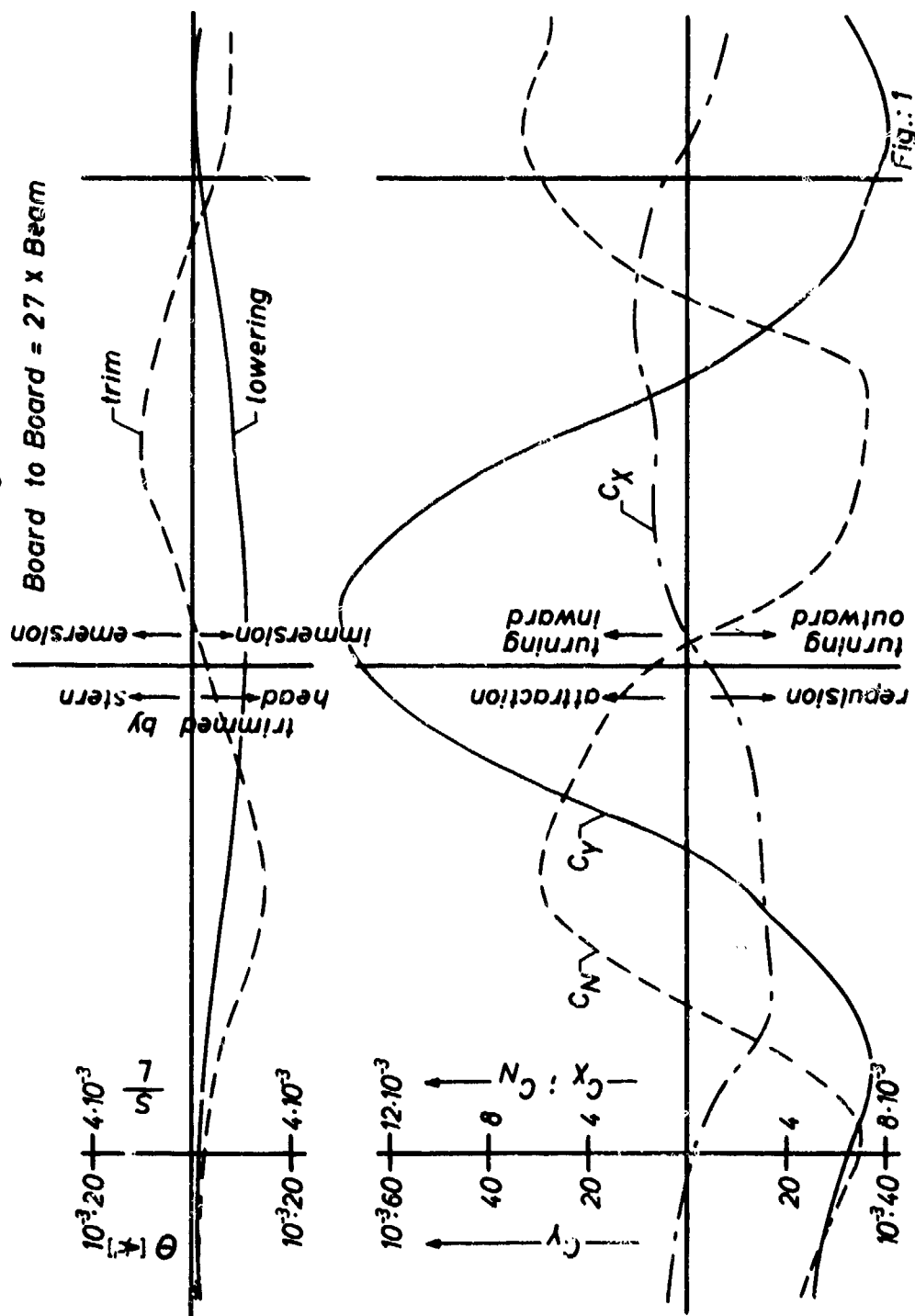
From the forces measured it might be expected that ships passing each other or passing a stationary obstacle are continually subjected to translatory and rotary dislocation. But this is not the case, as demonstrated by Figure 3. Here are shown 2 procedures of overtaking which have been carried out with different lateral distance between the models. The change of course has been caused — as illustrated — substantially by the initial impulse obtained.

For reasons of simplification of the trials the vessel passing ahead shown in Fig. 3 was guided on a straight compulsory course.

Encountering Trial (Captive Test)

Model, Carrying Instruments: $V \approx 14,0 \text{ km/h} = 7,6 \text{ kn}$ - Encountering model: $V \approx 15,6 \text{ km/h} = 8,4 \text{ kn}$

Board to Board = $27 \times \text{Beam}$



Lines of Const. Level $\frac{\Delta h}{L_{pp}} \cdot 10^3$
 River - Cargoship „J. Welker”

$h \approx 4,0 \text{ m}$; $T \approx 2,0 \text{ m}$; $V \approx 14,4 \text{ km/h}$; $h = 7,8 \text{ kn}$

$$F_{rh} = \frac{V}{\sqrt{g \cdot L}} = 0,639$$

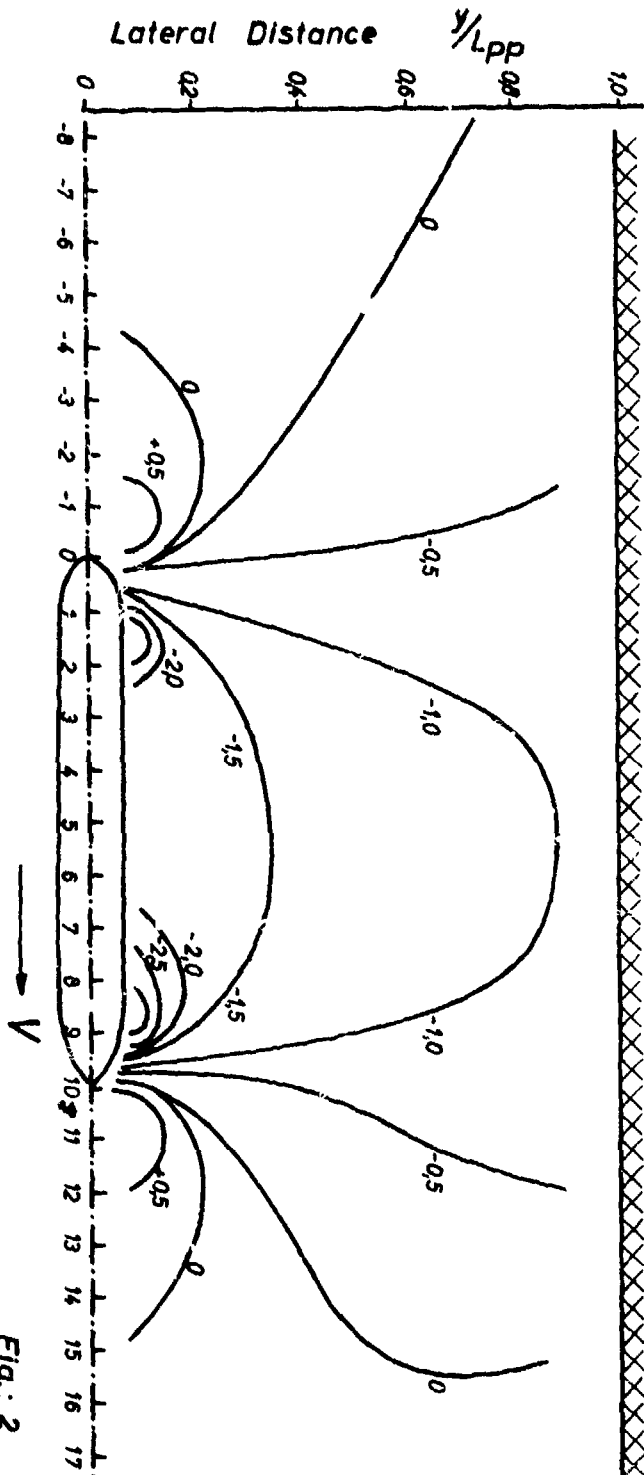


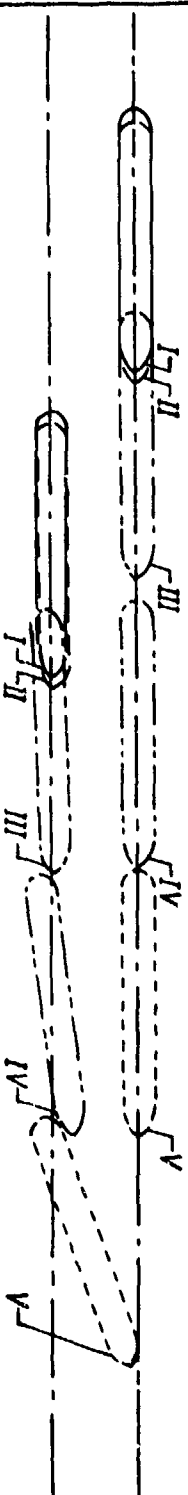
Fig. 2

Overtaking Trials (Free running Test)

$h \hat{=} 4,0 m$; $T \hat{=} 2,0 m$

$V \hat{=} 14,0 km/h = 7,6 kn$; $V \hat{=} 16,0 km/h = 8,6 kn$ (Overtaker)

Board to Board = $1,7 \times$ Beam



Board to Board = $3,1 \times$ Beam

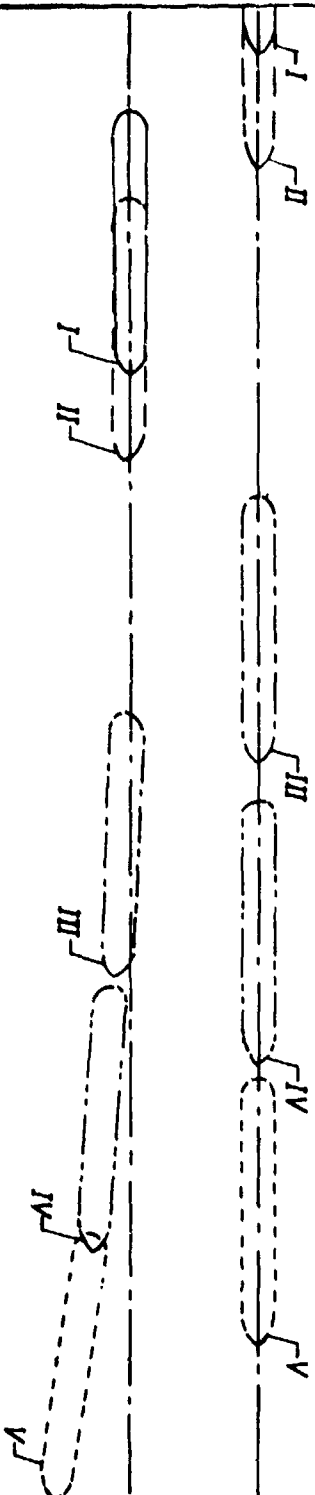


Fig. 3

The initial impulse for the case shown in the upper part of the illustration is produced by superposition of the increased pressure zones on the bow of the vessel passing ahead and on the stern of the vessel which is overtaken. This impulse has a repellent reaction on the stern of the ship overtaken. The vessel turns inward, and is brought on a collision course.

In the second case the lateral distance of both ships is so large that the increased pressure zone will no longer be effective. Already before overlapping of the models the stern of the slower ship is attracted by the large under-pressure area caused by the other vessel and the slower ship is turned outward.

Measuring forces (captive tests) is done simpler and more accurate than measuring translatory or rotary displacements (free-running tests), and under simplifying conditions, the resulting deviations of course can be obtained.

If the external forces are shifted to the centre of gravity of the ship and summarizing them to the resultant R , it may be concluded:

$$R = m \cdot \frac{dV}{dt} = m \cdot \frac{d^2e}{dt^2}$$

with: e = transversal displacement

m = mass

t = time

V = speed

Therefrom results

$$e = \int \int_{t_B}^{t_E} \frac{R}{m} dt^2$$

t_B = initial point of time

t_E = final point of time

Correspondingly, for the rotary motion:

$$N = I_{ZZ} \cdot \frac{d\omega}{dt} = \frac{d^2\psi}{dt^2}$$

with:

I_{ZZ} = moment of inertia referred to the vertical axis

N = moment around the vertical axis

ω = angular velocity

ψ = course angle

$$\psi = \int \int_{t_B}^{t_E} \frac{N}{I_{ZZ}} dt^2$$

By means of the results of the measurements of forces it is possible to determine with good approximation the range of the occurring course deviation on the assumption of $m = \text{const}$, and $I_{ZZ} = \text{const}$. Various examples of calculation which have been carried out have shown this.

AUTHOR'S REPLY

I am grateful to Mr. Earnest for his appearing in the discussion; it is only the exchange of experiences and findings between those engaged in the design and operation of narrow waterways — and of the ships moving in these waterways — that can make a continued effort in this field meaningful.

Mr. Earnest points out that current practice of ocean-going ship operation accepts an under-keel clearance of five feet in port areas, corresponding to $h/T = 1.15$ or even less. In scale model testing the viscous blockage of this small clearance will obscure the quantitative results, and, which is even more serious, the quality of the results. It may therefore well be better to extrapolate experimental values from moderate clearances into the small-clearance region, preferably according to a theoretical relationship. In as much as viscous effects become of importance also in the full scale world they may in principle be corrected for by introducing an effective clearance, which will be a function of ship and back flow velocities, and bed roughness. Such an approach should be especially applicable to the problem of lateral forces due to drift.

Mr. Earnest further advocates model tests for fine form ships. It is known from early tests that the fullness of the fore body of a hull may markedly influence the bank effects in a long canal, and it will certainly also influence the transients in meeting with a short bank. The model testing would perhaps present less problems than in the case of full forms, but, unfortunately, the amount of new money required is of the same order.

Mr. Martin refers to an interesting AEW experience of pressure field measurements around ship models, and of

computations using a simple source distribution along a longitudinal axis in the hull. This computational scheme should work well at a far distance from the body, but it is not equally easily applied to a body close to a wall or in a canal, where the original line of sources (or alternatively the hull form) is distorted. It is not clear to me if the fair agreement claimed by Mr. Martin relates to cases with wall interference.

Dr. Müller has contributed an interesting report on measurements on ship models during encountering tests, which has bearing not only on my paper but, perhaps even more, on the previous paper by Newman and Tuck.

The surface elevation survey reveals a zone of positive pressures forward of the bow of the model moving alone in the canal model, and a large area of negative pressures along almost the full length of the model. During the first phase of the encountering, when bow is in line with bow, each model experiences a repulsion from the other, and an outward turning moment. At the instant the two models overlap by a quarter of their length there is still a net repulsion, but now an inward turning moment. Again, as in the case of our measurements on a model meeting a finite bank, the pressure distribution over the total length of the hull must obviously be considered for an explanation of the force balance. With access to the variation of resultant force and moment with the longitudinal separation between the meeting models it will be a straight-forward operation to calculate the initial disturbance of the alternatively let-free model. But before doing so we must try to understand the origin of the force history.

DOUBLE-BODY FLOW THEORY—A NEW LOOK AT THE CLASSICAL PROBLEM

T. Y. Wu
California Institute of Technology
Pasadena, California

A. T. Chwang
California Institute of Technology
Pasadena, California

ABSTRACT

This study explores various methods for calculating potential flow around a double model of ship-like form. The discussion begins with the family of ellipsoids, which is the simplest of three-dimensional shapes possessing three unequal axes of length, beam and draft. For the potential flow past an ellipsoid moving with arbitrary velocity, the solution can be represented, equivalently, by a volume distribution of doublets, or a doublet-layer distributed over the limiting confocal ellipse, as well as by a source-layer or a doublet-layer distributed over the ellipsoid or over an interior confocal ellipsoid. The analytical behavior of these different representations of the solution (for an ellipsoid) is examined in detail with objective to throw light on the singularity method for arbitrary bodies in general. A simple relationship between the geometry of the confocal ellipse and the maximum principal curvature of confocal ellipsoids is obtained. This relationship seems to have a general validity as a rule for determining the center plane form of singularity distribution for arbitrary bodies with a plane symmetry.

Based on the singularity method new solutions are presented for the internal flow between two confocal ellipsoids in relative motion. These solutions may provide an order-of-magnitude estimate of the wall effects.

For arbitrary ship-like double models a general formulation of the potential flow problem is presented based on the representation of a body by a center plane distribution of doublets and moments of doublets for translational and rotational body motions. This construction results in an integral equation of the first kind for the doublet density. Several numerical methods investigated so far include an approximate direct method and an iteration scheme. The results for a double-elliptic hull form are presented.

1. INTRODUCTION

In naval hydrodynamics a continued interest has been directed to develop techniques for evaluating the wave resistance of ships more accurately than by the Mitchell theory, taking into account more exactly the

boundary conditions on the free surface and the ship hull. Of equal importance is to improve the methods for predicting the viscous resistance due to a three-dimensional boundary layer at the hull and a wake. For both purposes it is desirable to establish an effective method for calculating exactly the potential flow around a 'double-model' with the objective that the method can be easily generalized to consider the free-surface effects and the viscous effects on flow around ships. With this vision Professor Georg Weinblum stressed the importance of improving our knowledge about double-model flows, both theoretically and experimentally. It is with our profound appreciation of this viewpoint that we wish to dedicate this work to the fond memory of Georg Weinblum, whose wonderful stimulus and personal encouragement has inspired the present preliminary study.

For numerical calculations of potential flow past arbitrary bodies, the method of surface-source distribution developed by Hess and Smith (1966) and, independently, by Landweber (1974) is very successful. Its extension to ship wave problems, however, still seems to be a formidable task. On the other hand, the representation of a certain class of bodies (with a plane symmetry) by a center-plane distribution of singularities has some attractive features. First, this type of representation is actually an analytic continuation of the exterior flow into the body surface. In application to ship waves, the local analytic behavior, near and at the water line, of the flow quantities as provided by the center-plane singularity (CPS) method may eliminate some difficulties encountered by the surface-source method. Further, since the classical Mitchell-Havelock ship theory is equivalent to a linearized center-plane singularity method, the higher-order calculations of ship water waves based on the CPS-method are likely to be benefited by the previous analytical developments in the linear theory, thereby some numerical efforts could be curtailed as a result. For these reasons the present study will be directed to seek possible development of the center-plane singularity method. In this connection, Miloh (1972), as we have just

learned¹, has made a contribution to this subject, in which two general methods were explored, with a triaxial ellipsoid and a double parabolic chip (with pointed edges) worked out as examples, including a discussion of the second-order wave theory. Still, a central problem of the CPS method is thought to depend on a workable technique by which the unknown plan form of singularity distribution for round-edged bodies can be determined with sufficient accuracy so as to lead to a convergent calculation of the singularity density. This may be a major reason for some previous unsuccessful attempts.

In order to gain further insight on this point, the classical problem of potential flow past a triaxial ellipsoid has been investigated once again with objective to find all possible representations of an ellipsoid by different singularity distributions. Having found independently the results sought, we discovered that some of the results were stated, without proof, as 'well known' by Havelock (1931 a, b) in a fundamental, but with that passage much neglected, paper on the wave resistance of an ellipsoid. We have also found that major steps of proving Havelock's statement were given by Lunde (1951). Actually, a simple proof of these results can be traced back to a long history of major developments in gravitational potential theory. In this respect Havelock was right in implying that no basic aspects of a proof (for the potential flow problem) would be new, but the important link between the gravitational potential and velocity potential pertaining to an ellipsoid can probably be attributed to Havelock. In view of the elegance of the classical work relating to the subject, a brief account of the proof is reviewed together with the historical background. A different approach to the solution of potential flow involving ellipsoids has been discussed by Miloh (1973) by using the image singularities in terms of the ellipsoidal harmonics, which will be useful for treating the related water wave and other general problems. Along the same approach the water wave singularities have been determined by Newman (1972) in terms of the spheroidal harmonics. In this connection, we may add that Havelock's results were also discussed by Weinblum (1936) in finding forms of a slender body of minimum wave resistance.

From the known results for ellipsoids still different variations of representation by surface distributions of sources or doublets are deduced, and new solutions are presented for confocal ellipsoids in relative motion. Further, from these exact solutions a specific relationship is found between the plan form

of singularity distribution and the maximum principal curvature of the ellipsoid. In order to ascertain if this relationship may have validity as a general rule, it is applied to a double-elliptic hull, which has round edges on all sides. The results based on the numerical methods proposed here are quite satisfactory. The indication by the present preliminary study is thus clear that further development of the center-plane singularity method is most promising.

2. The Fundamental Problem of Ellipsoids -- Historical Background

The most fundamental of the exact solutions for potential flow involving truly three-dimensional bodies are, no doubt, those for triaxial ellipsoids in translational and rotational motions. Interestingly, it seems not widely known that the potential flow theory for ellipsoids is closely related in mathematics to the theory of gravitational potential of a homogeneous ellipsoid. The latter has been a major problem dating back to Newton, and having attracted over a century the remarkable efforts of Maclaurin, Jacobi, Laplace, Dirichlet, and other most eminent mathematicians of the time. In resolving the associated hydromechanical problems little new efforts are required if good use is made of the rich content of the gravitational potential theory.

As a brief review of the historical developments, we note first that for a homogeneous ellipsoid E , bounded by surface

$$S: \sum_{i=1}^3 \frac{x_i^2}{a_i^2} = 1 \quad (a_1 > a_2 > a_3), \quad (1)$$

the gravitational potential is simply given by the Poisson integral

$$\mathcal{V}(\underline{x}) = \rho \int_E \frac{1}{R} d^3\xi \quad (R = |\underline{x} - \underline{\xi}|), \quad (2)$$

ρ being the uniform mass density of the ellipsoid. (Here the universal constant of gravitation is omitted for brevity.) For an interior point ($\underline{x} \in E$), the integral in (2) can be carried out directly (see, e.g., MacMillan, 1930), giving (the representation of Gauss (1813) and Rodrigues (1815), see Todhunter (1873) and Chandrasekhar (1967))

$$\mathcal{V}(\underline{x}) = \pi\rho \left\{ A - \sum_{i=1}^3 a_i x_i^2 \right\}, \quad (3a)$$

where

$$A = a_1 a_2 a_3 \int_0^\infty \frac{d\lambda}{\Delta}, \quad a_i = a_1 a_2 a_3 \int_0^\infty \frac{d\lambda}{(a_i^2 + \lambda)\Delta}, \quad (3b)$$

¹ We are indebted to Prof. Louis Landweber for providing us with a copy of Miloh's thesis when this paper was being written.

$$\Delta = [(a_1^2 + \lambda)(a_2^2 + \lambda)(a_3^2 + \lambda)]^{\frac{1}{2}}, \quad (3c)$$

or

$$\mathcal{V}(\underline{x}) = \pi \rho a_1 a_2 a_3 \int_0^\infty \left(1 - \sum_{i=1}^3 \frac{x_i^2}{a_i^2 + \lambda}\right) \frac{d\lambda}{\Delta}. \quad (3d)$$

At an exterior point ($\underline{x} \notin E$), the gravitational potential may assume Dirichlet's representation:

$$\mathcal{V}(\underline{x}) = \pi \rho a_1 a_2 a_3 \int_\lambda^\infty \left(1 - \sum_{i=1}^3 \frac{x_i^2}{a_i^2 + \lambda}\right) \frac{d\lambda}{\Delta}, \quad (4a)$$

where $\lambda(\underline{x})$ is the ellipsoidal coordinate of \underline{x} , which is the algebraically largest root of

$$\sum_{i=1}^3 \frac{x_i^2}{a_i^2 + \lambda} = 1. \quad (4b)$$

This expression of Dirichlet for the exterior solution can be shown to follow immediately from the 'Splendid Theorem' of Maclaurin (as so referred to by Thomson and Tait 1883):

The gravitational potentials at the same \underline{x} exterior to two individual ellipsoids of confocal shapes

$$\sum_{i=1}^3 (x_i/a_i)^2 = 1, \quad \sum_{i=1}^3 (x_i'/a_i')^2 = 1, \quad (5)$$

$$a_i'^2 = a_i^2 + \lambda,$$

are equal if their total uniform masses are the same, that is

$$\rho a_1 a_2 a_3 = \rho' a_1' a_2' a_3'. \quad (6)$$

The above solution shows that $\mathcal{V}(\underline{x})$ is linear in x_i^2 within the ellipsoid E , continuous and continuously differentiable at the surface S , and falls off like R^{-1} at large distances from E .

2.1 Potential Flow Due to Translation of an Ellipsoid

These properties of \mathcal{V} immediately suggest that certain simple relationships exist between the gravitational potential and the velocity potential (of an ideal flow) involving ellipsoids. We first note that for an ellipsoid E undergoing translation with velocity $\underline{U} = U_1 \underline{e}_1 + U_2 \underline{e}_2 + U_3 \underline{e}_3$ denoting the base vectors and the summation convention being understood unless otherwise designated, the boundary condition on the velocity potential $\varphi(\underline{x})$ at the ellipsoid surface S (with normal vector \underline{n}) is

$$n_i \frac{\partial \varphi}{\partial x_i} = n_i U_i \quad (\underline{x} \in S), \quad (7a)$$

or

$$\frac{x_i}{a_i^2} \frac{\partial \varphi}{\partial x_i} = \frac{x_i}{a_i^2} U_i. \quad (7b)$$

This condition suggests that, since \mathcal{V} is quadratic in x_i within and on S , φ may be derived as a linear combination of the first derivatives of \mathcal{V} , or, by (2),

$$\varphi(\underline{x}) = \frac{1}{\rho} \beta_i \frac{\partial \mathcal{V}}{\partial x_i} = \beta_i \int_E \frac{\partial}{\partial x_i} \left(\frac{1}{R} \right) d^3 \xi. \quad (8)$$

In fact, the interior flow is a trivial uniform flow with the potential

$$\varphi(\underline{x}) = U_i x_i \quad (\underline{x} \in E). \quad (9)$$

For the exterior flow, substitution of (4) in (8) yields the potential

$$\varphi(\underline{x}) = -2\pi a_1 a_2 a_3 \beta_i x_i \int_\lambda^\infty \frac{d\lambda}{(a_i^2 + \lambda)\Delta} \quad (\underline{x} \notin E), \quad (10a)$$

$$\sum_{i=1}^3 \frac{x_i^2}{a_i^2 + \lambda} = 1, \quad (10b)$$

which satisfies the boundary condition (7) if

$$\beta_i = \frac{U_i}{2\pi(2-a_i)} \quad (i = 1, 2, 3). \quad (10c)$$

The relationship (8) between the velocity potential φ and the gravitational \mathcal{V} for ellipsoids was cited by Havelock (1931) as being then 'well known'.

The integral representation (8) for the exterior flow may be interpreted as a potential due to a volume distribution of doublets of uniform density β_i , pointing in the positive U_i -direction, respectively. By further invoking Maclaurin's theorem, the following alternative representations of the exterior flow can be obtained.

(i) Volume distribution of doublets within an interior confocal ellipsoid.

$$\varphi(\underline{x}) = \beta_i \int_{E'} \frac{\partial}{\partial x_i} \left(\frac{1}{R} \right) d^3 \xi \quad (\underline{x} \notin E'), \quad (11a)$$

where

$$\beta_i = \beta_1 \frac{a_1 a_2 a_3}{a_i^2} \quad (i = 1, 2, 3), \quad (11b)$$

a_1', a_2', a_3' being the axes of an interior confocal ellipsoid E' ,

$$\sum_{i=1}^3 (x_i/a_i')^2 = 1, \quad (a_i')^2 = a_i^2 + \lambda_0 \quad (-a_3^2 < \lambda_0 < 0). \quad (11c)$$

(ii) Center-plane distribution of doublets over the focal ellipse.

$$\varphi(\mathbf{x}) = \int_{E_0} \bar{\beta}_i(\xi, \eta) \frac{\partial}{\partial x_i} \left(\frac{1}{R} \right) d\xi d\eta \quad (2a)$$

$$[R^2 = (x_1 - \xi)^2 + (x_2 - \eta)^2 + x_3^2]$$

where E_0 is the limiting focal ellipse reached as $\lambda_0 \rightarrow -a_3^2$, or

$$E_0: \frac{x_1^2}{a_0^2} + \frac{x_2^2}{b_0^2} = 1 \quad (a_0^2 = a_1^2 - a_3^2, b_0^2 = a_2^2 - a_3^2), \quad (12b)$$

$$\bar{\beta}_i(\xi, \eta) = 2\beta_i \frac{a_1 a_2 a_3}{a_0 b_0} \left(1 - \frac{\xi^2}{a_0^2} - \frac{\eta^2}{b_0^2} \right)^{\frac{1}{2}} \quad (i = 1, 2, 3) \quad (12c)$$

Proof. By putting $\lambda_0 = \epsilon^2 - a_3^2$ in (11) and taking the limit as $\epsilon \rightarrow 0$ for the case $a_1 \geq a_2 > a_3$, the x_3 -coordinate of E' reduces to

$$x_3 = \pm \zeta_0 = \pm \epsilon \left(1 - \frac{x_1^2}{a_0^2} - \frac{x_2^2}{b_0^2} \right)^{\frac{1}{2}} (1 + O(\epsilon^2)), \quad (13a)$$

hence by (11),

$$\varphi(\mathbf{x}) = \lim_{\epsilon \rightarrow 0} \beta_i \frac{a_1 a_2 a_3}{a_0 b_0 \epsilon} \int_{E_0} \frac{\partial}{\partial x_i} \frac{\zeta_0(\xi, \eta)}{R} d\xi d\eta \cdot (1 + O(\epsilon^2)), \quad (13b)$$

which yields the result stated.

In this limiting case, the doublet distribution over the focal ellipse assumes the ellipsoidal density (12c) for all three components of translation. Though for the components $i = 1, 2$, $\varphi(\mathbf{x})$ can also be expressed in terms of source distributions over E_0 (by integration by parts), the source strengths, however, have a square-root singularity along the periphery of E_0 .

(iii) Focal-axis distribution of doublets for prolate spheroids. For the prolate spheroid ($a_1 > a_2 = a_3$),

$$\varphi(\mathbf{x}) = \beta_1 \frac{a_1 a_2}{a_0} \int_{-a_0}^{a_0} (a_0^2 - \xi^2) \frac{\partial}{\partial x_1} \left(\frac{1}{R} \right) d\xi \quad (14a)$$

This result can be obtained by a procedure similar to the above by putting $\lambda = \epsilon^2 - a_2^2 = \epsilon^2 - a_3^2$, and taking the limiting value of (11) as $\epsilon \rightarrow 0$. The doublet distribution now lies between the foci, $-a < x_1 < a$, and assumes a parabolic density, as noted by Chwang and Wu (1974a).

Further alternative representations of the exterior flow potential can be given by considering distributions of sources and normal doublets at ellipsoid surface.

(iv) Surface-source representation. The following simple manipulation on (8) yields

$$\varphi(\mathbf{x}) = \beta_1 \int_E \frac{\partial}{\partial x_1} \left(\frac{1}{R} \right) d^3 \xi = - \int_E \nabla_{\xi} \cdot \left(\frac{\beta}{R} \right) d^3 \xi$$

$$= - \int_S \frac{\mathbf{n} \cdot \beta}{R} dS \quad (15a)$$

which is an expression for φ in terms of a surface source distribution of strength

$$\sigma(\mathbf{x}) = \beta_1 n_1 = \left(\sum_{i=1}^3 \beta_i x_i / a_i^2 \right) \left(\sum_{i=1}^3 x_i x_i / a_i^2 \right)^{-\frac{1}{2}} (\mathbf{x} \in S). \quad (15b)$$

Alternatively, application of Maclaurin's theorem (eqs. 5 and 6) to (15) gives $\varphi(\mathbf{x})$ in terms of a source distribution over the surface S' of an interior confocal ellipsoid E' as

$$\varphi(\mathbf{x}) = \beta_1' \int_{E'} \frac{\partial}{\partial x_1} \left(\frac{1}{R} \right) d^3 \xi = - \int_{S'} \frac{\sigma'(\xi)}{R} dS \quad (\mathbf{x} \notin E'), \quad (16a)$$

$$\sigma'(\mathbf{x}) = \beta_1' n_1' = (\beta_1' x_1 / a_1'^2) (x_1 x_1 / a_1'^2 + a_1'^2)^{-\frac{1}{2}} (\mathbf{x} \in S'), \quad (16b)$$

where β_1' is related to β_1 by (11b).

(v) Surface-doublet representation. The potential of a doublet layer, orientated along the outward normal \mathbf{n} at S ,

$$\varphi(\mathbf{x}) = \int_S \mu(\xi) \frac{\partial}{\partial n} \left(\frac{1}{R} \right) dS, \quad (17a)$$

has the well-known properties

$$4\pi\mu = \varphi^- - \varphi^+ \quad (17b)$$

$$\partial\varphi^+ / \partial n = \partial\varphi^- / \partial n, \quad (17c)$$

where φ^+ and φ^- denote the values of φ on the outer and inner sides, respectively, of S .

From the known interior solution (9) and exterior solution (10) we immediately deduce that

$$\mu(\mathbf{x}) = \frac{1}{4\pi} (\varphi^- - \varphi^+) = \frac{1}{4\pi} (U_1 + 2\pi a_1 \beta_1) = \beta_1 x_1 \quad (\mathbf{x} \in S), \quad (17d)$$

in which the last step follows from (10c). This result shows that the density of the doublet layer is simply linear in x_i . By a similar procedure used in (iv), we also have

$$\varphi(\underline{x}) = \int_S \mu'(\underline{x}) \frac{\partial}{\partial n} \left(\frac{1}{R} \right) dS \quad (\underline{x} \notin E'), \quad (18a)$$

$$\mu'(\underline{x}) = \beta'_i x_i \quad (\underline{x} \in S'), \quad (18b)$$

where β'_i is again given by (11b). $\mu'(\underline{x})$ is also linear in x_i .

2.2 Potential Flow Due to Rotation of an Ellipsoid.

By an analysis similar to that shown above, the velocity potential of the flow past ellipsoid E rotating with angular velocity $\underline{\Omega} = \Omega_i \underline{e}_i$ in an ideal fluid can be given as

$$\varphi(\underline{x}) = (\underline{\gamma} \times \underline{x}) \cdot \nabla \int_E \frac{1}{R} d^3 \xi \quad (\underline{x} \notin E) \quad (19a)$$

$$= -\frac{3}{2} V \epsilon_{ijk} x_j x_k \int_{\lambda}^{\infty} \frac{1}{a_k^2 + \lambda} \frac{d\lambda}{\Delta}, \quad (19b)$$

$$\gamma_i = \frac{1}{2\pi} \Omega_i \left[2 + \frac{a_i^2 + a_k^2}{a_j^2 - a_k^2} (a_j - a_k) \right]^{-1}, \quad (19c)$$

where ϵ_{ijk} is the permutation symbol, $V = (4/3)\pi a_1 a_2 a_3$ is the volume of E, and (i, j, k) in (19c) stands for an even permutation of (1, 2, 3). Equation (19b) is obtained directly by converting (19a) into Dirichlet's form. This φ satisfies the boundary condition

$$\underline{n} \cdot \nabla \varphi = \underline{n} \cdot (\underline{\Omega} \times \underline{x}) \quad (\underline{x} \in S). \quad (20)$$

The above solution may be interpreted as a linear combination of moments of a doublet distribution. The original uniform distribution of doublets throughout the ellipsoid can again be converted, as shown in the previous case of translation, into various other forms of distributions for the exterior flow.

Some of the above relationships between the singularity distributions over confocal ellipsoids have also been discussed by Eggers (1960) from a different approach.

2.3 Virtual Mass Coefficients of Ellipsoid.

The virtual mass coefficients, M_{ij} , of ellipsoid E, defined in terms of the kinetic energy T of the fluid as

$$2T = \rho V M_{ij} U_i U_j + \frac{1}{5} \rho V a_i a_j M_{i+3, j+3} \Omega_i \Omega_j \quad (21)$$

have only diagonal components in virtue of the body symmetry. Determination of the components corresponding to translation is especially

simple by applying the extended Taylor theorem (Yih 1969), giving

$$M_{ii} = -1 + 4\pi \beta_i / U_i = a_i / (2 - a_i) \quad (i = 1, 2, 3). \quad (22a)$$

The components corresponding to rotation are given by

$$M_{i+3, i+3} = 2\pi (\gamma_i / \Omega_i) (a_j - a_k) (a_k^2 - a_j^2) / (a_j^2 + a_k^2), \quad (22b)$$

in which (i, j, k) stands for an even permutation of (1, 2, 3).

An example is given in Fig. 1 for the prolate spheroid ($a_1 = a$, $a_2 = a_3 = b$). In comparison, we note that in the strip theory for slender bodies ($b/a \ll 1$), the longitudinal virtual mass (M_{11}) is neglected while the transverse virtual mass (M_{22}) is taken sectionally to be the limit of vanishing b/a . For slender ships, b/a is typically about 1/6, in which case the strip theory would give a M_{22} approximately 10% too high.

3. Potential Flow Between Confocal Ellipsoids.

The above singularity method can be readily extended to consider the flow between two confocal ellipsoids in relative motion. Let the two confocal ellipsoids E and E' be specified as

$$E: \sum_{i=1}^3 (x_i/a_i)^2 = 1, \quad E': \sum_{i=1}^3 (x'_i/a'_i)^2 = 1, \quad (\lambda = a_i'^2 - a_i^2 > 0). \quad (23)$$

In the case of relative translation, let the outer ellipsoid E' move with velocity $-U$ with respect to the inner ellipsoid E, which is held at rest. Then the boundary conditions on the velocity potential are

$$\partial \varphi / \partial n = 0 \quad (\underline{x} \text{ on } S) \quad (24a)$$

$$= -U_i n'_i \quad (\underline{x} \text{ on } S') \quad (24b)$$

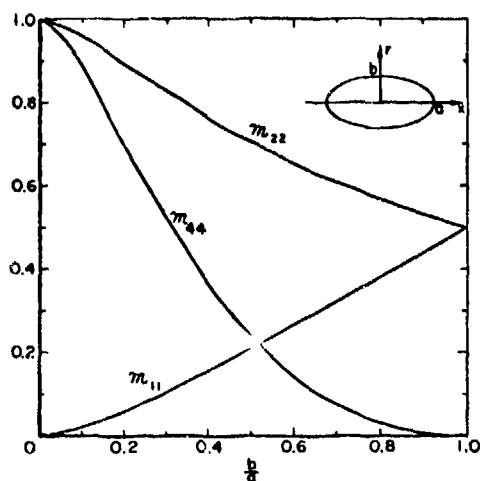


Figure 1. The virtual mass coefficients, m_{11} , m_{22} (translational motion) and m_{44} (rotational motion), of a prolate spheroid of axis-ratio b/a .

The solution can be constructed by a linear superposition of the interior and exterior types of flows, namely (9) and (10), as

$$\phi(\mathbf{x}) = B_i \left\{ -U_i x_i - 2\pi a_1 a_2 a_3 \beta_i x_i \int_{\lambda}^{\infty} \frac{d\lambda}{(a_i^2 + \lambda)\Delta} \right\}. \quad (25)$$

The two terms inside the brackets are actually the velocity potential of a solitary ellipsoid E written in the body frame of E , placed in a uniform stream of velocity $-U$. Therefore (24a) is satisfied if β_i is given by (10c). Further, (24b) is satisfied if

$$B_i = \left[1 - \frac{a_1 a_2 a_3}{a_1' a_2' a_3'} \frac{2 - a_i'}{2 - a_i} \right]^{-1}, \quad (26)$$

where $a_i = a_i(a_j)$ as defined by (3b), and $a_i' = a_i(a_j')$. Similarly, for rotation of E relative to E' with angular velocity $\underline{\Omega}$,

$$\begin{aligned} \phi(\mathbf{x}) &= C_i (-\Omega_i x_j x_k + \gamma_i \epsilon_{ijk} x_j \frac{\partial}{\partial x_k} \int_E \frac{1}{R} d\mathbf{x}) \\ &= C_i (-\Omega_i x_j x_k - \frac{3}{2} V \gamma_i \epsilon_{ijk} x_j x_k \int_{\lambda}^{\infty} \frac{1}{a_k^2 + \lambda} \frac{d\lambda}{\Delta}), \end{aligned} \quad (27)$$

$$\frac{\gamma_i}{\Omega_i} = \frac{1}{2\pi} \frac{a_1' a_2' a_3'}{a_1 a_2 a_3} \left[2 \frac{a_j^2 - a_k^2}{a_j^2 + a_k^2} + (a_j' - a_k')^{-1} \right], \quad (28a)$$

$$\begin{aligned} C_i &= \Omega_i \left\{ 2\pi \gamma_i \left[2 + \frac{a_j^2 + a_k^2}{a_j^2 - a_k^2} (a_j - a_k) \right] \right. \\ &\quad \left. - \Omega_i \frac{a_j^2 + a_k^2}{a_j^2 - a_k^2} \right\}^{-1}. \end{aligned} \quad (28b)$$

The corresponding virtual mass coefficients are, for $i = 1, 2, 3$,

$$m_{ii} = B_i a_i / (2 - a_i), \quad (29)$$

$$m_{i+3, i+3} = 2\pi (C_i \gamma_i / \Omega_i) (a_j - a_k) (a_k^2 - a_j^2) (a_j^2 + a_k^2) \quad (30)$$

The effect of the presence of an outer ellipsoid on the virtual mass coefficients of a moving inner ellipsoid is demonstrated in Fig. 2 and Fig. 3 for the case of two confocal prolate spheroids ($a_1 = a$, $a_2 = a_3 = b$, $a_1' = a'$, $a_2' = a_3' = b'$). This effect is seen to increase all the virtual mass coefficients; they increase more rapidly when the outer ellipsoid is drawn closer to E .

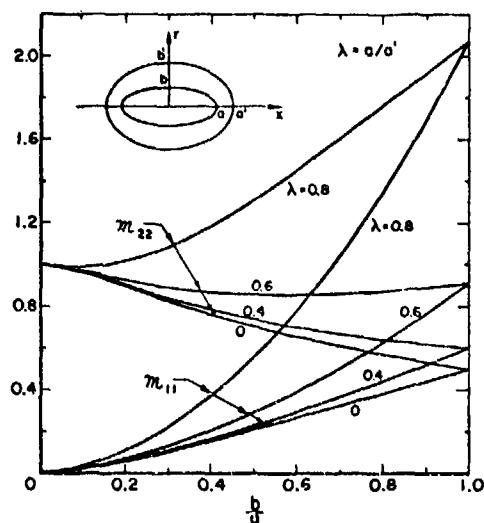


Figure 2. The translational virtual mass coefficients, m_{11} and m_{22} , of two confocal prolate spheroids with axis-ratio b/a and scale factor $\lambda = a/a'$.

4. Plan Form of Singularity Distribution.

At a point \underline{x} on an ellipsoid E , the total curvature (or the sum of principal curvatures), κ , is a local property:

$$\kappa(\underline{x}) = \text{div } \underline{n} = \kappa_1 + \kappa_2 = R_1^{-1} + R_2^{-1} \quad (\underline{x} \in S), \quad (31)$$

where $\underline{n}(\underline{x})$ is the unit outward normal vector, $\kappa_{1,2} = R_{1,2}^{-1}$ denote the principal curvatures

of S at \underline{x} . Since κ is a local property, there exists, in general, in the tangent plane at \underline{x} a direction in which the principal radius of curvature R_1 is minimum, equal to R_m say, while R_2 is maximum. At each longitudinal station ($\xi = \text{const.}$) R_m reaches a minimum at the center plane

$$S_c: \quad \frac{x_o^2}{a^2} + \frac{y_o^2}{b^2} = 1, \quad z = 0, \quad (32)$$

where $(x_1, x_2, x_3) \equiv (x, y, z)$, $(a_1, a_2, a_3) \equiv (a, b, c)$, used alternatively throughout for brevity. At S_c the x - and y -component of R_m can be shown to have the value

$$R_{mx} = R_m \frac{\partial x}{\partial n} = \frac{c^2}{a^2} x, \quad R_{my} = R_m \frac{\partial y}{\partial n} = \frac{c^2}{b^2} y, \quad (\underline{x} \in S_c) \quad (33)$$

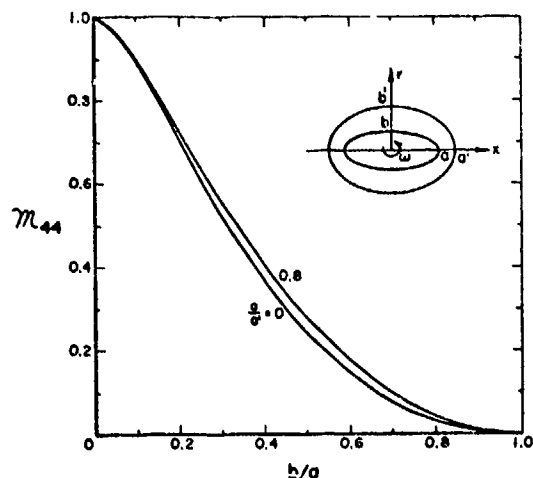


Figure 3. The rotational virtual mass coefficient m_{44} of two confocal prolate spheroids.

It is of significance to note that a boundary point \underline{x} of the center plane S_c , the minimum radius of curvature R_m at S_c , and a boundary point \underline{x}_o of the focal ellipse (see Eq. (12 b), designated there as E_o)

$$S_o: \quad \frac{x_o^2}{a^2 - c^2} + \frac{y_o^2}{b^2 - c^2} = 1, \quad z = 0, \quad (34)$$

are related by the following parametric equations

$$x_o^2 = x(x - R_{mx}), \quad y_o^2 = y(y - R_{my}) \quad (\underline{x} \in S_c). \quad (35)$$

In fact, substitution of (33) in (35) gives

$$\frac{x_o^2}{a^2 - c^2} + \frac{y_o^2}{b^2 - c^2} = \frac{x^2}{a^2} + \frac{y^2}{b^2} = 1.$$

The relationship (35) may provide a useful guideline for determining the region of singularity distribution in the center plane for a class of arbitrary bodies, as will be discussed next.

5. Center-plane Singularity Method for Arbitrary Double-model.

The general problem at hand is concerned with the potential flow generated by the motion of a double-model (with at least one plane of symmetry, taken to be $z = 0$), of arbitrary shape

$$S: \quad z = \pm \zeta(x, y) \quad (|x| \leq a, |y| \leq b), \quad (36a)$$

so that its center-plan-form is

$$S_c: \quad \zeta(x, y) = 0. \quad (36b)$$

The body-shape function $\zeta(x, y)$ is assumed to be continuous, continuously differentiable (except possibly at $\zeta = 0$), and bounded, $|\zeta| \leq c$, so that the body lies within a rectangular box of sides a, b, c . We shall further take $a > b > c$. The side edge (at $z = 0$) of a body is said to be pointed if $|\nabla \zeta| < \infty$ as $z \rightarrow \pm 0$, and round if $|\nabla \zeta| \rightarrow \infty$ in the limit. A round edge is further said to have a stationary, or non-stationary, curvature according to $\partial R_m / \partial s = 0$, or $\neq 0$, at $z = 0$, where s is the arclength of a curve formed by the interception of body surface S with a plane perpendicular to $z = 0$ and containing the normal vector \underline{n} to S at $z = 0$, and R_m is the minimum principal curvature defined in Section 4.

When the body moves with velocity $\underline{U} + (\underline{\Omega} \times \underline{x})$ through an ideal fluid, the velocity potential satisfies the condition

$$\frac{\partial \phi}{\partial n} = (\underline{U} + \underline{\Omega} \times \underline{x}) \cdot \underline{n} \quad (\underline{x} \in S). \quad (37)$$

According to the method of center-plane singularity distribution, the solution may assume the form

$$\varphi = \varphi_T + \varphi_R \quad (38a)$$

$$\varphi_T = \int_{S_0} \beta_1(\xi, \eta) \frac{\partial}{\partial x_1} \left(\frac{1}{R} \right) d\xi d\eta \quad (38b)$$

$$\varphi_R = \epsilon_{ijk} \int_{S_0} \gamma_1(\xi, \eta) x_j \frac{\partial}{\partial x_k} \left(\frac{1}{R} \right) d\xi d\eta \quad (38c)$$

$$S_0: f_0(x, y) = 0 \quad (S_0 \subset S_c). \quad (38d)$$

Here β_1, γ_1 are unknown densities of doublets and doublet-moments, and S_0 is the unknown region of distribution, which is assumed to lie within the center plane S_c and may have boundary points common with S_c . This integral representation of φ is suggested by the known exact solution for ellipsoids. Although only doublets are employed, it may still contain isolated point sources and line sources at the discontinuities of β and γ . It may also represent distributions of higher-order singularities when β and γ can be expressed as derivatives of some appropriate functions.

Application of condition (37) to (38) yields the following integral equations

$$\int_{S_0} \beta_1(\xi, \eta) K(x, y, z; \xi, \eta) d\xi d\eta = u_a n_a \quad (x \in S), \quad (39a)$$

$$K_1(x, y, z; \xi, \eta) = n_a \frac{\partial}{\partial x_a} \left[\frac{\partial}{\partial x_1} \left(\frac{1}{R} \right) \right]; \quad (39b)$$

$$\epsilon_{ijk} \int_{S_0} \gamma_1(\xi, \eta) Q_{jk}(x, y, z; \xi, \eta) d\xi d\eta = \epsilon_{ijk} \Omega_{jk} x_j n_k \quad (x \in S), \quad (40a)$$

$$Q_{jk}(x, y, z; \xi, \eta) = n_a \frac{\partial}{\partial x_a} \left[x_j \frac{\partial}{\partial x_k} \left(\frac{1}{R} \right) \right]. \quad (40b)$$

Strictly speaking, these integral equations are not linear, since the region of integration is also unknown. They are further characterized by the particular feature that the free variable x and integration variables (ξ, η) belong to different sets of space. Theory for this kind of integral equations is in its infancy. There is no known necessary and sufficient condition on the shape function S for ensuring existence of solution. Even when a solution is found, it is difficult to prove the uniqueness.

On a heuristic basis, this method may be applicable to a limited family of bodies (for instance, under certain conditions on the bound of variation in convexity of S). It may be

possible, however, to have the scope of body family enlarged with further modifications of the method, such as by adding lines of vortices and sources on body surface S to represent local discontinuities in slope and curvature of S and by introducing more interior planes of doublet layers, if necessary.

From the standpoint of calculation of solution by numerical means, the problem of the integral equations (39) and (40) may well be ill-posed. It is plausible that large errors in β_1 and γ_1 may produce only small errors of the integrals (for example, when β has a smooth error in the region where K is oscillatory, and vice versa). Actually, the kernels K_1 and Q_{jk} all have localized peaks, which become more pronounced with decreasing body thickness or slenderness. These peaks are manifested by the value of the following functions:

$$\frac{1}{R} = \frac{1}{[(x - \xi)^2 + (y - \eta)^2 + z^2]^{\frac{1}{2}}} \quad (x \in S) \quad (41a)$$

$$\nabla \frac{1}{R} = - \frac{(x - \xi) e_1 + (y - \eta) e_2 + z e_3}{R^3}, \quad (41b)$$

and their higher derivatives appearing in K_1 and Q_{jk} . Thus, for fixed (ξ, η) , R^{-1} has a peak at $\partial R / \partial x = \partial R / \partial y = 0$, or at

$$\xi = x + z e_x = \hat{\xi}(x, y), \quad \eta = y + z e_y = \hat{\eta}(x, y). \quad (42)$$

It follows that $\partial R^{-1} / \partial x$ has two peaks near $(\hat{\xi}, \hat{\eta})$, with one on each side of $\xi = \hat{\xi}$, and so forth for higher derivatives of R^{-1} . The peaking feature of these kernels actually enhances the hope of success in developing adequate numerical methods (though it may sound superficially strange), if this feature is used to advantage.

5.1 The Plan Form of Singularity Distribution.

Our experience with several numerical methods so far attempted indicates that the error of the solution is very sensitive to the error in S . When a first guess, $S^{(1)}$ say, of S_0 is either too large or too small, various finite-element methods that have been tried out generally produced poor results (as measured by the error of the solution in satisfying the integral equation at interpolated points), and computations by iteration methods may not converge. Satisfactory results, however, have been obtained when $S^{(1)}$ is sufficiently accurate. In the trial cases for bodies with round edges, the parametric equation (35) for S seems to have a general validity. We therefore propose the following rules for determining the region S_0 .

(i) Along round edges of non-stationary curvature. For bodies with non-stationary transverse curvature along the boundary points

(x, y) of its center plane S , the boundary points (x_0, y_0) of the distribution region S_0 are given by the parametric equations

$$x_0^2 = x(x + \zeta_x), \quad y_0^2 = y(y + \zeta_y), \quad (\partial R_m / \partial s \neq 0). \quad (43)$$

This set of equations are the same as (35) since for the shape function (36), $R_{mx} = -\zeta_x$, $R_{my} = -\zeta_y$. As has been shown (see the equation following (35)), this rule gives the exact S for triaxial ellipsoids (including spheroids and sphere as special cases).

For axisymmetric prolate bodies, the y -component of (43) automatically yields $y_0 = 0$, while the x -component provides the two terminals of axial distribution of singularities as

$$l = a \left[1 - \left(1 - \frac{R_a}{a} \right)^{\frac{1}{2}} \right], \quad (44a)$$

where l is the distance (towards the center) from the body nose at $x = a$, and R_a is the principal radius of nose curvature (since at the body end $x = a$, $x_0 = a - l$, $\zeta_x = -R_a$). For slender axisymmetric bodies ($R_a \ll a$), (44a) reduces to

$$l = \frac{1}{2} R_a \left[1 + \frac{1}{4} \left(\frac{R_a}{a} \right) + \frac{1}{8} \left(\frac{R_a}{a} \right)^2 + \frac{5}{64} \left(\frac{R_a}{a} \right)^3 + \dots \right], \quad (44b)$$

of which the leading term is well known, and the higher-order terms have been discussed by Landweber (1951), Lighthill (1951), Moran (1963), Handelsman and Keller (1967) and Miloh (1972).

(ii) Axisymmetric prolate bodies with ends of stationary curvature. The end-rule

(44), however, may not be valid for axisymmetric prolate bodies with ends of stationary curvature, such as the Rankine ovoid formed by a source-sink pair (or equivalently, a line of uniform doublets). For Rankine ovoids, of arbitrary eccentricity, we have the relationship between the body major axis a , nose radius of curvature R_a , and the 'focal length' $2x_0$ of line doublet as

$$a(a - R_a) = \frac{1}{3} x_0^2 (5a^2 + x_0^2) / (a^2 + x_0^2), \quad (45a)$$

or after solving for x_0 ,

$$l = a - x_0 = a \left\{ 1 - \left[2 \left(1 + \frac{9}{16} \frac{R_a^2}{a^2} \right)^{\frac{1}{2}} - \left(1 + \frac{3}{2} \frac{R_a}{a} \right) \right]^{\frac{1}{2}} \right\}. \quad (45b)$$

For very slender Rankine ovoids, (45b) reduces to

$$l = \frac{3}{4} R_a \left[1 + \frac{27}{512} \left(\frac{R_a}{a} \right)^3 + \dots \right], \quad (45c)$$

indicating that the singularity distribution stops at about $3/4 R_a$ from the nose.

For two-dimensional Rankine bodies, the relationships corresponding to (45) become

$$R_a = 3a(a^2 - x_0^2) / (3a^2 + x_0^2), \quad (46a)$$

$$l = a - x_0 = a \left\{ 1 - \left[3 \left(1 - \frac{R_a}{a} \right) / \left(3 + \frac{R_a}{a} \right) \right]^{\frac{1}{2}} \right\}, \quad (46b)$$

$$l = \frac{2}{3} R_a \left[1 + \left(\frac{R_a}{3a} \right)^2 + \left(\frac{R_a}{3a} \right)^3 + \dots \right]. \quad (46c)$$

The distribution of a uniform two-dimensional doublets for representing a thin Rankine body terminates at about $\frac{2}{3} R_a$ from the nose. This last result (46c) has also been obtained by Miloh (1972).

For the sphere, $R_a = a$, both (44a) and (45a) give the correct value $x_0 = 0$, implying that a single doublet at the origin will suffice. For slender (three-dimensional) bodies, the distinction between $l = \frac{1}{2} R_a$ (see 44b) and $l = \frac{1}{3} R_a$ (see 45c) (or between $l = \frac{1}{2} R_a$ and $l = \frac{2}{3} R_a$ for two-dimensional thin bodies) can be attributed to the difference that in the former case the doublet density vanishes at the end of distribution whereas in the latter it has a finite end value. This feature has also been noted before by Miloh (1972), and further found valid in low Reynolds-number flows as well (Chwang and Wu 1974b).

The remaining discussion will be given for the case of translational motions, since the methods of solution for rotational motions are quite similar.

5.2 Approximate Solution by a Direct Finite-Element Method.

The integral equation (39) can be reduced to linear algebra when $\beta(\xi, \eta)$ is approximated by piece-wise constant values in finite-element integration. Since each component U_i can be treated separately, we shall drop the component indices for brevity. Thus we discretize the integration by choosing a set base points

$$(\xi_i, \eta_j) \quad (i = 0, 1, 2, \dots, m; \quad j = 0, 1, 2, \dots, n), \quad (46)$$

of equal or unequal intervals, and keep only those base rectangles whose centers lie within S_0 . Let the number of these base rectangles be N . Next we choose N points of x on S by taking (x_i, y_j) as the solution of (42) corresponding to the center point $(\xi_{ci}, \eta_{cj}) = (\frac{1}{2}(\xi_i + \xi_{i+1}), \frac{1}{2}(\eta_j + \eta_{j+1}))$ of each base rectangle.

By approximating $\beta(\xi, \eta)$ in each base rectangle by its value at the center, that is $\beta(\xi, \eta) \approx \beta(\xi_{ci}, \eta_{cj}) \approx \beta_{ij}$, the integration in (39) can be carried out analytically for each element. Consequently, after reordering the elements β_{ij} and $n_{ij} = n(x_i, y_j)$ separately into a N -element vector, we obtain a linear algebraic equation, given symbolically as

$$K_{kl} \beta_l = \eta_k \quad (k = 1, 2, \dots, N). \quad (47)$$

Hence

$$\beta_l = K_{kl}^{-1} \eta_k \quad (l = 1, 2, \dots, N) \quad (48)$$

if the matrix K_{kl} is non-singular, and then β_l can be converted back to β_{ij} by inverting the original ordering. This method can be expected to yield only an approximate solution to (39); it may be useful, however, to provide a first approximation to $\beta(\xi, \eta)$ for some iteration scheme when an improved accuracy is required.

This approximate method has been applied to an ellipsoid of axis ratio $a:b:c = 1.5:1:1$. In comparison to the known exact solution, the numerical results of β_j have a root-mean-square error of 0.03 and a maximum error of +0.1 when the total number of elements, N , is 40; these errors decrease to 0.01 and +0.03, respectively, when N is increased to 100, and to 0.002 and +0.01 when $N = 200$. The computation took about 30 seconds for each case on an IBM 370/158 Computer at the W. H. Booth Computing Center.

5.3 Solution by Iteration

In order to improve the accuracy of the solution we have investigated a few iteration methods. Basically there are two approaches to appropriate handling of the peaks of the kernel in numerical integration. One approach is by approximating β by a family of known functions so that the resulting integrals can be integrated analytically. This approach is attractive since $\beta(\xi, \eta)$ is expected to be generally smooth and since analytical integrations help reduce errors due to the presence of large peaks of the kernel. When an interpolating polynomial is assumed for β , the analytical integration is readily carried out; this convenience is actually a noticeable advantage of the center-plane-singularity (CPS) method since the integration is over a plane. The second approach is by removing the peaks by adding and subtracting the values of β at the peaks of the kernel K and by appropriate re-grouping. These two methods are described below.

In the first method, consider, as an example, the case of longitudinal translation, $\mathbf{U} = (1, 0, 0)$. Since in this case the kernel K has a double peak parallel to the ξ -direction, it is desirable to carry out first the ξ -integration in (39a), then the η -integration. To begin with, we subdivide S_0 first by lines $\eta = \eta_j$, ($j = 1, 2, \dots, n$), $-b_1 = \eta_1 < \eta_2 < \dots < \eta_n = b_2$, where $-b_1$ and b_2 are the lower and upper bounds (in η) of S_0 . Let the interval of the line $\eta = \eta_j$ lying within S_0 be $-\xi_L(\eta_j) < \xi < \xi_R(\eta_j)$. It is also possible that, when the boundary of S_0 is convex towards the interior, the line $\eta = \eta_j$ may have two or more disconnected intervals lying within S_0 . When this happens, we treat each of these intervals

separately in the same manner. For each given η_j , the ξ -interval is subdivided at the base points.

$$\xi_{j,i} \quad (i = 1, 2, \dots, m), \quad -\xi_L(\eta_j) = \xi_{j1} < \xi_{j2} < \dots < \xi_{jm} = \xi_R(\eta_j). \quad (49)$$

The subintervals $\xi_{j,i+1} - \xi_{j,i} = h_j$ need not be uniform, and m may be different for different j . In each ξ -subinterval, we approximate the doublet strength $\beta(\xi, \eta)$ by a quadratic function

$$\beta(\xi, \eta) = \beta(\xi_i, \eta_j) + (\xi - \xi_i) \beta'(\xi_i, \eta_j) + \frac{1}{2} (\xi - \xi_i)^2 \beta''(\xi_i, \eta_j) \quad (\xi_i < \xi < \xi_{i+1}) \quad (50)$$

in which the subindex j of $\xi_{j,i}$ is omitted as understood. By using the continuity conditions on β and $\partial\beta/\partial\xi$ at ξ_i ($i = 2, 3, \dots, m-1$), and two appropriate end conditions (such as $\beta = 0$ for edges of non-stationary curvature), there results m_j unknown parameters for each j , or $\sum_j m_j (= N$ say) in total. An even

better approximation to β would be the cubic SPLINE representation, use of which is being investigated in a continued study.

An appropriate choice of N points (x_i, y_j) on S is made by taking (x_i, y_j) as the solution of (42) for each (ξ_i, η_j) , or

$$\xi_i = x_i + \frac{1}{2} \frac{\partial}{\partial x} \zeta^2(x_i, y_j), \quad \eta_j = y_j + \frac{1}{2} \frac{\partial}{\partial y} \zeta^2(x_i, y_j), \quad (51)$$

from which (x_i, y_j) can be solved by known methods. Conversely, we note that for any point $(x_i, y_j, \zeta(x_i, y_j))$ on S , the corresponding point (ξ_i, η_j) given by (51) always falls within S_0 determined by (43). Upon substituting (50) into (39), the ξ -integration can be carried out analytically for each (x_i, y_j) . Since the effect due to the peaks of the kernel K on the accuracy of numerical integration is already much suppressed after the ξ -integration, the remaining η -integration can be handled adequately by applying Simpson's rule if the η -subintervals are taken to be uniform and if some approximate values of the N unknowns β_{ij} are assigned. In the final step the required solution may be sought by applying the following iteration procedure

$$\beta_{ij}^{(n+1)} = \beta_{ij}^{(n)} + \lambda [n_1(x_i, y_j) - \int_{S_0} K(x_i, y_j; \xi, \eta) \beta^{(n)}(\xi, \eta) d\xi d\eta], \quad (52a)$$

in which the integration is computed as described above in each step, and λ is a relaxation parameter. This iteration procedure may be regarded as a generalization, to double integrals, of the method introduced by Landweber (1951) for axisymmetric potential flow problems. The rate of convergence of the iterations generally depends on the choice of λ . Based on the same procedure as Landweber's, a proper choice of λ for the present case is

$$\lambda^{-1} = \int_{S_0} K(x_i, y_j; \xi, \eta) d\xi d\eta. \quad (52b)$$

For the translation in the y -direction, $\underline{U} = (0, 1, 0)$, we interchange the order of integrations since the double peaks of K_2 are along the line $y = \text{const}$. For the translation in the z -direction the order of integrations is immaterial. For rotational motions the integrals involved are combinations of the cases already discussed.

The above technique has been applied to the ellipsoid of axis ratio $a:b:c = 1:1/2:1/4$, the result from the first iteration was found to have a relative mean error of 10^{-3} .

6. Example: A Double-elliptic Body.

As a representative example, we consider the following shape function:

$$z = \pm \zeta(x, y) = \pm c \left(1 - \frac{x^2}{a^2}\right)^{1/2} \left(1 - \frac{y^2}{b^2}\right)^{1/2} \quad (a > b > c). \quad (53)$$

This double-elliptic body has round edges except for the four sharp corners at $x = \pm a$ and $y = \pm b$ (see Fig. 4).

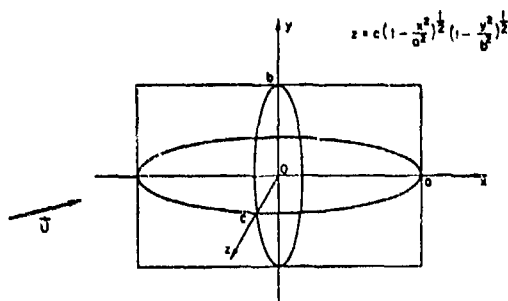


Figure 4. The shape function of a double-elliptic body.

According to the rule (43), the CPS region S_0 is bounded on four sides by two pairs of hyperbolas (see Fig. 5)

$$\frac{x^2}{c^2} - \frac{y^2}{b^2} = \frac{a^2}{c^2} - 1, \quad (54a)$$

$$\frac{y^2}{c^2} - \frac{x^2}{a^2} = \frac{b^2}{c^2} - 1. \quad (54b)$$

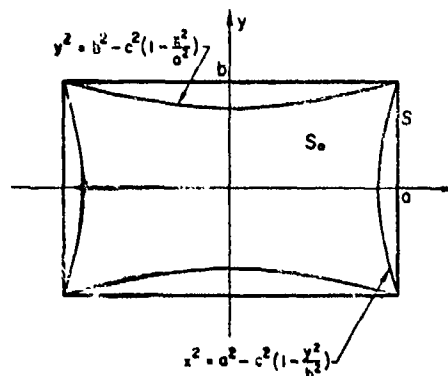


Figure 5. The singularity-distribution plan form S_0 of the double-elliptic body; S_0 is bounded by two pairs of hyperbolas.

Using this plan form of S_0 , the doublet strength has been computed by applying the direct finite-element method (Sect. 5.2) for the longitudinal translation in the x -direction.

The results of the doublet density are shown in Fig. 6 for double-model I with $a:b:c = 1:1/2:1/4$ and in Fig. 7 for double-model II with $a:b:c = 1:1/6:1/8$. We note that the doublet density β decreases to zero rather rapidly as the

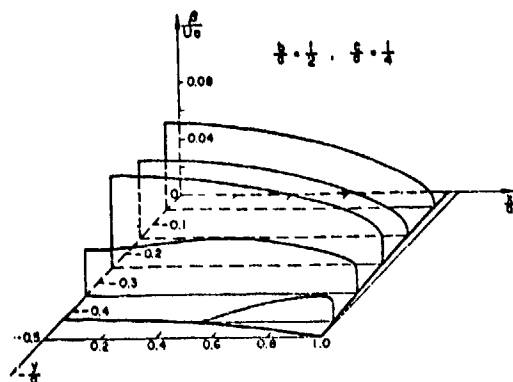


Figure 6. The computed center-plane doublet density used in representing the longitudinal translation of a double-elliptic body with axis-ratio $a:b:c = 1:\frac{1}{2}:\frac{1}{4}$ (double-model I).

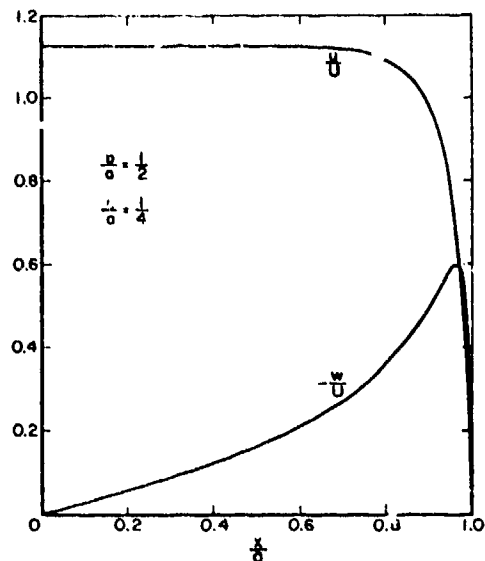


Figure 8. The computed surface velocity components of double-model I in longitudinal translation.

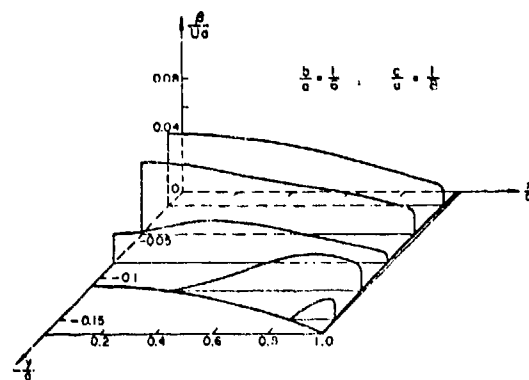


Figure 7. The same legend as in Figure 6 for double-model II with axis-ratio $a:b:c = 1:1/6:1/8$.

front and rear boundaries of S_0 are approached, and these two boundaries (given by 54a) are very close to the bow and stern line, whereas β decreases more slowly towards the upper and lower boundaries (Eq. 54b) of S_0 . The x - and z -components of velocity at the surface of Model I along the center line $y = 0$ are shown in Figure 8 in terms of the body frame. The corresponding pressure distribution (in the coefficient form) is presented in Figure 9.

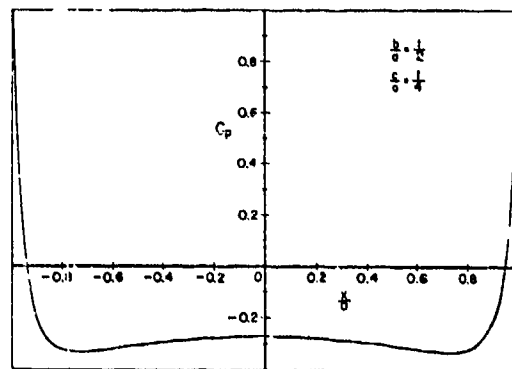


Figure 9. The computed pressure coefficient at $y = 0$ on the surface of double-model I in longitudinal translation.

With respect to the effect of error in S_0 on the accuracy of solution, we remark here that if an approximate S_0' is larger than S_0 , some negative values of doublets were invariably found in the region outside S_0 . On the other hand, if another S_0'' is smaller than S_0 , then the numerical results always exhibited large variations in β , fluctuating between positive and negative values. In either case, there is evidence that the solution becomes unsatisfactory at intermediate points of the base elements.

In conclusion, we feel that the present preliminary results have thrown much needed

light on the direction of further development of the center-plane-singularity method. Its possible generalization to water waves problems will be explored.

Acknowledgments

We are very much indebted to Professor Louis Landweber for stimulating discussions and for providing us with copies of related works by himself and his students.

This work was sponsored by the Office of Naval Research.

REFERENCES

- Chandrasekhar, S. 1967 Ellipsoidal figures of equilibrium - an historical account. *Comm. Pure & Appl. Math.* 20, 251-265.
- Chwang, A. T. & Wu, T. Y. 1974a A note on the potential flow involving prolate spheroids. *Schiffstechnik*, 21, 19-31.
- Chwang, A. T. & Wu, T. Y. 1974b Hydro-mechanics of low-Reynolds-number flow. Part I. Rotation of axisymmetric prolate bodies. *J. Fluid. Mech.* 63, 607-622.
- Eggers, K. 1960 Über Singularitätendarstellungen und Kraftwirkungen bewegter Körper in inkompressibler Flüssigkeit. *Schiffstechnik* 38, 3-15.
- Handelsman, R. A. & Keller, J. B. 1967 Axially symmetric potential flow around a slender body. *J. Fluid Mech.* 28, 131-147.
- Havelock, T. H. 1931a The wave resistance of a spheroid. *Proc. Roy. Soc. A* 131, 275-285.
- Havelock, T. H. 1931b The wave resistance of an ellipsoid. *Proc. Roy. Soc. A* 132, 480-486.
- Hess, J. L. & Smith, A. M. O. 1966 Calculation of potential flow about arbitrary bodies. *Progress Aeron. Sci.* 8, 1-138. New York: Pergamon Press.
- Landweber, L. 1951 The axially symmetric potential flow about elongated bodies of revolution. David Taylor Model Basin Rept. 761. Washington, D. C.
- Landweber, L. 1974 Private communication.
- Lighthill, M. J. 1951 A new approach to thin aerofoil theory. *Aeron. Quart.* 3, 193.
- Lunde, J. K. 1951 On the linearized theory of wave resistance for displacement ships in steady and accelerated motion. *Trans. SNAME* 59, 25-76.
- MacMillan, W. D. 1930 The theory of the potential. New York: McGraw-Hill Book Co. (reprint ed. 1958, New York: Dover Publ.)
- Miloh, T. 1972 Higher-order theory of ship waves from centerplane source distribution. Ph.D. Thesis. The University of Iowa, Iowa City, Iowa.
- Miloh, T. 1973 The ultimate image singularities for external spheroidal and ellipsoidal harmonics. IHR Report 146, The University of Iowa, Iowa City, Iowa.
- Moran, J. F. 1963 Line source distributions and slender body theory. *J. Fluid Mech.* 17, 285-304.
- Newman, J. N. 1972 Water wave singularities in a prolate spheroidal coordinate system. *J. Ship Research* 14, 41-46.
- Thomson, W. & Tait, P. G. 1883 Treatise on Natural Philosophy. Cambridge University Press, Cambridge, England.
- Todhunter, I. 1873 History of the Mathematical Theories of Attraction and the Figure of the Earth. London: Constable. (reprint ed. 1962, New York: Dover Publ.)
- Weinblum, G. 1936 Rotationskörper geringsten Wellenwiderstandes. *Ingenieur-Archiv*, 7, 104-117.
- Yih, C. S. 1969 Fluid Mechanics. New York: McGraw-Hill Book Co.

DISCUSSION

L. LANDWEBER

It was in a 1956 paper [1] that I first acknowledged my debt to George Weinblum. Since then there have been other papers, honoring him on his various birthdays; but since the first statement, written with the stimulation of a special occasion, symbolizes the inspirational influence he has had on his colleagues and students, it is again quoted: "We are also pleased, here, to mention George Weinblum of the University of Hamburg, that most inspiring teacher, who pointed out the power of the Lagally theorem and new fields of research for many of us." Sorrowfully, the present discussion, on a subject that was of close interest to him, is also dedicated to George Weinblum.

In the introduction, the authors have kindly mentioned the writer's method of computing the potential flow about arbitrary three-dimensional forms, but referred to it as (1974), unpublished. That reference should have been to his 1969 paper [2]. The authors will also be interested to know that the technique of applying the known gravitational potential of a solid ellipsoid to derive the potential flow about an ellipsoid is mentioned by Lamb [3] and developed by Munk [4]. In discovering this method independently, the authors have joined the ranks (including Havelock) of an illustrious group of hydrodynamicists.

Both in a previous paper, (Chwang and Wu, 1974a) as well as in the present one, focal axis distributions are presented for prolate spheroids. Evidently the authors were not aware of the Havelock formula [5]

$$P_n^s(u)Q_n^s(c)e^{is\phi} = \frac{1}{2} \left(\frac{\partial}{\partial y} + i \frac{\partial}{\partial y} \right)^s \cdot \int_{-1}^1 \frac{(1-\xi^2)^{s/2} P_n^s(\xi) d\xi}{[(x-\xi)^2 + y^2 + z^2]^{3/2}}$$

which expresses the general spheroidal harmonic in terms of a distribution of singularities between the foci. The distributions associated with each of the motions of a spheroid can be read immediately from this formula. Havelock did not present a proof of his formula; this was first demonstrated by Bottacini [6]. An alternative proof, given in the writer's class notes, was published with some modifications by one of his students, Miloh (1973). Indeed, it was the Havelock formula which inspired Miloh to seek and find an equivalent result for ellipsoids, which yields the centerplane distributions for the various motions of an ellipsoid, just as directly as the Havelock formula for spheroids.

In the section on virtual mass coefficients of ellipsoids, a more precise reference than (Yih 1968) for the "extended Taylor theorem" is the writer's paper [7]. The formulae for the added masses are also given by Lamb [3]. Munk [4] has expressed these in terms of elliptic integrals, which are better suited for numerical calculations.

A novel and important feature of the paper is the proposed formula (35) for determining the outer contour of a centerplane distribution. Applied to a two-dimensional section, with $x = 1$ and $x_0 = 1 - s$, this yields the solution

$s = 1 - \sqrt{1 - R_m}$, which is exact for an elliptical extremity. More generally, however, if a nose shape near $x = 0$ is represented by $y^2 = 2R_m x + cx^2$, the writer has shown [8]

$$\frac{s}{R_m} \approx \frac{\sqrt{49+40c} - 1}{2(5+c)}$$

which agrees approximately with the authors' result when $|c| \ll 1$ and $R_m \ll 1$. For other values of c , one sees from this expression that s varies from R_m to 0 as c varies from -1 to ∞ . It appears, then, that (35) is applicable only to forms which are locally ellipsoidal at the points of intersection with the centerplane, as the authors also found when attempting to apply (35) to a Rankine ovoid.

Two methods of solving the integral equation for a centerplane doublet distribution are described. One, in which piecewise constant distributions over rectangular area elements are assumed, is similar to von Kármán's early method [9] of determining axial distributions for bodies of revolution. Experience with the von Kármán method indicates that it can yield useful results if a moderate number of elements are assumed, $N = O(10)$, but that the results became erratic when a much larger number of elements are employed. This is consistent with the theory of Fredholm integral equations of the first kind, which indicates that, when an exact solution does not exist, a sequence of approximate solutions can at best satisfy the integral equation only "in the mean." It appears that the favorable results with this method are due to the fact that it was applied to a spheroid for which both an exact solution exists and the domain of the distribution is known. For other shapes, the experience with the von Kármán method would probably be repeated. The authors have used eq. (42), giving peaks in $1/R$ for fixed (ξ, η) , for the centers of the finite elements. Should not the peaks of kernel for fixed (x, y, z) have been used for this purpose?

The second method is more nearly similar to that of Miloh (1972) and Miloh and Landweber [8], although the philosophy of the methods are somewhat different. In the latter papers, the sharp peaks of the kernel which can be integrated exactly, and has peaks that nearly coincide with those of the original kernel. Subtracting the original kernel within the integral, and adding its exact value outside the integral, leaves the integral equation unaltered, but with a smoother integrand to which an accurate quadrature formula, of moderate order, such as that of Gauss, may be applied. The resulting set of linear equations is then solved by the same iteration formula, (52a).

Clearly there are many methods of obtaining useful solutions of the integral equation. The main problem remaining is to generalize the author's formula for determining the domain of the centerplane singularities.

References

1. L. Landweber and C.S. Yih, "Forces, Moments, and Added Masses for Rankine Bodies," *Journal of Fluid Mechanics*, Vol. 1, Part 3, 1956.

2. L. Landweber and M. Macagno, "Irrotational Flow about Ship Forms," IIHR Report No. 123, Dec. 1969.
3. H. Lamb, *Hydrodynamics*, 6th Edition, p.154, Cambridge University Press, 1932.
4. M.M. Munk, "Fluid Mechanics, Part II," Division C, Vol. 1 of *Aerodynamic Theory*, p.304, Edited by W.F. Durand.
5. T.H. Havelock, "The Moment on a Submerged Body of Revolution Moving Horizontally," *Quarterly Journal of Mechanics and Applied Mathematics*, Vol. 5, Part 2, 1952.
6. M.R. Bottem, "The Added Masses of Prolate Spheroids Accelerating under a Free Surface," Ph. D. Thesis, The University of Iowa, 1958.
7. L. Landweber, "On a Generalization of Taylor's Relation between Virtual Mass and Source Strength of Rankine Bodies," *Quarterly of Applied Mathematics*, Vol. 14, No. 1, 1956.
8. T. Miloh and L. Landweber, "Ship-Centerplane Source Distributions," in preparation.
9. T. von Kármán, "Calculation of Pressure Distribution on Airship Hulls," NACA Technical Memorandum No. 574, 1930.

T. MILOH

The first time I met Professor Weinblum was in the Summer of 1973. I then had the privilege of talking to

$$\bar{M}_{i+3, i+3} = M_{i+3, i+3} \left\{ 1 - \frac{V}{V'} \left(\frac{1 + M_{ii}}{1 + M'_{ii}} \right) \right\}^{-1}$$

$$1 - \frac{V[(a_j^2 + a_k^2) + a_i^2 \left(\frac{a_j^2 + a_k^2}{2} \right)^2 M_{i+3, i+3}]}{V'[(a_j'^2 + a_k'^2) + a_i'^2 \left(\frac{a_j'^2 + a_k'^2}{2} \right)^2 M'_{i+3, i+3}]} \right\}^{-1}$$

him and experience his warmth and friendliness. Sorrowfully this was also the last time. I remember that in our discussion Professor Weinblum was proposing to obtain potential flow solutions for ellipsoids in various motions in order to apply these results as a first order approximation to the motion of real ship forms. It is not a coincidence that the present paper which is dedicated to the memory of Professor Weinblum is concerned with the same problem.

The writer wishes to acknowledge the authors for referring to his work on ellipsoidal bodies, (Miloh (1973)) "which will be useful for treating the related water wave and other general problems." Before this can be done it is necessary to obtain a formal expansion for $1/R$ (here R denotes distance between two spatial points) in terms of ellipsoidal harmonics. Such an expansion has been recently derived and is given in [1]. It is now possible to make use of this expansion in obtaining the water wave singularities in terms of ellipsoidal harmonics in a similar manner to Newman's (1972) work with spheroidal harmonics.

The most general motion of an ellipsoid may be generated by a distribution of sources and doublets on the center-plane. The same motion may be also generated by only a surface source distribution. [1]. For this reason the derivation of a surface doublet representation in section 2.1 (v) seems to be of limited use.

Expressions for the six added mass coefficients of an ellipsoid, given in (22a) and (22b) have been given by Lamb [2] and were displayed graphically by Kochin et al [3]. Different expressions for these added mass coefficients in terms of the tabulated incomplete Legendre integrals are also given in [1]. A comparison between these results and the results given in the paper indicate that the term $(a_j^2 + a_k^2)$ appearing in (22b) should be replaced by $a_j'^2$, in accordance with the expression for the kinetic energy given in (21).

The solution of the potential flow problem between confocal ellipsoids may be found to be useful in obtaining blockage corrections and in estimating the effect of neighboring bodies or walls. It seems that they are two different definitions for γ_i in (19c) and in (28a). It is not clear which one of these will be used in (28b) and (30). The added mass coefficients for the case of a flow between two confocal ellipsoids, here denoted by M_{ij} , are related to the added mass coefficients for the unbounded case M_{ij} by,

$$\bar{M}_{ii} = M_{ii} \left\{ 1 - \frac{V}{V'} \left(\frac{1 + M_{ii}}{1 + M'_{ii}} \right) \right\}^{-1}$$

with

$$1 - \frac{V[(a_j^2 + a_k^2) + a_i^2 \left(\frac{a_j^2 + a_k^2}{2} \right)^2 M_{i+3, i+3}]}{V'[(a_j'^2 + a_k'^2) + a_i'^2 \left(\frac{a_j'^2 + a_k'^2}{2} \right)^2 M'_{i+3, i+3}]} \right\}^{-1}$$

where the prime denotes values corresponding to the outer ellipsoid. This is a somewhat simpler representation than (29) and (30).

The value of the longitudinal added mass coefficients for the parabolic ship was calculated in [4] by applying the Taylor theorem to the numerical solution of the integral equation for the center-plane source distribution. This value was compared with the longitudinal added mass coefficient of an equivalent ellipsoid which yields a closed form expression. The equivalent ellipsoid was chosen so as to yield the same volume, mid-section area and free surface area as real ship hull. The comparison was surprisingly good. A research along these lines for other modes of ship motion and their equivalent ellipsoids should be continued.

References:

- [1] Miloh, T. "Forces and Moments on a Tri-Axial Ellipsoid in Potential Flow", *Israel Journal of Technology*, Vol. 11, Nos. 1-2, 1973.

- [2] Lamb, H. "Hydrodynamics" 6th edition. Cambridge University Press. 1932. p. 164.
- [3] Kochin, N.E., Kibel, I.A. and Roze, N.V. "Theoretical Hydromechanics" Interscience Publishers. 1964. p. 150.
- [4] Miloh, T. and Landweber, L. "Ship Centerplane ~~Source~~ Distributions" in preparation.

AUTHOR'S REPLY

Professor Landweber and Professor Miloh have pointed out several references either not cited in our paper, or cited not precisely to the very origin. To them we are very grateful for helping set the record straight since the true source of the original ideas, to which their studies as well as ours are related, will be of good historical interest.

For instance, the relationship between the gravitational potential and the velocity potential involving ellipsoids, as noted by Lamb (1916, 4th ed. pp 148-149; 1932, 6th ed. pp. 153-154, in footnotes) and by Munk (1934, Vol. I, p. 304-referenced to by Dr. Landweber), must date back to earlier times since Havelock (1931a, b) already referred to that relationship as then being 'well known' (1931a, p. 276, Collected Papers, p. 313). In fact, the precise formula was explicitly discussed by Basset (1888, Vol. I, p. 141), and we can trace the original idea back to Green (1833, p. 56 footnote; Mathematical Papers, p. 317), to whom we may attribute the underlying thought relating the potential flow to the theory of attraction. Though we have rediscovered this interesting relationship (actually first through our recent work on low-Reynolds-number flow problems), we immediately become aware of its historical importance, and therefore include a discussion of it under the heading 'Historical Background'. In that Section a brief survey was given in terms of the classic works of Gauss, Rodrigues, Dirichlet and other great mathematicians, together with appropriate applications of Maclaurin's Theorem on the ellipsoid — an approach which may appeal to some as to bear certain classical simplicity and elegance. This approach, however, seemed to have been undertoned by the subsequently more popular method of orthogonal functions, thus becoming, in a sense, a sort of lost art.

We are indebted to Dr. Landweber for showing us a few alternative proofs of Havelock's formula. This formula, originally intended for prolate spheroids, has been extended by Dr. Miloh (1974) to the case of tri-axial ellipsoids. Undoubtedly, further development and fruitful applications of these formulas will be forthcoming.

We agree with Professor Landweber that the main problems remaining are (i) to generalize the formula for determining the domain S_0 of the centerplane singularities and (ii) to improve the numerical method, including the aspect of evaluating, by iteration if desired, the domain S_0 conjointly with the calculation of the singularity density. Dr. Landweber and Dr. Miloh have proposed a different formula (for two-dimensional sections) depending only on the nose shape near $x = 0$ (see the last equation provided in the Discussion). For an elliptic cylinder $x^2/a^2 + z^2/b^2 = 1$ ($a > b$), our equation (43) yields the exact solution $x_0 = \pm (a^2 - b^2)^{1/2}$, or $s = a - x_0$, for all eccentricities. The Landweber-Miloh formula gives the same result as ours for the circular cylinder (in their notation, $c = -1$, $R_m = 1$), but differs somewhat from our result at other values of the eccentricity. It will be welcome to see their formula extended to cover three-dimensional body shapes so as to permit further comparisons with our formula.

We choose to correlate the integration variables (ξ, η) with the point $(x, y, \zeta(x, y))$ on the body surface according

to the peaks of the kernel for fixed (ξ, η) , rather than for fixed (x, y, ζ) for the following reason. This choice may correlate those (ξ, η) near the boundary of the domain S_0 of the singularities with those points $(x, y, \zeta(x, y))$ on the body surface whose projections onto the centerplane will fall outside of S_0 , whereas the peaks determined for fixed (x, y, ζ) cannot include those values of (x, y) lying outside S_0 . The first method may be expected to improve the accuracy of solution beyond that which can be achieved by the latter one. As explained in the text, this choice of correlation may be subject to further modifications in our future development of the method.

On this note we would like to reiterate that much will need to be done on this interesting problem in which area, as well as along vast frontiers elsewhere, we have received a great deal of stimuli from Georg Weinblum, our mentor and benefactor, who once said, "The ellipsoid is God's gift to the Naval Architects".

References

- Basset, A.B. 1888 A Treatise on Hydrodynamics: Deighton, Bell & Co.; also Paperbound 1961 Dover Pub. Inc.
- Green, G. 1833 Researches on the vibration of pendulum in fluid medium. Trans. Roy. Soc. Edin. 13 54-62; Papers, p. 315-324.
- Lamb, H. 1916 Hydrodynamics, 4th ed. Cambridge University Press.
- Lamb, H. 1932 Hydrodynamics, 6th ed. Cambridge University Press.
- Miloh, T. 1974 The ultimate image singularities for external ellipsoidal harmonics. SIAM J. Appl. Math. 26, 334-344.

Reply to the Discussion by T. Miloh

T. Y. Wu and A. T. Chwang
California Institute of Technology
Pasadena, California

We acknowledge Professor Miloh's comments and appreciate his taking interest in checking carefully our calculations in detail.

As explained in our previous reply, we presented in Section 2.1 of our paper various integral representations of the potential flow involving the general motion of a tri-axial ellipsoid, after a very brief review of the colorful history of gravitational potential theory and its connection with potential flow in question, so that the salient features of the solution are exhibited by the simple and elegant method. The usefulness of a surface doublet representation need not be limited to naval hydrodynamics, but may also arise in electrodynamics and other branches of mathematical physics.

The normalization factor $a_i a_j$ in (21) should be a_{ij} which are related to the components of the moment-of-inertia tensor, I_{ij} , by

$$I_{ij} = \frac{1}{5} \rho V a_{ij}$$

where

$$I_{xx} = \rho \int_E (y^2 + z^2) dV, \quad I_{xy} = \rho \int_E xy dV, \text{ etc.}$$

By virtue of the body symmetry, a_{ij} and I_{ij} have only diagonal components, that is $a_{ij} = 0$ ($i \neq j$) and

$$a_{11} = a_2^2 + a_3^2, \text{ etc.}$$

Equations (22a) and (22b) are correct.

In order to avoid any possible confusion in notation, we should, perhaps, replace γ_i in (27), (28a, b) and (30) by another symbol, say $\bar{\gamma}_i$ for the case of confocal ellipsoids. The virtual mass coefficients given by (29) and (30) are correct. Alternatively, we could use a different representation as suggested by Miloh, which can be expressed as (for $i = 1, 2, 3$)

$$\bar{M}_{ii} = M_{ii} \left\{ 1 - \frac{V}{V'} \left(\frac{1 + M_{ii}}{1 + \bar{M}_{ii}} \right) \right\}^{-1}$$

$$\bar{M}_{i+3, i+3} =$$

$$M_{i+3, i+3} \left\{ 1 - \frac{V(a_j^2 + a_k^2)(a_j^2 - a_k^2)N_{i+3, i+3}}{V'(a_j^2 + a_k^2)(a_j^2 - a_k^2)N'_{i+3, i+3}} \right\}^{-1}$$

$$N_{i+3, i+3} = 1 + \left(\frac{a_j^2 + a_k^2}{a_j^2 - a_k^2} \right)^2 M_{i+3, i+3}.$$

We note, however, that the expression for $\bar{M}_{i+3, i+3}$ given in Miloh's Discussion is at variance with our result.

We are eagerly waiting to read the paper "Shipcenterplane source distribution" quoted by Professor Landweber (as his Ref. 8) and by Professor Miloh (as his Ref. 4). We share with the conviction of theirs and of Georg Weinblum's that much of the potential usefulness of the centerplane singularity method remains to be explored.

HYDRODYNAMICS FOR SAFETY — MANEUVERING

SESSION II

Monday, June 24, 1974
2:00 P.M. — 4:35 P.M.

Chairman: Dr. C. C. Bates
Science Advisor to the Cominadant,
U.S. Coast Guard
United States

Oscillatory Testing for the Assessment of Ship Maneuverability	109
R.E.D. Bishop and A.G. Parkinson, University College, London, England	
R.K. Burcher and W.G. Price, RCNC, England	
Large Amplitude PMM Tests and Maneuvering Predictions for a Mariner Class Vessel	131
L.W. Smitt and M.S. Chialett, Skibsteknisk Laboratorium, Lyngby, Denmark	
On a Study of Ship-Controllability of a Wide-Beam Tanker Using Large Scale Model	159
S. Sato, M. Takagi and T. Takai, Hitachi Shipbuilding & Engineering Co., Ltd. Osaka, Japan	
Digital Simulation Analysis of Maneuvering Performance	181
H. Eda, Davidson Laboratory, Stevens Institute of Technology, Hoboken, New Jersey	

OSCILLATORY TESTING FOR THE ASSESSMENT OF SHIP MANEUVERABILITY

R.E.D. Bishop
University College
London, England

R. K. Burcher
RCNC
England

A.G. Parkinson
University College
London, England

W. G. Price
RCNC
England

ABSTRACT

A mathematical model of the fluid forces and moments experienced by a ship model is described without invoking the conventional approximations associated with the use of slow motion derivatives. Experimental data derived from horizontal oscillatory tests with a Mariner model is shown by a linear analysis to depend on response functions in the time domain. In addition relationships are established between the components of the hydrodynamic loadings in phase with the displacement of the model and those in quadrature with the model's displacement.

The complementary nature of steady state tests and oscillatory tests is confirmed and a linear analysis is shown to interpret satisfactorily the experimental oscillatory data.

The mathematical model is extended to include the non-linear terms which may be needed to explain more wide ranging tests.

NOTATION

F arbitrary fluid force or moment with perturbations expressed as ΔF , $\Delta F[\]$
 F_x arbitrary slow motion velocity or angular velocity derivative
 $F_{\dot{x}}$ arbitrary slow motion acceleration or angular acceleration derivative
 N yaw fluid moment
 N_r slow motion yaw moment derivative with respect to yaw angular velocity
 N_v slow motion yaw moment derivative with respect to sway velocity
 $N_{\dot{v}}$ slow motion yaw moment derivative with respect to sway acceleration
 \bar{U} steady forward reference velocity
 $v(t)$ sway velocity
 $\dot{v}(t)$ sway acceleration
 v_0 amplitude of harmonic sway velocity
 \dot{v}_0 amplitude of harmonic sway acceleration
 X_{vv} hydrodynamic coefficient
 x arbitrary velocity or angular velocity
 \dot{x} arbitrary acceleration or angular acceleration

Y sway fluid force with perturbations expressible as $\Delta Y(t)$, $\Delta Y[\]$
 Y_r slow motion sway force derivative with respect to yaw angular velocity
 Y_v slow motion sway force derivative with respect to sway velocity
 $Y_{\dot{v}}$ slow motion sway force derivative with respect to sway acceleration
 $Y_v|v|$, Y_{v^3} , Y_{vr} hydrodynamic coefficients
 $Y_v(\omega) = Y_v^R(\omega) + iY_v^I(\omega)$ Fourier transform of $y_v(t)$
 $y(t)$ displacement to starboard
 y_0 amplitude of harmonic displacement to starboard
 $y_r(t)$ variation of ΔY following unit yaw angular displacement
 $y_{\dot{r}}(t)$ variation of ΔY following unit variation of r
 $y_v(t)$ variation of ΔY following unit step displacement to starboard
 $y_{\dot{v}}(t)$ variation of ΔY following unit step variation of v
 $y_v^*(t)$ function of $y_v(t)$ without delta function components
 $y_{\dot{v}}^*(t)$ function $y_{\dot{v}}(t)$ without delta function components
 $y_{x_i x_j}(\tau_1, \tau_2)$ higher order impulsive functions
 ΔY_{IN} harmonic component of ΔY in phase with y_0
 ΔY_{QUAD} harmonic component of ΔY in quadrature with y_0 (and in phase with \dot{y}_0)
 τ, τ_1, τ_2 time variables
 ω circular frequency

INTRODUCTION

When a ship, assumed rigid, departs from steady motion in a straight line, the water exerts a resultant force and resultant moment about the centre of mass as a consequence of that departure. It is commonly assumed that the force and moment are uniquely determined at any instant by the perturbation of the steady motion at that instant. Bryan (1911) proposed the use of 'slow motion derivatives' to represent the fluid forces and the underlying theory is sometimes referred to as one of

'quasi-steady flow' - or, perhaps better, of 'instantaneous forces'. In this approach, the fluid force or moment ΔF is considered to be proportional to the velocity x and acceleration \dot{x} of the perturbed motion. Thus if the body has a steady reference motion and then acquires a velocity perturbation x and an associated acceleration \dot{x} the fluid force or moment arising from the perturbed motion is expressed as:

$$\Delta F(x, \dot{x}) = F_x x + F_{\dot{x}} \dot{x}$$

where F_x and $F_{\dot{x}}$ are the slow motion derivatives relative to velocity and acceleration respectively. Bryan developed this approach intuitively and Garrick (1959) noted its likeness to a multi-variable Taylor series expansion of a function.

In manoeuvring theory, the conventional way of expressing a fluid force or moment of this kind is to employ a multi-variable Taylor expansion for departures from the steady reference motion. In mathematical terms we may say that, provided the multi-variable analytic function $F(x_1, x_2, \dots, x_n)$ is sufficiently regular in the region of $x_1 = 0 = x_2 = \dots = x_n$, then

$$\begin{aligned} F(x_1, x_2, \dots, x_n) &= F_0 + \sum_{i=1}^n \frac{\partial F}{\partial x_i} x_i + \\ &+ \frac{1}{2} \sum_{i=1}^n \sum_{j=1}^n \frac{\partial^2 F}{\partial x_i \partial x_j} x_i x_j + \dots \\ &= F_0 + \sum_{i=1}^n F_{x_i} x_i + \\ &+ \frac{1}{2} \sum_{i=1}^n \sum_{j=1}^n F_{x_i x_j} x_i x_j + \dots \end{aligned}$$

where F_0 is a constant. For a small perturbation of the variables x_i , we may write

$$\begin{aligned} \Delta F(x_1, x_2, \dots, x_n) &= F(x_1, x_2, \dots, x_n) - F_0 \\ &= \sum_{i=1}^n F_{x_i} x_i. \end{aligned}$$

The Taylor coefficient F_{x_i} gives the difference between the instantaneous value of F in the new motion of the system and that in the initial steady state due to a perturbation x_i alone, when the remaining motion parameters are held constant at their original steady-state values of zero. These coefficients are all assumed constant and independent of time. If the fluid force F is dependent on, say, velocity x and acceleration \dot{x} , then the coefficients F_x and $F_{\dot{x}}$ are the corresponding 'slow motion derivatives'. Physically, however, it is difficult to comprehend how \dot{x} can vary (according to the definition of the Taylor coefficient $F_{\dot{x}}$) while x is prevented from varying.

Ship hydrodynamicists are faced with the necessity of specifying fluid forces and moments applied to a ship when it departs from a steady reference motion. No satisfactory method has

been developed for measuring these quantities on a full scale ship. In any case, the application of a dynamic theory is useful in the preliminary design stage before the ship has been built. Resort is therefore taken to the testing of a ship model in which the forces acting on the model are measured during an imposed motion.

The simplest test is the oblique tow test, in which the ship model is towed at a constant velocity and at various drift angles to the direction of motion and the sway force (Y) and yaw moment (N) on the model are measured. The gradient of the curve at zero drift angle in the plot of force Y against drift angle gives an experimental value of the slow motion velocity derivative Y_v ; likewise the slope at zero drift angle in the moment curve gives the value of N_v . No comparable practical method has been devised for measuring such slow motion acceleration derivatives Y_a and N_a , however.

To obtain derivatives such as those of the sway force and yaw moment due to an angular velocity of yaw (represented by Y_r and N_r respectively), attempts have been made to employ curved models in a straight towing tank. That is to say a curved model is towed along a straight path rather than a straight model towed along a circular path. The theoretical basis of this substitution was set out by Gourjionko (1934) for the curvilinear flight of airships and also by Albring (1947) in his investigation of torpedo stability. The method is unsatisfactory in practice though, since a special model has to be constructed for each curvature.

Some testing establishments have a special facility - a 'rotating arm' - by means of which a straight model can be towed along circular paths. By this means it is possible to obtain slow motion derivatives of yawing. Apart from the high capital cost of a rotating arm operating in a large enough tank, a drawback is that only angular velocity derivatives can be obtained. There still remains the problem of measuring acceleration derivatives of angular motion such as Y_a and N_a .

It was partly to avoid the expense of special purpose facilities, but mainly to obtain acceleration derivatives, that the Planar Motion Mechanism (PMM) was developed. This mechanism, which was pioneered by Gertler (1959) and Goodman (1960) can be mounted on the carriage of a ship towing tank. It imparts an oscillatory motion to the model while it is being towed at constant speed down the tank. By imposing sinusoidal motions, e.g. of pure sway or pure yaw, the analyst seeks to measure all the slow motion sway or yaw derivatives of velocity and acceleration.

Unfortunately, the experimental results obtained by these techniques pose problems of analysis. For example:

- (i) For the oblique tow and rotating arm experimental tests it is found that the forces and moments do not produce straight lines when they are plotted against sway

or yaw velocity. This has led to a modification of the linear derivative theory to introduce constants of proportionality (sometimes loosely called 'derivatives') for higher powers of velocity. Such terms as $Y_v|v|$ or $Y_{vvv}v^3$ are included in expressions for sway force, for instance. In effect the analysis of such tests is thus made into an exercise in curve fitting, using an arbitrary power series. Unfortunately there is little agreement as to the terms required in the series; different testing establishments employ different terms, depending on the use to which the data is to be put and the computing facilities available. It is to be noted, however, that if (to take a simple case) the same experimental results are fitted by the alternative expressions

$$\Delta Y = Y_{vv} + Y_{v|v|} |v|$$

and

$$\Delta Y = Y_{vv} + Y_{vvv} v^3,$$

the value of Y_v obtained will, in general, be different as between the two formulations. The linear derivative has therefore lost its uniqueness and, if it is used subsequently in a linear stability analysis, different conclusions may well be reached.

- (ii) Rotating arm tests display cross coupling between sway and yaw or surge so that terms such as $Y_{v\psi}$ or $Y_{vv}v^2$ are sometimes included to fit the experimental data.
- (iii) The results from a PMM test raise further difficulties. Suppose that a PMM is used to impart a pure sinusoidal sway motion

$$y(t) = y_0 \sin \omega t$$

to a model while it is towed at constant speed along a towing tank. The sinusoidal applied sway force may be measured and expressed as

$$\Delta Y = Y_{IN} \sin \omega t + \Delta Y_{QUAD} \cos \omega t$$

According to the instantaneous force theory of slow motion derivatives,

$$\begin{aligned} \Delta Y &= Y_v v(t) + Y_{\dot{v}} \dot{v}(t) \\ &= Y_v (y_0 \omega \cos \omega t) + Y_{\dot{v}} (-y_0 \omega^2 \sin \omega t), \end{aligned}$$

so that the amplitudes of the ~~slow~~ force components that are in quadrature and in phase with the displacement $y(t)$ are

$$\begin{aligned} \Delta Y_{QUAD} &= Y_v y_0 \omega = Y_v v_0 \\ \Delta Y_{IN} &= Y_{\dot{v}} (-y_0 \omega^2) = Y_{\dot{v}} \dot{v}_0 \end{aligned}$$

where $v_0 (= y_0 \omega)$ and $\dot{v}_0 (= -y_0 \omega^2)$ are the amplitudes of velocity and acceleration respectively. Thus, in theory, if the amplitude of the quadrature component of force, ΔY_{QUAD} , is plotted against the

amplitude of the velocity v_0 , then the slow motion derivative theory predicts a straight line whose gradient gives the slow motion velocity derivative. In practice, however, the plot rarely gives a straight line and this has led some experimenters, Chislett and Ström-Tejsten (1966) and Glansdorp (1969) to define and obtain 'non-linear derivatives'.

A comparison of derivatives obtained from a PMM test and those from an oblique tow test often reveals a quite unsatisfactory disparity. In the ITTC, Gertler (1969) presented the results of co-operative tests on the Mariner form and the values of derivatives varied quite widely. Though some discrepancies are undoubtedly due to the use of different models and scales, the information presented illustrates the difficulties.

Although derivatives have been extensively and successfully used in aerodynamic theory, Newman (1966) has discussed the fundamental objections to this approach in the theory of ship manoeuvrability. In the theory it is assumed that fluid forces and moments are determined by the prevailing instantaneous motions of the ship and the weakness of the theory is that time history effects are ignored; this is the essential assumption of quasi-steady flow. Burcher (1974) has shown that the fluid forces and moments acting on a ship at any instant are greatly influenced by the previous motion. Nonweiler (1960), too, has drawn attention to this dependence on time history although it has been more rigorously considered by Cummins (1962) in studying surface effects and by Brard (1964) in the development of a vortex theory for a submerged manoeuvring body. Bishop, Burcher and Price (1973a, b) showed that by expressing the fluid force or moment in terms of a functional analysis the entire time history of the ship's motion may be included. In terms of this form of analysis, the slow motion derivative theory is merely a particular case.

In this paper we shall illustrate the usefulness of this previous work in the analysis of some experimental results obtained with a PMM. We shall find, in particular, that a striking degree of success is to be had with a purely linear theory. We shall then recall the more general non-linear form of the functional representation and give some indication of how it might, if necessary, be employed.

FUNCTIONAL REPRESENTATION OF FLUID FORCES

To start with it will be sufficient to introduce only the linear first approximation to a true functional representation. A much more complete presentation, in the present context of fluid forces and moments, is given by Bishop, Burcher and Price (1973a); an outline of it will be given later. As we shall see the linear representation can be established in the same manner as the familiar Duhamel Integral of elementary dynamics.

Suppose that a ship's model is travelling at

constant ahead speed \bar{U} having a small superimposed sway motion. In conventional linear quasi-steady flow analysis it is assumed that at any instant the perturbed sway force is

$$\Delta Y = Y_v v + Y_{\dot{v}} \dot{v}$$

Alternatively, Bishop, Burcher and Price (1973 c) have shown that, by employing the principle of superposition together with a linear functional representation, we may describe the perturbed sway fluid force in either of two more general forms:

(i) In terms of impulsive motion,

$$\Delta Y[v(t)] = \int_{-\infty}^{\infty} y_v(\tau) v(t-\tau) d\tau$$

where the function $y_v(\tau)$ is the variation of the sway force deviation ΔY caused by a unit impulse of sway velocity (i.e. by a sudden unit step to starboard) and is such that

$$\begin{aligned} y_v(\tau) &= 0 & \text{for } \tau < 0 \\ v(t-\tau) &= 0 & \tau > t \end{aligned}$$

(ii) In terms of an indicial motion,

$$\Delta Y[v(t)] = \int_{-\infty}^{\infty} y_{\dot{v}}(\tau) \dot{v}(t-\tau) d\tau$$

where the function $y_{\dot{v}}(\tau)$ is the variation of the perturbed sway force ΔY caused by an indicial sway motion (i.e. by a suddenly acquired unit sway velocity to starboard) and is such that

$$\begin{aligned} y_{\dot{v}}(\tau) &= 0 & \text{for } \tau < 0 \\ \dot{v}(t-\tau) &= 0 & \tau > t \end{aligned}$$

Unfortunately it is impossible to impose either an impulsive or an indicial motion with any precision. An alternative approach is needed for the purposes of testing.

The function $y_v(\tau)$ may be regarded as one member of a 'Fourier transform pair'. That is to say there exists a function $Y_v(\omega)$ which satisfies the relationship

$$Y_v(\omega) = \int_{-\infty}^{\infty} y_v(\tau) e^{-i\omega\tau} d\tau$$

or

$$y_v(\tau) = \frac{1}{2\pi} \int_{-\infty}^{\infty} Y_v(\omega) e^{i\omega\tau} d\omega$$

Thus it follows that if either $y_v(\tau)$ or $Y_v(\omega)$ is known and is mathematically well behaved, then it is possible for $Y_v(\omega)$ or $y_v(\tau)$ respectively to be deduced. This appears to present the experimenter with a practical proposition, since the real valued impulsive response function $y_v(\tau)$ has the complex valued inverse Fourier transform

$$\begin{aligned} Y_v(\omega) &= \int_{-\infty}^{\infty} y_v(\tau) \cos \omega\tau d\tau - i \int_{-\infty}^{\infty} y_v(\tau) \sin \omega\tau d\tau \\ &= Y_v^R(\omega) + i Y_v^I(\omega), \end{aligned}$$

in which the real quantities $Y_v^R(\omega)$ and $Y_v^I(\omega)$ can be measured from an oscillatory test on a model. These integral relationships between the frequency and time domains form the basis of the theoretical derivations of the Hilbert transform and the Kramers-Kronig relations as discussed by Kotik and Mangulis (1962) for ship motions.

Suppose that a sinusoidal sway motion

$$\begin{aligned} y(t) &= y_0 \sin \omega t \\ v(t) &= y_0 \omega \cos \omega t = v_0 \cos \omega t \\ \dot{v}(t) &= -y_0 \omega^2 \sin \omega t = \dot{v}_0 \sin \omega t \end{aligned}$$

is imposed on the model by a planar motion mechanism. The deviation of sway force that is measured during this motion is

$$\begin{aligned} \Delta Y[v(t)] &= \int_{-\infty}^{\infty} y_v(\tau) v(t-\tau) d\tau \\ &= v_0 \int_{-\infty}^{\infty} y_v(\tau) \cos \omega(t-\tau) d\tau \\ &= v_0 \cos \omega t \int_{-\infty}^{\infty} y_v(\tau) \cos \omega\tau d\tau \\ &\quad + v_0 \sin \omega t \int_{-\infty}^{\infty} y_v(\tau) \sin \omega\tau d\tau \\ &= \Delta Y_{QUAD} \cos \omega t + \Delta Y_{IN} \sin \omega t \end{aligned}$$

The amplitudes ΔY_{QUAD} and ΔY_{IN} can be measured so that $Y_v^R(\omega)$ and $Y_v^I(\omega)$ may be determined from the relationships

$$Y_v^R(\omega) = \frac{\Delta Y_{QUAD}}{v_0} \quad \text{and} \quad Y_v^I(\omega) = -\frac{\Delta Y_{IN}}{v_0}$$

In practice difficulties may arise in the evaluation of the inverse Fourier transform due to non-zero asymptotic values of the $Y_v(\omega)$ curve for large ω . It has been shown previously by Bishop and Price (1974) and Bishop, Burcher and Price (1973c, 1974a, b), however, that this difficulty may be overcome by expressing the fluid expressions in the form

$$\begin{aligned} \Delta Y[v(t)] &= \lim_{\omega \rightarrow \infty} \left(\frac{\Delta Y_{IN}}{-v_0 \omega} \right) \dot{v}(t) + \lim_{\omega \rightarrow \infty} \left(\frac{\Delta Y_{QUAD}}{v_0} \right) v(t) \\ &\quad + \int_{-\infty}^{\infty} y_v^*(\tau) v(t-\tau) d\tau \end{aligned}$$

or alternatively

$$\begin{aligned} Y[v(t)] &= \lim_{\omega \rightarrow \infty} \left(\frac{\Delta Y_{IN}}{-v_0 \omega} \right) \dot{v}(t) + \lim_{\omega \rightarrow 0} \left(\frac{\Delta Y_{QUAD}}{v_0} \right) v(t) \\ &\quad + \int_{-\infty}^{\infty} y_v^*(\tau) \dot{v}(t-\tau) d\tau, \end{aligned}$$

where $y_v^*(\tau)$ and $y_\phi^*(\tau)$ are now well behaved functions which possess Fourier transforms with zero asymptotic values as $\omega \rightarrow \pm\infty$. It also follows that there exists the relationship

$$\lim_{\omega \rightarrow 0} \left(\frac{\Delta Y_{\text{QUAD}}}{v_0} \right) = \lim_{\omega \rightarrow \infty} \left(\frac{\Delta Y_{\text{QUAD}}}{v_0} \right) + y_\phi^*(0)$$

Although, for illustration, we have dealt specifically with deviation ΔY of sway force that is dependent on sway motion $v(t)$, the representation may readily be extended in a similar manner to other deviations of force and moment and to other motions.

COMPARISON OF EXPERIMENT AND THEORY

An interesting check on the foregoing theory and an illustration of its application is provided by the results of some recent experiments performed by Glansdorp (1973) using a horizontal planar motion mechanism. The oscillatory tests were conducted with a $1/40$ th scale Mariner model having a rudder but neither appendages nor propeller. The model, of length 2.2906m, was towed at speeds of 0.922 ms^{-1} and 1.23 ms^{-1} and oscillated at frequencies which varied between 1 rad s^{-1} and 13 rad s^{-1} at intervals of 0.5 rad s^{-1} . In all the tests the amplitude of the lateral velocity (i.e. transverse to the tank centre-line) was kept constant, such that

$$y_0 \omega = 0.25 \text{ ms}^{-1},$$

by varying y_0 and ω in the appropriate way. For purposes of illustration only the results for the sway force produced by sway and yaw motions with a tow speed of 1.23 ms^{-1} are discussed here. A similar interpretation of the other experimental results will be published in the near future.

It has been shown previously that the response function $y_v(\tau)$ can be determined from either the real or imaginary parts of its Fourier transform and hence from either the in-phase or quadrature components of the corresponding harmonic sway force. In practice it is easier to use ΔY_{QUAD} for this purpose, as $Y_v^R(\omega)$ can be determined with the PMM for a range of frequency and $Y_v^R(0)$ can be measured as the conventional slow motion derivative Y_v in an oblique tow test. For the latter test one can write

$$\begin{aligned} \lim_{\omega \rightarrow 0} Y_v^R(\omega) &= \lim_{\omega \rightarrow 0} \int_{-\infty}^{\infty} y_v(\tau) \cos \omega \tau \, d\tau = \int_{-\infty}^{\infty} y_v(\tau) \, d\tau \\ &= \lim_{\omega \rightarrow 0} \left(\frac{\Delta Y_{\text{QUAD}}}{v_0} \right) = Y_v \end{aligned}$$

Thus the sway response function $y_v(\tau)$ can be deduced as the inverse Fourier cosine transform from the relation

$$y_v(t) = \frac{2}{\pi} \int_0^{\infty} Y_v^R(\omega) \cos \omega t \, d\omega.$$

Several graphical methods have been proposed for

this computation [see, for example, Solodovnikov (1960) and Burcher (1974)].

When the response function $y_v(t)$ has been evaluated in this way, the imaginary part of its Fourier transform, namely $Y_v^I(\omega)$, can be determined from the expression

$$Y_v^I(\omega) = - \int_{-\infty}^{\infty} y_v(\tau) \sin \omega \tau \, d\tau$$

We have seen, however, that Y_v^I can also be measured directly through an oscillatory sway test in the form

$$Y_v^I(\omega) = - \frac{\Delta Y_{\text{IN}}}{v_0}.$$

Thus, if values for ΔY_{IN} [or more usually $\Delta Y_{\text{IN}}/(-v_0)$] are also available from the PMM tests, then a comparison can be made between the directly measured experimental values for $Y_v^I(\omega)$ and those deduced numerically from $Y_v^R(\omega)$ via the appropriate Fourier transforms.

Since the use of Fourier transforms in this way relates to a linear functional approach, the comparison affords a sensitive check on the "linearity" of these oscillatory experiments. In addition the apparent slow motion acceleration derivative at zero frequency can be evaluated from the relation

$$\begin{aligned} \lim_{\omega \rightarrow 0} \left(\frac{\Delta Y_{\text{IN}}}{-v_0} \right) &= - \int_0^{\infty} y_v(\tau) \lim_{\omega \rightarrow 0} \left(\frac{\sin \omega \tau}{\omega} \right) d\tau \\ &= - \int_0^{\infty} \tau y_v(\tau) \, d\tau = Y_\phi \end{aligned}$$

after $y_v(\tau)$ has been computed. A comparable analysis can also be performed in terms of the indicial sway response function $y_\phi(\tau)$.

A similar analysis may be undertaken for yaw motion, in which case the sway force can be expressed in terms of the response functions $y_r(\tau)$ or $y_\phi(\tau)$ as

$$\Delta Y[r(t)] = \int_{-\infty}^{\infty} y_r(\tau) r(t-\tau) \, d\tau$$

or

$$\Delta Y[r(t)] = \int_{-\infty}^{\infty} y_\phi(\tau) \dot{r}(t-\tau) \, d\tau$$

The application of the above analysis and its counterpart for yaw motion is illustrated in figures 1 - 8. The response functions $y_v(\tau)$, $y_\phi(\tau)$, $y_r(\tau)$ and $y_\phi(\tau)$ in figures 3, 4, 7 and 8 are deduced from the appropriate components of the sway force. Figures 1 and 5 show the in-phase data which has been deduced numerically from the computed response functions. By using both sets of response functions it is possible to compare experimental and numerically deduced values for the real and imaginary parts of all the appropriate Fourier transforms.

The figures show that the calculated and experimental values are in good agreement. Further it must be emphasised that the slow

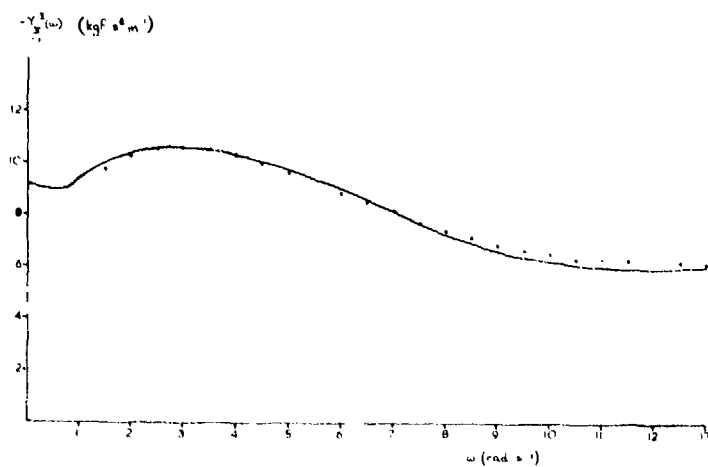


Figure 1. • experimental data
 — calculated from $y_v^*(t)$

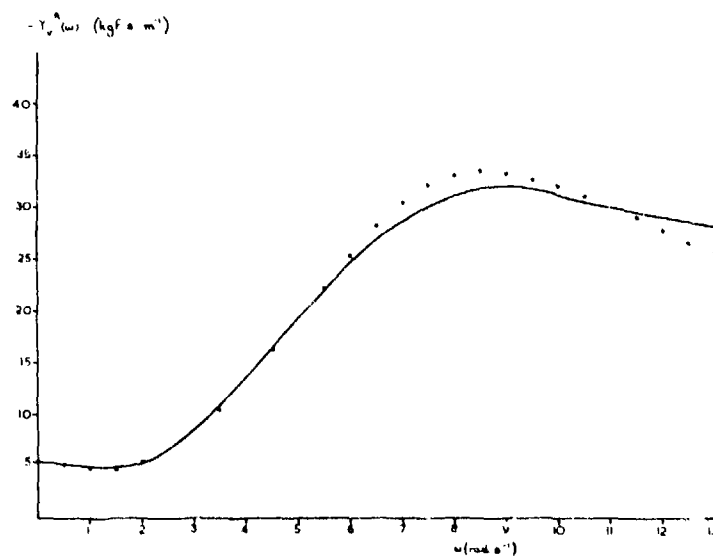


Figure 2. • experimental data
 — calculated from $y_v^*(t)$

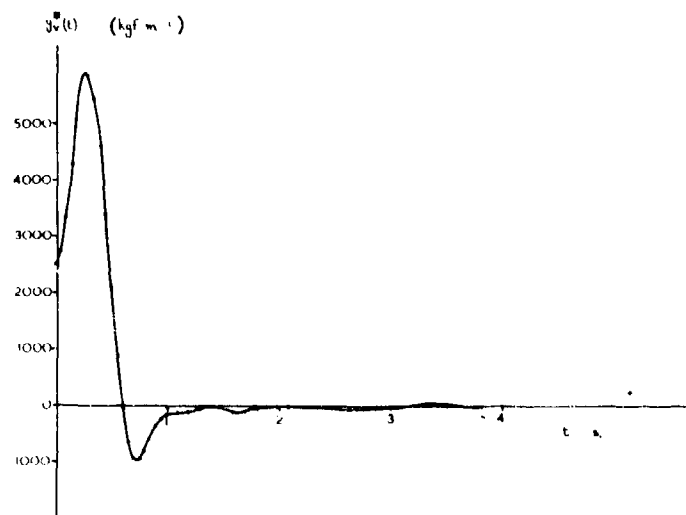


Figure 3. Impulse response function calculated from the experimental values of $Y_V^R(\omega)$

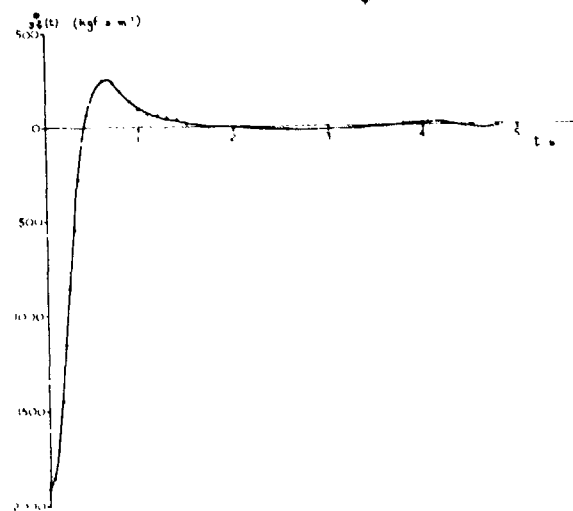


Figure 4. Indicial response function calculated from the experimental values of $Y_V^I(\omega)$

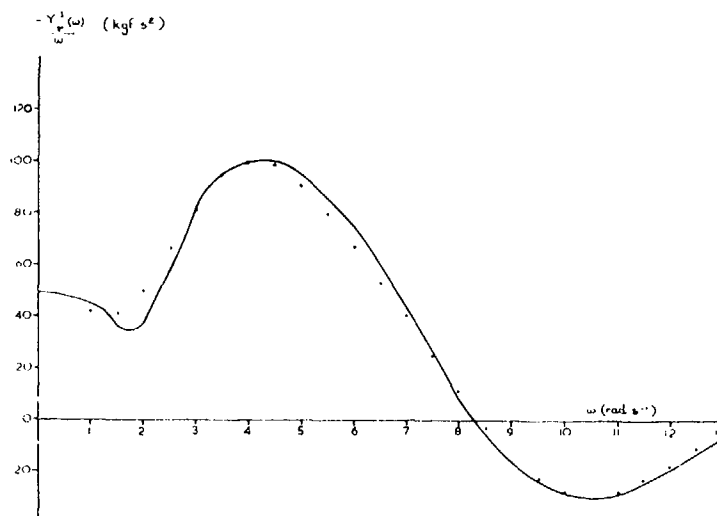


Figure 5. • experimental data
 — calculated from $y_r^*(t)$

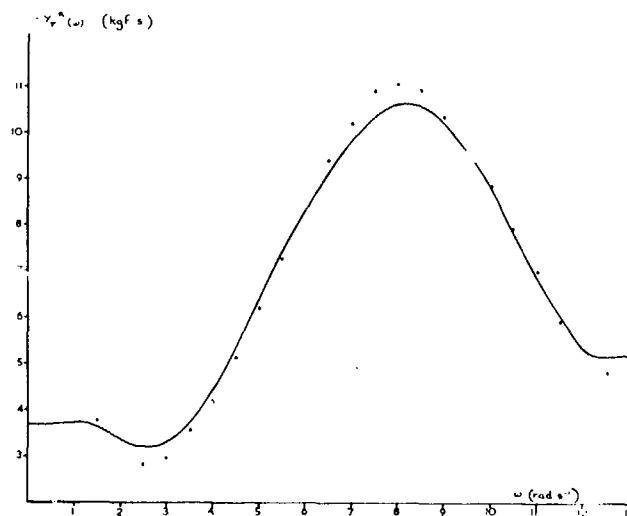


Figure 6. • experimental data
 — calculated from $y_r^*(t)$

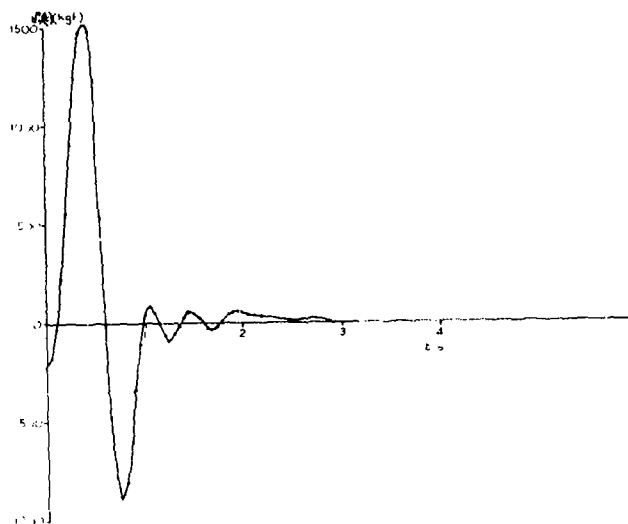


Figure 7. Impulse response function calculated from the experimental values of $Y_R^R(\omega)$

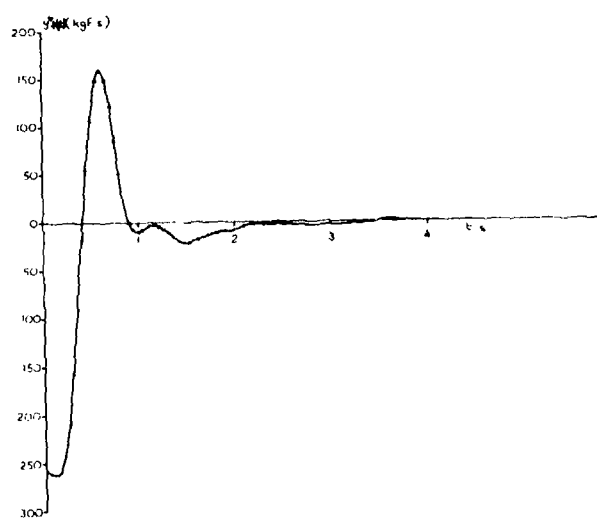


Figure 8. Indicial response function calculated from the experimental values of $Y_R^I(\omega)$

motion velocity derivative, which is normally measured by an oblique tow test, can also be deduced from the experimental values for ΔY_{IN} . The slow motion derivatives obtained from the above numerical investigation are as follows:

$$\begin{aligned} Y_v &= -5.36 \text{ kgf.s m}^{-1} \\ m - Y_{\dot{v}} &= 9.20 \text{ kgf.s}^2 \text{m}^{-1} \\ -Y_{\dot{v}} &= 4.56 \text{ kgf.s}^2 \text{m}^{-1} \quad (m = 4.64 \text{ kgf.s}^2 \text{m}^{-1}) \\ m\ddot{U} - Y_{\ddot{r}} &= 3.65 \text{ kgf.s} \\ Y_{\ddot{r}} &= -0.49 \text{ kgf.s}^2 \\ Y_{\ddot{r}} &= 2.057 \text{ kgf.s} \end{aligned}$$

Thus the steady state test and the planar motion mechanism test are complementary under certain controlled conditions. The numerical investigation also shows that the experimental results relate primarily to a linear system, even though they display a strong frequency dependence.

WIDER APPLICATION OF THE THEORY OF FUNCTIONALS

It has been shown above and previously by Bishop, Burcher and Price (1974a, b) that the results of oscillatory testing, in many cases previously considered non-linear, can be explained in terms of frequency effects employing a linear theory. The present interpretation of the oscillatory test results rests however on the existence of straight-line relationships (as between sway force ΔY and drift angle in a steady oblique tow test). There remain the so-called "nonlinearities" associated with steady state testing.

When the results of oblique tow or rotating arm tests are plotted as fluid force or moment against a velocity then the experimental data do not lie on a straight line. To be sure a region of small perturbations can usually be found in which a straight-line relationship can be found to good approximation, but this region can sometimes be rather small. It is by no means unusual for a ship to manoeuvre sufficiently violently to operate outside this region.

It should be mentioned that, in the oscillatory tests that have been cited, the (constant) sway velocity amplitude v_0 was so chosen that the operating conditions of the model remained within the linear region of the graph of ΔY against v that is obtained in a steady oblique tow test. Our purpose next will be to examine in a tentative fashion the possibility of relaxing this requirement.

Departures from straight line relationships in steady state testing are not at all easy to explain in physical terms. Possible reasons have been suggested by Newman (1966); for example he points out that separation drag may be dependent on being velocity squared. This might indeed account for the effect at large drift velocities but ships rarely develop such large motions. Similarly, the decrease of lift on an

aerofoil due to separation and breakdown of flow is also associated with large angles. Separation of flow and vortex shedding observed on full-bodied tanker forms may also be part of the answer but again for many ships this phenomenon is not observed. Tests performed with segmented models in which the distribution of force is measured on the hull have been reported by Clarke (1972) for a tanker form and by Burcher (1972) for a fast cargo form. Both these results showed that the forces on the forward 60 percent of the length behaved in a straight line (proportional) fashion up to quite large drift angles and rates of turn. The breakdown of proportionality occurs at the stern of the vessel and is noticeable at low rates of drift and turn. It has been suggested that this effect occurs because the stern of the vessel, and particularly the rudder, operates in the wake of the hull where the flow differs considerably from that in open water. At large angles of drift, the stern is in open water and less subject to the hull wake, which is swept sideways. These observations suggest that lack of proportionality may well be largely dependent on the ship's previous motions - i.e. on "memory effects".

For example the flow around the stern at a given time may depend on the conditions at the bows a short time earlier. Fluid disturbances shed by the bow of a ship will be left in a line roughly corresponding to the trajectory of the bow. The stern follows a different path. For example, in steady drift the stern will follow a parallel path, whilst in a turn the stern will travel along a path of larger radius than that of the bow. Under these circumstances the stern will suffer the effects of disturbances left by the bow. In general, therefore, if we assume that a fluid perturbation is left 'stationary' in the fluid then its influence at any point on a model passing near it will depend on their relative positions at any given time.

How are effects of this type incorporated in the functional analysis which has been introduced by Bishop, Burcher and Price (1973a)? It will be sufficient here merely to summarise the results. Suppose that the perturbed fluid action F depends upon motion variables $x_1(t)$, $x_2(t)$, ..., $x_n(t)$; then the deviation of this fluid action is of the form

$$\begin{aligned} \Delta F[x_1(t), x_2(t), \dots, x_n(t)] &= \int_{-\infty}^{\infty} \int_{-\infty}^{\infty} F_{x_1}(\tau_1) x_1(t-\tau_1) d\tau_1 \\ &+ \int_{-\infty}^{\infty} \int_{-\infty}^{\infty} \int_{-\infty}^{\infty} F_{x_i x_j}(\tau_1, \tau_2) x_i(t-\tau_1) x_j(t-\tau_2) d\tau_1 d\tau_2 \\ &+ \dots, \end{aligned}$$

provided that the system may be regarded as time-invariant.

Although we are not yet in a position to present a systematic development of non-linear theory, it is perhaps worthwhile to outline the forms taken by some preliminary studies.

* This is also the value predicted by the oblique tow test.

Consider, by way of example, the planar motion of a surface ship for which only disturbances in surge (u), sway (v) and yaw (r) relative to a steady state ahead motion with a speed \bar{U} are relevant. The general functional expression quoted above can be rewritten for ΔY as follows:

$$\begin{aligned}\Delta Y[u, v, r] = & \int_{-\infty}^{\infty} \sum_{i=1}^3 y_{x_i}(\tau_1) x_i(t-\tau_1) d\tau_1 \\ & + \int_{-\infty}^{\infty} \int_{-\infty}^{\infty} \sum_{i=1}^3 \sum_{j=1}^3 y_{x_i x_j}(\tau_1, \tau_2) x_i(t-\tau_1) x_j(t-\tau_2) d\tau_1 d\tau_2 \\ & + \int_{-\infty}^{\infty} \int_{-\infty}^{\infty} \int_{-\infty}^{\infty} \sum_{i=1}^3 \sum_{j=1}^3 \sum_{k=1}^3 y_{x_i x_j x_k}(\tau_1, \tau_2, \tau_3) x_i(t-\tau_1) x_j(t-\tau_2) x_k(t-\tau_3) d\tau_1 d\tau_2 d\tau_3 \\ & + \dots\end{aligned}$$

where we identify

$$x_1 = u, \quad x_2 = v, \quad x_3 = r.$$

The functions y_{x_i} are the first order impulsive response functions which we have discussed before, whereas $y_{x_i x_j}$, $y_{x_i x_j x_k}$, etc. represent higher order impulsive response functions. Some of these functions, for example $y_u(\tau_1)$ and $y_{uu}(\tau_1, \tau_2)$, may be zero for a ship with a fore and aft plane of symmetry. All the functions depend on the ahead reference speed, \bar{U} , and the hull form of the ship.

For simplicity we will now consider a motion for which the only disturbance is in sway. Thus

$$u = 0 = r, \quad v \neq 0.$$

In these circumstances the expression for ΔY reduces to

$$\begin{aligned}\Delta Y[v] = & \int_{-\infty}^{\infty} y_v(\tau_1) v(t-\tau_1) d\tau_1 + \int_{-\infty}^{\infty} \int_{-\infty}^{\infty} y_{vv}(\tau_1, \tau_2) v(t-\tau_1) v(t-\tau_2) d\tau_1 d\tau_2 \\ & + \int_{-\infty}^{\infty} \int_{-\infty}^{\infty} \int_{-\infty}^{\infty} y_{vvv}(\tau_1, \tau_2, \tau_3) v(t-\tau_1) v(t-\tau_2) v(t-\tau_3) d\tau_1 d\tau_2 d\tau_3 \\ & + \dots\end{aligned}$$

Moreover, if the motion corresponds to that of a steady inclined tow test, $v = v_0$ constant, the expression for ΔY can be simplified further and has the form

$$\Delta Y[v] = v_0 \int_{-\infty}^{\infty} y_v(\tau_1) d\tau_1 + v_0^2 \int_{-\infty}^{\infty} \int_{-\infty}^{\infty} y_{vv}(\tau_1, \tau_2) d\tau_1 d\tau_2 + v_0^3 \int_{-\infty}^{\infty} \int_{-\infty}^{\infty} \int_{-\infty}^{\infty} y_{vvv}(\tau_1, \tau_2, \tau_3) d\tau_1 d\tau_2 d\tau_3 + \dots$$

The expression for ΔY in the steady inclined tow test corresponds to that for oscillatory testing in the limit as $\omega \rightarrow 0$. Alternatively in an oscillatory sway test, for which $v = v_0 \cos \omega t$, the integrals can be expressed in terms of higher order Fourier transforms, which are functions of ω , and ΔY will also possibly depend on v_0^2 , v_0^3 , etc.

On the basis of the functional approach therefore we can make the following tentative observations concerning the interpretation of oscillatory tests for $v_0 = y_0 \omega$. For small values of v_0 the linear treatment in terms of first order functionals is valid. For larger values of v_0 higher order terms in v_0 are likely to contribute to ΔY . These terms introduce additional oscillatory components whose frequencies are multiples of the forcing frequency ω .

It should be realised that the magnitude of v_0 is not the only factor which determines the relative importance of the higher order terms. The Fourier transforms are functions of frequency, so that for a given v_0 different combinations of y_0 and ω may produce different higher order effects. Indeed the first order terms for small v_0 have been seen to depend on ω separately in addition to $v_0 = y_0 \omega$. In

conducting oscillatory tests, therefore, it would seem to be worthwhile to select a series of values of v_0 , for each of which a wide range of y_0 and ω should be used.

CONCLUSIONS

An allowance for memory effects can be made by suitable linear interpretation of PMM results. Although the analysis is more complex than one based on the assumptions of quasi-steady flow, considerably greater overall accuracy is now possible. The high accuracy that is obtainable has been illustrated by means of some experimental results.

The results used were obtained in tests with operating conditions that fell reasonably within the region of proportionality of steady state tests. The device of maintaining a constant amplitude of velocity in this region appears to have much to commend it where linear theory is to be employed in stability and control analysis. (It has been found by Bishop, Burcher and Price (1973d) and Parkinson and Price (1974) that the integro-differential equations of motion in such an analysis can easily be handled.)

Relaxation of the limitation to the region of proportionality in steady state testing takes us into the field of nonlinear analysis. A tentative approach has been illustrated and remains under investigation.

ACKNOWLEDGEMENT

The authors wish to thank Professor Ir. J. Gerritsma and Ir. C.C. Glansdorp of the Technische Hogeschool Delft for their helpful discussions and the experimental data provided for this paper. Also, Mr A.J. Vosper (Superintendent) and his staff at the Admiralty Experiment Works, Gosport, for their excellent co-operation and assistance in the preparation of this paper.

REFERENCES

- Albring, W., 1947, "Report on methods of experiment and calculation to determine the force and moment coefficients for a solid of revolution moving in a circular path" Monograph M.A.P.-V-120R.
- Bishop, R.E.D., Burcher, R.K. and Price, W.G., 1973a, "The uses of functional analysis in ship dynamics" Proceedings of the Royal Society, London, Vol. A.332, pp. 23-35.
- Bishop, R.E.D., Burcher, R.K. and Price, W.G., 1973b, "Application of functional analysis to oscillatory ship model testing" Proceedings of the Royal Society, London, Vol. A.332, 37-49.
- Bishop, R.E.D., Burcher, R.K. and Price, W.G., 1973c, "On the linear representation of fluid forces and moments in unsteady flow" Journal of Sound and Vibration, Vol. 29, pp. 113-128 [The Fifth Fairey Lecture]
- Bishop, R.E.D., Burcher, R.K. and Price, W.G., 1973d, "Directional stability analysis of a ship allowing for time history effects of the flow" Proceedings of the Royal Society, London Vol. A.335, pp. 341-354.
- Bishop, R.E.D., Burcher, R.K. and Price, W.G., 1974a, "A linear analysis of planar motion mechanism data" Journal of Ship Research (to appear)
- Bishop, R.E.D., Burcher, R.K. and Price, W.G., 1974b, "The determination of ship manoeuvring characteristics from model tests" The Naval Architect (to appear)
- Bishop, R.E.D. and Price, W.G., 1974, "On the slowness of a small departure from steady flow" Proceedings of Noise, Shock and Vibration Conference, Monash University (to appear)
- Brard, R., 1964, "A vortex theory for the manoeuvring ship with respect to the history of her motion" Proceedings of Fifth Symposium on Naval Hydrodynamics, Bergen, pp. 815-911.
- Bryan, G.H., 1911, Stability in Aviation Macmillan & Co. Ltd., London
- Burcher, R.K., 1972, "Developments in ship manoeuvrability" The Naval Architect, Vol. 1, pp. 1-32.
- Burcher, R.K., 1974, "Fluid forces acting on a manoeuvring ship" Ph.D. Thesis, London University.
- Chislett, M.S. and Strøm-Tejsen, J., 1966, "A model testing technique and method of analysis for the prediction of steering and manoeuvring of surface ships" Hy-A Report Hy-7.
- Clarke, D., 1972, "A two-dimensional strip method for surface ship hull derivatives: comparison of theory with experiments on a segmented tanker model" Journal of Mechanical Engineering Science, Vol. 14, No. 7 (Supplementary issue), pp. 53-61.
- Cummins, W.E., 1962, "The impulsive response function of ship motions" Schiffstechnik, Vol. 7, pp. 101-9.
- Garrick, J.E., 1959, "General Introduction" AGARD Manual on Aeroelasticity, Part II, pp. 1-26
- Gertler, M., 1959, "The DTMB planar motion mechanism system" Symposium on Towing Tank Facilities, Zagreb, Paper 6.
- Gertler, M., 1969, Twelfth International Towing Tank Conference, Rome
- Glansdorp, C.C., 1969, "Some notes on oscillator techniques" Rep. Shipbldg. Lab. Technol. Univ. Delft., No. 231.
- Glansdorp, C.C., 1973, "Horizontal high frequency PMM-tests with a Mariner model" Rep. Shipbldg. Lab. Technol. Univ. Delft. No. 381-M
- Goodman, A., 1960, "Experimental techniques and methods of analysis used in submerged body research" Proceedings of Third Symposium on Naval Hydrodynamics, Scheveningen, pp. 379-449
- Gourjienko, G.A., 1934, "Method of curved models and its application to the study of

curvi-linear flight of airships" N.A.C.A.
Tech. Mem. Nos. 829 and 830.

Kotik, J. and Mangulis, V., 1962, "On the
Kramers-Kronig relations for ship motions"
International Shipbuilding Progress, Vol. 97
pp. 3-10.

Newman, J.N., 1966, "Some hydrodynamic
aspects of ship manoeuvrability" Proceedings
of Sixth Symposium on Naval Hydrodynamics,
Washington, pp. 203-236.

Nonweiler, T.R.F., 1960, "The longitudinal
stability and control of deep submerged
submarines" Ph.D. Thesis, Queen's University,
Belfast.

Parkinson, A.G. and Price, W.G., 1974
"Assessment of directional stability by means of
oscillatory model tests" (to appear).

Solodovnikov, V.V., 1960, Introduction to
the Statistical Dynamics of Automatic Control
Systems Dover Publications, New York.

DISCUSSION

L.L. MARTIN

I would like to make an alternative approach to this problem, to that taken by the authors.

As an engineer, rather than a hydrodynamicist, what is required for simulation purposes is the impedance of the water as seen by the ship. This is obtained by frequency response testing using PMM or HPMM (even though they were not designed for this purpose).

Since the nature of the load is little understood as yet, it is unwise to make too many assumptions, but it is obvious that as the steady state force on the ship depends on velocity, not position, velocity should be taken as the reference motion and phase angles measured from it so that acceleration becomes the quadrature component and velocity the in-phase component (these being in any case only a convenient way of measuring the complex impedance by suitable instrumentation the magnitude and phase of the force could be measured directly).

We may then use the authors new data, or van Leeuwen's well known results which were the basis of their previous work, to take what they refer to as QUAD as in-phase and IN multiplied by frequency as quadrature and produce a Bode-plot. We immediately see, Fig. 1 (which is based on van Leeuwen's data), not only the lead term due (apparently) to the conventional "added mass" and damping, but also a resonant/anti-resonant pair, at least for $Y(V)$ and $N(R)$ ¹.

The impedance of the water is therefore representable by the transfer function:

$$\frac{Y(V)}{v} \text{ or } \frac{N(R)}{r} = \mu \frac{(1 + Ts)(1 + 2\zeta_1 T_1 s + T_1^2 s^2)}{(1 + 2\zeta_2 T_2 s + T_2^2 s^2)}$$

Derivation of the appropriate transfer function shows that the measured resonance/anti-resonance cannot be due to resilience in the HPMM mechanism combined with the damping and "added mass" of the water. We must accept that they are part of the impedance of the water.

In the case of $Y(R)$ and $N(V)$, Fig. 2 (also based on van Leeuwen's data), an additional lag appears necessary in the transfer function. $Y(R)$, having negative gain (Yr being positive) is not minimum phase and presents some unusual phase shifts.

Having established the transfer functions for the water impedances it is a trivial matter to include these effects in studies of the yaw stability of the ship, without, or more importantly, with autopilot control, roll-yaw interaction studies etc.

For simulation purposes, with which I am concerned, knowledge of the transfer function is more useful than the impulse response because it can either be programmed directly on an analogue computer or requires little addi-

tional storage and computer time for digital computation. Use of the impulse response and convolution integration necessitates a digital computer with considerable additional storage and increase in computer time for each iteration of the computation.

Now since the total damping of the system, which is measured by oblique tow or rotating arm tests, is known to be nonlinear, the transfer function will vary with the amplitude of the motion (becoming in fact a describing function for sinusoidal motion). If however we can identify a mechanical model with the transfer function and this model can be shown to correspond to some physical reality, there is a real possibility that the nonlinearities could be incorporated with the correct dynamic, as well as static, behavior. The simplest system giving a transfer function like $Y(V)$ or $N(R)$ is a spring | mass | dampers in parallel with the conventional "added mass" and damping. Further work should be directed at identifying the components of this resonant system and the measurement of the individual nonlinearities of the damping elements. (The spring may also of course be nonlinear—it is to be hoped the "masses" are constant). Whatever is the cause of these resonance effects it seems unlikely they are related to the "memory" effects due to the passage of vortices down the ship.

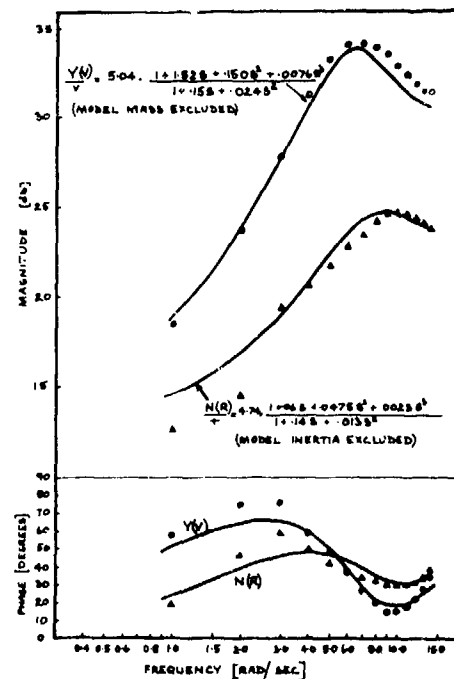


Fig. 1 — Magnitude and phase of $Y(V)$ and $N(R)$

¹ By $Y(V)$ we mean the side force due to sway velocity and by $N(R)$ we mean the moment due to rate of turn. Anti-resonance implies a quadratic term in the numerator of the transfer function, as resonance implies a quadratic term in the denominator.

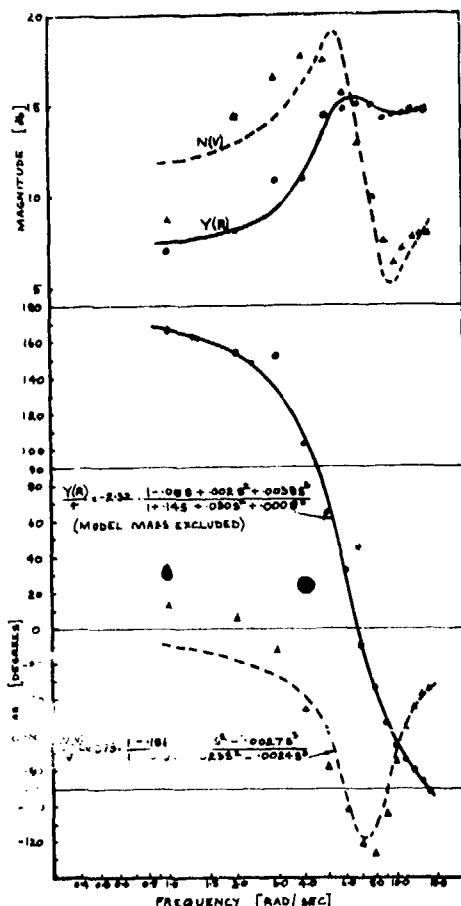


Fig. 2 - Magnitude and phase of Y(R) and N(V)

M. SCHMIECHEN

The authors have been as far as possible from using functional polynomials for the identification of non-linear ship dynamics

including memory effects. As has been pointed out previously this behaviouristic description in the time domain is hardly practical for simulation purposes even with very large computers (1).

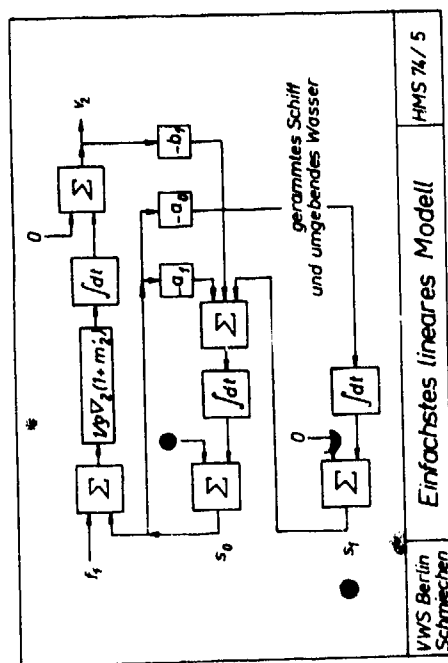
Much more simple are equivalent state space descriptions as is well known in many other fields but apparently not yet in our profession. An account of the general theory, of the linear theory, and applications to hydrodynamic systems has recently been published (2) and an application to the collisions of ships will be presented shortly (3).

From the slides prepared for the latter presentation slides 5 and 6 show the simplest linear state space model and a mechanical analogue, respectively, with only two additional fluid states for the sway motions of a ship initially at rest. The model, which does not include low and high frequency damping, is closely related to that suggested by Mr. Martin.

In slides 8 and 9 the hydrodynamic damping and mass of the simple model are compared with theoretical data for a scale model of the Japanese nuclear ship Mutsu Maru. For most applications the simple model will apparently be sufficient, and if it is not, the description may be improved by introduction of further fluid states, maybe two or four. Consequently the step responses as simulated and observed for the same scale model are quite close as shown in slide 10.

The example given is of course only the simplest application of the theory of state space models. Non-linear models will have to be developed for multidimensional situations not only in ship dynamics in the narrow sense. My own motivation in studying state space models was primarily the need for an adequate tool for investigation and design of marine traffic control systems for congested waters.

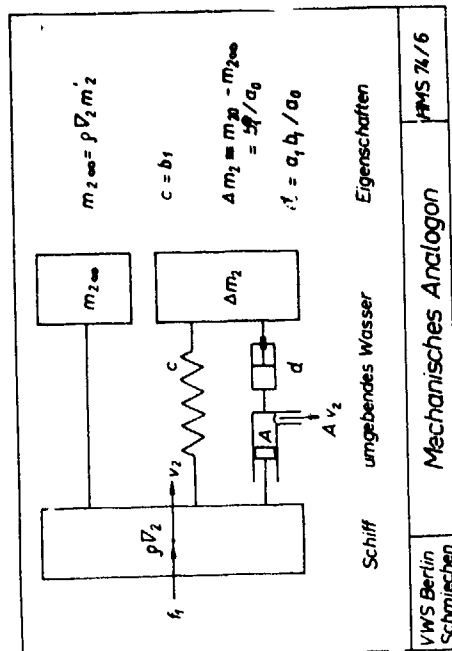
- (1) Schmiechen, M.: Design and evaluation of experiments for the identification of physical systems. Massachusetts Institute of Technology, Dept. of Naval Architecture and Marine Engg. 1969. Report No. 69-1.
- (2) Schmiechen, M.: On state space models and their application to hydromechanic systems. University of Tokyo, Dept. of Naval Architecture, 1973. NAUT Report 5002.
- (3) Schmiechen, M.: Zur Kollisionsdynamik von Schiffen. STG 68 (1974) to be published.



VWS Berlin
Schmiechen

Einfachstes lineares Modell

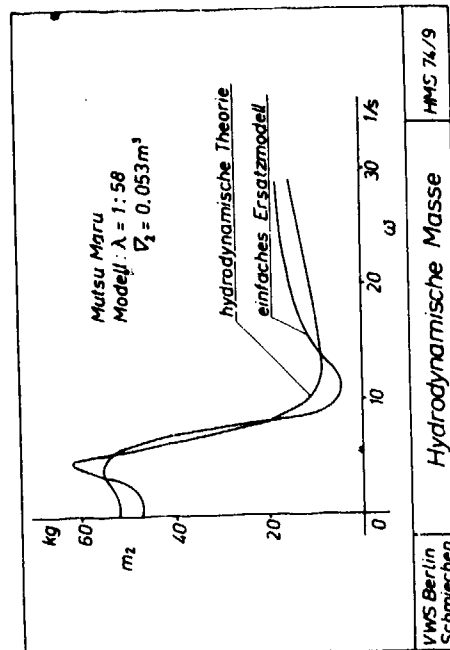
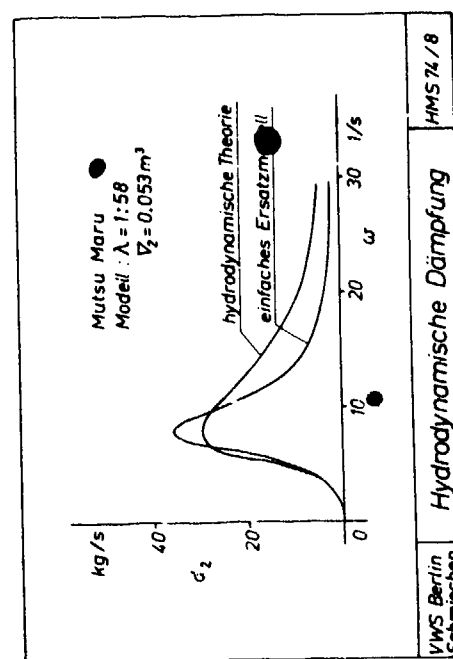
HMS 74/5



VWS Berlin
Schmiechen

Mechanisches Analogon

HMS 74/6





A. GOODMAN

In 1968 HYDRONAUTICS, Incorporated provided the Admiralty Experiment Works (AEW) with a complete PMM system for submarine model testing. This system was provided some twelve (12) years after the PMM system was first developed and applied to submarine model testing as shown in the enclosed Table. In addition, complete documentation was provided which described the theory and operation of the PMM system as well as the application of the results to solving engineering problems. Subsequent to 1968, the authors have published many papers, including the present one, which attempts to extend the usefulness of the PMM. It is obvious, however, that the authors have not read the basic papers by Gertler (1959) and Goodman (1960) nor the materials provided to AEW in 1968 which not only describe the PMM system but presents the philosophy behind its development. Statements such as, "It was partly to avoid the expense of special purpose facilities, but mainly to obtain acceleration deriv-

atives that the PMM was developed," indicates that the philosophy presented in these aforementioned papers either was not understood by the authors or ignored completely.

The facts really speak for themselves. The results determined for PMM model tests over the past twenty years have been used to predict the behavior of many submarine designs. Excellent model to full-scale correlations are available (unfortunately in the classified literature) which demonstrates the power of the PMM system approach.

The authors are attempting to show that a highly nonlinear problem can be represented adequately and more accurately by using a linear approach. This is an interesting theory and deviates from the approaches used in aircraft and submarine simulations over the past twenty years. It would be interesting to see how predictions of the performance of an actual submarine using this approach compares with full-scale data.

TABLE 1
HISTORY OF PMM AND PMM SYSTEMS

Date	Event	Location
July 1952	Concept of PMM first developed by A. Goodman for use in determining lateral stability coefficients of aircraft	NACA Langley Stability Tunnel, Langley Field, Virginia
October 1956- June 1957	PMM System (MARK I) conceived developed and placed into service for submarine model testing by A. Goodman and M. Gertler	DTMB, U.S.A.
May 1959	U.S. patent for PMM System filed	U.S.A.
September 1959	Paper presented by M. Gertler describing improved PMM System	Zagreb, Yugoslavia
September 1960	Paper presented by A. Goodman describing improved PMM System	Third ONR Symposium, Scheveningen, Holland
December 1961	PMM System MARK II placed into service	DTMB, U.S.A.
July 1962	PMM Built by J.R. Paulling	University of California
September 1962	U.S. Patent 3,052,120 granted	U.S.A.
October 1962	PMM System built by HYDRONAUTICS, Incorporated for use with High-Speed Channel-hydrofoil testing	U.S.A.
1962	PMM built by Delft University for ship model testing	Holland (Continued)

TABLE 1

(Cont'd)

Date	Event	Location
1963	PMM System supplied by HYDRO-NAUTICS, Incorporated to Bassin d' Essais des Carenes for submarine model testing	France
1964	PMM System built by Tokyo University for ship model testing	Japan
1964	PMM System built by HyA for ship model testing	Denmark
1965	PMM System built by Nagasaki Technical Institute	Japan
August 1966	Paper presented by J. Strom-Tejsen and M.S. Chislett on HyA PMM System used for ship model testing	Sixth ONR Symposium, Wash., D.C.
May 1968	PMM System supplied by HYDRO-NAUTICS, Incorporated to AEW for submarine model testing	U.K.
November 1968	PMM Instrumentation System supplied by HYDRONAUTICS, Incorporated to DTMB	U.S.A.
December 1968	PMM System built by HYDRO-NAUTICS, Incorporated for submarine model testing in HSMB	U.S.A.
1969	PMM System built by NSRDC for ship model testing	U.S.A.
April 1969	Lecture on PMM for ship model testing sponsored by AEW and University College, London	U.K.
December 1970	PMM System supplied by HYDRO-NAUTICS, Incorporated to Bassin d' Essais des Carenes for use with High-Speed Channel	France
January 1971	PMM adapted by HYDRONAUTICS, Incorporated for ship model testing in HSMB	U.S.A.
1972	Large-Amplitude PMM built by HyA for ship model testing	Denmark
Note: This list is by no means complete. However, it indicates that the PMM System concept has been adopted for marine vehicle testing throughout the world.		

T.F. OGILVIE

There are many important points presented in this paper, and I find that the attitude here is almost identical to my own in many ways. In particular, I believe that we should make every effort to determine just how far we can push a linear theory before we conclude that a nonlinear theory is essential. It may well be true, as Professor Newman said this morning that viscous separation phenomena are much significant than free-surface effects. However, we can hope to solve the linear free-surface problems, even numerically, in the near future, whereas the separation problem will be intractable for a long time yet. Therefore it seems prudent to investigate the free-surface problem absolutely thoroughly before jumping to a conclusion that it is unimportant. We even have some possibility of solving nonlinear free-surface problems before we make much progress on the separation problem. For these reasons, I welcome this paper and its point of view.

This paper could have been a landmark paper — if it had been written ten years ago. The connection between frequency domain and time domain is well-understood in ship hydrodynamics, at least for the linear problems. In 1970, for example, Salvesen, Tuck, and Faltinsen gave a paper at the Annual Meeting of the Society of Naval Architects and Marine Engineers in which they wrote "equations of motion" in a rather conventional form that appears to be in the time domain but is really in the frequency domain. In a written discussion, I objected to this misleading representation. However, the authors put me down quickly with a statement to the effect that I was

flogging a dead horse. They even said that Professor Ogilvie has raised an issue which has been discussed on many occasions. . . . But now, for the first time, there has been a sequence of recent papers by the present authors in which these relationships are rediscovered on behalf of naval architects.

More than ten years ago, various kinds of transient tests were conducted at the David Taylor Model Basin and elsewhere, in the attempt to obtain transfer functions from efficient time-domain test procedures. As far as I know, these attempts were largely abandoned because they required too much in the way of experimental precision. In particular, a bit of noise in the system ruined the results.

I do not know of any early attempts to use this experimental technique for the lateral motion problem. However, I should point out that in 1964 I treated the case of motions without restoring force terms and showed analytically how one can use either frequency or time domain descriptions. I think that the authors should review the ship motions literature a bit more thoroughly before making broad generalizations such as they have made here about the limitations of previous work.

Having said these things in defense of the honor of ship hydrodynamicists of long standing, I do now want to add that I welcome the energetic approach that these authors are taking in solving ship maneuvering problems, especially with regard to consideration of free-surface effects.

AUTHOR'S REPLY

Mr L.L. Martin

Mr Martin wishes to employ techniques that are familiar in control theory. He will find that three of us (REDB, RKB, WGP) have in fact discussed this standpoint in somewhat greater detail than he has in a paper that is in the course of publication by the RINA.

We are unable to accept that hydrodynamics is outside the province of an engineer who is concerned with simulation of ship manoeuvrability. Mr Martin in fact makes this point for us. He really accepts that hydrodynamic damping "is measured by oblique tow or rotating arm tests" and that this is as it should be, then by implication he asserts that memory effects are non-existent. The whole point of the paper is to show that memory effects do exist and that they appear to be very important.

Dr M. Schmiechen

The opening sentence of Dr Schmiechen's remarks appears to dispose of what he has written. For contrary to what he says, we have shown that, far from being "non-linear", the behaviour we have discussed is essentially linear even when memory effects are included. Furthermore, unless we have misunderstood his mechanical analogue, it does not represent the formulations that we attempted to outline.

Dr A. Goodman

We note Dr Goodman's rebuke but remain mystified. So far as we are aware - and Dr Goodman does not question this point - the PMM is a device that was originally designed to measure derivatives. Derivatives have no meaning, save only in the context of quasi-steady flow theory. Within that context, the PMM is the only device known to us that will measure acceleration derivatives. As it appears almost universally to be the case that quasi-steady flow is assumed, this is a compelling reason to employ a PMM and model testers are indebted to Dr Goodman for brilliantly meeting their need. If Dr Goodman disapproves of this, we are at something of a loss to know what the attraction of the PMM is.

We naturally accept that Dr Goodman and his colleagues deserve credit for producing the "PMM System", though we are not absolutely clear what the distinction is between the "PMM" and the "PMM System". It is, however, the technique of extracting results and not their acquisition that we have been moved to question, because the assumption of quasi-steady flow does not seem tenable after all.

Dr Goodman's historical survey seems quite irrelevant. Moreover it seems thoroughly misleading. In case anyone should be led to imagine that the first apparatus for oscillating models in wind tunnels was assembled and commissioned by NACA in July 1952 for the measurement of derivatives, we would mention a paper by R.L. Halfman: "Experimental Aerodynamic Derivatives of a Sinusoidally Oscillating Airfoil in Two Dimensional Flow", NACA Rep TN 2465,

November 1951. In fact an interesting account of this subject entitled "The Comparison of Theory and Experiment for Oscillating Wings" is given by W.E.A. Acum in chapter 10 of volume 2 of the AGARD Manual on Aero-Elasticity. Oscillatory testing of aircraft models appears to have been practised in the U.K. before World War II; presumably it required some rudimentary "PMM".

Prof T.F. Ogilvie

We note with amusement the epigrammatic opening of Prof. Ogilvie's second paragraph; but when he fails to grasp the point of a technical paper he is surely unwise to be rude about it by way of 'discussion'. Since he is evidently intent on high temperature discussion, however, we are by no means unhappy to fulfil his wish.

The sad fact is that Prof. Ogilvie seems to have missed several things:

1. Fluid memory effects can be allowed for with complete generality by functional analysis. Rightly or wrongly we think we are the first to suggest it.
2. A linear first approximation to a functional series is nothing more nor less than a convolution integral. This is a general result and it requires no decision from a hydrodynamicist about the nature of the hydrodynamic theory that will adequately describe the flow. It is quite independent of whether the motion is symmetric or antisymmetric, or even of whether or not there is a free surface; in short the comments on the matter in Prof. Ogilvie's first and last paragraphs are beside the point. Moreover the convolution integral approach provides a far better interpretation of the results of oscillatory testing than the conventional methods. Has any of this been the stock in trade of hydrodynamicists? We think not.
3. Previous writers have arrived at a convolution formulation by adding a hydrodynamic theory (that may or may not be accurate). Unfortunately, as Prof. Ogilvie says, their results could not be checked by experiment. We have pointed out that the PMM seems to remove that difficulty. If this, too, is something that has been known for years, it is surprising that there appears to be absolutely no literature on the matter. (Parenthetically, we should hesitate to suggest to an applied mathematician that time/frequency domain techniques were devised by a 20th century hydrodynamicist.)
4. On the basis of experimental results we have thus been able to measure memory effects and to show that they are by no means insignificant. Since theoretical naval hydrodynamics is hardly noted for its devastating accuracy, this demonstration does seem to be of some merit. Yet so far as

we know this too is a new departure.

5. If the first approximation to the functional series will not suffice, the behaviour being essentially non-linear, then a functional series of higher order can be used. Again we know of no previous statement, let alone development, of this point.

The second of these points is the crux of this matter. In his spirited defence of hydrodynamicists (who were not, by the way, under attack!), Prof. Ogilvie has overlooked that this is not a paper on hydrodynamics in his own very limited sense of the word.

The suggestion that we "should review the ship motions literature a bit more thoroughly before making broad generalizations ... about the limitations of previous work" seems a little patronizing. We do try. But the suggestion seems to come particularly ill from a critic who manifestly has not read what he is criticizing with any real depth of understanding. We know very well of Prof. Ogilvie's enormous contributions to naval hydrodynamics; this is not one of them and it is best forgotten.

LARGE AMPLITUDE PMM TESTS AND MANEUVERING PREDICTIONS FOR A MARINER CLASS VESSEL

L. W. Smitt
Skibsteknisk Laboratorium
Hjortekaersvej 99
DK 2800 Lyngby Denmark

M. S. Chislett
Skibsteknisk Laboratorium
Hjortekaersvej 99
DK 2800 Lyngby Denmark

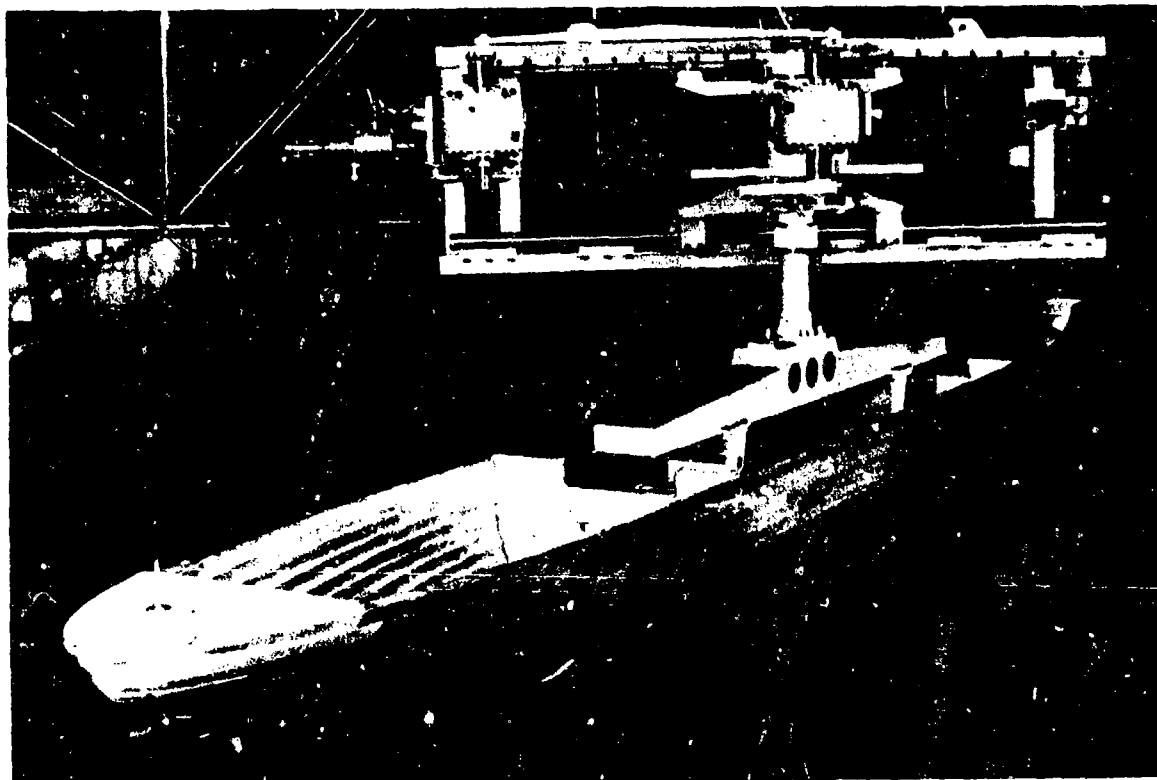


Fig. 1 Model, PMM & Towing Carriage

ABSTRACT

Simulation of ship steering and manoeuvring behaviour is becoming increasingly common, both as a training aid, and for research and development purposes. The behaviour of a projected design can, at present, best be simulated by obtaining the coefficients of the equations of motion from captive model tests.

The co-operative manoeuvring research programme initiated by the ITTC, which originally recommended the comparison of captive model measurements made by different model tanks, has been extended to include the comparison of simulated manoeuvres with full scale trial results

for the MARINER Class Vessel "USS Compass Island".

The new large amplitude Planar Motion Mechanism, (PMM) recently installed at Skibsteknisk Laboratorium (SL) has been used to measure a complete set of hydrodynamic coefficients covering the manoeuvres made with 15 kn approach speed. The raw data are expressed in coefficient form and used to simulate full scale manoeuvres, which are compared with the "Compass Island" trials.

Measurements made with the PMM at 20 kn are compared with rotating-arm results from other establishments.

NOMENCLATURE

The nomenclature used for steering and manoeuvring at SL is based on the SNAME Technical and Research Bulletin No. 1-5, "Nomenclature for Treating the Motion of a Submerged Body Through a Fluid," (1952). This nomenclature is identical, in every major respect, to that subsequently adopted by the 10th ITTC (1963), and to (1) (1967) which is the most commonly available source.

Symbols

x, y, z	axes fixed in ship/model
u, v, w	velocities referred to x, y, z
$\dot{u}, \dot{v}, \dot{w}$	accelerations - - - -
X, Y, Z	forces - - - -
p, q, r	angular velocities about x, y, z
$\dot{p}, \dot{q}, \dot{r}$	accelerations - - - -
K, M, N	turning moment - - - -

O	origin of axes, x, y, z
G	CG of ship/model
x_G	distance from O to G
U	equal to $\sqrt{u^2 + v^2 + w^2}$
δ	rudder angle
β	drift angle, $\sin \beta = -v/U$
m	mass of ship/model
I_z	mass moment of inertia about z
u	speed loss, equal to $u - U_0$
U_0	appr. ch (initial) speed
ω	circular frequency
x_0, y_0	axes fixed on earth
ψ	heading angle
g	gravitational acceleration
L_{pp}	length between perpendiculars
ρ	mass density of water

A given physical quantity is non-dimensionalized by considering its dimensions in terms of mass, length and time as fundamental units and dividing mass by $(\frac{1}{2} \rho L_{pp}^3)$, length by L_{pp} and time by L_{pp}/U .

The prime notation is used to indicate non-dimensionalized quantities and the dot notation to indicate time derivatives.

Abbreviations

SL	Skibsteknisk Laboratorium ¹
NSRDC	Naval Ship R & D Centre
AEW	Admiralty Experiment Works
PMM	Planar Motion Mechanism
DRT	Dead Reckoning Tracer
EM log	Electro-Magnetic Log

¹ Skibsteknisk Laboratorium (Danish Ship Research Laboratory) resulted from the merging of the former Hydro- and Aerodynamics Laboratory (HyA) and the Danish Ship Research Institute.

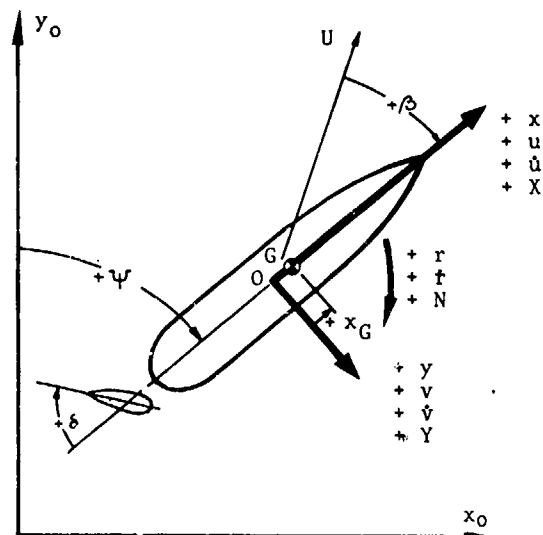


Fig. 2 Body and Earth Axes

INTRODUCTION

The development of new ship types for which very little experience exists - current examples are mammoth tankers with very low L/B ratios, and very fast container vessels - has given renewed impetus to the need for a method of evaluating steering and manoeuvring qualities in the design stages. It has become apparent that steering and manoeuvring behaviour has considerable bearing on economic, safety and ecological aspects of ship operation.

Simulation of steering and manoeuvring behaviour with the aid of a mathematical model and digital or analogue computers is now common both as a tool for research and development and for the training of masters, navigators and helmsmen etc.

For such simulation exercises to be meaningful, the design of the mathematical model must be tailored to the ship type and conditions, and the (hydrodynamic) coefficients of the equations must be accurately determined.

Hydrodynamic coefficients can be found in many ways, but although progress is being made with theoretical considerations and more recently with application of system-identification techniques, the most accurate and complete results are at present obtained from captive-model tests.

The ITTC Standard Captive-Model-Test Programme was set up in 1952 in an endeavour to assess the credibility of the various captive-model test techniques. The first phase, which consisted of a comparison of data from tests with a standardized model of a Mariner Class Vessel, has now been formally ended (2), even though few firm conclusions could be drawn due to variations of the test conditions. There still exists a need for test data that can form a basis for comparative studies of the different captive-model test techniques, and the Recommendations of the Manoeuvrability Committee adopted by the 13th ITTC (3) invite the submission of: "... any kind of information related to duplicate tests with Planar Motion Mechanisms, Rotating Arms or Straightline Towing".

The Committee urge that the second phase of the ITTC Standard Captive-Model-Test Programme "... be actively pursued to correlate computer predictions with free-running models and full-scale trial data".

Following the installation of a new large amplitude horizontal PMM at SL in the spring of 1971, about 30 different designs have been tested and simulated. The new PMM (4) was designed on the basis of 8 years experience with a medium amplitude PMM (5, 6), and is capable of generating the full range of motions encountered in ship manoeuvres. The data acquisition system, and in particular the data analysis, mathematical model and simulation procedures have been continuously refined through the years.

Opportunities for comparison with reliable full-scale trial results have, however, been scarce.

The extensive and unusually well documented full-scale trials conducted with the USS "Compass Island" Mariner Class Vessel (7), which form the basis for the ITTC Standard Captive-Model-Test Programme, furnish an almost unique opportunity.

The present paper describes the results of PMM-tests with a 61 m model of the USS "Compass Island" and a comparison of full-scale trial and simulated manoeuvres. The first part of the paper describes the results of tests made with 15 knots approach speed, the speed at which most full-scale trials were made. The general philosophy behind the design of the test programme is expounded and the measured values together with the analytical expressions which represent them in the mathematical model are given.

The second part of the paper contains the full-scale trial and simulated manoeuvres, and a discussion of the similarities and differences.

The third part of the paper relates to the ITTC plea for comparative PMM and Rotating Arm data, as it contains a comparison of test data (for 20 knots) measured with the SL PMM, and the NSRDC and AEW Rotating Arm Facilities.

TEST CONDITIONS

Model and Ship Particulars

A 61 m long model of varnished wood was used for the tests. The model conformed with the specifications for the ITTC Standard Captive-Model-Test Programme (2) and therefore differed from the USS "Compass Island" in that the model bilge-keels were longer, and no sonar-dome was fitted.

The stock propeller used for the tests had dimensions very close to those of the ship propeller. The propeller revolutions during the tests were accurate to within $\pm 1/4\%$ which was necessary for the consistent measurement of the longitudinal force. The model was entirely free to sink and trim, but restrained to zero heel.

The loading condition corresponded to the "Compass Island" trials and is given in Table 1.

Table 1 Condition Tested

Model Scale 1:25	Model	Ship
Length overall	m 6.748	171.80
Length between Perps.	m 6.437	160.93
Beam	m .927	23.17
Draft forward	m .274	6.86
Draft aft	m .323	8.08
Displacement	m ³ 1.064	16622
Propeller:	Right-Handed	
Designation number	6137	
Number of Blades	4	
Propeller Diameter	m .270	6.706
Pitch Ratio at .7R	.963	
Developed Area Ratio	.524	

Model Basin and PMM Particulars

The main particulars of the towing tank, carriage and PMM are listed in Table 2.

Table 2. Tank, Carriage, PMM Particulars

Length of Towing Tank	240	m
Width of	12	m
Water Depth	5.5	m
Max. Carriage Speed	14	m/s
Max. Practical Speed	8.5	m/s

PMM Bolted to Aft End of Carriage:

Max. Sway Amplitude	$\pm .75$ m
Max. Yaw Amplitude	$\pm 27.5^\circ$
Drift Angle Range	$\pm 180^\circ$ in steps of 2°
or during Static Runs	$\pm 27.5^\circ$ continuous
PMM revolutions	
continuously variable	0.5 - 15 rpm

A general impression of the layout of the PMM in relation to model and towing carriage can be obtained from Fig. 1.

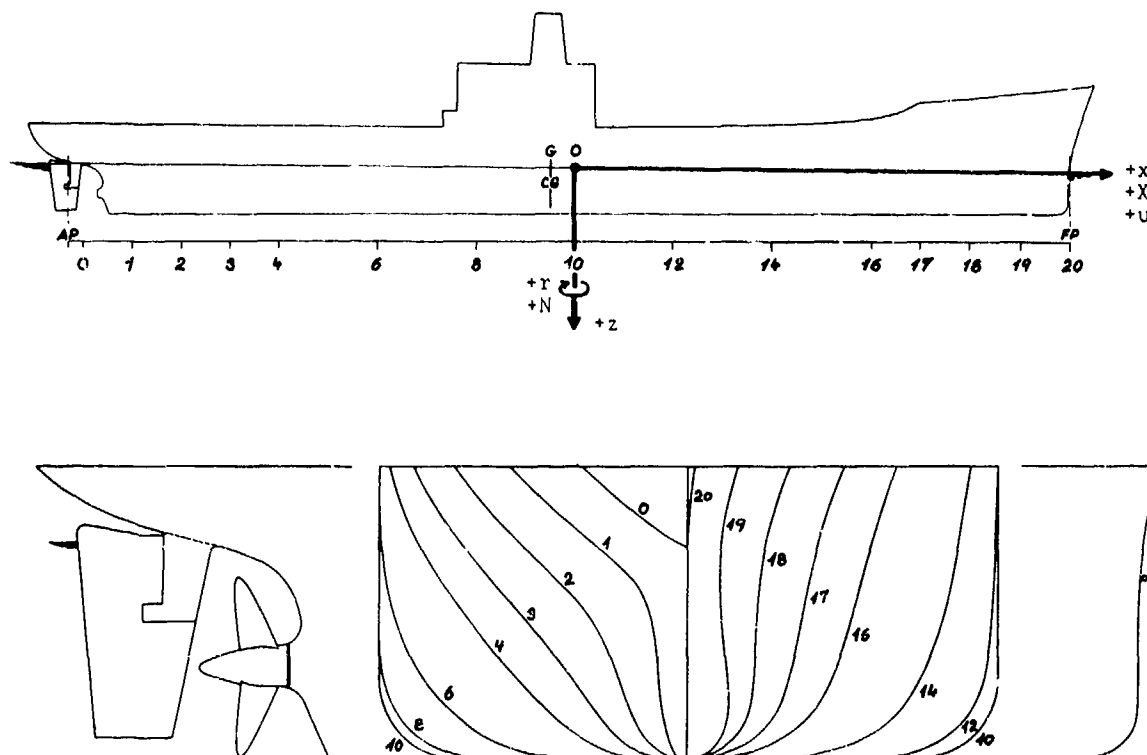


Fig. 3 The Mariner Class Vessel, USS "Compass Island"
Trial Condition

The PMM is based on a flat welded-up frame of hollow rectangular sections which, when bolted in position on the aft end of the towing carriage, forms a very stiff foundation.

A subcarriage runs on two horizontal rails which extend over the full width of the frame. The lower rail is of circular section and supports the weight of the subcarriage on two axial recirculating ball bearings. The upper rail is rectangular in section and the subcarriage is guided along it by two pairs of ball-bearing wheels.

Sinusoidal lateral (swaying) motions of the subcarriage are generated by an O'Dell linkage and rotary (yawing) motions of the main strut by a scotch yoke and tangent generator. These motions are generated using two identical but counter-rotating worm and wheel gearboxes driven by a common splined shaft powered by a variable speed d.c. motor. One gearbox is fixed on the frame of the mechanism and the other is incorporated in the subcarriage.

The amplitudes of the lateral and rotary motions are continuously variable by means of lead screws in the crank arms and the settings are indicated by mechanical digital counters on the cranks.

The main vertical strut connecting

model and mechanism is supported by bushed bearings in the top and bottom of the subcarriage and can be rotated relative to the subcarriage by a radial arm via a toothed coupling. The lower end of the strut is bolted to a strong-back of welded-up box section, the underside of which serves as a universal mounting surface to which the models are connected. In the case of normal displacement ship models, linkages permitting sinkage and trim, but preventing heel, are connected to each end of the mounting surface on the strong-back and by way of gimbals to force gauges in each end of the model.

Static drift angles from 0° to 360° can be set with 20° increments using the toothed coupling, or with a fine adjustment screw at the main strut to the strong-back connection which has a continuous range of $\pm 2^\circ$ and a zero adjustment facility. Using these settings, static drift angles can be superimposed on cyclic yawing or swaying modes. When making static measurements, the drift angle can be varied continuously from 0° to 55° while the carriage is in motion by manually varying the amplitude of the yaw crank.

A somewhat more complete description of the system is given in (4).

MODEL DATA, 15 KN INITIAL SPEED

General Philosophy

The test programme has been designed to provide a necessary and sufficient description of the hydrodynamic effects governing steering and manoeuvring qualities, within the performance envelope corresponding to 15 knots initial speed, and constant propeller revolutions.

Steering qualities, which characterize the ability to sail on straight course at constant speed, are associated with full (initial) speed and small rudder angles, drift angles, yaw rates etc. Manoeuvring qualities which characterize ability to change course, turn, pull-out etc., are associated with a speed loss, large rudder angles, drift angles, yaw rates etc. Due regard has been paid to these two distinct but related areas of the performance envelope in the design of the test programme, a full description of which is given in Table 3.

Account has also been taken of the fact that the "Compass Island" is a single-screw ship, and that the port and starboard symmetry is therefore imperfect due to the uni-directional rotation of the propeller.

In principle, the ranges of the variables δ , u , v , r , and their time derivatives, should be explored over the full range covered by the ship. In practice, care has been taken to cover the important areas thoroughly and other areas more sketchily.

Finally, care must be taken that a particular hydrodynamic effect is only included once in the mathematical model even though it may occur in more than one test.

The subsequent discussion of the individual test series serves to illustrate the application of these general principles.

The hydrodynamic effects are, in general, proportional to the square of the relevant water flow velocity. Deviations result from changes in wave-making, sinkage and trim variations with speed etc. but are generally fairly small. The variations of the dimensionless coefficients when non-dimensionalized with speed squared are thus also fairly small. The results of tests at different speeds can in many cases be expressed with analytical expressions that do not contain the variable, u , but do in fact account for minor speed effects.

The test data are weighted such that the coefficients give the best possible fit in important areas and a more relaxed fit in less important areas.

Table 3 Test Programme

Name of Test	Speed u knots Ship	Parameters Varied During Test	Flg	Relevant Coefficients	Parameters Constant During Test
STATIC SPEED & RUDDER ANGLE	15 13.5 12 10.5 9 7	$-35 \leq \delta \leq 35$ - - - - -	4 5	Y_0 Y_δ $Y_{\delta\delta}$ $Y_{\delta\delta\delta}$ Y_{0u} $Y_{\delta u}$ $Y_{\delta\delta u}$ $Y_{\delta\delta\delta u}$ N_0 N_δ $N_{\delta\delta}$ $N_{\delta\delta\delta}$ N_{0u} $N_{\delta u}$ $N_{\delta\delta u}$ $N_{\delta\delta\delta u}$ X_δ $X_{\delta\delta}$ $X_{\delta\delta u}$ X_0 X_u X_{uu} X_{uuu}	$\beta, r, \dot{r}, \dot{v}, \dot{u}$ - - - -
STATIC DRIFT ANGLE	15 10.5	$-8 \leq \beta \leq 8$ $-15 \leq \beta \leq 15$	6 7	Y_v Y_{vv} $Y_{v v }$ X_v N_v N_{vv} $N_{v v }$ X_{vv}	$r, \dot{r}, \dot{v}, \dot{u}$ -
STATIC DRIFT & RUDDER ANGLE	15	$\beta = -8$ $-20 \leq \delta \leq 35$ $\beta = 8$ $-35 \leq \delta \leq 20$ $\delta = -20$ $-8 \leq \beta \leq 8$ $\delta = 20$ $-8 \leq \beta \leq 8$	8 9	$Y_{\delta v }$ $X_{v\delta}$ $N_{\delta v }$ $X_{\delta vv}$	$u, r, \dot{r}, \dot{v}, \dot{u}$ - - -
PURE YAW	15 10.5 15 10.5	$0 \leq r \leq 0.3$ $0 \leq r \leq 0.7$ $0 \leq r \leq 0.6$ $0 \leq r \leq 1.7$	10 13	Y_r Y_{rrr} X_{rr} N_r N_{rrr} $Y_{\dot{r}}$ $N_{\dot{r}}$	$u, \delta, \beta, \dot{v}, \dot{u}$ - - -
YAW & DRIFT+ DRIFT & YAW	10.5 10.5 10.5	$r=0.4$ $0 \leq \beta \leq 10$ $r=0.6$ $6 \leq \beta \leq 14$ $\beta=12$ $0.3 \leq r \leq 0.7$	11	Y_{vrr} Y_{rvv} N_{vrr} N_{rvv} X_{vr}	$u, \delta, \dot{v}, \dot{u}$ - -
PURE SWAY	15	$0 \leq v \leq 0.3$	12	$Y_{\dot{v}}$ $N_{\dot{v}}$	$u, \delta, r, \dot{r}, \dot{u}$
PURE SURGE	0	$0 \leq \dot{u} \leq 0.07$	14	$X_{\dot{u}}$	$\delta, \beta, r, \dot{r}, \dot{v}$

Presentation of Results

The model test measurements are shown in Figures 4 through 14. The fairing expressions subsequently inserted into the mathematical model used to predict ship-scale manoeuvres are drawn through the measured values. The fairing expressions are indicated in the figures and the numerical values of the coefficients of the fairing expressions are given in Table 5. For example, in the case of the Pure Yaw Test, the side-force measurements plotted in Fig. 10 have been fairied with the expression:

$$Y' = Y'_r + Y'_{rrr} r^3$$

where the values:

$$Y'_r = 322.7 \times 10^{-5}, Y'_{rrr} = 552.8 \times 10^{-5}$$

are found in Table 5 and the fairing expression is given in the figure as:

$$Y'_r (f) = r, rrr$$

All of the measured data correspond to hydrodynamic effects, i.e. the force and moment components due to model mass and mass distribution have been subtracted. The data furthermore refer to a body axis system with origin at station 10 (and not at the CG) as shown in Fig. 3.

All of the results are in non-dimensional form except for the added mass in surge shown in Fig. 14, where, since the tests were made at zero speed, and \dot{u} is the same for model and ship, it was found reasonable to present the results dimensionally.

Apart from this one exception, all of the side-force (Y) data are plotted to the same scale, as are also all turning-moment (N) and all longitudinal force (X) measurements. This permits a ready evaluation of the relative importance of the different measurements especially when it is borne in mind that all of the excitation and damping effects (functions of u, δ, v and r) have been measured over ranges extending a little beyond the performance envelope of the ship. Thus for example measurements have been made for drift angles in the range $-140^\circ \leq \beta \leq 140^\circ$ while the ship range is approx. $-120^\circ \leq \beta \leq 120^\circ$ for maximum rudder angle.

In the case of the acceleration dependent effects shown in Figs. 12, 13 and 14, the tests extended considerably beyond the ship range, which is, however, indicated in the figures.

For those who are unfamiliar with these non-dimensional values of hydrodynamic force and moment, it may be helpful to give the following values for model and ship at speed equivalent to 15 knots:

$X' \times 10^3 = Y' \times 10^3 = 1$ corresponds to 80.6 metric tons force for ship and 5.2 kp for model.

$N' \times 10^3 = 1$ corresponds to 13.0 tons kilometre for ship and 33.5 kp m for model.

The relation between the scales for Y and N has been chosen such that the relative accuracy of the Y and N data is displayed with the same weight.

Data measured at approach speed (15 kn.) are indicated with solid points and full lines thus —●—, while data from tests at reduced speeds are, for the most part, shown with open points and dotted lines thus —○—□—▽—.

Static Speed & Rudder Angle Test Figures 4 & 5

The effects of rudder angle at full speed were investigated fairly extensively as they are important for both steering and manoeuvring.

The measurements are expressed by the dominant symmetrical coefficients:

$$Y_6, Y_{666}, N_6, N_{666}, X_{66}$$

together with the less important asymmetrical coefficients:

$$Y_0, Y_{66}, N_0, N_{66}, X_6$$

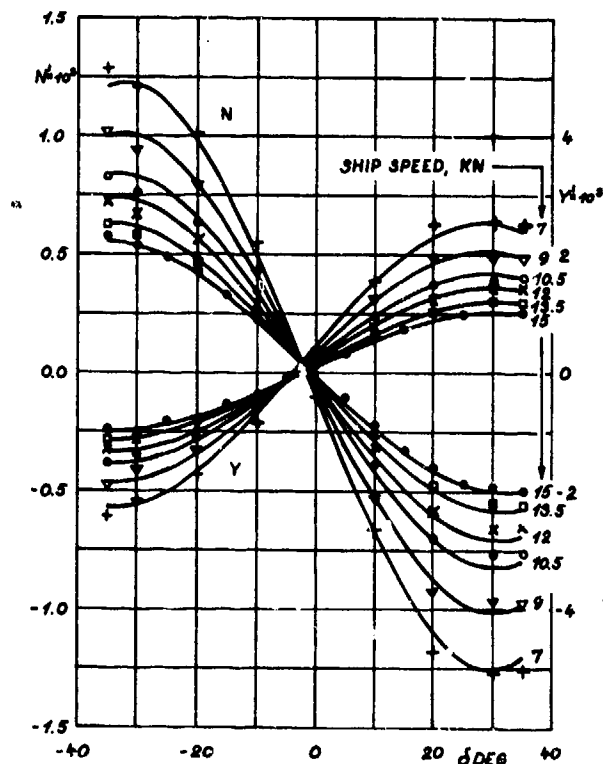


Fig. 4 Static Speed & Rudder Angle Test. Side-Force and Turning-Moment versus Rudder Angle for various Speeds

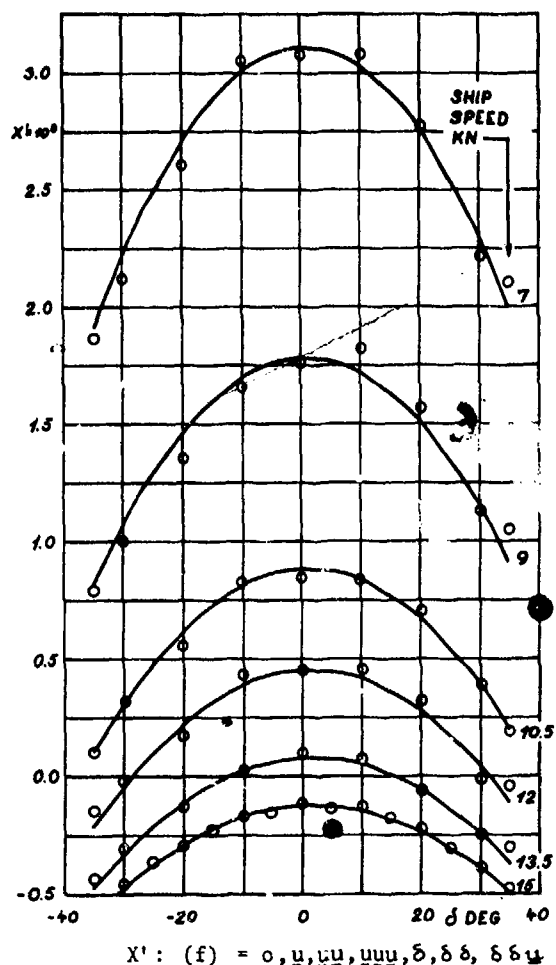


Fig. 5 Static Speed & Rudder Angle Test. Longitudinal-Force versus Rudder Angle for various Speeds

Contrary to "hull-forces" (which are dependent on r and β) and which are nearly proportional to hull-speed squared (U^2), the "rudder-forces" are very much dependent on the velocity of the propeller slip-stream for this single-screw centre-line rudder configuration. During a manoeuvre, hull-speed falls more than slip-stream speed. As slip stream speed, and hence average speed past the rudder is unknown, it is practicable to non-dimensionalize rudder-forces (as well as all others) with hull-speed, and to account for the "overload" effect with reducing speed with the aid of the speed-loss dependent coefficients:

$$\begin{aligned} Y_{0u} \quad Y_{\delta u} \quad Y_{\delta \delta u} \quad Y_{\delta \delta \delta u} \\ N_{0u} \quad N_{\delta u} \quad N_{\delta \delta u} \quad N_{\delta \delta \delta u} \\ X_{\delta \delta u} \end{aligned}$$

It is interesting to note that the centre-of-action of the rudder-forces expressed by the symmetrical coefficients

$$Y_{\delta} \quad Y_{\delta \delta \delta} \quad Y_{\delta u} \quad \text{and} \quad Y_{\delta \delta \delta u}$$

(obtained by dividing the N-coefficients by the corresponding Y-coefficients), are at -0.516, -0.520, -0.515 and -0.512 respectively (see Table 5), i.e. slightly aft of the rudder stock (which is at -0.508 for origin of axis system at station 10). For other designs tested at deeper drafts the corresponding centres-of-action are usually slightly forward of the rudder, indicating that the hull above and forward of the rudder carries part of the force due to rudder angle. However, possibly due to the light draft aft (see Fig. 3), little or no force acts on the hull in the present case.

The non-dimensional speed loss parameter

$$u = (u - U_0)/U$$

is seen to be zero at initial speed and the speed-loss dependent coefficients thus express the disparity between ship-speed and the speed of the flow past the rudder.

The coefficients Y_0 and N_0 express the asymmetrical side-force aft due to the single propeller, and the values of the coefficients Y_{0u} and N_{0u} the fact that this force is dimensionally rather independent of speed.

Static Drift Angle Test Figures 6 & 7

Measurements were made for small and moderate drift angles at initial speed, primarily to cover the steering area, and for larger drift angles at reduced speed, in the manoeuvring range. Both sets of side-force and turning moment data were then faired with the coefficients:

$$\begin{aligned} Y_0 \quad Y_{0u} \quad Y_v \quad Y_{vv} \quad Y_{v|v|} \\ N_0 \quad N_{0u} \quad N_v \quad N_{vv} \quad N_{v|v|} \end{aligned}$$

where the coefficients

$$Y_0 \quad Y_{0u} \quad N_0 \quad \text{and} \quad N_{0u}$$

were taken from the Speed & Rudder Tests. It was possible to fair the data for both speeds without the use of speed dependent coefficients as the "hull-forces" due to drift angle are largely proportional to speed squared. The coefficients Y_v and N_v are primarily based on the data for initial speed, whereas $Y_{v|v|}$ and $N_{v|v|}$ besides expressing the non-linearities with drift angle also account for any small speed effects since the measurements for large drift angles were made at reduced speed.

The asymmetrical terms Y_{vv} and N_{vv} reflect the influence of the single-

propeller, which is unusually pronounced, presumably due to the relatively large diameter and proximity to the free surface.

This is supported by the fact that $N_{vv}/Y_{vv} = -0.631$ (close to $-0.5l_{pp}$), which indicates that the effects causing the asymmetry are concentrated in the area of the propeller.

In order to obtain the best possible assessment of steering (course stability) ability, the coefficients N_v and N_v were also found by hand-fairing the results for small drift angles at full-speed. These values are given in brackets in Table 5 and are seen to compare extremely well with the linear coefficients from the overall fairing.

The asymmetrical variation of the longitudinal force with drift angle shown in Fig. 7 is largely influenced by the variation of propeller thrust, which is in turn dependent on the inflow velocity to the propeller. The inflow velocity varies with drift angle since the low-velocity frictional wake-belt is progressively deflected. Measurements of wake-fraction variation with drift angle for the same model at 20 kn have been taken from (8) and included in Fig. 7. The affinity is striking. The faired lines correspond to $X'_v = X'_{vv} = 0$, which is a better representation than that used for simulation and given in Table 5. The difference is small.

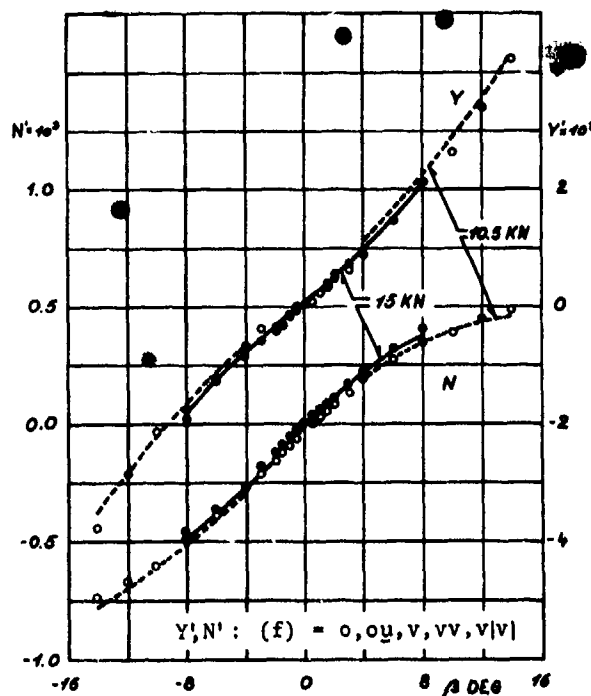


Fig. 6 Static Drift Angle Test. Side-Force and Turning-Moment versus Drift Angle for two Speeds

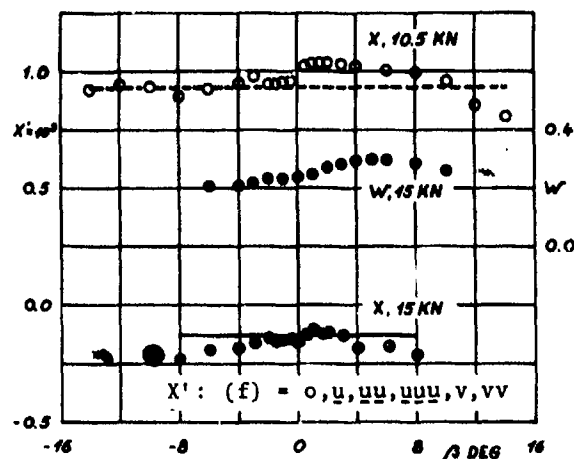


Fig. 7 Static Drift Angle Test. Longitudinal-Force versus Drift Angle for two Speeds.

Static Drift & Rudder Angle Test Figs. 8 & 9

These tests were made to investigate cross-coupling between the drift angle and rudder angle effects already characterized by the tests described in the above. The cross-coupling phenomena can be physically interpreted by recourse to the notion that drift angles primarily give rise to forces on the hull and that rudder angles primarily give rise to forces on the rudder. Cross-coupling terms then express deviations from these main effects.

The coefficients of the variable $\delta|v|$ thus expresses the "rudder-force" component due to drift angle. It can be viewed as the change of rudder lift-curve slope with drift angle resulting from the deflection from the centre-line of the low-velocity frictional wake-belt, with resultant increase of inflow velocity to the rudder. Hence the character of the variable $\delta|v|$ which has the same sign for both positive and negative drift angles. Note also that the centre-of-action, given by $N_{\delta|v|}/Y_{\delta|v|}$ is close to the rudder. The effect is small.

The variable $\delta|v|$ is preferable to the analogous but more powerful δv since the underlying phenomenon is more akin to a step function than a quadratic effect as once the wake is washed away the inflow remains more or less constant (at the new higher velocity) for further increase of drift angle.

As can be seen from Table 5, the mathematical model does not include terms of the form $v|\delta|$ (or $v\delta\delta$) which would account for change of drift angle lift-curve-slope with rudder angle.

Experience has shown that the values assigned to such terms by three-dimensional fairings of measured data are negligible, which is perhaps not surprising since no physical grounds for their existence are apparent.

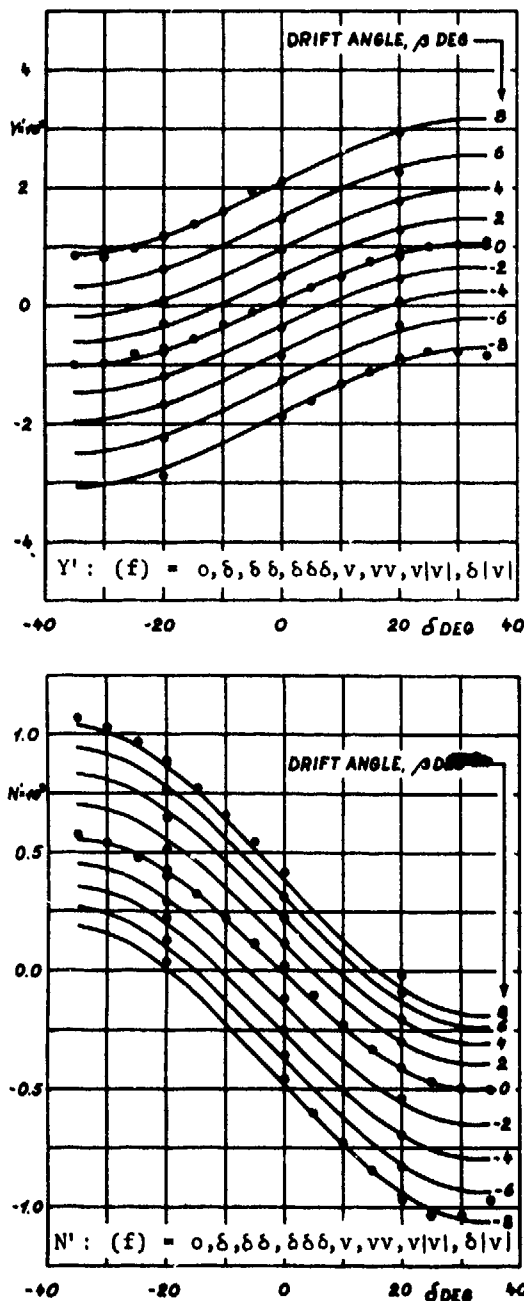


Fig. 8 Static Drift & Rudder Angle Test. Side-Force and Turning-Moment versus Rudder Angle for various Drift Angles

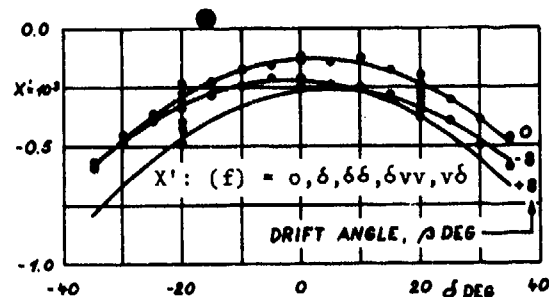


Fig. 9 Static Drift & Rudder Angle Test. Longitudinal-Force versus Rudder Angle for various Drift Angles

Cyclic Tests

All of the tests described so far have been so-called static tests, i.e. tests in which the motion parameters are time independent and where the model is moved along a straight-line path. Such tests are conveniently made with the SL-PMM, but its main function is the generation of cyclic yawing motions, where the yawing rate can be varied from zero to that corresponding to maximum turning rate for the full-scale ship.

Pure yawing motion is obtained (by definition) by moving the model along a sinuous path such that its centre-line (x-axis) is always tangential to the path at the origin of the axis system in the model. This is exactly accomplished by the SL-PMM, no approximations being involved, even the very small cyclic variation of model speed given by:

$$U_{\text{model}} = (U_{\text{carriage}}) / \cos \psi$$

being accounted for with good accuracy in the data analysis.

The general principles used for the resolution of the forces in-phase with the cyclic yaw rate and in-phase with the associated cyclic yaw acceleration, as well as the principles underlying the assessment of non-linear and cross-coupling effects, have been described in detail in (6). The not inconsiderable refinements in the logicality of the detailed reasoning and numerical methods, that have been made in connection with the introduction of the newer large amplitude PMM will be published shortly.

The SL analysis of PMM test data is founded on the assumption that the hydrodynamic effects measured in cyclic tests are, for all practical purposes, independent of the frequency of the motions. The frequency effects associated with:

- a) tank resonance (6)
- a function of tank dimensions and test frequency

b) translatory free-surface waves generated by a pulsating source (9), a function of model speed, test frequency and gravity, $\omega U/g$

c) unsteady lift or memory-effects, a function of normalized test frequency, $\omega L_{pp}/U$

are found to be negligibly small (for normal ships) when

a) test frequency is appreciably less than 14 cpm

b) $\omega U/g$ is appreciably less than $1/4$ (10)

c) $\omega L_{pp}/U$ is less than about 3

Yawing Tests Figs. 10, 11 & 13

Pure Yaw measurements with small r 's were made at 15 knots to cover the steering area, and with larger r 's at reduced speed in the manoeuvring range. The linear coefficients, Y_r and N_r , are based on the full-speed measurements, and the cubic coefficients, Y_{rrr} and N_{rrr} , represent both the non-linear effects and the small speed-effects.

The results of the Yaw & Drift + Drift & Yaw tests (analogous to the Static Drift & Rudder Angle Tests) can be interpreted as due to the integrated effects of local cross-flow drag. The coefficients Y_{rv} and N_{rv} can be viewed as expressing the influence of drift angle on the results of the Pure Yaw measurements, and the coefficients Y_{rr} and N_{rr} as expressing the influence of yaw rate on the results of the Static Drift Angle tests.

The values of the normalized frequency parameters for the yawing tests are given in Table 4.

Table 4 Parameters for Cyclic Yaw Tests

Speed ship	Speed model	N_{PMM}	$\frac{\omega L_{pp}}{U}$	$\frac{\omega U}{g}$	r' max	\dot{r}' max
knots	m/sec	cpm				
15	1.54	4	1.75	.07	.33	.58
10.5	1.08	4	2.50	.05	.68	1.69

The acceleration-dependent Y and N components measured in the Pure Yaw and the Yaw & Drift + Drift & Yaw tests are plotted in Fig. 13.

The longitudinal force components in-phase with the product of yaw rate and drift angle (which has the units of acceleration) are plotted in Fig. 13. The zero offset is due to the asymmetrical wake variation with drift angle mentioned in connection with the Static Drift Angle tests.

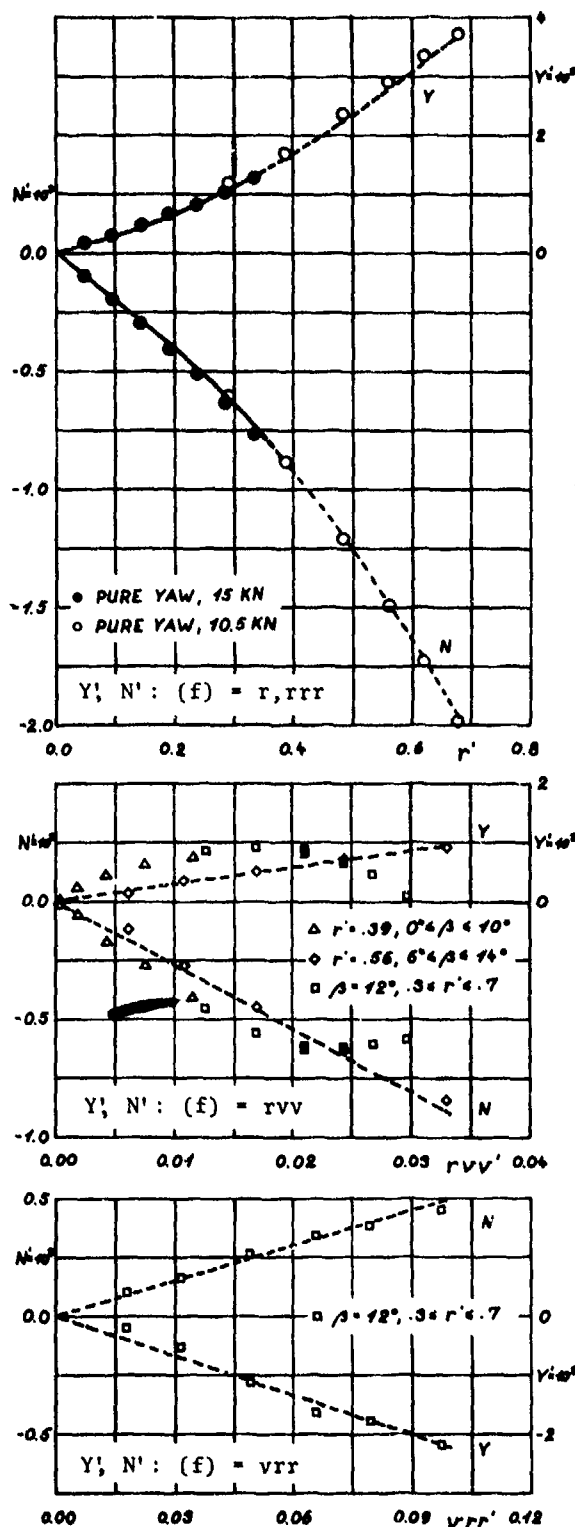


Fig. 10 Yawing Tests. Side-Force and Turning Moment versus Yaw Rate for various Drift Angles

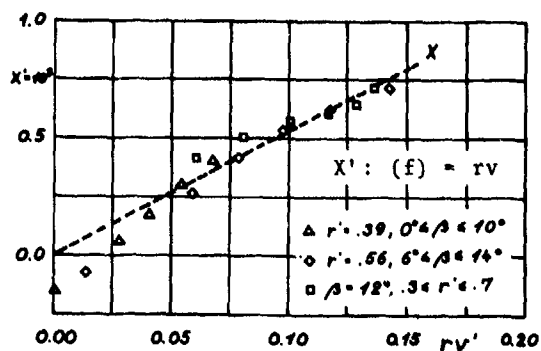


Fig. 11 Yawing Tests.
Longitudinal-Force versus
product of Yaw Rate
and Drift Angle

Pure Sway Test Fig. 12

The results of the Pure Sway test furnish the Y and N dependence on lateral acceleration (lateral added mass). Experience has shown that the damping components (in-phase with v) are more sensitive to frequency than are the damping components (in-phase with r) in yawing tests.

SL-practice is therefore to use the sway damping results given by the static tests and only use the cyclic Pure Sway test for the determination of the coefficients $Y\dot{v}$ and $N\dot{v}$.

The measurements shown in Fig. 12 were made with two sway amplitudes and various frequencies as follows:

Ship Speed, knots	15
Model Speed, m/sec.	1.54
PMM Frequency, cpm	2.5 to 10
ω_{Lpp}/U	1.09 to 4.36
$\omega U/g$	0.04 to 0.16
β_{max} , degrees	2, •, 4, ■

The measured values for $\omega_{Lpp}/U > 2$ have been disregarded as normal SL-practice is to make measurements at low frequency only. The measurements at higher frequencies in this case have been included for the sake of "new-comers" to the field, who are particularly interested in frequency-effects.

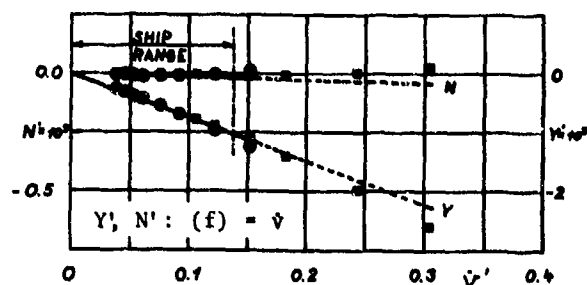


Fig. 12 Pure Sway Test.
Side-Force and Turning-Moment
versus Lateral Acceleration

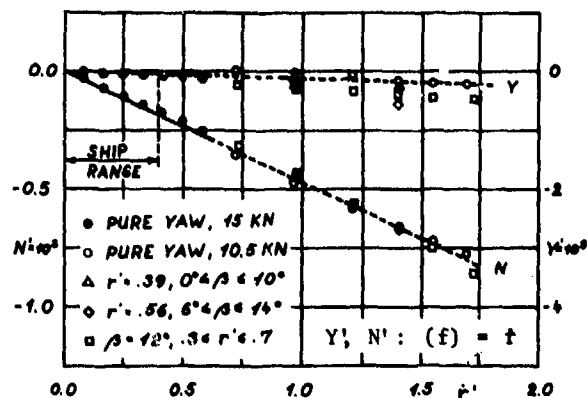


Fig. 13 Pure Yaw Test.
Side-Force and Turning-Moment
versus Yaw Acceleration

Pure Surge Test Fig. 14

The results of the Pure Surge test made at zero speed are included more for the sake of their curiosity value than for their importance. The hydrodynamic dependence on \dot{u} (added mass in surge) is very small compared with the ship's mass (see Table 5) but the results are interesting in that they illustrate the accuracy of the measuring system when free of carriage noise.

Sir Horace Lamb's coefficients of accession to inertia for an equivalent ellipsoid suggest an added mass of 3% of the displacement. Making allowance for the contribution of the propeller (which was not rotating) and for the influence of the boundary layer, the measured value of 4.55% seems very reasonable.

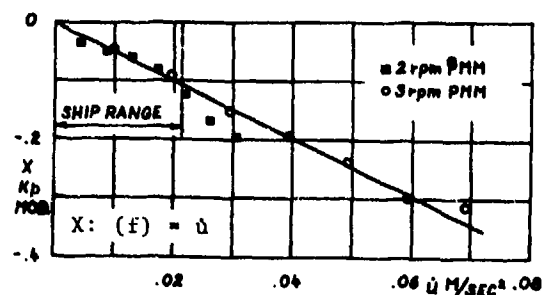


Fig. 14 Pure Surge Test.
Dimensional Longitudinal-Force
versus Dimensional Surge
Acceleration

Table 5 Coefficients of the Mathematical Model used for Simulation

X-EQUATION	non-dlm coeff $\times 10^5$	Y-EQUATION	non-dlm coeff $\times 10^5$	N-EQUATION	non-dlm coeff $\times 10^5$	Ncoeff Ycoeff
$X_{\dot{u}}$	-36.3	$Y_{\dot{v}}$	-740.0	$N_{\dot{v}}$	-11.0	.01
		$Y_{\dot{r}}$	-12.3	$N_{\dot{r}}$	-44.0	
$X_{\dot{u}}$	-160.8	$Y_{\dot{o}}$	6.2	$N_{\dot{o}}$	-1.5	-.52
$X_{\dot{u}\dot{u}}$	218.7	$Y_{\dot{o}\dot{u}}$	-33.6	$N_{\dot{o}\dot{u}}$	7.1	
$X_{\dot{u}\dot{u}\dot{u}}$	41.3	Y_{δ}	262.0	N_{δ}	-135.2	-.52
X_{δ}	8.4	$Y_{\delta\delta}$	-19.7	$N_{\delta\delta}$	12.8	
$X_{\delta\delta}$	-109.7	$Y_{\delta\delta\delta}$	-257.3	$N_{\delta\delta\delta}$	133.7	-.52
$X_{\delta\delta\dot{u}}$	204.4	$Y_{\delta\dot{u}}$	-419.4	$N_{\delta\dot{u}}$	216.0	
$X_{\delta\dot{v}\dot{v}}$	-151.2	$Y_{\delta\dot{u}\dot{u}}$	80.4	$N_{\delta\dot{u}\dot{u}}$	-11.7	-.51
$X_{v\delta}$	93.0	$Y_{\delta\delta\dot{u}}$	531.2	$N_{\delta\delta\dot{u}}$	-271.9	
		$Y_{\delta\dot{v}}$	180.9	$N_{\delta\dot{v}}$	-112.6	-.52
		$Y_{\delta\dot{v}}$	21.7	$N_{\delta\dot{v}}$	-6.0	
X_v	-17.1	Y_v	-1121.0	N_v	-385.4	.34
X_{vv}	-588.4	(Y_v)	-1114.7	(N_v)	-385.1	
X_{vr}	533.0	Y_{vv}	303.5	N_{vv}	-191.5	-.63
		Y_{vM}	-2038.6	N_{vM}	539.6	
		Y_{vrr}	-2220.0	N_{vrr}	500.0	
		Y_r	322.7	N_r	-201.5	
		Y_{rrr}	552.8	N_{rrr}	-199.4	
		Y_{rvv}	2833.0	N_{rvv}	-2700.0	
m	797.6	mx_G	-18.3	I_z	47.8	
Mass non-dlm with $1/2 \rho Lpp_3^3$ Inertia - $1/2 \rho Lpp_2^2$ X and Y Forces - $1/2 \rho Lpp_3 U_0^2$ Moments - $1/2 \rho Lpp U$ $u = (u - U_0)/U$ where U_0 is initial speed NB No Taylor Expansion Factorials are used						
u and v non-dlm with U δ^r - U/Lpp \dot{u} and \dot{v} - U^2/Lpp^2 \dot{r} - U/Lpp						

FULL-SCALE MANOEUVRES

PREDICTIONS & TRIALS

As discussed in the above, the model test programme was specifically designed to provide the coefficients of a mathematical model for simulation of the full-scale manoeuvres made with the USS "Compass Island" at 15 knots (?).

This section contains a very brief description of the structure of the mathematical model, a discussion of some aspects of the full-scale trial results, followed by a comparison of the full-scale trial and predicted manoeuvres.

Mathematical Model

The mathematical model is basically as described in (9.11) and consists of a de-coupled longitudinal-force equation together with interdependent side-force and turning-moment equations:

$$X: (m - X_{\dot{u}})\dot{u} = f_1(u, v, r, \delta) \quad (1)$$

$$Y: (m - Y_{\dot{v}})\dot{v} + (mx_G - Y_{\dot{r}})\dot{r} = f_2(u, v, r, \delta) \quad (2)$$

$$N: (mx_G - N_{\dot{v}})\dot{v} + (I_z - N_{\dot{r}})\dot{r} = f_3(u, v, r, \delta) \quad (3)$$

The functions f_1 , f_2 and f_3 are defined by the coefficients given in Table 5. As will be apparent from the discussion of the model test data, the number and character of the coefficients is tailored to the particular ship type, loading condition, speed range etc. The general computer programme in use at SL therefore contains all of the combinations and permutations that have so far been found necessary, giving a total of about 70 coefficients, (50 are used for the present case). Those not used in a particular case are set to zero.

Continuous time-base solutions for \dot{u} , \dot{v} and \dot{r} are calculated for predetermined rudder angle strategies, and integrated to give u, v , and r , which are in turn integrated to give x_0, y_0 and ψ .

As a digital computer is used to solve the equations, there is essentially no limit to the number of coefficients that can be included in the mathematical model. The computation time increases somewhat with number of coefficients, but this is not an important factor. If the equations were to be solved on an analogue computer, when the size of computer is roughly proportional to the number of coefficients, it would be feasible to reduce the number of coefficients considerably without serious loss of accuracy by eliminating and/or combining some of the analytical expressions.

Full-Scale Speed Measurements

A number of points seem to indicate that in the case of the full-scale trials the approach speed (the speed at the start of a manoeuvre) did not correspond to the equilibrium speed for the power output in question.

No acceleration trials were made with propeller revolutions corresponding to 15 knots nominal speed, but the measurements for revolutions corresponding to 10 knots nominal speed show the ship to be accelerating with 0.0075 m/sec^2 at 9 knots. This acceleration corresponds to an excess of thrust over resistance of at least 12% tons, i.e. a thrust of more than twice the resistance, indicating an equilibrium speed of over 11 knots instead of 10.

Fig. 18, showing final speed in turns for 15 knots nominal initial speed, indicates that at zero rudder angle the full-scale speed should have been closer to 16% knots than 15. This estimate is based on the inertial navigation system, which Morse & Price judged to be more accurate than the electro-magnetic log.

When combined with the unexpectedly large full-scale resistance, attributed by Morse & Price to fouling (the ship was 10 months out of dock) and the sonar dome, these points largely explain the rather high final speeds observed in the full-scale trials.

The model tests were made with constant propeller revolutions corresponding to the ship propulsion at 15 knots for a clean Mariner hull without sonar dome.

The use of constant revolutions, rather than constant power (as was the case for the ship) is believed, with hind sight, to have on average compensated for:

- a) the trial approach speeds being lower than the equilibrium speeds for the given revolutions.

- b) The ship resistance being greater than expected

and to account for the good agreement between trial and predicted final-speeds.

Full-Scale Path Measurements

The full-scale recordings of ship path, from which the parameters:

Advance after 90° change of heading
Transfer after 90° change of heading
Tactical diameter
Final turning radius

have also been derived, were obtained on board with the aid of a Dead Reckoning Tracer (DRT).

The inputs to the DRT were forward speed, u , from an electro-magnetic log and course, ψ , from the gyro-compass. The path was then calculated "by means of suitable integrators and resolvers" (7), presumably as follows:

$$x_0 \text{ DRT} = \int_0^T u \cos \psi dt \quad (1)$$

$$y_0 \text{ DRT} = \int_0^T u \sin \psi dt \quad (2)$$

The true path, however, is found by including the side-slipping effect of drift angle, when:

$$x_0 \text{ TRUE} = \int_0^T (u \cos \psi - v \sin \psi) dt \quad (3)$$

$$y_0 \text{ TRUE} = \int_0^T (u \sin \psi + v \cos \psi) dt \quad (4)$$

In order to be able to compare the full-scale trials and the predictions on a fair basis, special predictions of "DRT Path" have been made in addition to predictions of "TRUE Path".

Where the difference between the two was significant, both have been included in the figures comparing trials and predictions.

Simulations

Simulations have been made of each of the full-scale manoeuvres made with 15 knots nominal initial speed. The various manoeuvres are listed in Table 6, together with a list of the variables plotted in the figures that follow.

No attempts have been made to correct the model data for scale effects, but the tests were made with constant propeller revolutions corresponding to the self-propulsion point for ship at 15 knots, i.e. with ship revolutions scaled directly to model scale using a factor $\sqrt{\text{scale}}$ without making any allowance for the difference between model and ship wakes.

All of the coefficients in the mathematical model representing the ship have thus been taken directly from the model test results without any modifications or empirical changes. The good correlation between the simulations and full-scale trials seems to indicate that no pronounced scale effects are present in this case.

This should not, however, be generalized as applicable to all ship types. It should be borne in mind that the "Compass Island" is very different from, for example, large unstable tankers, which can experience drift angles and non-dimensional turning rates that are twice as big and where scale effect could be more important.

Nevertheless indications are, that predictions of zig-zag tests and spiral tests for tankers show quite satisfactory agreement with full-scale trials. More full-scale data on large full-bodied ships are required before possible scale effects on cross-flow drag can be assessed.

Turning Circles

Not unnaturally, there is a considerable difference between predicted DRT- and TRUE Paths, particularly for the turning circle turn-entry transients, as can be seen in Figs. 15 & 17. The predicted DRT Paths agree much better with the full-scale trial results than the predictions of TRUE Path do.

The full-scale trial results and the predictions both show a greater degree of port and starboard asymmetry than is usual, most probably due to the large propeller operating near the water surface, as mentioned in the comments on the model test data.

The predicted speed time histories in Fig. 16 are seen to agree quite well with the full-scale trials, when regard is paid to the truncated speed axis, although the agreement should perhaps be treated with reservation as discussed above.

The agreement between the predicted and full-scale trial results in Fig. 17 & 18 is otherwise very satisfactory.

Table 6 Full-Scale Trial & Predicted Manoeuvres

Type of Manoeuvre	Rudder Angle deg.	Approach speed kn.	Dependent Variable	Independent Variable	Fig. No.
<u>Turning Circles</u>					
Time Histories:	19.1 8.3 5.0 -10.4 -11.2 -19.8 -20.9	15.4 16.0 15.4 15.4 15.6 15.6 15.4	Typical Path Turning Rate Forward Speed	Time	15 16 16
Parameters:	-30 ¹ to +30 in steps of 5	15.5 ²	Advance after 90° Transfer after 90° Tactical Diameter Final Turning Radius " Drift Angle " Turning Rate " Speed	δ	17 17 17 18 18 18 18
<u>20-20 Zig-Zag</u>		15.0	Path Heading & Rudder Angle Drift Angle Turning Rate Speed	Time	19 19 19 19 19
<u>Spiral Manoeuvre</u>		15.0	Turning Rate	δ	20

¹ Turning Circle Parameters have only been calculated for $-30 \leq \delta \leq 30$ as no full-scale trials were made for rudder hard over.

² 15.5 knots is a good average of the full-scale approach speeds.

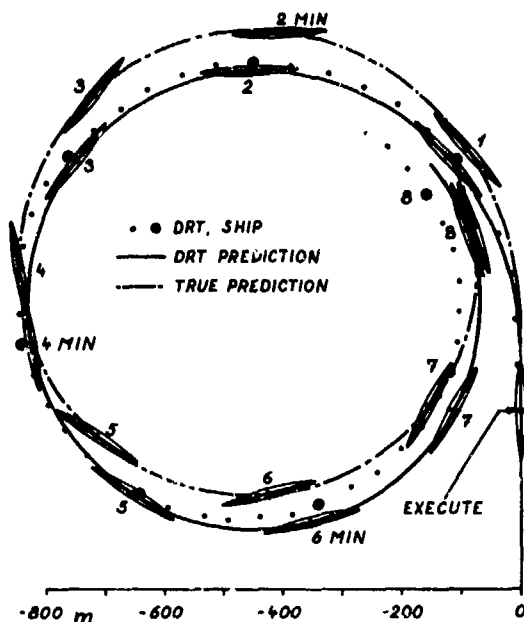


Fig. 15 Turning Circle Path.
Full-Scale Trial and Predictions
for 19.1 deg. Port Rudder Angle
and 15.4 knots Initial Speed

20-20 Zig-Zag Manoeuvre

In order to obtain the best possible basis for comparison, the predicted Zig-Zag was made by starting the rudder shifts at exactly the same heading angles as in the full-scale trials. The rudder angles were then changed with the same rudder rate to the same steady rudder angles. The heading angles, rudder rates and steady rudder angles were therefore different for each segment of the manoeuvre.

The trial and predicted results are shown in Fig. 19 and the general agreement leaves little to be desired, with the possible exception of the 3% difference in period.

Other small differences can be largely explained by minor deficiencies in the full-scale trial instrumentation:

- a) Difficulties were experienced with the inertial avigator used for deriving drift angles, particularly in transient manoeuvres.
- b) Although the trial and predicted average speeds after the first 2 minutes agree within 2%, the track lengths from the second to eighth minutes differ by 6%. As the tracks are almost identical for trial and prediction, this difference must either be due to inconsistencies between the speed used for the DRT and the average EM log speed time history, or due to a minor error in the DRT itself.

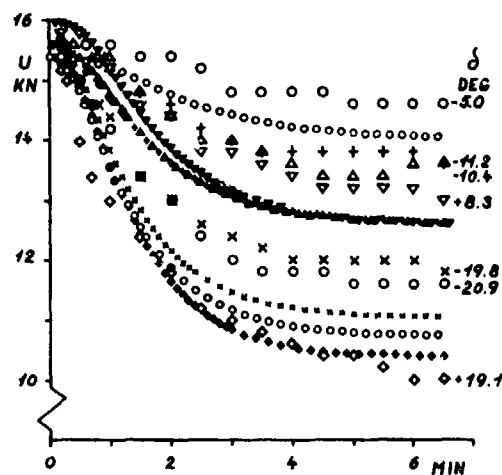
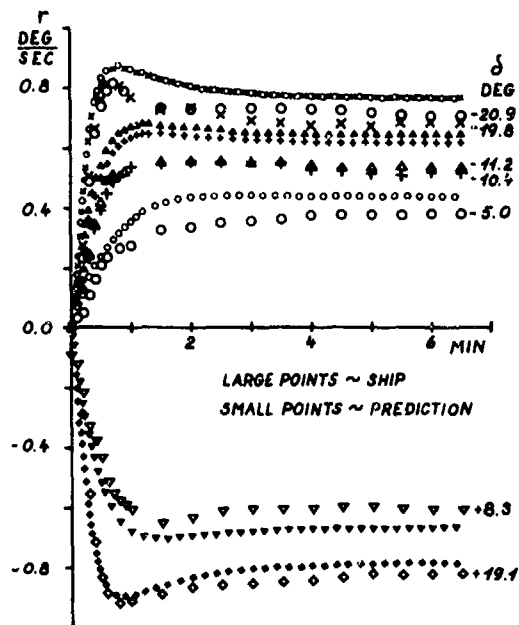


Fig. 16 Turning Circle Time Histories.
Turning Rate and Speed versus
Elapsed Time for various
Rudder Angles and Initial Speeds

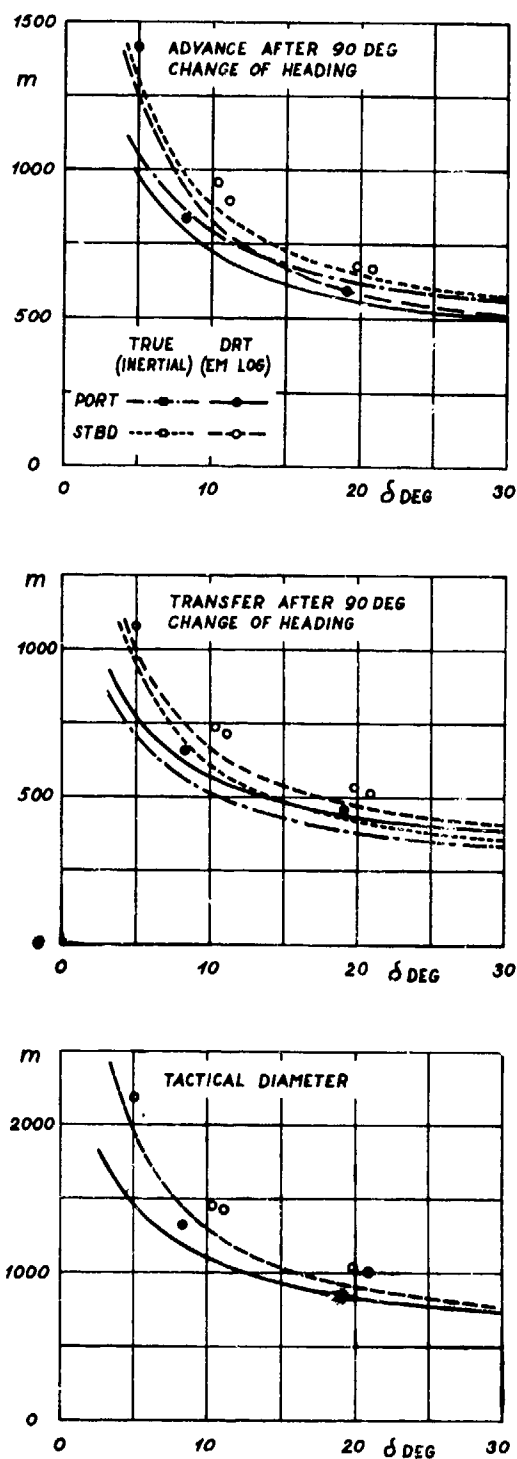


Fig. 17 Turning Circle Parameters. Advance and Transfer after 90 deg. Change of Heading, and Tactical Diameter. Trial Points & Predicted Lines

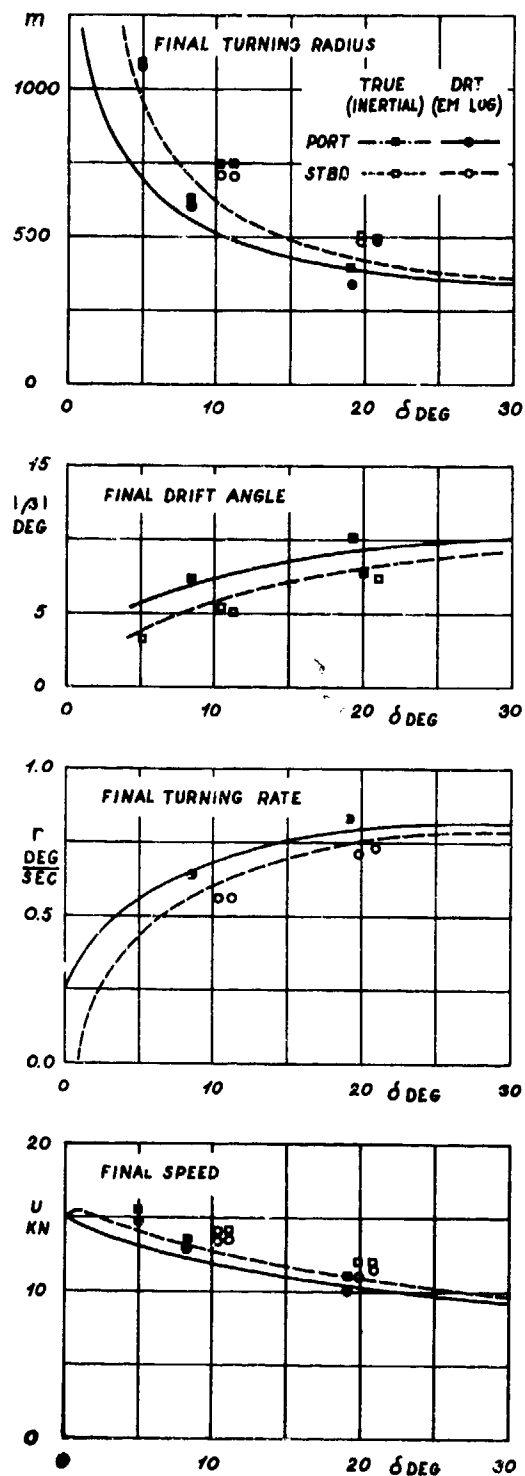
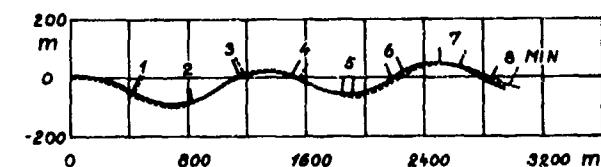
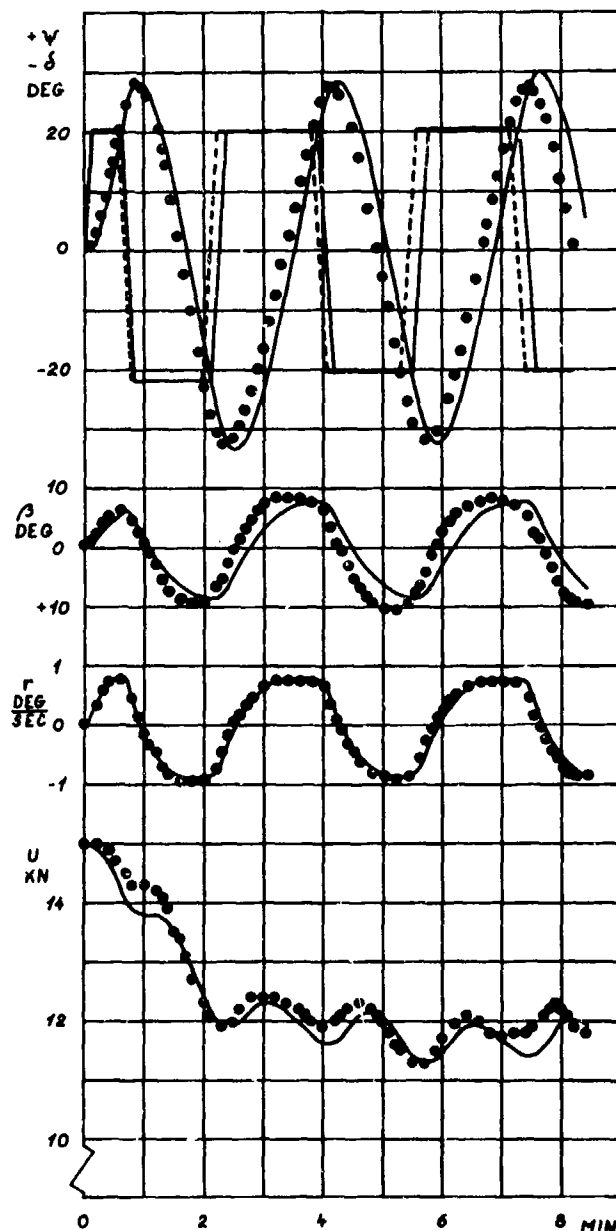


Fig. 18 Turning Circle Parameters. Final Turning Radius, Drift Angle, Turning Rate and Speed. Trial Points & Predicted Lines



DRT predicted and trial paths. The trial is shown with a dotted line, the predictions with a full line. Trial and predicted positions are indicated for each minute of elapsed time.



The prediction has been made with rudder rates, rudder angles and shift angles corresponding to the trial values.

The trial drift angle is from the inertial navigation system, with possibility of cyclic error.

The trial turning rate is from gyrocompass synchro, and probably accurate.

The trial speed is from EM-log, which is thought to be accurate for the moderate speed-loss and drift angles that occur here. Note the truncated speed axes.

Fig. 19 20-20 Zig-Zag Manoeuvre.

Path, Rudder Angle, Heading, Drift Angle, Turning Rate & Speed versus Elapsed Time. Trial Points & Predicted Lines

Spiral Manoeuvre

The full-scale trial and predicted Dieudonné Spiral Test results are shown in Fig. 20, which also includes the final turning rates from the turning circle trials.

Morse & Price interpreted the results of the trials as indicating a small but definite instability loop. It was later shown, however, (9) that the results of a spiral test can exhibit a so-called "sloped-loop" character unless ultra-extreme care is taken in waiting for the speed to settle down (or up) when making the measurements.

The trial results for 5 knots initial speed clearly show this sloped-loop character, which neither confirms nor precludes the existence of instability.

The trial results at 15 knots initial speed are more difficult to interpret, due to the limited number of measurements at small rudder angles, but it is suggested that they indicate the vessel to be marginally stable as is also indicated by the value of the predicted slope of the $r-\delta$ curve:

$$\left(\frac{\partial r}{\partial \delta}\right)_{r=0} = -0.567 \text{ deg/sec/deg.}$$

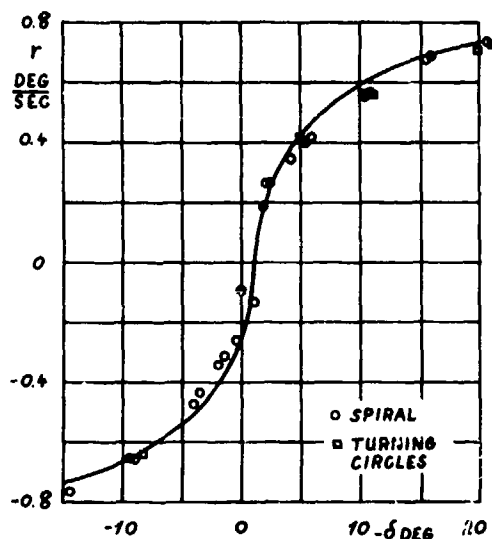


Fig. 20 Spiral Manoeuvre.
Final Turning Rate versus
Rudder Angle.
Trial Points & Predicted Lines

COMPARISON OF CAPTIVE-MODEL TEST TECHNIQUES

Background

The ability to predict full-scale manoeuvres with good accuracy on the basis of large-amplitude, low-frequency PMM tests has been demonstrated in the foregoing section. However, as also reflected in the recommendations of the 1972 ITTC, there is still a need for the comparison of different captive-model test techniques.

The foregoing PMM-tests made at 15 knots approach speed for comparison with full-scale trials at 15 knots, were therefore supplemented with PMM-tests at 20 knots for comparison with the published results of Rotating Arm tests at 20 knots made at NSRDC and AEW (12,13). These two sets of rotating-arm data were chosen for comparison as they were made with comparably large models and under very similar conditions as shown in Table 7.

All three sets of data were made with the ship loading condition defined in Table 1 and all three sets of results represent hydrodynamic effects only, i.e. mass effects, instrument tares etc. have been subtracted or corrected for.

Constraint in heel is one of the few points of difference between the three test conditions, and this can almost certainly be discounted as a source of differences, as the maximum heel angles due to drift angle and yaw rate were 6½ deg and 1 deg respectively for model (12), (maximum final roll angle for ship was 3 deg (7)).

Pure Yaw Results

The pure yaw results, i.e. for zero drift angle, are shown in Fig. 21. The PMM results are shown as measured points and faired lines, the analytical expressions for which are included in the figure.

The PMM results are, due to the nature of the integrating system used, averages of the results for port and starboard turning rates.

The NSRDC results are shown by the broken line which represents the hand-faired line drawn by the authors of (12) through their 16 measured values. The NSRDC tests were only made for starboard turns and the small zero- r' intercepts have been subtracted.

The AEW results are shown by the square points which are averages of the results for port and starboard turns.

The PMM tests were made at 5 and 7 cycles/min of the PMM, corresponding to the normalized frequencies shown in Table 7. As can be seen from Fig. 21, if the measurements are frequency dependent, the effect is negligibly small.

Table 7 Parameters for Cyclic Yaw Test

Speed ship knots	Speed model m/s	N _{PMM} cpm	$\frac{\omega L}{g}$ pp	$\frac{\omega U}{g}$	r' max	t' max
20	2.06	5	1.64	.11	.30	.49
20	2.06	7	2.29	.15	.61	1.40

No corrections have been made for the small difference in the positions of the origins of the axis systems in the models used for the PMM tests and the Rotating Arm tests (see Tables 1, 8 & Fig. 3). An idea of the magnitude of the influence of this difference can be obtained by calculating the changes in the linear coefficients Y_r and N_r using the transformations given in (1). If the PMM test values are transformed to correspond to the origin position used for the rotating-arm tests, the results are:

$$Y'_{r0} : Y'_{rG} :: 330.6 \times 10^{-5} : 315.5 \times 10^{-5}$$

$$N'_{r0} : N'_{rG} :: -234.5 \times 10^{-5} : -235.1 \times 10^{-5}$$

The change in N_r is negligible and the change in Y_r changes the PMM-test results such that they fall almost midway between the two rotating-arm test results.

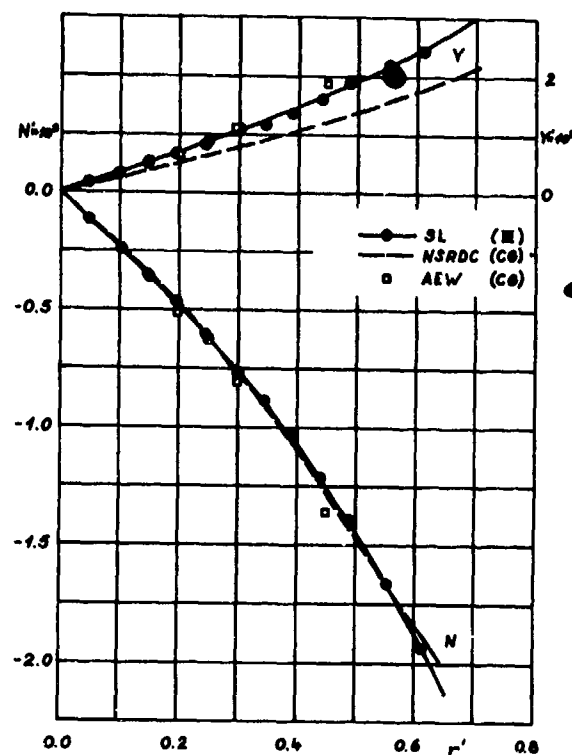
Yaw and Drift Angle Results

Figures 22 and 23 compare the results of the two sets of Rotating-Arm tests and the PMM-tests.

The PMM-test results are compounded from the Pure Yaw test results described above, and Yaw and Drift + Drift and Yaw test results that are completely analogous to those described for 15 knots ship speed.

No corrections have been made for the difference in position of the origins.

The three sets of data can be said to agree remarkably well, with the PMM test results, in general, lying between the two sets of Rotating-Arm data.



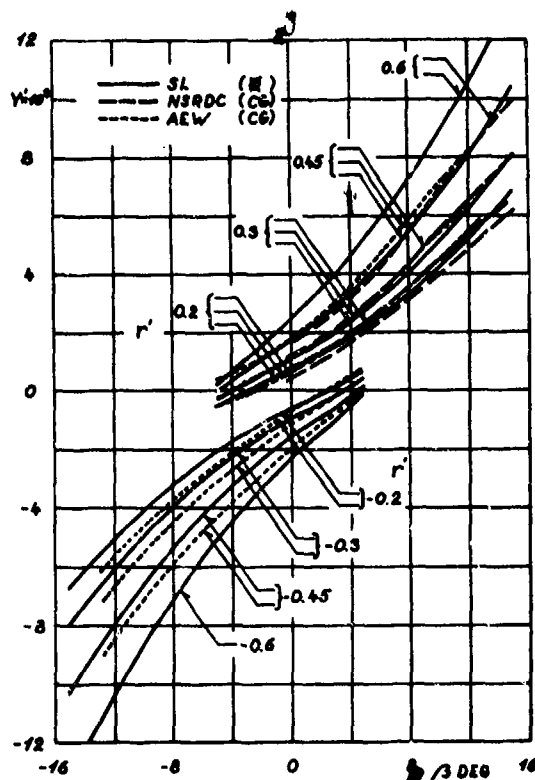
$$Y' \times 10^3 = 3.3055r' + 1.9396r'^3$$

$$N' \times 10^3 = -2.3452r' - 2.1594r'^3$$

Fig. 21 PMM and Rotating Arm Data. Side-Force and Turning-Moment versus Yaw-Rate for Zero Drift Angle.

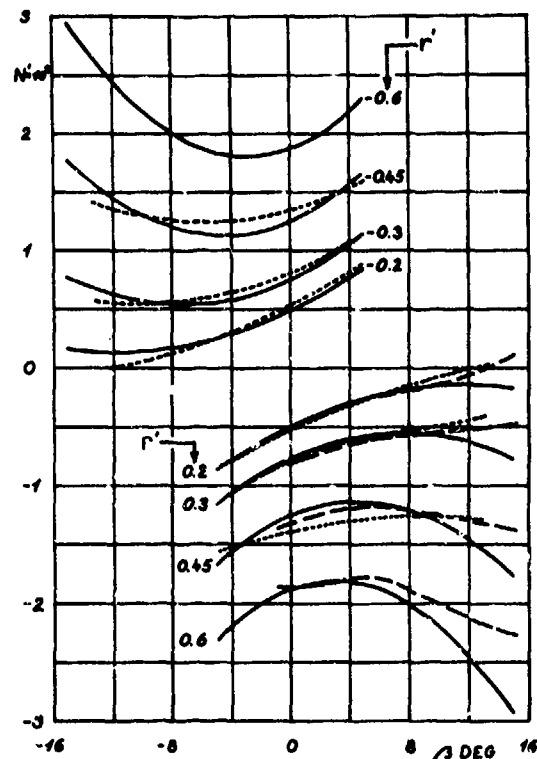
Table 8 Models and Facilities for PMM and Rotating-Arm Tests

	SL	NSRDC	AEW
Linear Ratio	25	24.175	34
Model Lpp, m	6.437	6.657	4.733
Propulsion-point	ship	ship	ship
Bilge-keels	yes	yes	yes
Sonar dome	no	no	no
Free to sink & trim	yes	yes	yes
Free to heel	no	yes	yes
Origin of body axes	stn. 10	nom. CG	nom. CG
Model speed, kn, ship	20	20	20
Facility	PMM	Rot. Arm	Rot. Arm
Basin	Towing Tank	Circular Tank	Offset Rect.



$$Y' \times 10^3 = 0.0478 - 11.5787v' - 25.699v'|v'| + 3.3055r' + 1.9396r'^3$$

Fig. 22 PMM and Rotating Arm Data. Side-Force versus Drift Angle for various Yaw-Rates.



$$N' \times 10^3 = -0.004918 - 3.5978v' + 0.055166v'|v'| - 2.3452r' - 2.1594r'^3$$

Fig. 23 PMM and Rotating Arm Data. Turning-Moment versus Drift Angle for various Yaw-Rates.

CONCLUSIONS

Captive model tests have been made with a 1:25 scale model of a Mariner Class vessel in the loading condition corresponding to the full-scale steering and manoeuvring trials with the USS "Compass Island".

The full capabilities of the SL large amplitude horizontal PMM were utilized to vary the motion parameters over the full range experienced by the ship. This was accomplished at very low normalized frequency by the use of large amplitudes. The added mass in surge was measured at zero speed.

The model test data have been used to simulate all of the full scale manoeuvres made with 15 knots approach speed, namely turning circles for rudder angles between -20° and $+20^\circ$, a 20-20 Zig-Zag and a Dieudonné spiral. The simulated and full-scale trial results have been compared, in accordance with the recommendations of the 1969 and 1972 ITTC's.

No attempts have been made to correct the model data for scale effects, but the tests were made with constant propeller revolutions corresponding to the self-propulsion point for ship at 15 knots, although the trials were made with approximately constant power. Extra simulations were made in order to permit a fair comparison with trial-records of ship path taken from the Dead Reckoning Tracer. The differences between "True" and "DRT" simulations were found to be substantial for turn-entry transients, but small for tactical diameter, steady turning radius and Zig-Zag trajectories.

The correlation between the simulations based on model-tests and the full-scale trial results is found to be excellent, indicating that for this type of ship, the normal SL PMM testing and analysis procedures and simulation techniques give accurate information on actual ship manoeuvring behaviour.

This conclusion should not, however, be generalized as applicable to all ship types.

The large asymmetry in manoeuvring behaviour for port and starboard turns shown by the full-scale trials is also predicted by the model results. It is suggested that the unusually pronounced asymmetry is due to the proximity of the large propeller to the water surface in the light loading condition tested.

Limited tests at the equivalent of 20 knots ship speed made with the SL-PMM have been compared with results obtained with the rotating-arm facilities at NSRDC and AEW. The three sets of data agree rather well, with the PMM results lying, in general, between the two sets of rotating-arm data.

The paper demonstrates the feasibility of using a PMM to measure non-linear and cross-coupling effects corresponding to tight turning manoeuvres, as well as linear effects corresponding to straight-line course keeping.

REFERENCES

1. Mandel, P., "Ship Manoeuvring and Control," Principles of Naval Architecture (revised), SNAME, 1967.
2. Gertler, M., "Final Analysis of First Phase of ITTC Standard Captive-Model-Test Programme," Report of Manoeuvrability Committee, App. III, part 2, Proceedings of the 12th ITTC, Rome, 1969, pp. 601-625.
3. Report of Manoeuvrability Committee, Proceedings of the 13th ITTC, Vol. 2, Berlin/Hamburg, 1972, pp. 993-1006.
4. Chislett, M.S., and Smitt, L.W., "A Brief Description of the HyA Large Amplitude PMM System," Hydro- and Aerodynamics Laboratory Report, Hy-16, Lyngby, 1973. Also Journal of Mechanical Engineering Science, Vol. 14, (No. 7, Supplementary Issue), London, 1972, pp. 80.
5. Chislett, M.S., and Strøm-Tejsten, J., "Planar-Motion-Mechanism Tests and Full-Scale Steering and Manoeuvring Predictions for a Mariner Class Vessel," Hydro- and Aerodynamics Laboratory Report, Hy-6, Lyngby, 1965.
6. Strøm-Tejsten, J., and Chislett, M.S., "A Model Testing Technique and Method of Analysis for the Prediction of Steering and Manoeuvring Qualities of Surface Vessels," Proceedings of the Sixth Symposium on Naval Hydrodynamics, 1966. Also HyA Report, Hy-7, 1966.
7. Morse, R.V., and Price, D., "Manoeuvring Characteristics of the Mariner Type Ship (USS Compass Island) in Calm Seas," Sperry Gyroscope Publication GJ-2233-1019, prepared for David Taylor Model Basin under Contract NOnr 3061(00), 1961.
8. Jørgensen, H.D., and Prohaska, C.W., "Wind Resistance," Report of Performance Committee, App. IV, Proceedings of the 11th ITTC, Tokyo, 1966, pp. 124.
9. Brard, R., "Introduction à l'étude théorique du tangage en marche," ATMA 1948.
10. van Leeuwen, G., "The Lateral Damping and Added Mass of an Oscillating Ship-Model," Shipbuilding Laboratory, Technological University - Delft, Publication No 23, July 1964.
11. Strøm-Tejsten, J., "A Digital Computer Technique for Prediction of Standard Manoeuvres of Surface Ships," Naval Ship Research and Development Center, Report No. 2130, December 1965.
12. Gertler, M., "Cooperative Rotating-Arm and Straight-Line Experiments with ITTC Standard Model (Mariner Type Ship)," David Taylor Model Basin, Report 2221, June 1966.
13. Burcher, R.K., "Co-operative Tests for ITTC, Mariner Class Ship, Rotating Arm Experiments," Written Contribution to 12th ITTC, Rome, 1966.

DISCUSSION

ALEX GOODMAN

The authors are to be congratulated on an excellent paper. It is obvious that the philosophy and application of the PMM system to engineering problems is clearly understood by the authors. They have demonstrated, as have other investigators, that the application of PMM test results and analysis procedures in combination with simulation techniques provide accurate information on actual ship maneuvering behavior. This is further substantiated by the comments of Mr. Uhlin of EXXON. As stated by the Chairman, Dr. C. Bates, "The proof of the pudding is in the eating."

Again let me state that the PMM system is a powerful engineering tool. When it is properly understood and applied, it can provide engineering excellent answers such as illustrated by the present paper.

R.C. UHLIN

I congratulate the authors on their excellent paper and the work they have done to advance this most useful method.

At Exxon we have found that a wide range of tanker maneuvering can be accurately performed by the use of the captured model PMM and computer simulation technique. This conclusion is based on a comparative study in which good full scale maneuvering data for the 190 MDWT ESSO MALAYSIA class tanker have been compared with 1:38 scale model results from the high amplitude and the medium amplitude PMM apparatus that the authors refer to in their paper. A comparison has also been made with free-running tests using this model.

The table below summarizes the differences found between the full scale and model test maneuvering data. The full scale data is based on the average of three sets of good trials on sister-ships.

	High Amplitude PMM	Medium Amplitude PMM	Free Running
Average Difference	+2.15%	+7.02%	-17.65%
Standard Deviation	8.69%	11.56%	13.49%

PERCENTAGE DIFFERENCE BETWEEN FULL SCALE SHIP AND MODEL TEST MANEUVERING DATA

The numbers in the table are calculated from certain measures of the turning circle, the Z-Maneuver, and the spiral test. For the turning circle the

maximum advance and maximum transfer of the ship's center is used, as well as the ratio of initial to final turning circle speed. For the Z-Maneuver the first overshoot angle and non-dimensional time to the first course intercept have been chosen. And finally, for the spiral test the total loop width has been used.

The table shows the average differences of full scale and PMM results to be quite small with the high amplitude PMM having the smaller difference. The plus sign indicates poorer maneuvering response than is found in full scale, while the negative sign indicates the opposite. The comparatively larger difference of the free running model can be attributed to model propeller-rudder forces being too large, a consequence of the hull alone having relatively more resistance than the full scale ship. These forces made the model turn much better than the ship as shown by the large negative value.

Besides using the average difference to indicate the central tendency of the data, it is also important to know how far from the average each of the measurements is located. An indication of this dispersion, or spread, within the data is given by the standard deviation figures appearing in the table. The standard deviation for the high amplitude PMM is seen to have the smallest value, indicating the least amount of data dispersion.

For the past several years we have used PMM test results as input to bridge maneuvering simulators for training and research. We have found that a wide range of maneuvers can be simulated quickly and with minimum cost once PMM results are available. Furthermore, controlled experiments can be conducted, ship motion in time can be properly scaled, and known wind and current effects can be added with comparative ease.

The Danish Towing Tank has gained experience with the operations of a PMM as an important experimental tool for approximately 10 years. The here presented paper shows that many improvements have been made in the PMM, in the measuring technique and in the mathematical model. PMM-techniques for the evaluation of the steering and manoeuvring behaviour of ships are becoming mature and they play an important role in the determination of the steering qualities in the design stage. Both authors have participated in the development from the very beginning. I want to congratulate them with their important contributions with respect to the progress of PMM-techniques.

I want to make a few remarks with respect to a number of details. The ratio of model length to PMM-amplitude is roughly 9. This means that in order to cover the whole range of yaw-speed and drift speed amplitudes one should apply rather high frequencies of oscillation. This is obvious when one looks to the graphs presenting acceleration forces and moments. The model ranges of yaw and drift acceleration are much higher than the ship ranges, because frequency squared appears in the relevant formulae for the accelerations. In this respect the Delft University Towing Tank has gained experience since 1964 when the horizontal PMM was put into service. The ratio between model length and amplitude of this device is about 10. Taking the dimensions of the PMM into account compared to actual ship behaviour when manoeuvring I would like to propose that devices like the Danish and the Delft PMM are called medium amplitude PMM's.

The authors state that the effects of frequencies upon the forces and moments are negligibly small when the dimensionless frequency $\omega L / U$ is smaller than 3. Delft Towing Tank practice has shown that this limit frequency is lower and lies in the vicinity of 1 to 1.5 for some sensitive hydrodynamic coefficients like Y' and N' .

From figure 5 one gets the impression that the coefficients describing the resistance of the ship and the delivered thrust have been determined from these experimental results. This is possible if the propeller rotates with a speed corresponding to the ship's self propulsion point and if a tow rope force is applied to correct for differences between the ship's scaled down resistance and the model resistance.

In this case the propeller revolutions were kept at a constant value. It is, however, possible to include a simple description of the propulsion dynamics together with a constant throttle setting for turbine ships respectively constant fuel supply for dieselships (1).

I like to ask the authors on their opinion with respect to simulation of manoeuvres with constant revolutions.

- (1) Brummer G.M.A., v.d. Voorde C.N., v. Wijk, W.R. Glansdorp C.C.
"Simulation of the Steering- and Manoeuvring Characteristics of a second Generation Containership"
TNO - NSS Report 1708, 1972.

S A R THULIN

I would like to comment on one of this, for manoeuvring people very interesting paper.

Inspired by reference [1], I have analysed the static speed and rudder angle tests, carried out at SL on behalf of SEPA on a twin screw/twin rudder model, by non-dimensionalising the forces and moments on the model due to rudder angles by dividing them by the mean velocity (squared) over the rudder surface.

This velocity approximately consists of two components - the propeller race velocity and the advance velocity at the rudder outside the race (Fig 1) - and can be written

$$v^2 = \frac{1}{A_R} \left[A_P (V_A + k u_{Aoo})^2 + (A_R - A_P) V_A^2 \right]$$

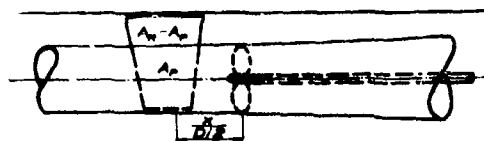


Fig 1. The Effective Rudder Advance Velocity

A factor k has been calculated [2,3,4] for the infinite blade propeller (Fig 2) expressing the induced mean axial velocity in the race, u_A , over the induced velocity far behind the actuator disk, u_{Aoo}

$$k = \frac{u_A}{u_{Aoo}}$$

k is a function of the axial distance from the propeller disk to, in this application, the quarter mean chord of the rudder.

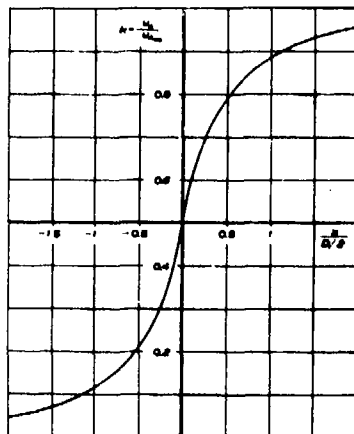


Fig 2. The Mean Axial Velocity Induced by a Semi-Infinite Tube of Ring Vortices Determined by the Law of Biot-Savart

To be able to compute the over-velocity in the propeller race, the momentum theory is applied to the race (Fig 3), see for instance [6].

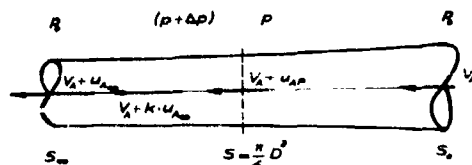


Fig 3. The Propeller Race According to Actuator Disk Theory

Introducing the propeller characteristics the induced axial velocity far behind the disk can be expressed

$$u_{Ao} = -V_A + \sqrt{V_A^2 + \frac{8}{\pi} K_T (nD)^2}$$

or

$$u_{Ao} = -V_A + \sqrt{\left(1 + \frac{8}{\pi} K_T' \right) V_A^2 + \frac{8}{\pi} K_T' (nD)^2}$$

where K_T' , based on $J' = V_A^2 [V_A^2 + (nD)^2]^{-1/2}$

is more suitable for computer calculations [5] and can be taken from Fig 4.

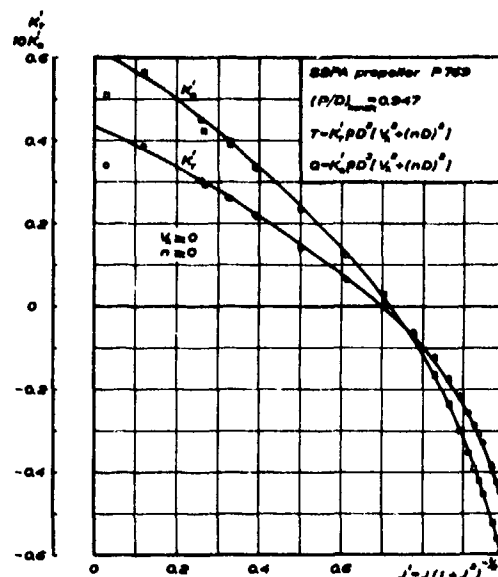
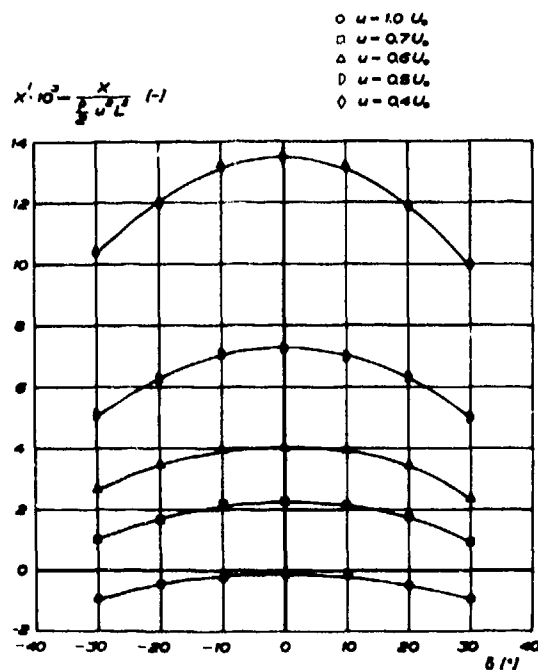
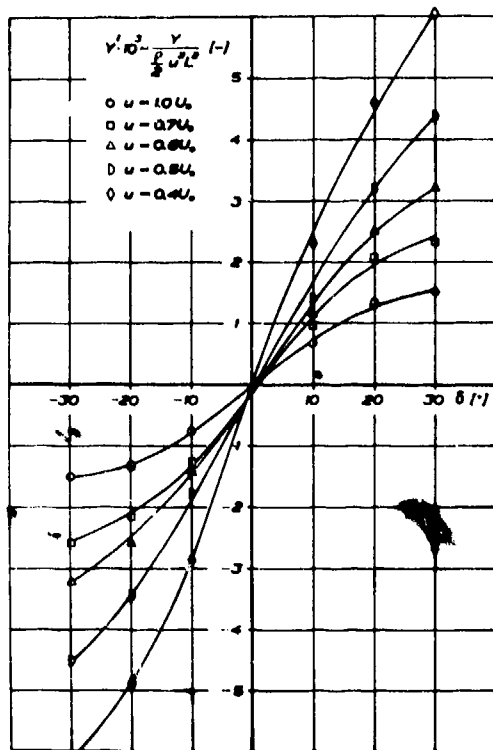


Fig 4. The Extended Propeller Characteristics

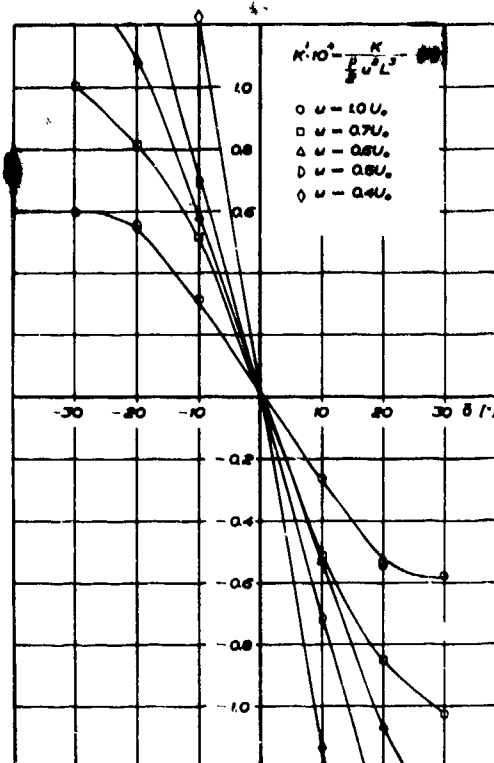
In Fig 5 a, b and c the measured forces and moments on the hull due to the rudder angle are non-dimensionalised with hull speed. Each curve corresponds to a certain overload due to reduced hull speed at constant rate of revolution.



a. Longitudinal-Force versus Rudder Angle



b. Side Force versus Rudder Angle



c. Rolling-Moment versus Rudder Angle

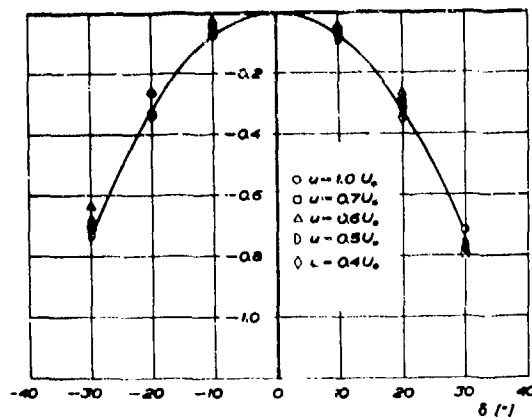
Fig 5. Static Speed and Rudder Angle Test for various Speeds at constant Rate of Revolution

The same measurements are reduced according to the above stated theory and are illustrated in Fig 6 a, b and c. The measured points coincide with the curve obtained from regression analysis with acceptable accuracy for manoeuvre simulation studies.

I think this approach should be very promising in this case and particularly useful when using a stock propeller for the model tests. It would be very interesting to know if this method is applicable with satisfactory result to for instance the model tests conducted with the "USS Compass Island".

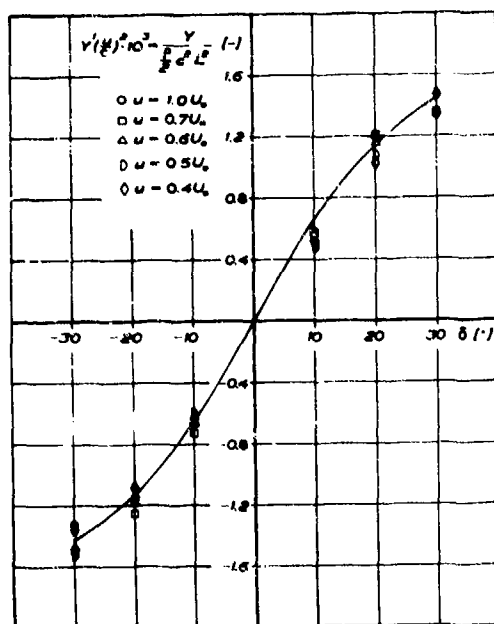
$$X'(\frac{U}{U_0})^2 \cdot 10^3 = (-223.6 \delta^2)$$

$$X'(\frac{U}{U_0})^2 \cdot 10^3 = \frac{X}{\rho U_0^2 L^2} \cdot 10^3 \quad (-1)$$



a. Longitudinal-Force versus Rudder Angle

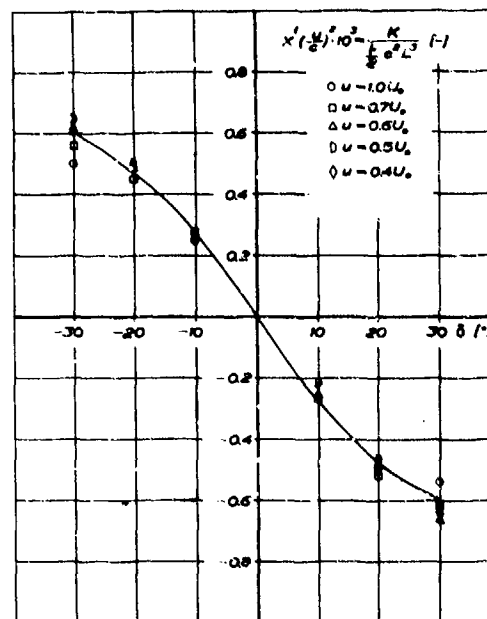
$$Y'(\frac{U}{U_0})^2 \cdot 10^3 = (422.4 \delta - 293.4 \delta^2)$$



b. Side-Force versus Rudder Angle

Fig 6. Static Speed and Rudder Angle Test
Reduced according to Actuator Disk
Theory, Constant Rate of Revolution

$$K'(\frac{U}{U_0})^2 \cdot 10^3 = (-172.4 \delta + 112.8 \delta^2)$$



c. Rolling-Moment versus Rudder Angle

REFERENCES

1. Norrbin, M H: "Theory and Observations on the Use of a Mathematical Model for Ship Manoeuvring in Deep and Confined Waters". SSPA Publ No 68, Göteborg 1971
2. Gutsche, F: "Die Induktion der axialen Strahlausatzgeschwindigkeit in der Umgebung der Schraubenebene". Schiffstechnik Bd 3 (1955) Heft 12/13 S 31-33
3. Okada, S: "Investigation on the Effect of the Propeller Race upon the Performance of Rudder". Hydrodynamical Research of Ship's Rudder. The Second Report". The Technical Research Laboratory, Hitachi Shipbuilding & Engineering Co Ltd 1959. Abstract of report also issued in Hitachi Zonen News No 21, 1961
4. Dyne, G: "A Method for the Design of Ducted Propellers in a Uniform Flow". SSPA Publ No 62, 1967
5. Stephenson, T: "Propeller Constants" ITTC 1960 Subject 7
6. von Mises, R: "Theory of Flight". Dover Publications, Inc New York, 1959

AUTHOR'S REPLY

Mr. Goodman's comments are welcomed by the authors, whose initial interest in captive model testing was inspired by Goodman & Gertler's application of the PMM test method to submarines.

Mr. Uhlin presents a rare and therefore extremely valuable comparison of model and full-scale steering and manoeuvring performance. He compares the average of three good full-scale manoeuvring trials on sister ships, with model results from tests with an 8 m. model, which was tested free-sailing, with the old SL PMM, and with the newer SL PMM. The comparison gives a clear and uncomplicated formulation of the differences. The good agreement in the case of the newer PMM is most gratifying and indicates that it is perhaps not necessary to go to model sizes above 8 m, as is currently under discussion. It would perhaps have been interesting to see the values of standard deviation for the three sets of full-scale trials included in the comparison.

Mr. Uhlin's contribution is especially significant as it deals with a tanker form, i.e. a ship type which because of its course instability can reach very high turning rates and large drift angles, and which therefore necessitates a more powerful test and simulation technique than is the case for the Liner Class of Vessels. It is very encouraging to have a practising shipping-company re-affirm the authors' opinion that PMM-tests can provide useful and commercially viable information.

Mr. Glansdorp is in a very good position to comment on this paper, as he and his colleagues at Delft have developed a sophisticated PMM and simulation system along lines similar to those followed at Lyngby. His proposal to call PMM's with sway amplitude to model length or order 10, "medium amplitude" is intriguing as it hints at a future need for the classification "large-amplitude". For merchant ship forms, sailing with speeds up to values of V/\sqrt{gL} equal to about 0.4, the present amplitude of the SL PMM has been found to be quite adequate. For the 6 to 8 m. models used in these cases, larger amplitude is precluded by the necessity for avoiding wall effects.

As indicated in the paper, the force and moment components due to the acceleration of the model mass and inertia were subtracted from the measured data and only the hydrodynamic components are included in the presentation of experimental results. The ship mass and moment of inertia were then inserted via equation (1, 2, 3) before simulating.

The limit $\omega L/U < 3$ applies to yaw-acceleration and yaw-damping coefficients. The authors agree that sway-damping and to a lesser extent, sway-acceleration responses are more sensitive to frequency effects. However, the ship range of sway-acceleration can easily be covered at low frequency, and as mentioned in the paper, results for $\omega L/U > 2$ have been disregarded in the determination of the coefficients Y_v and N_v . The sway damping terms Y_v and N_v are obtained from the static drift angle tests and the therefore correspond to zero frequency. The yaw damping coefficients N_r etc. have fortunately been found to be less sensitive to frequency, as e.g. demonstrated in Fig. 21, where results for $\omega L/U$ equal to 2.3, 1.6 and 0.0 show good agreement.

It is true that the coefficients $X_{\dot{u}}$, $X_{\dot{u}\dot{u}}$ and $X_{\dot{u}\dot{u}\dot{u}}$ were in this case derived from the model test results, and that the propeller revolutions corresponded to the ship's self-propulsion point. The two-rope force at 15 knots and zero rudder angle can be seen in Fig. 5.

The choice of engine characteristics and the resulting variation of propeller revolutions with speed is one of the flexible features of captive-model testing with a PMM. As mentioned in the paper, the choice of constant power as was the case for the ship, seems to have been counterbalanced by the high ship-resistance due to fouling.

Mr. Thulin's elegant analysis of the speed & rudder test tests for another model, where the measurements were also made with constant revolutions, shows how he uses the test results simply to characterize the interaction between hull, propeller and rudder. Having done this, he is free to make simulations for the ship in question, using any propeller (defined by its open-water characteristic) and for any engine characteristic or engine manoeuvre.

ON A STUDY OF SHIP-CONTROLLABILITY OF A WIDE-BEAM TANKER USING LARGE SCALE MODEL

S. Sato
Hitachi Shipbuilding
& Engineering Co., Ltd.
Osaka, Japan

M. Takagi
Hitachi Shipbuilding
& Engineering Co., Ltd.
Osaka, Japan

T. Takai
Hitachi Shipbuilding
& Engineering Co., Ltd.
Osaka, Japan

ABSTRACT

This paper presents the results of a study of the ship-controllability of a wide-beam tanker ($L/B=5.0$).

The report consists of the following three parts;

- 1) Estimation of the indices of the manoeuvring characteristics of the ship by the method of series tests using similar models which are 4M, 10M, 30M in length.
- 2) Determination of whether or not the ship is unstable in course keeping because of so-called "unusual phenomenon."
- 3) Determination of the feeling of control of the ship with manoeuvring characteristics as estimated by item 1), by means of simulation of the ship's manoeuvres.

The results of this study show that if a large wide-beam tanker has a large enough rudder area ratio, the ship will be controllable.

NOMENCLATURE

A_r =rudder area
 B =ship beam
 C_1 =rudder adjustment (deg/deg)
 C_2 =yaw rate adjustment (deg/deg/sec)
 C_N =normal force coefficient of rudder
 d =ship draft
 G_r =transfer function of steering gear
 G_{s1} =transfer function of ship to rudder action
 G_{s2} =transfer function of ship to wave
 $K, T, T_1, T_2, T_3, \rho$
 ρ =steering quality indices
 K', T' =nondimensional steering quality indices
 r =yaw rate

r' =nondimensional yaw rate
 s =slip ratio
 T_r =representative time of course change
 V =ship speed
 w =wake fraction
 δ =helm angle
 ρ =radius of gyration
 ψ =heading angle
 ψ_s =setting course
 ψ_w =noise, response of ship caused by waves

INTRODUCTION

It has been concluded that, under certain conditions, a large wide-beam ship is attractive from the viewpoint of building costs [1]. However such a hull form requires extensive testing and research before it may be considered to be practical. The controllability of the ship is one of the most important points to be investigated.

In dealing with the controllability of such a large ship there seem to be two important points to be considered. One of them is whether the ship is easy to steer or not. The other is whether the ship has enough stability in course keeping or not.

The former characteristics is confirmed by comparing the steering quality indices of the ship, which are estimated from model tests, to those of conventional ships. Moreover, if we want to check the feeling of the control of the full scale ship, useful conclusions may be drawn from the examination of the response of the ship obtained by a helmsman using a simulation device.

For the latter it is important to investigate the instability in course keeping due to so-called "unusual phenomenon" [2], [3]. As the mechanism of this phenomenon is not yet clear, it is difficult to predict the existence of such a phenomenon in the full scale ship before it is built. But practical conclusions may be obtained by careful experiments using similar models of various lengths [4].

Accordingly three similar models, 4M, 10M, and 29.9M in length, were selected and many kinds of manoeuvring tests were carried out paying particular attention to the scale effect. Basing on these results we confirmed that there would be no trouble in controlling the large wide-beam ship.

SCALE EFFECT AND SELECTION OF LENGTH OF SIMILAR MODELS

As shown above, models 4M, 10M and 30M in length were used in the model tests. Principal particulars of models and the designed ship are shown in Table 1. The profile and body plan are shown in Fig. 1 (which shows the side view of the arrangement of 30 M model). The values of the radius of gyration shown in Table 1 are as calculated for the 10M and 30M model and as measured for the 4M model.

It is obvious that as large a model as possible is desirable to avoid scale effect. However both from expense and also from the accuracy of the results of experiment, too large model

is not desirable.

For steering quality in large amplitude motion, scale effect seems to alter continuously according to Reynolds number. If the steering quality indices can be expressed as functions of frictional resistance C_f just as done in the field of propulsion and resistance of ships [5], the 30M model is large enough to estimate the indices of the full scale ship by extrapolation with sufficient accuracy. This length is also favorable compared with the area of the test, Maizuru-Bay. At least three models are needed to obtain the indices by extrapolation. Thus 4M and 10M models are chosen to provide a proper intervals for extrapolation.

As mentioned above, if the scale effect can be regarded to alter continuously according to Reynolds number, it is reasonable to carry out the tests using perfectly similar models and at same Froude number. All tests executed satisfy these conditions.

Table 1 Principal particulars of models and designed ship.

	4M Model		10M Model		30M Model		Actual ship	
	Full	Ballast	Full	Ballast	Full	Ballast	Full	Ballast
L_{pp} (m)	4.0		10.0		29.9		350.0	
B_{pp} (m)	0.8		2.0		5.98		70.0	
d_f (m)	0.253	0.105	0.632	-	1.885	0.793	22.15	9.12
d_a (m)	0.253	0.137	0.632	-	1.915	1.049	22.15	11.95
Displacement (t)	0.670	0.300	10.49	-	289.5	130.2	462,700	205,900
Ar/L_{xd} (%)	2.40	-	2.40	-	2.40	-	2.39	-
Ar (m ²)	0.0242		0.151		1.35		185.0	
K/L	0.244	0.258	0.234	-	0.230	0.260	-	-
Propeller								
Dia. (m)	0.1109		0.277		0.828		9.7	
Pitch ratio	0.6995		0.6995		0.6995		0.6995	
Number of blades	6		6		6		6	
Speed	0.858m/s	0.912m/s	1.355m/s	-	4.55kt	4.85kt	15.6kt	16.6kt

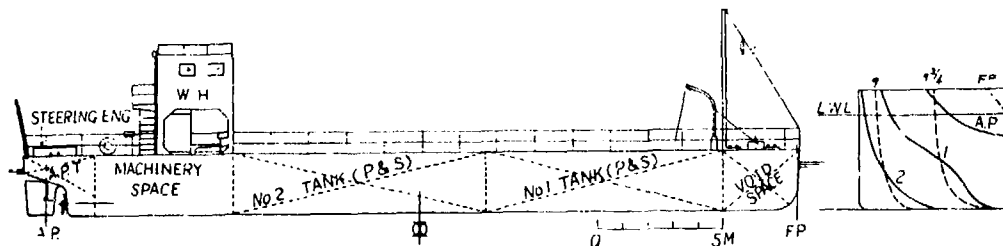


Fig. 1 Profile and body plan of 30 m model.

On the other hand for course keeping quality in relatively small amplitude motion, the flow field is expected to change discontinuously according to Reynolds number and there seem to be complex problems. At first because such a ship is regarded as a blunt body, it comes into question whether Reynolds number related to the dimension of the body perpendicular to the stream, namely ship width, exceeds the critical Reynolds number or not. For the 30M model this number amounts to about 2×10^7 and exceeds the critical Reynolds number $10^5 - 10^6$ sufficiently, so the generation and transformation of the vortices in the model can be regarded to have nearly the same qualitative character as in the full scale ship. The other problem is concerned with the periodic fluctuation of the flow field. If this phenomenon happens and the period of fluctuation coincides with the natural period of yawing motion decided from the autopilot system, the course stability of the ship will become extremely bad. But even in this case, if this periodic phenomenon can be seen to happen in a range of certain Strouhal number, the characteristics of the full scale ship can be estimated from the model test so long as they are carried out in the same Froude number as the one of the full scale ship.

ESTIMATION OF THE STEERING QUALITY OF FULL SCALE SHIP FROM MODEL TEST RESULTS

Manoeuvring Tests Using 4M Model

Method and kinds of model tests.

Model tests were carried out at the manoeuvring test facility of Osaka University. A free-sailing model with radio control was used in the tests. Zig-Zag tests and reversed spiral tests are carried out automatically by means of electronic circuits and the data are recorded on a recorder on board. Model speed which corresponds to the sea speed was produced by setting the propeller revolution to the value obtained from the speed trial. Only this model was not fitted with bilge keels.

Kinds of tests executed are as follows;

(1) Full load condition

i) Original hull + Original rudder

- a. Turning test ($\pm 40^\circ$, $\pm 35^\circ$, $\pm 25^\circ$, $\pm 15^\circ$, $\pm 10^\circ$, $\pm 5^\circ$).
- b. Spiral test and reversed spiral test
- c. Zig-Zag test ($\pm 20^\circ$, $\pm 15^\circ$, $\pm 10^\circ$, $\pm 7.5^\circ$, $\pm 5^\circ$).

ii) Original hull + Original rudder + Fin (fitted to emphasize "unusual phenomenon"[3])

- a. Spiral test.
- b. Zig-Zag test ($\pm 10^\circ$, $\pm 7.5^\circ$, $\pm 5^\circ$).

iii) Original hull + Small rudder (78% of original rudder area)

- a. Spiral test.
- b. Zig-Zag test ($\pm 10^\circ$, $\pm 7.5^\circ$, $\pm 5^\circ$).

(2) Ballast condition

i) Original hull + Original rudder

- a. Turning test ($\pm 40^\circ$, $\pm 30^\circ$, $\pm 20^\circ$, $\pm 10^\circ$, $\pm 7.5^\circ$).
- b. Spiral test and reversed spiral test.
- c. Zig-Zag test ($\pm 20^\circ$, $\pm 10^\circ$, $\pm 7.5^\circ$, $\pm 5^\circ$).

Test results

(1) Zig-Zag tests. Steering quality indices obtained from the usual K-T analysis of the Zig-Zag tests are shown in Figs. 2 and 3, in which the results were nondimensionalized using approach speed. (Same as in 10M and 30M model).

From these results the type of so-called "unusual phenomenon" which is characterized by stabilization in the range of small amplitude motion can not be found.

Results of the full load condition with fin are more stable and those of the small rudder are less stable than the results of the original type.

(2) Turning test, spiral test and reversed spiral test. The results analyzed by usual method are shown in Figs. 4 and 5.

Nondimensional turning rate was obtained from steady turning circle in the case of the turning test. In other cases it was calculated from the measured turning rate and model speed during the turning which was estimated from approach speed and speed drop curve derived from turning test.

Full width of the hysteresis loop is about $2 - 3^\circ$ for full load condition and in the case of ballast condition the ship is stable.

Another type of "unusual phenomenon", which is characterized by periodic yawing motion during the spiral test was not observed. But the data scatters a little in r/δ curve even though such the improper points as

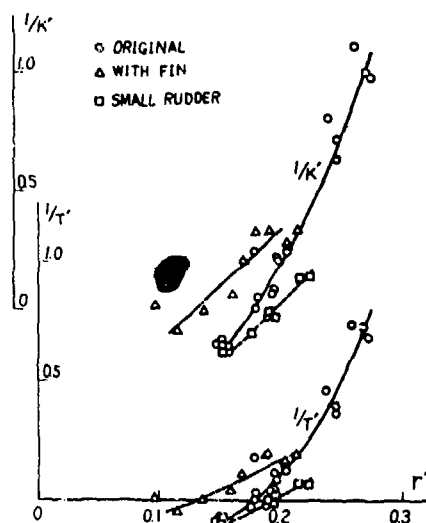


Fig. 2 Indices K' and T' derived from zig-zag test (4 m model) full load condition

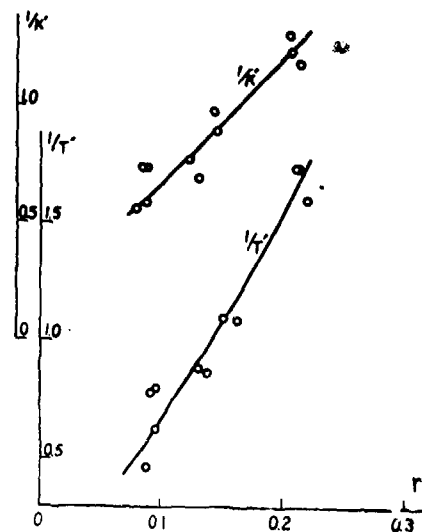


Fig. 3 Indices K' and T' derived from zig-zag test (4 m model, ballast condition)

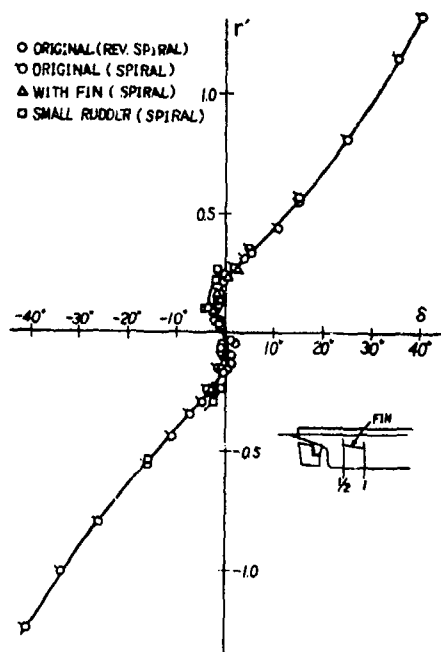


Fig. 4 Turning characteristics (4m model, full load condition)

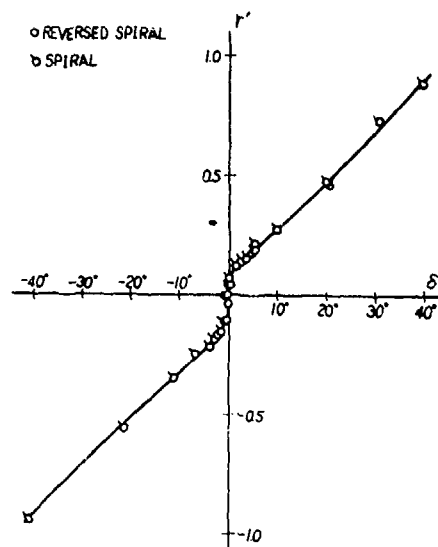


Fig. 5 Turning characteristics (4 m model, ballast condition)

affected by the wind were neglected. This phenomenon happened especially in port side turning with small helm angle but propeller revolution did not change during such tests in 4M model.

Manoeuvring Tests Using 10M Model

Method and kinds of tests.

Tests were conducted at an irrigation reservoir in southern part of Osaka City. This pond has about 200M x 500M area and about 4M depth and seems extensive enough for this model. The method of tests is the same as the conventional one but in this case the model was controlled by two persons on board and propelled by a D.C. motor. Kinds of tests are as follows;

(1) Full load condition

i) Original hull + Original rudder

- a. Turning test ($\pm 40^\circ$, $\pm 35^\circ$, $\pm 30^\circ$, $\pm 20^\circ$, $\pm 10^\circ$, $\pm 5^\circ$).
- b. Zig-Zag test ($\pm 20^\circ$, $\pm 15^\circ$, $\pm 10^\circ$, $\pm 7.5^\circ$, $\pm 5^\circ$).
- c. Spiral test and reversed spiral test.

ii) Original hull + Small rudder (83.9% of original rudder area)

- a. Spiral test and reversed spiral test.

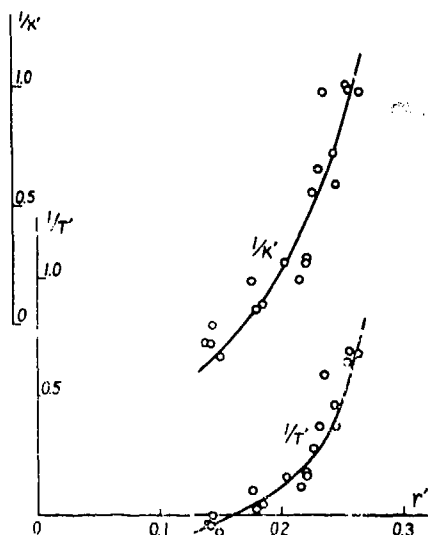


Fig. 6 Indices K' and T' derived from zig-zag test (10 m model, full load condition)

Test results

(1) Zig-Zag test. Steering quality indices obtained from the usual K-T analysis of the Zig-Zag test are shown in Fig. 6.

For the original rudder, "unusual phenomenon" of having stable indices in small amplitude motion is not seen.

(2) Turning test, spiral test and reversed spiral test. The results obtained from same analysis as 4M model are shown in Fig. 7. For the original rudder, the "unusual phenomenon" of having two or more equilibrium conditions in the $r'-\delta$ curve occurs more markedly than with the other models.

The details of this phenomenon are shown in Figs. 8 and 9 which were obtained from analysis of the reversed spiral test. As the experimenter found a change of propeller revolution during the test, the test was continued for many hours and repeated many times. Especially in the tests of the small rudder, this phenomenon was seen distinctly and the difference between mean values of helm angle are about 5 degrees as shown in Fig. 9.

In this case the change of state was distinguished by experimenter and a remarkable feature is that the propeller revolution changes at the same time. When the experimenter steers the ship so as to keep a certain yaw rate, the mean helm angle to keep this yaw rate decreases suddenly and the propeller revolution increases at the same time.

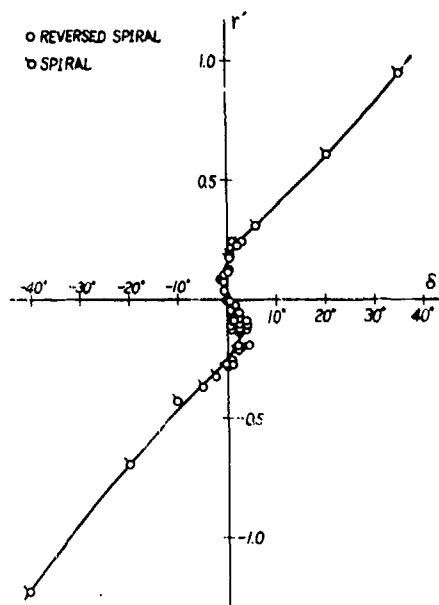


Fig. 7 Turning characteristics (10 m model, full load condition)

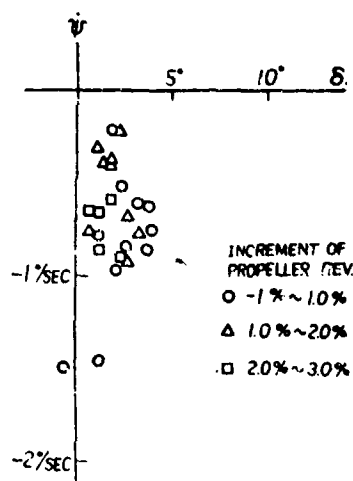


Fig. 8 Unusual phenomenon in turning characteristics (10 m model with original rudder, full load condition)

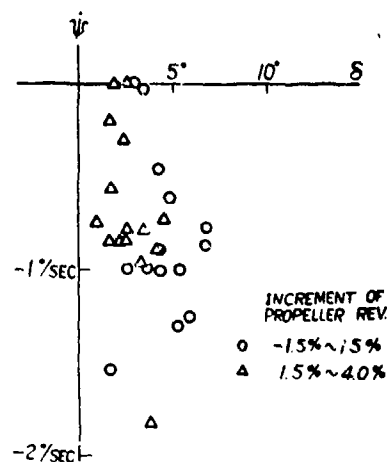


Fig. 9 Unusual phenomenon in turning characteristics (10 m model with small rudder, full load condition)

Manoeuvring Tests . g 30M Model

Model ship and measuring system.

(1) Ship hull and engine. The side view of the general arrangement is shown in Fig. 1. As shown before propeller, rudder, etc. are all similar to those of the ship. Only this model was made of steel and the model surface was prepared to keep the smoothness according to Japanese standards. The constructed surface was very smooth and accurate. The welding beads were smoothed by grinding except for the fore peak part which was regarded as a turbulence stimulator.

The main engine is a 40 PS marine diesel with reduction gear and clutch and it is controllable from the wheel house. The engine revolution was very steady even at slow revolutions.

(2) Steering gear. The steering gear is an important instrument in this experiment and was selected with great care. Principal particulars are as follows;

- i) Type; electro hydrolic
- ii) Maximum helm angle; $\pm 9.5^\circ$
- iii) Steering speed; 8.2 sec. from 35° to 30° of opposite side (Corresponds to 28 sec. for 350M ship).
- iv) Maximum error of actual helm angle to settled angle; 0.5°

A block diagram of the steering system is shown in Fig. 10. The difference between this system and that of the ship is as follows;

- i) Dead band of the steering gear is larger in the 30M model than in the ship.
- ii) On-off control was used for the 30M model while proportional control was adopted for the ship.

The above differences are considered to injure the stability of auto-pilot steering control loop. But in other kinds of tests such a difference does not affect the test results.

(3) Measuring system. The outline of the measuring system is shown in Fig. 11. With some exception, almost all instruments are similar to those used in manoeuvring tests of ships' trials. However since the current meter gave frequent trouble, the chip log method was used exclusively.

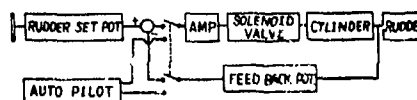


Fig. 10 Block diagram of steering system in 30 m model

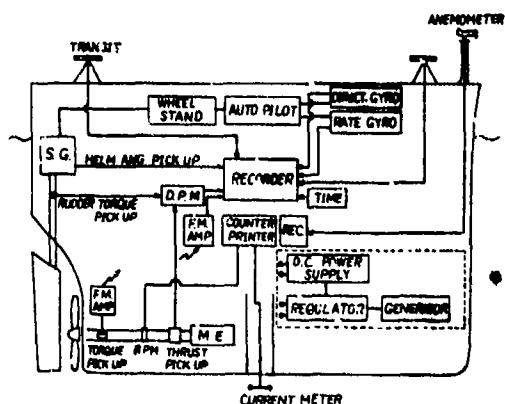


Fig. 11 Measuring system in 30 m model

(4) Auto pilot. The auto pilot system was constructed to simulate the ship motion controlled by auto pilot. The signals of the directional gyro and the rate gyro are fed into this system and the combined signal is fed to the steering gear. In this circuit, dead band or backlash can be added as a weather adjustment. Also, electric noise can be inserted for the purpose of simulation of course keeping in waves. Figs. 12 and 13 shows the circuit and block diagram of this system.

(5) Sea surface. Tests were carried out in Maizuru Bay. Water depth is 12-20M and shallow water effect can be neglected. As the bay is surrounded by mountains, the wind is relatively weak and as the fetch is short, the wave height was not over 50 cm even with 10 m/sec. winds. A condition with wind velocity of less than 3 m/sec. was chosen for the tests of very small amplitude motion.

Method and kinds of tests. Tests were carried out by operators and experimenters on board. The procedure of experiments and method of analysis are almost same as those of a ship trial. The relation between propeller revolution and ship speed was obtained from speed trials between mile posts. The turning circle was obtained from the continuous record of the angle between two transits on deck, by which experimenters traced a buoy fixed by anchors. The reversed spiral test was carried out by changing the rudder set switch while looking at the output of rate gyro indicated on a digital volt meter (Fig. 12). The same method was used in the Zig-Zag test. In the course keeping test, the model ship was set to run in a straight course with various auto-pilot gain settings. The same test was also conducted with noise. Course

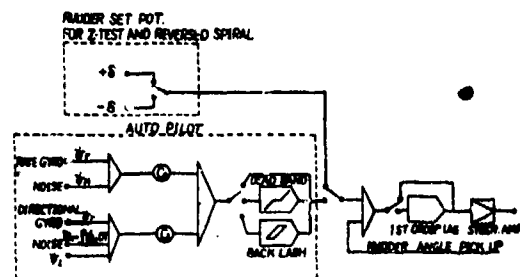


Fig. 12 Auto pilot circuit in 30 m model

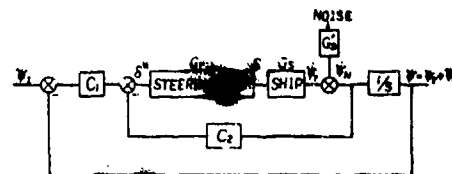


Fig. 13 Block diagram of auto pilot system

keeping tests by helmsman were also carried out. Rudder and hull used in the test was the original type only. Kinds of tests are as follows;

- (1) Full load condition
 - a. Turning test ($\pm 37.5^\circ, \pm 15^\circ, \pm 5^\circ$).
 - b. Spiral test and reversed spiral test.
 - c. Zig-Zag test.
 - d. Course keeping test.
- (2) Ballast condition
 - a. Turning test ($\pm 37.5^\circ$)
 - b. Spiral test and reversed spiral test.
 - c. Zig-Zag test.

Test results

(1) Turning locus. One of the results of the turning tests is shown in Fig. 14. The turning loci of the full load condition before steady turning and those of the ballast condition are not smooth and this can be considered to be due to the effect of wind. From the results of calculation, the loci drift by definite distance to definite direction under constant wind [6]. So the steady state loci were modified using direction and distance of drift which were obtained from the results of the steady state turning test. Modified loci are also shown in Fig. 14.

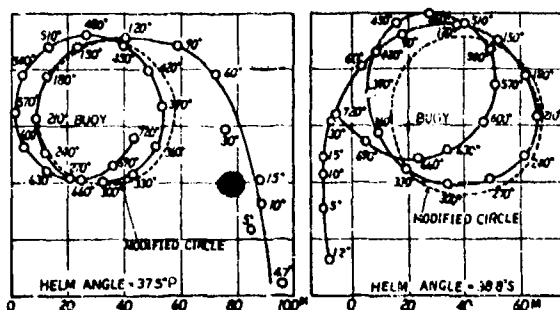


Fig. 14 Turning locus (30 m model, full load condition)

(2) Turning test, spiral test and reversed spiral test. The results are shown in Fig. 15 and 16. The ship speeds used to nondimensionalize the results were based on the chip log method.

The record of the heading in the spiral test shows a slight but not periodic fluctuation while the helm angle was fixed. The scattering of the $r'-\delta$ curve seems to be remarkable, which is regarded to be due to the fluctuation of the flow field. In this case, the qualitative trend of fluctuation of propeller revolutions was the same as that of the LOM model but not so remarkable as in the case of LOM model.

On the other hand, scattering in the $r'-\delta$ curve cannot be found in ballast condition. In this case, the stabilization at small helm angles is clearly seen as in the Zig-Zag test.

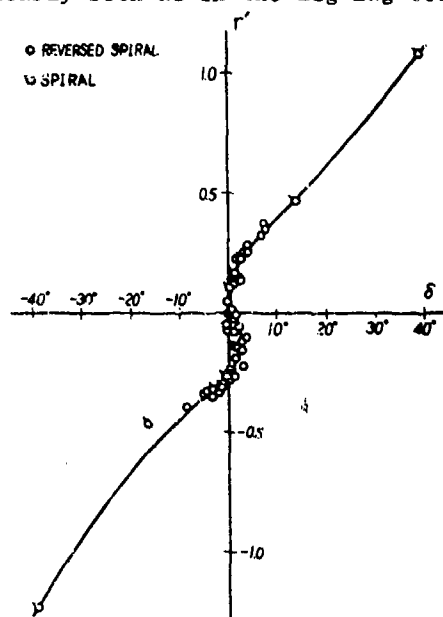


Fig. 15 Turning characteristics (30 m model, full load condition)

(3) Zig-Zag test. Results obtained from the usual K-T analysis are shown in Figs. 17 and 18. In the full load condition, the indices show more stable characteristics in the range of small helm angle.

In the ballast condition, the indices are considerably different from those of the 4M model and the "unusual phenomenon" of having stable indices in small amplitude motion seems to occur.

(4) Course keeping test.

a. Without electric noise. Some of results are shown in Figs. 21 and 22 in which rudder adjustment, rate adjustment and width of deadband were varied.

From these results a slight yawing of long period is observed. It must be examined carefully as to whether this is due to the deadband of the amplifier of the steering gear or due to abnormal fluid forces acting on the hull.

b. With electric noise. One of the results is shown in Fig. 23 which was obtained from the record of the course keeping test by auto-pilot in which electric noise was applied. The noise applied was calculated for this model length using the spectrum which was measured by Koyama during the voyage of a 150M length cargo ship in the North Pacific Ocean (in the condition Sea 6, Swell 7, Wind 15 m/sec.) [7].

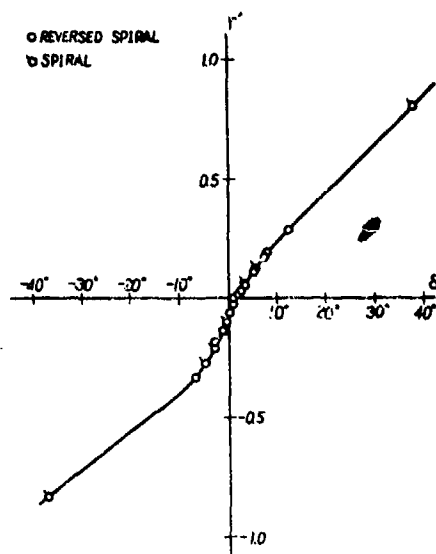


Fig. 16 Turning characteristics (30 m model, ballast condition)

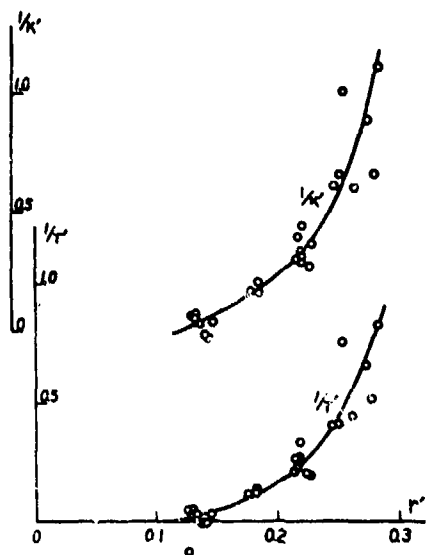


Fig. 17 Indices K' and T' derived from zig-zag test (30 m model, full load condition)

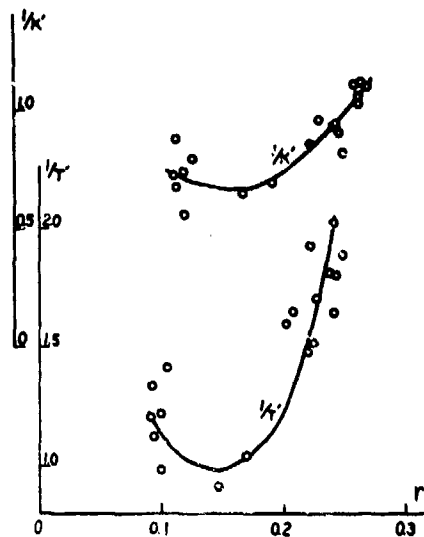


Fig. 18 Indices K' and T' derived from zig-zag test (30 m model, ballast condition)

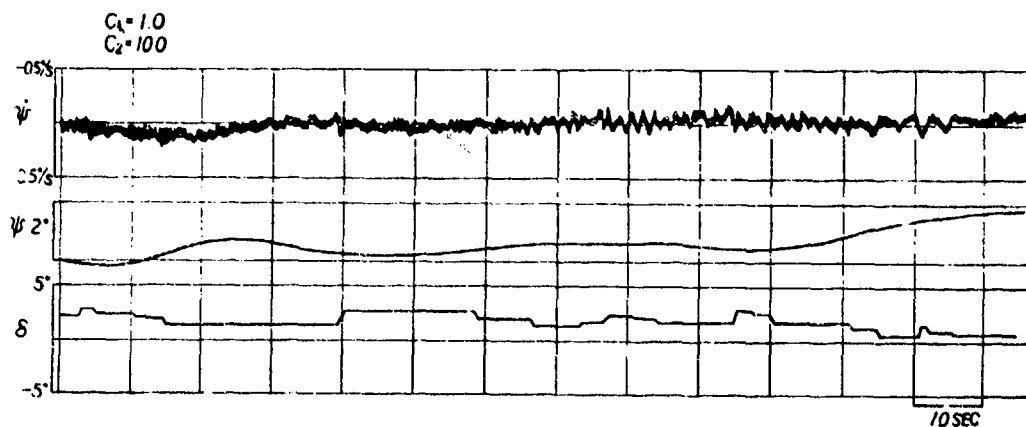


Fig. 19 Results of course stability test (30 m model, full load condition, without electric dead band and back lash)

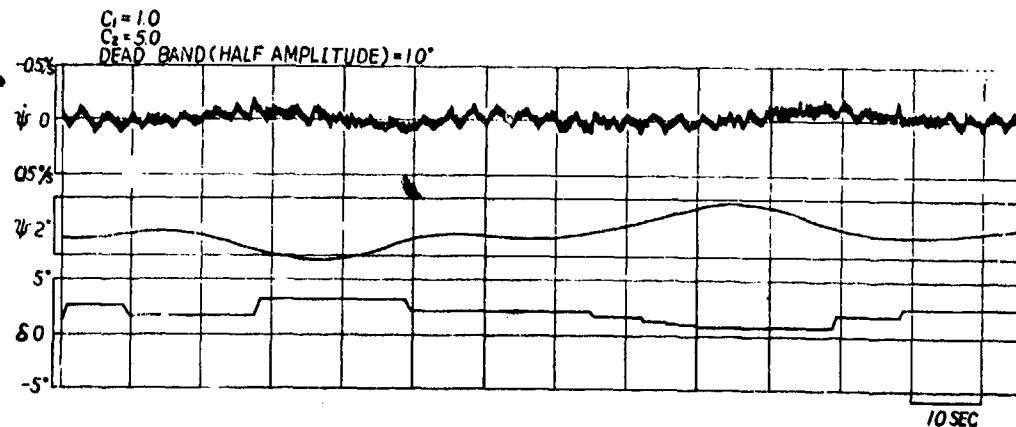


Fig. 20 Results of course stability test (30 m model, full load condition, with electric dead band)

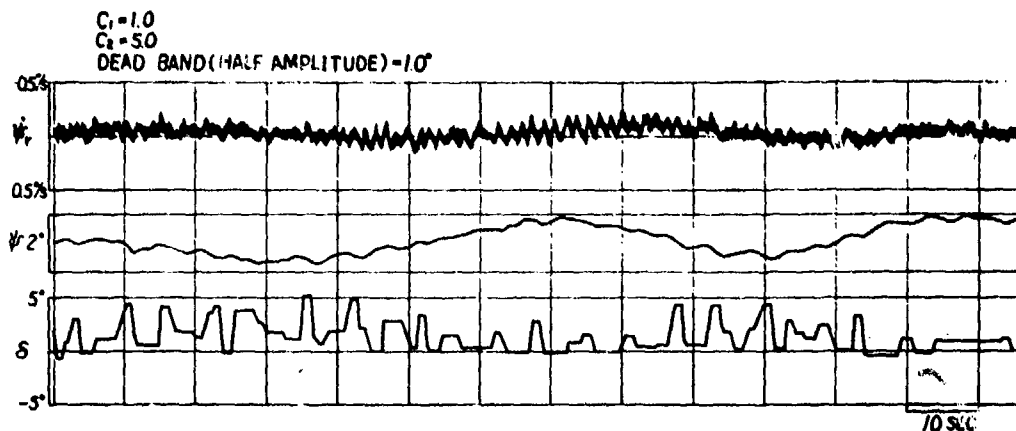


Fig. 21 Results of course stability test (30 m model, full load condition, with electric dead band and noise)

Comparison of variance of heading angle and helm angle with noise and without noise are as follows;

Variance	Without noise	With noise
$\psi (\text{deg}^2)$	0.438	0.677
$\delta (\text{deg}^2)$	0.775	1.478

REMARKS ON THE RESULTS OF THE MODEL TESTS

Scale Effect on Manoeuvrability

Mean lines of the results of the Zig-Zag tests for the three models are shown in Figs. 22 and 23.

From these results, it appears that the steering quality of this type hull form seems to be influenced slightly by Reynolds number in relatively large amplitude motion taking into account the scattering of the measured points and the difference of the radius of gyration. However, definite conclusions on scale effect must await the results of full scale ship trial.

On the other hand for small motions, an obvious scale effect exists even if the scattering of the measured points are considered. This effect has an opposite tendency to conventional results, in which the smaller model is more stable than larger one because the rudder force is larger in smaller model owing to strong propeller slip and because yaw damping moment due to trailing vortices tends to be generated in smaller model.

Two factors may explain the above phenomenon. It is mentioned that the trailing vortices, which produce a yaw damping moment, tend to be generated and to be strongest as the Reynolds number decreases because of the separation of the flow outside the boundary

layer. But, in a wide beam ship as this type, it can be considered that the flow pattern has a same tendency as a flat plate wing and the trailing vortices may actually become weaker as the Reynolds number decreases. We can also suppose that in a small model such vortices may be weak owing to the strong propeller suction. These factors seem to affect on the phenomenon, but we can not draw concrete conclusions because fundamental experiments have not yet been carried out.

Next we consider the normal force acting on a rudder which is placed in a strong wake as with the present ship. In the case of a very large tanker, there is considerable area of the rudder on which the propeller race has no influence. This part of the rudder produces a stronger normal force in a large model than in a small model. Thus, even though the rudder part in the propeller race generates a smaller force, the total rudder force may be larger in a large model than in a small model. To confirm this, a brief calculation was conducted under some assumptions. The value of wake fraction used in the calculation was obtained by extrapolating the value which was derived from 6.7M self-propulsion test, according to Yazaki's chart [8]. The propeller revolution was derived from the model tests for each model and estimated by conventional methods for the ship. In the calculation, the rudder was divided into two parts by the horizontal line tangent to the upper edge of the propeller blade and the normal force on each part was calculated separately. The horn was excluded from the parts. Aspect ratio of each part was decided on the assumption that each part has a same characteristics as a double mirror image body with respect to the boundary line. Normal force coefficient was cal-

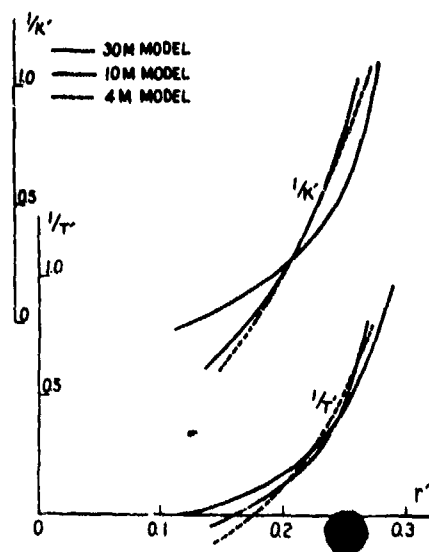


Fig. 22 Scale effect on the indices K' and T' (full load condition)

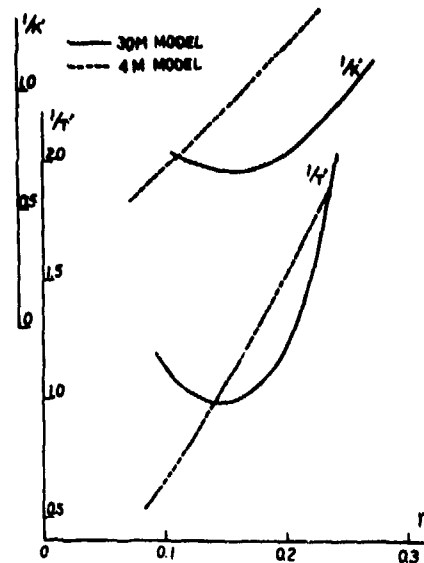


Fig. 23 Scale effect on the indices K' and T' (ballast condition)

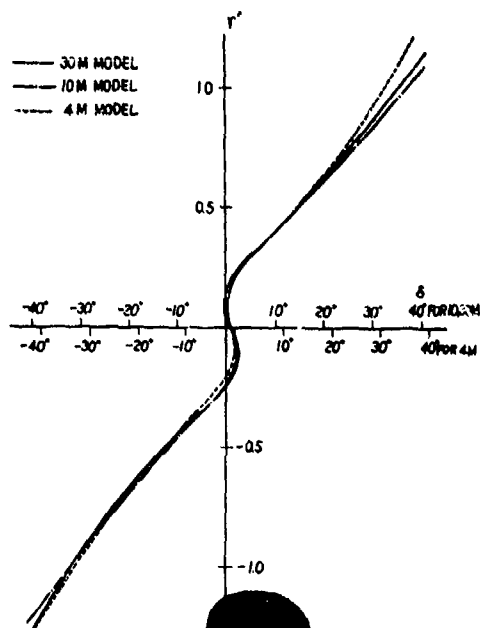


Fig. 24 Scale effect on the turning characteristics (full load condition)

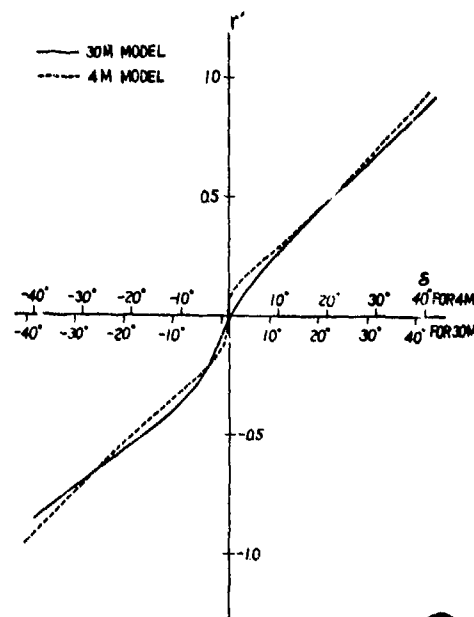


Fig. 25 Scale effect on the turning characteristics (ballast condition)

culated by Okada's formula [9] and shown in Table 2, in which C_{N2} shows the normal force coefficient for the part placed in propeller race, C_{N1} shows that for out of propeller race and C_N shows the total normal force coefficient.

From the calculation it can be seen that the normal force coefficient varies according to the change of wake fraction and the steering becomes stable as the model length increase.

There seems to be only a slight difference between the 30M model and the ship. It is notable that not only C_{N1} but also C_{N2} increase as the model becomes large. However for large motions the wake decreases and the differences of the results between each model becomes small.

As was stated earlier, the only 4M model was not fitted with bilge keels. The University of Osaka Prefecture was asked to examine this effect. From the results steering quality with bilge keels is more unstable than that of without bilge keels but the qualitative conclusion does not change.

In ballast condition 30M model ship is more stable in a range of small helm angle than 4M model. This seems to be due to so-called "unusual phenomenon" but not due to difference of normal force acting on rudder, because in ballast condition normal force is produced from C_{N2} mostly and increment of C_{N2} is very small. Unusual phenomena on K' , T' are discussed later.

Also in ballast condition there are obvious differences in K' and T' . However because ballast model tests with the 10M model were not conducted (as it was not considered to be important) and because we do not have other available data, we will put off any conclusions until the ship trial is carried out.

Mean lines of $r'-\delta$ characteristics of each model are shown in Figs. 24 and 25, in which the abscissas are shifted to coincide the point $r'=0$. In the range of small helm angle, the 30M model is clearly more stable than the 4M model but in full load condition the differences are not clear. This seems to be because the flow field is stable in the ballast condition while it is not in full load condition.

In the range of large amplitude motion there is only a small scale effect. The discrepancy of the tendency between turning characteristics and K' , T' may be due to the differences of the mode of the motion.

Table 2 Coefficients of normal forces acted on rudders.

L (m)	4.0	10.0	29.9	350
1-w	0.37	0.406	0.456	0.543
s	0.747	0.709	0.662	0.488
C_{N1}	0.331	0.400	0.503	0.712
C_{N2}	Star-board	1.80	2.06	2.44
	Port	2.11	2.38	2.70
C_N	Star-board	1.454	1.67	1.98
	Port	1.69	1.92	2.23

"Unusual Phenomenon"

"Unusual phenomenon" in manoeuvrability is the name used by Nomoto for a phenomenon that is characterized by the stabilization of manoeuvrability in small amplitude motion where yaw damping is essentially small [2]. This phenomenon is said to happen more frequently in small models, but in the present study the rather large model appears to indicate this phenomenon in the ballast condition.

Nomoto has stated that "unusual phenomenon" is apt to happen if two trailing vortices are generated from the bilges when the ship runs in a straight course. Such vortices become stronger as the Reynolds number increases if there is strong twisted flow outside of boundary layer (the flow field around a wing, a light draft ship and a wide beam ship in trim condition seem to correspond to this situation). Even if there is not such a strong twisted external flow, trailing vortices are generated when the external streamwise flow is apt to separate (full load condition rather corresponds to this case). In such a case trailing vortices are supposed to be stronger as the Reynolds number becomes small.

Accordingly, "unusual phenomenon" in ordinary ship forms tends to occur as the models become small. But if the flow field is affected by propeller suction, "unusual phenomenon" is supposed to happen in large models also. "Unusual phenomenon" in ballast condition shown in the present study seems to be subjected to twisted flow. But as there are few data for ballast condition, it is difficult to derive a certain conclusion.

In the full load condition, the type of "unusual phenomenon" as noted by Nomoto was not found, but another type of "unusual phenomenon" in small amplitude motion was found. The phenomenon of having two equilibrium conditions in $r'-\delta$ characteristics (we can not distinguish clearly but it seems to have two conditions on the average) can be supposed to have the same mechanism as mentioned before. But in this case, the

generation of vortices is not steady and the turning characteristics become unstable if such vortices are generated and vice-versa. And if the generation and extinction of vortices is periodic in connection with the stern flow field, the ship results in self-excitation during the course keeping by auto-pilot as shown in small cement carrier [3].

In the case of the present ship, the vortex generation and extinction does not seem to be periodic from the data of spiral test (helm angle is fixed in the test) and therefore the ship should not experience this problem.

Next we consider about the reason why the above mentioned phenomena tends to happen in port side turning and why the propeller revolutions increase when the steering quality becomes stable. (Figs. 8 and 9). As shown in Fig. 26 when the steering quality becomes stable, a vortex from the starboard side, which turns in a anti-clockwise direction, extincts and then the load of the propeller, which turns in a clockwise direction, decreases and the revolutions increase. If we can say that the generation and extinction of a vortex outside the bilge of turning ship is affected by the suction [10] in upper half propeller disk, the suction is weaker in the second quadrant in starboard side turning than the first quadrant in port side turning owing to the direction of propeller revolution. For this reason the vortex remains in port side when the ship turns to port side and stabilization is apt to occur.

In addition to this, the increase of propeller revolution contributes to stabilizing moment. But because more scattering is seen with the small rudder than with the original one, the former effect seems to dominate. Therefore in the case of such a wide beam ship as studied in this report, it is desirable to have a large rudder area.

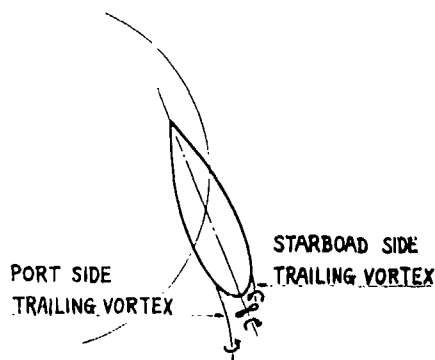


Fig. 26 Schematic diagram of the mechanism of unusual phenomenon

Investigation of Manoeuvrability from the View-point of Design

At first we consider the course keeping quality. As shown Fig. 19 if a weather adjustment such as dead band and backlash is not included in the auto-pilot system, maximum yawing amplitude is about 2 degrees and full-width of check helm is also about 2 degrees. This amplitude of yawing is by no means small but because an on-off control steering system was adopted in this study and also because it has some mechanical back lash, this is easily improved by adopting the excellent steering system in the actual ship.

Relation between width of hysteresis loop and amplitude of check helm is shown in Fig. 28 for several ships, which was obtained from the course keeping test during the speed trial. In this figure, "H" indicates the results of human operator and "A₁" and "A₂" indicate the results of auto-pilots of different manufacture. Because of large scattering in the relation between loop width and check helm, the range of scattering is shown in figure and the straight line shows the envelope of the maximum value of "A₁". As these actual ships did not get into trouble, we can conclude that in the case of 30M model 2 degrees of check helm versus about 2 or 3 degrees of hysteresis loop is an average value in comparison with the figure and the "unusual phenomenon" does not injure the course keeping quality.

Next we consider the period of yawing. Although the precise period can not obtain from Fig. 19 it seems to about 40 - 60 seconds. On the other hand the period of generation of vortex calculated from Strouhal number related to the ship width as the dimension of length comes to about 30 - 15 seconds. Because these periods differ from each other considerably, even when the flow fluctuates periodically, and because

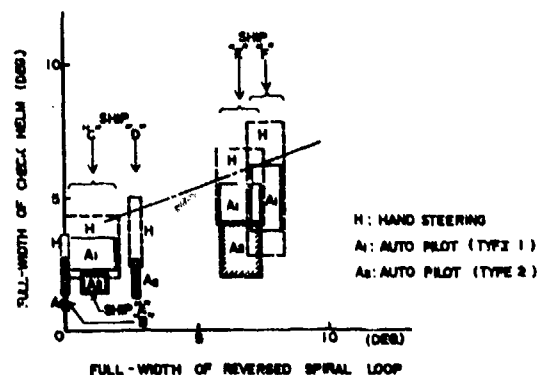


Fig. 28 Relation between loop width and check helm (full load condition)

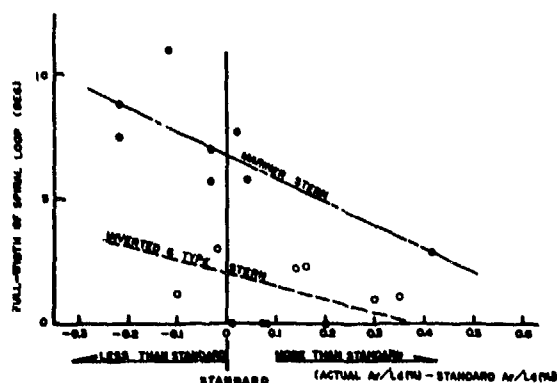


Fig. 27 Actual results of loop width in reversed spiral test (full load condition)

the record of yawing does not have a clear period, there is no fear of self-excitation in auto-pilot control.

Furthermore, in the case of navigation in rough seas, the standard variations of yawing and helm angle obtained are 0.82 degree and 1.21 degree respectively from the results of course keeping test with noise even in very rough condition of sea=6, swell=7 and wind=15 m/sec. As these standard variations are not large in comparison with conventional values, there seems to be no trouble in this point.

Finally we consider the steering quality indices. Fig. 29 shows the mean value of the results of 10° Zig-Zag test versus ship length. In the case of this ship, the value $K'=3.3$, $T'=4.0$ has enough stability by comparison with this value.

Fig. 27 shows the variation of the width of the hysteresis loop from the reversed spiral test versus the deviation of rudder area from the standard value derived from Yamada's method [11]. The straight line in the figure shows the mean line of the various data. For the present ship, the width of the hysteresis loop estimated from model tests is about 2 - 5 degrees while from this figure it may become 6 degrees. But even so, there will be no trouble in steering as shown next section if the ship does not show periodic yawing due to periodic fluctuation of the flow field [3].

EXAMINATION OF FEELING OF CONTROL OF SHIP BY SIMULATION

Object and method of simulation

As we have shown so far as we compare the model test results with those of actual ship, it may be said that 400,000 D.W. tons tanker of the present type will not get into trouble. But the steering quality indices are dealt

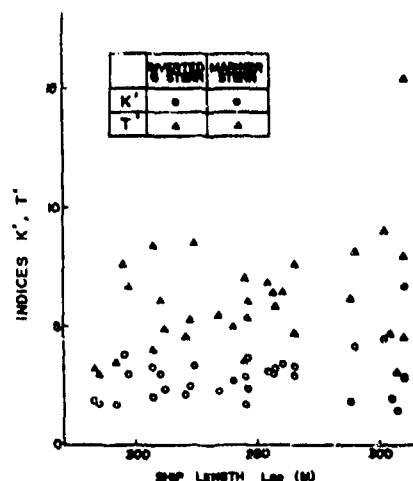


Fig. 29 Actual results of indices K' and T' in 10° zig-zag test (full load condition)

in nondimensional value so we must examine whether or not any trouble will occur in the view point of the feeling of control by checking the motion of the ship due to steering in real time, because the actual ship of the present type is larger in length than conventional 200,000 D.W. tons type tankers. In the present study the problem of the actual steering motion was examined by the method that helmsmen steer a simulator in which the steering quality indices estimated from 30M model test were applied.

The experiment was conducted using the manoeuvring simulator at Hiroshima University. This device can simulate the motion of ships having various steering qualities, lengths and speeds in the laboratory. The details of the device were already published [12]. For reference, an experiment using collision avoidance simulator was also carried out.

The equation of motion applied to the simulator is

$$T_1 T_2 \ddot{\psi} + (T_1 + T_2) \dot{\psi} + \psi + \nu \dot{\psi}^3 = K \delta + K T_3 \delta$$

Each coefficient of the equation was derived from the results of the experiments of the 30M model in the full load condition. In general, the results of model tests are more stable than the ship trials. So a modified imaginary model having 8 degrees width of hysteresis loop was also examined.

The tests were carried out at two speed conditions which were 15.6 knots and 8.0 knots (both in the full load condition) for the actual ship and those speeds correspond to 4.56 knots and 2.34 knot for the 30M model respectively.

Table 3 Coefficients of equation of motion.

SYMBOL	$L_{pp}(m)$	$V_S(kt)$	Full-width of Loop	$T_1(sec)$	$T_2(sec)$	$T_3(sec)$	$K(1/sec)$	$\mu(sec^2)$
M1	29.9	4.56	1.9 ⁰	-136.7	4.21	15.05	-0.423	- 0.90
M2	29.9	2.34	1.9	-266.4	8.14	29.24	-0.217	- 3.42
S1	350	15.6	1.9	-466.3	14.37	51.17	-0.124	-10.46
S2	350	8.0	1.9	-909.1	28.01	99.76	-0.064	-99.79
S'1	350	15.6	8.0	-309.5	14.73	51.17	-0.042	- 5.21
S'2	350	8.0	8.0	-603.4	28.72	99.76	-0.022	-19.87

The coefficients of equation of motion are shown in Table 3.

The process of examination is shown in Fig. 30. To take into account of the effect of individual differences, the same test was executed by two helmsmen.

Helmsman (A); a helmsman who controlled the 30M model ship and has much experience controlling medium size ships but no experience controlling very large tankers.

Helmsman (B); a helmsman who has much experience steering very large tankers and controlled the 30M model ship for two days.

Course control simulation was conducted after the sequence shown in Fig. 31. Helm angle was restricted to 15° at the beginning of course change but not restricted after that.

Collision avoidance simulations were carried out in the cases of avoidance of an anchored ship and crossing the course of other ship perpendicularly in which helm angle was not restricted.

Results on the analysis of simulation

In course control simulation, the performance of a course change is judged from the time which is required until the ship sets on new course, the magnitude of helm angle and the amplitude of motion. In this paper, the time history during the course change, the relation between L/V and Tr which represents the time of the course change and the relation between L/V and

mean helm angle $\sqrt{\Sigma \delta^2/N}$ during the course change are shown in Figs. 32, 33 and 34 for a typical example, where

$$Tr = \frac{1}{\psi_x} \times \int_0^{\infty} (\psi_I - \psi) dt$$

In Fig. 33, Tr for an ideal course change as calculated approximately from the first order system equation is also shown.

Namely

$$Tr = L/V \times \frac{2}{3} \sqrt{\frac{T_1}{K}} \frac{\psi_x}{\delta}$$

We can not find any indication of trouble in steering from the time history shown in Fig. 32. The maximum turning rate shown becomes 0.25 degree/sec even in the minimum case, which is large enough in comparison with the value 0.12 degree/sec. [13] which is the minimum value necessary to make an other ship notice the motion of own ship. And this value is not less than the above mentioned value even if we consider the 50% loss of turning rate due to shallow water effect [14].

As shown in Fig. 33 the value of Tr derived from simulation test agrees well with that of ideal steering and the control is also well. The results of the 30M model show rather large values. This seems to be because the helmsman hesitates to steer in a small ship. This phenomenon is also indicated in the value of helm angle shown in Fig. 34. On the other hand, in the case of a large ship, the motion of the ship is slow and the helmsman tends to turn the ship actively with large helm

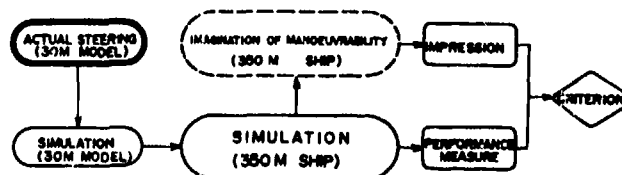


Fig. 30 Flow chart of criterion for feeling of ship-control

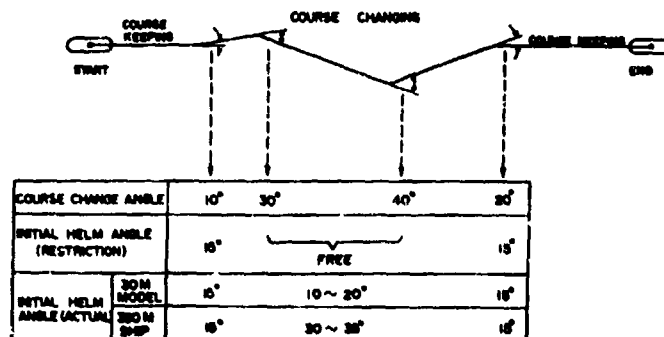


Fig. 31 Steering pattern

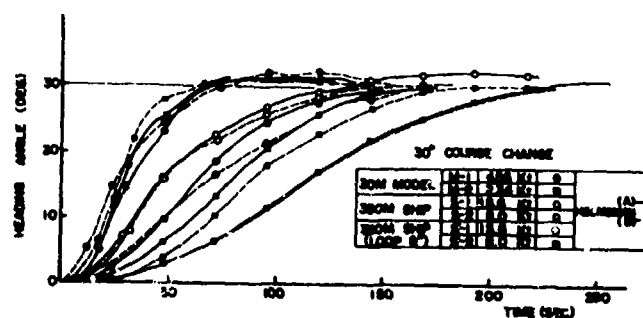


Fig. 32 An example of time history of heading angle

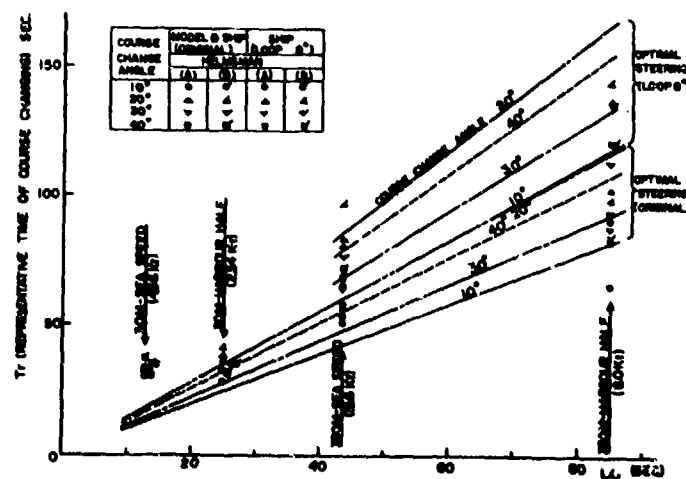


Fig. 33 Tr(Representative time of course changing) versus 1/V curve

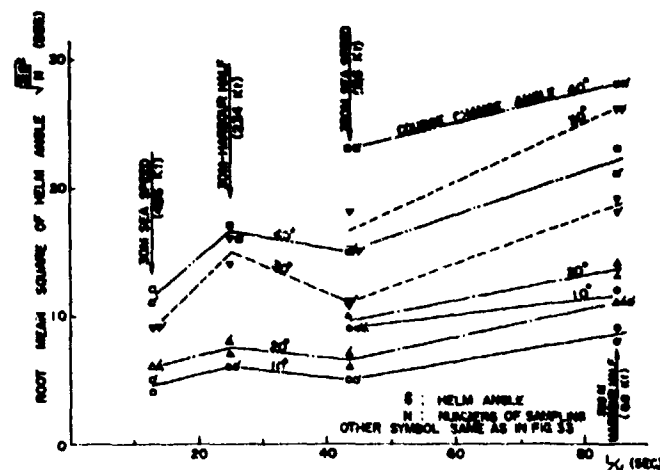


Fig. 34 Root mean square of helm angle versus L/V curve

angles. In the case of the wide hysteresis loop, a difference between ideal steering and the actual results exists. But it is not obvious whether this is due to the difficulty of steering or an error from first order system approximation. Because T_r is not so different from the ideal one and also because T_r is proportional to L/V and there is no trouble in 200,000 D.W. tons tanker, any trouble will not occur for such a L/V as studied in the present paper.

Course keeping test was carried out before and after the course changing test. Because the object of this test is to see the effect of difference of L/V , noise corresponding to a sea disturbance is not put in and the simulation corresponds to steering motion in a calm sea. Accordingly, yawing motion and helm angle is very small and the record is omitted here. It is interesting that helmsman (B), who has much experience steering large ships steers just like the rate-adjust control and helmsman (A), who has much experience steering small ships, steers just like proportional control and the helm angle is rather large in this case.

Also, in the collision avoidance simulation no trouble was found. We cannot obtain certain conclusions from the few results of this test but it seems that as L/V increases the helmsman tends to steer the ship actively and as a result the overshoot becomes large and the distance between the obstacle and the ship enlarges when the ship passes the obstacle.

To examine the relation between the results of simulation and feeling of control of the helmsman, impressions

of helmsman were recorded. These are gathered and as follows;

(1) The feeling of control of the 30M simulation model is very similar to that of the actual 30M model ship. (helmsman (A) and (B))

(2) In the case of the 350M simulated ship at 15.6 knots and 8.0 knots speed, the reaction to the steering is same as or more excellent than that of a conventional 200,000 D.W. tons type vessel (helmsman (B)).

(3) No trouble will occur in the case of "S1" and "S2" although I have no experience controlling very large tanker (helmsman (A)).

(4) In the case of "S1" and "S2" (having 8 degrees width of hysteresis loop) a large check helm is needed and the reaction to the steering is slow in comparison with "S1", "S2" but even so it is not so bad as get into trouble. (helmsman (A) and (B)). As mentioned above there is no discrepancy between the feeling of helmsmen and the results of analysis and this simulation test is considered to give rational results.

If the turning characteristics of the 350M actual ship is same as that of the 30M model in nondimensional representation, there will be no trouble even we consider the effect of L/V .

And even if the 350M actual ship is more unstable than the 30M model with a 8 degrees wide hysteresis loop, no particular problem in control will happen.

CONCLUSION

Unexpected phenomena found from various manoeuvring tests using three similar models are as follows;

(1) In the full load condition, scale effect appears in the range of small helm angle and (unlike conventional results) the steering quality indices of the large model indicate more stable characteristics than that of small model. The reason for this phenomenon is assumed to be that, owing to the large wake, the normal force acting on rudder has an inverse tendency.

(2) In the full load condition, the "unusual phenomenon" in which the turning characteristics are not defined uniquely is found in the 30M and the 10M model while it is not found in the 4M model. The scattering becomes marked as the rudder area becomes small and is apt to occur in port side turning. This phenomenon has a relation with the propeller revolutions, namely the turning characteristics become stable when the revolutions increase and vice-versa.

(3) In the ballast condition, the "unusual phenomenon" of having stable steering quality indices in the range of small helm angle occurs in the 30M model while it does not occur in the 4M model.

The reason for this phenomenon seems to be that the mechanism of the generation of vortices (which is the cause of yaw damping) resembles that of a wing and it becomes marked as the Reynolds number increases.

Next the steering quality of the ship is expected as follows;

(1) The indices K' , T' and the width of the hysteresis loop are stable in comparison with conventional ships.

(2) The yawing motion due to "unusual phenomenon" is not a periodic one and the results of the course keeping test show almost the same value of the variance of heading angle as a conventional ship.

(3) No difficulty in steering the ship could be found in the simulation test by helmsmen.

From these results it seems that no trouble will occur in actual navigation if the same rudder area and the same stern form as the model ship is adopted.

As to the scale effect of steering quality, we must wait till we shall get the results of the full scale trials.

And it is beyond question that we need to make more fundamental studies in order to clarify of the mechanism of the above mentioned "unusual phenomena".

ACKNOWLEDGEMENT

In executing this study we received many instructions and support. Especially Professor Matora, University of Tokyo, and Professor Nomoto, Osaka University, directed us from the beginning of this study. Professor Taguchi, University of Osaka Prefecture, and members of his staff carried out the experiments about the effect of bilge keels. Dr. Kose, lecturer of Hiroshima University, carried out the simulation test. Dr. Koyama, assistant Professor of University of Tokyo, gave us a valuable advice. Many members of Ship Design Head Office, Maizuru Shipyard and Technical Research Laboratory of Hitachi Shipbuilding & Eng. Co., Ltd. supported us very earnestly in the accomplishment of this study. The completion of this study owes much to these people and the authors wish to thank to them heartily.

REFERENCES

1. S.Seto, I.Nakamura, M.Kano, S.Uetake and Y.Kutomi, "On the Study of Optimal Design of ULCC under Restricted Draught" J. of the Society of Naval Architects of Japan, vol.134, 1973.
2. K.Nomoto, "Unusual scale effect on manoeuvrabilities of ships with blunt bodies" Proceeding of 11th I.T.T. C. 1966.
3. S.Matora, M.Takagi, A.Kokumai, H.Kato and T.Koyama, "An Analysis of the Maneuvrability of a Ship Associated with Unusual Characteristics under Steerage" J. of the Society of Naval Architects of Japan, vol. 128, 1970.
4. H. Okamoto, H. Tamai and H. Oniki, "Correlation Studies of Manoeuvrability of Full Ships" J. of the Society of Naval Architects of Japan, vol. 131, 1972.
5. The 107 Research Committee, The Report of the Shipbuilding Research Association of Japan, No.142, 1972.
6. A.Ogawa, "Calculation on the Steered Motion of a Ship under the Action of External Forces" J. of the Society of Naval Architects of Japan, vol. 126, 1969.
7. T.Koyama, "On the Optimum Auto Pilot Steering System of Ship at Sea" J. of the Society of Naval Architects of Japan, vol. 122, 1967.

8. A.Yasaki and E.Kuramochi, Technical Note of Transportation Technical Research Institute, No.43, 1962.

9. S.Okada, "On the Results of Experiments on Rudders Placed behind the Ships" J. of the Society of Naval Architects of Japan, vol.105, 1959.

10. K.Watanabe, K.Yokoo, T.Fujita and H.Kitagawa, "Study on Flow Pattern around the Stern of Full Ship Form by Use of the Geosims" J. of the Society of Naval Architects of Japan, vol.131, 1972.

11. K.Yamada, "A Method of Judging Manoeuvrability and Rudder Area Design for Large ships" J.of the Kansai Society of Naval Architects of Japan, vol.134, 1969.

12. K.Nowoto and K.Kose, "Some simulator Studies on the Directional Stability of Ships under Manual Steering" J. of the Society of Naval Architects of Japan, vol. 132, 1972.

13. K.Yamada, Technical Note of Hitachi Shipbuilding & Eng. (Unpublished), 1972.

14. The '8 Research Committee, The Report of the Shipbuilding Research Association of Japan, No.95, 1969.

DISCUSSION

H.H.W. THIEME

The progress in developing wide-beam large ships - may be some kind of forerunner of extreme "flounder" hulls - as achieved by the authors leads to a welcome insight in very interesting problems, specially for the maneuvering people too. My contribution must be restricted to a more or less probable suggestion to explain the newly observed phenomena.

The shown scale effect favouring the larger models is unusual indeed, but very different from Prof. Nomoto's "Unusual Scale Effect" /2/. The latter is an overstabilizing effect due to increased rudder force from unusual side-wash angle past the rudder induced by strong separation on the turning inside stern part. Comparable results, and the same possible explanation, were reported by Dr. Okamoto at the Third NSMB-Symposium 1973; an overstabilizing effect only for the smaller models of 2.0 and 6.0 meters in length.

Differently with the new results of the Wide-Beam Tanker geosims. They are showing no overstabilizing at all, turning instability for the full load condition, stability for the very large model and a marginally unstable small model in ballast condition. If one calculate roughly the influence of trim and light load, the governig parameter for the latter may be $V/(T.L^2)$,

on the turning stability, an equivalent enlargement of about 30 % for the rudder area is found. This may good enough explain the good results for the ballast condition.

More difficult I think is a reliable explanation of the first mentioned phenomenon of increased turning stability with increased model size. I would have more appreciated, when more details would be published on hull-form and rudder-section, speed-loss and drift angle during turning. It must be very emphasized the author's conclusion, that there is a need for more fundamental studies in this field. As a contribution to such an extended program of investigation I may once more suggest Less Rudder Turning Tests and rudder force measurements during normal spiral-tests, in order to separate the hull-phenomena from the rudder-phenomena.

In case all the model rudders are geometric similar not only in area-profile but also in hydrofoil-section, e.g. a normal, thick section familiar to NACA 0018 or so, it must be afraid an essential, direct and real scale effect on the rudder force of the 4-M-model. The Reynolds Number of this rudder is in the range from about 0.1 million up to below 0.2 million with respect to the slip-stream influence. And this is somewhat too low; the use of a plate-rudder might have a remarkable effect.

AUTHOR'S REPLY

The authors thank the discussor who took the time and effort to prepare valuable contributions to this paper.

In a full load condition, the results are different from Prof. Nomoto's "Unusual Scale Effect" and the phenomenon of increased stability with increased model size is unusual. However we think that this phenomenon is caused by the difference of the rudder force due to the difference of the wake fraction and the slip ratio. And we agree with Mr. Thieme's suggestion that rudder force measurements are useful.

In a ballast condition, the larger model is more stable than the smaller model. This phenomenon is quite unusual. The authors think that the reason of this phenomenon is an overstabilizing effect due to unusual fluid force which happens in the larger model only. This assumption is opposite to Prof. Nomoto's "Unusual Scale Effect" and we also think that the more fundamental studies are necessary.

As for the scale effect on a rudder force, the authors think that there seems to be no essential scale effect on the rudder force of the 4M model even though the Reynolds Number of the rudder is small. Because the rudder is placed in fully disturbed flow field.

DIGITAL SIMULATION ANALYSIS OF MANEUVERING PERFORMANCE

H. Eda
Davidson Laboratory
Stevens Institute of Technology
Hoboken, New Jersey

ABSTRACT

Results obtained in a series of digital simulations are given in the area of standard maneuver motion predictions, hull form design (e.g., effect of dynamic course instability), control systems design (e.g., effect of rudder rate), and maneuvering control in narrow channels. Hydrodynamic data obtained in captive model tests were used to achieve a realistic modeling of ship dynamic systems. Encouraging correlations are shown for the case of a typical large tanker between digital simulations and available full-scale trial data obtained in various maneuvers, including highly nonlinear ones such as enter-a-turn with a 40-degree rudder angle and emergency stopping from the design speed. Effects of inherent dynamic instability due to wide full-form configurations are examined in digital simulations as well as eigenvalue analysis. Results indicate that a ship with a large degree of inherent instability requires a relatively high sensitivity feedback in yaw-rate to achieve directional stability. Evaluation of maneuvering performance at the design stage is recommended particularly for full-form configurations.

INTRODUCTION

During the past ten years significant progress has been made in the area of ship maneuvering hydrodynamics stimulated by the ever-increasing size of ships, such as tankers and bulk carriers. An effective means frequently used to examine ship dynamic response involved digital simulations combined with captive model data as well as the use of free-running models.

The objective of this paper is to present typical examples of our recent results obtained from digital simulations of ship maneuvering control in the following areas:

- Standard maneuver motion predictions.
- Control systems design (e.g., effect of rudder rate).
- Maneuvering safety in restricted channels.
- Hull form design (e.g., effect of wide beam).

To ensure a realistic modeling of ship dynamic response, the mathematical model should be formulated with inclusion of nonlinear

hydrodynamic coefficients because ship maneuvering motion is highly nonlinear. The basic mathematical models used in these studies are described in the Appendix.* Linear and nonlinear hydrodynamic coefficients used in the mathematical model were determined in captive model tests carried out at the Rotating-Arm Facility of Davidson Laboratory, Stevens Institute of Technology.

STANDARD MANEUVER MOTION PREDICTIONS

The following are representative maneuvers frequently employed in full-scale trials to obtain the maneuvering characteristics of a ship:

- Enter-a-turn.
- Z-maneuver.
- Stopping maneuver.

Responses to these standard maneuvers were obtained in a series of digital simulations for a typical large tanker (i.e., the 250,000 DWT type) at a fully-loaded condition. Full-size principal characteristics of the tanker are given in Table 1. The tanker model had been tested previously in the Rotating-Arm Facility of Davidson Laboratory. Figures 1-6 show typical examples of predicted response to the above-mentioned standard maneuvers having an approach speed of 16 knots in most cases.

Figure 1 shows computer-plotted LCG locations at 20-second intervals, starting at the time of rudder command. High turning performance (e.g., high-turning rate versus rudder angle) is shown in these trajectories, which are typical for full-form tanker configurations at the fully-loaded condition.

Figure 2 shows predicted heading angle changes at every 10 seconds during Z-maneuvers of 10° - 10° , 20° - 20° , and 30° - 30° . These three response curves reveal fairly well the maneuvering characteristics of this particular tanker.

The 10° - 10° Z response curve, for example, shows an oscillatory divergent pattern of heading angle change, indicating the ship is unstable under the condition where magnitude of

*Most nomenclature appearing in this paper follows that used in SNAME publications such as References 1-3.

yaw-rate and sideslip are relatively small. The tanker is dynamically unstable on straight course having a positive index ($\alpha' = 0.17$).

On the other hand, the 20° - 20° Z response curve shows a stable pattern of heading angle change, having approximately a constant heading angle amplitude (or overshoot angle). Nonlinear hydrodynamic effect is increased during the 20° - 20° Z-maneuver due to an increase in yaw-rate and sideslip velocity, making the inherently unstable ship on the straight course stable during this maneuver.

The 30° - 30° Z response curve shows an overshoot angle (or heading amplitude) that reduces with time, having a maximum value which is shown in the first overshoot angle. During this maneuver, the speed reduction due to yaw-rate and sideslip reaches a substantial degree with time, thereby introducing greater rudder effectiveness during the later portion of this maneuver. As a result, the overshoot angle is reduced with time.

It should be noted, in Figure 2, that the same ship at the same loading condition behaves differently, as a stable ship or as an unstable ship, depending on the degree of nonlinear hydrodynamic contribution due to motion parameters (e.g., yaw-rate and sideslip). It should also be pointed out here that this tanker, which is inherently unstable on straight course in open-water, can be highly stable in restricted water as revealed in recent studies.³ Furthermore, the same tanker is extremely stable at ballast load conditions as indicated in full-scale experience and from results of our recent rotating arm tests.

Stopping is one of the most critical maneuvers for ships. The complexity in dynamic simulations of stopping maneuvers is increased by deviations in heading and path due to reversed propeller revolutions.⁴ Including this reversed propeller effect into nonlinear equations of yaw, sway, and surge, digital simulations were made for stopping maneuvers.

Figure 3 shows the computer-plotted ship speed and longitudinal distance traveled at every 30 seconds for approach speeds of 16, 11, and 6 knots, after the propeller command of -55 rpm was given.

Correlations between these simulations and available full-scale trials are shown in Figures 4-6.

Figure 4 shows a comparison of turning trajectory for rudder angle of 40 degrees at approach speed of 15 knots. Extremely encouraging agreement is evident in these highly nonlinear maneuvers.

Figure 5 shows a comparison of the 20° - 20° response, where a fairly good correlation is indicated.

Comparisons of predictions with full-scale stopping maneuvers are shown in Figure 6. It should be pointed out that it probably will be difficult to obtain consistent and accurate

results in full-scale stopping trials because external disturbances could have significant effects, particularly at slow speeds in open seas. Considering such disturbances, the correlation shown in the figure indicates a reasonably realistic modeling of the present digital simulations.

The realistic modeling of ship maneuvering response, shown in the above example, formulates a firm basis for many applications such as ship design, control system design, maneuvering safety procedures, and ship-handling trainers.

CONTROL SYSTEMS DESIGN (Effect of Rudder Angular Rate)

Presently a minimum rudder angular rate of 2-1/3 deg/sec, which is independent of ship parameters, is required by ship classification societies and regulatory agencies. Rudder angular rate, however, can be better described as a function of rudder size, ship form, proportions, length and speed.^{5,6} This is particularly important for recent large ships such as VLCC (very large crude-oil carriers) because of the huge capacity of steering gear. Accordingly, a limited computer study has been made to evaluate the effects of rudder system (particularly rudder angular rate in this paper) on the performance of the 250,000 DWT tanker through a series of digital simulations.

Figures 7 and 8 show examples of turning trajectories with application of 35-deg rudder angle at approach speeds of 16 and 4 knots, respectively. These trajectories show that the effect of rudder angular rate is greatly reduced at low speeds (i.e., 4 and 8 knots) relative to the full speed of 16 knots.

Figures 9 and 10 show examples of 20° - 20° Z-maneuver response at approach speeds of 16 and 4 knots. These figures also indicate a similar effect of rudder angular rate as in the case of turning.

A summary chart is shown in Figure 11 as a result of a series of entering-a-turn maneuvers. Advance and transfer in terms of ship length are shown on the basis of rudder angular rate for three different approach speeds (16, 8, and 4 knots). Advance and transfer are longitudinal and lateral distances traveled from the time of rudder command to the time of 90-deg heading change.

The figure shows that the magnitude of advance is reduced with an increase of rudder angular rate but that the rate of reduction becomes insignificant after rudder rate reaches a certain value. The effect of rudder rate on advance becomes significant at high speeds. At all speeds examined, transfer is very slightly influenced by the rudder angular rate.

Figure 12 shows a summary chart as an example of results obtained from a series of 20° - 20° Z-maneuver at approach speeds of 16, 8 and 4 knots. Time to the second and third rudder executions, yaw overshoot, and lateral path overshoot are shown on the basis of rudder angular rate in these charts. Results revealed

that quickness of response and overshoots in yaw and sway are all improved with an increase in rudder rate but these improvements become insignificant at high rudder rate and, particularly, at low speed.

MANEUVERING SAFETY IN RESTRICTED CHANNELS

During meeting and passing in restricted channels, hydrodynamic interactions between two ships are fairly significant, thereby introducing a problem in ship operations. Accordingly, a simulation study was carried out for the case of large full-form tankers. Using recently obtained hydrodynamic data^{4,5} for tanker forms, the mathematical model was formulated on a digital computer and a series of computer runs were carried out.⁷

Figure 13 shows the geometry of the canal and the courses of two ships A and B. The dynamic motions of Ship A were simulated due to the interaction with Ship B while meeting and passing. Interaction forces and moments during meeting and passing, previously measured by Moody in captive model tests of full-form ships were applied to digital simulations (Case 1).

Simulations of ship motions were carried out on the digital computer in the following manner:

Initially, the ship moved from the canal centerline course to the off-centerline course and maintained the off-centerline straight course with a rudder angle required for retaining the equilibrium condition. Then, time histories of hydrodynamic interactions in yaw moment and side force were applied to the ship. A series of simulation runs was continued for 1000 seconds in full scale ($t' \approx 9$, i.e., for a period of time to travel nine ship lengths.)

Figures 14 and 15 show computer-plotting of trajectories (heading angle and path deviations, respectively) for a period of 900 seconds ($t' \approx 8$) during meeting and after passing. The following control system characteristics were used:

- (1) no control, $a=b'=c'=0$, shown by in the figures
- (2) typical control, $a=3$, $b'=1.5$, $c'=0$, shown by *****

The figures show that the ship deviates very little from the initial course during a period of meeting. This small deviation is because the inertial terms of ships (including added inertial terms which are greatly increased in the canal) are relatively larger than hydrodynamic interactions, which are somewhat oscillatory with relatively short duration. This small deviation during meeting justifies the simulation procedure in the present study, which utilizes hydrodynamic interactions measured in captive model tests. Without control, the trajectory is divergent with slow oscillation due to bank effects. It should be noted that potential hazards are still great after passing, and that adequate control must be continued for a long time after passing until the

disturbance due to meeting diminishes.

During 1960-1962, a series of full- and model-scale tests carried out in the Netherlands for the North Sea Canal studies included measurements of two-way traffic in narrow canals.⁸ Comparisons are made here between simulation trajectories and test results.

Table 2 gives ship and canal dimensions for three cases as follows:

- CASE 1. Digital simulation of large full-form tankers examined in this study utilizing captive model test results.
- CASE 2. Full-scale test of the ASTYANAX and the WILLEM BERENDSZ in the North Sea Canal to Amsterdam.⁸
- CASE 3. Manned-model of tanker form.⁸

Figure 16 compares time histories of rudder activity. In digital simulations, yaw and yaw-rate gains of 3 and 1.5 were employed. Time and yaw-rate in test results are scaled to Case 1 (i.e., simulations) in these figures. A fairly good correlation in behavior of yaw-rate and rudder activity is shown in three cases. All cases indicate three major peaks in yaw-rate and rudder activity at corresponding time. Since the canal size relative to the ship is the largest in Case 1 (shown in Table 1), the time history of yaw-rate and rudder activity is the least pronounced in Figure 16.

Considering the difference in ship and canal configurations in these cases, the comparisons presented in the figures are encouraging. It is considered that the results fairly well verify realistic modeling of the ship-waterway system.

HULL FORM DESIGN (Effect of Wide Beam)

While a wide-beam, full-form hull is one of the most promising designs for large tankers, it is important to evaluate the maneuvering characteristics at its design stage because of possible inherent dynamic course instability due to its particular configuration. Accordingly, the effect of inherent dynamic course stability on ship handling was examined for three ship configurations having various degrees of inherent stability through computer-based analyses.

The dynamic behavior of the following ship configurations having various degrees of stability was examined:

- SHIP A: Inherently stable (slender, fine form)
- SHIP B: Inherently unstable (wide beam, full form)
- SHIP C: Inherently very unstable (very wide, full form)

These three ships were at fully-loaded conditions (even keel) and were compared on the basis of the same ship length of 910 feet.

Principal dimensions of these ships are given in Table 3.

Digital simulations and eigenvalue analysis have been made for these ships with inclusion of feedback control systems to examine the effect of various degrees of inherent course stability on ship maneuvering performance.

Region Of Directional Stability

Directional stability (i.e., capability to maintain a given heading by utilizing rudder) is one of the most basic requirements for satisfactory ship performance. In most cases, inherently unstable ships can achieve directional stability without any difficulty by the use of feedback control due to helmsman or autopilot, just as stable ships do. However, unstable ships require more refined control characteristics to achieve directional stability under greater limitations (e.g., less amount of disturbances due to wind and waves) compared with the case of stable ships. Typical examples are shown in the following stability analysis.

Feedback control of helmsman or autopilot can be fairly well expressed by the following equation:

$$\delta_d = a(\psi - \psi_d) + b'\dot{\psi}' + \delta_e = \delta + t_r'\dot{\delta}'$$

where δ_d = rudder command

δ_e = rudder at equilibrium condition

δ = actual rudder angle

ψ = heading

ψ_d = desired heading

a = yaw gain

b' = yaw-rate gain

t_r' = time constant in rudder response

Yaw and yaw-rate gain constants*, a and b' , respectively, are based on nondimensional values (e.g., nondimensional time t' = ship length of travel = tl/A). Stability of heading angle can be examined in the following set of solutions of perturbation equations, which are derived from equations of yaw and sway motions and rudder control:³

$$\psi = \sum_{n=1}^4 Y_n e^{\sigma_n t'} \quad (\text{heading angle})$$

$$v' = \sum_{n=1}^4 V_n e^{\sigma_n t'} \quad (\text{sideways velocity})$$

$$\delta = \sum_{n=1}^4 \Delta_n e^{\sigma_n t'} \quad (\text{rudder angle})$$

where Y_n , V_n , and Δ_n are constant depending upon the initial conditions, and σ_n are eigenvalues of the system which are determined by nontrivial solutions of the following characteristic equations:

$$p_0 \sigma_n^4 + p_1 \sigma_n^3 + p_2 \sigma_n^2 + p_3 \sigma_n + p_4 = 0$$

*Yaw gain constant of 2 means, for example, that a rudder angle of 2 degrees is ordered when the heading deviation is 1 degree.

When the real parts of all roots of the characteristic equation have the negative sign (i.e., $\text{Re} \sigma_n < 0$), the system is stable (i.e., the system eventually converges to the initial equilibrium state after a small perturbation is given). In determining whether or not the system is stable, it is sufficient to know the sign of the real parts of the roots only. Hurwitz (or Routh) criteria, for example, can be applied.

On the other hand, if all the roots are determined, more detailed characteristics of the system can be obtained. Time constant and frequency of the system are determined from the real and imaginary parts of the roots, respectively. Furthermore, the solution vector can be determined from the initial conditions, and the actual ship dynamic response to any disturbance can be computed readily, if required. Accordingly, instead of using Hurwitz criteria, eigenvalues of the system were directly determined on a digital computer for a wide range of control gain constants for three ships.

Stability roots were determined for three ships with the following range of control system characteristics:

Yaw gain	$a = 0$ to 10
Yaw-rate gain	$b' = 0$ to 5.0
Time constant	$t_r' = 0$ to 2.0

Figure 17 shows directionally stable regions for three ships where the abscissa and the ordinate represent yaw-rate and yaw gain, respectively. The figure reveals the following:

1. Yaw gain must be positive to achieve directional stability whereas yaw-rate gain can be negative under certain conditions (e.g., when the ship has sufficient inherent dynamic stability or when sufficiently large yaw gain is simultaneously used).
2. Three ships, having various degrees of dynamic stability, show a similar trend in stability change with changes in yaw and yaw-rate gains. Slopes of curves for neutral stability are roughly the same for these three ships; the only major difference is in the location of the intersection on the transverse axis (i.e., the yaw-rate gain axis).
3. Inherent dynamic instability can be compensated by adding hydrodynamic damping due to yaw-rate gain control. A ship with a greater degree of inherent instability requires a greater value of yaw-rate gain to achieve directional stability than that for a ship with a lesser degree of instability (when yaw gain is constrained).

A large yaw-rate gain constant (e.g., $b' > 0.75$) would not be acceptable for operation in a seaway because excessive rudder activity could be introduced due to yawing in waves. This possible limit is shown by a dotted line in Figure 17. It is seen that Ship C has only a

limited acceptable and stable region compared with those for Ships A and B. This clearly indicates a possible difficulty in handling of the very unstable Ship C.

It should be stated that stable regions shown in Figure 17 are results of the eigenvalue analysis of the linear system so that the results are only valid for the case where deviations from the equilibrium conditions are very small. For example, a limit in available rudder angle in actual system is not included in the analysis. When large values of gain constants are used, there exists a great possibility of a large degree of saturation in rudder angle which can introduce the instability into the system during actual operation. Accordingly, the dynamic behavior of these ships is also examined in a series of digital simulations, which is a more realistic representation of ship motions with inclusion of nonlinear hydrodynamic terms.

Predictions of Steady-Turning Conditions

Based on hydrodynamic data of yaw moment and sway force obtained from the Rotating-Arm Facility, it is possible to make predictions of maneuvering motions. To compare the dynamic course stability and maneuvering performance, steady-turning conditions (or spiral test results) are predicted for three ships through numerical analysis of hydrodynamic data.

Solid-line curves in Figure 18 show steady-turning rates predicted for Ships A, B, and C. Arrows along the curves show the sequence of results predicted for spiral tests. Dotted lines indicate jump in steady-turning rate during spiral tests of dynamically unstable Ships B and C. In other words, an unstable ship exhibits hysteresis loops in spiral test results.

With respect to a given steady-turning state (r'_1, v'_1), where r'_1 and v'_1 are steady-turning and sideslip velocities, respectively, dynamic stability of the system can be examined (i.e., whether the dynamic quantities of r'_1 and v'_1 are convergent or not after a small perturbation is given). The dynamic stability roots (σ'_1 and σ'_2) determined from nonlinear equations of yaw and sway motions are shown in Figure 19. When the stability root σ'_1 is negative (where σ'_1 is algebraically greater than σ'_2), the system is stable. Therefore, this figure tells us the stability of steady-state conditions shown in Figure 18.

For example, the positive-slope portion of the solid-line curve for Ship C between vertical dotted lines in Figure 18 corresponds to the positive-value portion of the σ'_1 curve for the same Ship C in Figure 19. Since the positive

value of σ'_1 means dynamical instability, the positive-slope portions of curves in Figure 18 are unstable. Similarly, the negative-slope portions of curves are stable in the same figure.

Figure 20 shows numerically computed speed reduction due to the resistance increase introduced by yaw-rate and sideslip during the steady turning. The ordinate is the ratio of ship speed during turning to approach speed. Whereas speed change is continuous for stable Ship A during the spiral test, there exists a large jump in speed change for unstable Ships B and C. Since it takes a long time to reach a steady ship speed after a jump, much more time is required to complete spiral tests for an unstable ship than that for a stable ship.

Nonlinear terms in hydrodynamic yaw moment and sway force have a great effect on height and width of hysteresis in spiral test results of unstable Ships B and C as shown, for example, in Figure 21 where nonlinear terms are changed relative to the original values keeping all linear terms unchanged as follows:

$$C_n = 0.75, 1.0, 2, \text{ and } 4$$

where

$$C_n = (\text{magnitude of all nonlinear terms}) / (\text{original values})$$

Since linear terms are not changed, the dynamic course stability with respect to the straight course ($r'_1=0, v'_1=0$) remains the same. Accordingly, slopes of curves at $r'_1=0$ remain unchanged in Figure 21. With an increase in nonlinear terms (i.e., an increase in C_n), a reduction in height and width of hysteresis loops in spiral test results are shown in the figure. This introduces a substantial improvement in maneuvering performance in actual ship operations as indicated in predictions of zig-zag maneuvers.

Predictions Of Zig-Zag Maneuvers*

Based on rotating-arm data, zig-zag maneuver trajectories were computed for three ships at an approach speed of 14.5 knots. Results of a series of digital simulations indicated dynamic behavior of these ships during Z-maneuvers as follows:

The dynamically stable Ship A has small overshoot angle and can finish a zig-zag test in a short time (see Figure 22). The unstable Ship B has a larger overshoot angle and it took more time to finish the test than that for Ship A. While Ship B finished the $15^\circ-15^\circ$ Z-test in a stable fashion (due to stabilizing effects of nonlinear hydrodynamic terms), it could not finish Z-tests of $7.5^\circ-7.5^\circ$ and $5^\circ-5^\circ$ in a stable manner (i.e., heading angle is oscillatory

*An ordinary Z-maneuver is accomplished as follows: With the ship on steady-state straight course, the rudder is deflected to a certain angle (e.g., 5°) at maximum rudder rate and maintained at that position. When the change of heading reaches the same magnitude as the rudder angle, a second rudder execution takes place shifting the rudder to the opposite direction. This procedure is continued. In a modified Z-maneuver, the rudder angle is shifted to the opposite direction when heading angle deviation reaches to a certain amount, e.g., 1° (or when heading-rate reaches to a certain magnitude).

divergent in unstable patterns). In the case of the very unstable Ship C where the heading angle is divergent after the first execution of rudder angle, recovery could not be achieved by the use of the opposing rudder angle at the second execution (see Figure 22). The ship finished the 15°-15° Z-test in stable fashion because of the significant contribution of nonlinear terms.

Since unstable ships cannot finish ordinary zig-zag tests in a stable manner when contributions of nonlinear terms are relatively small, as in the case of 5°-5° Z-test shown in Figure 22, modified methods have been proposed to obtain test results in a stable manner.⁸ Figure 23 shows predictions of heading angle response during a modified zig-zag maneuver where the rudder angle of 5° is shifted to the opposite direction when heading angle deviations reach to 10° instead of heading change equal to rudder angle (i.e., $\psi = -\delta = 5^\circ$).

Figure 23 indicates that stable Ship A finished the modified Z-tests, of course, in a stable manner. It is important to note in Figure 23 that the unstable Ship B finished the modified Z-maneuvers tested (i.e., 5°-10°) in a stable manner whereas the same ship could not finish some of the ordinary Z-maneuvers (e.g., 5°-5°) as shown in Figure 22. In the case of Ship C with a large degree of inherent dynamic instability, however, an unstable divergent pattern of trajectory is shown even in the modified Z-maneuvers (e.g., 5°-10°) as shown in Figure 23, indicating possible difficulties in handling of this particular ship at sea. Accordingly, it is recommended that maneuvering performance be thoroughly evaluated at its design stage, particularly of wide-beam full-form ships, to ensure satisfactory ship performance.

CONCLUDING REMARKS

A series of digital simulation analyses has been made in the area of standard maneuver response predictions, correlations, hull form design, control systems design and maneuvering control in narrow channels. Hydrodynamic data obtained in captive model tests were used in an effort to achieve a realistic modeling of ship dynamic response.

Encouraging correlations were shown for the case of the 250,000 DWT tanker between digital simulations and available full-scale trial data obtained in various maneuvers, including highly nonlinear ones such as enter-a-turn with a 40-degree rudder angle and emergency stopping from the design speed. It should be noted that adequate representations of linear and nonlinear hydrodynamic effects are essential for ship maneuvering simulations because of high-turning performance of ships relative to other kinds of vehicles. Based on these encouraging correlations, the simulation model can be effectively used for many applications such as ship design, control systems design and maneuvering safety problems. The major findings obtained in these applications are summarized as follows:

1. Effects of inherent dynamic course

instability due to wide-beam full-form configurations were examined in digital simulations as well as eigenvalue analysis. Results indicate that a ship with a large degree of inherent instability requires a relatively high sensitivity in yaw-rate in its feedback to achieve directional stability. Evaluation of maneuvering performance at the initial design stage is recommended for new designs, particularly for full-form configurations.

2. An application was made to examine the effect of rudder angular rate on maneuvering performance of the tanker. Summary charts were presented as guidelines to determine adequate rudder rate.

3. Dynamic behavior of tankers during two-way traffic in channels was examined with variations in control system characteristics. Results reveal a basic pattern of ship behavior and rudder activity during meeting, which was favorably compared with records previously obtained from full-scale studies in the North Sea Canal. The analysis can be effectively applied to the maneuvering safety procedure development.

ACKNOWLEDGMENTS

This paper is based on research supported by the Naval Ship Systems Command under the General Hydrodynamic Research Program (Contract N00014-67-A-0202-0029, technically administered by the Naval Ship Research and Development Center), the Corps of Engineers (DACW 17-68-C-0072) and The Society of Naval Architects and Marine Engineers (P.O. No. 658). The author wishes to acknowledge many valuable suggestions given by Mr. J. B. Hadler of NSRDC, Dr. A. Strumpf of Davidson Laboratory, and the members of the SNAME H-10 Panel (Ship Controllability) during the course of these studies.

REFERENCES

1. PRINCIPLES OF NAVAL ARCHITECTURE, SNAME 1967 Publication.
2. Ede, H. and Crane, C.L., Jr., "Steering Characteristics of Ships in Calm Water and Waves," TSNAME, Vol. 73, 1965.
3. Ede, H., "Directional Stability and Control of Ships in Restricted Channels," TSNAME, Vol. 79, 1971.
4. Crane, C.L., Jr., "Maneuvering Safety of Large Tankers: Stopping, Turning and Speed Reduction," TSNAME, Vol. 81, 1973.
5. Mandel, P., "Some Hydrodynamic Aspects of Appendage Design," TSNAME, 1953.
6. Moody, C.G., "Study of the Performance of Large Bulk Cargo Ships in a Proposed Inter-oceanic Canals," Naval Ship Research & Development Center Report 374-H-01, 1971.
7. Ede, H., "Dynamic Behavior of Tankers During Two-Way Traffic in Channels," Marine Technology, Vol. 10, July 1973.
8. "Noorzeekanaal, Parts I-IV," Waterloopkundig

Laboratorium, Delft, The Netherlands.

9. Motora, S. and Fujino, M., "Modified Zig-Zag Maneuver and Its Application," Jour. of Soc. of N.A. of Japan, 1970.

APPENDIX Basic Mathematical Models

Longitudinal and transverse horizontal axes of the ship are represented by the x- and y-axes with origin fixed at the center of gravity. By reference to these body axes, the equations of motion of a ship in the horizontal plane can be written in the form

$$\begin{aligned} I_z \ddot{\psi} &= N & (\text{Yaw}) \\ m(\dot{v} + ur) &= Y & (\text{Sway}) \\ m(\dot{u} - vr) &= X & (\text{Surge}) \end{aligned} \quad (A-1)$$

where N, Y, and X represent total hydrodynamic terms generated by ship motions, rudder and propeller.

Hydrodynamic forces are expressed in terms of dimensionless quantities N' , Y' , and X' based on non-dimensionalizing parameters ρ (water density), U (resultant ship velocity relative to the water), and A , i.e.,

$$N' = \frac{N}{\frac{\rho}{2} U^2 A L}, \quad Y' = \frac{Y}{\frac{\rho}{2} U^2 A}, \quad \text{etc.} \quad (A-2)$$

Hydrodynamic coefficients vary with position, attitude, rudder angle, propeller revolution, and velocity of the ship. For example, in the case of hydrodynamic yaw moment coefficient,

$$N' = N'(v', r', \delta, y_o', \dot{v}', \dot{r}', n', u') \quad (A-3)$$

where

$$\begin{aligned} v' &= \frac{v}{U}, \quad r' = r \frac{L}{U}, \quad y_o' = \frac{y_o}{L}, \quad n' = \frac{n}{n_e} \\ u' &= \frac{u}{u_e}, \quad \text{etc.} \end{aligned}$$

Finally, the following polynomials were obtained for predictions of ship dynamic motions:

$$\begin{aligned} N' &= a_1 + a_2 v' + a_3 r' + a_4 \delta + a_5 y_o' + a_6 v'^2 r' + a_7 v' r'^2 \\ &+ a_8 v'^3 + a_9 r'^3 + a_{10} \delta^3 + a_{11} y_o'^3 + a_{12} \dot{v}' + a_{13} \dot{r}' \\ Y' &= b_1 + b_2 v' + b_3 r' + b_4 \delta + b_5 v' y_o' + b_6 v'^2 r' + b_7 v' r'^2 \\ &+ b_8 v'^3 + b_9 r'^3 + b_{10} \delta^3 + b_{11} y_o'^3 + b_{12} \dot{v}' + b_{13} \dot{r}' \\ X' &= c_1 + c_2 v' r' + c_3 v'^2 + c_4 \delta^2 + c_5 \dot{u}' + X'_p \end{aligned} \quad (A-4)$$

where coefficients of rudder force and moment are functions of propeller slip as follows:

$$a_3 = \frac{(1 + k s_e^{1.5})}{(1 + k s_e)} a_{3e} \quad (A-5)$$

$$a_6 = \frac{(1 + k s_e^{1.5})}{(1 + k s_e)} a_{6e}, \quad \text{etc.} \quad (A-5)$$

and

$$s = \text{propeller slip} = 1 - \frac{U}{pn}$$

p = propeller pitch
n = propeller revolutions per second
k = constant (semi-empirical)
subscript e indicates the value at the equilibrium conditions

The hydrodynamic force coefficients of X' differ in form from the lateral force coefficients Y' in Eq. (A-4), e.g.,

$$\begin{aligned} c_1 &= X'_0 \\ c_2 &= X'_{vr}, \quad \text{etc.} \end{aligned} \quad (A-6)$$

and X'_p = propeller thrust depending on K_t , K_q and J (i.e., u' and n'). Lower constant characteristics are used assuming a steam turbine for the ship in this study.

The following rudder control characteristics are employed:

$$\delta_d = a(\psi - \psi_e) + b'\dot{\psi} + c'\ddot{\psi} + \delta_e + t_r'\dot{\delta}' \quad (A-7)$$

where

δ_d = rudder command
 δ_e = rudder at equilibrium condition
 δ = actual rudder angle
 a, b', c' = gain constants

and $t_r' = 0.1$, $\dot{\delta}' = 2.3$ deg/sec, $\delta' \leq 35$ deg in most simulations.

TABLE 1
PRINCIPAL PARTICULARS

LBP, ft	1085
Beam, ft	170
Depth, ft	84
Draft	65', 5-3/4"
Draft, molded	65', 4-3/4"
Displacement, tons	285,944
Midship coefficient	0.995
Prismatic coefficient	0.834
Block coefficient	0.830
Waterline coefficient	0.909
KG, ft	45.4
LCG, forward amidships, ft	23.4
Gyradius, yaw, % LBP	23.8
Rudder area/(length x draft)	0.019

TABLE 2
SHIP AND CANAL DIMENSIONS

Tc c Description	CASE 1 Computer Simulation		CASE 2 Full-Scale Test		CASE 3 Manned Model Test	
Canal	CANAL 1		CANAL 2		CANAL 3	
Width at the bottom, W_b Width at the surface, W_a Water depth, D_w	810 ft 810 ft 78 ft		75m 160m 12.5m		135m 235m 15m	
Ship	SHIP A	SHIP B	SHIP A	SHIP B	SHIP A	SHIP B
Description of Ship	Tanker 250,000 DWT	Tanker 170,000 DWT	ASTYANAX	WILLEM BARENDZ	Tanker 70,000 DWT 1/50 Scale	Tanker 70,000 DWT
Ship length, L Beam, B Fore draft, H_f Aft draft, H_a Speed, U	1085 ft 170 ft 65 ft 65 ft 6.1 kt	965 ft 151 ft 58 ft 58 ft 9.1 kt	137.2m 18.9m 4.3m 5.9m 6.1 kt	190m 27.6m 7.0m 7.9m 5.2 kt	241m 34.6m 13.3m 13.3m 6.1 kt	241m 34.6m 11.0m mean 6.5 kt
RATIO W_b/B D_w/H_m	4.75 1.2	5.36 1.35	4.0 2.45	2.7 1.68	3.9 1.13	3.9 1.36
DATE	Feb 1972		17 Oct 1962		1960 to 1962	

TABLE 3. PRINCIPAL PARTICULARS

	A	B	C
Length, ℓ , ft	910	910	910
ℓ/B	6.95	5	4
ℓ/H	19.56	16.2	16.2
B/H	2.81	3.24	4.03
Block Coefficient, C_b	0.613	0.820	0.810
Prismatic Coef., C_p	0.625	0.823	0.813
LCG forward m/ℓ	-0.015	0.026	0.019
Rudder Area/ ℓH	1/45	1/53	1/48

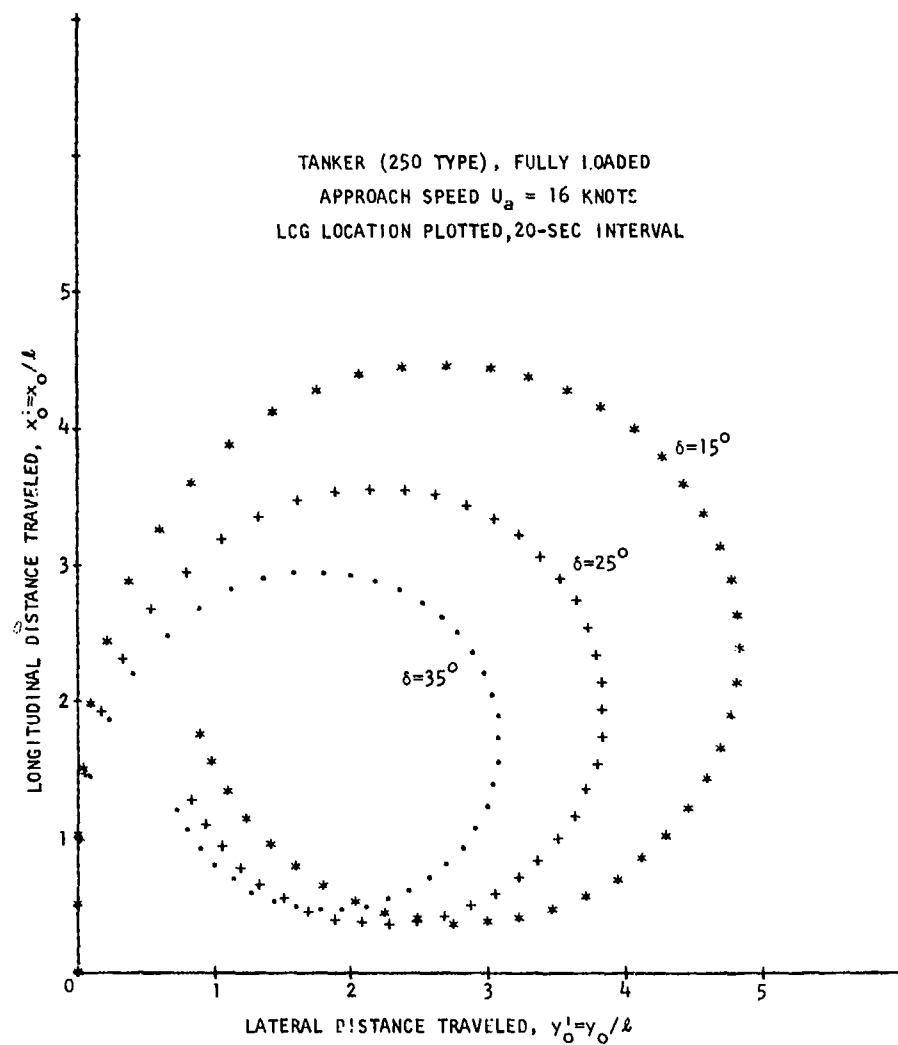


FIGURE 1. COMPUTED TURNING TRAJECTORY

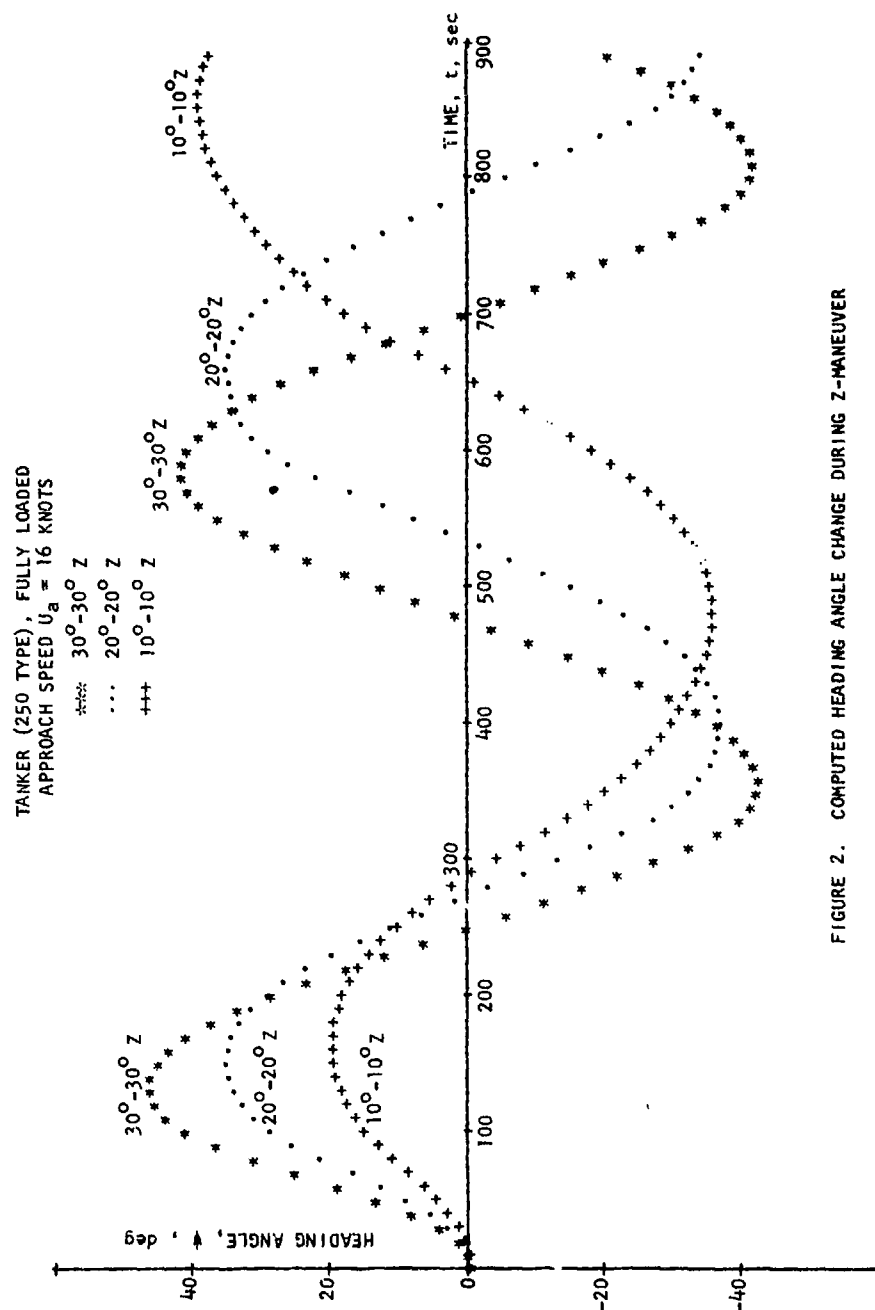


FIGURE 2. COMPUTED HEADING ANGLE CHANGE DURING Z-MANEUVER

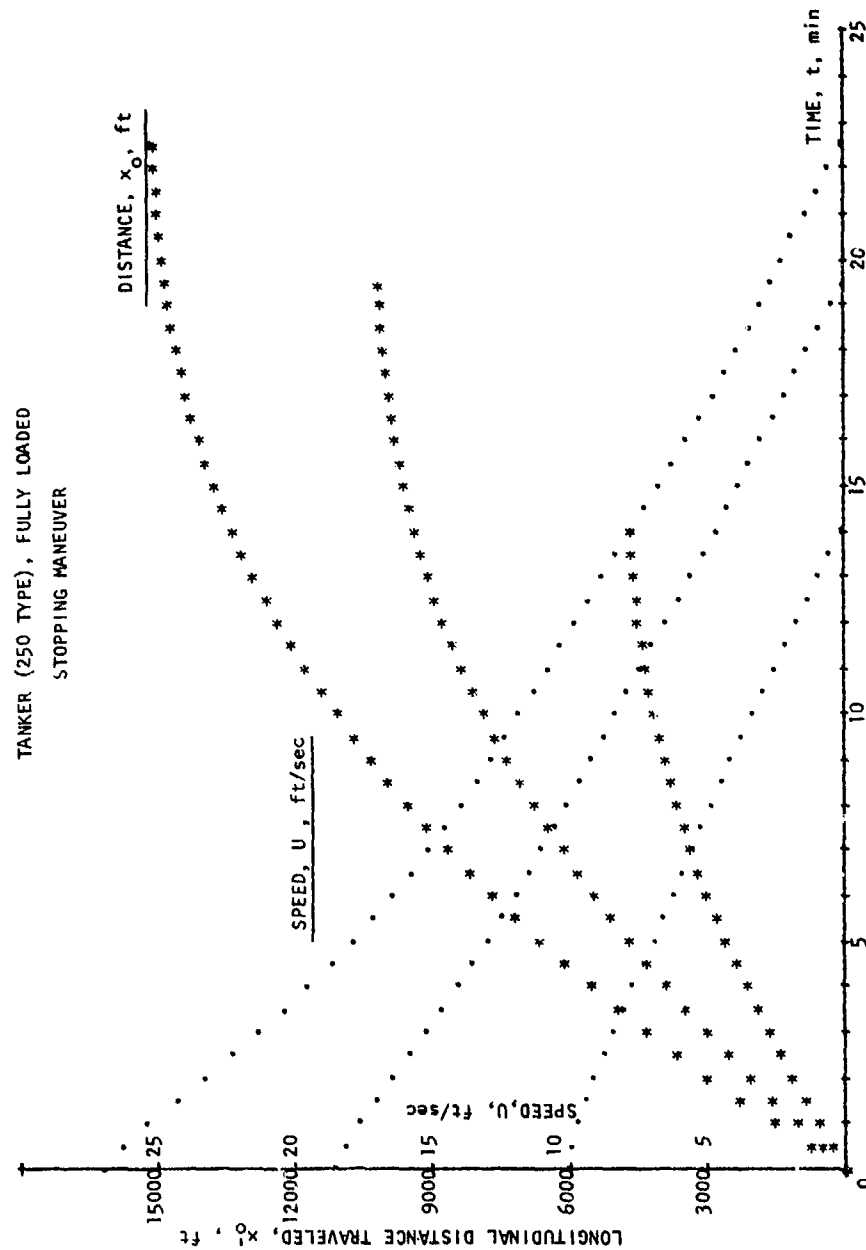


FIGURE 3. COMPUTED SPEED AND LONGITUDINAL DISTANCE TRAVELED DURING STOPPING

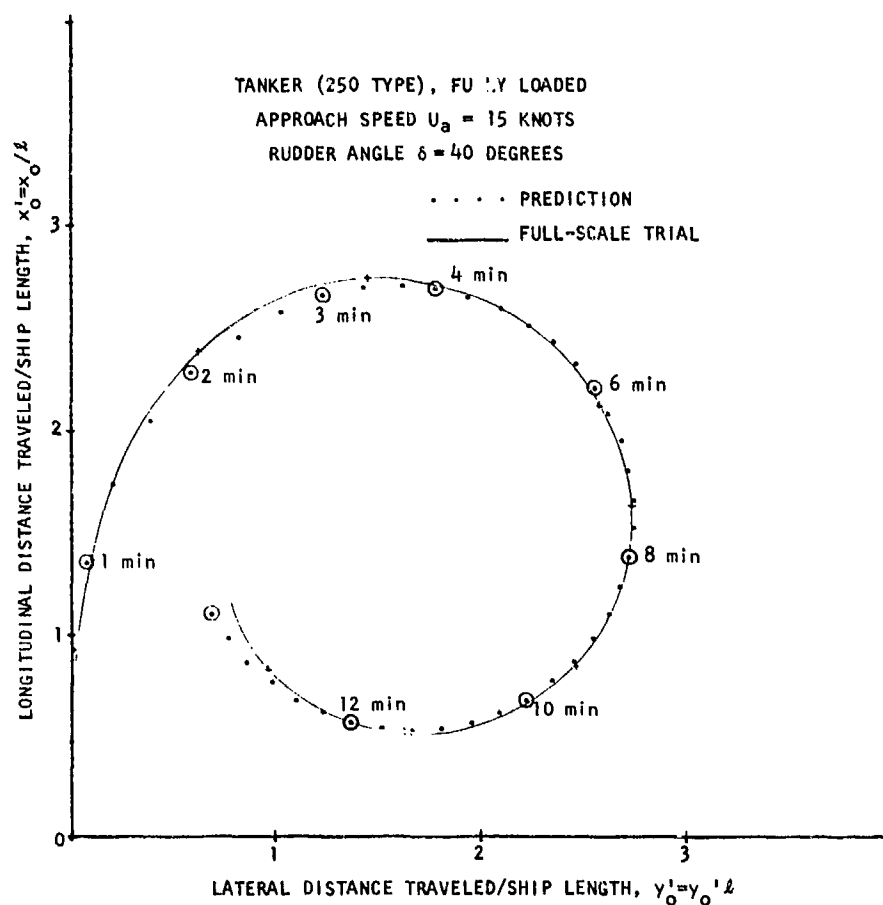


FIGURE 4. TURNING TRAJECTORY CORRELATIONS

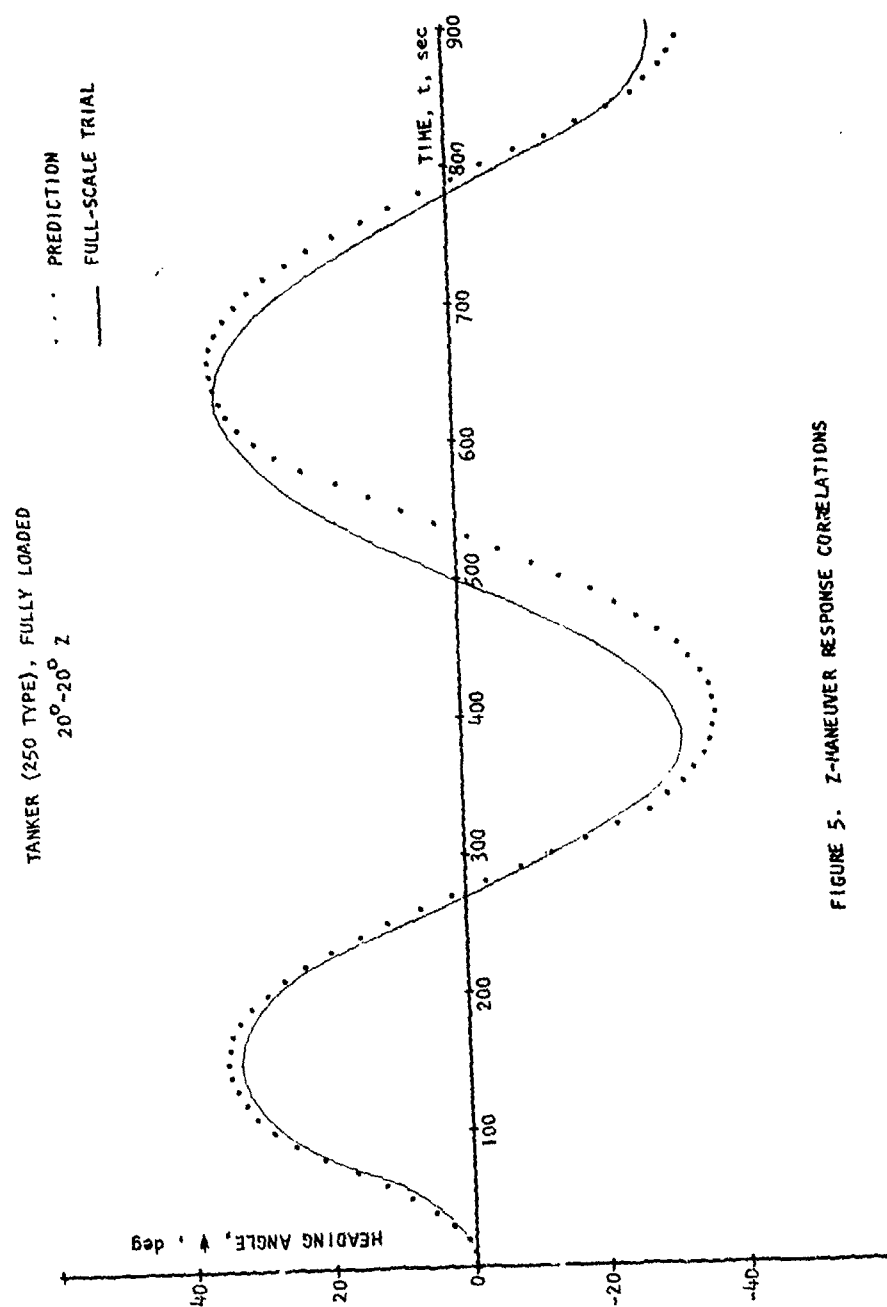


FIGURE 5. Z-MANEUVER RESPONSE CORRELATIONS

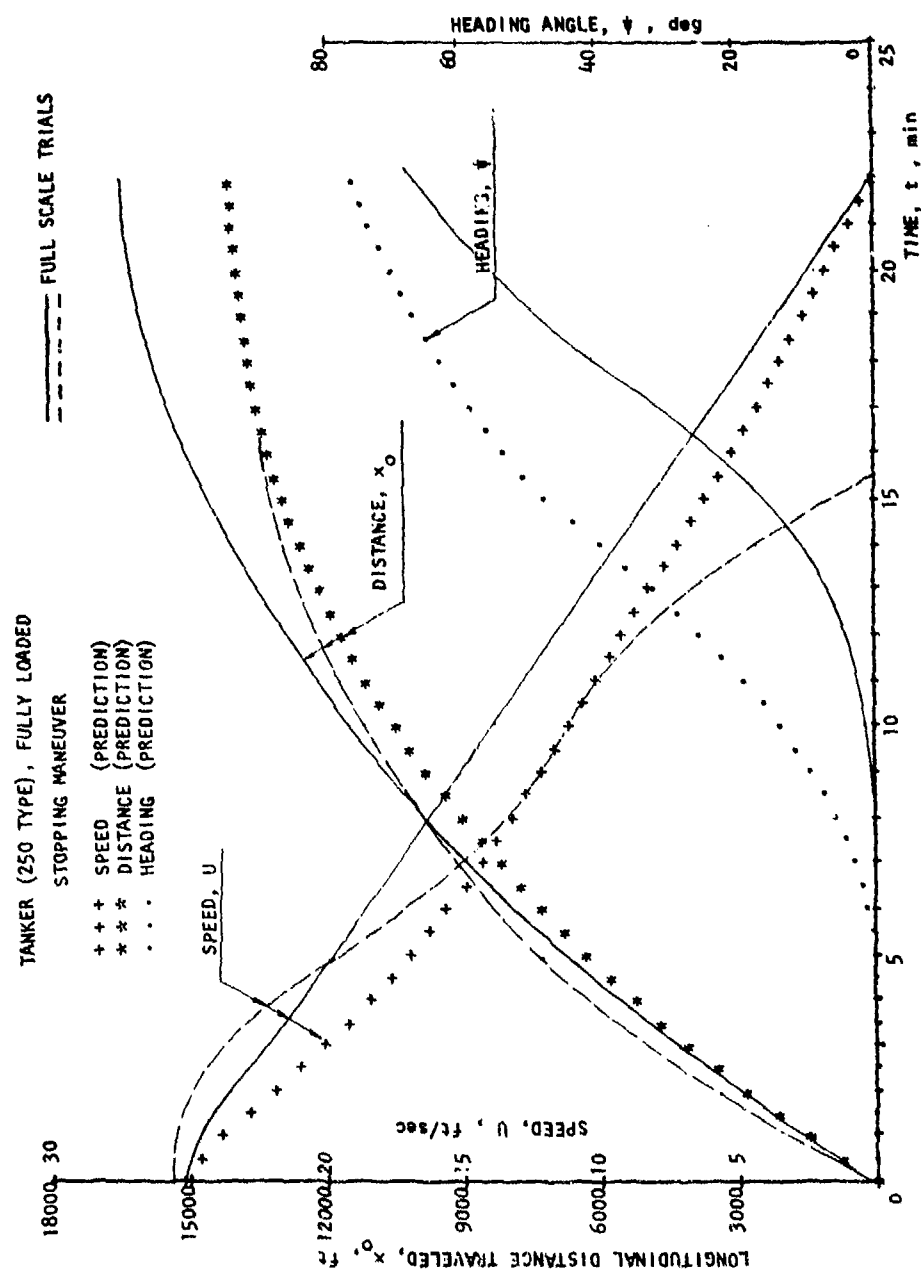


FIGURE 6. STOPPING TRAJECTORY CORRELATIONS

TANKER (250 TYPE), FULLY LOADED

Approach speed = 16 knots

Rudder angle $\delta = 35$ deg

Approach speed = 4 knots

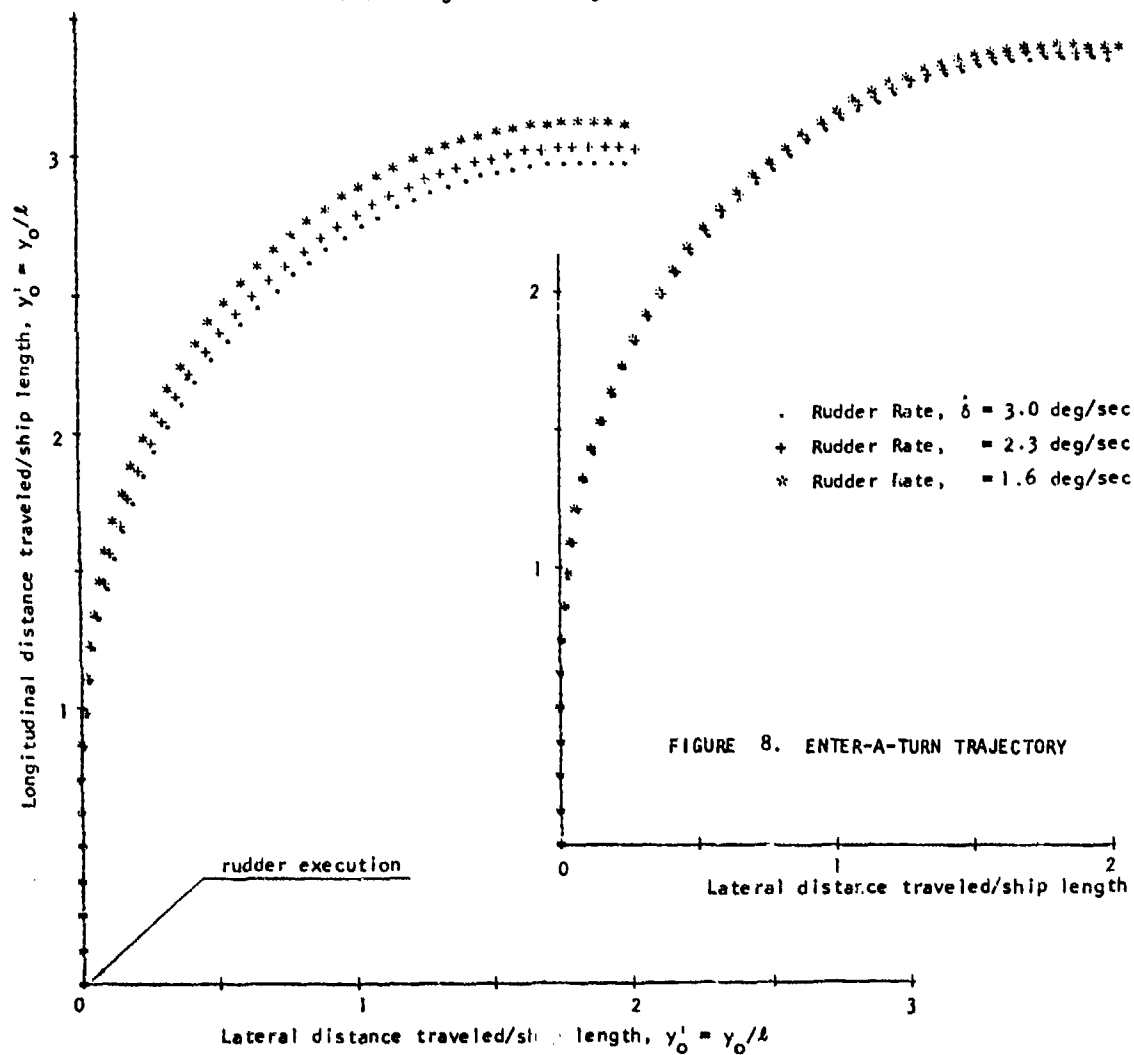


FIGURE 8. ENTER-A-TURN TRAJECTORY

FIGURE 7. ENTER-A-TURN TRAJECTORY

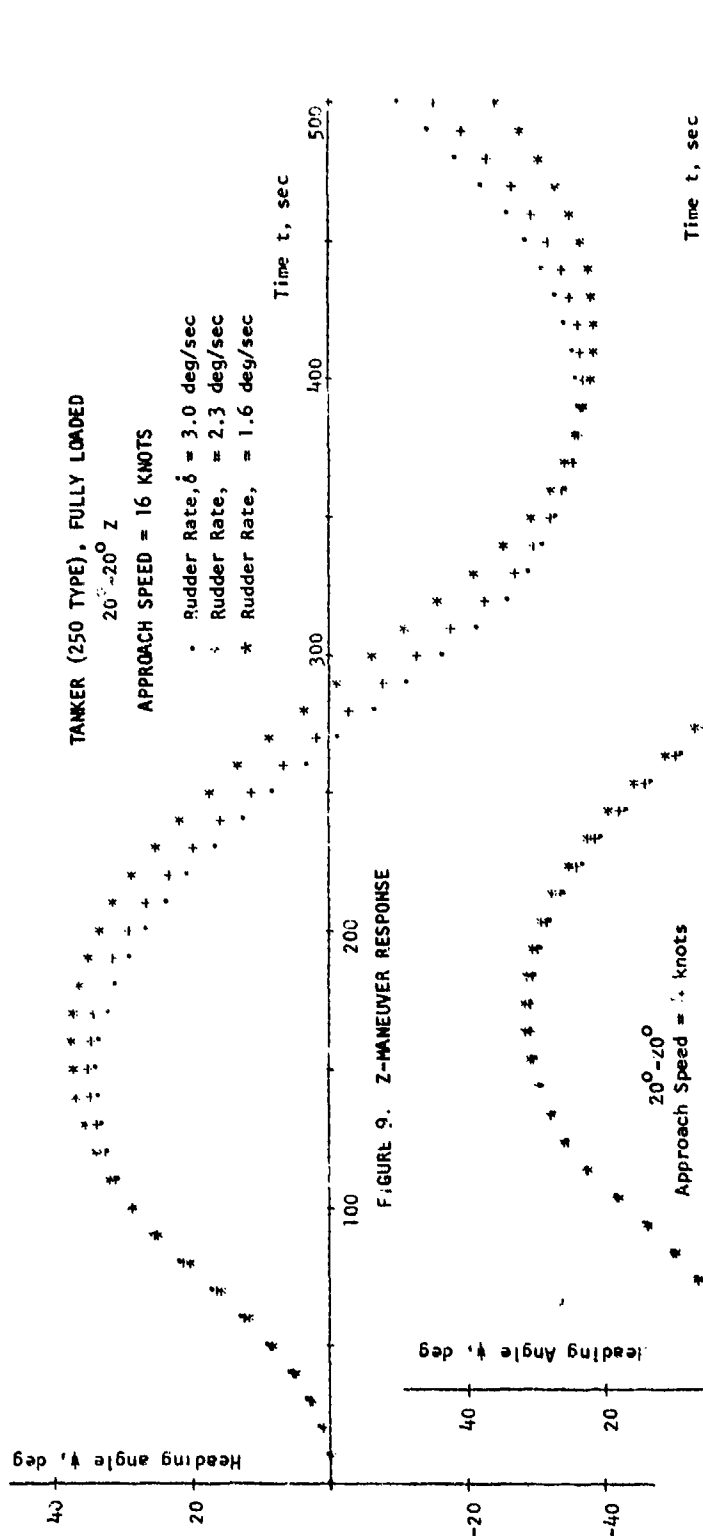


FIGURE 9. Z-MANEUVER RESPONSE

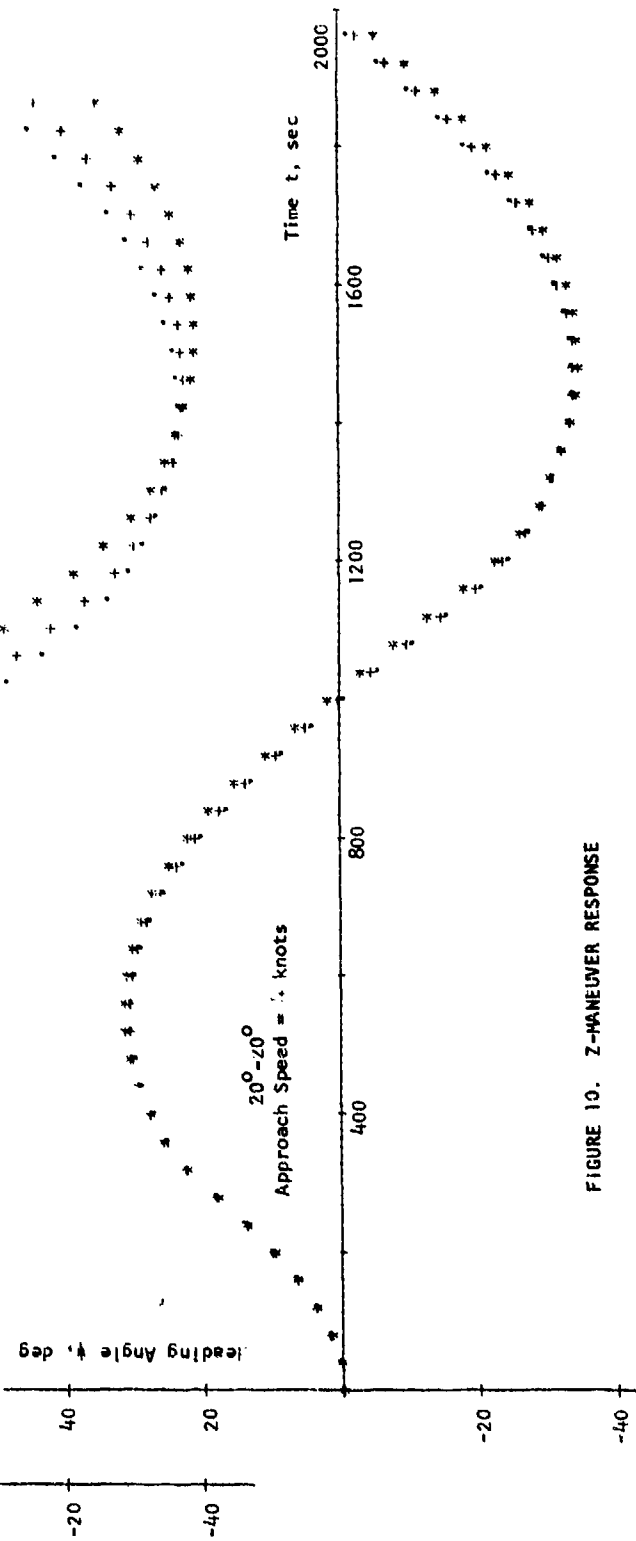


FIGURE 10. Z-MANEUVER RESPONSE

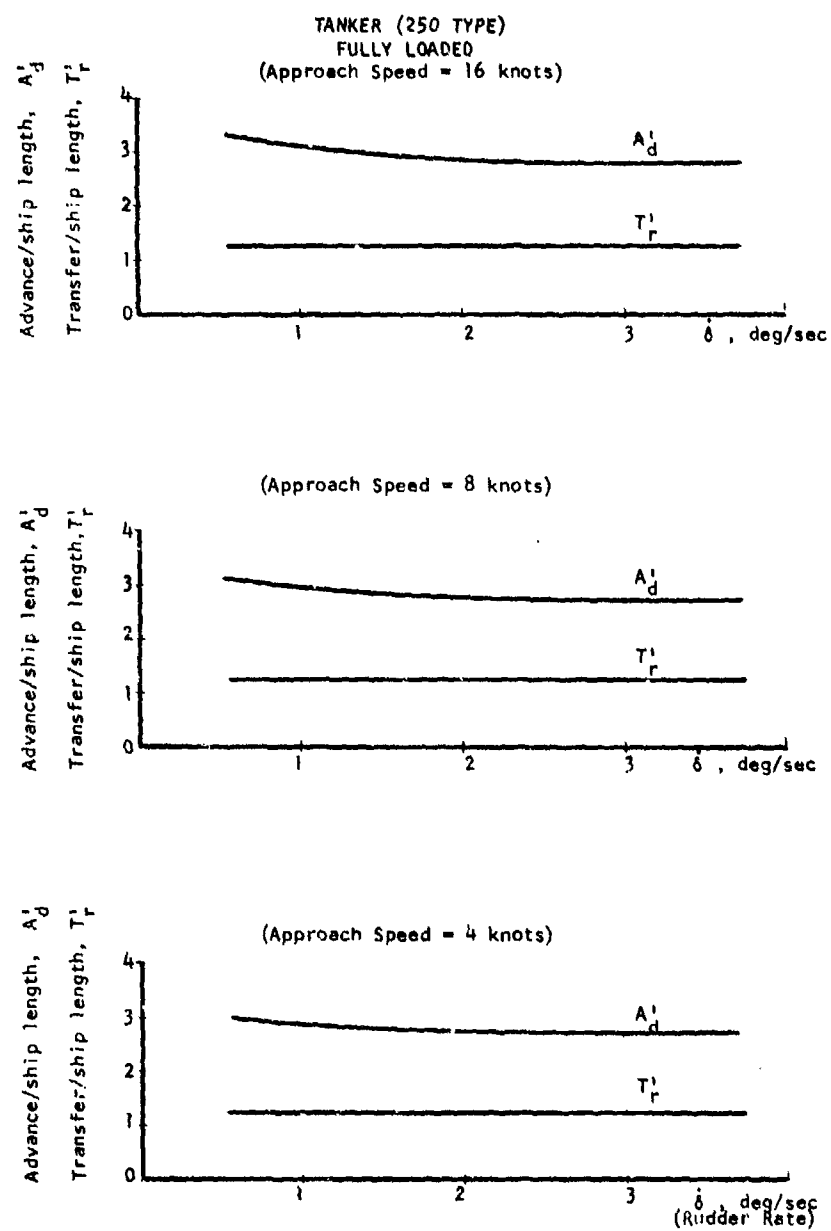


FIGURE 11. EFFECT OF RUDDER RATE ON TURNING TRAJECTORY

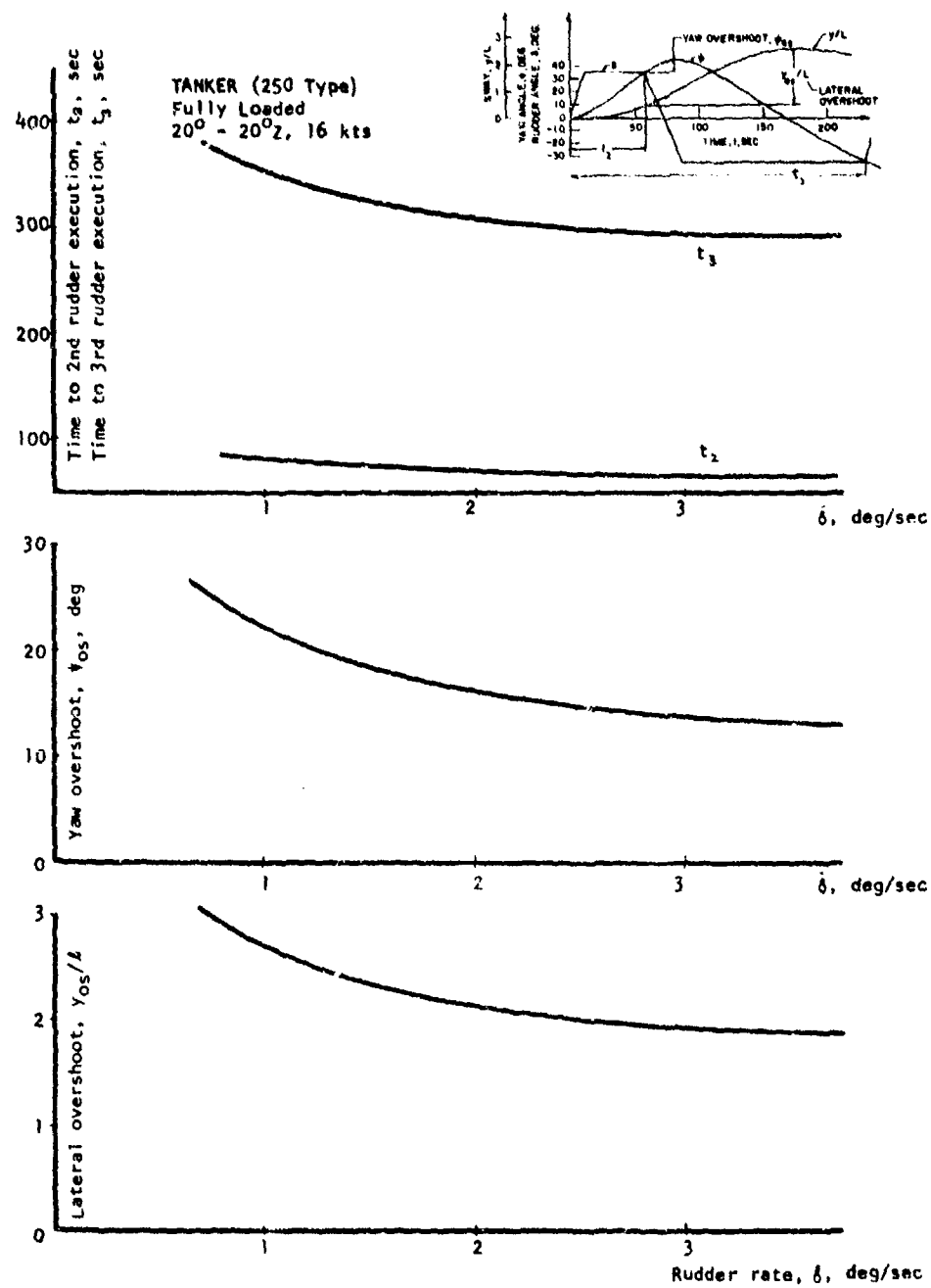


FIGURE 12. EFFECT OF RUDDER RATE DURING Z-MANEUVER

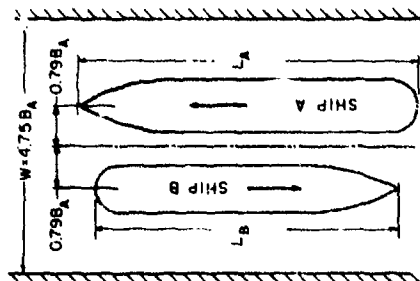
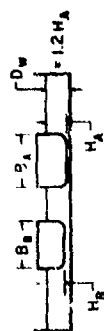


FIGURE 13. MEETING OF SHIPS
IN A CANAL

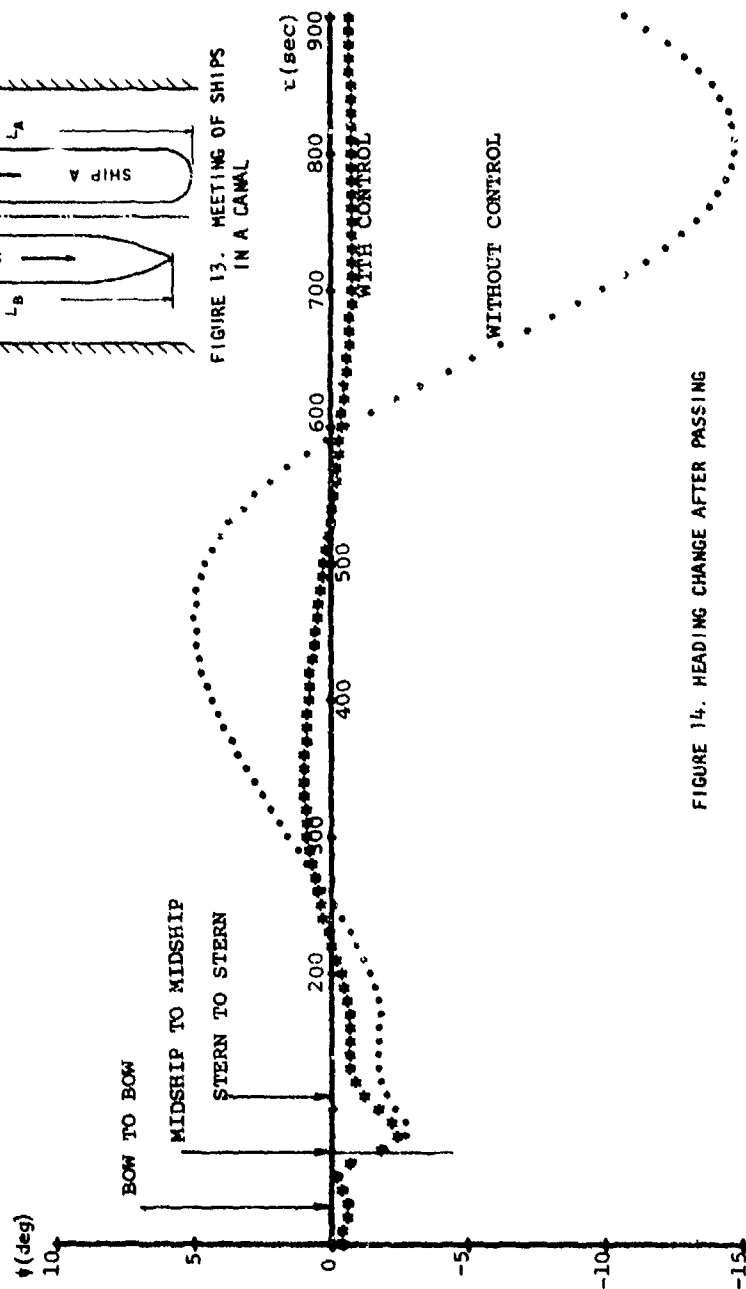


FIGURE 14. HEADING CHANGE AFTER PASSING

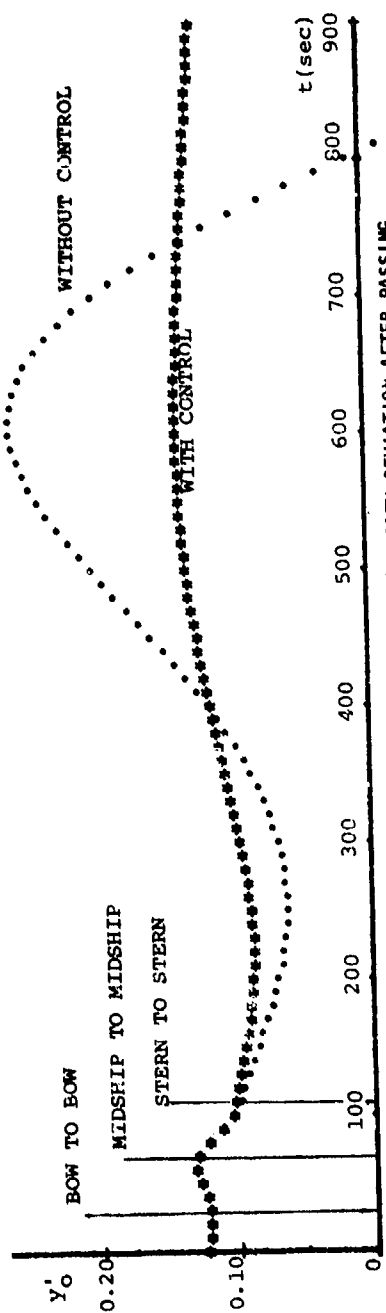


FIGURE 15. PATH DEVIATION AFTER PASSING

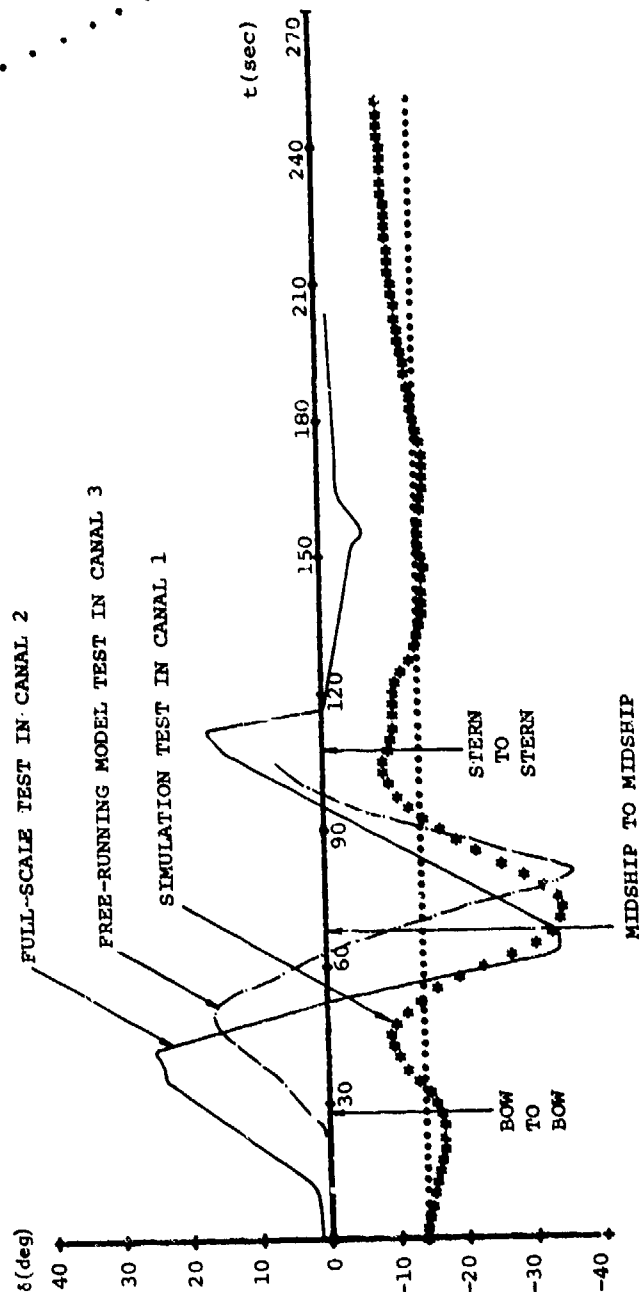


FIGURE 16. COMPARISON OF RUDDER ACTIVITY

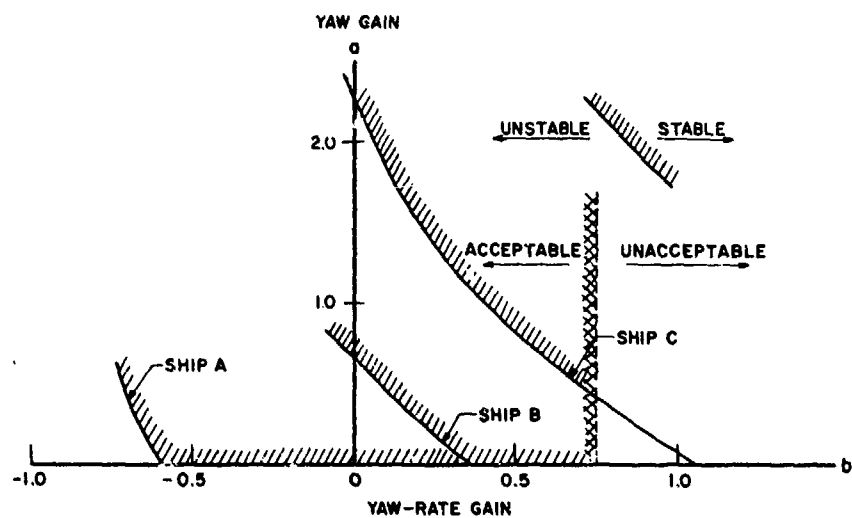


FIGURE 17. REGION OF DIRECTIONAL STABILITY

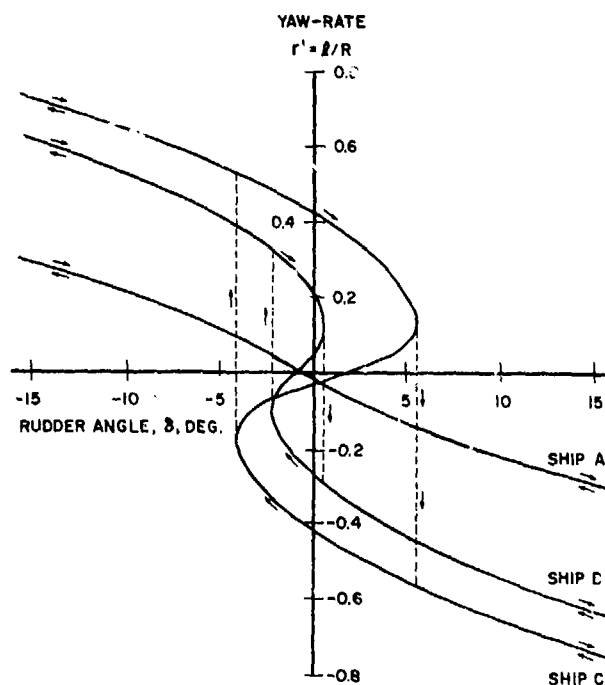


FIGURE 18. STEADY-TURNING VS. RUDDER ANGLE

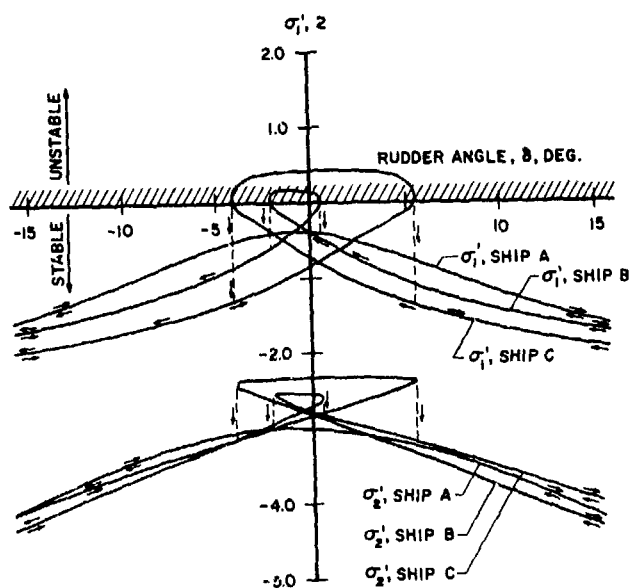


FIGURE 19. DYNAMIC STABILITY ROOT LOCUS

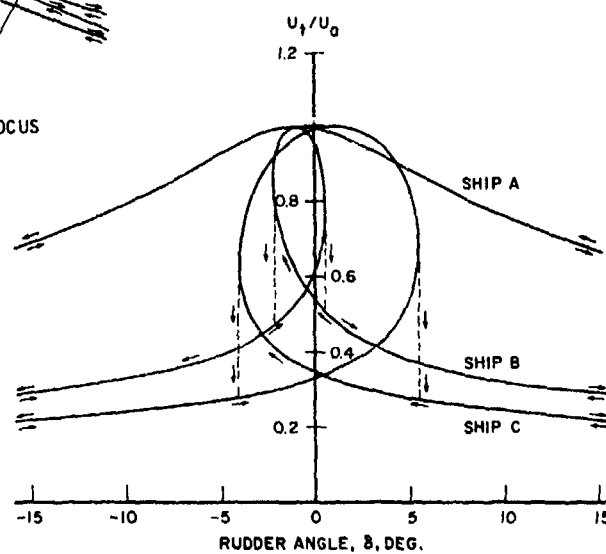


FIGURE 20. SPEED REDUCTION DURING STEADY TURNING

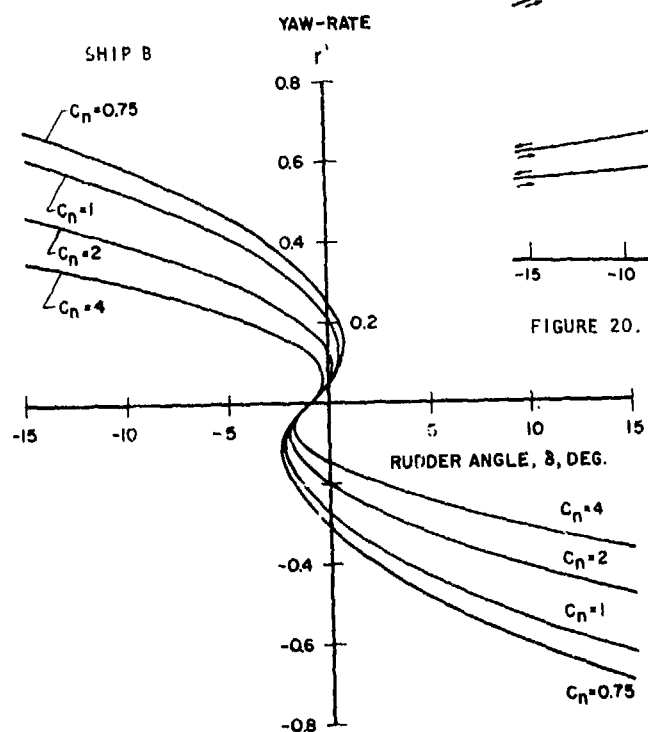


FIGURE 21. EFFECT OF NONLINEAR HYDRODYNAMIC TERMS ON STEADY TURNING

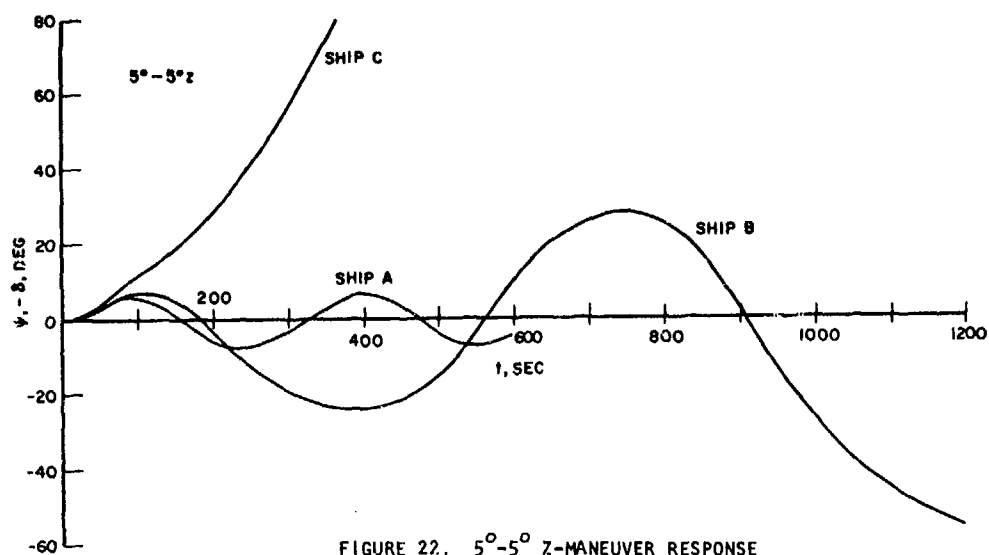


FIGURE 22. 5°-5° Z-MANEUVER RESPONSE

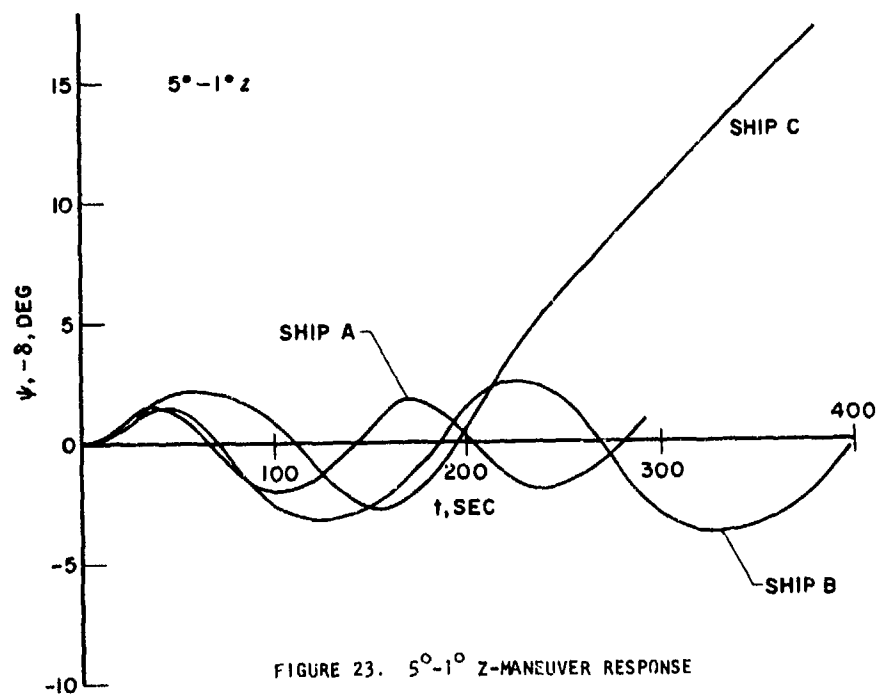


FIGURE 23. 5°-1° Z-MANEUVER RESPONSE

DISCUSSION

ALEX GOODMAN

Doctor Eda, as usual, has contributed a very fine paper on the subject of digital simulation analysis as applied to the maneuvering performance of ships. Again this paper illustrates the power of the captive-model, computer-simulation approach to providing engineering solutions to the maneuvering problems of ships operating under various environmental conditions. However, I have a few questions which I hope he can answer.

(a) How is the influence of the propeller slipstream on the rudder forces accounted for? For the model size

used by Dr. Eda (i.e., 5-ft long) the propeller size and model wake will not produce meaningful data.

(b) Are the static derivatives Y'_v , N'_v , Y'_r , and N'_r obtained by extrapolating rotating arm data to infinite radius ($r' = C$)?

AUTHOR'S REPLY

At Davidson Laboratory, we measure forces and moments acting on the model for a range of rudder angles and propeller revolutions (including both ship-propulsion point and model-propulsion point). Thus, we can obtain the necessary data regarding the effect of the propeller slipstream on rudder forces.

It should be pointed out here that yaw moment and lateral forces due to the rudder located in the propeller stream are hydrodynamic moments and forces mainly due to lifts acting on the rudder, and that these measurements

are not critically influenced by the model size (or Reynolds number) as expected in other tests, such as resistance tests.

We determine static derivatives Y'_v , N'_v , Y'_r , and N'_r at infinite radius ($r' = 0$) by oblique towing in our regular towing tank (Tank No. 3 of Davidson Laboratory), and also by interpolating (not extrapolating) of rotating-arm data from data obtained at $\pm r'$.

HYDRODYNAMICS FOR SAFETY — MANEUVERING

SESSION III

Tuesday, June 25, 1974
9:00 A.M. — 12:10 P.M.

Chairman: Mr. J. A. H. Paffett
Superintendent, Ships Division
National Physical Laboratory
England

Hybrid Computation for the Simulation of the Maneuvering Ships	209
G. Mak and G.M. van der Bend, Netherlands Ship Model Basin, Wageningen, The Netherlands	
Simulation of Vessel Encounters in Confined Waters	221
J. Patell, N. Norrbin, J.W. Devanney III, N. Szasz. Carnegie-Mellon University Pittsburgh, PA., and Swedish State Shipbuilding Experimental Tank Goteborg, Sweden, M.I.T. Cambridge, MA.	
The Analysis of Safety Margins in the Maneuvering of Large Ships in Confined Waters	245
I. Oldenkamp, Royal Institution of Engineers, Netherlands and P.J. Paymans, Ergonomics Society, Netherlands	
Some Aspects of Maneuvering in Collision Situations in Shallow Water	261
I.W. Dand, National Physical Laboratory, Feltham, Middlesex, England	
When is Collision Unavoidable?	277
W.C. Webster, University of California, Berkeley, California	

HYBRID COMPUTATION FOR THE SIMULATION OF THE MANEUVERING SHIPS

G. Mak
Netherlands Ship Model Basin
Wageningen, The Netherlands

G. M. van der Bend
Netherlands Ship Model Basin
Wageningen, The Netherlands

INTRODUCTION

Since the end of 1970 the Netherlands Ship Model Basin has put into operation a ship manoeuvring simulator. On this simulator sailing conditions can be encountered according to the actual situations.

In Fig. 1 a rough indication is given of the working procedure of the simulator. It can be seen that the computation consists of mainly two

parts viz. the calculation of the ship motions and the calculation of the setting of instruments on the bridge and the projection system from which the mariner gets the impression about the motions of the ship.

For the computation of the ship motions a hybrid computer is chosen because of its special advantages like continuous integration and parallel computation in relation with the real-time simulation.

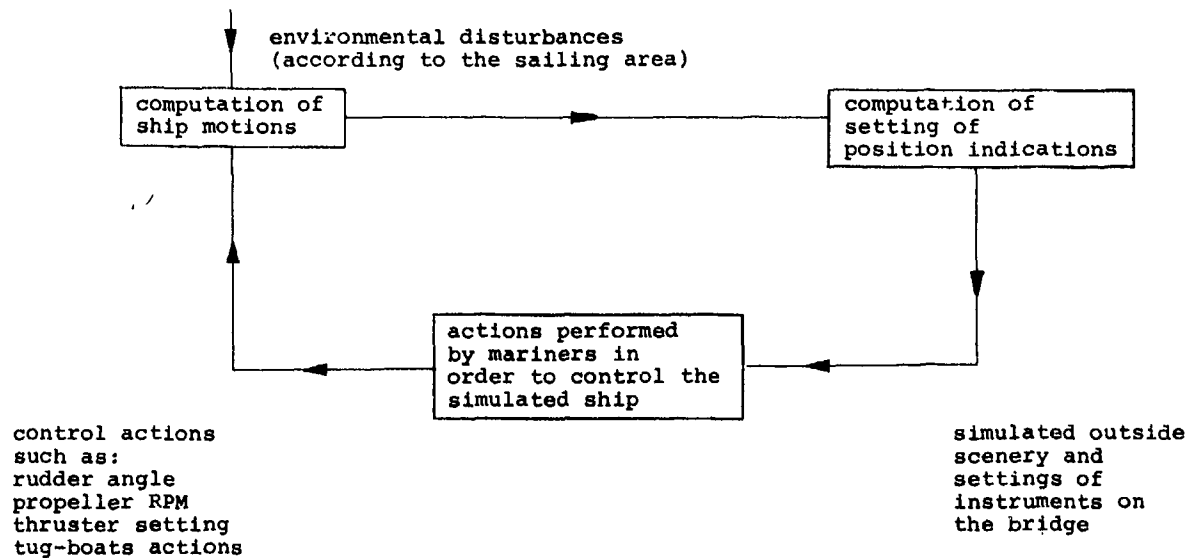


Fig. 1 Schematic system of the working procedure of the simulator.

A special purpose servo-computation unit with a mechanical integration unit to determine the course of the ship has been developed to enable infinite course changes and a synchro-coupling with the compass on the bridge.

Also connected with the analog computer is the radar simulator on the bridge. The coastline image is generated from a photographic picture. The input for this is the position of the ship. Further there are two moving targets installed. These targets can be controlled manually or by the analog computer.

SET-UP OF THE SIMULATOR

An impression of the set-up of the simulator is given in Fig. 2. The wheelhouse (width 6m, depth 4m, height 2,15 m) is equipped with instruments found on board modern big ships. The instrument consoles include a rudder control unit with rudder angle indicator and automatic pilot,

engine telegraph (which can be adapted to both single and twin screw arrangement), engine remote control, bridge control, repeater compass, RPM indicator, log, wind velocity and direction meters, echo sounders, V.H.F., intercom and control (RPM and pitch) for bow and stern thrusters.

Further there are a Raytheon 16-inch display and a doppler docking system available. In the center of the wheelhouse the chart table and Decca navigator are placed. The location of all instruments can be changed and adapted to the desired type of bridge.

Before reaching the bridge one first passes a ship's corridor and an acclimatization room (see Fig. 3), to make a gradual change-over from full daylight to the simulated daylight. This room is furnished like a captain's office.

The simulation of the outside view is accomplished by means of a point-light-source projection method. At the top of the wheelhouse a point-

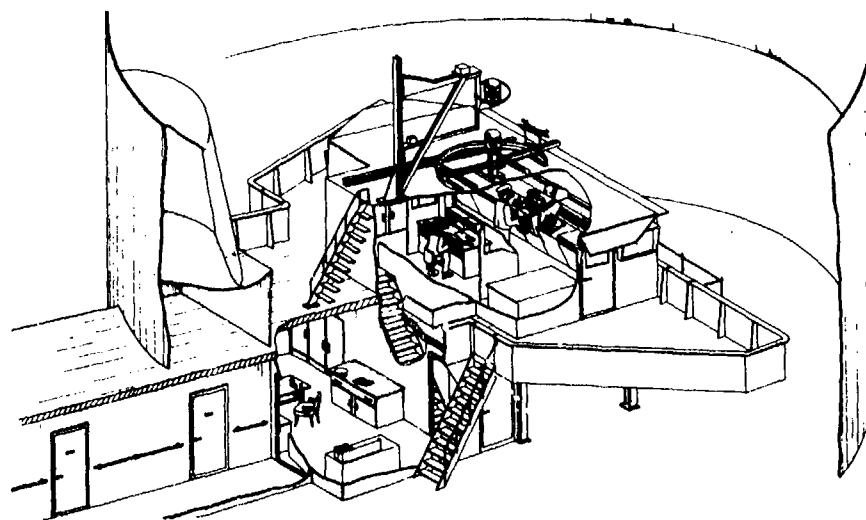


Fig. 2 Lectional perspective drawing of the simulator



Fig. 3 Acclimatization room

light-source is mounted. Around this lamp a three-dimensional object is moving according to the ship's movement.

The shadow of this object on the cylindrical projection screen (diameter 20 m) which surrounds the wheelhouse gives the outside view of for instance a harbour entrance. The picture of the ship in front of the bridge is obtained by the projection of a slide. With this projection system a realistic view is perceptible when looking aside or astern from any point of the wheelhouse.

Fig. 4 gives the outside view of a channel with a width of 400 meter and the entrance of a harbour.

The computer is situated in a control room (Fig. 5) where also registration instruments (like an eight-channel pen recorder and magnetic tapes), an instrument console

(duplicating all bridge indicators) and a t.v.-circuit to observe the forward view from the bridge, are located, so that manoeuvres can be followed in the control room without disturbing the officers on the bridge.

THE MATHEMATICAL DESCRIPTION OF THE MANOEUVRING SHIP

To study the manoeuvring of surface ships, it is common practice to consider three degrees of freedom: only the horizontal motions of the ship are taken into account.

For certain applications, however, it may be necessary in the future to include also one or more vertical motions in the mathematical model of the manoeuvring ship.

In the case of third generation container ships, for instance, it has been observed that these vessels can attain considerable heel angles during

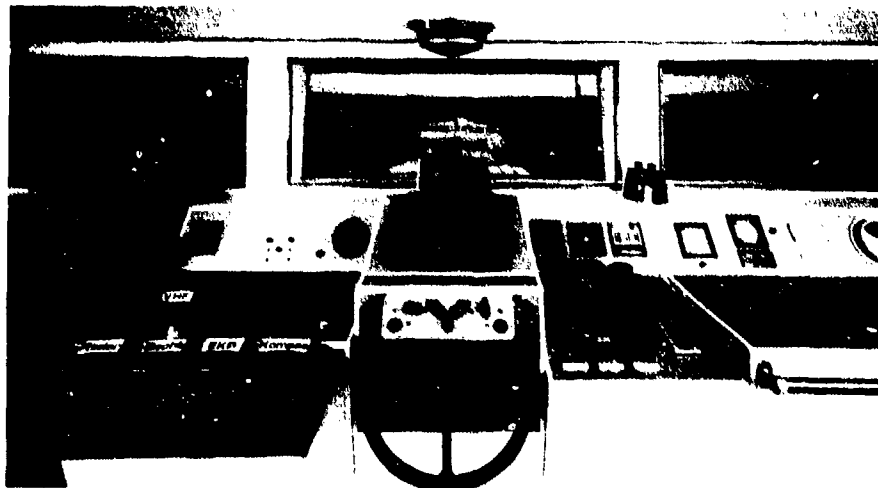


Fig. 4 Outside view of harbour-entrance and manoeuvre
in a channel



Fig. 5 Control room with hybrid-computer

course changes when running at high speeds, due to the low initial transverse stability and a large heeling moment caused by the rudders.

The hydrodynamic forces will be affected by the heeling of the ship. Another phenomenon which may necessitate an extension of the conventional manoeuvring equations is the sinkage and trim of ship in very shallow water. The hydrodynamic forces are very sensitive for a change in the keel clearance of the ship. For the case of a ship running at a constant speed in water of constant depth this effect imposes no special problems, but if these conditions are not met the introduction of squat and trim as additional degrees of freedom may be needed.

According to Newton's law, the horizontal motions of a ship with respect to a right-handed, space

fixed system of axes as defined in Fig. 6, are given by:

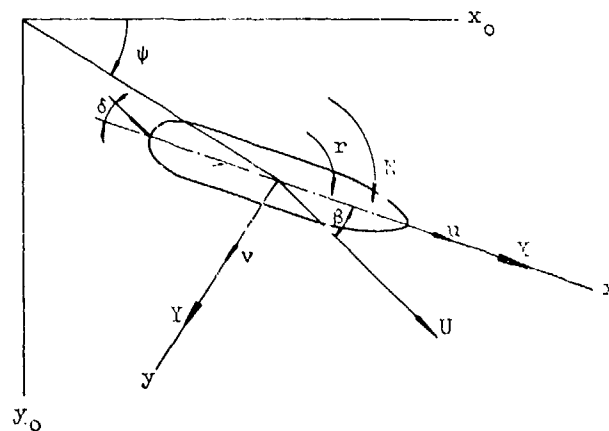


Fig. 6 Axes of reference

$$X_0 = m\dot{x}_0$$

$$Y_0 = m\dot{y}_0$$

$$N = I_z \dot{\psi}_0$$

where m = mass of the ship

I_z = moment of inertia around the vertical axis through the centre of gravity of the ship

When using the moving system of axes $x y z$ with its origin in the centre of gravity of the ship, the motions can be described by:

$$\begin{aligned} X &= m (\dot{u} - vr) \\ Y &= m (\dot{v} + ur) \\ N &= I_z \dot{r} \end{aligned} \quad (2)$$

in which X = longitudinal force on the ship

Y = transverse force on the ship

N = moment around vertical axis

u = speed component in x -direction

v = speed component in y -direction

r = angular velocity

U = direction of motion $U = (u^2 + v^2)^{1/2}$

δ = rudder angle

ψ = drift angle

X , Y and N are the total forces and moment exerted on the ship which are composed of:

- hydrodynamic forces due the motion of the ship
- rudder and propeller forces
- external disturbances caused by wind, waves, current, passing ships, banks, tug boats etc.

At a constant waterdepth, the hydrodynamic forces and rudder forces are a function of the motions of the ship,

the mean forward velocity, the rudder angle, the number of revolutions of the propeller:

$$\begin{aligned} X &= X(u, v, r, \dot{u}, \dot{v}, \dot{r}, n, \delta) \\ Y &= Y(u, v, r, \dot{u}, \dot{v}, \dot{r}, n, \delta) \\ N &= N(u, v, r, \dot{u}, \dot{v}, \dot{r}, n, \delta) \end{aligned} \quad (3)$$

Usually, the hydrodynamic forces and rudder forces are expanded in a Taylor series (see ref. [1]).

If the expansion is restricted to the first order, and if only small deviations from a straight course of a ship running at constant speed are considered, the following linear equations are obtained:

$$\begin{aligned} (m - Y_v) \dot{v} - Y_v v - Y_r \dot{r} - (Y_r - mU) r - \\ Y_\delta \delta = Y \\ -(I_z - N_r) \dot{r} + N_v v + N_v v + N_r r + N_\delta \delta = -N \end{aligned} \quad (4)$$

Y and N are the external disturbances, acting on the ship. U is the ship's speed. The derivatives Y_v and Y_r are called added masses, the derivatives N_r and N_v added moments of inertia and Y_v , Y_r , N_v and N_r are damping coefficients.

The equations presented in (4), are mostly used for the determination of the ship's stability indices.

Since, however, ship motions have to be performed which need not be small deviations from a straight course at constant speed, a further elaboration of equation (4) is necessary when simulating the ship's manoeuvrability.

HYDRODYNAMIC FORCES

When considering the hydrodynamic forces it is assumed that all variables (such as propeller RPM, rudder angle and waterdepth) other than the ship motions are constant. It then can be assumed that:

1. all forces are symmetric to port and starboard
2. the cross-coupling between acceleration and velocity parameters can be neglected.

One then finds:

$$\begin{aligned}(m-X_{\dot{u}}) \dot{u} &= X(u, v, r) \\ (m-Y_{\dot{v}}) \dot{v} - Y_r r &= Y(u, v, r) \\ -N_{\dot{v}} \dot{v} + (I_z - N_r) \dot{r} &= N(u, v, r)\end{aligned}\quad (5)$$

Added Mass: It should be noted that due to retardation effects (see ref. [2]) the added mass coefficients depend on the frequency of which the ship motions can be composed of. When this frequency dependency is important, time integrals of the retardation function have to be added in equation (5). In deep water the horizontal motions of large ships are so slow that it can be assumed that the added mass coefficients are constant for different frequencies of oscillations.

In shallow water, however, it can be shown that the addition of a retardation function will provide a better simulation of the ship's manoeuvrability than the use of constant added mass coefficients only (see ref. [3]).

In the present simulation, however, even in shallow water constant coefficients are still used which are the averaged values over as large a frequency range as considered necessary.

From the above considerations and assumptions it can be concluded that added mass coefficients only depend on the ship's geometry and the waterdepth while no influences from other aspects such as the ship's speed, propeller RPM are to be taken into account.

Added mass coefficients can be determined from model tests with oscillation techniques as well as from

computer calculations based on potential theories.

The good agreement between model test results and the results from potential theories justify the assumption that viscosity has little influence on the added masses which is in agreement with the earlier conclusions.

Damping: The forces on the right hand side of equation (5) are called damping forces which are determined by the ship's velocity component relative to the water. It is generally accepted that for larger motions of the ship the damping forces are influenced by higher order terms, which means that these forces contain terms which are proportional to the second and third order of velocities. At the same time cross-coupling effects play an important role which means that these forces contain terms which are proportional to the product of the velocity components.

In addition to this, one should be aware for the following aspects:

- the damping forces are influenced by the waterdepth (see ref. [4]) In the simulation process a set of coefficients is stored for a number of specific waterdepths. At each time during the manoeuvre the waterdepth is known (as a function of time of the tide and of the ship's position) after which the coefficients used for the calculation of the ship motions are found after an interpolation process between the coefficients known at the pre-conditioned waterdepth.
- Though the propeller RPM sometimes will affect the sway and yaw damping forces this influence yet has been neglected so far. The same holds for the influence of lateral thrusters on the damping force.

The damping coefficients are mostly obtained from model tests since no calculation method has been developed yet. Calculation of these coefficients is especially very difficult since pressure forces due to separation effects play an important role. This also means that one has to be aware of scale effects in the coefficients obtained from model test results.

For the experimental determination of the damping coefficients mostly captive model tests are performed in a statical way by means of force measurements on a restrained model (under a towing carriage or a rotating arm) or in a dynamical way by means of force measurements on an oscillated model. Both these methods are based on the principle that the motions are predetermined and the forces are measured.

At the Netherlands Ship Model Basin use is also made of free running tests, especially for the determination of the turning damping coefficients. In this case the motions of a free running model are measured accurately at a given stationary external force. Mostly this force is generated by a certain rudder angle (see next section about rudder forces). In this method at least as many runs have to be made as the largest amount of unknown coefficients in one of the three equations of motion.

This method will only lead to more accurate values of the coefficients at larger motions of the ship model.

It will be obvious that these free running tests are performed at the self propulsion point of model. It now is assumed that, except for the longitudinal resistance, all coefficients are not influenced by scale effects. In the longitudinal equation of motion the resistance as a function of the

ahead speed has to be corrected for scale effects by means of an extrapolation method. In this aspect the Δ log A-method is very much recommended for shallow water.

RUDDER AND PROPELLER FORCES.

In order to examine the rudder forces which excite the ship motions, it will be necessary to consider first a stationary condition of the ship (zero drift and yaw motion).

It will be obvious that when a single ship is kept on a straight course with zero rudder angle some resulting lateral force and yawing moment can be detected due to the propeller action. This force and moment will depend on the propeller RPM and ship's speed.

When putting the rudder at some angle, a force will be generated on the ship's hull which can be assumed to be composed of the following two contributions:

1. when the rudder lies in the propeller stream, the rudder acts as a guiding vane by which a force is generated on the rudder as a result of the declination of the propeller stream.
2. due to this declination of the propeller stream a circulation around the ship's hull will be generated which will result in an additional hull force. This phenomenon will become more dominant in shallower water.

From this consideration it will be obvious that the rudder force (so called because it is the force due to a rudder angle) does not depend only on the rudder angle but as much on the propeller RPM and the ship's speed.

$$F_{rud.} = F(u, n, \delta) \quad (6)$$

It also will be obvious now that the point of application of the resultant force on the ship's hull will lie some distance before the rudder.

In this aspect it also should be remembered that the rudder force, on the merchant ships considered, shows hardly any discontinuity at the stall angle of the rudder profile.

When performing captive model tests at several combinations of ship's speed, propeller RPM and rudder angles, the rudder force in equation (6) can be expressed by polynomials.

It should be born in mind that there will be a coupling between the hydrodynamic force in equations (5) and the rudder force in equation (6). The most important coupling is mostly found between the influence of the rudder angle and of the sway motion. For this reason additional captive model tests have to be performed at a combination of ship's drift and rudder angle.

EXTERNAL DISTURBANCES

External disturbances like current, wind, bank suction, meeting and overtaking vessels will also influence the ship's manoeuvres. Therefore the mathematical model should include these effects.

For the simulator manoeuvres it is most practical to determine the external forces on the ship at each moment, dependent on the ship's position together with the environmental situation. In this way all ship motions are obtained relatively easily.

The current force mostly can be calculated from the relative motion concept. This means that the force of a moving ship in still water will be equal to the force on a stationary ship in streaming water. In this way one finds from the earlier determined

forces F in still water:

$$F \left[\begin{array}{l} \text{moving ship in still} \\ \text{water with speed } u_j \end{array} \right] \quad (7)$$

$$= F \left[\begin{array}{l} \text{moving ship in current} \\ \text{with speed } u_{jc} \end{array} \right] = F(u_j - u_{jc})$$

in which: u_j = ship's speed relative to earth

u_{jc} = current speed relative to earth

j = number of direction indicating surge or sway.

From equation (7) it will be obvious that due to higher order terms there will be a coupling between influence of the ship's velocity and current speed, both relative to earth.

In equation (7) only the forces are described in a homogeneous current. However, when the current velocity and direction change a rotation of the ship relative to the water can be discerned according to:

$$r_c = \frac{\Delta V_c}{L} \quad (8)$$

$$\dot{r}_c = \frac{\Delta \frac{\Delta V_c}{L}}{L} + \frac{\delta \frac{\Delta V_c}{L}}{\delta t}$$

in which:

r_c = apparent rotation between current and ship

v_c = change of lateral component of current velocity over the ship's length

\dot{v}_c = change of v_c due to change of current velocity with time.

When taking into account equation (8) the excitation forces due to an instationary current the following relative influences on the current force have to be regarded (see equation (7)), like $(\dot{u} - \dot{u}_c)$, $(\dot{v} - \dot{v}_c)$ etc.

in which:

$$\dot{u}_C = v \frac{\delta u_C}{\delta y} + \frac{\delta u_C}{\delta t}$$

$$\dot{v}_C = u \frac{\delta v_C}{\delta x} + \frac{\delta v_C}{\delta t}$$

Comparison between the results of this calculation method with measurements of captive models through inhomogeneous currents (which change smoothly) have shown good results. For the determination of the forces due to more discontinuous current distributions captive model tests seem the most appropriate method.

Other external forces and moments are introduced in equation (2) as additional exciting forces. These forces and moments depend on a lot of variables. The wind for example is depending on the angle of incidence, the relative velocity and the exposed projected area of the ship and can be described by polynomials like (see ref. [5])

$$X_W = \frac{1}{2} \rho_a V_W^2 A_T \left[X_{W0} + \sum_{n=1}^5 X_{Wn} \cos n\alpha_W \right]$$

$$Y_W = \frac{1}{2} \rho_a V_W^2 A_L \left[\sum_{n=1}^5 Y_{Wn} \sin n\alpha_W \right]$$

$$N_W = \frac{1}{2} \rho_a V_W^2 A_L L \left[\sum_{n=1}^5 N_{Wn} \sin n\alpha_W \right]$$

in which:

X_W = steady longitudinal wind force

Y_W = steady transversal wind force

N_W = steady yaw wind moment

ρ_a = density of air

V_W = wind velocity with respect to the ship

A_T = exposed transverse area

A_L = exposed lateral area

L = length of the ship

X_{Wn}, Y_{Wn}, N_{Wn} = constants

α_W = the angle of incidence of the wind

after which the coefficients can be determined with model tests.

In the same way the other external disturbances like bank suction and meeting and overtaking vessels can be included. It should be noticed that these kinds of disturbances depend on a high number of variables so that the number of model tests to determine the coefficients in the polynomials can be extremely large.

PROGRAMS CARRIED OUT ON THE SIMULATOR

Up to now two kinds of programs have been carried out on the manoeuvring simulator.

- training courses
- research programs

These training courses are used to familiarize the mariner manoeuvring VLCC's under conditions as different waterdepths, currents and wind. The manoeuvres are changing during the course like changing of course with leading lines or entering a harbour.

From each manoeuvre the position is recorded on a Decca-plot (see Fig. 7) and variables like velocities, rudder angle on an eight-channel pen-recorder (see Fig. 8). These registrations are used to discuss the manoeuvres with the mariners.

Research programs are carried out e.g. for developing new harbour lay-outs or design of new navigational aids like track-predictors. During such a program a number of mariners are making the same manoeuvres; the conditions of, for example, wind or current, are systematically varied and of each manoeuvre position, heading, velocity and human orders like rudder and engine are recorded on an eight-channel pen-recorder and digital tape-recorder.

These pen-recordings are used to

check the registration signals while the digital recordings are used for statistical calculations like average manoeuvre (see ref. [6]). From these calculation advices can be given to the principals.

NEW DEVELOPMENTS OF THE SIMULATOR

The history of the use of a ship manoeuvring simulator is relatively short, and as may be expected the development goes fast. A lot of effort therefore will be devoted to the improvement of the simulation techniques. The set-up of experiments has been improved and will be improved further as insight in the problems of ship handling increases. As safety in waterways and harbours is of great importance, there is need of a second simulator so that two ships can simultaneously be simulated in a certain area. Also the process of analysing the registration from rough data on a recorder to meaningful results has improved very much. It is obvious

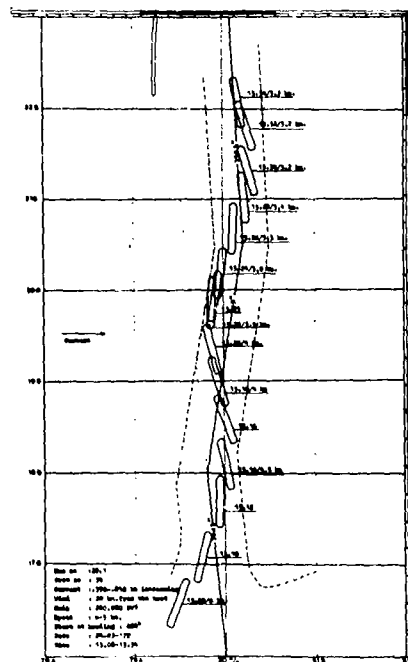


Fig. 7 Decca-plot of a manoeuvre

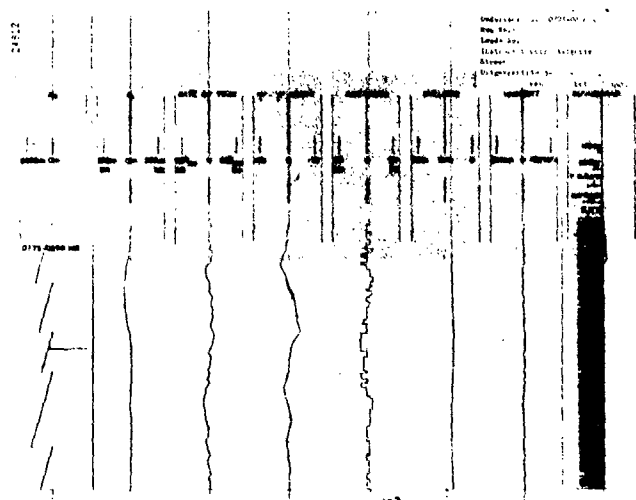


Fig. 8 Registration on an eight-channel pen-recorder

that this process will continue; new fields of research will be discovered

as knowledge about ship handling increases.

REFERENCES

- [1] Ph. Mandel - Ship Manoeuvring and Control in Principals of Naval Architecture, New York 1967
- [2] W.E. Cummins - The forces and moments acting on a body moving in an arbitrary potential stream
T.M.B. Report 780, 1953
- [3] G. van Oortmerssen - Influences of the waterdepth on the manoeuvring characteristics of ships
Symposium of "Ship Handling" Wageningen, 1973
- [4] J.P. Hooft - "Manoeuvring large ships in shallow water"
Journal of Navigation Vol.26 - No. 2, 1973
- [5] G.F.M. Remery and G. van Oortmerssen - The mean Wave, Wind and Current Forces on Offshore Structures and Their Role in the Design of Moving systems.
Offshore Technology Conference - Paper number OTC 741
- [6] I. Oldenkamp - The Analysis of Safety Margins in the Manoeuvring of large Ships in Confined Waters.
Tenth Symposium on Naval Hydrodynamics, 1974

SIMULATION OF VESSEL ENCOUNTERS IN CONFINED WATERS

J. Patell
Carnegie-Mellon
University
Pittsburgh, PA

N. Norrbin
Swedish State
Shipbuilding
Experimental Tank
Gothenburg, Sweden

J. W. Devanney III
M.I.T.
Cambridge, MA

N. Szasz
M.I.T.
Cambridge, MA

ABSTRACT

An existing analog three-dimensional, vessel maneuvering model was modified and reprogrammed in digital form. Results of program are compared with analog runs and full-scale trials. The model is then exercised over a number of possible vessel encounters. Results indicate the desirability of full forward throttle in close-in maneuvers and of coordination of maneuvers.

1. INTRODUCTION AND SUMMARY

Objective

The objective of the research described in this report is to:

1. Develop a digital program for simulating vessel responses to given control commands in harbor situations.

2. Exercise this program on a number of different vessel encounters in order to obtain insight on the possible investments society might make in vessel harbor control.

To this end, a vessel maneuvering model developed by Norrbin to drive the analog simulator at the Swedish State Experimental Tank was extended, put into digital form, and programmed in PL/I. One feature of this program is that it does not require the hydrodynamic coefficients of a given hull as input but rather estimates these coefficients from a limited set of physical characteristics of the ship.

This program was validated by comparison with trial results of seven vessels, including several large tankers, a fleet oiler, and a moderate-sized break-bulk cargo ship. With some exceptions, the accuracy of the program in deep water was deemed acceptable given the wide range of ships considered. Validation of the model's shallow-water results was hampered by paucity of full-scale data.

Computer run times proved moderate and it is quite feasible to simulate the movements of four or five ships simultaneously for rather long periods.

The basic model has been implemented in a variety of forms:

1. A validation package which

takes a given hull and outputs:

- a. steady-state speed as a function of throttle setting;
- b. the results of a spiral test;
- c. turning circles as a function of initial speed and helm angle;
- d. the results of an overshoot (zigzag) test.

The purpose of this set of routines is to test the model's results against actual maneuvering trials.

2. An encounter simulator which takes as inputs the physical characteristics of two ships initially on a collision course together with their initial speeds, relative headings, and separations, and exercises this pair of ships over a wide range of maneuvers. For those maneuvers which avoid collision, the program outputs the closest point of approach. For those maneuvers which result in collision, the program outputs who hit whom, which portions of each ship were involved, and the relative speed and relative bearing at impact. The logic of this program is quite comprehensive and it catches stern-swing collisions as well as bow-on collisions. A variant of the encounter simulator allows the ships to make double moves (first turning away and then turning into in order to get their sterns out of trouble).

3. The harbor control simulator. This program takes as input a description of a harbor by depth, the physical characteristics and the initial positions, headings and velocities of an arbitrary number of ships, and outputs the track, velocity, and heading of these ships under an arbitrary user-supplied control routine. Periodically, the control routine is allowed to observe the entire situation and to give each ship throttle and desired heading orders at this time.

Major Results

1. The vessel encounter simulator has been exercised over a wide range of encounters, and a wide range of possible evasive maneuvers in deep water. One major theme runs through all the results: once you get in trouble, the best maneuver invariably involves full forward throttle both as a means of turning more quickly and slowing down faster. Once

you get in trouble, sharply reduced or astern throttle is poor seamanship. The larger the ship, the more drastic the advantage of full ahead over reduced throttle. The Rules of the Road and the principles by which admiralty courts operate should be changed to encourage full-throttle maneuvers in close quarters and to discourage zero or astern throttle, once you get into trouble.

2. Even very large tankers can get rather close to each other on collision course and still miss, provided the maneuvers are coordinated. For example, two 200,000-ton tankers approaching each other end on at ten knots each can come within 1,800 meters of each other before initiating a maneuver if one ship is not allowed to maneuver. If both ships are allowed to make one maneuver, this distance drops to 1,400 m. If both ships are allowed to make two maneuvers (turning away for a while and then turning back to avoid a stern-swing collision), this distance drops to 1,000 m or a little over three ship lengths. In every case, the optimal maneuver involves full forward throttle. Reducing throttle can increase the minimum distance at which a collision-avoiding maneuver can be initiated by 70% even if the turn is made in the proper direction, in certain crossing situations. Directly end-on situations are less sensitive to throttle reduction.

3. As part of the study not directly connected to the simulation of vessel maneuvering, we surveyed what is known about actual collisions. Almost all vessel collisions occur in periods of poor visibility in end-on encounters. Generally, the vessels are aware of each other on radar in plenty of time to initiate collision-avoiding maneuvers. Often the collision occurs because the maneuvers were not coordinated. Despite this fact, vessels in international waters rarely, if ever, communicate with each other. In extremis, the vessels usually reduce throttle sharply or put the throttle astern.

4. While cost-benefit analyses were not undertaken, it is our feeling that investment in shoreside control stations may be premature. We believe that the above collision summary points to bridge-to-bridge communications as a cheaper, much more comprehensive, and much more likely to be effective alternative. Further, if identification proves to be a problem, we think a transponder-based system should be as seriously considered as shore-based control. Only if communication-channel saturation proves to be a problem does shore-based control appear to offer anything that cannot be obtained more cheaply and much more comprehensively than vessel-to-vessel communication with respect to collision.

Major Limitations and Intended Future Research

1. In its present form, the model tends to underestimate yaw rates in hard-over maneuvers for large tankers, especially for twin-screw ships. Further refinement of the coefficient-generating routine is indicated.

2. In its present form, the model cannot simulate a ship backing down, and while it is logically capable of simulating a ship going ahead with the propeller going astern, this capability has never really been validated.

3. The shallow-water terms need considerable work. The present program assumes that variations in depth in the vicinity of the ship are small enough to be ignored. Full-scale maneuvering trials in shallow water are quite rare. Further validation of the present flat-bottom model is indicated and extension to bank and channel effects would be useful.

4. The collision logic developed for the vessel encounter simulator should be incorporated into the harbor control model.

2. THE HYDRODYNAMIC MODEL

The hydrodynamic model used in the vessel encounter summations is that developed by Norrbin. The model proper consists of seven equations relating forward velocity, sway, yaw, propeller revolutions, thrust, rudder flow, and effective rudder angle. The model is described in detail in reference 1.

Several changes were made to the original model as described in reference 1 for the purposes of this application.

1. In the original model, sway acceleration and yaw acceleration were coupled in the sense that yaw acceleration occurred explicitly in the sway acceleration equation and vice versa. In order to obtain a model that was less sensitive to digital integration, these equations were manipulated so that yaw acceleration and sway acceleration never occur in the right-hand sides. The integration method used is discrete time-step summation. During development of the model, a range of time steps from .5 to 10 seconds simulated time was investigated. At 3 seconds, some oscillations in yaw acceleration were observed, and at 5 seconds or more, the oscillations grew and generally became unstable. An integrating interval of 2 seconds was chosen and is used in the computations in this paper. More advanced integration techniques were investigated but with one exception, the additional computation more than balanced the increase in time step possible. That exception was the yaw acceleration equation, where a Runge-Kutta method was used to prevent underestimating yaw during hard-over maneuvers due to assuming that the

rudder was at its original position throughout the time interval.

2. It was found necessary to modify, refine, and extend some of the equations relating the physical parameters of the ship to the hydrodynamics coefficient. Principal areas involved were:

- a. Propeller thrust and torque;
- b. Propulsion machinery inertia;
- c. A Froude number-dependent

cubic term was added to the straight-ahead resistance;

d. Changes to the rudder flow and angle of attack equations to accommodate different screw-rudder geometry and propeller going astern.

These changes are described in reference 2.

In its present form, the program takes as input the following eighteen physical parameters of each vessel to be simulated.

From these parameters it computes, as a first step, eighty odd hydrodynamic coefficients according to the relations given in references 1 and 2.

For the purposes of validation, the basic model has been implemented in a form which takes as input a given hull and outputs:

1. Steady-state speed as a function of throttle setting;
2. The results of a spiral test;
3. Turning circles as a function of initial speed and helm angle;
4. The results of an overshoot test.

A sample set of results is shown in Figs. 1 through 7. These are the results for the Swedish State Experimental Tank, single-screw, single-rudder tanker, 1521B. For this tanker, the speed versus throttle curve reached the design speed of 16 knots at a throttle setting of 1.02, indicating a good estimate of resistance. When compared with the analog results in which measured hydrodynamic coefficients were used, the turning transients test indicated that the digital yaw rate is somewhat low. The radius of the 10° helm angle turning circle is predicted to be 1,060 m by the analog

Table 1 Input Parameters

Parameter		(Unit)	Symbol
Hull	Length	(m)	L
	Beam	(m)	B
	Draft	(m)	T
	Block coefficient		C_B
Propulsion machinery	Design speed	(Kt)	V_0
	Design RPM	(min ⁻¹)	N_0
	Design shaft horsepower	(shp)	SHP
	Power plant type	(steam or diesel)	
	Number of propellers		
	Propeller diameter	(m)	D
	Propeller pitch/diameter ratio		A_E/A
	Propeller blade area ratio		sd
Steering system	Depth of propeller shaft	(m)	
	Number of rudders		
	Type of rudders	(all-movable or fixed horn)	
	Rudder area	(m ²)	A_r
	Rudder height	(m)	b
	Depth to top of rudder	(m)	a

3. VALIDATION

1. The program was validated by comparing the program's results against the results of the original analog model when the analog model was using experimentally measured hydrodynamic coefficients. This was done for the four SSPA tankers shown in Table 2, which are roughly similar in size but differ in number of propellers and number of rudders.

2. Comparing the program's results with model tests or actual full-scale maneuvering trials for the final three vessels shown in Table 2. Shallow-water trials were available only for the "Esso Bernicia".

model (3), while the digital program claims 1,250 m. In the 30° turn, the analog prediction is 650 m and the digital, 750 m. In the overshoot test (helm swung to +20° and held there until yaw equals 20° and then helm swung to -20° and held there until yaw equals helm and so on), both the analog and the digital models predicted an overshoot of 34°. Again the digital yaw rate was lower. As a result, the analog model required 4.8 minutes to complete first half cycle whereas the digital model required 5.3 minutes. The spiral test correctly predicted dynamic instability and the shape of the hysteresis loop as well as the displacement of the center of the loop

Table 2 Overall Dimensions of Ships Tested

Ship	Type	Length	Beam	Draft	Design Speed	Engine	Screws	Rudders
SSPA 1521-A	Tanker	335.7 m	59.4 m	19.8 m	16.0 kt	Steam	2	1
SSPA 1521-B	Tanker	335.7 m	59.4 m	19.8 m	16.0 kt	Steam	1	1
SSPA 1521-D	Tanker	335.7 m	59.4 m	19.8 m	16.0 kt	Steam	2	2
SSPA 1575-D	Tanker	328.4 m	61.6 m	20.6 m	16.0 kt	Steam	2	2
Mandalay	Cargo liner	135.6 m	18.9 m	7.8 m	17.5 kt	Diesel	1	1
USS A0108	Fleet oiler	160.2 m	22.9 m	8.00m	18.0 kt	Steam	2	1
Esso Bernicia	Tanker	304.9 m	47.2 m	18.1 m	16.5 kt	Steam	1	1

to a slight negative helm. The intercepts for 0° helm matched for both models and the intercepts for $0^\circ/\text{sec}$ yaw rate were within 1° of helm. The yaw rate for large helm angles (15°) was about $.28^\circ/\text{sec}$ for both models.

The results for the other Swedish State Experimental Tank tanker stern configurations were not as good. In general, the digital program underestimated straight-ahead resistance by about 8%-10%, as compared to the analog, and yaw rates were still lower, generating turning circles which were as much as 30% larger than the analog results for hard-over maneuvers.

The worst results were for the twin-screw, single-rudder, with the twin-screw, twin-rudder hulls intermediate. The pattern of the errors indicates further work on design resistance, thrust deduction and the partial of sway with respect to the product of rudder flow squared and helm angle. The lift generated by the deadwood for twin-screw, single-rudder tanker forms might stand some investigation.

The first experimental test vessel, "Mandala", is a single-screw, single-rudder cargo liner form and the only diesel-powered vessel used to validate the model. In this case, the digital simulation results were compared with those generated by radio-controlled model tests at the Swedish State Experimental Tank. The model generated a very poor estimate of straight-ahead speed as a function of throttle setting, predicting the design speed of 17.5 knots at .65 throttle. This is probably due to errors in the routine which attempts to model the δ^2 . However, by adjusting throttle settings according to the results of the straight-ahead resistance tests, the desired approach speeds for the other tests can be obtained.

Only limited maneuvering data were available for this vessel, namely the relative size of turning circles and a nondimensionalized spiral curve. Comparison with the results indicated once again the yaw rate is low in hard-over maneuvers by as much as 20%. However, the program's spiral test correctly predicted a dynamically stable hull. In short, aside from straight-ahead speed as a function of throttle

setting, which errors we believe are in the diesel throttle setting logic, the program exhibits the kind of accuracy it displayed for the large tankers--qualitatively correct response with somewhat depressed yaw rate--despite the very much finer hull.

The second actual ship against which the model was compared was the USS "Pawcatuck" (A108), a member of the A105 class of fleet oilers. In this case, the model's results were compared against full-scale trials. Once again, the speed versus throttle setting curve reached design speed at too low a throttle (80%), although this may be due to the very conservative estimate of design speed which the Navy employs. Except for this, the digital results agreed extremely well with the full-scale trials, despite the fact that this is a twin-screw, single-rudder hull. Overshoot tests were conducted at approach speeds of 8 and 16 knots. In both cases, the time required for the first half-cycle was correctly predicted by the model and the overshoot yaw angle predicted was within 5% of the full-scale results. Spiral tests were also conducted at approach speeds of 8 and 16 knots. The model correctly predicted narrow hysteresis loops and the 0° helm and $0^\circ/\text{sec}$ yaw rate intercepts. In this case, the yaw rate predicted for large helm angles was within 5% of trial results. We are somewhat at a loss to explain the accuracy of the model on this hull compared with its much poorer performance on the twin-screw, single-rudder SSPA tanker, although this is a much finer hull.

The third ship against which the model was tested was the "Esso Bernicia," a 193,000-ton tanker. This is the only ship for which we were able to obtain both deepwater and shallow-water results. The available experimental data consisted primarily of turning circles at various approach speeds and loading conditions in 75 and 25 m deep water. Both the turning circles for the deep (75 m) water and the shallow were about 35° larger in maximum advance and maximum transfer than the fullscale results indicating once again we are underestimating yaw rate. However, the similarity of the errors in the shallow and

deepwater case indicate that the shallow water terms are at least qualitatively correct.

4. THE HARBOR CONTROL SIMULATOR

General Description

The hydrodynamic model described in Sections 2 and 3 has been implemented in several forms. The basic version of the model is the Harbor Control Simulator. The Harbor Control Simulator takes as input a description of a harbor (water depth on an x-y array and current speed and direction on the same grid), the physical characteristics of the ships where movements are to be simulated, and the initial location and velocity of these ships. The program is designed to accept a user-supplied subroutine, the Traffic Controller, which contains the harbor control logic being studied and returns desired heading and speed for each ship.

The Harbor Control Simulator does not account directly for changes in depth (bank rejection or suction effects), but rather uses the water depth under the vessel's center of gravity. Nor does it account for current shear. The program assumes the current at the vessel's center of gravity is also the current affecting the entire hull. Rapid changes in depth or current are not modeled.

The structure of the Harbor Control Simulator is presented in the flow chart on the following page. In order to initiate the program, the operator specifies the number of ships in the simulation, and the number of minutes of real time to be simulated, in order to allocate storage space. The harbor depth chart is loaded, and the input dimensions and characteristics of each vessel are stored. The coefficients of the equations of motion are computed and stored for each ship, and the main simulation loop is then entered. As indicated, the decision cycle time is thirty seconds; that is, the simulation is interrupted every thirty seconds and the position, depth, speed, acceleration, etc. of all the ships are passed to the Traffic Controller. The Controller is allowed to change any desired headings or speeds, and the simulation then proceeds for another thirty seconds. The depth is also updated every thirty seconds.

As constructed, the program will accept an unlimited number of ships for an unlimited amount of time. However, storage capacity and costs of the computer may limit economic tests to around three hours of simulated time. In a sample test in which four ships were run for thirty minutes of simulated time, 310,000 bytes of storage space were required. Execution costs for this test (excluding compilation) were approximately \$4.50. For a one-ship run, the program requires 280,000 bytes of core.

Figs. 9 through 11 contain output for a simulation of nine ships for thirty minutes. In Fig. 9, the vessels were initially placed at the positions marked by a B at 10 knots heading east. The topmost ship was instructed to make a hard left turn with full astern throttle; the second ship from the top was instructed to make a hard left turn with 0 throttle; the third ship down, a hard left turn with 50% throttle; the fourth ship down, a hard left turn with full-ahead throttle. The middle ship was told to continue straight ahead with full-astern throttle. The bottom four ships were told to make a hard right turn with 100%, 50%, 0%, and -100% throttle respectively from top to bottom. Fig. 10 shows the resulting speed reductions and Fig. 11 the headings as a function of time.

Description of the Harbor

The model is constructed to accept a square harbor chart 10 km (6.2 mi) on a side. A square grid with a 250 m grid spacing is overlaid on the chart, and the depth at each grid point is read into the program, resulting in a 41 x 41 member depth array (1,681 data points). At the close of each simulation time interval (30 sec), a new depth is computed for each ship position. The depth is computed by a two-dimensional linear interpolation of the four grid points surrounding any given ship position in the harbor.

The model also accepts a steady-state current of specified heading and speed. The correction to ship position caused by this velocity field is made continuously during the actual simulation. The current direction is displayed on the output trajectory plot.

Auto-Pilot

Each vessel's helm is controlled by a simulated proportional auto-pilot. The auto-pilot receives an instruction from the Traffic Controller in the form of a "desired heading", and also knows the present heading and rate of yaw of the vessel. The auto-pilot then "calls for" a rudder angle according to the following relation.

$\delta^* =$ rudder angle called for

H = present heading

H* = desired heading

$\dot{\psi}$ = present rate of yaw

$$\delta^* = \gamma(H - H^*) + \alpha(\dot{\psi}) \quad (1)$$

The rudder angle called for is therefore proportional to both heading error and yaw rate. The constants of proportionality are given by:

Rudder ratio $\gamma =$

- { 3 for normal course-keeping and maneuvers
- { 4 for high-speed (panic) maneuvers

$$\sigma = 2.5 \frac{L}{V_0} \quad (2)$$

where L = length (m)

V_0 = design speed (m/sec)

The rudder angle called for is then passed to the steering mechanism, which is modeled by:

Rudder turning rate = 2.3 deg/sec (3)

Maximum rudder deflection = 35 deg (4)

The desired throttle setting is made directly and instantaneously upon command.

Traffic Controller

At present, the Traffic Controller is treated as a black-box internal subroutine. Various simple maneuvers, such as the one illustrated in Fig. 9, have been implemented. At each decision interval (every thirty seconds), the following data on all the ships in the model is made available to the Controller:

1. Position
2. Depth
3. Running variables (speed, acceleration, RPM, etc.)
4. Control variables (throttle setting, helm setting)
5. Last instructions received from Controller.

On the basis of this information and its own internal traffic control logic, the Controller sends the following three instructions to each ship:

1. Desired throttle setting
2. Desired heading
3. If turn must be made, execute as normal turn or high-speed (panic) turn

These instructions are transmitted to each ship, and the simulation then proceeds for another thirty seconds. The auto-pilot aboard each ship carries out these instructions as described previously.

Availability

The Harbor Control Simulator program, together with operating instructions, may be obtained on deck or tape by contacting the Department of Ocean Engineering at MIT.

5. SIMULATION OF SIMPLE VESSEL ENCOUNTERS

Introduction

In its present form, the Harbor Traffic Controller does not really simulate collisions in the sense that two ships could proceed right through each other without the program's being aware of it. The problem of efficiently determining whether or not a collision has occurred is not completely trivial. Further, it was judged that, at the present stage of the game, more insight could be obtained by working in the

context of simple, two-vessel encounters, studying these in detail, before working in the context of an entire harbor. Therefore, further development of the Harbor Traffic Controller was deferred in favor of simple vessel encounter studies.

For this purpose, a variant of the basic hydrodynamic model known as the Encounter Simulator was developed. This program takes as input the physical characteristics of two ships and their initial speed, heading, and separation. The initial conditions are chosen so that in absence of a maneuver, a collision will occur. The program exercises these ships over twelve simple maneuvers:

- 1a. Throttle setting to -100% (full astern), rudder hard over to port.
1. Throttle setting to 0%, rudder hard to port.
2. Throttle setting to 50%, rudder hard to port.
3. Throttle unchanged, rudder hard to port.
4. Throttle setting to +100%, rudder hard to port.
5. Do nothing, maintain course and throttle setting.
- 5a. Throttle setting to full astern, maintain course.
6. Throttle setting to +100%, rudder hard to starboard.
7. Throttle unchanged, rudder hard to starboard.
8. Throttle to 50%, rudder hard to starboard.
9. Throttle to 0%, rudder hard to starboard.
- 9a. Throttle to -100%, rudder hard to starboard.

All maneuvers are exercised under the control of the auto-pilot described in the last section operating in the panic mode. Strictly speaking, the order is not "rudder hard over" but rather "come to new course 110° to the right (left) of present course."

For each maneuver, the program determines whether or not a collision occurs and if so, returns the particulars of that collision (who hits whom, position of impact, relative speed at impact, and relative angle of impact). If no collision occurs, the program returns the closest point of approach.

In order to execute the above orders involving astern throttle, a modification of the auto-pilot was required. Our original auto-pilot became quite confused by the reversal in rudder flow in hard astern maneuvers and began hunting wildly. This was corrected by changing the sign of the rudder movement when the rudder flow went negative. Once this change was made, the auto-pilot was able to steer the ship in propeller astern, ship still going ahead situations. Needless to say, no real-world auto-pilot has this capability, and

even very experienced helmsmen have a great deal of difficulty in determining when they should reverse the helm with the ship going ahead and the propeller going astern.

Results of Vessel Encounter Simulations

The key result of our vessel encounter simulations can be expressed in one sentence. Large ships, especially very large tankers, will not only turn much more sharply but also will slow down more quickly if the throttle is advanced rather than retarded during the maneuver. In general, crash astern appears to be an extremely ineffective means of avoiding collision once the ships are in close quarters.

This result is illustrated by Figs. 9, 10, and 11 which display the track speed and heading for a large tanker under eight hard-over maneuver with a range of changes in throttle. Note that full-ahead throttle resulted in the sharpest turn and the sharpest drop in speed.

The fact that slowing down the engines is an ineffective maneuver once a ship is in trouble is not an original observation. Tani in 1968 gave a rather detailed comparison of head reach under hard-over and hard-astern maneuvers and cites references going back to 1875 on the undesirable effect of going astern (4). Recently, Crane displayed a series of full-scale trials on 191,000-ton tankers in which head reach under crash action was four times that under hard-over at service power (5). Interestingly enough, the side reach, for these single-screw ships, under the full-action order was approximately the same as that under hard-over. However, the fact that you not only turn sharper but also slow down faster under advanced throttle has not been sufficiently emphasized.

These basic hydrodynamic facts seem to have had no effect on the Rules of the Road or actual operator responses in collision situations. (See first section.) Discussions with operators indicate that while they are quite aware of "the loss in rudder control" associated with sharp throttle decrease, no one wants to go into court in a collision which occurred after he had called for full ahead. The operators claim that court policies effectively rule out this option. The recent revision of the Rules of the Road is no improvement in this regard. The new Rule 8(e) states specifically, "If necessary to avoid collision, a vessel shall slacken her speed or take all way off by stopping or reversing the means of propulsion." No mention is made of advancing throttle as a collision avoidance mechanism. Clearly, we might do well to rethink our legal attitude toward throttle changes in encounter situations.

Minimum Separations At Which Collision-Avoiding Maneuver Can Be Initiated

Following Kenan, the Vessel Encounter Simulator can be used to estimate the minimum separation at which maneuvers can be initiated for a given situation and a collision still be avoided and the maneuver which leads to this minimum separation (6). This is done for given initial speeds and relative bearings which would result in a collision in the absence of a maneuver, by looping over initial separation. The results for two large tankers in which one tanker is moving at 10 knots and does not alter course and speed (the stand-on vessel) while the other, the give-way vessel, is also at 10 knots, are displayed in Fig. 12. The ship used in these runs is the 193,000 ton tanker "Bernicia". The separation decrement used in these studies was 100 m. The minimum separations ranged from 1800 m (bow on) to 0 m ("overtaking"). The minimum separations were achieved by non-book maneuvers: throttle full ahead and hard turn to starboard when initial relative bearings were less than 50° (bow on to slightly overtaking) and throttle full ahead and hard turn to port when relative bearings were greater than 50°.

The advantage of the unusual hard turn to port over the more obvious turn to starboard under the privileged vessel's stern when "overtaking" is a product of stern swing. Turning into the privileged vessel rather than away prevents the stern from swinging into the privileged vessel. The minimum separation in these cases is quite small, one or two ship lengths.

Note the increase in minimum separation for the crossing cases with decrease in throttle. Minimum separation can be increased by as much as a factor of two in some orientations by sharp reductions in throttle even if the ship turns the right way. The end-on cases are much less sensitive to throttle decreases as long as some turn is made. Maneuver A is the throttle astern, maintain course alternative. As the figure indicates, this is not a particularly bad maneuver for the overtaking cases but becomes progressively worse as the angle on the bow decreases.

These analyses were iterated over a number of burdened ship maneuvers including hard astern, maintain course, a hard port turn (full ahead, port helm) and a hard starboard turn. The results for the hard astern maneuver were quite similar to Fig. 12. There was very little change in minimum separation and no change in the optimal maneuver on the part of the burdened vessel. Fig. 13 indicates the results for a port turn on the part of the formerly privileged vessel. A port turn with full ahead throttle on the part of the formerly privileged vessel results in about a 25% reduction in minimum

separation for direct meeting situations if combined with a hard port turn on the part of the burdened vessel. There is no change in minimum separation for the intermediate relative bearings even if the moves are coordinated and a drastic increase if they are not. A hard port turn results in an increase of 500 m or so in minimum separation distance in overtaking situations over no maneuver, even if the burdened vessel does the best he can against this move. Most importantly, the burdened vessel's optimal maneuver against a port turn is quite different from that against no maneuver, for headings greater than 84° (relative bearings less than 48°).

Not surprisingly, the most attractive move on the part of the burdened vessel was a hard starboard turn. The results for this maneuver are shown in Fig. 14. The decrease in direct meeting situations is again about 25% over no maneuver and more importantly the burdened vessel's optimum maneuver is the same as it is if the privileged vessel made no maneuver. Minimum separation for intermediate relative bearings are the same as no maneuver. However, by performing a hard starboard turn, the privileged vessel gains some separation if the burdened vessel does something other than the optimum. The overtaking cases are about the same. According to the program, the privileged vessel has nothing to lose and something to gain by executing a starboard turn, provided of course he has sufficient sea room.

In short, according to our calculations, for large tankers proceeding at 10 knots, allowing both vessels to maneuver will decrease the minimum separation at which a maneuver can be initiated from something like six ship lengths to five ship lengths for end-on situations if the privileged vessel makes the right move or the moves are explicitly coordinated. Allowing the privileged vessel to maneuver in crossing situations gains almost nothing as long as the burdened vessel makes the right move. It can have rather disastrous results if the privileged vessel makes the wrong move.

Multi-Turn Maneuvers

In the above analysis, each ship was allowed at most one maneuver. Especially in end-on situations, the possibility arises that the ships could do better if they were allowed a double maneuver, i.e. first turn away and then turn back toward each other in order to swing their sterns out of the way. To investigate this possibility, a variant of the encounter simulator was concocted in which two ships meeting end-on both turned to starboard and then, after a time, turned back to the original course. Some of the results are shown in Tables 3 through 7. These tables are based on two 200,000-ton tankers each at

initial speed of 10 knots. The tables show, as a function of initial separation distance (range) and the time that the helm is held over (in thirty-second intervals) before being brought back, either of two things. If no collision occurs, the program outputs CPA=xxx where xxx is closest point of approach in meters. If a collision occurs, the computer prints out xx.yyyy where xx is relative speed at impact. yy are two letters which take one of the following forms:

BB--bow of ship 1 collides with bow of ship 2
 BM--bow of ship 1 collides with midsection of ship 2
 BS--bow of ship 1 collides with stern of ship 2
 MB--bow of ship 2 collides with midsection of ship 1
 SB--bow of ship 2 collides with stern of ship 1
 SM--stern of ship 1 collides with midsection of ship 2
 MS--stern of ship 2 collides with midsection of ship 1
 SS--stern of ship 1 collides with stem of ship 2.

For the purposes of this analysis, bow is defined to be the forward 10% of waterline length and stern the aftmost 10%.

In Table 3, which refers to the situation when the throttle is advanced to full ahead throughout the maneuver, the best maneuver shown is to hold the first turn for two half-minutes, resulting in a miss distance of something over 1000 m. This compares favorably with the 1400 m when both ships were allowed to maneuver once and 1600 m when only one ship was allowed to maneuver once. Note that by holding the first maneuver for only one-half minute, the minimum miss distance increases to something over 1300 m. Approximately the same miss distance is obtained if he holds the first maneuver for four half-minutes. However, note that in the latter case we have a stern-swing collision at 17 knots, while in the former we have a bow-on collision at 20 knots.

Tables 4 through 6 show the similar results for throttle setting of 50%, 0%, and -100% throughout the maneuver. The effect of reducing throttle is to increase the minimum distance at which the maneuver can be initiated, with no decrease in relative speed on impact, if a collision does occur. Reducing throttle also leads to bow-on collisions in situations where increasing throttle leads to stern-swing collisions. In the final table, the throttle was initially set full astern but when the turn back to original course was made, the throttle was moved back to full ahead. This resulted in a slight improvement over the throttle full astern throughout but is still definitely inferior to throttle full ahead throughout.

A word of caution is in order in interpreting these results. They are all deepwater runs of a model which appears to underestimate yaw rates and does not account for a hydrodynamic interaction between the two hulls.¹ The model has not been validated with the propeller going astern and employs a rather too clever auto-pilot which is able to steer the ship with the propeller going astern. Nonetheless, we believe these results offer some interesting insights.²

We performed the same analysis for the case of 5 knot approach speeds. In this situation, the differences between the alternative throttle maneuvers becomes even more striking. Once again, the optimal maneuver is full ahead and hold the first turn for two half-minutes. The resulting minimum separation at which the maneuver can be initiated is something over 700 m, barely two ship-lengths. Dropping the throttle setting to 48% increases minimum separation distance only about 100 m. But dropping the throttle to 0% increases the minimum separation distance to over 1300 m and throwing the throttle astern increases the distance to over 1600 m, at which point the ships are practically stopped. Under the sharply decreased throttle settings, the optimum time to hold the first maneuver increases, as might be expected given the more gradual turn.

ACKNOWLEDGEMENTS

The work described in this paper was supported by the National Science Foundation, Applied Mechanics Division.

REFERENCES

1. Norrbin, Nils H., "Theory and Observations on the Use of a Mathematical Model for Ship Maneuvering in Deep and Confined Waters," Publication of the Swedish State Shipbuilding Experimental Tank, No. 68, Göteborg, Sweden, 1971.
2. Patull, J., "Preliminary Report on Vessel Maneuvering Project," MIT Commodity Transport Lab Report MITCTL 72-2, Cambridge, Mass., 1972.
3. Norrbin, N., "300,000 TDW Tankfartyg-Styrning Segenskaper Prognoser och Jämförande Simulatorstudier

För en Begränsad Modellfamilj," Swedish State Shipbuilding Experimental Tank Report 1633-4, Göteborg, Sweden, 1971.

4. Tani, H., "The Reverse Stopping Ability of Supertankers," Journal of the Institute of Navigation, Vol. 21, No. 2, April 1968.

5. Crane, C. Lincoln, "Maneuvering Safety of Large Tankers: Stopping Turning and Speed Selection," Maritime Reporter and Engineering News, Jan. 1, 1974.

6. Kenan, G., "Collision Avoidance Between Surface Ships at Short Range," paper presented to Northern California Section, Society of Naval Architects and Marine Engineers, San Francisco, 1972.

¹ By coincidence, the underestimated deepwater yaw rates are about equal to the observed shallow-water rates for the tanker being exercised.

² Also the bow to midsection results in column 1 of these tables are undoubtedly actually bow to bow. At these relative speeds, the ships can travel "through" the bow before the program realizes that a collision has occurred.

Table 3 Double Maneuver, Initial Speeds 10 knots, Both Ships Advance
Throttle to Full Ahead Throughout Maneuver

SEPARATION (m)	TIME HOLDING FIRST MANEUVER (SECONDS)							
	30	60	90	120	150	180	210	240
1000	20.BB179	19.SB179	19.BS179	19.BS179	19.BS179	19.BS179	19.BS179	19.BS179
1100	20.MB179	CPA=70	18.MS179	18.MS179	18.MS179	18.MS179	18.MS179	18.MS179
1200	20.MB179	CPA=93	CPA=98	18.MS179	18.MS179	18.MS179	18.MS179	18.MS179
1300	20.MB179	CPA=118	CPA=133	17.SS179	17.SS179	17.SS179	17.SS179	17.SS179
1400	CPA=51	CPA=143	CPA=172	CPA=170	CPA=170	CPA=170	CPA=170	CPA=170

Table 4 Double Maneuver, Initial Speeds 10 knots, Both Ships
Use Half-Ahead Throttle Throughout Maneuver

SEPARATION (m)	TIME HOLDING FIRST MANEUVER (SECONDS)							
	30	60	90	120	150	180	210	240
1000	19.BB179	19.BB179	19.BB179	19.BB179	19.BB179	19.BB179	19.BB179	19.BB179
1100	19.BB179	19.SB179	19.SB179	19.BS179	19.BS179	19.BS179	19.BS179	19.BS179
1200	19.BB179	CPA=63	18.MS179	18.SM179	18.SM179	18.SM179	18.SM179	18.SM179
1300	19.MB179	CPA=80	CPA=88	18.MS179	18.MS179	18.MS179	18.MS179	18.MS179
1400	CPA=48	CPA=98	CPA=113	CPA=113	17.SS179	17.SS179	17.SS179	17.SS179
1500	CPA=53	CPA=116	CPA=141	CPA=143	CPA=142	CPA=142	CPA=142	CPA=142

Table 5 Double Maneuver, Initial Speeds 10 knots, Both Ships
Stop Engines Throughout Maneuver

SEPARATION (m)	TIME HOLDING FIRST MANEUVER (SECONDS)							
	30	60	90	120	150	180	210	240
1000	19.BB179	19.BB179	19.BB179	19.BB179	19.BB179	19.BB179	19.BB179	19.BB179
1100	19.BB179	19.BB179	19.BB179	19.BB179	19.BB179	19.BB179	19.BB179	19.BB179
1200	19.BB179	19.MB179	18.MB179	18.MB179	18.MB179	18.MB179	18.MB179	18.MB179
1300	19.BB179	18.MS179	18.MS179	18.MS179	18.MS179	18.MS179	18.MS179	18.MS179
1400	18.MB179	CPA=64	18.SS179	18.MS179	18.MS179	18.MS179	18.MS179	18.MS179
1500	18.SS179	CPA=77	CPA=85	CPA=85	CPA=85	CPA=85	CPA=85	CPA=85
1600	CPA=60	CPA=92	CPA=102	CPA=104	CPA=104	CPA=104	CPA=104	CPA=104

Table 6 Double Maneuver, Initial Speeds 10 knots, Both Ships
Use Full Astern Throttle Throughout Maneuver

SEPARATION (m)	TIME HOLDING FIRST MANEUVER (SECONDS)							
	30	60	90	120	150	180	210	240
1000	19.BB179	19.BB179	19.BB179	19.BB179	19.BB179	19.BB179	19.BB179	19.BB179
1100	19.BB179	19.BB179	19.BB179	19.BB179	19.BB179	19.BB179	19.BB179	19.BB179
1200	19.BB179	19.BB179	19.BB179	19.BB179	19.BB179	19.BB179	19.BB179	19.BB179
1300	19.BB179	19.BB179	18.BB179	18.BB179	18.BB179	18.BB179	18.BB179	18.BB179
1400	18.BB179	18.MB179	18.MB179	18.MB179	18.MB179	18.MB179	18.MB179	18.MB179
1500	18.BB179	17.SM179	17.MS179	17.MS179	17.SM179	17.SM179	17.SM179	17.SM179
1600	17.MS179	17.SS179	17.SS179	17.SS179	17.SS179	17.SS179	17.SS179	17.SS179
1700	16.SS179	CPA=72	CPA=75	CPA=76	CPA=76	CPA=76	CPA=76	CPA=76
1800	CPA=64	CPA=84	CPA=88	CPA=89	CPA=90	CPA=90	CPA=90	CPA=90

Table 7 Double Maneuver, Initial Speeds 10 knots, Both Ships Initially Go Full Astern and Then Go Full Ahead on Commencement of Second Turn

SEPARATION (m)	TIME HOLDING FIRST MANEUVER (SECONDS)							
	30	60	90	120	150	180	210	240
1000	19.BB179	19.BB179	19.BB179	19.BB179	19.BB179	19.BB179	19.BB179	19.BB179
1100	19.BB179	19.BB179	19.BB179	19.BB179	19.BB179	19.BB179	19.BB179	19.BB179
1200	19.BB179	19.BB179	19.BB179	19.BB179	19.BB179	19.BB179	19.BB179	19.BB179
1300	19.BB179	19.BB179	18.BB179	18.BB179	18.BB179	18.BB179	18.BB179	18.BB179
1400	19.BB179	18.MB179	18.MB179	18.MB179	18.MB179	18.MB179	18.MB179	18.MB179
1500	19.BB179	CPA=50	18.MS179	18.MS179	17.SM179	17.SM179	17.SM179	17.SM179
1600	20.BB179	CPA=58	CPA=64	CPA=64	17.SS179	17.SS179	17.SS179	17.SS179
1700	20.BB179	CPA=65	CPA=75	CPA=76	CPA=76	CPA=76	CPA=76	CPA=76
1800	20.BB179	CPA=72	CPA=87	CPA=89	CPA=90	CPA=90	CPA=90	CPA=90

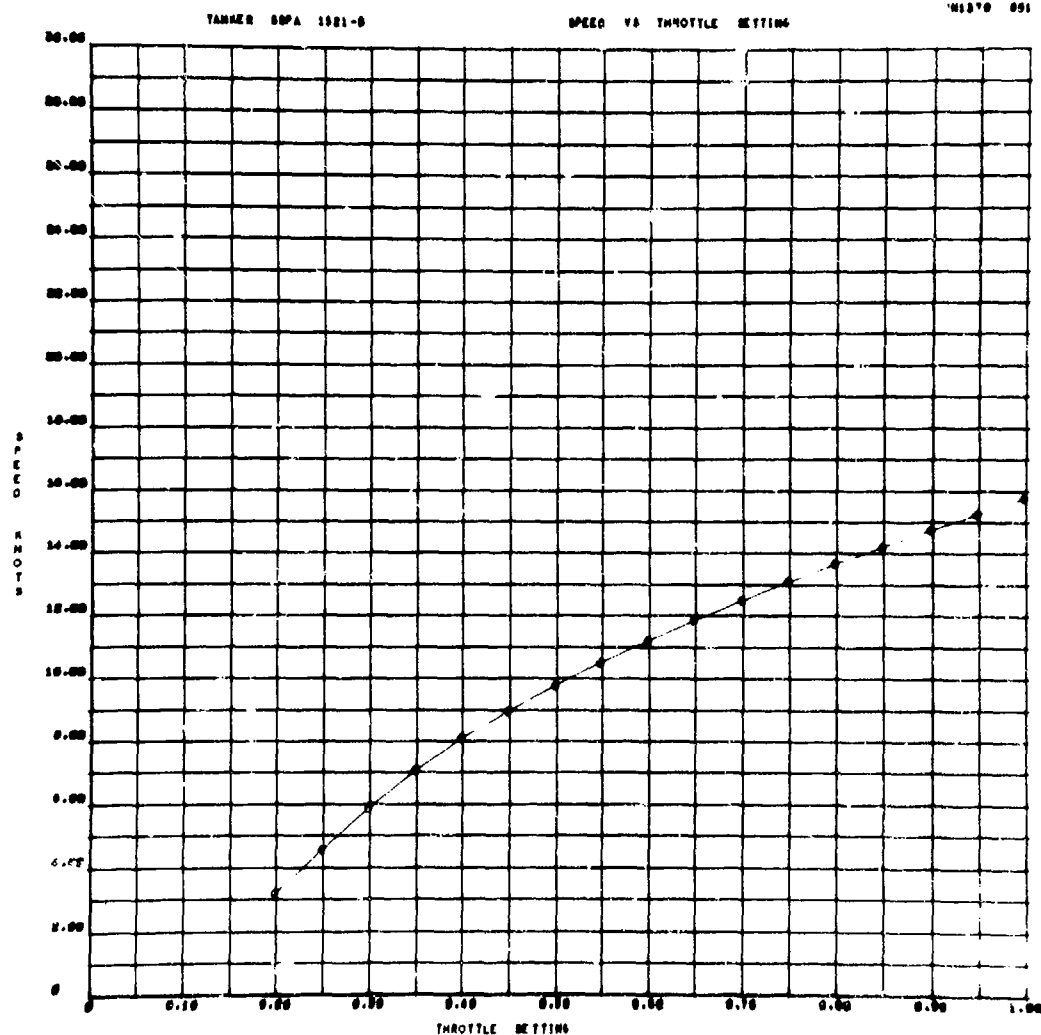


Fig. 1 Straight-Ahead Resistance--Steady-State Speed Versus Throttle

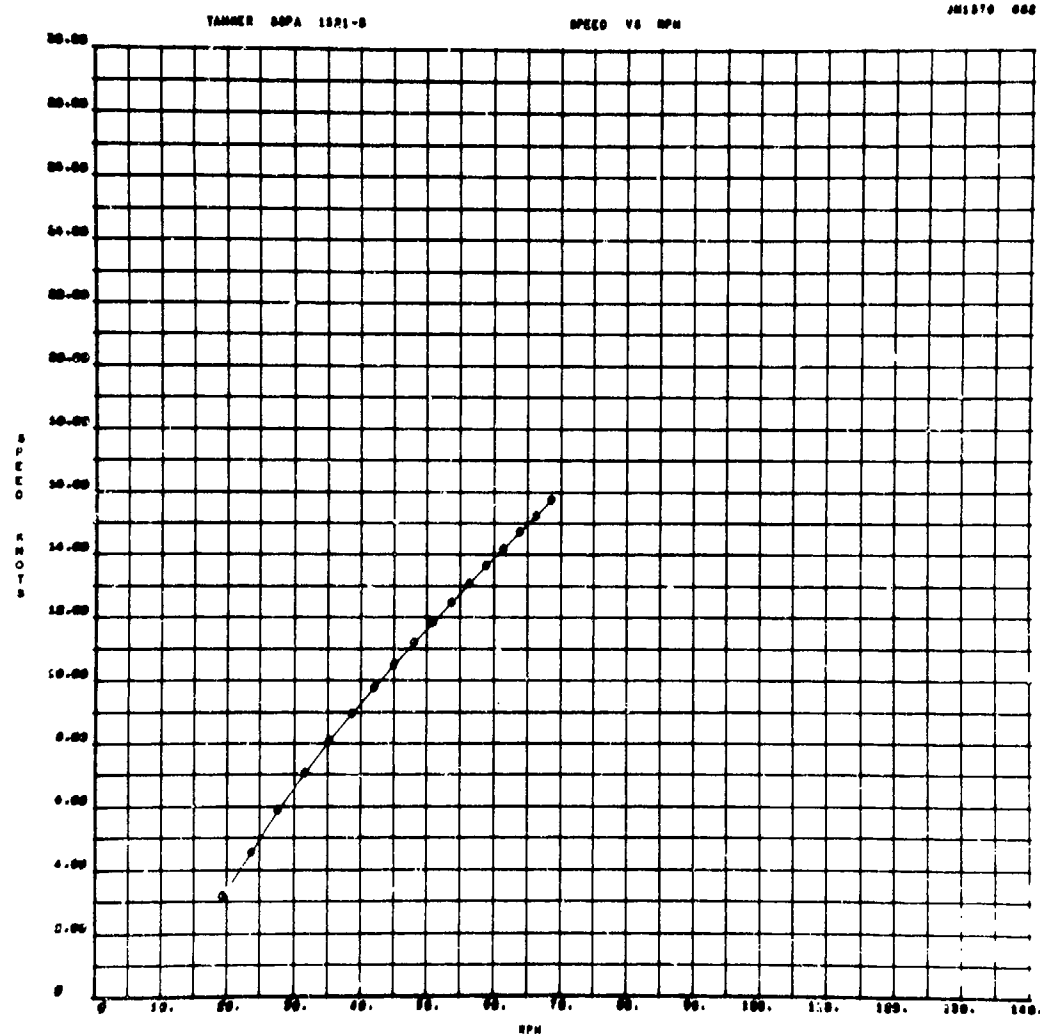


Fig. 2 Straight-Ahead Resistance--Speed Versus RPM

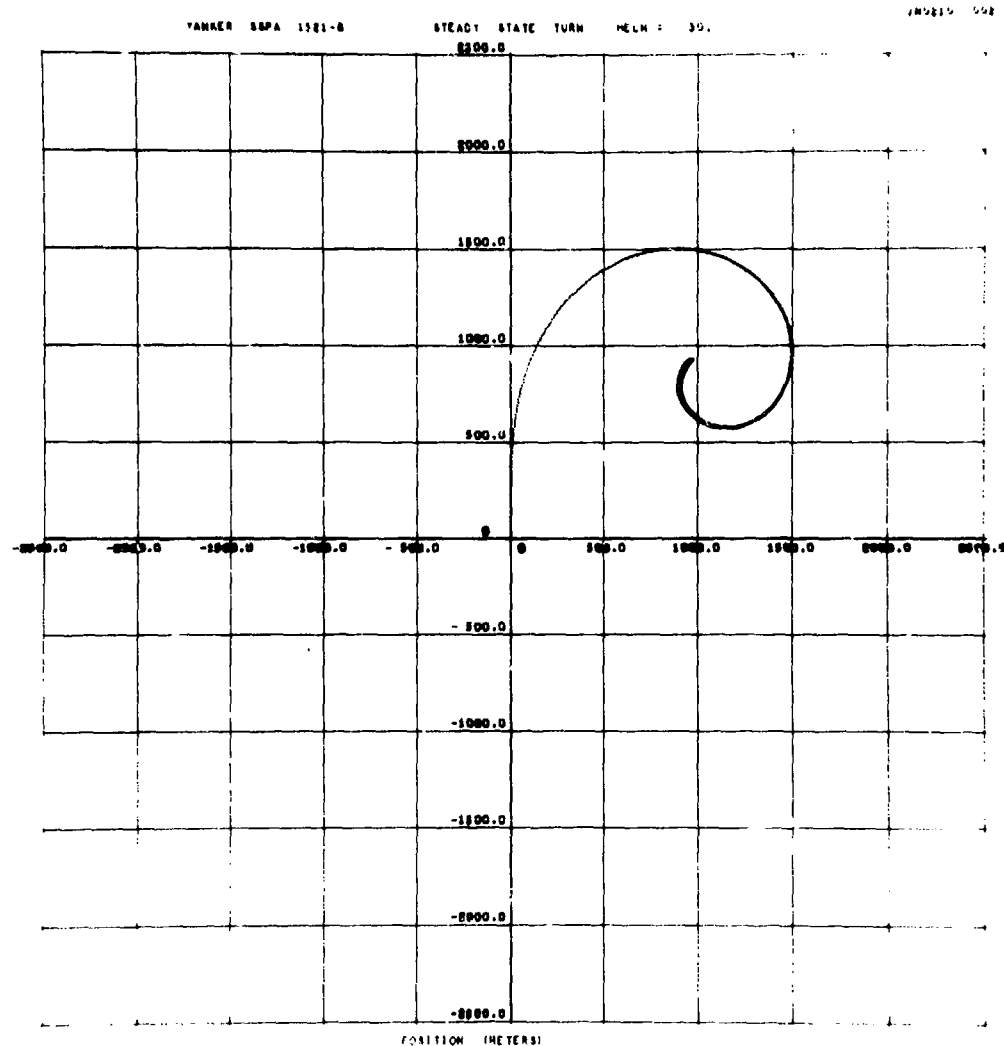


Fig. 3 Turning Circle for 30° Helm--16 Knots Approach Speed

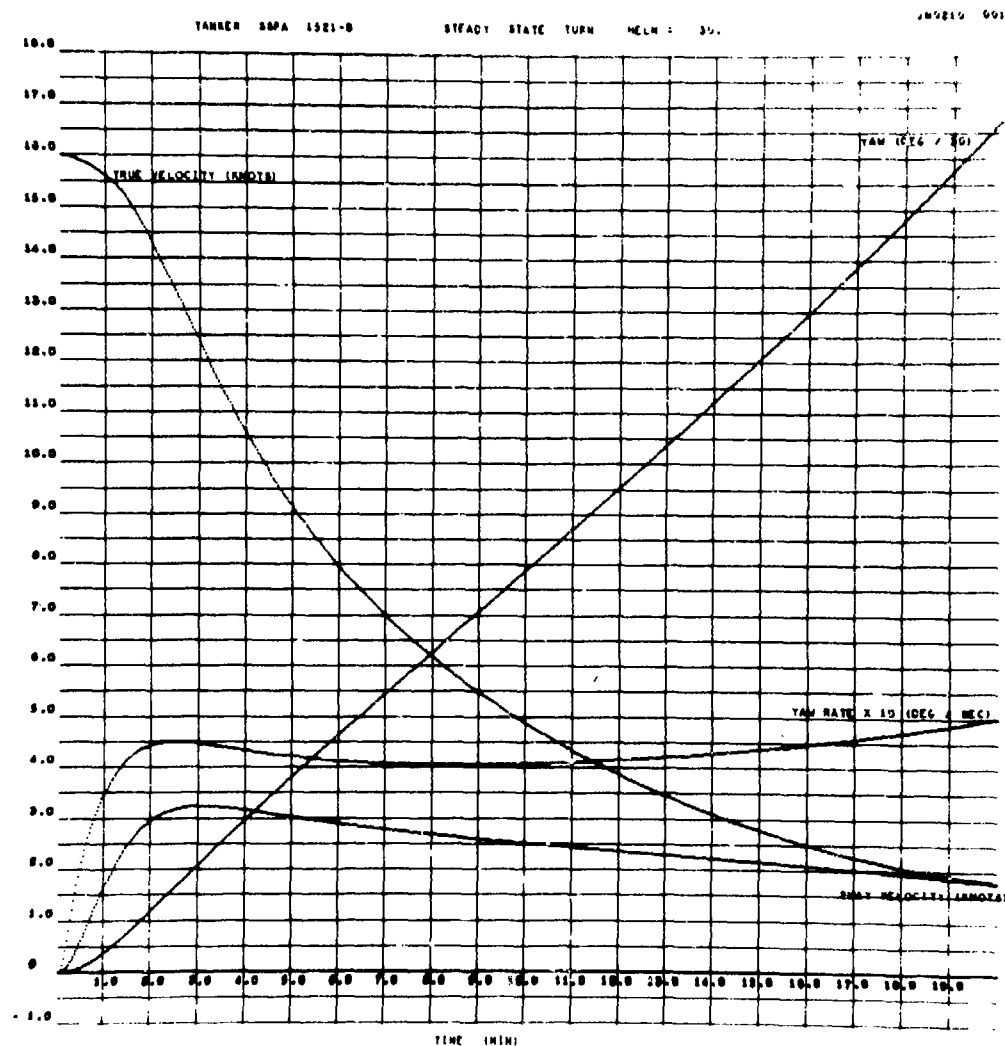


Fig. 4 Forward Velocity, Sway Velocity and Yaw Rate in 30° Turn--
Approach Velocity 16 Knots

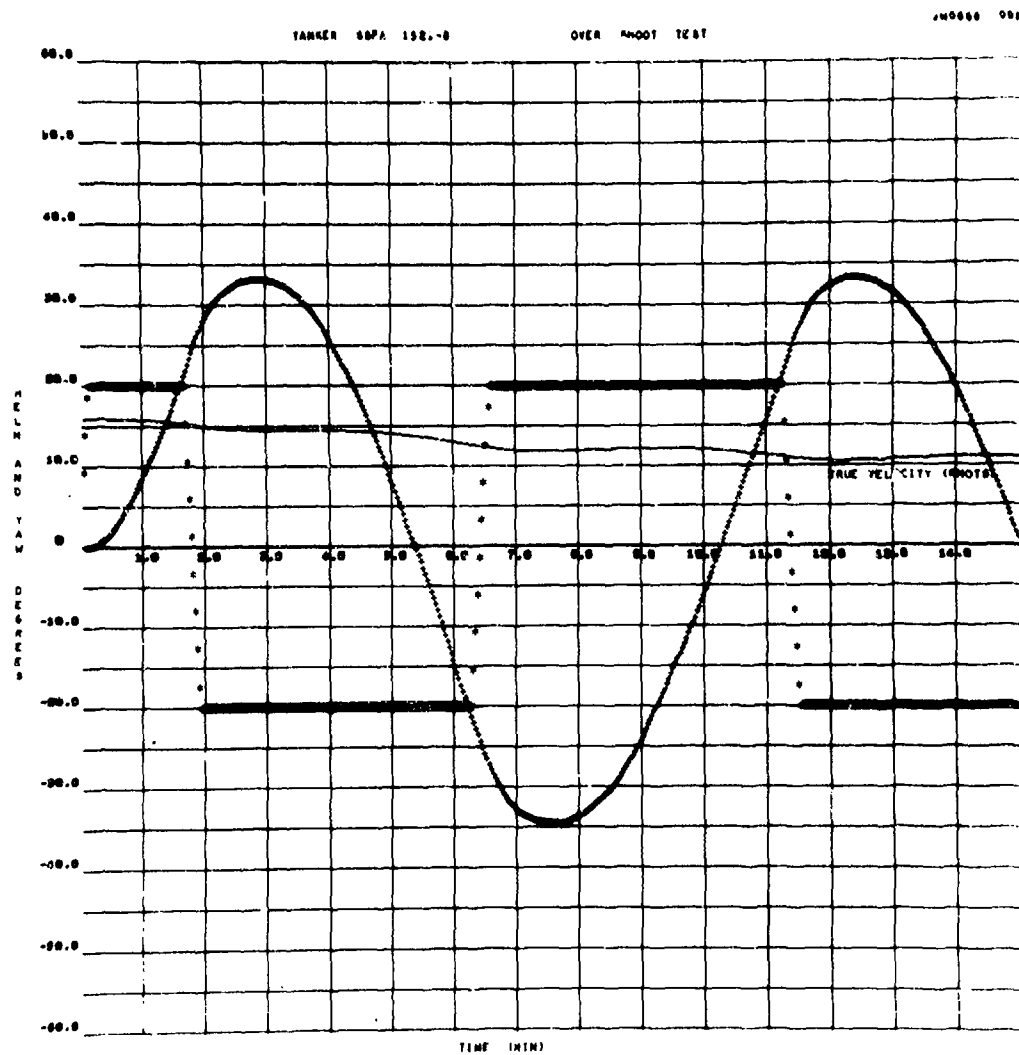


Fig. 5 Helm and Forward Velocity in 20° Zigzag Test

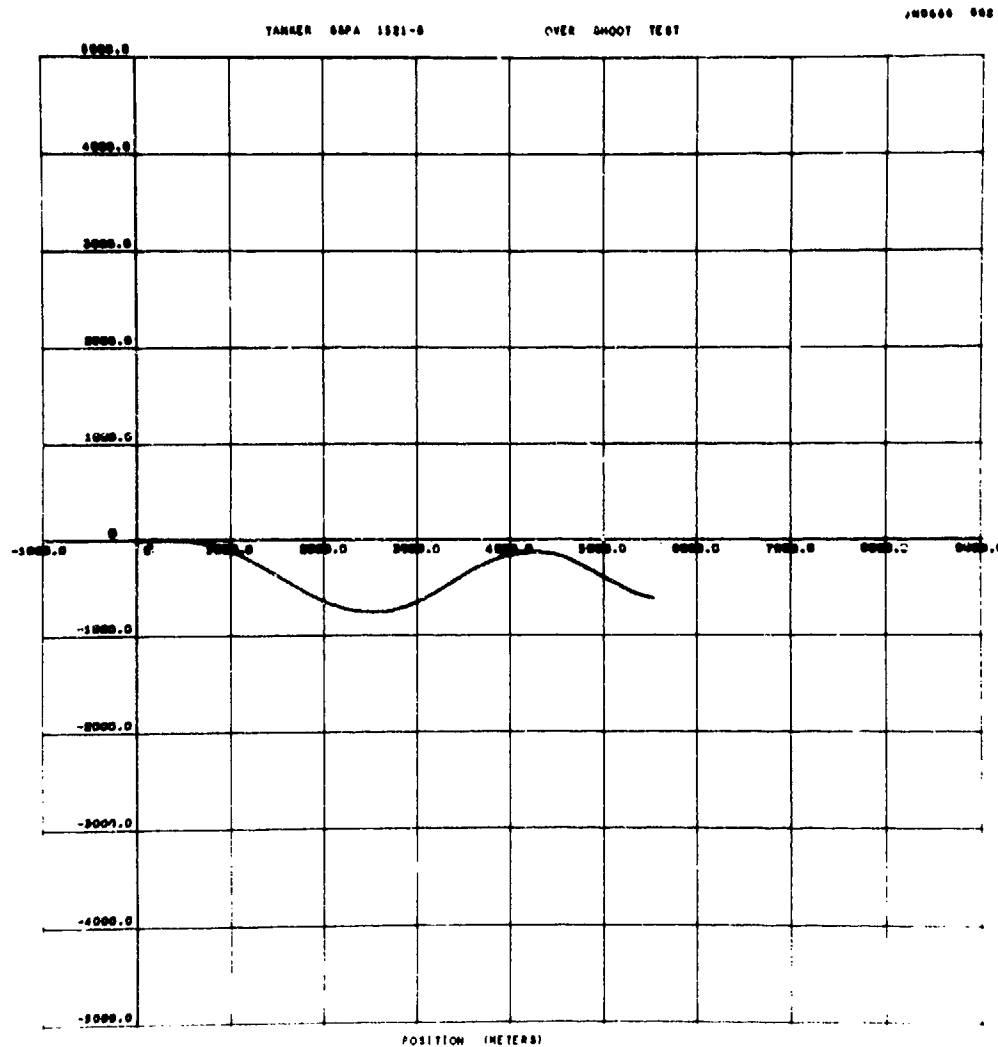


Fig. 6 Track in 20° Zigzag Test

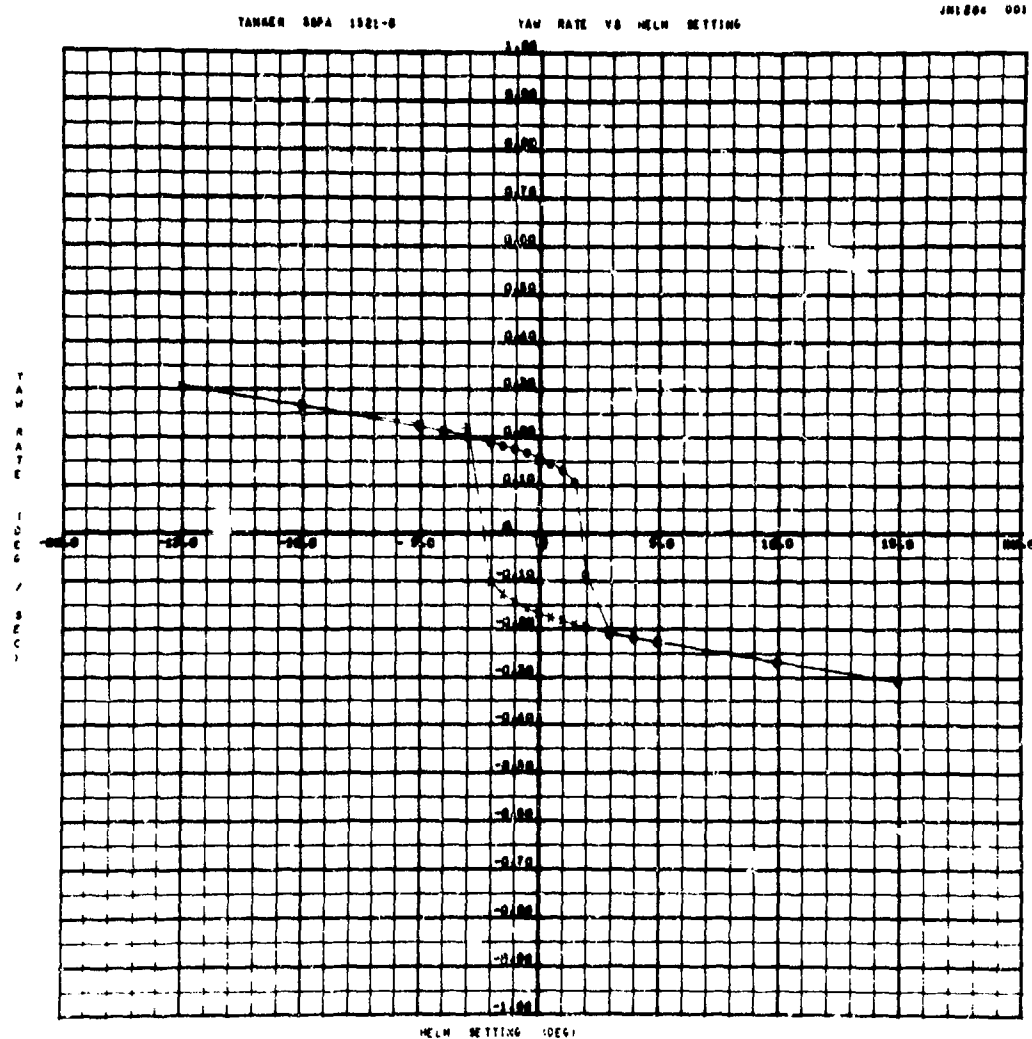


Fig. 7 Hysteresis Curve From Spiral Test
 O = increasing rudder angle
 X = decreasing rudder angle

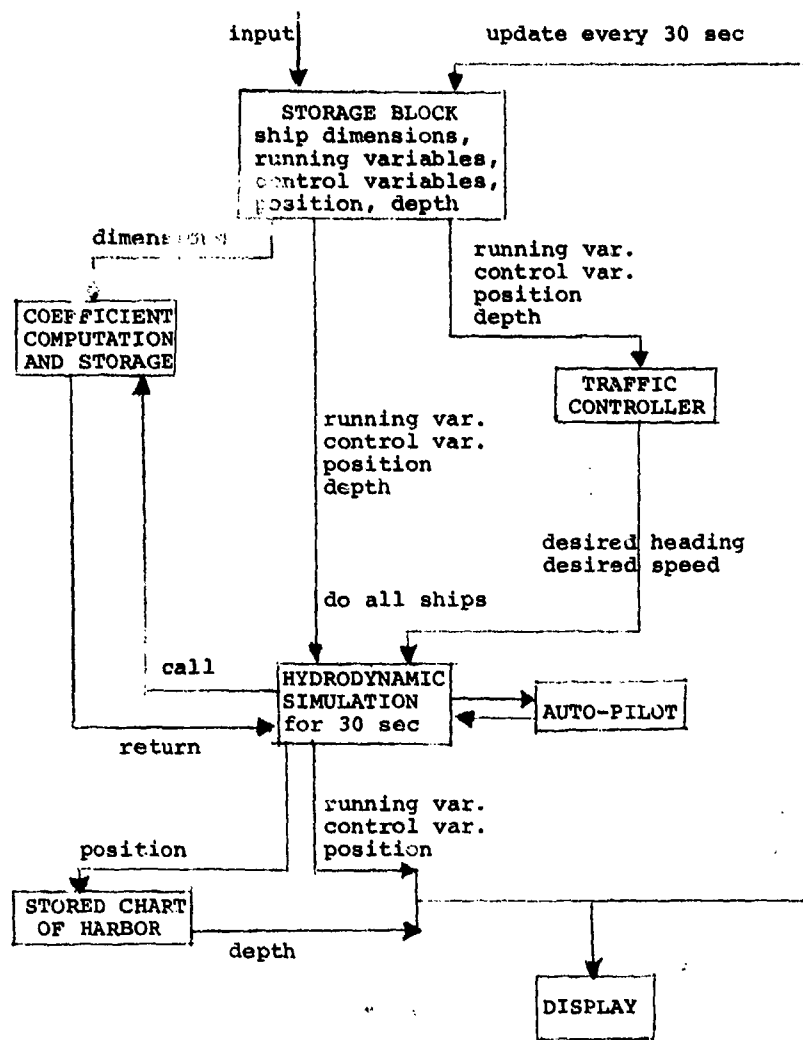


Fig. 8 Harbor Traffic Simulation Program

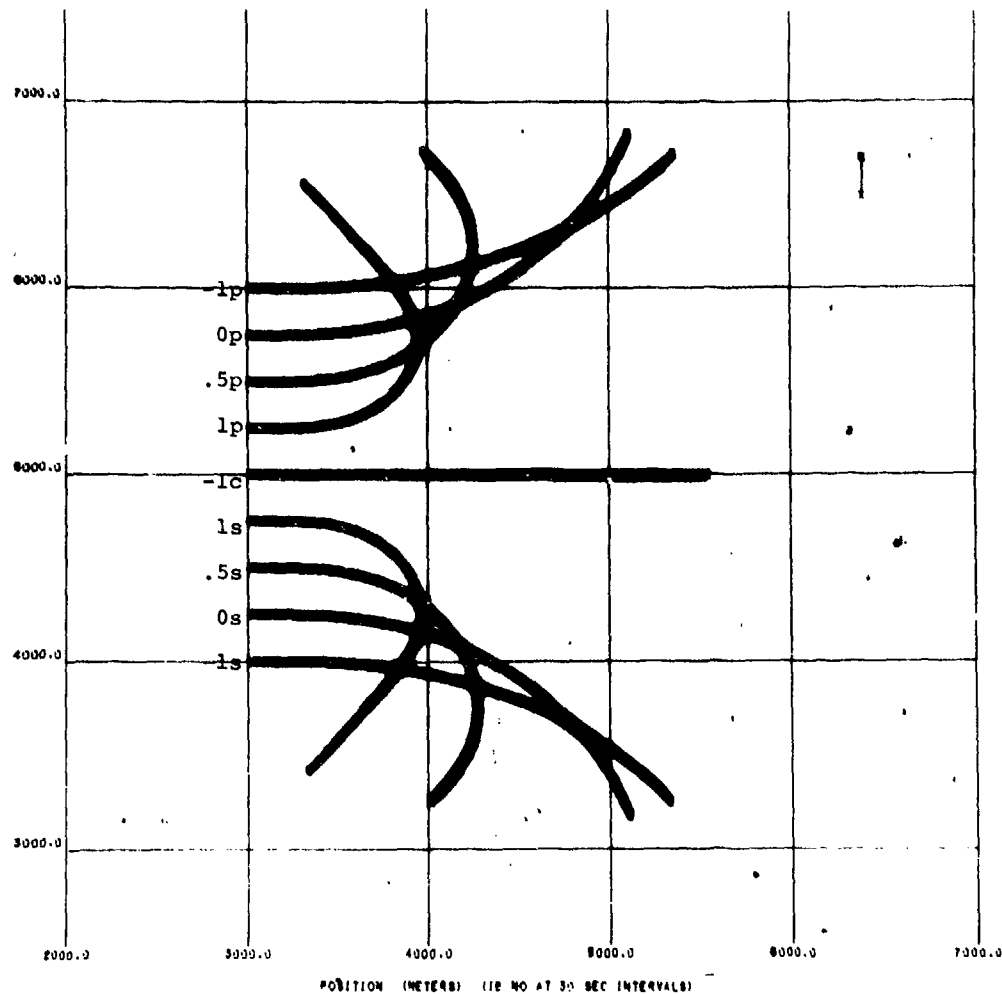


Fig. 9 Track as a Function of Maneuver, "Esso Bernicia" Initially at 10 knots
Simulation Ended After 10 Minutes

<u>Throttle Code</u>	<u>Helm Code</u>
1 full ahead	p helm hard to port
.5 half ahead	s helm hard to stbd
0 stop	c maintain course
-1 full astern	

HARBOR TRAFFIC SIMULATION

J01804 002 L

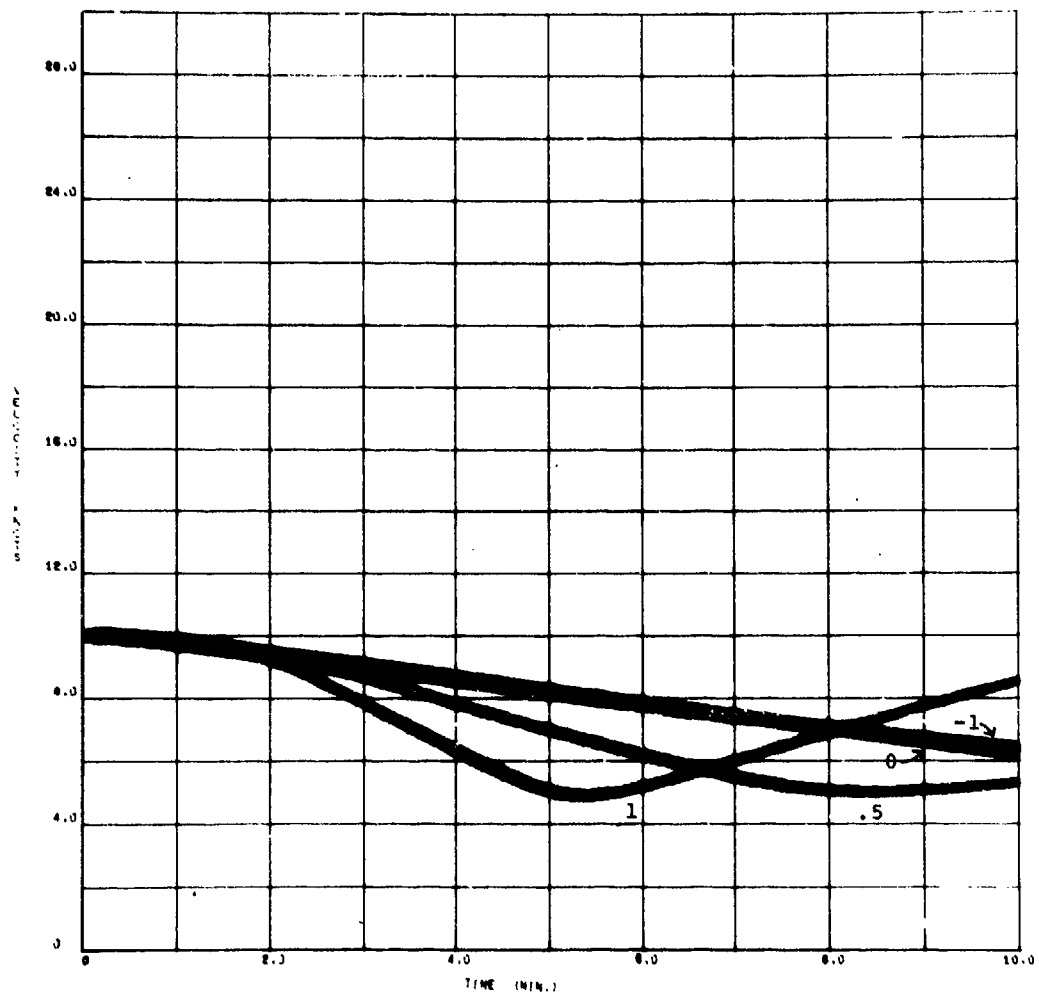


Fig. 10 Speed Reduction as a Function of Maneuvers in Fig. 9

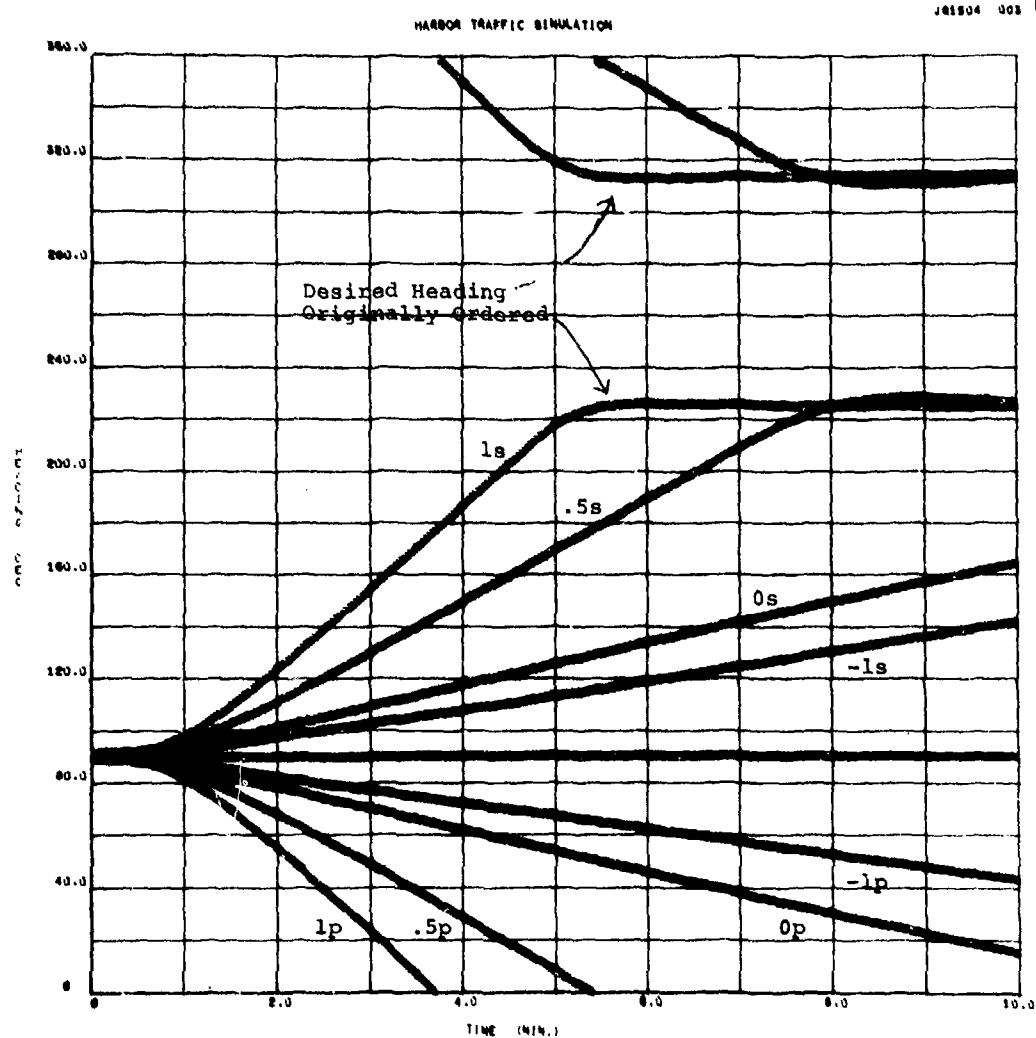
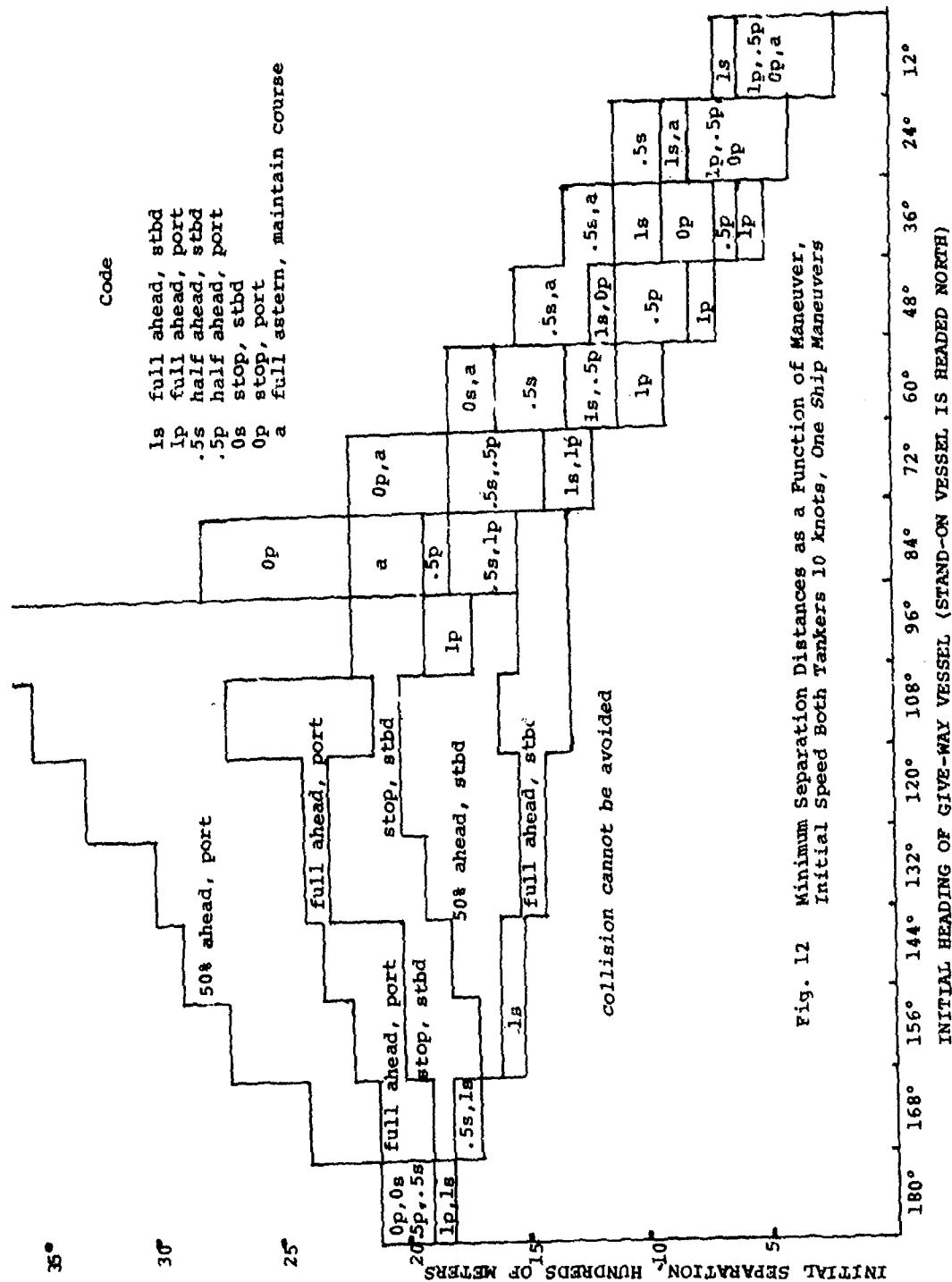
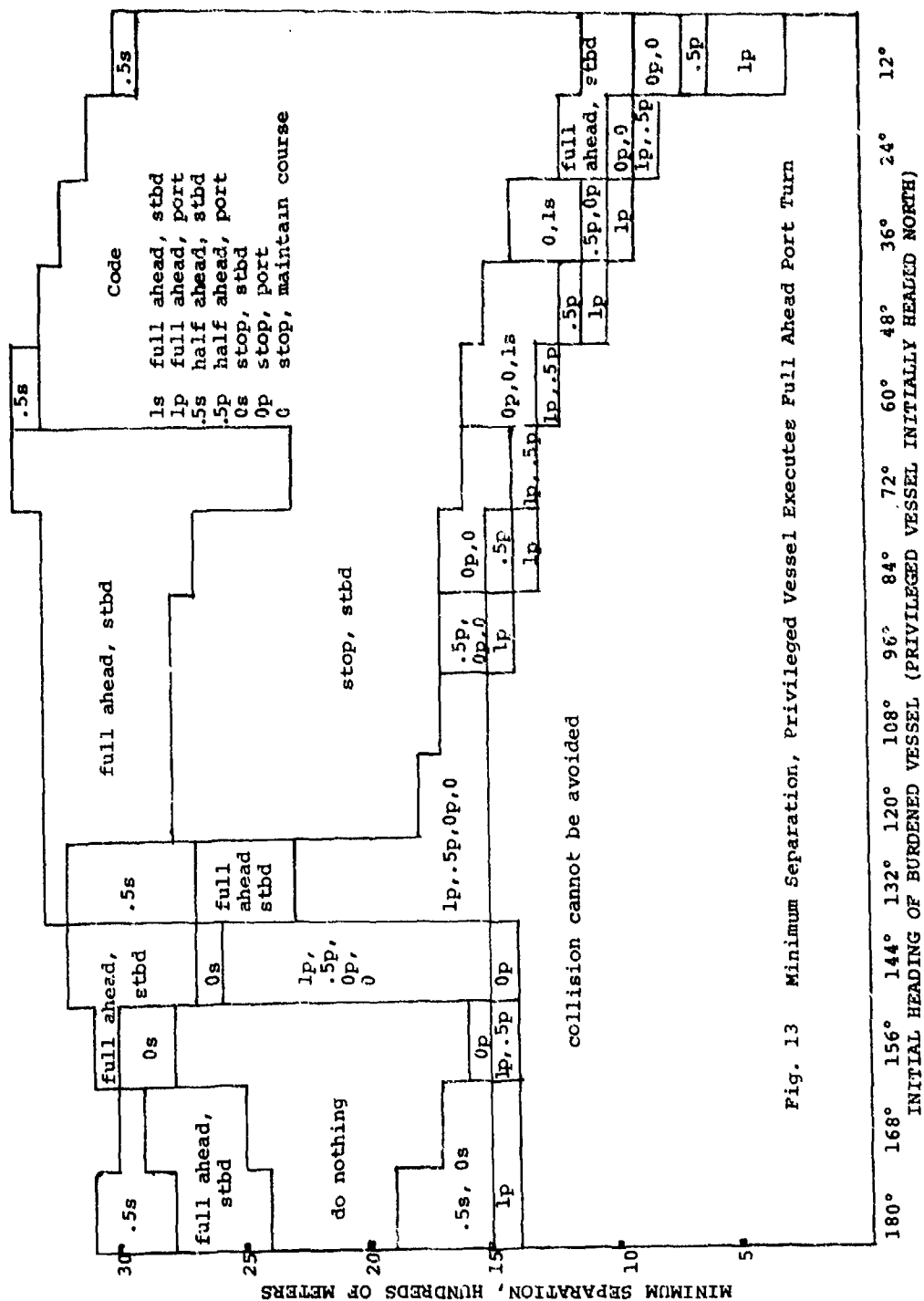


Fig. 11 Heading as a Function of Maneuvers in Fig. 9





Code

1s full ahead, stbd
 1p full ahead, port
 .5s half ahead, stbd
 .5p half ahead, port
 0s stop, stbd
 0p stop, port
 0 stop, maintain course

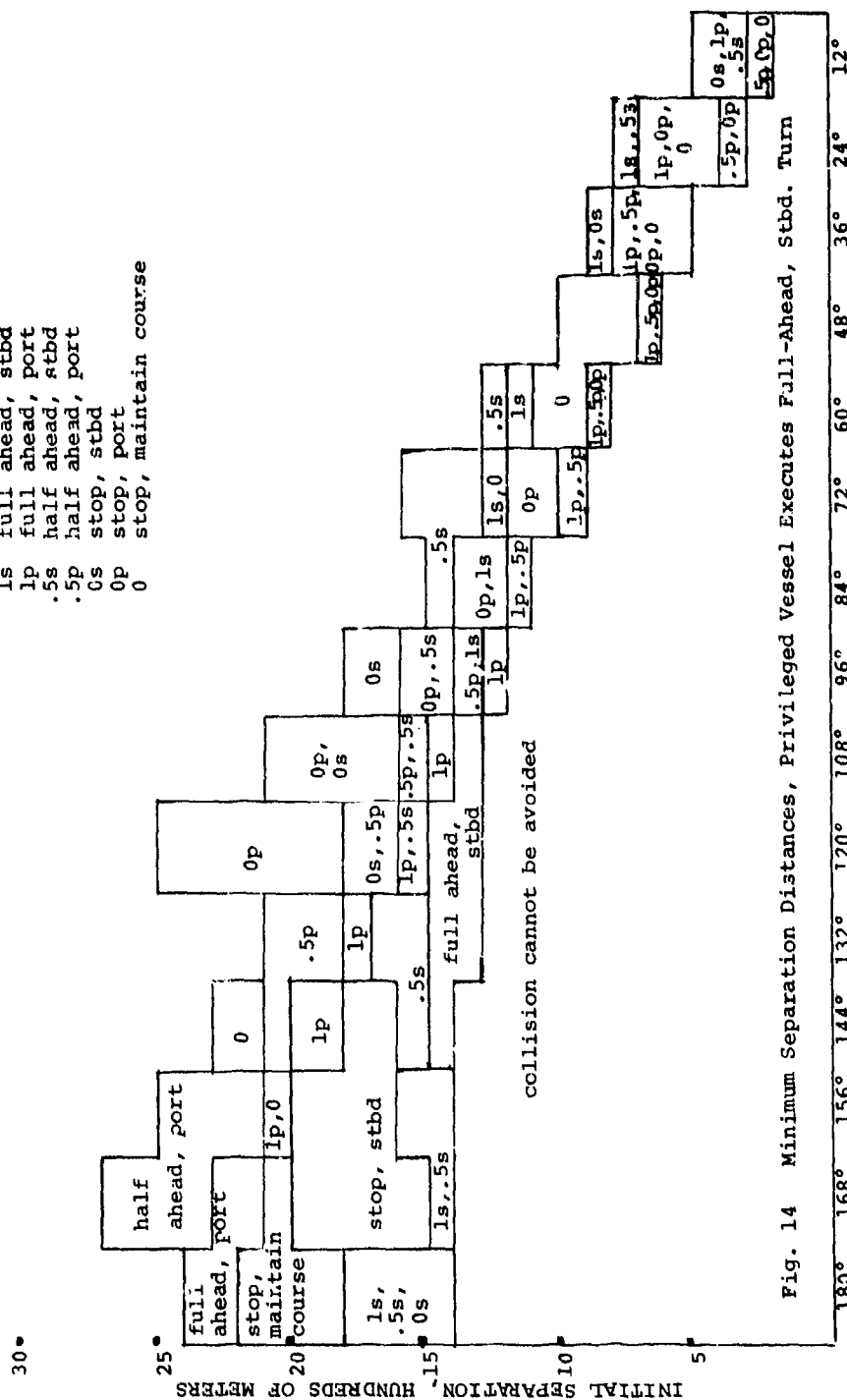


Fig. 14 Minimum Separation Distances, Privileged Vessel Executes Full-Ahead, Stbd. Turn

INITIAL HEADING OF BURDENED VESSEL (PRIVILEGED VESSEL INITIALLY HEADED NORTH)

THE ANALYSIS OF SAFETY MARGINS IN THE MANEUVERING OF LARGE SHIPS IN CONFINED WATERS

I. Oldenkamp
Royal Institution of Engineers
Netherlands

P. J. Paymans
Ergonomics Society
Netherlands

SUMMARY

In the present paper ship manoeuvres are considered as the output of a stochastic process. The main reason for the process being stochastic is the fact that the ship is steered by a human controller. A mathematical description of manoeuvres is derived which shows resemblance with the description of other irregular signals. The analysis is applied to an experiment executed on the manoeuvring simulator of the Netherlands Ship Model Basin. Results of these experiments are presented, showing the large influence the mariner has on handling capabilities of the steered ship.

INTRODUCTION

In the present paper the analysis of safety margins in the manoeuvring of large ships will be elucidated by results of simulator studies. The same type of analysis can be performed for actual manoeuvres when systematic records are available of those manoeuvres.

The simulator considered consists of a ship's bridge with the instruments usually found on board modern ships. Fig. 1 shows the interior of the bridge. The bridge is situated in the middle of a cylindrical screen with a diameter of 60 ft. on which the outside view is projected, Fig. 2 and 3.



Fig. 1 The bridge of the simulator during an approach manoeuvre to a harbour entrance.

The ship's characteristics as well as the influences of wind, current and for example bank suction are programmed on a hybrid computer, so that the ship's reactions on for example a rudder call are the same as the reactions of the real ship in a corresponding situation.



Fig. 2 Sectional perspective view of the simulator.

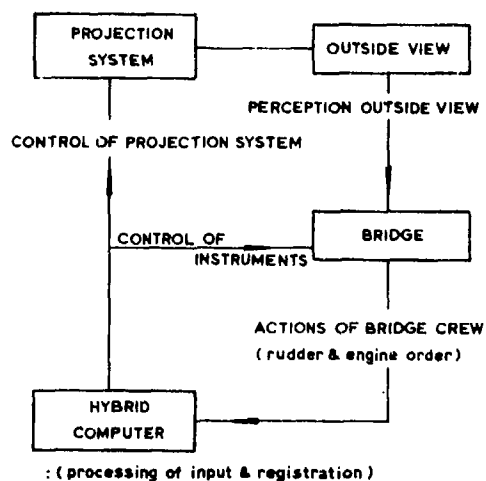


Fig. 3 Pictural block diagram of the simulator

These properties are used to investigate the influences of external disturbances, ship's characteristics, navigational aids and the mariners skill on the safety of the manoeuvres performed.

THE SYSTEM

Manoeuvring a ship can be schematized in its simplest form as a feed-back control system as shown in Fig. 4.

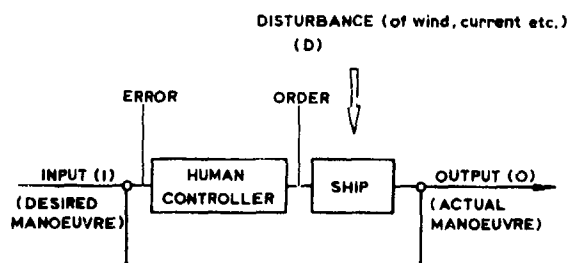


Fig. 4 Block diagram of a man-steered ship.

The ship responds to rudder calls with a certain output (O). The human operator which may be the helmsman, the captain or the pilot, compares this output with the input (I) which means that he checks whether the ship is performing the desired manoeuvre.

On a discrepancy between the input and output, called the error, the human controller decides for corrective reactions.

The blocks shown in Fig. 4 have an in- and output. For the block representing the ship this is quite obvious.

In the example shown, the input is the rudder angle set by the helmsman, calls to a bow thruster or calls to tugboats. The output is the reaction of the ship on the input and on disturbances of wind, current, bank suction etc., the latter indicated as (D) in Fig. 4.

There is an important difference in the blocks representing the human controller and the ship. For the ship there is a unique relation between the input plus the disturbance and the output. This means that a manoeuvre repeated under the same external condition and the same rudder calls, results in exactly the same manoeuvre. The human operator is quite different in this respect, he generally will not nor can repeat the same manoeuvre under the same conditions.

The fact that there is no unique relation between man's in- and output makes that it is not possible to predict exactly how a manoeuvre will be performed. There can only be a prediction with a certain probability that the manoeuvre is executed between some boundaries. For a better understanding of the prediction a great deal of effort has to be devoted to the description and interpretation of recorded manoeuvres.

DESCRIPTION OF MANOEUVRES

Consider a ship sailing through a canal. This manoeuvre can be described by registration of the distance of the centre of gravity of the ship to a reference line, for example the centre line of the canal, and furthermore by registration of speed, heading, rudder angle and any further signal which may be of interest. The registration of the manoeuvre performed is also the registration of the output (0) of the model presented in Fig. 4.

This output is a stochastic signal, since the human operator is unable to reproduce a manoeuvre even if the

circumstances of wind, current etc. were constant. This means that when a number of canal transits are recorded, the ship's trajectories will deviate from each other. Different measures have been developed to describe the manoeuvres considered. The average manoeuvre has been called the result of the procedure in which the ship's trajectory, the rudder angle, the speed and any further signal for a set of manoeuvres have been averaged. Fig. 5 shows how by this procedure the average trajectory is accomplished.

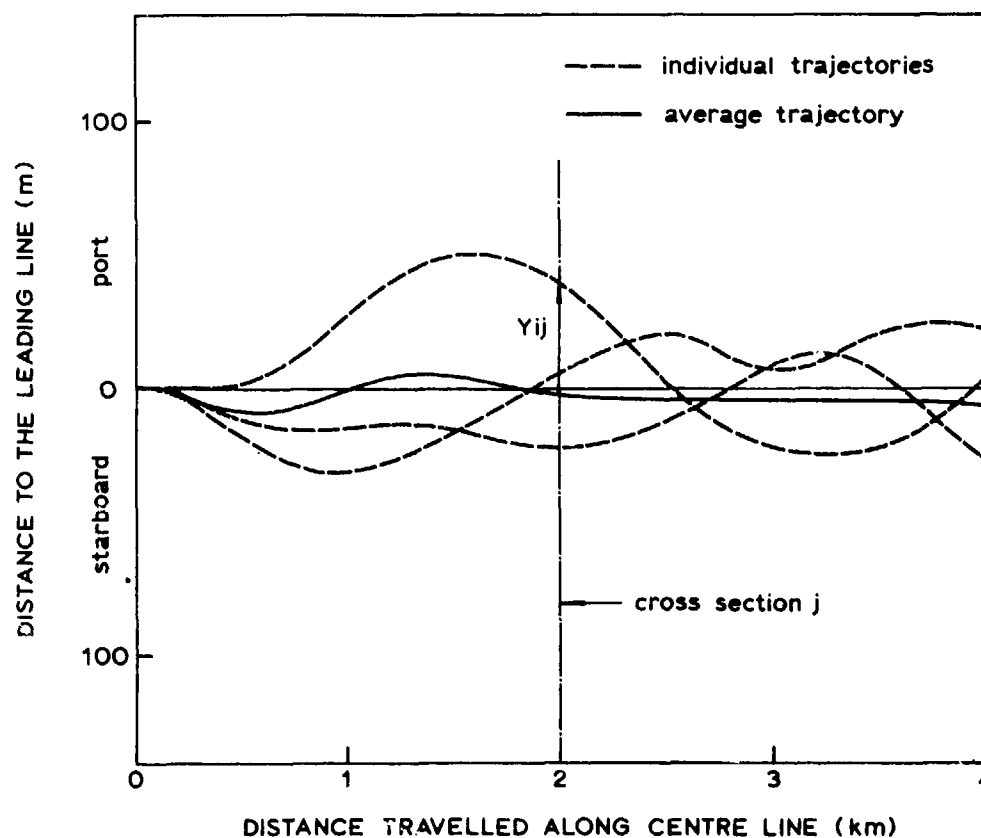


Fig. 5 Example of the determination of the average trajectory from N individual trajectories.

$$Y(\text{average})_j = \frac{1}{N} \sum_{i=1}^N Y_{ij}, \quad j = 1 \dots M = \text{average value of } Y \text{ at cross section } j.$$

The standard deviation of the signal describes how signals of individual manoeuvres are spread around the average signal. Particularly important is the standard deviation of a set of the ship's trajectories. The average trajectory may be near the centre of the canal, safe manoeuvring requires that during each individual run the trajectory remains within the channel boundaries. As a result of experiments carried out so far, it has been found that trajectories are spread around

the average trajectory, according to the Gaussian distribution. The fact that the distribution has been identified, implicates that the deviation of the trajectories is fully defined by the standard deviation.

In Fig. 6 an example is given of the distribution of individual trajectories around the average trajectory.

In this figure the distance to the average track is plotted on the horizontal axis on a linear scale, the frequency that the distance was below a

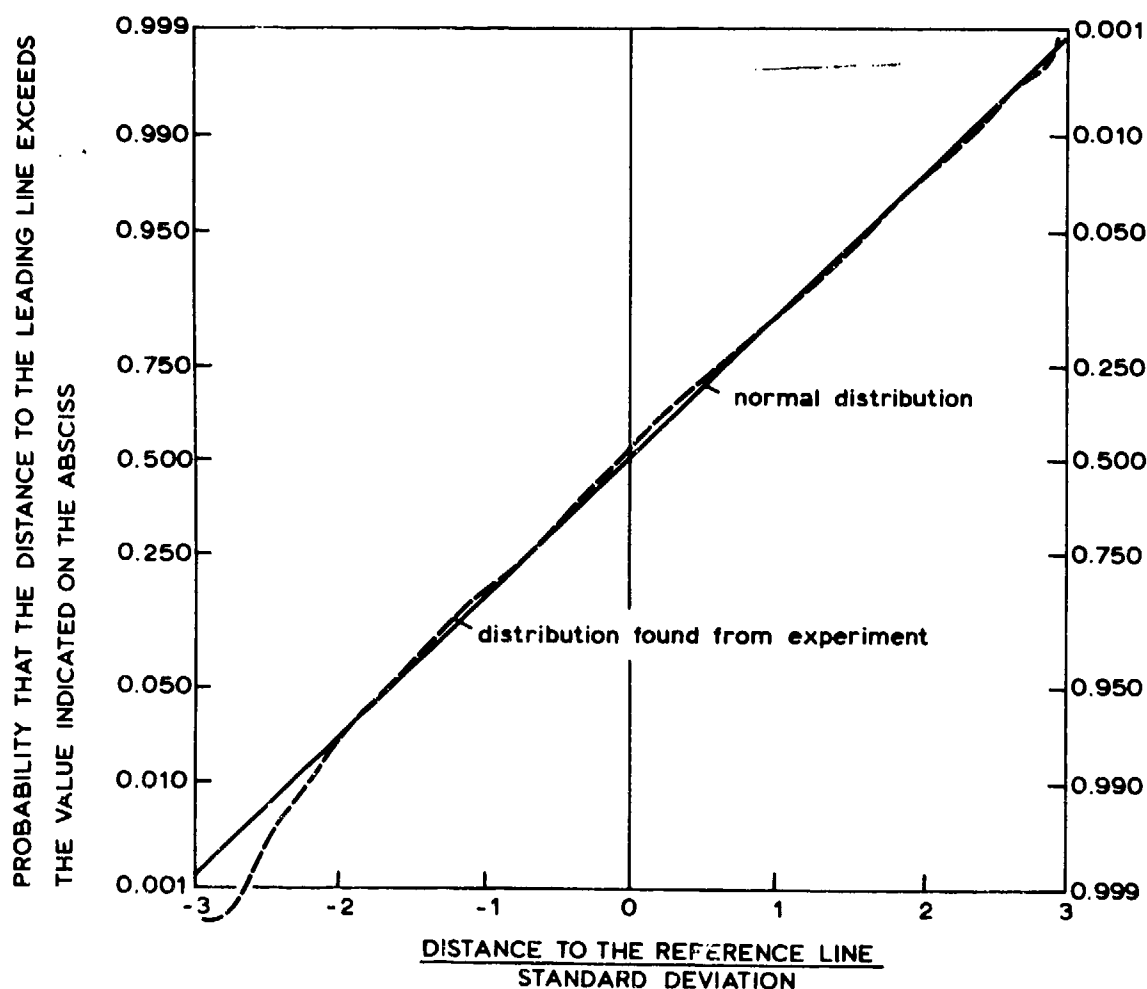


Fig. 6 Cumulative distribution function of distance to the reference line.

certain level on the vertical axis on a non-linear scale. If the distribution is normal, a straight line appears. Here indeed this condition is satisfied.

With this standard deviation, however, the width of lane cannot be determined directly yet. This can be illustrated as follows. Take for example an average trajectory with around it a collection of trajectories from individual runs, Fig. 7.

If now, as an experiment of mind, two piers would be placed at a certain cross section, the standard deviation defines the probability that a track chosen at random passes between the

ends of the piers. If there were another pair of piers at another cross section, again the probability could be calculated from the formula:

$$P(\text{track lies between both pair of piers}) = P(\text{track lies between piers A}) \times P(\text{track lies between piers B under the condition that the track was between piers A}) \dots(1)$$

This last probability cannot be calculated if we have the standard deviation of the trajectories only. To illustrate this, point I in Fig. 7 should be considered where a trajectory

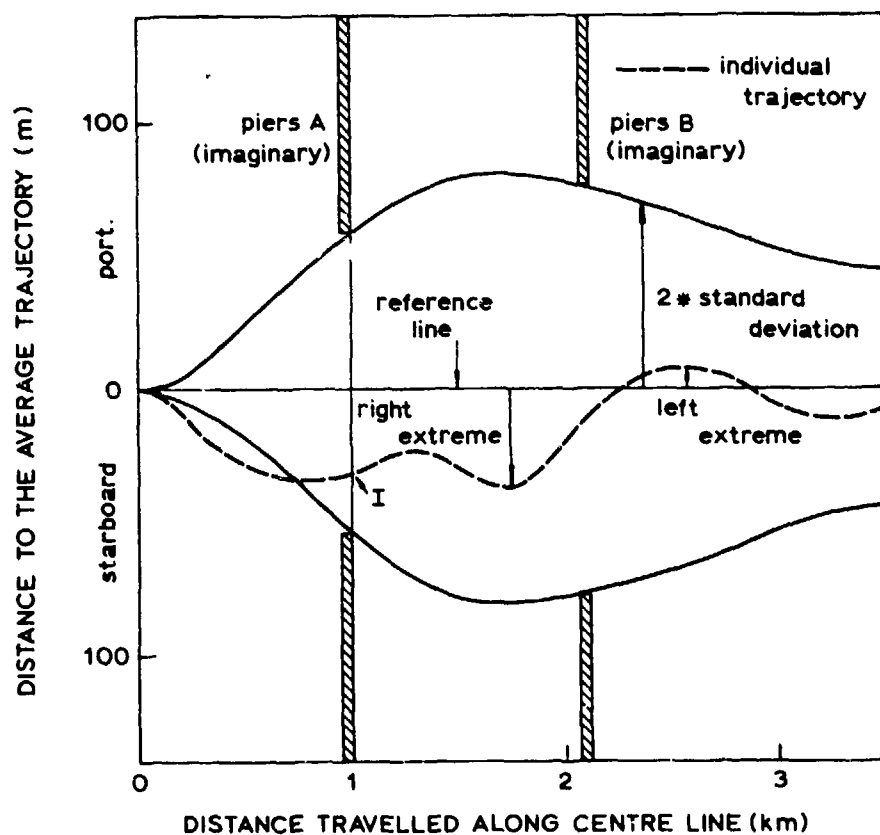


Fig. 7 Two times the standard deviation has been plotted on both sides of the average trajectory as a function of the distance travelled.

$$P(\text{track goes between both pair of piers}) = P(\text{track goes between piers A}) \times P(\text{track goes between piers B under the condition that the track went between piers A})$$

intersects section A. The probability that this trajectory passes between piers B depends on the nature of the oscillation around the average track. If the number of oscillations per unit length is high, it will be less certain that this trajectory passes between piers B. So the calculation of the possibility that a track will pass between sets of piers or in the case of an infinite number of piers (a channel) requires knowledge about the distribution of the amplitudes of the oscillations around the average track and the number of oscillations per unit length.

In Fig. 7 the track of a run is given, together with a reference line. The track oscillates more or less around this line if this line is the average track of a number of runs. In the trajectory left and right extremes can be discerned. A left extreme is defined to occur if the distance of the track to the reference line (in this case the average track) reaches an extreme value pointing to Port. In the same way a right extreme is defined. An essential and sufficient condition for the requirement that the track does not exceed the sides of a channel with sides parallel to the average track is that the extremes are smaller than half the channel width.

The occurrence of an extreme is the result of a stochastic process; its size and its likelihood of occurrence therefore have to be given in the form of probability density functions defining respectively the probability of the occurrence of a certain size of an extreme and the number of extremes per unit of length of the channel. For the calculation of the safety of manoeuvres the probability density function of the extremes has to be known. The hypothesis is now that this probability function is similar to that of an irregular signal which has the

following properties:

- a. The average of the signal is zero and is distributed according to the Gaussian distribution around this average.
- b. The signal is ergodic.
- c. If the signal is thought to be composed of sine functions, the phase differences between the sine functions should be random.

Knowing these properties, the distribution of the extremes of the signals is known; see Rice (1). Condition (a) is satisfied if we deduct from the individual trajectories the average trajectory. When enough manoeuvring space is available the trajectories are distributed according to the Gaussian distribution. Condition (b) is in general not satisfied since first of all the standard deviation is not constant over the manoeuvre. However, this can be overcome by dividing the extremes by the local value of the standard deviation. Consider a part of the manoeuvre. The trajectories can be assumed to be composed of an infinite number of sine functions. The expected number of extremes per trajectory will in general be different from the expected number of extremes of another part of the manoeuvre of the same length. If the difference is too large, a separate calculation has to be made for both parts of the manoeuvre. The condition (c) needs to be checked after each experiment.

Some indications led to the conclusion that this condition may not be entirely satisfied when in a particular point of the manoeuvre the situation is different, such as near a location where the channel is narrowing, another ship is meeting or when a different phase of the manoeuvre begins.

The distribution of the magnitude of the extremes is given in Fig. 8 in the form of a cumulative distribution function. Since for the present problem one is only interested in the very large extremes, which seldom appear, the vertical scale of Fig. 8 is logarithmic to permit interpretation.

There appears another factor, the parameter ϵ . It has been stated before that for a part of the manoeuvre the trajectories can be considered as being composed of an infinite number of sine functions of different "frequency". It should be noted that the frequency here has the dimension of number of oscillations per unit of length. From the distribution of the frequencies of the sine functions which compose the trajectories, the

distribution of the size of the extremes can be calculated.

If the trajectories are composed of sine functions of nearly the same frequency, ϵ equals zero and the distribution of the size of the extremes equals the Rayleigh distribution function. When ϵ equals unity it is the Gaussian distribution. In this case sine functions of all frequencies are present. In the experiments carried out so far it has been found that the parameter ϵ is close to the unity.

From Fig. 8 the probability can be calculated that one extreme exceeds a given magnitude. Since many more extremes are likely to appear during a number of manoeuvres a certain probability has to be chosen that sequential extremes do not exceed a

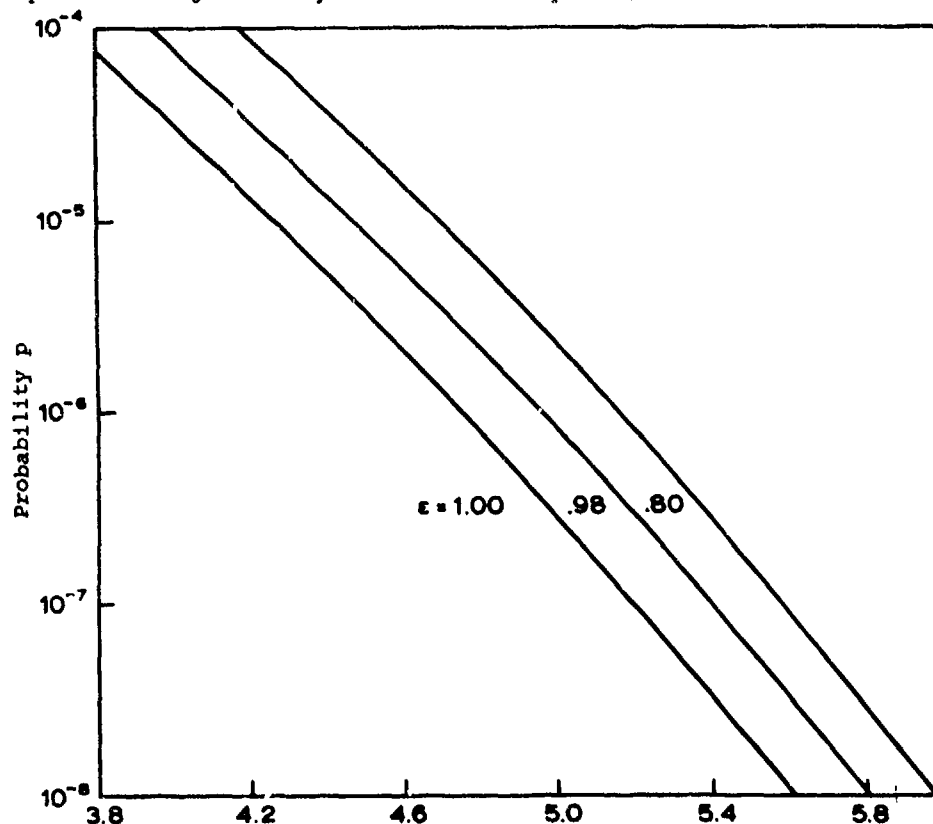


Fig. 8 The probability p that one extreme is larger than η (The probability that n sequential extremes will be smaller than η equals $n \times p$, since for small values of p the following approximately yields: $1-(1-p)^n = n.p.$)

given value. As the extremes are not correlated the probability that sequential extremes do not exceed the given value follows from the formula:

$$P = 1 - (1 - p)^n$$

P = probability that n subsequent extremes will not exceed a given magnitude

p = probability that one extreme exceeds a given magnitude

n = number of extremes concerned.

It should be mentioned that the number of manoeuvres is very large. From the above formula it follows that the probability p of one extreme exceeding a certain magnitude should be very close to zero to allow a reasonable value of P , the probabi-

lity that n sequential extremes do not exceed the given magnitude.

Fig. 9 shows the relation between P and p for some values of n .

As an example it is supposed that a probability of .60 is required that no accidents occur in a certain period of time, say 10 years. From Fig. 9 the required value of p then can be determined. The total number of extremes during this period of time can be estimated from the average number of extremes per manoeuvre and the expected number of ships. Knowing the value of n , n then follows from Fig. 8; the required width of lane then can be determined by multiplying n with the standard deviation. In the next section an illustration of the method is given based on manoeuvres made on the simulator during an experiment.

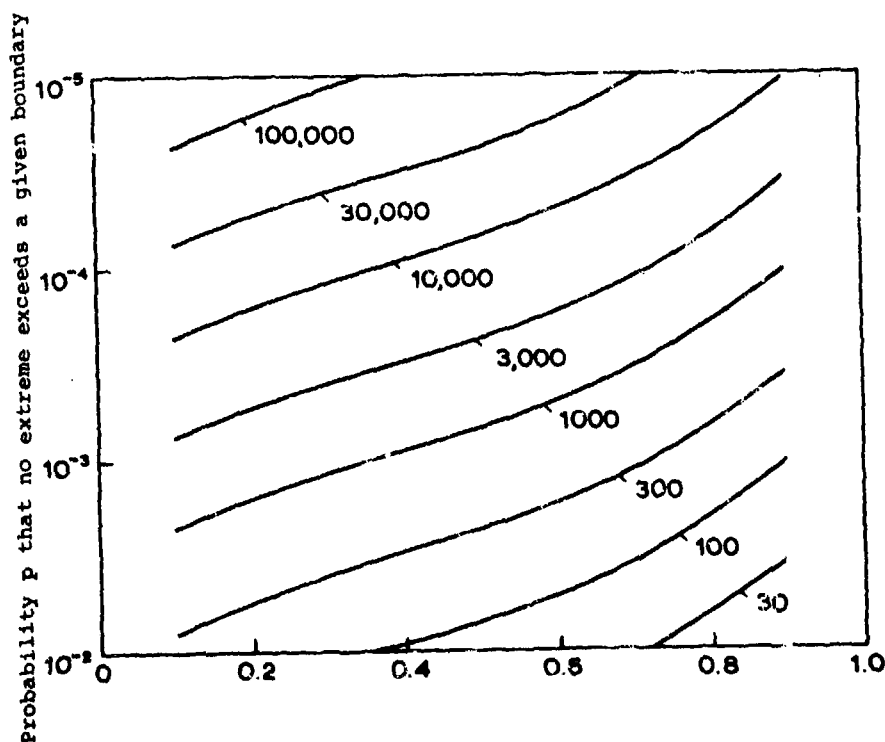


Fig. 9. Probability P that no extreme exceeds the given boundaries during n extremes
In the Figure, lines are given for n equals 30; 100; 300 ... 100,000

THE EXPERIMENT

A canal was simulated with a width of 400 m, see Fig. 10.

The sides of the canal could be seen from the bridge, though not so sharply as in ordinary daylight due to some limitations of the projection system. In the canal there were no obstacles as meeting or overtaking ships. The ship was a tanker of 200,000 DWT. The ship's particulars are shown in Table 1. The subjects of the experiment were four experienced Europort pilots aged between 55 and 63. During the experimental runs the ship's speed was either 12 or 16 knots and the subjects were asked to keep the ship either in the centre of the canal or on a line parallel to the centreline, 100 meters to starboard. To investigate what the influence was of bank suction half of the experimental runs were carried out with bank suction, the other half without. Further the schedule was arranged so that the improvement in the performance of the subjects could be analysed. Table 2 gives an outline of the experimental conditions.

The entire experiment was composed of 64 runs.

RESULTS

Fig. 11 shows the average trajectories and the standard deviations for the conditions of the line to be followed and first eight runs of each subject and his last eight runs. It shows some very interesting results.

With regard to the average trajectory in all conditions the reference line was followed very well with deviations not larger than 20 meters. The standard deviation shows, however, that individual runs deviated much more than 20 meters from the reference line. At the start of the manoeuvre the standard deviation is zero, since all manoeuvres started precisely on the reference lines. As the runs continue, the subjects start to make corrections which causes the phenomenon that the trajectories deviate from each other. This is something special for the human controller. If they had not used the rudder at all, the ship would have sailed perfectly on the reference line, except for those runs during which bank suction

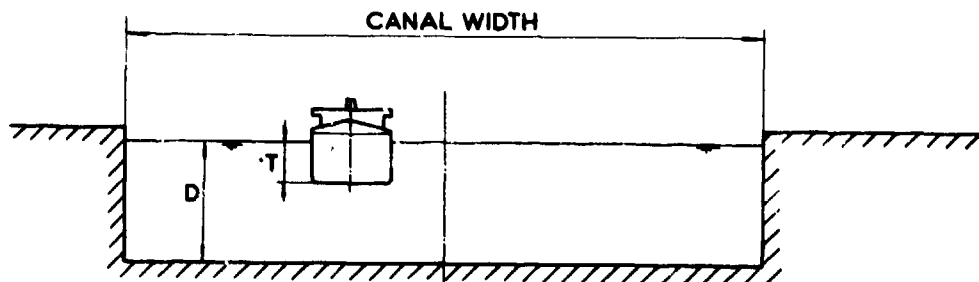


Fig. 10 Dimensions of the simulated canal.

$T = 65'$

$D > 3 \text{ times } T$

Canal width = 400 m.

The length of the canal was infinite.

The simulator runs covered 12 km.

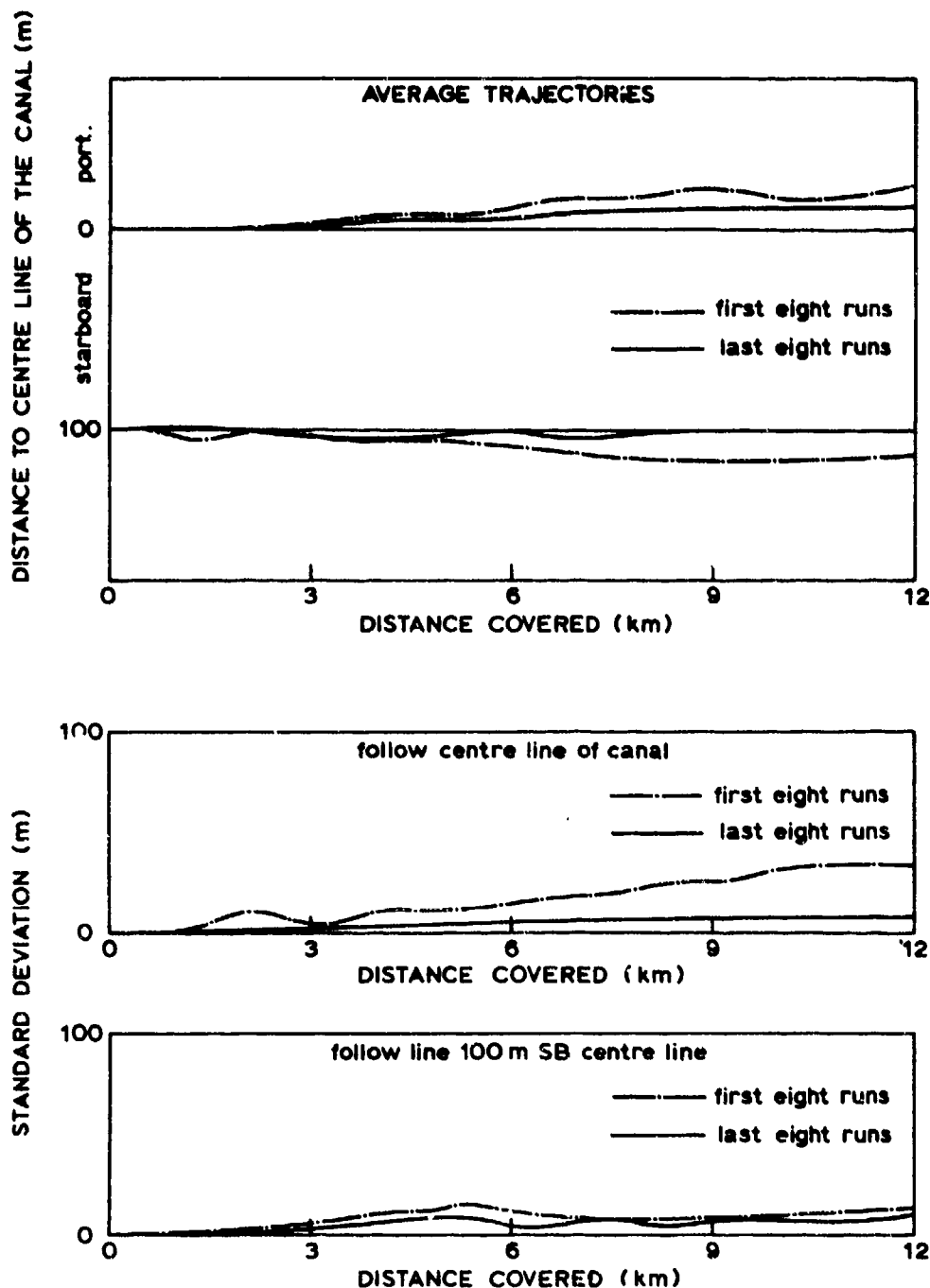


Fig. 11 Average trajectories and standard deviation as function of the distance travelled.

was simulated and the reference line was 100 meters starboard from the centre line. A plausible explanation for this is that the subjects could only estimate their position with a

limited accuracy, so that they falsely believed to have sailed away from the reference line. Another (less obvious) reason could be that the subject liked to use the rudder just to see if the

ship responded as they expected her to respond.

Once the subjects had introduced the first error, they had to use the rudder from time to time to correct their subsequent errors. After some four to five kilometers the manoeuvre is completely "developed", which means that the standard deviation has reached a more or less stable level and the manoeuvre is not influenced any more by the fact that the runs were started four to five kilometers ago on the reference line.

Great differences appear when the first eight runs are compared with the last eight. The required width of lane drops by a factor four in case the

centreline of the channel had to be followed and reduces with a factor two when the reference line 100 meters to starboard had to be followed.

Apparently, subjects could improve a lot as they got more acquainted with the ship and the manoeuvre. Also one observes a striking difference in the factor with which the performance improves depending on which reference line had to be followed.

An explanation for this phenomenon is that in the beginning of the experiment the subject needed a lot of space to manoeuvre. In case the centre line had to be followed more space was available, than when the other reference line had to be followed. With some

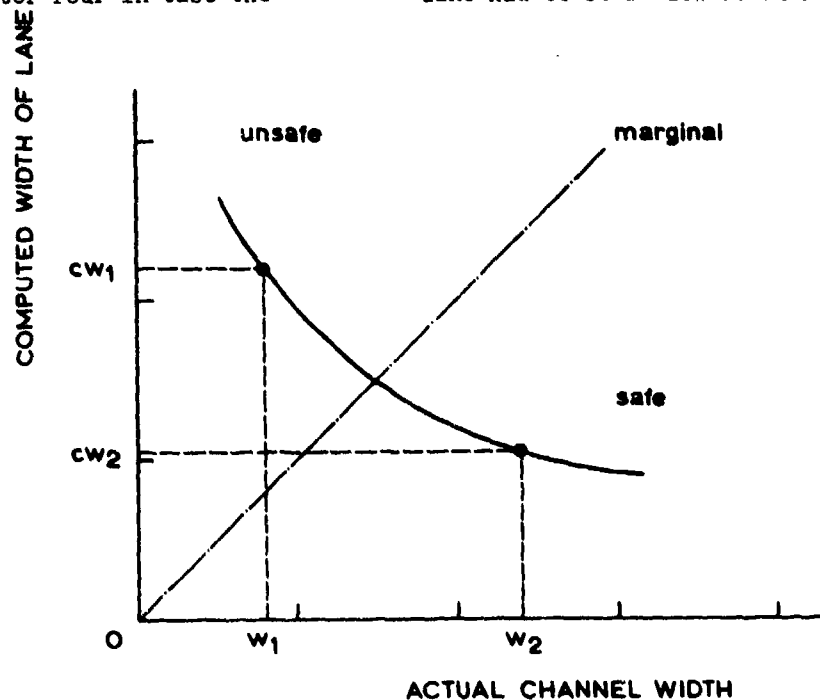


Fig. 12 Illustration of finding the optimal channel width.

When a too narrow channel is tested, the mariner has great difficulty to steer the ship, with the result that the standard deviation of the trajectories is large and therefore the computed width of lane will be larger than the actual channel width. When the actual channel width is very large, the computed width of lane will be small.

extra effort the subject succeeded in using the smaller space available. As the subjects got trained, the easier task was performed better. This phenomenon was also observed during other experiments. When the task to manoeuvre the ship becomes more difficult, the steered ship behaves more unstable. This has some peculiar consequences when designing a channel. An illustration is given in Fig. 12. If the channel with width w_1 is tested and the computed width of lane cw_1 is found to be larger than w_1 ,

this does not mean that the actual required width of lane has to be equal or larger than cw_1 . When a channel with width w_2 is tested (w_2 being larger than w_1) the required width of lane cw_2 found will in general be smaller than cw_1 . When optimizing the channel width it is therefore necessary to perform tests with the approximate final channel width under conditions equally difficult as those the channel is designed for. The question what type of influences have a great consequence is a very important one. The following results

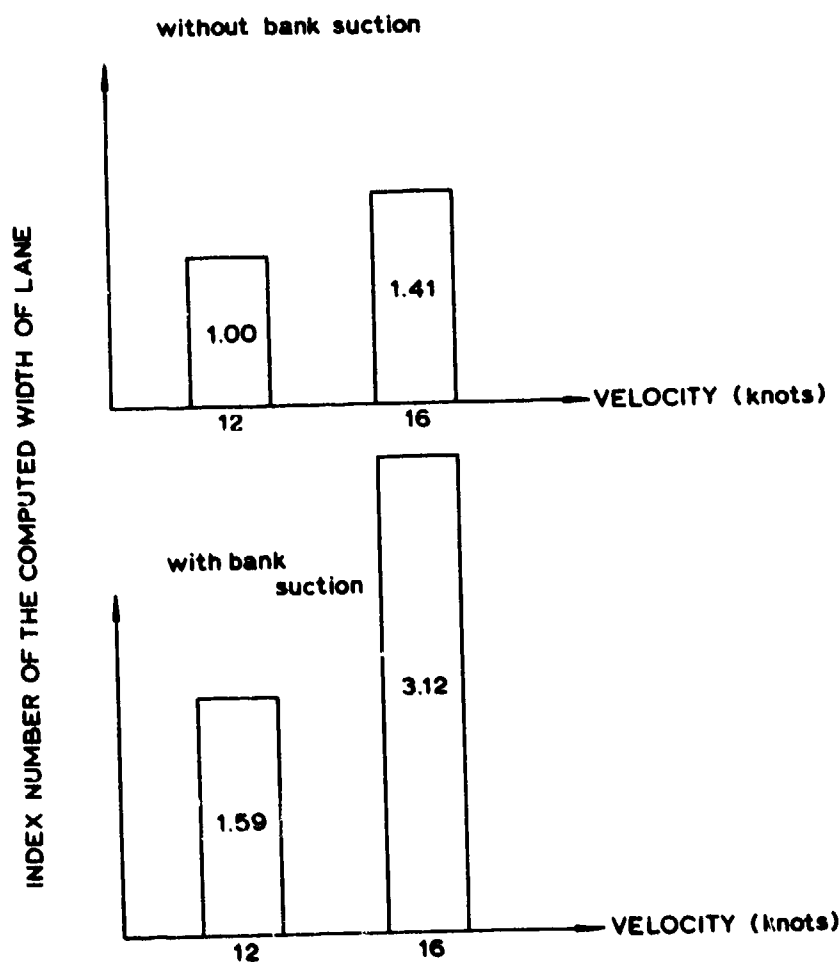


Fig. 13 Influence of forward speed and bank suction on the computed width of lane. The condition forward speed and no bank suction has been set at 1.00

of the experiment give some indication. See Fig. 13.

The effect of the ship's speed and the presence or absence of bank effects had a complex, but in quantity not so large effect as the effect of training.

The presence of bank suction caused the task to be a little more difficult than without bank suction. Under the first condition the required channel width was about 60 percent larger at the speed of 12 knots.

High speed is a disadvantage when sailing through a channel, especially when bank effect is experienced. This finding is in accordance with findings of Bindel (2). A ship in a canal becomes course unstable at increased speeds.

The increase in required channel width was more than 100 percent.

When no bank suction was simulated, the effect of the ship's speed was not so large. The required channel width was 40 percent larger at 16 knots than at 12 knots.

During other experiments it has been found that the ship dynamics have no great influence on the ship's trajectories provided that the manoeuvre is not too close to the physical limits of the ship to make the manoeuvre. Usually this is a requirement for safe manoeuvring. Much more important is the influence of the human controller as was demonstrated here by the huge learning effect. Also disturbing conditions like from wind, current, bank suction etc. influence the safety of manoeuvring very much. If now the block diagram of Fig. 4 is considered again, the elements which have the greatest influence on ship's trajectories are presented with a double line. The human controller and the external disturbances working on the ship are

meant in the broadest sense. Considering the human operator, the following factors are found to be of importance:

- The skill with which the mariner performs his task, which includes his motivation to perform the manoeuvre; his knowledge about the local conditions as from harbour layout and tidal current.
- Availability of navigational aids. This means both instruments on board and ashore including landmarks. Essential again is to what degree the mariner is trained in the use of his equipment. The effect of navigational equipment is very complex. A great many sources of information is often undesirable no matter how accurate the information may be. Few instruments giving the essential information is preferable. Which information is given and the way in which it is presented is of importance.
- Disturbing conditions like those of current, wind, bank suction etc. Not only the magnitude of the disturbance, but also its variation during the manoeuvre as well as the degree to which the mariner is informed about it.

Naturally this summary is far from complete, but it indicates some important factors.

FINAL REMARKS

In this paper a mathematical description of ship manoeuvres has been given. It permits the calculation of the probability that during a manoeuvre channel boundaries are exceeded. In this way different conditions like the available navigational aids, trained or untrained mariners etc. can be compared

with respect to safety.

It is recognized that the mathematical description presented has up to now been applied to only a few cases. The method has to be evaluated further. At present an experiment is

conducted in which the results of simulator tests will be compared with manoeuvres made in reality. The results of these studies will be presented in the near future.

LIST OF REFERENCES

- 1 Rice, S.D.; "Mathematical Analysis of Random Noise"
from Bell System Technical Journal, Vols. 23 and 24.
2. Bindel, S.; "Experiments on Ship Manoeuvrability in
Canals as carried out in the Paris Model Basin"
presented at First Symposium on Ship Manoeuvrability
at the David Taylor Model Basin (1960)

TABLE 1. PRINCIPAL DIMENSIONS OF THE SHIP.

Displacement	200.000 DWT
Length	290 m
Breadth	47 m
Draft	65 ft.
Number of propellers	1 (right turning)
Number of rudders	1

TABLE 2 PARTICULARS OF THE EXPERIMENTAL CONDITIONS

Size of the experiment 64 runs

Effect	Levels	Remarks
Bank suction	2	with/without bank suction
Learning period	2	first 8/last 8 runs
Reference line to be followed	2	centre line/line 100 m to starboard of centre line
Speed	2	12/16 knots
Subjects	4	Europoort pilots

SOME ASPECTS OF MANEUVERING IN COLLISION SITUATIONS IN SHALLOW WATER

I. W. Dand
National Physical Laboratory
Feltham, Middlesex, England

ABSTRACT

Hydrodynamic effects which could contribute to a collision between ships in shallow water are discussed. A numerical method for the computation of interaction forces and moments is presented and it is used qualitatively in the discussion of two particular types of collision which have been reproduced on model scale. The effect of water depth on manoeuvring and the crash stop are mentioned where they are relevant to collision situations in shallow water.

NOMENCLATURE

a	length of major axis of ellipse
b	maximum beam of ship
C_N	moment coefficient $N/\rho b^2 U^2$
C_X	longitudinal force coefficient $X/\rho b U^2$
C_Y	transverse force coefficient $Y/\rho b U^2$
h	water depth
l	longitudinal separation of centroids of two ellipses
L_A, L_B	lengths of ships A and B
N	$N_u + N_s$
N_s	steady Lagally moment
N_u	unsteady moment
\vec{n}	outward-drawn normal vector of magnitude n
\vec{r}	position vector of magnitude r
δs	length of source panel
t	time
δt	time increment
T	draught of ship at rest
U_A, U_B	velocities of ships A and B
U_R	relative velocity of ships A and B
u_i	normal component of velocity on i th source panel
u, v	perturbation velocities in x and y directions of body axes
X	$X_u + X_s$
X_s	longitudinal Lagally force
X_u	unsteady longitudinal force

X_o	overlap parameter = $x_{\text{bow}}(\text{ship B}) - x_{\text{bow}}(\text{ship A})$
δx	projected length of source panel on centreplane
Y	$Y_u + Y_s$
Y_s	transverse Lagally force
Y_u	unsteady transverse force
Y_o	transverse separation of centreplanes of ships A and B
y	ordinate of source panel in question
y_o	local half-beam of hull
α	angle of U_R to space axes
β	depression angle of camera
δ	helm angle
η	ordinate of source panel other than that in question
θ	angle between directions of U_R and U_B
ξ	abscissa of source panel other than that in question
ρ	water density
σ	surface source distribution
σ_i	contribution to σ from i th source panel
ϕ	velocity potential of undisturbed flow
ϕ_b	velocity potential of body singularities
ϕ_j	potential of source on j th source panel
Φ	potential of total flow
ψ	angle between course of Ship B and that of ship A

1 INTRODUCTION

Collisions at sea occur for a variety of reasons. They may be due, among other things, to human error, mechanical failure, weather and sea conditions, or they may be 'assisted' by the use of radar (ref 1). It is with none of these aspects that this paper is concerned, but rather with the hydrodynamic interaction between two ships and the effect of depth of water, both of which can change the manoeuvring characteristics of ships in close proximity and may in fact lead to a collision where one might suppose none would occur.

We consider collisions which occur in shallow water only, for it is often in confined waters of limited depth that ships find them-

selves in conditions of close proximity where the risk of collision is high. In water of limited depth it seems reasonable to assume that the flow becomes more nearly two-dimensional and Weinblum has shown theoretically (ref 2) that interaction forces are far larger in two-dimensional than three-dimensional flow. This, coupled with deterioration in manoeuvring characteristics in shallow water, makes the problem of navigating two ships in close proximity all the greater, thereby increasing the likelihood of a collision.

2 INTERACTION BETWEEN TWO SHIPS IN SHALLOW WATER

2.1 General

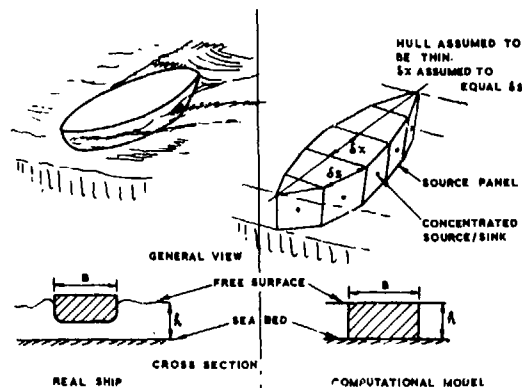
When two ships approach each other in deep or shallow water, some measure of hydrodynamic interaction occurs which may cause one or both of the ships to deviate from her course, possibly resulting in a collision (ref 3). The vessels are subjected to interaction forces in the longitudinal and transverse directions which may cause either ship to be repelled from or attracted to the other, as well as a moment in the horizontal plane which may cause either ship to turn towards or away from the other.

Such effects are intensified in shallow water and have been the subject of some model studies (ref 4). However, such studies have of necessity been restricted to particular occurrences and have usually dealt with cases where the models are constrained in some way so that they pass on parallel courses with no collision.

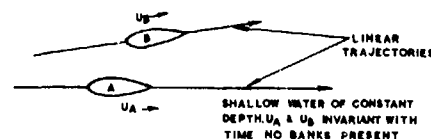
Model results have been used, however, to deduce manoeuvring characteristics when passing in confined waters when the vessels are not allowed to deviate too much from a parallel course (refs 5,6,7). Furthermore, the types of hull form to which such analytical studies are applicable are restricted to those used in the model experiments. Finally, such studies do not allow for the case where the ships are on converging courses.

It would therefore seem desirable to investigate interaction between ships from an entirely theoretical point of view and use this, in conjunction with model tests, to investigate the likely behaviour of ships in danger of collision. An early investigation of interaction, applicable to deep water, was due to Havelock (ref 8), and this was extended by Silverstein (ref 9) who presented results of calculated interactions experienced by two deeply-submerged Rankine ovoids. More recently, Collatz (10) presented a solution of the two-dimensional problem of two elliptical cylinders moving on parallel courses, taking into account unsteady terms in the calculation of interaction forces and moments, but neglecting any free surface effects.

The approach below follows Collatz but uses a numerical rather than analytical solution to the problem to allow extension to the case of ships of more realistic plan form than an ellipse, moving on non-parallel courses at different speeds. Calculated results are then compared qualitatively with results of experiments using free-running models, thereby enabling sample collisions to be analysed and discussed.



HULL REPRESENTATION



TRAJECTORY REPRESENTATION

Fig. 1 Main Assumptions of Computational Scheme

2.2 Theoretical Approach

2.2.1 Assumptions. In the calculation method, which is outlined briefly below, the following assumptions are made or implied (see Fig 1):

i) The flow is everywhere two-dimensional, irrotational and possesses a velocity potential.
ii) Free surface effects are negligible.
iii) Interaction forces may be represented by the potential flow field alone, ie frictional forces and the effect of the wake and propeller slipstream are neglected.

iv) The ship may be represented by a strut whose plan form is the same as the load water-plane of the ship, but whose body sections are everywhere rectangular. This implies that the water is very shallow indeed.

v) The ships move at constant, but not necessarily equal, speeds on linear trajectories which need not be parallel.

A computer program has been written to compute forces and moments according to these assumptions, but at its present stage of development it incorporates two further limitations:

vi) The ships are sufficiently far away from any channel bank so that bank suction effects are negligible.

vii) The hull surface slopes are small enough to permit linearisation of the basic hydrodynamic equations. This limitation is at present dictated by limits of computer size and speed and it is intended to lift this limitation at a later stage of program development.

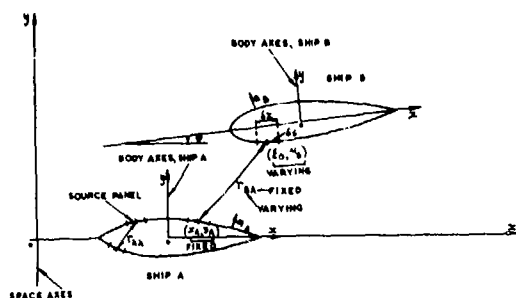


Fig. 2 Axis Systems

2.2.2 Axis Systems. Three axis systems are used, one fixed in space, and two moving and body-centred in ship A and ship B, as in Fig 2. The position of ship B relative to ship A at any instant of time is found from their relative velocity U_R and the course ψ of ship B relative to ship A. Ship A is assumed to have a linear course which lies parallel to the x-axis of the space axes. Thus

$$U_R = (U_A^2 + U_B^2 - 2 U_A U_B \cos \psi)^{1/2} \quad (1)$$

with a direction α to the space axes where

$$\alpha = \theta + \psi$$

$$\theta = \sin^{-1} \left(\frac{U_A \sin \psi}{U_R} \right) \quad (2)$$

2.2.3 Computation of Source Distributions. We represent each ship by a two-dimensional surface source distribution σ which is recalculated at each instant of time from the relative positions of each ship.

We consider the waterline of each ship to be subdivided into plane panels of length δs , upon each of which is a uniform source distribution of strength σ_i . In the absence of any other such source panels, the body boundary condition is satisfied by

$$\frac{\sigma_i}{2} = U_{n_i} \quad (3)$$

where U_{n_i} is the local component of velocity along the outward-drawn normal on the i th panel.

Equation (3) is modified, however, by the presence of all the other source panels representing both the hull in question and the other hull which induce a normal component of velocity on the i th panel. We assume that these other source panels may be adequately represented by point sources located at the centre of each panel. The velocity potential of such a two-dimensional source is given by

$$\phi_j = \frac{1}{2\pi} \sigma_j \ln r_j \delta s_j \quad (4)$$

where r_j is the distance from the j th source panel to the centre of the panel under consideration (see Fig 2). The normal component of velocity to be added or subtracted from

equation (3) is given by

$$\frac{\partial \phi_j}{\partial n} = \frac{1}{2\pi} \sigma_j \frac{\partial}{\partial n} (\ln r_j) \delta s_j \quad (5)$$

where n is the outward-drawn normal for each ship.

We adopt a system of subscripts used by Collatz to differentiate between the source distributions. The surface source distribution representing ship A is given the subscript A while that representing ship B is given the subscript B. The distance r is given two subscripts; the first refers to the panel in question while the second refers to the location of the source panel inducing a velocity on the first (see Fig 2).

Therefore the source distributions may be found from a solution of the following simultaneous equations

$$\begin{aligned} \frac{\sigma_{Ai}}{2} + \frac{1}{2\pi} \sum_{j=1}^m \sigma_{Aj} \frac{\partial}{\partial n_A} (\ln r_{jAA}) \delta s_A + \\ \frac{1}{2\pi} \sum_{j=1}^m \sigma_{Bj} \frac{\partial}{\partial n_A} (\ln r_{jBA}) \delta s_B = U_{An} \\ \frac{\sigma_{Bi}}{2} + \frac{1}{2\pi} \sum_{j=1}^m \sigma_{Bj} \frac{\partial}{\partial n_B} (\ln r_{jBB}) \delta s_B + \\ \frac{1}{2\pi} \sum_{j=1}^m \sigma_{Aj} \frac{\partial}{\partial n_B} (\ln r_{jAB}) \delta s_A = U_{Bn} \end{aligned} \quad (6)$$

where the summations exclude the panel in question.

These equations are similar to those presented in ref 10 as integral equations which Collatz solved using a Fourier Series method for the special case of two elliptic cylinders of the same size on parallel courses.

We now apply the simplifying assumptions that the ships are sufficiently thin to allow the substitutions

$$\frac{\partial}{\partial n} \approx \frac{\partial}{\partial y}; \quad \delta s \approx \delta x; \quad \frac{\partial}{\partial s} \approx \frac{\partial}{\partial x}$$

and we have, for example, when the ships are on parallel courses and using

$$\begin{aligned} r^2 &= (x - \xi)^2 + (y - \eta)^2 \\ \frac{\partial (\ln r)}{\partial y} &= \frac{(y - \eta)}{r^2} \end{aligned} \quad (7)$$

$$\begin{aligned} \frac{\sigma_{Ai}}{2} + \frac{1}{2\pi} \sum_{j=1}^m \sigma_{Aj} \frac{(y_A - \eta_A)}{r_{jAA}^2} \delta x_A + \\ \frac{1}{2\pi} \sum_{j=1}^m \sigma_{Bj} \frac{(y_A - \eta_B)}{r_{jBA}^2} \delta x_B = U_A \frac{\partial y_{oA}}{\partial x_A} \\ \frac{\sigma_{Bi}}{2} + \frac{1}{2\pi} \sum_{j=1}^m \sigma_{Bj} \frac{(y_B - \eta_B)}{r_{jBB}^2} \delta x_B + \\ \frac{1}{2\pi} \sum_{j=1}^m \sigma_{Aj} \frac{(y_B - \eta_A)}{r_{jAB}^2} \delta x_A = U_B \frac{\partial y_{oB}}{\partial x_B} \end{aligned} \quad (8)$$

where $\frac{\partial y_o}{\partial x} = (y_{oi+1} - y_{oi})/\delta x$

y_0 = local half breadth of hull at source
panel under consideration in body
axis system of each ship

y = ordinate of panel under consideration in body axis system of ship A or B

η = ordinate of source panel other than that under consideration.

Equations (8) are a set of $2m$ simultaneous equations which were solved using pivotal condensation to yield source distributions for each hull.

The equations were found to be well-behaved and typical results of calculated distributions for $m = 20$ are shown in Fig 3.

It should be noted that the terms $\partial(\ln r)/\partial y$ in equation (8) refer to the local body axes of each ship so that when considering two ships on non-parallel courses, account must be taken of this in the numerical calculation of the derivatives.

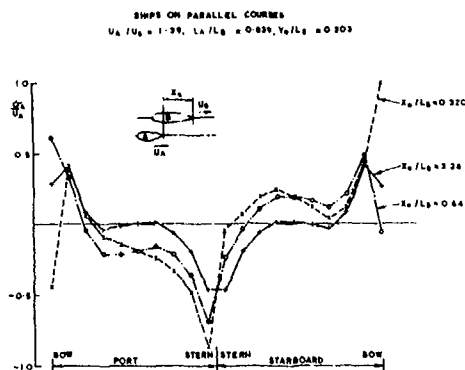


Fig. 3 Computed Source Distributions for Ship A

2.2.4 Computation of Forces and Moments.

To calculate interaction forces and moments, use is made of Lagally's Theorem as generalised by Cummins (ref 11) to the case of non-steady flow. We consider the steady and unsteady or time-dependent components separately.

Steady Forces and Moments. It is shown in refs 10 and 11 that for a continuous distribution of sources and sinks the steady-state forces and moment may be written, using Lagally's Theorem

$$\begin{aligned} X_s &= -\rho \int_s \sigma u \, ds \\ Y_s &= -\rho \int_s \sigma v \, ds \\ N_s &= -\rho \int_s \sigma (xv - yu) \, ds \end{aligned} \quad (9a)$$

which in our simplified scheme become

$$\begin{aligned} X_s &= -\rho \sum_{i=1}^m \sigma_i u_i \delta x \\ Y_s &= -\rho \sum_{i=1}^m \sigma_i v_i \delta x \\ N_s &= -\rho \sum_{i=1}^m \sigma_i (x_i v_i - y_i u_i) \delta x \end{aligned} \quad (9b)$$

where the σ_1 and δx are appropriate to the ship in question and the local perturbation velocities u and v are those induced on the ship in question by the other ship. For example, following Coillatz the values of u and v for ship A, induced by ship B are given at the i th hull panel on ship A by

$$\begin{aligned} u_{Ai} &= \frac{1}{2\pi} \sum_{j=1}^m \sigma_{Bj} \left[\frac{\partial(\ln r_{BA})}{\partial x_A} \right]_j \delta x_A - u_A \\ v_{Ai} &= \frac{1}{2\pi} \sum_{j=1}^m \sigma_{Bj} \left[\frac{\partial(\ln r_{BA})}{\partial y_A} \right]_j \delta x_A \end{aligned} \quad (10)$$

where

$$\frac{\partial(\ln r_{BA})}{\partial x_A} = \frac{x_A - \xi_B}{(x_A - \xi_B)^2 + (y_A - \eta_B)^2}$$

$$\frac{\partial(\ln r_{BA})}{\partial y_A} = \frac{y_A - \eta_B}{(x_A - \xi_B)^2 + (y_A - \eta_B)^2}$$

Unsteady Forces and Moments. Unsteady forces and moments are calculated according to the extended Lagally Theorem given in ref 11 and arise from the variation with time of the singularity distributions representing the flow.

For a ship moving at constant speed with no rotation the unsteady forces are given by

$$\begin{aligned} X_u &= -\rho \sum_{i=1}^m \frac{\partial \sigma_{Ai}}{\partial t} x_{Ai} \delta x_A \\ Y_u &= -\rho \sum_{i=1}^m \frac{\partial \sigma_{Ai}}{\partial t} y_{Ai} \delta x_A \end{aligned} \quad (11)$$

for ship A with similar expressions for ship B.

In order to compute numerically the time rate of change of the surface source strength on one panel, the following expression was used at time $t = t_i$.

$$\left. \frac{\partial \sigma_i}{\partial t} \right|_{t=t_i} \approx \frac{\sigma_i(t_j + \delta t) - \sigma_i(t_j - \delta t)}{2 \delta t} \quad (12)$$

Thus the computational method calculated source distributions and steady forces at some instant in time $t = t_j$ whereas the unsteady forces were calculated at $t = t_j$ only after the source distribution at $t = t_j + \delta t$ was known. For a ship on a linear trajectory, approximation (12) may be used as it stands, but in the case of more general motion involving curved trajectories the problem would be more difficult as all forces and moments must be known at $t = t_j$ before the relative positions of the two ships at $t = t_j + \delta t$ can be projected.

Expressions similar to (11) for the calculation of the unsteady moment were not obtained by Cummins in ref 11. Instead the unsteady moment was left in the form

$$N_u = \rho \int_S \frac{\partial \Phi}{\partial t} [\vec{r} \times \vec{n}] ds \quad (13)$$

for a continuous distribution

where ϕ is the potential of the total flow

\vec{r} is a position vector

\vec{n} is the outward-drawn normal.

Resolving the vector terms into their component parts, we find that (13) becomes, for this investigation,

$$N_u = \rho \int_s \frac{\partial \phi}{\partial t} (x u_y - y u_x) ds$$

$$= \rho \int_s \frac{\partial \phi}{\partial t} \left[x \frac{\partial x}{\partial s} - y \frac{\partial y}{\partial s} \right] ds \quad (14)$$

where the term in square brackets is evaluated at the body surface. Applying our assumptions that $\partial x / \partial s = 1$ and that $\partial y / \partial s$ is negligible in comparison with unity we have

$$N_u = \rho \int \frac{\partial \phi}{\partial t} x dx$$

or

$$N_u = \rho \sum_{i=1}^m \frac{\partial \phi_i}{\partial t} x_i \delta x \quad (15)$$

for m source panels.

In order to compute $\partial \phi_i / \partial t$ use was made of a numerical approximation similar to that given in equation (12) above.

Now ϕ is given by

$$\phi = \phi_a + \phi_b$$

where ϕ_a is the potential of the undisturbed flow

ϕ_b is the potential of the body singularities.

As the ships are assumed to have linear trajectories and velocities which are invariant with time, we have

$$\frac{\partial \phi}{\partial t} = \frac{\partial \phi_b}{\partial t}$$

Values of ϕ_b were calculated at the hull surface from

$$\phi_{bi} = \frac{1}{2\pi} \left\{ \sigma_i \int_{-\delta x/2}^{\delta x/2} \ln(x^2 + y^2)^{1/2} dx + \sum_{j=1}^m \sigma_j \ln r_j \delta x \right\}$$

$$= \frac{1}{2\pi} \left\{ \sigma_i [\ln(\delta x/2) - 1] \delta x + \sum_{j=1}^m \sigma_j \ln r_j \delta x \right\} \quad (16)$$

where the first term in brackets represents the contribution to the velocity potential of the distributed sources on the i th source panel and the summation represents the contribution from all the other source panels ($j \neq i$).

$U_a = U_b = U$, $Y/E = 2.0$, $Y_0/E = 2.0$; COURSES PARALLEL
BOTH ELLIPSES IDENTICAL; FORCE & MOMENT ON ELLIPSE 'A' SHOWN

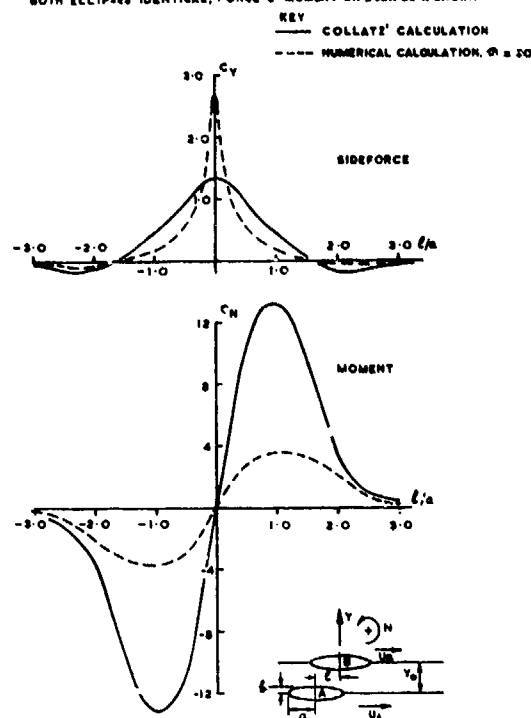


Fig. 4 Interaction Forces and Moments on two Ellipses

2.2.5 Comparison with Collatz' Theory.

A Fortran computer program has been written to calculate interaction forces and moments using the methods outlined above. Forces and moments per unit draft were non-dimensionalised using the scheme

$$C_X = \frac{X}{\rho b U^2}; \quad C_Y = \frac{Y}{\rho b U^2}; \quad C_N = \frac{N}{\rho b^2 U^2}$$

where b = maximum beam of ship
 U = velocity of ship
 ρ = water density.

Although values of C_X were calculated, these were in general very small and we concern ourselves only with C_Y and C_N values in the discussion which follows.

The theory outlined above is to be used initially to help gain an insight into trajectories taken by models in collision situations. It is to be used in a qualitative rather than a quantitative sense. Further, we are concerned at present with only the overtaking type of situation where we make the further assumption that the unsteady Lagally force and moment terms are negligibly small. This is probably not unreasonable for the overtaking situation provided the relative velocity of the two ships is not high.

With this further assumption a comparison may be made with calculated results given in ref 10 for the case of two identical ellipses proceeding on parallel courses at the same speed but with different longitudinal separations, l/a .

This is the case treated by Collatz which most closely resembles the overtaking case.

The comparison is shown in Fig 4, where each ellipse has been represented in the numerical scheme by twenty source panels, i.e. $m = 20$. It is seen that although qualitatively the agreement between the two methods of calculation is reasonable, quantitative agreement is poor. This lack of quantitative agreement is probably due in part to the treatment of the ends of the ellipse in the numerical calculations and this is borne out by the under-estimation of C_N values. Values of dy/dx at the ends of an ellipse are infinite whereas a finite value is assumed in the numerical calculation. Furthermore, each side of the ellipse is represented by only 10 source panels, so that under-estimation of surface slopes at the ends is greater.

Clearly this could be overcome by the use of more source panels near the ends, but it should be remembered that the numerical method is intended ultimately for use with ship-like forms where the surface slopes near the ends are in general finite.

2.3 Model Experiments

To investigate interaction between ships in collision situations, several experiments have been made at Ship Division NPL using two small radio-controlled free-running models. The use of free-running models was preferred to force measurements on towed models for the following reasons:

- i) Both models were free to interact with each other and not constrained to move on prescribed and possibly unrealistic courses.
- ii) The ultimate aim of this investigation is the prediction of the likely trajectories of ships in close proximity using a combination of future developments of the theory outlined in section 2.2 and the known manoeuvring characteristics of the ships in question. For this, realistic model/ship trajectories must be known.

A disadvantage of using free-running models is that it is very difficult not to impose some human element into the trajectories due to control exerted by the operators. To attempt to minimise this, all trajectories of the models when in close proximity were obtained with the helm set amidships and no control was applied during the collision/passing phase of the manoeuvre. This seemed to high-light the changes of course due to interaction.

2.3.1 The Models. The models themselves were made of wood, were 1.524 m and 1.817 m between perpendiculars and had block coefficients of 0.70 and 0.76 respectively. They were each powered by printed circuit motors running from 6 volt lead acid batteries. Two channels of radio-control were provided, one enabling the drive motor to be set at any one of three speeds, ahead or astern, and the other enabling control over rudder movement which was continuous from 35° port to 35° starboard. Hard-over-to-hard-over times were arranged to give scale values on each model.

Before experiments commenced, the rotational radius of gyration of each model was measured on a bifilar suspension which gave a value of about 23% of the length for both models after some adjustment of internal ballast.

2.3.2 Measurement of Model Trajectories.

The experiments were run in the shallow water section of NPL No 2 towing tank which was sealed off from the main tank to give a working area measuring 36.6 m x 6.1 m. The depth of water was varied to give water depth/at rest draft (h/T) values ranging from 1.1 to 7.7 with most of the shallow water interaction work done at a water depth giving an h/T of 1.4 for the smaller model and an h/T of 1.1 for the larger model.

The trajectories of each model were measured photographically using a motorised Canon F1 camera. This was situated in the roof of the tank and due to the comparatively low roof height, was mounted with a depression angle of some 17°. Each photograph had therefore to be corrected for perspective and scaled. To do this, two datum buoys were fixed in the water surface known vertical and horizontal distances from the centre of the camera lens. Furthermore, two vertical masts were fitted fore and aft on each model, the tops of each being in the same horizontal plane, so that the position of each model at any instant could be determined (see Fig 5).

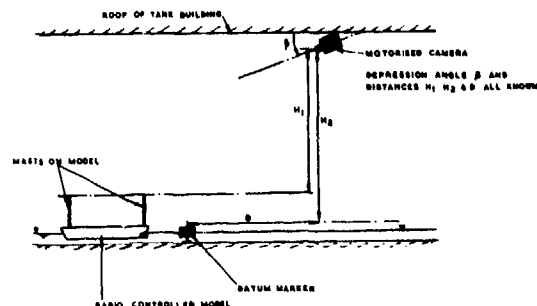


Fig. 5 Experimental Arrangement for Model Tests

A computer program was written to accept data obtained from each photograph after projection onto a digitiser. The program corrected for perspective, scaled and printed out trajectories and other data such as trajectory curvature, rate of turn, speed on the trajectory (obtained from a knowledge of the time-lapse of the motorised camera) and drift angle.

Experiments were conducted not only into collision situations but also into simulated crash-stop and steady-state turning manoeuvres in various depths of water. In all cases the models were run where possible close to the longitudinal centreline of the tank to minimise bank suction effects.

3 THE 'OVERTAKING' COLLISION

We now discuss two collision situations which were measured when the smaller, faster model was allowed to overtake the larger. Both models were on approximately parallel courses and we show how the theory outlined in 2.2 above can be used to explain some of the features of the trajectories of each model.

Interaction effects are more likely to predominate in the overtaking-type of collision for

the ships are in close proximity for long periods of time, and course changes due to interaction may build up slowly and then rapidly magnify.

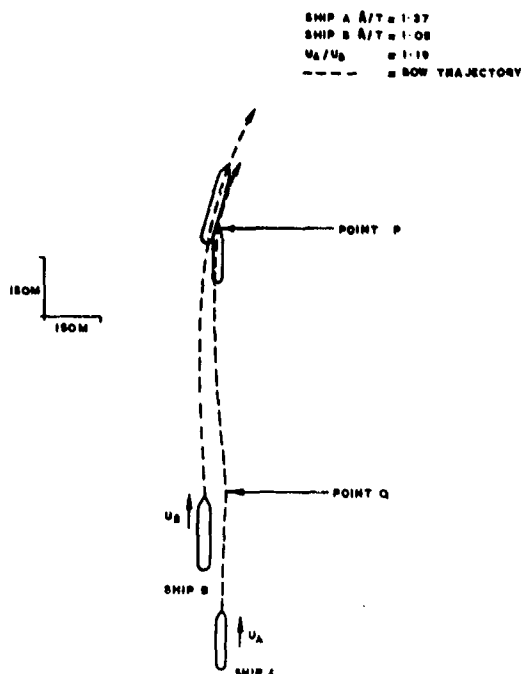


Fig. 6 Overtaking Collision - 'Bow to Stern' Collision

3.1 The 'Bow-to-Stern' Collision

The first type of overtaking collision occurred when the bow of the overtaking model collided with the stern or aftbody of the slower model. As shown in fig 6 the trajectories of both models are approximately parallel apart from a slight tendency to turn to starboard prior to collision which is discussed in section 4 below.

It was quite apparent when observing the behaviour of the models that, as the faster began to overhauled the slower, it suddenly sheered into its neighbour and a collision occurred at point P. Both rudders remained amidships for the duration of the experiment. It is also of interest to note that the models apparently experienced some repulsion at point Q.

Calculations for two overtaking ships are shown in Figs 7 and 8. These results were obtained with the numerical method outlined above using as input data the load water lines of each ship, each represented by 20 source panels. In the Figures the smaller, faster ship is designated ship A. Calculated force and moment coefficients

are plotted against a non-dimensional overlap parameter X_0/L_B where X_0 is given by

$$X_0 = x_{\text{bow}} (\text{ship B}) - x_{\text{bow}} (\text{ship A})$$

and L_B is the length of ship B.

It is seen in Fig 7 that for reducing X_0/L_B , as the faster ship begins to overtake, the interaction forces cause a repulsion for $X_0/L_B > 0.78$ and then change sign to cause an attraction between the two vessels for $-0.65 < X_0/L_B < 0.78$ with the maximum attraction force occurring when the bows of each vessel are very nearly level. In company with this the interaction moments initially attain large positive values, particularly for ship B, then change sign for both ships in the region of $X_0/L_B = 0$, subsequently attain large negative values and then decrease as the overtaking ship moves clear of its neighbour. The effects of lateral separation are shown in Fig 8 which indicates the reduction in force and moment to be obtained when the lateral separation is increased by 50%. It should be noted that these calculations were made for ships on parallel courses.

Therefore if Figs 7 and 8 can be taken to give a general picture of the interaction forces and moments during an overtaking manoeuvre, it may be seen that the overtaking ship may enter the 'attraction zone' and be attracted toward the larger ship while turning toward it as its neighbour turns away. Because of this, the distance between the vessels reduces, the forces and moments increase and a collision occurs. It is perhaps relevant that most of the bow-to-stern overtaking collisions observed in the model tests occurred with the overtaking model striking the larger model in about the vicinity of the beginning of the 'attraction zone' at $X_0/L_B = 0.78$.

In the model experiments the larger model had a depth/draught ratio of about 1.1 whereas that of the smaller model was about 1.4. This suggests that the larger model would be less responsive to interaction forces and moments due to its increased inertia in very shallow water.

A further point about interpretation of Fig 6 is that both models had a tendency to turn to starboard with helm amidships. This is apparent in the trajectories prior to collision.

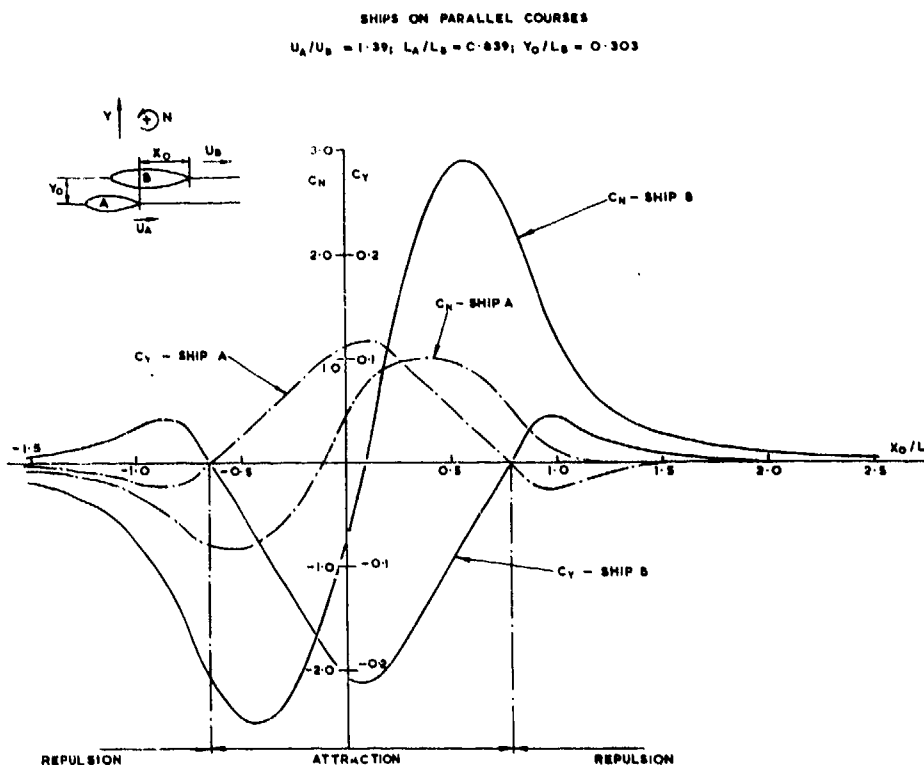
3.2 The 'Stern to Stern' Collision

If the courses and speeds of the two ships are such that the interaction forces and moments of Fig 7 do not give rise to a collision, it appears that both ships will begin to turn in the same direction with the result that

their trajectories may diverge. Further calculations have shown that, when the trajectories diverge, the attraction forces between the ships diminish and the positive turning moment of ship A becomes negative before that of ship B indicating that she will turn away from her neighbour. Moreover the inertia of ship B may be such that it continues the turn to port initiated by the large positive interaction moment of the earlier stages of overtaking regardless of any subsequent smaller interaction moments applied as the courses diverge. Such an occurrence is shown in Fig 9 where the models were seen to diverge violently from each other, with the possibility of a stern-to-stern collision at point R. The behaviour of both models during the run shown in Fig 9 was similar to

that obtained when each model experienced 'rejection' by a steep bank.

Thus we see that discussion of both types of overtaking collision is illuminated by the calculated interaction forces and moments. It is of interest to note that the calculated results were obtained for ships on parallel courses in courses which, one might suppose, would not lead to a collision. But, due to interaction, collisions did occur, at times very violently. Clearly, as interaction forces and moments act on each ship their courses change and any extensions to the theory should take some account of this, but it is apparent that at this stage of development plausible qualitative results can be obtained.



SHIPS ON PARALLEL COURSES
 $U_A/U_B = 1.39$; $L_A/L_B = 0.839$; $Y_0/L_B = 0.455$

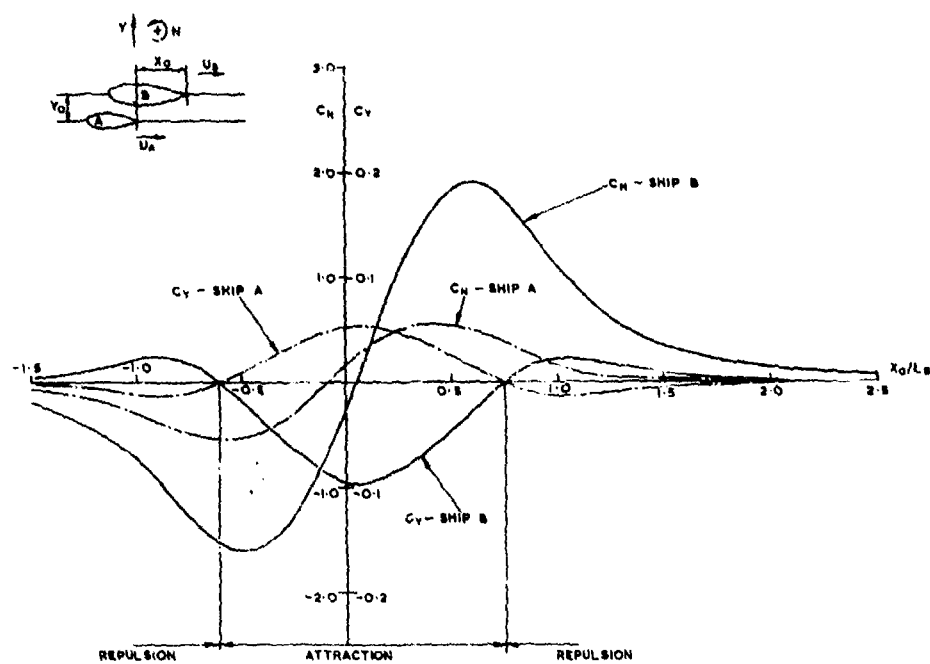


Fig. 3 Interaction Forces and Moments between two Overtaking Ships

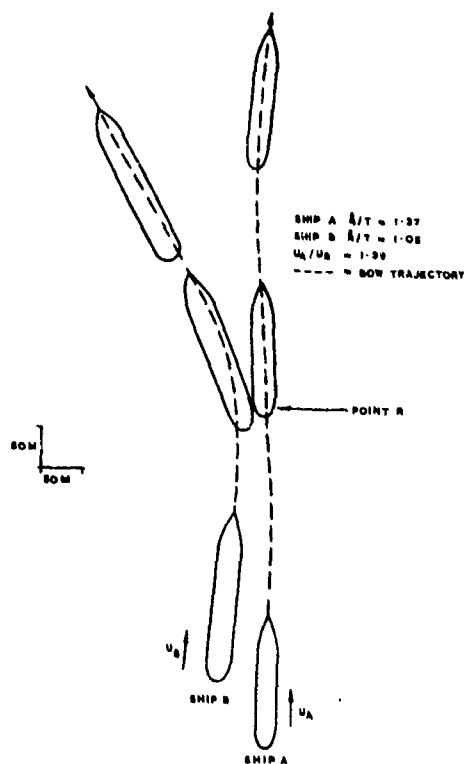


Fig. 9 Overtaking Collision - 'Stern to Stern' Collision

4 THE EFFECT OF WATER DEPTH ON MANOEUVRING

Although we do not intend to discuss the effect of water depth on manoeuvring in detail, it is relevant to the collision problem in shallow water to mention that manoeuvring characteristics change with reducing water depth (ref 12). This was confirmed in the model experiments described above where turning circle diameters were increased and rates of turn and drift angles reduced as water depth reduced.

A particular feature noted was that rates of turn for small rudder angles were sensitive to water depth for the smaller model which gave rise to rapid rates of turn in moderately shallow water. This is relevant to the collision problem because, although both vessels are moving in the same depth of water, the depth/draft ratios will differ and therefore so will the manoeuvring characteristics. For the experiments described above, the slow model was very close to the bottom whereas the smaller, faster model was reasonably well clear. Therefore, the slower model responded to the helm more sluggishly, unlike the smaller, faster model, and a collision situation could build up gradually before the final violent interaction phase which may lead ultimately to collision.

A measure of the size of the interaction forces and moments may therefore be obtained from manoeuvres as in Fig 9 where interaction has caused a violent movement off-course from the larger and apparently more sluggish model.

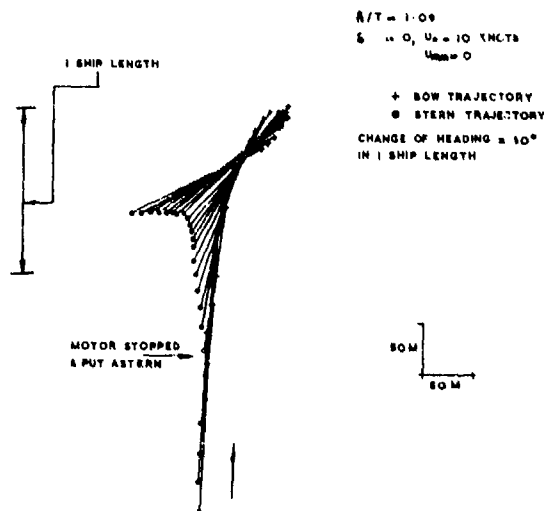


Fig. 10 Crash Stop Manoeuvre

A feature also noted and mentioned above was the tendency for each model to turn slightly to starboard with helm amidships. This tendency was less pronounced for very shallow water, whereas in deep water an initial tendency to turn to port was followed by a sheer to starboard. The models were checked and no lateral asymmetry was found.

5 THE CRASH STOP

A manoeuvre which may feature in some potential collision situations in crowded and confined waters is the crash stop. Simulated crash stops were run on each model and the track of one for the larger, fuller model is shown in Fig 10.

During this manoeuvre, at a depth/draft ratio of 1.1, the model was brought up to speed on a straight course, the drive motor was stopped and, after a short interval, put astern. Throughout the whole manoeuvre, the helm remained amidships.

It is seen from Fig 10 that the results were quite dramatic. The ship's head falls away to starboard with the stern simultaneously moving to port, causing change of heading of about 60° in the example shown. Clearly if such a manoeuvre were used to avoid a head-on collision, it would make matters worse by exposing most of the ship's side to the oncoming ship.

Further crash-stop experiments were carried out with this model, whereby attempts were made to reduce the change in heading with appropriate use of helm before the model had lost all headway. The results showed that use of the helm did little to alter the trajectory shown in Fig 10.

6 GENERAL DISCUSSION AND CONCLUSIONS

The purpose of this paper has been to raise some hydrodynamic issues relevant to collision situations. Where it has helped to illuminate the behaviour of models in close proximity, use has been made of an interaction theory. This theory, in spite of many approximations and assumptions and a neglect of free surface conditions, appears to produce, qualitatively at least, plausible forces and moments which may occur when two ships interact, while one overtakes the other.

Discussion has centred on the overtaking type of collision for this is perhaps the one which builds up most slowly and inevitably. To the ship's officer, problems of perception arise when overhauling another ship, due to the difficulty of assessing distance off. Further, as Figs 7 and 8 show, interaction forces act suddenly, by which time it may be too late or impossible to take avoiding action. It would appear that the vessels will also interact in different ways depending on their relative velocities. It is interesting that for four separate model runs, two had values of U_A/U_B of about 1.4 and a stern-to-stern collision resulted, whereas for the other two values of U_A/U_B were about 1.2 and bow-to-stern collisions occurred.

Furthermore, interaction forces have been shown to reduce with increasing lateral separation so it would appear that there is some 'danger zone' round every ship, dependent on its relative velocity, into which another ship strays at its peril.

It is also important to note that the trajectories shown were obtained with self-propelled models and no discussion has been made of the effect of the propeller and its wake in manoeuvring prior to a collision. In Figs 6 and 9 ship A has to overhaul ship B by running alongside the wake of B and in the type of collision shown in Fig 9 the final collision of sterns could be magnified by the increasing proximity of the low-pressure regions around the propellers of each ship.

Recommendations for collision avoidance have been made, based on aircraft practice (ref 13). Clearly when using such recommendations for framing rules for the avoidance of collision at sea, some account should be taken of the hydrodynamic behaviour of ships in close proximity. Collisions can build up slowly and human reaction to such a slow sequence of events may not be adequate to deal with the potentially violent manoeuvres which may follow.

REFERENCES

1. Cockcroft, A.N., "A Radar-assisted Collision," *Safety at Sea International*, Sept 1973, pp. 18-21.
2. Weinblum, G., "Theoretische Untersuchungen der Stromungsbeeinflussung zweier Schiffe aufeinander beim gegenseitigen Begegnen und ueberholen auf tiefem und beschränktem Wasser," *Schiffbau*, Vol 34, 1933, pp. 113.
3. Robb, A.M., "Interaction between Ships. A record of some experiments and evidence on wall effect," *Trans RINA*, Vol. 91, 1949, pp. 324.
4. Moody, C.G., "The handling of ships through a widened and asymmetrically, deepened section of Gaillard Cut in the Panama Canal," DTMB (now NSRDC) Report 1705, Aug. 1964.
5. Eda, H., "Ship control during two-way traffic in channels. (Case of large full-form ships)," 3rd Ship Control Symposium, paper IX B-1, Bath, 1972.
6. Eda, H., and Savitsky, D., "Experimental and analytical studies of ship controllability in canals," 12th ITTC, Rome 1970.
7. Eda, H., "Dynamic behaviour of tankers during two-way traffic in channels," *Marine Technology*, Vol. 70, 1973 July, pp. 254.
8. Havelock, T.H., "Wave resistance: the mutual action of two bodies," *Collected Works, ONR/ACR 193*, pp. 408.
9. Silverstein, S.L., "Linearised theory of the interaction of ships," *University of California Report 3, Series 82*, 1957.
10. Collatz, G., "Potentialtheoretische Untersuchung der hydrodynamischen Wechselwirkung zweier Schiffskörper," *Jahr der Schiffbautechnischen Gesellschaft*, Band 57, 1963, pp. 281.
11. Cummins, W.E., "The forces and moments acting on a body moving in an arbitrary potential stream," DTMB (now NSRDC) Report 780, June 1953.
12. Fujino, M., "Experimental studies on ship manoeuvrability in restricted waters," *International Shipbuilding Progress*, Vol. 15, No. 168, August 1968, pp. 279.
13. Hollingdale, S.H., "The mathematical principles of collision avoidance," *Joint RINA/RIN Conference on Marine Traffic Engineering*, London 1973, pp. 141.

ACKNOWLEDGEMENTS

This paper is published with the permission of the Director of the National Physical Laboratory. The author is particularly grateful to his colleagues Mr. G.L. Taylor and Dr. G.E. Gadd for their invaluable assistance throughout the experimental and theoretical investigations described in the paper.

DISCUSSION

E. O. TUCK

As mentioned in the paper by Professor Newman and myself, the work of Collatz (ref.10) is of limited practical utility because of failure to allow for circulation around the bodies, and a similar objection applies to the present paper by Dand. Additional information bearing upon this question is contained in a paper of my own (J. Fluid Mech., Vol.50, 1971, pp.481-491) in which a numerical analysis quite similar to that of Dand was carried out on thick bodies in ground effect, but in which an arbitrary circulation κ was allowed. The analogy is with the steady problem for two identical ships at zero stagger.

The resulting force Y is a quadratic expression in κ , and a typical result (for an automobile-like shape of length L , moving at speed U) is

$$Y = -0.21(\frac{1}{2}\rho U^2 L) + 1.26(\rho U \kappa) - 0.69(\frac{1}{2}\rho \kappa^2 / L).$$

The value of F at $\kappa = 0$ corresponds to the type of force to be expected from the Collatz or Dand approaches, and for thin bodies will vary like the square of body thickness. On the other hand, the circulation-dependent terms are numerically much larger, depending only on the first power of body thickness for thin bodies. For such bodies the circulation can be determined by satisfying a Kutta condition, as in the Tuck-Newman paper, and gives in general a very much increased value for the side force, but less effect on the moment.

I am rather surprised by the large discrepancy between the Dand and Collatz estimates of the forces and moments in Fig.4, and disturbed by Dr. Dand's explanation of this discrepancy as due to numerical inaccuracy. The discrepancy appears to be particularly bad for the moment, so that circulation is not to be blamed for this. I should very much like to see this agreement improved, since it seems to me that Dr. Dand's procedure is capable of being extended to include circulation.

Aside from the above critical comments, I should like to commend Dr. Dand for a very interesting paper. I feel that the experimental aspect of the paper is of especial interest and importance in view of the appalling lack of such measurements in the past. I hope that Dr. Dand will make actual force measurements in any future experiments.

PETER OLTMANN

I would like to comment on one special point of this very interesting paper, which gives a good insight into the mechanics of possible collision situations in shallow water.

The Author follows Collatz in his theoretical approach toward calculating the hydrodynamic interactions between ships in close proximity to each other, and emphasizes that the outlined theory is to be used rather in a qualitative than a quantitative sense. In a recent experimental investigation an examination of the theoretical results obtained by Collatz, using two identical elliptical cylinders with a ratio of $a/b = 8.0$, had been undertaken, Ref. 1. The transverse force coefficient $C_Y = P/P_0$ and the moment coefficient $C_N = M_z/M_z^0$ for a transverse ratio of $y_0/b = h/b = 5.0$ with $U_A = U_B = U$ are given in two graphs, see Ref. 1 (Fig. 8a and Fig. 9a). There is good qualitative agreement between the experimental and theoretical results, but quantitatively they are far apart. The discrepancy, especially in case of the transverse force coefficient, is due to the fact that Collatz only takes into consideration the displacement flow, although it is known that a vortex flow must exist. Furthermore, a pronounced asymmetry can be noticed, which is not indicated by the theory of Collatz. A quite plausible interpretation of this effect has been given by Tuck and Newman in their paper at this symposium.

Collatz has also considered the case of unsteady motion, i.e. when one body is at rest and the other moves with a constant velocity U on a parallel course. As can be seen from two graphs, Ref. 1 (Fig. 18a and Fig. 19a), the experimental results for the condition $U_A = 0$ and $U_B = U$ with $y_0/b = 5.0$ are in excellent agreement with the theoretical prediction. The explanation might be that in contrast to the steady motion case of $U_A = U_B = U$ here a vortex flow can not develop and hence the hydrodynamic forces and moments may be represented by displacement flow alone.

Reference:

1. Oltmann, P.: Experimentelle Untersuchung der hydrodynamischen Wechselwirkung schiffsähnlicher Körper. Schiff und Hafen, 22. Jahrg. (1970), S. 701-709

M. SCHMIECHEN

Similar tests as those mentioned by Dr. Dand and Dr. Müller have previously been carried out in the Berlin Model Basin to establish limits for the size of passing ships in the Kiel canal (1). These tests have been successfully simulated on analogue computers using the simple relative motion concept mentioned in the contribution to Prof. Tuck's and Prof. Newman's paper presented earlier at this Symposium, and including bank effects (2). Some corrections found necessary in the general theory of relative motions as developed in the last reference will be published shortly together with a contribution to the theory of centrifuges (3).

1. Hoffmann, M.: Contribution to Collatz, G.: Potentialtheoretische Untersuchung der hydrodynamischen Wechselwirkungen zweier

Schiffkörper.

STG 57 (1963) S. 281/329.

STG 57 (1963) S. 388/370.

2. Schmiechen, M.: Fragen der Kurstabilität und Steuerfähigkeit von Schiffen.
STG 58 (1964) S. 319/340.
3. Schmiechen, M.: Relativkinetik von Schiffen.
To be published.

other, it is conceivable that viscous effects may be important, especially if the overtaken ship is of full form, with a boundary layer flow in the stern region close to separation. Then the additional pressure gradients induced by the overtaking ship may give rise to an asymmetrical separation over the stern of the overtaken one. It would be of interest to look at the flow with tufts to see if any such effects take place.

G. E. GADD

Regarding the interaction which occurs in the overtaking case, when the bow of one ship comes close to the

AUTHOR'S REPLY

The author is particularly grateful to Professor Tuck for his contribution to the discussion which contains much useful and constructive criticism. It is fully appreciated that the computational method outlined in the paper is deficient in that circulation around the bodies is ignored and steps are now being taken to include the effects of this in the computer program.

The reason for the poor agreement between the Collatz calculations and my own as shown in Fig. 4 is due to the fact that the computer program would only allow the source panels to be of equal length dx . This meant that the treatment of the ends of the ellipses was very approximate and this was reflected in the calculated interaction moment. This has been confirmed recently by re-writing the program to accept a variable panel size and the results show that the moment is predicted well when smaller panel sizes are used at the ends of the ellipse. The practical implementation of the numerical method still suffers however from the small number of panels which can be used to represent the hull and this will be remedied in the future.

We are at present actively engaged on an experimental investigation of two-ship interaction in shallow water during which it is intended to measure the forces and moments arising. It is hoped to publish the results in due course.

Mr. Oltmann also mentions circulatory flow and refers to his interesting experiments using ellipses. The asymmetry in the forces and moments to which he refers has been noted and we intend to investigate this as well as any possible Froude number effects in the experiments at NPL referred to above.

I am grateful to Dr. Schmiedchen for providing some useful additions to the references given in the paper and look forward to the publication of his paper on the general theory of relative motions and centrifuges.

Dr. Gadd raises the important point of the effect of viscosity mentioned also in the paper on interaction presented by Tuck and Newman at this conference. It is not known if the flow was separating on the overtaken ship in the model tests described in the paper, but it is hoped to investigate this further.

Finally the author thanks all the contributors for an interesting and useful discussion.

WHEN IS COLLISION UNAVOIDABLE?

N. C. Webster
University of California
Berkeley, California

ABSTRACT

The motions of a large super tanker in response to various maneuvering commands is computed using the non-linear hydrodynamic coefficients presented by van Berlekom and Goddard (18). The results of the simulations were analyzed to determine the critical range (the range at which collision is unavoidable) and the simple maneuvers necessary to minimize this range. The study shows that the critical range depends strongly on the two ships' headings and speeds, and on the permissible maneuvers. The effect of design features, such as rudder size and radar accuracy does not appear very significant. The effect of operating procedures such as "Rules of the Road" or the "Right Turn Rule" does seem significant.

INTRODUCTION

The collision of ships at sea has recently and justly become a topic of great interest. A study by the Committee on Oceanography of the National Academy of Science predicted the potential world losses from strandings and collisions during the mid-nineteen seventies at around \$500 million a year (1). In 1970, one out of every fourteen ships of 500 gross tons or more was involved in a collision. Of these involved in collision, one out of twenty-five resulted in total loss (2). That is, in 1970, one out of 350 large ships sailing the ocean was completely lost. When one considers all of the ships at sea, it is easy to appreciate the magnitude of the problem.

Ship collision is one of those problems which so intertwines diverse disciplines that it is hard to develop a good perspective of one facet without at least an awareness of the whole problem. For example, we must at least consider the following factors:

Hydrodynamics. The ability of a ship to avoid a collision, once a collision course has inadvertently been attained, depends on its ability to change course and speed. This ability is determined by the hull size and form,

rudder size and location, steering machinery response, propeller design and propulsion system response, etc. All of these can be prescribed during the design of the ship. If it were known what effect they had on ship collision, a prescription of them based on collision performance might become an important aspect of ship design.

Current designs are evaluated for maneuvering performance by conducting model tests (such as planar motion mechanism tests) and full-scale trials. In the latter, spiral tests and zig-zag tests are common. What is not known is the direct relation of these measurements to the avoidance of collision. The theoretical prediction of the maneuvering performance (such as measured in trials) to a given and untested ship configuration is only somewhat understood, which means that the overall relation between ship configuration and collision avoidance performance is cloudy indeed.

Human factors. When two ships are on a collision course, the master of each vessel must make a decision of what command to give to avoid the impending catastrophe. Generally, these decisions are uncoordinated (made independently of each other, without communication). The pressure on these men is tremendous. If a collision does occur, it is almost certain that one of them will be denied another command, perhaps shattering his career. Maritime law does not have a "no-fault" provision and one master will almost inevitably be deemed responsible.

In order to cope with this difficult decision making process, many ship maneuvering simulation facilities have been developed in which masters can be trained using either physical models or complicated, computer driven simulators. This on-shore experience at least helps the master know the abilities of his ship in a collision situation.

The "Rules of the Road" (12). These international maritime rules define the actions that masters should take in case

of an impending collision. Unfortunately these rules have the force of law and, accordingly, are written in a fuzzy way, wide open to interpretation. For example, Rule 18 requires vessels meeting "end on, or nearly end on, so as to involve risk of collision" to alter course to starboard. What does "nearly end on" mean in quantitative terms? What amount of risk is necessary in order for this rule to apply? When the ships are five miles apart? ten miles apart?

A close examination of these rules indicates that almost all specificity of the required decision criteria has been eliminated, resulting in an extra burden for the master. The irony is that, in a survey of court decisions, 99 percent of the cases of collision were a result of the "failure to obey the Rules of the Road" (2). Of course, since there is no "no-fault" provision, and the purpose of these court actions is to produce a culprit on the basis of the single legal document, "The Rules of the Road", this is hardly a surprising conclusion.

Sensing equipment. In addition to visual perception of impending collisions many masters rely on other devices, particularly radar. It is unfortunate that radar requires the user to acquire a significant amount of training to interpret the situation from just the observation of the radar screen. The term "Radar-Assisted Collision" has become a synonym for misinterpretation of data (6). A classical example is the "Andrea Doria"-Stockholm disaster, where both radar equipped ships were aware of each other's position for 27 minutes before the collision!

The development of true-motion radar has eliminated some of the problems involved with the original, relative-motion devices, but interpretation of the display still requires skill.

Environmental considerations. The "Torrey Canyon" case (although a grounding) has played a major role in transforming sea-borne disasters of tankers from little publicized insurance statistics to a topic of international public concern. In a recent case of collision between two tankers in San Francisco Bay, the clean up costs due to the resulting oil spill exceeded the value of either ship. The cleanup of the spillage of oil from, say, a 200,000 DWT supertanker could easily be a hundred million dollar, hurculean task [see (3), (4) and (5)].

Traffic. Increased shipping density, higher speeds, reduced turn-around times and increased ship sizes all lead to severe traffic problems. One often stated rule is that the master should

strive to maintain at least two nautical miles separation between ships. The density of shipping in the Dover Straits is now so high that this objective is a practical impossibility. Projections of the future great increases in traffic in this area can only lead to grave difficulties since "near-misses" are already relatively common place here. The question which arises here is how safe is the two mile separation figure?

When all of these factors are put together, the picture which emerges is one in which all of the burden is placed on the masters of the endangered ships. The guidance which he is given is incomplete, fuzzy, and, in the case of radar, difficult to understand. It is perhaps a wonder that so few ships are involved in collisions! Efforts have been made recently to improve the situation in several ways. The advent of small, inexpensive computers means that it is now possible for these electronic devices to help with the interpretation of the radar signals, and to aid the master in determining a safe, non-collision path. Many of these collision avoidance, radar-computer systems are now available. As a general rule, these devices are still limited to avoidance of collision when the ship ranges are large. The target ship is treated as a point and course changes result in highly simplified trajectories. There is no assurance that these devices will be significantly helpful if the situation arises when collision is imminent, since neither ship can be considered a point, or for that matter, any elementary geometric figure. Further, ships' trajectories are very complicated and the usual assumptions incorporated in these devices of instantaneous course change, or of parabolic trajectory shape is not appropriate in the last few instants before the time when collision is unavoidable. The shore-based ship maneuvering simulators do give the masters (at least those in the more affluent shipping lines) many lifetimes-worth exposure to collision situations without the danger of real loss.

These advances have omitted from consideration two other avenues of improvement: increasing ship maneuvering performance by means of design changes and changes in the "Rules of the Road." It is not hard to see why these aspects have been ignored (or overlooked). First, direct knowledge of the relation between maneuvering performance (as measured in a ship full-scale trial or model test) and collision avoidance performance is not clearly known. Second, a change in international regulations, although not unknown, is a terribly ponderous undertaking.

THE OBJECTIVE

The objective here is to define the boundary between situations in which collision is avoidable and when it is not. This boundary has significance to many aspects of the ship collision problem mentioned in the Introduction.

This boundary will be expressed here as a critical range. That is, the distance between the two ships at which collision just becomes unavoidable. This range will depend on a variety of things: each ship's speed, heading, size, and maneuvering characteristics, the governing operating procedure (for instance, the "Rules of the Road") and, of course, whether or not the masters make good decisions. Nonetheless, the critical range does provide a quantitative measure of the collision performance so that one can weigh all of these factors and sift out the most important ones.

Consider Rule 21 of the "Rules of the Road." This rule states that the "privileged vessel" is required to maintain course and speed as long as the "burdened vessel" by its action alone can avoid collision. The master of the privileged ship must rely on nothing but experience to determine when this criteria is met, and must rely on faith that the burdened master will not execute a disastrous maneuver.

When collision does become inevitable both masters should abandon all attempts at avoidance and join in to make the collision as gentle as possible. This normally means a set of maneuvers approaching the ideal bow-to-bow collision, where each vessel exposes only the best damage-sustaining part of the hull. Determination by the master that collision is unavoidable is rarely early enough for him to introduce the proper collision maneuvers. Again, the master currently has no information on this subject to guide him and it is hoped that the critical range information developed in this study will at least lead to some insights into this decision process. The variation of critical range with the bearing of the other ship delineates the bearings which involve the greatest danger, that is, the bearings with the greatest critical range.

It is not clear that the current "Rules of the Road" are the best operating procedures for minimizing the possibility of collision, even if they are stripped of their fuzziness. The current "Rules of the Road" were predated by a rather less codified rule known as the "Right Turn Rule." This rule stated, in essence, that in case of the danger of collision, neither ship is to make a left turn. It is

instructive to examine this ancient rule as well in order to see the impact of operating procedures on the collision performance.

Finally, and most important for the naval architect, is the impact of the details of the design of the ship on the collision performance. It is relatively easy to assess the increased cost involved in, say, making the rudder larger, increasing the slewing speed of the steering machinery, or decreasing the reaction time required to reverse the engines. It is within the technology to determine linear and non-linear motions derivatives for a given hull form by use of a planar motion mechanism. These derivatives can be used to model quite adequately the results of standard maneuvering tests (spiral and zig-zags). What is missing in order to select the appropriate design features is a way to convert the maneuvering characteristics into a rational metric of collision performance, so that the added costs involved in installing larger rudders or more sophisticated machinery can be balanced against improvements in the ability to avoid a collision. The concept of critical range can provide this metric. If some improvement in the ship design can lead to a measurable decrease in the critical range then this means that the master will have a longer time to sift out the facts and make the best decision before collision is unavoidable.

DETERMINATION OF THE CRITICAL RANGE

In order to determine the critical range between two given ships on a collision course it is necessary to know in detail how each ship will react to any command of the master and to know the ship's geometry. The reaction of each ship to a given command is information not usually available. During sea trials the ship is subjected to maneuvering tests which include spiral tests and zig-zag tests. The results of these tests are usually represented by global answers such as the turning radius for a given rudder angle or the overshoot in a zig-zag test. In order to predict the critical range, one needs to know the whole trajectory resulting from a given command. Further, in an emergency, the master may elect to change speed as well as rudder angle, and it is unusual to have such combinations tested in full-scale trials. The prediction of trajectories has been accomplished successfully by the use of linear and non-linear hydrodynamic derivative data measured in a towing tank. The work of Strom-Tejsen (13) and van Berlekom and Goddard (18) represent the advanced levels of trajectory prediction now available.

For the purposes of this study, the characteristics of a super tanker were chosen, since these ships are not only

of high capital value but represent a severe environmental hazard as well. Van Berlekom and Goddard (18) present detailed hydrodynamic coefficients for a particular ship (an Esso 190,000 DWT tanker). These coefficients are based on nondimensional equations of motion developed by Norrbin (19), the so-called "bis" system. The coefficients include not only those required for the equations of surge, sway, and yaw, but also include equations for propeller thrust and torque (together with the dynamics of the propulsive system). An important feature of this presentation is that it explicitly includes the effect of the propeller race on the forces developed by the rudder. The "blanketing" of the rudder during crash astern maneuvers is a well known phenomena and van Berlekom's coefficients reflect this.

As a preliminary to the computation of critical range, a computer program was written to determine the trajectories of the tankers presented by van Berlekom (including the geosium series and the rudder variation series). The programs were checked against the data presented in his paper for standard maneuvers. In the process of this development it was discovered that, although the coefficients referred to the "bis" system, the notation appears to be somewhat different from Norrbin in that the $(1/n!)$ factors arising from the Taylor's expansions of the forces seem to be incorporated into the published hydrodynamic derivatives.

As part of this numerical simulation, two features were included which were not in van Berlekom's work. First, the rudder angle deflection was assumed to have a delay of two seconds (to reflect the time between the master's command and the turning of the helm by the helmsman). Once the rudder did respond, it was restricted to a rate of three degrees per second, a typical figure for a large ship. Second, the change in power level was assumed to have a delay of five seconds, representing the time between the initiation of the command, its transmission through the telegraph, and the reaction of the engine room watch officer. The subsequent change in engine RPM is given by the dynamics presented by van Berlekom.

A second preliminary to the computation of critical range involved developing a program to determine the minimum distance between two ships of arbitrary orientation. If the actual ship geometries were used, this would be an exceptionally difficult task. Instead, following Kenan (20), a simplified form was selected to represent the shape of the deckedge. The

form was a flat oval, a rectangle with a semicircular closure bow and stern (see Figure 1).

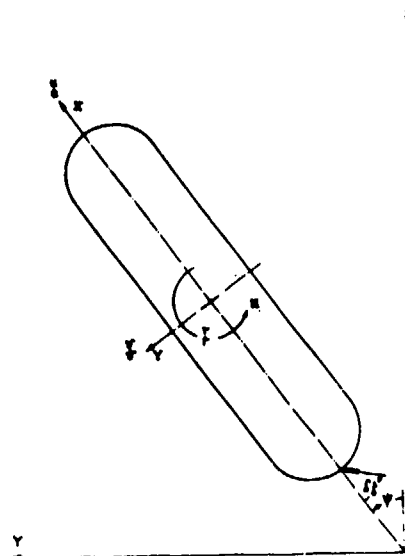


Figure 1. Definition of Coordinates

For two such forms, the algorithm to determine the shortest distance, M , between them is given by (see Figure 2)

$$M = \max \{(\min\{d, p\} - R_1 - R_2), 0.0\}$$

where

$$d = \min \{D(I, J)\},$$

$$p = \min \{P(I, J)\}, \text{ subject to the requirement that the intersection is within the line connecting the bow and stern centers.}$$

M is zero whenever the forms intersect or touch. An additional algorithm is required to detect the case of the ships overlapping one another. If the intersection of the two ship centerlines lies within the line connecting bow stern centers for both ships then, again, M is set equal to zero.

Consideration was given to many other geometric forms, but this one seems to be a good representation as well as a simple one to analyze.

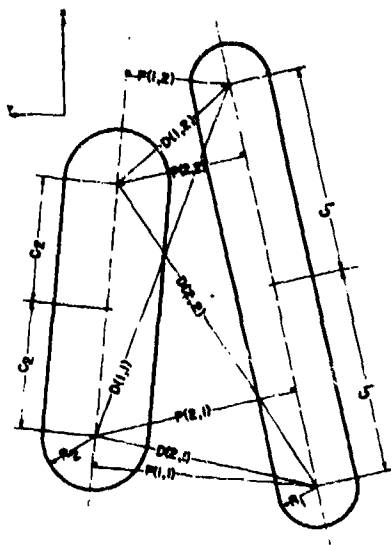


Figure 2. Definitions for Determining the Minimum Distance.

The Ships

The ship assumed for this study is a relatively conventional super tanker with the following specifications given by van Berlekom (18):

Length between perps. (ft.)	1000
Beam (ft.)	154.75
Draft (ft.)	60.56
Total displacement (long tons)	222,000
Ship's speed (knots)	16
Nominal propeller RPM	80

It is assumed that both ships involved in this collision have the same overall dimensions as above. Of course, it would be interesting to consider the collision of ships of different sizes. It is hoped that this might be investigated at some future date. For this ship the values of C , the distances between centers, and R , the radius of the ends, was chosen as

$$C = 422.625 \text{ ft.}$$

$$R = 77.375 \text{ ft.}$$

The Maneuvers

It was assumed that both ships were proceeding along a given course at a fixed speed. At time equal to zero, one or both of the ships' masters perform a collision avoidance maneuver. The maneuver consists of two parts: a rudder command, and a speed command. It is assumed that the rudder command could be any of the seven following commands:

- turn to starboard -
 - rudder angle = $+12^\circ$, $+24^\circ$ or $+36^\circ$
- no turn -
 - rudder angle = 0°
- turn to port -
 - rudder angle = -12° , -24° or -36°

The hydrodynamic terms corresponding to the steady state sway force and yaw moment due to the propeller's rotation which lead to a non-zero rudder angle for a straight line course were omitted so that a zero rudder angle would correspond to a straight course. It is realized that a rudder angle of 36° is a little bit larger than the usual 35° maximum rudder angle, but this range was selected so as to have a convenient, equally spaced set of rudder commands.

It was also assumed that the speed control was limited to two options, 16 knots and 8 knots. Because of the "blanketing" of the rudder by the propeller, van Berlekom's model virtually makes the rudder ineffective for propeller RPM's less than or equal to zero. As a result, if controllability is desired to be maintained, the commanded RPM (equivalent to a commanded steady speed) must remain positive. Only two speeds were chosen so that the number of combinations of maneuvers was minimized. It should be pointed out that if a ship is at 16 knots and the commanded speed is 8 knots, it will take a very long time for this new speed to be achieved. In fact, this time is so long compared to the time required for collision to occur, that the commanded speeds represent really a slow acceleration (or deceleration) during the final moments before collision. The simulation model shows that the fastest way to decrease forward speed is to execute a turn. This is in keeping with practical experience.

With seven rudder settings and two speed commands, there were fourteen different maneuvers investigated. It was assumed that once a given maneuver was executed, it was maintained. No sequential maneuvers were considered.

The Search Procedure

The process of determining the critical range for a pair of maneuvers (one maneuver per ship) is straightforward, but tedious. For the given initial headings and speeds of each ship, and an assumed value of critical range, coordinates of the centers of both ships were determined such that if no maneuvers were executed by either master, the ships would collide along a path which would bring their centers into coincidence. In other words, a perfect collision course is assumed. The internal axes of Ship 1 were assumed to be aligned initially with the geographic axes (X pointing North and Y to the West). The locations of each ship are determined in an earth-fixed coordinate system which coincides with the internal coordinate system of Ship 1 at time $t = 0$. From their given initial conditions the motions were simulated by a stepwise integration of van Berlekom's equations of motion. After the end of

each time step, the distance between the two ships was computed. This process continued until the ships collided or until well after the time of the minimum distance had passed. If the ships collided, then the assumed range between them was increased; if they did not collide, the assumed range was decreased. When a range was found such that the ships just touched, this was set equal to the critical range for this specific maneuver pair. The search process was continued over all possible combinations of maneuver pairs and over the complete range of relative headings.

It should be noted that any hydrodynamic interaction between the ships when they are in close proximity has been ignored.

Coordination of Maneuvers.

In a collision situation we can consider many possible groups of maneuver. For instance, only one ship might perform a maneuver while the other does not. In another case, both ships might simultaneously perform a maneuver. The choice could, if selected properly, improve the situation (decrease the critical range) or worsen the situation (increase the critical range) over that which would occur if only one ship maneuvered. The study presented here presents five basic variations. These are:

1. The best maneuver of both ships. The critical ranges for each possible maneuver pair are examined. Selection of the minimum critical range amongst these determines the best set of coordinated maneuvers.
2. The best maneuver of one ship coupled with the worst maneuver of the other. The purpose here is to determine the maneuver that one ship master must make in order that there will not be a collision, irrespective of the choice of maneuver of the other ship. For this situation, for each maneuver of Ship 1 the maneuver of Ship 2 which maximizes the critical range is determined. The minimization of these maximum critical ranges determines the best maneuver of Ship 1. The corresponding maneuver of Ship 2 represents its most disastrous maneuver. Again, the roles of Ship 1 and Ship 2 can be reversed to obtain the best maneuvering of Ship 2 coupled with the worst maneuver of Ship 1.
3. The best maneuver of just one ship. If it is assumed that Ship 1 maintains course and heading, then selection of the minimum critical range for the range of possible maneuvers of Ship 2 determines its best maneuver. By reversing the roles of Ship 1 and Ship 2, one can

determine the optimum maneuver of Ship 1.

These three different procedures yield an ordered set of critical ranges. That is, the critical ranges determined for 2 above must be larger than those determined for 3, which, in turn, are larger than those for 1.

Operating Procedures.

Two different operating procedures were considered. The first one allows course changes both port and starboard. The second, the "Right-Turn Rule", assumes that only turns to starboard are allowed.

Time before Collision.

Two different times were determined in association with each critical range. The first is the "nominal" time before collision. This is the time which would be required for the centers of both ships to become coincident at the critical range if no avoidance maneuver was adopted. The second time is the time required for the ships to just touch, if the proper maneuver was selected just at the critical range. Generally, this latter time is somewhat longer than the "nominal" time for collision and represents the time after the maneuver is begun before it is known that a collision will not occur.

THE RESULTS

The evaluation of critical ranges was made for several different combinations of conditions. In these studies both ships were identically sized tankers, as described above. These studies were:

Both Tankers at 16 Knots.

The critical ranges for this situation are tabulated in Table 1 and shown in Figures 3 and 4.

1. Unrestricted turning.

a) Both Ships Maneuvering (Curve a on Figure 3). The critical range varies from 4164 ft. when the ships are approaching end-on to 0 ft. when the ships are on the same heading. Only the headings of Ship 2 which result in bearings relative to Ship 1 between 0° and 90° are tabulated. The results for critical range for bearings between 0° and 270° are identical to those between 0° and 90°, from symmetry. However, the maneuvers for the port bearings require rudder angles which are the negative of those for starboard bearings.

Curve a on Figure 3 shows the variation of critical range with bearing as seen by Ship 1. This polar plot corresponds to what one might see on a radar screen on Ship 1. If the radar image

HEADING SHIP 2 DEGREES	BEARING OF SHIP 2 SEEN BY SHIP 1	BEARING OF SHIP 1 SEEN BY SHIP 2	CRITICAL RANGE	COMMAND-SHIP1		COMMAND-SHIP2		NOMINAL TIME BEFORE COLLISION	TIME UNTIL SHIP TOUCHES
				SPEED	RUDDER	SPEED	RUDDER		
a. Both Ships Maneuvering									
180	0	0	4164	16	+36	16	+36	77.2	95.7
210	15	345	4037	16	+36	16	+36	77.2	94.5
240	30	330	4107	16	+36	16	+36	87.5	87.5
270	45	315	3464	16	-36	16	+36	90.5	145.4
300	60	300	2200	16	-36	16	+36	81.2	118.6
330	75	285	1095	16	-36	16	+36	78.3	91.1
360	90	270	0	--	--	--	--	----	-----
b. Best Maneuver of Ship 1 and Worst Maneuver of Ship 2									
180	0	0	9070	16	+36	8	+24	167.9	274.8
210	15	345	8550	16	-36	8	+12	163.9	273.0
240	30	330	8275	16	-12	8	+12	176.6	271.3
270	45	315	5564	16	-36	8	-12	145.4	184.8
300	60	300	4404	16	-36	16	-12	162.7	182.3
330	75	285	2641	16	-36	16	-24	188.8	163.5
360	90	270	0	--	--	--	--	----	-----
c. Only Ship 1 Maneuvering									
180	0	0	5602	16	+36	16	0	103.8	107.2
210	15	345	4415	16	+36	16	0	84.7	99.1
240	30	330	4121	16	+36	16	0	88.2	85.9
270	45	315	3978	16	+36	16	0	102.6	96.5
300	60	300	2731	16	-36	16	0	100.9	148.4
330	75	285	1176	16	-36	16	0	84.1	106.9
360	90	270	0	--	--	--	--	----	-----
d. Right Turn Rule - Both Ships Maneuvering									
180	0	0	4164	16	+36	16	+36	77.2	95.7
210	15	345	4037	16	+36	16	+36	77.2	94.5
240	30	330	4107	16	+36	16	+36	87.5	87.5
270	45	315	3895	16	+36	16	+24	102.0	96.9
300	60	300	2731	16	0	16	+36	100.9	148.4
330	75	285	1176	16	0	8	+36	84.1	106.9
360	90	270	0	--	--	--	--	----	-----
e. Right Turn Rule - Best Maneuver of Ship 1 and Worst Maneuver of Ship 2									
0	270	90	0	--	--	--	--	----	-----
30	285	75	2641	16	+36	16	+24	188.8	163.5
60	300	60	4404	16	+36	16	+12	162.7	182.3
90	315	15	5564	16	+36	8	+12	145.4	184.8
120	330	30	8032	16	+12	16	0	171.4	186.6
150	345	15	6709	16	36	16	0	128.6	140.1
180	0	0	5602	16	+36	16	0	103.8	107.2
210	15	345	4505	16	+36	8	0	86.4	103.4
240	30	330	4188	16	+36	8	+36	89.3	90.6
270	45	315	4083	16	+36	8	0	106.7	100.8
300	60	300	3591	16	+36	8	0	132.7	114.1
330	75	285	2702	16	+36	8	0	192.8	126.9
f. Right Turn Rule - Only Ship 1 Maneuvering									
0	270	90	0	--	--	--	--	----	-----
30	285	75	1176	16	+36	16	0	84.1	106.9
60	300	60	2731	16	+36	16	0	100.9	148.4
90	315	45	5017	16	+36	16	0	131.2	202.3
120	330	30	8032	16	+12	16	0	171.4	186.6
150	345	15	6709	16	+36	16	0	128.6	140.1
180	0	0	5602	16	+36	16	0	103.8	107.2
210	15	345	4415	16	+36	16	0	84.7	99.1
240	30	330	4121	16	+36	16	0	88.1	85.9
270	45	315	3978	16	+36	16	0	104.1	96.6
300	60	300	3478	16	+36	16	0	128.7	108.9
330	75	285	2576	16	+36	16	0	184.2	120.1

Table 1. Critical Ranges for Two 190,000 Dwt. Tankers at 16 Knots.

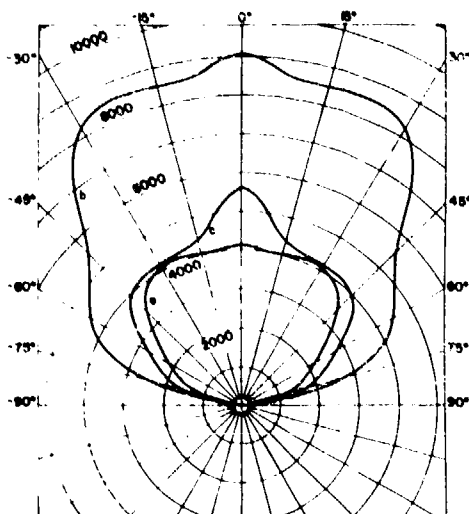


Figure 3. Critical Ranges for Two 190,000 DWT Tankers at 16 knots.

of Ship 2 lies within this curve and Ship 2 is on a collision course, then collision is unavoidable, even if both ships make the best evasive maneuvers.

Notice from Table 1 that the best maneuvers are those in which the ships maintain the commanded speed (although the actual speed decreases as a result of the added drag in the turn), and the ships execute a maximum turn. For Ship 2 bearings equal to or less than 30°, the best maneuver is for both ships to execute the same turn either starboard or port. For bearings equal to or greater than 45°, Ship 1 should execute a port turn while Ship 2 should execute a starboard turn. This means that the best strategy changes dramatically for some heading between 30° and 45°.

The nominal time to collision is remarkably independent of bearing even though the critical ranges are not. Unless action on the part of both ships is taken about 80 seconds before the predicted time of collision, the collision is unavoidable.

b) Best Maneuver of Ship 1 and Worst Maneuver of Ship 2. (Curve b on Figure 3). If Ship 2 makes the worst possible maneuver, then Ship 1 must make its best maneuver soon enough to avoid the collision. Table 1 shows that these maneuvers of Ship 1 are not always identical to those given for the best maneuver of both ships. In general, the critical range and nominal time to collision is doubled if Ship 2 makes a catastrophic maneuver.

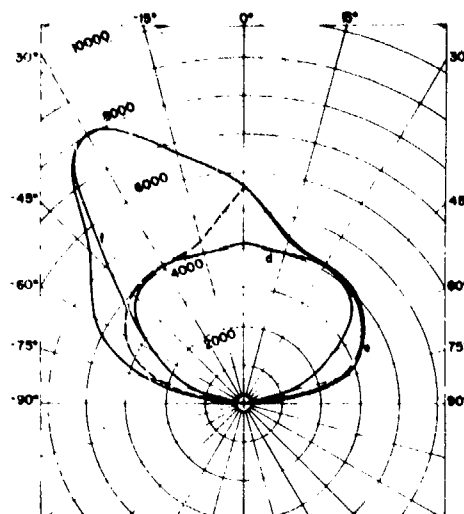


Figure 4. Critical Ranges for "Right Turn Rule" for 190,000 DWT Tankers at 16 knots.

c) Only Ship 1 Maneuvering. (Curve c on Figure 3). If only Ship 1 maneuvers, then it is seen from Table 1 or Figure 3 that the critical ranges are only somewhat larger than for the cases of both ships maneuvering, except for the case of the ships approaching end on (a bearing of 0°), in which the critical range is about 40 percent larger. Again the best commands are not quite the same as for both ships maneuvering. The avoidance maneuver must be executed about 90 seconds before the predicted time of collision.

An interesting conclusion is that not too much is to be gained by communication between the ships in order to coordinate evasive maneuvers. The comparison between the three curves in Figure 4 shows that there is a much greater increase in critical range if both ships maneuver but with one picking the wrong maneuver, than there is gained by both ships picking the best maneuver. Apparently, this is the rationale behind the concept of "privileged" and "burdened" ships in the "Rules of the Road."

2. Right Turn Rule." Situations similar to those presented above were computed for the case in which all port turns are excluded and these results are tabulated in Table 1 and shown on Figure 4.

a) Both Ships Maneuvering. (Curve d in Figure 4.). The restriction to starboard turns only affects the critical ranges for bearings between 45° and 90°, and here it is increased

only slightly. As before, the critical range polar is symmetric about 0° bearing. For bearings between 0° and 270°, the maneuvers of Ship 1 and Ship 2 are to be interchanged.

b) Best Maneuver of Ship 1 and Worst Maneuver of Ship 2 (Curve e in Figure 4.) It is assumed that Ship 2 makes the worst maneuver, but does not make a port turn. In this situation, the polar critical range plot is no longer symmetric. When Ship 2 has a bearing between 0° and 90°, the structure against starboard turns prevents it from making a very disastrous turn. However, for bearings between 0° and 270°, it is possible to have Ship 2 make a bad decision and critical range results are comparable to 1.a) above. On the average, the critical ranges for this situation are greatly reduced over those when turning is unrestricted. Only in a narrow bearing range are they excessively large, and if a "Right Turn Rule" were to be adopted, the master would know that ships on his port quarter would represent his greatest danger.

c) Only Ship 1 Maneuvering. (Curve f on Figure 4). Similar to 2.b) above, the critical range polar is not symmetric and bearings of Ship 2 on the port quarter represent the greatest hazard. If the "Right Turn Rule" were expanded to include the concept of "burdened" and "privileged" vessels so that the "burdened" vessel is the one which lies on the port side of the other ship, then the critical ranges for only one ship maneuvering would be the symmetric image of curve f from 0° to 90° shown as a dotted curve on Figure 4. In this case for bearings of Ship 2 between 0° and 90°, Ship 1 would maneuver. For bearings between 270° and 0° Ship 2 would maneuver. Examination of the results in Table 1 indicate that for this situation the critical ranges between the "Right Turn Rule" and unrestricted turning compare favorably.

One can conclude that the "Right Turn Rule", if the concept of "burdened" and "privileged" ships is adjoined to it, produces similar results to the current "Rules of the Road" except that it produces less disastrous results if one ship chooses the wrong command. In other words, the "Right Turn Rule" eliminates a significant number of bad decision possibilities.

Both Tankers at 8 Knots

The calculations performed for the 16 knot case above were repeated for the situation in which both tankers were at 8 knots, and the results are tabulated in Table 2. The features of the results are generally similar to

those for the 16 knot case but with two major exceptions. First, although the critical ranges are much smaller, the nominal time before collision is larger. In the best of situations, in which both ships maneuver, the decision to maneuver must be made fully two minutes before the time of expected impact or else the collision is unavoidable. Second, the optimum maneuver appears to be most often to speed up (to a commanded speed of 16 knots). This is just a reflection of the numerical model which shows that the ship is more controllable when the propeller race is faster. It is probably rare indeed for a master to order full speed ahead in a collision emergency, however, these calculations show that it is in his best interest.

Ship 1 Travelling at 8 knots and Ship 2 at 16 knots.

The results for these calculations are tabulated in Table 3. The critical ranges for the case of both ships maneuvering lie in between those for both ships travelling at 16 knots and both ships travelling at 8 knots. Notice that the bearings which Ship 1 appears to Ship 2 are limited to ±30°. For heading of Ship 2 near 0°, Ship 1 is in front of and is being overtaken by Ship 2. For headings of Ship 2 near 180°, Ship 1 and Ship 2 meet bow to bow. The optimum commands of each vessel vary considerably with bearing. When Ship 2 is overtaking Ship 1 the optimum speed command for Ship 1 (originally steaming at 8 knots) is 16 knots. In other words, speeding up appears to be a good strategy in this situation. Also note that it is not always true that the best strategy is to put the rudder hard over.

An investigation was made for the case of only one ship maneuvering. Here different results are obtained for Ship 1 alone maneuvering and those for Ship 2 alone maneuvering. It is shown that the critical range for only Ship 1 maneuvering is about twice that for Ship 2 maneuvering. This means that the master of Ship 2 has the ability to avoid the collision by his maneuver at a much later time than that of Ship 1. In other words, if only one ship maneuvers (which is generally the case following the "Rules of the Road"), the faster ship is the last one to avoid the collision.

The Effect of Rudder Size.

The situation in which the rudder of Ship 1 was increased 20 percent in size over the standard tanker referred to above was considered for the case of both ships travelling at 16 knots. The appropriate hydrodynamic derivatives for this case are given by van Berlekom. The results of this calculation are shown in Table 4. For both ships maneuvering and for only Ship 1 maneuvering, the critical range decreases marginally due to the

HEADING SHIP 2 DEGREES	BEARING OF SHIP 2 SEEN BY SHIP 1	BEARING OF SHIP 1 SEEN BY SHIP 2	CRITICAL RANGE	COMMAND-SHIP1		COMMAND-SHIP2		NOMINAL TIME BEFORE COLLISION	TIME UNTIL SHIP TOUCHES
				SPEED	RUDDER	SPEED	RUDDER		
a. Both Ships Maneuvering									
180	0	0	3219	16	+36	16	+36	119.1	148.2
210	15	345	3117	16	+36	16	+36	119.7	148.6
240	30	330	2876	16	+36	16	+12	122.5	161.1
270	45	315	2370	16	-36	16	+36	124.3	179.5
300	60	300	1614	16	-36	16	+36	119.7	146.0
330	75	285	856	16	-36	16	0	122.0	125.9
360	90	270	0	--	--	--	--	-----	-----
b. Best Maneuver of Ship 1 and Worst Maneuver of Ship 2									
180	0	0	6055	16	+36	8	+24	223.7	329.4
210	15	345	5743	16	-36	8	+12	220.3	326.4
240	30	330	5988	16	-36	16	0	255.1	320.2
270	45	315	4028	16	-24	8	0	211.0	305.7
300	60	300	3263	16	-24	16	-12	241.1	202.0
330	75	285	2382	16	-24	16	-12	340.5	268.0
360	90	270	0	--	--	--	--	-----	-----
c. Only Ship 1 Maneuvering									
180	0	0	4617	16	+36	8	0	170.5	165.5
210	15	345	3411	16	+36	8	0	130.7	146.0
240	30	330	2876	16	+36	8	0	122.5	118.3
270	45	315	2741	16	+36	8	0	143.4	120.7
300	60	300	1770	16	-36	8	0	131.2	173.2
330	75	285	856	16	-36	8	0	122.0	125.9
360	90	270	0	--	---	--	--	-----	-----
d. Right Turn Rule - Both Ships Maneuvering									
180	0	0	3219	16	+36	16	+36	119.1	148.2
210	15	345	3117	16	+36	16	+36	119.7	148.6
240	30	330	2876	16	+36	16	+ 8	122.5	116.3
270	45	315	2801	16	+36	16	+ 8	146.3	123.4
300	60	300	1770	16	0	16	+36	131.2	173.2
330	75	285	856	16	0	16	+36	122.0	125.9
360	90	270	0	--	---	--	---	-----	-----
e. Right Turn Rule - Best Maneuver of Ship 1 and Worst Maneuver of Ship 2									
0	270	90	0	--	---	--	---	-----	-----
30	285	75	2382	16	+24	16	+12	340.5	268.0
60	300	60	3263	16	+24	16	+12	241.1	202.0
90	315	45	4028	16	+24	8	0	211.0	305.7
120	330	30	5988	16	+36	16	0	255.1	320.2
150	345	15	5637	16	+24	16	0	215.6	205.2
180	0	0	4617	16	+36	8	0	170.5	161.5
210	15	345	3411	16	+36	8	0	130.7	146.0
240	30	330	3079	16	+36	8	+36	131.1	140.2
270	45	315	2945	16	+36	8	+36	154.4	136.4
300	60	300	2649	16	+36	8	+36	196.0	152.8
330	75	285	2101	16	+36	8	+36	300.0	172.0
f. Right Turn Rule - Only Ship 1 Maneuvering									
0	270	90	0	--	---	--	---	-----	-----
30	285	75	856	16	+36	8	0	122.0	125.9
60	300	60	1770	16	+36	8	0	131.2	173.2
90	315	45	3232	16	+36	8	0	169.4	236.4
120	330	30	5988	16	+36	8	0	255.1	320.2
150	345	15	5637	16	+24	8	0	215.6	205.2
180	0	0	4617	16	+36	8	0	170.5	161.5
210	15	345	3411	16	+36	8	0	130.7	146.0
240	30	330	2876	16	+36	8	0	122.5	116.3
270	45	315	2741	16	+36	8	0	143.4	120.7
300	60	300	2446	16	+36	8	0	181.0	134.7
330	75	285	1886	16	+36	8	0	269.4	148.3

Table 2. Critical Ranges for Two 190,000 Dwt. Tankers at 8 Knots.

HEADING SHIP 2 DEGREES	BEARING OF SHIP 2 SEEN BY SHIP 1	BEARING OF SHIP 1 SEEN BY SHIP 2	CRITICAL RANGE	COMMAND-SHIP 1		COMMAND-SHIP 2	
				SPEED	RUDDER	SPEED	RUDDER

a. Both Ships Maneuvering

0	180	0	1430	16	+36	16	+36
30	234	24	1447	16	+12	16	-36
60	270	30	2063	16	+36	16	-36
90	297	27	2804	16	-36	16	+36
120	319	19	2883	16	-24	8	0
150	340	10	3352	8	-12	16	+36
180	0	0	3551	8	+36	16	+36

b. Only Ship 2 Maneuvering

0	180	0	1527	8	0	16	+36
30	234	24	1457	8	0	16	-36
60	270	30	2469	8	0	16	-36
90	297	27	3013	8	0	16	+36
120	319	19	3090	8	0	16	+36
150	340	10	3375	8	0	16	+36
180	0	0	4301	8	0	16	+36

c. Only Ship 1 Maneuvers

0	180	0	2941	16	+12	16	0
30	234	24	2174	16	+36	16	0
60	270	30	2970	16	+36	16	0
90	297	27	4585	16	-36	16	0
120	319	19	4279	16	-36	16	0
150	340	10	5137	16	-36	16	0
180	0	0	6516	16	+36	16	0

d. Right Turn Rule - Both Ships Maneuvering

0	180	0	1430	16	+36	16	+36
30	234	24	1457	8	0	16	+36
60	270	30	2469	8	0	16	+36
90	297	27	3642	16	+36	16	+36
120	319	19	3751	16	+36	16	+36
150	340	10	3512	16	+36	16	+36
180	0	0	3551	8	+36	16	+36

Table 3. Critical Ranges for Two 190,000 Dwt. Tankers
(Ship 1 = 8 kts., Ship 2 = 16 kts.)

HEADING SHIP 2 DEGREES	BEARING OF SHIP 2 SEEN BY SHIP 1	BEARING OF SHIP 1 SEEN BY SHIP 2	CRITICAL RANGE	COMMAND-SHIP 1		COMMAND-SHIP 2		CHANGE IN CRITICAL RANGE DUE TO RUDDER	
				SPEED	RUDDER	SPEED	RUDDER	FEET	%

a. Both Ships Maneuvering

180	0	0	4117	16	+36	16	+36	-47	-1.1
210	15	345	3895	16	+36	16	+36	-147	-3.5
240	30	330	3864	16	+36	16	+12	-243	-5.9
270	45	315	3354	16	-36	16	+36	-110	-3.2
300	60	300	2173	16	-36	16	+36	-47	-2.1
330	75	285	1731	16	-36	16	+24	-14	-1.3
360	90	270	0	--	---	--	---	----	0

b. Only Ship 1 Maneuvering

180	0	0	5539	16	+36	16	0	-63	-1.1
210	15	345	4339	16	+36	16	0	-73	-1.8
240	30	330	3864	16	+36	16	0	-257	-6.2
270	45	315	3741	16	+36	16	0	-237	-6.0
300	60	300	2528	16	-36	16	0	-203	-7.4
330	75	285	1119	16	-36	16	0	-57	-4.8
360	90	270	0	---	---	--	---	----	----

Table 4. Critical Ranges For Two 190,000 Dwt. Tankers at 16 Knots.
(Ship 1 has a 20% larger rudder)

increased rudder size. An average critical range reduction is approximately 100 feet for both ships maneuvering and 150 feet for only Ship 1 maneuvering. It is felt that this reduction in critical range is very marginal and probably is not worth the added cost of the larger rudder and steering machinery in this case. It should be emphasized, however, that the decrease in critical range does give the naval architect here a useful metric to make this decision of rudder size.

The Effect of the Radar Information.

Unless extremely high resolution radar is used, the image of a ship on the radar screen is a circular or oval patch. Since the radar "sees" only reflective surfaces such as the ship side and deckhouse front, the center of this patch may not be and probably is not the center of the ship. Determination of whether an approaching ship is on a collision course or not is somewhat difficult and it is improbable that one can differentiate to within 200 feet what the collision situation is. In all of the above calculations it was assumed that the ship paths were such that, without avoidance maneuvers, the centers of each ship would become exactly coincident. Suppose the following situation occurs. The paths of the two ships cross, but when the center of Ship 1 crosses the path of Ship 2, the center of Ship 2 is some distance, d_s , from this. The inaccuracy in interpreting the radar signal is equivalent to a variation in d_s .

The following set of variations were performed for two tankers at 16 knots and with the heading of Ship 2 at 270° (that is, for a bearing of Ship 2 relative to Ship 1 of 45°). In the first case, it was assumed that Ship 1 was either on a perfect collision course ($d_s = 0$ ft.) or ±100 feet from the perfect collision course ($d_s = ±100$ ft.). The critical ranges for each of these three Ship 1 initial situations was determined for each maneuver pair. The maximum value of the three was set equal to the critical range for the maneuver pair under the uncertainty of d_s . Variations assuming uncertainties of ±200 ft. and ±300 ft. were also performed. The results are shown in Table 5. The bearing error presented in this table represents the variation in bearing caused by the variation in d_s at the critical range. It can be seen that even relatively large bearing errors do not change the critical range much.

a. Both Ships Maneuvering:

d_s , ft.	bearing error	critical range	change in critical range, ft.
0	0	3464	0
0, ±100'	±1.3°	3520	56
0, ±200'	±2.6°	3553	89
0, ±300'	±3.9°	3586	122

b. Only Ship 1 Maneuvering:

0	0	3968	0
0, ±100'	±1.0°	4083	115
0, ±200'	±2.0°	4172	204
0, ±300'	±3.0°	4200	234

Table 5. Effect of Radar Inaccuracy
(Ship 2 Heading = 270°)

Optimal Commands.

In a collision situation a typical command issued by a master might be: full astern, rudder hard to starboard (or port). Although this seems at first glance to be a good course of action, the results of this section do not substantiate this. Full speed astern causes the rudder to be ineffective, as discussed above. It is also not always true that the maximum rudder commands (such as hard to port, hard to starboard) are the best commands. It is well known that in simple mechanical systems, bang-bang control systems using maximum commands are best. The major difference here is that the two ships considered have great size and are not considered to be points. For instance, consider the case of one ship overtaking another when both are on the same course and track (see the first entry of Table 3a for a Ship 2 heading of 0°). If Ship 2 does not maneuver, then Ship 1 must, in order to avoid the collision. Detailed examination of the trajectories indicated that a rudder angle of +36° (right turn) swings the stern quite far to the left before the ship gets out of its original track. As a result, the overtaking ship (Ship 2) collides with Ship 1 on the starboard side of the stern. For the case of a 12° rudder angle, the leftward swing of the stern is much less and, even though the ultimate turning radius is larger, this command more rapidly removes the whole ship from the path of Ship 2 than the maximum command of hard right rudder.

CONCLUSIONS

Based on the above studies a number of conclusions can be reached. Of course these conclusions are based on one ship type and a limited number of maneuvers. It is felt, however, that the trend of these results is applicable to a wide variety of ships and ship types.

Coordinated Maneuvers

It is appealing to think that if both endangered ships were in communication and could thus coordinate their maneuvers that collision would be significantly reduced. The calculations presented here do not bear this out. The improvement in critical range when both ships execute the best maneuver is not large compared to the case when just one ship executes its best maneuver. Further, if both ships maneuver, it is possible that one will execute a disastrous maneuver and the calculations show that this will lead to a doubling of the critical range. In other words, there is a lot more to be lost by both ships maneuvering than there is to be gained.

"Right Turn Rule"

The "Right Turn Rule" has significant advantages. In a collision situation if the ships may not turn to port and if the "burdened" ship is the one facing the port side of the other ship then the possibility for a disastrous combination of maneuvers is greatly reduced. With such a rule it would be possible to codify the requirements explicitly. For instance, "end-on or nearly end-on" could safely be interpreted as bearings less than 10°. For all other headings the above burdening rule would apply. The removal of half of the possible maneuvers not only eases the master's choice but does not substantially increase the critical range.

Ship Speed.

The study shows that if the two ships are both travelling at the same speed, the slower this speed, the smaller the critical range. However, the slower speed ships require that an evasive maneuver be executed a longer time before the impending collision.

Speed Commands.

It appears that a commanded increase in speed is more often than not the best strategy. The increase in controllability with increases in water velocity in the propeller race, as reflected in the numerical model, leads to this conclusion.

Fast Ships vs. Slow Ships.

The calculations indicate that the faster of the two ships involved will be the last ship capable of avoiding collision. This result should be considered only for ships of the same size as studied here. It would be an appropriate extension of this current work to see if this conclusion also applies to ships of different sizes.

Rudder Size.

It does not appear that moderate increases in rudder size will lead to large changes in critical range.

Radar Information.

The uncertainty in detecting the exact nature of the collision situation does not greatly affect the critical range.

Optimum Commands.

The optimum command is not always the maximum command.

ACKNOWLEDGEMENT

The author would like to extend his thanks to Mrs. Helen Strauch and Mrs. Marylou Newby of the University of California for their invaluable help in typing the manuscript, and to Ship Research, Incorporated, for help in preparing the figures.

BIBLIOGRAPHIC REFERENCES

1. Christopher, Nicholas S. "Marine Integrated Navigation Systems", Navigation, Journal of the Institute of Navigation, vol. 16, no. 4, 1969, pp. 419-423.
2. Glen. "Ship Collisions - What's Being Done to Prevent Them", Ocean Industry, vol. 6, no. 12, Dec. 1971, pp. 19-37.
3. Flore, Alfred E., Cdr. USMS. "Practical Aspects of Merchant Marine Navigation", Navigation, Journal of the Institute of Navigation, vol. 15, no. 1, 1968, pp. 16-21.
4. Chase, K. H., Tiblin, D. V. "INCAS- Integrated Navigation and Collision Avoidance System", Navigation, Journal of the Institute of Navigation, vol. 18, no. 2, 1971, pp. 205-214.
5. Beer, W. J., "Analysis of World Merchant Marine Losses", R.I.N.A. Trans., vol. 111, 1969, pp. 97-112.
6. Pansmith, Jack, "The Navigational on True Radar Plot for Collision Prevention", Navigation, Journal of the Institute of Navigation, vol. 16, no. 4, 1969, pp. 333-345.
7. Oliver, Edward F., Cdr., USCG. "International Development on Merchant Marine Training", Navigation, Journal of the Institute of Navigation, vol. 16, no. 3, 1969, pp. 249-253.
8. Riggs, Robert F. "Lad - A New Family of Devices for the Avoidance of Collisions at Sea", Presented at SNAME Great Lakes Section Meeting, Jan. 1969.
9. Mara, Thomas D. "Automation of Merchant Ship Navigation Systems", Navigation, Journal of the Institute of Navigation, vol. 18, no. 2, 1971, pp. 215-220.

10. Ratcliff, S. "The Avoidance of Collisions in the Air", Published by NATO-AGARD, Navigation, 1962, pp.372-399.

11. Frye, E. O., Killham, D.C. "Aircraft Collision Avoidance Systems", IEEE Spectrum, Jan. 1966, pp. 72-80.

12. United States Coast Guard. "Rules of the Road, International - Inland", USCG Issue, Sept. 1, 1965.

13. Strom-Tejsen, J. "A Digital Computer Technique for Prediction of Standard Maneuvers of Surface Ships", David Taylor Model Basin, Report No. 2130, December 1965.

14. Abkowitz, Martin A. "Lectures on Ship Hydrodynamics - Steering and Maneuverability", Hydro- and Aerodynamics Laboratory, Lyngby, Denmark, Report Hy-5, May 1964.

15. Carr, J. B. "Probable Developments in Marine Navigation 1966-1976", Ship's Gear, A Symposium on Control Engineering Equipment and Ship Operation, London 1966, published by Fishing News LTD.

16. Riggs, Robert F. "A Short Study of Statistics of Collisions Between Merchant Vessels", Navigation, Journal of the Institute of Navigation, vol. 12, no. 3, 1965, pp. 206-217.

17. Thompson, Robert P. "Size and Ocean Distribution of the World Merchant Fleet: Present and Future", Navigation, Journal of the Institute of Navigation, vol. 18, no. 2, 1971, pp. 176-187.

18. van Berlekom, W.B., Goddard, T. A., "Maneuvering of Large Tankers", Trans. of the Society of Naval Architects and Marine Engineers, vol. 80, 1972, pp. 264-298.

19. Norrbin, N. H., "Theory and Observations on the Use of a Mathematical Model for Ship Maneuvering in Deep and Confined Waters", Swedish State Shipbuilding Experimental Towing Tank Publication No. 68, 1971.

20. Kenan, G., "Collision Avoidance Between Surface Ships at Short Ranges", presented at the Northern California Section of SNAME, March 1972.

DISCUSSION

J.C. CARD

I wish to thank the organizers of the Symposium and Professor Webster for the opportunity to comment on this paper about collisions. The topic is one of great concern to those of us in the business of promoting maritime safety and environmental protection. While I find Professor Webster's paper thought provoking and I feel that he has presented a method which could help evaluate the effects of vessel design on collision situations, I think the paper is weak in practical marine application. I do not agree with some of the assumptions made or conclusions drawn. My comments will be limited to the areas of "Rules of the Road" and communications between vessels.

Professor Webster leaves us with the impression that the International Regulations for the Prevention of Collisions at Sea (Rules of the Road) are of little or no help to the mariner in avoiding collisions and that there is little hope for improving these Rules. The Rules presently in force may not be clear in all areas. However, they do represent an internationally agreed upon set of regulations by which ships can safely navigate when in proximity of other ships. Without the Rules, or if they did not have the force of law, safe navigation into and out of ports would be greatly impaired.

The Rules came into acceptance in 1895 and were changed in 1948, 1960 and most recently in 1972. This latest change took place at a special international conference of recognized experts in the maritime field. At the conference consideration was given to the significant changes that have occurred in marine transportation since 1960 and to the deficiencies in the 1960 Rules. The result of the conference was an extensive rewrite of the Rules. The opinion of those experts associated with the rewrite of the Rules is that they are substantially superior to the 1960 Rules. Particular areas of improvement are:

- a. Simplification of the individual rules which removed extraneous information and moved detailed technical information to an annex. The new language is more easily understood by the mariner than that found in the present Rules.
- b. Recognition was given to vessels restricted in their ability to maneuver due to operational constraints. Also recognition was given to vessels restricted in maneuvering because of draft limitations.
- c. Recognition of vessel maneuverability when determining safe speed.
- d. Incorporation of traffic separation schemes.
- e. Clarification of old Rule 18 the "meeting situation." The new Rule 14 "Head-on-Situation" is:

The opinions expressed in this paper are those of the author and do not necessarily reflect those of the United States Coast Guard.

"(a) When two power-driven vessels are meeting on reciprocal or nearly reciprocal courses so as to involve risk of collision each shall alter her course to starboard so that each shall pass on the port side of the other.

"(b) Such a situation shall be deemed to exist when a vessel sees the other ahead or nearly ahead and by night she could see the masthead lights of the other in a line or nearly in a line and/or both sidelights and by day she observes the corresponding aspect of the other vessel.

"(c) When a vessel is in any doubt as to whether such a situation exists she shall assume that it does exist and act accordingly."

The 1972 Rules will come into force on 1 January 1976 provided 15 major maritime nations ratify the convention prior to 1 January 1975.

Professor Webster's conclusion that communication between ships would not reduce collisions is not supported by investigations into vessel collisions. A major cause of collisions in the past twenty years has been failure of the vessels to understand each others intentions. Whistle signals of the past just are not adequate in today's crowded and restricted waterways. The late Vice Admiral E. L. Cochrane headed a special committee which studied the collision of the M/V STOCKHOLM and the S/S ANDREA DORIA. One of this committee's recommendations was the increased use of bridge-to-bridge radio communications as "an important navigational safety tool." Several major collisions since that time could have been prevented if the vessels had been in communication with each other and had established passing agreements. Recognizing the need for this avenue of communication a joint committee of the Coast Guard and the Federal Communications Commission released in the summer of 1965 a report advocating requirements for bridge-to-bridge capabilities. After several delays in the Congress, the Vessel Bridge-to-Bridge Radio Telephone Act was passed in August 1971. Coast Guard regulations which resulted from this law became effective on 1 January 1973.

Putting a quantitative evaluation on the effectiveness of bridge-to-bridge radio telephone requirements is not an easy task because of the complexity of the collision situation. However, several studies conducted for the Coast Guard put the effectiveness in reducing collisions no lower than 25% and maybe as high as 75%. In addition, the Great Lakes and the Delaware Bay and River systems have had bridge-to-bridge communications in effect since 1954 and 1960 respectively. Both areas reported a substantial decrease in collisions after the implementation of bridge-to-bridge communications. On Delaware Bay during the 5 years and 10 months prior to the program's implementation there was an average of 1.27 collisions per month. That average dropped to 0.91 collisions per month during the first few years of the program and in 1966 and 1967 the figures fell even lower to 0.23 per month. The years 1968 and 1969 brought the program to fruition as no collisions were recorded

involving vessel equipped with bridge-to-bridge capabilities.

I feel certain that the ports of the United States are safer when pilots and masters of vessels are capable of directly communicating with one another. While my comments have been somewhat critical, I do feel this paper is an interesting study which adds to the knowledge of maneuvering safety. Moreover, I would encourage Professor Webster and others in the field to pursue similar studies because the need exists to develop practical safety regulations for ship maneuvering based on vessel designs, human factors, harbor configurations and environmental conditions.

S.D. SHARMA

The discussor considers this to be a paper of fundamental importance both for its underlying philosophy and the results obtained. Within the framework of a "Special Research Pool" a small group at Hamburg and Hanover has been working for some time on a similarly motivated project entitled "Safety of Ships against Collisions" as part of a broader effort to rationalize and reconcile the concepts of economy and safety in shipping and shipbuilding. If safety is understood as the probability of avoiding the occurrence of certain undesirable events in the life of a ship of given physical properties in an essentially stochastic environment, it becomes evident that absolute safety cannot be achieved. In fact an optimum level of finite safety can be determined either from considerations of economy, if only material values are at stake, or from the principle of minimum total mortality, if human lives are also involved.

Like the Author, we think that a rational evaluation of design features for improving the maneuverability of ships is impossible as long as maneuverability is expressed only in terms of physical properties such as advance and tactical diameter in a turning circle test etc. We set out to find a formal quantitative relationship between the cost of design features and their ultimate economic benefit. It was shown by Krappinger (1972) that the rate of collision is a suitable concept for evaluating the economic benefits of maneuverability. The problem then is to find how the rate of collision is affected by the physical properties of the ship and the statistical properties of the environment. The solution presupposes a mathematical model for ship collisions including a basic concept for their causes. Here we have found the Author's "critical range" under which collision becomes unavoidable between ships at steady bearing quite useful. However, in the ultimate analysis only human error and machine failure seem to be the true causes of collisions. Poor maneuverability and even instrument errors can be overcome, at least in the open sea, by an appropriate strategy of anti-collision maneuvers. Thus collisions are caused not so much by poor hardware as by a poor assessment of the true maneuverability by the ship's master. Hence significant gains will accrue from a better training of the ship's command and from improved software rather than from better ship design, a somewhat disappointing result from the naval architect's point of view!

Reference

Krappinger, O.: Die Kollisionsrate als Element des Systemansatzes im Schiffbau. IFS-Bericht Nr. 289, Hamburg, January 1972.

AUTHOR'S REPLY

The author would like to thank LCDR Card for his interesting reply to this paper. It is apparent that LCDR Card sees a great disparity between the results and proposals of this paper and the experience of the Coast Guard. The author would like to suggest that this difference is illusory and deeper examination reveals a harmony between LCDR Card's comments and the results of this paper.

The paper shows that little is to be gained in going from the situation in which one ship performs the best maneuver to the situation in which both perform the best maneuver. For this purpose only does it appear that communication between the ships does not seem fruitful. The fact that experience shows that ship-to-ship communication does reduce collisions dramatically, is *prima facie* evidence that one or the other of these ships

would have selected a bad maneuver without the communication.

It is the author's thesis that the ambiguity of the "Rules of the Road" is a contributing factor in the selection of such bad maneuvers. The reader is invited to reread the new rule 14 presented by LCDR Card and to judge the level of ambiguity for himself.

The author would like to thank Dr. Sharma for his useful comments. It is particularly important that his group's research appears to come to the same conclusion as this paper, that ship design improvements do not appear to be the way to reduce collisions. Since design improvements are easier to implement than improvements in human judgement, we can conclude that the subject of ship collisions still represents a significant challenge.

HYDRODYNAMICS FOR SAFETY – OTHER

SESSION IV

Tuesday, June 25, 1974
2:00 P.M. – 5:10 P.M.

Chairman: ADM A. Castera
Director, Paris Model Basin
France

Ship Motions and Capsizing in Astern Seas	297
O.H. Oakley, Jr., J.R. Paulling, and P.D. Wood, University of California, Berkeley, California	
Design Acceleration and Ship Motions For LNG Cargo Tanks	351
A.E. Baitis, S.L. Bales, and W.G. Meyers, NSRDC Bethesda, Maryland	
Liquid Slosh in LNG Carriers	371
H.N. Abramson and R.L. Bass, Southwest Research Institute San Antonio, Texas and O. Faltinsen and H.A. Olsen, Det Norske Veritas, Oslo, Norway	
The Hydrodynamic Influence on the Non-Linear Motion of an ACV Over Waves	389
L.J. Doctors, University of New South Wales, Sydney, Australia	
Semi-Submerged Air Cushion Vehicle (SSACV)	421
T.K.S. Murthy, Portsmouth, U. K.	

SHIP MOTIONS AND CAPSIZING IN ASTERN SEAS

O. H. Oakley, Jr.
University of California
Berkeley, California

J. R. Paulling
University of California
Berkeley, California

P. D. Wood
University of California
Berkeley, California

ABSTRACT

An analytical and experimental study of ship motions and capsizing in extreme seas has been conducted. The analysis of linear and quasi-linear one-dimensional roll models has revealed motion anomalies not apparent from the usual nonlinear ship motion theory. Extensive tests have been conducted using a radio-controlled model in the wind generated seas of San Francisco Bay. Directional spectra were computed, using a variety of techniques, from the wave measurements by an array of wave gages. Comparisons of the experimentally determined motions and a linear strip theory prediction are presented. A time domain numerical simulation program for motions and capsizing has been used to investigate motions in a variety of wave group configurations. The results show good agreement with observed capsizing phenomena and have revealed a number of important characteristics associated with large geometry changes in waves.

I. INTRODUCTION

Stability against capsizing in heavy seas is one of the most fundamental requirements considered by the naval architect when designing a ship. At the same time it is one of the least understood phenomena in the realm of ship motion theory. By its very nature, stability is concerned with extreme motion both of ship and waves. Therefore, the linearized methods of wave and ship motion analysis which have received so much attention in recent years cannot be applied here with any expectation of obtaining directly useable results, but may be used only for general guidance. Statistically, capsizing falls into the category of events of rare occurrence, again calling for special techniques in studying its probability distributions.

The basic purpose of studying capsizing is to establish prediction techniques which may be used by naval architects during the design process.

Even though traditional empirical methods have apparently been successful in insuring adequate stability of conventional ships built in the past, it is expected that the future will see more rapid evolution in ship size, speed, geometry, and performance requirements. Some of the new, high performance ship types may be expected to experience motion, control, and even stability problems when operating in severe seas which are not susceptible to prediction or remedy by traditional empirical methods. The more general goal of our study, therefore, is to establish a basis of understanding of phenomena associated with the operation of ships in severe seas and to relate these ship behavior phenomena to the geometrical and operational characteristics of the ship.

Model experiments conducted under conditions which are as realistic as possible in simulating a severe storm sea environment offer the best means of gaining this understanding. At the present time, there are no towing tanks which have the capability of producing realistic short-crested seas of sufficient severity. Further, the infrequent nature of the capsizing event indicates that experimental runs of considerable length will be required, especially in following seas where the frequency of wave encounter is low. The testing of free-running radio-controlled models in an open water area in natural wind generated waves is an alternative to tank testing that has been successfully used for this purpose in the past.

As is the case of all experiments conducted in a natural environment, there is the difficulty of controlling the conditions of the test. However, the two principal requirements enumerated above: steep short-crested waves and virtually unlimited length of run are available only in this way.

The first experiments of this type were conducted by a group working under the direction of Professor Kurt Wendel

at the universities of Hamburg and Hannover in Germany. Their work clearly pointed out the value of open water testing as a means of studying capsizing. Partly as a result of the success of Wendel, a ship capsizing study was initiated at the University of California under sponsorship of the U.S. Coast Guard starting in 1969. This research started with a program of model testing in the open waters of San Francisco Bay. Experiments have now been completed with two models, one a conventional cargo ship and the other, a fast twin screw container ship. As a result of these experiments, a great deal has been learned about the mechanical process of capsizing. This has enabled the development of a mathematical model to be initiated and good progress is being made in that direction. Finally the probability of capsizing is found to be closely associated with the probability of the ship encountering a single especially steep wave or group of several especially steep and regular waves in the random sea environment. This has led to the necessity of studying the statistics of wave groups as they relate to the overall characteristics of the seaway. This subject appears to have received relatively little attention in the literature of physical oceanography. It, therefore, forms a subject of study under the present program in order to round out our treatment of the capsizing problem.

II. LINEAR AND QUASI-LINEAR MOTION COMPUTATIONS

As noted in the Introduction, modern ship motion research has been mostly concerned with small amplitude motion which is amenable to a linearized dynamic-hydrodynamic analysis. The practical implementation of such procedures has been most successfully obtained in the strip-method of computation as exemplified by the work of Salvesen, Tuck, and Faltinsen (1970). It is safe to say that the strip calculation now provides a workable design tool for predicting the average seakeeping performance of a proposed ship early in the design process.

Performance predictions, however, are usually concerned with the average behavior of the ship over long periods of time encompassing, e.g., the length

of a voyage and tens of thousands or hundreds of thousands of wave encounters, rather than the short intervals which the ship spends in extremely severe seas. Performance characteristics which have been successfully described by linear procedures are ship motion, structural loads, stresses and even occurrence of seemingly nonlinear large-amplitude phenomena such as the frequency of slamming and bow immersion. Prerequisite to a study of performance but not part of it is survivability. In contrast to the average conditions with which performance estimates are concerned, survivability addresses itself to the extreme sea and motion conditions having a very low probability of occurrence. Thus, by definition, in studying capsizing of ships in extreme seas, we are concerned with the largest, steepest waves which the ship may encounter during her lifetime (sometimes at its very end!), and with motions of large amplitude, usually well beyond the range of a linear ship motion analysis. Nevertheless, it is useful to review some of the features of linear motion theory in hopes that its results may provide some guidance and insight into certain phenomena of concern in a study of capsizing. Further insight and new phenomena may also be revealed by certain nonlinear theoretical procedures which have been developed to augment linear ship motion theory.

What results of concern in a study of capsizing may be obtained from linear motion theory? The first which suggests itself is resonant rolling. Although a linear analysis of roll does not accurately describe the details of the motion at large amplitudes, some of the properties of this mode of motion may be revealed. For example, there is substantial evidence that rolling motion in beam seas in the absence of other effects is not likely to result in danger to the ship. The vessel may roll to very large angles if the frequency content of the sea is in the right relationship to the natural frequency of the ship, but in order for her to be placed in danger of capsizing, additional factors must be present. These may include strong wind heeling moments, damage to the watertight envelope resulting in the flooding of a portion of the ship, and the entrapment of large quantities of water on deck by bulwarks.

Tests of the range of applicability of the linear ship motion technique have been made by Dalzell, and some of his results for the Mariner-type ship were reported in a discussion to a paper by Ochi (1964). Pitch and heave motions were measured in regular waves of various steepness. For waves more than 1.75 times the model length these motions show a linear behavior with wave height for values of wave height to length ratio up to 1/12. In the shorter waves, the pitch motion appeared to drop somewhat below a straight line relationship for the higher waves, i.e. the graph of pitch versus wave height was concave downward in these waves.

Figure 1 shows some results obtained at the Univ. of Calif. from experiments and corresponding calculations of the relative rolling motion between the ship model and the wave surface. The experiments and calculations were carried to moderately large angles and show reasonably good correlation. The important characteristic of this motion is its tendency to level off in increasingly higher sea states. Since the relative rolling motion is more important than the absolute roll in relation to such effects as water entrapment on deck, this suggests that the effects of increasingly severe sea states tends to level off.

These calculations were made using a linear approximation to the ship righting arm curve equal to displacement times the initial metacentric height. The quadratic roll damping was approximated by an equivalent linear damping coefficient. The trend of this curve illustrates the degree of agreement that may be expected in comparing linear calculations with experiments. The maximum wave steepness, however, is not in the extreme or survival range.

It is also useful, at this point, to look at some results of nonlinear ship motion theory. Two topics of ship dynamics have been studied using nonlinear equations of motion: maneuvering in calm water, and rolling in beam seas. In both cases, the procedure has been to include terms in the equations of motion representing forces which depend in a nonlinear manner upon some of the unknown motion

variables. Most commonly, these have been damping forces assumed to vary as the square of velocity or more general forces which, by reason of symmetry, behave as odd functions and may therefore be expressed by cubic terms in all velocities and accelerations. In principle, these terms represent higher order terms in a Taylor series expansion of the total force on the ship, assumed to depend in some unknown way on the relevant motion variables. Many of the terms can, in fact, be related to specific physical effects, e.g., the above noted viscous drag which varies in a nonlinear manner with velocity.

The results of including nonlinear terms in the equations of motion are twofold: First, behavior which might be obtained by a conventional linear analysis is modified somewhat without changing its basic nature. Second, new phenomena may be revealed which are not present in the linear results. We shall look at examples of each of these cases and attempt to relate them to the capsizing problem.

In studying the large amplitude rolling motion of ships in beam seas, the method of equivalent linearization has been utilized by several investigators, e.g. Vassilopoulos (1971) and St. Denis (1967). Equivalent linearization is a method which is generally suitable for describing a dynamic system in which large deviations from linear behavior are not anticipated, (weak nonlinearity). A reasonable approximation to the exact behavior of the real system, therefore, is given by an equivalent linear system having linear coefficients appropriately selected. The principal shortcoming to the method, in common with most approximation methods, is that the limits of applicability or degree of approximation are difficult to estimate.

In applying equivalent linearization, one selects coefficients of the equation of motion such that their effect on the behavior of the system is equivalent in some way to the exact system. Consider the simple uncoupled single degree of freedom roll motion described by

$$I_x \ddot{\phi} + D(\dot{\phi}) + R(\phi) = K_e(t) \quad (\text{II-1})$$

where D and R are the damping and restoring moments respectively. Let us

further restrict the problem by assuming sinusoidal excitation and a damping moment which varies quadratically with roll velocity

$$D(\phi) = C_q \dot{\phi} |\dot{\phi}|. \quad (\text{II-2})$$

The equivalent linear damping coefficient, C_L , for this case has been derived by Blagoveshchensky and is

$$C_L = \frac{8\omega}{3\pi} \phi_0 C_q \quad (\text{II-3})$$

where ϕ_0 is the amplitude, and ω the frequency of the rolling motion. This expression is obtained by requiring that the linear damping results in the same dissipation of energy per cycle of motion as the quadratic resisting moment.

In the case of random seas, the concept of energy interchange "per cycle" is not meaningful since the motion is no longer periodic. Rather, one must deal with time averages, but the concept of equivalent energy interchange still applies. Both St. Denis and Vassilopoulos estimated equivalent linear coefficients for roll motion in random beam seas by the following procedure. Assume that the actual force (moment) which is a function of motion variable X_j , is given by $F_i(X_j)$. This is to be approximated by an equivalent force consisting of a linear term in the appropriate motion variable plus an error term, E

$$F_i(X_j) = C_i X_j + E. \quad (\text{II-4})$$

We shall require that C_i be selected such that the time average of the mean square of the error term, E , will be a minimum.

$$\frac{\partial \langle E^2 \rangle}{\partial C_j} = 0 \quad (\text{II-5})$$

For the case of quadratic damping this leads to the following expression

$$\sqrt{8/\pi} \sigma_\phi C_q \quad (\text{II-6})$$

Thus it is seen that the evaluation of (II-5) leads to an equivalent linear force coefficient for random motion which, as in the case of sinusoidal motion, is a function of the motion amplitude itself, in this case, σ_ϕ , the RMS value of the motion.

Applying the same reasoning to a nonlinear restoring moment, let us represent the righting moment curve by a fifth-order, odd polynomial in the roll angle ϕ ,

$$R(\phi) = C_1 \phi + C_3 \phi^3 + C_5 \phi^5. \quad (\text{II-7})$$

Designating the equivalent linear restoring moment by an error term plus $C_E \phi$, and again assuming the roll motion to be a zero mean Gaussian process having an RMS amplitude given by σ_ϕ , minimization of the error term, equation (II-5) leads to

$$C_E = C_1 + 3C_3 \sigma_\phi^2 + 15C_5 \sigma_\phi^4 \quad (\text{II-8})$$

By introducing equivalent linear forces and moments for the "exact" nonlinear terms, we see that we have obtained a linear system in which these forces depend on the mean amplitude of the motion. The solution, for a given amplitude of the excitation, must therefore be obtained by iteration. That is, one begins with an estimate of σ_ϕ , and computes the moment coefficients by (II-6) and (II-8). These are then inserted into the roll equation of motion. The solution for roll amplitude is then obtained and its RMS value compared with the assumed σ_ϕ . Convergence is usually quite rapid.

Now consider the nature of the coefficients appearing in (II-8) for a typical ship. Referring to Figure 2 it is noted that C_1 will normally be

positive and is, in fact, the product of the metacentric height and displacement, C_1 will be positive corresponding to the concave upward nature of the initial part of the curve, and C_5 is negative corresponding to the reversal of the curvature beyond approximately 30° . Thus, it is seen that if the RMS roll is in the medium range, the equivalent linear coefficient will be greater than the small angle linear value (stiff restoring spring) and the ship will have maximum roll response to wave component frequencies higher than the small angle natural frequency. For large average roll amplitude however, C_5 predominates resulting in a soft equivalent effective spring constant, and the maximum response is to frequencies lower than the small angle natural frequency.

This, qualitatively, describes a situation in which the consideration of certain nonlinear forces in the equations of motion has the effect of modifying the results that might have been obtained by a linear analysis, but without introducing any radical changes in the behavior.

Let us now consider another kind of nonlinear term which may be included in the roll equation of motion. Recall that the higher order damping and restoring terms in (II-2) and (II-7) may be considered as higher order derivatives in a Taylor Series expansion of the perturbation force about a mean state of motion of the ship. In such an expansion, there will be higher order mixed derivatives as well, exemplified by a roll restoring moment term of the following form

$$R(\phi, y) = K_{\phi y} \phi y. \quad (\text{II-9})$$

This may be thought of as expressing the change in the linear restoring moment coefficient, C_1 , with changes in the heave position of the ship designated by y . The method of calculating $K_{\phi y}$, as well as details of the analysis whose results are given here, are found in a paper by Paulling and Rosenberg (1959). Including just this nonlinear term, the roll equation of motion (II-1) becomes

$$I_x \ddot{\phi} + C_L \dot{\phi} + C_1 \phi + K_{\phi y} \phi y = K_\phi(t). \quad (\text{II-10})$$

Let us now assume that the ship is proceeding in regular head or following seas so that, by symmetry, the roll excitation, $K_\phi(t)$ is zero. In this case, the heave motion is sinusoidal and is given by $y_0 \cos \omega t$. Equation (II-10) then becomes

$$I_x \ddot{\phi} + C_L \dot{\phi} + \phi(C_1 + K_{\phi y} y_0 \cos \omega t) = 0 \quad (\text{II-11})$$

For the time being, ignore the damping, C_L . The resulting equation is known as Mathieu's equation and has solutions expressible in the form of special functions. It should be noted that this is a linear differential equation in ϕ . The unique feature of the equation is the presence of a time-dependent coefficient of the roll motion variable ϕ .

The solutions to Mathieu's equation have a property of considerable importance in ship rolling problems in that for certain values of the frequency, ω , the solution is unstable. Physically, this implies that if the roll motion described by (II-11) is taking place in an unstable region, the amplitude will grow until limited by a physical constraint not included in this equation. The unstable frequency may be found as follows.

Introducing the change of variable $\tau = \omega t$, equation (II-11) (with C_L neglected) may be rewritten

$$\frac{d^2 \phi}{d\tau^2} + (\delta + \epsilon \cos \tau) \phi = 0 \quad (\text{II-12})$$

where

$$\delta = \frac{C_1}{I_x \omega^2} = \left(\frac{\omega_n}{\omega} \right)^2$$

$$\epsilon = \frac{K_{\phi y} y_0}{I_x \omega^2}$$

$$\omega_n = \sqrt{C_1 / I_x} = \text{natural frequency in roll.}$$

Figure 3 is a graph of ϵ versus δ for the Mathieu equation in which regions corresponding to stable solutions have been shaded. It is seen that for small values of ϵ , corresponding to small heave motion, y_0 , we have unstable

solutions of Mathieu's equation and therefore, unstable rolling motion occurring for

$$\delta = 1/4, 4/4, 9/4, \dots = (n/2)^2; n=1, 2, 3, \dots$$

Since δ is the square of the ratio of the natural frequency to exciting frequency, this means that unstable roll occurs when this frequency ratio takes on half-integer values. The lowest and widest unstable region occurs at an exciting frequency of one-half the natural frequency. Thus unstable roll will be excited if the ship encounters head or following seas with a frequency of encounter equal to one-half the natural frequency of roll. For usual ship-wave proportions of interest, this occurs only in following seas. Note also that the instability may occur at an encounter frequency equal to the natural frequency of roll, $3/2$ times the natural frequency and so on. The width of the unstable region for these higher frequencies is less however than that at the lowest frequency with the practical result that for unstable motion to be excited at the higher frequency, the amplitude of the variable term, ϵ , and therefore y_0 , must be greater. For practical purposes, only the two lower frequencies have any significance.

The existence of this parametrically induced unstable motion has been investigated theoretically and experimentally by Grim (1952), Kerwin (1955), and Paulling and Rosenberg (1959). The former two utilized a ship model equipped with a pair of weights which rotated at constant angular velocity in the vertical plane. In this way, the vertical position of the center of gravity, thus the metacentric height was forced to vary sinusoidally. The latter performed a constrained model experiment in which the ship model was mechanically forced to oscillate vertically in heave but with mechanical attachment to the oscillating mechanism which allowed freedom in roll. Thus the condition of sinusoidal heave was induced artificially in calm water. In both types of experiments, an unstable rolling motion was found to be set up at frequencies predicted by the Mathieu instability chart. Grim showed that the motion would ultimately reach a steady state value determined by nonlinear damping. Kerwin, in addition to his experiments, carried out a numerical integration of the equation of roll motion. He concluded from this solution that the

transient behavior in the region of instability was quite sluggish and that a large number of oscillations would be experienced before the amplitude of roll, starting from a small arbitrary disturbance, would grow to appreciable magnitude. This conclusion is not in accord with observations of the model behavior during some of the experiments which form the subject of later parts of the present paper and we shall return to this point.

The above discussions has described the phenomenon of parametrically induced unstable roll motion. The excitation consists of the periodic variations in static transverse stability which result from the variation in geometry of the immersed hull during periodic heave oscillation of the ship. When the ship moves through head or following seas, the immersed geometry variations result from the changing water profile along the ship or wave surface, as well as from the ship motion. The relationship between transverse stability and the wave proportions in following seas has been investigated by Paulling (1961). It is shown that significant variations in the righting arm curve are caused by the changes in the immersed geometry as the ship is overtaken by successive crests and troughs in following or head seas. In general, for waves of length nearly equal to the ship length, the ordinates of the righting arm curve are increased if a wave trough is near amidships and decreased when a crest is near amidships. The effect is more pronounced in steep waves and for ships of low freeboard. Typical curves of righting arm for these two conditions, crest amidships, and trough amidships are shown in Figure 2.

If the ship is moving through a following sea, it is, therefore, apparent that the ship will experience periodic variations in its transverse stability, and these variations will affect the roll motion of the ship. Although the preceding discussion was concerned with regular waves, a somewhat similar phenomenon but perhaps of a transient nature might be expected if the ship encounters a wave group having sufficient regularity and steepness. Such behavior has, in fact, been observed during some experiments to be described in the next section and the nature of this observed motion suggests

that the wave induced stability changes and resulting parametrically induced roll play an important role in extreme motions and capsizing.

The examples just described illustrate the point that contemporary linear and nonlinear ship motion theory can reveal many features of ship behavior of interest to a study of capsizing, but it falls short of describing all aspects of the problem. This suggests that experiments, conducted in conditions which are as realistic as possible, offer the best possibility for an initial study of capsizing. The primary objective will be to gain insight and understanding of the basic phenomena. A second purpose will be to gather some data upon which to base conclusions and to be used as calibration for a possible later theoretical study.

As noted in the Introduction, experiments utilizing radio-controlled free running ship models have been conducted several times in the past to study aspects of ship behavior and control for which adequate theory is lacking or for which conventional towing tanks are inadequate. In order to conduct free running experiments, one requires, in addition to a suitable test site, certain hardware items.

These include the test model itself, complete with radio controls, scaled autopilot steering systems, self-contained propulsion and monitoring instrumentation to record the pertinent motion variables, apparatus for recording the wave conditions in the test area, and some kind of floating platform from which to conduct the experiment. Such experiments performed in San Francisco Bay during the past three years are described in the following section.

III. THE EXPERIMENTS

Test Site and Sea Spectra Measurements and Analysis

San Francisco Bay offers a unique combination of wind, sea, and topography that makes it well suited for model experiments that could not be conducted in a laboratory. The test area is a region of gradually shoaling water with an average depth of from eight to twelve feet and a mud bottom.

Tidal currents are generally under one knot and the test area is outside of the regular commercial traffic lanes.

During the summer months, the overall wind pattern is extremely stable and repeats itself day after day. The hot air rising in the central valley draws the cooler ocean air through the Golden Gate. The test site is located down wind and slightly off to one side. The fetch is between three and six nautical miles in the form of a diverging funnel, two miles wide at the Gate and over four just before the test area. The overall geometry of the area is shown in Figure 4. On a typical test day, the winds would be light in the early morning and build gradually to about fifteen knots, depending on location, by mid afternoon. The waves are a typical "wind sea". Ocean swell is rarely noticeable in the Bay and is of no consequence in the test area.

The waves were measured using an array of step type wave gages. Three of the gages were mounted on arms extending from a wave buoy and the fourth gage was located at the center. The wave buoy is of the tension leg variety, each interconnected column being held down with its own anchor line. The buoy is very stable and has virtually no motion in heave and probably less than ten degrees in yaw in extreme conditions. Since the support vessel supplied electrical power and carried the tape recorder, it was necessary to anchor and connect with the buoy via a long electrical cable on the bottom. The wave measurements were monitored with a strip chart recorder and the observed wind and sea conditions recorded. The analog records were later digitized at 0.2 second intervals. The spectral analysis was conducted using a fast Fourier analysis technique with 2048 points and a 0.4 second time interval. Smoothing was done by block averaging over eight or sixteen frequencies.

The waves were recorded for fifteen minutes approximately every hour and one half or when there was a significant change in conditions. Figure 5 shows the four spectra measured on 17 SEP 1973. The growth of the spectrum appears to follow the general description of a fetch limited sea as reported by JONSWAP, the Joint North Sea Wave Project

[Hasselmann, et al (1973)]. A parameterized one-dimensional spectrum was used to fit that data. The spectrum was given as the product of a Pierson-Moskowitz (1964) type spectrum with parameters α and f_m :

$$S^{PM}(f) = \alpha g^2 (2\pi)^{-4} f^{-5} \exp[-1.25(f_m/f)^4] \quad (III-1)$$

and a "peak enhancement" factor:

$$\gamma \exp[-(f - f_m)^2 / 2\sigma^2 f_m^2], \quad (III-2)$$

where $\sigma = \begin{cases} \sigma_a & \text{for } f \leq f_m \\ \sigma_b & \text{for } f \geq f_m \end{cases}$ width of the spectral peak

f_m = frequency of the peak

$$\gamma = S^{OBS}(f_m) / S^{PM}(f_m)$$

Typical values of the constants can be estimated from the non-dimensional fetch

$$\tilde{x} = xg/U_{10}^2$$

where x is fetch and U_{10} is the wind velocity at ten meters, using

$$f_m = \frac{g}{U_{10}} 3.5 \tilde{x}^{-0.33} \alpha = 0.076 x^{-0.22} \quad (III-3)$$

the (JONSWAP) estimates of γ , σ_a , and σ_b showed much scatter but were assumed to be approximately 3.3, 0.07, and 0.05, respectively. The fetch derived from Equation (III-3), given the spectral peak f_m and the measured wind velocity $U_s = U_{10}/1.11$, ranged from approximately one nautical miles at low wind speeds to about seven nautical miles at the higher wind speeds. The scatter in the present data is due in part to inaccuracies in wind speed measurements since these were not taken over the full fifteen minute wave recording period. However, the derived fetch appears to correlate with the direction of the current in the generating area. The peak ratio γ , unlike JONSWAP, varied smoothly from approximately 3.3 for low spectra to 0.98 for the highest. The fit of the parameterized model with the experimental spectrum is also shown in Figure 5. The parameterized model was

computed using the observed peak frequency f_m and amplitude $S^{OBS}(f_m)$

and appears to agree reasonably well. It may be possible to use such models as aids in interpolating for spectra at times other than those measured.

On one occasion, ten wave recordings were made during a four hour period in order to investigate wave stationarity. Consecutive records yield similar spectra with amplitude and directional properties that correlate very well with the observed values. Furthermore, the changes appeared to be smooth functions of time. If there were no unusual changes in the observed wind and wave characteristics, it is therefore probably reasonable to interpolate between consecutive measurements for an estimate of intermediate sea conditions.

At a scale ratio of $\lambda=30$, the two largest spectra of Figure 7 correspond to Pierson-Moskowitz spectra with RMS wave heights of 16 ft and 22.25 ft respectively (based on the peak spectral ordinate). The miss-match in frequency is of little concern since the actual experimental spectra are to be used in analyzing the results.

All of the spectra peaked at $f = 0.38$ Hz or above with one exception which peaks at approximately 0.32 Hz. The large spectrum on that day is the only one with any energy at $f = 0.3$ Hz, which corresponds to a deep water wavelength of 56.9 feet. Even at this frequency there is only a nine percent decrease in the wavelength due to shallow water. Since this is still 3.1 times longer than the models being tested, the effect of the shallow water is not considered to be significant.

Some spectra exhibited a small spike below $f = 0.03$ Hz peaking at zero frequency. These correlate well with rapid changes in the tide at the time of recording.

The major reason for experimenting in the open water of San Francisco Bay was the desire to investigate ship capsizing in more or less "reasonable extreme" sea conditions. This of course implies the possibility that the sea spectrum could be multi-directional. A measure of the directionality was considered vital for the interpretation

of the resulting motions so a number of analysis techniques were evaluated. The first method involved computing the first few terms of a Fourier series expansion of the directional spreading function at each frequency [Oakley (1973)]. This method has not proven to be well suited to the analysis of a small number of gages. Spurious peaks and negative spectral estimates are frequent problems. The peak direction can be accurately computed but not the amount of spreading. Knowing the peak direction, θ_0 , a $\cos^n(\theta - \theta_0)$ spreading function could be assumed. The current literature on the subject of directional spreading advocates a cosine squared spreading function within the generating area. A narrower spreading relation is more appropriate the farther one moves from the region of wave generation. The test area appears to be within the wind wave generating region so a moderately broad spreading function should be applicable. However, this does not appear to be the case from observations. The waves appear to be quite unidirectional and relatively narrow band in character. Another analysis technique investigated was the maximum likelihood filter developed by Capon (1969). This procedure requires only the inverse of the cross-spectral matrix and is therefore rather simple to use. The frequency-wavemaker spectrum estimate is given by

$$\hat{S}(k, f) = \sum_{j, l=1}^K [\hat{Q}_{jl}(f) \exp(-ik \cdot X_{jl})]^{-1}$$

where

$[\hat{Q}_{jl}(f)]$ = the inverse of the cross spectral matrix with elements corresponding to the gage pair $j-l$.

k = wave number (directional)

X_{jl} = distance between gage pair $j-l$ in an array of K gages.

This method offers significantly improved resolution over the Fourier series method and yields positive definite spectral estimates. Cross plots of the directional spectrum $S(\theta, f)$ sequence number (3), at selected frequencies as shown in Figure 6. The directions shown are relative to the

buoy. The peak direction and relative narrowness agree very well with observation. The narrowest peak corresponds to a cosine spreading function raised to the 6.8 power. Resolution appears to be acceptable for wave lengths up to an order of magnitude longer than the average distance between gage pairs. Resolution is not unlimited, however, with four gages. The filter is only able to resolve a pair of sine waves unambiguously if they are separated by at least 15 or more degrees in azimuth. Since the spectral estimate is given by the inverse of a trigonometric series, there is a tendency to spread energy into all directions. The amount of spreading increases with a decrease in frequency or the number of gages. Spreading also increases with the amplitude of the peak of the distribution with such a small array. Care must therefore be taken in applying the results. Small amounts of spurious energy, relative to the peak, going in the wrong direction may show up in the prediction of ship accelerations, for example.

Improved resolution is possible using a linear programming approach [Oakley (1973)]. This technique attempts to minimize the largest deviation between the measured cross spectrum and a parameterized estimate. The method is capable of achieving a very high degree of resolution, even for a limited number of gages, by looking only at those directions containing energy. If pushed too far, however, the directional distribution estimate begins to resemble a distribution of spikes even if the actual distribution is smooth. Some care in interpreting the results is therefore in order. If the spectrum is known to be "smooth", a smoother parameterization than the tent functions used in Oakley (1973) should be considered. The linear programming technique was used to check the results using Capon's analysis. The results support the previous observation that the directional distributions tend to be very narrow, especially for the higher seastates and lower frequencies.

Model Experiments

The experiments were conducted using two models of the same length. The first was a medium speed, full form hull ($\lambda = 30$ American Challenger Class) of wood construction (Haddara, et al, 1971). The second model represented a high speed, narrower hull form ($\lambda = 55$, Sealand-7 Container Class). (Chou, et al 1973). The latter was most fully instrumented and will be described below, but comparisons will be made on the basis of a $\lambda = 30$ scale ratio.

The second model is a fiberglass reinforced epoxy sandwich construction with a balsa core. Large hatches with O-ring seals were provided for easy access and proved to be completely watertight. Table I lists the particulars of the model. The model is self-propelled, using a 24 volt DC PM field motor, and radio controlled. The rechargeable battery circuitry is divided to provide power to the instruments and propulsion separately. Four batteries are also used as moving

The autopilot system was designed to simulate a typical full scale system with a dead zone circuit. The error signal is the sum of the scaled yaw and yaw rate signals.

The righting arm curves for the model in calm water and in waves are given in Figure (2a,b).

After recording the waves, the wave buoy cable was disconnected and left with the anchored dingy. The model was then launched such that the wave buoy would be passed close aboard at approximately half way through the run. The compass heading of the model was recorded but the heading characterizations, i.e., following, quartering, or beam, were selected strictly by eye. During the course of the run the model would occasionally deviate from the desired heading due to initial heading errors during uncaging, drift of the yaw gyro (small), or a change in the observed principal direction of the

TABLE I

CHARACTERISTIC OF THE 1973 SL-7 MODEL

CONDITION	LIGHT	HEAVY
Length Overall	17.12 ft	-
Length Between Perpendiculars	16.36 ft	-
Beam	23.125 in.	-
Depth	13.375 in.	-
Draft	7.000 in.	8.49 in.
Displacement	630 lb	814 lb
Block Coeff.	.535	.570
Midship Section Coeff.	.940	.950
Water Plane Coeff.	.669	.719
KM	9.827 in.	9.796 in.
δ GM (Six Steps)	0.113 in.	0.091 in.
GM Position 2	0.102 in. (.44%B)	0.090 in. (.39%B)
GM Position 4	0.328 in. (1.18%B)	0.272 in. (1.18%B)
GM Position 6	0.554 in. (2.44%B)	0.453 in. (1.97%B)
Speed Setting 1	4.65 fps (0.100Fn)	4.53 fps (.181Fn)
Speed Setting 2	6.00 fps (0.240Fn)	6.10 fps (.244Fn)
Speed Setting 3	7.45 fps (0.298Fn)	7.58 fps (.303Fn)

ballast for GM changes.

A tape recorder is available to record seven channels of data selected from the following:

- pitch, roll, yaw, and yaw rate angles (gyros)
- heave, sway & surge accelerations (located as near to the CG as possible)
- motor RPM, relative water speed, and rudder angle.

seas. Course corrections were radiced to the model in the form of two degree steps in the yaw gyro heading angle. If the model was able to maintain course, the realtive heading was held substantially constant. Since the sea conditions were often extreme, the model would occasionally experience a broach or a series of large yaw forces and be thrown off course into a large quartering or even beam sea heading. At high speeds there was sufficient directional control for the rudder (generally hard over) to bring the model slowly back on course as soon as the large group of waves had passed. At the lowest Froude number and largest seas, the model on a

number of occasions was unable to recover for long periods and wallowed in beam seas until a long lull arrived. The spectral analysis of these runs generally show very large values at low frequencies in the yaw and rudder angles.

If capsize occurred before the end of a fifteen minute run, the model was recovered, the yaw gyro re-caged, and the procedure repeated until there was a noticeable change in sea conditions or approximately one hour had elapsed since the last wave measurements. Launching and recovery in high seas was a tricky operation requiring both skill and time. Two long runs or three to four short runs were generally all that could be done between wave measurements. Nevertheless, a substantial number of experiments were conducted in a variety of sea conditions, speeds, GM's, and headings.

At the completion of the day's testing the onboard model tape recorder was removed and the analog signal inspected on a strip chart recorder. The data were digitized each week and the results preserved in both analog and digital form.

Many runs were too short to make either a statistical or spectral analysis meaningful. Only runs over seven minutes have been selected for statistical analysis, the majority being over ten minutes. Many of these involve rather violent motions, especially in roll, yaw, and rudder deflections. These are necessary conditions for a capsize to be likely, but this makes a comparison with a linear theory analysis rather difficult.

The mean relative speed between the model and water was measured on numerous runs using a paddle wheel type speedometer. Figure 7 is a plot of the mean speed versus significant wave height (interpolated to the time of the run) for the various headings. The measured speed is seen to decrease with increasing significant wave height, even in following seas. If there were significant surge motions, the speedometer would be expected to read a lower value due to the decrease relative velocity between the model and water velocity on the face of the wave. Computations were made with a linear ship motions

program using both the calm water speeds and the lower speeds reported by the speedometer. Due to the nature of the folding of the motion spectra for conversion to the encounter domain, the frequency distribution is quite sensitive to speed changes. Good frequency agreement was found for speeds close to the speedometer readings, rather than the calm water values. This would suggest that the velocity did indeed decrease and that in the main surging was not too significant. This agrees with the observations made in the Bay. An estimate of surging is possible by using the surge accelerometer data taken on about a third of the runs. The RMS surge motion and RMS surge velocity was obtained by integrating the acceleration spectrum. Typical motion amplitudes were less than 0.5 feet and speed deviation less than eight percent about the mean in the larger seastates.

The principal cause of the speed decrease is presumably due to the large rudder deflections required to keep the model on course in the following and quartering seas. A plot of the RMS rudder deflections versus significant wave height, speed, and headings showed a large amount of scatter. This points to the need for some further experiments expressly to evaluate the speed decrement due to rudder motions.

Motor RPM was not recorded due to channel limitations. It was checked, however, and found to be sufficiently constant.

The heave and sway accelerometers ($\pm 1.0g$) were adjusted to have gains of approximately two-thirds of a g . Subsequent analysis suggests inadequate resolution may be a problem in the low seastates where the accelerations are only a small percentage of full scale readings. The surge accelerometer ($\pm 0.5g$) had a higher gain factor and is believed to have worked well.

Pitch and roll angle measurements appear to be accurate. Since full scale yaw range needs to be large, it should be remembered that very small yaw motions are only a small percentage of the calibration figure.

Observations

All capsizes observed in the course of our experiments occurred in following

or quartering seas, and these, as was pointed out in an earlier section, are the headings of ship relative to waves in which the stability is most strongly affected by the waves. By observing the capsize and the motion picture records of them, it became clear that the attenuation of stability by the waves played a very important role in nearly all capsize. Further, it was possible to distinguish three distinct modes of capsizing which may be described as follows.

Mode 1: Low Cycle Resonance. This refers to an oscillatory rolling motion which builds up rapidly, i.e., in two to five cycles, to a very large amplitude, culminating in a capsize.

The phenomenon appears to occur in approximately the following sequence. The model, while operating in following or quartering seas, encounters a group of especially steep and regular waves. When the crest of a wave is about amidships, the stability of the model is greatly reduced and it takes a large roll. This wave moves on past the model and a trough comes into the amidships position while the model is heeled over, resulting in sharply increased stability. This causes the model to "snap" back upright, acquiring a high roll angular velocity by the time it reaches the upright position. Another wave crest, meanwhile, is moving into the amidships position, resulting in diminished stability once again as the ship starts rolling past upright and to the other side. The ship then rolls far over to the side against a diminished restoring moment. If now another trough moves into the amidships position with the correct timing, the roll will be stopped and the model snaps upright again. This process continues until either the model capsizes or it moves out of the wave group and the motion dies down. This mode of capsize is seen to be related to the Mathieu motion instability. It results directly from the periodic stability variations experienced by the ship moving through waves and in its most pronounced form takes place at one-half the encounter frequency, thus at the first Mathieu unstable frequency.

Mode 2: Pure Loss Of Stability. This usually occurs in a following sea at high speed. The model is observed

to encounter one or more very steep and high waves and, with little or no preliminary rolling motion, simply loses all stability when a crest moves into the amidships position and "flops" over. The essential prerequisite for this to occur is a model speed nearly equal to the wave phase velocity so that the model remains almost stationary relative to the crest for a sufficient length of time to capsize. The necessary wave would be of about the same length as the model and the height would be sufficient to immerse the deck in the crest with the model upright. This, of course, implies a high model speed since a Froude number of 0.4 is required for the model speed to be exactly equal to wave speed in waves of length equal to model length. From motion picture records of several capsize of this nature, it appeared that a model speed lying between the group velocity (one-half the phase velocity) and the phase velocity could result in this mode of capsize.

Mode 3: Broaching. This is the most dynamic mode, in appearance, and has received the most attention in the previous literature. In this mode of capsize, the model is struck from astern by three or four steep breaking seas in succession. As each wave strikes it, the model is forced to yaw off course to such an extent that the steering system is unable to correct the heading in the time interval between waves. The breaking seas striking the model and the dynamic heeling moment resulting from the turn combine to cause capsizing, again with the crest of a wave amidships. The essential features of broaching are the breaking waves striking the model in series, and the large heading deviation and associated angular velocity.

On several occasions, broaching was observed to occur without capsizing but with such total loss of directional control that the model swung through ninety degrees from a following sea course to beam seas. This was observed to occur most frequently in the light displacement condition where the rudder was less deeply immersed and therefore less effective. On several occasions, at low speed, the model was totally unable to regain its original course, but

remained in the beam sea condition even with the rudder hard over.

Wave Encounter Phenomena

A number of striking phenomena are observed in the wave pattern encountered by a vessel moving in following seas. None of these observations are new, yet some discussion of waves in the encounter domain is in order in light of the capsizing modes discussed above.

The most dramatic event in the encounter domain occurs at zero frequency. A vessel moving at or near the velocity of a wave crest may experience a significant non-oscillating force and a critical loss of stability. Capsizing due to broaching or to a pure loss of stability can result. The zero occurs at an absolute wave frequency of $g/(U \cos X)$ where $U \cos X$ is the ship velocity in the direction of wave travel. A singularity appears at this frequency in the prediction of the unrestored motions using linear theory. Normally few displacement vessels move at such large Froude numbers. Exceptions might be forthcoming as the speed of container ships increases and fast vessels are driven at their limit. Small craft, such as fishing boats and tugs, can experience problems when they operate in shallow water. The phase speed of wave travel can be reduced to sufficiently small values that such craft have no difficulty in running with a crest amidships. For example, a modern tuna seiner 144 feet on the waterline with a design speed of approximately 15 knots travels at the phase speed of a 125-foot wave. In thirty feet of water a deep water wave of 160 feet will have a length of approximately 140 feet, it will be steeper, and will run at this same ship speed.

The folding of the wave spectrum in the encounter domain is also familiar. Figure 8 shows a typical experimental wave spectrum in the absolute and in the frequency of encounter domain for two speeds. The collapse of virtually all of the energy to a narrow band of rather low frequencies should be noted and is potentially significant for purposes of mathematical simulation. The frequency collapse with respect to wave length is dramatically shown in Figure 9 presented by Kastner (1973). It is evident that, for a given ship speed U , a quartering situation may involve the

most serious concentration of energy. The situation could be serious if this frequency is near the natural frequency of rolling or in the neighborhood of the frequency for low cycle resonance. It has often been stated that the seaway appears to be a confused collection of waves with random phasing and the only thing regular about the sea is its irregularity. Intuition would therefore suggest that extended excitation at a single frequency or a very narrow frequency band is unlikely, especially when the spectrum tends to be rather broad band. It is apparent, however, that in following seas the picture is radically altered.

Excitation by a series of large waves at or near a single frequency appears to be a requirement for capsizing due to low cycle resonance. These conditions may be a far more common event than might first be assumed. For purposes of discussion, it will be convenient to consider a wave group or packet formed by the superposition of two regular wave components:

$$\eta(x,t) = \frac{1}{2} \{ \cos(k_1 x - \omega_1 t) + \cos(k_2 x - \omega_2 t) \}.$$

The number of waves in a group at any instant of time is given by

$$N[t=0] = \frac{k_1 + k_2}{2(k_1 - k_2)}$$

and is the number that would be observed from a photograph or film. This is not the same group size obtained from a record made at a fixed point, however. A wave probe located at $x=0$ would observe

$$N[x=0] = \frac{\omega_1 + \omega_2}{2(\omega_1 - \omega_2)}$$

waves in each group. Figure 10a is a plot of the sum of two waves of frequency 0.433 and 0.601 rad/sec. The number of waves in each group therefore represents an increase by a factor of 1.9 over the number that would be observed at a fixed instant. This

discrepancy is often overlooked when comparing wave records with motion records.

A dramatic change occurs with forward speed in following seas. The number of waves encountered by a vessel moving a speed $U \cos \chi$ is

$$N = \frac{(k_1 + k_2) U \cos \chi - (\omega_1 + \omega_2)}{2 \{ (k_1 - k_2) U \cos \chi - (\omega_1 - \omega_2) \}}$$

Here the observed wave frequency is

$$f_e = \{ (k_1 + k_2) U \cos \chi - (\omega_1 + \omega_2) \} / (4\pi)$$

which is zero when

$$U \cos \chi = \frac{\omega_1 + \omega_2}{(k_1 + k_2)}$$

As noted earlier, this is often a very high speed for more dangerous waves of sufficient length and amplitude. The ratio of the number of waves encountered at forward speed to the number observed at any one instant is therefore

$$\frac{U \cos \chi - \frac{(\omega_1 + \omega_2)}{(k_1 + k_2)}}{U \cos \chi - \frac{(\omega_1 - \omega_2)}{(k_1 - k_2)}}$$

Figure 10b shows the same set of waves pictured above but viewed in the encounter domain where $U \cos \chi = 22.7$ fps. There is a gain by a factor of 4.5 in the number of waves in each group over an observation at fixed time and a gain of 3.1 over an observation at a fixed point. These facts are well known but need to be repeated to be appreciated. If the ship moves at or near the group velocity it will encounter a very large number of waves even when the observed wave group or packet appears to be rather small. This also implies that the frequency of encounter could be very pure during such a wave group. If the wave group contains one or more large waves, their repeated encounter in the moving domain could become a favorable situation for low cycle resonance or a combination of resonance and large stability loss.

IV. LINEAR ANALYSIS & EXPERIMENTAL COMPARISONS

This chapter is an attempt to investigate the applicability of linear ship motions theory to the case of extreme following seas. There are a number of obvious reasons for pursuing a linear analysis. No other three-dimensional theory is so well developed. Strip theory has yielded surprisingly good comparisons with measurements despite a flagrant disregard of the restrictions on the input wave frequency, wavelength, and amplitude. Capsizing is a rare event and should be viewed in a probabilistic sense. A spectral description of the motions is far more amenable to long term extreme motion prediction than a time series derived from a nonlinear model.

On the other hand, there are numerous reasons why we should not expect particularly good agreement. Strip theory requires the input wavelength to be of the order of the beam. The solution is singular for the unrestored motions in stern seas when $\omega_e = 0$. The important variations in the righting arm curve discussed above are not included since only linearized hydrostatics are available.

Any rudder-autopilot system is likely to be quite nonlinear and it is not clear that an equivalent linearization will be sufficient. Obtaining a good linearized estimate of the roll damping (including the viscous contribution) and a measure of the waves actually encountered are also complications.

These are all potential problems. The significance of each one must be evaluated under actual tests conditions. The aim here is to see if there is sufficient agreement between theory and experiment to warrant further refinements in the linear prediction procedure.

The linear prediction of motions was made using the Salveson, Tuck, Faltinsen theory (1970). The computer program, developed at U.C. Berkeley, uses a modified version of the Frank close-fit method for calculating the two dimensional hydrodynamic coefficients. The first and second

"irregular frequencies" have been removed. Coefficients at the desired encounter frequencies are then obtained by interpolation from the coefficient table. The program will generate a Pierson-Moskowitz sea spectrum or accept either a point or a directional spectrum as input. The point spectrum can be spread using a cosine to the power r distribution if desired. An additional feature is the Froude-Krylov computation of surge motion. Surge is assumed to be a second order quantity in most linear, head sea ship motion predictions. This is not the case, however, for long waves in following and quartering seas where the surge exciting force can be significant.

No rudder-autopilot system has been included in the following calculations. The linear predictions for yaw have in general been low. The lack of a rudder is probably not too serious since the rudder-auto-pilot combination acts as a course stabilizing device.

Viscous effects become apparent in roll in the neighborhood of resonance. To account for this, a constant proportional to the significant roll amplitude is added to the roll damping coefficient. The total roll damping was computed from the results of roll decay experiments conducted in calm water at both zero and forward speeds. The linear damping term showed a marked increase with forward speed, approximately a factor of three over the zero speed estimate. The changes between the three Froude numbers, however, were not great and were not as significant as the changes with GM. The additional constant term was taken as the difference between the total damping and the computed wave or mechanical damping near resonance.

Virtually all of the experiments were conducted in rather large following and quartering seas. For completeness a few tests were also made in head and beam waves. Comparisons with the linear computations in many cases are probably not valid or particularly fair. Large waves and motions present a totally new geometry with substantially altered stability characteristics, both in the horizontal and vertical planes.

A large number of computations have been performed using the directional spectra computed by Capon's maximum likelihood filter. The comparisons of computations for all six degrees of freedom with the measured values has shown a large amount of scatter. No one experiment has yielded perfect agreement in all modes. In fact, the agreement has in general been poor. Much of this is attributable to the effects of deck wetness, broaching, and imperfect knowledge of the wave system actually encountered by the model. Nevertheless, the linear computations often show the correct trends and frequency bands. It is not obvious that the linear analysis should be rejected as a starting point for the estimation of ship capsizing potential in extreme following and quartering seas. In order to indicate the degree of agreement, a few experimental runs will be discussed in some detail.

Two days were devoted to head sea experiments as a supplement to the 1973 test season with the model in the heavy condition. The righting arm curve is given in Figure 2b. One of these suffered from very erratic wind, current, and sea conditions. The motions were extremely violent. The model experienced large amounts of slamming and green water on deck due to the relatively high speeds. Surprisingly, the linear motion estimates tended to underpredict pitch RMS in most cases by about 20%. Heave acceleration was not measured. Yaw, roll, and rudder experimental spectra had large values at low frequencies. This low frequency energy results from the nonperiodic motion induced by large slamming or bow submersion and the short term motions excited while the model is at reduced speed.

The second set of sea conditions were not quite as extreme, however some slamming and deck wetness was experienced. Unlike the following sea tests, the wave spectra were recorded during the model runs. A wave directional distribution is shown in Figure 11. It appears to be quite broad, a characteristic of the comparatively low amplitude waves. The significant wave height for this run was only 0.61 feet. The predicted and experimental pitch RMS agreed well for some runs and was low in others. The

experimental motion spectra and the linear estimate, using the directional distribution shown in Figure 11, for one of the head sea tests are shown in Figure 12. Pitch shows good frequency agreement but is somewhat low. Heave and sway acceleration were also very good considering their very low amplitude. Only roll is poor. This may have been caused by an increase in the effective righting arm in large waves at high frequencies of encountered. Most head sea runs showed good agreement in heave acceleration; reasonable surge and yaw comparisons, and somewhat erratic sway acceleration spectra.

Few head sea tests were conducted and a large number of uncertainties are involved in such complicated experimental and theoretical comparisons. Nevertheless, the above analysis suggests that the overall experimental and analytical procedures are substantially correct and might reasonably be extended to following seas.

As noted earlier, only a few of the model runs performed are likely to provide even a reasonable agreement with theory. In order to make a comparison of motion spectra valid, the model should be expected to run with only a small deviation from the mean speed and direction since the linear analysis assumes them constant. The runs long enough for meaningful spectral analysis occasionally involved severe rolling and varying degrees of broaching. It is also possible that some of these long runs encountered somewhat different spectra than those observed at the wave buoy before and after the run. The analysis of many runs show rather erratic agreement with theory. For purposes of discussion, a few examples having reasonable correlations in pitch have been selected for presentation.

All model runs were bracketed by wave spectral measurements. Interpolation between wave spectra for the time of the model run should be possible for many of these experiments. However, little is known about the changes in spectral shape and direction with time. The following results, with one exception, show the experimental motion spectrum bracketed by the linear computations using the two closest wave spectra measured before and after the run.

The motion spectra for a following sea run at Froude number 0.244 and GM number 6 is shown in Figure 14. The wind shifted suddenly to the North prior to this run and only the spectrum measured immediately afterwards is considered relevant. The directional distribution is shown in Figure 13 and is seen to be much narrower than the previous distribution. Roll, pitch, and surge show reasonable agreement. Yaw and sway, not shown, agree nicely in frequency content but not magnitude. The experimental spectral peak in yaw is a factor of five over the predicted value while the sway prediction is twice the experimental. The calculated heave acceleration spectrum differs wildly from the measured, however. This is surprising since good agreement was obtained for head seas. Part of the explanation may be due to the relatively low amplitude, resulting in experimental error. A more plausible explanation involves the input directional spectrum. A significant amount of broadening of the directional spectrum occurs using the maximum likelihood filter coupled with its approximation for input to the linear motions program. The head sea components were usually down by at least an order of magnitude from the peak of the directional distribution, yet there still appears to be enough energy to result in large heave accelerations. Truncating the input spectrum to a quadrant about the peak direction removes this large computed acceleration peak only if the ship sees nothing forward of the beam. As shown below, relatively better heave acceleration agreement was obtained by using such a truncated spectrum. The other modes of motion showed only slight changes and do not appear to be so sensitive to head and beam sea components.

Figure 16 shows the type of agreement obtained using an input spectrum truncated to a 120° sector about the peak. The point spectra for this day are given in Figure 15. The directional distributions were quite narrow and correspond to cosine spreading to the power 19, 10, and 30 for sequences 1, 2, and 3 respectively. The pitch spectrum agrees well. Yaw and sway were both underpredicted and the roll spectra are smaller than the measured value. The calculated heave spectra have an order of magnitude larger peak than the experimental one at high frequencies if the input spectrum

is not truncated. The low frequency peak at 0.25 Hz in Figure 16b is unaffected by truncation. Truncation is not the complete answer, however. A following sea run was made at speed and GM position 4 between spectra numbers (1) and (2) of September 17, 1973, Figure 5. The linear computations were made using both the untruncated and truncated distributions of which sequence 2 is given in Figure 6. Note that the secondary peak is at a considerably higher frequency than the primary direction. The motion spectra are shown for the "truncated" run in Figure 17. As before, only heave is materially altered by the input wave truncation. Pitch and surge show remarkably good agreement since the experiment was conducted midway between the two measured wave spectra. The rather good agreement between the measured surge and the Froude-Krylov computation in general indicates that diffraction forces are small.

The computed heave acceleration spectra are far too small. Without truncation of the wave input spectrum, the computed spectral peak of heave is too large by a factor of almost five. The frequency distribution, on the other hand, is better in the latter case. Roll exhibits some anomalous behavior in Figure 17c. Rolling appears to be taking place at three distinct frequencies, none of which agrees with the linear prediction. Figure 18 shows a portion of the time series of both pitch and roll for this run. The pitch record appears to contain some noise which can be ignored. For low frequencies, pitch has been shown to follow the wave slope and can therefore be used as a measure of the encounter frequency. Much of the rolling does occur at the pitch period which corresponds to the center peak of the roll spectra. The roll time history also shows what appears to be a low frequency component, slightly less than one-half the pitch frequency, superimposed on the higher roll frequency. It is not clear whether this represents intermittent low cycle resonance or some sort of flopping, possibly due to water on deck. The extreme low frequency rules out the probability of a wave system existing only at the time of the run.

TABLE II

CHARACTERISTICS OF THE
AMERICAN CHALLENGER USED FOR TIME
DOMAIN SIMULATION

LBP	529.0 ft	17.523 ft
L, for		
ordinates	521.0 ft	17.258 ft
B, molded	75.0 ft	2.484 ft
Depth molded		
to main deck		
at side	42.5 ft	16.894 in.
Depth molded		
to main deck ^a	46.5 ft	18.484 in.
Draft, fwd	33.5 ft	13.318 in.
Draft, aft	26.0 ft	10.336 in.
Δ	19652.5 tons	1600 lbs
Speed	27.7 ft/sec	2.99 ft/sec
Froude No.	0.215	0.215
Metacentric		
Heights:		
GM pos. 2	0.257 ft	0.102 in.
GM pos. 3	0.558 ft	0.222 in.

^aThis depth is greater than the depth of the actual ship because the model was constructed up to the level of the top of the bulwark rather than the main deck level of the ship.

V. NUMERICAL SIMULATION OF THE MOTION IN ASTERN SEAS

A complete analytical solution for the motion of a ship in waves requires first that the hydrodynamic forces acting on the ship be found. Solutions of the hydrodynamic problems have heretofore been obtained only under the assumption of small motion amplitudes, in which case the forces acting on the ship are computed as though the instantaneous position of the ship differs but little from its mean position. Such an assumption cannot be used in the present case where large deviations in position from the mean are an essential feature of the phenomenon. Instead, we observe that at high speed in following and quartering seas the frequency of wave encounter will be low and the ship motion will be determined largely by the hydrostatic forces. This enables us to retreat from the necessity of determining the hydrodynamic forces with great accuracy but to concentrate instead on the hydrostatic forces which may be computed for the exact position of ship and waves. These forces, plus additional external forces representing, e.g., the steering and controls, plus a simplified approximation to the relatively unimportant hydrodynamic terms then are used as the right hand side of the rigid body equations of motion. A standard numerical procedure is employed to integrate the equations of motion leading to a step-by-step approximation of the vessel's motion.

Formulation of the Problem

The ship is assumed to behave as a rigid body having six degrees of freedom. Newton's second law may be written for the body in the form

$$\frac{d}{dt} m \underline{v} = \underline{F} \quad (V-1)$$

and

$$\frac{d}{dt} I \underline{\omega} = \underline{M} \quad (V-2)$$

where

t = time,

m = mass of the body (ship)

\underline{v} = velocity vector of the mass center,

\underline{F} = force vector,

I = inertia matrix,

$\underline{\omega}$ = angular velocity vector, and

\underline{M} = moment of the force about the mass center.

The force and moment result from the gravitational force acting at the mass center and the interaction between the ship and the sea. The force and moment, in general, depend on the time history of the position of the ship in the sea. Under appropriate circumstances, however, this history may be characterized by the instantaneous position, velocity, and acceleration of the ship. The general problem is nonlinear in the motion variables in that the force and moment are nonlinear functions of the motion of the ship, and the rate of change of angular momentum in equation (V-2) contains nonlinear terms. As noted previously, we shall focus on an exact computation only of the hydrostatic part of the force.

Coordinate Systems

Since large amplitude motions are to be computed, it is necessary to clearly define the relationships between several coordinate systems to be used in describing the ship and water motion. The coordinate systems described below are right hand Cartesian systems.

A Newtonian reference frame is formed by the $\bar{O}\bar{x}\bar{y}\bar{z}$ system which is fixed in space and so oriented that the $\bar{x}\bar{z}$ -plane is the equilibrium sea surface, and the \bar{y} -axis is directed upwards.

A body coordinate system $Gxyz$ is fixed in the ship such that the origin, G , coincides with the center of gravity of the ship. In a ship of usual form, the x -axis is parallel to the baseline and directed forward, the xy -plane is parallel to the centerplane of the ship, the y -axis is directed upward and the z -axis to starboard.

The position of the ship mass center, G , may be specified in the fixed coordinate system by

$$\bar{x} = x_G$$

$$\bar{y} = y_G$$

$$\bar{z} = z_G$$

This may be represented by the vector

$$\vec{r}_G = \begin{Bmatrix} x_G \\ y_G \\ z_G \end{Bmatrix} \quad (V-3)$$

The velocity of the mass center is represented by the vector

$$\vec{v} = \frac{d}{dt} \vec{r}_G = \begin{Bmatrix} \frac{d}{dt} x_G \\ \frac{d}{dt} y_G \\ \frac{d}{dt} z_G \end{Bmatrix} \quad (V-4)$$

Any rotation of the ship coordinate system is uniquely defined by the modified set of Eulerian angles described below. These angles are similar to the ones given by Blagoveshchensky (1962), but differ from the ones used by Euler. The angles are defined as follows.

Consider the ship coordinates in a position before rotation with the $x, y,$ and z -axes parallel to the fixed $\bar{x}, \bar{y},$ and \bar{z} -axes. This is the orientation of $Gx_1y_1z_1$ in Figure 19. Rotate the triad about the y_1 axis to the yaw angle ϕ . This positions the frame as $Gx_2y_1z_2$ in the figure. Next, rotate about the z_2 -axis to the pitch angle ψ . The figure shows the yawed and pitched orientation as $Gx_3y_2z_3$. The final rotation is about the x -axis to the roll angle θ . The orientation of the ship coordinates, $Gxyz$, is indicated in the figure.

The Eulerian angles ϕ, ψ and θ are represented by the vector

$$\vec{\alpha} = \begin{Bmatrix} \phi \\ \psi \\ \theta \end{Bmatrix} \quad (V-5)$$

The angular velocities about the ship coordinate axes are denoted by $p, q,$ and r corresponding to components of the angular velocity vector along the $x, y,$ and z -axes. These angular velocities

may be expressed in terms of the Eulerian angles and their derivatives:

$$p = \frac{d\theta}{dt} + \frac{d\phi}{dt} \sin \psi$$

$$q = \frac{d\phi}{dt} \cos \theta \cos \psi + \frac{d\psi}{dt} \sin \theta \quad (V-6)$$

$$r = \frac{d\psi}{dt} \cos \theta - \frac{d\phi}{dt} \sin \theta \cos \psi$$

The notation is simplified by representing the angular velocities by the vector

$$\vec{\omega} = \begin{Bmatrix} p \\ q \\ r \end{Bmatrix} \quad (V-7)$$

If we define the matrix

$$B = \begin{bmatrix} 1 & \sin \psi & 0 \\ 0 & \cos \theta \cos \psi & \sin \theta \\ 0 & -\sin \theta \cos \psi & \cos \theta \end{bmatrix} \quad (V-8)$$

and note that

$$\frac{d\vec{\alpha}}{dt} = \begin{Bmatrix} \frac{d\theta}{dt} \\ \frac{d\phi}{dt} \\ \frac{d\psi}{dt} \end{Bmatrix} \quad (V-9)$$

then equations (V-6) are represented by

$$B \frac{d\vec{\alpha}}{dt} = \vec{\omega} \quad (V-10)$$

The moments and products of inertia in the angular momentum equation (V-2) are represented by the matrix

$$I = \begin{bmatrix} I_{xx} & -I_{xy} & -I_{xz} \\ -I_{xy} & I_{yy} & -I_{yz} \\ -I_{xz} & -I_{yz} & I_{zz} \end{bmatrix} \quad (V-11)$$

The moments of inertia are defined as

$$\begin{aligned} I_{xx} &= \sum m' (y^2 + z^2), \\ I_{yy} &= \sum m' (z^2 + x^2), \end{aligned} \quad (V-12)$$

and

$$I_{zz} = \sum m' (x^2 + y^2),$$

where the summations are taken over all particles of mass m' comprising the ship. The products of inertia are

$$\begin{aligned} I_{xy} &= \sum m' xy, \\ I_{xz} &= \sum m' xz, \end{aligned} \quad (V-13)$$

and

$$I_{yz} = \sum m' yz.$$

These moments and products of inertia are constants in the moving ship coordinate system, $Gxyz$.

In the $Gxyz$ coordinate system, the rate of change of angular momentum is given by

$$\frac{d}{dt} I \omega = I \frac{d}{dt} \omega + \omega \times I \omega, \quad (V-14)$$

Computation of Force and Moment

The present version of the computer program for the time-domain simulation of large amplitude ship motions assumes that the force and moment acting on the ship may be modeled using an accurate computation of the hydrostatic or Froude-Krylov forces plus an approximation to the hydrodynamic forces. The hydrodynamic approximation consists of using constant added mass coefficients, and constant linear and quadratic damping coefficients for computing the forces resulting from ship acceleration and velocity. Also, constant two-dimensional added mass and linear damping coefficients are used with averages of the water acceleration and velocity over each station to correct for the diffraction of the incident waves by the ship. The hydrodynamic approximations are not expected to

lead to serious errors if the Froude-Krylov force is dominant. This, as noted, is expected to be the case in the most severe capsizing situations in following or quartering seas.

Since large amplitude motions and finite amplitude waves are assumed, the hydrostatic restoring and coupling coefficients computed for the equilibrium position cannot be used. It has been shown by Paulling (1961) and others that there can be significant variations in the roll restoring moment as a wave progresses along the ship's length as well as the change in this moment caused by large amplitude roll angles. The Froude-Krylov force that is computed by the numerical simulator includes both the motion exciting force and the restoring force and moment that result from the situation of the ship in the system of waves at any time step during the simulation.

The sea surface elevation is given by the sum of sinusoidal waves in the fixed, $Oxyz$, coordinate system. The water surface is given by

$$\bar{\eta}(t, \bar{x}, \bar{z}) = \sum_{i=1}^N \eta_i(t, \bar{x}, \bar{z}) \quad (V-15)$$

where

$\bar{\eta}$ = the \bar{y} coordinate of the surface,

and

N = the number of wave components (in the present version of the program $0 \leq N \leq 20$).

The component wave amplitude is:

$$\begin{aligned} \eta_i &= A_i \cos(\bar{x}k_i \cos \delta_i \\ &\quad - \bar{z}k_i \sin \delta_i + \phi_i - \sigma_i t) \end{aligned}$$

where

A_i = the amplitude of the i -th wave,

σ_i = the circular frequency,

ϕ_i = initial phase angle,

$k_i = \sigma_i^2/g$ = wave number,

g = the gravitational acceleration,
and

δ_i = the direction of the wave
propagation.

The wave pressure is

$$p(t, \bar{x}, \bar{y}, \bar{z}) = -\rho g \bar{y} + \sum_{i=1}^N p_i(t, \bar{x}, \bar{y}, \bar{z})$$

$$p_i = \rho g e^{k_i \bar{y}} \eta_i \quad (V-16)$$

where

ρg = the specific weight of the water.

The Froude-Krylov force and moment may be obtained by integrating the pressure over the entire wetted surface of the ship. By applying Gauss' Theorem the force and moment are given by integrals of the pressure gradient over the submerged volume of the ship. The components of the force and moment in the ship coordinate system, $Gxyz$, are

$$F_x = - \iiint \frac{\partial p}{\partial x} dV$$

$$F_y = - \iiint \frac{\partial p}{\partial y} dV$$

$$F_z = - \iiint \frac{\partial p}{\partial z} dV \quad (V-17)$$

$$M_x = \iiint (z \frac{\partial p}{\partial y} - y \frac{\partial p}{\partial z}) dV$$

$$M_y = \iiint (x \frac{\partial p}{\partial z} - z \frac{\partial p}{\partial x}) dV$$

$$M_z = \iiint (y \frac{\partial p}{\partial x} - x \frac{\partial p}{\partial y}) dV$$

In equation (IV-17) the volume element is dV ; F_x , F_y , and F_z are forces in the x , y , and z -directions; and M_x , M_y , and M_z are moments about these x , y , and z axes. The integrals are taken over all volume up to the instantaneous sea surface within the envelope of the ship.

The hydrodynamic force resulting from the diffraction of the waves is approximated in the following manner. Two-dimensional added mass and damping coefficients for heave, sway, roll and roll-sway coupling are entered into the program as constants for each station of

the ship. Each time the sectional Froude-Krylov forces are computed by integrating the pressure gradient over a station of the ship, average values of vertical, horizontal and "roll" water velocities and accelerations are also evaluated for the station. The "roll" velocity and acceleration components are the first and second time derivatives of the slopes of constant pressure lines in the plane of the station. The products of the average velocities and accelerations with appropriate coefficients yield two-dimensional diffraction forces which are added to the two-dimensional Froude-Krylov forces before the longitudinal integrations are performed.

The ship hull is approximated by a number of polygons representing the stations of the ship. Each polygon is in a plane defined by a constant value of x in the ship coordinate system. A maximum of 24 line segments are used for each closed polygon station in the ship and a maximum of 25 stations may be used. The stations may be unsymmetrical and unequal station spacings are permitted. The position of the center of gravity may be in any fixed position relative to the ship.

The integrals of the pressure gradients, velocities and accelerations over each station made up with straight line segments are evaluated exactly, but with two restrictions on the angle of pitch. First, the pitch angle must not become so large as to cause the intersection of a station plane and the instantaneous sea surface to define multiple regions or a closed contour in the station plane. Second, the magnitude of a quantity like the product of the pitch angle and the slope of all component waves must be "small". These two restrictions are satisfied for vessels of usual proportions in waves with realistic slopes.

The two-dimensional forces and moment at each station are evaluated as functions of the form

$$f(x) = V' + \sum_{i=1}^N [C_i \cos(k_i' x) + S_i \sin(k_i' x)] \quad (V-18)$$

where

V' is obtained from the static $(\rho g \bar{y})$ part of the pressure,

C_i and S_i result from the sinusoidal pressure fluctuation for the i -th wave component, and

k_i' is a projection of the wave number onto the x -axis of the ship.

The relative magnitude of C_i and S_i depends on the phase of the waves relative to the center of ship coordinates at each instant of time. The integrals and moments of the functions like (IV-18) along the length of the ship are evaluated with the assumption that V' , C_i , and S_i vary linearly in x between adjacent stations of the ship.

The velocity dependent damping force is approximated in the following manner. Let P be one of the components of the force or moment M in the ship coordinate system, and let v be the corresponding component of linear or angular velocity. The force or moment is computed from

$$P = P_{wave} - vL - v|v|Q \quad (V-19)$$

where

P_{wave} = exciting force or moment due to the wave,

L = coefficient of linear damping for the particular motion component,

and

Q = coefficient of quadratic damping for the particular motion component.

There are three force equations and three moment equations in the form of (V-19). The equations are referred to the x , y , and z -directions in the ship coordinate system. Velocity dependent coupling between the directions of motion are not included in the present version of the program.

The constant added mass moments and products of inertia are added to

the rigid body elements of the inertia matrix that is given in equation (V-11). Added masses in the linear momentum equation are included by modifying the component of the force in each of the ship coordinate directions with an equation of the form

$$P' = P/(1 + \mu/m) \quad (V-20)$$

where

P' = the force modified by the added mass,

P = the component of the force as computed by (V-19),

μ = the added mass for the particular motion component, and

m = the mass of the ship.

There is one equation of the form of (V-20) for each of the x , y , and z directions in the ship coordinate system. After the forces are computed by equation (V-20) they are resolved into the Newtonian coordinate directions x , y , and z for integration of the linear momentum equation (V-15).

Time Domain Integration

The equations of motion are solved by numerical integration in the time domain. In order to perform the integration using standard algorithms, the equations of motion are rewritten as first order ordinary differential equations.

The position of the ship's center of gravity is determined by the linear momentum equation (V-1). This equation and equation (V-4) are rewritten as

$$\frac{d}{dt} v = \frac{1}{m} F \quad (V-21)$$

and

$$\frac{d}{dt} \omega = \tau \quad (V-22)$$

In equations (V-21) and (V-22) the vectors are referred to the Newtonian reference frame, $Oxyz$.

The rotations of the ship are governed by the angular momentum equation (V-2). Combining equations (V-2) and (V-14) and rewriting equation (V-10) give

$$\frac{d}{dt} \tilde{\omega} = I^{-1} [M - \tilde{\omega} \times I \tilde{\omega}] \quad (V-23)$$

and

$$\frac{d}{dt} \tilde{\alpha} = R^{-1} \tilde{\omega} \quad (V-24)$$

In equation (V-23) the moment vector M is referred to the ship coordinate system, $Gxyz$.

The vector equations (V-21), (V-22), (V-23), and (V-24) form a system of twelve simultaneous first order ordinary differential equations which may be integrated by standard numerical procedures. The current version of the program uses a fifth-order Adams type predictor-corrector algorithm developed by Glauz (1960).

Examples of Numerical Simulations

Several examples of motions simulated by the numerical time domain integration are presented here. These computations were performed for the *American Challenger* class of cargo ship for which a model was previously tested on San Francisco Bay. Details of the experiments with this vessel are given in the reports by Haddara, et al (1971) and Paulling, et al (1972). Characteristics of the vessel and its displacement condition for the simulations are given in Table II, located at the end of Chapter IV. The motion calculations were carried out at ship scale rather than at the scale of the model used for the experiments. The ratio of ship length to model length is 30.189, and the time scale for Froude number similarity is about 5.5. Metacentric heights corresponding to model ballast weight positions 2 and 3 were used for the simulations. The righting arm curves for the *Challenger* are shown in figure 20. In addition to the curve for still water, the righting arm for the ship in a longitudinal wave with crest amidship and trough amidship are plotted.

The simulated wave system for these examples was the sum of two sinusoidal waves traveling in the same direction. The circular frequencies of the waves were 0.133 and 0.601 sec^{-1} , which correspond to wave lengths of 1076 and 558 ft. The amplitudes of both wave components were equal in magnitude.

Three simulation runs for following seas are shown in Figures 22 through 30. The metacentric height for these runs is 0.550 ft. (GM position 3).

To initiate rolling, the waves approach the ship from the direction of ten degrees to starboard of dead astern. The amplitude of each component wave is five feet making a twenty foot maximum wave height in the group. The first simulation begins with the two wave components in phase at the position of the ships center of gravity. To decrease the effect of starting transients caused by the choice of initial conditions, all forces applied to the ship are multiplied by a ramp function which increases linearly with time from zero to one for the first 60 seconds of the run. Figure 21 shows the wave amplitude at the position of the center of gravity of the ship. The roll record is displayed in Figure 22. After about 120 seconds the rolling begins to take place at one half of the frequency of wave encounter. As the wave amplitude builds, the rolling becomes erratic rolling alternately with the encounter frequency and one half of that frequency. Figure 23 shows the pitch record for this run. The ramp function used for starting the simulation caused the attenuation of the pitch at the beginning of the record. Note that the pitch angle gives good indication of the wave slope for these waves which are longer than ship length. The pitch and roll experiment records for the SL-7 model are shown in Figure 18 exhibit this same erratic rolling with the roll frequency occurring at the wave encounter frequency and then at one half of this frequency.

Figures 24, 25 and 26 show the wave, roll, and pitch records for a simulation with the same initial conditions as before, except that the phase angles of the two waves are initially one half cycle apart causing the amplitudes to cancel. The starting ramp was reduced to 30 seconds. In this run the rolling is at the same frequency as the wave encounter, and the amplitude is less than half that of the previous example.

The last example, for following seas, shows the wave, roll and pitch records in Figures 27, 28 and 29. The initial conditions are the same as for the previous example except that an initial roll angle

of fifteen degrees to starboard has been added. Rolling begins at one half the encounter frequency which is close to the natural roll frequency for calm water and this roll amplitude. As the wave amplitude and roll exciting moment build up the ship is forced to roll at the encounter frequency.

Figure 30 shows a *Challenger* model experiment in following seas for the corresponding speed and GM condition. Although the experiment ended in a capsize with low cycle resonance and these simulations did not, both the experiment and the first and last following sea calculations show a tendency for the roll frequency to switch back and forth between the encounter frequency and one half the encounter frequency.

Two examples of capsize simulations in quartering seas are shown in Figures 31 through 37. The waves are the same as used for the following sea runs, but the direction was such that the waves approach the ship from 35 degrees to starboard of dead astern. At the beginning of the runs the two wave components are in phase.

The first quartering example is for a metacentric height of 0.257 ft (GM position 2). The wave record for this run is shown in Figure 31. The starting ramp was 60 seconds in length, and ended near the end of the first wave group. Roll and pitch records are in Figures 32 and 33. At about forty seconds from the start a wave crest comes amidship and the vessel takes a 14 degree roll to port. The next wave crest comes amidships at about sixty seconds and a starboard roll into the wave of 4 degrees is reached. The next roll is 22 degrees to port just after the next crest passes. The ship rolls to starboard as the waves begin to build in the second wave group. The maximum starboard roll of 23 degrees is reached as the next crest moves away. The roll momentum imparted the ship by the increased righting arm of the next trough coming amidship together with the reduced stability in the crest that follows causes the ship to capsize to port, clearly an example of low cycle resonance. Figure 34 shows the last two and a half minutes of a model run corresponding to the same speed, heading relative to the waves and GM condition. The experiment also ended with a capsize to port caused by low cycle resonance.

An example of pure loss of stability is shown Figures 35 through 37. The metacentric height was 0.557 ft. (GM position 3). The wave amplitude at the center of gravity of the ship is shown in Figure 35. Roll and pitch are in Figures 36 and 37. Rolling is at one half the frequency of wave encounter between 40 and 110 seconds into the run. After that the wave amplitude and the roll moment are so large that the ship is forced to roll at the encounter frequency. The vessel finally capsizes with the combination of a large port roll and a wave crest amidships.

VI. CONCLUSIONS

In this paper we have attempted to point out some of the difficulties in using available theoretical means to predict ship capsizing in heavy seas. In addition, special attention has been given to the usefulness of experiments conducted with radio-controlled free running ship models in wind-generated waves on open water.

In Summary

1. Linear ship motion can only broadly outline areas of speed, heading, and ship characteristics which may lead to trouble.
2. Classical ship motion theories which are augmented by some nonlinear terms may reveal phenomena, not apparent in results of linear theory, which may lead to severe motion. The ability to predict capsizing is still not available through such theories.
3. The open water experiments mentioned above yield great insight into the mechanics of capsizing. The phenomenon is a "rare event" in the statistical sense, however, and very extensive experimental programs would be required to adequately describe the probability of capsize of just one ship configuration.
4. An important side benefit of these experiments has been the development of methods of deducing the directional properties of wind generated waves from measurements made by a sparse gage array. These measurements show that good similarity exists between the wave conditions in the model test area and full scale storm waves at sea.

5. The knowledge gained in the experiments has led to the development of a time-domain numerical simulation of the large amplitude motion of a ship in following and quartering seas. Records of severe motions including capsizes have been computed by this technique, and the computed motions resemble, in general, the motions of the model under similar sea conditions.

6. The characteristics of wave groups encountered by the model have considerable influence on the tendency to capsize. Some of these characteristics are discussed here, and it is expected that the statistical nature of wave groups is a fruitful subject for future study.

ACKNOWLEDGMENT

A large number of individuals have participated in this project at various stages. Especial mention should be made of the contributions of Dr. Sigismund Kastner who brought much valuable experience from Hamburg when he joined the project in its early stages. Several graduate students, especially Shian-Jiun Chou, Robert J. VanSlyke, and Peter F. Zink, have assisted greatly, particularly in the conducting of experiments and in processing of experimental data. The patience and assistance of Marylou Newby in typing the manuscript is also greatly acknowledged.

This work has been sponsored by the U. S. Coast Guard under Contract DOT-CG-84,549A.

REFERENCES

Blagoveshchensky, S.N., "Theory of Ship Motions," Translation ed. by L. Landweber, Dover, Vol.1, pp 140-143, 1962.

Capon, J., "High-Resolution Frequency Wave Number Spectrum Analysis," Proc. IEEE, Vol.57, No.8, Aug. 1969.

Chou, S.J., et al, "Capsizing Experiments in San Francisco Bay -- Annual Report 1973," Dept. of Naval Architecture, Univ. of Calif. Berkeley, June, 1973.

Grim, O., "Rollschwingungen, Stabilitat und Sicherheit in Seegang," Schiffstechnik, Vol.1, pp 10-21, 1952.

Glauz, R.D., "Adams Method of Integration of Differential Equations," Computing Services Report No. 13, Aerojet-General, Sacramento, Calif., May 12, 1960.

Haddara, M.R., et al., "Capsizing Experiments with a Model of a Fast Cargo Liner in San Francisco Bay," U.S. Coast Guard Project 723411, Naval Architecture Department, Univ. of California, Berkeley, Jan. 1972.

Hasselmann, K., "Measurements of Wind Wave Growth and Swell Decay During the North Sea Wave Project (JONSWOP)," Report by the Deutsches Hydrographisches Institut, Hamburg, 1973.

Kastner, S., "Analysis and Evaluation of Capsizing Experiments in San Francisco Bay 1971," Department of Naval Architecture, Univ. of Calif., Berkeley, Mar. 1973.

Kerwin, J.E., "Notes on Rolling in Longitudinal Waves," International Shipbuilding Progress, Vol.2, pp 597-614, 1955.

Oakley, Jr., O.H., "Directional Wave Spectra Measurement and Analysis Systems," SNAME Panel H-7 Seakeeping Symposium, Webb Institute of Naval Architecture, Oct. 1973.

Ochi, K.M., "Extreme Behavior of a Ship in Rough Seas," Transname Vol.72, pp 143-202, 1964.

Paulling, J.R., "The Transverse Stability Of A Ship In A Longitudinal Seaway," Journal Of Ship Research, Vol.4, No.4, pp 37-49, March 1961.

Paulling, J.R., "Stability and Ship Motions in a Seaway," USCG Office of Research and Development Project 713111, Dept. of Naval Architecture, Univ. of Calif., Berkeley, Sept. 1970.

Paulling, J.R., Kastner, S. and Schaffran, S.D., "Experimental Studies of Capsizing of Intact Ships in Heavy Seas," Technical Report. Dept. of Trans., U.S. Coast Guard, Contract DOT-CG-84, 549-A, Project 5940.1.1/GDST-3411, Nov. 1972.

Paulling, J.R. and Rosenberg, R.M., "On Unstable Ship Motion Resulting from Nonlinear Coupling," Journal of Ship Research, Vol. 3, No. 1, pp 36-46, June 1959.

St. Denis, M., "On a Problem in the Theory of Nonlinear Oscillations of Ships" Schiffstechnik, Bd 14, H 70, pp 11-14, 1967.

St. Denis, M., "Some Cautions on the Employment of the Spectral Technique to Describe the Waves of the Sea and the Response Thereto of Oceanic Systems," OTC 1819, Offshore Technology Conference, Houston, pp 827-840, 1973.

Vassilopoulos, L., "Ship Rolling at Zero Speed in Random Beam Seas with Nonlinear Damping and Restoration" Journal of Ship Research, Vol. 15, No. 1, pp 289-294, Dec. 1971.

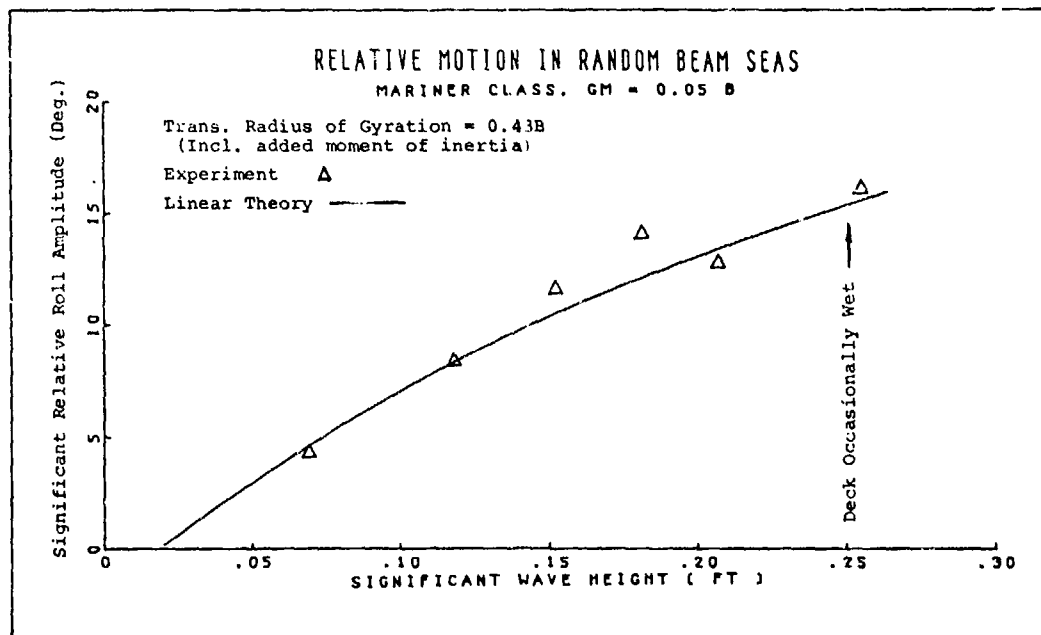


Figure 1.

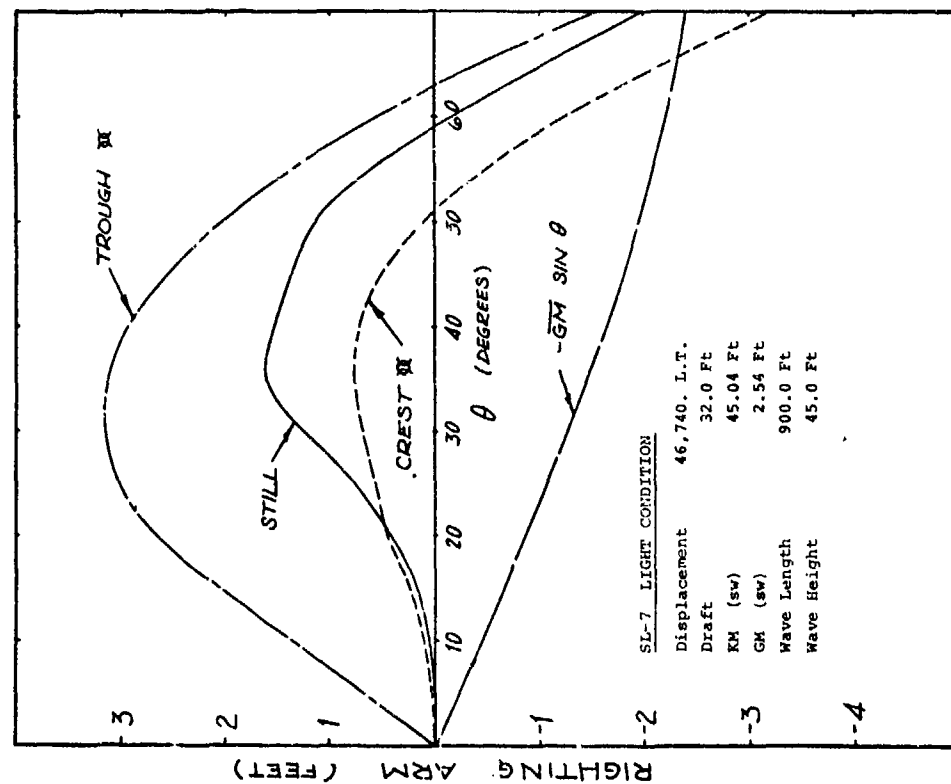


Figure 2 (a)

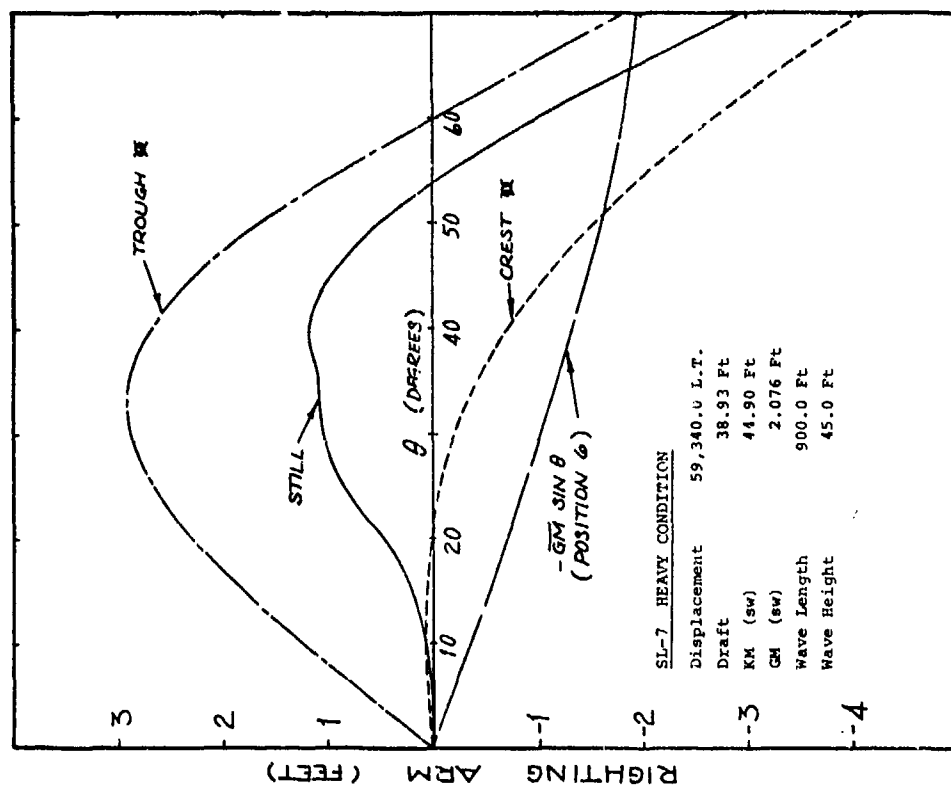


Figure 2 (b)

Righting Arm Curves for the Sealand-7. Full Scale. (See also Table I).

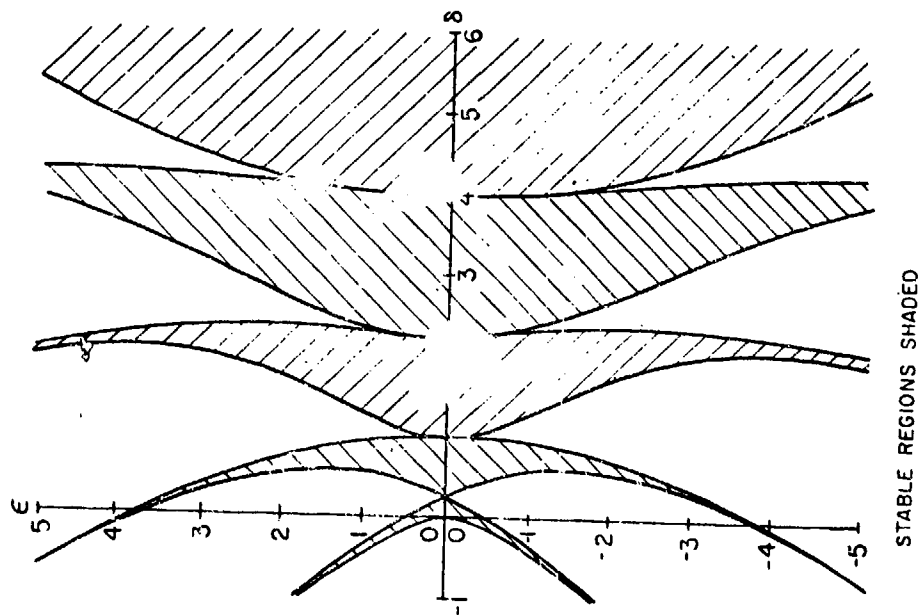


FIG. 3 STABLE AND UNSTABLE REGIONS
FOR THE MATHIEU EQUATION

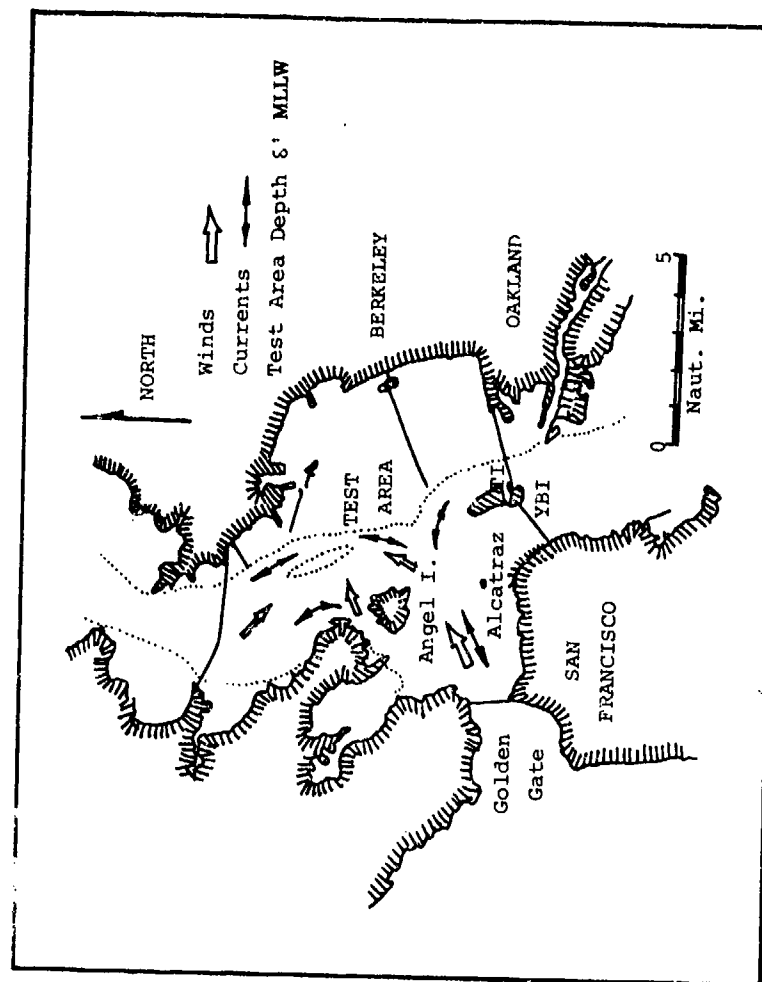


Figure 4 Test Site and San Francisco Bay Area

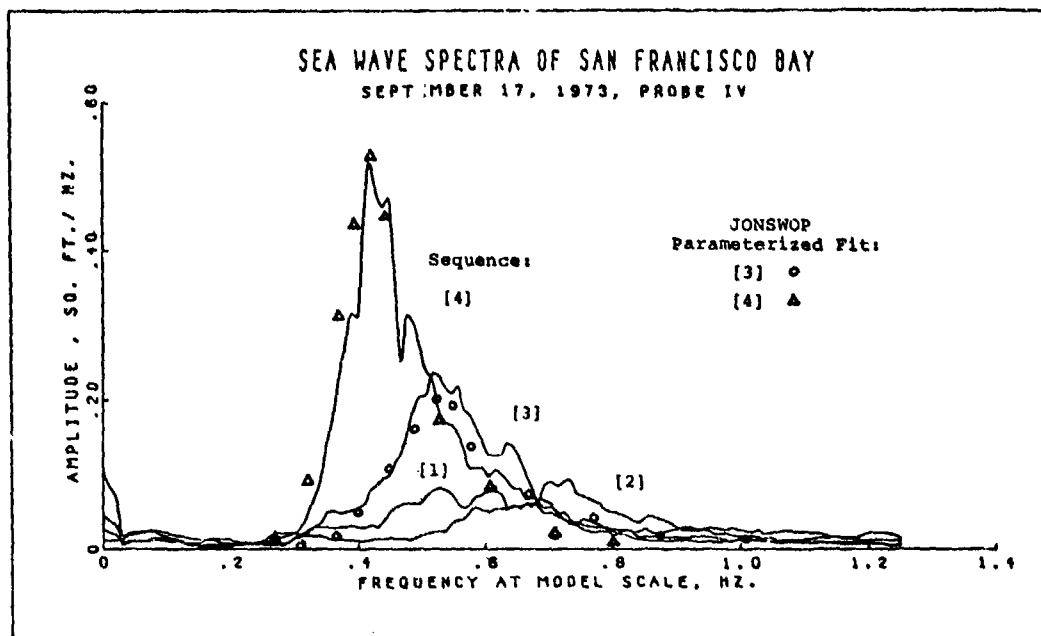


Figure 5

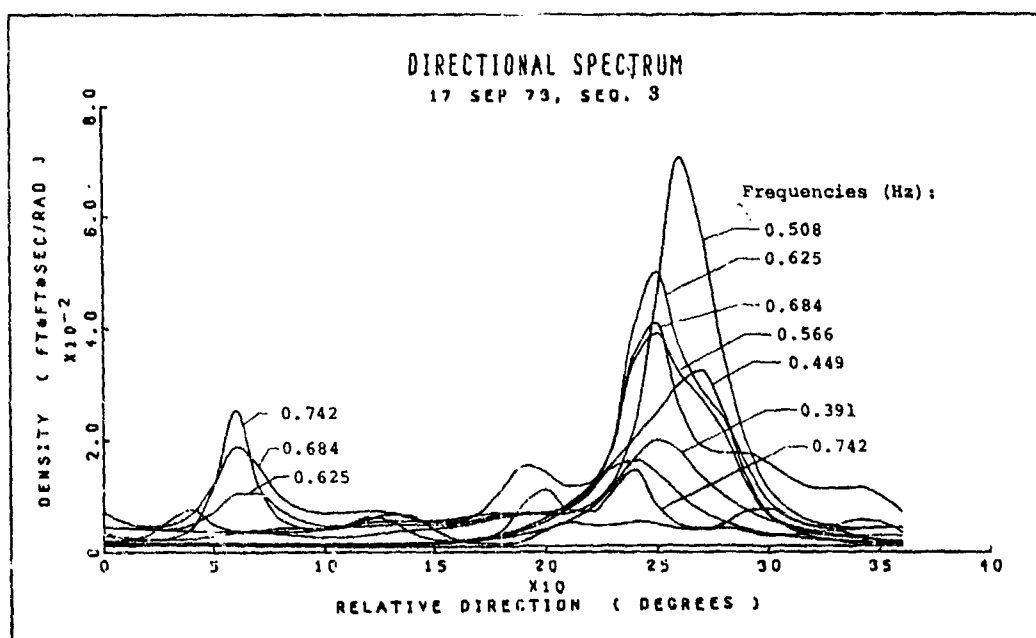


Figure 6

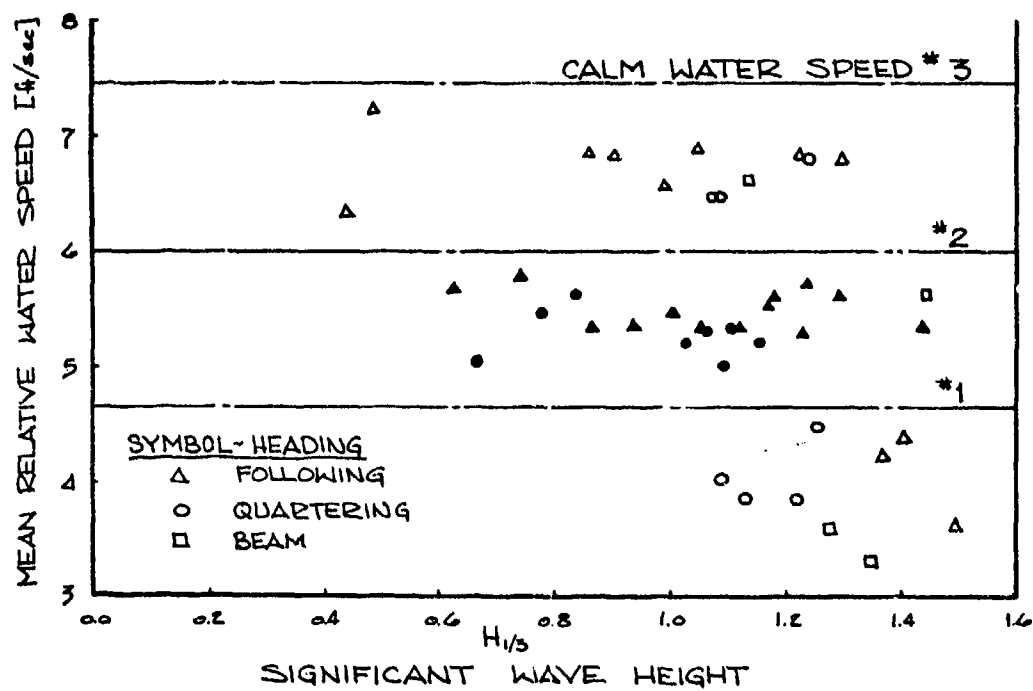


Figure 7

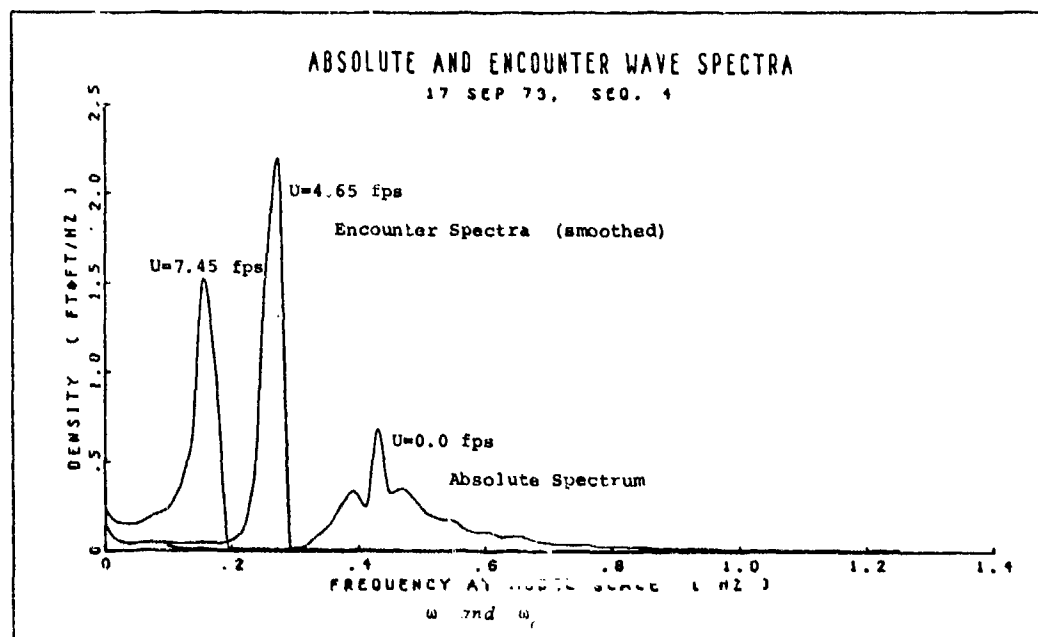


Figure 8

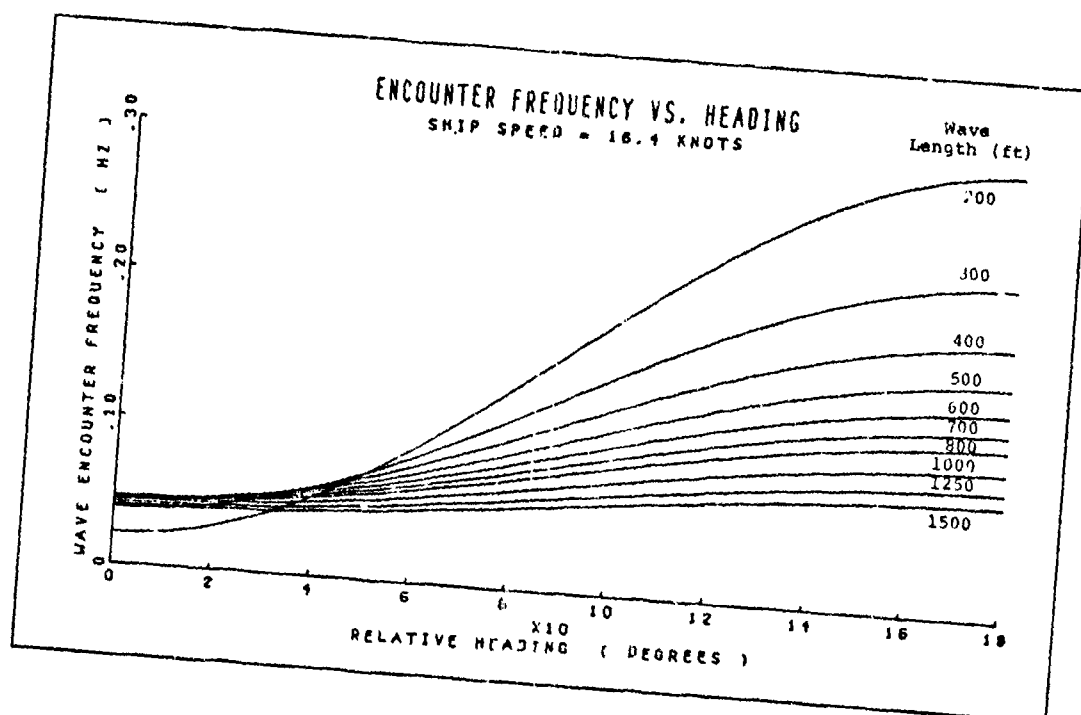


Figure 9

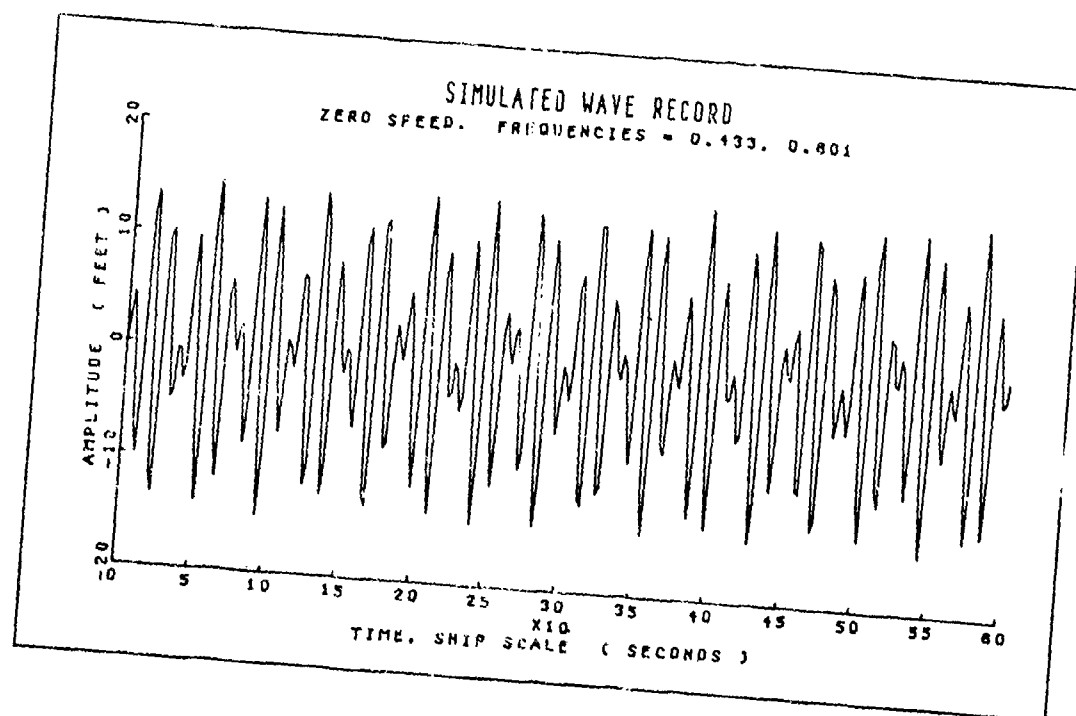


Figure 10a

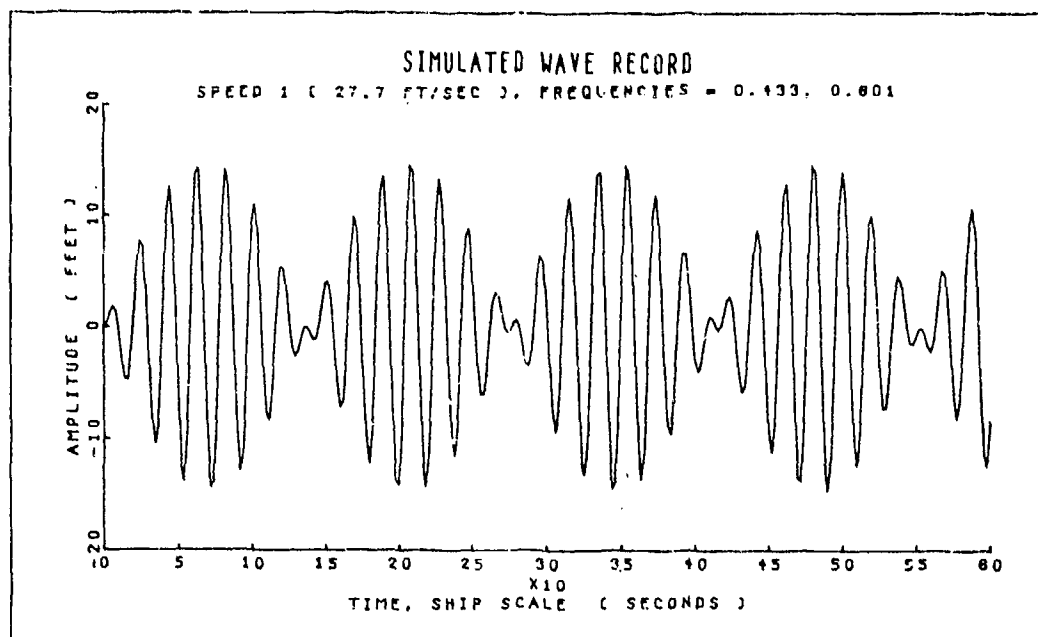


Figure 10b

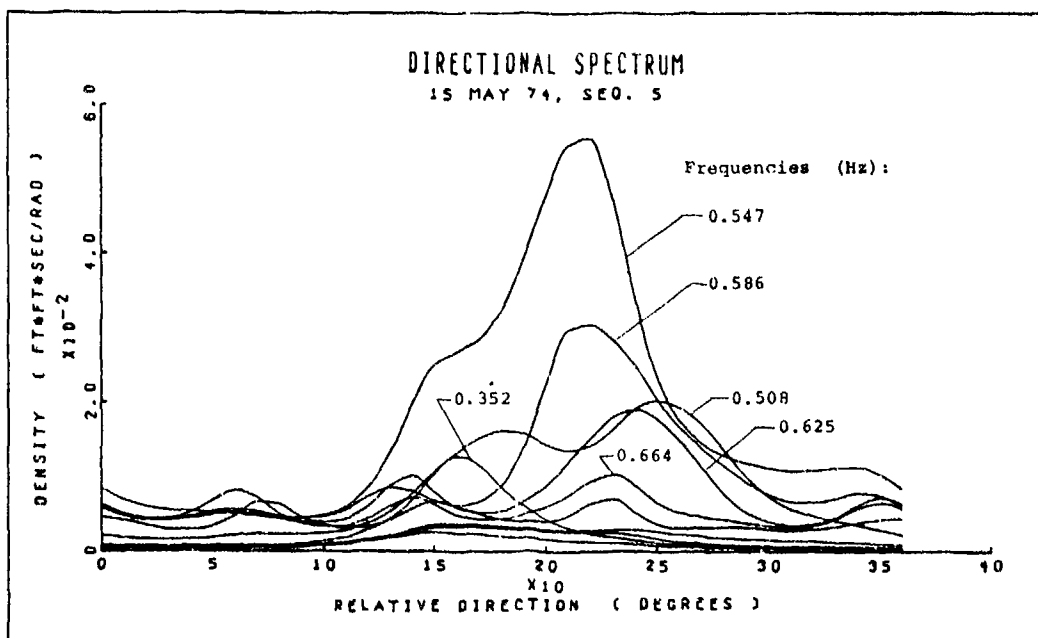


Figure 11

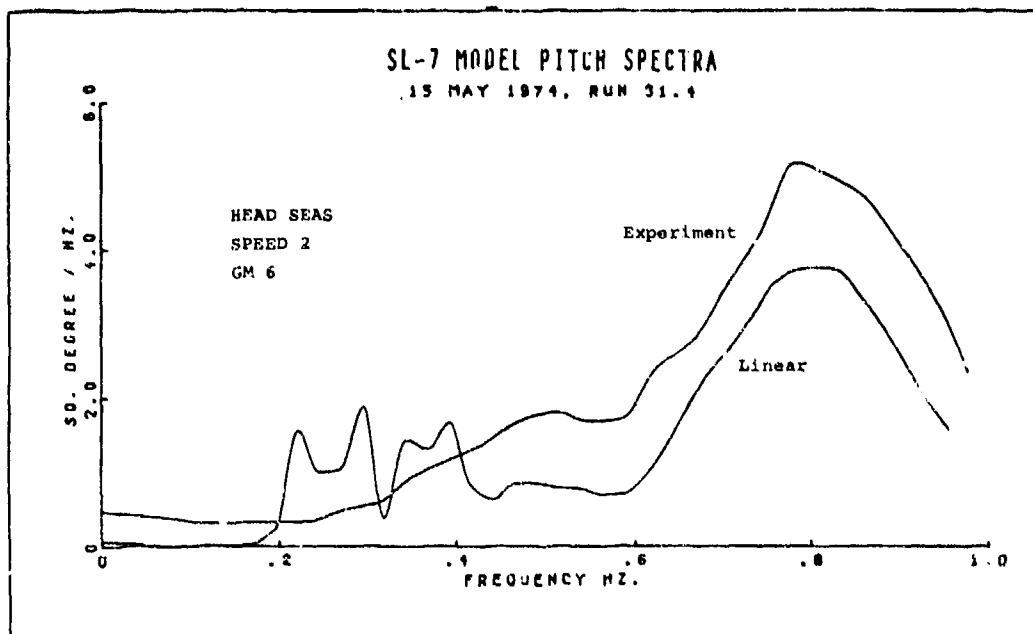


Figure 12a

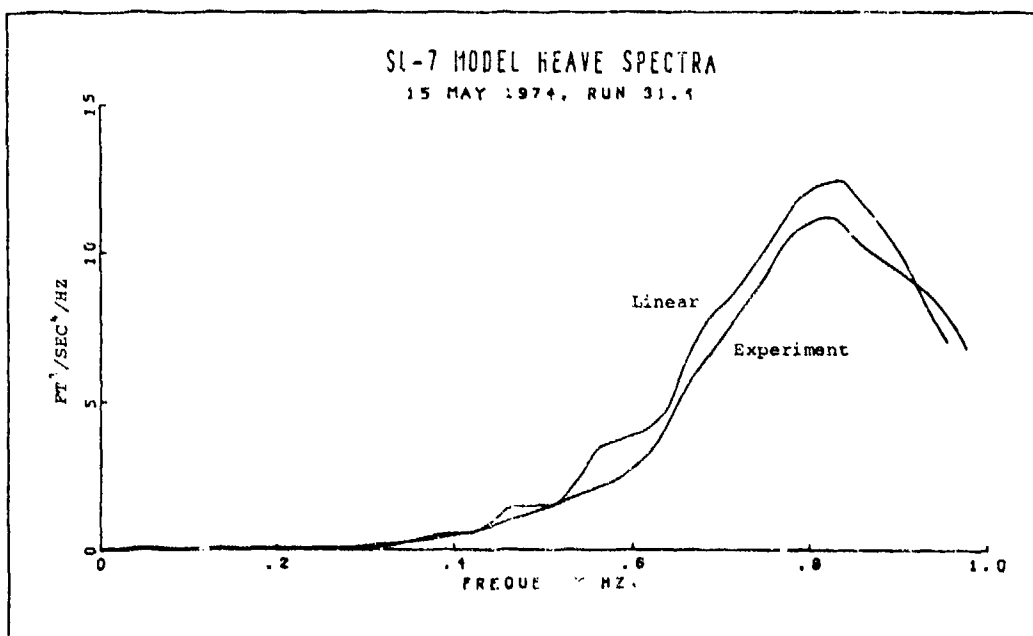


Figure 12b

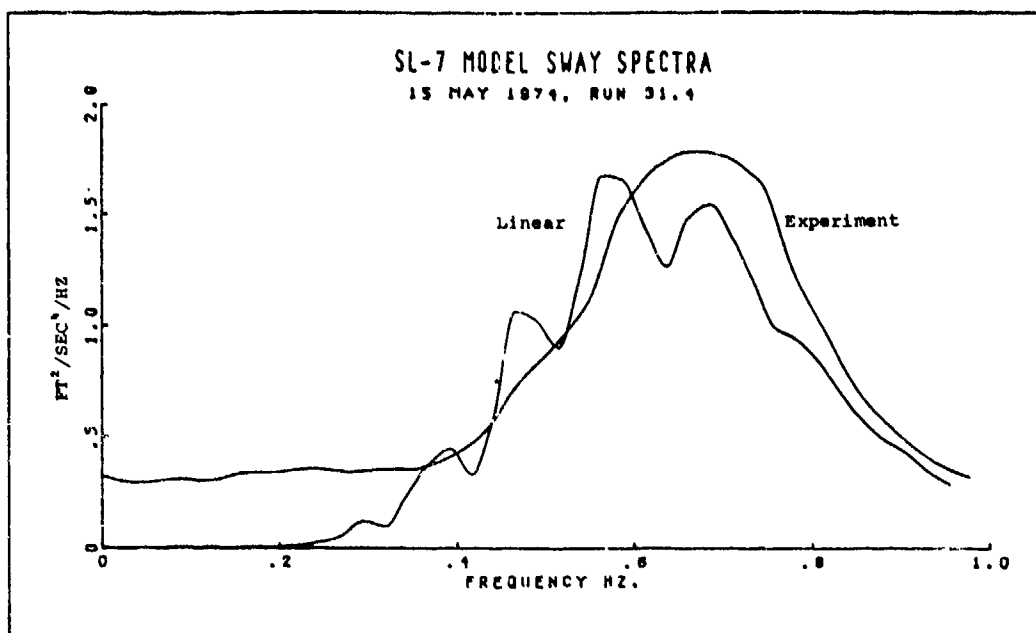


Figure 12c

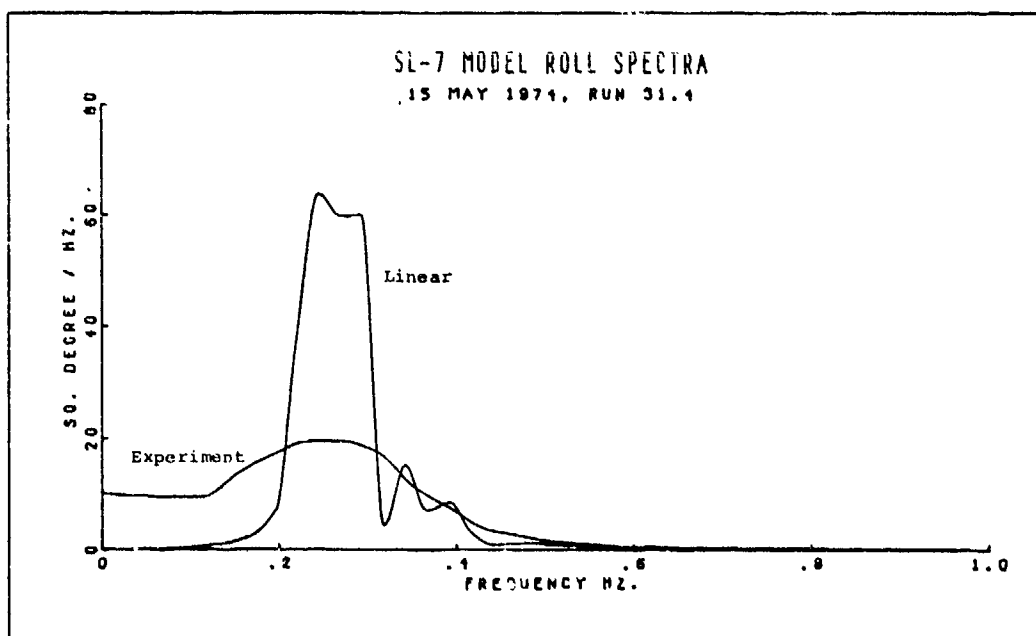


Figure 12d

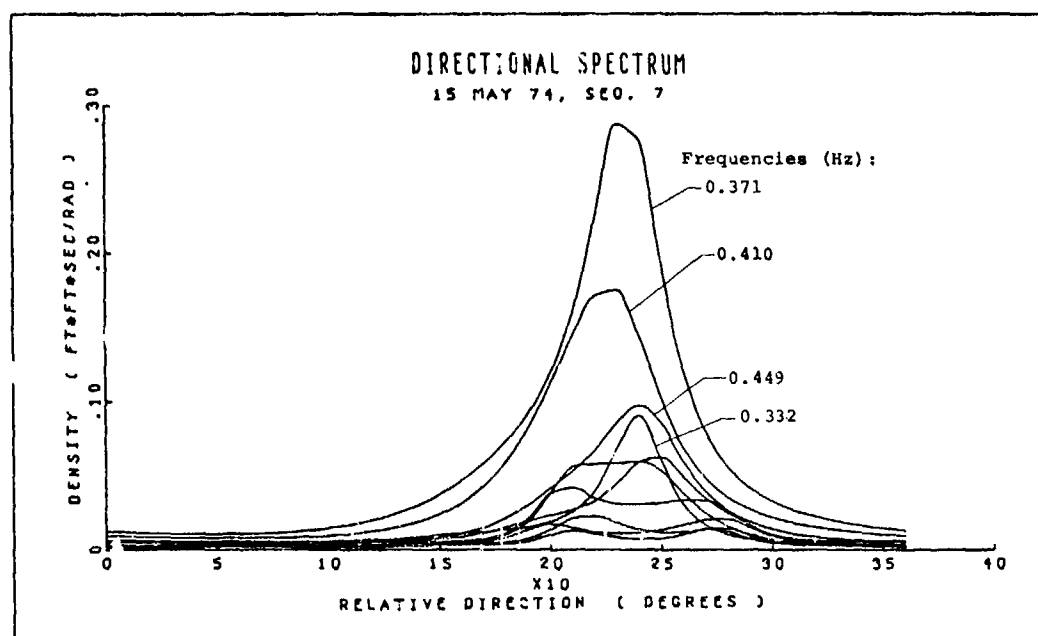


Figure 13

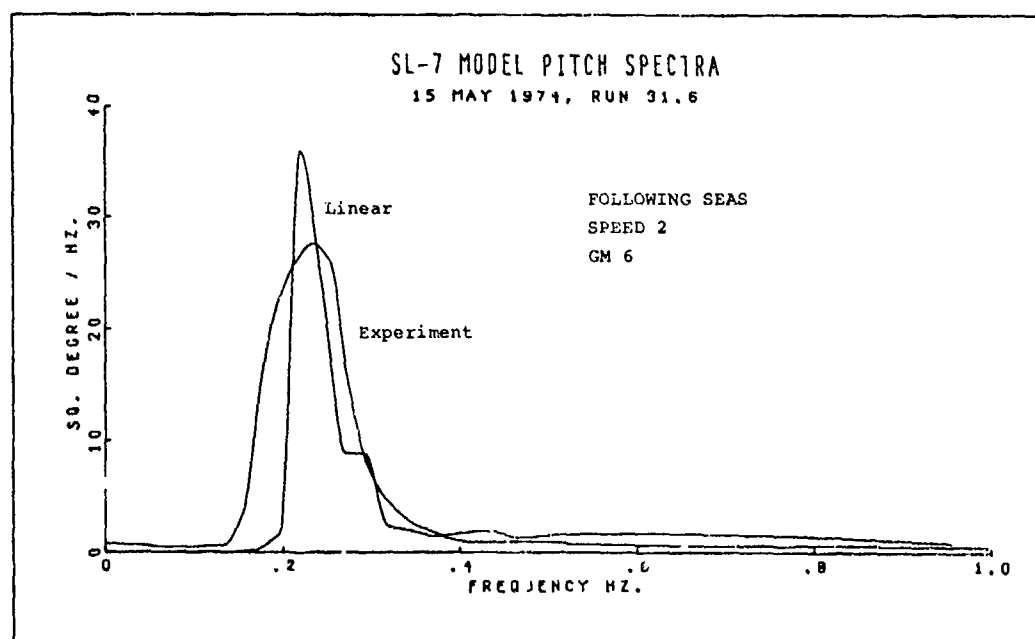


Figure 14a

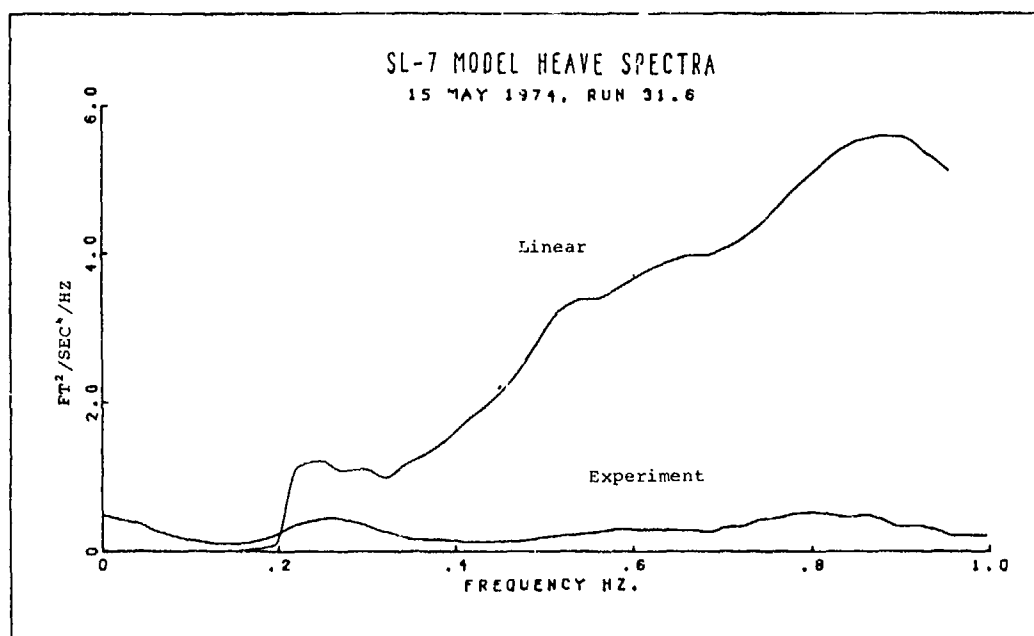


Figure 14b

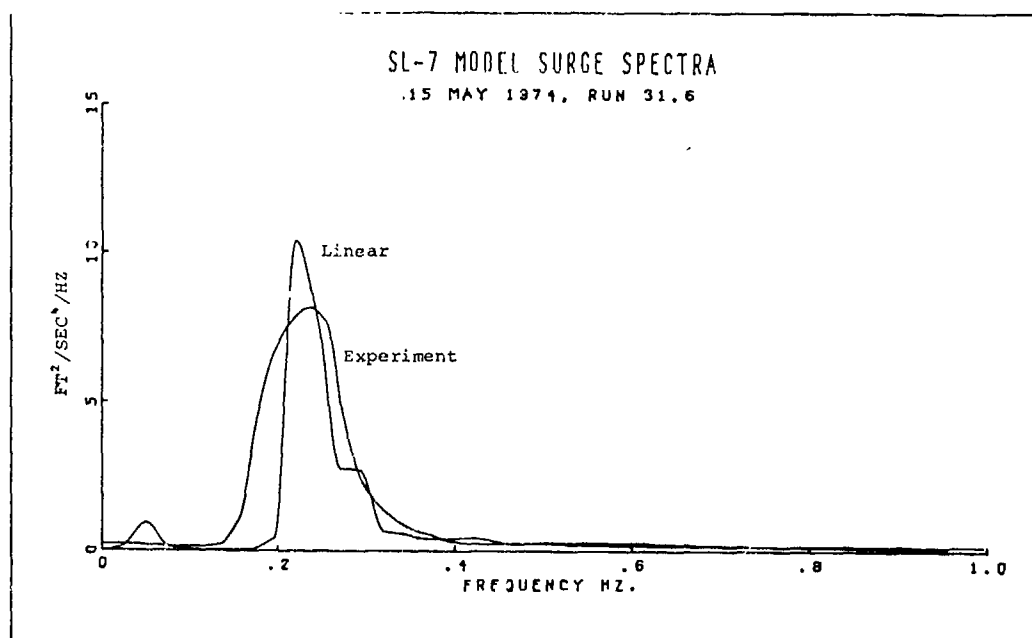


Figure 14c

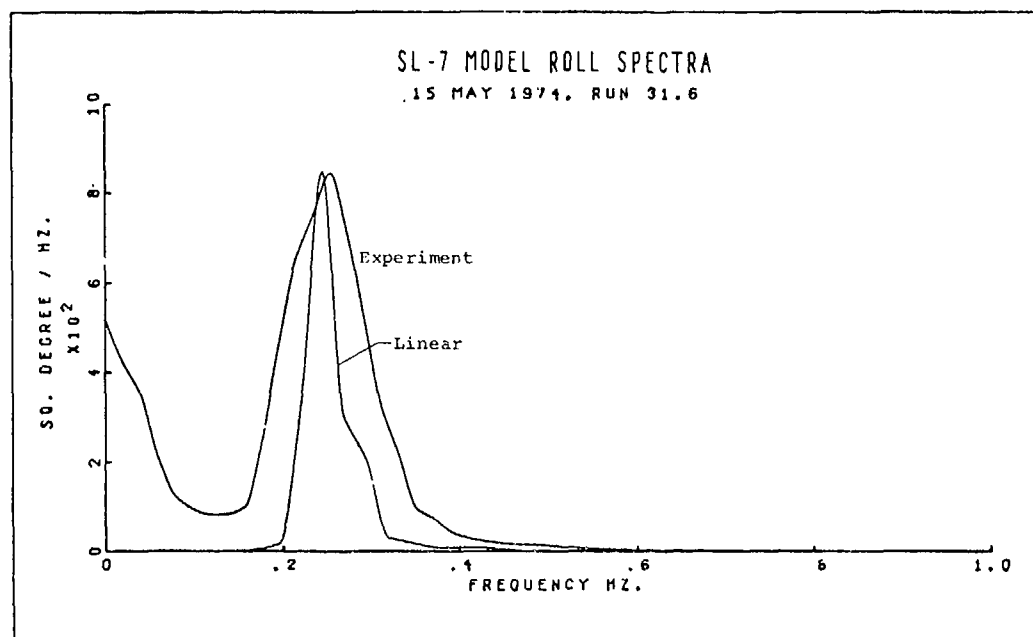


Figure 14d

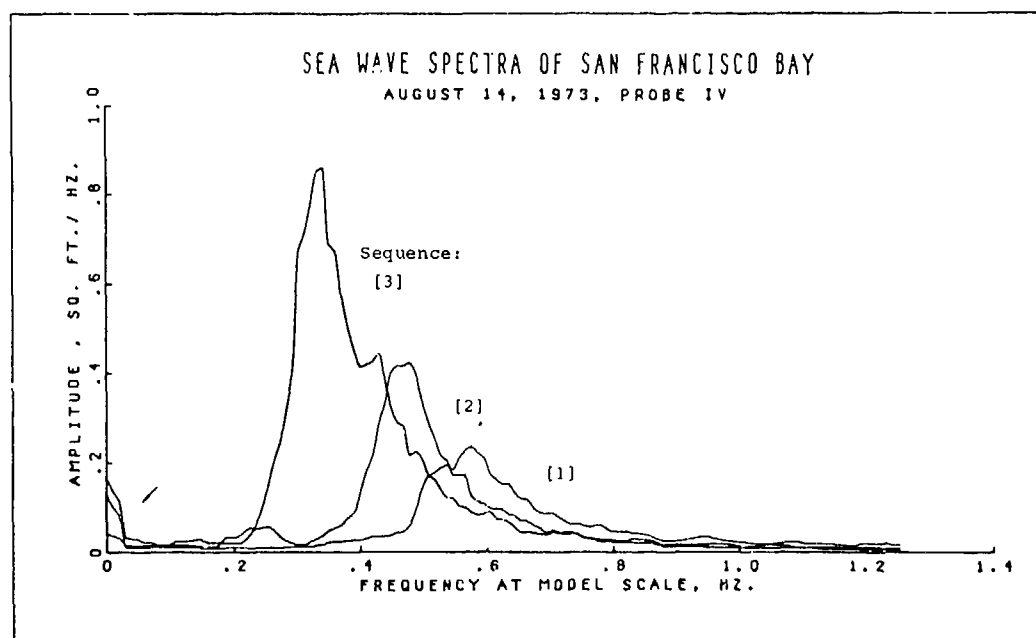


Figure 15

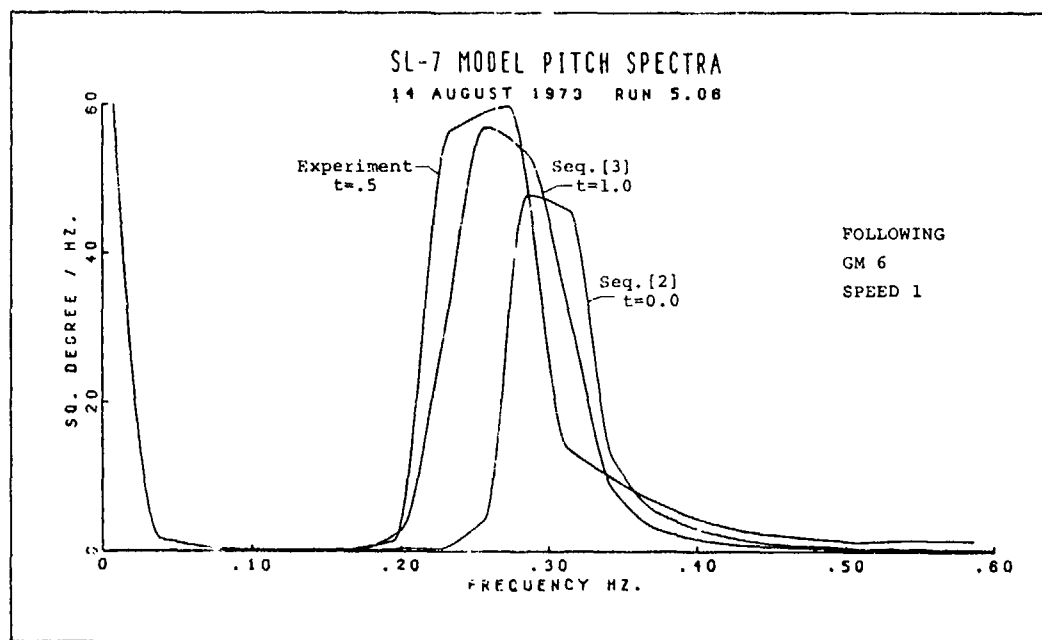


Figure 16a

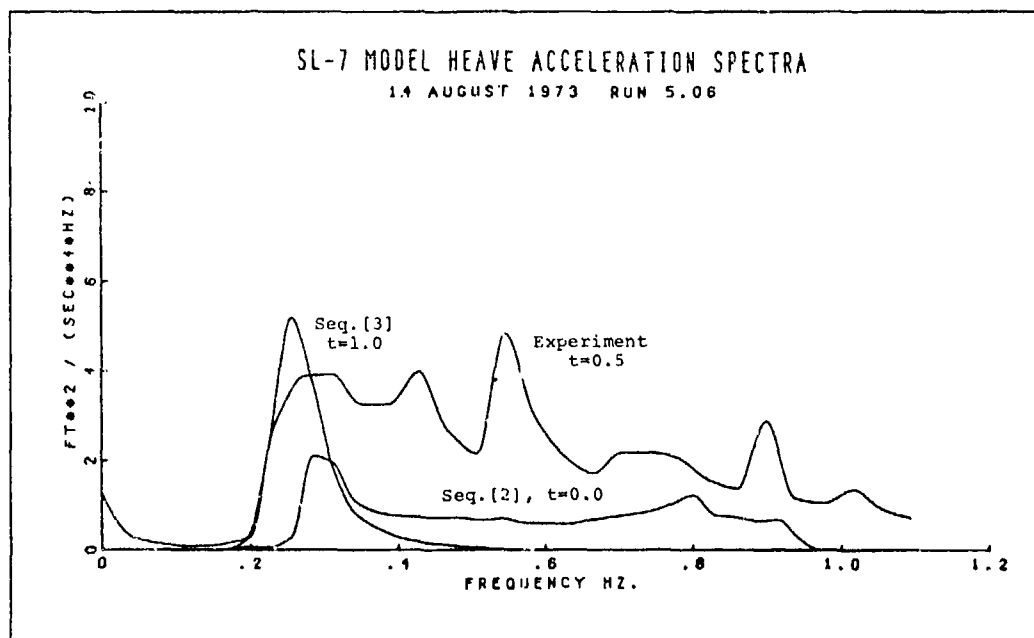


Figure 16b

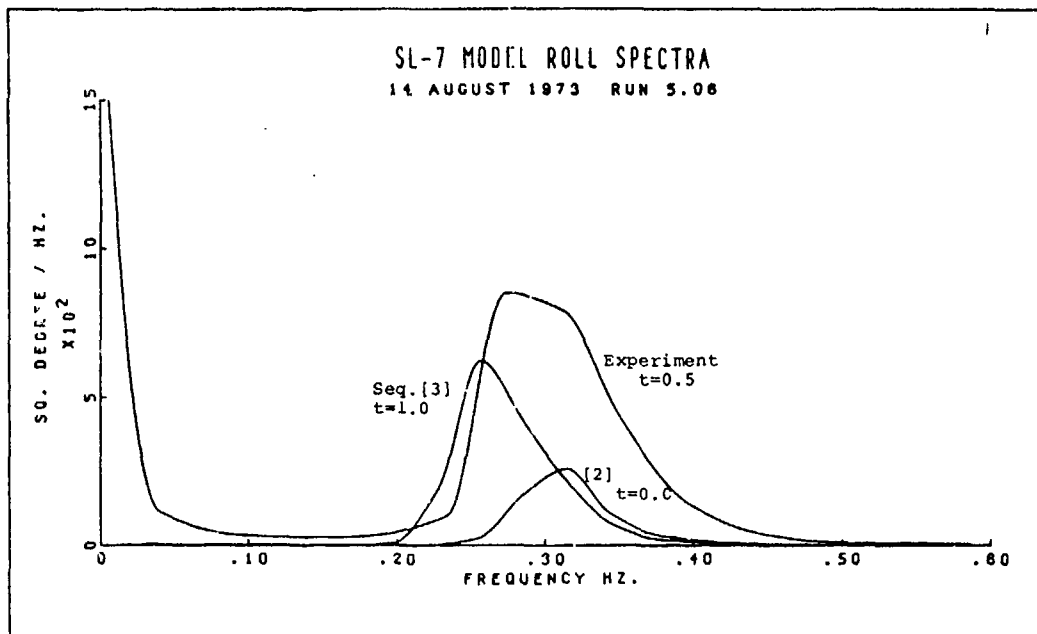


Figure 16c

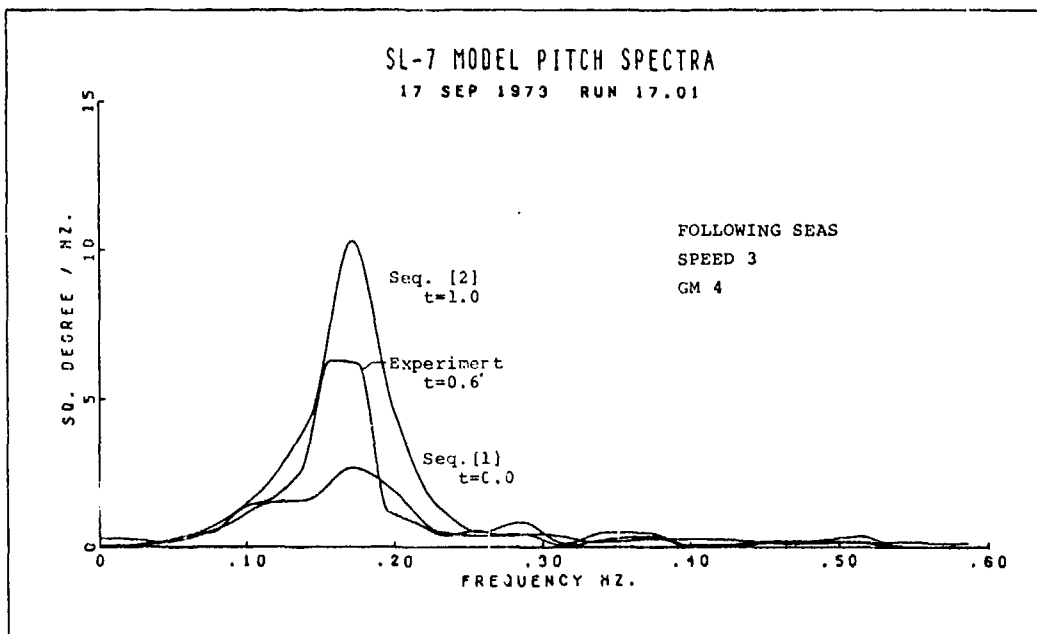


Figure 17a

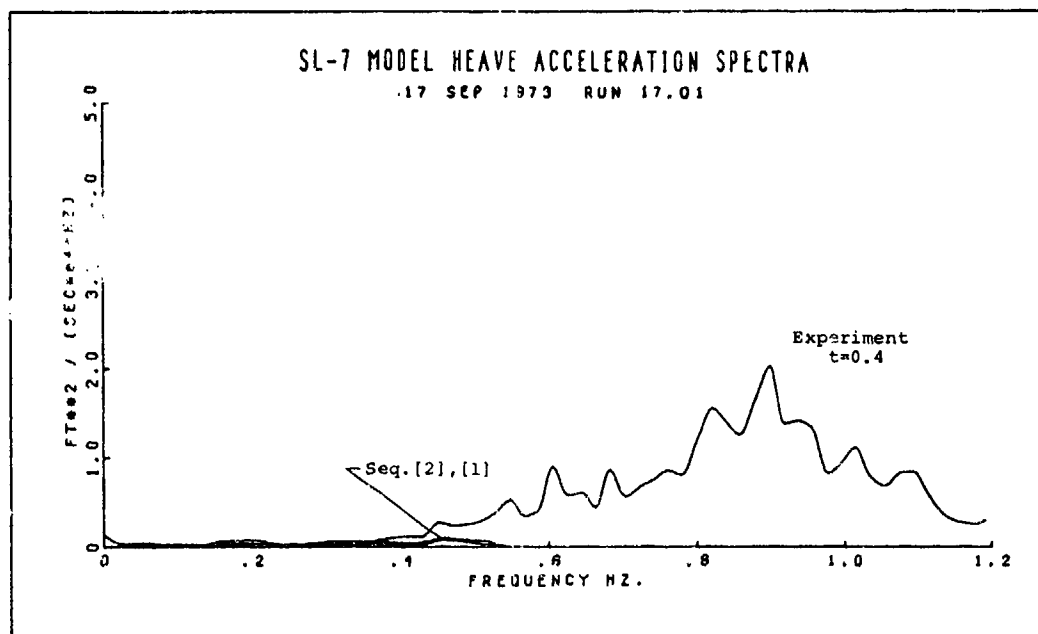


Figure 17b

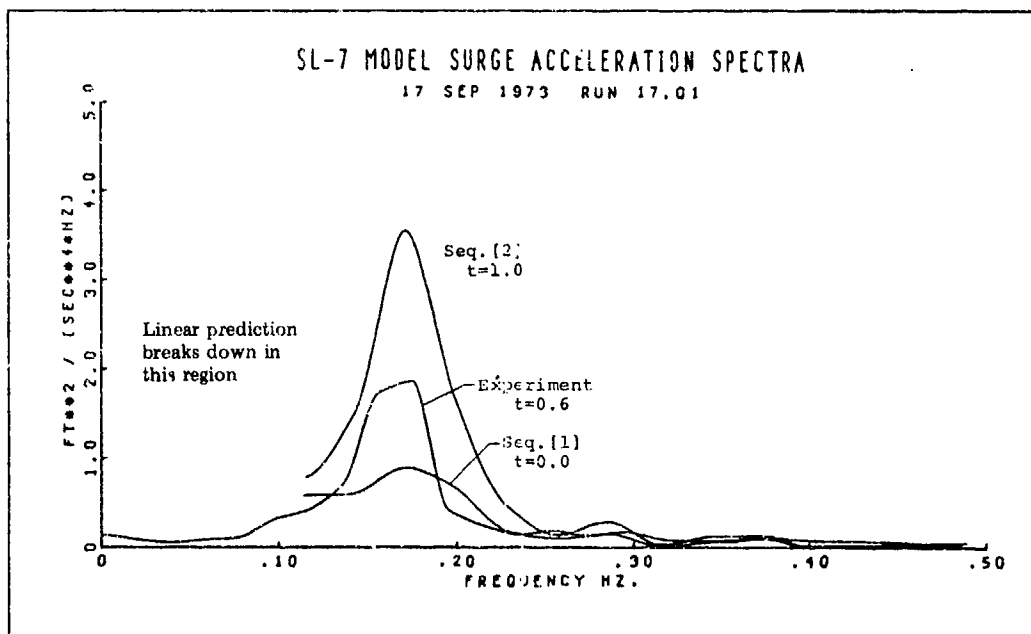


Figure 17c

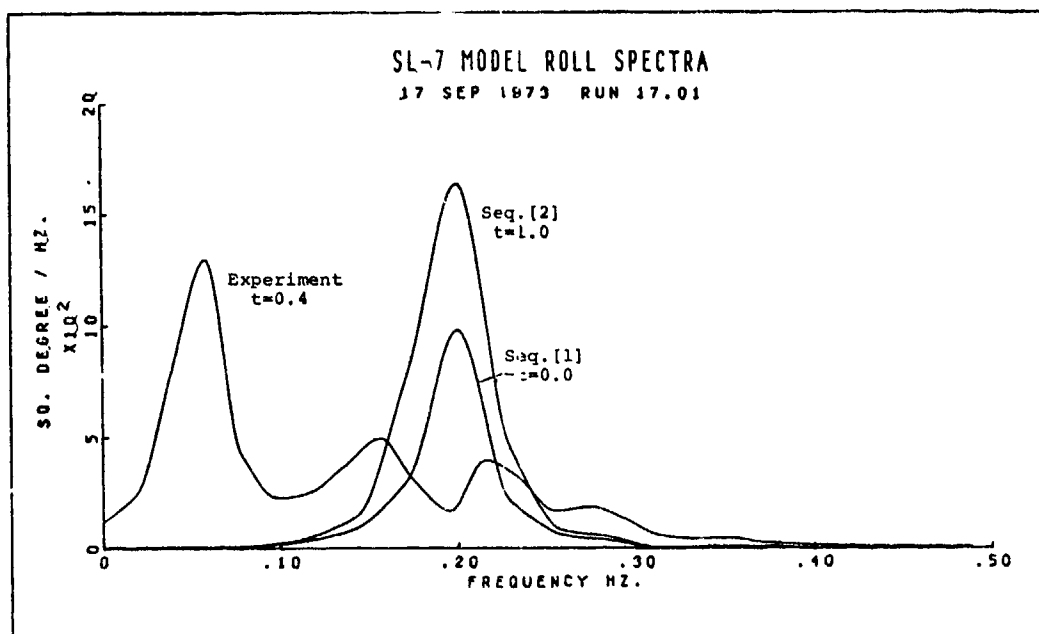


Figure 17d

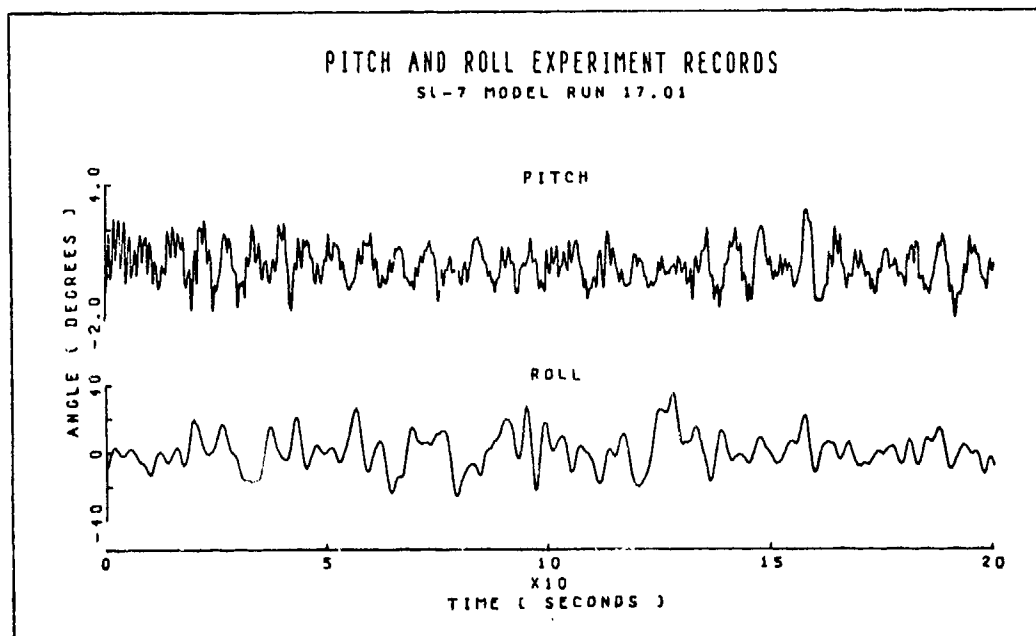


Figure 18

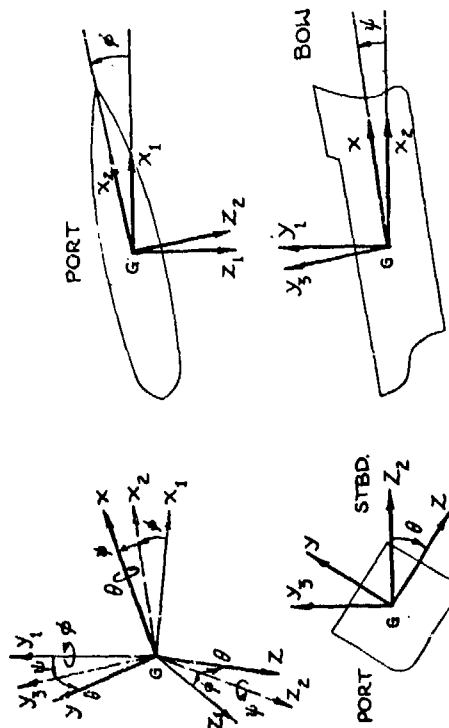


Figure 19 Coordinate Rotations

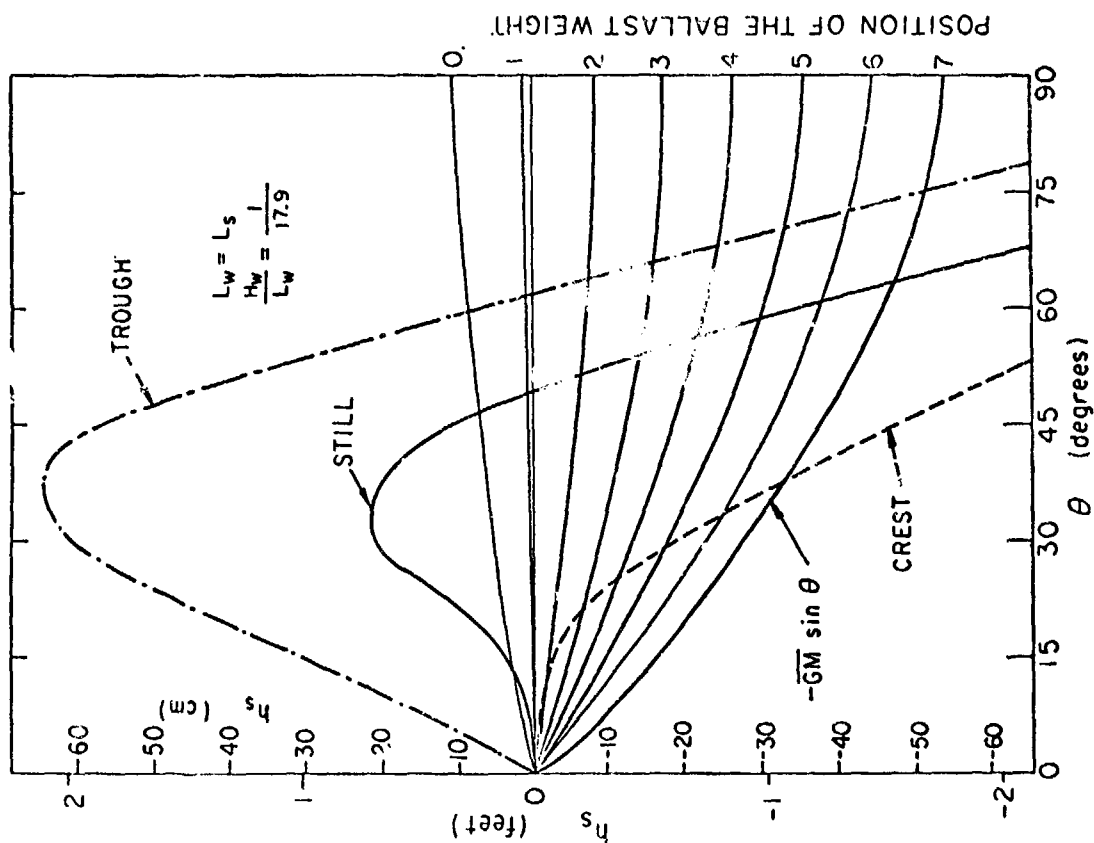


Figure 20 RIGHTING ARM CURVES, SHIP "CHALLENGER" FOR HEAVY MODEL CONDITION

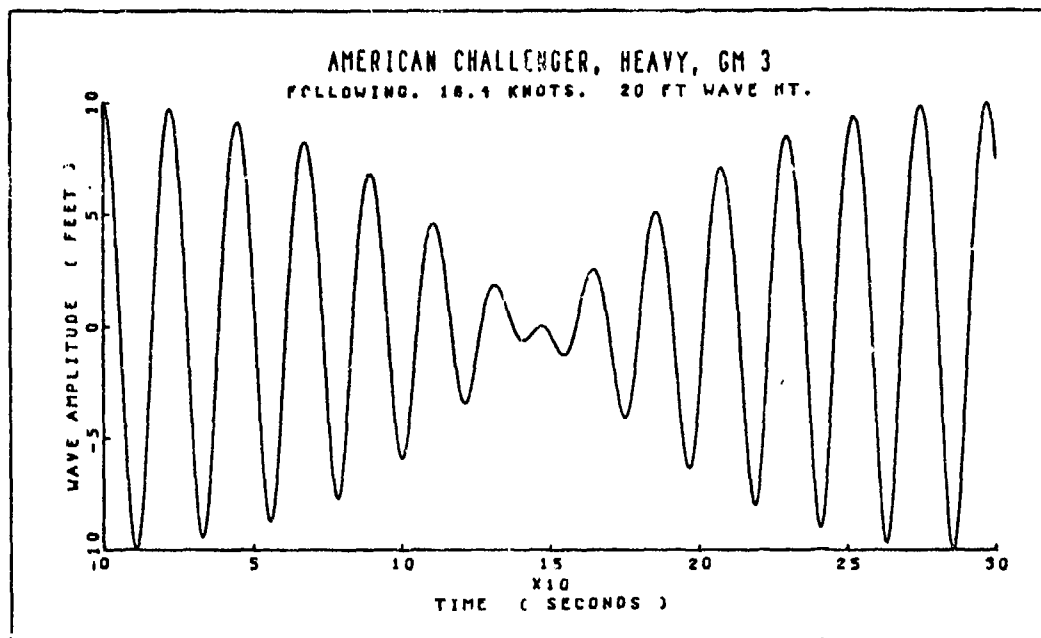


Figure 21

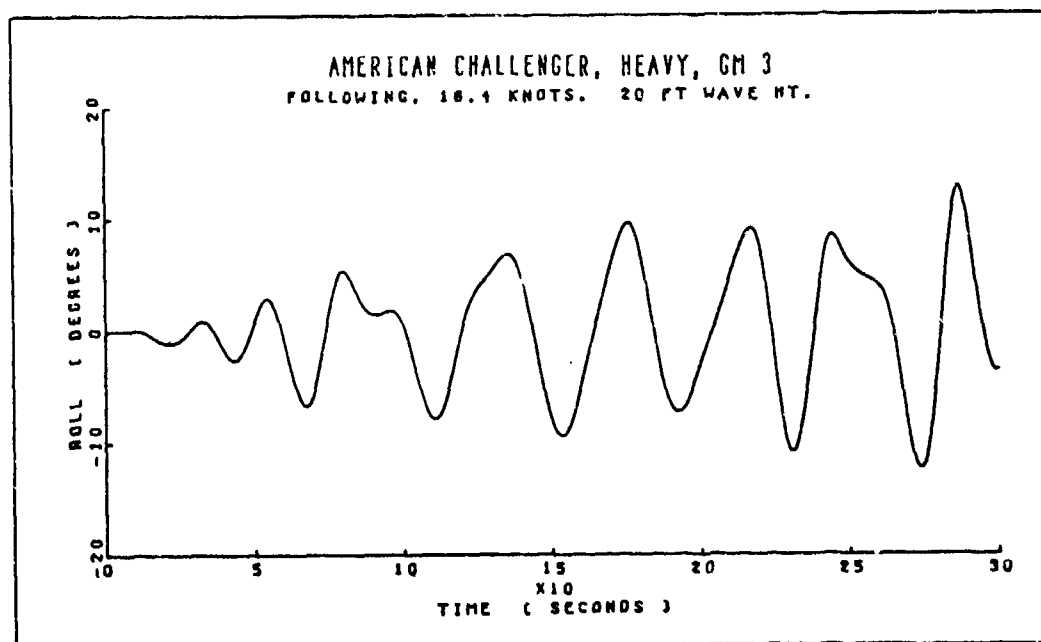


Figure 22

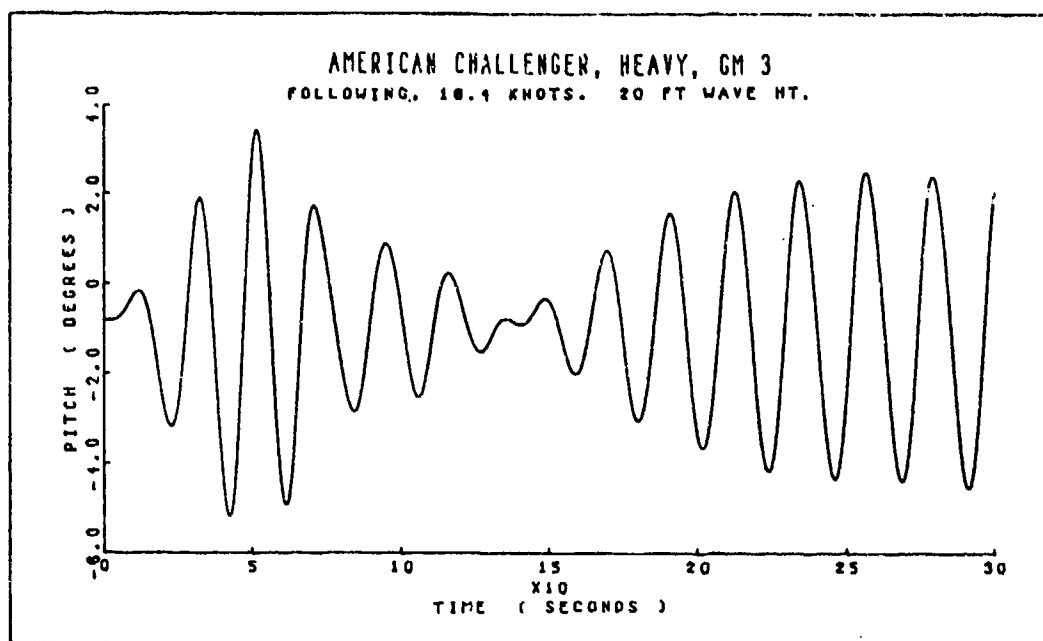


Figure 23

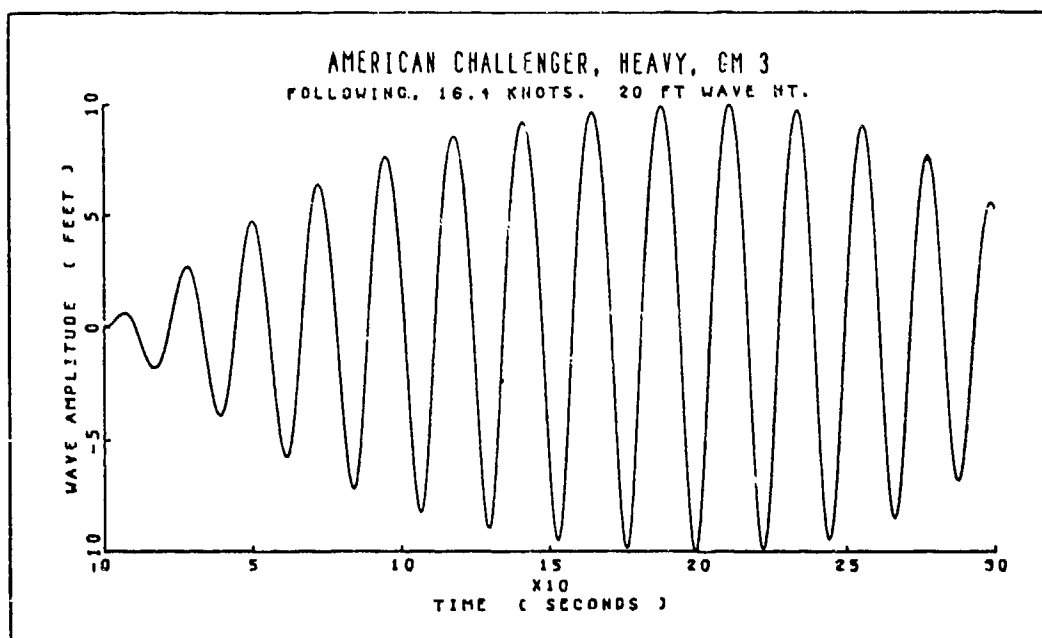


Figure 24

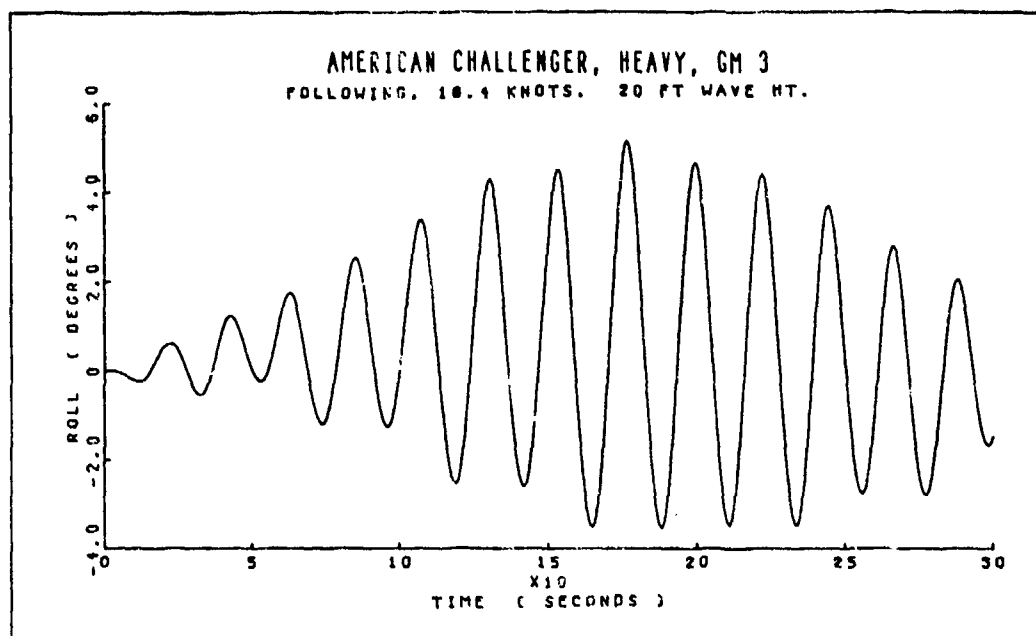


Figure 25

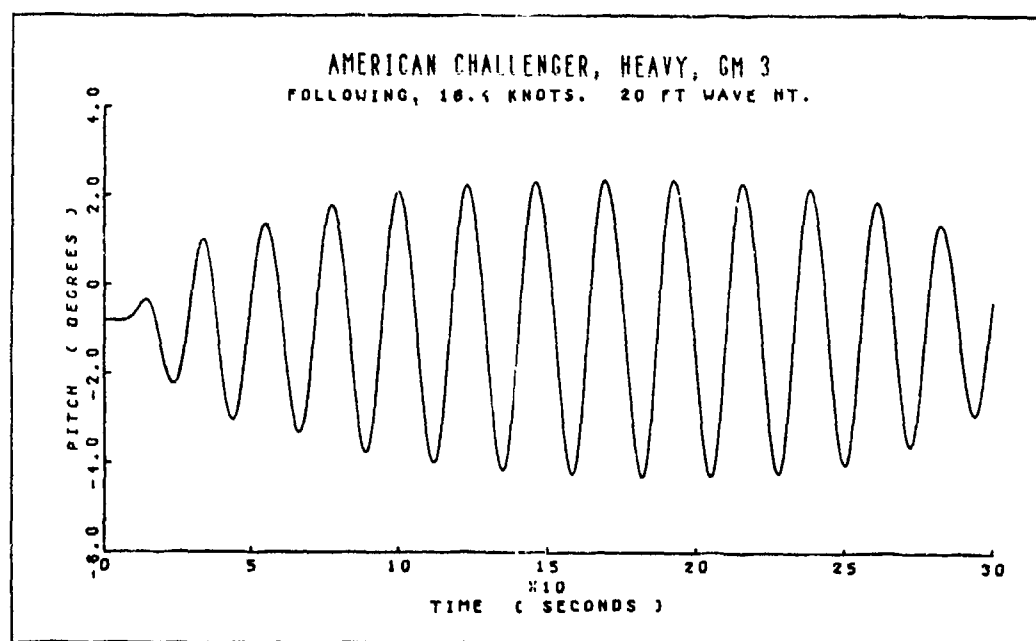


Figure 26

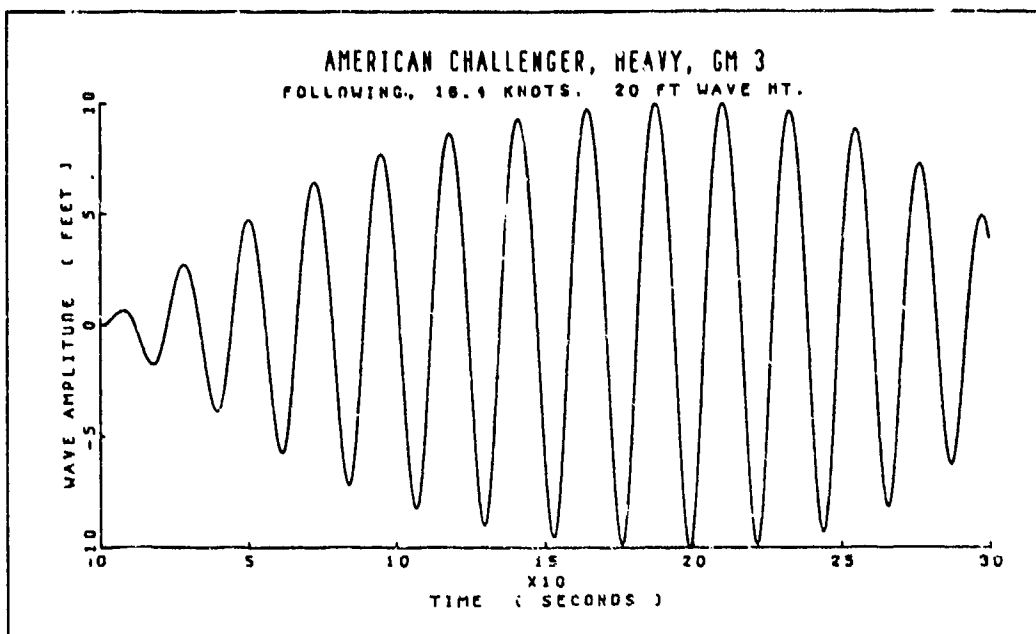


Figure 27

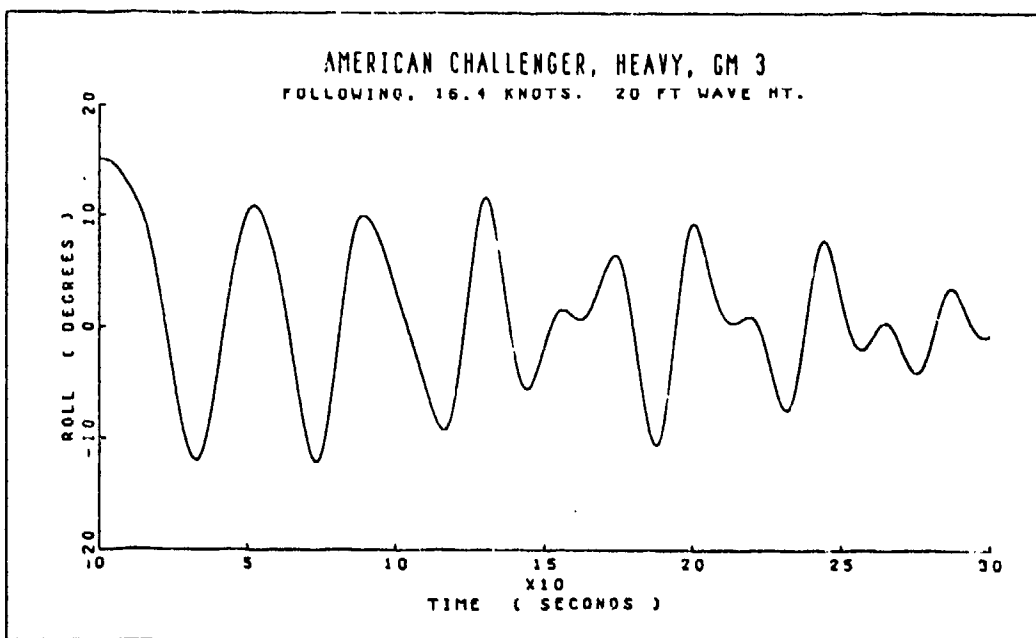


Figure 28

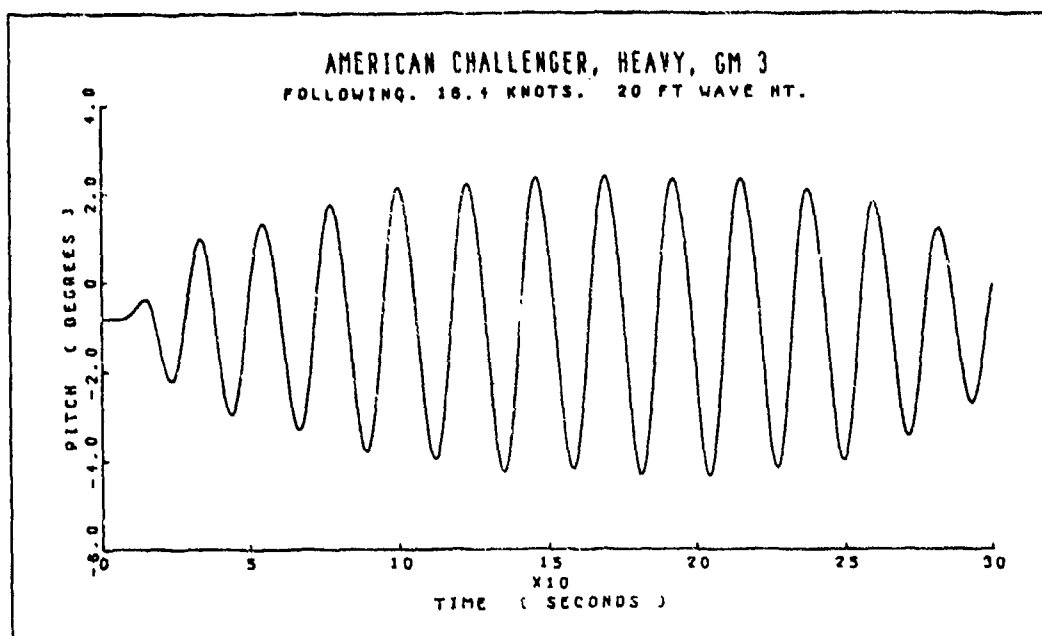


Figure 29

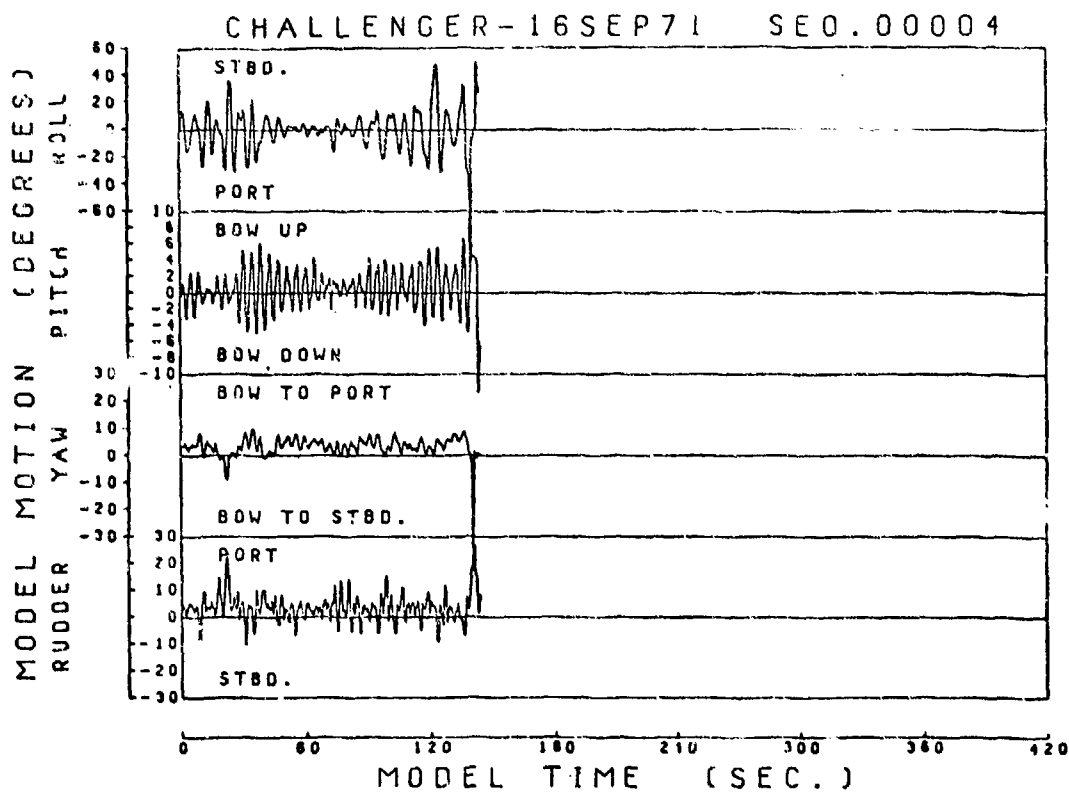


Figure 30

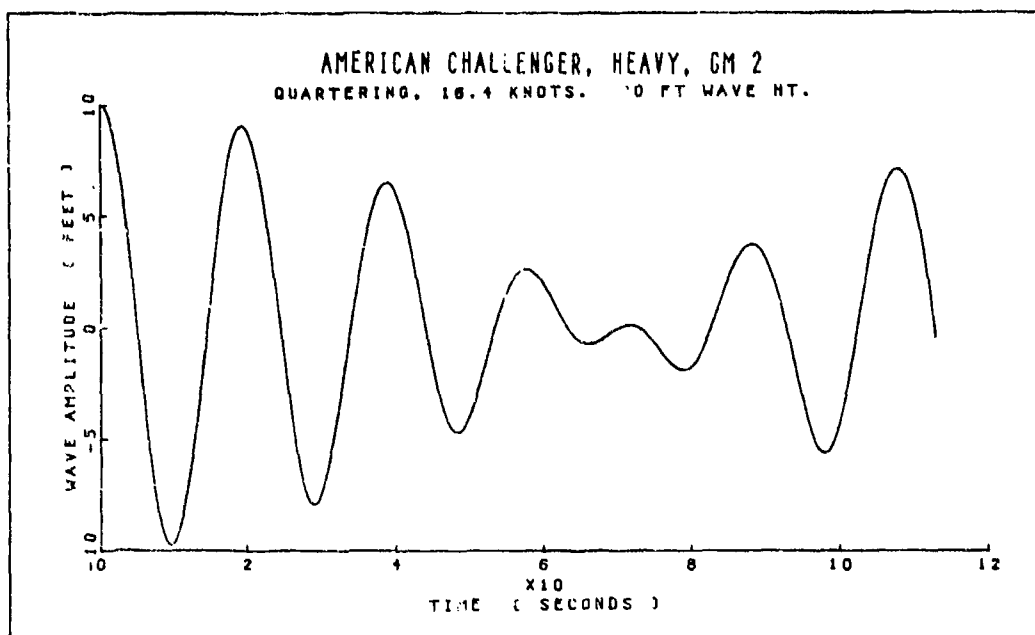


Figure 31

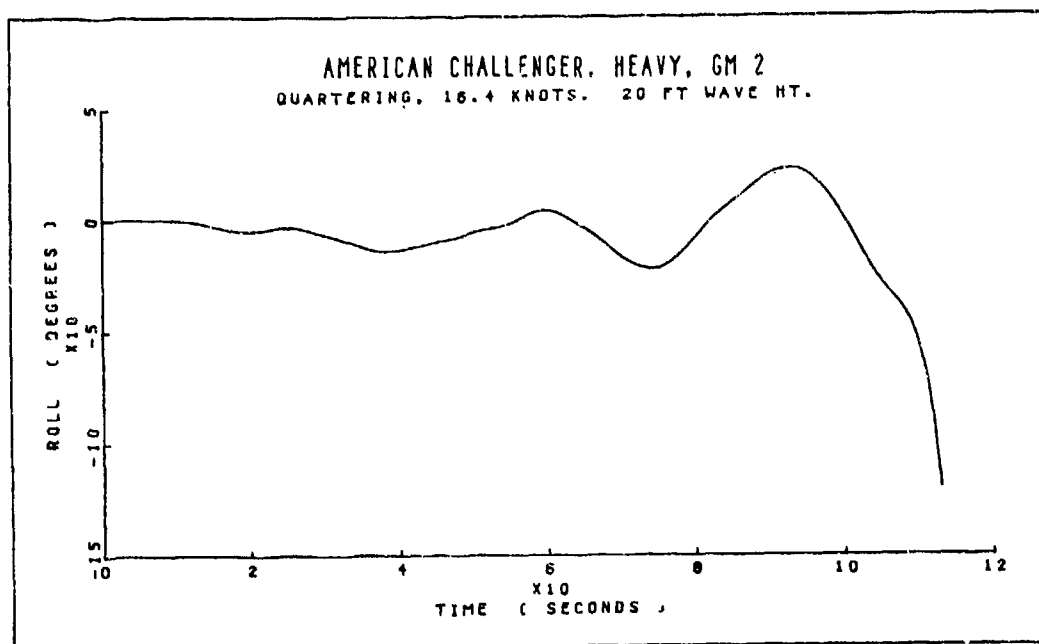


Figure 32

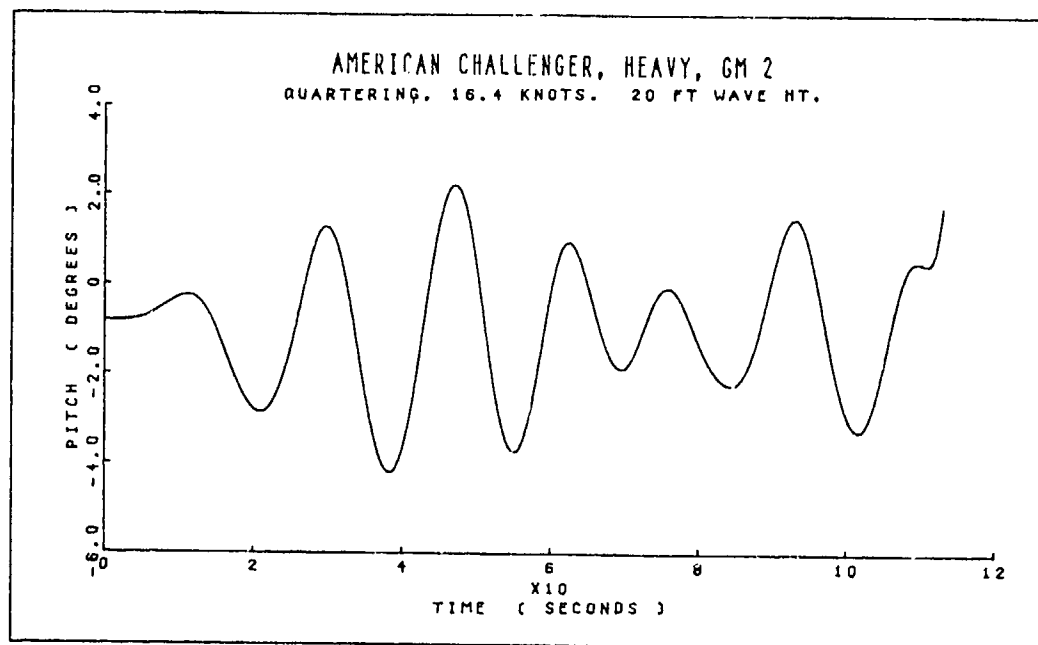


Figure 33

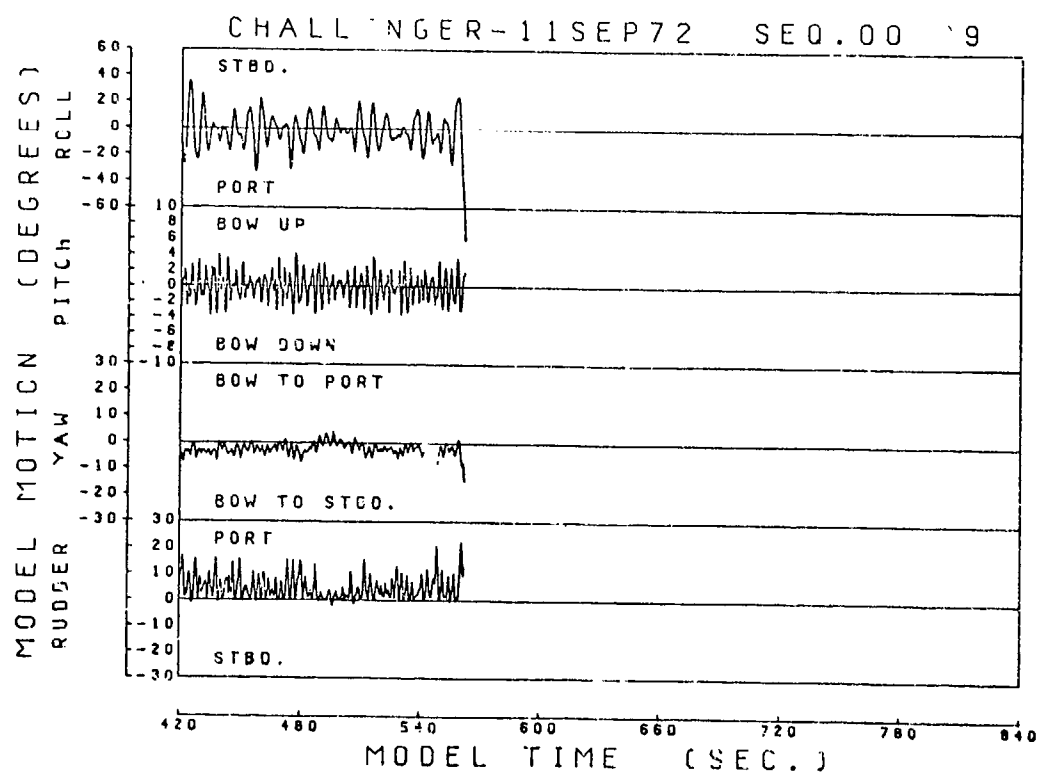


Figure 34

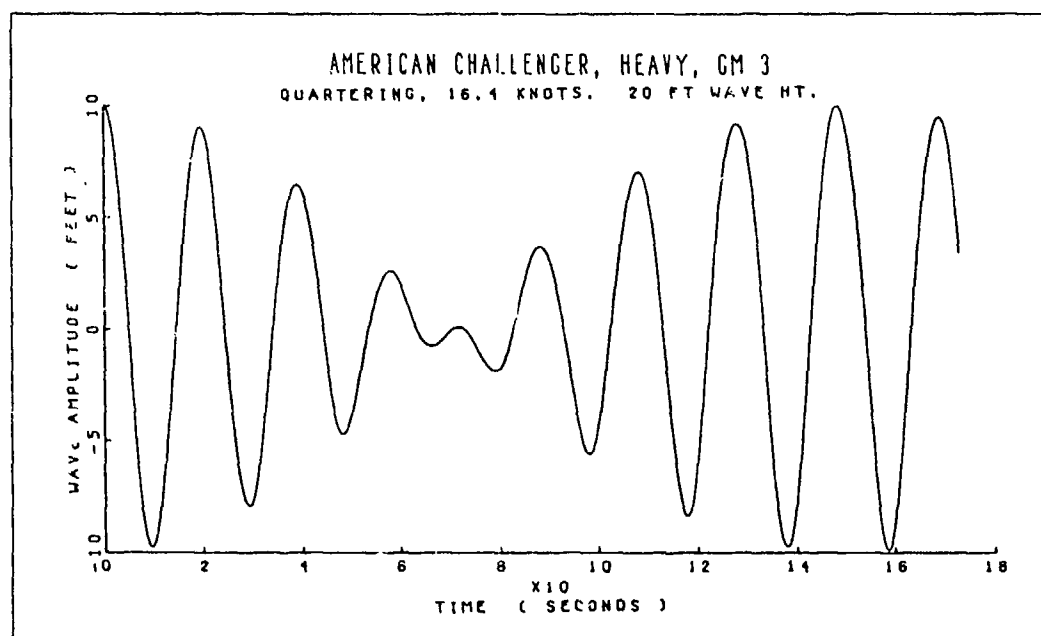


Figure 35

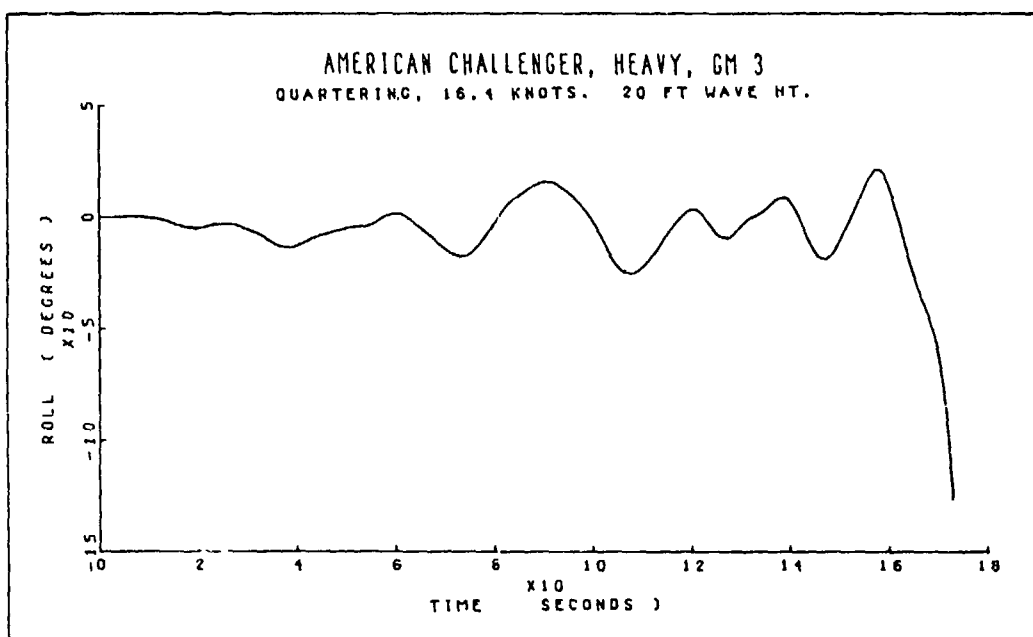


Figure 36

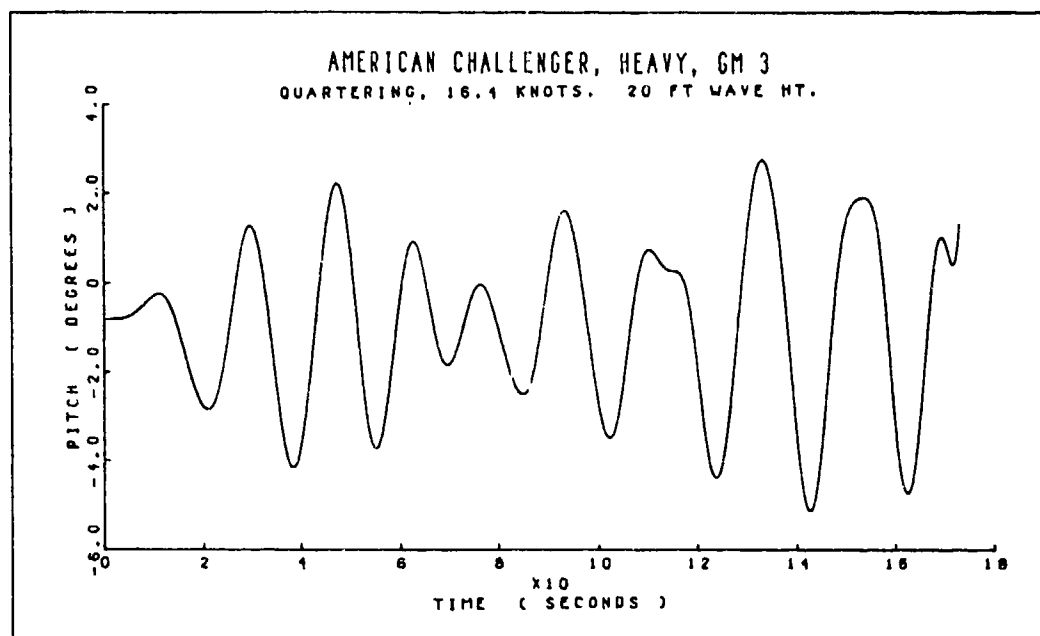


Figure 37

DISCUSSION

C.M. LEE

This paper provides us valuable knowledge on ship capsizing. The authors should be congratulated for their excellent work.

One point still not clear to me is the large values of the spectral density at the zero frequency which are shown in several figures, particularly, in Figures 16a and 16c.

For second-order d.c. effects, the motion spectral density at the zero frequency (Figures 16a and 16c) seem to be extremely large. I wonder if they were caused by the difficulty of offsetting the d.c. shifts of the recording devices.

L.L. MARTIN

It appears that the authors did not obtain broaching in their simulations as they did in their experiments. Have they considered the effect the wind may have had in their experiments? When moving with the wind a small change in heading, such as was caused by the waves striking the vessel will require a large rudder angle to maintain control (the angle depending on the ratio of the speeds of wind and ship). If this exceeds the maximum rudder angle available or is not applied in time control will be lost and the ship will broach as described by the authors.

AUTHOR'S REPLY

We wish to thank Messrs. Lee and Martin for their comments.

In regard to Dr. Lee's question, the occasional large spectral density values at and near zero frequency have a number of possible causes. Smoothing of the Fast Fourier Transform raw spectral ordinates results in the spreading of low frequency energy ($f < 0.02$ Hz) into the zero frequency ordinate. Such low frequency energy could represent signal or instrument (rare) drift, second order effects, and other nonlinear events that may occur only rarely during the course of an experiment. The low frequency spike in the wave spectra is almost entirely a tidal effect. Erratic motions, e.g. broaching in the yaw signal, stop-to-stop motions in the rudder angle, and intermittent low cycle type roll often yield much low frequency spectral energy outside the rather narrow excitation encounter band. Few experiments were conducted in very low sea states where the low frequency contribution could be ascribed purely to second order d.c. effects.

In regard to Mr. Martin's remarks, steering and wind have not been included for the results shown here. The format of the simulation program is such that they will be included in the future. It is also probable that the simplified model of some of the hydrodynamic forces used in the simulation do not adequately represent some forces of importance in broaching. This is a topic to which continuing improvements will be made as experience with the simulator accumulates.

Under certain conditions inadequate rudder action, either in time or maximum deflection, may contribute to broaching. With proper representation of the steering system, including such effects as time lags, rudder angle limits, and proper autopilot gain coefficients, it is expected that this behavior can be simulated.

DESIGN ACCELERATION AND SHIP MOTIONS FOR LNG CARGO TANKS

A. E. Baitis
NSRDC
Bethesda, Maryland 20034

S. L. Bales
NSRDC
Bethesda, Maryland 20034

W. G. Meyers
NSRDC
Bethesda, Maryland 20034

ABSTRACT

A procedure is developed to predict extreme accelerations and ship motions for design of cargo tanks in LNG ships. The procedure is a building block approach in which each of four stages involves essentially independent professional disciplines.

The first stage provides ship responses to all combinations of headings and modal wave periods.

The second stage provides extreme seas that may be expected during a ship's lifetime on different trade routes.

The third stage provides a probability of exceeding the extreme acceleration.

The fourth stage provides design values selected from extreme response surfaces which are the result of the product of the first three stages. Design values are selected by strategies based on current operating procedures in extreme seas.

Validity of the procedure is discussed by comparing results with model and full scale experiments and with current Chemical Transportation Industry Advisory Committee (CTIAC) design rules.

NOMENCLATURE

B = maximum waterline beam
C_T = confidence factor
K_φ = roll radius of gyration
L = ship length
m₁ = 1st moment of response spectrum $\int_0^\infty \omega^1 S_\zeta(\omega) d\omega$
n = number of observations
rms = root mean square response
S_ζ = wave spectrum
T = ship exposure time to extreme sea

T₋₁ = energy averaged wave period
T₀ = modal wave period, peak period of frequency wave spectrum
T_{obs} = observed wave period
 \bar{T} = mean wave period
 \bar{T} = mean apparent wave period
 \bar{X}_T = most probable extreme value in T hours of ship exposure
 \hat{X}_T = extreme value for time T with a probability of being exceeded
α = probability that extreme value \hat{X}_T is exceeded
ε = bandwidth parameter $(1 - m_2^2 / m_0 m_4)^{1/2}$
τ_{obs} = observed wave height
τ_w = mean wave height
(τ_w)_{1/3} = significant wave height
μ = ship heading angle
ν = short crested spreading angle
σ = root mean square response single amplitude, m₀
ω = wave frequency

INTRODUCTION

The increasing importance of liquefied natural gas (LNG) as a source of energy in the U.S. and Japan as well as Western Europe, has resulted in the development of rather specialized ships to transport this fuel from Algeria and Alaska to the U.S. and Japan. It has been found, as was the case with oil tankers, that the best way to improve the efficiency of these ships is to vastly increase their cargo capacity. As a result, ships are being built to classification rules that are currently under revision as LNG tank construction experience and research in LNG tank loads expands. The United States Coast Guard (USCG) regulates the design safety of all ships, including LNG carriers, entering or leaving U.S. harbors. The USCG therefore contracted the Naval Ship Research

and Development Center (NSRDC) [1]¹ to explore procedures which may result in classification or design rules for LNG cargo tanks that are more realistic than the ones specified in the current Code of Federal Regulations [2].

At present, the Code of Federal Regulations [2] states that cargo tanks in large LNG vessels must be designed to withstand, simultaneously, the following dynamic loadings:

- a) Rolling 30° each side, 10 second period;
- b) Pitching 6° single amplitude, 7 second period; and
- c) Heaving 1/80' single amplitude, 8 second period.

This rule imposes requirements which may be inappropriate for larger vessels such as many of the proposed LNG carriers. Recently, foreign classification societies have adopted rules which are reputed to be more realistic for the new large vessels. This paper presents a building block procedure for determining realistic extreme accelerations based on hull geometry and the operating procedures of the ship in extreme seaways.

The accelerations, computed at various ship locations, consist solely of the rigid body accelerations due to ship motions; the effect of slamming is not considered. The NSRDC Ship Motion and Sea Load Computer Program [3] and the NSRDC Irregular Sea Response Prediction Computer Program [4] provide predicted values of the root mean square (rms) acceleration in the longitudinal, lateral, and vertical directions for specified sea conditions. By applying short-term statistics to these predictions, the required extreme accelerations are found.

The seaways are analytically represented by short crested, two-parameter wave spectra of the form developed by Bretschneider [5]. Defining parameters of the spectra, i.e., mean wave height and mean wave period, are taken from published observations on specified trade routes.

The results of a pilot study on a typical, large LNG tanker, called SHIP D for purposes of this paper, are used as a detailed example for determining LNG cargo tank extreme acceleration values. These are compared to the proposed 1 October 1972 CTIAC rules for cargo tank accelerations [6]. The procedure to determine these extreme accelerations is outlined in the following section.

PROCEDURE

The procedure used to develop the extreme response surface from which the design accelerations are to be determined is divided into four distinct stages. It is felt that this building block approach to the development of design accelerations is flexible and suited to the rapidly varying technologies represented by the individual stages of the extreme response surface.

Stage one (see Figure 1a) consists of the determination of the rms ship unit response surface. This surface represents the unit wave height rms ship response, σ , for all combinations of headings and modal wave periods. A unique surface is computed for each ship speed, load condition, and location on the ship.

Stage two consists of the determination of the extreme seas on the different trade routes of interest in the design. The extreme accelerations are computed by using a sea representation based on visual wave heights and periods collected over a period of many years. The extreme sea conditions are used to compute the extreme cargo tank accelerations that may be expected over the life of the ship. The short-term Rayleigh amplitude distribution is then used to

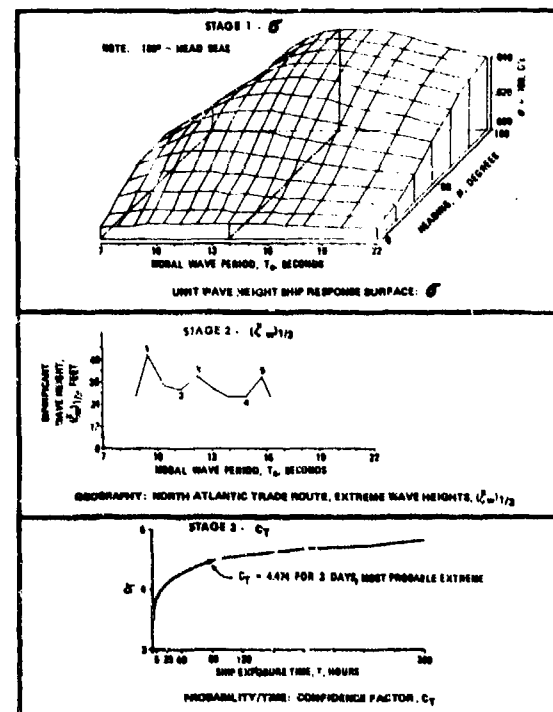


Figure 1a - Development of Extreme Response Surface.
(Sample Building Blocks.)

¹ Numbers in brackets refer to references listed on pages

predict the extreme accelerations at various probability levels. The short-term prediction is used for the prediction of these extremes because the ship will be exposed to the extreme seas generally for a very short period (on the order of few days) over its lifetime.

Stage three consists of the determination of the confidence factor, C_T , required to predict ship motions which will not be exceeded at various probability levels. This confidence factor is a function of the ship exposure time to the seas, the probability of the response not being exceeded, and the individual ship motions and sea conditions.

The fourth stage is the determination of the extreme response surface which consists entirely of the product of the previous three stages.

Figure 1 presents a graphic representation of the development of a sample extreme response surface. The results from these stages, see Figure 1a, are multiplied by one another to yield the extreme response surface shown in Figure 1b. A detailed explanation of the various components of Figure 1 follows in the next three sections.

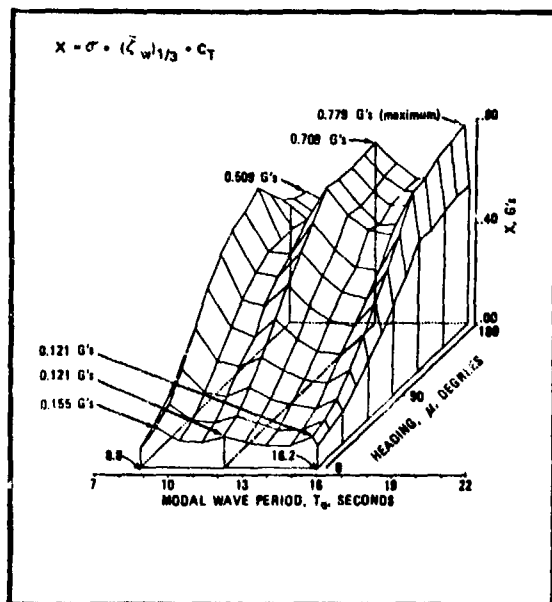


Figure 1b - Development of Extreme Response Surface. (Sample Extreme Response Surface for the LNG Carrier SHIP D. Most Probable Extreme Vertical Accelerations Over 3 Days at 20 Knots, Full Load, on the North Atlantic Trade Route for Point 1, Near Bow.)

It is considered that at each stage different professions enter into the determination of the design accelerations. For example, in stage one the evaluation of the rms unit ship response is made primarily by naval architects. In stage two the interpretation of various observed sea conditions is best made by oceanographers. Also in stage two the selection of the trade routes for which the ship is to be designed is best made by the ship owner and the regulatory agencies. The selection of the confidence factor in stage three is best made jointly by the naval architect/designer, the ship owner, and the regulatory agencies. Finally, the selection of the design acceleration from the extreme response surface in stage four is made by the regulatory agencies in consultation with the ship owners. The owners in turn decide on the design trade routes and the operating instructions for the ships' masters. It is recognized, of course, that the USCG bears the final responsibility for the selection of the design values. The extreme ship cargo accelerations experienced in a ship's life are regarded as being significantly influenced by the operating procedures for the ship in extreme seas as well as by the trade routes on which the ship is employed.

RMS Response Surface for Unit Wave Height

The rms ship unit response surface illustrated in Figure 1a is computed using the NSRDC Ship Motion and Sea Load Computer Program [3] and the NSRDC Irregular Sea Response Prediction Computer Program [4]. This surface consists of the collection of the rms ship responses computed for all possible modal wave periods and headings for a specific ship load, speed, and location on the ship. The individual rms responses which compose the surface are determined from the products of the ship response amplitude operators and wave spectra with one foot of significant wave height.

The use of the rms ship unit response surface presupposes that the ship responses are linear, an assumption which has been demonstrated for certain ship types in recent years by model experiments and full scale ship motion trials. The question of the validity of the linearity assumption for ship roll for SHIP D is not very important since roll does not seriously influence the extreme ship acceleration for this large ship.

Detailed investigations into the significance of load variations on the acceleration response have been carried out and are presented in Appendix A. This Appendix also presents results of the investigation into the sensitivity of the acceleration responses to position along the ship or alternately into the influence of specific motion components

such as pitch on the predicted accelerations. In addition, the validity of the ship motion prediction programs is examined by comparing predicted results with measured model results for SHIP D and full scale results for the USS GUAM (LPH-9).

It should be noted that the modal period of the wave spectrum (peak of the wave spectrum) or equivalently the shape of the wave spectrum and its location on the frequency axis is another major influence on the ship response. The details of this variable will be discussed in the following section.

Extreme Seas

The proposed procedure for the determination of LNG cargo tank design accelerations differs from long-term bending moment prediction procedures proposed by Abrahamson of Norske Veritas [7], Mansour of MIT [8], and Lewis of Webb [9]. The distribution of extreme sea conditions for the trade route in question is taken directly for all wave periods. Thus, the design results are based directly on the observed extreme wave height and period combinations rather than on long-term distribution functions (e.g. Weibull or log-normal) fitted to these observations. The extreme conditions thus derived are shown for the North Atlantic (Trade Route 1) in Figure 2.² The variability of the extreme sea conditions is shown in Figure 3 which is discussed in detail in Appendix B.

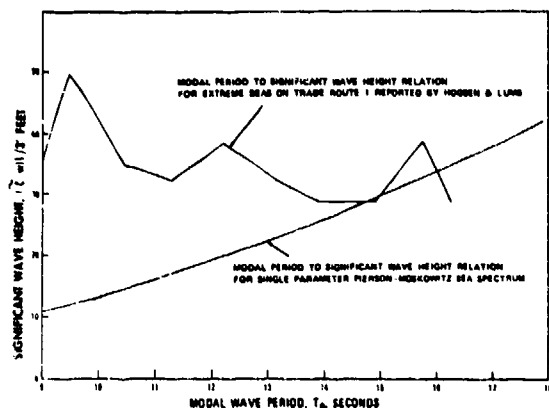


Figure 2 - Comparison Between Modal Period Wave Height Relation Required by Single Parameter Pierson-Moskowitz Sea Spectrum and Observed Modal Period to

²The significant wave height in Figure 2 should be 49.5 rather than 32.1 feet. (Hogben and Lumb). Accordingly, Figure 1a (Stage 2), 1b, 3, and 6 should have values plotted at $T_o = 11.3$ seconds increased by a factor of $49.5/32.1 = 1.5$.

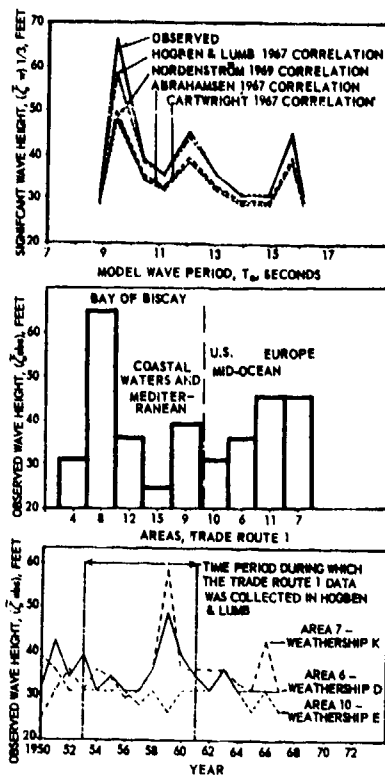


Figure 3 - Variability of Extreme Sea Conditions on Trade Route 1

No long-term distribution for wave heights and periods is assumed. Neither has a fixed significant wave height to mean wave period relation such as the one represented by the single-parameter Pierson-Moskowitz spectrum been employed. The observations based on results from Hogben and Lumb [10], see Figure 2, clearly show that the extreme seas do not follow, as expected, a fixed height/period relationship. The figure illustrates that only for modal wave periods ranging from 14 to 16 seconds will the height/period relationship indicated by the single-parameter Pierson-Moskowitz spectra agree with observations.

Because of this rather obvious discrepancy between an "average" and the observed height/period relationship (height or wind speed), the two-parameter (height and period) Bretschneider spectrum [5] was selected.

$$S_c(\omega) = \frac{1}{8} A \omega^{-5} \exp [-B/\omega^4] \quad (1)$$

where

$$A = 5356.7 \zeta_w^2 / T^4 \quad (2)$$

and

$$B = 1052 / T^4 \quad (3)$$

$S_c(\omega)$ is the wave spectrum

$\bar{\zeta}_w$ is mean wave height and

T is mean wave period

The mean wave height is related to the significant wave height by

$$\begin{aligned} \bar{\zeta}_w &= 0.625 (\bar{\zeta}_w)_{1/3} = 0.625 (4 m_0)^{1/3} \\ &= 2.5 m_0^{1/3} \end{aligned} \quad (4)$$

The mean wave period is the crest to trough period used by Bretschneider/Putzz [11]. This period is related to the wave spectrum by

$$T = 2\pi m_{-1} / m_0 \quad (5)$$

where

$$m_1 = \int_0^\infty \omega^1 S_c(\omega) d\omega \quad (6)$$

Although many expressions have been proposed by various authors to describe the directional spread of the waves, cosine squared spreading was selected for this investigation, i.e.,

$$S_c(\omega, \nu) = S_c(\omega) \cdot \left[\frac{2}{\pi} \cos^2(\nu - \mu) \right] \quad (7)$$

where μ is the heading angle of the ship and ν is the spreading angle. This spreading is the most frequently observed function describing the data of Rudnick [12].

Observed wave heights, ζ_{obs} , and periods, T_{obs} , were converted into the parameters required ($\bar{\zeta}_w$, T) for the Bretschneider spectral representation of the sea. Cartwright's [13] correlations between measured and observed wave heights and periods were used for this conversion, i.e.,

$$(\bar{\zeta}_w)_{1/3} = 2.55 + 0.66 \zeta_{obs} \text{ meters} \quad (8)$$

and

$$T_0 = 6.58 + 0.448 T_{obs} \text{ seconds} \quad (9)$$

The relationship between the modal, T_0 , and mean, T , period for the Bretschneider spectrum, i.e.,

$$T_0 = 1.166 T \quad (10)$$

and the relation between the mean apparent (or zero crossing period, T , and Bretschneider/Putzz [11] mean crest to trough period \bar{T} , i.e.,

$$\bar{T} = T/0.83 \quad (11)$$

was used to relate the mean apparent period \bar{T} with the modal period of the Bretschneider spectrum. This gives

$$T_0 = 1.166 T/0.83 = 1.4 T \quad (12)$$

It should be noted that Cartwright [13] derived his relationship between observed and measured wave periods for the mean apparent wave period

$$\bar{T} = (4.7 + 0.32 T_{obs}) \quad (13)$$

so that

$$\begin{aligned} T_0 &= 1.4 (4.7 + 0.32 T_{obs}) \\ &= (6.58 + 0.448 T_{obs}) \end{aligned} \quad (9)$$

The procedure for the selection of sea conditions, on the trade routes specified by the USCG, the validity of the Bretschneider spectral representation for extreme seas, the variability in extreme seas due to the correlation uncertainties between observed and actual wave heights, the variability in extreme seas due to geography constraints of trade routes, as well as the long-term (18 years) variability in extreme seas for the North Atlantic Trade Route are all treated in Appendix B.

Confidence Level and Exposure Time

In order to predict the ship motions in extreme seas which will not be exceeded at various levels of probability, two elements are required. The first is the expected length of time that the ship will be exposed to the seas, i.e., the ship exposure time; and the second is the probability distribution function of the wave heights.

The prediction of extreme ship responses is here regarded as designing for ship responses during a single severe storm or for a relatively short time period for a series of storms. The sea conditions are considered to be stationary, i.e., statistically unchanging for the time period for which response predictions are made. By considering a ship lifetime of 20 years, a total downtime of 25 percent (5 years) for the ship, a loading and unloading turnaround time in port of 1.5 days, it can be shown that the ship may be expected to be exposed to any particular extreme sea condition characterized by a given modal wave period and significant wave height for a rather short time. It is assumed, for this calculation, that the ship will spend its entire 4210 days at sea on Trade Route 1 (North Atlantic). The days at sea are derived from an assumed sustained ship speed of 20 knots, and a trade route length of 4800 nautical miles. 421 separate ocean crossings on Trade Route 1 are thus expected from the above assumptions. During these 421 ocean crossings the ship is certain to encounter a large number of storms. However, only a few storms are likely to be encountered which have extreme seas on the order of the ones presented by the most extreme seas observed at

various modal wave periods tabulated in reference 10, see Figure 2. The exposure times of the ship to the extreme seas may be computed directly from the percentage of occurrence of the extreme seas, see Appendix B (Table 3). If this is done, very short exposure times ranging from 0.0126 to 0.50 days are obtained. These times, in general, correspond to the persistence of extreme waves in a single storm, see Reference 14. To account for the occurrence of several extreme storms in the lifetime of a ship, it is considered appropriate to use longer exposure times than those for a single storm. A total ship exposure time of three days, corresponding to several such storms, has been selected as being an appropriately conservative design exposure time. The significance of variations in exposure times is shown in Figure 4. It can be seen from this figure that once the ship exposure time exceeds three days, relatively little increase in the confidence factor C_T occurs.

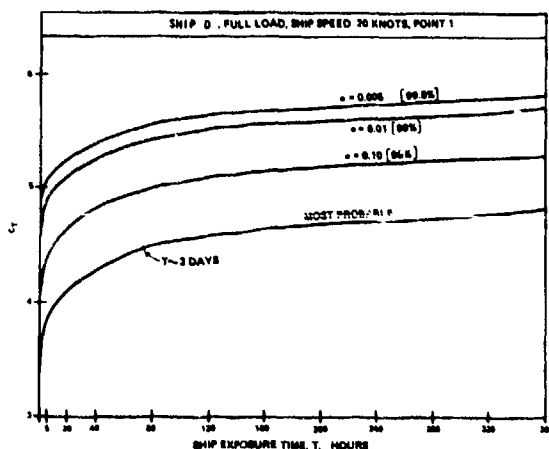


Figure 4 - C_T Versus Ship Exposure Time for Most Probable Extreme Value and Extreme Values not to be Exceeded 90, 99, and 99.5% of the Time

For short-term predictions of ship motions in statistically unchanging seas, it has been repeatedly shown by various oceanographers and naval architects in the past 20 years that the wave height and ship motions are distributed according to the Rayleigh distribution. This

distribution assumes that the wave height and linear ship responses are narrow-band processes. Based on these characteristics of wave height and ship responses Cartwright and Longuet-Higgins discuss in reference 15, the most probable extreme value, \bar{X}_T ,

$$\bar{X}_T = C_T \cdot \sigma \quad (14)$$

where the confidence factor C_T is

$$C_T = [2 \ln n]^{\frac{1}{2}} \quad (15)$$

and

$$\hat{X}_T = C_T \cdot \sigma \quad (16)$$

where

$$C_T = [2 \ln \frac{n}{\alpha}]^{\frac{1}{2}} \quad (17)$$

for the extreme value, \hat{X}_T , having a probability α (where α is small) of being exceeded, see Reference 16. n is defined as the number of observations. It should be noted that Ochi [16] extended this concept to include the more realistic case of wide-banded processes, i.e., $\epsilon \leq 0.9$, where

$$\epsilon = [1 - \frac{m_2^2}{m_0 m_4}]^{\frac{1}{2}} \quad (18)$$

Ochi also defined extreme values as a function of time T , in hours, by using

$$n = (60)^2 \frac{T}{2\pi} (\frac{m_2}{m_0})^{\frac{1}{2}} \quad (19)$$

for the case $\epsilon = 0$. Therefore,

$$C_T = \{2 \ln [(60)^2 \frac{T}{2\pi} (\frac{m_2}{m_0})^{\frac{1}{2}}]\}^{\frac{1}{2}} \quad (20)$$

for the most probable extreme value and

$$C_T = \{2 \ln [(60)^2 \frac{T}{2\pi \alpha} (\frac{m_2}{m_0})^{\frac{1}{2}}]\}^{\frac{1}{2}} \quad (21)$$

for the case where the extreme value has a probability α (α small) of being exceeded. Therefore,

$$\bar{X}_T = C_T \cdot \sigma \quad (22)$$

using equation (20)

and

$$\hat{X}_T = C_T \cdot \sigma \quad (23)$$

using equation (21).

The most probable extreme value, \bar{X}_T , has been selected for the calculations of the pilot study presented in this paper. Due to other large uncertainties in the extreme response surface, the most probable value was considered appropriate here. A more conservative extreme value, say \hat{X}_T with $\alpha = 0.005$ (99.5 percent level) causes approximately a 24 percent increase in predicted extreme accelerations.

The relative significance of various α levels in comparison to variations due

to different proposed wave height and period correlation procedures can be determined by comparing the percentage variation in C_T due to more conservative design levels than the most probable extreme, and the percentage variation in $(\dot{\xi}_w)_{1/3}$ due to a change in the correlation equation. This comparison, made on the basis of Figures 3 and 4, indicates quite clearly that they are of comparable importance. That is, both types of variations can independently vary the predicted extreme values up to 24 or 22 percent. A far more significant influence on the predicted extreme accelerations is the variation in the extreme heights reported for the different modal wave periods. This variation is reflected directly in the contours of the extreme response surface.

Extreme Response Surface

The extreme response surface is the product of unit response surface, the extreme sea conditions, and the confidence factor, see Figure 1. The irregularity (across modal period) of this surface is due primarily to variations of up to 71 percent in the observed extreme wave heights across modal period, see Figure 2. The "jaggedness" of the observed extreme wave height to period curve of Figure 2 is also apparent in the extreme response surface (product with unit wave height surface and C_T) of Figure 1b. Until a great deal more extreme wave height/period data is collected, it is not clear whether or not this large 71 percent variation in wave heights for different wave periods can be either neglected or smoothed over in some fashion, e.g. the average extreme over modal period. It should be noted that the 71 percent variation in wave height does not mean that there is 71 percent uncertainty in the selected design accelerations. The selection procedure could delete, for example, this extreme variation in design wave conditions. However, the variations due to varying a level or wave height correlation do indicate up to 24 percent uncertainty in the selected design accelerations.

Once the extreme response surface of the ship is determined for the design range of speeds and load conditions, the task is to select from this group of surfaces a realistic value that can be regarded as an adequately safe design value. For the particular example shown in Figure 1, one strategy for the selection of a design value is to take the largest value, or the average of the three largest values, or a similar scheme. The main point, however, is that a rational procedure for selecting the design value from a group of extreme response surfaces is required. It is considered essential that the regulatory agencies, the ship owners, as well as research naval architects, participate in the development of a rational procedure for

selecting design values from the extreme response surfaces. Several such procedures will be discussed briefly in the following Results Section of the paper.

RESULTS

Three figures summarize the main results of this work. Figure 1 presents the prediction process in graphical form; Figure 5 presents the significance of spatial variations along the ship on predicted extreme responses; and Figure 6 presents a comparison between the predicted extreme accelerations for two different selection strategies and the CTIAC proposed rules of 1 October 1972.

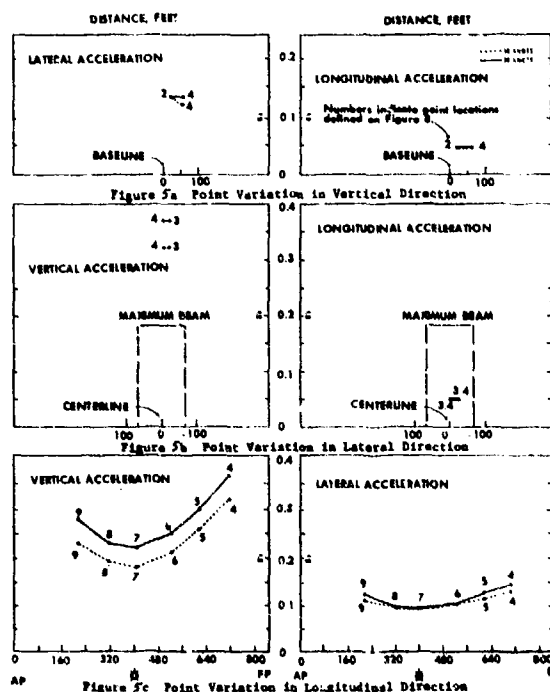


Figure 5 - Variations in Point Response Predictions with Variations in Point Locations for SHIP D, Full Load, Ship Speeds 10 and 20 Knots, Ship Heading 120 Degrees, Modal Wave Period 12.2 Seconds

All other results are regarded as being of secondary importance and are thus presented only briefly in the Appendices. It should be noted, however, that for shorter ships the significance of load variations, modal wave periods, and roll is expected to increase.

Interpretation of Extreme Accelerations

The predicted extreme accelerations are the result of a multiplication of three separate terms, as shown in Figure 1. Each term has associated with it a given uncertainty. The rms response, for example, can be considered to be accurate within the 10 percent range dictated by the worst spectral fit of a Bretschneider spectrum to true extreme sea conditions, see Appendix B. The extreme significant wave height has associated with it the 20 to 22 percent difference that can be obtained by using the various height correlation relations of Cartwright, Hogben and Lumb, Nordenström and Abrahamsen and the up to 71 percent variation over modal period. Finally, it is clear that the individual designers can readily influence the design by selecting design values that are based on a more conservative probability level (up to 24 percent more) than the most probable extreme value. Thus, it is important to note that the process of developing an extreme response surface consists of the multiplication of three variables each of which has associated with it variations which can independently vary the predicted extreme responses by 10 (due to σ), 22 to 71 (due to $(\bar{\zeta}_w)_{1/3}$), or 24 (due to C_T) percent.

Application of Extremes to Design

Figure 5 illustrates the acceleration response variations that may be expected when changes of location in the longitudinal, lateral, and vertical directions occur on or in the ship. It is evident that significant response variations occur only when very large location changes are made. In the context of ship design, this means only the longitudinal location of a point on the ship has a significant bearing on the magnitude of the acceleration response. The verification of this conclusion for other ships and additional ship speeds and headings is required. It should also be pointed out that only the vertical accelerations and, to a lesser extent, the lateral accelerations vary substantially with location on the ship.

A comparison is made at both 10 and 20 knots between the predicted extreme longitudinal, lateral, and vertical most probable accelerations and the comparable values based on the proposed 1 October 1972 CTIAC rules. Figure 6 shows the results of this comparison. Two different strategies for selecting extreme values from the extreme response surface are shown. The first is designated as the "Worst Heading" strategy. This strategy selects from the extreme response surface the largest predicted response at each modal wave period. The second strategy is regarded as being more realistic and is designated as the "Most Likely Heading" strategy. It is considered that when a ship encounters the extreme seas which are the basis for

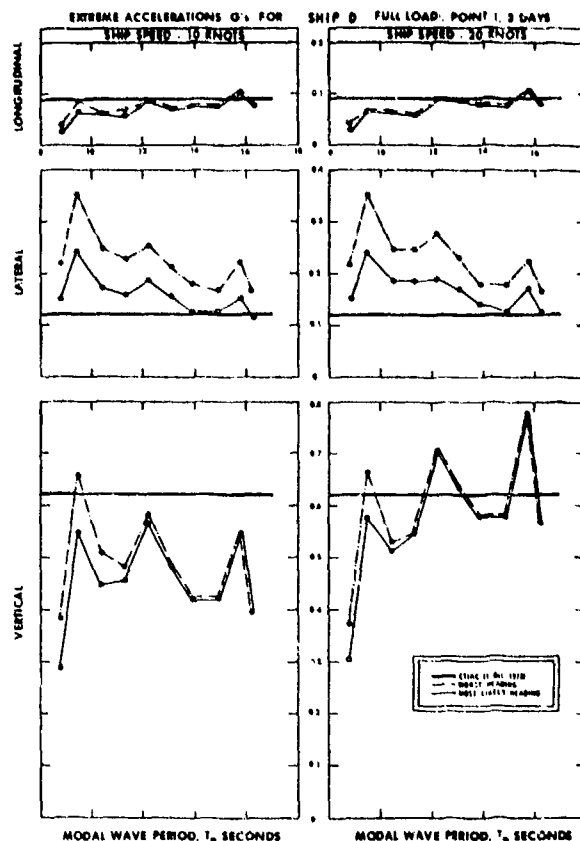


Figure 6 - Comparison of Predicted Extreme Accelerations (Most Probable), Point 1, SHIP D, Ship Speed 10 and 20 Knots. [CTIAC (1 Oct 1972), Worst Heading, Most Likely Heading]

these predictions, the captain will consider these storms as seas which significantly endanger his ship. As a consequence, it is expected that the tried and true "head directly into the wind and sea" will be followed. It is similarly considered unlikely that the visual estimate of the sea will be off from the true predominant sea direction by more than 30 degrees. The "Most Likely Heading" strategy thus consists of selecting the largest predicted response for headings between 180 and 150 degrees at each modal wave period. It should be noted at this time that both strategies select the largest values for a particular acceleration, such as lateral or vertical, independently. Thus, the longitudinal, lateral, and vertical accelerations shown do not correspond to the same identical heading. In this connection, the realism introduced by the use of spreading function for the waves is evident in the realism displayed in the results. Clearly, extreme wind driven seas are not long crested. Unlike the unrealistic case of long crested seas, longitudinal accelerations do not go to zero in beam seas,

nor do lateral accelerations go to zero in head seas, nor do vertical accelerations necessarily reach a maximum value directly in head seas, see Appendix B.

The extreme vertical accelerations (most probable) for both the "Worst Heading" and the "Most Likely Heading" of Figure 6 reflect the strong variation in response with modal wave period. It is evident that at modal periods somewhat above 11 seconds, both strategies result in essentially the same extreme values. Below 11 seconds the more realistic "Most Likely Heading" strategy results in substantially lower predicted extremes, i.e., approximately 20 percent, than the "Worst Heading" strategy. In general, the predicted extreme vertical accelerations vary above and below the proposed CTIAC rule value. The predicted extreme longitudinal accelerations are much less sensitive to the variations in the extreme seas with modal period. The agreement between both strategies and the proposed CTIAC rule for longitudinal acceleration is very good.

Lateral acceleration predictions unfortunately reflect the sea variations much more strongly than longitudinal accelerations. The differences in the results for the two strategies are greater than was the case for vertical accelerations and also these differences appear to be independent of modal period. It is significant here to note that the highest lateral acceleration predictions occur at the smaller modal periods. Thus, for lateral accelerations the significance of extreme seas which are properly related to wave period is evident. Unlike both longitudinal and vertical accelerations, the lateral acceleration predictions are much greater than those required by the proposed CTIAC rules. Clearly, the discrepancy between the present lateral acceleration rule and the predicted extremes is large and significant.

Further, it is considered essential to adopt a realistic speed limiting strategy in the determination of LNG cargo tank design values. One such speed limiting criterion actually employed by the operators of the present LNG tankers POLAR ALASKA and ARCTIC TOKYO [17] limits speed by avoiding pitch angles in excess of 3 degrees. This is considered a voluntary speed loss criterion. Another speed limiting criterion considers only the added drag (resistance) in extreme seas. This is considered an involuntary speed loss. Although ideally a combination of voluntary and involuntary speed limiting criteria might be used, it is considered that a more conservative and safe approach is to use only the involuntary speed loss. This involuntary speed loss due to the added drag in waves is less than the voluntary speed reductions in extreme seas. In addition,

the involuntary speed loss is less variable with operator actions than voluntary speed loss.

CONCLUDING REMARKS AND RECOMMENDATIONS

The CTIAC lateral acceleration rule (proposed 1 October 1972) may be too low for LNG cargo tank design. For example, for SHIP D the proposed rule is noticeably lower than both the "Worst Heading" and "Most Likely Heading" values. An investigation into this phenomenon for the entire range of actual and proposed LNG ships is therefore recommended. Subject to the resulting findings, modifications to the proposed 1 October 1972 CTIAC rules should be considered to improve the design lateral accelerations--if these values are to be adopted.

It is recommended that the USCG adopt the building block procedure developed here as an interim standard in specifying design acceleration, e.g. the average extreme across modal wave period could be readily used. The use of this interim standard should be encouraged until sufficient ships have been designed to the standard that a simpler rule can be deduced from an adequately large data/experience base. The interim standard could then be retained as an option for the design rule, at the discretion of the owner/designer. This process should be preferred over the one which specifies the design accelerations by very simple rules which do not take ship geometry or trade route into account.

In the above context, it is also recommended that an effort be made to adopt a realistic strategy for the selection of design accelerations from the extreme response surface. This refinement effort should include the ship owners, designers, the research naval architects, and the regulatory agencies.

The collection of more realistic wave height and period data (joint distributions as presented in Reference 10) for the Pacific is also strongly recommended. This is based on the rather strong influence that short modal period extreme seas have on lateral accelerations. It may be expected that the influence of modal period will be much more pronounced for smaller LNG tankers than was the case for SHIP D.

ACKNOWLEDGMENTS

The authors wish to express their appreciation to Mr. Joseph J. Ricci, Jr. of NSRDC, for his assistance in the computation of load response variations and the validity checks of two-parameter spectrum representation, and to Mr. Terrence Applebee and Mrs. Paula Thornton, both of NSRDC, for their assistance in preparation of the manuscript.

REFERENCES

1. Department of Transportation, USCG ltr 73350 Ser 743S, dtd April 1972 to Department of Defense, NSRDC.
2. "Rules and Regulations for Tank Vessels - Subchapter D," Department of Transportation, United States Coast Guard, May 1, 1969.
3. Salvesen, Nils et al., "Ship Motions and Sea Loads," Transactions of The Society of Naval Architects and Marine Engineers, Vol. 78, 1970, pp. 250-287.
4. Meyers, William G. and Bales, Susan Lee, "Manual-NSRDC Irregular Sea Response Prediction Computer Program," NSRDC, Bethesda, Maryland, Report 4011 (in preparation).
5. Estuary and Coastline Hydrodynamics, Edited by Arthur T. Ippen, McGraw-Hill, Inc., 1966, "Wave Generation by Wind, Deep and Shallow Water," (C.L. Bretschneider), pp. 133-196.
6. CTIAC/LNG-LPG Group Proposed Draft to 46-Code Federal Regulations Part 38, 1 October 1972 Revision.
7. Abrahamsen, Egil, "Recent Developments in the Practical Philosophy of Ship Structural Design," The Society of Naval Architects and Marine Engineers, Spring Meeting, Montreal, Canada, 1967.
8. Mansour, Alaa E., "Probabilistic Design Concepts in Ship Structural Safety and Reliability," Transactions of The Society of Naval Architects and Marine Engineers, Vol. 80, 1972, pp. 64-97.
9. Lewis, E.V., "Predicting Long-Term Distributions of Wave-Induced Bending Moment on Ship Hulls," The Society of Naval Architects and Marine Engineers, Spring Meeting, Montreal, Canada, 1967.
10. Hogben, N. and Lumb, F.E., Ocean Wave Statistics, Her Majesty's Stationary Office, London, 1967.
11. Bretschneider, C.L., "Wave Variability and Wave Spectra for Wind Generated Gravity Waves," Technical Memorandum No. 118, Beach Erosion Board, U.S. Army Corps of Engineers, 1959.
12. Rudnick, P., "Wave Directions from a Large Spar Buoy," Journal Marine Research, Vol. 27, No. 1, 1969.
13. Report of 3rd International Ship Structures Congress-Committee 1, "Environmental Conditions," 1967.
14. Snider, Robert H. and Chakrabarti, "High Wave Conditions Observed over the North Atlantic in March 1969," Journal of Geophysical Research, Vol. 78, No. 36, 1973, pp. 8793-8807.
15. Cartwright, D.E. and Longuet-Higgins, M.S., "The Statistical Distribution of the Maxima of a Random Function," Proceedings of the Royal Society of London, Series A, Vol. 237, 1956.
16. Ochi, Michel K., "On Prediction of Extreme Values," Journal of Ship Research, Vol. 17, No. 1, 1973, pp. 29-37.
17. Department of Transportation, USCG ltr OCMT, Marine Inspection Office Alaska, Ser 5923 dated 30 Nov 1972 to USCG (GMMT), Washington, D.C.
18. Dommershuijzen, R.J., "Seakeeping Model Experiments for a 120,000 m³ L.N.G. Tanker," Netherlands Ship Model Basin, Wageningen, Holland, Report No. 70-351-ZT, 1972.
19. Baitis, A.E. and Wermter, R., "A Summary of Oblique Sea Experiments Conducted at the Naval Ship Research and Development Center," Appendix 8 of the Seakeeping Committee Report, 13th International Towing Tank Conference, 1972.
20. Cragin, J.O., "Ship Response Instrumentation Aboard the Container Vessel SS Boston: Results from Two Operational Seasons in North Atlantic Service," Report SSC-214, Ship Structure Committee, 1970.
21. Yamanouchi, Y. and Ogawa, A., "Statistical Diagrams of the Winds and Waves on the North Pacific Ocean," Ship Research Institute, Tokyo, Japan, 1970.
22. Report of 4th International Ship Structures Congress-Committee 1, "Environmental Conditions," 1970.
23. Report of 2nd International Ship Structures Congress-Committee 1, "Environmental Conditions," 1964.
24. "Wave Spectra Estimated from a Stratified Sample of 323 North Atlantic Wave Records," Minutes of Meeting No. 53 of The Society of Naval Architects and Marine Engineers Panel H-7, November 1969.

APPENDIX A EVALUATION (VALIDITY) OF RESULTS

RESPONSE VARIATIONS

A pilot study has been conducted to investigate the procedure outlined in this paper. The ship selected for the pilot study is a large LNG tanker, SHIP D. Figure 7 shows the important particulars of SHIP D. The pilot study included investigations into variations of ship parameters which might affect extreme acceleration predictions as well as investigations into the validity of the computer programs used to predict the ship responses.

Effect of Load Variation

Two types of load variations were examined. The first considered changes in roll radius of gyration, or effectively the natural roll period; and the second considered draft changes and the related displacement change. The effect of roll on acceleration was obtained by varying the roll radius of gyration, K_{ϕ} , by 10 percent of the base value (0.40 Beam). These gyration variations were examined for a realistic range of sea conditions. RMS accelerations were computed for $K_{\phi}/B = 0.32, 0.36, 0.40$, and 0.44, and are given in Table 1.

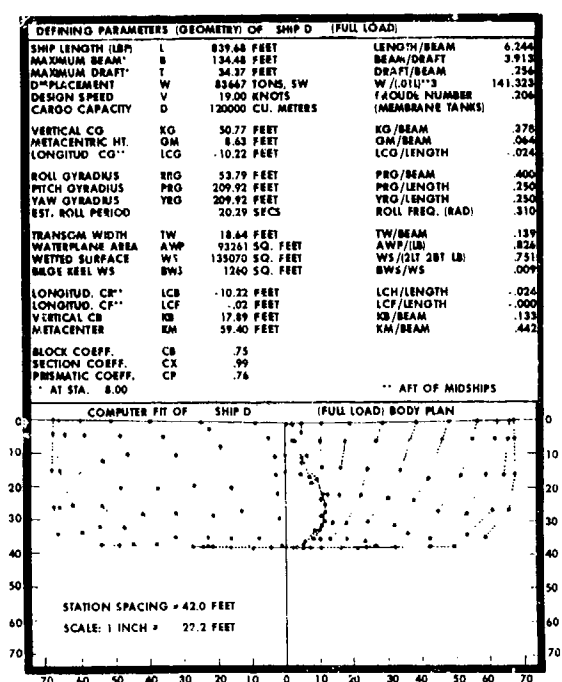


Figure 7 - Ship Particulars of SHIP D (Full Load)

Although rms roll response varied from 0.2° to 3.7° for the sea states investigated, the lateral accelerations varied by less than two percent, and the vertical and longitudinal accelerations varied by even less. The conclusion is that roll is not a significant factor in the determination of extreme design accelerations for this ship. This conclusion is borne out by LNG ship operator reports

which indicate that roll is not a problem for these ships. In this connection, it should be noted that a precise specification of the roll radius of gyration is therefore not necessary for such a large ship.

The draft/displacement effect on accelerations is shown in Table 2. Although rms roll increased up to 6° for the light draft condition, the largest difference in rms acceleration due to realistic draft changes is 0.005 g's. It is therefore concluded that the investigated draft variations do not significantly influence the acceleration responses for as large a ship as SHIP D. It is expected that the load variation will be much more significant for shorter ships.

Effect of Location

In order to examine the acceleration response variations that may be expected when location is changed in the longitudinal, lateral, or vertical direction on or in the ship, the responses were computed at ten distinct points, see Figure 8. Six of these points correspond to the centers of the six LNG tanks. Three points are located in the forward LNG tank and serve to define the importance of lateral and vertical position on acceleration responses. The tenth point, point 0, is at the origin of the calculation procedure, as defined in Reference 4.

An example of the results is shown in graphical form in Figure 5. The scales on both the response and the position axes of the graphs are the same and the extremities of the ship are also located on the scales. The results of this position investigation indicate that the most significant variations in acceleration responses (vertical and lateral) occur with shifts along the length of the ship rather than with shifts in the lateral or vertical direction.

TABLE 1 - EFFECT OF VARYING K_B/B ON ROOT MEAN SQUARE ACCELERATIONS AT POINT 1, SHIP D, FULL LOAD, 20 KNOTS, LONG CRESTED BEAM SEAS

Sea Condition		Roll (Deg)				Longitudinal Acc. (g's)				Lateral Acc. (g's)				Vertical Acc. (g's)			
$(\zeta_w)^{1/4}$ (FT)	T_0 (SEC)	K_B/B				K_B/B				K_B/B				K_B/B			
		.32	.36	.40	.44	.32	.36	.40	.44	.32	.36	.40	.44	.32	.36	.40	.44
23.8	7.3	.3	.3	.2	.2	.001	.001	.001	.001	.050	.049	.049	.048	.046	.046	.046	.047
23.9	12.24	.9	.4	.3	.2	.001	.001	.001	.001	.045	.044	.044	.044	.061	.061	.061	.061
23.8	13.9	2.7	2.0	1.3	.8	.001	.001	.001	.001	.041	.040	.040	.040	.056	.056	.056	.056
32.4	13.9	3.7	2.8	1.8	1.1	.001	.001	.001	.001	.056	.054	.054	.054	.076	.076	.076	.076

TABLE 2 - EFFECT OF DRAFT VARIATION ON ROOT MEAN SQUARE
ACCELERATIONS, SHIP D, POINT 1, 20 KNOTS,
LONG CRESTED SEAS

Sea Condition		Roll (Deg)				Longitudinal Acc. (g's)				Lateral Acc. (g's)				Vertical Acc. (g's)			
(F _W) (PM)	T _O (SEC)	Head		Beam		Head		Beam		Head		Beam		Head		Beam	
		Lt	Full	Lt	Full	Lt	Full	Lt	Full	Lt	Full	Lt	Full	Lt	Full	Lt	Full
23.8	7.3	0	0	.2	.2	.001	.001	.001	.001	0	0	.046	.049	.020	.015	.056	.046
23.9	12.24	0	0	3.0	.3	.010	.011	.001	.001	0	0	.040	.044	.094	.090	.065	.061
23.8	13.9	0	0	4.4	1.3	.013	.014	.001	.001	0	0	.036	.040	.106	.104	.059	.056
32.4	13.9	0	0	5.9	1.8	.017	.018	.001	.001	0	0	.049	.054	.144	.142	.081	.076

Load	K _s /B	GM/B	Draft (FT)	Displacement (Tons)
Light	.44	.14	32.2	75159
Full	.40	.06	34.4	83667

It should be noted that:

- a) longitudinal ship response is constant along any longitudinal line through the ship, for example, the longitudinal acceleration is the same for points 4 through 9 in Figure 8;

- b) lateral ship response is constant along any lateral line through the ship, for example, the lateral acceleration is the same for points 3 and 4 in Figure 8; and

- c) vertical ship response is constant along any vertical line through the ship, for example, the vertical acceleration is the same for points 2 and 4 in Figure 8.

VALIDITY OF ACCELERATION PREDICTIONS

Comparison With Model Experiments

The regular wave response predictions output by the computer programs, see References 3 and 4, have been compared at three speeds with the results of model experiments for SHIP D conducted at the Netherlands Ship Model Basin, Wageningen, Holland [18]. This experimental verification of the computer program involves pitch, heave, and roll in addition to vertical acceleration at the center of the forward tank. The ship model was ballasted to a condition very close to the full load condition given in Figure 7.

The heave displacement and vertical bow acceleration comparisons are shown in Figure 9, with pitch and roll comparisons shown in Figure 10. Comparisons are made on the basis of response transfer functions, i.e., the square root of the ship response amplitude operators. One of the components of the vertical acceleration, heave, does not compare very well with measured model results. However, the remaining components (pitch and roll) and most importantly the resultant vertical acceleration (at the center of the forward LNG tank), agree satisfactorily with the measured results. It is therefore concluded that the computer programs adequately predict the vertical accelerations which are under investigation. Additional experimental verification

POINT	DEFINITION	LONGITUDINAL DISTANCE FROM 4TH PERPENDICULAR (FEET)	LATERAL DISTANCE FROM 4TH PERPENDICULAR AXIS (FEET)	VERTICAL DISTANCE FROM BASELINE (FEET)
0	ORIGIN WATERPLANE	430.1	0.0	34.4
1	FORWARD POINT OF FORWARD TANK	743.5	35.0	16.7
2	BOW CENTER OF GRAVITY OF FORWARD TANK	75.7	0.0	16.7
3	TO SIDE OF CENTER OF GRAVITY OF FORWARD TANK	708.7	35.0	33.7
4	CENTER OF GRAVITY OF FORWARD TANK	708.7	0.0	33.7
5	CENTER OF GRAVITY OF 2ND TANK	615.5	0.0	33.1
6	CENTER OF GRAVITY OF 3RD TANK	521.0	0.0	33.0
7	CENTER OF GRAVITY OF 4TH TANK	401.4	0.0	33.0
8	CENTER OF GRAVITY OF 5TH TANK	314.9	0.0	33.0
9	CENTER OF GRAVITY OF LAST TANK	215.0	0.0	32.9

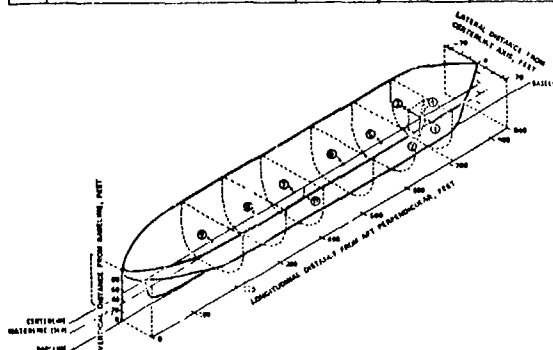


Figure 8 - Point Locations for Prediction of Extreme Accelerations for SHIP D

of ship motions predicted by the program can be found in Reference 19.

vertical acceleration ratios on the order of 0.6 were obtained. In this connection, it should be noted that even large lateral acceleration response ratios were measured on board the SS Boston, see Reference 20, although there is some question as to the measurement process employed on this ship. It is concluded from these results that the computer programs predict reasonably accurate values of longitudinal and lateral accelerations.

APPENDIX B REPRESENTATION AND VARIABILITY OF EXTREME SEA CONDITIONS

SOURCES OF EXTREME SEA CONDITIONS

Because the extreme accelerations developed in this paper depend on observations of the actual sea for the extreme seas, a literature search for

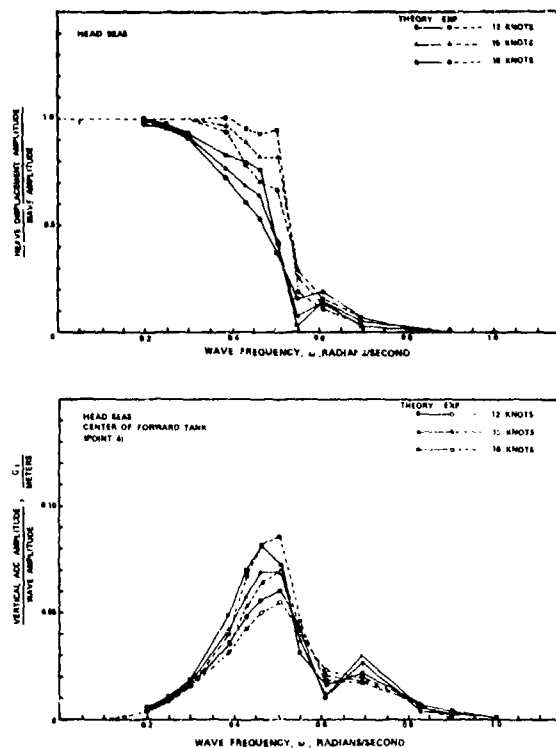


Figure 9 - Comparison of Predicted (Theory) and Measured (Exp.) Responses in Regular Waves of SHIP D, Full Load

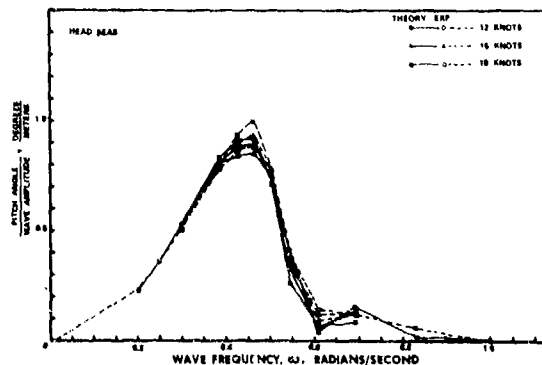
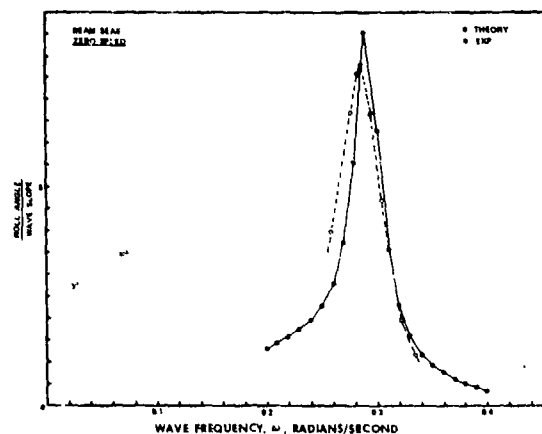


Figure 10 - Comparison of Predicted (Theory) and Measured (Exp.) Responses in Regular Waves of SHIP D, Full Load

Comparison With Full Scale Trials

Experimental verification for the lateral and longitudinal accelerations is somewhat more difficult to obtain. Only limited experimental data on lateral motions and accelerations is available. Reference 3 shows limited sway motion comparisons. To develop some basis for broadly verifying the predicted lateral and longitudinal acceleration levels, full scale values measured by NSRDC in 1972 and 1973 on the USS GUAM (LPH-9) were examined. Figure 11 shows a comparison of the relative magnitudes of longitudinal, lateral, and vertical accelerations. These accelerations were all referenced to the vertical acceleration. It should be noted that rather large lateral accelerations were obtained. Both measured and predicted lateral to

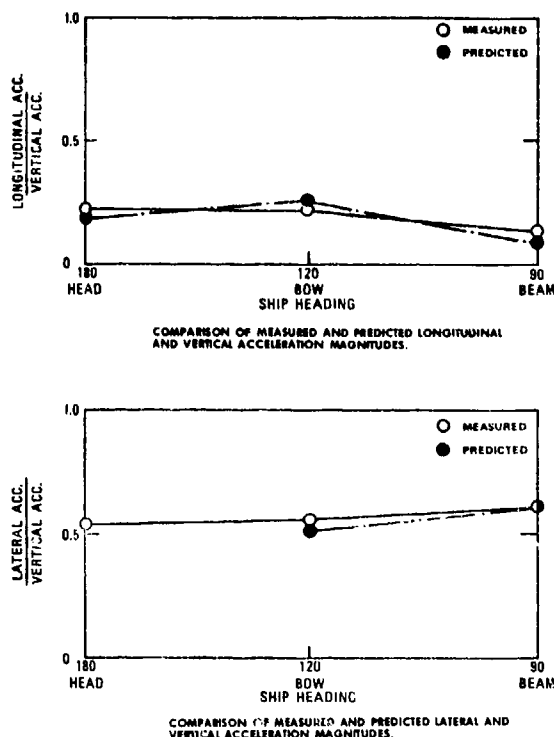


Figure 11 - Comparison of Measured and Predicted Acceleration Magnitudes, near the Stern of LPH-9, Ship Speed of 5 Knots

such measured or observed sea data has been conducted. Of particular interest was the joint compilation of wave heights and periods over eight years given by Hogben and Lumb [10]. These data were compiled in a format directly applicable to the use of two-parameter wave spectra. In addition, the rather wide geographic area covered by Hogben and Lumb simplified the search for extreme sea conditions for the Atlantic Trade Route, designated as Trade Route 1 in Figure 12a. The USCG specified the areas shaded in Figure 12a as representing the most realistic, foreseeable trade route in the Atlantic.

Attempts at locating equally good observed or measured ocean data for the other most realistic, foreseeable trade route in the Pacific failed. The massive oceanographic data compiled by Yamanouchi and Ogawa [21], see large shaded area Figure 12b, were unsuitable for the prediction process developed. The method of presentation and data reduction chosen by Yamanouchi and Ogawa makes it impossible to reconstruct the joint wave height/wave period distri-

bution which is essential for the prediction of extreme accelerations.

The reports of the Environmental Committee of the International Ship Structures Congress [13], [22], [23] were also examined in order to locate extreme sea data (height and period) which would be representative of the Pacific. Only two extreme wave height/wave period observations were located in Reference 13. These are the observations, shown in Figure 12b, made in 1963 aboard two Japanese freighters. It should be noted that other reported extreme wave height/wave period sets were essentially subsets of the Atlantic trade route data [23]. Figure 13 presents the extreme sea conditions located thus far.

The conclusion that the North Pacific may be regarded as a subset of the North Atlantic cannot, at this time, be drawn

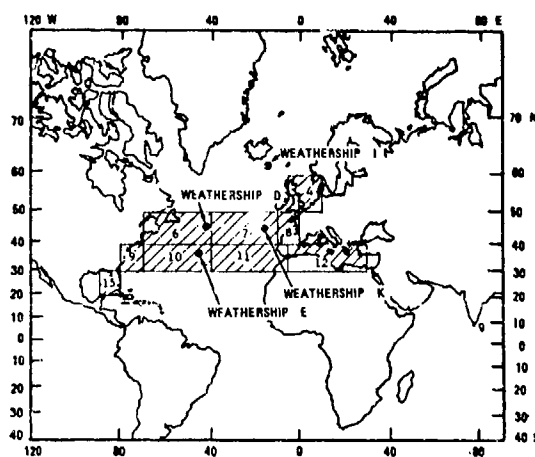


Figure 12a. North Atlantic, Trade Route 1

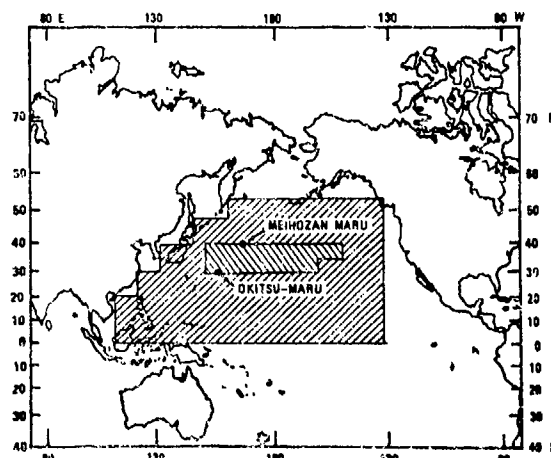


Figure 12b. North Pacific, Trade Route 2

Figure 12 - Assumed Trade Routes for North Atlantic and North Pacific

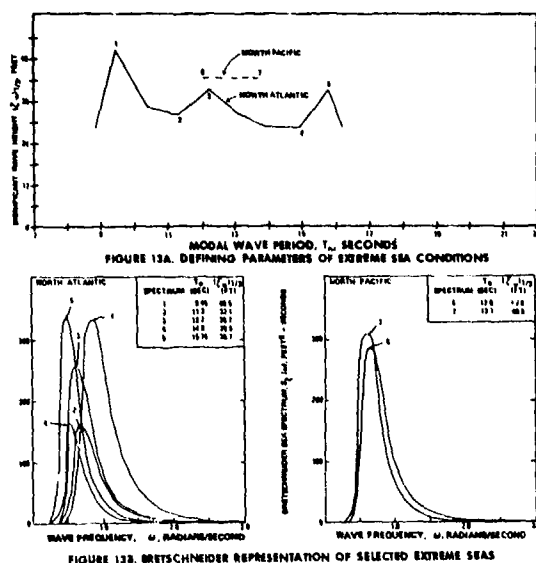


Figure 13 - Extreme Sea Conditions Selected for the North Atlantic and the North Pacific

since far too little extreme joint wave height/wave period data have been collected or located and reduced in a suitable format for the North Pacific. It can only be concluded at this time that more suitably reduced oceanographic data for the Pacific are required.

REPRESENTATION OF EXTREME SEAS

Validity of Two-Parameter Spectral Representation

The effect of using the idealized two-parameter Bretschneider spectral formulation to represent realistic, extreme sea spectra was investigated. A series of measured wave spectra of very high seas was used to examine the adequacy of the Bretschneider spectral fit to real, extreme seas. These measured spectra were recorded (see Figure 12a) on weatherships at Station India in the North Atlantic [24]. As a measure of the adequacy of the spectral fit, differences in computed ship responses based on the measured spectra and the Bretschneider spectral fit to these measurements were computed.

The energy-averaged period, T_{-1} , and the significant wave height $(\bar{\zeta}_w)_{1/3}$, of the measured spectra were used to calculate the corresponding Bretschneider spectra. Thus, the period parameter, T ,

in the Bretschneider spectrum corresponding to the measured Station India spectrum is

$$T = T_{-1} = 2\pi m_{-1}/m_0 \quad (24)$$

Similarly, the height parameter, $\bar{\zeta}_w$, for the Bretschneider spectrum was computed from the significant wave height, $(\bar{\zeta}_w)_{1/3}$, of the measured spectra by

$$\bar{\zeta}_w = 0.625 (\bar{\zeta}_w)_{1/3} = 0.625 (4m_0^{1/4}) = 2.5 m_0^{1/4} \quad (25)$$

Longitudinal, lateral, and vertical accelerations were computed in head and beam seas at three ship locations using the Bretschneider (B) and Station India (SI) spectra. An example of the results is shown for three different measured wave spectra in Figure 14. These results represent the worst comparisons between ship accelerations in the measured and the Bretschneider fit sea spectra. Differences between B and SI longitudinal and lateral root mean square accelerations were less than 0.003 g's. The

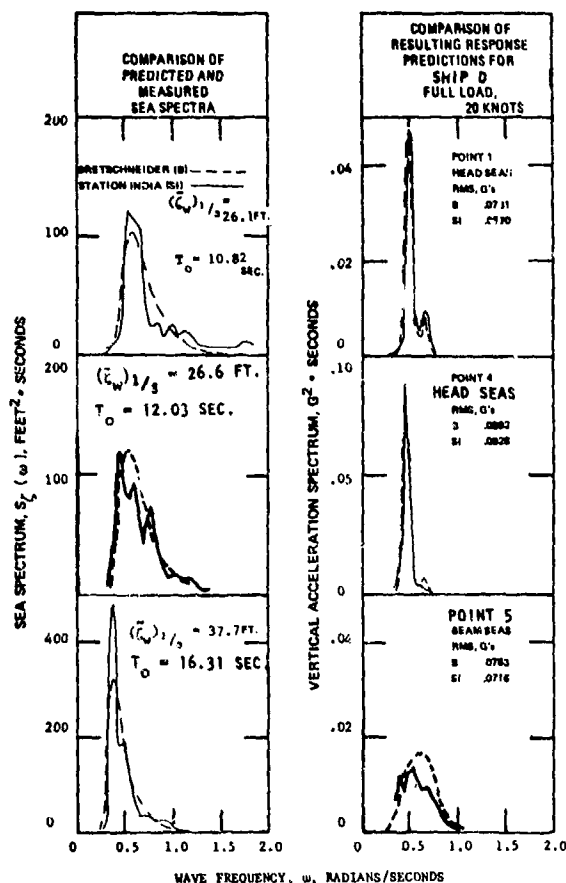


Figure 14 - Comparison Between Predicted Bretschneider Spectra and Wave Spectra Measured at Station India and Resulting Response Predictions

differences between B and SI vertical acceleration rms values range from 0.0036 to 0.0067 g's and are less than 10 percent of the SI values. It is therefore concluded that the Bretschneider spectral formulation provides an adequate representation for the extreme sea conditions investigated.

Short Crested versus Long Crested Representation

The effect of assuming a more realistic short crested rather than a long crested seaway is shown in Figure 15. Characteristics of each acceleration are as follows:

- the short crested longitudinal acceleration remains fairly constant across heading, whereas the long crested prediction is zero in beam seas;
- the short crested lateral acceleration is greater in head and following seas but less in beam seas than the long crested lateral acceleration; and
- the short crested vertical acceleration does not exhibit the double peak characteristic of the long crested prediction; the short crested value is greater in head, quartering, and following seas and less in bow seas than the long crested value.

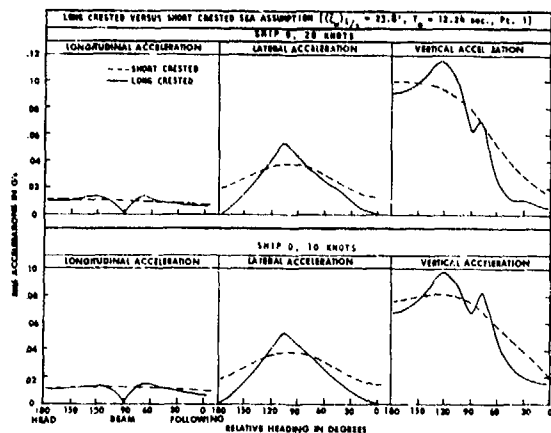


Figure 15 - Comparison Between Long Crested and Short Crested Predictions

In general, the short crested predictions do not exhibit the sharp resonances of the long crested form at certain headings. In addition, they show significant increases in the lateral and vertical accelerations in head and following seas. It is concluded that the more realistic short crested seas be used in the prediction of extreme accelerations.

VARIABILITY IN OBSERVED EXTREME SEAS

Three specific questions regarding the variability of the observed seas were examined to establish to some extent, the validity of the extreme accelerations calculated on the basis of these sea observations. The results are shown in graphic form in Figure 3.

Height Correlation for Observed Wave Heights

Several different wave height correlation equations have been proposed by various authors to relate the visually observed wave heights and periods to characteristic wave heights and periods that will describe the spectral distribution of the waves. The wave height variability that results from the use of different "correlation equations" is demonstrated in Figure 3a. The visually observed wave heights, also shown in this figure, illustrate the significance of this "correlation variability." A similar effort was not conducted for wave periods.

All height correlation equations tend to reduce the most extreme wave heights observed. The Hogben and Lumb correlation was made between weather-ship observations (i.e., observations by trained professionals), and measured results [10]. This correlation appears to result in only slight reductions between the observed heights and the characteristic measured significant wave heights.

It is interesting to note another group of correlation relations due to Nordenström [13], Abrahamsen [7], and Cartwright [13], result in substantially lower wave heights than the ones based on Hogben and Lumb [10]. The results from all three sets of correlation relations are quite similar. Cartwright's correlation [13] was selected for this work because it explicitly related the wave heights and periods observed by voluntarily cooperating ships with wave measurements. Cartwright's correlation was considered to be the most realistic one to use because, by far the majority of all observations come from voluntarily cooperative ships with relatively untrained observers rather than weather-ships with trained observers.

Since the use of different wave height correlation results in variations in extreme significant heights of more

than 10 feet, it is considered that the extreme observed heights are not likely to be much more accurate than this value. This large uncertainty in the actual reported wave height must, therefore, be taken into consideration in the final determination of the design accelerations.

Table 3 presents a tabulation of the correlated (Cartwright) observed data from Hogben and Lumb [10] for the North Atlantic Trade Route of Figure 12a. The table includes the frequency of occurrence of each height/period combination accumulated over the entire trade route for the years 1953-61. The curve denoted "Cartwright 1967 Correlation" in Figure 3a is taken as the highest significant wave height occurring in each modal period range in Table 3. The influence of geography on the highest observed height over all wave periods as well as the variation of highest observed heights with time are discussed in the following sections.

Geographic Influence on Largest Observed Wave Heights

The variability in the reported extreme height for the various areas in Trade Route 1 is examined in Figure 3b. Only the largest height for all wave periods in a particular area of the trade route is considered. It is

interesting to note that the relatively sheltered coastal waters (areas 4, 8, 12, 15 and 9, see Figure 12) contain the highest reported wave height in the trade route. The very large difference of more than 40 feet between area 8 (Bay of Biscay) and area 15 (Caribbean) demonstrates the strong influence of geography on this trade route.

Long-Term Variation in Largest Observed Wave Heights

The question of the applicability of the extreme sea conditions reported by Hogben and Lumb [10], for use in lifetime extreme or design determination was examined, see Figure 3c. The yearly extreme wave height, observed by three weatherships which are located on the Atlantic trade routes (noted on Figure 12a) were plotted for 18 consecutive years. Figure 3c clearly shows that the largest yearly extreme occurred in 1959. Thus, it can be tentatively concluded that the extremes on Trade Route 1 are realistic representations of sea conditions that might be expected to be encountered over a ship's 20-year life on the specified North Atlantic trade route. It is not possible to reach a similar conclusion with regard to the North Pacific trade route due to the scarcity of suitable long-term wave data.

TABLE 3 - SIGNIFICANT WAVE HEIGHT AND MODAL WAVE PERIODS FROM OBSERVATIONS, TRADE ROUTE 1 (NORTH ATLANTIC)

T ₀ (Sec) (FT)	Calm Undetermined Periods	<8.8	9.2 - 9.7	10.2 - 10.6	11.1 - 11.5	11.9 - 12.5	12.9 - 13.3	13.7 - 14.1	14.7 - 15.1	15.5 - 16.0	>15.0	Total
8.92	3.29	3.88	0.11	0.04	0.02	0.01	*	*	*	0.07	0.05	7.47
9.45	0.19	9.23	0.51	0.20	0.08	0.03	0.01	*	*	0.02	0.34	11.01
10.53	0.32	14.28	5.77	1.19	0.35	0.13	0.05	0.02	0.01	0.03	0.13	22.28
11.61	0.34	6.17	7.32	3.11	0.82	0.26	0.09	0.03	0.01	*	0.02	18.17
12.69	0.25	1.56	5.63	4.02	1.28	0.33	0.09	0.03	*	*	*	13.19
13.78	0.17	0.59	2.84	3.15	1.54	0.46	0.15	0.04	0.01	*	*	9.95
14.86	0.12	0.21	1.29	1.95	1.26	0.33	0.15	0.04	*	*	*	5.35
15.94	0.10	0.12	0.71	1.28	0.97	0.48	0.16	0.05	0.02	*	*	3.89
17.02	0.05	0.05	0.36	0.63	0.63	0.35	0.14	0.05	0.01	*	*	2.34
18.10	0.06	0.04	0.27	0.55	0.56	0.31	0.15	0.06	0.02	*	*	2.02
19.19	0.02	0.01	0.03	0.10	0.10	0.66	0.02	*	*	*	*	0.94
20.27	0.01	0.01	0.03	0.08	0.10	0.06	0.03	0.01	*	*	*	0.33
21.35	0.01	0.01	0.06	0.12	0.15	0.10	0.04	0.01	*	*	*	0.50
22.43	*	0.01	0.05	0.10	0.14	0.08	0.04	0.01	*	*	*	0.43
23.53	*	*	0.01	0.05	0.05	0.03	0.01	*	*	*	*	0.15
24.57	*	*	0.02	0.04	0.06	0.04	0.02	*	*	*	*	0.18
25.65	*	*	0.01	0.03	0.04	0.04	0.02	*	*	*	*	0.14
26.73	*	*	*	0.01	0.03	0.02	0.01	*	*	*	*	0.07
27.81	*	*	*	0.01	0.02	0.02	*	*	*	*	*	0.05
28.89	*(22)	*(3)	*	0.02	0.04	0.03	0.02	0.01(45)	*(26)	*	*(7)	0.12
32.13			*(2)	*(2)	*(2)	*(3)	*(1)					
34.29			*(1)	*(1)		*(3)						
38.61						*(4)				*(1)		
49.50			*(1)		*(1)							
Total	4.93	36.17	25.42	16.75	8.24	3.77	1.20	0.36	0.08	0.12	0.54	97.58

*Less than 0.01%

Number of observations listed for the highest wave height for each range of periods and for wave heights 19.9 feet or greater. Total number of observations 373,952.

DISCUSSION

EDWARD V. LEWIS

There are two approaches to the problem of predicting extreme ship responses to ocean waves. One is to develop a mathematical model covering the ship's response to all sea conditions and hence to obtain a cumulative distribution of all responses. The value to be exceeded in the lifetime of the ship -- or of a fleet of ships -- can then be read off. The other approach is to deal only with the extreme values of response, which are presumably associated with the most severe wave conditions.

The first approach has advantages in simplicity and easy full-scale verification. The second -- which is used in this paper -- is appealing because it is not encumbered with a large quantity of low-value data. However, there are some dangers that show up in the treatment given here, and these will be pointed out.

First, the highest wave spectrum of a given characteristic period may not produce the largest response. There are two reasons: (a) spectral shapes vary considerably, and (b) exposure time will be greater for the not-quite-highest waves.

Second, the final answer depends greatly on the extreme sea conditions selected. It is hard to be satisfied that the five shown in Figure 13 (from Table 3) are the real lifetime maxima to be expected. If three times as many observations had been made over the same period, or if the observations had continued over three times as long a period, one would expect that some more severe seas would have been reported.

Third, the determination of exposure time is a problem: "To account for the occurrence of several extreme storms in the lifetime of a ship, it is considered appropriate to use longer exposure times

than those for a single storm". Apparently a single Rayleigh distribution is used over a time period of three days, covering several storms. Such a procedure requires justification, since the continuous exposure to a single storm is not the same statistically as the separate exposure to several different storms.

On the basis of the above it appears to this discussor that, although the proposed procedure for establishing rational standards for accelerations on LNG ships is sound in principle, further steps are needed to make it more rigorous and acceptable. In particular, it is felt that the wave data (Table 3) should be fit to a suitable distribution function in order to obtain a more reliable maximum height for each period group. A more rigorous procedure should then be developed to determine the highest expected accelerations, considering exposure time not only to the maximum expected seas, but to the other severe seas near to the maximum.

It is recognized that the paper represents a pilot study, but it is important that, once the basic procedure is decided upon, systematic calculations be carried out over a range of ship sizes -- as recommended in the paper. It is also felt that the whole problem is so important that it is essential for independent calculations to be carried out by the other well-established approach mentioned in this discussion, and results compared. See [7] [8] [9].

The authors have rightly given considerable attention (Appendix B) to the effects of variability of wave spectral shapes. Current work by Dr. Dan Hoffman at Webb Institute has a bearing on this subject. He is also analyzing spectral data obtained by the Sea Use Council under MarAd sponsorship for Station Papa in the North Pacific. This work should help to fill in some of our gaps in knowledge of the Pacific Ocean.

D.L. FOLSOM

The authors are to be congratulated for the development of this building block procedure for determining design accelerations. This method provides a means to readily identify the stages of the procedure which will require further study and decisions by the regulatory bodies.

Certainly it is clear that there is a need for an improved wave data base, just as there is for any procedure which requires ship motion information.

The action which the Coast Guard takes on LNG tank design criteria must consider this work and the criteria recommended by the International Association of Classification Societies as well as the criteria recommended by the Chemical Transportation Industry Advisory Committee. One step that has been taken by these groups, that is not taken in this paper, is to provide a means to combine the accelerations into a resultant maximum acceleration vector. They accomplish this by simply adding the maximums. I would like to know if the authors agree with this procedure or do they have a more rational procedure for determining the resultant acceleration vector.

AUTHOR'S REPLY

We wish to thank Professor Lewis and LCDR Folsom for their penetrating comments on our paper. We agree with Professor Lewis that additional work is required in order to establish valid standards for the design of LNG cargo tanks. We believe that the emphasis in the next steps should be to improve the accuracy of the predicted design accelerations. In short, we believe that more physics or real data is required to improve design acceleration predictions. We do not believe that more rigorous mathematics or statistics would improve the realism of the predicted design accelerations.

In reply to Professor Lewis' cautionary statement that the largest responses do not necessarily occur in the seas with the highest waves, the following comments are offered. First, we are aware that there is full scale container ship data, such as from the SS BOSTON, which appear to confirm Professor Lewis' observation. However, the reason for this apparent confirmation is that the ships' masters employ operating strategies which tend to reduce objectionable ship responses, i.e., they voluntarily reduce speed or alter course. However, it is not considered to be appropriate for regulatory or design purposes to depend on voluntary operator strategies to reduce extreme ship responses. Thus, our use of the highest wave heights to define sea conditions in which the largest accelerations occur rests on the conservative assumption that involuntary factors, such as involuntary speed loss, reduce the design accelerations in extreme seas.

The influence of spectral shape variations in extreme seas on ship responses is treated by our use of the wave spectra at different modal periods. We are pleased to hear that Professor Hoffman is also analyzing Station Papa North Pacific wave data. We are using Station Papa extreme wave data to compare acceleration variations due to different measured wave spectra with acceleration variations that result when our series of wave spectra at different modal wave periods are employed.

When the ship exposure times for the not-quite-highest waves are considered (see Table 3) in the calculation of extreme ship responses, the largest ship responses still occur in the highest seas. We have verified this by simple calculations using Table 3 and varying

C_T and $(\zeta_w)_{1/3}$ in our building block approach to the prediction of design accelerations.

We agree with Professor Lewis' point that larger design accelerations than the ones given in this paper are possible, if these accelerations were based on extreme wave data selected from a larger wave data base than the one employed. That is of course, as noted by LCDR Folsom, the reason for an improved wave data base.

We have considered that the highest measured or visually recorded wave height/period combination is a valid extreme storm condition on which to base design acceleration predictions. We have employed only the visual data from Hoghen and Lumb. It is considered essential to update regularly (yearly) the wave data base from which the extreme design accelerations are calculated. Thus, it is intended that the design accelerations be improved yearly as more extreme sea measurements and observations become available. We do not concur with the approach which fits distribution functions to the measured or observed wave data base and then "extrapolates" the extremely rare events to some convenient level of statistical confidence. We do not consider that the added layer of sophistication in treating rare, extreme sea data adds any confidence to the predicted level of the extreme seas and the extreme sea ship responses.

It has been concluded that results will be conservative when exposure times greater than the ones for a single storm are used along with the associated assumption that a single Rayleigh distribution is valid over this entire exposure time at a constant wave condition. Results indicate that predictions of extreme wave heights, and thus ship responses, based on the above assumptions may be as much as 20 percent larger than values that may be expected from measurements based on a large series of 1/2 hour wave height measurements.

In response to LCDR Folsom's question regarding our opinion of the present IAX and CTIAC acceleration combination rule, let me state that we have as yet not formed an opinion. However, we are presently examining the validity of the present rule by using predicted, correlated time histories of all three acceleration components, i.e., vertical, lateral, and longitudinal.

LIQUID SLOSH IN LNG CARRIERS

H. N. Abramson
Southwest
Research Institute
San Antonio, Texas

R. L. Bass
Southwest
Research Institute
San Antonio, Texas

O. Faltinsen
Det Norske Veritas
Oslo, Norway

H. A. Olsen
Det Norske Veritas
Oslo, Norway

ABSTRACT

Results of several research programs to investigate sloshing in Liquid Natural Gas (LNG) Carriers are presented. The history of slosh-related problems in LNG carriers is discussed including a listing of recorded tank damages from LNG sloshing. Sloshing considerations for different tank designs are also presented. In addition theoretical and experimental studies for determining liquid response characteristics for different tank geometries and fill levels are delineated. The scaling of LNG slosh loads from model data to full scale is also discussed and available full scale load measurements are presented. Areas requiring further investigation are also enumerated as well as design implications from the studies to date.

INTRODUCTION

History of Slosh Problem

The initial attempt at LNG transport by water was accomplished in the early 1950's when a barge called "Methane" was constructed with five cylindrical balsa lined tanks with a total capacity of 6000 cubic meters. In spite of several technical problems with the balsa insulation the project was considered a success but was abandoned for economic reasons. In subsequent years increasing gas shortages and energy demands in Europe and Japan made LNG transport economically feasible, and by the early 1960's commercial transport of LNG was occurring in ships with cargo capacities of approximately 25,000 cubic meters. Since the mid 1960's, LNG ship technology has advanced considerably and ships of numerous designs and capacities have evolved (Figure 1). At present, LNG carriers are under construction with capacities of 125,000 cubic meters with ships as large as 150-200,000 cubic meters anticipated for use in the near future.

As the various LNG ship designs have evolved, several important types of unique ship loads have been considered by the designers of LNG carriers. One of the most important ship loads results from sloshing of the LNG in the

cargo tank. These slosh generated loads have a considerable influence on the tank and support structure design. Accounting for liquid impact loads in cargo tanks is not restricted to LNG carriers since similar problems have been experienced in other types of liquid transport ships such as bulk oil carriers. However, several factors make slosh loads more important with regard to LNG ship design. A tank failure in a LNG ship merits special consideration because of 1) the risk of brittle fracture of the primary structure (low temperature shock), 2) the expensive repair cost of the complicated tank designs, 3) the high out-of-service costs and 4) a potentially explosive cargo. In addition, special requirements result in LNG tanks being partially full; a condition creating the highest impact loads from liquid sloshing. Partial filled conditions occur because 1) chill-down liquid is needed to maintain cold tanks on return trips, 2) higher specific gravity liquids than LNG are transported in tanks designed for LNG weight, 3) partial unloading is desirable when multi-port stops are made and 4) loading or unloading at sea creates significant time periods at undesirable fill depths. Also, the complexity of the tank design in LNG carriers is such that at least some LNG tanks are more susceptible to damage from slosh loading than tanks for transporting oil or other petroleum products.

There are presently over 10 designs of LNG tanks (1) that are either currently in use or under major consideration. These tanks generally fall into two categories; namely, free-standing (independent) and non-free-standing (membrane) tanks (Figure 2). Integral tanks used for LPG transport are not acceptable for LNG since their use is restricted to temperatures greater than -10°C . The freestanding or independent tank is usually of the spherical or cylindrical design and because of its geometry it is amenable to stress analysis and other conventional analytical techniques. Because the stresses can be calculated, a secondary barrier system is not required as is the case of the non-free-standing tanks. An exception is the prismatic freestanding tank which does require a secondary barrier. Freestanding tanks are

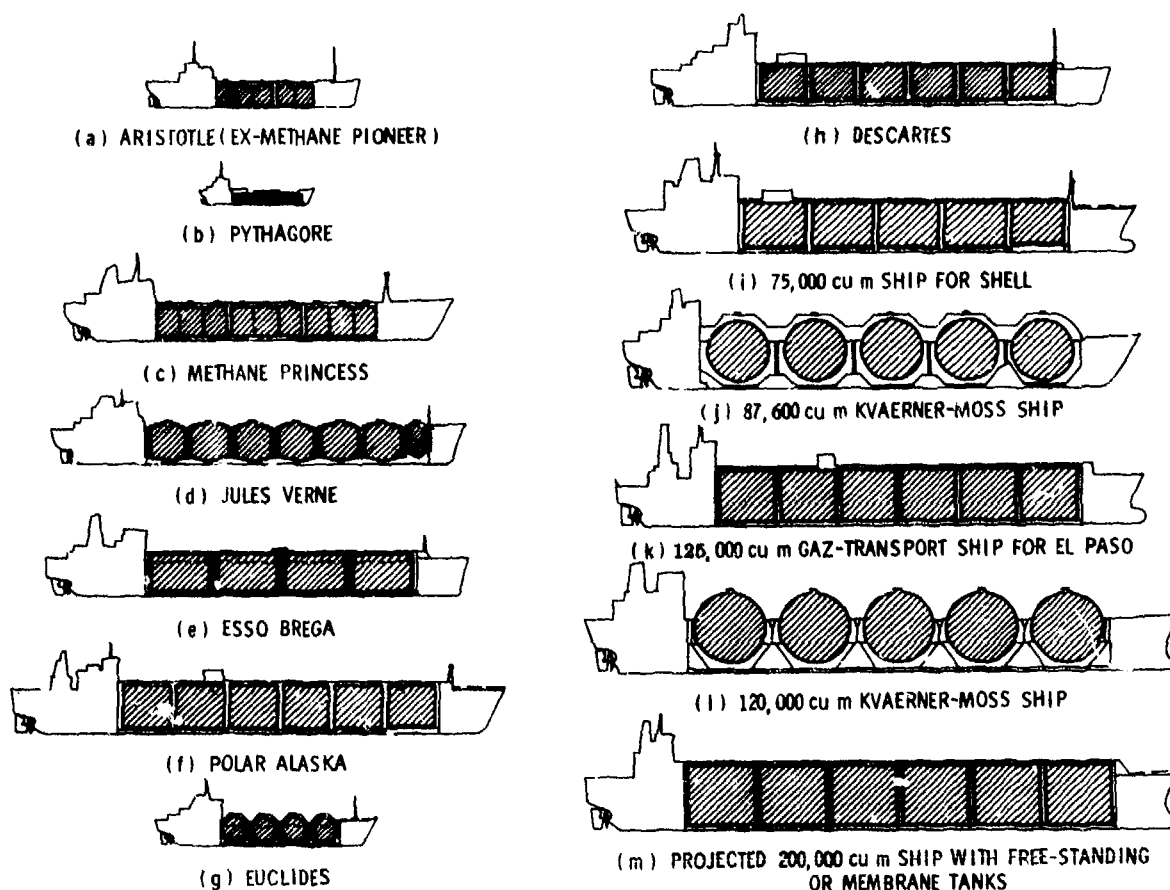


Fig. 1 LNG Carriers: The Current State of the Art

also easier to fabricate, and the insulation is easier to install than on other systems. One drawback to the freestanding design is the disadvantage of requiring a larger ship per given cargo volume. Since freestanding tank walls can be designed to withstand large impact pressures, the primary problem associated with LNG sloshing in freestanding tanks results from the slosh loads on internal components and on the tank support structure.

Sloshing Considerations vs Tank Design

Liquid sloshing in spherical and cylindrical containers has been studied in the past for space applications, both analytically and experimentally (2). The nature of slosh loading in these types of tanks and its prediction is probably better understood than for prismatic tanks, but analytical techniques for predicting large amplitude sloshing are still not fully developed, and such loads are extremely important in designing the tank support structure and internal tank components. In addition, much of the sloshing technology developed for space applications is not useful because emphasis was placed on frequencies and total forces as they related to control system requirements and, therefore, the effects of local peak impact

pressure on structural requirements were not studied to any extent. Further, the excitation amplitudes considered in space applications were too small for ship motion simulation.

The second general tank type, the non-freestanding or membrane tank, affords the maximum utilization of space as the tanks are essentially built into the ship's hold making use of the ship's structure for support. The membrane tanks use a thin internal layer of metal to act as a liquid barrier and are directly supported by insulation material. The insulation is applied directly to the hull with no access space which makes this type of tank difficult to repair after material fracture or other damage. Because of the complex structure, membrane tanks are not amenable to analysis. In addition, because of this and the thinness of the membrane, a complete secondary liquid barrier is required. The primary problem associated with sloshing in membrane tanks is the potential damage to the tank walls from peak impact slosh pressures. Since this type of tank cannot be analyzed to determine its failure strength, special load tests must be performed on representative segments of the structure to determine its load bearing strength.

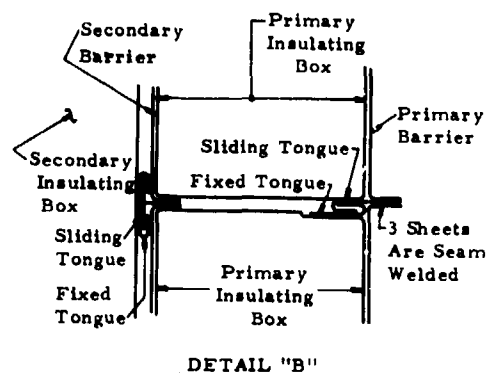
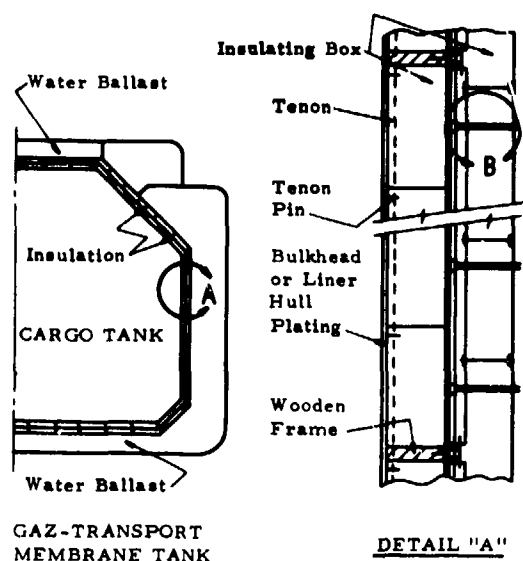


Fig. 2a Non-Freestanding (Membrane) Tank Design

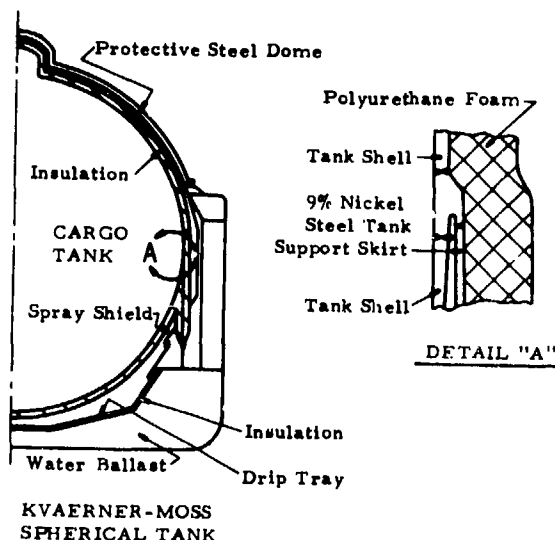


Fig. 2b Freestanding (Spherical) Tank Design

An estimate of the slosh loads that occur in these types of tanks is then utilized to determine if the structure has the required strength. Severe slosh loads in the membrane tank can occur at small fill depths resulting from large amplitude traveling wave impact which is not amenable to analysis. Also, severe slosh loads can occur on or near the tank top as a consequence of standing slosh waves in partially filled tanks. Therefore, tests with geometric scale models of LNG membrane tanks are needed to obtain liquid impact pressure data for tank design.

Recorded Damage From Sloshing

As of 1973 over fifty years of experience has been gained with numerous ships of various tank designs. During these years, several structural problems have been recorded which have resulted from slosh loads on LNG cargo tanks. Slosh related loads causing tank damage have occurred on two ships with membrane tanks, the "Polar Alaska" and the "Arctic Tokyo". On the "Polar Alaska", supports of the electric cables supplying the cargo pumps were broken by liquid sloshing loads. This occurred when the tank was approximately 15 - 20% full. The broken cable supports resulted in damage to the bottom of the membrane tank. On the "Arctic Tokyo", a leak in the number 1 tank was caused from liquid sloshing when the tank was about 20% full. Inspection revealed that the leak was located, along with four deformed points in the membranes, in the aft corners of the transverse and longitudinal bulkheads at about the liquid surface level. Subsequent model tests (3, 4) performed on scale models of the damaged "Arctic Tokyo" tank revealed that a 15 - 30% fill depth with respect to tank length resulted in appreciable impact loads from sloshing. As a result of these studies operations with partially filled tanks other than nearly full or nearly empty have been prohibited, and no additional problems have been reported. The model tests were not successful, however, in establishing peak impact pressures (5) which could have caused the damage. As a result, additional work has been undertaken to investigate more thoroughly all aspects of modeling LNG sloshing and to provide a greater understanding of the slosh generated loads and their implications to tank and ship design.

In this paper a description of recent activities in studying liquid slosh in LNG carriers is presented. Fundamental, analytical and experimental studies in this area are discussed as well as the implications this research has for LNG ship design.

MODELING OF LNG SLOSH BEHAVIOR

Scaling Criteria

The important loads associated with sloshing of LNG in transport ship tanks are not well understood and at present cannot be adequately described mathematically. To circumvent this problem, studies have been performed utilizing scale models of LNG cargo tanks to 1) determine the nature of the slosh phenomena for various fill depths and tank geometries, 2) provide loads data for use in estimating prototype reactions and 3) help determine the factors responsible for damage to full scale tanks. In order to utilize model test results, the scaling criteria to convert model test data to full scale loads need to be established.

In general, modeling requires a selection of a set of significant parameters and the combining of these parameters into pi terms using the principles of similitude. A test program is then designed so the model size is properly scaled for whatever parameters are chosen. If a proper simulation is obtained, the results from model tests can be scaled directly to full scale conditions without significant error. On the other hand, if tests have been performed out of simulation, then enough test information must be obtained so correction factors can be applied to the data to indicate full scale conditions. In examining modeling requirements for LNG slosh studies, the following questions must be answered. 1) What are the appropriate scaling criteria? 2) Have previous model tests been performed in or out of scale, and if out of scale, what can be done with the data to relate it to prototype conditions? 3) If tests were performed in scale, was enough data compiled to draw any conclusions and allow meaningful expressions to be developed to predict prototype behavior? In an attempt to answer these questions the following important parameters are considered in modeling the liquid motions in a typical LNG tank geometry:

P	pressure exerted on tank by liquid
g	gravitational acceleration
L	tank length or diameter (selected characteristic dimension)
h	liquid height
S _i	other pertinent tank dimension (i = 1, 2, ... n)
X ₀	excitation amplitude
τ	excitation period
μ	liquid viscosity
ρ	liquid density

σ surface tension

E_L bulk modulus of liquid

E_s tank elastic modulus

ΔP = P₀ - P_v, where

P₀ pressure at free surface

P_v liquid vapor pressure

Using the Pi Theorem and choosing impact pressure as the dependent variable results in the following functional relationship:

$$\frac{P}{\rho(L/\tau)^2} = F \left[\frac{g}{L/\tau^2}, \frac{\rho L (L/\tau)}{\mu}, \frac{\rho(L/\tau)^2 L}{\sigma}, \frac{\rho(L/\tau)^2}{E_L}, \frac{\Delta P}{\rho(L/\tau)^2}, \frac{E_s}{\rho(L/\tau)^2}, \frac{X_0}{L}, \frac{h}{L}, \frac{S_i}{L} \right] \quad (1)$$

The first pi term represents a pressure coefficient (Euler number) which is a function of the remaining pi terms. Pi terms 2 - 6 represent Froude, Reynolds, Weber, Cauchy and cavitation number, respectively. Pi term 7 accounts for wall elasticity with the remaining pi terms accounting for geometric similitude.

In all model testing to date, only Froude and geometric scaling have been considered important. Therefore, no attempt to simulate pi terms 3 - 7 has been undertaken. Since for any free surface condition Froude scaling is always important, considering this pi term is a must. The importance of the remaining terms is now evaluated by comparing magnitudes of each dimensionless group using typical model and prototype values for the parameters. A summary of comparisons is given in Table 1.

Surface Tension Effects

The surface tension parameter, σ, appears in the Weber number or π₄ term. The product of the Froude and the Weber number forms the Bond number

$$B_0 = \rho g L^2 / \sigma \quad (2)$$

Table I. Model to Prototype Scaling Comparisons

	Model - m	Prototype - p
Length (meters)	1.0	30
Scale (L_m/L_p)	1/30	--
Liquid	H ₂ O	LNG
Density - ρ (kg/m ³)	1000	474
Viscosity - μ (CP)	1.0	0.139
Kinematic Viscosity - ν (cm ² /sec)	0.01	0.00290
Surface Tension - σ (Dynes/cm)	72.8	496*
Speed of Sound - C (m/s)	1505	1700
Bulk Modulus - E_L (Dynes/cm ²)	20.6×10^9	13.8×10^9
Wave Speed - V (m/s)	1.0	8.0
$Re = \rho V L / \mu$	1×10^6	8.3×10^8
$\bar{Re} = \rho L^{3/2} g^{1/2} / \mu$	3.1×10^6	1.7×10^9
$Bo = \rho g L^2 / \sigma$	1.35×10^5	8.43×10^6
$Ca = \rho g L / E_L$	4.75×10^{-6}	101×10^{-6}
$\rho CV/g$ (kg/cm ²)	15.3	65.7
$\Delta P / \rho g L$	10	~ 0
* Maximum value for liquids, LNG value unknown		

The Bond number represents the ratio of inertia to surface tension forces, and if greater than 1, surface tension can be neglected when modeling a free surface. The estimated Bond numbers (Table I) are 1.35×10^5 and 8.43×10^6 for the model (m) and prototype (p), respectively. The magnitude of these numbers indicate that surface tension effects can be neglected and one pi term eliminated.

Viscous Effects

The viscosity of the fluid appears in the Reynolds number (π_3) given by

$$Re = \rho V L / \mu \quad (3)$$

In most fluid mechanics applications viscous effects become more important with decreasing values of Reynolds number. An estimate of the Reynolds number for both the model and prototype was made utilizing the values given in Table I, with the characteristic velocity V taken to be the longitudinal liquid velocity of the order of magnitude as measured or esti-

mated in (3). The resulting Reynolds numbers are $\sim 10^6$ and 10^9 for the model and prototype. While the magnitude of these numbers is large, the importance of viscosity cannot be determined on this basis alone. Previous slosh studies, (2) showed that viscosity affects the magnitude of the peak pressures and forces exerted on tank walls at resonant conditions but only slightly alters the slosh frequency at resonance. These results indicate that viscous scaling may be important in predicting prototype LNG slosh impact loads.

A new parameter, formed by combining Froude and Reynolds number, is given by

$$Re = \rho L^{3/2} g^{1/2} / \mu \quad (4)$$

For both Reynolds and Froude number scaling to be satisfied, the model scale is given by

$$L_R = \frac{L_m}{L_p} = \left(\frac{\nu_m}{\nu_p} \right)^{2/3} \quad \text{for } g_m = g_p \quad (5)$$

This equation is plotted in Figure 3 which shows that the kinematic viscosity ratio of the model (H₂O) to prototype fluid (LNG) is about 3 orders of magnitude too high even for the largest model tested. Conversely, for proper viscous scaling a model liquid would have to be found whose kinematic viscosity was approximately 1/100th that of LNG, and no such liquid exists. Unfortunately since the kinematic viscosity of water is higher than that of LNG, if viscosity is an important factor, then the data obtained in model tests to date are nonconservative since out of scale damping is present.

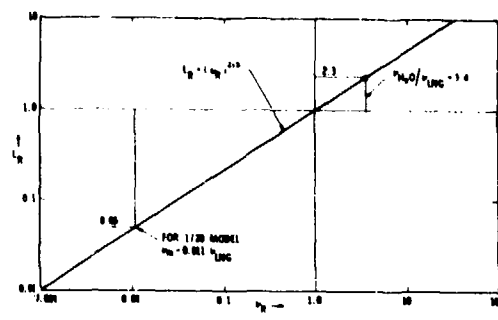


Fig. 3 Froude and Reynolds Number Scaling

Some data and discussion relating to the effects of viscosity on measured impact pressures, as pertinent to LNG sloshing, are given in a later section of this paper.

Compressibility Effects

The Cauchy or π_5 term accounts for the compressibility of the liquid. After introducing Froude scaling, the Cauchy number is given by

$$C_a = \frac{\rho g L}{E_L} \quad (6)$$

The Cauchy number given by equation (6) (Table I) for the model and prototype is 4.75×10^{-6} and 100×10^{-6} , respectively, indicating that previous model tests have also been performed out of scale with respect to compressibility effects. An alternate technique for evaluating compressibility effects is to scale pressures by the method used in (6). For this type of loading, impact pressures¹ are proportional to the impact velocity V , liquid speed of sound C , and liquid density ρ , or $P = K \rho CV$. The proportionality constant, K , assumes a maximum value of 1 at the stagnation point, but numerous factors in actual situation result in K being much smaller, usually on the order of 0.1 to 1. The final value of K is dependent on the relative slope of the impact surface, the amount of gas entrapped between the impacting liquid and sur-

face, the amount of gas bubbles entrained in the liquid and the environmental pressure. For $K = 1.0$, impact pressures (Table I) are 14.6 kg/cm² and 66 kg/cm² for the model and prototype, respectively, compared to reported crushing strengths of 5-7 kg/cm² for typical LNG membrane tanks. This would indicate that the proportionality constant, K , must be considerably less than 1, (i.e., as low as .005) if compressibility scaling is pertinent.

Impact pressure traces recorded in previous LNG slosh modeling studies (3, 4) are similar in wave form to slamming pressure traces given in (6). Since the pressure traces indicate that a slamming type pressure is present, the effects of compressibility and the appropriate scaling criteria for these type of pressures still remain in doubt.

Test data obtained in previous model studies were scaled with the dimensionless ratio represented by π_1 or Euler scaling. This approach results in pressure scaling proportional to the length and density ratio. If $P/\rho CV$ is the proper scaling parameter, then the addition of Froude scaling requires that

$$P_p = P_m \frac{\rho_p C_p}{\rho_m C_m} \sqrt{\frac{L_p}{L_m}} \quad (7)$$

or pressure scale as a square root of the length ratio. Therefore, the current scaling of model pressures by L_p/L_m results in a conservative estimate of peak impact pressures.

Cavitation Effects

Since the vapor pressure of LNG is approximately equal to the tank static pressure, the cavitation parameter, π_6 , has a value near zero. Model testing of H₂O at $P = 1$ atm has a much larger value of the cavitation parameter (~ 10) and therefore cavitation scaling is not achieved in model tests with H₂O. Tests have been performed at Det Norske Veritas with iso-pentane and boiling H₂O to simulate LNG. The preliminary results indicate little difference between non-boiling H₂O and boiling H₂O and iso-pentane test results; however, additional tests with cavitation scaling should be conducted. It is possible that the vapors produced by boiling will affect impact pressures by allowing more entrained gas in the impacting liquid. Thus, boiling (or cavitation) can in essence affect scaling from a compressibility standpoint so that the interaction of these two scaling criteria should therefore be considered.

Wall Elasticity

Another potentially important parameter in modeling liquid sloshing is the rigidity of the liquid container. If the wall is highly elastic

¹ For predicting ship slamming pressures, the relationship $P = K \rho V^2$ is normally used.

then liquid and structural motions can couple and drastically alter the slosh pressures and forces.

No attempt has been made to simulate the tank wall (membrane, insulation, boxes, hull) in previous model testing. To determine if the elasticity of the wall can be neglected, the natural frequency of typical plywood boxes of membrane tanks was computed and compared to the slosh frequency. The plywood segments were assumed to act as clamped plates yielding a natural wall frequency of $f_w = 250 \text{ Hz}^2$. The more rigid freestanding tanks will exhibit even larger natural frequencies. Since typical slosh periods are on the order of 1 to 10 seconds (0.1 to 1.0 Hz), it is unlikely that the wall will be excited to resonance by sloshing. However, it should be noted that the duration of the pressure pulse is of the order of the natural period of the wall response so that dynamic amplification is possible.

Conclusions from Modeling Considerations

The previous discussion indicates that surface tension and wall elasticity effects can be neglected for purposes of scaling. However, viscous, compressibility and cavitation contributions cannot be neglected until additional tests are performed to ascertain their effects. Eliminating the two appropriate pi terms and including Froude scaling in the others results in:

$$\frac{P}{\rho g L} = F^2 \left[\frac{\rho g^{1/2} L^{3/2}}{\mu} \right. \\ \left. \frac{\Delta P}{\rho g L}, \frac{\rho g L}{E_L}, \right. \\ \left. \text{Geometry} \right] \quad (8)$$

Figure 4 is a plot of reasonable ranges which can be obtained for the first three parameters in the functional form of the above equation. The region where the ranges for each pi term overlap represents the area where all three pi terms can be scaled simultaneously. This figure indicates that for simultaneous scaling of viscous, compressibility and cavitation effects would require about a $3/4$ scale model which is, of course, unreasonable. Therefore, additional experimental testing needs to be undertaken to determine which, if any, of these three pi

2

This value is computed in free air. The presence of liquid will add an apparent mass reducing the natural frequency, but not appreciably when compared to the small slosh frequency.

terms can be neglected so that the scaling problem may be simplified. Once the important terms are established then the test can be performed to account for the important parameters and allow data to be converted to full-scale. Such testing is currently underway at SwRI and DnV and some of the initial test results are presented herein.

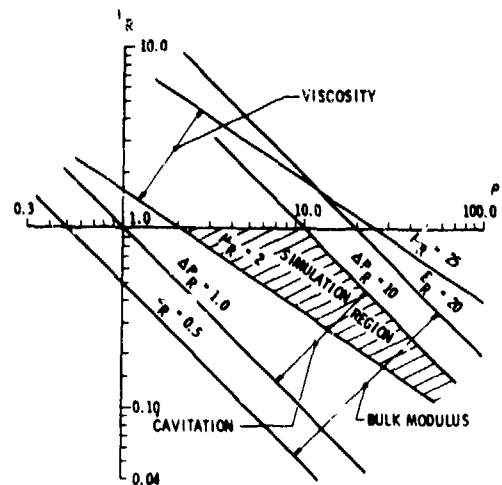


Fig. 4 Simulation Plot for Simultaneous Viscous, Cavitation and Compressibility Scaling

LIQUID RESPONSE CHARACTERISTICS

Background

The liquid motion inside a tank has an infinite number of natural periods, but it is the lowest mode that is most likely to be excited by the motions of a ship. Studies have therefore concentrated on investigating forced harmonic oscillations in the vicinity of the lowest natural period where the natural period is defined as that predicted by linear theory. Nonlinear effects result in the frequency of maximum response being slightly different from the natural frequency and dependent on amplitude. The mode corresponding to the lowest natural period is asymmetric so studies consider only forced surge, sway, roll and pitch oscillation since yaw oscillation is normally of no interest. The LNG tanks are also assumed to be rigid and without baffles and tank geometry, liquid level and excitation waveform dictate whether two-dimensional or three-dimensional flow effects should be considered.

Two-Dimensional Flow

Tanks with two dimensional flow are divided into two cases; shallow and non-shallow liquid depths. The shallow depth case is represented by $h/b \lesssim 0.2$ where h is the still liquid depth and b is the tank length in the direction of motion. The shallow depth case is characterized by the formation of hydraulic jumps and traveling waves for excitation periods around the

natural period. On the other hand, in the non-shallow depth case large standing waves are formed in the resonance frequency range.

The natural periods for any two-dimensional tank-shape can be determined by use of a modified Frank close-fit method (7). This method has been shown to give very good results for tank shapes with trapezoidal cross sections (8). The method consists of finding a Green's function $G[X, Z; \xi(s), \eta(s), t]$ for the problem and writing the velocity potential as

$$\phi = \int_S Q(s) G[X, Z; \xi(s), \eta(s), t] ds \quad (9)$$

where the integration is over the average wetted surface of the tank and $\xi(s), \eta(s)$ are the coordinates of points on the wetted surface. $Q(s)$ is found by satisfying the tank boundary condition, and (X, Z) is the coordinate of a point in the fluid. Since there is no damping for a potential flow problem inside a tank, the linear theory predicts an infinite response for the natural periods. To predict a reasonable response near resonance one has to rely on nonlinear theory.

An estimate of the lowest natural slosh frequency for rectangular tanks is given by

$$\omega_0 = \sqrt{(g\pi/b) \cdot \tanh(\pi h/b)} \quad (10)$$

Similar equations for other tank shapes are given in (2).

Shallow Liquid Depth. In the shallow depth case, hydraulic jumps are formed around resonance. The hydraulic jumps can result in very high impact pressures at the end walls and for a general tank shape there exists no adequate theory to describe the hydraulic jump. However, for a rectangular tank Verhagen and van Wijngaarden (9) derived an analytical solution for forced harmonic roll oscillation of small amplitude δ and with frequency ω near the lowest resonance frequency. The case of forced harmonic sway oscillation can easily be obtained by letting the distance H between the axis of roll and mean liquid level go to infinity and δ go to zero, so that δ multiplied by H approaches the forced sway amplitude. This theory is based on the nonlinear "shallow liquid theory" [Wehausen and Laitone (10), Stoker (11)], where the only assumptions are potential flow, and the hydrodynamic pressure is static below the instantaneous free surface. Verhagen and van Wijngaarden wrote their solution as a power series in

$$\epsilon = \left(\frac{b\delta}{\pi h} \right)^{1/2} \quad (11)$$

where ϵ is assumed to be a small quantity. When a solution exists, it represents a hydraulic jump traveling back and forth between the walls of the container. The condition with roll

excitation for existence of a hydraulic jump is

$$\left| 1 - \frac{\omega}{\omega_0} \right| \leq \frac{\sqrt{24}}{\pi} \sqrt{\frac{b\delta}{h} (1 + \pi^2) \frac{h}{b} \frac{H}{b}} \quad (12)$$

where ω is the forced oscillation frequency and ω_0 is the natural frequency. In the case of forced sway oscillations the condition is

$$\left| 1 - \frac{\omega}{\omega_0} \right| \leq \frac{\sqrt{24}}{\pi} \sqrt{\frac{\pi}{b}} \quad (13)$$

where η is the forced sway amplitude.

The velocity of the hydraulic jump is approximately

$$v \approx \sqrt{gh} \quad (14)$$

The fluid velocity and the surface elevation are of the order ϵ , and are nonlinear functions of the oscillation amplitude. Comparisons of this theory with experiments performed with small excitation amplitudes reveal reasonable agreement.

This theory was utilized to predict slosh impact forces for comparison to forces measured on a typical LNG model-tankform. A cross-section of the experimental model tank is shown in Figure 5. The liquid depth in the tests was $h = 0.12 b$ and forced harmonic sway excitation amplitudes were $\eta = 0.01 b$ and $0.1 b$. The $\eta = 0.1 b$ condition corresponds to a realistic extreme sway motion of a ship. Liquid slosh impact pressure was measured at point P_1 (see Figure 5) in the center of the aft tank wall. In addition, the total horizontal sloshing force was measured.

NOTE: ALL DIMENSIONS IN MILLIMETERS

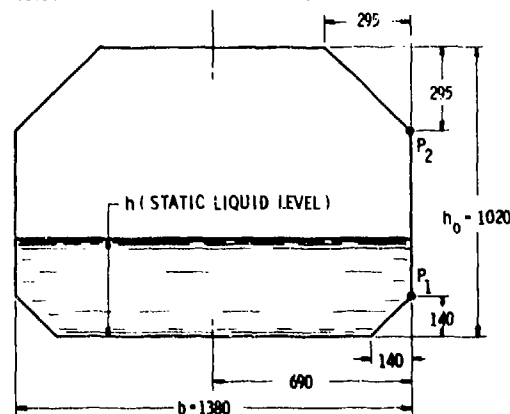


Fig. 5 Prismatic Tank Model for LNG Slosh Studies

During the testing, several sloshing modes were observed. When $\eta/b = 0.01$ and $1.99 \text{ sec} < T < 2.3 \text{ sec}$, where T is the excitation period, a single traveling wave was present (Figure 6). For the larger oscillation amplitude, $\eta/b = 0.1$, and $1.6 \text{ sec} < T < 2.95$



Fig. 6 Traveling Wave Profile for $h/b = 0.12$ & $n/b = \pm 0.01$ @ $T = 2.0$ secs

sec there exists a strong shock traveling wave (figure 7). When $2.95 \text{ sec} < T < 3.25$ and $n/b = 0.1$, there was a single traveling wave present. According to the nonlinear rectangular tank theory, hydraulic jumps occur for $n/b = 0.01$ and 0.1 when $1.86 \text{ sec} < T < 2.5 \text{ sec}$, and $1.5 \text{ sec} < T < 3.7 \text{ sec}$, respectively. These values are in reasonable agreement with experiment.

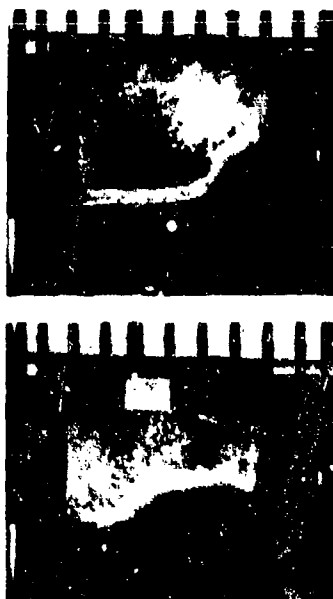


Fig. 7 Hydraulic Jump Wave Profile for $h/b = 0.12$ & $n/b = \pm 0.1$ @ $T = 2.0$ secs

The impact pressures occurring when the wave front hits the vertical bulkhead are of

particular interest. Experiments show that even under harmonic oscillations, the pressure variation is neither harmonic nor periodic since the magnitude and duration of the pressure peaks vary from cycle to cycle. A typical histogram for the distribution of peaks is shown in Figure 8. The most frequently occurring pressure peaks will reach 0.4 times the pressure level exceeded by 10 percent of all peaks. The 1 percent exceedence limit is two to three times the 10 percent exceedence limit. The test data samples obtained so far are of too small a size for a reliable prediction of extreme values. However, a study of the data available seems to indicate that a three parameter Weibull distribution may be used to describe the peak pressure probability distribution.

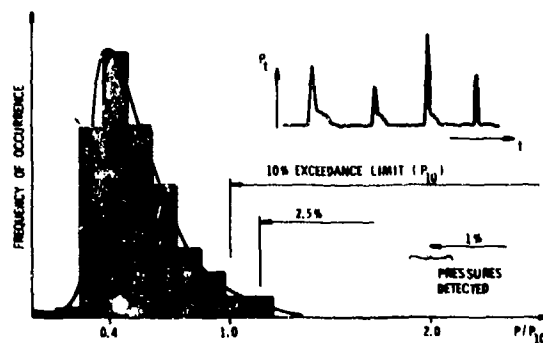


Fig. 8 Distribution (P.D.F.) of Impact Pressure Peaks

Experimental values for the ten percent exceedence level of impact pressures as a function of excitation period, are shown in Figures 9 and 10 for excitation amplitudes $n/b = 0.01$ and 0.1 , respectively, and shallow fill depths of $h/b = 0.12$. The pressures are nondimensionalized by γb where $\gamma = \rho g$. Several liquids (fresh water, 63% glycerol/water and reginol oil) were used

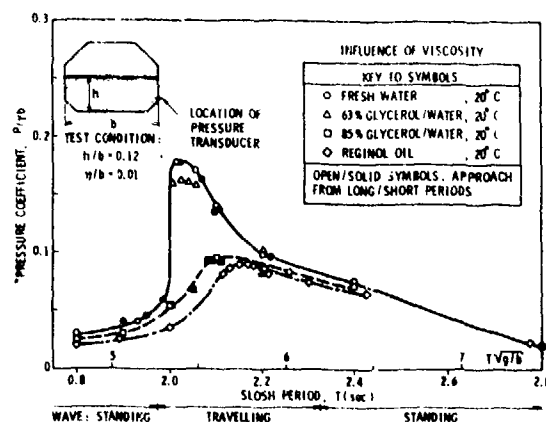


Fig. 9 Impact Pressures (10% Exceedence Limit) With Shallow Fill Depth and Small Excitation Amplitude

in the experiments. The excitation periods were approached both by starting at high periods and at low periods with no effect on the results (see Figure 9) which is contrary to theory for the case of non-shallow liquid depth (Faltinsen (12)). The test results show that the frequency of maximum response depends somewhat on the test liquid. Further for the same liquid, but different excitation amplitudes, the frequency of maximum response differs. The

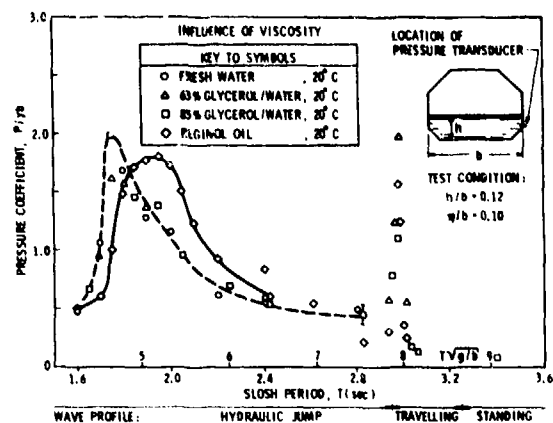


Fig. 10 Impact Pressures (10% Exceedance Limit) With Shallow Depth and Large Excitation Amplitude

higher the excitation amplitude, the lower the period of maximum response. This is opposite to the behavior for larger filling depths. When $\eta/b = 0.1$ all the liquids seem to give approximately the same maximum value for the 10% exceedance limit. For a full scale ship with tank breadth $b = 40$ m, this maximum value would correspond to a pressure of approximately 8 atmospheres, which is the same order of magnitude as in ship slamming.

For $\eta/b = 0.01$ the maximum impact pressure value for fresh water and 63% glycerol/water is approximately 1/10 of the maximum value for $\eta/b = 0.1$. But the maximum values for 85% glycerol/water and reginol oil, for $\eta/b = 0.01$, are approximately 1/20 of their maximum values for $\eta/b = 0.1$. An explanation might be due to differences in wave-forms because of viscous effects. When $\eta/b = 0.1$ the wave or shock has maximum steepness for all liquids. However, when $\eta/b = 0.01$ the steepness is not large and appears to be influenced by the viscosity of the fluid.

The horizontal sloshing forces were also measured in these model tests. The horizontal force predicted by the Verhagen and van Wijngaarden-theory (9) is compared to experiment in Figures 11 and 12 for $\eta/b = 0.01$ and 0.1, respectively. Fair agreement is observed. When $\eta/b = 0.01$ both measured and calculated

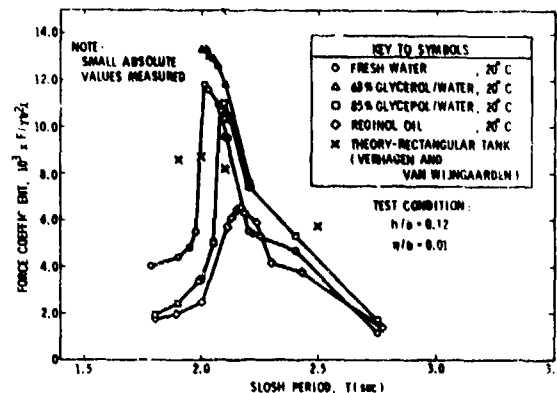


Fig. 11 Lateral Hydrodynamic Force With Small Fill Depth and Excitation Amplitude

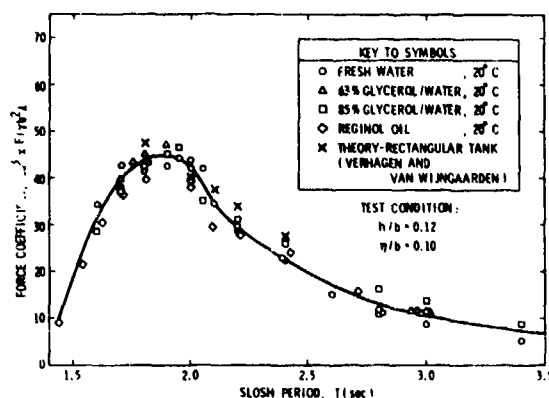


Fig. 12 Lateral Hydrodynamic Force With Small Fill Depth and Large Excitation Amplitude

forces are very small and the measured values appear to depend on viscosity. When $\eta/b = 0.1$ viscosity does not affect the measured forces.

Non-Shallow Liquid Depth. In the non-shallow liquid case large standing waves can cause very high impact pressures against the tank top. This is possibly the most important problem from a design point of view, but the horizontal forces and moments are also important.

There exists no adequate theory that can be used to describe the liquid motion for any arbitrary tank shape and filling depth. In the case of a rectangular open tank, Faltinsen (12) has derived an analytical solution based on the general procedure proposed by Moiseyev (13) for any tank shape. The excitation is assumed to be harmonic with small sway or roll ampli-

tudes. The breadth of the tank b and the depth of the fluid h is assumed to be of the order of unity, $O(1)$. The excitation is $O(\epsilon)$ and the response is $O(\epsilon^{1/3})$. The solution is found as a power series in $\epsilon^{1/3}$ correctly to $O(\epsilon)$. The response variable as a function of excitation frequency for $h/b > 0.34$ is shown in Figure 13 where σ_1 is the lowest natural

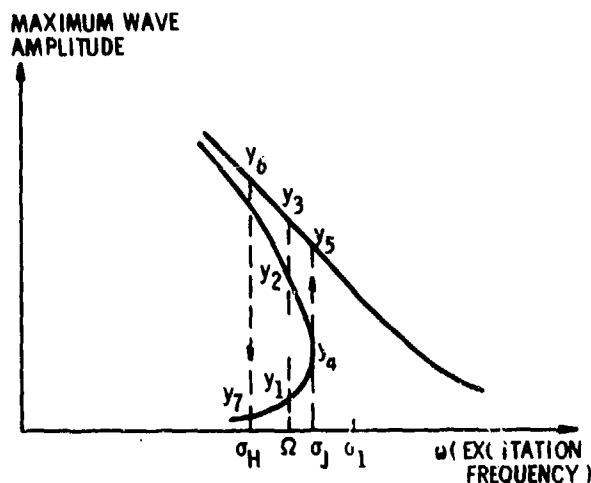


Fig. 13a Possible Solutions From Theory of Faltinsen (12) at $h/b > 0.34$

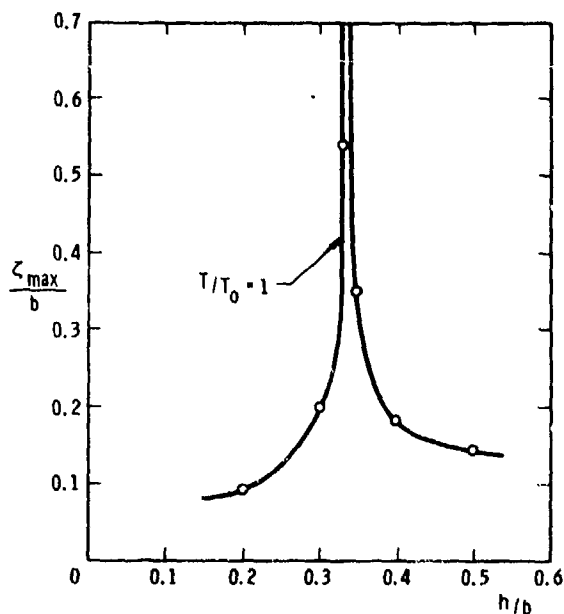


Fig. 13b Maximum Surface Elevation, z_{\max} , as a Function of Water Depth at Resonance Frequency (Roll Amplitude, $\omega = 0.01$ Radians, Axis of Roll Position, $C = 0.2$)

period for the fluid inside the tank. For $\omega = \Omega < \sigma_1$ there are three different mathematical solutions. The correct solution for the physical system will depend on how the frequency Ω is approached. If one starts to oscillate a tank with a much lower frequency than Ω and then approach Ω , the solution will be y_1 . If one does the opposite and approaches Ω from above, the solution will be y_3 . The physical system will never select y_2 , as it is an unstable solution. If σ_J is approached from below with increasing ω , the solution will suddenly jump from y_4 to y_5 . On the other hand, if one starts with a high frequency and decreases, the mathematical solution will follow the upper branch. There are obviously limitations (provided by damping) on how large a response can be, and in reality the solution will jump down from y_6 to y_7 for some frequency σ_H . Due to the potential flow assumptions in the theory one cannot predict σ_H . This kind of jump phenomena has been observed in experiments. The jump frequency σ_J will depend on the excitation amplitude. The higher the excitation amplitude, the lower the jump frequency, σ_J , which will always be lower than the natural frequency. When $h/b < 0.34$ the response characteristics are similar to a hard spring response. Therefore, the higher the excitation amplitude, the higher the jump frequency and in this case σ_J will always be higher than the natural frequency. In the vicinity of $h/b = 0.34$ and close to the natural period, the theory is not applicable. This is illustrated in Figure 13b, where maximum wave amplitude at the natural period T_0 is shown as a function of h/b . A separate expansion is needed for $h/b = 0.34$ which will probably require that the lowest order term be $O(\epsilon^{1/5})$.

Reasonable agreement between theory and experiments was found for a rectangular tank with $h/b = 0.5$. When the fluid impacted the tank top the agreement between theory and experiment became poor due to violations of the basic assumptions in the theory.

The theory of Faltinsen (12) was used to predict lateral hydrodynamic force for the model tank shown in Figure 5 with results compared to experimental values for a still water level of $h = 0.4 b$. The forced sway amplitudes were $\eta/b = 0.01$ and 0.1 . In addition, experimental impact pressure was measured at point P_2 (see Figure 5). The test liquids used were the same as for the shallow liquid case with the addition of 74% glycerol/water. Experimental results of 10% exceedance limit for impact pressures are shown as a function of excitation period in Figures 14 and 15. Figure 16 shows impact pressure as a function of exceedance limit for $T = 1.48$ sec and $\eta/b = 0.1$. The 1% exceedance value is 1.7 times the 10% exceedance value. The data of Figure 16

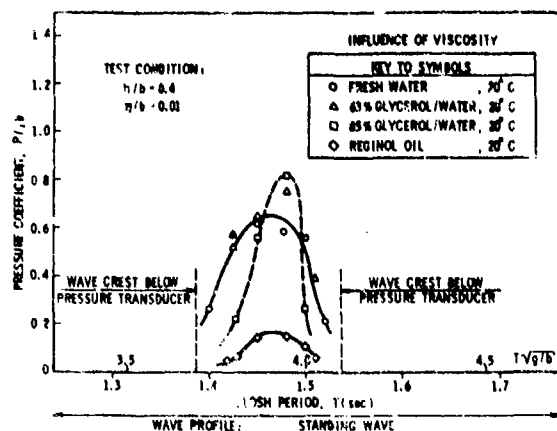


Fig. 14 Impact Pressures (10% Exceedance Limit) With Large Fill Depth and Small Excitation Amplitude

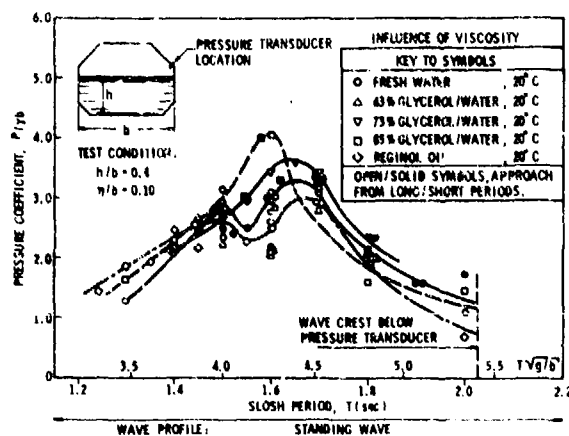


Fig. 15 Impact Pressures (10% Exceedance Limit) Large Fill Depth and Excitation Amplitude

will fit to the probability function

$$Q(\bar{P}) = \exp \left(- \left(\frac{\bar{P} - 1.0}{0.55} \right)^{0.85} \right) \quad (15)$$

where $\bar{P} = P/\gamma b$. As in the shallow liquid case, the frequency of maximum response depends on the liquid used and for the same liquid the frequency of maximum response is dependent on excitation amplitude. The higher the excitation amplitude, the higher the period of maximum response, which is opposite the behavior for the shallow liquid case. All test liquids give approximately the same maximum value for the 10% exceedance-limit which is roughly twice as large as the shallow liquid case. When $\eta/b = 0.01$ the maximum value depends on the liquid used, with the highly viscous reginol oil pressures being significantly lower than the other test liquids. When

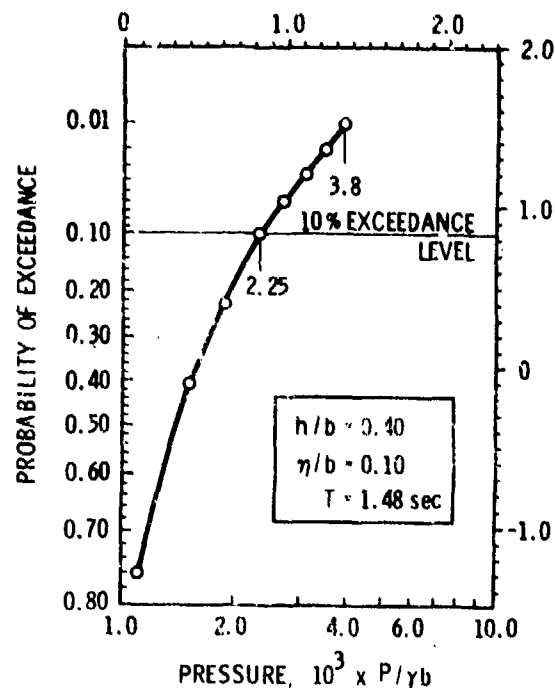


Fig. 16 Probability of Exceedance vs Peak Impact Pressure Coefficient

$\eta/b = 0.01$ impact (resonance) occurs when $1.39 \text{ sec} < T < 1.54 \text{ sec}$ compared to $1.38 \text{ sec} < T < 1.53 \text{ sec}$ as predicted by Faltinsen (12).

The measured horizontal forces are shown in Figures 17 and 18 for $\eta/b = 0.01$ and $\eta/b = 0.1$, respectively. For $\eta/b = 0.01$ theoretical values for rectangular tanks are plotted. To obtain the theoretical horizontal force, the pressures from the theory of

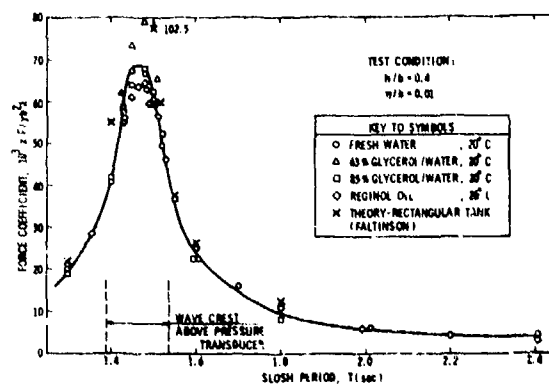


Fig. 17 Lateral Hydrodynamic Force With Large Fill Depth and Small Excitation Amplitude

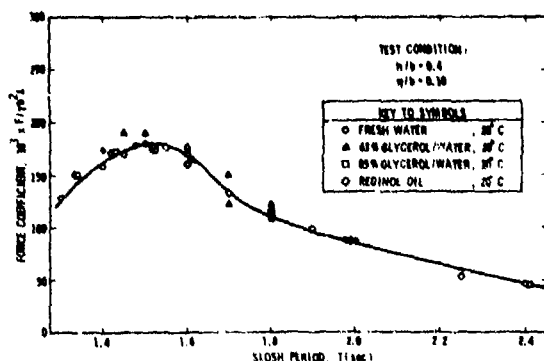


Fig. 18 Lateral Hydrodynamic Force With Large Fill Depth and Excitation Amplitude

Faltinsen (12) were integrated by the procedure used by Abramson, Chu and Kana (14) for vertical cylindrical tanks. The integration was performed over the actual wetted surface of the tank. As long as the wave does not hit the tank top there is good agreement between theory and experiment. However, when $T = 1.5$ sec the experiment revealed wave impact on the tank top and the theoretical solution is more than twice the experimental value. One reason for this disagreement could be the suppression effect of the tank top on the liquid motion. Figure 18 shows the experimental values for $\eta/d = 0.1$ which appear similar to the response of a highly-damped system. Wave impact on the tank top was observed for all experimental conditions and the theory did not agree well with experiments as it consistently gave values too high.

Three-Dimensional Flow

To determine the natural periods for any three-dimensional tank, one may generalize the procedure used for two-dimensional tanks. Faltinsen and Michelsen (15) have developed a computer program to compute added mass and damping coefficients for three-dimensional bodies oscillating in a fluid. The procedure which is a generalization of the Frank close-fit method (7) for two-dimensional bodies has been adapted to the three-dimensional slosh problem. For a general tank shape there exists no adequate theory to describe the nonlinear fluid behavior around resonance. However, for a vertical cylindrical tank shape Hutton (16) has derived an analytical solution based on the general procedure proposed by Moiseyev (13). Abramson, Chu and Kana (14) have shown good agreement between theoretical and experimental values of horizontal force for small excitation amplitudes of a vertical cylinder using an extension of Hutton's method.

The most common LNG tank with three-dimensional flow is the spherical tank. For a spherical tank the most important load is the resulting hydrodynamic force, the predominant component of which is the lateral force. Rotational motion of the liquid occurs readily so there is in general a force component normal to the oscillation direction. Abramson, Chu and Kana (14) did experiments for a spherical tank that was half filled. A vertical splitter plate was installed in the spherical tank (parallel to the direction of excitation) in order to suppress the liquid swirl mode. The experimental results show the jump phenomena discussed earlier for rectangular tanks with non-shallow liquid depth. Further, the larger the excitation amplitude, the larger the period of maximum response.

In experiments performed at Det Norske Veritas in 1972 for Moss - Rosenberg Verit A/S the liquid swirl mode was not suppressed thus changing the response characteristics described in (14). The excitation in their experiments was harmonic sway oscillation with amplitudes $\eta/d = 0.0278, 0.0555$ and 0.167 where d is the diameter of the sphere. The maximum still water depths were $h/d = 0.289, 0.5$ and 0.65 . Representative results are presented in Figures 19 and 20 for the transverse and longitudinal force components. The swirling prevents

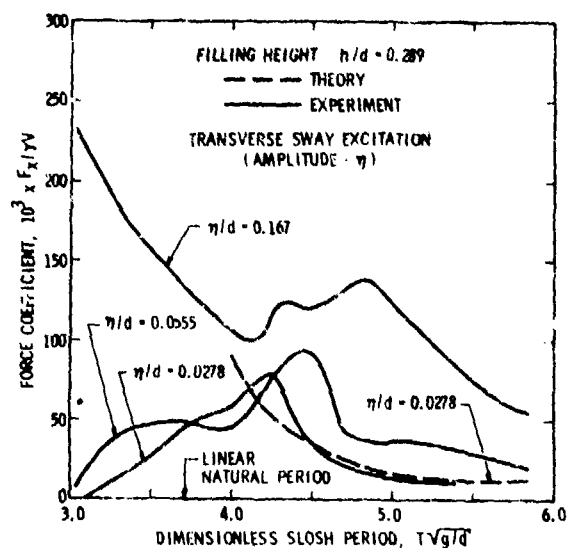


Fig. 19 Spherical Tank Horizontal Force in Transverse Direction

easy observation of the resonance phenomena, especially for the largest excitation amplitude. The maximum response occurs for much smaller periods than the range of periods where maximum response is expected when swirling is suppressed.

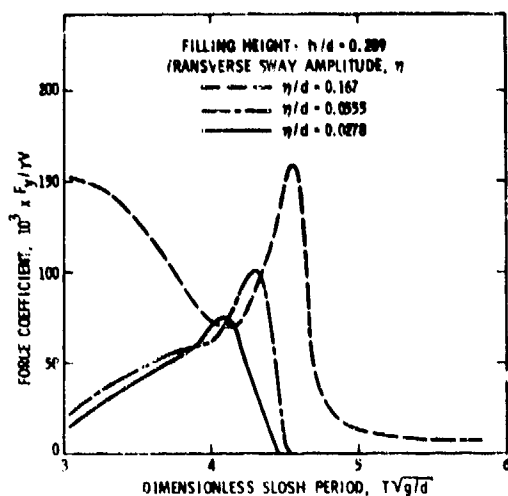


Fig. 20 Spherical Tank Horizontal Force in Longitudinal Direction

The linear theory described in Faltinsen and Michelsen (15) was used to predict spherical tank transverse forces. For excitation periods T sufficiently larger than the natural period it agrees well with the experiments. In this period range, however, there is not much swirling. No swirling is predicted by the theory and at lower periods where swirling occurs, theory does not agree well with experiment. The linear natural period calculated by the theory has been plotted and agrees well with experience formulas which may be found in Abramson (2).

FULL SCALE MEASUREMENTS

Full scale data on LNG sloshing are very scarce. The data that exists have been obtained during a short period of time under moderate sea conditions, rendering no possibility to predict long-term effects of sloshing.

Some stress measurements on horizontal girders in a crude oil carrier have been presented by Hagiwara and Tani (17). These results might have some relevance to Conch LNG tanks, but the amount of data is very small.

More recently (1972) some measurements were carried out at Det Norske Veritas for The International Chamber of Shipping (ICS) who has sponsored an investigation into the conditions around a number of explosions in OBO carrier holds. The results from these experiments are also limited; however, some interesting and useful information was obtained. A number of pressure gauges were installed at different locations in an OBO tank carrying water ballast and simultaneous recordings of pressures and the ship's roll motion were taken with different filling heights during a voyage from Japan to the Persian Gulf. As part of a

subsequent model test program, recorded roll motions of the ship were imposed on a tank model (scale 1 : 30), and the pressures at corresponding locations measured. Extremely high impact pressures were recorded at the underside of the top wingtank. Generally it was found that fewer impacts occurred in the model than in the prototype. However, the magnitudes of the pressure peaks were quite similarly distributed. An example (for the condition which could best be simulated on the model) is given in Table II. The pressures obtained in model scale, have been scaled according to Froude's Law of similarity, i.e., in proportion to the linear scale ratio. Tabulated is the percentage of all peaks in a sample that lie within different pressure intervals.

PRESSURE (ATM)	Percent of Peaks in Pressure Range		TEST CONDITION
	MODEL	PROTOTYPE	
0 - 6	83.1	86.0	$h/b = 0.215$
6 - 12	13.6	10.0	Random rolling
12 - 18	3.1	2.5	(Max. roll angle 7.4 deg.)
18 - 24		1.5	RMS of roll angle 2.9 deg.) $T_R/T_0 \approx 1.0$

Table II - Comparison of Model to Prototype OBO Impact Pressures

As long as the number of actual impacts (i.e., the probability of occurrence) in model and prototype is of the same order of magnitude, the prediction of extreme values will not be affected seriously and model test results can be taken as a basis for such predictions. It should be noted that both model and prototype liquids were water and therefore the question of modeling LNG with H_2O is not resolved. It will be noticed that the highest measured full scale pressures exceeded corresponding highest pressures measured on the model. However, Figure 21 indicates this perhaps is more a question of data sample size.

Besides the magnitude of the peak pressure, the width of duration of the pressure pulse may become an important parameter. A typical pressure pulse obtained in the full scale measurements is illustrated in Figure 22 and has a very short rise time and a somewhat slower decay time. Normally in ship slamming terminology the time Δt_0 elapsed between the zero-upcrossing and the zero-downcrossing is taken as a measure for the pulse width. In the present case of slosh-induced pulses, however, the width Δt at the half-height of the peak was

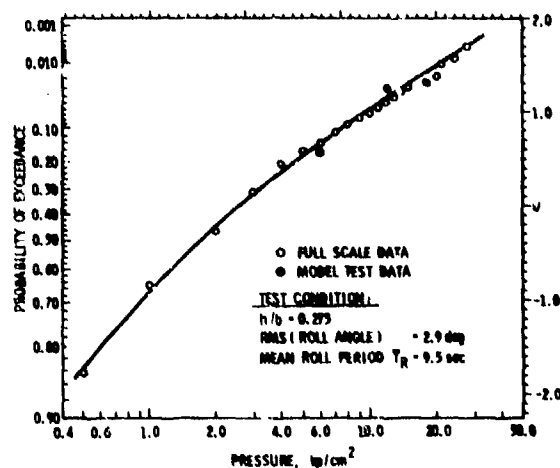


Fig. 21 Distribution of Peak Pressures Recorded at Underside of Top Wingtank

adopted, as it was found to offer a much more precise definition. The pressure data indicate (Figure 22) that the higher peaks will have smaller width (smaller Δt). The total pulse duration (~ 2 times Δt) varied in a range of 1 - 10 milliseconds for the measured data, which is significantly shorter than normally considered in ship's slamming (18).

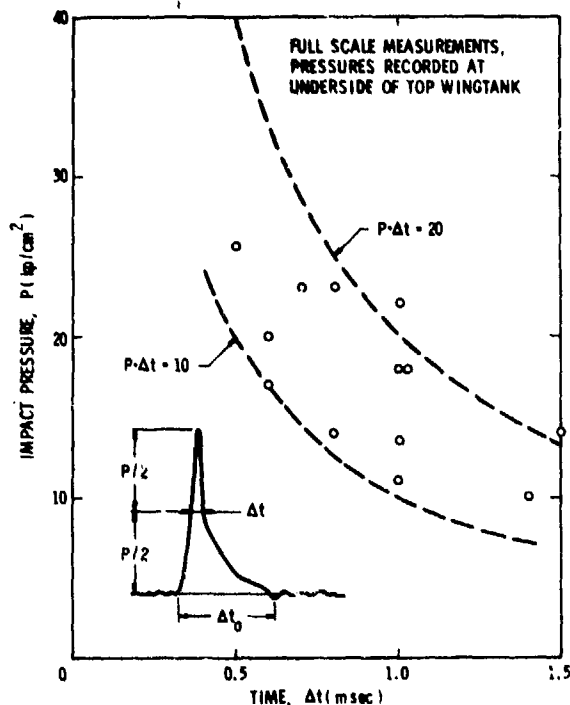


Fig. 22 Correlation Between Height and Width of Pressure Peak

Figure 23 presents some comparisons between model and full scale results for different depths under harmonic roll excitation. Values corresponding to the 1% exceedance level have been used as a reference. It appears from Figure 23 that the pressures do not vary significantly in the range $h/h_0 \sim 0.6 - 0.9$, but outside this range they drop rapidly. For the best simulation of full scale conditions, fairly good agreement has been achieved; however, not enough motion data was obtained to simulate all conditions.

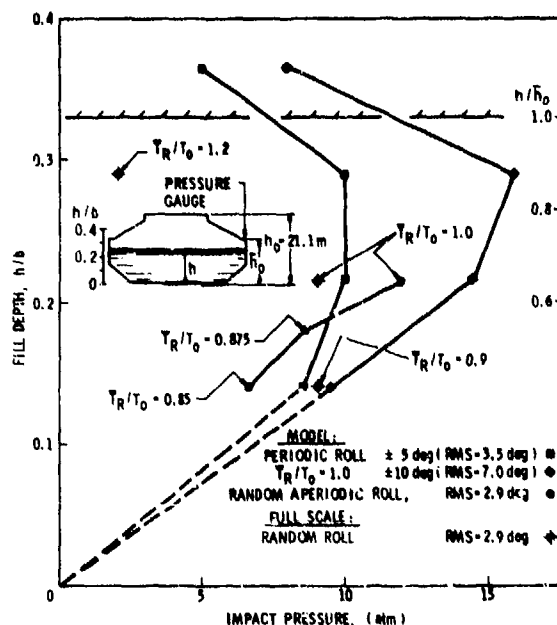


Fig. 23 Measured Impact Pressures Underneath Top Wingtank (1% Probability of Exceedance)

As a measure of the degree of resonance ("tuning") in the experiments with random (field measured) motions, the ratio between the average roll period \bar{T}_R and the (theoretical) natural period of liquid motions (T_0) has been used. In reading Figure 23, attention should be given to the fact that the change in \bar{T}_R/T_0 from 1.0 to 0.8 or 1.2 will theoretically bring the sloshing liquid out of a resonant state. Another important feature which should be noticed is that within the range of measured data there appears to be no trend towards an ultimate limit of pressure.

Finally it is admitted that the simulations made are by no means complete. For example, they include only one mode of motion (rolling) which for the present case was believed to govern the response to be studied.

DESIGN IMPLICATIONS

General

The theoretical and laboratory research previously conducted and currently underway is pointed at establishing methods for predicting pressures and forces resulting from LNG slosh impact. This information will be extremely beneficial to the design of LNG ships. Out of these studies reasonable tank loading criteria can be established to insure that realistic methods are available to design safe LNG cargo tanks. These studies can also be of use in unifying current rules and criteria regarding LNG tank design.

The work to date has shown that LNG sloshing and the resultant loads are highly dependent on numerous parameters. In general, the slosh loads are determined by tank acceleration, liquid fill depth, and tank geometry.

Tank Acceleration and Fill Depth

Resonant sloshing creates the largest impact loads in LNG tanks. Studies to date have indicated that model test results as well as calculations, can be successfully used to estimate the lowest frequency resonant conditions through Froude scaling ($\omega_p = \omega_m \sqrt{L_m/L_p}$). The question arises, can this mode be excited by the ship's motion. The spectrum of each mode of ship motion is a time-dependent function of the sea state as well as the ship's loading condition, speed and course. Also, the motion spectra for the different modes will be located differently, and the spectral density distributed differently along the frequency axis. Considering that each of the modes of ship motion is a random variable represented by a spectrum composed of contributions over a wide range of frequencies, the possibility exists for exciting the lowest frequency mode regardless of the tank design. Practically, this indicates that it is impossible to avoid all resonance conditions. For example, Figure 24a illustrates a family of sway acceleration spectra, corresponding to several sea state conditions, which may occur. Figure 24b shows that different sized tanks with different filling levels yield peak response amplitudes within the range of sway periods to be expected.

The designer has to accept that the tank will be subjected to the ship's motions and accelerations. Therefore, the designer's problem cannot be limited to a determination of tank geometry and fill depths where resonance will not occur. In principle, the determination of loads should follow a probabilistic procedure involving the response at different conditions and their probability of occurrence. However, a good estimate of the possibility of resonance slosh problems to occur can be achieved through consideration of natural slosh frequen-

cies and pertinent motion spectra.

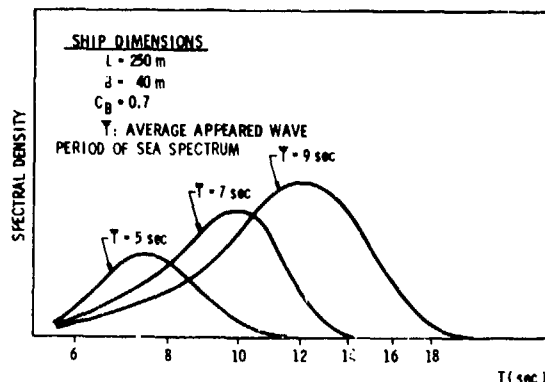


Fig. 24a Ship Acceleration Spectra (Sway)

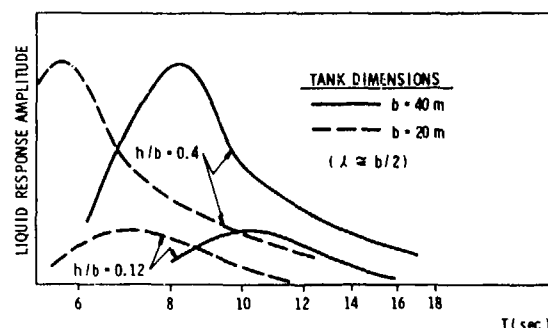


Fig. 24b Liquid Response Amplitude

In a partially filled prismatic tank that is basically rectangular in form, the standing wave liquid motion response is particularly violent in a fill depth range $0.20 \lesssim h/b \lesssim 0.50$, with a theoretical maximum severity at $h/b = 0.35$. Below this range, say $0.05 < h/b < 0.20$, a traveling slosh wave can easily occur. This implies that all of the following loads may be relevant:

Impacts on tank and intervals in the lower region of the tank, due to a traveling wave (shallow liquid, $h/b < 0.2$).

Impacts on tank and intervals in the upper region, due to a standing type of wave (non-shallow depth).

Integrated (total) hydrodynamic forces acting on the tank due to a standing type of wave (non-shallow depth).

For other tank geometries, e.g., the spherical tank, the sloshing wave phenomena will also depend on filling depth. Therefore, the resulting sloshing loads at different filling depths must be established for each basic tank geometry. In estimating these loads the design-

er must turn to model test data for setting prototype structural requirements.

The impact loads require consideration for local scantlings, while integrated loads are needed in the design of tank supporting structure.

Tank Geometry

The overall geometry of a tank will be selected primarily on other criteria than the prevention of liquid slosh. However, it may well be advantageous to adjust tank shape and dimensions to improve tank characteristics with respect to slosh prevention, at least in some range of fill depth. This will normally mean designing for high natural slosh frequencies. Locally, the tank boundary should, if practicable, be designed with curved surfaces in order to prevent structural damages in areas where liquid impacts may be expected.

Structural Response to Impact

The fact that extremely high impact pressures may occur, will in general require the structural response to such loads be investigated, taking into account the duration of impact pressures and the correlation between magnitude and duration of these pressures. The natural frequencies of the structure subjected to impact will be of great importance in these calculations, as well as any significant damping parameters. Since the general trend is that the natural frequencies of many parts of ship structures will decrease with increasing ship size, this aspect should require increased consideration in the future.

AREAS REQUIRING FURTHER INVESTIGATION

The limitations to adequate modeling, set by the laws of dynamic similitude and the lack of suitable liquids to fulfill these requirements, call for more correlation between full scale and model response. One could suggest in particular liquid movements to be measured in full scale, simultaneously with ship motions in (preferably) all degrees of freedom. Subsequent simulation in model scale should be made, with a thorough analysis and correlation of the recorded signals.

ACKNOWLEDGEMENTS

We express our appreciation to the following organizations for permitting us to utilize information and data obtained during the course of research conducted under their sponsorship:

The El Paso Natural Gas Co.

The International Chamber of Shipping

Moss-Rosenberg Verft A/S

The U. S. Maritime Administration

Also, special appreciation is extended to the following SwRI and DnV personnel who aided either in conducting the research or in preparing the manuscript:

V. Hernandez
S. Hyden
T. Hysing
K. Rygg Johnsen
M. Sissung

REFERENCES

1. Bailey, M. S., Report prepared for the U. S. Maritime Administration, National Maritime Research Center-Galveston, Dec. 1972.
2. Abramson, H. N., The Dynamic Behavior of Liquids in Moving Containers, NASA SP-106, 1966.
3. Olsen, Harald, "Slack LNG Tank Study--3-Dimensional Model Liquid Responses Caused by Surge and Pitch motions," Det norske Veritas Report No. 71-35-0, May 1971.
4. Bureau Veritas Technical Note BM. 1 at 27 Gas-Transport Study (Confidential Report).
5. Bass, R. L., III, "Liquid Impact Loads in LNG Carriers," Tech. Report No. 1, Aug. 1972, El Paso Natural Gas Company, Southwest Research Institute.
6. Gerlach, C. R. and Astleford, W. J., "Investigation of Water Impact of Blunt Bodies," Final Report, Contract No. N00014-67-C-0213, SwRI Project No. 02-2036, Southwest Research Institute, Dec. 1970.
7. Frank, W., "Oscillation of Cylinders In or Below the Free Surface of Deep Fluids," U. S. Naval Ship R&D Center Report 2357, 1967, Washington, D.C.
8. Aalen, A.S. and Olsen, H., "Natural Frequencies of Liquid Motion in Tanks of Different Shapes," Report No. 72-16-S, 1972, Det norske Veritas.
9. Verhagen, J. H. G., and Van Wijngaarden, L., "Nonlinear Oscillations of Fluid in a Container," Journal of Fluid Mechanics, Vol. 22, Part 4, 1965.
10. Wehausen, J. V. and Laitone, E. V., "Surface Waves," Article in Encyclopedia of Physics (ed. S. Flügge), Vol. IX, Berlin: Springer-Verlag, 1960, p. 446.
11. Stoker, J. J., Water Waves, New York: Interscience, 1957.
12. Faltinsen, O., "A Nonlinear Theory of Sloshing in Rectangular Tanks," accepted for publication in Journal of Ship Research.
13. Moiseyev, N. N., "On the Theory of Nonlinear Vibrations of a Liquid of Finite Volume," Appl. Math. Mech. (PMM), Vol. 22, No. 5, 1958.
14. Abramson, H. N., Chu, W. H., and Kana, D. D., "Some Studies of Nonlinear Lateral Sloshing in Rigid Containers," Journal of Applied Mechanics, Vol. 33, No. 4, Dec. 1966,

pp. 777-784.

15. Falkneen, O. and Michelsen, F., "Motions of Large Structures in Waves at Zero Froude Number," Presented at the International Symposium on the Dynamics of Marine Vehicles and Structures in Waves, University College London, April 1974.

16. Hutton, R. E., "An Investigation of Resonant, Nonlinear, Nonplanar Free Surface Oscillations of a Fluid," NASA TN D-1870, 1963.

17. Hagiwara, K. and Tani, A., "Study on Dynamic Pressure Produced in Long Tanks by the Motion of Ship," Mitsubishi Heavy Industries, Inc. Technical Review, Jan. 1968, pp. 46-52.

18. Ochi, M. K. and Motter, L. E., "Prediction of Slamming Characteristics and Hull Responses for Ship Design," Paper No. 4, SNAME Annual Meeting, Nov. 1973.

THE HYDRODYNAMIC INFLUENCE ON THE NON-LINEAR MOTION OF AN ACV OVER WAVES

L. J. Doctors
University of New South Wales
Sydney, Australia

ABSTRACT

The nonlinear behavior of an air-cushion vehicle (ACV) during coupled heave and pitch motion over a sinusoidal wave is studied. The vehicle is of the plenum-chamber type with a transverse stability skirt, which greatly contributes to the nonlinearity of the response. Nonlinearity also results from the contact of the flexible skirt with the water surface. Linearized potential flow theory is used to compute the elevation of the free surface induced by the pressure distribution under the air cushion. The air flow is considered to be incompressible.

Numerical computations were made for the craft response in regular head seas. The compliance of the water is found to increase the damping of the heave motion and it greatly modifies the effective mass of the ACV. However, as the motion is strongly damped, the heave amplitude is only increased by up to ten percent when the effect of the water is considered. On the other hand, it increases the pitch motion by as much as one third, and is therefore an important feature of ACV motion.

NOMENCLATURE

A = discharge area
B = beam of craft measured at skirt
c = forward velocity of craft
C = coefficient
e = skirt hem clearance
F = Froude number = c/\sqrt{gL}
g = acceleration of gravity
h = height
I = second moment of mass of craft about transverse axis through the c.g.
k = wavenumber
 k_0 = fundamental wavenumber = g/c^2
 l = distance measured around skirt hem
L = length of craft measured at skirt
m = mass of craft
M = moment
N = number of terms in the cushion-pressure Fourier series which are used
p = pressure
Q = volume flow
R = reaction
S = cushion planform area
t = time

V = volume under the free surface, and above the datum

w, = longitudinal and transverse wave-
u numbers
x, = right-handed orthogonal system, with
y, x in the forward direction, and z
z vertically upwards. Craft position
relative to datum also given by x
and z

α = local wave slope, or amplitude of
wave slope

β = angle between skirt hem and x axis,
as seen in plan view,
i.e. $\cos \beta = dx/dl$

ϵ = longitudinal position of transverse
skirt, ahead of midpoint, as a frac-
tion of L

ζ = free-surface elevation induced by the
pressure

η = skirt-force deflection constant

θ = craft pitch angle, or wave angle

$\lambda = \lambda_0 \cos \theta$

λ_0 = speed-frequency parameter = $4\sigma c/g$

μ = coefficient of friction between skirt
and the operating surface, or Rayleigh
viscosity

ρ = density (of water, usually)

σ = radian frequency of pressure distri-
bution

ϕ = potential function (fluid perturbation
velocity being its positive gradient)

ω = wave-encounter radian frequency

Subscripts

a = air
c = out-of-phase (cosine) component
d = discharge
e = escape
f = fan
g = center of gravity
h = horizontal
i = inlet
k = skirt
max = maximum
min = minimum
rms = root mean square
r = craft
s = in-phase (sine) component
v = vertical
w = wave
 ζ = induced by pressure acting on water
surface
1, = forward, aft and stability regions
2&3

Superscripts

- = average
- = $\partial/\partial t$
- * = indicates a variable related to its mean value during the craft motion, divided by h_w , and nondimensionalized with L , g and ρ . However, craft pitch angle is divided by α_w , instead.

INTRODUCTION

Previous Work

Experimental Results. The motion of an air-cushion vehicle (ACV) was studied by Swaan and Wahab [1]. They conducted towing-tank tests on a peripheral-jet model and tested it both with, and without, flexible skirts. The model was run in regular waves of various direction. The curves which displayed craft heave and pitch response as a function of forward speed (for a particular wavelength) were fairly flat indicating a high level of damping. Results were also presented for waveheights varying up to about one tenth of the craft length, and these indicated some nonlinearity in that the response was not proportional to the height of the waves.

Dyne [2] restricted his model tests (also on a peripheral-jet craft) to regular head seas. The air cushion was compartmented into six sections. The model was excited on a flat surface and the stiffness and damping factors were measured and found to be in agreement with his theory. From these results, a prediction for the motion over a regular wavy surface was made, using a linear theory.

Van den Brug and Van Staveren [3,4] also performed model tests on an essentially plenum-chamber design. Forced oscillation tests in heave, pitch and roll above ground without forward velocity, and above water with forward velocity were carried out with a view to determine the coefficients in the linearized equations of motion. The manner in which these coefficients vary with forward speed and encounter frequency was displayed graphically. In particular, the added mass of the water was found to be negative - in sharp contradistinction to a ship, where it is positive, and of the order of the ship mass.

A method of "equivalent linearization" was suggested by Murthy [5] for the determination of the response spectrum of an ACV travelling in an irregular wind-generated seaway. He gave an example of the technique which requires a knowledge of the craft response to a regular wave.

The practical operation of ACVs in realistic waves has been entirely due to the development of the flexible skirt, and a review of the history of this work was given by Jones [6]. Jones quoted model tests on a skirted annular-jet craft which indicated that the damping ratio in heave was approximately 0.5, and for the pitch motion was somewhat lower, being

about 0.25. Some results were also given for a craft fitted with finger skirts. These indicated a higher damping ratio (of the order of 0.75) compared to the annular-jet-skirt case. Thus the craft motion was measurably improved by the fitting of finger skirts. Jones also noted that the unit response was less in higher waves, and that this would be a measure of the nonlinearity in the system.

Theoretical Work. In the theoretical field, Lin [7] computed the dynamic heave and pitch behavior of an unskirted annular-jet craft fitted with a transverse stability jet. The equations of motion were linearized. Comparisons were made with model tests and good agreement was found, particularly as the natural frequencies and general magnitudes of the pitch and heave response were well predicted. The spring constants for both the static and dynamic cases for a peripheral-jet ACV executing a simple heaving motion were calculated by Ozawa [8], and then used to predict the linear heave motion due to a sinusoidal input.

Hogben [9], in his review of the behavior of ACVs over water, also gave the basic theories for simple heave motion, and linearized these for both annular-jet and plenum-chamber craft. In addition, he covered various empirical approaches in his article.

The heaving response of an ACV moving over regular waves was studied by Reynolds [10], and later extended to include pitching by Reynolds, West and Brooks [11]. The vehicle considered is shown in Fig. 1. In both cases the equations of motion were linearized. In the latter paper, the plenum-chamber vehicle considered had a single lift fan feeding an intermediate chamber (corresponding to the ducting and flexible supply bag utilized by many ACVs). The air was then fed to the fore and aft compartments of the cushion, which had a transverse stability skirt. The incompressible Bernoulli equation and the usual equations of continuity were used in this analysis, and the coupled heave and pitch motion for a particular vehicle was computed as a function of the ratio of craft length to wavelength.

One aspect of the problem which renders this linearization questionable is that the daylight clearance under the skirt is usually quite small, so that skirt contact and deflection occur in most situations, and this is ignored - as pointed out by Reynolds et alia. This would be a very strong nonlinear effect. A second point of concern is related to the crossflow under the transverse stability skirt. The pressure drop across the skirt is proportional to the square of the flow and has the same sign. Consequently, the linearization process is only valid, if there is a crossflow in the equilibrium condition, and if the changes during motion are

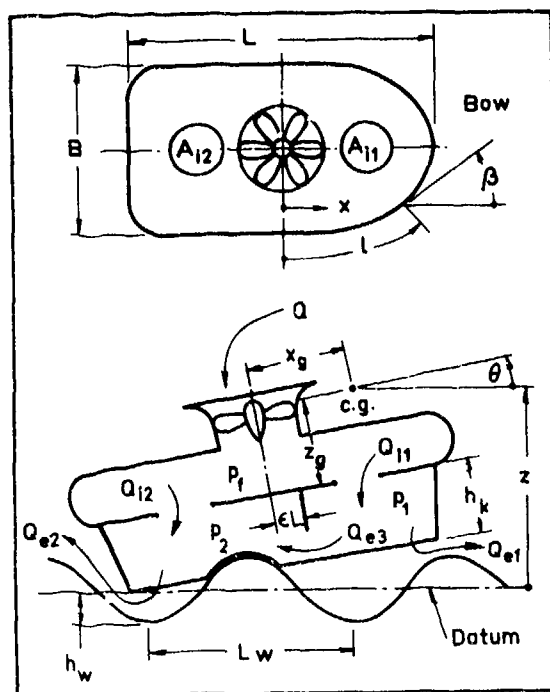


Fig. 1. General layout of Craft and Notation

small compared to it. In fact, the equilibrium crossflow itself is usually very small in practice (the equilibrium pressures in the fore and aft compartments are virtually identical). Hence the changes in crossflow during the heave and pitch cycle swamp it entirely, so that this physical mechanism is essentially nonlinear to the first order.

Nonlinearity. These objections to linearized theory were considered recently by Doctors [12], who used the various nonlinear equations describing the air flow. He also took into account the effect of skirt contact with the wave surface. This was found to be of major importance, since the usual air clearance under the skirt is a fraction of both the encountered waveheights and the skirt depth. The equations were solved iteratively.

It was found that both the heave and pitch response per unit waveheight at low frequencies were essentially independent of waveheight, and the harmonic content of the motion was low. However, at higher frequencies, the unit response was a strong function of waveheight, being either an increasing, or a decreasing function, depending on the craft speed, skirt configuration, etc. Only cases in which the equilibrium cross flow was zero were considered. The calculations showed that for asymptotically small waveheights, the unit heave response approached

a constant value (a suggestion of linearity), but the unit pitch response became unbounded (thus indicating nonlinearity).

Yamamoto [13] studied nonlinear pure heaving motion of a plenum-chamber ACV, including the effect of air compressibility.

Compressibility. Other workers who have considered the compressibility of air for simple heaving motion include Leatherwood, Dixon and Stephens [14], Guienne [15], Leatherwood [16] and Genin, Ginsberg and Ting [17]. All of these employed linearized equations, which would be valid, since their main interest lies in the application to high-speed tracked ACVs and no contact with the track will then be permitted. Incidentally, all of these reports except the last, while assuming the air within the cushion obeys the polytropic process, used the *incompressible* Bernoulli equation for the disc-charge of the cushion air to atmospheric conditions.

Coupled pitch and heave motion of a multiple-skirt ACV was analysed by Bickford and Olson [18], utilizing the above-mentioned assumptions, and solving the equations on an analog computer.

Other aspects of the mechanics of ACV motion over waves were considered by Breslin [19], Richardson [20] and Trillo [21]. It was noted that if compressibility is to be represented correctly on a model ACV, then one must scale the atmospheric pressure accordingly.

Hydrodynamic Influence. The effect of the ACV on the water can be most logically represented by a pressure distribution acting on the free surface. If we consider periodic coupled heave and pitch motion of angular speed ω , over regular waves, then this pressure can be decomposed into a Fourier series. Furthermore, if one linearizes the hydrodynamic aspect of the problem, it is only necessary to consider the effect of a pressure patch with a simple-harmonic timewise variation. This problem is very similar to that for the disturbance created by an oscillating point source, studied by Brard [22,23], Haskind [24], Hanaoka [25], Sretenskii [26], Eggers [27], Becker [28,29] and Wehausen and Laitone [30]. These all pointed out the singularity in the solution for the flow when the parameter $\lambda_0 = 4\omega c/g = 1$, where σ is the radian frequency of the source, c its speed of translation and g is the acceleration due to gravity. As a consequence, the damping of a ship, for example, also changes markedly at this point, as pointed out by Havelock [31] and Newman [32].

The problem of the oscillating pressure appears to have been examined in two dimensions only. Kaplan [33] and Wu [34] considered the forward motion of twodimensional oscillatory pressure distributions over deep water. Debnath

and Rosenblat [35] extended this work to include the effect of finite depth, deriving an expression relating σ , c , g and the water depth for which the above-mentioned singularity occurs. Ogilvie [36] solved the problem of a stationary pulsating pressure band contained within sidewalls. This problem was used principally to model a pneumatic wave maker, but Ogilvie also applied it to a captured air bubble ACV.

Present Work

This paper is directed at computing the effect of the compliance of the water surface - as opposed to a solid one - on the coupled heave and pitch motion of an ACV. We shall assume the water to be inviscid and incompressible so that the potential function, ϕ , may be used.

First the problem of a travelling oscillating pressure distribution will be solved. This is just a generalization to three dimensions of the results given by Wu [34]. From the resulting free-surface elevation, the added mass, damping and spring constant due to the water may be found.

Then these results will be applied to a rectangular ACV, and its response over a sinusoidal wave will be determined. These results will be compared to those in a previous paper by the writer [12], in which the hydrodynamic effect was neglected.

HYDRODYNAMIC REPRESENTATION

The Velocity Potential

We consider a timewise oscillating pressure distribution,

$$p(x, y) = \hat{p}(x, y) \cos \sigma t \cdot H(t),$$

acting on the free surface, and travelling with a velocity c . Here t is the time, and H is the Heaviside step function. The coordinate system x, y, z moves with the pressure, in the x direction, and z is measured vertically upwards from the undisturbed free surface. Under the usual assumptions of linearized potential flow (see Stoker [37]), ϕ satisfies the Laplace equation,

$$\phi_{xx} + \phi_{yy} + \phi_{zz} = 0, \quad (1)$$

the kinematic free-surface condition,

$$\left[\phi_z \right]_{z=0} - \zeta_t + c \zeta_x = 0, \quad (2)$$

and the dynamic free-surface condition,

$$\left[\phi_t - c \phi_x + \mu \phi \right]_{z=0} + p/\rho + g\zeta = 0. \quad (3)$$

Here ζ is the free-surface elevation and ρ is the water density. The radiation condition is satisfied by employing the Rayleigh viscosity μ , which is made to approach zero from the positive direction at a later stage. Some discussion of this technique is given by De Prima and Wu [38], for example. If the water

is infinitely deep, then we may also impose

$$\left[\phi_z \right]_{z=-\infty} = 0. \quad (4)$$

The combined free-surface condition is obtained from Eqs (2) and (3) by eliminating ζ :

$$\phi_{tt} + c^2 \phi_{xx} - 2c \phi_{xt} - \dot{c} \phi_x + g \phi_z + \mu(\phi_t - c \phi_x) = (c p_x - p_t)/\rho \text{ on } z=0. \quad (5)$$

The set of equations (1), (4) and (5) may be solved using the Fourier transform pair:

$$\phi(w, u; z, t) = \frac{1}{2\pi} \int_{-\infty}^{\infty} \int_{-\infty}^{\infty} \phi(x, y, z, t) \cdot \exp[-i(wx+uy)] dx dy$$

(6)

and

$$\phi(x, y, z, t) = \frac{1}{2\pi} \int_{-\infty}^{\infty} \int_{-\infty}^{\infty} \phi(w, u; z, t) \cdot \exp[i(wx+uy)] dw du$$

Here w and u are the longitudinal and transverse wavenumbers and are related to the circular wavenumber k and the wave angle θ by

$$w = k \cos \theta \quad (7)$$

and $u = k \sin \theta$.

The solution to Eqs (1) and (4) is then

$$\phi = A(w, u; t) \cdot c^{kz}, \quad (8)$$

in which A satisfies the transformed free-surface condition (5):

$$\ddot{A} - 2icw\dot{A} + A(gk - c^2w^2 - ic\dot{w}) + \mu(\dot{A} - icwA) = \frac{P}{\rho}(icw \cos \sigma t + \sigma \sin \sigma t), \quad (9)$$

where P is the Fourier transform of \hat{p} . This may be simplified by the substitution

$$A = \chi \exp[iws(t)], \quad (10)$$

where s is the distance travelled by the craft from rest. Thus we obtain

$$\ddot{\chi} + \mu \dot{\chi} + gk \chi = \frac{P}{\rho}(icw \cos \sigma t + \sigma \sin \sigma t) \cdot \exp[-iws(t)].$$

We now take the Laplace transform defined by

$$L(\chi) = \int_0^{\infty} \chi \exp(-qt) dt. \quad (11)$$

Assuming the craft starts from rest with a constant velocity, then we obtain

$$(q^2 + \mu q + gk) L(\chi) = \frac{P}{\rho} L\{\exp(-i\omega ct) \cdot (i\omega \cos \sigma t + \sigma \sin \sigma t)\}.$$

The convolution theorem is now employed to obtain the inverse Laplace transform, and Eq. (10) is used to give

$$A = \sum_{l=\pm 1} \frac{\rho P}{2i\rho\sqrt{gk}} \int_0^t (i\omega \cos \sigma \tau + \sigma \sin \sigma \tau) \cdot \exp[(-\mu + li\sqrt{gk} + i\omega c)(t - \tau)] d\tau$$

$$= \sum_{l,m=\pm 1} \frac{\rho P(c\omega - m\sigma)}{4\rho\sqrt{gk}} \int_0^t \exp[m i \sigma \tau + (-\mu + li\sqrt{gk} + i\omega c)(t - \tau)] d\tau.$$

Partial integration with respect to τ yields

$$A = \sum_{l,m=\pm 1} \frac{\rho P}{4i\rho\sqrt{gk}} \left[\exp[(i\omega c - \mu + li\sqrt{gk})t] - \exp(m i \sigma t) + (\mu - li\sqrt{gk}) \times \int_0^t \exp[(i\omega c - \mu + li\sqrt{gk})(t - \tau) + m i \sigma \tau] d\tau \right].$$

For large values of t , one is left only with the steady-state solution, which comes from the integral term in this expression. This is integrated to give

$$A = \frac{iP}{4\rho} \sum_{l,m=\pm 1} \exp(m i \sigma t) \cdot \left[\frac{1 - \exp[i(c\omega + i\mu + li\sqrt{gk} - m\sigma)t]}{-(c\omega + i\mu + li\sqrt{gk} + m\sigma)} \right].$$

Now we substitute Eq. (8) and take the inverse Fourier transform (6):

$$\phi = \frac{1}{16\pi^2 i \rho} \iint \hat{p}' ds' \int_{-\pi}^{\pi} d\theta \int_0^{\infty} dk \cdot \exp[i\{w(x - x') + u(y - y')\} + kz].$$

$$\cdot \left[e^{i\sigma t} \left(\frac{1 - e^{i\omega_1 t}}{\omega_1} + \frac{1 - e^{i\omega_2 t}}{\omega_2} \right) + e^{-i\sigma t} \left(\frac{1 - e^{i\omega_3 t}}{\omega_3} + \frac{1 - e^{i\omega_4 t}}{\omega_4} \right) \right], \quad (12)$$

$$\text{where } \omega_1 = c\omega \pm \sqrt{gk} - \sigma + i\mu$$

$$\omega_2 = c\omega \pm \sqrt{gk} + \sigma + i\mu \quad (13)$$

The integration of the peak pressure, $\hat{p}(x', y')$ is taken over the surface on which it acts, namely S' .

Finally, the limit of this expression is required as $t \rightarrow \infty$. The locations of the four poles in the k inte-

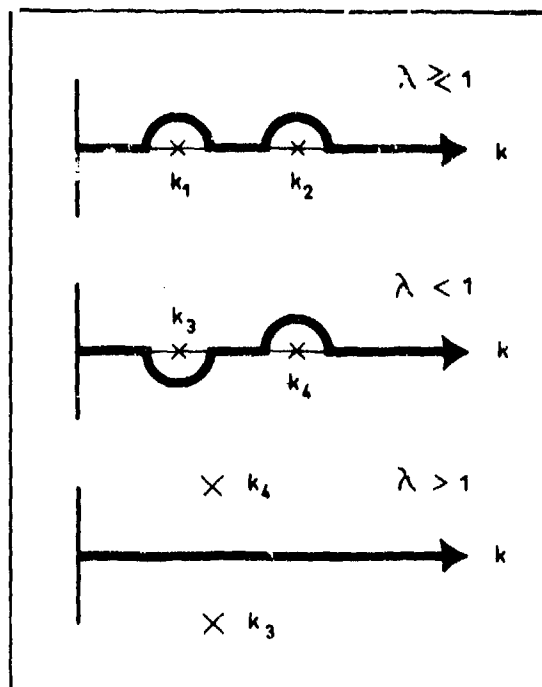


Fig. 2. Path of Integration in the k Plane

gration are given by the zeroes of Eq. (13). This results in the imaginary part of k_1 and k_2 being negative and of order μ . For $\lambda < 1$, the imaginary part of k_3 is positive and that of k_4 negative, again being of order μ . This suggests we deform the path of integration around the poles as indicated in Fig. 2, as $\mu \rightarrow 0$. The poles are therefore given by

$$k_1 = \frac{1}{4} k_0 \sec^2 \theta (\sqrt{1 + \lambda} + 1)^2$$

$$k_2 = \frac{1}{4} k_0 \sec^2 \theta (\sqrt{1 + \lambda} - 1)^2 \quad (14)$$

$$\text{and } k_3 = \frac{1}{4} k_0 \sec^2 \theta (1 + \sqrt{1 - \lambda})^2,$$

$$\text{where } k_0 = g/c^2 \quad (15)$$

$$\text{and } \lambda = \frac{4\sigma c}{g} \cos \theta = \lambda_0 \cos \theta. \quad (16)$$

If $\lambda_0 > 1$, then for part of the θ integration, namely $0 < \theta < \theta_1$, where

$$\cos \theta_1 = 1/\lambda_0, \quad (17)$$

the two poles k_3 and k_4 are complex conjugate (see Fig. 2). In this case the path of the contour integral need not be deformed.

The consequence of this path selection is that the integrals of the expressions containing the $\exp(i\omega_1 t)$, $\exp(i\omega_2 t)$, etc. factors contribute nothing in the limit as $t \rightarrow \infty$. Thus

$$\phi(x, y, z, t) = \frac{1}{16\pi^2 i \rho} \iint \hat{p}' ds' \int_{-\pi}^{\pi} d\theta \int_0^{\infty} dk \quad (18)$$

$$k \cdot \exp[i\{w(x - x') + u(y - y')\} + kz] \cdot \left[e^{i\sigma t} \left(\frac{1}{\omega_1} + \frac{1}{\omega_2} \right) + e^{-i\sigma t} \left(\frac{1}{\omega_3} + \frac{1}{\omega_4} \right) \right] dk.$$

(The path of integration for each of the four terms is interpreted as previously indicated.)

Free-Surface Response

The elevation of the free surface is given by Eq. (3). We substitute the potential from Eq. (18) and simplify the expression using the relations (13):

$$\zeta = \frac{1}{8\pi^2 \rho g} \iint \hat{p}' ds' \int_{-\pi}^{\pi} \sec^2 \theta d\theta \int_0^{\infty} dk \quad (19)$$

$$k \cdot \exp[i\{w(x - x') + u(y - y')\}] \cdot \left[\frac{e^{i\sigma t} \left(\frac{k_1}{k-k_1} - \frac{k_2}{k-k_2} \right) + \frac{e^{-i\sigma t} \left(\frac{k_3}{k-k_3} - \frac{k_4}{k-k_4} \right)}{k_3-k_4} \right].$$

It is now convenient to reduce the range of the θ integration to $0 < \theta < \pi/2$, and to perform the contour integration in the k plane. We make use of the even and odd properties of the trigonometrical functions, and obtain the following expressions after some reduction:

$$\zeta = \zeta_c \cos \sigma t + \zeta_s \sin \sigma t, \quad (20)$$

where

$$\zeta_c = \frac{-1}{2\pi^2 \rho g} \int_0^{\pi/2} d\theta \int_0^{\infty} dk k U \cdot \left[\frac{1}{\sqrt{1+\lambda}} \left(\frac{k_1}{k-k_1} - \frac{k_2}{k-k_2} \right) + \frac{1}{\sqrt{1-\lambda}} \left(\frac{k_3}{k-k_3} - \frac{k_4}{k-k_4} \right) \right] - \frac{1}{2\pi \rho g} \left[\int_0^{\pi/2} \frac{1}{\sqrt{1+\lambda}} (k_1^2 V_1 - k_2^2 V_2) d\theta - \int_0^{\pi/2} \frac{1}{\sqrt{1-\lambda}} (k_3^2 V_3 + k_4^2 V_4) d\theta \right], \quad (21)$$

and

$$\zeta_s = \frac{1}{2\pi^2 \rho g} \int_0^{\pi/2} d\theta \int_0^{\infty} dk k V \cdot \left[\frac{1}{\sqrt{1+\lambda}} \left(\frac{k_1}{k-k_1} - \frac{k_2}{k-k_2} \right) - \frac{1}{\sqrt{1-\lambda}} \left(\frac{k_3}{k-k_3} - \frac{k_4}{k-k_4} \right) \right] - \frac{1}{2\pi \rho g} \left[\int_0^{\pi/2} \frac{1}{\sqrt{1+\lambda}} (k_1^2 U_1 - k_2^2 U_2) d\theta + \right. \quad (cont.)$$

$$\left. + \int_0^{\pi/2} \frac{1}{\sqrt{1-\lambda}} (k_3^2 U_3 + k_4^2 U_4) d\theta \right],$$

$$U = P_e \cos wx \cos uy + P_o \sin wx \sin uy + Q_e \sin wx \cos uy + Q_o \cos wx \sin uy, \quad (22)$$

$$V = P_e \sin wx \cos uy - P_o \cos wx \sin uy - Q_e \cos wx \cos uy + Q_o \sin wx \sin uy,$$

$$P_e = \iint \hat{p}(x, y) \frac{\cos(wx)}{\sin(wx)} \frac{\cos(uy)}{\sin(uy)} ds \quad (23)$$

and

$$Q_e = \iint \hat{p}(x, y) \frac{\sin(wx)}{\cos(wx)} \frac{\cos(uy)}{\sin(uy)} ds.$$

(The subscripts on U and V in Eq. (21) refer to the four poles in Eq. (14).)

To simplify computation, we shall now limit our consideration to a space-wise constant pressure p_0 acting on a rectangular area defined by $|x| < a$ and $|y| < b$. Hence

$$P_e = 4 p_0 \frac{\sin aw}{w} \frac{\sin bu}{u} \quad (24)$$

$$\text{and } P_o = Q_e = Q_o = 0.$$

The free-surface response given by Eq. (21) can now be simplified. The usual rules for combining products of trigonometric functions allow us to write the k integral in terms of the sine- and cosine-integral auxiliary functions given by Abramowitz and Stegun [39]:

$$f(z) = \int_0^{\infty} \frac{\sin t}{t+z} dt \quad (25)$$

$$\text{and } g(z) = \int_0^{\infty} \frac{\cos t}{t+z} dt.$$

The results for the in-phase and out-of-phase components of the free-surface elevation are

$$\zeta_c = \frac{p_0}{4\pi^2 \rho g} \sum_{l,m,n=\pm 1} \sum_{l,m,n=\pm 1} \int_0^{\pi/2} \sec \theta \operatorname{cosec} \theta \cdot \left[\frac{1}{\sqrt{1+\lambda}} [g_1 - g_2 - \pi s_1 + \pi s_2 + 2\lambda \pi (s_1 - s_2)] + \frac{1}{\sqrt{1-\lambda}} [g_3 - g_4 - \pi s_3 + \pi s_4 - 2\lambda \pi (s_3 + s_4)] \right] d\theta \quad (26)$$

and

$$\zeta_s = \frac{p_0}{4\pi^2 \rho g} \sum_{l,m,n=\pm 1} \sum_{l,m,n=\pm 1} \int_0^{\pi/2} \sec \theta \operatorname{cosec} \theta \cdot \quad (cont.)$$

$$\cdot n \left[\frac{1}{\sqrt{1+\lambda}} [\ell v(f_1 - f_2 - \pi c_1 + \pi c_2) + \pi(c_1 - c_2)] - \frac{1}{\sqrt{1-\lambda}} [\ell v(f_3 - f_4 - \pi c_3 + \pi c_4) - \pi(c_3 + c_4)] \right] d\theta$$

in which the following shorthand notation has been used:

$$\begin{aligned} f_1 &= f|rk_1|, \quad f_2 = f|rk_2|, \text{ etc.}, \\ g_1 &= g|rk_1|, \text{ etc.}, \\ c_1 &= \cos|rk_1|, \text{ etc.}, \\ s_1 &= \sin|rk_1|, \text{ etc.}, \end{aligned} \quad (27)$$

and $v = \text{sgn}(r)$,

where $r = (a + \ell x) \cos \theta + (b + my) \sin \theta$.

The underlined terms in Eq. (26) should be omitted for $\theta < \theta_1$, as given by Eq. (17).

The case of a nonvarying pressure distribution, corresponding to $\sigma = 0$, may be recovered from Eq. (26). We use the fact that

$$f(z) \rightarrow \frac{1}{2} \text{ and } g(z) \rightarrow -\gamma - \ln(z) \text{ as } z \rightarrow 0, \quad (28)$$

γ being the Euler constant. Taking the limit, one can show that

$$\begin{aligned} \zeta_c &= \frac{P_0}{2\pi^2 \rho g} \sum_{\ell, m, n=\pm 1} \sum_{\theta=0}^{\pi/2} \sec \theta \operatorname{cosec} \theta \cdot \\ &\cdot n [-g|rk_0 \sec^2 \theta| + \pi(1 - \ell v, \sin|rk_0 \sec^2 \theta|) - \\ &- \frac{P_0}{2\pi^2 \rho g} \sum_{\ell, m, n=\pm 1} \sum_{\theta=0}^{\pi/2} n \int \sec \theta \operatorname{cosec} \theta \cdot \\ &\cdot \ln|rk_0 \sec^2 \theta| d\theta, \end{aligned} \quad (29)$$

and $\zeta_s = 0$.

The second integral can be shown to equal the depression of the free surface from hydrostatic considerations alone:

$$\zeta_{\text{stat}} = - \frac{P_0}{4\rho g} \sum_{\ell, m=\pm 1} \operatorname{sgn}(a + \ell x) \cdot \operatorname{sgn}(b + my)$$

Induced Free-Surface Escape Areas and Volumes

The motion of the ACV over water is modified by two effects. These are the change in the clearance under the skirt, given by Eq. (26), and the volume under the free surface relative to the datum, as this alters the cushion-pumping effect. The notation used for number of these terms is presented in Fig. 3. In this way an ACV with a forward and an aft compartment may be modelled. Many of the terms indicated influence cross coupling between the two cushions.

The escape areas corresponding to sides 1, 2 or 3 are obtained by integrating Eq. (26) with respect to x . This process requires the formulas

$$\int \operatorname{sgn}(z) f|z| dz = g|z| + \ln|z|$$

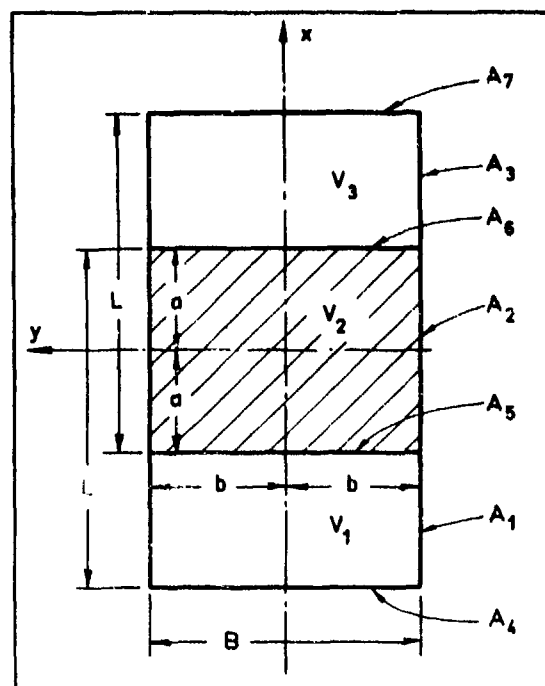


Fig. 3. Notation for Escape Areas and Volumes

$$\text{and } \int g|z| dz = \operatorname{sgn}(z) \left[\frac{\pi}{2} - f|z| \right], \quad (30)$$

which may be derived from Eq. (25). The result for these three areas (for both sides) is

$$A_{\zeta c} = A_{\zeta c} \cos \sigma t + A_{\zeta s} \sin \sigma t, \quad (31)$$

where

$$\begin{aligned} A_{\zeta c} &= \frac{P_0}{2\pi^2 \rho g} \sum_{i, \ell, n=\pm 1} \sum_{\theta=0}^{\pi/2} \sec^2 \theta \operatorname{cosec} \theta \cdot \\ &\cdot \ln \left[\frac{1}{\sqrt{1+\lambda}} \left[\ell v \left(\frac{\pi c_1 - f_1 - \pi/2}{k_1} - \frac{\pi c_2 - f_2 - \pi/2}{k_2} \right) - \right. \right. \\ &\quad \left. \left. - \pi(c_1/k_1 - c_2/k_2) \right] + \right. \\ &\quad \left. + \frac{1}{\sqrt{1-\lambda}} \left[\ell v \left(\frac{\pi c_3 - f_3 - \pi/2}{k_3} - \frac{\pi c_4 - f_4 - \pi/2}{k_4} \right) + \right. \right. \\ &\quad \left. \left. + \pi(c_3/k_3 + c_4/k_4) \right] \right] d\theta \end{aligned} \quad (32)$$

and

$$\begin{aligned} A_{\zeta s} &= \frac{P_0}{2\pi^2 \rho g} \sum_{i, \ell, n=\pm 1} \sum_{\theta=0}^{\pi/2} \sec^2 \theta \operatorname{cosec} \theta \cdot \\ &\cdot \ln \left[\frac{1}{\sqrt{1+\lambda}} \left[\frac{g_1 + L_1 - \pi s_1}{k_1} - \frac{g_2 + L_2 - \pi s_2}{k_2} + \right. \right. \\ &\quad \left. \left. + \ell v \pi (s_1/k_1 - s_2/k_2) \right] - \right. \end{aligned} \quad (\text{cont.})$$

$$- \frac{1}{\sqrt{1-\lambda}} \left[\frac{q_3 + L_3 - \pi r_3}{k_3} - \frac{q_4 + L_4 - \pi s_4}{k_4} - \frac{\pi (c_3/k_3^2 + c_4/k_4^2)}{2} \right] d\theta,$$

$$- \frac{\lambda v \pi (s_3/k_3 + s_4/k_4)}{2} \Big] d\theta$$

The notation used here is

$$L_1 = \ln|rk_1|, \quad L_2 = \ln|rk_2|, \text{ etc.}, \quad (33)$$

as well as that given in Eq. (27) with the changes:

$$my = b, \quad x = x_1,$$

where x_1 and x_2 are the endpoints of the interval under consideration.

In a similar way, one can obtain the areas along sides 4, 5, 6 and 7, by integrating Eq. (26) with respect to y . The result is the same as that in Eq. (32), but with the "i" summation replaced by an "m" summation, and with an additional factor " $i \cot \theta$ " placed inside the integral. Also different is r , which is now given by Eq. (27) with $x = x_1$ (the position of the transverse side) and with $y = b$.

The volume between the datum plane $z = 0$ and the free surface $z = \zeta(x, y, t)$ may be obtained by a double integration of Eq. (26) with respect to x and y over the particular area of interest, or more directly, by integrating Eq. (32) with respect to y over the range $-b \leq y \leq b$. The result, after using the formulas (30), is:

$$V_{\zeta} = V_{\zeta c} \cos \sigma t + V_{\zeta s} \sin \sigma t, \quad (34)$$

where

$$V_{\zeta c} = \frac{P_0}{2\pi^2 \rho g} \sum_{i,l,m,n=1}^{\infty} \sum_{\theta=0}^{\pi/2} \sec^2 \theta \operatorname{cosec}^2 \theta \cdot$$

$$\cdot i \operatorname{Im} \left[\frac{1}{\sqrt{1+\lambda}} \left[\frac{\pi s_1 - g_1 - L_1 - \frac{\pi}{2} M_1}{k_1^2} - \frac{\pi s_2 - g_2 - L_2 - \frac{\pi}{2} M_2}{k_2^2} - \frac{\lambda v \pi (s_1/k_1^2 - s_2/k_2^2)}{2} \right] + \right.$$

$$+ \frac{1}{\sqrt{1-\lambda}} \left[\frac{\pi s_3 - g_3 - L_3 - \frac{\pi}{2} M_3}{k_3^2} - \frac{\pi s_4 - g_4 - L_4 - \frac{\pi}{2} M_4}{k_4^2} + \right.$$

$$\left. \left. + \frac{\lambda v \pi (s_3/k_3^2 + s_4/k_4^2)}{2} \right] \right] d\theta,$$

and

$$(35)$$

$$V_{\zeta s} = \frac{P_0}{2\pi^2 \rho g} \sum_{i,l,m,n=1}^{\infty} \sum_{\theta=0}^{\pi/2} \sec^2 \theta \operatorname{cosec}^2 \theta \cdot$$

$$\cdot i \operatorname{Im} \left[\frac{1}{\sqrt{1+\lambda}} \left[\frac{\pi c_1 - f_1 + M_1 L_1 - \frac{\pi}{2}}{k_1^2} - \frac{\pi c_2 - f_2 + M_2 L_2 - \frac{\pi}{2}}{k_2^2} - \frac{\pi (c_1/k_1^2 - c_2/k_2^2)}{2} \right] - \right.$$

$$- \frac{1}{\sqrt{1-\lambda}} \left[\frac{\pi c_3 - f_3 + M_3 L_3 - \frac{\pi}{2}}{k_3^2} - \frac{\pi c_4 - f_4 + M_4 L_4 - \frac{\pi}{2}}{k_4^2} + \right.$$

in which $M_1 = |rk_1|$, $M_2 = |rk_2|$, etc. and r is given by Eq. (27), but with $y = b$ and $x = x_1$.

Finally, from Eqs (34), the induced volume flux under the free surface is

$$Q_{\zeta} = (\sigma V_{\zeta c}) \cos \sigma t + (-\sigma V_{\zeta s}) \sin \sigma t. \quad (36)$$

Numerical Evaluation

The results for the induced free-surface elevation, escape areas and volumes, Eqs (26), (29), (32) and (35), were computed by use of the trapezoidal rule in the θ integration. The change of variable given by

$$\theta' = \sin \theta / \cos^2 \theta \quad (37)$$

was also made. This results in a fairly uniform oscillation in the various integrals, instead of an infinite accumulation near $\theta = \pi/2$. The range of the θ' integration is 0 to ∞ , but it was found that less than 1% error was involved by truncating at $\theta' = 64$ (for $0 < \lambda_0 < 6$). For $\lambda_0 = 0$, the steady-state case, 512 points were needed, but for $0.2 < \lambda_0 < 6$, only 256 points were required.

For the supercritical part of the integral ($\lambda_0 \cos \theta > 1$ or $\theta < \theta_1$), which only occurs if $\lambda_0 > 1$, the underlined terms are to be omitted. Furthermore, the remaining terms which are functions of k_3 and k_4 become complex. It was found convenient to combine these (they do so into a purely real result), and to leave them in the form of the k integral, and perform this integration numerically, since there are no poles on the real axis in this case. About 1% error was incurred by truncating this integration at $ka = 16$ and by using 64 points.

Wave profiles for $\sigma = 0$ and $F = 1.5$ were found to agree with the steady-motion results of Huang and Wong [40], whose numerical technique was different. Another check involved comparing the induced escape areas with those obtained by numerically integrating the free-surface elevation.

Results

Some numerical calculations are shown in Figs 4 to 7. These all pertain to a pressure acting on a square area ($b/a = 1$), so that this would model either the fore or aft cushion of a rectangular ACV with a beam-to-length ratio $B/L = 0.5$, and with a central transverse skirt. The Froude number based on the craft length is 0.5. Calculations were performed for $\lambda_0 = 0(0.2)0.8, 0.9, 0.95, 1.1, 1.2(0.2)2.0(0.5)3.0(1.0)6.0$.

Fig. 4a depicts the cosine, or in-phase components of the longitudinal free-surface profiles along the sides of the craft, for various values of the speed-frequency parameter λ_0 . The steady case ($\lambda_0 = 0$) shows the usual rise of the water at the bow of the cushion ($x/a = 1$),

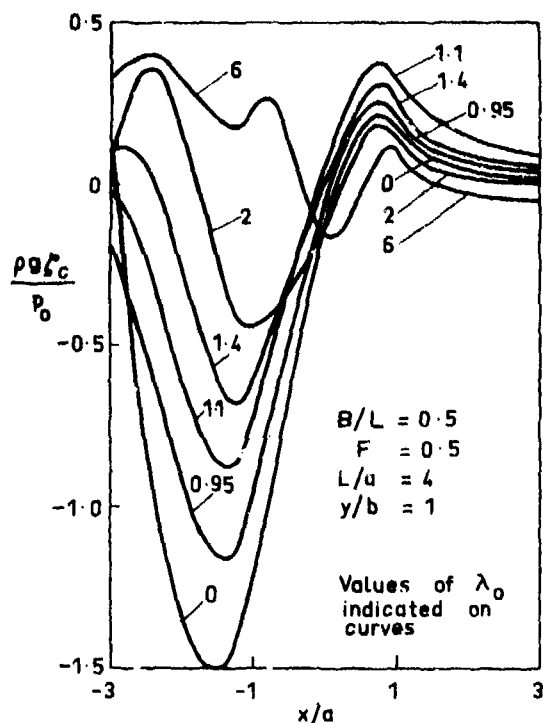


Fig. 4. Induced Free-Surface Elevation (Longitudinal)
(a) In-Phase Component.

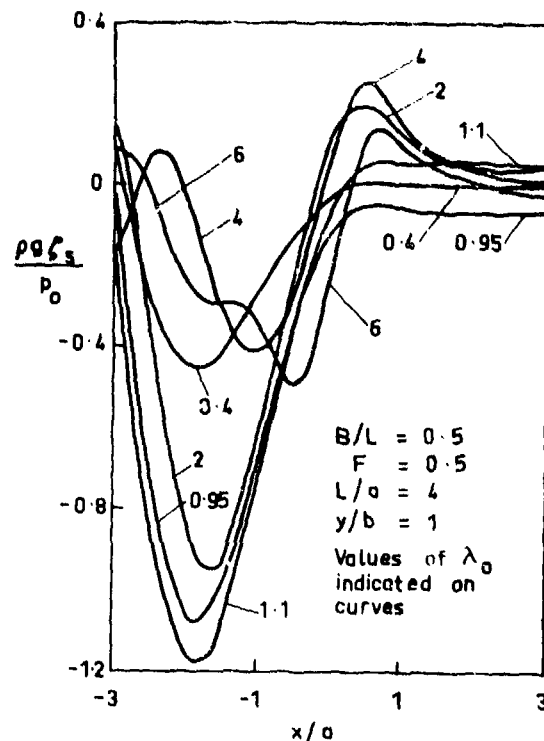


Fig. 4. Induced Free-Surface Elevation (Longitudinal)
(b) Out-of-Phase Component

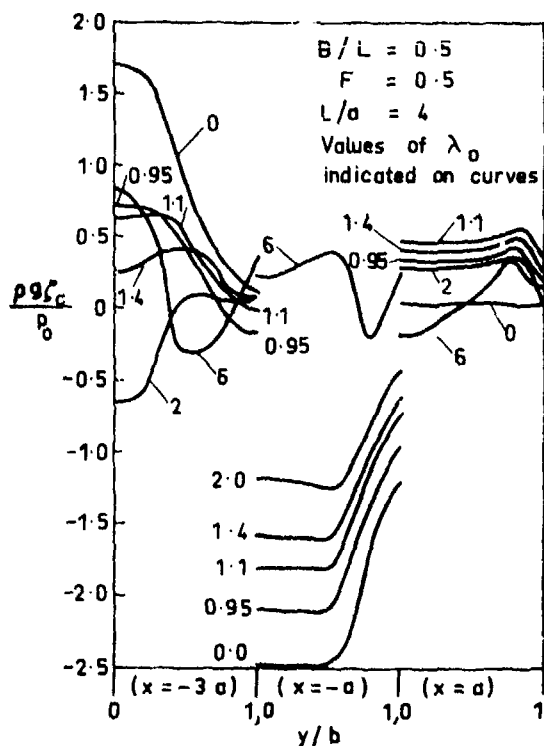


Fig. 5. Induced Free-Surface Elevation (Transverse)
(a) In-Phase Component

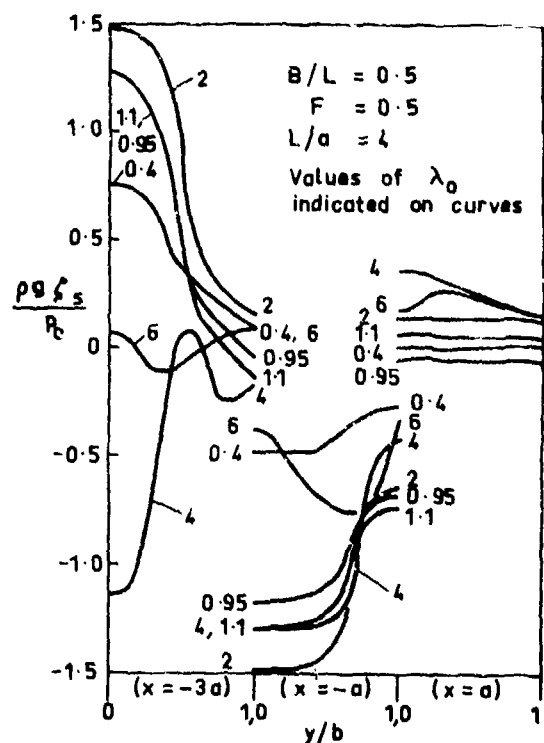


Fig. 5. Induced Free-Surface Elevation (Transverse)
(b) Out-of-Phase Component

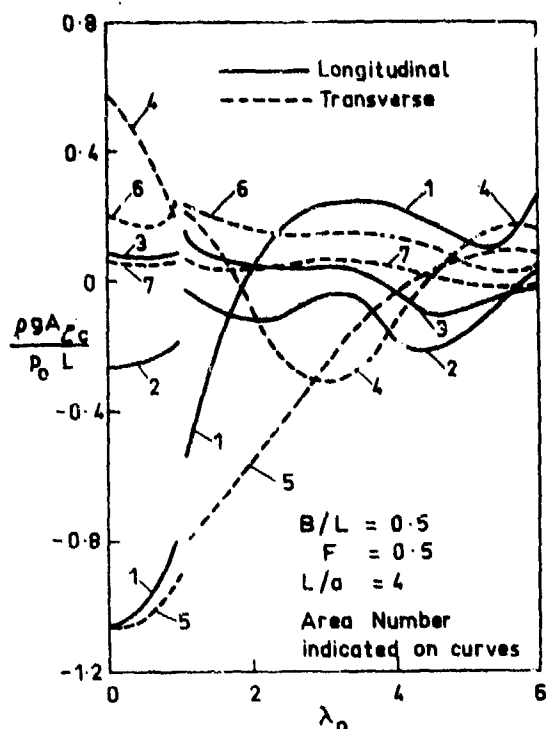


Fig. 6. Induced Free-Surface Escape Areas
(a) In-Phase Component

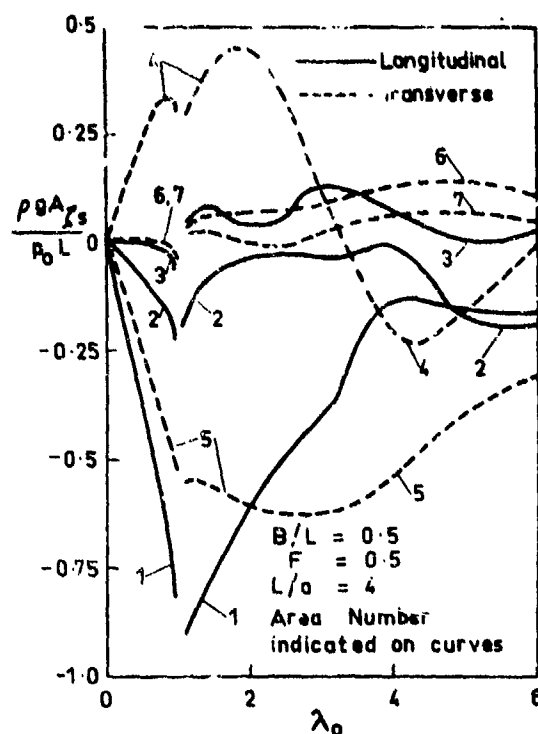


Fig. 6. Induced Free-Surface Escape Areas
(b) Out-of-Phase Component

with a wave developing downstream (due to the k_1 , k_2 and k_4 terms in Eq. (26)). A smooth change in the character of the curves occurs as λ_0 increases, but the upstream effect ($x/a > 1$), due to the k_3 term, is always small. The sine, or out-of-phase components are given in Fig. 4b. The case of $\lambda_0 = 0$ is not shown as this is identically zero. Again there is little upstream effect and a downstream wave profile is developed in all cases. Transverse wave profiles are shown in Fig. 5. Transverse cuts corresponding to $x/a = 3$ are not shown as these are so small. As in Fig. 4, the character of the in-phase components (Fig. 5a) and that of the out-of-phase components (Fig. 5b) are quite similar.

The induced areas under the wave profiles are shown in Fig. 6. These, of course, only have relevance in a linear theory which negates skirt contact. For both the cosine and sine components, the square-root singularity produced by the linear theory at $\lambda_0 = 1$ is evident in varying degrees. The curves tend to follow the same direction as one passes through the singularity, this being interrupted by a break in either the positive or negative direction. (The tendency of the departure appears to be the same on both sides of the singular point, although there are not enough computed points in all cases to illustrate this feature.) At high value of λ_0 the curves display

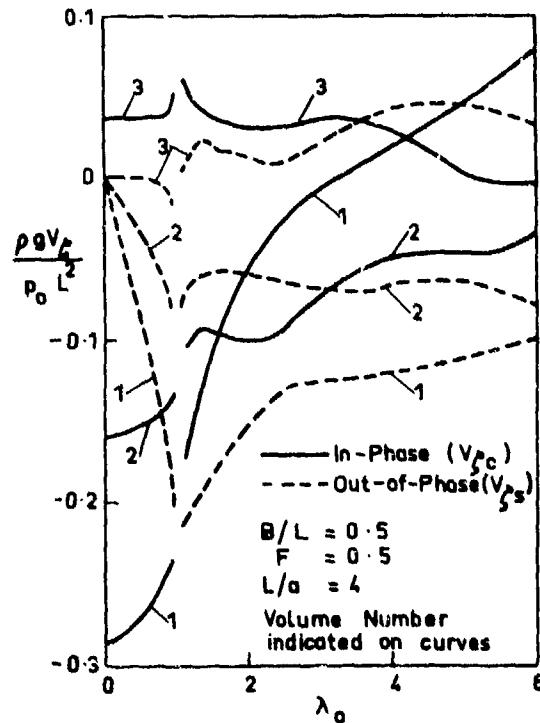


Fig. 7. Induced Free-Surface Volumes

oscillations, and presumably they eventually approach zero.

The induced volumes under the free surface are depicted in Fig. 7. The varying degrees of localization of the singular effect are again to be noted.

APPLICATION TO ACV MOTION

Theoretical Model

The craft under consideration is shown in Fig. 1. The vehicle executes planar motion, so that its center of gravity, which is at (x_g, z_g) relative to the longitudinal midpoint and above the baseline, is defined by the heave and pitch, z and θ . The air from the lift fan(s) discharges into an intermediate chamber before feeding the forward and aft cushions through the equivalent areas A_{i1} and A_{i2} , respectively.

We assume that the total pressure in the intermediate chamber is given by

$$P_f = C_{f1} + C_{f2}Q + C_{f3}Q^2, \quad (38)$$

where Q is the inlet flow, and the C_f are constants which incorporate the fan characteristics as well as those of the intake duct.

Volume Flow Terms

The fan flow equals the sum of the cushion inlet flows:

$$Q = Q_{i1} + Q_{i2}. \quad (39)$$

The cushion inlet flows, and escape flows Q_e are given in terms of the appropriate pressure differences:

$$Q_{i1} = \text{sgn}(p_f - p_1) A_{i1} C_{di1} \sqrt{2|p_f - p_1|/\rho_a}, \quad (40)$$

$$Q_{i2} = \text{sgn}(p_f - p_2) A_{i2} C_{di2} \sqrt{2|p_f - p_2|/\rho_a},$$

$$Q_{e1} = \text{sgn}(p_1) A_{e1} C_{de1} \sqrt{2|p_1|/\rho_a},$$

$$Q_{e2} = \text{sgn}(p_2) A_{e2} C_{de2} \sqrt{2|p_2|/\rho_a} \text{ and } (41)$$

$$Q_{e3} = \text{sgn}(p_1 - p_2) A_{e3} C_{de3} \sqrt{2|p_1 - p_2|/\rho_a}.$$

The stability cross flow Q_{e3} can clearly have either sign. The other four flows are normally positive, but as pointed out by Doctors [12], can be negative for high encounter frequencies. These flows are interrelated, by continuity, as follows:

$$Q_{i1} = Q_{e1} + Q_{r1} - Q_{w1} + Q_{e3} - Q_{\zeta 1} \quad (42)$$

$$\text{and } Q_{i2} = Q_{e2} + Q_{r2} - Q_{w2} - Q_{e3} - Q_{\zeta 2}.$$

The flux terms due to craft pumping under the two compartments, Q_{r1} and Q_{r2} are given by

$$Q_r = [\dot{z} + (\bar{x} - x_g)\dot{\theta}] S, \quad (43)$$

S being the area of either compartment, and \bar{x} its centroid.

The flux terms due to pumping because

of the water surface compliance Q_ζ can be obtained if the vehicle motion is periodic (with angular frequency ω) and the Fourier series cosine and sine components (a_n and b_n , say) of the two cushion pressures p_1 and p_2 are known. Since a linear theory for the water flow is employed, we may sum the effect of each frequency component using Eq. (36). One must also consider the interference between the two cushions. The result is

$$Q_{\zeta 1} = \sum_{n=1}^{N-1} n\omega. \quad (44)$$

$$\begin{aligned} & \cdot \left[(a_{n1} V_{\zeta s2}(n\omega) + b_{n1} V_{\zeta c2}(n\omega) + \right. \\ & \quad + a_{n2} V_{\zeta s1}(n\omega) + b_{n2} V_{\zeta c1}(n\omega)) \cos(n\omega t) + \\ & \quad + (b_{n1} V_{\zeta s2}(n\omega) - a_{n1} V_{\zeta c2}(n\omega) + \\ & \quad \left. + b_{n2} V_{\zeta s1}(n\omega) - a_{n2} V_{\zeta c1}(n\omega)) \sin(n\omega t) \right]. \end{aligned}$$

The expression for $Q_{\zeta 2}$ is the same, but with the subscripts of $V_{\zeta c}$ and $V_{\zeta s}$ reduced by 1. Here we are considering the first N terms in the Fourier series:

$$p = \sum_{n=0}^{\infty} \epsilon_n [a_n \cos(n\omega t) + b_n \sin(n\omega t)], \quad (45)$$

in which $\epsilon_0 = \frac{1}{2}$ and $\epsilon_n = 1$ for $n \neq 0$. The first term ($n = 0$) does not contribute to the fluxes.

The volume fluxes due to wave pumping are given by

$$Q_w = \int \frac{\partial}{\partial t}(z_w) B(x) dx, \quad (46)$$

in which B is the local craft beam (constant here) and z_w is the forcing wave which we define as

$$z_w = h_w \cos[k_w(x_w - c_w t)],$$

where h_w , k_w and c_w are respectively the amplitude, wavenumber and velocity of the wave, and x_w is measured in a stationary reference frame. We reexpress this as

$$z_w = h_w \cos(k_w x - \omega t), \quad (47)$$

where ω is the encounter frequency, and substitute in Eq. (46) to give

$$Q_{w1} = \frac{h_w B \omega}{k_w}. \quad (48)$$

$$\begin{aligned} & \cdot \left[(\pm \cos(\frac{1}{2}k_w L) \mp \cos(\frac{3}{2}k_w L)) \cos(\omega t) + \right. \\ & \quad \left. + (-\sin(\frac{1}{2}k_w L) \pm \sin(\frac{3}{2}k_w L)) \sin(\omega t) \right]. \end{aligned}$$

The Escape Areas

Assuming the craft position to be known, then the clearance under the hem of the skirt may be calculated:

$$e = z + x\theta - h_k - z_w - z_\zeta, \quad (49)$$

where h_k is the local skirt depth, and z_ζ is the induced free surface elevation due to the action of the cushion pressure on the water surface. It may be calculated in a way similar to the flux terms in Eq. (44) using the same Fourier series components of the pressure. For example, the pressure-induced elevation on side 1 is:

$$z_{\zeta 1} = \sum_{n=0}^{N-1} \epsilon_n \cdot \quad (50)$$

$$\begin{aligned} & \cdot \left[\{a_{n1} \zeta_{c1}(nw) - b_{n1} \zeta_{s1}(nw) + \right. \\ & + a_{n2} \zeta_{c2}(nw) - b_{n2} \zeta_{s2}(nw)\} \cos(nwt) + \\ & + a_{n1} \zeta_{s1}(nw) + b_{n1} \zeta_{c1}(nw) + \\ & \left. + a_{n2} \zeta_{s2}(nw) + b_{n2} \zeta_{c2}(nw)\} \sin(nwt) \right]. \end{aligned}$$

The escape area along the appropriate segment of the skirt is obtained by integration with respect to the distance along the skirt hem, l :

$$A_e = \int e H(e) dl, \quad (51)$$

where H is the Heaviside step function. The escape area under the stability skirt is simply

$$A_{e3} = R e H(e), \quad (52)$$

e being evaluated at $l = x = eL$.

Skirt Contact Forces and Moments

We consider each element of skirt to act independently, so that the vertical force on the craft due to skirt deflection is

$$R_V = - \int p \eta e H(-e) dl. \quad (53)$$

Thus we assume the local force is proportional to the cushion pressure. The constant η is essentially the tangent of the angle between the skirt and the vertical.

The horizontal component of the skirt force can be decomposed into two causes. The first, being frictional, is due to the relationship between a horizontal and vertical force moving over a surface:

$$dR_h'/dR_V = (\alpha_w + \mu) / (\alpha_w - 1), \quad (54)$$

where α_w is the slope of the water surface,

$$\alpha_w \doteq (\Delta z_w + \Delta z_\zeta) / \Delta x, \quad (55)$$

and μ is the equivalent coefficient of friction, a concept admittedly rather tenuous in our situation, considering

the mechanics of the skirt contact with the water surface. The horizontal force is also partly due to the pressure acting on the skirt wall. That component in the x direction is given by

$$dR_h'' = p e H(-e) \sin \beta dl, \quad (56)$$

where β is the angle between the skirt and the x direction. (Thus the sides of the rectangular ACV in our problem do not contribute to Eq. (56)). We use Eqs (53), (54) and (56) to give the longitudinal horizontal skirt force on the ACV,

$$\begin{aligned} R_h &= R_h' + R_h'' \\ &= \int p \left[\sin \beta - \eta \frac{\alpha_w + \mu}{\mu \alpha_w - 1} \right] e H(-e) dl, \end{aligned} \quad (57)$$

and the bow-up moment on the vehicle about the center of gravity

$$\begin{aligned} M &= \int p \left[(z_g + h_k + h_e) \sin \beta - \right. \\ & \left. - \eta (x - x_g + (z_g + h_k + e) \frac{\alpha_w + \mu}{\mu \alpha_w - 1}) \right] e H(-e) dl. \end{aligned} \quad (58)$$

Equations of Motion

Newton's laws of motion for heave and pitch give

$$m(\ddot{z} + g) = p_1 S_1 + p_2 S_2 + R_V \quad (59)$$

$$\begin{aligned} \text{and } I\ddot{\theta} &= p_1 S_1 (\bar{x}_1 - x_g) + p_2 S_2 (\bar{x}_2 - x_g) + M + \\ & + p_1 B(h_{k1} - h_{k3}) [z_g + \frac{1}{2}(h_{k1} + h_{k3})] + \\ & + p_2 B(h_{k3} - h_{k2}) [z_g + \frac{1}{2}(h_{k3} + h_{k2})], \end{aligned} \quad (60)$$

where m and I are the vehicle mass and its second moment about the transverse axis through the center of gravity, respectively.

Numerical Solution

The motion of the ACV was computed numerically from initial conditions of

$$\begin{aligned} z &= z_g + h_{k, \min} - h_w, \\ \text{and } \dot{z} = \ddot{z} = \theta = \dot{\theta} = \ddot{\theta} &= 0, \end{aligned} \quad (61)$$

with a forward velocity of c , over the waves travelling at a speed c_w .

The time t was incremented in steps, with the new craft position z and θ and velocity \dot{z} and $\dot{\theta}$ computed from a simple extrapolation, using \ddot{z} , $\ddot{\theta}$ and $\ddot{\theta}$ from the previous point in time. Thus, at each time step, it was first necessary to solve the set of equations (38) to (42). It is possible to reduce this set to a pair of nonlinear algebraic equations in p_1 and p_2 which are soluble by the Newton-Raphson technique. The skirt forces given by

Eqs (53), (57) and (58) can then be obtained, leading to values of the acceleration from Eqs (59) and (60).

The vehicle was run over a sufficient number of cycles until a stable periodic motion resulted. Details of the procedure and numerical information pertaining to the computer program may be found in Doctors [12], where the hydrodynamic effect (namely the calculation of z_L in Eq. (50) and Q_L in Eq. (44)) was neglected. The technique implies that the values of z_L and Q_L will always be those corresponding to the previous cycle, since a Fourier analysis of a complete cycle is required for their evaluation. This possibly explains why the number of periods required for a repetitive motion to result typically increased from 3 to 4 or 5.

Encounter Frequency

We consider the frequency resulting from waves, whose wavenumber is

$$k_w = 2\pi/L_w = 1/L \cdot F_w^2, \quad (62)$$

where L_w is the wavelength. If the craft Froude number is $F = c/\sqrt{gL}$, then the wave speed may be found for a particular frequency ω :

$$F_w = [-1 \pm \sqrt{1 + 4F(\omega\sqrt{L/g})}] / 2(\omega\sqrt{L/g}). \quad (63)$$

In general, there are four possible values of F_w satisfying Eq. (63), if positive or negative values of ω are allowed. If $\lambda_0 = 4\omega F > 1$, there are only two possible wave speeds.

In this paper we shall restrict our interest to head waves ($F_w < 0$), for which there is always just one solution.

RESULTS

Calculations were carried out for the ACV whose particulars are presented in Table 1. The craft response in the low frequency range in head seas is shown in Fig. 8. The hydrodynamic effect is considered to the extent of two terms ($N = 2$ in Eqs (44) and (50)), and the results are compared to those in which the hydrodynamic effect is ignored ($N = 0$). Root-mean-square heave response is given in Fig. 8a. For a dimensionless frequency greater than 1.5, it is seen that the compliance of the water increases the response by 5 or 10%. However, the pitch of the craft (Fig. 8b) is affected to a much greater degree, being increased by as much as 30% in the frequency range considered. A series of peaks are apparent for $\omega\sqrt{L/g} \approx 2$, but these are not related to the critical condition of $\lambda_0 = 1$, which occurs at $\omega\sqrt{L/g} = 0.5$ for a Froude number of 0.5. Surprisingly, in fact, none of the calculations showed any peaks near the critical condition, so that one must assume that the singularity is highly localized.

The phase angles, ahead of the

B/L	=	0.5
ϵ	=	0.0
$m/\rho L^3$	=	0.006
$I/\rho L^5$	=	3.25×10^{-4}
x_g/L	=	0.0
z_g/L	=	0.1
h_{k1}/L	=	0.08
h_{k2}/L	=	0.08
h_{k3}/L	=	0.08
η_1	=	1.0
η_2	=	1.0
η_3	=	0.0
μ	=	0.0
$C_{f1}/\rho g L$	=	0.04
$C_{f2}\sqrt{L^3/g\rho^2}$	=	0.0
$C_{f3}L^4/\rho$	=	-30.0
A_{i1}/L^2	=	0.005
A_{i2}/L^2	=	0.005
C_{di1}	=	1.0
C_{di2}	=	1.0
C_{de1}	=	0.55
C_{de2}	=	0.55
C_{de3}	=	0.6
ρ_a/ρ	=	0.00125

Table 1. Craft Particulars

incident wave, of the fundamentals of the heave and pitch motion are plotted in Figs 8c and 8d. As the frequency increases from zero, the heave phase becomes negative (i.e. lags the input wave). On the other hand, if the wave is considered solid, then the opposite trend is predicted. The pitch phase angle, in Fig. 8d, also is more negative when the hydrodynamic effect is included.

Nonlinearity is evident in Fig. 8 by the noncoincidence of the various curves for different waveheights. This effect is more clearly displayed in Fig. 9. For a solid wave ($N = 0$), the maximum, minimum and root-mean-square heave responses (the latter is multiplied by $\sqrt{2}$) are seen to approach each other, and become constant, as $h_w/L \rightarrow 0$, in Fig. 9a. Thus the heave motion would appear linear in this limit. The pitch response as a function of waveheight appears in Fig. 9b, where the strong nonlinearity (with, or without water compliance) is evident. At larger waveheights, the difference in the response due to the water compliance become relatively less important.

The heave and pitch accelerations are shown in Figs 10a and 10b respectively. The accelerations are only approximately related by a factor of $\omega^2 L/g$ to the motions in Figs 8a and 8b - due to

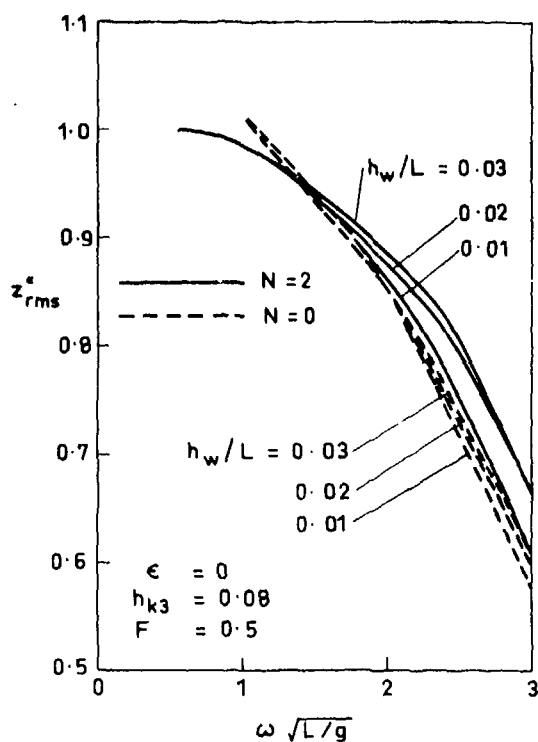


Fig. 8. Craft Response as a Function of Frequency (a) Heave

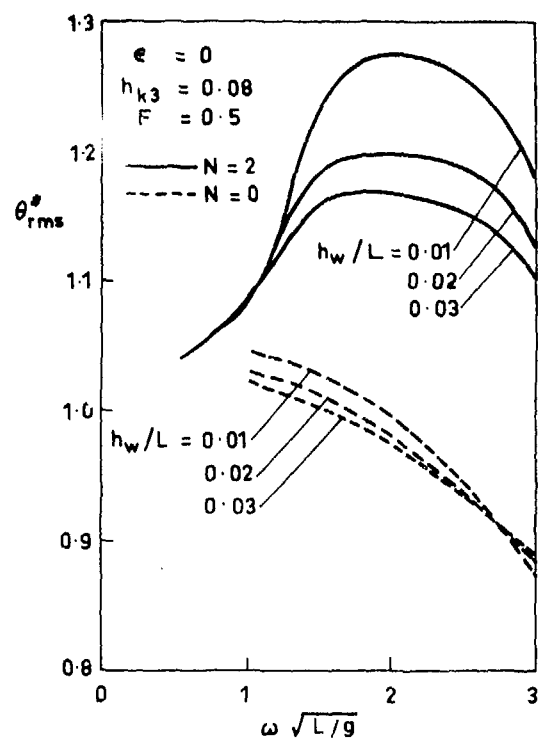


Fig. 8. Craft Response as a Function of Frequency (b) Pitch

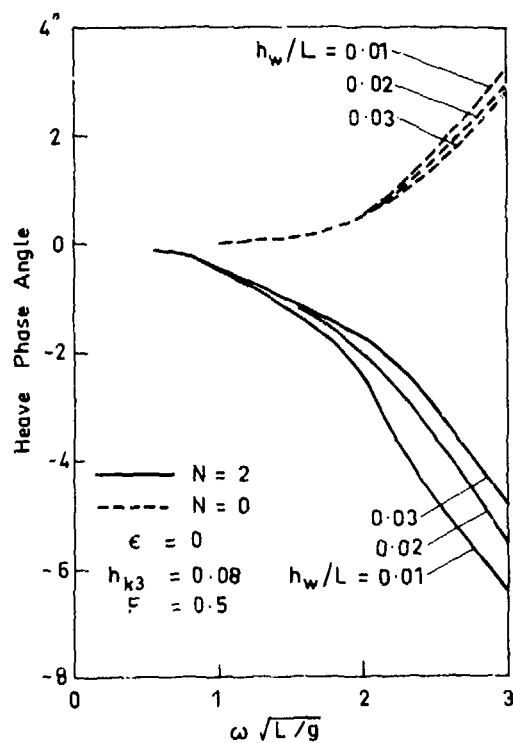


Fig. 8. Craft Response as a Function of Frequency (c) Heave Phase Angle

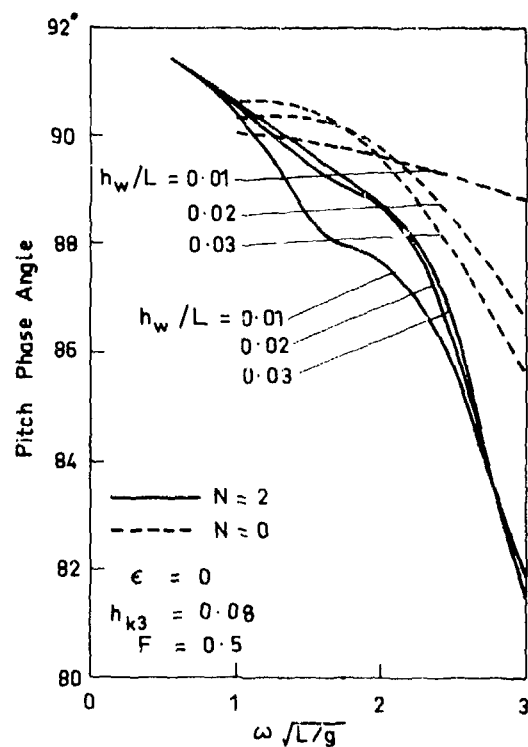


Fig. 8. Craft Response as a Function of Frequency (d) Pitch Phase Angle

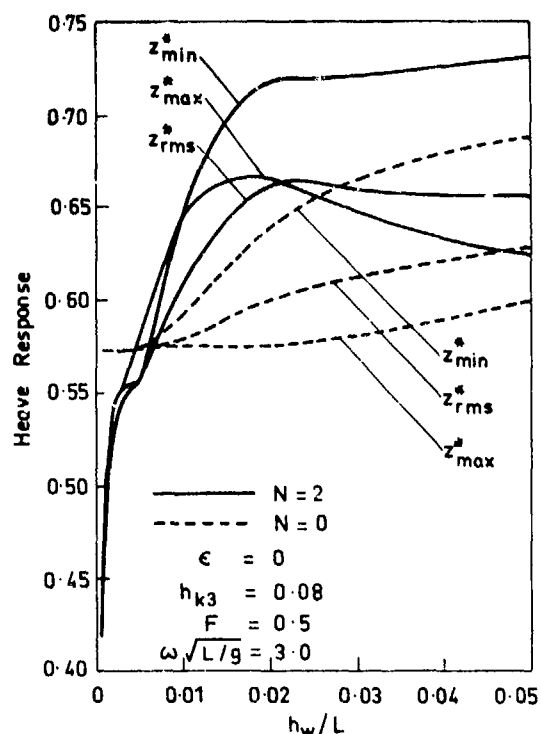


Fig. 9. Craft Response as a Function of Waveheight (a) Heave

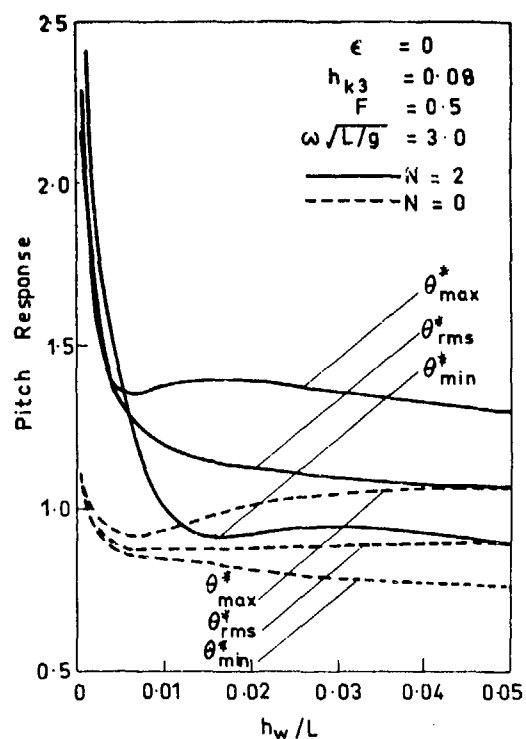


Fig. 9. Craft Response as a Function of Waveheight (b) Pitch

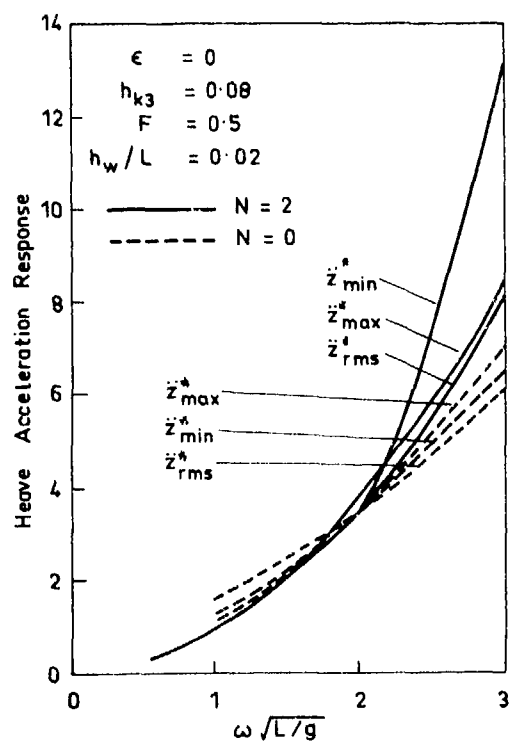


Fig. 10. Craft Acceleration as a Function of Frequency (a) Heave

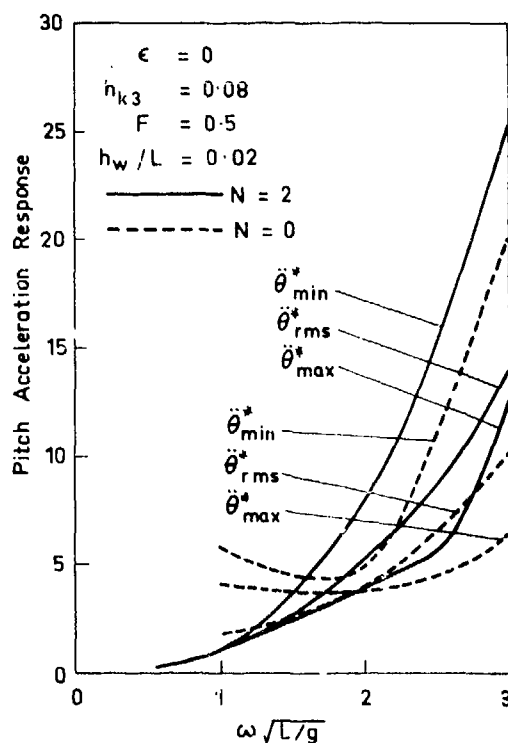


Fig. 10. Craft Acceleration as a Function of Frequency (b) Pitch

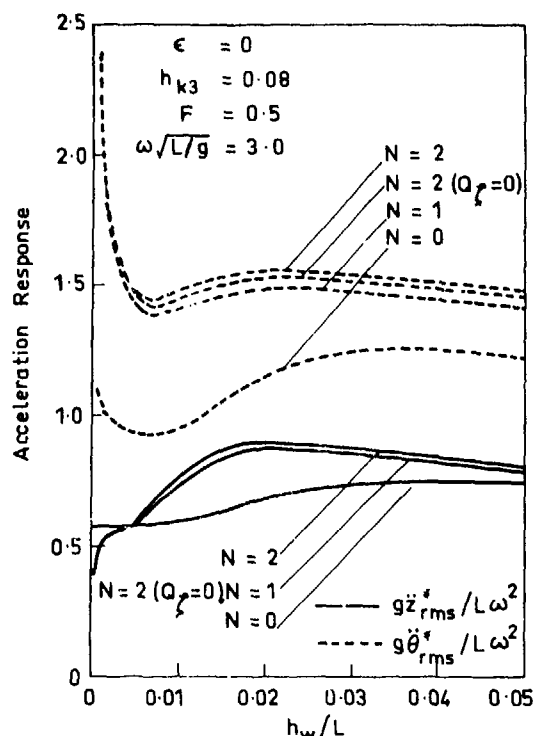


Fig. 11. Effect of the Considered Number of Harmonics in the Cushion Pressures

the harmonic content in the motion. In the vicinity of $\omega/L/g = 1$ in Fig. 10b, the hydrodynamic effect results in a substantial reduction of the pitch motion. It may be, coincidentally, that the singular effect near $\lambda_0 = 1$ is such as to oppose the aerodynamic forcing.

The acceleration response for heave and pitch again appears in Fig. 11, as a function of waveheight. Here, a comparison is made for $N = 0$ (a solid wave), $N = 1$ (just the hydrodynamic effect due to the mean pressure under the ACV), $N = 2$ (the first two terms of the Fourier series) and $N = 2$ with $Q_z = 0$ (the first two terms, but with the pumping due to the induced free surface neglected). It is evident that the greatest influence is due to the static term (the step from $N = 0$ to $N = 1$). A relatively much smaller increase in the same direction occurs if the fundamental frequency component is included (the step from $N = 1$ to $N = 2$). The pumping effect from the fundamental (the step from $N = 2$ with $Q_z = 0$ to $N = 2$) is also minor.

The second harmonics in the craft response and in the cushion pressures are plotted in Fig. 12. The relative increase when the water compliance is included is particularly large for the forward cushion (p_1) at large waveheights, but for the aft cushion (p_2) at small waveheights. While the second harmonics seem to practically disappear for small

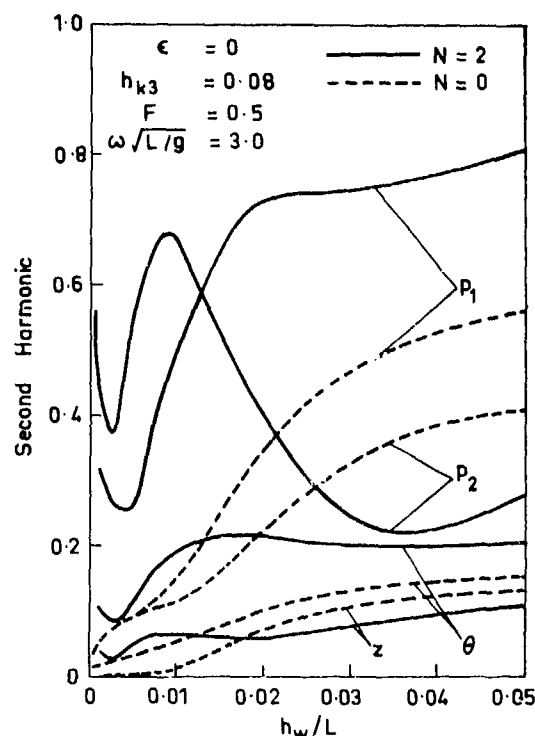


Fig. 12. Second Harmonics in the Craft Motion and Cushion Pressures

waveheights over a solid wave, the opposite is true when the water compliance is considered.

Finally, the skirt contact forces and moment are shown in Fig. 13. The forces are always greater, typically by a factor of 2, when the compliance is included. In Fig. 13a, it is seen that there is no skirt contact for $\omega/L/g < 2$ over a solid wave, but there is over water, due to the distortion of the latter. As the waveheight increases (Fig. 13b), the differences between the forces during motion over a solid wave, and over a water wave are seen to become relatively less. This is not unexpected, as the depression of the water is almost independent of waveheight (i.e. it is basically a steady effect) and becomes less important for higher waves.

LINEARIZED HEAVE THEORY

It was pointed out in the Introduction that one may not properly apply a linear theory to the motion of the ACV due to the behavior of the air flow under the stability skirt. Nevertheless, this only affects pitch stability. It is possible to appreciate some of the effect of the hydrodynamics by considering the heave motion alone (without the presence of the stability skirt). The linear theory is then, to some extent, analogous

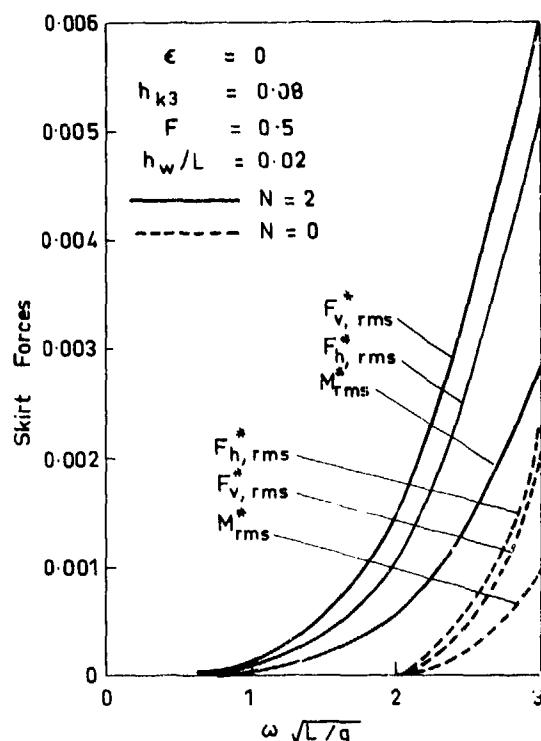


Fig. 13. Skirt Contact Forces and Moment
(a) As a Function of Frequency

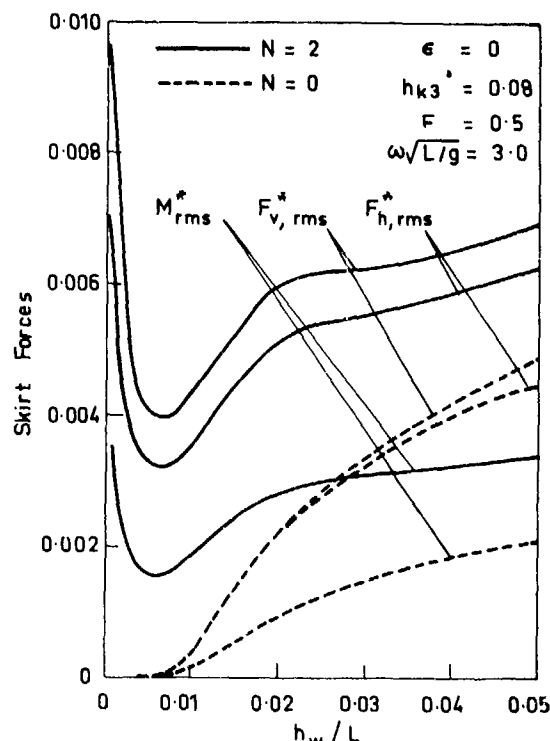


Fig. 13. Skirt Contact Forces and Moment
(b) As a Function of Waveheight

to that of Reynolds [10], except that we may only consider harmonic motion. The final result for the equation of pure heave motion is

$$\begin{aligned} & \left[1 + \left(\frac{mA_{\zeta C}}{\rho g B \ell} + e \left(\frac{m}{BLQ_e P_Q} - \frac{1}{2g} \right) \right) \omega^2 + \frac{emLV_{\zeta S} \omega^3}{\rho g B Q_e} \right] \cdot \hat{z} \cos(\omega t + \phi) + \\ & + \left[-\frac{B \ell e \omega}{Q_e} + \frac{mA_{\zeta S} \omega^2}{\rho g B \ell} - \frac{emLV_{\zeta C} \omega^3}{\rho g B Q_e} \right] \hat{z} \sin(\omega t + \phi) \\ & = \frac{[B \cos(\frac{1}{2} k_w L) + \frac{2}{k_w} \sin(\frac{1}{2} k_w L)]}{B + L} h_w \cos(\omega t) - \\ & - \frac{2e B \sin(\frac{1}{2} k_w L)}{Q_e k_w} h_w \sin(\omega t). \end{aligned} \quad (64)$$

Here e is the clearance under the skirt and p_Q is the slope of the fan curve, both evaluated at the equilibrium condition, and ℓ is the skirt perimeter. The amplitude of the heave motion is \hat{z} , and this is ahead of the encountered wave by the phase angle ϕ .

The equilibrium clearance e/L may be shown to be 0.003844 for the craft studied. From this one may evaluate the coefficients of the cosine and sine terms on the left-hand side of Eq. (64). These are:

$$\begin{aligned} & [1 + (0.00400 A_{\zeta C} - 0.002744) \omega^2 + \\ & + 0.00166 V_{\zeta S} \omega^3] \\ & \text{and} \\ & [-0.0692 \omega + 0.00400 A_{\zeta S} \omega^2 \\ & - 0.00166 V_{\zeta C} \omega^3] \end{aligned} \quad (65)$$

respectively.

The induced escape areas and volumes here pertain to the whole craft, so that

$$\begin{aligned} A_{\zeta C} &= A_{\zeta C2} + \sum_{i=1}^7 A_{\zeta Ci}, \\ A_{\zeta S} &= A_{\zeta S2} + \sum_{i=1}^7 A_{\zeta Si}, \\ V_{\zeta C} &= V_{\zeta C2} + \sum_{i=1}^3 V_{\zeta Ci} \\ \text{and } V_{\zeta S} &= V_{\zeta S2} + \sum_{i=1}^3 V_{\zeta Si}. \end{aligned} \quad (66)$$

The damping term is the second one in Eq. (65). One must extract the factor " $-\omega$ " to determine the effect on the purely aerodynamic heave damping of 0.0692 (corresponding to a damping ratio of 0.660). In the range $0 < \omega\sqrt{L/g} < 3$ (see Figs 5 to 7) both $A_{\zeta S}$ and $V_{\zeta C}$ are negative. Thus the area effect increases the damping, but the volume

effect decreases it. The magnitude of the former is larger than the second here, so that one may conclude that water compliance increases the heave damping of this ACV. At $\omega L/g = 1, 2$ and 3 the percentage increase of damping is respectively $3.8, 7.1$ and 11.7 .

The first term in Eq. (65) actually combines the added mass and spring constant effect due to the water, and could be split into these two components by studying the compliance of the air/water system at zero frequency - assuming the second component to be frequency independent. Instead, we shall just consider A_{LC} and V_{LS} , both of which are negative for the range of frequency examined - except that the former does become positive just before $\omega L/g = 3$. Eq. (65) has been nondimensionalized so that, without the water, the added mass is represented by the "0.002744" term, and the spring constant by the "1".

If one arbitrarily considered the hydrodynamics to modify only the effective mass part of the in-phase term, then this is increased by 274% at zero frequency and decreased by 44% at $\omega L/g = 3$.

CONCLUSIONS

Present Work

Comparisons between the motion of an ACV over water, and over a solid wave, show considerable differences in some instances. Particularly with regard to the pitch motion, we see that this can be increased by up to one third, for the particular craft studied, and for the range of conditions examined. It is clear that the compliance of the water should be included in calculations of this nature.

However, it is noteworthy that the major hydrodynamic effect is due simply to the steady depression of the water surface (at $\lambda_0 = 0$), resulting from the average cushion pressure. Nevertheless, it is seen that the water increases the heave damping by up to 12% in the range of frequency studied, and it considerably changes the effective mass of the ACV. Due to the high damping in the system, the virtual mass of the water is such as to increase the motion of the vehicle only slightly.

The usual singularity in ship-motion theory which occurs at $\lambda_0 = 1$ ($\omega L/g = 0.5$ for $F = 0.5$) was not detected in the numerical results, so is presumably a very localized phenomenon. One must assume that the aerodynamic connection between the water and the craft smooths the singularity.

Future Work

The present work can be logically extended in two directions. The first encompasses an increase in the range of frequencies covered by the computation. For more realistic encounter frequencies - greater than $\omega L/g = 3$ - it should be

possible to derive simplified expressions for the free-surface response, valid for large values of the parameter λ_0 . This would greatly reduce the computational effort, which is centered on this aspect - rather than on the calculation of the motion itself. However, it should be pointed out, that one would expect the greatest hydrodynamic effect to occur near $\lambda_0 = 1$. Thus, a negligible influence at the greater frequencies would not be surprising.

A second line of extension would include the effect of compressibility of air. This could be adequately represented by the polytropic ideal-gas equations. Compressibility would probably be more important at large encounter frequencies.

ACKNOWLEDGEMENTS

The writer is very grateful to the Australian Research Grants Committee which partially supported the costs of computing for this work during 1973 and 1974, under project number 71/17726.

In addition, he would like to express his appreciation to Mr J. Fein of the Naval Ship Research and Development Center, Washington, for providing data typical of ACVs.

BIBLIOGRAPHY

1. Swaan, W.A. and Wahab, R.: "The Behaviour of a Ground Effect Machine over Smooth Water and over Waves", *Hovering Craft and Hydrofoil*, 4, 8, pp 18-24 (1965)
2. Dyne, G.: "An Investigation Concerning the Motions of a Hovercraft in Regular Head Seas", *Trans. Royal Inst., Naval Architects*, 110, 4, pp 465-477, (1968)
3. Van den Brug, J.B.: "The Dynamic Stability of a Ground Effect Machine Model, Determined by Static- and Forced-Oscillation Tests", *Proc. Seventh Symposium on Naval Hydrodynamics*, Office of Naval Research, Washington, 4 pp (1968)
4. Van den Brug, J.B. and Van Starveren, P.: "An Experimental Study on the Dynamic Stability of a Ground Effect Machine Model in Heave, Pitch and Roll", *Int. Shipbuilding Progress*, 16, 181, pp 277-297 (1969)
5. Murthy, T.K.S.: "Motions of Marine Craft in a Wind Generated Seaway", *Proc. Seventh Symposium on Naval Hydrodynamics*, Office of Naval Research, Washington, 74 pp (1968)
6. Stanton-Jones, R.: "Hovercraft Skirt Development - an Engineering and Performance Review", *Trans. Royal Inst., Naval Architects*, 110, 4, pp 499-524, (1968)
7. Lin, J.D.: "Dynamic Behavior of GEMs in Motion over Waves", *J. Ship Research*, 6, 4, pp 1-10 (1963)

8. Ozawa, S.: "Spring Constants of a Peripheral-Jet Air Cushion Vehicle in Heaving Motion", *J. Japan Soc. Aeronautical and Space Sciences*, 18, 193, pp 69-73 (in Japanese) (1970)
9. Hogben, N.: "Hovering Craft over Water", National Physical Laboratory, Ship Division, Tech. Mem. 119, 78 pp + 29 figs (1966)
10. Reynolds, A.J.: "A Linear Theory for the Heaving Response of a Hovercraft Moving over Waves", *J. Mechanical Engineering Science*, 14, 2, pp 147-150 (1972)
11. Reynolds, A.J., West, R.P. and Brooks, B.E.: "Heaving and Pitching Response of a Hovercraft Moving over Regular Waves", *J. Mechanical Engineering Science*, 14, 5, pp 340-352 (1972)
12. Doctors, L.J.: "The Nonlinear Motion of an Air-Cushion Vehicle over Waves", submitted for publication in *J. Hydrodynamics*, 36 pp (1974)
13. Yamamoto, A.: "Nonlinear Heaving Motion of Plenum-Chamber-Type Air Cushion Vehicles", *J. Japan Soc. Aeronautical and Space Sciences*, 18, 193, pp 73-78 (in Japanese) (1970)
14. Leatherwood, J.D., Dixon, G.V. and Stephens, D.G.: "Heave response of a Plenum Air Cushion Including Passive and Active Control Concepts", Nat. Aeronautics and Space Administration, Tech. Note D-5202, 42 pp (1969)
15. Guienne, P.: "Air Cushion Vehicle Suspension", *Aeronautique et l'Astronautique*, 24, pp 17-28 (in French) (1970)
16. Leatherwood, J.D.: "Analog Analysis of the Heave Response and Control of a Plenum-Type Air-Cushion Vehicle", Nat. Aeronautics and Space Administration, Tech. Note D-6257, 30 pp (1971)
17. Lin, J., Ginsberg, J.H. and Ting, E.C.: "Fluid Suspension Model for Air-Cushioned Vehicles", *J. Sound and Vibration*, 25, 1, pp 83-93 (1972)
18. Bickford, L.L. and Olson, G.K.: "Dynamics of a Multiple-Skirt Air-Cushion Vehicle", *J. Aircraft*, 6, 6, pp 564-565 (1969)
19. Bickford, J.P.: "The Dependence of SES Heave Response on Model Scaling Parameters as Deduced from a Simplified Linear Approach", Davidson Lab., Stevens Inst. Technology, Tech. Mem. 157, 20 pp (1969)
20. Richardson, J.R.: "A Scaling Technique for Hovercraft Models", Nat. Physical Lab., Hovercraft Unit, Rep. 13, 12 pp (1970)
21. Trillo, R.L.: "Marine Hovercraft Technology", Leonard Hill, London, 245 + xxiii pp (1971)
22. Brard, R.: "Introduction à l'étude théorique du tangage en marche", *Bull. Assoc. Tech. Mar. Aéro.*, 47, pp 455-471, Discussion pp 472-479 (1948)
23. Brard, R.: "Vague engendrées par une source pulsatoire en mouvement horizontal rectiligne uniforme. Application au tangage en marche", *Comptes Rendus Acad. Sci.*, 226, pp 2124-2125 (1948)
24. Haskind, M.D.: "The Hydrodynamic Theory of Ship Oscillations in Waves", *Prikl. Mat. Mekh.*, 10, pp 33-66, (in Russian) (1946). Translated by Soc. Naval Architects and Marine Engineers, Tech. and Res. Bull., 1-12, pp 3-43 (1953)
25. Hanaoka, T.: "On the Velocity Potential in Michell's System and the Configuration of the Wave Ridges due to a Moving Ship", *J. Zosen Kyokai*, 93, pp 1-10 (1953)
26. Sretenskii, L.N.: "The Spatial Problem of Steady Waves of Finite Amplitude", *Vestnik Moskov. Univ.*, 9, 5, pp 3-12 (in Russian) (1954)
27. Eggers, K.: "Über das Wellenbild einer pulsierenden Störung in Translation", *Schiff und Hafen*, 9, pp 874-878 (1957)
28. Becker, E.: "Das Wellenbild einer unter der Oberfläche eines Stromes schwerer Flüssigkeit pulsierender Quelle", *Z. angew. Math. Mech.*, 38, pp 391-399 (1958)
29. Becker, E.: "Die pulsierende Quelle unter der freien Oberfläche eines Stromes endlicher Tiefe", *Ingenieur Archive*, 24, pp 69-76 (1956)
30. Wehausen, J.V. and Laitone, E.V.: "Surface Waves", *Encyclopedia of Physics*, 9, Fluid Dynamics 3, ed. by S. Flügge, Springer-Verlag, Berlin, pp 446-815 (1960)
31. Havelock, T.H.: "The Effect of Speed of Advance upon the Damping of Heave and Pitch", *Trans. Inst. Naval Architects*, 100, 2, pp 131-135 (1958)
32. Newman, J.N.: "The Damping and Wave Resistance of a Pitching and Heaving Ship", *J. Ship Research*, 3, 1, pp 1-19 (1959)
33. Kaplan, P.: "The Waves Generated by the Forward Motion of Oscillatory Pressure Distributions", *Proc. Fifth Midwestern Conf. Fluid Mech.*, Ann Arbor, Michigan, pp 316-329 (1957)
34. Wu, T. Yao-Tsu: "Water Waves Generated by the Translatory and Oscillatory Surface Disturbance", Eng. Div., Calif. Inst. Tech., Rep. 85-3, 36 pp (1957)
35. Debnath, L. and Rosenblat, S.: "The Ultimate Approach to the Steady State in the Generation of Waves on a Running Stream", *Quart. J. Mech. and Appl. Math.*, 22, Part 2, pp 221-233 (1969)
36. Ogilvie, T.F.: "Oscillating Pressure Fields on a Free Surface", Dept. of Naval Arch. and Marine Eng., Univ. of Michigan, Rep. 30, 52 pp (1969)
37. Stoker, J.J.: "Water Waves", *Pure and Applied Mathematics*, 4, ed. by R. Courant et alia, Interscience, New York, 567 + xxiv pp (1957)
38. De Prima, C.R. and Wu, T. Yao-Tsu: "On the Theory of Surface Waves in Water Generated by Moving Disturbances", Eng. Div., Calif. Inst. Tech., Rep. 21-23, 40 pp (1957)
39. Abramowitz, M. and Stegun, I.A.: *Handbook of Mathematical Functions*, Nat. Bureau of Standards, Applied Mathematics Series - 55, U.S. Govt. Printing Office, Washington, 1046 + xiv pp (1965)
40. Huang, T.T. and Wong, K.K.: "Disturbance Induced by a Pressure Distribution Moving over a Free Surface", *J. Ship Research*, 14, 3, pp 195-203 (1970)

DISCUSSION

N. KING

It has been my experience to study the papers of L. J. Doctors with interest. The interest is generated by the author's ability to investigate areas which are both difficult and relevant in ACV technology. This paper is typical of the author's work. It is well researched, it continues on where earlier investigations have stopped and, most important, it is a theoretical investigation that has strong avenues to experimental studies.

My major regrets with the author are twofold. One regret is that the paper leaves me wishing to see more results. The second regret is that the author has not found time to direct his work more towards a captured air bubble ACV, as a former mentor, Prof. T. F. Ogilvie, did. The latter regret results from the fact that my interests lay primarily in the side-walled ACV which is better known as the surface effect ship (SES).

This paper cannot be overlooked with respect to SES and I will now direct my discussion from such a viewpoint.

Since a SES has rigid sidewalls, it was comforting to see that the sides of the rectangular ACV considered in this paper did not contribute to Eq. (56) which is used in the development of skirt contact forces and moments. The author's conclusion that the major hydrodynamic effect is due simply to the steady depression of the water surface ($\lambda_0 = 0$), resulting from the average cushion pressure is encouraging when I attempt to correlate some of the results of this paper to SES data.

Experimental investigations of SES in regular waves have also shown strong nonlinear responses that are not proportional to the height of waves -- as well as strong dampening of the heave responses.

A preliminary look at SES data [data for a rectangular SES of similar B/L in the same h_w/L and frequency ranges for $F = 0.6$] has provided results comparable to results for the $N = 2$ case given in Figures 8(a) and 8(b) which give the craft's heave and pitch responses, respectively, as a function of encounter frequency. Although the majority of available SES data are at higher frequencies and for higher speeds, the trends indicated in the cited figures for $N = 2$ have tantalizing similarities to the SES data trends. I thus encourage strongly that future work be extended to higher frequencies -- a direction the author is considering.

Higher speed data are not directly applicable due to the fact that SES heave and pitch responses show a strong speed dependency as one might expect. This brings up the last point that I wish to make.

In the author's discussion of linearized heave theory, the developed Eqns. (64) and (65) relating to heave motion are highly dependent on the induced free-surface escape areas and volumes given by Eq. (66). [It is to be noted that the presented heave theory does not contain the midship transverse stability skirt, a craft component not applicable to SES.] The heave damping is shown to be quite sensitive to the values of the escape areas and volumes given in the frequency range studied for a $F = 0.5$.

It is my experience that the induced free-surface elevations for ACV and SES traveling over calm water, regardless of an imposed sinusoidal wave, are highly speed dependent. The cushion pressure region alone will change the escaped area and volume values as a function of craft speed. In addition, the induced free-surface elevation is such that the magnitude of the skirt contact forces will be a function of speed.

Thus, it is suggested that the author in future work consider craft speeds associated with the highest two wave-making drag hump speeds and post-hump speeds. The wave-making drag hump speeds at approximately $F = 0.35$ and $F = 0.65$ for $B/L = 0.5$ are where one might expect the most pronounced free-surface distortions and therefore where one may expect the greatest fluctuations of escape areas and volumes as well as the largest amount of skirt contact with the free-surface. The post drag hump speeds of say $F = 1.0$ or greater are suggested since such speeds are included in the optimum operational speed area of ACV's.

I wish to commend the author again on this excellent paper. More investigations such as contained in this paper are needed in advancing ACV technology.

ALLEN MAGNUSON

To this discussor's knowledge this is the first time the linear hydrodynamic boundary value problem (the moving oscillatory pressure patch) has been solved in conjunction with the nonlinear craft dynamics, and for which corresponding numerical results have been obtained for the motions of a typical ACV design. The author is to be congratulated on presenting a valuable contribution to a very complex and difficult problem.

The author's analysis is similar in many respects to a linearized heave analysis developed by the discussor. A condensed treatment of this analysis and a discussion of the results will be given. A comparison of the two analyses and appropriate comments reflecting the discussor's opinions may be appropriate:

1. The general nature of the interaction of the free surface disturbance and the craft/cushion dynamics is

essentially the same. That is, the craft dynamics is affected by the increment in cushion volume and leakage area resulting from the free surface depression, which is in turn caused by the unsteady component of the pressure. The details of computing the effects of the interaction differ. Doctors applies a frequency domain approach that is a logical extension of his earlier work on the accelerating pressure patch. The discussor's approach is based on a time-domain interpretation of linear systems theory (Equations 6 and 7 below), which reduces the problem to the evaluation of a kernel function associated with a generalization of the classical Cauchy-Poisson problem. The discussor is presently developing a solution to the hydrodynamic problem along these lines. In the absence of a direct solution, the kernel function was estimated using plausible physical arguments. The results agree with Doctors at least to the extent that the hydrodynamic interaction was found to be an important first order effect.

2. The discussor has relied (to date) on a linearized analysis because of the obvious ease in computation. In addition, model data and the recently-obtained trial data on the 50 ton ACV imply that the heave and pitch behavior of the craft in the frequency domain is similar to the simple damped oscillator. In this respect the linearized frequency-domain heave equations are similar in form (Doctors' Equation 64 and the discussor's Equation 8 given below). Both analyses exhibit the frequency dependence of the dissipative and the reactive (added-mass) components of the response. At any rate, the issue of the importance of the nonlinearities on the response can only be satisfactorily resolved by carefully designed and executed model-scale experiments in the towing tank.

ANALYSIS OF HEAVE DYNAMICS

This simplified analysis treats the problem of an air cushion supported vehicle running with a constant speed and heading in a seaway. The cushion pressure force is assumed to dominate the heave dynamics, so forces produced by the skirt and/or seal system and sidewalls are neglected.

One may separate the dynamic variables into a constant component or mean value and a time dependent or fluctuating component; e.g., for the cushion pressure we write

$$p_c(t) = p_{c0} + \Delta p(t). \quad (1)$$

The heave motion is governed by the usual force equation and two equations describing the air cushion dynamics: the adiabatic gas law and the continuity or flow equation. These three equations may be written as follows:

$$m\ddot{z} = -A_c \Delta p(t) \quad (2)$$

$$p_c/p_A = (\rho_c/\rho_A)^{1.4} \quad (3)$$

and

$$\dot{m}_c = \rho_A (Q_{IN} - Q_{OUT}), \quad (4)$$

where z , A_c , p_A , ρ , m_c , Q are the heave displacement, cushion area, absolute atmospheric pressure, air density, cushion air mass and volume flow rate, respectively. The inlet flow rate Q_{IN} is related to the differential cushion pressure through the lift fan characteristic curve, and the leakage Q_{OUT} is governed by the orifice flow relation. Both of these relations are highly nonlinear, as the gas law.

We linearize these equations so that insight may be obtained by use of frequency domain techniques. The linearization is performed by separating each variable into a mean and a perturbation component, as was done in Equation (1) for the cushion pressure. The linearization results in a set of two coupled linear differential equations, one for the heave equation and another governing the air mass flow. The differential equations are supplemented by a linearized pressure relation obtained by expanding Equation (3). The linearized equations contain terms involving the perturbations in cushion volume (ΔV) and leakage area (ΔA_L) may be set to zero on the assumption that the flexible skirt follows the water surface perfectly for frequencies of practical interest. The volume perturbation (ΔV) can be separated into three components: one due to the heave motion, one due to the undeformed wave profile encountered by the craft and a term describing the interaction of the craft with the water surface. One may write

$$\Delta V(t) = -A_c z + \Delta V_w + \Delta V_{FS}. \quad (5)$$

The wave term ΔV_w may be computed in regular waves as a function of wavelength λ for a given geometry. The interaction term ΔV_{FS} may be related to the cushion pressure fluctuation Δp_c .

Linear systems theory tells us that one may express the output or response of a system as a convolution integral containing a kernel function and the input or stimulus. In this case the response is the volume change and the input is the pressure fluctuation, so we may write

$$\Delta V_{FS}(t) = \int_{-\infty}^{\infty} K_V(\tau) \Delta p_c(t - \tau) d\tau, \quad (6)$$

where

$$K_V(\tau) = 0 \text{ for } \tau < 0.$$

Equation (6) states that the response is computed by integrating the weighted past history of the pressure. The kernel function is casual, or zero for negative values of the argument to ensure that the response does not anticipate the stimulus. If the pressure is impulsive, one sees from the sifting property of the Dirac delta function that the kernel function represents the volume change due to

an impulsive pressure, or

$$\Delta V_{FS}(t) = K_V(t) \quad (7)$$

for

$$\Delta p(t) = \delta(t)$$

One may separate the free surface disturbance into two components: the steady-state wave pattern associated with the wavemaking drag and the time dependent diffracted wave pattern created by the cushion pressure fluctuations. For small disturbances the two components will be independent of each other; i.e., if each wave pattern is considered to have an infinitesimal amplitude the linearized potential fluid theory can be used to analyze each component separately. From Equation (7) one sees that the kernel function $K_V(t)$ may be obtained by computing the volume change due to an impulsive pressure. This means that we do not have to concern ourselves with the steady Froude number dependent wave patterns: all one has to do is compute the interaction volume change from Equation (6). This, in turn, reduces to finding an expression for the kernel $K_V(\tau)$ appearing in the convolution integral. Since the kernel function is associated with an impulsive surface pressure disturbance, the problem is essentially a generalization of the Cauchy-Poisson problem⁽¹⁾. This surface disturbance or radiated wave pattern may be calculated most conveniently in a fixed reference frame due to the impulsive time dependence of the surface pressure. That is, the wave pattern will be the same regardless of whether the vessel creating the impulsive pressure is moving or not. The craft translates relative to the fixed point where the impulse was applied. This translation must be taken into account when the volume change for the moving craft is computed by integrating the water surface depression over the cushion area.

The evaluation of the kernel function by analytical means requires, then, a near field solution of a generalized Cauchy-Poisson radiation problem whereby an impulsive pressure is applied over a finite area having the same shape as the cushion platform. One sees from Equation (6) that the solution to the motions (diffraction) problem is obtained by superposition of solutions to the radiation problem.

To obtain a frequency domain solution we restrict ourselves to regular sinusoidal waves and a specific heading. In the linearized equations we replace time differentiation by an $i\omega$, where ω is the encounter frequency. The convolution integral (6) becomes a multiplication in the frequency domain. One may solve directly for the heave motion by elimination of the other two dynamic variables; the fluctuations in air cushion mass and pressure. The resulting heave dynamics equation may be written in the following form:

$$[\omega_n^2(\omega) - \omega^2 + i\omega 2\zeta(\omega)\omega_n(\omega)]z(\omega) =$$

$$\omega_n^2(\omega)f_1(\lambda)\eta_w(\lambda,\omega), \quad (8)$$

where ω_n and ζ are the frequency dependent natural frequency and damping, respectively. The wave height is η_w and the $f_1(\lambda)$ factor is a normalized function of wavelength that describes the cushion volume pumping due to the undeformed wave train. The right hand side represents the heave force excitation. Equation (8) has the form of a second order damped oscillator, except for the frequency dependence of the natural frequency and damping. The frequency dependence arises from the free surface interaction through $K_V(\omega)$, the Fourier transform of the kernel function.

COMPARISON WITH FULL SCALE DATA

Heave response amplitude operators (RAOs) for a 50 ton hovercraft were computed from the linearized analysis (Equation 8) using published engineering data. Experimental RAOs obtained from full scale seakeeping trials described elsewhere⁽²⁾ were available for the same craft. Since the boundary value problem has not been solved it was necessary to estimate the kernel function associated with the water surface interaction. The kernel function was assumed to have the form of an exponential decay. The speed dependence was taken into account by estimating the extent to which the craft translates relative to the free surface depression. The resulting kernel function may be written in the frequency domain as a simple time lag:

$$K_V(\omega) = \frac{\tau_e}{1 + i\omega\tau_e} \quad (9)$$

The effective time constant (τ_e) takes into account the relaxation time of the free surface (τ) and the speed dependence. This is the simplest non-trivial qualitative representation of the effect of the pressure on the free surface, and requires the specification of only one time constant.

The results are shown in the three figures. The first figure is a linear plot of heave RAO as a function to encounter frequency in head seas. Predicted RAO are shown for two time constants. One sees that correlation with trial data is good at high frequencies for the 110 second time constant. The low frequency correlation is better for the 70 second time constant. The calculated heave RAO with the free surface interaction suppressed ($\Delta V_{FS} = 0$) is shown in the second figure. The correspondence is not particularly good in either frequency range. The third figure shows the RAO plotted against a log-log scale with and without the water surface interaction. The $\tau = 70$ second curve exhibits the resonant behavior at the low frequencies seen in the trial data as well as the straight line dropoff at high frequencies. The "no interaction" curve does not exhibit low frequency resonance and the high frequency behavior is characterized by null points at wavelengths where the volume pumping is zero, i.e., at $\lambda/L = 1, 1/2, 1/3$, etc. The high frequency behavior appears to be particularly unrealistic, as one would not expect significant response in this frequency range.

These results show that the inclusion of pressure-free surface interaction improves correlation with experimental

data. The overall behavior is similar to the simple underdamped oscillator whereby the existence of a natural frequency is indicated by the resonant behavior of the heave RAO. The linearized frequency response function in heave (Equation 8) takes the form of an oscillator with frequency dependent damping and reactive components. By contrast, the response with interaction suppressed appears to be dominated by geometrical effects (the volume pumping). The generally applied assumption that dynamic free surface interaction effects are unimportant appears to be erroneous. One must include this effect to obtain even qualitative agreement with reality.

These results are intended to illustrate in a qualitative way the nature of the dynamic interaction of the craft with the water surface. One sees that the free surface affects the heave dynamics through the perturbation in volume of the air cushion (Equation 5). The volume interaction is characterized by a convolution integral (Equation 6) involving the past history of the pressure. The problem

then reduces to solving a generalized Cauchy-Poisson radiation problem in order to find the kernel function in the convolution integral. The boundary value problem has not been solved to date, so the kernel function was estimated using simple physical arguments. Good qualitative agreement with trial data has been obtained with the estimated kernel functions.

REFERENCE

1. Lamb, H. "On Deep-Water Waves," Proceedings of the London Mathematical Society, Second Series, Vol. 2, 1905.
2. Fein, J.A., Magnuson, A.H. and Moran, D.D., "Dynamic Performance of an Air Cushion Vehicle in a Marine Environment," AIAA Paper No. 74-323, Presented at AIAA/SNAME Advanced Marine Vehicles Conference, San Diego, California, February 1974.

HEAVE R.A.O. FOR 50 TON A.C.V.

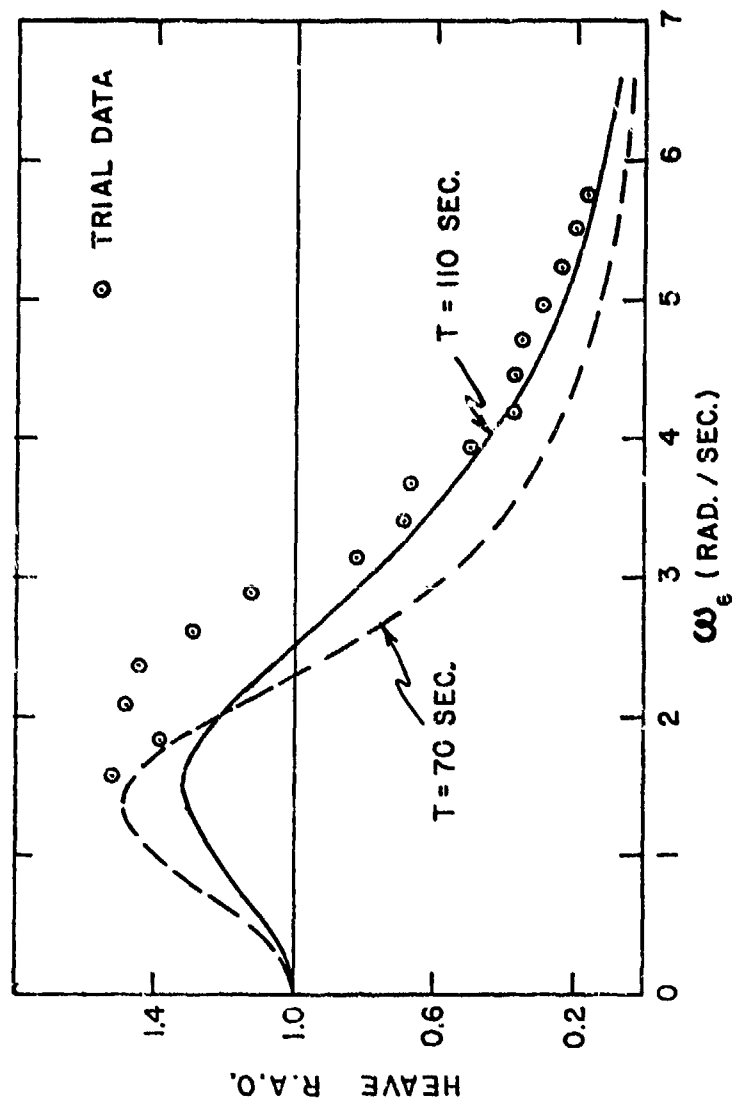


Figure 1 - Heave RAO for 50 Ton ACV Including Estimated Effect of Water Surface Interaction

HEAVE R.A.O FOR 50 TON A.C.V.

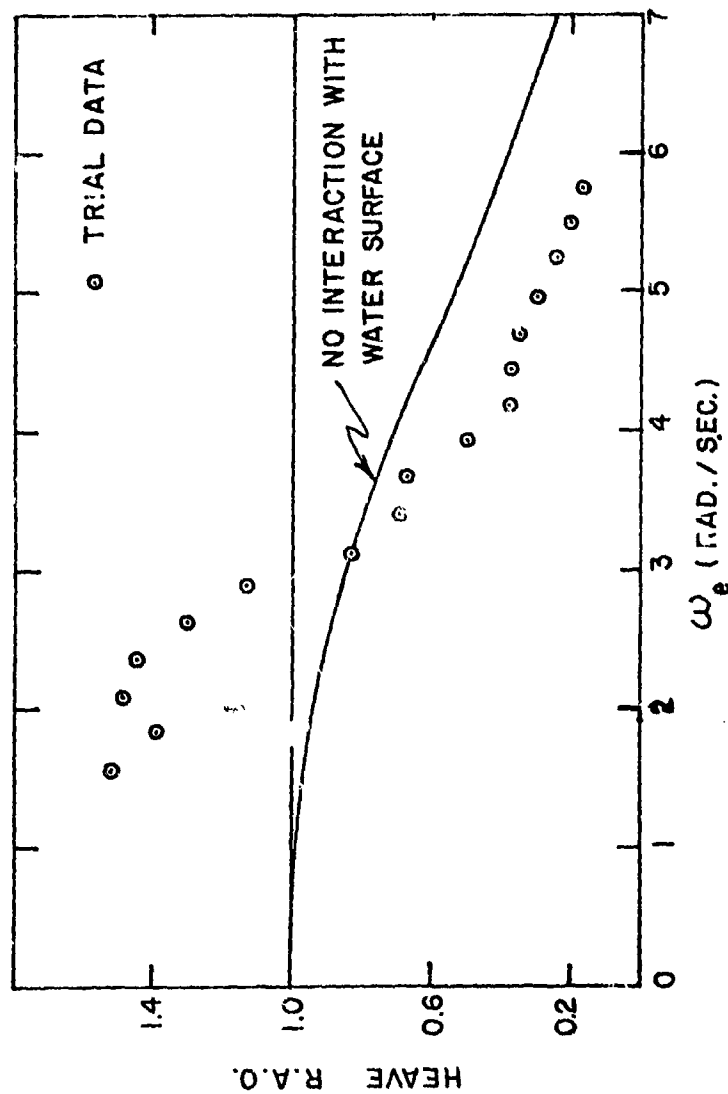


Figure 2 - Heave RAO for 50 Ton ACV, No Pressure - Water Surface Interaction

HEAVE R.A.O.
FOR
50 TON A.C.V.

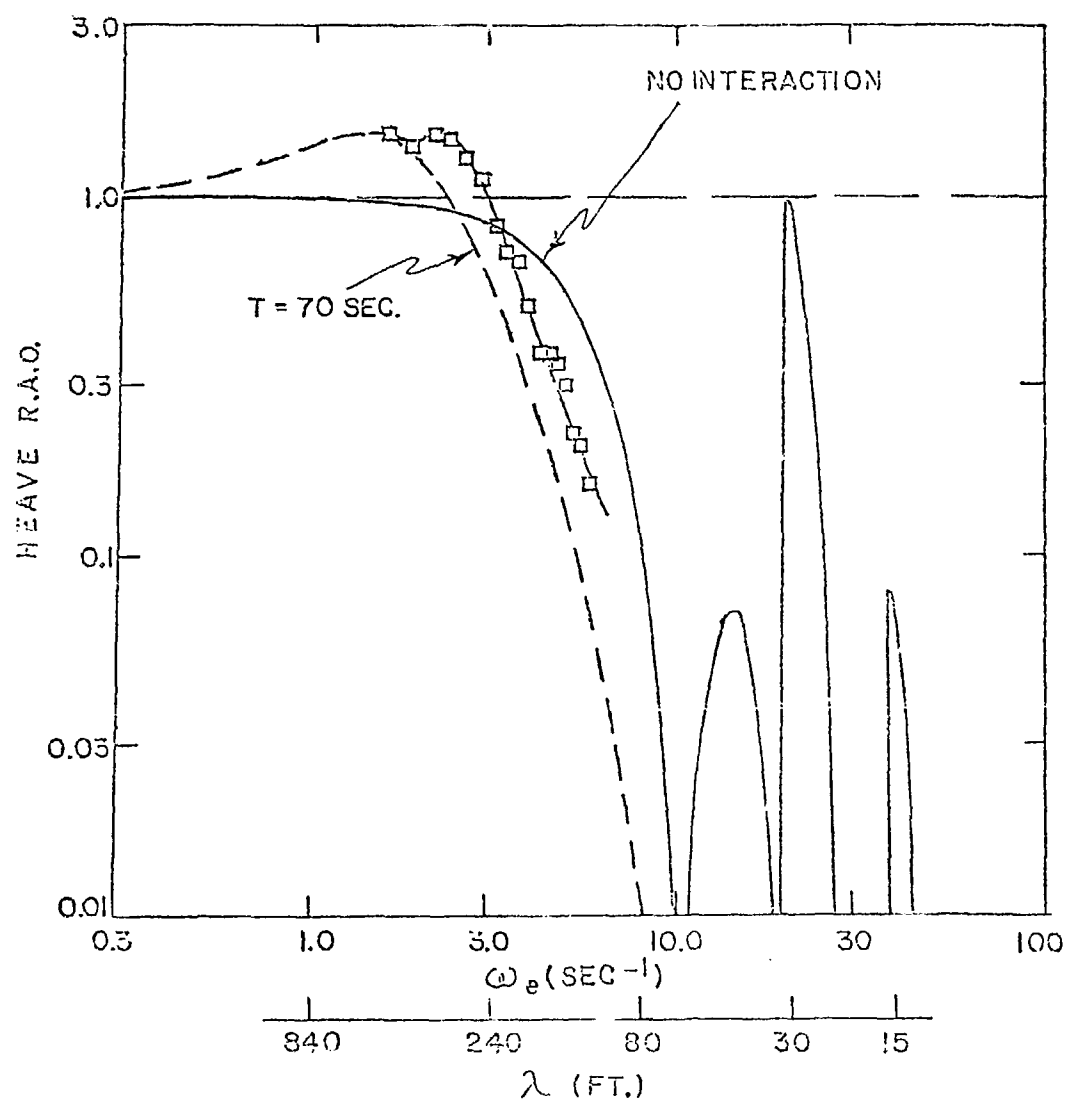


Figure 3 - Logarithmic Representation of Heave RAOs for 50 ton ACV

T. T. HUANG

The author is to be congratulated for his fine work. It would be very interesting to consider a practical case while Equation (41) is approximated by

$$Q_{e1} = \frac{\text{Sgn} \left(P_1 - \frac{1}{2} \rho_a c^2 \alpha(y) \right) A_{e1} C_{de1}}{\sqrt{2 |P_1 - \frac{1}{2} \rho_a c^2 \alpha(y)| / \rho_a}}$$

$$Q_{e2} = \frac{\text{Sgn} (P_2 - P_w(y)) A_{e2} C_{de2}}{\sqrt{2 |P_2 - P_w(y)| / \rho_a}}$$

where $\alpha(y)$ depends upon geometry of the vehicle and wake pressure $P_w(y)$ may be slightly negative.

DR. DAVID D. MORAN

The author has obviously succeeded in the difficult task of constructing a solution to the ACV dynamics problem from sources of varying degrees of non-linearity. The linear free surface boundary-value problem has been handled well, following the classical technique employing an artificial (Rayleigh) viscosity. The resultant free surface perturbation solution has been incorporated into a nonlinear model for the cushion flow dynamics in a way which prompts only minor comments from this discussor.

The discharge functions presented beginning with equation 39 reveal a good insight by the author on the nonlinear behavior of the air flow in the cushion. It is especially encouraging to see that the stability cross flow Q_{e3} and the forward discharge Q_{e1} are allowed the freedom of changing sign.

The author may find the fan-duct characteristic equation 38 presented, presumably as an example, in this study limiting in future work. Although this steady flow equation is presented in nonlinear form, its applicability in a dynamic context may be questioned. Depending upon fan characteristics, scale, and cushion ducting the fan-duct characteristic equation may show increased deviation from the steady flow form given by equation 38 as the frequency of excitation is increased. This point is discussed further in a subsequent paragraph.

The development of a model for skirt-contact forces and moments may also need elaboration by the author in his continued research. The skirt support or

cushion seal system on an air-cushion-supported vehicle is a dynamic system with responses coupled to the craft motions, surface conditions, and cushion characteristics. The dynamic behavior of the support system has been neglected in this analysis (see equation 49). This is comparable to assuming an instantaneous skirt or seal response to external excitation. This assumption can be valid only for heavily loaded light cushion seals.

The nonlinear (discontinuous) behaviour of the leakage properties of skirts included in this analysis again shows excellent insight by the author. It would be of interest to pursue the benefits or limitations of matching the linear wave-perturbation profiles to the nonlinear geometric functions for exit area.

The section of the paper concerned with skirt-contact forces may require refinement. First, it would appear that the vertical force on the craft due to skirt deflection is more properly a function of skirt bag or seal pressure than cushion pressure. The value of vertical force computed by equation 53 will probably be negligible unless the skirt is inclined at a rather large angle. Under normal conditions for realistic ACV designs, the angle \tan^{-1} (angle between the skirt element and the vertical) will approach zero. Perhaps a clarification of the geometrical conditions assumed in the author's analysis would suffice to answer this point.

The horizontal skirt drag given by equation 54 should include viscous and wave making contributions as well as the induced drag included in the author's formulation. If this is done properly, the the sides of the ACV support system will also contribute to the longitudinal horizontal skirt forces on the ACV, perhaps with magnitude comparable to the transverse sections.

The author is also to be congratulated for the summary of previous efforts in this area of research. It is most encouraging to see a complete summary of the significant efforts of previous researchers. The references to studies on compressibility and scaling were of special interest to this discussor. It is unfortunate that the magnitude of the effects of scale on the vertical plane dynamics of air-cushion-supported vehicles is still unresolved. There have been published indications of scaling effects of both major and minor proportion but to this discussor's knowledge a formal comparison of the dynamic behavior of well-scaled, air-cushion-supported vehicles is still lacking. Although

scale effects may be identified analytically for several portions of the air-cushion-support system these effects have not received a thorough experimental verification. There is a definite need to establish the full scale craft dynamics predictions based upon model scale sea-keeping studies. This verification is vital for the determination of the sea-keeping characteristics of the proposed 2000-ton, surface effect ships currently in design for the U.S. Navy.

The identifiable problems associated with the dynamic scaling of ACVs are first that the RMS values of vertical accelerations appear to be under predicted by model tests. This is in contradiction to the intuitive hypothesis that the stiffer cushion (aerodynamically) of the model should yield conservative estimates of craft accelerations. The second visible problem in a macroscopic sense is that the natural frequency of the craft in heave is over predicted through model tests. These two characteristics both results from the basic problem that the total craft-dynamics response as characterized by the systems response amplitude operators for various modes of motion is not directly Froude scaled.

The three mechanisms contributing to the difficulty in scaling the heave and pitch dynamics of air-cushion-supported vehicles may be identified as follows. First, the stiffness of the cushion volume (often called aerodynamic or sometimes thermodynamic stiffness) of the craft is not modeled correctly on the model scale. The cushion pressure-heave gradient $\partial p / \partial z$ which should be the same for both ∂z model and prototype is given for a perturbed static model as

$$\left(\frac{\partial p}{\partial z}\right)_r = \frac{\gamma_r p_r}{\lambda_r} \left(\frac{\gamma_r p_r}{\lambda_r} \frac{P+1}{P+1} \right) \quad (1)$$

where the subscript r denotes a prototype-to-model ratio of the property, p is the absolute cushion pressure which is the sum of the atmospheric and cushion gauge pressures, λ is a characteristic length scale, and γ is the ratio of thermodynamic specific heats at constant pressure and volume, respectively, for the cushion medium. The static deflection of the free surface is incorporated in the variable P in the form.

$$P = \left(\frac{\gamma_p}{\rho g (h + \delta)} \right) \text{Full-Scale Conditions} \quad (2)$$

where the water density ρ , mean cushion depth h, and static water deflection δ are included in the denominator. Neglecting all hydrodynamic effects and assuming a rigid free surface corresponds to setting $P = 0$ in equation 1. It is obvious from the first equation that parity in cushion stiffness can be maintained only if the product of the thermodynamic constant and absolute cushion pressure are scaled by the model scale ratio. This can be done by performing model dynamics studies in a variable pressure towing tank as noted by the author in his reference to previous work. A more novel technique which may possibly be employed is to substitute cushion media during a seakeeping test, eg., γ (Argon, Helium) ≈ 1.66 , γ (Air) ≈ 1.40 , γ (Carbon Dioxide) ≈ 1.28 . Although the resultant scale ratios are small, changes in the cushion medium may prove useful in some experimental studies.

The second mechanism associated with scaling errors involves the fan dynamic response to transient loadings. It is not sufficient to model the lift-fan character in terms of steady load pressure-discharge function. The unsteady loading on a lift-fan system, produced by the craft motions as it responds to sea excitation results in a frequency dependent stage-discharge hysteresis function which may differ dramatically between full scale and model. An ideal experimental solution would be to model the prototype lift-fan response exactly through an electro-mechanical feedback system.

The third obvious source of scaling errors is associated with the mechanical properties and material dynamics of the skirt or seal system of an air-cushion-supported vehicle. The difficulty in scaling a model according to both inertial and elastic criteria often results in either a distortion in skirt material thickness or modulus of elasticity. The dynamic response of this structural system can under certain conditions characteristically, affect the overall craft seakeeping response.

The overall approach to the study of dynamic scaling in air-cushion-supported vehicles underway by several investigators (without specific citations) includes on the theoretical level three different approaches and on the experimental level two approaches. These include:

1. Solution of the hydrodynamic-aerodynamic, free-surface interaction problem in closed form. This analysis when complete will constitute a total solution to the dynamic behavior of air-cushion-supported vehicles in both the vertical and horizontal planes. The author of the paper under discussion has made a significant contribution to the ultimate complete solution as was previously noted.

2. Numerical solutions of motion equations for simulation. This effort is proceeding on various levels of sophistication by several investigations.

3. Stochastic behavior of craft in waves. The dynamic behavior of an air-cushion-supported vehicle in waves may be examined statistically, independently from other analytic considerations. The craft response may thereby be characterized without a knowledge of the detailed nature of wave-excited motion mechanisms.

---and on the experimental level:

4. Full-scale to model correlation. The dynamic characteristics of two geometrically similar ships of different scale can be compared directly to illustrate total system scaling difficulties. The dynamic characteristics under consideration must include response amplitude operators for motion freedom, e.g., heave, pitch, and roll and similar operators for craft dynamic characteristics such as pressure. The craft in question are ideally a full-scale vessel and its model; however, any two geometrically similar models with a sufficient difference in scale could serve this purpose.

Full-scale to model correlation results in an evaluation of total system response, including cushion stiffness, fan dynamic characteristics and the effect of the skirt on seal structural response on the dynamic behavior of the craft. Experience with full-scale model correlation may result in techniques for tuning model characteristics so that the model and full-scale responses match. Ideally this approach should result in matching techniques applicable to all craft design-model experiments.

5. Since the stiffness of the cushion medium is the most significant identifiable nonscalable item necessary to characterize the dynamics of an ACV, most experimental work has centered

around the various methods for modifying cushion stiffness. Besides those methods already listed, we should include changes in stiffness through modifications of the mechanical system, such as adding a spring-mass-damping system in series with the cushion system.

RODERICK A. BARR

I would like to comment on the author's treatment of the fans. He has used a purely static representation of the fan (equation (38)). It seems probable, however, that fan dynamics or the dynamics of the fan-intermediate chamber cannot be neglected.

I would also be interested in knowing the basis for the fan characteristic coefficients, Cf_1 , Cf_2 and Cf_3 given in Table 1, and knowing whether these are representative values or values appropriate to a particular design.

More rigorous analysis of ACV and SES dynamics are needed and the author's contribution is thus all the more valuable.

DR. PAUL KAPLAN

This paper by Doctors is a very fine job, treating a complicated problem with the aid of a number of simplifications. However there are some points that have been neglected and also certain effects that may have been over-emphasized in regard to their extent of applicability. The major problem in ACV motions over waves is due to heave accelerations, which affect habitability. Since the largest accelerations occur at high speeds, which is the intended regime of operation of ACV craft, emphasis should be put on that area.

In that case compressibility will definitely be important, and the pressures must be found using differential equation relations rather than algebraic solutions as used here. That increases the computational complexity of the system, demands smaller time steps in digital integration with attendant increase in computer time, etc. Also, in work which we have carried out at Oceanics and presented only recently this year, we have ignored the effect of unsteady wave formation. This is based upon our emphasis on the high speed case for ACV craft, which reduces the free surface to a constant pressure surface limit condition of the potential function, i.e. $\phi = 0$. It would certainly have been more elucidating to have seen the results of computations of the influence of the surface compliance of the water at Froude numbers in the range of 1.0-2.0 in order to determine the significance of the water surface in this more practical speed regime. I hope that the author can provide such computations in the future, or at least comment on his expectations for these conditions.

Another point, perhaps of smaller significance, concerns the effect of skirt forces. The simplified representations given in the paper do not account for effects that are known to be significant for different types of craft that employ different types of skirt systems. Whenever a bag

on a skirt makes contact with the water, as well as develops frictional forces during lateral (or longitudinal) displacement, the bag shape deforms and hence the bag pressure changes. This effect interacts with the cushion pressure (dependent of course on the details of the configuration) and causes changes in the vertical force as well as the pitch mo-

ment due to a shift of the craft center of pressure. While such effects are certainly configuration-dependent, their influence should still be considered as one proceeds with more detailed consideration of the many features that affect ACV motions in waves.

AUTHOR'S REPLY

I would firstly like to thank those who discussed my paper for their very kind comments. Most of the contributors suggested refinements of the physical model used to represent the ACV. These ideas are most welcome as they will assist in the development of this work. The theoretical model employed in the present calculations was deliberately kept simple, so that the effect of compliance of the free surface could be more easily studied.

Referring firstly to Mr. King's remarks, the author agrees that the work should be extended to cover the case of the SES. This would involve an additional study - that of the interactions between the sidewalls, water and the cushion.

Furthermore, most of the pitch stability of an SES is derived from water contact with the planing fore and aft seals which are themselves complicated mechanisms. On the other hand, the ACV studied here achieves stability by use of the athwarships skirt. Thus there are inherent differences between these two craft.

It is pleasing to learn that a preliminary comparison of the theoretical results with practical data reveals some similarities. Much more correlation is required to advance the computation of ACV motions.

It would be worthwhile to study the theoretical response at both higher speeds and frequencies. These were deliberately kept low in the present study in order to examine the expected singularity in the craft motion when the speed-frequency parameter passes through unity. As noted, this did not occur. The next stage is to compute cases corresponding to the usual (much higher) values of this parameter.

The author read Dr. Magnuson's analysis with great interest, and agrees with the general approach he followed within the limitations of the linearised heave theory used. However, it is suspected that linearised theory for the cushion aerodynamics, etc. is a poor substitute for the actual phenomena. That is, the brute-force technique of solving the craft motion by an initial-value representation must be employed. This is particularly so when pitch motion is included.

The idea of representing the hydrodynamic effect by using a kernel function with a timewise exponential decay has no precise basis, of course. On the other hand, it does introduce the compliance of the water into the equations of the motion in a realistic manner, and appears to improve the fit with experimental data provided by Dr. Magnuson in his discussion. One wonders if this concept could be expanded in order to eliminate the large amount of computing effort required to evaluate the free-surface response.

Dr. Huang suggested a modification to the equations for the discharge of the cushion air to the surrounding air - on the basis that this air is not at static atmospheric pressure. The idea includes a ram effect due to the velocity head of the airthrough which the craft moves (at the bow) and a wake effect (in the stern region). This suggestion is most welcome, as it is certain to improve the physical modelling of the craft.

The author had originally thought the inertia of the fan and engine/gear-box system to be so high that one could assume it ran at a constant speed. However, he is now inclined to agree with Dr. Moran that the unsteady effects of variable fan speed should be included. This could possibly be done by assuming the fan performance curves are still valid - but in a quasi-steady manner.

There are many ways in which the modelling of the skirt behavior could be improved. The only limitation here is computer time. The skirt on the ACV under study was assumed to consist of separate segments independently suspended (like a "finger" skirt). Such skirts typically have an inclination of 45° to the vertical, and this value was used. No deflection of the upper portion of the skirt system, known as the bag on some designs, was considered.

The skirt along the sides of the craft do contribute to the total drag on the craft, as given by Eq. (54). The sides just don't contribute to one aspect of this force, in Eq. (56).

In practice the skirt/water interaction gives rise to viscous forces and wavemaking, as indicated by Dr. Moran. However, the author sees no way of including these realistically in a computer model at present. Empirical techniques would be necessary, instead.

The contribution of Dr. Moran about SES model scaling is appreciated by the author.

Dr. Barr commented on the treatment of the fans. As noted before, this aspect of the total system should be considered dynamic, so that the fan speed would vary in time. The three coefficients of the fan characteristics, used in Eq. (38) and referred to in Table 1, were obtained by fitting to the actual characteristics of the fans of a 150-ton AALC under study by the U.S. Navy. These coefficients may therefore be considered to be representative.

The author agrees with Dr. Kaplan with regard to compressibility of the air within the craft. This is certainly an important factor at higher frequencies. In this case, every feature of the aerodynamic system of the craft will have to be considered to be unsteady and compressible. Incidentally, within the range of frequencies studied, the author found that fewer time steps were required per cycle as the frequency increased. (This is because the actual

maximum time step, for stable computation, was sensibly independent of frequency.)

It is not entirely clear whether the compliance of the water surface is less important at higher speeds and frequencies, or not. It is known that the surface response per unit of pressure will be reduced. On the other hand, the magnitude of the unsteady pressure fluctuations under the cushion also greatly increase as shown in previous work [12]. Thus the product of these two factors is the important thing.

Dr. Kaplan's comments about skirts are, of course, accepted. Such refinements can be included at the expense of computer time.

SEMI-SUBMERGED AIR CUSHION VEHICLE (SSACV)

T. K. S. Murthy
Portsmouth Polytechnic
Portsmouth, U. K.

ABSTRACT

A new concept of the air cushion vehicle is presented which shows some promise in fulfilling the requirements for a high performance vehicle with a degree of operational flexibility in open water not possessed by conventional types of ACVs or displacement vessels. The proposed concept comprises the use of a composite type of vehicle which will take advantage of the high speed capability of an ACV and combine with this the inherent stability and course keeping ability of a pair of submerged hulls.

Some tentative calculations have shown that the total power requirements of the SSACV are likely to be less than those of ACVs or semi-submerged ships of comparable size up to a speed of 60 or 65 knots. Above this speed the drag of the submerged hulls increases excessively and the economic advantages of the SSACV are not present unless considerations of habitability or the avoidance of excessive power requirement.

A dual configuration is therefore proposed for the SSACV by suggesting the use of cushion power to raise the hulls to the water surface for short bursts of high speed of the order of 100 knots with the available power and reverting to the semi-submerged configuration after the mission is completed.

INTRODUCTION

A requirement exists for a high performance vehicle with a degree of operational flexibility in open water not possessed by conventional types of ACVs or displacement vessels. Thus, in terms of military applications, such as in anti-submarine warfare (ASW), the vehicle should be capable of sustained all-weather operation in the open ocean with a long endurance at relatively low or moderate speeds, for initial search and detection, and with additional capability of bursts of very high speed operation of the order of 100 knots at least for short periods during interception and attack. The vehicle should also possess a high degree of seakeeping, particularly in the attack role, capable of "platforming" the waves in

rough seas by retaining a steady mean height and level trim over the mean water surface without undesirable motions or accelerations even in the high speed role. In addition, the vehicle should also possess a high degree of manoeuvrability.

A conventional type of displacement vessel operating on the irregular interface between air and water does not possess this exacting type of capability. Even in calm water the vessel has a very high resistance to motion comprising wave resistance, form drag and skin friction, and propulsion beyond moderate speeds is impractical without an inordinate expenditure of power which roughly follows the speed-cubed law. Also, the vessel will undergo very severe motions and accelerations at high speeds in waves as it is very much subject to the adverse effect of the rough water surface with which it is in intimate contact. It is therefore obvious that the hull should be kept away from the disturbed water surface in order to travel at a high speed with a minimum of motions and accelerations. Thus, the fully skirted amphibious air cushion vehicle (ACV) has its hard structure raised well above the mean water surface so that it is clear of the crests of all but the highest waves and it has been demonstrated in recent years that this type of vehicle is capable of high speeds in moderate sea states as the resistance to motion over water is now only that due to the generation of surface waves (the so-called wave resistance which is very small indeed at speeds well above the hump) apart from the momentum drag, if the form drag and skin friction of the immersed part of the flexible extensions is ignored. This means a considerable improvement over the conventional type of interface vehicle. It will be remembered, however, that the elevation of the hard structure of the ACV above the water surface, i.e. the increase of the potential energy of the vehicle which also enables the increase of its kinetic energy may call for the expenditure of a great deal of power. This may, however, be considered worthwhile if the speed is the main objective. But it has been shown (1) that this type of ACV is subject to severe motions even if the vehicle is ideally assumed to be free from water contact at all stages of its motions and oscillations.

There is inadequate damping available if no part of the vehicle is immersed in the water, apart from the damping characteristics of the air cushion itself.

An alternative method would be to immerse the hull of the vehicle well below the free surface so that it will not be subject to the pressure fluctuations caused by the orbital velocities of the water particles due to the surface waves or sub-surface waves. Ideally, the depth of immersion should be at least one-half of the length of the longest wave on the surface, but a depth equal to one-half of the length of the hull may be found adequate. In the case of a very long hull this depth of immersion will be structurally impractical and a depth equal to two or three times the diameter of the hull is actually used in practice with the hope that the wave effect will be very much smaller at this depth than at the surface. Semi-submerged ships of this type have been built and Lang (2) has described the small motions exhibited by this type of vessel in waves compared with surface vehicles. However, the use of this type of submerged hull (or hulls) will still entail a large expenditure of power for propulsion at high speeds, for although wave resistance may be considered to have been nearly eliminated and form drag reduced to a minimum by a proper streamlining of the hulls, the skin friction will be considerable as the area of the wetted surface will now be very much larger than in the case of surface vehicles. But, although these types of vehicles may not be economical for very high speed operation, they have an inherent static and dynamic stability. The submerged hulls will have zero stiffness by themselves and the stiffness of the semi-submerged ship is limited to that appropriate to the small waterplane area of the surface-piercing struts which carry the platform above the water. However, the submerged hulls will provide a large measure of damping due to vortex shedding in all modes of oscillation and particularly in heave.

It appears to be a law of nature that the faster the ride over an irregular surface, such as in a seaway, the rougher the ride will be. An amphibious ACV or an ACV with rigid side-walls can be made to attain an arbitrary value of high speed if sufficient power is installed although there is no guarantee that the habitability, i.e. the oscillatory motions and accelerations in various degrees of freedom, will be within acceptable bounds. In fact, the ride quality will invariably deteriorate with increasing speed exactly as in the case of planing boats, hydrofoils and displacement vessels in general. On the other hand, a semi-submerged ship may provide a very stable platform, but the speed is not likely to be very high without an inordinate and impractical expenditure of power.

A new design concept is therefore necessary in order to satisfy the very stringent and conflicting requirements of a very high speed and a smooth ride which are separately satisfied by the above two types of vehicles. As it appears that the satisfaction of each of the two separate requirements is mutually exclusive in the case of each type, it may be expected that a combination of the two will produce a type of vehicle which may also hopefully combine the merits of each without attracting too many of the disadvantages.

It is suggested that the new concept of the Semi-Submerged Air Cushion Vehicle (SSACV) to be described presently may provide a true compromise between the above two conflicting requirements of a high speed and a smooth ride.

Starting with a conventional surface ship such as a destroyer, Lewis and Breslin (3) have indicated three directions for seeking higher ship speed; firstly going well below the surface and thereby eliminating surface wavemaking resistance; secondly staying on the surface

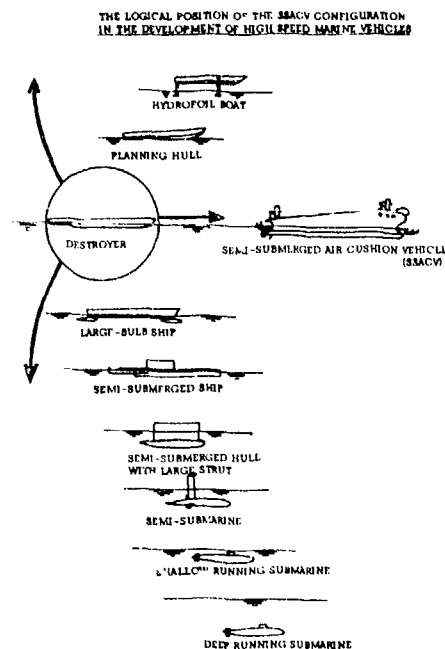


Fig. 1 Possible directions in which to seek higher speeds at sea (Reproduced from Reference 2)

and reducing wavemaking drastically by making the hull longer and more slender; and thirdly, raising the hull above the surface. Fig. 1 is reproduced from their work (3) and also now includes the new concept of the SSACV which involves movement in all three directions, namely, raising the deck and buoyancy chamber well above the water surface, lengthening the vehicle and submerging the hull well below the water surface.

THE SSACV CONCEPT

The proposed Semi-Submerged Air Cushion Vehicle (SSACV) concept comprises the use of a composite type of vehicle which will take advantage of the high speed capability of an air cushion vehicle and combine with this the inherent stability and course-keeping of a pair of submerged hulls. For this purpose, the hard structure of an ACV of the conventional type is supported well above the water surface by a pair of long, thin, streamlined struts along the sides of the vehicle which carry at the lower end a pair of long, slender torpedo-shaped hulls immersed at an adequate depth well below the water surface. Flexible seals extend below the base of the vehicle down to the water surface at the bow and at the stern enabling the retention of the air cushion. The sustentation of the vehicle above the water surface is therefore partly due to the pressure of air generated in the cushion and partly due to the buoyancy of the submerged hulls and the immersed part of the surface-piercing side struts. The mass flow of air into and out of the cushion, the size of the side struts and of the submerged hulls are all determined for an arbitrary ratio of cushion lift to buoyancy which can be optimised from considerations of (a) maximum speed that can be achieved for a given total installed power (lift and propulsion); and (b) habitability, i.e. minimum of motions and accelerations. It is realised that these requirements may be conflicting and that a compromise may therefore be necessary.

A general configuration of the SSACV is shown in Fig. 2.

POWER REQUIREMENTS

If σ is the proportion of air cushion lift in the total sustentation of the SSACV above the water surface, $(1 - \sigma)$ denotes the proportion of buoyancy lift due to the immersed portion of the side struts and the two submerged hulls. When $\sigma = 1$, the SSACV becomes simply the familiar amphibious ACV and when $\sigma = 0$ the vehicle degenerates to the case of a semi-submerged ship such as that described by Lang (2). In the case of a sidewall hovercraft σ takes a value slightly less than unity. The buoyancy contribution in this case is only the

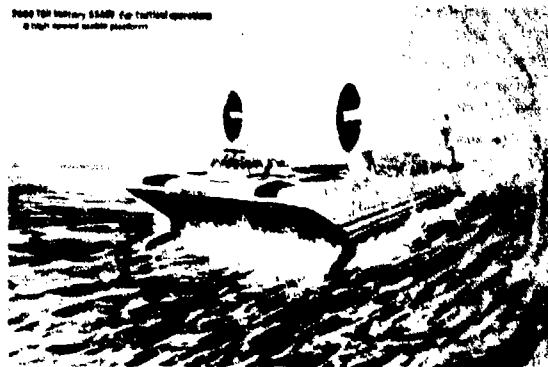


Fig. 2 General Configuration of the SSACV

small amount due to the lightly immersed side-walls.

As σ is always less than unity in the case of the SSACV the cushion pressure, p_c , will be less than that of an amphibious ACV of the same total weight and cushion area. The power required for the generation of the air cushion ($\propto p_c^{3/2}$), the wave resistance ($\propto p_c^2$) and the momentum drag ($\propto p_c^2$) will all therefore be less. However, the power required for the propulsion through water of the surface-piercing struts and the submerged hulls whose displacement is $(1 - \sigma)$ times the total weight of the vehicle will have the value $D(1 - \sigma)^{2/3}$ where D is a constant obtained by theoretical calculation or from tests. This power is an additional item, although since σ is always greater than zero in the case of the SSACV, this will be less than that for the equivalent semi-submerged ship.

It may be possible to optimise the σ -value from considerations of (a) maximum speed achievable for a total installed power (lift and propulsion); and (b) habitability (motions and accelerations). So far as (a) is concerned σ may be obtained by the minimisation of an expression of the form.

$A \sigma^{3/2} + B \sigma^2 + C \sigma^{1/2} + D (1 - \sigma)^{2/3}$ where the constants depend upon the characteristics of the air cushion, the side struts and the submerged hulls. A similar optimisation may be carried out in respect of (b). The two values of σ so derived may be different and a compromise may therefore have to be reached in regard to the above two conflicting requirements.

It may be pointed out that the true optimum to be sought for the SSACV whether designed for civil or military applications is not so much a minimisation of the total installed power with a further optimum subdivision into lift and propulsive powers, but more in the nature of optimisation of performance and ride quality. The latter may be very important for certain types of military

operations, such as weapons deployment in anti-submarine warfare and other tactical operations, for helicopter and V/STOL aircraft operations on deck, etc. The ride comfort is equally important for the carriage of fare paying passengers in the civil transport role.

A preliminary analysis of the power requirements of the SSACV has been made in some very simple terms. The following characteristics of the vehicle have been assumed or derived. (Tables 1 and 2).

Table 1 2000-ton SSACV
General Particulars

Weight, W 2000 tons =	4.42×10^6 lb
Cushion length, L	220 ft
Cushion width, B	80 ft
Cushion height, H	8 ft
Side strut length	220 ft
Side strut width	3 ft (average)
Hull length	220 ft
Hull diameter	6 ft - 10 ft (uniform)
Depth of immersion of hulls	12 ft along longitudinal axis

Table 2 Values of σ for Various Hull Sizes

DIAMETER OF HULL ft	BUOYANCY lb	CUSHION LIFT lb	CUSHION PRESSURE lb/ft ²	σ
6	1.56×10^6	2.92×10^6	166	0.65
7	1.80×10^6	2.68×10^6	152	0.60
8	2.09×10^6	2.39×10^6	136	0.53
9	2.42×10^6	2.06×10^6	117	0.46
10	2.80×10^6	1.68×10^6	95	0.37

The power required to propel the SSACV at various speeds has been calculated for different values of σ , the ratio of cushion lift to the total weight (2000 tons) of the vehicle. The method of prediction recommended in reference (4) has been used so far as the air cushion is concerned. As for the side struts and the submerged hulls it has been assumed that

$$\text{power} = C_D \cdot \frac{1}{2} \rho_w \cdot V^3 / n \quad (1)$$

as suggested by Lang (2) for his semi-submerged ship. A strict assessment of the drag coefficient, C_D , is difficult without controlled model tests for the present configuration. Chapman (5) has indeed made a theoretical study of the wave drag and spray drag of surface-piercing struts as well as hull drag including various interactions, but he considers the use of two struts of fairly large thickness/chord ratio in tandem on each side of the vessel. We are, however, considering the use of a very long continuous strut of very low thickness/chord ratio and our hulls are also of smaller diameter than that of the semi-submerged ship. Lang has used a C_D value of 0.05, but we may use a much lower value, say, 0.02 as appropriate to our case.

The estimated power requirements of a 2000 ton SSACV are shown in Fig. 3 together with the curves given by Lang for other types of 3000 ton vehicles including the Surface Effect Ship. It will be seen that the curves for the SSACV with the air cushion providing a lift of about one-third to two-thirds of the total

weight all lie within a narrow band and that the curves cross at a speed of approximately 60 knots. Above this speed, the SSACV power requirements appear very excessive.

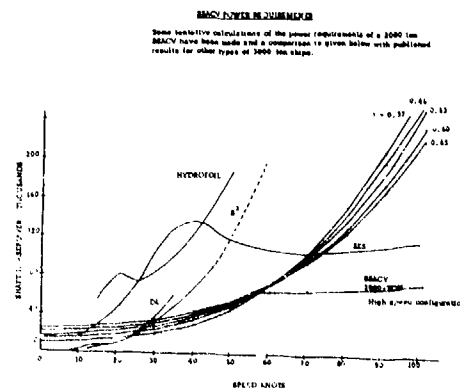


Fig. 3 2000-ton SSACV Power Requirements
Curves for Hydrofoil, Destroyer, S³ and SES
relate to 3000-ton ships and are reproduced
from Reference (2)

Even after allowing for a proper scaling down of the ordinates of the curves for the 3000-ton ships to represent the power requirements

for 2000 tons, it will be seen that the SSACV will require generally much less power than the hydrofoil, the semi-submerged ship, the destroyer and even, possibly, the SES of comparable size up to a speed of 60 or 65 knots, although the power may slightly be higher than that of the destroyer or the semi-submerged ship at very low speeds, say, below 25 knots. This is because the resistance of the air cushion is very high at low speeds up to and slightly beyond the so-called "hump speed" compared to the resistance of the hulls. The reverse is true at higher speeds when the resistance of the air cushion becomes very small whilst the resistance of the hulls increases steadily, following roughly the speed-cubed law in terms of power requirements. A dual configuration is therefore proposed below for the SSACV.

THE HIGH SPEED SSACV

Although the semi-submerged feature of the SSACV can provide a smooth ride with an economy of power at speeds up to 60 or 65 knots, the submerged hulls will cause an excessive resistance to motion at higher speeds of the order of 100 knots and provision of the necessary power is neither economical nor practical. However, if the hulls are raised above the water so that the vehicle is just skimming the water surface, they will still provide a lateral boundary for the air cushion and the skin friction will now be simply that due to the small area of contact of the lower surfaces of the hulls with the water surface. This could be less than that of the immersed part of the sidewalls of the SES and the power required for the high speed SSACV could be therefore less than the equivalent SES.

Fig. 3 shows that the power required for the high speed SSACV at high speeds does not greatly exceed that at about 60 knots provided the hulls are raised above the water. It is therefore perfectly possible to reach a speed of 100 knots with a little more than the power required to propel the SSACV in the semi-submerged condition. It is, however, true that the inherent stability of the semi-submerged condition is now lost, but as stated above, the power required may now be less than that of the SES due to the lower skin friction of the lateral rigid boundaries of the air cushion.

The raising of the hulls above the water is simply effected by lowering the hemline of the flexible extensions at the bow and at the stern and increasing the mass flow of air through the lift fans. The hulls will have zero stiffness to being raised through the water surface and if they come up too high air will escape from the cushion along the entire side-boundaries underneath the hull surfaces. This will cause the cushion pressure to drop and the vehicle will settle down on the water surface. However, the

hulls on contact with the water will have considerable stiffness against immersion due to the buoyancy which is developed. A steady position will soon be reached and this position is obviously a stable one.

WAVE PUMPING AND WAVE EXCITATION

The principal merit of the SSACV concept lies in the possibility of a mathematical design of the size and geometry of the submerged hulls to match the characteristics of the air cushion. When traversing waves in a seaway, the surface waves will pass through the air cushion under the flexible extensions in more or less undistorted form and will act in the nature of a piston causing alternatively compression and rarefaction of the air contained in the cushion. This "wave pumping" has the effect of introducing a fluctuating component to the steady design cushion pressure.

The result will be an undesirable vertical heaving motion and also pitching and rolling of the vehicle. The frequency of the oscillatory motions will be the frequency of encounter of the waves which depends upon the forward speed of the vehicle and the length of the incident waves.

The surface waves will also induce orbital velocities of the water particles below the surface and the effect will be a variation of the steady hydrostatic pressure around the hulls to which a fluctuating component will be added also with a frequency equal to the frequency of encounter. This again will produce a vertical fluctuating force on the hulls and a fluctuating pitching moment and, possibly, a rolling moment. This is a hydrodynamic effect as compared with "wave pumping" which is simply a pneumatic effect.

The mechanisms producing pressure fluctuations due to wave pumping of the air cushion and wave excitation of the submerged hulls are different in the two cases. The former is simply a pneumatic effect dependent upon the depth of the air cushion, i.e. the height of the base of the vehicle above the water, whilst the latter arises from hydrodynamic reasons and depends upon the depth of submergence of the hulls.

It appears therefore possible by designing the air cushion system and the buoyancy system as complementary systems in a suitable manner, to balance the adverse effects of the surface waves in the ocean on the two systems taken together so that the overall effect on the vehicle, considered as a rigid body, may be negligible and thus enabling a true "platforming" of the waves to be achieved in rough seas, subject to slight modification by the drag and lift forces on the flexible extensions which are likely to contact and get immersed in the rough water surface.

The ideal response would be with the SSACV platforming the waves although contouring all

the longer waves may be acceptable without detriment to the habitability of the vehicle as the accelerations in the oscillatory motions depend upon the square of the frequency of encounter which is fairly small over the long waves. A comparatively smooth ride is thus possible in heavy seas.

A simple analysis of the two effects is carried out in Appendix I. This analysis overestimates the effect of wave pumping as it is assumed that the air does not escape out of the cushion during the adiabatic compression. In actual practice, air will escape out of the cushion through the lift fan air intake and through the fluid seals under the flexible extensions at the front and the rear. A strict analysis would involve fan characteristics and the actual response of the vehicle to the pressure fluctuations in the cushion due to wave pumping and around the hulls due to wave excitation. Also, the wave form has been assumed to travel through the cushion without distortion and that it is also not modified by the motion of the hulls through the water. The results are therefore based on the so-called Fronde-Krylov hypothesis which postulates that the waves affect the vehicle but that the vehicle does not affect the waves.

It is shown in Appendix I that the vertical forces due to wave pumping in the air cushion and wave excitation of the hulls are exactly in anti-phase when the wave length exceeds a certain minimum value. As short waves are unlikely to produce much effect as regards wave pumping or wave excitation it is clear that it is possible to balance out the two effects over a range of wave lengths of practical significance. Similar calculations can also be made in respect of the pitching moment.

MOTIONS IN A SEAWAY

The linearized problem of the motions and oscillations of a sidewall hovercraft in a seaway has been formulated and the velocity potential derived in 1972 (6) by the use of Green's theorem and appropriate Green's functions. The separate potentials due to the motion of the air cushion and of the sidewalls can be directly applied to the SSACV configuration, but it is now necessary to derive also the potential due to the motion of the submerged hulls. This derivation is indicated in Appendix II.

The velocity potential can be used to study the steady motion of the SSACV in calm water. For example, the resistance to motion including all interference effects between the air cushion, the side struts and the submerged hulls can be calculated together with the steady trim and sinkage in calm water. The added mass and damping of water during forced oscillation in calm water and the response amplitude operators for free oscillation in waves can also be calculated by the methods previously established.

It must, however, be emphasised that the above results are based entirely on the basis of a linearised theory of an inviscid fluid and separate account should therefore be taken of such non-linear and viscous effects such as wave pumping, spray drag, skin friction resistance, etc. in empirical form or on the basis of tests as they are not easily amenable to mathematical treatment.

GENERAL FEATURES OF THE SSACV

The SSACV is a stable high-speed marine vehicle which combines the advantages of the low resistance to motion of an air cushion vehicle with the inherent static and dynamic stability as well as course-keeping and sea-keeping qualities of a pair of submerged hulls.

The propulsion of the SSACV may be

- (a) air propulsion from the deck; and/or
- (b) water-screw or water-pump propulsion from the hulls.

Air propulsion will naturally be required for the high speed configuration when the hulls are raised above the water. In the semi-submerged condition it may be found to be more economical to use water screw or water pump propulsion but the air propulsion units may have to be used for control purposes.

The submerged hulls will have zero stiffness when displaced in the vertical or horizontal directions, but they will have considerable damping, particularly due to vortex shedding in all modes of oscillation except, perhaps, in surge. The small waterplane areas of the immersed parts of the two side struts will produce a certain measure of stiffness for static stability. Their stiffness may be increased by shaping the cross-section in the form of an inverted triangle within the limits of the requirements of streamlining. There is also a considerable amount of stiffness available from the air cushion.

The submerged hulls should be designed for laminar flow over their entire length as far as possible in longitudinal motion at all speeds. They should be designed to be "non-lifting" even at small angles of attack in the horizontal and vertical planes. It is important not to build up circulation around them with the possibility of incipient separation and cavitation at high speeds causing instability. In other words, the submerged hulls are to be designed solely from considerations of hydrostatic buoyancy. No hydrodynamic forces are to be expected to be produced, nor are these forces desirable on account of possibly adverse effects at high speeds.

The side struts and immersed hulls will provide a great deal of directional stability and course-keeping ability. Directional control is available from swivelling air propellers or contra-rotating water screws (or variable flow water pump systems) in the hulls. The use of stabi-

lisers or rudders on the submerged hulls or side struts will present a difficult problem at high speeds due to cavitation and separation. Reliance will therefore have to be placed on the well-established methods of control by aerodynamic forces from above the deck as in the case of amphibious ACV's. The air cushion may be used as an active stabilising device although this involves the generation of large volumes of low pressure air very quickly and at frequent intervals depending upon the frequency of encounter of the waves. The lift fan speed can be suitably adjusted to counteract heave motion.

The geometry of the flexible extensions at the bow and at the stern can also be varied to provide trim control and thus obviating the need for ballast in the hulls which is very necessary in the case of purely semi-submerged ships. When swivelling air propellers are used there is adequate control in the horizontal plane.

The hulls are very suitable for housing machinery and fuel and for mounting sonar or other equipment. Compressed air can also be produced and stored in the hulls during "slack periods" when the power plants are not being used to their full capacity. The air can then be bled to the cushion in a suitable manner for taking corrective action to control the motions of the vehicle in rough weather.

It has to be borne in mind that there may be an increased structural weight due to the dispersal of the structural members and having considerable buoyancy at a great depth below the base of the vehicle. But the problems can be overcome. The minimum width of the side struts may have to be determined mainly from structural considerations.

The side struts and submerged hulls may be considered to be the "legs and feet" supporting the SSACV above the water surface with the air cushion system and the propulsion units constituting the muscular power for counteracting undesirable motions. The immersion of these appendages in the water need not constitute an embarrassment to the unique characteristics of an air cushion vehicle, for it may well be the only means of enabling the vehicle to steady itself in rough seas. It will be remembered that it is very necessary to seek the considerable damping of the motions available from the water itself.

It is to be expected that the SSACV is likely to require considerable power and be of complex design, but it may well be the only answer when a high speed and habitability are to be simultaneously satisfied as the desired objectives for all weather operations in the open ocean where a large draught is not a disadvantage. The SSACV concept also poses some very difficult structural problems, particularly in respect of a suitable strengthening of the hulls to withstand wave impact in the high speed configuration.

The SSACV combines the technologies of the air cushion vehicle and the semi-submerged ship whose individual development is proceeding at a rapid pace.

The spray drag of the SSACV in the high speed configuration with the hulls lightly skimming the water surface need not be unduly high as the hulls do not produce any hydrodynamic lift like a planing surface but simply constitute the lower edge of the lateral boundaries of the air cushion. In any case it is very likely that air will escape from the cushion under part of the hulls keeping them dry locally and eliminating the generation of spray.

CONCLUSIONS

A new concept of a high speed marine vehicle is presented for flexible operation in open water with a high speed and a considerable degree of habitability. At moderate speeds up to 60 or 65 knots, the vehicle will be in the normal configuration of a sidewall ACV with a pair of submerged hulls, the latter contributing to the sustention of the vehicle and providing sea-keeping ability and overall economy of power. The "legs and feet" of the SSACV need not constitute an embarrassment to the unique characteristics of an air cushion vehicle but may well be the means of steadying the vehicle in rough seas as it is very necessary to seek the damping of the motions from the water itself.

In the high speed role the hulls are raised just above the water by depressing the hemline of the flexible extensions at the bow and stern and by a judicious adjustment of lift fan speed. Although the advantages of the submerged hulls are now lost, it is possible for the SSACV to attain very high speeds with the available power for specific missions of short duration before reverting to the normal configuration.

The dual configuration proposed for the SSACV is very necessary as the resistance of the air cushion is very high and the hull drag low at moderate speeds. At high speeds the air cushion drag is negligible but the hull drag becomes excessive. This dual configuration also enables the draught of the SSACV to be reduced as necessary in very shallow waters.

The economy in power demonstrated for the SSACV in the submerged condition at moderate speeds is worthy of attention when designing vehicles for passenger-carrying transport. It is thus possible to achieve a fast and smooth ride.

It is realised that considerable effort and expenditure mainly in the area of theoretical studies and model tests will be involved in the successful evolution of the SSACV concept which shows great promise for tactical military operations and for civil transport applications.

The SSACV concept has been registered with the U.K. Patent Office under Provisional

Specification number 35705/73.

ACKNOWLEDGEMENTS

The author is indebted to the President of Portsmouth Polytechnic, Portsmouth for the facilities provided for the preparation of this paper.

REFERENCES

1. Murthy, T.K.S. "A Linearized Potential Flow Theory for the Motions of Air Cushion Vehicles in a Seaway", University of Southampton, Department of Aeronautics and Astronautics, A.A.S.U. Report No. 299, June 1970.
2. Lang, T.G. "Hydrodynamic Design of an S³ Semi-Submerged Ship", Ninth Symposium on Naval Hydrodynamics, Paris, August 1972.
3. Lewis, E.V. and Breslin, J.P. "Semi-Submerged Ships for High Speed Operations in Rough Seas", Third Symposium on Naval Hydrodynamics, September 1960.
4. National Physical Laboratory (U.K.), Hovercraft Unit, Report No. 10, September 1969.
5. Chapman, R.B. "Hydrodynamic Drag of Semi-Submerged Ships", Transactions of the A.S.M.E., Paper No. 72-WA/Oct-5.
6. Murthy, T.K.S. "A Linearized Potential Flow Theory for the Motions of Amphibious and Non-Amphibious Air Cushion Vehicles in a Seaway", Ninth Symposium on Naval Hydrodynamics, Paris, August 1972.

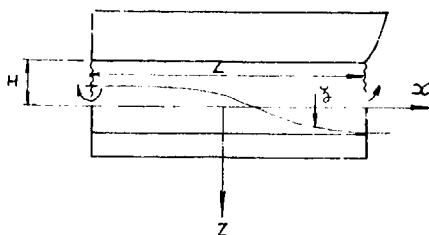
APPENDIX I

WAVE PUMPING AND WAVE EXCITATION

Wave Pumping

The instantaneous wave elevation may be written,

$$\zeta(x,t) = \frac{h_w}{2} \cos\left(\frac{2\pi x}{\lambda} + \omega_e t + \epsilon\right)$$



where h_w is the wave height, λ the wave length, ω_e the frequency of encounter and ϵ the phase angle.

If H is the height of the base of the SSACV above the mean water level, the instantaneous cushion volume is

$$\begin{aligned} V_C(t) &= B \int_{-L/2}^{L/2} (H + \zeta) dx \\ &= BLH + \frac{Bh_w}{2} \int_{-L/2}^{L/2} \cos\left(\frac{2\pi x}{\lambda} + \omega_e t + \epsilon\right) dx \\ &= V_{C_0} + \frac{B\lambda h_w}{2\pi} \sin\left(\frac{\pi L}{\lambda}\right) \cos(\omega_e t + \epsilon) \end{aligned}$$

where V_{C_0} is the steady cushion volume and the change in cushion volume is therefore

$$\delta V_C = V_C(t) - V_{C_0} = \frac{B\lambda h_w}{2} \sin\left(\frac{\pi L}{\lambda}\right) \cos(\omega_e t + \epsilon)$$

It is assumed in the above derivation that the wave form is unchanged as it passes through the cushion. This is in accordance with the Froude-Krylov hypothesis which postulates that the waves affect the vehicle but that the vehicle does not affect the waves.

If we also assume that when the frequency of encounter with the waves is high, the air in the cushion under the frequent pumping action of the waves has insufficient time to escape either through the lift fan intake or through the "daylight gap" under the flexible extensions, the compression of the cushion will follow the adiabatic law

$$(p_c + p_a) V_C^\gamma = \text{constant}$$

where p_c is the cushion pressure and p_a is the atmospheric pressure, γ being the adiabatic constant. This relation gives

$$\begin{aligned} \delta p_c &= -\frac{\gamma(p_c + p_a)}{V_C} \delta V_C \\ &= -\frac{B\lambda h_w \gamma}{2\pi} \frac{(p_c + p_a)}{V_a} \sin\left(\frac{\pi L}{\lambda}\right) \cos(\omega_e t + \epsilon) \end{aligned}$$

so that the vertical force on the base of the SSACV in the upward direction is the heave force.

$$\begin{aligned} F_C \uparrow &= (\text{cushion area}) \times \delta p_c \\ &= -\frac{B\lambda h_w \gamma}{2\pi} \frac{(p_c + p_a)}{H} \sin\left(\frac{\pi L}{\lambda}\right) \cos(\omega_e t + \epsilon) \\ &= -\frac{1}{2} \zeta_0(t) \left(\frac{B\lambda}{\pi H}\right) \gamma(p_c + p_a) \sin\left(\frac{\pi L}{\lambda}\right) \end{aligned}$$

where $\zeta_0(t)$ is the wave elevation at the centre of the cushion.

We have assumed in the above simple analysis that the air pumped by the wave does not escape out of the cushion and also that the vehicle does not respond in heave, pitch or roll and take up an attitude appropriate to the modified cushion pressure. These are drastic assumptions and a stricter analysis will be necessary taking into account the stiffness and damping of the air cushion and the added mass and damping of the submerged hulls which will naturally have an important effect on the motion of the vehicle as a rigid body.

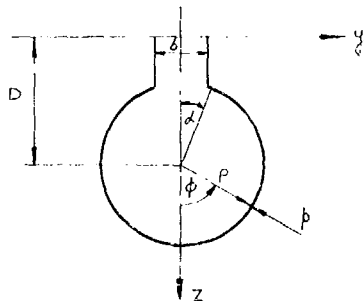
Wave Excitation

We will now obtain an approximate expression for the heaving force on a submerged hull at the lower end of a surface-piercing strut due to the passage of a surface wave along the length of the hull. For the purposes of a simple analysis we may use the Froude-Krylov hypothesis mentioned above and neglecting hull-wave interaction, the pressure on the hull due to the orbital motion of the water particles below the surface of the wave is in the usual notation

$$p = -\rho_w g \left(\frac{h_w}{2} \right) e^{-\frac{2\pi z}{\lambda}} \cos \left(\frac{2\pi x}{\lambda} + \omega_e t + \epsilon \right)$$

assuming that the water is deep. This shows that the pressure is increased above the hydrostatic head $\rho_w g z$ directly below the crest of a wave ($z = -\frac{h_w}{2}$) and decreased below a trough ($z = \frac{h_w}{2}$)

Considering an element of area $\rho d\phi dx$ of the cross-section of the hull and integrating



along the entire length of the hull we have for the heaving force on both hulls

$$F_H \uparrow = 4 \int_{-L/2}^{L/2} dx \int_0^{\pi-\alpha} \rho(x) p \cos \phi d\phi$$

where $\alpha = \arcsin \frac{b}{2\rho}$

and setting

$$z = D + \rho \cos \phi$$

we may write

$$F_H \uparrow = -2\rho_w g h_w \int_{-L/2}^{L/2} \rho(x) \cos \left(\frac{2\pi x}{\lambda} + \omega_e t + \epsilon \right) \int_0^{\pi-\alpha} e^{-\frac{2\pi}{\lambda} (D + \rho \cos \phi)} \cos \phi d\phi$$

If we assume that

we may set $\rho \ll \lambda$

$$e^{-\frac{2\pi \rho}{\lambda} \cos \phi} \approx 1 - \frac{2\pi \rho}{\lambda} \cos \phi$$

so that

$$\begin{aligned} & \int_0^{\pi-\alpha} e^{-\frac{2\pi}{\lambda} (D + \rho \cos \phi)} \cos \phi d\phi \\ &= e^{-\frac{2\pi D}{\lambda}} \int_0^{\pi-\alpha} \left(1 - \frac{2\pi \rho}{\lambda} \cos \phi \right) \cos \phi d\phi \\ &= e^{-\frac{2\pi D}{\lambda}} \left[\frac{b}{2\rho} - \frac{\pi \rho}{\lambda} \left\{ \pi - \sin^{-1} \frac{b}{2\rho} - \frac{b}{2\rho} \sqrt{1 - \frac{b^2}{4\rho^2}} \right\} \right] \end{aligned}$$

i.e. the downward force

$$F_H \downarrow = \rho_w g h_w e^{-\frac{2\pi D}{\lambda}} \int_{-L/2}^{L/2} \left[\frac{b}{2\rho} - \frac{2\pi \rho}{\lambda} \left\{ \pi - \sin^{-1} \frac{b}{2\rho} - \frac{b}{2\rho} \sqrt{1 - \frac{b^2}{4\rho^2}} \right\} \right] \rho(x) \cos \left(\frac{2\pi x}{\lambda} + \omega_e t + \epsilon \right) dx$$

If we now assume that the hull is of uniform cross-section throughout its length, i.e. that it is in the form of a circular cylinder we may set

$$\rho(x) = \rho, \text{ a constant}$$

and integrating along the length of the cylinder we get

$$\begin{aligned} F_H \downarrow &= \rho_w g h_w e^{-\frac{2\pi D}{\lambda}} \left[b - \frac{2\pi \rho^2}{\lambda} \left\{ \pi \sin^{-1} \frac{b}{2\rho} - \frac{b}{2\rho} \sqrt{1 - \frac{b^2}{4\rho^2}} \right\} \right] \sin \left(\frac{\pi L}{\lambda} \right) \cos \left(\omega_e t + \epsilon \right) \\ &- 2 \rho_w g h_w \left(\frac{\rho_w g h_w}{\lambda} \right) e^{-\frac{2\pi D}{\lambda}} \sin \left(\frac{\pi L}{\lambda} \right) \left[b - \frac{2\pi \rho^2}{\lambda} \left\{ \pi \sin^{-1} \frac{b}{2\rho} - \frac{b}{2\rho} \sqrt{1 - \frac{b^2}{4\rho^2}} \right\} \right] \end{aligned}$$

This is only an approximate expression. A stricter analysis would take into account the response of the vehicle to wave excitation when the added mass and damping of the hulls would be pertinent.

It is clear that the integral force on the hulls is zero where the wave length is such that

$$\frac{L}{\lambda} = 1, 2, 3, \dots$$

and also when $\lambda = \lambda_0$ given by

$$\frac{2\pi \rho}{\lambda_0} = \rho \left[\pi - \sin^{-1} \frac{b}{2\rho} - \frac{b}{2\rho} \sqrt{1 - \frac{b^2}{4\rho^2}} \right]$$

When the waves are longer than λ_0 , the heave force is i.e. in the same direction as the cushion heave force, but over shorter waves ($\lambda > \lambda_0$) the heave excitation of the hulls is in the opposite direction, thus reducing the effect of wave pumping.

APPENDIX II

DERIVATION OF THE VELOCITY POTENTIAL

The derivation of the velocity potential for the motion of sidewall hovercraft through the water surface has been derived in 1972 (6) by the use of Green's theorem with appropriate Green's functions. The separate potentials due to the air cushion and the sidewalls derived previously can be directly applied to the air cushion and side struts of the SSACV but it is now necessary to derive in addition the potential due to the submerged hulls.

A part of the domain of integration in Green's theorem is the surface of the immersed part of the surface-piercing struts and the submerged hulls. The former has already been dealt with in the earlier work and in the case of the submerged hulls we will have to evaluate in addition

$$\frac{1}{4\pi} \iint_{H_1+H_2} \left(G \frac{\partial \phi}{\partial n} - \phi \frac{\partial G}{\partial n} \right) dS$$

taken over the surface of the hulls with the normal derivatives taken into the hulls.

It has been shown earlier (6) that the kinematic condition on the side struts

$$y' + b = \delta h_1(2) (x', z')$$

is

$$\frac{\partial \phi}{\partial n} = \delta \left[\dot{x} \cos \theta - \dot{z} \sin \theta + (z + h_G) \dot{\theta} + V \cos \theta \right]$$

$$\frac{\partial h_1(2)}{\partial x'} + \left\{ \frac{\dot{x}}{x} \sin \theta - \frac{\dot{z}}{z} \cos \theta - x' \dot{\theta} + V \sin \theta \right\} \frac{\partial h_1(2)}{\partial z'}$$

where x, z and θ are the small displacements in surge, heave and pitch.

A similar boundary condition may be derived for the submerged hulls whose surface may be represented by an equation of the form

$$H(x, y, z, t) = \gamma \rho (x') - \sqrt{(y' + b)^2 + (z' - d)^2} = 0$$

where $\gamma \rho$ is the small radius of cross-section which may vary along the longitudinal axis

$$y' = \pm b, \quad z' = d$$

Thus, in the case of the starboard hull, H_1 , we may write

$$y' - b = \gamma \rho \sin \phi$$

$$z' - d = \gamma \rho \cos \phi$$

where ϕ is the angle made by the radius vector to the point (y', z') on the surface with the z' -axis which is taken vertically downwards.

It can be shown that

$$\frac{\partial H}{\partial x} = \gamma \frac{d\rho}{dx} \cos \theta - \cos \phi \sin \theta$$

$$\frac{\partial H}{\partial y} = \frac{dH}{dy} = -\sin \phi$$

$$\frac{\partial H}{\partial z} = -\gamma \frac{d\rho}{dx} \sin \theta - \cos \phi \cos \theta$$

$$\text{and } \frac{\partial H}{\partial t} = \gamma \frac{d\rho}{dx} \left[\frac{\dot{x}}{x} \sin \theta - \frac{\dot{z}}{z} \cos \theta - (z' + h_G) \dot{\theta} \right] - \cos \phi \left[x' \dot{\theta} - \frac{\dot{x}}{x} \sin \theta - \frac{\dot{z}}{z} \cos \theta \right]$$

so that

$$|\nabla H| = 1 + \left(\gamma \frac{d\rho}{dx} \right)^2$$

and

$$\frac{\partial \phi}{\partial n} = - \frac{\frac{\partial H}{\partial t} - V \frac{\partial H}{\partial x}}{|\nabla H|}$$

$$= \left[x' \dot{\theta} - \frac{\dot{x}}{x} \sin \theta - \frac{\dot{z}}{z} \cos \theta - V \sin \theta \right] \cos \phi$$

$$+ \left[\frac{\dot{x}}{x} \cos \theta - \frac{\dot{z}}{z} \sin \theta + (z' + h_G) \dot{\theta} + V \cos \theta \right] \left(\gamma \frac{d\rho}{dx} \right)$$

$$+ O(\gamma^2)$$

The expression for the normal velocity on the port hull is identical.

This expression may be directly used for the evaluation of the first term in the surface integral

$$\frac{1}{4\pi} \iint_{H_1+H_2} G \frac{\partial \phi}{\partial n} dS$$

$$H_1+H_2$$

after expanding G from the hull surface to the longitudinal axis and substituting

$$dS = \gamma \rho d\phi dx'$$

It will be noted that this integral is of $O(\gamma)$ which is exactly the order of the potential due to the motion of the hulls.

The second term

$$- \frac{1}{4\pi} \iint_{H_1+H_2} \phi \frac{\partial G}{\partial n} dS$$

$$H_1+H_2$$

may be ignored in evaluating the lowest order potential for ϕ is of $O(\gamma)$ as is also dS so that the integrand becomes of $O(\gamma^2)$.

DISCUSSION

PAUL KAPLAN

This paper is very disturbing to me, and represents publication of a concept that has previously been discussed with the author by the present discussor as well as personnel at the U.S. Navy SESPO office. In each case the negative impressions of the concept have been provided to the author, based upon the judgment of all the reviewers, but now my comments will deal with precise facts related to the proposed vehicle. The original concept initially looked impractical since the inclusion of simple appendages, such as propulsion pods for use of submerged propellers, was not considered practical for SES craft due to the large resistance associated with appendages. If such an addition seemed impractical, then the inclusion of the submerged hulls, large struts, etc. of the present concept implies a greater impracticality. Rather than discuss the concept generally, the various analyses provided by the author are considered with an appropriate critical engineering evaluation.

Examining the drag estimates first, it seems that the basis for a much lower drag coefficient, as compared to that of the semi-submerged ship of Lang, is not a practical choice. The spray drag is not the largest factor for this particular design, especially in view of the small slenderness ratio of the strut thickness-to-length ratio proposed for this design. The major component of drag for the submerged portions of struts and hulls is due to friction drag, and computations have been made of the necessary power to overcome the frictional drag alone (based on use of total wetted surface area, for a 9 ft. diameter hull, 3 ft. strut width, and use of the Schoenherr friction coefficient applied to the total wetted surface, at the appropriate Reynolds number), assuming a propulsion efficiency of approximately 85%. On that basis the power requirements, just to overcome friction drag, are 36,000 hp at a speed of 50 kt. and 60,000 hp at a speed of 60 kt. Additional power is required to overcome the following drag components that have not been considered in the above evaluation: viz. form drag of all the submerged hulls and struts, spray drag of the struts, wave drag of the struts, wave drag of the submerged hulls, momentum drag of the air cushion, wave drag of the air cushion, and also the power required for generation of the air cushion. Without going into any detailed computations of all of these effects, and noticing by comparison with Figure 3 of the paper that the friction drag power requirement alone is about the same value as that proposed by the author, it can be seen that the total drag for the proposed system can easily be twice as much (if not more) as the author's tabulated values. There is just no physical reason for expecting this vehicle to have reduced drag in comparison with other craft that will be competitive with it in its operating speed range, so that the author's power requirements seem to be severely underestimated.

It is even more obvious that the computations of power provided by the author are erroneous when examination is made of the drag associated with his so-called "high speed configuration". In that case his vehicle then operates in the same way as a full SES craft. Since the water level within the cushion is depressed by the action of the cushion wave generation, which is of the order of

a 1-deg. slope, that would depress the water approximately 4 ft. at the stern of the craft relative to that at the bow. In order for the craft to properly seal the cushion, the circular hulls must be submerged into the water at least this much. Comparing the actual shape of the sidewalls associated with SES craft, which usually have very sharp leading edges and a gradual increase toward the stern where the propulsion system is located, it appears that there would be much more area of cylindrical hulls in the water than for an SES craft. In addition I would certainly expect a more significant spray problem to be associated with such a ship having cylinders in the surface, which lead to much greater restrictions for the proposed configuration as compared to any SES design I have ever seen.

Another practical consideration for an SES type of craft is the necessity to have a sufficient submergence at the stern so that the water propellers can operate properly. The alternative proposal for use of air propulsion is not presently being considered for any practical multi-thousand ton SES craft under U.S. Navy development. This is due to the low efficiency, noise, and habitability problems associated with such an air propulsion system for the maximum speed range of 80-100 kt. Thus the inference of an air propulsion system for this range is counter-productive. Furthermore, no dual propulsion system (separate water and air propulsion systems) is envisioned for any functional ship system. Such a redundancy in power plants is not practical from the points of view of engineering, cost and payload reasons. After all, that (i.e. payload) is the function of any vehicle, which will be compromised by any such design suggestions.

The author's statement regarding a lack of hydrodynamic forces acting on the hulls in any configuration he envisions is an unreal and ridiculous expectation. Effects due to circulation, near surface forces, turbulent drag, etc. are certainly present and cannot be dispensed with by desire, in accordance with the physical principles I am aware of. The hydrodynamic forces on a hull near the surface running at high speed, which is similar to the problem of submarines near the surface, result in difficulties in maintaining appropriate depth control. That sort of operation requires the use of continuous active controls to maintain a desired depth, even in smooth water, and this problem has not even been considered by the author.

A number of the statements about SES craft subsystems such as the action of adjusting the fairs, varying the characteristics of the bow and stern seals, etc. are made without any consideration of the actual behavior of such real systems. Extensive work has been carried out to deal with those particular problems for a number of years, and they represent important problems for the development of SES craft. There is obviously a lack of appreciation and understanding associated with the operation of these various subsystems, together with their effect on the craft, when considering the subsystem behavior as part of an SES craft.

However, the most important point made in the paper, which is indicated to be the most significant virtue

of the craft, is the ability to obtain better heave motion characteristics in a seaway. The author presents an analysis comparing the effects of the vertical forcing function due to the "wave pumping" action and that due to the action of the waves on the submerged hulls. While it is indicated that there is a definite range of wavelengths wherein the vertical force on the hulls reduces the forcing action of the pressure fluctuations, no consideration has been given to determine their relative magnitudes, i.e. nowhere in the paper is there any numerical evaluation of the magnitudes of these two components.

In order to determine where the wave forces on the submerged hulls are significant in achieving a benefit for the craft motion in waves I carried out some computations to determine the force magnitudes, based upon the formulas given in Appendix I. The computations were carried out for cases that would be expected to be conditions with significant craft motions. The first case chosen was that of a wavelength of 150 ft. which is approximately 2/3 of the craft cushion length, a condition that is known to result in large vertical accelerations of SES craft at high speed. The relative magnitude of the force due to the wave pumping, as compared to that of the hull forces, is 227:1!!!! While it is expected that the formula given for the force due to wave pumping, based upon the model of an enclosed box, is known to be too large, we have carried out model studies together with a theoretical analysis that has been verified by the model test data (thereby overcoming an objection to the use of model values which do not scale) which indicates that the wave pumping effect is too large by a factor of the order of 10. Even in that case, the wave pumping effect is so much larger than the force on the submerged hulls that they cannot be expected to have any significant effect on the craft. An actual evaluation of the hull forces for this particular wavelength results in a value of 3265 lb./ft. of wave amplitude, which is quite small when considering its influence on a 2000 ton craft. This is not surprising to any hydrodynamist who is aware that a submerged body near the surface does not generate any significant wave force until the waves are somewhat longer than 1/2 the length of the body. Thus it is obvious that one cannot gain any benefit from the forces generated on the submerged form in this case.

Another computation was made for the case of a 500 ft. wavelength which results in the wave pumping effect to be 59 times as large as the force on the submerged hulls. Even accounting for the deficiency of the box model used by the author, the relative magnitudes are such that the benefits to be gained in heave motion are marginal. This is even more obvious when considering the fact that the craft motions themselves do not result in large accelerations for such a large wavelength, with the craft heave tending to follow the wave elevation like a particle, in the limit (i.e. close to vertical contouring).

In conclusion, my own opinion is that this concept has no engineering utility as a replacement for an SES craft in the high speed operating regime. In a lower speed range there may be some benefit for a particular restrictive operating range, but I cannot see one based on the examination given above. There is always an opportunity to investigate the practicality of this concept, or any other concept, by use of some detailed numerical computations

rather than leaving expressions in mathematical or integral form without any numerical evaluation that can indicate feasibility, or otherwise. While all of the above represents my opinion regarding this concept, at least a choice can be made (when considering this proposed design) which is based on perhaps more rational reasoning than has been presented in the paper itself.

R.A. BARR

Interest in hybrid ship concepts is growing rapidly. Any contribution to the meager literature in this area is therefore welcome, although I think the present paper is technically not well founded. I would like to make a number of comments on the paper.

1. The use of a drag coefficient of 0.02 seems optimistic. Using the authors dimensions and a representative C_f of 0.0024, the drag due to friction alone is approximately 0.02.
2. It does not appear feasible to make the hulls non-lifting bodies or to achieve laminar flow over a large portion of the hull length given in nature of the near-surface environment.
3. It seems likely that cavitation at or near the hull-strut intersection will present a difficult problem at speeds of 60 knots or greater.
4. Configurations with equal hull and strut lengths, and with no stabilizing appendages, as proposed by the author, seem likely to be directionally unstable.
5. The use of swiveling CRP propellers at high speeds is not practical.
6. There is likely to be a significant drag peak or hump associated with the hulls breaking the surface as required to achieve the high speed configuration.
7. At high speeds, with the hulls "planing", both spray drag and frictional drag will be significant. A significant hull "submergence" will be required to maintain a satisfactory leakage rate and to account for the differential waterlines created by the pressure difference of about 250 pst.
8. The "lowering of the skirt or seal hemline", is far from simple since the seals must be lowered 15 feet or more. It is likely that such seals will not perform adequately in waves.

Many of the question raised here can only be answered by model tests or detailed engineering studies. There is little doubt in my mind, however, that the authors drag estimates, particularly for the high speed configuration, are highly optimistic.

L.J. DOCTORS

Regarding the power related to (a) the air cushion supply, (b) the wave resistance of the air cushion and (c) the momentum flux, the discussor tends to be in agreement. However, the submarine/sidewall drag is difficult to understand. Approximating these by circular cylinders, one can obtain their volume and the power to drive them through the water:

$$\nabla = \frac{1}{4} \pi D^2 L \times 2$$

and

$$P = V \cdot \frac{1}{2} \rho V^2 \cdot C_D \cdot \pi D L \times 2,$$

in the usual notation (neglecting free surface effects). Thus

$$P \propto \nabla^{1/2} V^3 \text{ and not } P \propto \nabla^{2/3} V^3$$

as assumed by the author in his Eq. (1). In addition, a

choice of drag coefficient, C_D , of 0.02 instead of 0.06 seems rather arbitrary.

Secondly, could the author explain qualitatively the nature of the curves in Fig. 3? Why is there so little difference between the cases given by $0.37 < \sigma < 0.65$, while there is a big change for $0.65 < \sigma < 1$?

The technique of the high-speed dash mode appears impractical to the discussor. One problem here would be the very high wave forces due to slamming, since the lower surfaces of the sidewalls are horizontal. Also there would be excessive venting under these sidewalls in anything but clean water, due to their zero nominal immersion.

The last paragraph before the conclusion concerning the spray, appears to be incorrect. Where there is a gap under the skirt or sidewall, the escaping air will generate spray not eliminate it.

AUTHOR'S REPLY

I must thank Dr. Kaplan for his lengthy comments. The printed comments occupy a space almost as much as my paper itself and they are all invariably of an adverse nature. This type of criticism was probably directed against the hovercraft principle itself when first introduced to the engineering public some fifteen years ago. However, ACVs are now well-established no doubt due to the considerable amount of research and development of the basic principle over the years. I do not think there is any need for Dr. Kaplan to be "disturbed" by the SSACV concept which simply attempts to combine the advantages of two established technologies, namely those of the ACV and the semi-submerged ship. This concept has been prompted by the simple idea, namely that if you must have sidewalls immersed in the water as obviously envisaged for the SES craft, let us make the sidewalls pay for the added resistance by providing a contribution to the sustentation of the vehicle. Planing surfaces are out of the question as they cause instability at high speeds and it is therefore necessary to rely entirely on the hydrostatic buoyancy of the immersed hulls.

With regard to the specific comments made by Dr. Kaplan, there are some very good reasons for choosing a lower C_D than that used by Lang for his semi-submerged ship. The drag coefficient is a function of the prismatic coefficient, C_p , and the L/D ratio. Lang's hulls are 14 ft in diameter, but the diameter proposed for the 2000 ton SSACV could well be only 6 or 8 ft. Also, our struts are continuous and the drag will be less than in the case of a pair of struts in tandem used in the semi-submerged ship. In addition, the wetted surface of the hulls in the case of the SSACV will be less on account of the induced wave formation in the air cushion which will cause reduced wetting on the inboard side of the hulls and struts. However, the power requirements for the SSACV given in Fig. 3 appear to be on the low side as surmised by Dr. Kaplan. Further calculations have since been made on a stricter basis which show that although a correction is required, the SSACV will still require less power (lift and propulsion) than other types of marine vehicles at least up to a speed of 60 knots. This may be sufficient for most types of operation, but it appears that the advantage may also be extended to the high speed configuration. It is not practical to set down the lengthy calculations here, but it is proposed to circulate separately a technical document containing a stricter analysis of the predicted performance of the SSACV to those who have expressed a critical interest,

favourable or otherwise, in the concept.

As regards the propulsion system for the SSACV it was not the intention to specify any particular type. Air propulsion was only indicated as a possibility, particularly as control from the deck may be preferred to control surfaces in the water which may not be very efficient at high speeds. However, there may be other considerations dictating the choice of water screw or water jet propulsion.

I agree that hydrodynamic forces on the hulls will arise particularly when running at a high speed near the free surface and these will have to be contended with. However, there may be considerable stiffness available from the air cushion which may make depth control easier. This is the particular advantage of the SSACV which is not available in the case of submarines or semi-submerged ships.

As regards the relative magnitudes of the effects of wave pumping and wave excitation, it was mentioned during the presentation that the simple formula given for adiabatic compression in a closed container gives unrealistic values for the increase in pressure. I tentatively decided to use a scaling down factor of 100:1 to reduce the level of the forces due to wave pumping to that observed in the actual operation of hovercraft. This is also supported by Mantle's (7) statement in a recent paper that the simple one-dimensional theory correctly predicts the trends but over-estimated the actual experienced accelerations by an order of magnitude. Mantle's Fig. 4 would indicate that a scaling down factor of, say, 25:1 may be more appropriate. Dr. Kaplan is prepared to settle for a factor of 10:1. It is also to be noted that forward speed effects are not included in the simple formula for wave excitation which considers the situation when a surface wave travels over a stationary hull.

I am glad to note that Dr. Kaplan concedes at least that there may be some benefit to be gained by the use of the SSACV concept in some particular operating range although he cannot readily see one. Fortunately, the comments received from a number of other sources and in other countries indicate that they have an open mind in the matter.

Dr. Barr also queries the use of a drag coefficient of 0.02 and I would refer him to the explanation given above. The skin friction has been calculated from the ITTC (1957) formula and actually works out to 0.0016 at 20 knots for C_f to 0.0013 at 100 knots. Also, as stated above, the wetted surface of the struts and hulls has to be suitably calculated taking into account the depression of the water surface on the inboard side.

Hydrodynamic forces on the hull and the possibility of cavitation have indeed to be studied in detail but these may be hopefully overcome. The other points referred to by Mr. Barr also require serious consideration and I fully agree with him that model tests and detailed engineering studies have to be carried out before serious development of the concept can be considered.

Dr. Doctors queries the use of the expression

$$\text{Drag power} = C_D \nabla^{\frac{2}{3}} \frac{1}{2} \rho_w V^3 / \eta$$

This is in conformity with similar expressions used in ship resistance studies and is strictly correct for ∇ has dimensions of L^3 and $\nabla^{\frac{2}{3}}$ has therefore the dimensions of wetted surface area, i.e. L^2 . It should of course be remembered that C_D is a function of the prismatic coefficient, C_p , and L/D ratio, so that the resistance of long slender hulls of similar shape may be compared by using the above formula.

Referring to the query regarding Fig. 3 I wonder whether Dr. Doctors has misinterpreted the situation. The cluster of curves relates to $0.37 < \sigma < 0.65$ and the curves are closely spaced indeed throughout the speed

range. They also appear to cross each other at a speed of about 60 knots and it was therefore suggested that the hulls may be taken out of the water at this speed, beyond which the hull resistance increases very steeply. The single curve for the high speed SSACV beyond 60 knots assumes only a nominal contact of the hull with the water surface.

I agree that the hulls have to be suitably strengthened to withstand the very high wave forces. As regards the venting of the air cushion the situation is no worse than in the case of the amphibious ACV which the SSACV now resembles.

Dr. Doctors has also raised the point that air escaping under the hulls will generate spray and not eliminate it. I should like to keep an open mind about this. Experience with amphibious ACVs seems to indicate that spray is essentially a low speed problem there being a significant absence of spray at high speeds.

Reference 7. Mantle, P.J. "Large High-Speed Surface Effect Ship Technology". Paper presented at the International Hovering Craft, Hydrofoil and Advanced Transit Systems Conference, Brighton, England, May 1974

FUNDAMENTAL HYDRODYNAMICS

SESSION V

Thursday, June 27, 1974
9:00 A.M. - 12:10 P.M.

Chairman: Mr. P. Eisenberg
President, Society of Naval Architects
and Marine Engineers
United States

Small Parameter Expansives in Ship Hydrodynamics	439
R. Timman, Delft University of Technology, Delft, The Netherlands	
Extension, Analysis, and Improvement of Perturbation Series	449
M. Van Dyke, Stanford University, Stanford, California	
Calculation of Vortex Sheets in Unsteady Flow and Applications in Ship Hydrodynamics	463
P.T. Fink and W.K. Soh, University of New South Wales, Sydney, Australia	
The Force and Moment on a Twin-Hull Ship in a Steady Potential Flow	493
Wen-Chin Lin, Naval Ship Research and Development Center, Bethesda, Maryland	
Second-Order Hydrodynamic Forces Due to Stochastic Excitation	517
Eddie Neal, Naval Ship Research and Development Center, Bethesda, Maryland	

SMALL PARAMETER EXPANSIVES IN SHIP HYDRODYNAMICS

R. Timman
Delft University of Technology
Delft, The Netherlands

ABSTRACT

The flow pattern at the bow of a ship is considered from the exact solution for the flow round a three axial ellipsoid. For a vertical ellipsoid the slender body solution is shown to be similar to Ogilvie's wedge flow, for a horizontal ellipsoid the pattern is similar to the pattern calculated by Hermans for the two dimensional flow round a cylinder. The equations for the two cases are shown to be similar.

INTRODUCTION

The theory of ship hydrodynamics is so complicated, that an exact analytical (or even numerical) theory is still far from a completion, so the only way to obtain a tractable set of results is to introduce asymptotic methods. So as a sequence to the classical Michell paper the slender body theory was introduced, which assumed that everywhere the tangent plane to the ship hull makes a small angle with the axis of the ship. The theory has been worked out and applied to a great number of cases and several reviews are available (Newman 1, Ogilvie 2).

The hypothesis that the slope of tangent plane is small, however, gives a severe restriction to its applicability. Essentially, as in supersonic aerodynamics, where the theory is much simpler, it is only valid for a conical bow, where the condition of small slope is fulfilled. Even a wedge shaped bow requires a modification, which was given by Ogilvie (3). For a round bow the conditions are quite different. Another extreme was considered in a recent paper by Hermans (4).

He considered the two dimensional forward flow

round a horizontal circular cylinder, perpendicular to the incoming flow.

In this paper a synthesis between the two approaches will be tried, based upon an analysis of the infinite fluid flow round the ship, which will be replaced by a three axial ellipsoid.

THE FLOW PATTERN ROUND A THREE-AXIAL ELLIPSOID

The flow round a three-axial ellipsoid in translational motion was first calculated by Green (1833, Lamb, Chap. V). If the half axis of the ellipsoid are a, b, c ($a \geq b \geq c$) the disturbance velocity potential for a flow in the direction of the x axis with velocity U is

$$\varphi(x, y, z) = \frac{U}{2 - \alpha_0} a b c \int_1^\infty \frac{d\lambda}{(a^2 + \lambda) \Delta(\lambda)}$$

where

$$\Delta(\lambda) = \{(a^2 + \lambda)(b^2 + \lambda)(c^2 + \lambda)\}^{\frac{1}{2}}$$

and

$$\alpha_0 = a b c \int_0^\infty \frac{d\lambda}{(a^2 + \lambda) \Delta(\lambda)}$$

which can be reduced to an elliptic integral.

λ, μ, ν are confocal coordinates, defined as the roots of the equation

$$\frac{x^2}{a^2 + \theta} + \frac{y^2}{b^2 + \theta} + \frac{z^2}{c^2 + \theta} = 1$$

with the domains

$$\lambda > -c^2, -c^2 > \mu > -b^2, -b^2 > \nu > -a^2$$

$\eta = 0$ corresponds to the ellipsoid.

For a slender ellipsoid the stream pattern is calculated by asymptotic expansions. (Appendix A).

On the middle part $-a < x < +a$ of the ellipsoid we obtain, putting $b = \xi \bar{b}$, $c = \xi \bar{c}$ the results of slender body theory, two dimensional flow in a plane perpendicular to the x axis with a source distribution along the axis. For our purpose, however the behaviour at the forward stagnation point is of primary interest. We do not consider an ellipsoid of revolution but the opposite case: $a \gg b$, $b \gg c$, a flattened three axial ellipsoid.

At the forward stagnation point the stream lines

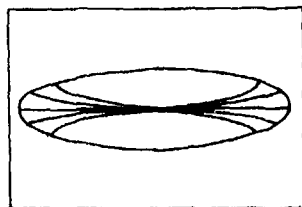


Fig. 1.

form a nodal point (Fig. 1). They travel along the equator of the ellipsoid and at a certain point leave this equator and change into nearly "straight" lines parallel to the x axis over the surface of the ellipsoid. (fig. 2).

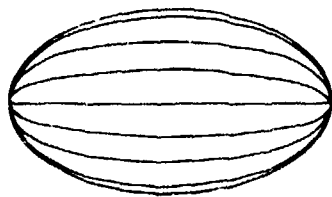


Fig. 2.

This behaviour is the basis for the following considerations.

THE FLOW AROUND AN ELLIPSOID WITH FREE SURFACE

The preceeding calculations for an ellipsoid in an infinite fluid gave a result with $\frac{\partial \psi}{\partial z} = w = 0$ on the plane $z = 0$. We now consider the case of a semi submerged ellipsoid and we have to take account of the free surface condition. An analytic solution to this problem is, because of the non-linear character of this condition not possible. So we have to take recourse to a case where a linearized free surface condition is admissible.

The Bernoulli law is valid on the free surface $z = \zeta(x, y)$

$$\frac{1}{2}(u^2 + v^2) + g\zeta = \text{const.}$$

Now at $x = -\infty$ the flow has velocity U in the x direction and the elevation of the free surface is zero, at the stagnation point $u = v = 0$. This gives for the elevation $\zeta(0, 0)$

$$\zeta(0, 0) = \frac{U^2}{2g}$$

a length, which must be compared to the characteristic length of the configuration: i.e. the half axis b or c of the ellipsoid. Hence for an acceptable theory we require

$$\frac{U^2}{2gb} \ll 1$$

(For a tanker with length 300 m and beam 50 m at a speed of 10 knots $\frac{U^2}{2gb} = 0,05$, the slenderness parameter is $\frac{25}{150} = 0,07$ at 20 knots the velocity parameter is 0,20).

The basic flow pattern is different for the case where the middle axis is vertical and for the case where it is horizontal.

In the first case the beam of the ship at the bows is small and, the stream lines will, except for a very small vertical region, follow the main flow, i.e. the flow pattern will resemble a wedge flow, as considered by Ogilvie.

In the case, where the middle axis is horizontal the free surface meets the bow over a relatively broad part of the front. Here again the stream lines will follow the direction of the x axis, projected on the surface. The flow pattern now will resemble the two dimensional flow as con-

sidered by Hermans. There is one difference, in the purely two dimensional flow there is a line of stagnation points along the front, here however there is only one stagnation point and the velocity increases along the equator.

OGILVIE'S SOLUTION FOR A WEDGE-SHAPED BOW

For a wedge shaped bow

$$y = \pm b(x, z)$$

with the condition $\frac{\partial b}{\partial x} = O(\epsilon)$.

Ogilvie has given the correction to the slender body theory. The vertical ellipsoid has a stream line pattern which is similar to this case, but although the vertical streamline is only limited to a narrow ship and the horizontal streamline starts very closely to the symmetry plane, the crucial condition $\frac{\partial b}{\partial x} = O(\epsilon)$ is not satisfied. Hence we must extend Ogilvie's analysis to the case, where $\frac{\partial b}{\partial x} = O(\epsilon x^{-\beta})$, which is allowed since a small region near $x = 0$ is excluded, where we assume $0 \leq \beta < 1$. For the ellipsoid $\beta = \frac{1}{2}$.

Following his derivation, we put for the potential

$$u_x + \phi(x, y, z)$$

consider the region near the front $x = O(\epsilon^\alpha)$
 $0 < \alpha < 1$. Then the estimation of the orders of magnitude in

$$0 = \phi_{xx} + \phi_{yy} + \phi_{zz}$$

gives

$$\phi \epsilon^{-2\alpha}, \phi \epsilon^{-2}, \phi \epsilon^{-2}$$

with the result

$$\phi_{yy} + \phi_{zz} = 0$$

where the approximation is worse if α is closed to 1. The boundary condition on the hull gives; since $b = O(\epsilon^{1-\alpha\beta+\alpha})$

$$0 = \pm u b_x \pm \phi_x b_x - \phi_y \pm \phi_z b_z$$

$$\epsilon^{1-\alpha\beta}, \phi \epsilon^{-\alpha+1-\alpha\beta}, \phi \epsilon^{-1}, \phi \epsilon^{-1+1-\alpha\beta+\alpha-1}$$

Since $b = O(\epsilon^{1-\alpha\beta+\alpha})$ and $1-\alpha\beta+\alpha > 1$ we can assume the condition on the plane $y = 0$.

Comparison of the terms of lowest order gives because of $1-\alpha\beta > -1$ and $\alpha-\alpha\beta-1 > -1$

$$\phi = O(\epsilon^{2-\alpha\beta})$$

which leads to the boundary condition

$$\frac{\partial \phi}{\partial n} \sim \phi_y \sim u b_x$$

With these simplifications we attack the free boundary condition, again following Ogilvie's reasoning:

$$0 = g\zeta + u\phi_x + \frac{1}{2}(\phi_x^2 + \phi_y^2 + \phi_z^2)$$

$$[\zeta], \epsilon^{2-\alpha\beta-\alpha}, \epsilon^{4-2\alpha\beta-2\alpha}, \epsilon^{4-2\alpha\beta-2}, \epsilon^{4-2\alpha\beta-2}$$

together with

$$0 = u\zeta_x + \phi_x \zeta_x + \phi_y \zeta_y - \phi_z \zeta_z$$

$$[\zeta] \epsilon^{-\alpha}, [\zeta] \epsilon^{2-\alpha\beta-2\alpha}, [\zeta] \epsilon^{2-\alpha\beta-2}, \epsilon^{2-\alpha\beta-1}$$

The first equation leads to

$$\zeta = O(\epsilon^{2-\alpha\beta-\alpha})$$

and in the second equation we must have

$$2-\alpha\beta-2\alpha = 2-\alpha\beta-1$$

or $\alpha = \frac{1}{2}$.

This leads to Ogilvie's boundary conditions

$$0 = g\zeta + u\phi_x$$

$$0 = u\zeta_x - \phi_z$$

or

$$x\phi_{xx} + \phi_z = 0$$

$$with \quad x = u/2$$

on the undisturbed free surface $z = 0$.

Since $b = O(\epsilon^{1+\alpha-\alpha\beta})$ we have (in a rough approximation) the conditions in the yz plane on the line $y = 0, z > -H(x)$.

$$\frac{\partial \phi}{\partial y} = U \epsilon_x$$

Apparently the problem is reduced to Ogilvie's problem. In Appendix B the results are derived in our case in a slightly different way.

HERMANS' SOLUTION FOR A HORIZONTAL CYLINDER

If the ellipsoid is horizontal the streamlines in infinite flow all follow the equator in a region near the stagnation point and suddenly break away and follow the main flow over the surface. This behaviour is similar to the behaviour of the flow round an elliptic cylinder at right angle to the oncoming flow direction with the difference that here only the point $x = -a, y = z = 0$ is a stagnation point and the other points on the equator have a steadily increasing velocity.

In this analysis it is essential, that $\frac{U^2}{2g}$, i.e. the height of the stagnation point in the free surface above the original stagnation point is small with respect to the radius of the cylinder. The total solution is written as

$$\phi(x, y) = \phi^0(x, y) + \varphi(x, y)$$

where $\phi^0(x, y)$ is the outer solution of the problem, as a solution of

$$\Delta \phi^0 = \phi_{xx}^0 + \phi_{yy}^0 = 0$$

for which

$$\phi = Ux \quad \text{as } x \rightarrow \infty$$

together with the condition on the wall

$$\frac{\partial \phi}{\partial n} = 0$$

and the non-linear free surface condition

$$\frac{1}{2} U^2 = g\zeta + \frac{1}{2} (\phi_x^2 + \phi_y^2)$$

$$0 = \phi_x \zeta_x - \phi_y^2$$

The basic solution for the determination of ϕ^0 is the infinite fluid solution, with rigid free surface, which can be perturbed by a series in the small parameter. It does not, however, represent the correct wave character of the flow.

In the case of the ellipsoid this basic solution along the front part does not have a pure two-dimensional character. Hence in writing down the perturbation conditions we use the basic solution $\phi^0(x, y, z)$, where z is the coordinate along the equator. The free surface condition takes the form

$$\frac{1}{2} U^2 = g\zeta + \frac{1}{2} (\phi_x^2 + \phi_y^2 + \phi_z^2)$$

$$\phi_y = \phi_x \zeta_x + \phi_z \zeta_z$$

Elimination of ζ gives the condition

$$\phi_x^2 \phi_{xx} + 2 \phi_x \phi_y \phi_{xy} + \phi_x \phi_z \phi_{xz} + \phi_y^2 \phi_{yy} + \phi_y \phi_z \phi_{yz} + g \phi_y = 0$$

on $\zeta = \zeta(x, z)$.

Hermans introduces the perturbation potential φ is $O(\phi^0)$ if $U \rightarrow 0$ in coordinates along the equator streamline, which are stretched with the length U^2/g in the field

$$x' = \frac{xg}{U^2}, \quad y' = \frac{yg}{U^2}, \quad z = z$$

Then

$$\frac{\partial \varphi}{\partial z} \ll \frac{\partial \varphi}{\partial x}, \quad \frac{\partial \varphi}{\partial y}$$

and φ satisfies the 2D Laplace equation

$$\varphi_{x'x'} + \varphi_{y'y'} = 0$$

In these coordinates the non-linear surface condition for $(\phi + \varphi)$ is linearized with respect to φ . We put $\phi = U\chi(x, y, z)$ and remark that χ_y is of order U^2 . So with U small, we retain only

$$\varphi_y + \frac{U^2}{g} [\chi_x^2 \varphi_{xx} + 2 \chi_x \chi_{xz} \varphi_x + 2 \chi_z \chi_{xz} \varphi_z] = 0$$

Remark, that in the 2D case for $x = x' = 0$:

$\chi_x = 0$, but in our case χ_x, χ_z and χ_{xz} do not vanish.

Anyhow, compared to the "wave length" U^2/g χ is

a slowly varying quantity with $\chi_x = O(1)$.
Hence we follow Hermans in putting as the free surface condition for φ in the stretched coordinates at $y' = 0$

$$\varphi_{y'} + \chi_x \varphi_{x'x'} = 0$$

where $\chi_x \rightarrow 1$ for $x' \rightarrow \infty$.

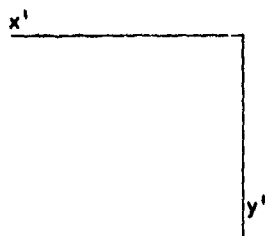
Remark, that in our case, in contrast to the 2D case $\chi_x = k$ can be considered as a slowly varying function because of the absence of a stagnation point. Hence with a reasonable approximation we can write the boundary value problem for φ in the stretched coordinates

$$\varphi_{x'x'} + \varphi_{y'y'} = 0$$

for $x' < 0$ $y' < 0$

$$\varphi_{y'} + k(x) \varphi_{x'x'} = 0, \quad y' = 0$$

$$\varphi_{x'} = f(y') \quad \text{for } x' = 0$$



The solution is given in the paper of Hermans and is reproduced in a simplified version in Appendix C.

REFERENCES

1. J.N. Newman, "Applications of slender body theory in ship hydrodynamics" Annual Review Fluid Mechanics, 1970, 2, 67-94.
2. T.F. Ogilvie, "Singular Perturbation problems in ship hydrodynamics", 8th O.N.R. Symposium, Pasadena.
3. T.F. Ogilvie, "The waves generated by a fine ship bow", 9th Symposium on Naval Hydrodynamics", Paris 1972.
4. A.J. Hermans, "A matching principle in non linear ship wave theory at low Froude number" Delft Progress Reports, Series F. Vol.1 (1974)
5. H. Lamb, "Hydrodynamics 8th ed."
6. J.V. Wehausen and E.V. Laitone, "Handbuch der Physik", Band 9, Strömungsmechanik III, Springer Verlag, p. 489.

APPENDIX A

The flow round a three axial ellipsoid.

The transformation formulae to ellipsoidal coordinates are

$$x^2 = \frac{(a^2 + \lambda)(a^2 + \mu)(a^2 + v)}{(a^2 - b^2)(a^2 - c^2)}$$

$$y^2 = \frac{(b^2 + \lambda)(b^2 + \mu)(b^2 + v)}{(b^2 - c^2)(b^2 - a^2)}$$

$$z^2 = \frac{(c^2 + \lambda)(c^2 + \mu)(c^2 + v)}{(c^2 - a^2)(c^2 - b^2)}$$

$$\frac{dx}{d\lambda} = \frac{x}{2(a^2 + \lambda)}, \quad \frac{dy}{d\lambda} = \frac{y}{2(b^2 + \lambda)}$$

$$\frac{dz}{d\lambda} = \frac{z}{2(c^2 + \lambda)}, \quad \text{e.t.c.}$$

$$\frac{d\lambda}{dx} = 2x \frac{(b^2 + \lambda)(c^2 + \lambda)}{(\lambda - \mu)(\lambda - v)}$$

$$\frac{d\lambda}{dy} = 2y \frac{(a^2 + \lambda)(c^2 + \lambda)}{(\lambda - \mu)(\lambda - v)}$$

$$\frac{d\lambda}{dz} = 2z \frac{(a^2 + \lambda)(b^2 + \lambda)}{(\lambda - \mu)(\lambda - v)}$$

and the perturbation potential is

$$\varphi = \frac{Ux}{2 - \alpha_0} abc \int_1^\infty \frac{d\lambda}{(a^2 + \lambda) \Delta(\lambda)}$$

This gives the velocity components at the surface $\lambda = 0$

$$U + \frac{\partial \varphi}{\partial x} = \frac{U}{2 - \alpha_0} - \frac{2Ux}{2 - \alpha_0} \frac{x^2}{a^2} \frac{b^2 c^2}{\mu v},$$

$$\frac{\partial \varphi}{\partial y} = -\frac{2U}{2 - \alpha_0} \frac{xy}{a^2} \frac{a^2 c^2}{\mu v},$$

$$\frac{\partial \varphi}{\partial z} = -\frac{2U}{2 - \alpha_0} \frac{xz}{a^2} \frac{a^2 b^2}{\mu v}$$

The product μv is found from the fact, that the equation

$$\frac{x^2}{a^2 + \theta} + \frac{y^2}{b^2 + \theta} + \frac{z^2}{c^2 + \theta} = 1$$

has one root $\lambda = 0$. The result is

$$\begin{aligned} \mu v &= a^2 b^2 + \frac{b^2(c^2 - a^2)}{a^2} x^2 + \frac{a^2(c^2 - b^2)}{b^2} y^2 = \\ &= a^2 c^2 + \frac{c^2(b^2 - a^2)}{a^2} x^2 + \frac{a^2(b^2 - c^2)}{c^2} z^2 = \\ &= c^2 b^2 + \frac{b^2(a^2 - c^2)}{c^2} z^2 + \frac{c^2(a^2 - b^2)}{b^2} y^2. \end{aligned}$$

We now put

$$\frac{x}{a} = \xi, \quad \frac{y}{b} = \eta, \quad \frac{z}{c} = \zeta$$

then

$$\xi^2 + \eta^2 + \zeta^2 = 1$$

Near the forward stagnation point, $\eta = -1, \zeta = 0$ we have for small values of η and ζ

$$\xi = -\left(1 - \frac{1}{2}(\eta^2 + \zeta^2) - \dots\right)$$

$$u = \frac{2U}{2 - \alpha_0} \left[1 - \frac{1 - \eta^2 - \zeta^2}{1 - \left(\frac{a^2}{c^2} - 1\right)\eta^2 + \left(\frac{a^2}{b^2} - 1\right)\zeta^2} \right]$$

$$v = \frac{2U}{2 - \alpha_0} \frac{\eta \sqrt{1 - \eta^2 - \zeta^2}}{1 - \left(\frac{a^2}{c^2} - 1\right)\eta^2 + \left(\frac{a^2}{b^2} - 1\right)\zeta^2} \sim$$

$$\sim \frac{2U}{2 - \alpha_0} \frac{a}{b} \eta \left\{ 1 + \left(\frac{a^2}{c^2} - \frac{3}{2}\right)\zeta^2 - \left(\frac{a^2}{b^2} - \frac{1}{2}\right)\eta^2 + \dots \right\}$$

$$w = \frac{2U}{2 - \alpha_0} \frac{\zeta \sqrt{1 - \eta^2 - \zeta^2}}{1 - \left(\frac{a^2}{c^2} - 1\right)\eta^2 + \left(\frac{a^2}{b^2} - 1\right)\zeta^2} \sim$$

$$\sim \frac{2U}{2 - \alpha_0} \frac{a}{c} \zeta \left\{ 1 + \left(\frac{a^2}{c^2} - \frac{3}{2}\right)\zeta^2 - \left(\frac{a^2}{b^2} - \frac{1}{2}\right)\eta^2 + \dots \right\}$$

These expansions are only valid for

$$\left| \frac{a}{c} \zeta \right| \ll 1$$

and

$$\left| \frac{a}{b} \eta \right| \ll 1$$

i.e. for small values of $\frac{c}{a}$ and moderate values of $\frac{b}{a}$ there is only a small band along the equator where this behaviour is representative.

The behaviour of the streamlines close to the origin follows from

$$v = b \dot{\eta} = \frac{2U}{2 - \alpha_0} \frac{a}{b} \eta$$

$$w = c \dot{\zeta} = \frac{2U}{2 - \alpha_0} \frac{a}{c} \zeta$$

or

$$\eta = C_1 \exp\left\{ \frac{2U a}{(2 - \alpha_0) b} t \right\}$$

$$\zeta = C_2 \exp\left\{ \frac{2U a}{(2 - \alpha_0) c} t \right\}$$

This gives for the streamlines the equation

$$\zeta = C \eta^{(b/c)^2}$$

For moderate values of b/c the streamlines follow closely the equator, dependent on C .

As soon as ζ reaches a value where the approximation is no longer valid, there is a rapid change in behaviour and the streamlines follow the middle region, to which we now turn our attention.

We assume

$$\frac{c}{a} = \varepsilon \ll 1 \quad \text{and} \quad \delta = \frac{c}{b} < 1$$

We introduce coordinates $\eta = \frac{y}{a\varepsilon}$ and $\xi = \frac{z}{a\varepsilon}$

and remark that

$$\left(\frac{x}{a}\right)^2 = 1 - \delta^2 \eta^2 - \xi^2$$

Then the velocity field is

$$\begin{aligned} u &\approx U \frac{2}{2 - \alpha_0} - \frac{2U}{2 - \alpha_0} \left(\frac{x}{a}\right)^2 \cdot \\ &\quad \cdot \frac{\delta^2 \varepsilon^2}{\delta^2 \eta^2 + \xi^2 \delta^{-2} + \delta^2 \eta^2} \sim \\ &\sim \frac{2U}{2 - \alpha_0} \left(1 - \left(\frac{x}{a}\right)^2 \frac{\varepsilon^2}{\delta^2 \eta^2 + \xi^2 \delta^{-2} + \delta^2 \eta^2} \right) \end{aligned}$$

$$v \approx \frac{-2\kappa}{2-\alpha_0} \frac{x}{a} \varepsilon \frac{\eta \gamma^4}{\xi^2 + \gamma^4 \eta^2}$$

$$w \approx \frac{-2\kappa}{2-\alpha_0} \frac{x}{a} \varepsilon \frac{\xi \gamma^4}{\xi^2 + \gamma^4 \eta^2}$$

i.e. the perturbation on the x component is of order ε^2 , but the y and z components are of order ε .

They correspond exactly to the result of the slender body theory, except for the factor α_0 , which can be shown to be of order $\varepsilon^2 \ln \varepsilon$.

APPENDIX E

Solution of the boundary value problem for the vertical ellipsoid.

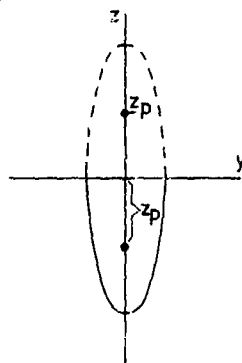
For the vertical ellipsoid (Ogilvie's problem), we have to determine a function $\phi(y, z, x)$ from the conditions

$$\phi_{,y} + \phi_{,zz} = 0$$

with

$$\kappa \phi_{,xx} + \phi_{,z} = 0, \quad z = 0$$

$$\phi_y = \pm U b_x(x, z), \quad y = 0$$



We try to obtain the solution by a superposition of sources of strength Ub_x along the negative z axis, but in order to avoid differentiation of the intensity with respect to x (x is a parameter in the problem.) we add a set of negative sources in the upper half plane.

Hence we assume, with $\xi = y + iz$

$$\begin{aligned} \tilde{\phi}(\xi; x) &= \phi(y, z; x) + i \psi(y, z; x) \\ &= \frac{\sigma(x)}{2\pi} \left\{ \log(\xi - iz_p) + \log(\xi + iz_p) \right\} \\ &\quad + \mathcal{F}(\xi; x) \end{aligned}$$

where $\mathcal{F}(\xi; x)$ is regular in the neighbourhood of iz_p and $-iz_p$.

The boundary condition for $z = 0$ becomes:

$$\text{Im} \{ -i \kappa \tilde{\phi}_{,xx} + \tilde{\phi}_{,\xi} \} = 0$$

or

$$\begin{aligned} \text{Im} \{ -i \kappa \mathcal{F}_{,xx} + \mathcal{F}_{,\xi} \\ - i \kappa \frac{d^2}{dx^2} \frac{\sigma(x)}{2\pi} \log(\xi^2 + z_p^2) \} = 0 \end{aligned}$$

on $z = 0$.

The function

$$f(\xi; x) = -i \kappa \mathcal{F}_{,xx} + \mathcal{F}_{,\xi} - i \kappa \frac{d^2}{dx^2} \frac{\sigma(x)}{2\pi} \log(\xi^2 + z_p^2)$$

is regular in the entire ξ plane and is real for $z = 0$, hence it is identically zero and \mathcal{F} is the solution of the non-homogeneous diffusion equation

$$\mathcal{F}_{,\xi} = i \kappa \mathcal{F}_{,xx} + i \kappa \frac{d^2}{dx^2} \frac{\sigma(x)}{2\pi} \log(\xi^2 + z_p^2)$$

From the condition that for $x \rightarrow \infty$ the solution must pass into the ordinary slender body solution we derive that $\mathcal{F} \rightarrow 0$ for $x \rightarrow \infty$.

The theory of the diffusion equation gives for the Green's function

$$\int_0^{\xi} \frac{d\xi}{\{i\pi(\xi_p - \xi)\}^{\frac{1}{2}}} e^{-\frac{(\xi - x_p)^2}{4i\pi(\xi_p - \xi)}}$$

and so the solution of the non-homogeneous equation is:

$$\begin{aligned} \bar{\phi}(\xi_p; x_p) &= \frac{\sigma(x)}{2\pi} \log(\xi^2 + \xi_p^2) + \\ &+ \int_0^{\xi_p} \frac{d\xi}{\{i\pi(\xi_p - \xi)\}^{\frac{1}{2}}} \int_0^{\infty} \frac{e^{-\frac{(\xi - x_p)^2}{4i\pi(\xi_p - \xi)}}}{\xi^2 + \xi_p^2} \frac{d\xi}{2\pi} \log(\xi^2 + \xi_p^2) d\xi \end{aligned}$$

For the function

$$\bar{\phi} = \frac{\sigma(x)}{2\pi} \log(\xi^2 + \xi_p^2) + \bar{\phi}^*$$

we obtain the representation

$$\begin{aligned} \bar{\phi}(\xi_p; x_p) &= \int_0^{\xi_p} \frac{d\xi}{\{i\pi(\xi_p - \xi)\}^{\frac{1}{2}}} \frac{2\xi}{\xi^2 + \xi_p^2} \\ &\int_0^{\infty} \frac{e^{-\frac{(\xi - x_p)^2}{4i\pi(\xi_p - \xi)}}}{\xi^2 + \xi_p^2} \sigma(\xi) d\xi \end{aligned}$$

Application of the method of stationary phase shows that for $x_p \rightarrow \infty$ $\bar{\phi}(\xi_p, x_p)$ approaches the ordinary slender body theory result.

APPENDIX C

Solution of the boundary value problem for the horizontal ellipsoid.

The boundary value problem is

$$\phi_{yy} + \phi_{zz} = 0, \quad z < 0, \quad y < 0$$

with

$$\frac{\partial \phi}{\partial z} + k(y) \frac{\partial^2 \phi}{\partial y^2} = 0, \quad z = 0, \quad y < 0$$

$$\frac{\partial \phi}{\partial y} = g(z), \quad z < 0, \quad y = 0$$

We solve this problem by a superposition of source potentials on the negative z axis.

Such a source potential G has a logarithmic singularity in a point $z = z_p$ ($z_p < 0$) and satisfies the boundary condition at $z = 0$.

Hence we put, with $\xi = y + iz$

$$G(\xi, z_p) = \ln(\xi - iz_p) + \alpha(\xi)$$

which has to satisfy the condition

$$\Im \left(ik \frac{\partial^2 G}{\partial \xi^2} - \frac{\partial G}{\partial \xi} \right) = 0 \quad \text{on } \Im \xi = 0$$

Consider now

$$\begin{aligned} f(\xi) &= ik \frac{\partial^2 G}{\partial \xi^2} - \frac{\partial G}{\partial \xi} = \\ &= ik \frac{\partial^2}{\partial \xi^2} \ln(\xi - iz_p) - \frac{1}{\xi - iz_p} + \\ &+ ik \frac{\partial^2 \alpha}{\partial \xi^2} - \frac{\partial \alpha}{\partial \xi} \end{aligned}$$

which has a singularity near $\xi = iz_p$. $f(\xi)$ is an analytic function which assumes real values on the real axis and from Schwartz's principle of symmetry

$$f(\bar{\xi}) = \overline{f(\xi)}$$

Hence $f(\xi)$ must also have a singularity near $\xi = -iz_p$. This leads to put

$$\begin{aligned} f(\xi) &= ik \frac{\partial}{\partial \xi} \frac{1}{\xi - iz_p} - \frac{1}{\xi - iz_p} + \\ &- ik \frac{\partial}{\partial \xi} \frac{1}{\xi + iz_p} - \frac{1}{\xi + iz_p} + f_1(\xi) \end{aligned}$$

where $f_1(\xi)$ is holomorphic in the complete plane including infinity and hence can be taken to vanish.

This leads to the equation for G

$$ik \frac{\partial^2 G}{\partial \xi^2} - \frac{\partial G}{\partial \xi} = -ik \frac{\partial}{\partial \xi} \frac{2z_p}{\xi^2 + z_p^2} - \frac{2\xi}{\xi^2 + z_p^2}$$

We now put

$$G = \ln(\xi - iz_p) - \ln(\xi + iz_p) + H(\xi)$$

and obtain the following equation for

$$\frac{dH}{d\xi} = K(\xi)$$

$$ik(\xi) \frac{dK}{d\xi} - K = \frac{2}{\xi - iz_p}$$

With the function

$$s(\xi) = \int \frac{d\xi'}{k(\xi')}$$

we obtain the solution for this function K

$$K(\xi) = 2e^{-is(\xi)} \int_L^\xi \frac{e^{is(\xi')}}{\xi' - iz_p} d\xi'$$

where the contour avoids the singular point.

The function

$$\frac{dG}{d\xi} = \frac{2\xi}{\xi^2 + z_p^2} + 2e^{-is(\xi)} \int_L^\xi \frac{e^{is(\xi')}}{\xi' - iz_p} d\xi'$$

gives the velocity distribution of the source potential.

If $k(\xi)$ has a constant value we find back

the well known formula for a moving point source. (e.g. Wehausen p. 489).

About the function

$$s(\xi) = \int \frac{d\xi}{k(\xi)}$$

we remark that the integral diverges and hence $s(\xi)$ is infinite if $k(\xi) = 0$ at the lower end of the path of integration, i.e. if we have a stagnation point of the first approximation. In this case the integral $K(\xi)$ does not exist. In the 2D case the whole equator is a line of the stagnation points but for the ellipsoid this is only the case in the forward point, now along the equator $k(0)$ has a finite value, so here we have a wave travelling from the ellipsoid, i.e. a bow wave. More accurate calculations, based on a second approximation for the undisturbed non-wave flow should be carried out.

EXTENSION, ANALYSIS, AND IMPROVEMENT OF PERTURBATION SERIES

M. Van Dyke
Stanford University
Stanford, California 94305

ABSTRACT

A three-step program is described for enlarging the range of utility of the power-series solution of a regular-perturbation problem. First, the number of terms is extended by delegating the arithmetic labor to a computer. Second, the coefficients are examined to reveal the analytic structure of the solution. Third, transformations suggested by that structure are applied to improve the accuracy and extend the range of convergence. The potentialities of this approach are illustrated by four examples from various branches of fluid mechanics, including gas dynamics, laminar viscous flow, and water waves.

INTRODUCTION

Most perturbation solutions are based on a systematic expansion procedure, so that in principle the approximation can be continued to indefinitely high order. If the scheme proves successful, however, the first or second approximation is usually adequate for practical purposes. This happens when the perturbation quantity, which has been regarded as infinitesimal in the formal expansion, actually assumes only small values in practice.

This happy situation does not prevail, however, when the perturbation quantity is not naturally small, but has been assumed small only out of desperation, in order to open a chink in an intractable problem. Then one wants to apply the results to values of the perturbation quantity that are large — perhaps even infinite. Under these circumstances one might hope to extend the range of utility of the approximation by calculating a great many terms.

Two major difficulties stand in the way of thus enlarging the range of a perturbation series. First, the labor involved — and hence also the possibility of error in hand calculation — grows rapidly with the number of terms. Thus, although a great variety of problems in fluid mechanics has been treated in this way, the writer knows of no expansion for a significant problem that has been carried beyond ten terms by hand; and it is typical that many of those calculations turn out to suffer from errors in the last few coefficients.

Second, if a few terms prove inadequate, it is likely that the series is being used close to (or even beyond) its limit of convergence. If so, its utility cannot be appreciably improved simply by adding

more terms.

Fortunately, both these difficulties can be alleviated. The labor of calculating higher terms can be delegated to a digital computer, which executes it not only thousands of times faster than a human computer, but without error. Then analysis of a sufficiently large number of coefficients will reveal at least the main analytic structure of the solution. Finally, that knowledge often serves to suggest one or more of a battery of transformations that can be applied to improve and enlarge the convergence of the series.

The combination of these three steps is essential: extension, analysis, and improvement — each is of little value without the other two. Together, in favorable problems they can produce dramatic results.

This three-step program has so far been significantly developed only for regular perturbations — approximations where the solution is found as a formal series in integral powers of the perturbation quantity. For singular perturbations, where the series may involve fractional powers and logarithms, neither extension, analysis, nor improvement has yet been systematically developed to any useful extent.

In this paper we illustrate the potentialities of this program by applying it to four problems in fluid mechanics. Our examples necessarily date only from the age of mass computers, which began in the 1950's; but each has its roots in an older hand computation. Other examples are discussed in reference 1, which presents a general survey of computer extension; and a more detailed discussion of the analysis and improvement of perturbation series, based on a set of examples from viscous flow theory, is given in reference 2.

COMPUTER EXTENSION OF SERIES

Principles of computer application

We are not concerned here with programming the computer to do our algebra. Non-numerical computer languages have been developed that carry out the literal operations of algebra and trigonometry; and they have been used to calculate the successive terms of a perturbation series in symbolic form. (Reference 3 gives an excellent survey of this subject.) However, that technique is typically applied to problems so complicated that only a few terms can be calculated even by machine. In any case, there

remains the task of numerically evaluating the symbolic results.

We consider instead problems sufficiently simple that recursion relations for successive terms in the perturbation series can be conveniently derived by hand, but the arithmetic labor mounts so rapidly that no more than five or ten terms can be evaluated by hand. When this arithmetic is delegated to the computer, dozens or even hundreds of terms can be calculated in a few seconds or minutes. The limiting factor is usually storage or loss of significance, rather than cost in computing time.

Thus the extension can be carried out using a standard language such as Fortran. A program typically consists mainly of nested "do" loops. In principle the coefficients, which are usually rational fractions, could be calculated precisely using integer arithmetic. However, it ordinarily seems preferable to accept the gradual erosion of significance that results from floating-point arithmetic; for integer arithmetic complicates the program, the integers quickly become enormous, and the unwieldy fractions must ultimately be evaluated as floating-point numbers in order to be comprehended. Repeating the calculations with single- and double-precision arithmetic appears to provide an adequate if not rigorous estimate of accuracy.

Flow Behind a Detached Bow Shock Wave

The earliest computer extensions were made in gas dynamics. The first appears to be Richtmyer's attempt (4) in 1957 to calculate axisymmetric supersonic flow past a blunt body using the inverse approach of supposing the bow shock wave known, and expanding the flow downstream in a double Taylor series. This approximation, introduced in 1948 by Lin and Rubinov (5), had been carried furthest by hand by Cabannes, who used cylindrical coordinates and calculated the coefficients of the fifth approximation (6) for adiabatic exponent $\gamma = 7/5$ and arbitrary free-stream Mach number M , and the seventh approximation (7) for $M = 2$. Richtmyer programmed the Univac computer to calculate the 15th approximation for a hyperboloidal shock wave at $M = 12$, using sheared coordinates with origin on the shock wave (Fig. 1). These calculations were later extended by Moran (8) and others.

As an example, we consider a paraboloidal shock wave of unit nose radius at $M = \infty$ with $\gamma = 7/5$. Cabannes's series gives the dimensionless Stokes stream function as

$$2\psi = r^2(1 - 10x - 5x^2 + \frac{550}{9}x^3 - \frac{15,515}{54}x^4 + \dots) + r^4(5 + 20x + \frac{75}{9}x^2 + \dots) + r^6(-\frac{25}{4} + \dots) + \dots \quad (1)$$

If for simplicity we restrict attention to the neighborhood of the axis $r = 0$, Moran's computer extension of this series gives

$$\frac{2\psi}{r^2} = 1 - 10x - 5x^2 + \frac{550}{9}x^3 - \frac{15,515}{54}x^4 + 1.289877 \times 10^3 x^5 - 9.031236 \times 10^4 x^6$$

$$\begin{aligned} &+ 8.628293 \times 10^3 x^7 - 8.047653 \times 10^5 x^8 \\ &+ 7.856042 \times 10^6 x^9 - 7.979608 \times 10^7 x^{10} \\ &+ 8.359180 \times 10^8 x^{11} - 8.979015 \times 10^9 x^{12} \\ &+ 9.845870 \times 10^{10} x^{13} - 1.098497 \times 10^{12} x^{14} \\ &+ \dots \end{aligned} \quad (2)$$

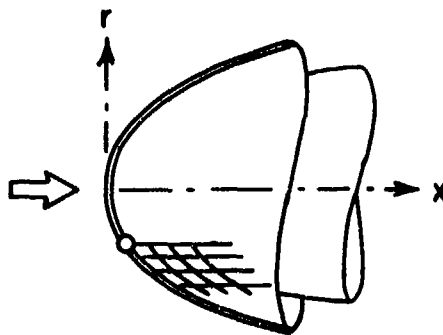


Fig. 1 Cylindrical (above) and sheared (below) coordinates for axisymmetric shock wave

Transonic Flow Through a Nozzle

In 1908 Meyer (9) calculated the potential flow near the throat of a symmetric plane Laval nozzle (Fig. 2). Assuming a linear velocity distribution along the axis: $u(x, 0) = 1 + x$ in dimensionless terms, he expanded the velocity potential in a double Taylor series in Cartesian coordinates, and computed the coefficients of terms up to sixth order in x and y .

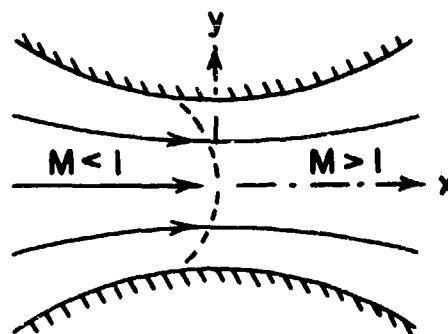


Fig. 2 Flow near throat of symmetrical nozzle

Fifty years later Martensen and von Sengbusch (10) programmed the Göttingen G2 computer to extend that series (and its axisymmetric counterpart) to 23rd order. Thus, for example, they find the axial velocity component as

$$u(x, y) = \sum_{i=0}^{i+2j=22} \sum_{j=0} a_{ij} (8x)^i (4y)^{2j} \quad (3)$$

(The scale factors 8 and 4 were inserted to suppress excessive growth of the coefficients.)

For simplicity, we consider conditions at the section $x = 0$. There only 23 of the 144 coefficients remain, giving for $\gamma = 7/5$

$$u(0, y) = 1 + \frac{3}{40}(4y)^2 + \frac{141}{16,000}(4y)^4 + \frac{6453}{3,200,000}(4y)^6 + 6.08975 \times 10^{-4}(4y)^8 + 2.096460 \times 10^{-4}(4y)^{10} + 7.76981 \times 10^{-5}(4y)^{12} + 3.02114 \times 10^{-5}(4y)^{14} + 1.21556 \times 10^{-5}(4y)^{16} + 5.0183 \times 10^{-6}(4y)^{18} + 2.1137 \times 10^{-6}(4y)^{20} + 9.048 \times 10^{-7}(4y)^{22} + \dots \quad (4)$$

Laminar Flow Through Slowly Varying Channel

In 1910 Blasius (11) calculated the steady viscous flow through a symmetrical plane channel (Fig. 3) by perturbing the Poiseuille solution for constant width.

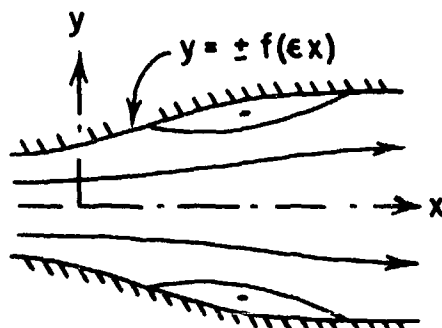


Fig. 3 Laminar flow through slowly varying channel

It is convenient to describe a slowly varying channel by $y = \pm f(\epsilon x)$. Then expanding the stream function in powers of ϵ gives

$$\psi = \left(\frac{3}{2}\eta - \frac{1}{2}\eta^3\right) + \frac{3}{280}\epsilon R f'(5\eta - 11\eta^3 + 7\eta^5 - \eta^7) + \epsilon^2 \left\{ \frac{3}{20}(ff'' - 4f'^2)(-\eta + 2\eta^3 - \eta^5) + \frac{R^3}{431,200}(ff''(-1213\eta + 3279\eta^3 - 3234\eta^5) + 1519\eta^7 - 385\eta^9 + 35\eta^{11}) + f'^2(2875\eta - 8222\eta^3 + 8778\eta^5 - 4488\eta^7 + 1155\eta^9 - 88\eta^{11}) \right\} + O(\epsilon^3). \quad (5)$$

Here R is the Reynolds number based on half the volumetric flow rate, and $\eta = y/f$ is the fractional distance across the channel at any station. The first term is due to Poiseuille, the second to Blasius, and part of the third was given by Abramowitz (12).

Lucas (13) observes that this series has the general form

$$\psi = \sum_{n=0}^{\infty} \epsilon^n \sum_{m=n, n-2, \dots}^{(m \geq 0)} R^m \sum_{k=1}^{K(n)} F_k^n(f) \sum_{i=1, 3, \dots}^{n+3m+3} A_{nmki} \eta^i \quad (6)$$

where F_k^n is a two-dimensional array with elements that depend on f through its first n derivatives, and $K(n)$ is the number of distinct ways that n indistinguishable objects can be placed in n indistinguishable boxes. He programmed the IBM 360/87 computer, using the PL/1 programming language, and in 23 minutes of execution time calculated the 227,018 coefficients of this series through ϵ^{12} . He also extended the series to higher order for special channel shapes and specific values of Reynolds number.

We quote one of his results for the exponential channel, described by $f(\epsilon x) = e^{\epsilon x}$, at $R = 17.5$. The dimensionless skin friction on the wall is given by the series in $X = \epsilon e^{\epsilon x}$

$$\psi_{\eta\eta/\eta=1} = 3 - 6X - \frac{393}{55}X^2 + 10.274X^3 + 10.938X^4 - 17.568X^5 + 23.511X^6 - 43.083X^7 + 105.11X^8 - 489.76X^9 + 2574.6X^{10} - 17.074X^{11} + \dots - 2.0999 \times 10^{17}X^{23} + 3.9561 \times 10^{18}X^{24} - \dots \quad (7)$$

Steady Periodic Waves in Deep Water

In 1849 Stokes (14) approximated the steady motion of plane periodic surface waves in deep water by expanding for small amplitude. Thus, for example, he found for the free surface (Fig. 4), the series

$$y = a \cos x + \frac{1}{2}a^2(1 + \cos 2x) + \frac{1}{8}a^3(9 \cos x + 3 \cos 3x) + \dots \quad (8)$$

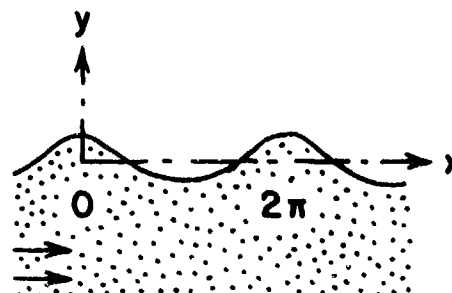


Fig. 4 Steady gravity waves

Evidently this is an expansion in powers of the amplitude of the infinitesimal wave. The higher terms tend to sharpen the crests and flatten the

troughs; and Stokes conjectured that his series would converge up to a highest wave having the sharp 120-degree cusp implied by a local analysis.

Thirty-one years later, while preparing his collected papers for publication, Stokes noticed that the calculations could be simplified by taking the velocity potential and stream function as independent rather than dependent variables; and he thus extended his series to fifth order. In 1914 Wilton (15) carried the computation to tenth order.

Schwartz (16) has programmed the IBM 360/67 computer in the Fortran IV language to extend Stokes's series, and calculated the 70th approximation in less than a minute. He finds that Wilton's hand computation is erroneous beyond the seventh order. A significant derived quantity is the wave height, for which Schwartz finds

$$h = \frac{1}{2}[y(0) - y(\pi)] = a + \frac{3}{2}a^3 + \frac{163}{24}a^5 + \frac{62047}{1440}a^7 + \frac{12,106,343}{37,800}a^9 + 2.607438 \times 10^3 a^{11} + 2.251536 \times 10^4 a^{13} + \dots + 5.414178 \times 10^{32} a^{69} + 5.868697 \times 10^{33} a^{71} + \dots \quad (9)$$

Parameter and Coordinate Expansions

A perturbation series is usefully classified as to whether the small quantity is a parameter in the problem or a coordinate. We see that both parameter and coordinate perturbations have been extended by computer. Stokes's series (8) for water waves is a parameter expansion, whereas the series for flow behind a detached shock wave and Meyer's series (3) for transonic flow in a nozzle are both double coordinate expansions. The Blasius series for laminar flow in a channel is a quadruple expansion (6), double in coordinates and parameters; but for the skin friction on an exponential channel at fixed Reynolds number (7) it reduces to a single coordinate expansion.

This distinction is of physical significance, and affects the details of computer extension. It is irrelevant, however, for the analysis and improvement that we discuss next.

ANALYSIS OF COEFFICIENTS

A great deal of information lies concealed in the multiple digits of the many coefficients in each of the preceding examples. In particular, the analytic structure of the solution awaits unveiling. We show how an analysis of the coefficients reveals that structure to a greater or lesser extent in each problem.

The Pattern of Signs

In each of our four examples a regular pattern of signs is established no later than the fifth term of the series. The signs ultimately alternate in the series for the blunt body (Eq. 2) and the viscous channel (Eq. 7), and become fixed for the transonic nozzle (Eq. 4) and the gravity waves (Eq. 9).

If a power series has a finite radius of convergence, fixed signs indicate that the nearest singularity lies on the positive real axis, as for the model function

$$\frac{1}{1-\epsilon} = 1 + \epsilon + \epsilon^2 + \epsilon^3 + \epsilon^4 + \dots \quad (10)$$

whereas alternating signs mean that it lies on the negative axis, as for

$$\frac{1}{1+\epsilon} = 1 - \epsilon + \epsilon^2 - \epsilon^3 + \epsilon^4 - \dots \quad (11)$$

If the radius of convergence is infinite, fixed signs mean that the function grows most rapidly along the positive real axis and most slowly along the negative axis, and conversely for alternating signs. If the radius of convergence is zero, the signs usually alternate in a physical problem, though not always.

A Graphical Ratio Test

Our most useful analytical device is a graphical version of the D'Alembert ratio test, according to which the radius of convergence R of the power series $\sum c_n \epsilon^n$ is

$$R = \lim_{n \rightarrow \infty} |c_{n-1}/c_n| \quad (12)$$

Domb and Sykes (17) observed that this limit is most accurately estimated from a finite number of coefficients by plotting the inverse ratio c_n/c_{n-1} versus $1/n$, and extrapolating to $1/n = 0$ to find $1/R$. The reason is that in many physical problems the nearest singularity is of the form

$$\text{const.} \begin{cases} (R \pm \epsilon)^\alpha, & \alpha \neq 0, 1, 2, \dots \\ (R \pm \epsilon)^\alpha \log(R \pm \epsilon), & \alpha = 0, 1, 2, \dots \end{cases} \quad (13)$$

and for these simple functions the extrapolation is precisely linear:

$$\frac{c_n}{c_{n-1}} = \mp \frac{1}{R} \left(1 - \frac{1+\alpha}{n}\right) \quad (14)$$

The nature of the nearest singularity can be estimated at the same time, since Eq. (14) shows that the exponent α is related to the ultimate slope of c_n/c_{n-1} versus $1/n$. Hence in making the linear extrapolation one naturally tends to favor slopes that correspond to simple values of that exponent.

Paraboloidal Bow Shock Wave

We analyze our four examples using these ideas. For the flow downstream of a paraboloidal shock wave, the alternation of signs in Eq. (2) means that the singularity that limits convergence does not lie in the region of physical interest, but rather in its analytical continuation upstream through the shock.

The radius of convergence can be estimated from the Domb-Sykes plot of Fig. 5. After some initial oscillation, the ratios become remarkably linear; and it seems clear that the slope corresponds to a $3/2$ -power singularity. On that basis the intercept is

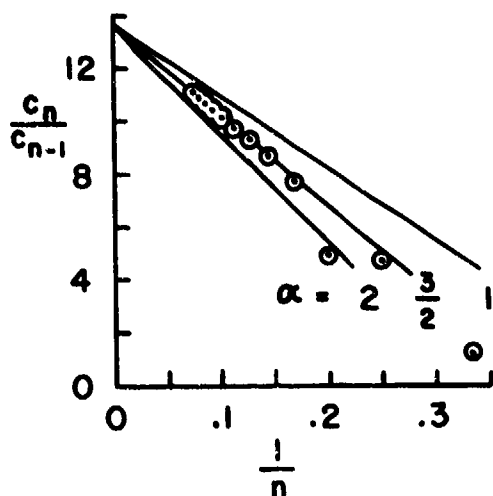


Fig. 5 Domb-Sykes plot for stream function near axis of paraboloidal shock wave

found as 13.6 to three figures, so that the radius of convergence is 0.074.

These results agree with the writer's conclusion (18) in 1958 that a limit line, or envelope of characteristics, lies ahead of the shock wave in the analytic continuation of the disturbed flow upstream (Fig. 6). For at a limit line the velocity has square-root behavior, so that its integral the stream function must show a $3/2$ -power singularity. Accurate numerical solutions (19) have shown that in this problem the nose of the body lies at $x = 0.09897$. Thus the shock wave is closer to the limit line than to the body, so that the series does not include the body in its radius of convergence.

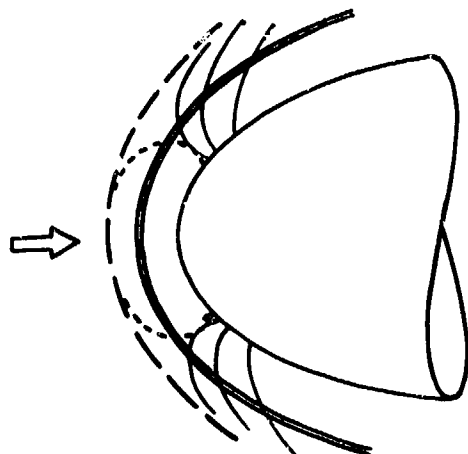


Fig. 6 Analytic continuation of disturbed flow upstream through shock wave

Transonic Nozzle

The fixed signs in Eq. (4) mean that the nearest singularity lies in the physical field for transonic flow in a nozzle. Again the Domb-Sykes plot (Fig. 7) is remarkably straight; and it clearly points to a

square-root singularity located at $(4y)^2 \approx (0.495)^{-1}$, or $y = 0.356$. This singularity is again symptomatic of a limit line, since the dependent variable is now a velocity component.

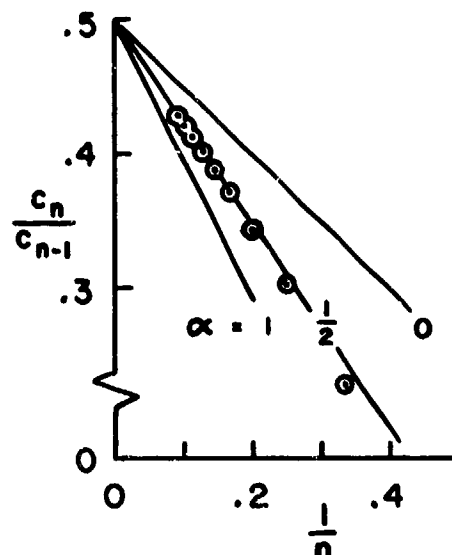


Fig. 7 Domb-Sykes plot for u across throat of transonic nozzle

No analog of the Domb-Sykes plot has been invented for double Taylor series. We can however locate other points on the boundary of convergence of the full series (Eq. 3) by examining the single series to which it reduces along various other rays through the origin. These contain odd as well as even powers of the distance except in the case just considered. However, the ratios become increasingly erratic as the slope decreases. The absence of odd powers from Eq. (4) suggests plotting the ratios of alternate terms. This gives a smoother variation, as shown in Fig. 8 for the 45-degree ray. The extrapolation must then be reinterpreted, according to

$$\frac{c_n}{c_{n-2}} = \frac{1}{R^2} \left(1 - 2 \frac{1+\alpha}{n} + \dots \right). \quad (15)$$

In this way we have traced out the domain of convergence of Meyer's double series, which is bounded by a doubly symmetric set of limit lines, as shown in Fig. 9. This may be compared with the result of Martensen and von Sengbusch, who made ingenious application of the classical method of majorants to calculate a finite region within which convergence is certain. That bound is seen to give roughly the proper shape, but to be very conservative.

Laminar Flow in Exponential Channel

Lucas observed that his series (Eq. 7) for the skin friction in an exponential channel appears to have zero radius of convergence. He therefore reinvented the ratios, plotting the classical c_{n-1}/c_n versus $1/n$, as shown in Fig. 10. This yields a linear plot

in the familiar situation of an asymptotic series whose coefficients grow like $n!$, and it seems plausible that this is the case here.

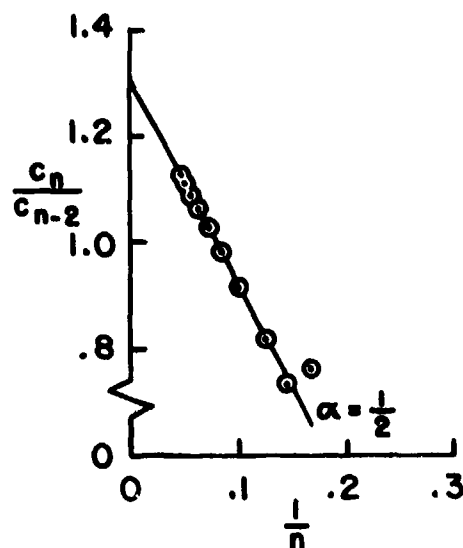


Fig. 8 Domb-Sykes plot of ratios of alternate terms for u on 45° ray from origin

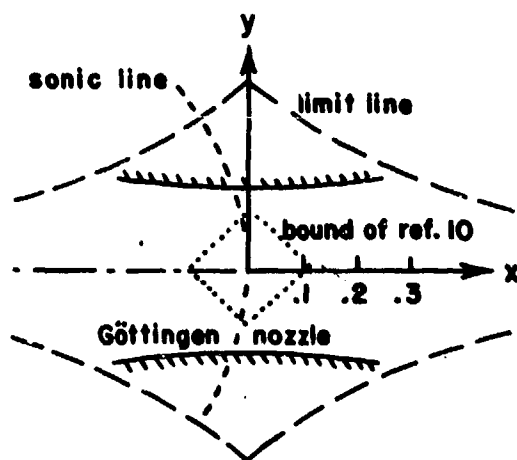


Fig. 9 Region of convergence of Meyer's series for nozzle

Gravity waves

The fixed signs in Schwartz's series (Eq. 9) for the wave height suggest that the nearest singularity has physical significance. The Domb-Sykes plot (Fig. 11) clearly indicates a square-root singularity at $a = 0.2972$. However, Schwartz noticed that this differs from the accepted value of $a = 0.292$ for the highest wave, calculated numerically by several investigators. Hence the nearest singularity appears not to correspond to the highest wave. We describe his resolution of this paradox in the following section.

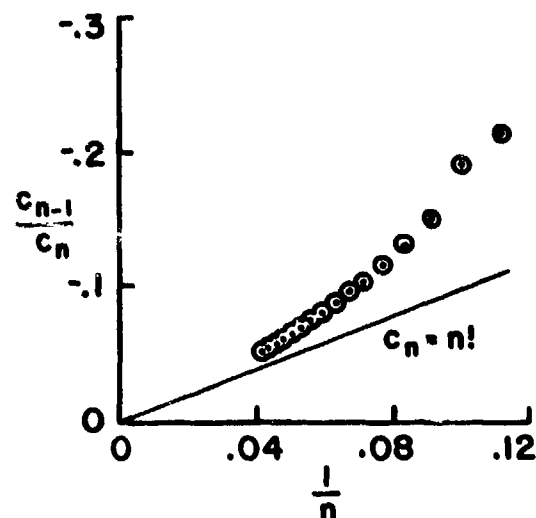


Fig. 10 Inverse Domb-Sykes plot for skin friction in exponential channel

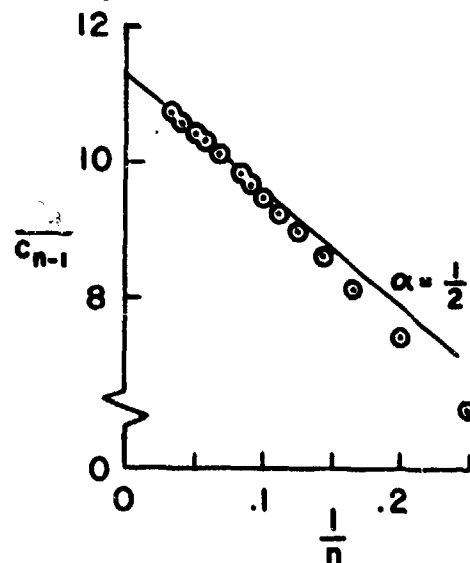


Fig. 11 Domb-Sykes plot for height of gravity waves in deep water

IMPROVEMENT OF CONVERGENCE

We have at our disposal a half dozen or more useful transformations for improving the convergence of a power series. These can be applied singly, but are often more effective in combination. An appropriate choice of transformations depends on understanding the analytic structure of the solution, at least to the extent of estimating the direction, distance, and nature of the nearest singularity, as discussed in the preceding section.

In particular, different techniques may be appropriate according as the nearest singularity lies on the positive real axis or elsewhere. On the axis, it usually represents a limit beyond which the problem loses physical meaning. Elsewhere in the complex

plane of the perturbation quantity, however, it has no direct physical significance; and we then want to perform analytic continuation of the solution as far as possible along the real axis.

We describe four of the most generally useful transformations, as applied to our four computer-extended series. Further examples, details, and discussion of other techniques are given in Ref. 2.

Reversion of Series

Stokes's series for water waves is an exception to our remark that a singularity on the positive real axis usually represents a physical limit. Schwartz (16) recognized that the square root indicated by Fig. 11 simply means that the wave height h is a double-valued function of the parameter a . At first a and h increase together, but a reaches a maximum about ten per cent short of the highest wave (Fig. 12).

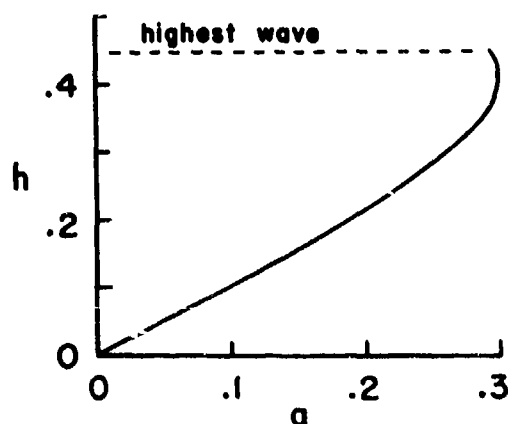


Fig. 12 Variation of wave height with Stokes's perturbation parameter

The singularity can therefore be eliminated simply by interchanging the roles of the independent and dependent variables, for a is a single-valued function of h up to the highest wave. Schwartz thus reverted the series (Eq. 9), and at the same time extended it to order 117. (This required 15 minutes on a CDC computer.) The result has the form

$$a = h - \frac{3}{2}h^3 - \frac{1}{24}h^5 - \frac{3007}{1440}h^7 - \frac{1,617,319}{302,400}h^9 - 19.16197h^{11} - 70.55874h^{13} - \dots - 1.461613 \times 10^6 h^{27} - 6.365499 \times 10^6 h^{29} - \dots - O(h^{117}) - \dots \quad (16)$$

The signs are still fixed, corresponding to a singularity on the real axis; and Schwartz has confirmed that it now corresponds to the corner in the highest wave.

Extraction of Singularity

When the nearest singularity has physical reality, it can usefully be extracted from the series to accelerate the convergence. We consider the series (Eq. 4) for u across the throat of a transonic nozzle. Figure 4 shows that it has a square-root singularity, corresponding to a limit line, at $(4y)^2 = (0.495)^{-1}$.

If u vanished there, we could either suppress the singularity by forming the series for u^2 or extract it by dividing out a factor $[1 - 495(4y)^2]^{1/2}$, and then examine the new series for additional singularities. An example from boundary-layer theory is given in reference 2. However, here the new Domb-Sykes plots indicate a square root remaining at the same location in the series for u^2 , and an inverse square root in the series from which the original square root has been extracted. This means that the square root is not the leading term, but that near the limit line u behaves like

$$u = A + B[1 - 495(4y)^2]^{1/2} + \dots \quad (17)$$

Under these circumstances the singularity has to be extracted by subtracting it rather than dividing it out. This is less accurate, because it requires an estimate of the coefficient B . Gaunt and Guttman, in a useful survey of techniques for analyzing coefficients (20), describe several systematic ways of making that estimate. However, in our example it suffices to choose B so that the coefficient of $(4y)^2$ in Eq. (17) agrees with that in the original series (Eq. 4). This gives

$$u(0, y) = -0.25943[1 - 495(4y)^2]^{1/2} + 0.74157 + 1.1039 \times 10^{-2}(4y)^2 + 7.849 \times 10^{-4}(4y)^4 + 5.76 \times 10^{-5}(4y)^6 + 2.91 \times 10^{-6}(4y)^8 - 3.5 \times 10^{-7}(4y)^{10} - 2.66 \times 10^{-7}(4y)^{12} - 1.11 \times 10^{-7}(4y)^{14} - 3.97 \times 10^{-8}(4y)^{16} - 1.22 \times 10^{-8}(4y)^{18} - 2.9 \times 10^{-9}(4y)^{20} - 0 \times (4y)^{22} - \dots \quad (18)$$

The later coefficients are now several hundred times smaller than before. Moreover, a new Domb-Sykes plot suggests (though the new coefficients are too small to be certain) that the radius of convergence is now infinite. In any case, this recast series converges very rapidly out to and including the limit line.

Euler Transformation

When the nearest singularity lies off the axis of physical significance, we are not ordinarily interested in its details. Then the simplest method of analytic continuation is to map that singularity away to infinity. This is easily accomplished by applying an Euler transformation: recasting the series in powers of the new perturbation quantity $\epsilon/(\epsilon + \epsilon_0)$ for a singularity located at $\epsilon = -\epsilon_0$. The range of convergence is thus extended to some other singularity — the nearest one

in the plane of $\epsilon/(\epsilon+\epsilon_0)$, which of course has physical significance.

We apply this transformation to the series of Eq. (2) for the paraboloidal shock wave. Figure 5 indicates a singularity at $x = -(13.6)^{-1}$. Recasting in powers of $X = x/(x+1/13.6)$ gives

$$\begin{aligned} \frac{2\psi}{r} = & 1 - .73594X - .762327X^2 - .765066X^3 \\ & - .751908X^4 - .728482X^5 - .699218X^6 \\ & - .667934X^7 - .638089X^8 - .612927X^9 \\ & - .595588X^{10} - .589072X^{11} - .596513X^{12} \\ & - .621064X^{13} - .666103X^{14} - \dots \end{aligned} \quad (19)$$

The pattern of signs shows that the nearest singularity now lies on the positive axis, and we shall see that it is inside the body. This is evidently almost a geometric series with unit radius of convergence; and that fact could be used to further improve its utility. However, the series is sufficiently accurate as it stands. It gives the zero that corresponds to the nose of the body at $X = 0.574$. Thus the surface of the body, which fell outside the range of the original series, now lies well within the radius of convergence. In terms of the original abscissa, Eq. (19) locates the nose of the body at $x = 0.0990$, which is correct to four decimals.

Padé Approximants

From a power series of order $M+N$ one can form any one of $M+N+1$ different Padé approximants — a rational fraction with numerator of degree M and denominator of degree N that reproduces the power series to order $M+N$ when expanded. In a convenient notation this is now often called the $[M/N]$ approximant. The approximants with M and N nearly equal have especially useful, though still somewhat mysterious, properties of analytic continuation. The best introduction to the use of Padé approximants is the article by Baker (21).

In particular, Padé approximants have the remarkable property of summing a divergent series whose coefficients grow like the factorial. We saw that just such a series (Eq. 7) is obtained for the skin friction in an exponential channel. Lucas (13) has recast that series using Padé approximants. Figure 13 shows that whereas the original series oscillates wildly, the $[12/11]$ and $[13/12]$ approximants are in close accord until far past the separation point.

Moran (8) used Padé approximants with great success in his solution for a detached bow shock wave. Because the classical Padé approximant deals with series in only one variable, he applied it to various fixed ratios of the coordinates in his double series. Recently Chisholm has generalized Padé approximants to two variables in a somewhat different way (22).

REFERENCES

1. Van Dyke, Milton, "Computer Extension of Perturbation Series," paper presented at Sydney

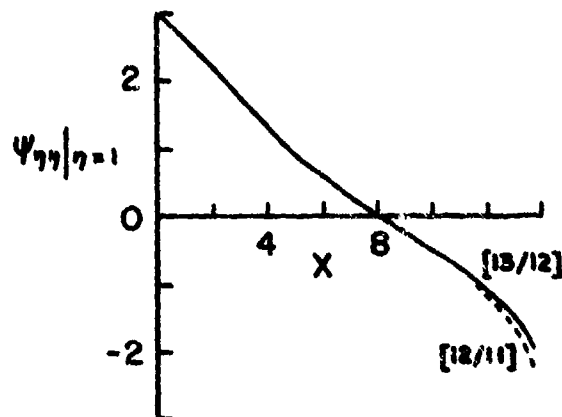


Fig. 13 Skin friction along exponential channel at $R = 17.5$

Goldstein's 70th anniversary symposium, to be published.

2. Van Dyke, Milton, "Analysis and Improvement of Perturbation Series," *Quarterly Journal of Mechanics and Applied Mathematics*, to appear.
3. Barton, D., and Fitch, J. P., "Applications of Algebraic Manipulation Programs in Physics," *Reports on Progress in Physics*, Vol. 35, 1972, pp. 235-314.
4. Richtmyer, R. D., "Detached-Shock Calculations by Power Series, I," NYO-7973, Oct. 1957, Institute of Mathematical Sciences, New York Univ., NY.
5. Lin, S. C., and Rubinov, S. I., "On the Flow Behind Curved Shocks," *Journal of Mathematics and Physics*, Vol. 27, No. 2, July 1948, pp. 105-129.
6. Cabannes, Henri, "Détermination Théorique de l'Écoulement d'un Fluide Derrière une Onde de Choc Détachée," Note Technique No. 5, 1951, Office National d'Études et de Recherches Aéronautiques, Chatillon-sous-Bagneux, France.
7. Cabannes, H., "Tables Pour la Détermination des Ondes de Choc Détachées," *La Recherche Aéronautique*, No. 49, Jan.-Feb. 1956, pp. 11-15.
8. Moran, J. P., "The Inverse Blunt-Body Problem," Part II of Ph.D. Thesis, 1966, Cornell Univ., Ithaca, N. Y. (available from University Microfilms, No. 66-4485, Ann Arbor, Mich.)
9. Meyer, Th., "Ueber zweidimensional Bewegungsvorgänge in einem Gas, das mit Ueberschallgeschwindigkeit strömt," Dissertation, 1908, Univ. of Göttingen, Germany; also *Forschungsarbeiten auf dem Gebiete des Ingenieurwesens des Vereins deutscher Ingenieure*, Vol. 62, 1908, pp. 31-67; reprinted in Carrier, G. F., ed., *Foundations of High Speed Aerodynamics*, Dover, New York, 1951, pp. 50-89.
10. Martensen, E., and von Sengbusch, K., "Numerische Darstellung von ebenen und rotations-symmetrischen transsonischen Düsenströmungen mit gekrümmtem Schalldurchgang," *Mitteilung Nr. 19*,

1958, Max-Planck-Institut für Strömungsforschung und der Aerodynamischen Versuchsanstalt, Göttingen, Germany.

11. Blasius, H., "Laminare Strömung in Kanälen wechselnder Breite," Zeitschrift für Mathematik und Physik, Vol. 58, 1910, pp. 225-233.

12. Abramowitz, M., "On Backflow of a Viscous Fluid in a Diverging Channel," Journal of Mathematics and Physics, Vol. 28, 1949, pp. 1-21.

13. Lucas, R. D., "A Perturbation Solution for Viscous Incompressible Flow in Channels," Ph. D. Dissertation, May 1972, Stanford Univ., Stanford, Calif.

14. Stokes, G. G., "On the Theory of Oscillatory Waves," Transactions of the Cambridge Philosophical Society, Vol. 8, 1849, pp. 441-455; "Supplement to a paper on the Theory of Oscillatory Waves," Mathematical and Physical Papers, Vol. 1, Cambridge Univ. Press, 1880, pp. 314-326.

15. Wilton, J. R., "On Deep Water Waves," Philosophical Magazine, Series 6, Vol. 27, 1914, pp. 385-394.

16. Schwartz, L. W., "Computer Extension and Analytic Continuation of Stokes' Expansion for Gravity Waves," Journal of Fluid Mechanics, Vol. 62, Part 3, Feb. 1974, pp. 553-578; additional details in "Analytic Continuation of Stokes' Expansion for Gravity Waves," Ph. D. Dissertation, Nov. 1972, Stanford Univ., Stanford, Calif.

17. Domb, C., and Sykes, M. F., "On the Susceptibility of a Ferromagnetic above the Curie

Point," Proceedings of the Royal Society of London, Series A, Vol. 240, 1957, pp. 214-228.

18. Van Dyke, M. D., "A Model of Supersonic Flow Past Blunt Axisymmetric Bodies, with Application to Chester's Solution," Journal of Fluid Mechanics, Vol. 3, Part 5, Feb. 1958, pp. 515-522.

19. Van Dyke, Milton, "Hypersonic Flow behind a Paraboloidal Shock Wave," Journal de Mécanique, Vol. 4, No. 4, Dec. 1965, pp. 477-493.

20. Gaunt, D. S., and Guttman, A. J. "Series Expansions: Analysis of Coefficients," Phase Transitions and Critical Phenomena, C. Domb and M. S. Green, eds., Vol. 3, Academic, New York and London, to appear.

21. Baker, G. A., Jr., "The Theory and Application of the Padé Approximant Method," Advances in Theoretical Physics, K. A. Breuckner, ed., Vol. 1, Academic, New York and London, 1965, pp. 1-58.

22. Chisholm, J. C. R., "Rational Approximants Defined from Double Power Series," Mathematics of Computation, Vol. 27, No. 124, Oct. 1973, pp. 841-848.

ACKNOWLEDGEMENTS

This work was supported by the Air Force Office of Scientific Research under Contract AFOSR 74-2649 and its predecessors.

DISCUSSION

J. M. Witting

Van Dyke has given us clear examples of how the combination of numerical analysis and the high speed digital computer can generate new ideas in certain problems in fluid mechanics. Another example should be added to van Dyke's list, that of a solitary wave in water.^{1,2,3} In reference 1 an expansion which is valid to the ninth order in wave amplitude was derived. By using a method which extracts the limit of well-behaved sequences of partial sums,⁴ Fenton was able to estimate properties of the highest wave in water. Very recently, Longuet-Higgins and Fenton² and Witting³ have applied several of the techniques described by van Dyke to the solitary wave problem, with marked success. Both conclude that expansions in powers of wave amplitude, e.g. reference 1, are asymptotic and, indeed, yield a highest wave amplitude that is a few percent too high.

In reference 2 the reversion of the series from powers of wave amplitude to one in powers of a parameter closely related to the fluid speed at the wave crest (in laboratory, not wave coordinates) yields results which are analogous to those of Schwartz for Stokes waves. Liberal use of diagonal Padé approximants is employed to deduce many important properties of solitary waves up to and including the highest wave. One of the most significant results of this research is that the highest wave is not the most energetic. Longuet-Higgins and Fenton are able to conclude that something drastic must happen to solitary waves propagating up a gently sloping beach before the highest wave is reached. This is an example of a qualitative discovery born out of some of the techniques described by van Dyke.

In reference 3 an expansion about the point at the extreme flank of the solitary wave is employed which facilitates computation to very high order (551 for the highest wave--apparently a record at this date). Except possibly for the highest wave, the expansion is shown to result in a non-solitary wave, and Witting concluded that perturbation expansions in powers of amplitude are incomplete at all amplitudes except infinitesimal, and, therefore, that such expansions are asymptotic. The analysis relies to some extent upon

finding the "direction of singularities" in a complex plane. As van Dyke has pointed out, most physical problems result in coefficients A_n with the same or with alternating signs. In the solitary wave problem the signs of A_n were found to be periodic at particular values of a parameter, but with periods greater than two. If the periodic sign structure behaves so that rotation by an angle $-\theta$ results in the signs of all real parts of $A_n > N$ being the same, then the closest singularity to the expansion point must lie at an angle of θ from the real axis of the original problem.⁵ This fact was used to deduce (with some reservations) the fact that the amplitude of the highest solitary wave is exactly $3/3^{1/2}\pi = 0.82699\dots$, which agrees perfectly with the result of Longuet-Higgins and Fenton of 0.827. By employing the Domb-Sykes tests described by van Dyke for a non-highest wave, one can conclude that the approach to near-breaking periodic waves taken by Havelock⁶ and others is probably better than recently thought.⁷

¹Fenton, J. A ninth-order solution for the solitary wave. J. Fluid Mech. 53, 257-271 (1972).

²Longuet-Higgins, M.S. and Fenton, J.D. On the mass, momentum, energy and circulation of a solitary wave. II. To appear in Proc. Roy. Soc. Lond. A.

³Witting, J. The highest solitary wave, and others. Presented at "Modern developments in fluid dynamics--an international symposium in honour of the 70th birthday of Sydney Goldstein" (December 1973).

⁴Shanks, D. Nonlinear transformations of divergent and slowly convergent sequences. J. Math. Phys. 34, 1-42 (1955).

⁵Hille, E. Analytic Function Theory Blaisdell Publishing Co., New York p. 133 and 136 (1959).

⁶Havelock, T.H. Periodic irrotational waves of finite height. Proc. Roy. Soc. Lond. A 95, 38-51.

⁷Grant, M.A. The singularity at the crest of a finite amplitude progressive Stokes wave. J. Fluid Mech. 59, 257-262 (1973).

M. S. Longuet - Higgins

In addition to the computations of the solitary wave by Longuet-Higgins

and Fenton which have already been mentioned by Dr. Witting, I would like to mention that I have carried out further computations on the speed of periodic waves in deep water by methods similar to those outlined by Professor van Dyke. The results are remarkable.

In the Stokes expansion outlined by Professor van Dyke, the complex velocity $(u + iv)$ is expanded as a power series in the complex potential ζ , in fact

$$\frac{1}{u-iv} = (1 + a_1 \zeta + a_2 \zeta^2 + \dots + a_n \zeta^n + \dots) / c^2$$

The coefficients a_1, \dots, a_n, \dots and the phase velocity c are then expanded in powers of some small parameter. Schwartz took as his parameter the wave amplitude h (= half the crest-to-trough wave height).

However in some respects it is more convenient to take as the expansion parameter

$$\omega = 1 - \frac{q_{\text{crest}}^2 \times q_{\text{trough}}^2}{c^2 c_0^2}$$

where q_{crest} and q_{trough} are the particle speeds at the crest and the trough respectively (in the steady flow seen by an observer travelling with the wave). c_0 denotes the speed of waves of infinitesimal amplitude. For waves with a sharp angle at the crest q_{crest} vanishes, giving $\omega = 1$ precisely. In general, $0 < \omega < 1$. Moreover ω can be expanded as a power series in h^2 (not h), and on reversion both h and c^2 can be expressed as power series in ω .

Using the $[N, N]$ Padé approximant to sum this series I obtained excellent

convergence right up to the limiting value $\omega = 1$ (see Figure 1). In fact with the quadratic precision (31 decimal places) available on the IBM 360, and at the 30th order in ω , (i.e., the 60th order in h) the wave speed c converges numerically to better than one part in 10^5 for all $0 < \omega < 0.98$ and better than one in 10^4 for $0.98 < \omega < 1$.

From Figure 1, however, it will be seen that while h increases monotonically with ω , the wave speed c appears to have a maximum of about $\omega = 0.95$, similar to the apparent maximum in the solitary wave speed found by Longuet-Higgins and Fenton.

Should one believe in the existence of this maximum? The author knows of no rigorous argument either for or against. The apparent values of c^2 and h^2 at $\omega = 1$ are respectively 1.1931 and 0.19641 for a wavelength normalized to 2π ($c_0 = 1$), giving a maximum wave steepness

$$\frac{2h}{2\pi} = \frac{h}{\pi} = 0.14107$$

This compares with Schwartz's preferred value of 0.14118 derived from the poles of $[N, N]$. The two values are indistinguishable graphically. Schwartz calculated a few values of c^2 at values of h near the maximum, the nearest being $c^2 = 1.1930$ at $A/L = 0.14$. He suggested that the tangent to c^2 might be horizontal at the maximum. By a quite different method Yamada found a limiting value $c^2 = 1.1932$.

In conclusion we may say that results obtained in this way can be highly interesting and suggestive. At the same time it is appropriate to regard them as being provisional, until confirmation is available by other methods.

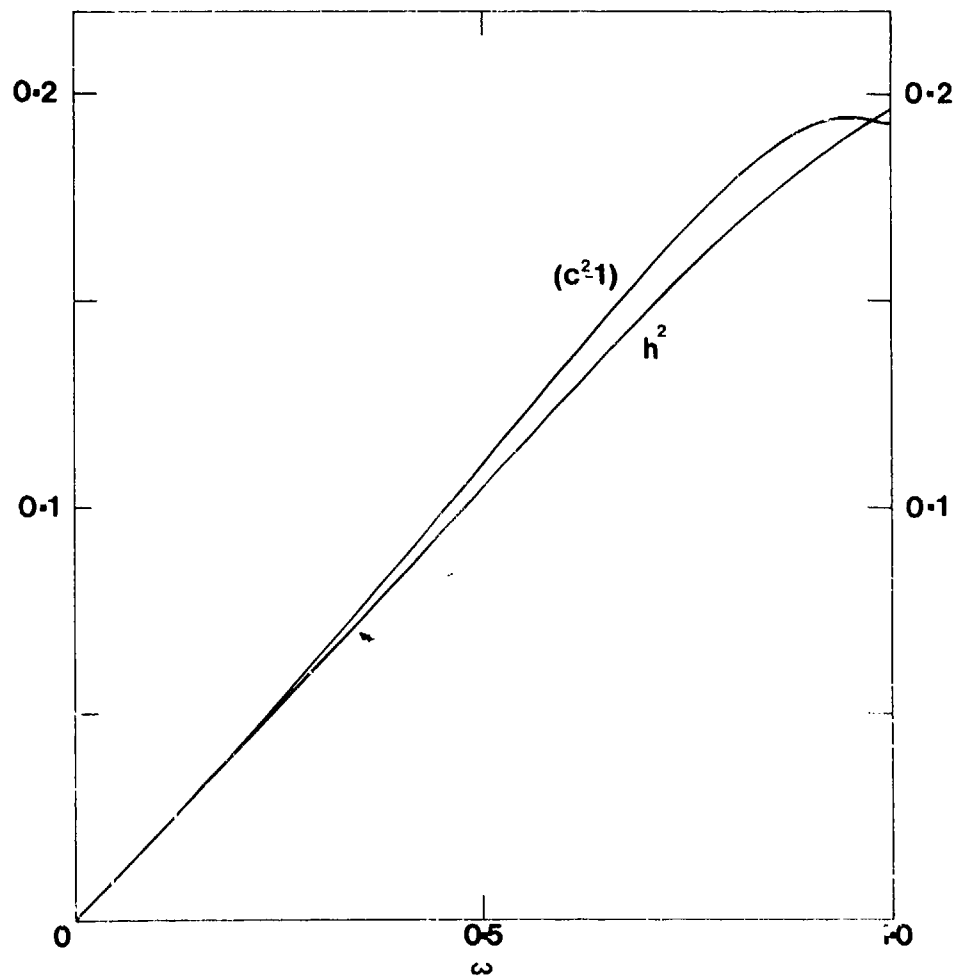


Figure 1. The squares of the wave amplitude h and wave speed c , as functions of ω , computed by Padé approximants.

AUTHOR'S REPLY

The author thanks Dr. Witting and Professor Longuet-Higgins for their supplementary comments.

CALCULATION OF VORTEX SHEETS IN UNSTEADY FLOW AND APPLICATIONS IN SHIP HYDRODYNAMICS

P.T. Fink
University of New South Wales
Sydney, Australia

W.K. Soh
University of New South Wales
Sydney, Australia

ABSTRACT

The numerical calculation of the movement of free shear layers in two-dimensional and quasi-three-dimensional flow has been in vogue since Rosenhead published his method of discretisation of vortex sheets into elemental vortices of constant strength in 1931. The many writers to use the technique in the next 42 years have met more or less severe difficulties in applying the method to a variety of problems involving memory effects. These troubles were due to Rosenhead's incomplete consideration of the principal value integrals which are implicit in the calculation.

A new method is put forward here in which numerical error associated with principal value integrals is much reduced. New sets of equivalent vortices are created at each time step in the computation, giving rather better simulation of the behaviour of vortex sheets. We review the most important of the earlier papers and recalculate some of their results. Solutions for vortex sheet development for several other problems of interest are also presented.

I. INTRODUCTION AND REVIEW OF EARLIER WORK

1.1 Introduction

The practical importance of boundary-layer separation and the formation of shear layers in two and three dimensions is so great that approximate calculations have been attempted by very many workers. These cover such areas as the self-induced movement of sheet layers; the rolling up of vortex sheets behind wings, propellers and other lifting bodies; lee vortices above slender wings, bodies and wing-body combinations; two-dimensional starting flows past all manner of bodies, particularly those with sharp edges such as ships' keels, Fig.1.

Although the viscosity of the fluid is responsible for the formation of all the shear layers mentioned above, it is neglected in potential flow calculations, save indirectly by the imposition of Kutta-type conditions on the solutions of the Laplace equation which is always involved, at any rate for subsonic flow.

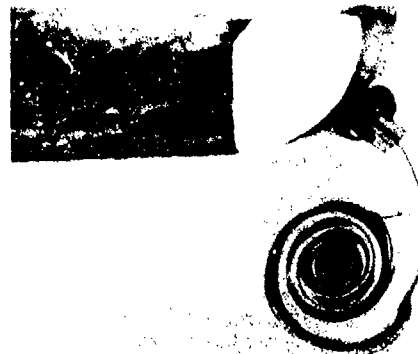


Fig. 1 Vortex Separation at Bilge Keel:
Segmented Model in Uniform
Vertical Motion following
Impulsive Start

This procedure appears to be justified for high Reynolds number steady flows and for many unsteady flow situations of practical importance during periods in which inertial effects predominate.

Rosenhead was the first worker to replace a vortex sheet by an equivalent distribution of discrete vortices. He used this method to consider the non-linear Helmholtz instability of a two-dimensional vortex sheet of initially constant strength in a paper published over forty years ago. The results were plausible and the method has been used repeatedly by research workers to the present day.

Unfortunately the method is unsound. After 1959, criticisms of Rosenhead's work were made by Birkhoff and Fisher, Hama and Burke and others. It was pointed out that groups of discrete vortices moving under their own influence in two-dimensional flow will inevitably tend to a random distribution. However, there is no proof that this will also happen to potential flow models of continuous vortex sheets. It seems certainly to be the case that experimentally observed starting flow situations are free of randomness. Thus it can be expected that Rosenhead's device of following a system of discrete vortices, chosen to represent some initial distribution of continuous vorticity, will lead to increasing irregularity in equivalent

vortex position and must finally make it impossible to reconstitute a coherent vortex sheet. A careful reading of the many papers using Rosenhead's discretisation, written between 1931 and the present day shows this to be the case. In many of these, the phenomenon of increasing randomisation has been brushed aside or ascribed to numerical error with an inference that better numerical accuracy would prevent the emergence of a random arrangement of equivalent vortices. In others, the randomisation was suppressed by arbitrary smoothing techniques.

In the present work a different process of discretisation is recommended which appears to improve the situation considerably. This is an extension to free vorticity of the care normally taken with principal value integrals occurring in bound vortex theory. Some of the most important applications published since 1931 have been reworked using the new procedure and rather more consistent results have been arrived at. Several new results involving memory effects have also been obtained.

The present section is intended to be a critical survey of some of the most significant published papers relevant to the subject of vortex sheet development in unsteady two-dimensional potential flow and of the allied subject of vortex separation from slender wings and other slender three-dimensional bodies.

1.2 Formation of Vortices from Unbounded and Planar Surfaces of Discontinuity

Rosenhead's Treatment of Helmholtz Instability. The reader will recall that Helmholtz instability [1] refers to the situation when adjacent portions of fluid of the same density move with different speeds. Rosenhead [2] investigated perturbations of a basic case of two initially uniform streams in two dimensions flowing over one another with equal speeds in opposite directions. Thus he was concerned with the self-induced distortion of an initially plane vortex sheet of constant strength. Rayleigh's method of applying small oscillation theory was used; i.e. the surface of discontinuity was given a sinusoidal displacement of small amplitude and arbitrary length. The work was extended by the inclusion of a second order term for the disturbance potential which generated disturbances anti-symmetrical about the crests of the initial sine-waves. The method was only claimed to be applicable for the very early stages of the development of instability. It appeared that within the assumptions of the analysis all wavelengths were unstable.

A most significant part of Rosenhead's work is his subsequent numerical treatment of the instability phenomenon for longer durations. To quote the original paper, "the

vortex sheet is replaced by a distribution of finite elemental vortices along its trace, and the paths of these vortices are determined by a numerical step-by-step method. The line joining these vortices at any instant is assumed to be an approximation to the actual shape of the surface at that time. It is shown that the effect of instability upon a surface of discontinuity of some form is to produce concentrations of vorticity at equal intervals along the surface, and it is also shown that the surface of discontinuity tends to roll up round these points of concentration with an accompanying increase in the amplitude of the displacement. For comparison, the effect of putting 2, 4, 8, 12 elemental vortices of equal strength initially equally spaced along the surface, is investigated, but the results are of the same nature". Fig. 2 is copied from Rosenhead's paper and shows both the abovementioned concentrations of vorticity and the increasing amplitude of the disturbance as calculated when 12 elemental vortices are used to represent one wavelength of the sheet.

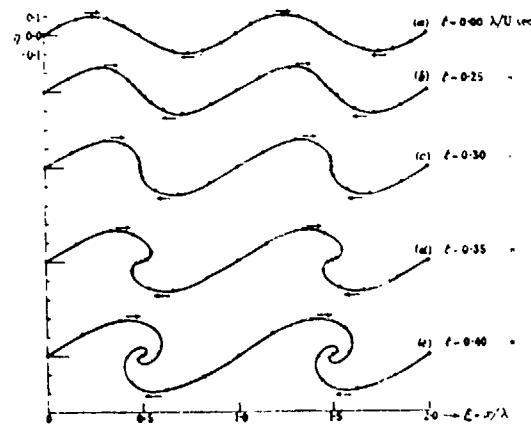


Fig. 2 Rosenhead calculation:
Initial vorticity
density constant and
 $(\eta)_{t=0} = 0.1 \sin 2\pi\xi$

Rosenhead gave an estimate of the error introduced at each step of the calculation. He supposed this to arise merely from the truncation of the Taylor series for the displacement of his elemental vortices during each step. He also mentioned that the method could not be used for a large number of steps since "the accumulation of the errors introduced at each step may become large enough to destroy the value of the approximation". Further, he speculated that "an increased accuracy in determining the shape of the surface would be obtained by taking (more vortices) than eight". It appears that Rosenhead's calculations

were not performed in sufficient detail to exhibit the tendency towards randomisation of vortex position which was brought out in recalculations of this now classical work, by later authors as discussed below.

In fact the question of the accuracy of calculations, in which vortex sheets are represented by elemental vortices, is rather more subtle and the criticisms of Birkhoff and his co-workers (see later) have to be considered when judging the merits of any of the investigations using that representation. Rosenhead's results are recalculated later, using the technique recommended in this paper.

Abernathy and Kronauer's Treatment of Vortex Sheets. The purpose of Abernathy and Kronauer's [3] contribution was to explain the essential features of the mechanism of the formation of vortex streets from two initially parallel uniform vortex sheets of opposite sign. The paper includes a small perturbation analysis and it was found that no argument based solely on a linearised theory of disturbances was able to generate the asymmetry commonly associated with the interaction of the two sheets.

Their non-linear analysis of this configuration employed the same numerical discretization of vortex sheets as Rosenhead's. Fig. 3 shows a typical outcome of the calculation. The non-linear calculation proceeded from a small amplitude sinusoidal disturbance in the same manner as Rosenhead's - as is evident from the positions of the equivalent elemental vortices shown for zero value of the time parameter. The method appears to be successful in calculating the subsequent distortion of the sheets for the next three values of the time parameter shown at the right side of the figure. For greater times, a degree of randomness appears to enter into the computation of the coordinates of the equivalent elemental vortices which finally becomes so pronounced that "there was no longer sufficient evidence to suggest the existence of vortex sheets". However, Abernathy and Kronauer consider it reasonable to draw solid lines around so-called clouds of vorticity, as shown at the bottom of Fig. 3. In fact the major concentrations of vorticity of one sign or another shown there, do include a few elemental vortices of opposite sign. Abernathy and Kronauer conclude that the concentrated clouds of vorticity have "a net strength diminished by the vorticity swept into the cloud by the opposite vortex row". We have not recalculated these results but it may be worthwhile repeating them using the method of this paper.

Michalke's Treatment of the Effect of Thickness. The work of Rosenhead and

of Abernathy and Kronauer was generalised by Michalke [4] to include the effect of thickness of a shear layer - at any rate for a simple Rayleigh type linear velocity profile. Michalke also began with a linearised treatment of his problem. This led to the discovery that the presence of the additional dimension in the analysis removed the arbitrariness

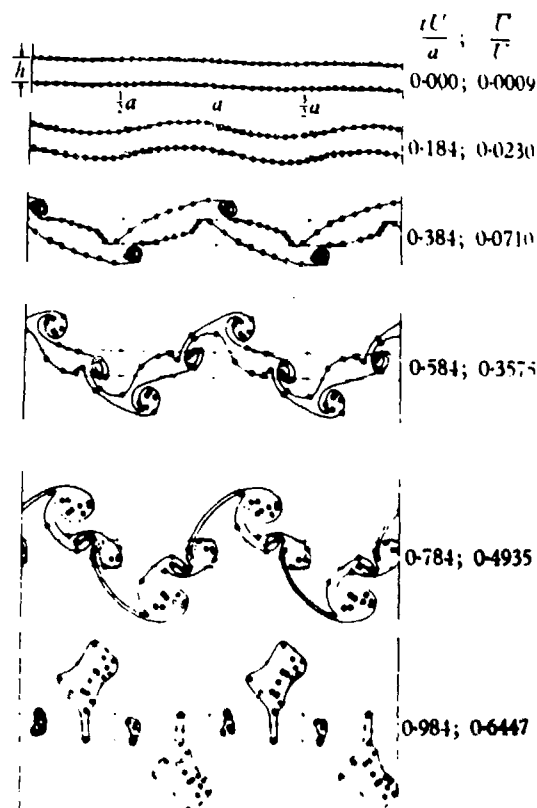


Fig. 3 Abernathy & Kronauer calculation:
Initial vorticity density
constant and initial
amplitude = 0.0125a

of disturbance wavelength stipulated in the earlier papers and that it was possible to find a wavelength for maximum amplification of disturbance.

The non-linear calculation proceeded in similar fashion to Rosenhead's except that the constant surface distribution of vorticity representing the initially linear velocity profile of the shear layer was represented by a discrete number of surfaces of discontinuity - each of which was simulated by a finite number of elemental vortices. The initial disturbance was chosen to have the wavelength which suffered maximum amplification according to the author's linearised theory. Fig. 4 shows a typical development of a disturbed shear layer when the latter is represented by three sheets of 24 elemental vortices per wavelength. No very great irregularity of vortex position appears to have

developed for the interval shown but some licence has had to be used to draw the vortex spirals shown due to the relatively small number of elemental vortices used. The number of apparent vortex cores developing in the layer with time seems to equal the initial number of surfaces of discontinuity. Thus it is unlikely that one can conclude anything detailed about the concentrations of vorticity which occur as time goes on. It appears that the surfaces of discontinuity used to represent a thick shear

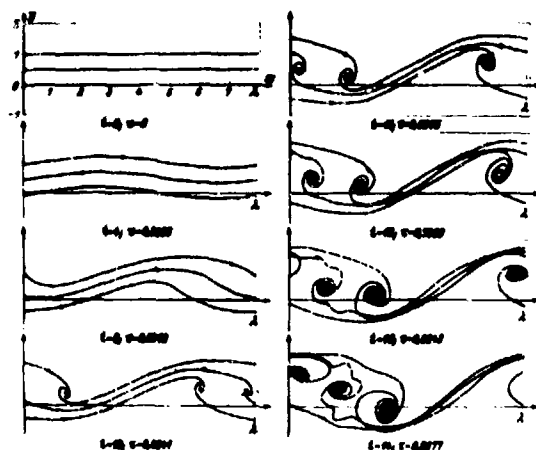


Fig. 4 Michalke calculation: Initial conditions are, sheets parallel, vorticity density has sinusoidal initial perturbation

layer retain a degree of independence. To the extent that this is true, the conclusions following from our recalculation of Rosenhead's problem may also have application here. One might also criticise Michalke's assumption that the development of a shear layer of finite thickness may be represented by the development of a number of elemental surfaces of discontinuity, each retaining the same circulation per unit wavelength of initial disturbance. The improvements recommended later relate only to the calculation of surfaces of discontinuity. Corresponding improvement to the calculation of the development of surface rather than line distributions of vorticity; i.e. shear layers with thickness, remains to be worked out in detail.

Criticism by Birkhoff, Hama and Others. Rosenhead's flow patterns for Helmholtz instability were so realistic that the validity of his calculations appears to have remained unsuspected for nearly thirty years. The first criticism

of Rosenhead's work was made in 1959 by Birkhoff and Fisher [5] in a little known publication¹ entitled 'Do vortex sheets roll up?' Their grounds for criticism were further examined by Hama and Burke [6]. The present writers learned a great deal respecting the computation of the motion of clusters of vortices from these papers but we would dispute the inference that conclusions about such motions are immediately relevant to the later development of vortex sheets which were initially represented by earlier configuration of the same discrete vortices.

Birkhoff and Fisher pointed out that any decrease of distances between pairs of vortices would be accompanied by increases for other pairs. This conclusion is based on the theorem that a system of vortex filaments in two-dimensional inviscid fluid flow has an energy invariant, see also Lamb [1], Batchelor [7], which is determined - when all vortices are of equal strength - by the product of all initial distances. Hence, no two vortex lines can coalesce unless some other pair has its separation increased indefinitely. Thus, Birkhoff and Fisher, having seized on a concept of rolling up which suggests an infinite concentration, asymptotically, assert their "Theorem I.: the vorticity in a periodic array of point vortices cannot tend to become concentrated". The inference in the paper that a similar conclusion may be applied in relation to the rolling up of vortex sheets; i.e. as represented in a potential flow model, derives from their persistence - after all! - with Rosenhead's assumption that such a continuous sheet of vorticity can be modelled by an appropriately chosen but unchanging set of discrete elemental vortices.

On recalculating Rosenhead's results they found that the motion of the elemental vortices became very complicated in domains where some concentration took place thus making it impossible to reconstitute smooth vortex sheets. Their re-examination also showed that the results were sensitive with respect to the assumed initial conditions. Furthermore, they tried a method in which local equality of arc length between elemental vortices was maintained. However this still led to irregular results as shown in Fig. 5.

These circumstances led Birkhoff and Fisher to look for - and find, subject to a plausible assumption - arguments that discrete vortex arrays might exhibit a tendency towards randomisation of position. Given that expectation, Poincaré's recurrence theorem was then invoked to prove that any "rolling up must be followed by unrolling with probability one". ('Rolling up' of vortex arrays was

¹ We are indebted to Professor John W. Miles for drawing our attention to Birkhoff's work.

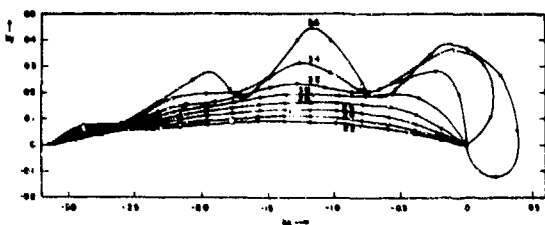


Fig. 5 Birkhoff calculation of Helmholtz instability:
Development of half wavelength

not defined.) The build-up of randomness in Birkhoff and Fisher's recalculation of Rosenhead's work, and also in similar and earlier recomputation by Birkhoff and Carter [8] was such as lead these writers to the conclusion that effective randomisation had taken place in a few wavelengths of relative motion.

The validity of Rosenhead's results and Birkhoff and Fisher's work were further considered by Hama and Burke [6] in a paper inspired by the wish to compute the effect of background vorticity on the rolling up process. A number of parameters were varied but the paper persists with Rosenhead's representation of the development of a vortex sheet by the motion of a given set of discrete elemental vortices. Hama and Burke's final conclusions are that "this result does not necessarily exclude the concentration (of vorticity) in a certain area" and that "the stability problem with background vorticity still remains open."

1.3 The Rolling up of Trailing Edge Vortex Sheets

Westwater's Calculations. In 1935 Westwater [9] attempted to calculate the rolling up of a trailing edge vortex sheet using the same numerical technique as Rosenhead. He considered the wing to have an elliptic span loading giving a corresponding strength of the trailing vortex sheet. The effect of the bound vorticity on the flow direction was neglected. Thus the problem was reduced to a two-dimensional one such that the region of interest would be a cross-section plane normal to the direction of travel of the wing. The time parameter involved would be the time interval from the instant the wing had passed this normal plane. Initially the trace of the vortex sheet was taken to be straight and coincident with the wing span. Its vorticity density was of the well-known cotangent form appropriate to an elliptically loaded bound vortex line. Westwater replaced the sheet by 20 unevenly spaced discrete vortices of equal strength in order to simulate the

correct vorticity density.

A step-by-step calculation was used to trace the movements of these vortices and the shape of the vortex sheet at any instant was taken to be the smooth line joining the discrete vortices. A typical result is shown as a solid line in Fig. 6. Westwater stated that the spiral portion of the vortex sheet could not be represented accurately by a small number of discrete vortices. "On the other hand, there are strong grounds for supposing that the approximate method gives a good representation of the form of the sheet near the centre and, in fact, anywhere except near the edges. Presumably these 'strong grounds' related to experimental observation rather than any more exact theoretical formulation.

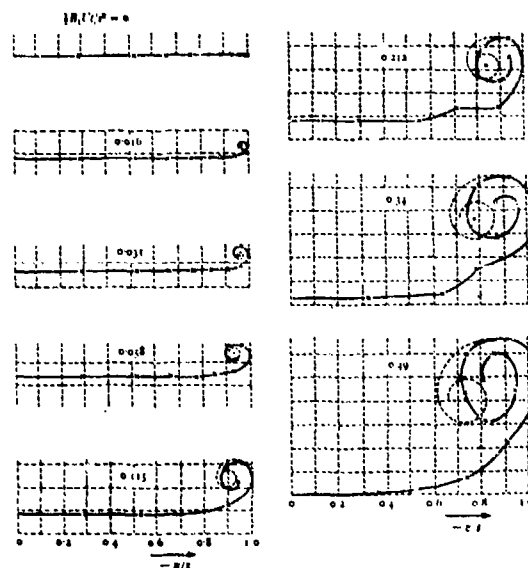


Fig. 6 Westwater calculation of development of trailing vortex sheet from elliptically loaded wing; elemental vortices identical in strength

He found that initially the discrepancy between the velocity of a point on the sheet and that of the equivalent vortex at this point was small even for the relatively few vortices used in his representation. In fact if only one vortex is used to represent the trailing vortex sheet from each half wing and is placed at the centroid of the shed vorticity as required in Westwater's scheme, the velocity at the position of that vortex will be error by a factor of only $8/\pi^2$. Of course this favourable state of affairs applies only at the beginning of

the calculation. Westwater believed that the error was due not so much to the discretisation of the sheet but to the step-by-step process of time integration - especially where the velocities of the vortices undergo rapid changes as in the spiral portions. He suggested that this calculated spiral portion could well be replaced by a matched spiral of the kind derived by Kaden's theory [10] for a two-dimensional infinite spiral sheet. Westwater shows this as a dotted line in Fig. 6.

A little time after the start of the motion, a kink appeared in Westwater's representation of the trailing vortex sheet, as shown in Fig. 6. Westwater's paper reproduced some flow pictures of Kaden's which seemed to have similar kinks. Yet, the photographs are not clear and it is debatable whether they really substantiate the existence of such kinks. However the general appearance of Kaden's photographs is similar to Westwater's prediction of the development of the sheet and he is confident that they "appear to give confirmation to the view that the numerical method gives a good approximation to the motion".

Later workers shed more doubt on his numerical approximation. The error analysis of the representation of a vortex sheet by a series of discrete vortices as given by Westwater is far from complete. It will be shown in the next chapter that Rosenhead's discretisation, as implemented by Westwater, must lead to an ever less coherent description of the movement of the sheet as time goes on.

Takami and Moore's Numerical Experiments. Takami [11] re-examined Westwater's calculations in light of the criticisms of Rosenhead's work by Birkhoff and others. He used a better numerical method, he employed a modern digital computer and he represented the trailing vortex sheet by rather more discrete vortices than the number used by Westwater. A Runge-Kutta integration was employed with much smaller time steps. The truncation error was small and a check of the coordinates of each elemental vortex computed for different values of the time step revealed that they differed only in the third significant figure. Fig. 7 gives one of Takami's results using twice the number of elemental vortices used by Westwater. The vortices moved in complicated orbits around each other so that the sheet they were supposed to represent would have had to cross itself repeatedly. He ascribed this to the rapid circling motions arising from the strong interaction among vortices which had come into close proximity. He found that the detailed picture of this region could not be improved by increasing the number of elemental vortices.

It is worth remarking that the characteristic kinks observed in Westwater's representation of the sheet were not present in any of Takami's calculations, i.e. not even when Westwater's

smaller number of elemental vortices was used. Thus it appears that Takami's use of a better method of numerical integration was enough to remove a feature which Westwater felt to be a reproduction of experimental observation.

Takami also attempted to calculate the development of trailing vortex sheets springing from wings with loadings other than the elliptic loading treated by Westwater. He considered spanwise loading curves which were square and cube of this - so reducing the strength of the trailing vortex sheet at the wing tip to constant and zero values respectively. He clearly expected greater regularity of flow near the ends of the sheet but appears not to have appreciated that his intermediate case was bound to require a logarithmic velocity distribution near the ends and he confesses that "... we still end up with a random distribution near the tip". Indeed this randomness became more pronounced as the number of elemental vortices was increased from eight to twenty-four. For the elliptical loading 'cubed' we quote Takami's graphic words "... At first thought, we would expect the vortices to have more regular distribution because the initial distribution is the least singular in this case.

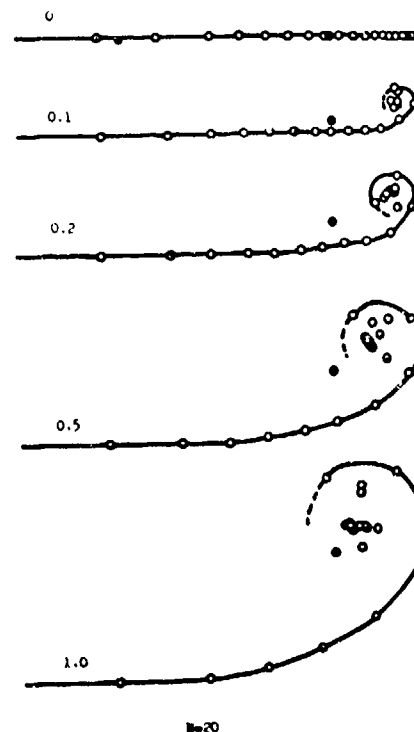


Fig. 7 Takami's recalculation of Westwater case; 40 elemental vortices of identical strength. Black spot is centroid of vorticity for half span

On the contrary, however, vortices move irregularly on a larger portion of the sheet than in the preceding cases, and we clearly see that the increase of the number of vortices makes the approximation meaningless". It is believed that the method developed in this paper resolves these difficulties - as demonstrated later when the method is applied to several of the problems tackled by Takami.

In his conclusion, Takami disagrees with Birkhoff's argument concerning the significance of the random distribution of elemental vortices as follows: ".... the randomness which we encountered in our computation is no more than an indication of the instability of the equation of motion and has nothing to do with the randomness in the statistical sense - it would take far longer time for this randomness to develop". The proposition that the equations are always unstable is not borne out by the results obtained in later sections of this work.

Moore [12] recalculated Takami's work using even larger numbers of elemental vortices to represent the vortex sheet for the Westwater case - of an elliptically loaded wing - and he further reduced the time steps. However, he found no improvement in the randomness which developed in Takami's calculations. Following on a careful numerical analysis, Moore ruled out the possibility of numerical error as the cause of this randomness and he concluded that Rosenhead's discretisation of vortex sheets was inappropriate. He claimed that ".... it is shown by examination of a special case that the approximation of replacing a finite vortex sheet by an array of line vortices can be unreliable, however many vortices are used". We agree with this statement and show later how the above randomness can, in principle, be avoided for periods of time which are significantly long in relation to many of the problems reviewed here.

Other Contributions. Many other workers have considered a variety of problems involving the rolling up of trailing vortex sheets shed from wings and, particularly, wing-body combinations. The position up to 1950 was summarised in an important paper by Spreiter and Sacks [13]. They were concerned to find ".... the proper vortex distribution to be used for 'downwash calculations'" and they used a similarity argument to show how very much more rapidly a trailing vortex sheet rolled up for a wing of small aspect ratio than for one of larger aspect ratio. Thus they pinpointed areas for application of the Rosenhead/Westwater method which they reported without criticism. However, they did not advocate its widespread use for downwash calculations behind low aspect ratio wings, presumably because the potential of electronic digital computers had hardly been tapped at that time. In the intervening years aerodynamic interference problems assumed greater importance and

digital computer power became more widely available. This led to an increase in the number of papers attempting to use Rosenhead's discretisation for those aerodynamic (vortex) interference calculations for which non-linearity was important. We mention now merely some of those writers who had some particular comment to make regarding the shortcomings of the method.

Rogers [14] applied two-dimensional non-linear vortex theory to the prediction of flow fields behind wings of wing-body combinations at subsonic and supersonic speeds in 1954. He found a number of interesting trends, including qualitative agreement with experimental findings that the trailing vorticity shed from a particular wing panel in supersonic flow distorted into an S-shape on the way to rolling up into a pair of cores rotating about each other. In respect of discretisation, Rogers found that a relatively small number of elemental vortices was needed for computation of downwash in regions of interest for missile designers. He used elemental vortices of equal strength spaced as necessary and he commented that care had to be taken to avoid what he called ".... the loss of a vortex caused by excessive induced velocity" due to close proximity to neighbouring elemental vortices. In view of the limited range of parameters considered and, particularly, because he did not wish to use fine sub-division of his sheets, the 'loss-of-vortex' phenomenon proved to be no great embarrassment.

In 1968 D.E. Cummings [15] published an M.I.T. report on a preliminary study of vortex interaction in the wake of heavily loaded marine propellers. He began with a re-examination of the case of an elliptically loaded lifting line using a discrete vortex approximation to the sheet, modified by analytic calculation near the ends. The latter naturally led him to use a Cauchy principal value integral and he recognised that this may be important in the numerical calculation also. He suggested that induced velocities should only be determined at points midway between discrete vortices. However, consideration of the segments of the continuous distribution represented by these vortices along the lines of the theory given in the next section, shows that this procedure cannot eliminate errors associated with Cauchy principal value integrals.

Hackett and Evans' paper of 1971 on vortex wakes behind high lift wings [16] attempts to use the Westwater method and discusses some of the difficulties. They wished to achieve greater accuracy than had been sought before and they also wished to investigate the effect of height above ground on the development of the sheets when non-linear effects were important. They found that small time steps in the integration led to 'tighter vortex grouping'; i.e. near the

edges of the sheet, but that "..... the vortex sheet had crossed itself, which is physically impossible in real flow". It was also noted that there was "ostensibly quite a wide choice of (elemental) vortex arrangements ranging from equal strength vortices to (initially) equal spaced vortices of differing strength". They show significantly different development of sheet geometry with time for these two forms of initial discretisation and express a preference for the latter while warning the reader about "..... the dangers of looking in too much detail near the singularities (cores)". They felt that there might be "a kinematic optimum between the two extremes".

Butter and Hancock [17], also in 1971, published an investigation of the effect of sweep-back angle on the rolling up process of the trailing vortex sheet behind a wing. Thus, they had to generalise Westwater's work by including the effects of bound vorticity. We note the paper here because of this and also because of their recognition that some of their more useful results were obtained "..... more by good fortune than numerical insight"; i.e. by use of relatively few initially equispaced elemental vortices of unequal strength. They also reported that "... if too great a number of vortices is chosen, numerical difficulties may arise ...".

The most recent paper, 1973, relating purely to wing trailing vortex sheet development appears to be Clements' and Maull's [18] attempt to find wing load distributions "which alter the rolling-up characteristics of the sheet in such a way as to decrease the vorticity finally contained in (any of the several resulting) vortex cores". They continue to follow Westwater and use elemental vortices of constant strength. This led to unacceptably large induced velocities near the edges of the sheets. Clements and Maull therefore placed an upper bound on the initial velocity of the vortices near the edges 'and if these velocities were exceeded at the first time step, the two tip vortices were amalgamated'. This arrangement never resulted in more than two vortices being amalgamated.

1.4 The Shedding of Vortex Sheets from Two-Dimensional Bodies

Anton and Wedemeyer's Treatments of Flow Separation from Impulsively Started Plates. The potential modelling of flow round a sharp edge requires that vorticity is shed from it in order to prevent a velocity infinity. This assumes a spiral form covering increasing area as more vorticity is added. It follows from the conservation of energy, that this vorticity cannot be concentrated into a point but that a core

structure very similar to the well-known solution given by Kaden [10] is expected to form.

The first calculation of vorticity shedding from a sharp edge is that of the flow round a semi-infinite plate which was made by Anton [19] in 1939 following on much earlier work by Prandtl. This system does not have a characteristic length and so a similarity solution exists. Anton found that the total vorticity shed is proportional to a one third power of time and that the distance from the edge to a marked point on the vortex sheet is proportional to the two thirds power of time. The similarity law does not give enough information to describe the entire shape and vorticity distribution of the sheet but Anton devised a numerical method to find the necessary constants. The existence of the similarity law allows the time dependent movements of the vortex sheet to be reduced to a steady state configuration by appropriate scaling in the time parameter. Anton divided the vortex sheet into two sections: an inner core and an outer loop linking it to the shedding edge. The inner core was approximated by a Kaden-type spiral. For smooth matching, the two portions were arranged to have a common tangent and continuous vorticity at the join. This determined the centroid of the inner core in relation to the sharp edge. The core portion was then replaced by a discrete vortex at this centroid having the same strength as the core which it replaced. The problem having been reduced to the steady state, it became possible to find the shape of the vortex sheet by an iterative process. The constraints for this iteration were that the vortex sheet must convect with the surrounding fluid and that a Kutta condition was applied at the shedding edge. Wedemeyer [20] published a recalculation of Anton's result in 1961 using a different form of iteration and this gave 8 per cent more vorticity in the sheet plus core combination. Despite the use of iterative procedures, neither solution can be viewed as exact because of the oversimplified representation of the core region.

Both Anton and Wedemeyer suggested use of the semi-infinite plate solution as a starting point for similar calculations for an impulsively started plate of finite width moving with uniform velocity transversely to its width. Step-by-step integrations were performed graphically. Wedemeyer's results are more complete and include useful information on the growth and distribution of vorticity density in the fluid as well as on the shape and total circulation of the shed vortex sheets, at any rate when there is a symmetric pair.

It is worth noting that Anton's similarity solution for the starting flow near a semi-infinite plate was recently generalised by Blendermann [21]

to include convex corners of any angle moving with velocity equal to time raised to any power in fluid otherwise at rest. Biendermann's results may serve as useful starting solutions in fuller analyses of vortex shedding from more complicated boundaries in more general motion.

Some Other Contributions. We refer to three further writers whose work relates to the shedding of vorticity in two-dimensional flow. Giesing has used non-linear (vortex) representations for the study of two-dimensional aerofoils in unsteady motion in a number of papers published from 1968. His discussion [22] of the kinematics of vortex shedding is noteworthy in that he claimed that the Kutta condition could be approximated as requiring zero velocity difference at non-cusped trailing edges and he showed that the surface velocity distribution is in error only in the immediate vicinity of the edge. We have not felt obliged to approximate conditions at shedding edges in this way.

Clements' model of the starting flow in the near wake of a bluff-based body, 1973, [23] exhibits some new features in the treatment of shedding conditions, when only discrete elemental vortices are used. It will be appreciated that for that case the velocity at a shedding edge must be infinite or zero; there is no scope for non-zero finite velocity unless a continuous sheet is used in the immediate vicinity of the edge. Clements dealt with the problem by letting the shed vortices travel with a velocity evaluated a small distance away from the shedding point. This appears to have replaced the Kutta condition with a fair measure of success. Some interesting results were obtained for the rate of shedding of vorticity into shear layers from two separation points - but the validity of these results must be subject to the general criticism made here of the Rosenhead model.

We also refer to Gerrard's numerical computation of 1967 of the magnitude and frequency of the lift on a circular cylinder [24]. This paper confronts the difficult problem of separation from a body without sharp edges by introducing a pair of elemental vortices into the flow some distance downstream at each time step. The - constant - strengths of these vortices were derived from experimentally obtained shedding rates. Despite the appearance of irregularity of elemental vortex position, see earlier discussion of Birkhoff's criticisms, the calculated values of lift force and scale of formation region agree well with experiment for a range of Reynolds number.

1.5 Vortex Separation from Slender Wings and Bodies

Boundary layer separation of an interesting kind is found to take place

at the sides of slender wings and bodies even for angles of incidence which are not very large. Boundary layer fluid is fed into the flow on the lee sides of the bodies, as is usual at separation, but it is also convected downstream. Thus coherent vortex sheets are formed and these lend themselves to analysis within the framework of slender body theory. The non-linear and memory effects associated with this so-called vortex separation are of significance in aeronautics, with respect to non-linear lift, nature of roll-up of shed vorticity etc; ship hydrodynamics, with respect to non-linear force and moment in ship manoeuvrability, action of bilge keels, fins, etc; and other areas. The reader is referred to Küchemann's excellent report [25] of the I.U.T.A.M. symposium on concentrated vortex motions in fluids held at Ann Arbor in 1964 and to his important survey [26] published in 1966. We now refer more particularly to work which contributes to the numerical treatment of such vortex sheets and associated forces.

Slender Wings and Wing-Body Combinations. The phenomenon of leading edge separation from slender wings and particularly delta wings, is now very well-known. Major contributions were made to the understanding of the subject by Roy and Legendre in France in the early 1950s but much remained to be done and many workers were attracted by the good prospects for theoretical treatment implied in the experimentally observed coherence of leading edge vortex sheets. The most successful attempt to create a purely analytical model was published by Brown and Michael [27] in 1954. Each sheet was represented in the crossflow plane by a point vortex and a cut joining the vortex to its shedding point. Neither was force-free alone but the condition of zero force on a vortex sheet was approximated by arranging for the forces on cut and point vortex to be equal and opposite. Although Brown and Michael's results for vortex position, pressure distribution, etc, were only in qualitative agreement with experiments, the method has been used in many attempts to include the effects of non-conical planform, thickness and even those of unsteady motion for the calculation of stability derivatives. A number of the papers on leading edge separation review earlier work and a useful review of this kind is included in a recent paper by Pullin [28].

The major numerical methods available hitherto were Smith's iteration technique [29] and the multivortex model of Sacks, Lundberg and Hanson [30]. Validation of any new models would involve comparison with these techniques - both of which are in moderate to good agreement with experiment. Smith's method is not easy to generalise for non-conical geometries although the attempt

has been made. Sacks' method is very adaptable but suffers from the shortcomings of multivortex representation as discussed later. Both these methods have been used by other writers who have extended the work to cover vortex separation from slender bodies alone and from wing-body combinations as discussed below.

Smith's is perhaps the most sophisticated model published so far. In developing his conical flow theory for a slender delta wing of zero thickness, he considered the trace of the separation vortex sheet in a transformed plane as being composed of two parts; the outer part, joining the leading edge was divided into an arbitrary number of segments while the remainder was represented by a Brown and Michael type force-free combination of isolated vortex plus cut connecting to the outer part. A procedure involving three nested iterations was used to ensure this, to satisfy boundary conditions at points on the outer part which were intermediate to the pivotal points at which the shape and strength of the sheet were defined and, thirdly, to satisfy a smooth outflow condition. It would appear that the pressure continuity condition was satisfied close to but not at the shedding edge. Convergence was very satisfactory for many quantities of interest, such as pressure distribution and normal force which agreed quite well with experiment. However, the proportion of total circulation carried by the isolated vortex ("core") depended strongly on the number of pivotal points chosen to represent the outer part of the spiral. Smith states that "..... the only evidence for the existence and uniqueness of a solution is the success of calculations". It is worth noting that Smith's success in modelling the flow is probably due to his avoidance of the Rosenhead-type of discretisation, tempting though that must have been. At the same time, this makes it harder to extend Smith's procedure for more general wing geometries. Such attempts have been published, see for example Levinsky, Wei and Maki [31]. Successful as they have been, they have not as yet been extended to the important problem of sheet roll-up behind wings.

Sacks, Lundberg and Hanson did use a Rosenhead discretisation in their model of leading edge vortex separation from wings alone or in combination with fuselage type bodies. Neither wings nor bodies were constrained to have conical geometry. Elemental vortices were shed from each edge at successive chordwise crossflow planes. These vortices were allowed to convect with the stream, their strength remaining unaltered. Kutta conditions were satisfied exactly but the shedding process was modelled only approximately in that the effect of finite sweep angle was neglected in the equation expressing the pressure continuity condition at the leading edges. The

predicted shapes of vortex sheets exhibited the considerable irregularity to be expected in applications of the Rosenhead method as the number of vortices representing a sheet was increased, see Fig. 8. Surface pressure distributions were not presented but estimates of normal force for delta wings were in fair agreement with experiment. The adaptability of the method enabled the authors to obtain results for various double delta wing arrangements and also for some elementary wing-body combinations. Alternative results were also derived using a semi-empirical procedure to determine local shedding rates. These were in better agreement with experiment than those using the above mentioned model of the shedding process.

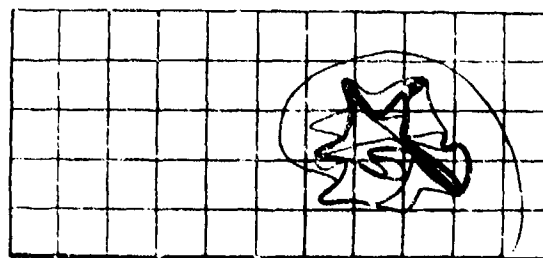


Fig. 8 Sacks, Lundberg and Hanson's result for delta wing of unit aspect ratio at angle of incidence 15° ($\alpha/K = 1.07$)

Finkleman [32] extended the Sacks method in his work on non-linear vortex interactions on wing-canard configurations. He corrected the expression for pressure continuity at leading edges used in [30] by including the effect of sweep and he analysed the vorticity shed from the trailing edge of the forward wing. Finkleman gave a frank description of the difficulties involved in his application of the Sacks method: "..... 'old' vortices near the vortex centroid become quite confused and cannot logically be connected"; when elemental vortices were sufficiently close to the surface, components of velocity normal to the surface had to be suppressed; Rogers' 'loss of vortex' phenomenon was also found and treated by amalgamating any pair of elemental vortices whose separation had become less than an arbitrary proportion of the local span. Finkleman's critical approach to these problems is exemplified by his comment that "..... Westwater's original figures reveal considerable imagination on the author's part when he connected the vortices".

The Sacks method was also used by Angelucci [33] in his multi-vortex method for axisymmetric bodies at incid-

ence (1971). Empirical separation lines were included to enable the analysis to proceed and agreement between predicted force and experiment was good. At the same time Angelucci reported that "..... internal spirals start to show significant irregularity when more than 30 to 40 vortices have been shed" - thus indicating the need for an improved model for this geometry as well as for the wings and wing-body combinations discussed previously.

Some Contributions from Ship Hydrodynamics. Usually, ships are more or less slender bodies and boundary layer separation leading to the formation of coherent shear layers would not be an unexpected phenomenon in normal straight ahead motion for many practical hull shapes. Also, much of the non-linear force and moment met in ship manoeuvrability is due to such vortex separation effects and we are currently using vortex sheet analysis to investigate these effects for appropriate geometries in order to improve on existing cross flow drag theories. We are preceded in this endeavour by Hennig [34] whose paper (1970) reported use of a single pair of discrete vortices to represent the non-linear side force due to sideways on slender ships with Lewis form cross sections. The theory required experimental input. Professor K. Nomoto recently supplied us with an advance copy of a paper by Fuwa [35] which appears to refine Hennig's work by using a multi-vortex model somewhat along the lines of Angelucci's work for the bilge vortex separation on a ship in oblique towing. At the time of writing we have been unable to obtain a translation but it appears that experimental inputs were required for the solutions, that bilge keels were not modelled and that some good agreement with experiment was reported.

Bilge vortices produced near the bows of full ships have been described by several writers and an approximate semi-empirical treatment of the corresponding increment in ship resistance, or vortex drag, is due to Tatinclaux [36]. The roll damping due to bilge keels has been the subject of a useful semi-empirical analysis by Martin [37] and others; a later review was published by Gadd [38]. To our knowledge, vortex sheet models have not yet been applied to any of these problems.

During 1971 we became interested in potential flow modelling of vortex separation at ships' bilge keels in the heaving mode - see Fig. 1 - and we presented a discrete vortex approximation for the sheets [39] which we took to be standard practice in aerodynamics; i.e. we used the Rosenhead method. The problem was simplified into the study of the motion of a plate normal to itself. At that stage we were unaware of most of the work reviewed in this section and we

quickly encountered the random vortex arrangements discussed by Birkhoff and his collaborators. The use of constant time steps promoted early onset of breakdown of the calculation in the sense of crossing vortex sheets. Considerable improvement was obtained by allowing the time steps to vary so as to ensure that the shedding point and the last two elemental vortices to be shed formed an equi-spaced set of points. This discovery led us to the more thorough analysis given in the next section from which it appears that error is least when elemental vortices are equi-spaced for the entire sheet at every instant for which the motion is calculated.

II. COMPLEX POTENTIAL TREATMENT OF VORTEX SHEETS IN UNSTEADY TWO-DIMENSIONAL FLOW OF INCOMPRESSIBLE FLUID

2.1 Introduction

The use of vortex sheets to help represent some of the effects of viscosity in otherwise inviscid flow theory is well-known. The technique is particularly valuable for two-dimensional situations and those many three-dimensional cases which are quasi-two-dimensional. It will generally be necessary to calculate the movement of the vortex sheets and this invariably leads to the problem of evaluating singular integrals.

In this section we recall and set down the necessary complex functions to the point where numerical methods may be applied. That is done in Section III in which a new numerical scheme is developed for the calculation of the movement of vortex sheets in unsteady motion. The distribution of pressure and the force on bodies in the vicinity of vortex sheets are often of interest and the method of calculation is then described. Proof of uniqueness of solution is perhaps too much to hope for at present but some aspects of the accuracy of the approximate method of solution proposed here, are examined in Section 3.4.

2.2 Complex Velocity Field Associated with a Vortex Sheet

In two-dimensional flow, a vortex sheet is a line of discontinuity of velocity and we require a notation such as is shown in Fig. 9. For a free vortex sheet which convects with the fluid, we follow Helmholtz in defining the complex velocity q_{vs} of a point on the sheet as the mean of the complex velocity vectors q_+ , q_- immediately on either side of the sheet at that point. Thus

$$q_{vs} = \frac{1}{2}(q_+ + q_-) \quad (1)$$

The vorticity density $\gamma(s)$, taken to be positive in the counter-clockwise sense, is defined in terms of the distance s along the sheet measured from some reference point.

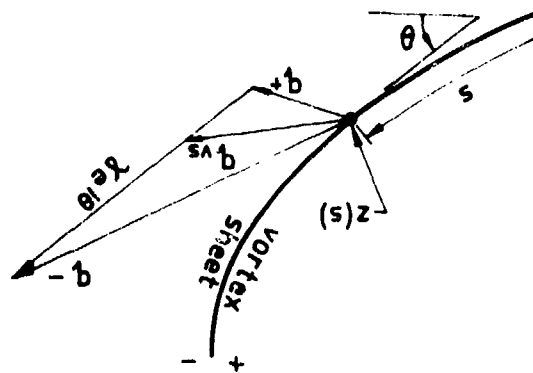


Fig. 9 Notation

The complex conjugate velocity $\bar{q}(z)$ at some point z induced by a segment of vortex sheet extending from s_a to s_b is usually given as:

$$\bar{q}(z) = \frac{1}{2\pi i} \int_{s_a}^{s_b} \frac{\gamma(s_1) ds_1}{z - z_1} \quad (2)$$

Whenever the field point z lies on the vortex sheet, $z = z(s)$ and for $s_a \leq s \leq s_b$, the Cauchy principal value has to be taken for the integral. Converting to integration with respect to the complex variable z_1 , we write $dz_1 = e^{i\theta} ds_1$ where θ is the inclination of the tangent to the sheet at $z_1(s_1)$ to the real axis. Equation (2) then becomes

$$\bar{q}(z) = \frac{1}{2\pi i} \int_{z_a}^{z_b} \frac{\gamma e^{-i\theta} dz_1}{z - z_1} \quad (3)$$

Where necessary we assume that the function $\gamma e^{-i\theta}$ satisfies the Hölder condition for the existence of a principal value integral. When the point z lies on the vortex sheet, the velocity is to be interpreted in the sense of Plemelj, viz

$$\frac{1}{2\pi i} \int_{z_a}^{z_b} \frac{\gamma e^{-i\theta} dz_1}{z - z_1} = \frac{1}{2} [\bar{q}_+(z) + \bar{q}_-(z)] = \bar{q}_{vs} \quad (4)$$

$$\gamma e^{-i\theta} = -[\bar{q}_+(z) - \bar{q}_-(z)]$$

Thus it appears that the velocity of points on the vortex sheet given by the above formulation agrees with Helmholtz's definition, see equation (1). For details of Hölder's condition and the Plemelj formulae, see e.g. L.C. Woods, [40].

Consistently with equation (3), the velocity potential is given by

$$w = \frac{1}{2\pi i} \int_{z_a}^{z_b} \ln(z - z_1) \gamma e^{-i\theta} dz_1 \quad (5)$$

We shall require the time derivative $\frac{\partial w}{\partial t}$. This is obtained as

$$\frac{\partial w}{\partial t} = \frac{1}{2\pi i} \int_{z_a}^{z_b} \frac{q_{vs}(z_1) \gamma(z_1) e^{-i\theta_1} dz_1}{z - z_1} \quad (6)$$

by invoking Kelvin's theorem for $d\Gamma = \gamma(s_1) ds_1 = \text{constant}$ and by taking care with (usually vanishing) terms arising from variability of the limits of integration. It can be shown that the expression (6) is valid at points on boundaries from which vorticity is shed.

Equations (3), (6) may also be used to demonstrate the continuity of pressure on free vortex sheets as follows. The appropriate Bernoulli equation is

$$-\frac{1}{\rho}(p_+ - p_-) = \left[\frac{\partial \phi}{\partial t} \right]_+ - \left[\frac{\partial \phi}{\partial t} \right]_- + \frac{1}{2}(|q_+|^2 - |q_-|^2) \quad (7)$$

and continuity of pressure is assured if the right side of (7) vanishes. The relevant Plemelj formula yields

$$\left[\frac{\partial \phi}{\partial t} \right]_+ - \left[\frac{\partial \phi}{\partial t} \right]_- = \text{Re}(q_{vs} \gamma e^{-i\theta}) \quad (8)^2$$

and this result together with equation (4) is easily shown to cause the right side of (7) to vanish, as required for the continuity of pressure condition which is an important constraint on the calculation of motion of vortex sheets. For the sake of simplicity we have omitted all mention of the effects of a free stream or of boundaries. The same arguments will apply when these are present.

2.3 Nature of Vortex Sheet at Shedding Point

In potential flow theory, separation from sharp edges is usually modelled by means of vortex sheets shed from those edges - or points for flow in two dimensions. Kutta's well-known condition ensures finite velocity at such points but it is not sufficient to determine other details of the shedding process. The static pressure must be continuous across a vortex sheet at the shedding point as much as at any other point on the sheet. Reference to equation (8) then indicates how the rate of

² This equation was derived differently by Cooper [41]

change $\dot{\Gamma}$ of circulation³ of the total shed vorticity is related to the vorticity density and velocity at the shedding point. Generally that point may have a vector velocity V and the pressure continuity condition at the shedding edge then becomes

$$\dot{\Gamma} = Re \left| (q_{VS} - V) \gamma e^{-i\theta} \right|_{\text{edge}} \quad (9)$$

This form of the condition is particularly convenient for application of numerical methods.

Mangler and Smith [42] give an interesting argument to determine the orientation of the vortex sheet shed in the flow past a convex corner. In order to avoid the infinite velocity at the corner which would violate Kutta's condition or zero velocity which would infer zero vorticity generation at the corner, the sheet is recognised as leaving the corner tangentially to one of the sides. The local vorticity density then reduces to the finite speed parallel to the appropriate arm of the corner.

III. NUMERICAL METHOD

3.1 Discretisation of Vortex Sheets

Here we first consider the discretisation of the continuous distribution of vorticity density in a vortex sheet; i.e. the manner in which the corresponding line singularity is treated numerically. Time integrations involved in following the convecting sheet are considered next and the section is concluded with discussion of the numerical representation of the shedding conditions mentioned previously.

Clearly, vortex sheets are made amenable to numerical calculation by breaking them up into simple segments whose movements are traced as a means of representing the motion of the sheets. We split a sheet into n segments, letting the boundaries lie at $s_{k+\frac{1}{2}}$ with integral values of k , $1 < k < n$.⁴ Equation (2) for the induced velocity then becomes.

$$\begin{aligned} \bar{q}(z) &= \frac{1}{2\pi i} \sum_{k=1}^n \int_{s_{k-\frac{1}{2}}}^{s_{k+\frac{1}{2}}} \frac{\gamma(s_1) ds_1}{z - z_1} \\ &= \frac{1}{2\pi i} \sum_{k=1}^n \frac{\Gamma_k}{z - z_k} \end{aligned} \quad (10)$$

The point z_k lies within the segment

$(s_{k-\frac{1}{2}}, s_{k+\frac{1}{2}})$. $\Gamma_k = \int_{s_{k-\frac{1}{2}}}^{s_{k+\frac{1}{2}}} \gamma(s_1) ds_1$ is the circulation round the segment and the

point z is taken to lie not in the vortex sheet.

When the point under consideration z_j does lie in the vortex sheet, the integration over the segment containing that point will require special treatment. If the segment is short enough to warrant the assumptions that its radius of curvature is large compared with its length and that the vorticity density may be taken as constant, then the appropriate Cauchy principal value will be well represented in the second term of the following equation,

$$\begin{aligned} \bar{q}(z_j) &= \frac{1}{2\pi i} \sum_{k \neq j}^n \frac{\Gamma_k}{z_j - z_k} \\ &\quad - \frac{1}{2\pi i} \frac{\Gamma_j e^{-i\theta_j}}{|s_{j+\frac{1}{2}} - s_{j-\frac{1}{2}}|} \times \ln \left| \frac{z_j - z_{j+\frac{1}{2}}}{z_j - z_{j-\frac{1}{2}}} \right| \end{aligned} \quad (11)$$

Equation (11) resembles the equation for the induced velocity field due to a series of n discrete vortices - or point singularities - except for the logarithmic term. When the equivalent vortex Γ is placed at the mid-point of its segment; i.e. $z_j = (z_{j-\frac{1}{2}} + z_{j+\frac{1}{2}})$ that term vanishes.

It is understandable that much of the previous work reviewed in this paper makes that assumption - perhaps intuitively! Thus it would appear that sufficiently fine subdivision of an initial vortex sheet would be likely to lead to indefinitely small error in the predicted velocity field. Certainly Rosenhead satisfied himself that his calculation tended to converge with increasing subdivision - coarse though that was in terms of modern computing power - in the limited number of subsequent steps used to follow the motion of his perturbed vortex sheet. However, the reader will recall Birkhoff's and Hama's experience that finer subdivision of an initial sheet leads to earlier failure of the representation!

Fine subdivision is clearly desirable for accuracy of calculation of flow quantities at a given instant but this is not to say that the Γ_k and their associated coordinates z_k can continue to represent a given vortex sheet as it distorts and convects with time. This is because each segment of the original sheet will suffer its own distortion and change of length. Thus a set of mid-points of segments will generally not remain mid-points as time goes on and each of the logarithmic terms associated in principle with each of the segments may become significant. Hence the predicted velocity at any point on the sheet will need to include an increasing number of logarithmic error terms as the subdivision of the initial sheet is refined. Thus the process of discretisation using Rosenhead's multivortex representation is

³ Clearly at a fixed shedding point $\Delta\phi(t) = \dot{\Gamma}$ and $\Delta\phi(t+\delta t) = \dot{\Gamma} + \delta\ddot{\Gamma}$
 $\frac{\partial}{\partial t} \Delta\phi(t) = \dot{\Gamma}$

⁴ See error analysis at end of this section.

inconsistent. Coarse subdivision is also undesirable - for obvious reasons - but some earlier work gave the appearance of success by using this for short enough times to avoid evident failure of the calculation. Thus, the difficulties encountered by the writers reviewed earlier appear to be explained. It is not possible to calculate the motion of a vortex sheet from the motion of the series of discrete vortices used to represent that sheet for more than infinitesimal intervals of time.

3.2 Method of Stepwise Rediscretisation of Vorticity

In general it would appear that equation (11) for the convection of points on a vortex sheet requires computation of a logarithmic term at every segment in the sheet for each time step as well as the velocity induced by the multivortex system used to represent the rest of the sheet. However, we have already shown that the logarithmic term vanishes when the z_j are placed at the mid-points of the j th segments. We ensure that this is done by a simple procedure. At some arbitrary time we have a series of discrete vortices at points predicted by an appropriate time integration of the velocity field existing one time step earlier. This movement will generally lead to a new set of coordinates of the equivalent vortices which no longer bisect the segments of the sheet they are intended to represent. Rather than calculate the logarithmic term of equation (11) at each time step, we represent the vorticity density by an entirely new set of equi-distant discrete vortices whose strengths are adjusted to give a good representation of that density. Thus we are no longer interested in the self-convection of a particular group of discrete vortices. Of course the time steps need to be reasonably small to ensure success of even this procedure for subduing the logarithmic terms. Otherwise they will make themselves evident again.

Thus the numerical integrations to be performed need not be particularly sophisticated. The loss of computing efficiency involved in using small time steps is compensated here by using a simple method of numerical integration, viz.

$$z_j(t+\Delta t) = z_j(t) + q(z_j)\Delta t + \frac{1}{2} \left[\frac{dq(z_j)}{dt} \right] (\Delta t)^2 \quad (12)$$

We now consider how to incorporate the various conditions applying at a shedding point. An additional segment Δs of vortex sheet will need to be introduced at the shedding point at each time step Δt . It will be oriented as described earlier. The strength of the circulation Γ_n and the values of Δs , Δt are related because of the need to satisfy the Kutta

condition and the pressure continuity condition, equation (9) which then becomes

$$\Gamma_n/\Delta t = (\Gamma_n/\Delta s) \operatorname{Re} \left[(q_{vs} - V) e^{-i\theta} \right]_{\text{edge}} \quad (13)$$

The determination of Γ_n from Kutta's condition has been found straight forward in all cases examined in this paper.

Although equation (13) is available, together with the Kutta condition for all values of n , we have to give special attention to the manner in which the calculation is started. The single vortex representation of the segment of sheet shed initially, i.e. for $n=1$, is unlikely to be satisfactory. However if the calculation converges to a solution of known character for increasing n , we may have some confidence in the details predicted as n becomes large. It will be shown that this is the case for a number of corner flows, including the special case of zero included angle, viz. that of flow past a semi-infinite flat plate in uniform motion normal to itself following on an impulsive start. These all have similarity solutions for the time dependence of the parameters describing the shed vorticity - but for unknown constants. These constants emerge in our calculations as n increases; i.e. the present method may also be viewed as an iteration technique for finding all the details of such flows. Thus, if an accurate representation of the shed vorticity is required for small times, or even at the first time step, we may begin with an arbitrarily large number of elemental vortices obtained from the appropriate similarity solution. Hence, the similarity solutions for semi-infinite corners serve to represent vorticity shed from points on quite general bodies with corners for small time. These solutions provide the starting configurations for the present method.

3.3 Calculation of Pressure and Force

The calculation of pressure in the flow using the Bernoulli equation is almost trivial but some points require attention. A numerical expression for the velocity is available in equation (10). The unsteady term of the Bernoulli equation is the real part of $\partial w/\partial t$, equation (6). This is represented numerically, in line with previous procedure as

$$\frac{\partial w}{\partial t} = - \frac{1}{2\pi i} \sum_{k=1}^n \frac{q_{vs}(z_k) \Gamma_k}{z - z_k} \quad (14)$$

Generally we will need to evaluate the pressure at points in flows with boundaries. In this work we consider only those boundaries which can be readily transformed on to the real axis of a $\zeta(z,t)$ plane. The shed vorticity will then appear in the upper half plane $\operatorname{Im}(\zeta) > 0$ together with its image in $\operatorname{Im}(\zeta) < 0$. Also, there will often be a stream with velocity $U(\zeta)$ parallel to the real axis at

$z \rightarrow \infty$. In place of the numerical equations (10), (14) - neither of which apply at points on vortex sheets - we then have

$$\bar{q}(z) = \frac{d\zeta}{dz} \left\{ U(t) + \frac{1}{2\pi i} \sum_{k=1}^n \frac{\Gamma_k}{\zeta - \zeta_k} - \frac{1}{2\pi i} \sum_{k=1}^n \frac{\Gamma_k}{\bar{\zeta} - \bar{\zeta}_k} \right\} \quad (15)$$

$$\frac{\partial w(\zeta)}{\partial t} = \frac{\partial}{\partial t} [U(t)\zeta] + \frac{1}{2\pi i} \sum_{k=1}^n \left(\frac{\partial \zeta}{\partial t} - \frac{d\zeta_k}{dt} \right) \frac{\Gamma_k}{\zeta - \zeta_k} - \frac{1}{2\pi i} \sum_{k=1}^n \left(\frac{\partial \bar{\zeta}}{\partial t} - \frac{d\bar{\zeta}_k}{dt} \right) \frac{\Gamma_k}{\bar{\zeta} - \bar{\zeta}_k} \quad (16)$$

It will be noted that this pair of expressions allows the boundary to change its geometry with time. Evidently this will be useful in applications of the theory to the flow past slender wings and bodies with non-linear force and moment arising from vortex separation.

The calculation of the distribution of pressure over a boundary from which vortex sheets are shed, will require attention for points $z(\zeta, t)$ close to the shedding edges/points because a discrete vortex representation of the segment which is attached to the shedding point - as suggested by equations (15), (16) - must misrepresent conditions in the immediate vicinity of that point. We improve the representation by approximating the attached segment by a straight short length of sheet with constant vorticity density and, by assuming that q_{vs} within the segment is $(q_{vs})_{edge}$. Thus, the segment is used in place of the n th elemental vortex referred to in equations (15), (16). Some results of using this procedure are given later.

The force on a body may be obtained by direct integration of pressure or by application of Blasius' theorem for unsteady motion. The latter is generally preferred since it involves less calculation and the former serves as a useful check. The expression for force, derived from Blasius' theorem will consist of the sum of an inertia term associated with the added mass of the body and of a further term associated with the memory effect of the shed vorticity. Consider for example a flat plate lying between $z = +ih(t)$ moving with velocity $U(t)$ normal to itself. The normal force $X(t)$ is readily determined by use of contour integration, when it is found that the memory term takes the form of line integrals along the vortex sheets shed into the flow:

$$\frac{X(t)}{\rho} = \frac{d}{dt} (\pi h^2 U) - 2 \text{Im} \int_{\text{sheet}} \left[\frac{dh}{dt} \zeta_1 + h \left(\frac{\partial \zeta_1}{\partial t} \right) \right] \Gamma_1 ds_1 \quad (17)$$

This equation is compatible with results obtained by Sacks [43] for discrete vortex systems. The numerical treatment of the equation follows the method of the previous sub-section. However, it is clear that special care must be taken in the neighbourhood of the shedding points $z = +ih$ as was the case in the determination of pressure in the same region. The segmentation and representation of the vortex sheet by equivalent elemental vortices is not taken right up to the shedding points. Instead, the contribution to the integral of the final segment is obtained analytically with the plausible assumptions that $\gamma_1(z)$, $q_{vs}(z)$ and $\theta_1(z)$ are constant and equal to the values pertaining at the shedding points. We found that it was necessary to treat the integrals in this way in order to obtain close agreement with the normal force obtained from integration of pressure.

3.4 Accuracy of Calculations

The predictions of our work will be in error due to the manner in which exact integrals occurring in equations (2), (6) as well as the condition (9) are approximated. Errors will arise from the discretisation and also from the technique of time integration. Comment will be made in this section on both these sources of inaccuracy. Fortunately there are a few similarity solutions for flows of interest with which the results of this paper agree well when the appropriate vortex sheets are sufficiently subdivided.

The error in induced velocity q_i at a point z_j on a vortex sheet is treated in two parts: error in induced velocity arising from discretisation of all of the sheet excepting the j th element and its immediate neighbours together with the error arising from the latter. We rewrite equation (10)

$$\bar{q}(z_j) = \sum_{k=1}^n \Delta \bar{q}_{jk} \quad (18)$$

$$\text{where} \quad \Delta \bar{q}_{jk} = \frac{1}{2\pi i} \int_{s_{k-1/2}}^{s_{k+1/2}} \frac{\gamma_1 ds_1}{z_j - z_1} \quad (19)$$

and the integral of equation (19) is taken as a Cauchy principal value for $k=j$. When $k \neq j$, we expand the denominator $(z_j - z_1)$ of (19) in terms of $(z_k - z_1)$, we express the vorticity density as $\gamma_1 = \gamma_k + \gamma'_k(s_1 - s_k) + \dots$ and the infinitesimal arc length $ds_1 = e^{-i\theta_k} dz$. We also assume that θ is constant within each segment. Equation (19) then becomes

$$\Delta \bar{q}_{jk} = \frac{1}{2\pi i} \frac{\Gamma_k}{z_j - z_k} \left[1 + \frac{e^{2i\theta_k}}{12} \left(\frac{s_{k+1/2} - s_{k-1/2}}{z_j - z_k} \right)^2 \left(1 + \frac{\gamma'_k}{\gamma_k} e^{-i\theta_k} \right) + \dots \right] \quad (20)$$

The first term of (20) arises from the discretisation of (10) as given in (11) with error of order

$$\frac{1}{12} \left| \frac{s_{k+\frac{1}{2}} - s_{k-\frac{1}{2}}}{z_j - z_k} \right|^2.$$

This error is small for most of the elements in the sheet and is perhaps only of significance for a few values of k in the neighbourhood of the j th element.

The error produced by discretisation at and near the j th element becomes important not only for the above reason but also because the induced velocity at z_j of the elemental vortices $\Gamma_{j-1}, \Gamma_j, \Gamma_{j+1}$ differs significantly from that induced by the corresponding portion $s_{j-\frac{1}{2}} < s < s_{j+\frac{1}{2}}$ of the original sheet due to the effects of local curvature. We demonstrate this by considering the sheet to have a linear vorticity density as before, viz. $\gamma_1 = \gamma_j + \gamma_j s$ and constant radius of curvature R for the three segments under consideration. With these approximations we easily integrate (19) to give

$$\sum_{j-1}^{j+1} \Delta \bar{q}_{jk} = \frac{-i\beta_j}{2\pi i} \left[\alpha \gamma_j + 3i\Delta s \gamma_j' + O(\alpha^3) \right]$$

where $\text{Re } \beta_j$ is the vectorial distance of z_j from the centre of curvature, Δs is the arc length of each of the three segments and $2\alpha R = 3\Delta s$. The approximate answer obtained from consideration of the effects of the corresponding elemental vortices $\Gamma_{j-1}, \Gamma_{j+1}$ follows readily as

$$\begin{aligned} \sum_{j-1}^{j+1} (\Delta \bar{q}_{jk})_{\text{approx}} &= \frac{1}{2\pi i} \left(\frac{\Gamma_{j-1}}{z_j - z_{j-1}} + \frac{\Gamma_{j+1}}{z_j - z_{j+1}} \right) \\ &= \frac{-i\beta_j}{2\pi i} \left[\frac{2}{3} \alpha \gamma_j + 2i\Delta s \gamma_j' + O(\alpha^3) \right] \end{aligned} \quad (22)$$

Hence, the principal error due to discretisation in our calculations will arise from the discrepancy in the leading terms in the parentheses in (21), (22). Thus, the contribution of the immediately adjacent elements to the velocity at z_j as given in (22) must be increased by one half even for small curvature of the sheet.

The error in the time integration may be estimated in the normal way but it must be remembered that the velocity field being integrated is itself in approximated form due to discretisation of the vortex sheets. In fact this leads to the conclusion that sophisticated procedures of the Runge-Kutta type are best avoided. In a Runge-Kutta integration the velocities of the elemental vortex coordinates are calculated at several intermediate times within each time step and there are as many additional opportunities for the creation of further logarithmic error in the induced velocity field since the elemental vortices will generally deviate

more and more from their original mid-element positions, see equation (11). The simple Euler integration (12) is free of this severe handicap.

We should also mention the method used to translate the unequally spaced elemental vortex coordinates, which occur at every time step in the calculation, into a new - and different - set of equi-spaced elemental vortices. The Lagrangian interpolation formula was used throughout for this purpose. For small steps, the error will be small since the deviations of the elemental vortices from their mid-segment positions will then also remain small.

Increasingly fine segmentation of a vortex sheet will evidently improve the accuracy of the discrete vortex representation of a continuous distribution of vorticity at the instant of subdivision. It will also ensure that the radius of curvature of the sheet is large cfd. the length of the segments. This implies that the time steps in the integration need to be small in our method because that ensures that in each time step the deviation per unit segment length from equi-spacing of the equivalent elemental vortices is kept small. We explained the vital importance of this matter earlier.

Perhaps we should point out that, like all other writers in the field, we have not produced a fully satisfactory numerical treatment of regions close to the centres of vortex spirals. Mostly, it is satisfactory to represent these regions by relatively few elemental vortices despite inaccuracy due to curvature and proximity of neighbouring turns. Where more precision is necessary, we invoke the now classical similarity solutions which give all the necessary information except for constants used to match these inner regions to our solutions. Our method throws these up readily.

Finally we refer to the use of certain invariants to check the accuracy of our calculations. The energy invariant for a vorticity distribution has already been referred to. However, where we use approximate treatments of the inner regions of vortex spirals we replace infinite lengths of vortex sheet by a relatively few discrete vortices and we cannot expect the relevant Hamiltonians to remain constant. To this extent we agree with Birkhoff's observations [5]. The moment of vorticity is invariant with time in many flow situations involving shed vorticity. All of the work reviewed in the first part of this paper used multivortex representation in which the strength of the elemental vortices remained unchanged. Thus, a running check on the moment of vorticity would have been little more than trivial. However, in the present method elemental vortices of different strengths are generated at every time step and observation of any change of moment of vorticity provides a worthwhile

check of overall accuracy.

IV. SOME APPLICATIONS OF THE METHOD

4.1 Introduction

In this section we give a survey of some of the results we have obtained with our stepwise rediscritisation method, more detailed accounts to be published elsewhere. We thought it worthwhile to recalculate some of the more critical results obtained in the papers which were reviewed earlier. These include a further attack on Rosenhead's and other free vortex sheet problems such as calculation of rolling up of trailing vortex sheets behind lifting surfaces with different loadings. We also recalculated the development of vortex sheets which grow with time for several cases, including those shed from edges at impulsively started plates and corners. Our method appears to give generally more satisfactory results - although this needs to be qualified with respect to the recalculation of Helmholtz instability for which we too are unable to present reliable conclusions.

We also report some of the results of our investigation of cases which have not been solved, or fully solved hitherto. The initial stimulus for much of that work followed on our review and revision of earlier calculations of the shape and vorticity distribution of vortex sheets shed from impulsively started plates moving at uniform speed. We extended these Anton/Wedemeyer calculations to include surface pressure distributions and force-time curves and then generalised the calculations to include the effect of time variation of both velocity and dimension of the plate itself; i.e. we obtained results which were immediately applicable for the estimation of surface pressure distribution and normal force on small aspect ratio lifting surfaces of arbitrary camber and planform - at any rate within the framework of slender wing theory. At time of writing we have not completed extensions to include the effects of thickness for lifting surfaces but we present some calculations of lee vortex development behind rectangular and other sections which have application in ship hydrodynamics. In principle, the method lends itself to consideration of much more realistic boundaries and some of these applications are the subject of current work.

4.2 Free Vortex Sheets

Helmholtz Instability. The result of repetition of one of Rosenhead's calculations using 16 and 32 elements per half wavelength of vortex sheet, as against Rosenhead's use of six discrete vortices of permanent strength is shown in Fig. 10. This development is for the same initial disturbance as for the case shown in Fig. 2 at the time $t = 0.4 \lambda/U$, i.e. for the lowest record shown there. It is

seen that increasing the number of elemental vortices no longer promotes breakdown of calculation, see Fig. 5, but our finer subdivision of the sheet has revealed the appearance of a shorter wavelength. It is possible that more detailed investigation of this inviscid model might indicate instability for all wavelengths.

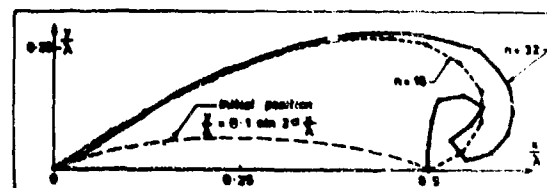


Fig. 10 Helmholtz instability

Roll-up of Trailing Vortex Sheet.

Application of the stepwise rediscritisation method to the problem of trailing vortex sheet roll-up behind an elliptically loaded wing - ignoring the contribution of wing bound vorticity following Westwater (Fig. 6) and Takami (Fig. 7) - gave results such as the configuration for $t = 0.5 s/U$ shown in Fig. 11.

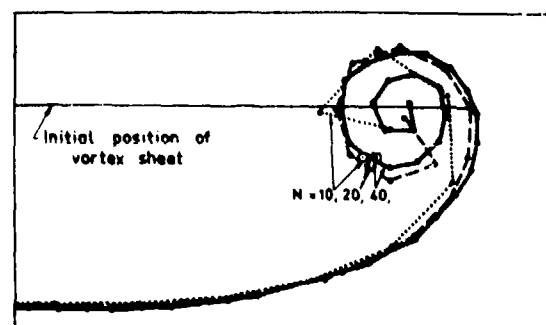


Fig. 11 Roll-up of trailing vorticity behind elliptically loaded wing

It is seen that increase in the number of segments from 10 to 40 per half wing indicates improvement rather than deterioration of results. The patterns should be compared with the final arrangements of discrete vortices shown in Figs. 6,7. It is interesting to note that our time steps were set at $\Delta t = 5 \times 10^{-3} s/U$, a rather coarser value than the range $5 \times 10^{-4} < \frac{U \Delta t}{s} < 1 \times 10^{-3}$ used by Takami in his Runge-Kutta method.

The calculation could have been made more accurate by a more careful initial approximation to the singular vorticity

⁵ The conventional notation of wing theory is used:

s = semi-span

U = wing velocity relative to stationary fluid.

density near the tip. This was revealed by testing our result for constancy of the spanwise position of the centroid of the distribution of trailing vorticity from each semi-span. Our very first discretisation removed that centroid from its theoretical position at $\pi/4s$. The reader may feel that the abandonment of the popular concept of following a particular group of discrete vortices might of itself lead to considerable inaccuracy because a curve fitting error is incurred in the process of interpolation at every time step. However, we found that the centroid remained at $0.7915s \pm 0.0008s$ during the interval of interest $0.1 < \frac{Ut}{s} < 0.5$, the deviation of $3/4s$ from the theoretical value, having occurred at the initial time of calculation $t = 0$. Of course, the initial subdivision may be made less coarse.

We also recalculated Takami's results [11] for vortex sheet roll-up behind a distribution for which the values of local load were proportional to the cube of the values for elliptic loading; i.e. a trailing vorticity distribution of the form $\frac{d}{dx}(s^2-x^2)^{3/2}$ in place of $\frac{d}{dx}(s^2-x^2)^{1/2}$ in Takami's notation. This was the case for which Takami found that even the absence of a singularity at the edge of the sheet $x=s$ did not prevent the tendency to random vortex positioning when using the Rosenhead method at times $t \geq 0.4 s/U$. Fig. 12 shows the result of applying the present method, using 24 segments in place of Takami's 24 discrete vortices of constant strength at time $t = 0.4 s/U$. It is evident that no irregularity was found.

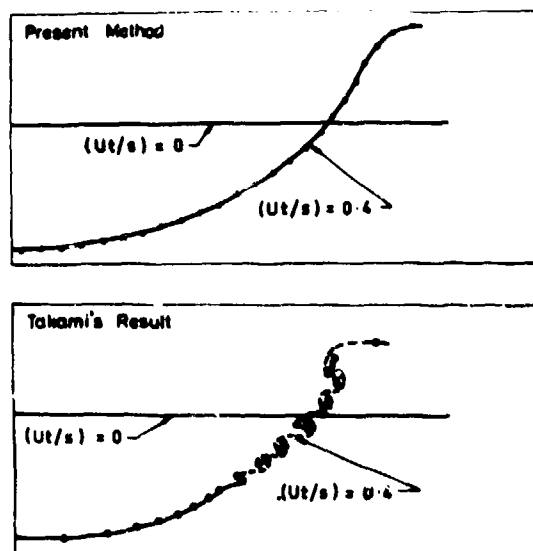


Fig. 12 Development of trailing vorticity distribution

$$\frac{d}{dx}(s^2-x^2)^{3/2} \text{ from } t=0 \text{ to } t=0.4 s/U$$

4.3 Vortex Shedding from Two-Dimensional Bodies

Vortex Shedding in Similarity Flows.

The similarity solutions of Anton [19], Wedemeyer [20] and Blendermann [21] for starting flows near the tips of plates and convex corners involve the computation of constants of proportionality, e.g. in the power law for the growth of circulation of shed vorticity with time. It is important to have these available as near-field solutions, valid early in the shedding process, for patching into the computation of vortex separation from finite bodies for longer times.

The analysis of the previous section is easily adapted to include the presence of boundaries. For the case of the semi-infinite plate we move to a ζ -plane with the transformation

$$\left. \begin{aligned} z &= \frac{i}{2} H \zeta^2 \\ \frac{dz}{d\zeta} &= f(\zeta) = -iH\zeta \end{aligned} \right\} \quad (23)$$

and equation (11) for the velocity of the j th vortex point in the shed sheet becomes

$$\begin{aligned} \dot{\zeta}_j &= \frac{1}{f(\zeta_j)} \left\{ UH + \frac{1}{2\pi i} \sum_{k \neq j}^n \left\{ \frac{\Gamma_k}{\zeta_j - \zeta_k} - \frac{\Gamma_k}{\zeta_j - \bar{\zeta}_k} \right\} \right. \\ &\quad \left. - \frac{\Gamma_j}{2\pi i} \cdot \frac{f'(\zeta_j)}{2f(\zeta_j)} - \frac{1}{2\pi i} \frac{\Gamma_j}{\zeta_j - \bar{\zeta}_j} \right\} \end{aligned} \quad (24)$$

where the logarithmic error term has been taken to vanish due to use of our discretised vorticity method, the variable $\bar{\zeta}_k$ arises from the image system, the penultimate term in parentheses arises from distortion of elemental lengths in the transformation and U is the fluid speed at the arbitrary point $z = -iH$ in steady flow with no vortex shedding. In our method the computation begins with the shedding of one segment of vortex sheet, which we generally represent by one equivalent vortex. Additional equivalent vortex points arise as the computation progresses, see Fig. 13 in which results for a semi-infinite plate are scaled for $Ut/H = 1$ to enable the convergence of the calculation to be exhibited as the number of segments increases from $n=5$ to $n=70$ in steps of 5. The similarity law is $z/H = (Ut/H)^{2/3}$ for this case.

Anton's similarity law for the development of the total circulation $\Gamma(t)$ of the vorticity shed into the fluid in time t is $\Gamma(t)/2\pi UH = C(Ut/H)^{1/3}$ and we found that our solution converged rapidly to the value $C=0.611$, viz.

n	1	10	25	40	55	70
C	0.241	0.539	0.595	0.609	0.610	0.611

This may be compared with values of 0.587, 0.635, 0.586 obtained respectively by Anton, Wedemeyer and Blendermann. The

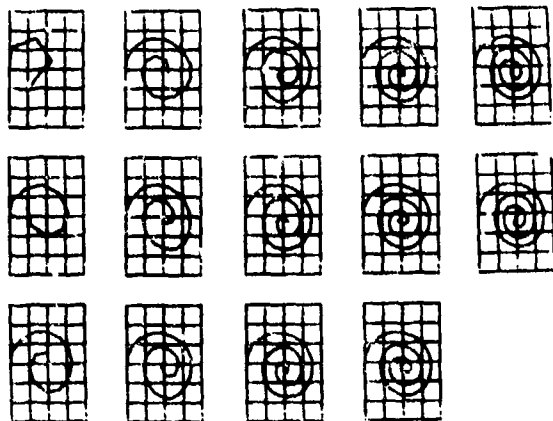


Fig. 13 Starting flow for semi-infinite plate: Scaled representation of sheet by 5, 10, ---, 65, 70 segments

first two of these writers used approximately one turn of outer spiral together with one discrete vortex to represent the inner turns. Anton's lumped central vortex accounted for 54% of the total circulation, Blendermann's accounted for 61% although he used $2\frac{1}{2}$ turns for the outer winding. However, the innermost segment of our 70 segment representation carried only 1.6% of the total circulation. Thus we appear to come rather closer to the character of the Kaden spiral which must obtain in the core and it is quite possible that our solution is the most accurate of the four discussed above.

The constant velocity starting flow near a right angled corner with vortex separation is handled in like manner, the transformation, and similarity laws being given by $z = \frac{1}{2} H \zeta^2$, $z/H = (U t/H)^{1/2}$, $\Gamma(t)/2\pi UH = B(U t/H)^{1/2}$. We again found quite rapid convergence for the constant B to a value of 0.429, viz.

n	1	10	25	40	55	69
B	0.248	0.389	0.441	0.432	0.430	0.429

This may be compared with a value of $B = 0.474$ obtained by Blendermann. Our previous remark in respect of comparative accuracy of the methods may apply here also. Corners with included angles other than zero and $\pi/2$ have not been examined but they are not thought to present any special difficulty.

Vortex Shedding from Finite Plate.

The similarity solutions for starting flow past semi-infinite plates were used by Anton and Wedemeyer as starting points for iterative solutions of the finite plate problem. In principle we should have done likewise but this proved to be not necessary for our purposes. We used the previously described procedure with

the elementary transformation $z = H(\zeta^2 - 1)^{1/2}$ to obtain results for a plate of width $2H$ moving normal to itself - initially at constant speed - following on an impulsive start. Our vortex sheet development was of the same general character as Wedemeyer's except for our rather greater definition of the core region. Fig. 14 shows the development for $(U/tH) = 1.924$ and $(U t/H) = 2.814$, the corresponding number of segments in the sheet being 55, 70.

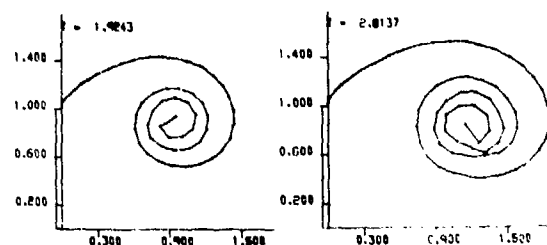


Fig. 14 Starting flow for finite plate: Onset of irregularity due to insufficiently fine subdivision

The pattern shown at the left has a smooth appearance but it is clear that there are several points for which the separation between turns of the spiral has become less than the chosen length of segments. Thus we find growing disturbances and the pattern at the right is the last for which no serious irregularity was observed. The sequence illustrates that the present method is not foolproof but that it gives adequate warning of danger so that the computing scheme may be adjusted. The development of circulation $\Gamma(t)$ shed into the stream at each edge is almost identical with that calculated by Wedemeyer as shown in Fig. 15.

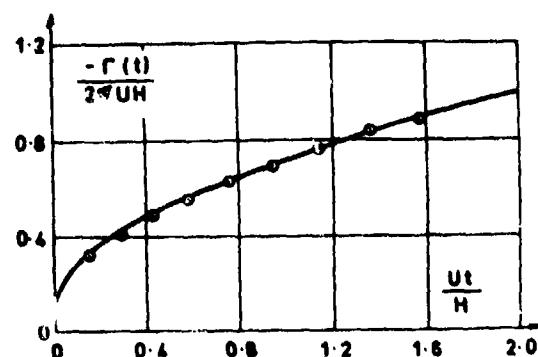


Fig. 15 Finite plate: Time development of circulation
— Wedemeyer's solution
○ Present method

We extended the work of earlier writers by also calculating surface pres-

sure distribution and normal force on plates of constant and time-varying finite width - the latter serving as the unsteady two-dimensional flow which may be incorporated into the theory of slender lifting surfaces with leading edge or vortex separation - with time-varying stream $U(t)$ which, incidentally, provides the means to include the effect of camber on the above slender lifting surfaces. A typical set of pressure distributions is shown in Fig. 16. This is for the special case $U(t) = \text{const}$ and shows both the decay and the inward movement of the surface suction peak in

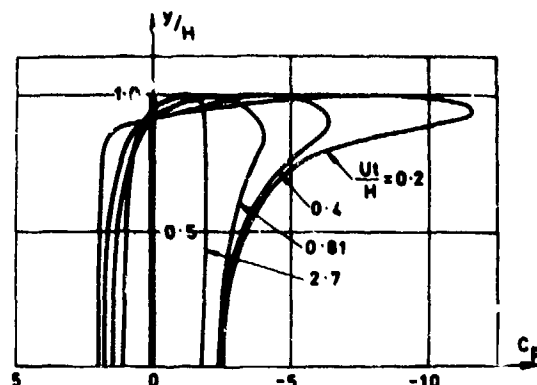


Fig. 16 Pressure distribution on half width of finite plate in uniform motion after impulsive start

the interval $0.2 \leq Ut/H \leq 2.7$. The decline of the front stagnation pressure coefficient towards its steady state value $C_p = +1.0$ may also be noted. Integration of these pressure distributions yielded normal force coefficients C_N which were within one percent of values obtained by careful application of Blasius' theorem, as explained previously, when 70 segments were used to represent a sheet. The discrepancy increased with reducing number of segments reaching nearly 5% when only 15 segments were employed in the representation. Fig. 17 shows an early result of using the Blasius-based method for $0.01 \leq Ut/H \leq 7.5$, the present vorticity discretisation being used after 25 time steps⁶. This is a difficult case for the method since C_N tends to infinity at $t=0$. If any sort of precision is required for small time, the segmentation of the sheet has to be fine, even for small Ut/H . Three curves are drawn for increasingly short final segments Δs_p of the sheets. Since only 70 time steps were employed in each case

⁶ It will be seen that every curve suffers a corresponding kink at the sixth point after the start; i.e. when 30 time steps have elapsed.

the useful range of Ut/H is correspondingly reduced. It might be noted that application of these results to slender lifting surfaces of rectangular planform of aspect ratio A at incidence will involve values of $Ut/H = 2\alpha/A$. This would normally leave us with values of Ut/H rather less than the range shown in Fig. 17 except perhaps when modelling the action of very small aspect ratio fins on ships' hulls.

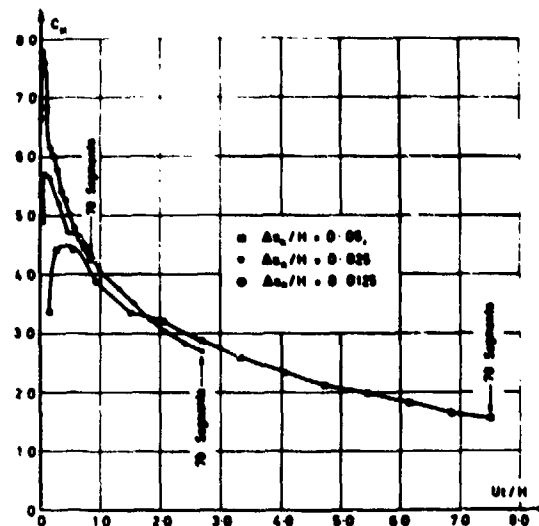


Fig. 17 Normal force coefficient for finite plate, $U=\text{constant}$. Effect of increasing subdivision of sheet

We also examined cases in which $U(t)$ was not constant, including uniform acceleration and the simple harmonic motion $U = \sin t$, which we pursued as part of an attempt to investigate the effect of bilge keel vortex separation on heave damping [39], see also Fig. 1. A specimen result is given in Fig. 18 which indicates the interaction of portions of shed vorticity of opposite sign. Towards the end of the first cycle a finer segmentation of the sheet is required for accuracy than we provided for. In Fig. 19 we present a normal force/displacement diagram in which some overlap of the sheets during the final eighth of the cycle has been ignored. The values of $C_N(t)$ plotted exclude added mass contributions defined in the first term of equation (17). It is clear that the non-linear force is not in phase with the motion of the plate, as is evident from the disposition of the shed vortex sheets. The net area enclosed within the curve represents the work done in generating the vortex system during the first cycle. We aim to extend this analysis when more computer power becomes available to us. Gadd [38] has drawn attention to the need for this type of analysis for an approxim-

ate theory of the action of bilge keels when their 'span' is small compared with the local bilge radius.

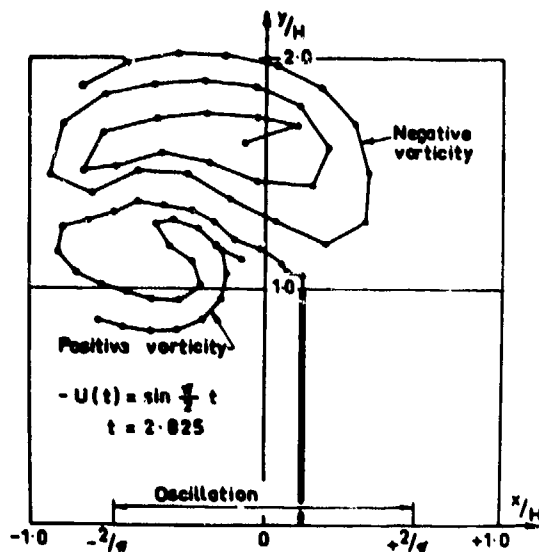


Fig. 18 Vortex sheet configuration in first cycle of simple harmonic motion

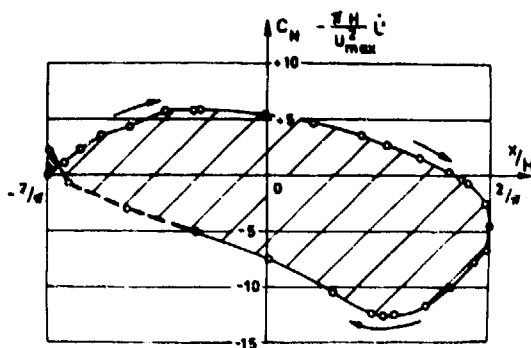


Fig. 19 Non-linear force on oscillating plate

Vortex Shedding from Slender Lifting Surfaces. We have already stated that our discretised vorticity method, together with our extension of the Anton/Wedemeyer/Blendermann work to finite plates of time-varying width is applicable, in respect of vortex separation, to the calculation of aero/hydrodynamic properties of lifting surfaces of arbitrary slender planform with camber. Initially, we applied the method to some slender delta wing configuration for which the well reputed solutions of Smith [29] and Sacks [30] already existed. We next investigated lee vortex disposition above lifting surfaces with curved leading edges. We also obtained some results for non-conical lifting surfaces for which the local span was constant or of linearly decreasing amount downstream of a maximum value.

We give a typical example of separation vortex sheet development in Fig. 20 together with Smith's prediction for the same value of the incidence parameter $\alpha/K = 1.00$, for a delta wing of zero thickness, K being the tangent of the semi-apex angle. The sheet was represented by 70 segments in this example, the central segment carrying 3 percent of the total circulation. The reader is referred back to Fig. 8 for Sacks, Lundberg & Hanson's prediction for the nearly equal value $\alpha/K = 1.07$. Smith's result is based on the use of 21 pivotal points to define the outer spiral together with a cut joining a concentrated vortex carrying 50% of the total circulation. Thus one could not expect close agreement between the predicted shapes of the vortex sheets. Despite the difference in shape of sheet, the two methods give almost identical pressure distributions, as shown in Fig. 21.

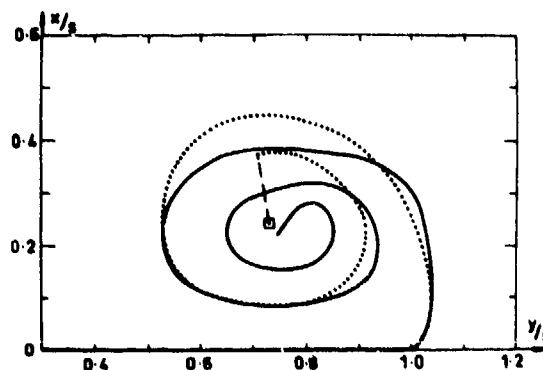


Fig. 20 Vortex Separation on Slender Delta:
 $\alpha/K=1.00$
... Smith,
— Present Method

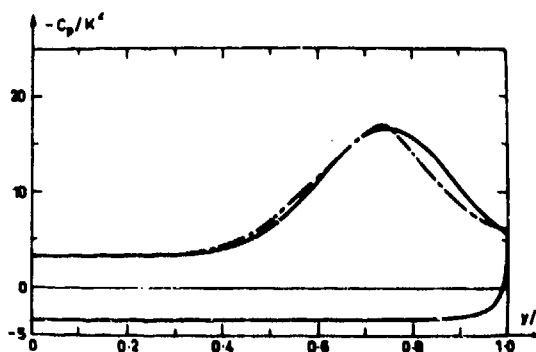


Fig. 21 Pressure Coefficient across Semi-span: Delta, $\alpha/K=1.00$
— Smith,
— Present Method

Perhaps not surprisingly, our prediction for non-linear force is closer to Sacks et al. than to Smith's as shown in Fig. 22. Further reference to Fig. 8 would seem to show that a fair degree of disorganisation of sheet shape can be tolerated in respect of estimation of non-linear normal force on slender delta plan forms.

Linearised theory has it that no lift is found downstream of the maximum span of a plane slender wing and that trailing vorticity shed from the retreating edges remains coplanar with the wing ahead of the trailing edge. We were interested in the effect of roll-up of the retreating edge vorticity on the above near-classical result. Fig. 23 shows the extent of this roll-up at the rear apex of a diamond shaped slender wing operating at the same angle of incidence 21.8° as the semi-apex angle of the diamond ($\alpha/K=1.06$). Flow over the front half wing was arranged to be un-separated. The number of segments used to represent the sheet was 47. Roll-up appeared to be significant for the entire extent of the retreating edges at the substantial angle of incidence chosen for this example. We also considered the same wing for $\alpha/K=1$ but with flow separation from the front apex. A few examples of the development of the shed vorticity, for this case, downstream of the maximum span are shown in Fig. 24. Immediately downstream of the maximum span, the retreating edge vorticity is of opposite sign to the vorticity shed from the leading edge. In the example shown, this changes back to the original sign at a station distant 36% of the half chord downstream of the maximum span. This accounts for the mushroom appear-

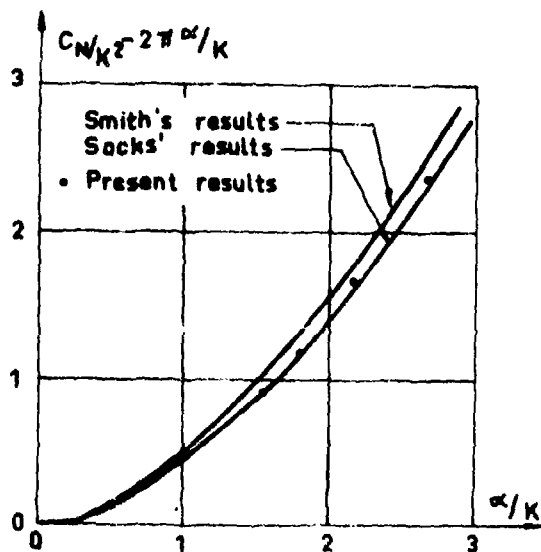


Fig. 22 Non-linear normal force increment for slender delta

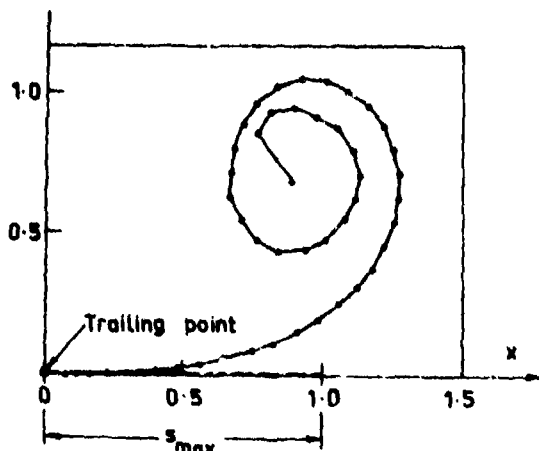


Fig. 23 Roll-up of Trailing Vortex Sheet at Rear Apex of Slender Diamond Wing: $\alpha/K=1.06$, Front Half with Attached Flow



Fig. 24 Roll-up of Trailing Vortex Sheet at Retreating Edge of Slender Diamond Wing: $\alpha/K=1.00$, Front Half with Separated Flow

ance of part of the sheet. Thus it appears that the now well-known bound vortex pattern associated with leading edge separation of slender lifting surfaces merges back into a conventional pattern when a contracting rear portion is fitted downstream of the maximum span. We have constructed plausible bound vortex patterns but we prefer to await the outcome of current calculations of surface pressure distribution for non-conical wings before committing the patterns to paper.

The chordwise distributions of local load coefficient C_n for the non-conical cases discussed above and also for a delta shape followed by a portion of constant span s_{max} are shown in Fig. 25 incidence now being set to 0.1 radian. The linearised slender wing theory attached flow result is shown for reference as a heavy dashed line. Our non-linear theory has perforce to predict infinite C_n when free vorticity is first shed; i.e. at the station immediately downstream of the maximum span. The chordwise loading falls to zero as shown by the light dashed line. The effect of roll-up is to induce lift at all stations upstream of the rear apex.

When leading edge separation occurs on the front half of the lifting surface the loading is of course increased. It appears to decay quite rapidly but not monotonically for the diamond wing, the latter feature presumably being associated with the abovementioned changes of sign of the retreating edge vorticity. When the rear portion is parallel-sided, the local load coefficient decays even less rapidly, as might be expected since the shed vorticity then passes much closer to the lifting surface. For this geometry we have not shown a prediction for attached flow over the delta portion followed by separation over the parallel-sided portion since the latter would be expected to show a $C_N(x)$ distribution equivalent to the two-dimensional flat plate solution for $C_N(t)$, Fig. 17. In any case the slenderness assumptions made here do not apply near the discontinuity in ds/dx . It is planned to investigate these matters in greater detail.

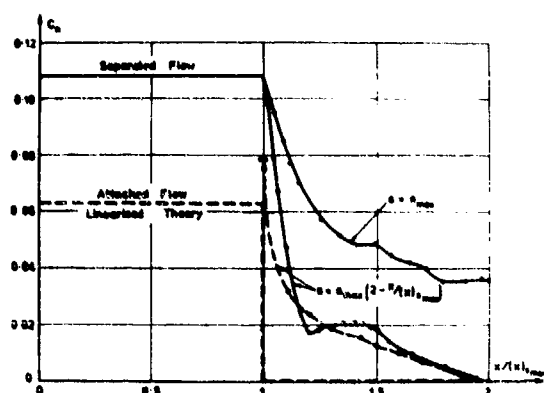


Fig. 25 Chordwise Loading for Two Non-Conical Lifting Surfaces: $\alpha/K=1.00$ for front delta

Vortex Shedding in Ship Manoeuvrability. The present method is applicable to the calculation of zero-Froude number values of non-linear force and moment on slender ships in manoeuvre situations. As a start we have considered the development of bilge vortex sheets and non-linear force for rectangular sections of beam/draft ratios 0.11, 0.60, 0.83, 1.23, 2.09, the geometry of the sections remaining invariant with time in the first instance. In Fig. 26 we show the two dissimilar separation vortex sheets - each modelled by 65 segments - shed from the square bilges of the beamiest of these sections at time $t = 1.80D/BU$. The drift (sideslip) velocity BU is written in terms of the sway angle β . If we replace the time t by distance x/U , this may be taken as an approximate representation of the state of affairs at the aft end of a box-shaped vessel of length/draft ratio 10:1 when $\beta = 10^\circ$. The cal-

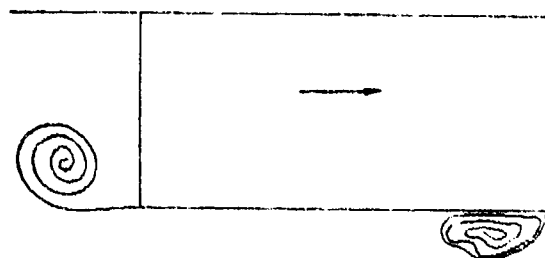


Fig. 26 Vortex Shedding from Rectangular Section: $B/D=2.09$, $BUt=1.80$

ulation was started with 15 segments per sheet, disposed according to our own similarity solution for vortex separation at a right-angled corner. The spirals assumed different shapes after relatively few time steps. Fig. 27 gives first results for the dependence of the non-linear side-force coefficient $C_N(t)$ on beam/draft ratio B/D . It will be noticed how increasing B/D reduces non-linear forces, perhaps due to the straightening of the flow component across the hull and also because the singularities at the shedding edges are less strong for rectangular sections than for a flat plate so that all curves other than $B/D = 0$ (see Fig. 17) have a finite starting value. This work is being extended to check results of oblique towing experiments, on a lenticular model with constant draft, recently made by a student of Professor Nomoto's at Osaka University. The method

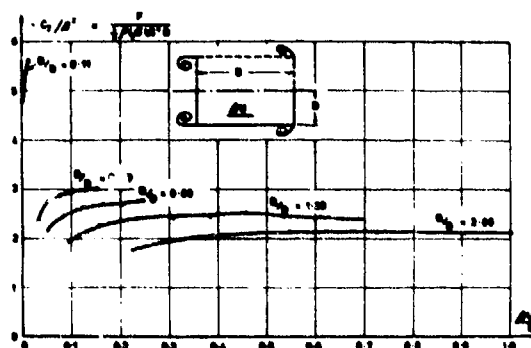


Fig. 27 Sideforce due to Sidesway for Rectangular Sections

is also being developed for more general sections. The zero frequency effect of rate of yaw r on bilge vortex shedding on a ship of length L travelling with speed V , may be studied by setting the two-dimensional stream velocity to $(L/2-Vt)r$.

ACKNOWLEDGEMENTS

We thank Mr Ralph D. Cooper of the U.S. Office of Naval Research, whose invitation to us to contribute to the 10th Symposium on Naval Hydrodynamics produced this paper. One of us (W.K.S.) held a C.S.I.R.O. studentship and, subsequently, a University of New South Wales Postgraduate Research Award while working on this project. In the course of this study one of us (P.T.F.) had the benefit of useful discussion with a number of workers in the field and he would like to make special acknowledgement of Mr J.H.B. Smith of the Royal Aircraft Establishment, Farnborough, U.K. who also provided us with a number of key references.

REFERENCES

1. Lamb, H., Hydrodynamics, 6th ed., Dover, New York, 1945.
2. Rosenhead, L., "The Formation of Vortices from a Surface of Discontinuity", Proceedings of the Royal Society, London, A, Vol. 134, 1931, pp. 170-192.
3. Abernathy, F.H., Kronauer, R.E., "The Formation of Vortex Streets", Journal of Fluid Mechanics, Vol. 13, Part 1, May, 1962, pp. 1-20.
4. Michalke, Von A., "Zur Instabilität und nichtlinearen Entwicklung einer gestörten Scherschicht", Ingenieur-Archiv, 33. Band, 4. Heft, 1964, pp. 264-276.
5. Birkhoff, G. and Fisher, J., "Do Vortex Sheets Roll Up", Circolo Matematico Di Palermo Rendiconti, Tomos 8, Series 2, 1953, pp. 77-89.
6. Hama, F.R. and Burke, E.R., "On the Rolling-Up of a Vortex Sheet", TN 60-1069, Sept. 1960, U.S. Air Force Office of Scientific Research.
7. Batchelor, G.K., An Introduction to Fluid Dynamics, 1st ed., Cambridge University Press, 1967, pp. 528-532.
8. Birkhoff, G. and Carter, D., "Calculation of Interface Motion", Appendix F to Report 1A-1927, Sept. 1955, Los Alamos Scientific Laboratory, University of California.
9. Westwater, F.L., "The Rolling Up of the Surface of Discontinuity behind an Aerofoil of Finite Span", R & M 1692, Aug. 1935, Aeronautical Research Council, Great Britain.
10. Kaden, H., Ingenieur-Archiv, Bd. II, 1931, pp. 140-168.
11. Takami, H., "A Numerical Experiment with Discrete-Vortex Approximation, with Reference to the Rolling Up of a Vortex Sheet", AFOSR 64-1536, Sept. 1964, U.S. Air Force Office of Scientific Research.
12. Moore, D.W., "The Discrete Vortex Approximation of a Finite Vortex Sheet", AFOSR - 1804-69, Oct. 1971, U.S. Air Force Office of Scientific Research.
13. Spreiter, J.R. and Sacks, A.H., "The Rolling Up of the Trailing Vortex Sheet and its Effect on the Downwash behind Wings", Journal of the Aeronautical Sciences, Vol. 18, No. 1, Jan. 1951, pp. 21-32.
14. Rogers, A.W., "Application of Two-Dimensional Vortex Theory to the Prediction of Flow Fields behind Wings of Wing-Body Combination at Subsonic and Supersonic Speeds", NACA TN-3227, Sept. 1954.
15. Cummings, D.E., "Vortex Interactions in a Propeller Wake", Ph.D. Thesis, June 1968, M.I.T.
16. Hackett, J.E. and Evans, M.R., "Vortex Wakes behind High-Lift Wings", Journal of Aircraft, Vol. 8, No. 5, May 1971, pp. 334-340.
17. Butter, D.J. and Hancock, G.J., "A Numerical Method for Calculating the Trailing Vortex System behind a Swept Wing at Low Speed", The Aeronautical Journal of the Royal Aeronautical Society, Vol. 75, Aug. 1971, pp. 564-568.
18. Clements, R.R. and Maull, D.J., "The Rolling Up of a Trailing Vortex Sheet", The Aeronautical Journal of the Royal Aeronautical Society, Vol. 77, Jan. 1973, pp. 46-51.
19. Anton, L., "Ausbildung eines Wirbels an der Kante einer Platte", Göttinger Dissertation, Ingenieur-Archiv Band 10, 1939, pp. 411-421. (English translation: NACA TM-1398, 1956).
20. Wedemeyer, E., "Ausbildung eines Wirbelpaares an den Kanten einer Platte", Ingenieur-Archiv, Band 30, 1961, pp. 187-200.
21. Blendermann, W., "Der Spiralwirbel an translatorisch bewegten Kreisbogenprofil; Struktur, Bewegung und Reaktion", Schiffstechnik, Band 16, Heft 80, Feb. 1969, pp. 3-13.
22. Giesing, J.P., "Vorticity and Kutta Condition for Unsteady Multienergy Flows", Transactions of the ASME, Series E, Journal of Applied Mechanics, Vol. 36, No. 3, Sept. 1969, pp. 608-613.
23. Clements, R.R., "An Inviscid Model of Two-Dimensional Vortex Shedding", Journal of Fluid Mechanics, Vol. 57 Part 2, Feb. 1973, pp. 321-336.
24. Garrard, J.H., "Numerical Computation of the Magnitude and Frequency of the Lift on a Circular Cylinder", Philosophical Transactions of the Royal Society, Vol. 261, Jan. 1967, pp. 137-162.
25. Küchemann, D., "Report on the I.U.T.A.M. Symposium on Concentrated Vortex Motions in Fluids", Journal of Fluid Mechanics, Vol. 21, Part 1, Jan. 1965, pp. 1-20.
26. Küchemann, D. and Weber, J., "Vortex Motions", Zeitschrift für Angewandte Mathematik und Mechanik, Band 45, Heft 7/8, Dec. 1965, pp. 457-474.
27. Brown, C.E., and Michael, W.H. Jr., "Effect of Leading-Edge Separation on the Lift of a Delta Wing", NACA TN-3430, April 1955.
28. Pullin, D.I., "A Method for Calculating Inviscid Separated Flow about Conical Slender Bodies", Aerodynamics Report 140, May 1973,

Department of Supply, Australian Defence Scientific Service, Aeronautical Research Laboratories, Australia.

29. Smith, J.H.B., "Improved Calculations of Leading-Edge Separation from Slender, Thin, Delta Wings", Proceedings of the Royal Society, Series A, Vol. 306, 1968, pp. 67-90.

30. Sacks, A.H., Lundberg, R.E., and Hanson, C.W., "A Theoretical Investigation of the Aerodynamics of Slender Wing-Body Combinations Exhibiting Leading-Edge Separation", NASA CR-719, 1967.

31. Levinsky, E.S., Wei, M.H.Y. and Maki, R.L., "Theoretical Studies of Vortex Flow on Slender Wing-Body Combinations", Sp.-228, 1969, NASA.

32. Finkleman, D., "Nonlinear Vortex Interaction on Wing-Canard Configurations", Journal of Aircraft, Vol. 9, No. 6, June 1972, pp. 399-406.

33. Angelucci, S.B., "A Multivortex Method for Axisymmetric Bodies at Angle of Attack", Journal of Aircraft, Vol. 8, No. 12, Dec. 1971, pp. 959-966.

34. Hennig, G., "Ebene Umströmung von Querschnitten mit Wirbelpaar und Querkraftverteilung infolge Schräganströmung an Körpern mit kleinem Seitenverhältnis", Schiffbau Forschung, Band 9, 1970, pp. 229-245.

35. Fuwa, T., "Hydrodynamic Forces Acting on a Ship in Oblique Towing", Autumn Meeting, Society of Naval Architects of Japan, November 1973. Preprint, pp. 161-173.

36. Tatinclaux, J.C., "Experimental Investigation of the Drag Induced by Bilge Vortices", Schiffstechnik, Vol. 17, No. 87, May 1970, pp. 37-44.

37. Martin, M., "Roll Damping due to Bilge Keels", Contract Nonr 1611(01), November 1958, Iowa Institute of Hydraulic Research, State University of Iowa, Iowa City.

38. Gadd, G.E., "Bilge Keels and Bilge Vanes", Ship Rep. 64, December 1964, Ship Division, National Physical Laboratory, England.

39. Soh, W.K. and Fink, P.T., "On Potential Flow Modelling of Action of Ships' Bilge Keels", Proceedings of Fourth Australasian Conference on Hydraulics and Fluid Mechanics, Monash University, Melbourne, Australia, December 1971, pp. 266-271.

40. Woods, L.C., "The Theory of Subsonic Plane Flow", Cambridge University Press, 1961.

41. Cooper, R.K., "Boundary Conditions on a Vortex Sheet in Non-Steady Flow", ARC 34,074, Aero. Res. Council, London, 1972.

42. Mangler, K.W. and Smith, J.H.B., "Behaviour of the Vortex Sheet at the Trailing Edge of a Lifting Wing", The Aeronautical Journal of the Royal Aeronautical Society, Vol. 74, November 1970, pp. 906-908.

43. Sacks, A.H., "Vortex Interference on Slender Airplanes", NACA TN 3525, November 1955.

DISCUSSION

L. LANDWEBER

Fink and Soh have refined previous treatments of the problem of calculating the motion of vortex sheets. In performing these calculations, it appears to be necessary to assume a distribution of vorticity strength on the sheet. The basis for this selection, and, indeed, the various distributions employed in the examples presented in the paper are not given. It is requested that the authors discuss this question.

The improvement in the numerical treatment consists of evaluating the Cauchy-principal-value integral (2) more carefully in the neighborhood of the singularity. The contribution to the velocity at a point of the vortex sheet from other elements of the sheet is treated by means of the trapezoidal quadrature formula, as was also done by previous investigators.

Discussor suggests that the integral (2) may be discretized almost as simply, but much more accurately, by using a form of the Simpson quadrature rule suitable for treating Cauchy-principal-value integrals, which yields, instead of (11),

$$\bar{q}(z) = \frac{1}{2\pi i} \left[\sum_{k \neq j}^n \frac{\lambda_k \Gamma_k}{z_j - z_k} + \lambda_j \Gamma_j' \right] \quad (1)$$

where $\lambda_1 = \lambda_n = 1$, n an odd number; for other values of k , $\lambda_k = 2$ or 4 according as k is even or odd; and $\Gamma_j' = \gamma_j' \Delta s$. A proof of this rule, which is due to the discussor, was given by Kobus (with due credit) in Appendix 1 of "Examination of Eggers' Relationship Between Transverse Wave Profiles and Wave Resistance," Journal of Ship Research, Vol. 11, No. 4, Dec. 1967. The result is valid for j even or odd, although the proof is given only for j even in the foregoing reference. Since Simpson's rule takes into account the curvature of the curve representing the integrand, the discretization errors should be much smaller and it should be possible to continue the calculations closer to the centers of vortex spirals.

A simple proof of the Cauchy-principal-value quadrature rule, valid for j either even or odd, is as follows. For $a < c < b$, and $f(x)$ a continuous function with a derivative $f'(c)$ at c , we may write

$$\int_a^b \frac{f(x)}{x-c} dx = \int_a^b \frac{f(x)-f(c)}{x-c} dx + \int_a^b \frac{f(c)}{x-c} dx \quad (2)$$

We now divide the interval $a < x < b$ into sub-intervals Δx at points $x_1 = a, x_2, \dots, x_j = c, \dots, x_n = b$. Applying Simpson's rule, we obtain

$$\begin{aligned} \int_a^b \frac{f(x)}{x-c} dx &= \frac{\Delta x}{3} \left[\sum_{k \neq j} \frac{\lambda_k (f_k - f_j)}{x_k - x_j} + \lambda_j f_j' \right] \\ &+ \int_a^{x_{j-e}} \frac{f_j}{x-x_j} dx + \int_{x_{j+e}}^b \frac{f_j}{x-x_j} dx, \quad e = \begin{cases} 1, & j \text{ even} \\ 2, & j \text{ odd} \end{cases} \end{aligned}$$

the remainder of the Cauchy-principal-value integral vanishing because of symmetry. It is now seen that the terms of the above sum containing f_j are either canceled when the last pair of integral are discretized by Simpson's rule, or vanish because of symmetry. The resulting rule is then

$$\int_a^b \frac{f(x)}{x-c} dx = \frac{\Delta x}{3} \left[\sum_{k \neq j} \frac{\lambda_k f_k}{x_k - x_j} + \lambda_j f_j' \right] \quad (3)$$

K. WIEGHARDT

To this valuable review with an improvement of the calculation method, just two supplementary remarks.

1) The finite pressure in the core of an edge vortex might become interesting for cavitation inception. Blendermann /1/ calculated e.g. the vortex sheet when a thin vertical plate ($2B =$ breadth) is accelerated horizontally with constant acceleration a in a fluid at rest (density ϱ). As long as the vortex spiral is small the pressure minimum in the core is, for time $t \ll \sqrt{B/a}$, $p \approx p_{\infty} - 7\varrho(a^2 B t)^{2/3}$.

2) For the plane motion of vortices in unbounded fluid (without shedding of new vorticity) Hamilton's principle might perhaps be used to check numerical computations. The generalised potential U of the Kutta-Joukowski forces on the vortices, which are proportional to their velocity, is $\frac{\varrho}{2} \sum [\vec{v}_k \times \vec{r}_k] \cdot \vec{r}_k$ or, in the notation used here, the imaginary part of $\frac{\varrho}{2} \sum \Gamma_k \bar{z}_k$. Then $U = \frac{\varrho}{2} \sum \Gamma_k (\dot{x}_k y_k - x_k \dot{y}_k)$ and the force $X_k = -\frac{\partial U}{\partial x_k} + \frac{d}{dt} \frac{\partial U}{\partial \dot{x}_k} = \varrho \sum \Gamma_k \dot{y}_k$ and $Y_k = -\varrho \sum \Gamma_k \dot{x}_k$.

The kinetic energy due to the vortices is $E = \frac{\varrho}{2\pi} \sum \Gamma_k \Gamma_l \ln |z_k - z_l| + E_{\infty}$, where E_{∞} (energy of the vortex cores) is infinite, yet independent of position of the vortices. The variational principle $\delta \int_0^t (E - U) dt = 0$ gives e.g. Prandtl's equation for the down wash far behind a lifting line /2/.

/1/ Blendermann, W. Schiffstechn. 20, 1973, pp. 76-80
/2/ Wieghardt, K. ZAMM 22, 1942, p. 59-60.

L. J. DOCTORS

The discussor would like to raise a question concerning computing effort, as the time (t) becomes large. It seems that the computation time will not be proportional to the time of development of the vortex sheet — due to the increasing number of vortices. Could the authors give an indication of the relationship — either as found in theory, or based on theory?

Should the computing time be dependent on a power of t not too much greater than unity, then the results shown in Fig. 19 could be extended to give the steady-state response due to a simple-harmonic motion of the flat plate (or ship section).

G. E. GADD

The authors have demonstrated that their numerical techniques have increased the stability of the computed results as compared with those obtained by earlier workers.

In the case of the problem of Fig. 18, an oscillating plate, presumably after many oscillations the influence of the vorticity shed in the earliest oscillations must become negligible, and a quasi-steady picture should be obtained, dependent only on the phase of the oscillation in its present cycle, and not on the number of previous oscillations that has taken place. Would it help to achieve such a result numerically if an artificial damping were introduced, so that the shed vortices slowly decayed with time?

AUTHOR'S REPLY

We thank our discussors for their comments and suggestions.

The answer to Professor Landweber's question is that the method of stepwise, rediscritisation does not involve explicit computation of the vorticity $\gamma(s, t)$. Instead, we use the circulation of each segment

$$\Gamma_k = \int_{s_{k-1/2}}^{s_{k+1/2}} \gamma(s) ds. \quad \text{When the vortex}$$

sheet is not attached to a boundary, as in Rosenhead/Westwater/Moore type calculations, the discretisation proceeds from a given initial distribution of vorticity. The pivotal points z_k move in accordance with the equation (2) so that Kelvin's theorem applies and the Γ_k do not change with time. To achieve equi-spacing of pivotal points before the next step is undertaken, rediscritisation is used and a new set of Γ_k emerges in an interpolation process which conserves the partial circulation function $K(s)$; i.e. the circulation of the portion of the sheet of length s measured from a reference point on the sheet, such as the midpoint in Westwater type calculations. Thus

$$K(s_k) = \int_0^{s_k} \gamma(s) ds = \frac{1}{2} \Gamma_k + \sum_{m=0}^{k-1} \Gamma_m.$$

When the sheet is attached to a boundary, the calculation is similar but additional vorticity is shed into the fluid in accordance with conditions described in the paper; otherwise the interpolation process is the same.

We believe that Professor Landweber's equation (3) is strictly applicable only to situations for which curvature of the vortex sheets is negligible. When the trace of the sheet is not a straight line, an additional factor appears in the last term on the right side:

$$\begin{aligned} -2\pi i \bar{q}(z_j) &= \int_a^b \frac{\gamma(s) ds}{z(s) - z_j} \\ &= \frac{\Delta s}{3} \left[\sum_{k \neq j} \frac{\lambda_k \gamma_k}{z_k - z_j} + \lambda_j e^{-\theta_j} \gamma_j^1 \right] \end{aligned}$$

where θ_j is the inclination of the tangent to the vortex sheet at z_j . We believe that this use of a form of Simpson's rule is not particularly advantageous. Both γ_k and γ_k^1 are needed in the calculation although our method does not throw these quantities up in explicit form. Since $\gamma = K'(s)$, the above formula becomes sensitive to error in numerical differentiation of the function $\gamma^1(s) = K''(s)$. A further difficulty arises from the fact that application of Simpson's rule requires knowledge of the value of the integrated

function at the ends of the segments whereas our method yields information at midpoints of segments. Thus we would need to extrapolate at the ends of the sheet in addition to interpolating within it for each time step.

We wrote the above reply after attempting to recalculate the semi-infinite plate case of section 4.3 using an adaption of Professor Landweber's form of Simpson's rule for evaluation of the velocity of pivotal points. We immediately encountered irregularity of shape of sheet near the shedding point and then arrived at the above conclusions.

In reply to Professor Wiegardt we are happy to acknowledge that we found Blendermann's work helpful - see our ref. 21 - and the additional reference is also useful. Estimations of cavitation number should be possible for two-dimensional situations. However, when our theory is adapted to slender three-dimensional flow situations, there may be problems in respect of pressure calculations since we are unable to model the strong axial velocities usually found in these circumstances.

In principle we agree with Professor Wiegardt's comment that the energy principle is not violated for exact solutions and we have ourselves commented in section 3.4 on the use of the relevant Hamiltonians. That statement was based on a limited number of checks we had made ourselves. For example our recalculation of Westwater's computation of trailing vortex roll-up behind an elliptically loaded lifting surface (section 4.2) gave changes of the Hamiltonian, in arbitrary units which were typically as follows for the case when $N=40$.

Ut/s	Hamiltonian
0.05	-4.09
0.1	-4.10
0.2	-3.99
0.3	-3.91
0.4	-3.85
0.5	-3.79

It is seen that the form of interpolation used in our stepwise rediscritisation of vorticity leads to changes in the Hamiltonian but that the variation is not large in the examples tested so far.

There are several aspects to Dr. Doctors question re computing time. Ordinarily, the time increases with the number of segments n as $n(n+1)$. However, as explained in section 4.3, it will be necessary to adopt increasingly fine segmentation when the separation between neighbouring loops of vortex sheet is of the same order as the length of the chosen segments and computing time will increase at a greater rate. It may of course be possible to coalesce elemental vortices for certain purposes

and thus save computing time. A carefully executed example of this procedure is given in a recent paper by Moore [44] which was not available to us when writing the review section of our paper. Computing effort must also depend on the magnitude of time step chosen. In our examples the stepwise rediscritisation method was found to be stable so that time steps were made large and only limited by considerations of accuracy as described in relation to the recalculation of Takami's computation of trailing vortex sheet roll up in section 4.2.

We agree that it would be desirable to approach the steady state for an oscillating plate rather more closely than in the calculations presented in section 4.3.

Dr. Gadd's interesting suggestion would force us to declare something like a half life for a portion of vorticity! We would prefer to find asymptotic conditions for the oscillating plate by plotting some appropriate quantity such as the work done per cycle against the number of cycles. Presumably it will be satisfactory to represent distant vortex sheets by single equivalent vortices and to apply obvious approximations for the effect of vortices which have become very remote.

44. Moore, D.W., "A Numerical Study of the Roll-Up of a Finite Vortex Sheet", Journal of Fluid Mechanics, Vol. 63, Part 2, 1974, pp. 225-235

THE FORCE AND MOMENT ON A TWIN-HULL SHIP IN A STEADY POTENTIAL FLOW*

by

Wen-Chin Lin

Naval Ship Research and Development Center
Bethesda, Maryland

ABSTRACT

The linearized problem of potential flow around a twin-hull ship is solved by two sheet distributions of sources and normal doublets. The thickness problem is solved by the thin-ship approximation, while the lifting problem is solved by a slender-ship approximation. General formulas for the steady hydrodynamic force and moment acting on a hull are obtained as an extended form of Lagally's theorem for two floating lifting bodies. This theory is applied to the prediction of wave resistance of Small-Waterplane-Area Twin-Hull (SWATH) ships. Computed and experimental results are compared and presented.

1. INTRODUCTION

Recently, there has been a considerable amount of interest in developing a particular type of twin-hull configuration, namely, the Small-Waterplane-Area Twin-Hull (SWATH) ship, as a new design concept for a number of specific Navy applications. As part of the initial effort to investigate the hydrodynamic performance of SWATH ships, an analytical tool for predicting wave resistance was developed. This paper presents the results of subsequent efforts to extend the scope of analysis to include an investigation of the steady hydrodynamic force and moment on a twin-hull ship of a more general shape.

The wave resistance problem of catamarans has been investigated by Lunde (1951) and Eggers (1955). In both papers, a catamaran was treated as two separate but identical thin ships, and the velocity potential of the problem was obtained from two sheet distributions of simple sources (or, more precisely, Havelock sources). However, since each hull is in proximity to the other, and since each will generally experience an asymmetrical flow field around it, distributions of simple sources alone are insufficient for solving the problem. To account for the asymmetric flow field around each hull, distributions of doublets normal to the sheets should be simultaneously considered. Fortunately, by virtue of linearization, the effects of doublet distributions may always be superimposed to refine the results initially obtained from source distributions without jeopardizing the initial results.

In this paper, the twin hulls are represented by two distributions of sources and normal doublets on their planforms (which, in the case of a symmetric ship, correspond

to the ship centerplane). The normal-doublet distribution is also extended into the infinite downstream in the wake regions which trail each hull. Hence, the so-called "lifting" effect is also included in the present analysis. The mathematical problem is formulated within the context of the linearized thin-ship theory. Therefore, the "thickness problem," i.e., the determination of the source density, may be solved immediately upon application of the boundary conditions. For the "lifting problem," i.e., the determination of the doublet density, an integral equation is initially derived with the full expression of the Havelock doublet as its kernel.

As a first approximation, the kernel function of the original integral equation is replaced by the so-called "zero-Froude-number" Green's function. This equation is further reduced to a singular integral equation of one variable by introducing low draft-to-length ratio and small hull separation distance-to-length ratio approximations. For this reduced problem, both the source density and doublet density of the distributions have been obtained. General formulas for force and moment expressed in terms of these singularity-distribution densities have been derived. The result, as might be expected, is an extended form of Lagally's theorem for thin lifting bodies making a uniform motion in the free surface. In addition to the expressions obtained by Cummins (1957) for the steady case, terms involving integrations along the waterline and the trailing edge of a hull now appear in these formulas. The significance of these additional terms for making better predictions of force and moment on a floating lifting body is being assessed by actual computations and by comparison of the computed results with experimental data.

As an example of the application of the theory presented in this paper, the wave resistance of two SWATH ships has been investigated. The results of computations together with their comparisons with experimental results are presented. Unfortunately, the entire scope of the investigation of force and moment on a twin-hull ship is not covered in this paper since the work is still in progress and further computations are being made. We shall continue to report the results of such investigations as they become available.

2. FORMULATION OF THE PROBLEM

Consider a twin-hull ship moving with constant forward speed U into otherwise calm water of infinite depth. The

* Read at the Tenth Symposium on Naval Hydrodynamics, June 24-28, 1974, M.I.T., Cambridge, Mass., U.S.A.

NOMENCLATURE

(Additional nomenclature are defined as they appear in the text)

$C(x,z)$	= mean camber surface of a demihull	$\underline{A} \wedge \underline{B}$	= vector product of two vectors
$t(x,z)$	= half thickness of a demihull	Σ	= bounding surface of a control volume excluding ship wetted surface
$2b$	= hull-separation distance	∇_c	= control volume bounded by Σ and the wetted surface of Hull 1, S_1
Φ	= total velocity potential	∇'_c	= ∇_c plus the displacement of Hull 1
ϕ	= disturbance potential	\underline{n}	= $(0,1,0)$ = the unit normal to $S_{1b}^{(0)}$
\underline{q}	= total fluid velocity relative to the ship	\underline{q}_t	= tangential component of \underline{q} with respect to $S_{1b}^{(0)}$
\underline{v}	= disturbance velocity	\underline{q}_n	= normal component of \underline{q} with respect to $S_{1b}^{(0)}$
$S_{1b}^{(0)}$	= planform of Hull 1	$\underline{q}_t^{(+)} - \underline{q}_t^{(-)}$	= the difference in \underline{q}_t at both sides of $S_{1b}^{(0)}$
$S_{1w}^{(0)}$	= wake sheet trailing Hull 1	$\hat{\underline{q}}$	= averaged value of the fluid velocities at both sides of the singularity distribution
ϕ_a	= disturbance potential due to source distribution	\underline{F}	= hydrodynamic force acting on Hull 1
ϕ_μ	= disturbance potential due to normal doublet distribution	\underline{N}_0	= hydrodynamic moment acting on Hull 1 with reference to the origin of the Oxyz-frame
σ	= local density of the source distribution	R_w	= total wave resistance
μ	= local density of the normal doublet distribution	\oint	= Cauchy principal value integral
H	= ship draft		
L	= ship length		
B	= ship beam		
$\underline{A} \bullet \underline{B}$	= scalar product of two vectors		

two hulls will be referred to as Hull 1 and Hull 2, respectively. Let Oxyz be a right-hand Cartesian coordinate system moving together with the ship, with Oz directed upward (against gravity), Ox in the direction of motion, Oy to port, and Oxy coinciding with the undisturbed free surface.

As usual, we shall assume that each hull is "thin" and has small camber, and that the two hulls are mirror images of each other. We shall further assume that Hull 1 is situated approximately in the Oxz plane, and Hull 2 is situated approximately in the plane $y = 2b$. Thus, the hull separation distance is $2b$, and the plane $y = b$ is a plane of symmetry for the whole flow field.

Using this coordinate system, the ship geometry may be described as follows:

$$\text{Hull 1: } \begin{cases} y_{1P} = f^+(x, z), \\ y_{1S} = f^-(x, z), \end{cases} \quad (2.1a)$$

$$\text{Hull 2: } \begin{cases} y_{2P} = -f^-(x, z) + 2b, \\ y_{2S} = -f^+(x, z) + 2b, \end{cases} \quad (2.1b)$$

where the subscript S and P indicate the starboard and port sides of the hull, respectively.

For convenience, let us define the mean camber surface and the half-thickness function, respectively, as follows:

$$C(x, z) = \frac{1}{2} \{ f^+(x, z) + f^-(x, z) \} \quad (2.2a)$$

$$t(x, z) = \frac{1}{2} \{ f^+(x, z) - f^-(x, z) \} \quad (2.2b)$$

Then,

$$\begin{cases} f^+(x, z) = C(x, z) + t(x, z), \\ f^-(x, z) = C(x, z) - t(x, z). \end{cases} \quad (2.3)$$

Finally, we shall assume that the draft of the ship is H and the ship length is L , extending from $-L/2$ to $L/2$.

We shall now develop a potential flow of an inviscid fluid for a twin-hull ship. This development will be based upon the linearized theory of ship waves using the thin-ship approximation.

Let the total velocity potential Φ be given by

$$\Phi = -Ux + \phi$$

so that its gradient gives the total fluid velocity relative to the ship as follows:

$$\underline{q} = \nabla \Phi = -U\underline{e}_1 + \nabla \phi, \quad (2.4)$$

where

$$\nabla \phi = (u, v, w) = \underline{v}, \quad (2.5)$$

which represents the disturbance velocity due to the ship. We shall use the notation e_i , $i = 1, 2, 3$ to represent the three base vectors of the $Oxyz$ coordinate system. Then, by a systematic perturbation expansion based on the thin-ship assumption, we may obtain the following boundary-value problem appropriate for the first-order approximation of the disturbance potential ϕ .

$$\left. \begin{aligned} \frac{\partial^2 \phi}{\partial x^2} + \frac{\partial^2 \phi}{\partial y^2} + \frac{\partial^2 \phi}{\partial z^2} &= 0, \quad \text{for } z < 0, \\ \frac{\partial^2 \phi}{\partial x^2} + k_0 \frac{\partial \phi}{\partial z} &= 0, \quad \text{at } z = 0, \\ \text{where } k_0 &= g/U^2, \\ \phi &= \begin{cases} O\left(\frac{1}{\sqrt{x^2 + y^2}}\right), & \text{for } x > 0, \\ O(1), & \text{for } x < 0, \end{cases} \quad \text{as } x^2 + y^2 \rightarrow \infty \\ \lim_{z \rightarrow \infty} \frac{\partial \phi}{\partial z} &= 0. \end{aligned} \right\} \quad (2.6)$$

In addition, ϕ is required to satisfy the following approximate kinematic conditions at the ship:

$$\left. \begin{aligned} \frac{\partial \phi}{\partial y}(x, +0, z) &= -U \frac{\partial f^+}{\partial x} = -U \left\{ \frac{\partial C}{\partial x} + \frac{\partial t}{\partial x} \right\}, \\ \frac{\partial \phi}{\partial y}(x, -0, z) &= -U \frac{\partial f^-}{\partial x} = -U \left\{ \frac{\partial C}{\partial x} - \frac{\partial t}{\partial x} \right\}, \\ \text{and} \\ \frac{\partial \phi}{\partial y}(x, 2b+0, z) &= U \frac{\partial f}{\partial x} = U \left\{ \frac{\partial C}{\partial x} - \frac{\partial t}{\partial x} \right\}, \\ \frac{\partial \phi}{\partial y}(x, 2b-0, z) &= U \frac{\partial f^+}{\partial x} = U \left\{ \frac{\partial C}{\partial x} + \frac{\partial t}{\partial x} \right\}, \end{aligned} \right\} \quad \begin{matrix} \text{for } (x, 0, z) \in S_{1b}^{(0)} \\ \text{for } (x, 2b, z) \in S_{2b}^{(0)} \end{matrix} \quad (2.7)$$

where $S_{1b}^{(0)}$ and $S_{2b}^{(0)}$ represent projections of the wetted surfaces of Hull 1 and Hull 2 onto the vertical planes $y = 0$ and $y = 2b$, respectively, when the ship is at rest. In wing theory terminology, $S_{1b}^{(0)}$ and $S_{2b}^{(0)}$ are the planforms of Hulls 1 and 2, respectively.

Before proceeding further, let us observe the flow situation around the ship. Because each hull is now cambered and is situated in proximity to the other, each will experience a uniform flow coming from an angle. Hence, in addition to the usual thickness effect of a symmetric monohull ship, the so-called cross-flow effect must also be considered. This is true even if the camber is reduced to zero since, for two identical monohull ships sailing abreast, the flow around each ship will still be asymmetric with respect to its centerplane.

Since both the differential equation and the boundary conditions (2.6) and (2.7) are linear, we may consider the effect of thickness and the effect of the position of the mean camber line (which now includes the incidence) separately. This can be done by assuming $C(x, y) = 0$ and $t(x, z) = 0$ in (2.7), respectively, and superimposing the results. Thus, for example, the flow around Hull 1 may be decomposed into two problems as follows: (1) the flow around a symmetric hull (with respect to the plane $y = 0$) without the presence of Hull 2, and (2) the flow around a very thin hull (zero thickness), with or without camber, in the presence of Hull 2. Subsequently, these two problems will be referred to as the "thickness" and the "lifting" problems, respectively. The flow around Hull 2 may be similarly decomposed. This suggests that the disturbance potential ϕ may have the following decomposition:

$$\phi = \phi_{1\sigma} + \phi_{1\mu} + \phi_{2\sigma} + \phi_{2\mu}, \quad (2.8)$$

such that

$$\left. \begin{aligned} \frac{\partial \phi_{1\sigma}}{\partial y}(x, \pm 0, z) &= \mp U \frac{\partial t}{\partial x}, \\ \frac{\partial \phi_{1\mu}}{\partial y}(x, 0, z) + \frac{\partial \phi_{2\mu}}{\partial y} &= -U \frac{\partial C}{\partial x} - \frac{\partial \phi_{2\sigma}}{\partial y}, \end{aligned} \right\} \quad \begin{matrix} \text{for } (x, 0, z) \in S_{1b}^{(0)}, \\ (2.9) \end{matrix}$$

$$\left. \begin{aligned} \frac{\partial \phi_{2\sigma}}{\partial y}(x, 2b \pm 0, z) &= \mp U \frac{\partial t}{\partial x}, \\ \frac{\partial \phi_{2\mu}}{\partial y}(x, 2b, z) + \frac{\partial \phi_{1\mu}}{\partial y} &= U \frac{\partial C}{\partial x} - \frac{\partial \phi_{1\sigma}}{\partial y}, \end{aligned} \right\} \quad \begin{matrix} \text{for } (x, 2b, z) \in S_{2b}^{(0)}. \\ (2.10) \end{matrix}$$

In view of these boundary conditions and the corresponding flow problem each component potential represents, we may expect the potentials $\phi_{1\sigma}$ and $\phi_{2\sigma}$ to be symmetrical about the planes $y = 0$ and $y = 2b$, respectively, while $\phi_{1\mu}$ and $\phi_{2\mu}$ should be antisymmetrical about these two planes. Hence,

$$\left. \begin{aligned} \phi_{1\sigma}(x, y, z) &= \phi_{1\sigma}(x, -y, z), \\ \phi_{1\mu}(x, y, z) &= -\phi_{1\mu}(x, -y, z), \end{aligned} \right\} \quad (2.11)$$

and

$$\left. \begin{aligned} \phi_{2\sigma}(x, y, z) &= \phi_{2\sigma}(x, -y+4b, z), \\ \phi_{2\mu}(x, y, z) &= -\phi_{2\mu}(x, -y+4b, z). \end{aligned} \right\} \quad (2.12)$$

Our next task is to find solutions to the boundary-value problems given by (2.6), (2.9), and (2.10). We shall try to find the respective solutions by the method of Green's functions.

2.1 Solution to the Thickness Problem

Let us first find the solution to $\phi_{1\sigma}$ which is required to satisfy the requirements in (2.6) and the first equation in (2.9).

Since $\phi_{1\sigma}$ is expected to be symmetrical with respect to the plane $y = 0$ (see 2.11), it suggests that $\phi_{1\sigma}$ may be obtained by a distribution of sources and sinks over the planform of Hull 1, $S_{1b}^{(0)}$. Thus

$$\phi_{1\sigma}(x, y, z) = - \iint_{S_{1b}^{(0)}} \sigma(x_0, z_0) G(x, y, z; x_0, 0, z_0) dx_0 dz_0, \quad (2.13)$$

where $\sigma(x_0, z_0)$ is the local surface density of the distribution, and $G(x, y, z; x_0, y_0, z_0)$ is known as a Green's function. This function satisfies all the requirements in (2.6), except at $(x, y, z) = (x_0, y_0, z_0)$, and has the form

$$G(x, y, z; x_0, y_0, z_0) = \frac{1}{r} + H(x - x_0, y - y_0, z + z_0), \quad (2.14)$$

In this expression $r = [(x - x_0)^2 + (y - y_0)^2 + (z - z_0)^2]^{1/2}$ and H is harmonic everywhere in the lower half space. The explicit expression of the function G is well known (see, for example, page 149 of Wehausen (1973)), and may be written in the following form:

$$\begin{aligned} G(x, y, z; x_0, y_0, z_0) = & \frac{1}{r} + \frac{1}{r_1} \\ & - \frac{4}{\pi} \int_0^{\pi/2} d\theta \int_0^\infty dk k \frac{\exp k(z+z_0)}{k - k_0 \sec^2 \theta} \\ & \times \cos[k(x - x_0) \cos \theta] \cdot \cos[k(y - y_0) \times \sin \theta] \\ & - 4k_0 \int_0^{\pi/2} d\theta \sec^2 \theta \cdot \exp[k_0(z+z_0) \times \sec^2 \theta] \\ & \times \sin[k_0(x - x_0) \sec \theta] \cdot \cos[k_0(y - y_0) \times \sin \theta \sec^2 \theta], \end{aligned} \quad (2.15)$$

where $r_1 = [(x - x_0)^2 + (y - y_0)^2 + (z + z_0)^2]^{1/2}$, $k_0 = g/U^2$, and the integral with respect to k is a Cauchy principal-value integral.

The function G for this specific case is called a "Havelock source" and, in addition to having the properties of a source potential, satisfies the linearized free-surface condition in (2.6). Thus, it is obvious from (2.13) and (2.14) that $\phi_{1\sigma}$ has the properties of a single-layer potential, and, in particular, has the following jump property at the surface of distribution, $S_{1b}^{(0)}$:

$$\frac{\partial \phi_{1\sigma}}{\partial y}(x, \pm 0, z) = \pm 2\pi \sigma(x, z). \quad (2.16)$$

From (2.16) and the first equation of (2.9), the local surface density, $\sigma(x_0, z_0)$, of the distribution is found to be related to the half-thickness function of a hull as follows:

$$\sigma(x, z) = - \frac{U}{2\pi} \frac{\partial t}{\partial x} \quad (2.17)$$

In a similar manner, we may conclude that

$$\phi_{2\sigma}(x, y, z) = - \iint_{S_{2b}^{(0)}} \sigma(x_0, z_0) G(x, y, z; x_0, 2b, z_0) dx_0 dz_0, \quad (2.18)$$

where $S_{2b}^{(0)}$ is the planform of Hull 2. Since we assume that Hull 2 is a mirror image of Hull 1, the local surface density of the source distribution for Hull 2 in (2.18) will still be given by (2.17).

Thus, both $\phi_{1\sigma}$ and $\phi_{2\sigma}$ are now completely determined. Our next task is to determine $\phi_{1\mu}$ and $\phi_{2\mu}$.

2.2 Solution to the Lifting Problem

Suppose that Hull 1 is of zero thickness, but cambered, and is situated in close proximity to Hull 2 which has finite thickness. As was previously discussed, $\phi_{1\mu}$ describes this portion of the flow field around Hull 1. By (2.11), $\phi_{1\mu}$ is antisymmetrical with respect to the plane $y = 0$. This suggests that $\phi_{1\mu}$ can be represented by a distribution of doublets of surface density μ in the x, z -plane. To satisfy the antisymmetrical property of (2.11), the orientation of the doublet distribution should be normal to the x, z -plane. Analogous to the situation of an incident flow past a finite thin wing, we shall assume that there is now a steady vortex wake trailing the stern of Hull 1 and remaining in the x, z -plane. We shall also assume a similar physical picture for Hull 2. Furthermore, since the wake is now a sheet of discontinuity, the doublet distribution extends over the wake $S_{1w}^{(0)}$ as well as over the planform $S_{1b}^{(0)}$ of Hull 1. Thus,

$$\phi_{1\mu}(x, y, z) = \iint_{S_{1b}^{(0)} + S_{1w}^{(0)}} \mu(x_0, z_0) \frac{\partial}{\partial y} G(x, y, z; x_0, 0, z_0) dx_0 dz_0, \quad (2.19)$$

where the suffix $S_{1b}^{(0)} + S_{1w}^{(0)}$ indicates that the integral is taken over the planform of Hull 1 and the wake trailing behind it.

Similarly, for Hull 2, we have

$$\phi_{2\mu}(x, y, z) = \iint_{S_{2b}^{(0)} + S_{2w}^{(0)}} \mu(x_0, z_0) \frac{\partial}{\partial y} G(x, y, z; x_0, 2b, z_0) dx_0 dz_0, \quad (2.20)$$

where the distribution is now extending over the planform of Hull 2 and its wake. The minus sign in (2.20) is due to the assumption that Hull 2 is a mirror image of Hull 1; hence, the doublet density for Hull 1 is equal in magnitude and opposite in orientation from that of Hull 2. From (2.14), (2.19), and (2.20), it is clear that both $\phi_{1\mu}$ and $\phi_{2\mu}$ have the properties of a double-layer potential. In particular, we have:

$$\phi_{1\mu}(x_0, +0, z_0) - \phi_{1\mu}(x_0, -0, z_0) = -4\pi\mu(x_0, z_0) \quad (2.21)$$

for $(x_0, 0, z_0) \in S_{1b}^{(0)} + S_{1w}^{(0)}$,

and

$$\phi_{2\mu}(x_0, 2b+0, z_0) - \phi_{2\mu}(x_0, 2b-0, z_0) = +4\pi\mu(x_0, z_0) \quad (2.22)$$

for $(x_0, 2b, z_0) \in S_{2b}^{(0)} + S_{2w}^{(0)}$.

Since, by (2.11) $\phi_{1\mu}$ is an odd function of y , (2.21) gives

$$\mu(x_0, z_0) = -\frac{1}{2\pi} \phi_{1\mu}(x_0, +0, z_0). \quad (2.23)$$

Similarly, for Hull 2, we have from (2.22)

$$\mu(x_0, z_0) = \frac{1}{2\pi} \phi_{2\mu}(x_0, 2b+0, z_0). \quad (2.24)$$

A few more observations can be made for the doublet density μ . The expression for the pressure appropriate for the first-order approximation may be obtained from Bernoulli's law as

$$p = \rho U \frac{\partial \phi}{\partial x} = \rho U \cdot \frac{\partial}{\partial x} \{ \phi_{1\mu} + \phi_{1\mu} + \phi_{2\mu} + \phi_{2\mu} \}. \quad (2.25)$$

Since, in (2.25), $\partial \phi_{1\mu} / \partial x$ is the only function which suffers a jump discontinuity across the sheet $S_{1b}^{(0)} + S_{1w}^{(0)}$, the pressure difference on both sides of this sheet is

$$\begin{aligned} p^{(+)} - p^{(-)} &= p(x, +0, z) - p(x, -0, z) \\ &= \rho U \left\{ \frac{\partial \phi_{1\mu}}{\partial x}(x, +0, z) - \frac{\partial \phi_{1\mu}}{\partial x}(x, -0, z) \right\} \\ &= -4\pi\rho U \frac{\partial \mu}{\partial x}. \end{aligned} \quad (2.26)$$

The assumption that the pressure is continuous across the wake implies that

$$\frac{\partial \mu(x_0, z_0)}{\partial x} = 0, \text{ or, } \mu(x_0, z_0) = \mu\left(\frac{L}{2}, z_0\right) \quad (2.27)$$

in the wake $S_{1w}^{(0)}$. That is, μ is constant along lines which are parallel to the direction of flow in the wake. Similarly, we may also set $\partial \mu / \partial x = 0$ along the keel if we assume continuity of pressure. At the keel we shall further assume that the function $\phi_{1\mu}$ is continuous. This means that

$$\mu(x_0, -H) = 0, \quad (2.28)$$

everywhere.

Since $\mu(x_0, z_0)$ is no longer related directly to the local geometry of the ship, it is more difficult to determine $\phi_{1\mu}$. However, the second equation of (2.9) may now be used. If we substitute expressions in (2.15), (2.18), (2.19), and (2.20) into (2.9), we may write

$$\begin{aligned} \lim_{y \rightarrow 0} \iint_{S_{1b}^{(0)} + S_{1w}^{(0)}} \mu(x_0, z_0) \frac{\partial^2}{\partial y^2} \{ G(x, y, z; x_0, 0, z_0) \\ - G(x, y, z; x_0, 2b, z_0) \} dx_0 dz_0 \\ = -U \frac{\partial \zeta}{\partial x} + \iint_{S_{1b}^{(0)}} \sigma(x_0, z_0) \frac{\partial G}{\partial y} \\ \times (x, 0, z; x_0, 2b, z_0) dx_0 dz_0 \end{aligned} \quad (2.29)$$

This is an integral equation to be solved for the unknown doublet density μ . The right-hand side of (2.29) involves only known quantities, since the source density $\sigma(x_0, z_0)$ is already related to the local slope by (2.17). However, this equation becomes extremely complex if the complete expression of the kernel function G is to be substituted from (2.15). A closed-form solution of this complete integral equation appears to be beyond our resources. Although we may try to solve this equation numerically it is not advisable to take a brute-force approach to evaluate the function G in the form given by (2.15) without further reduction. Since, in this expression, G contains a double-integral term with a highly oscillating integrand, a direct numerical evaluation of this term is not only time-consuming but prone to inaccuracy.

Hu (1961) has shown that for a simpler case, i.e., for $y = 0$ and $y_0 = 0$, the k -integral of the double-integral term in (2.15) may be expressed in terms of the exponential integral function. Since the exponential integral function is well behaved and is also extensively tabulated, the degree of numerical difficulty appears to be considerably reduced.

To fill the need of the problem here, Hu's approach has been extended to a general case of G . It is shown in Appendix A that (2.15) may be written in the following form:

$$G(x, y, z; x_0, y_0, z_0) = \frac{1}{r} + \frac{1}{r_1} + \frac{1}{\pi} \frac{\partial}{\partial a} \int_{-\pi}^{\pi} d\theta \cdot e^{\nu(a+i\tilde{\omega})} \cdot E_1(\nu(a+i\tilde{\omega})) + 4 \frac{\partial}{\partial a} \int_{\pi/2}^{\pi/2+\beta} d\theta \cdot e^{\nu a} \cdot \sin[\nu \rho \cos(\theta - \beta)], \quad (2.30)$$

$$\text{where } a = z + z_0, \rho = \sqrt{(x - x_0)^2 + (y - y_0)^2},$$

$$\beta = \tan^{-1}[(y - y_0)/(x - x_0)], \tilde{\omega} = (x - x_0) \cos \theta + (y - y_0) \sin \theta$$

$$\text{and } \nu = k_0 \sec^2 \theta.$$

the rest of the variables are already defined in (2.15). The special function E_1 is the "exponential integral function" as defined by Equation (A.4) of Appendix A.

In (2.30), the double-integral term has been reduced to a single integral. Since the function E_1 is extensively tabulated and its method of computation well studied, an efficient numerical scheme for evaluating G may be developed from (2.30).

As an alternate approach, we may also try to solve the integral Equation (2.29) by an iterative perturbation technique. In fact, for a yawed-ship problem, Hu (1961) assumed perturbation expansions for both G and the doublet density μ , and solved the integral equation of the problem by an iterative procedure.

In terms of (2.30), the expansion for G used in Hu may be written as follows:

$$\{G - G^{(0)} - G^{(w)}\} \sim G^{(1)} + G^{(2)} + G^{(3)} + \dots \quad (2.31)$$

where

$$G^{(0)} = \frac{1}{r} + \frac{1}{r_1}, \quad (2.32)$$

and

$$G^{(w)} = 4 \frac{\partial}{\partial a} \int_{\pi/2}^{\pi/2+\beta} d\theta e^{\nu a} \cdot \sin[\nu \rho \cos(\theta - \beta)]. \quad (2.33)$$

The remaining terms of (2.31), $G^{(n)}$, $n = 1, 2, 3, \dots$, are obtained by making use of the asymptotic expansion of the E_1 function. Their explicit expressions are given by Equations (A.18) and (A.19) of Appendix A. Since the asymptotic expansion of the E_1 function is valid only for large arguments, and since the argument of the E_1 function in (2.30) is now $\nu(a + i\tilde{\omega})$ which is related to the inverse of the Froude

squared, the expansion (2.31) is valid only for low Froude numbers.

In fact, $G^{(0)}$ in (2.31) corresponds to the limiting case of setting Froude number equal to zero, and is referred to as the "zero-Froude-number" approximation of G . Hu further reasoned that $G^{(0)}$ and $G^{(w)}$ represent the lowest- and highest-order terms in the expansion, respectively, and pursued the iterative approximations accordingly.

In Hu's report, the computational results so obtained compared favorably with corresponding experimental data. Therefore, it may be inferred that a similar technique may be applied here to solve the integral Equation (2.29). On the other hand, some investigators have experienced difficulty in using the iterative technique based on a perturbation expansion which has the zero-Froude-number approximation as its first term in the series, and have warned that such a technique may not be valid. In any case, the information available in this regard seems inconclusive in proving or disproving the validity of such a technique. Continuing efforts are being made to solve the integral Equation (2.29) both by a direct numerical scheme and by the iterative perturbation technique. It is felt that, short of rigorous mathematical proof, one can draw a conclusion about the validity of the iterative perturbation technique only after a careful examination of the computed results obtained by different methods, such as those mentioned above, and by comparison between the computed results and experimental data.

2.3 Zero-Order Solution

In the following we shall attempt to derive an approximate solution to the integral Equation (2.29) by replacing the complete expression of G by $G^{(0)}$. Such a solution is equivalent to the zero-order approximation in the asymptotic expansion (2.31). The problem will be further simplified by adding three more assumptions concerning ship geometry: (1) that each hull has a rectangular planform, (2) that the draft-to-length ratio is small, and (3) that the ratio between the hull separation distance and ship length is also small and is of a comparable order of magnitude as the draft-to-length ratio.

Thus, (2.29) shall now be written as

$$\lim_{y \rightarrow 0} \iint_{S_{1b}^{(0)} + S_{1w}^{(0)}} \mu(x_0, z_0) \frac{\partial^2}{\partial y^2} \{G^{(0)}(x, y, z; x_0, 0, z_0) - G^{(0)}(x, y, z; x_0, 2b, z_0)\} dx_0 dz_0 = -U \frac{\partial C}{\partial x} + \iint_{S_{2b}^{(0)}} \sigma(x_0, z_0) \frac{\partial G^{(0)}}{\partial y} \times (x, 0, z; x_0, 2b, z_0) dx_0 dz_0. \quad (2.34)$$

In the above equation, $G^{(0)}$ is to be substituted from (2.32). After such a substitution, however, each term in (2.34) must be further manipulated into a form suitable for taking the limit as indicated. Thus, the first term on the left side of (2.34) becomes

$$\begin{aligned} v_{1\mu}(x, y, z) &= \iint_{S_{1b}^{(0)} + S_{1w}^{(0)}} \mu(x_0, z_0) \frac{\partial^2 G^{(0)}}{\partial y^2} \\ &\quad \times (x, y, z; x_0, 0, z_0) dx_0 dz_0 \\ &= \int_{-\infty}^{L/2} dx_0 \int_H^0 dz_0 \mu(x_0, z_0) \frac{\partial^2}{\partial y^2} \\ &\quad \times \left\{ \frac{1}{\sqrt{(x-x_0)^2 + y^2 + (z-z_0)^2}} \right. \\ &\quad \left. + \frac{1}{\sqrt{(x-x_0)^2 + y^2 + (z+z_0)^2}} \right\} \\ &= \int_{-\infty}^{L/2} dx_0 \int_H^0 dz_0 \mu(x_0, z_0) \frac{\partial^2}{\partial y^2} \\ &\quad \times \left\{ \frac{1}{\sqrt{(x-x_0)^2 + y^2 + (z-z_0)^2}} \right\}, \quad (2.35) \end{aligned}$$

if we assume

$$\mu(x_0, z_0) = \mu(x_0, -z_0). \quad (2.36)$$

Since $r^{-1} = [(x-x_0)^2 + y^2 + (z-z_0)^2]^{-1/2}$ satisfies Laplace's equation, (2.35) may be replaced by

$$\begin{aligned} v_{1\mu}(x, y, z) &= \int_{-\infty}^{L/2} dx_0 \int_H^0 dz_0 \mu(x_0, z_0) \left\{ \frac{\partial^2}{\partial x_0^2} \left(\frac{1}{r} \right) \right. \\ &\quad \left. + \frac{\partial^2}{\partial z_0^2} \left(\frac{1}{r} \right) \right\}. \quad (2.37) \end{aligned}$$

Next we adapt the usual assumptions made for a rectangular wing (for example, Robinson and Laurmann, p. 232) that: (1) $\mu(x_0, z_0) = 0$ along the finite boundaries of $S_{1b}^{(0)} + S_{1w}^{(0)}$; (2) $\partial\mu/\partial z_0 = 0$ along the bow profile and its reflection, $x = L/2$; and, (3) $\partial\mu/\partial x_0 = 0$ along the keel and its reflection, $z_0 = \pm H$. Then, by making use of these assumed boundary conditions, of integration by parts, and of the fact that $\partial\mu/\partial x_0 = 0$ in the wake, the following results may be established:

$$- \int_{-\infty}^{L/2} dx_0 \int_H^0 dz_0 \mu(x_0, z_0) \frac{\partial^2}{\partial x_0^2} \left(\frac{1}{r} \right) \quad (2.38)$$

$$= \int_{-L/2}^{L/2} dx_0 \int_H^0 dz_0 \frac{\partial^2 \mu}{\partial x_0 \partial z_0} \cdot \frac{(x-x_0)(z-z_0)}{[(x-x_0)^2 + y^2] \cdot r},$$

and

$$\begin{aligned} &- \int_{-\infty}^{L/2} dx_0 \int_H^0 dz_0 \mu(x_0, z_0) \frac{\partial^2}{\partial z_0^2} \left(\frac{1}{r} \right) \\ &= \int_H^0 dz_0 \frac{\partial \mu}{\partial z_0} \left(-\frac{L}{2}, z_0 \right) \cdot \frac{z-z_0}{y^2 + (z-z_0)^2} \quad (2.39) \\ &+ \int_{-L/2}^{L/2} dx_0 \int_H^0 dz_0 \frac{\partial^2 \mu}{\partial x_0 \partial z_0} \cdot \frac{(x-x_0)(z-z_0)}{[y^2 + (z-z_0)^2] r}. \end{aligned}$$

The algebraic details for deriving these results may be found in Robinson and Laurmann (1956, pp. 232-237). After substitution from (2.38) and (2.39) into (2.37), we obtain

$$\begin{aligned} v_{1\mu}(x, y, z) &= \int_{-L/2}^{L/2} dx_0 \int_H^0 dz_0 \frac{\partial^2 \mu}{\partial x_0 \partial z_0} \\ &\quad \times \left(\frac{1}{(x-x_0)^2 + y^2} + \frac{1}{y^2 + (z-z_0)^2} \right) \\ &\quad \times \frac{(x-x_0)(z-z_0)}{\sqrt{(x-x_0)^2 + y^2 + (z-z_0)^2}} \\ &\quad + \int_{-H}^H dz_0 \frac{\partial \mu}{\partial z_0} \left(-\frac{L}{2}, z_0 \right) \cdot \frac{(z-z_0)}{y^2 + (z-z_0)^2} \\ &= \int_{-H}^H dz_0 \frac{z-z_0}{y^2 + (z-z_0)^2} \\ &\quad \times \left(\int_{-L/2}^{L/2} dx_0 \frac{\partial^2 \mu}{\partial x_0 \partial z_0} \cdot \frac{(x-x_0)\sqrt{(x-x_0)^2 + y^2 + (z-z_0)^2}}{(x-x_0)^2 + y^2} \right) \\ &\quad + \int_{-H}^H dz_0 \frac{z-z_0}{y^2 + (z-z_0)^2} \\ &\quad \times \left(\int_{-L/2}^{L/2} dx_0 \frac{\partial^2 \mu}{\partial x_0 \partial z_0} \cdot \frac{y^2}{\sqrt{(x-x_0)^2 + y^2 + (z-z_0)^2}} \right) \end{aligned}$$

Equation (2.40) (Continued)

$$\begin{aligned}
& \times \frac{x - x_0}{(x - x_0)^2 + y^2} \\
& + \int_{-H}^H dz_0 \frac{\partial \mu \left(-\frac{L}{2}, z_0 \right)}{\partial z_0} \cdot \frac{z - z_0}{y^2 + (z - z_0)^2}.
\end{aligned} \quad (2.40)$$

The integrals in (2.40) are singular for $y = 0$. It can be shown that in this case the correct limiting value is obtained by taking the principal values of the integrals. Thus, upon taking the limit,

$$\begin{aligned}
v_{1\mu}(x, 0, z) &= \int_{-H}^H dz_0 \int_{-L/2}^{L/2} dx_0 \frac{\partial^2 \mu}{\partial x_0 \partial z_0} \\
& \times \frac{\sqrt{(x - x_0)^2 + (z - z_0)^2}}{(x - x_0)(z - z_0)} \\
& + \int_{-H}^H dz_0 \frac{\partial \mu \left(-\frac{L}{2}, z_0 \right)}{\partial z_0} \cdot \frac{1}{z - z_0} \\
& = \int_{-H}^H dz_0 \int_{-L/2}^{L/2} dx_0 \frac{\partial^2 \mu}{\partial x_0 \partial z_0} \\
& \times \left(\frac{\sqrt{(x - x_0)^2 + (z - z_0)^2}}{(x - x_0)(z - z_0)} - \frac{1}{z - z_0} \right).
\end{aligned} \quad (2.41)$$

Note that upon taking the limit $y \rightarrow 0$, the second double integral in (2.40) tends to zero. Hence, only the principal values of the first double integral and the last single integral of (2.40) remain.

Next, let us derive a similar result for the second term on the left of (2.34). Clearly, this term represents the component velocity normal to $S_{1b}^{(0)} + S_{1w}^{(0)}$ due to the doublet distribution over the planform and its wake of Hull 2. Hence, we shall write

$$\begin{aligned}
v_{2\mu}(x, y, z) &= - \iint_{S_{1b}^{(0)} + S_{1w}^{(0)}} \mu(x_0, z_0) \\
& \times \frac{\partial^2 G^{(0)}(x, y, z; x_0, 2b, z_0)}{\partial y^2} dx_0 dz_0 \\
& = \int_{-\infty}^{L/2} dx_0 \int_{-H}^0 dz_0 \mu(x_0, z_0) \frac{\partial^2}{\partial y^2}
\end{aligned}$$

Equation (2.42) (Continued)

$$\begin{aligned}
& \times \left\{ \frac{1}{\sqrt{(x - x_0)^2 + (y - 2b)^2 + (z - z_0)^2}} \right. \\
& \left. + \frac{1}{\sqrt{(x - x_0)^2 + (y - 2b)^2 + (z + z_0)^2}} \right\} \\
& = \int_{-\infty}^{L/2} dx_0 \int_{-H}^0 dz_0 \mu(x_0, z_0) \frac{\partial^2}{\partial y^2} \\
& \times \left(\frac{1}{\sqrt{(x - x_0)^2 + (y - 2b)^2 + (z - z_0)^2}} \right) \\
& = \int_{-\infty}^{L/2} dx_0 \int_{-H}^0 dz_0 \mu(x_0, z_0) \\
& \times \left\{ \frac{\partial^2}{\partial x_0^2} \left(\frac{1}{r} \right)_{y_0=2b} + \frac{\partial^2}{\partial z_0^2} \left(\frac{1}{r} \right)_{y_0=2b} \right\},
\end{aligned} \quad (2.42)$$

where we have again made use of (2.36) and the fact that $1/r$ satisfies Laplace's equation.

Following a similar manipulation as in the case of $v_{1\mu}$, we obtain

$$\begin{aligned}
v_{2\mu}(x, y, z) &= - \int_{-L/2}^{L/2} dx_0 \int_{-H}^0 dz_0 \frac{\partial^2 \mu}{\partial x_0 \partial z_0} \\
& \times \left(\frac{1}{(x - x_0)^2 + (y - 2b)^2} + \frac{1}{(y - 2b)^2 + (z - z_0)^2} \right) \\
& \times \frac{(x - x_0)(z - z_0)}{\sqrt{(x - x_0)^2 + (y - 2b)^2 + (z - z_0)^2}} \\
& + \int_{-H}^0 dz_0 \frac{\partial \mu \left(-\frac{L}{2}, z_0 \right)}{\partial z_0} \cdot \frac{z - z_0}{(y - 2b)^2 + (z - z_0)^2}.
\end{aligned} \quad (2.43)$$

Since there is no longer any singularity at $y = 0$ in (2.43), $v_{2\mu}(x, 0, z)$ may be obtained immediately from (2.43) as

$$\begin{aligned}
v_{2\mu}(x, 0, z) &= - \int_{-L/2}^{L/2} dx_0 \int_{-H}^0 dz_0 \frac{\partial^2 \mu}{\partial x_0 \partial z_0} \\
& \times \left(\frac{(x - x_0)^2 + 8b^2 + (z - z_0)^2}{\{(x - x_0)^2 + 4b^2\} \cdot \{4b^2 + (z - z_0)^2\}} \right. \\
& \left. \times \frac{(x - x_0)(z - z_0)}{\sqrt{(x - x_0)^2 + 4b^2 + (z - z_0)^2}} - \frac{z - z_0}{4b^2 + (z - z_0)^2} \right).
\end{aligned} \quad (2.44)$$

The remaining term to be similarly manipulated is the last term on the right side of the equal sign in (2.34). This term represents the component velocity normal to $S_{lb}^{(0)} + S_{lw}^{(0)}$ contributed by the source distribution over the planform of Hull 2. Hence, let us write

$$\begin{aligned} v_{2o}(x, 0, z) &= \iint_{S_{2b}^{(0)}} \sigma(x_0, z_0) \frac{\partial G^{(0)}(x, 0, z; x_0, 2b, z_0)}{\partial y} dx_0 dz_0 \\ &= \int_{L/2}^{L/2} dx_0 \int_H^0 dz_0 \sigma(x_0, z_0) \\ &\quad \times \left(\frac{2b}{[(x-x_0)^2 + 4b^2 + (z-z_0)^2]^{3/2}} \right. \\ &\quad \left. + \frac{2b}{[(x-x_0)^2 + 4b^2 + (z+z_0)^2]^{3/2}} \right) \\ &= \int_{L/2}^{L/2} dx_0 \int_H^0 dz_0 \sigma(x_0, z_0) \\ &\quad \times \left(\frac{2b}{[(x-x_0)^2 + 4b^2 + (z-z_0)^2]^{3/2}} \right), \end{aligned} \quad (2.45)$$

where we have assumed

$$\sigma(x_0, z_0) = \sigma(x_0, -z_0). \quad (2.46)$$

Because of the relationship between the source-distribution density and the local ship-hull slope as given by (2.17), the assumption (2.46) means that the ship geometry is also an even function of z , i.e., symmetric with respect to the Oxy-plane, so that $\partial C(x_0, z_0)/\partial x = \partial C(x_0, -z_0)/\partial x$.

The integral equation for the doublet-distribution density appropriate for the flow around a ship with two thin hulls may now be obtained by substituting the results obtained in (2.41), (2.44), and (2.45) into (2.34). Hence,

$$\begin{aligned} \int_H^H \int_{L/2}^{L/2} \frac{\partial^2 \mu}{\partial x_0 \partial z_0} &\left\{ \left(\frac{\sqrt{(x-x_0)^2 + (z-z_0)^2}}{(x-x_0)(z-z_0)} - \frac{1}{z-z_0} \right) \right. \\ &- \left(\frac{(x-x_0)^2 + 8b^2 + (z-z_0)^2}{[(x-x_0)^2 + 4b^2][4b^2 + (z-z_0)^2]} \cdot \frac{(x-x_0)(z-z_0)}{\sqrt{(x-x_0)^2 + 4b^2 + (z-z_0)^2}} \right. \\ &\left. \left. - \frac{z-z_0}{4b^2 + (z-z_0)^2} \right) \right\} dx_0 dz_0 \\ &= -U \frac{\partial C(x, z)}{\partial x} \end{aligned}$$

Equation (2.47) (Continued)

$$+ \int_{-H}^H \int_{L/2}^{L/2} \sigma(x_0, z_0) \left(\frac{2b}{[(x-x_0)^2 + 4b^2 + (z-z_0)^2]^{3/2}} \right) dx_0 dz_0. \quad (2.47)$$

This is an integral equation of the first kind for $\partial^2 \mu / \partial x_0 \partial z_0$. Although we may try to solve this equation numerically, it appears that, for the problem considered here, further simplifying assumptions may be introduced. To do this, we observe that the draft of a ship is generally much smaller than its length. Furthermore, for the steady forward motion of a twin-hull ship, the cross-flow effect becomes a problem of concern only when the two hulls are sufficiently close to each other. Hence, the two assumptions introduced earlier concerning the draft-to-length ratio and separation distance-to-length ratio will now be used. They may be stated as

$$\frac{H}{L} \ll 1 \text{ and } \frac{2b}{L} \ll 1. \quad (2.48)$$

That is, H/L and $2b/L$ are both small and their orders of magnitude are comparable, so that the usual approximations made for low-aspect ratio wings may be applied here. Thus the radicals $[(x-x_0)^2 + (z-z_0)^2]^{1/2}$ and $[(x-x_0)^2 + 4b^2 + (z-z_0)^2]^{1/2}$ may both be replaced by $|x-x_0|$ in (2.47). For example, two of the terms in (2.47) will be approximated as follows:

$$\frac{\sqrt{(x-x_0)^2 + (z-z_0)^2}}{(x-x_0)(z-z_0)} \approx \frac{|x-x_0|}{(x-x_0)(z-z_0)}. \quad (2.49)$$

$$\begin{aligned} \frac{(x-x_0)^2 + 8b^2 + (z-z_0)^2}{[(x-x_0)^2 + 4b^2][4b^2 + (z-z_0)^2]} &\cdot \frac{(x-x_0)(z-z_0)}{\sqrt{(x-x_0)^2 + 4b^2 + (z-z_0)^2}} \\ &\approx \frac{(x-x_0)}{|x-x_0|} \cdot \frac{z-z_0}{4b^2 + (z-z_0)^2}. \end{aligned} \quad (2.50)$$

After making substitutions from (2.49) and (2.50) and carrying out the integration with respect to x_0 , the left side of the equal sign in (2.47) becomes:

$$2 \int_{-H}^H dz_0 \frac{\partial \mu(x, z_0)}{\partial z_0} \cdot \left(\frac{1}{z-z_0} - \frac{z-z_0}{4b^2 + (z-z_0)^2} \right). \quad (2.51)$$

To treat the last double-integral term in (2.47) similarly, we integrate by parts with respect to x_0 first before replacing the radical $[(x-x_0)^2 + 4b^2 + (z-z_0)^2]^{1/2}$ with $|x-x_0|$. Thus, this term becomes:

$$\begin{aligned}
& \int_H^H dz_0 \int_{L/2}^{L/2} dx_0 \sigma(x_0, z_0) \\
& \times \left(\frac{2b}{[(x-x_0)^2 + 4b^2 + (z-z_0)^2]^{3/2}} \right) \\
& = 2b \int_H^H dz_0 \frac{1}{4b^2 + (z-z_0)^2} \\
& \times \left\{ \left[\frac{(x-x_0) \sigma(x_0, z_0)}{\sqrt{(x-x_0)^2 + 4b^2 + (z-z_0)^2}} \right]_{x_0=L/2}^{x_0=L/2} \right. \\
& \left. - \int_{L/2}^{L/2} dx_0 \frac{\partial \sigma}{\partial x_0} \cdot \frac{x-x_0}{\sqrt{(x-x_0)^2 + 4b^2 + (z-z_0)^2}} \right\} \\
& \approx 2b \int_H^H \frac{1}{4b^2 + (z-z_0)^2} \left\{ \left[\frac{(x-x_0) \sigma(x_0, z_0)}{x-x_0} \right]_{x_0=L/2}^{x_0=L/2} \right. \\
& \left. - \int_{L/2}^{L/2} \sigma(x_0, z_0) \cdot \frac{(x-x_0)}{x-x_0} dx_0 \right\} dz_0 \\
& = 4b \int_H^H \frac{\sigma(x, z_0)}{4b^2 + (z-z_0)^2} dz_0. \quad (2.52)
\end{aligned}$$

Substituting (2.51) and (2.52) into (2.47), we obtain an approximate integral equation for $\partial\mu/\partial z_0$ as follows:

$$\begin{aligned}
& 2 \int_H^H \frac{\partial \mu(x, z_0)}{\partial z_0} \left(\frac{1}{z-z_0} - \frac{z-z_0}{4b^2 + (z-z_0)^2} \right) dz_0 \\
& = U \frac{\partial C}{\partial x} + 4b \int_H^H \frac{\sigma(x, z_0)}{4b^2 + (z-z_0)^2} dz_0. \quad (2.53)
\end{aligned}$$

This equation, aside from being simpler than the original one in (2.47), has an interesting physical significance which shall be discussed here. It can be shown, by integrating by parts and by making use of the fact that $\log [(y-y_0)^2 + (z-z_0)^2]^{1/2}$ satisfies Laplace's equation in the plane perpendicular to the x-axis (i.e., in y- and z-variables), that (2.53) is precisely the same equation as

$$\begin{aligned}
& \frac{\partial}{\partial y} \int_H^H \mu(x, z_0) \left[\left(\frac{\partial}{\partial y_0} \log \sqrt{(y-y_0)^2 + (z-z_0)^2} \right)_{y_0=0} \right. \\
& \left. - \left(\frac{\partial}{\partial y_0} \log \sqrt{(y-y_0)^2 + (z-z_0)^2} \right)_{y_0=2b} \right] dz_0 \\
& = \frac{U}{2} \frac{\partial C}{\partial x} - \frac{\partial}{\partial y} \int_H^H \sigma(x, z_0) \\
& \times \left(\log \sqrt{(y-y_0)^2 + (z-z_0)^2} \right)_{y_0=2b} dz_0, \quad (2.53a)
\end{aligned}$$

at $y = 0$.

In the cross-sectional plane, $x = \text{constant}$, the left side of the equal sign in (2.53a) represents the net y-component velocity contributed by the two line-distributions of horizontal doublets, located at $y_0 = 0$ and $y_0 = 2b$ and extending from $z_0 = -H$ to $z_0 = H$. On the other hand, the right side of this equation represents the cross-flow velocity due to both the camber of Hull 1 and the source distribution representing Hull 2. Thus (2.53a) states that the doublet density μ may be determined by equating these two velocities when evaluated at $y = 0$ (which corresponds to the planform of Hull 1). Hence, μ is now to be determined two-dimensionally at each cross-section. This is in agreement with one of the familiar conclusions obtained from the slender-body approximation.

To find the doublet density μ , we note first that (2.53) is a complete singular integral equation. Except for some particular types (see, for example, Gakhov, § 51) for which closed-form solutions may be obtained, the solution of such an equation is generally carried out by a reduction to a Fredholm integral equation. A number of techniques are available. Here, we shall use the method of Carleman-Vekua. Namely, we shall eliminate the singular integral by solving the corresponding dominant equation (for example, Gakhov, pp. 186-194).

Morgan (1962) derived an integral equation of this type for a ducted propeller problem, and used the same method to solve the equation. A similar approach will be applied here to solve (2.53). First, let us rewrite (2.53) in the following form:

$$\int_H^H \frac{\partial \mu(x, z_0)}{\partial z_0} \cdot \frac{1}{z-z_0} dz_0 = F_0(x; z), \quad (2.54)$$

where

$$\begin{aligned}
F_0 = & \frac{U}{2} \frac{\partial C}{\partial x} - \frac{bU}{\pi} \int_H^H \frac{\partial \mu(x, z_0)}{\partial x} \cdot \frac{dz_0}{4b^2 + (z-z_0)^2} \\
& + \int_H^H \frac{\partial \mu}{\partial z_0} \cdot \frac{z-z_0}{4b^2 + (z-z_0)^2} dz_0. \quad (2.55)
\end{aligned}$$

Note that in (2.55) we have made a substitution for σ from (2.17).

By making use of a known inversion formula, (2.54) may be solved in a closed form if F_0 is regarded temporarily as a known function. Thus, according to this formula, (2.54) may yield the following result:

$$\frac{\partial \mu(x, z)}{\partial z} = \frac{1}{\pi^2 \sqrt{(H-z)(H+z)}} \int_{-H}^H F_0(x; z_0) \frac{\sqrt{(H-z_0)(H+z_0)}}{z_0 - z} dz_0 + \frac{1}{\pi \sqrt{(H-z)(H+z)}} \int_{-H}^H \frac{\partial \mu(x; z_0)}{\partial z_0} dz_0. \quad (2.56)$$

But

$$\int_{-H}^H \frac{\partial \mu(x; z_0)}{\partial z_0} dz_0 = \mu(x, H) - \mu(x, -H) = 0, \quad (2.57)$$

since we have assumed that μ is even in z and also vanishes along the keel. Hence, upon substitution from (2.55) for F_0 , (2.56) becomes:

$$\begin{aligned} \frac{\partial \mu(x, z)}{\partial z} &= \frac{1}{\pi^2 \sqrt{H^2 - z^2}} \int_{-H}^H K_0(z, z') \frac{\partial \mu(x, z')}{\partial z'} dz' \\ &= \frac{1}{\pi^2 \sqrt{H^2 - z^2}} \int_{-H}^H F_1(x, z_0) \frac{\sqrt{H^2 - z_0^2}}{z_0 - z} dz_0, \end{aligned} \quad (2.58)$$

where

$$K_0(z, z') = \int_{-H}^H \frac{(z_0 - z') \sqrt{H^2 - z_0^2}}{(z_0 - z) [4b^2 + (z_0 - z')^2]} dz_0, \quad (2.59)$$

$$F_1(x, z_0) = \frac{U}{2} \frac{\partial C}{\partial x} - \frac{bU}{\pi} \int_{-H}^H \frac{\partial t(x, z_0)}{\partial x} \cdot \frac{dz'}{4b^2 + (z_0 - z')^2}. \quad (2.60)$$

Note that (2.58) is a Fredholm equation of the second kind for $\partial \mu / \partial z$. However, it may not be solved in this form since there are singularities at $z = \pm H$. Instead, let us define

$$\frac{\partial \mu^*(x, z)}{\partial z} = \sqrt{H^2 - z^2} \cdot \frac{\partial \mu(x, z)}{\partial z}. \quad (2.61)$$

Then, in terms of this new unknown function, (2.58) may be written as

$$\begin{aligned} \frac{\partial \mu^*(x, z)}{\partial z} &= \int_{-H}^H K(z, z') \cdot \frac{\partial \mu^*(x, z') / \partial z'}{\sqrt{H^2 - z'^2}} dz' \\ &+ F_2(x, z). \end{aligned} \quad (2.62)$$

where

$$K(z, z') = \frac{1}{\pi^2} \int_{-H}^H \frac{(z_0 - z') \sqrt{H^2 - z_0^2}}{(z_0 - z) [4b^2 + (z_0 - z')^2]} dz_0, \quad (2.63)$$

$$F_2(x, z) = \frac{1}{\pi^2} \int_{-H}^H F_1(x, z_0) \frac{\sqrt{H^2 - z_0^2}}{z_0 - z} dz_0. \quad (2.64)$$

The kernel function $K(z, z')$ and the known function $F_2(x, z)$ are both defined by Cauchy principal-value integrals. In general, for a given ship geometry, (2.62) may be solved for $\partial \mu^* / \partial z$ by a numerical scheme without much difficulty. Finally, the doublet density $\mu(x, z)$ may be completely determined from the solution for $\partial \mu^* / \partial z$.

3. HYDRODYNAMIC FORCE AND MOMENT

Thus far, both the thickness and lifting problems previously formulated have been solved. That is, both the corresponding source and doublet densities may now be determined explicitly for a given ship geometry. The logical next step is to find the hydrodynamic force and moment acting on the ship in terms of these known singularity densities. Formulas derived for such purposes are generally referred to as Lagally's theorem.

Recall that we have obtained the flow field of our problem by two sheet-distributions of sources and normal (or transverse) doublets. Across such surface distributions of singularities, two important properties of the fluid velocity are of particular interest to our investigation, namely: (1) that part of the velocity generated by a source distribution which has a jump discontinuity in its component normal to the surface, and (2) that part generated by a normal doublet distribution which has a jump discontinuity in its component tangential to the surface. These two properties shall now be used to derive general expressions for force and moment.

In the subsequent development, we shall derive formulas for force and moment acting on Hull 1 alone. Let S_1 and S_2 be the wetted surface of Hull 1 and Hull 2, respectively. Let S_{1w}^+ and S_{1w}^- represent the plus and minus sides of the wake sheet of Hull 1, respectively. Next, consider a volume of fluid, V_c , which is bounded by the wetted surface S_1 and a control surface Σ enclosing Hull 1 and its wake sheet. Thus, part of Σ consists of the free surface and both sides of the wake sheet. Hence, the combined surface S_1 and Σ bounds only fluid. As before, we shall define the positive direction of the unit normal to this bounding surface $S_1 + \Sigma$ to be pointing away from the fluid volume V_c . We shall assume that V_c contains no singularities, and therefore Hull 2 lies outside of V_c . For a steady-state problem we shall assume that the control surface Σ moves with the ship.

3.1 Force

The total momentum of the fluid in the volume V_c is

$$Q = \iiint_{V_c} \rho \mathbf{q} dV, \quad (3.1)$$

where ρ is the mass density of the fluid, and \underline{q} is the total fluid velocity relative to the ship as defined by (2.4). Then, by making use of the momentum theorem (see, for example, Wehausen (1973), p. 102), we may obtain an expression for the force acting on Hull 1 as

$$\underline{F} = \iint_{\Sigma} [p \underline{n} + \rho \underline{q} (\underline{q} \cdot \underline{n})] ds, \quad (3.2)$$

in which p is the pressure, and \underline{n} is the unit normal to Σ . Next, recall that the generating singularities representing Hull 1 are distributed only on its planform $S_{1b}^{(0)}$. Let $(S_{1b}^{(0)})_+$ and $(S_{1b}^{(0)})_-$ represent the plus and minus sides of $S_{1b}^{(0)}$, respectively. To simplify our derivation, we shall assume that the planform of Hull 1 lies entirely within S_1 , the wetted surface of Hull 1. Then, the volume bounded by the combined surface Σ , $(S_{1b}^{(0)})_+$ and $(S_{1b}^{(0)})_-$ also contains no singularities. Let this volume be denoted by V_c' . Note that the difference between V_c' and V_c in this case is the displacement of Hull 1.

Let us now rewrite (3.2) as follows:

$$\begin{aligned} \underline{F} = & \iint_{\Sigma + (S_{1b}^{(0)})_+ + (S_{1b}^{(0)})_-} [p \underline{n} + \rho \underline{q} (\underline{q} \cdot \underline{n})] ds \\ & + \iint_{(S_{1b}^{(0)})_+ + (S_{1b}^{(0)})_-} [p \underline{n} + \rho \underline{q} (\underline{q} \cdot \underline{n})] ds. \end{aligned} \quad (3.3)$$

Applying Gauss' theorem to the first surface integral in (3.3) results in

$$\iiint_{V_c'} [\nabla p + \rho (\underline{q} \cdot \nabla) \underline{q}] dV, \quad (3.4)$$

where we have used a variant of Gauss' theorem,

$$\iint_S \underline{A} (\underline{B} \cdot \underline{n}) ds = \iiint_V [(\underline{B} \cdot \nabla) \underline{A} + \underline{A} (\nabla \cdot \underline{B})] dV$$

and the fact that $\nabla \cdot \underline{q} = 0$ for an incompressible fluid. Note that Euler's equation of motion may be written with reference to the Oxyz frame as follows:

$$\frac{\partial \underline{q}}{\partial t} + (\underline{q} \cdot \nabla) \underline{q} = -\frac{1}{\rho} \nabla p + \underline{X}.$$

If we neglect the external body force \underline{X} , then for steady-flow problems we have

$$\nabla p + \rho (\underline{q} \cdot \nabla) \underline{q} = 0. \quad (3.5)$$

From (3.5) and (3.4) it is clear that the first surface-integral term in (3.3) vanishes identically. Hence, the expression for the force, (3.3), becomes simply:

$$\begin{aligned} \underline{F} = & \iint_{(S_{1b}^{(0)})_+ + (S_{1b}^{(0)})_-} [p \underline{n} + \rho \underline{q} (\underline{q} \cdot \underline{n})] ds \\ = & \iint_{(S_{1b}^{(0)})_+ + (S_{1b}^{(0)})_-} \left[\frac{1}{2} \rho q^2 \underline{n} + \rho \underline{q} (\underline{q} \cdot \underline{n}) + \frac{1}{2} \rho U^2 \underline{n} \right] ds, \end{aligned} \quad (3.6)$$

in which a substitution has been made from Bernoulli's equation for the pressure p .

Let us now define the unit normal vector to the planform $S_{1b}^{(0)}$ to be \underline{v} such that it is pointing in the positive y-direction. Then, according to our convention, the normal vector \underline{n} in (3.6) is related to \underline{v} as follows:

$$\left. \begin{aligned} \underline{n} &= \underline{v} \quad \text{on } (S_{1b}^{(0)})_+ \\ \underline{n} &= -\underline{v} \quad \text{on } (S_{1b}^{(0)})_- \end{aligned} \right\} \quad (3.7)$$

Recognizing the planform $S_{1b}^{(0)}$ to be a sheet of discontinuity, let us also define

$$\left. \begin{aligned} p^{(+)} &= p(x, +0, z), & \underline{q}^{(+)} &= \underline{q}(x, +0, z) \quad \text{on } (S_{1b}^{(0)})_+ \\ p^{(-)} &= p(x, -0, z), & \underline{q}^{(-)} &= \underline{q}(x, -0, z) \quad \text{on } (S_{1b}^{(0)})_- \end{aligned} \right\} \quad (3.8)$$

Furthermore, we shall decompose the fluid velocity \underline{q} on either side of $S_{1b}^{(0)}$ into the normal and tangential components as follows:

$$\underline{q}^{(\pm)} = \underline{q}_t^{(\pm)} + \underline{q}_v^{(\pm)} = \underline{q}_t^{(\pm)} + q_v^{(\pm)} \underline{v}. \quad (3.9)$$

Substituting (3.9), (3.8), and (3.7) into (3.6) and working out the necessary algebraic manipulations, we may obtain an expression for \underline{F} as

$$\begin{aligned} \underline{F} = & \rho \iint_{S_{1b}^{(0)}} \left\{ (q_t^{(+)} q_v^{(+)} - q_t^{(-)} q_v^{(-)}) + \frac{1}{2} (q_v^{(+)} + q_v^{(-)}) \right. \\ & \left. \times (q_v^{(+)} - q_v^{(-)}) \underline{v} + \frac{1}{2} (q_t^{(+)} + q_t^{(-)}) \cdot (q_t^{(+)} - q_t^{(-)}) \underline{v} \right\} ds. \end{aligned} \quad (3.10)$$

In view of the decomposition (2.8), let us write

$$\left. \begin{aligned} \underline{q} &= \underline{q}_e + \underline{V}_{1\sigma} + \underline{V}_{1\mu}, \\ \underline{q}_e &= \nabla(\phi_{1\sigma} + \phi_{2\sigma} + \phi_{2\mu}) \\ &= -U\underline{e}_1 + \underline{V}_{2\sigma} + \underline{V}_{2\mu}, \\ \underline{V}_{1\sigma} &= \nabla\phi_{1\sigma}, \quad \underline{V}_{1\mu} = \nabla\phi_{1\mu}. \end{aligned} \right\} \quad (3.11)$$

Thus, \underline{q}_e represents the uniform stream and the disturbance velocity due to Hull 2. On the other hand, $\underline{V}_{1\mu}$ and $\underline{V}_{1\sigma}$ represent the disturbance velocities due to the normal doublet and source distributions on $S_{1b}^{(0)}$, respectively. If we now decompose $\underline{V}_{1\sigma}$ and $\underline{V}_{1\mu}$ into the normal and tangential components according to (3.9), then from (2.16) and (3.11) we have

$$q_p^{(+)} - q_p^{(-)} = \left(\frac{\partial \phi_{1\sigma}}{\partial y} \right)^+ - \left(\frac{\partial \phi_{1\sigma}}{\partial y} \right)^- = 4\pi\sigma. \quad (3.12)$$

On the other hand, the discontinuity in the tangential component will be written as

$$q_t^{(+)} - q_t^{(-)} = \gamma_t. \quad (3.13)$$

In terms of (3.12) and (3.13), the three terms in the integrand of (3.10) become:

$$\begin{aligned} \text{(i)} \quad \underline{q}_t^{(+)} q_p^{(+)} - \underline{q}_t^{(-)} q_p^{(-)} &= \frac{1}{2} (q_p^{(+)} + q_p^{(-)}) (\underline{q}_t^{(+)} - \underline{q}_t^{(-)}) \\ &+ \frac{1}{2} (q_p^{(+)} - q_p^{(-)}) (\underline{q}_t^{(+)} + \underline{q}_t^{(-)}) \\ &= \hat{q}_p \cdot \underline{\gamma}_t + 4\pi\sigma \hat{q}_t, \end{aligned}$$

$$\text{(ii)} \quad \frac{1}{2} (q_p^{(+)} + q_p^{(-)}) (q_p^{(+)} - q_p^{(-)}) \underline{e}_1 = 4\pi\sigma \hat{q}_p,$$

$$\text{(iii)} \quad \frac{1}{2} (\underline{q}_t^{(+)} + \underline{q}_t^{(-)}) \cdot (\underline{q}_t^{(+)} - \underline{q}_t^{(-)}) \underline{e}_1 = (\hat{q}_t \cdot \underline{\gamma}_t) \underline{e}_1,$$

in which we have defined

$$\left. \begin{aligned} \hat{q}_t &= \frac{1}{2} (\underline{q}_t^{(+)} + \underline{q}_t^{(-)}), \\ \hat{q}_p &= \frac{1}{2} (q_p^{(+)} + q_p^{(-)}). \end{aligned} \right\} \quad (3.14)$$

With substitutions of the results obtained in (i), (ii), and (iii), the expression for the force in (3.10) becomes:

$$\begin{aligned} \underline{F} &= 4\pi\rho \iint_{S_{1b}^{(0)}} \sigma \cdot (\hat{q}_t + \hat{q}_p) ds \\ &+ \rho \iint_{S_{1b}^{(0)}} [\gamma_t \hat{q}_p \cdot (\underline{\gamma}_t \wedge \hat{q}_t) \underline{e}_1] ds \\ &= 4\pi\rho \iint_{S_{1b}^{(0)}} \sigma \cdot \hat{q} ds \\ &+ \rho \iint_{S_{1b}^{(0)}} \hat{q} \wedge (\underline{\gamma} \wedge \underline{\gamma}_t) ds, \end{aligned} \quad (3.15)$$

where $\hat{q} = \hat{q}_t + \hat{q}_p$ represents the average value of the velocities on both sides of $S_{1b}^{(0)}$. The first term of (3.15) is exactly the familiar form of Lagally's theorem for the force acting on a source distribution. However, (3.15) states that for a continuous sheet distribution, across which the velocity suffers a jump discontinuity, the average value of the velocities on both sides of the sheet should be used when applying Lagally's theorem to compute the force.

Since (3.15) represents the force due to a simultaneous distribution of sources and normal doublets, the second integral must represent the force on the doublet distribution. Nevertheless, it is not in the familiar form of Lagally's theorem since it is now expressed in terms of vorticity rather than explicitly related to the density of the doublet distribution.

It will be shown next that the second integral in (3.15) can indeed be brought into the familiar form of Lagally's theorem for doublets. However, because the singularity distribution now represents a lifting body, additional terms must be added to the usual form of Lagally's theorem for doublets. To derive this result, we shall make use of the properties of the potential of normal-doublet distribution. Since the subsequent analysis involves integration by parts, in order to simplify our derivation we shall assume that Hull 1 has a rectangular planform. Hence, the boundary conditions imposed, following (2.37), on the doublet density γ_t and its derivatives for a rectangular planform will still be used. Extension to a planform of a more ship-like shape is straightforward but adds additional complications to the final result.

To begin with, let us write the second integral of (3.15) as

$$\underline{F}_\mu = \rho \iint_{S_{1b}^{(0)}} \hat{q} \wedge (\underline{\gamma} \wedge \underline{\gamma}_t) ds. \quad (3.16)$$

Recall that in (3.13) we defined γ_i as the jump discontinuity in that component of \underline{q} which is tangential to $S_{lb}^{(0)}$. Thus from (3.13), (3.11), and (2.21) we have

$$\begin{aligned}\gamma_i &= q_i^{(+)} - q_i^{(-)} = \gamma_{i\mu}^{(+)} - \gamma_{i\mu}^{(-)} \\ &= -4\pi \left(\frac{\partial \mu(x, z)}{\partial x}, 0, \frac{\partial \mu}{\partial z} \right).\end{aligned}\quad (3.17)$$

Substituting (3.17) into (3.16) and noting that $\underline{v} = (0, 1, 0)$ and $\hat{\underline{q}} = (\hat{q}_1, \hat{q}_2, \hat{q}_3)$, the expression for \underline{F}_μ becomes

$$\underline{F}_\mu = 4\pi\rho \iint_{S_{lb}^{(0)}} \left(\hat{q}_2 \frac{\partial \mu}{\partial x}, \hat{q}_1 \frac{\partial \mu}{\partial x} - \hat{q}_3 \frac{\partial \mu}{\partial z}, \hat{q}_2 \frac{\partial \mu}{\partial z} \right) ds. \quad (3.18)$$

Let us now examine each component of \underline{F}_μ in (3.18). After integration by parts, the x-component gives

$$\begin{aligned}F_{\mu 1} &= 4\pi\rho \iint_{S_{lb}^{(0)}} \hat{q}_2 \frac{\partial \mu}{\partial x} ds \\ &= 4\pi\rho \int_H^0 \int_{-L/2}^{L/2} \hat{q}_2 \frac{\partial \mu}{\partial x} dx dz \\ &= -4\pi\rho \int_{-H}^0 (\hat{q}_2 \mu)_{x=-L/2} dz - 4\pi\rho \iint_{S_{lb}^{(0)}} \mu \frac{\partial \hat{q}_2}{\partial x} dx dz.\end{aligned}$$

But if we define

$$\begin{aligned}\frac{\partial \hat{q}_1(x, 0, z)}{\partial y} &= \lim_{y \rightarrow 0} \left\{ \frac{\partial \hat{q}_1}{\partial y}(x, y, z) \right\} \\ &= \lim_{y \rightarrow 0} \frac{\partial}{\partial y} \left\{ \frac{1}{2} \left(\frac{\partial \phi_1(x, y, z)}{\partial x} + \frac{\partial \phi(x, y, z)}{\partial x} \right) \right\}\end{aligned}\quad (3.19)$$

that is, the limit $y \rightarrow 0$ is to be taken after the partial differentiation with respect to y , then

$$\frac{\partial \hat{q}_2}{\partial x} = \frac{\partial \hat{q}_1}{\partial y}, \text{ on } S_{lb}^{(0)}. \quad (3.20)$$

With substitution from (3.20), the last expression for $F_{\mu 1}$ becomes

$$\begin{aligned}F_{\mu 1} &= -4\pi\rho \iint_{S_{lb}^{(0)}} \mu \frac{\partial \hat{q}_1}{\partial y} dx dz \\ &\quad + 4\pi\rho \int_H^0 (\mu \hat{q}_2)_{x=-L/2} dz.\end{aligned}\quad (3.21)$$

The first term of (3.21) is the standard form of Lagally's theorem for a distribution of doublets with its axis in the positive y -direction. The second term of (3.21), on the other hand, can be identified with the induced drag of a wing. As is indicated in (3.21), the doublet density μ and the "averaged" velocity normal to $S_{lb}^{(0)}$ are both to be evaluated at $x = -L/2$, which is the trailing edge (i.e., the stern) of the planform of Hull 1. Note also that (3.21) appears to provide an interesting insight into the difference between a lifting and a nonlifting body.

For simplicity, let us consider the case of a thin asymmetric body making a uniform motion in an infinite fluid (which is incompressible and inviscid). So long as the flow field is to be generated by a distribution of singularities on the planform of the body, both sources and normal doublets will be required. Since in the wake the doublet density remains constant along the direction of the uniform stream, i.e., $\mu(x, z) = \mu(-L/2, z)$, if we assume $\mu(x_0, z) = 0$ for any $x_0 < -L/2$, then there will be no wake trailing the thin asymmetric body. In this case the induced-drag term in (3.21) vanishes. Thus the flow problem is solved as a nonlifting potential problem which has its velocity field continuous everywhere outside the body. On the other hand, if μ is nonzero at the trailing edge, then there will be both a wake trailing behind the body and induced drag due to the wake. Clearly, in this case, the flow problem is solved as a lifting problem.

Applying a similar analysis to the two remaining components of \underline{F}_μ in (3.18), we may obtain the following results:

$$\begin{aligned}\underline{F}_\mu &= -4\pi\rho \iint_{S_{lb}^{(0)}} \mu \frac{\partial \hat{\underline{q}}}{\partial y} dx dz \\ &\quad + 4\pi\rho \int_H^0 (\mu \hat{q}_2, \mu \hat{q}_1, 0)_{x=-L/2} dz \\ &\quad + 4\pi\rho \int_{-L/2}^{L/2} (0, \mu \hat{q}_3, \mu \hat{q}_2)_{y=0} dx,\end{aligned}\quad (3.22)$$

in which the second term is to be integrated along the trailing edge, and the third term is to be integrated along the waterline.

In summary, let us write the force acting on Hull 1 as

$$\underline{F} = \underline{F}_D + \underline{F}_\mu, \quad (3.23)$$

where

$$\underline{F}_\sigma = 4\pi\rho \iint_{s_{1b}^{(0)}} \sigma \hat{q} \, dx \, dz, \quad (3.24)$$

and \underline{F}_μ has already been given by (3.22).

3.2 Moment

To obtain formulas for the hydrodynamic moment acting on Hull 1, we may use an analysis similar to that used for deriving the force expression. However, moment of momentum will be used rather than momentum. We shall use the origin of the Oxyz frame as the point of reference for the moment expression. Thus, in place of (3.1), the momentum, we shall consider the moment of momentum with respect to the origin $O = (0,0,0)$ in the control volume V_c as follows:

$$\underline{K}_0 = \iiint_{V_c} \rho \underline{x} \wedge \underline{q} \, dV, \quad (3.25)$$

in which $\underline{x} = (x, y, z)$ is the position vector of a point $P = (x, y, z)$ in the control volume.

Then, by a similar analysis applied to \underline{K}_0 , we may obtain the expression for the moment acting on Hull 1 with reference to the origin of the Oxyz frame as follows:

$$\begin{aligned} \underline{N}_0 &= \iint_{s_1} \rho \underline{x} \wedge \underline{n} \, ds = -4\pi\rho \iint_{s_{1b}^{(0)}} \sigma \cdot (\underline{x} \wedge \hat{q}) \, ds \\ &+ \rho \iint_{s_{1b}^{(0)}} \underline{x} \wedge \hat{q} \wedge (\underline{v} \wedge \underline{\gamma}_1) \, ds = \underline{N}_{0\sigma} + \underline{N}_{0\mu}, \end{aligned} \quad (3.26)$$

where $\underline{N}_{0\sigma}$ and $\underline{N}_{0\mu}$ represent the first and second integrals in (3.26), respectively.

By a similar analysis following (3.16) we may obtain the final expression for $\underline{N}_{0\mu}$ as follows:

$$\begin{aligned} \underline{N}_{0\mu} &= 4\pi\rho \iint_{s_{1b}^{(0)}} \mu \underline{x} \wedge \frac{\partial \hat{q}}{\partial y} \, dx \, dz \\ &- 4\pi\rho \iint_{s_{1b}^{(0)}} (\mu \underline{v}) \wedge \hat{q} \, dx \, dz \\ &+ 4\pi\rho \int_{-L/2}^0 \left\{ \mu \underline{x} \wedge (\hat{q}_2, \hat{q}_1, 0) \right\} \Big|_{x=-L/2} \, dz \\ &+ 4\pi\rho \int_{-L/2}^{L/2} \left\{ \mu \underline{x} \wedge (0, \hat{q}_3, \hat{q}_2) \right\} \Big|_{z=0} \, dx. \end{aligned} \quad (3.27)$$

Again, in this expression, the first two integrals represent the well known result of Lagally's theorem. The last two integrals in (3.27) are required only if the flow problem is being solved as a lifting-surface problem. In particular, the last integrals in (3.22) and (3.27) appear only for surface ship problems since they are to be evaluated along the undisturbed waterline, $z = 0$. These integrals are obtained as the result of integration by parts. Their physical meaning and numerical importance to a better prediction of the force and moment are not yet well understood. Hence, further investigations are required to assess their contributions.

4. APPLICATION TO SWATH SHIPS

With the source density $\sigma(x_0, z_0)$ and doublet density $\mu(x_0, z_0)$ obtained in Chapter 2, and the general formulas for force and moment derived in Chapter 3, we may now proceed to compute all three components of force and moment. However, since this work is still in progress and further computations are being made, we shall not be able to cover the entire scope of this investigation here, but shall continue to report the results as they become available. In this paper, we shall present the results of our specific application of the theory, namely: the prediction of wave resistance of the Small-Waterplane-Area Twin-Hull (SWATH) ships.

A SWATH demihull is characterized by having a combination of an elongated, slender, round body which is totally submerged, and a thin strut which joins the submerged main body and extends above the free surface. There has been a considerable amount of interest in developing such configurations as a new design concept. As a part of the effort to investigate the hydrodynamic performance of SWATH ships, an analytical tool for predicting the wave resistance was developed. Such a tool may be obtained by applying the theory presented in this paper.

To begin with, observe that the main body of a SWATH demihull has a round shape, and its transverse dimension is wider than that of the strut. Such a configuration tends to prevent the flow from going around the keel. Hence, a SWATH demihull is less likely to behave as a lifting surface as compared to a conventional catamaran. Thus, in applying the theory to SWATH ships, it was assumed that wake may be neglected in the initial investigation. Such an approach does not represent a serious compromise in accuracy since, as a consequence of linearization, the effect of the wake may be superimposed on the results of the initial investigation as a later refinement, if necessary.

To obtain the wave resistance formula, we only have to be concerned with the x-component of Equation (3.23). Since we have assumed that Hull 2 is the mirror image of Hull 1, the resultant wave resistance of the twin-hull ship is twice that experienced by Hull 1. Thus, with the effect of wake neglected, we may obtain from (3.23):

$$\begin{aligned} R_w &= -2\hat{e}_1 \cdot \underline{F} = -2\hat{e}_1 \cdot (\underline{F}_\sigma + \underline{F}_\mu) \\ &= 2(R_{\sigma\sigma} + R_{\mu\sigma} + R_{\sigma\mu} + R_{\mu\mu}), \end{aligned} \quad (4.1)$$

where

$$R_{\sigma\sigma} = 16\pi\rho K_0^2 \int_0^{\pi/2} d\theta \sec^3 \theta [1 + \cos(2bK_0 \sec^2 \theta \sin \theta)] \times [P_\sigma^2 + Q_\sigma^2], \quad (4.2)$$

$$R_{\mu\sigma} + R_{\sigma\mu} = 32\pi\rho K_0^2 \int_0^{\pi/2} d\theta \sec^3 \theta \sin(2bK_0 \sec^2 \theta \sin \theta) \times [P_\sigma Q_\mu + P_\mu Q_\sigma], \quad (4.3)$$

$$R_{\mu\mu} = 16\pi\rho K_0^2 \int_0^{\pi/2} d\theta \sec^3 \theta [1 - \cos(2bK_0 \sec^2 \theta \sin \theta)] \times [P_\mu^2 + Q_\mu^2], \quad (4.4)$$

$$\begin{Bmatrix} P_\sigma \\ Q_\sigma \end{Bmatrix} = \iint_{S^{(0)}} dx dz \sigma(x, z) e^{K_0 z \sec^2 \theta} \begin{Bmatrix} \cos \\ \sin \end{Bmatrix} (K_0 x \sec \theta), \quad (4.5)$$

$$\begin{Bmatrix} P_\mu \\ Q_\mu \end{Bmatrix} = K_0 \sec^2 \theta \sin \theta \iint_{S^{(0)}} dx dz \mu(x, z) \times e^{K_0 z \sec^2 \theta} \begin{Bmatrix} \sin \\ \cos \end{Bmatrix} (K_0 x \sec \theta), \quad (4.6)$$

$K_0 = g/U^2$, and $S^{(0)}$ is the projection of $S_{1b}^{(0)}$ and $S_{2b}^{(0)}$ onto the Oxz plane.

The quantity $R_{\sigma\sigma}$ represents the wave resistance experienced by one hull contributed by the source distribution alone. Similarly, $R_{\mu\mu}$ is that due to the transverse dipole distribution alone, and $R_{\sigma\mu} + R_{\mu\sigma}$ is due to the interaction between the sources and the transverse doublets.

4.1 No-Cross-Flow Assumption and Its Consequence

Here we shall discuss a special condition on camber. Under such a condition, each demihull will experience no cross-flow effect. Recall the integral Equation (2.34) which is to be solved for the unknown doublet density μ . Suppose now that a demihull is so designed that its camber satisfies the following relationship:

$$\frac{\partial \zeta}{\partial x} = \frac{1}{2\pi} \iint_{S^{(0)}} \left(\frac{\partial t}{\partial x_0} \right) \frac{\partial \zeta^{(0)}}{\partial y} (x, 0, z; x_0, 2b, z_0) \cdot x_0 dz_0, \quad (4.7)$$

Then, since the right side of Equation (2.34) vanishes, we may conclude that

$$\mu(x_0, z_0) = 0, \quad (4.8)$$

if the integral equation has a unique solution. Thus, if the condition (4.7) is satisfied, then the force and moment associated with μ vanish. In particular (4.1), the wave resistance formula, simplifies to merely

$$R_w = 2 R_{\sigma\sigma}. \quad (4.9)$$

Thus, the relationship (4.7) represents an interesting design application. If we apply the low draft-to-length ratio and the small separation-distance-to-length ratio approximations used in obtaining (2.52), the relationship (4.7) may be further simplified as follows:

$$C(x, z) = \frac{2b}{\pi} \int_H^H \frac{t(x, z_0)}{4b^2 + (z - z_0)^2} dz_0, \quad (4.10)$$

with the boundary condition $t(-L/2, z) = 0$ and $C(-L/2, z) = 0$. According to (4.10), the no-cross-flow camber varies with z as well as with x . In practice, however, it would be more convenient and sufficiently accurate to use an averaged value of $C(x, z)$ so that it would be constant along the draft and would vary only along the length. If we let \tilde{C} be such an averaged value, then from (4.10) we have:

$$\begin{aligned} \tilde{C}(x) &= \frac{1}{2H} \int_{-H}^H C(x, z) dz \\ &= \frac{1}{2H\pi} \int_H^H t(x, z) \left\{ \tan^{-1} \left(\frac{H-z}{2b} \right) - \tan^{-1} \left(\frac{H+z}{2b} \right) \right\} dz. \end{aligned} \quad (4.11)$$

Thus, the averaged no-cross-flow camber may now be determined for each station by using (4.11).

4.2 Results of Computations and Comparison with Experimental Data

In making wave resistance computations for SWATH ships, we have assumed that the ship either has camber which satisfies the no-cross-flow requirement of (4.11), or a low beam-to-separation-distance ratio. Under such an assumption, the simplified formula (4.9) may be considered an acceptable approximation. Thus, with this simplification, only the source distributions are now involved. Nevertheless, as can be seen from (4.2) and (4.5), the actual computation is still quite involved for an arbitrarily given ship geometry.

To take advantage of SWATH geometry, the source distribution is further simplified to the sum of a sheet distribution representing the thin strut, and a line distribution representing the body. With this simplification, only the thickness of the strut and the cross-sectional area of the body appear explicitly in the wave-resistance formula. However, carrying out the

computation still requires the strut thickness and body sectional area to be described analytically. This may present problems since hull geometry is usually given in terms of offsets.

To solve this problem, a special curve-fitting technique has been developed. This technique employs the Chebyshev series, utilizes the offsets of strut thickness and area curve of the body, and provides analytical expressions for the strut-thickness function and the body area curve. Analytical development of this technique is presented in Appendix B.

With two Chebyshev-series representations, one for the strut thickness function and one for the body area curve, the expression for wave resistance may be put in the following final form:

$$R_w = 2(R_S + R_B + R_{SB}) \quad (4.12)$$

where R_S , R_B , and R_{SB} represent the wave resistance of one strut, one body, and the interaction between strut and body, respectively. Furthermore, each of the three components is now expressed as a finite sum of the products of Chebyshev coefficients and auxiliary functions. For example, R_S is given as follows:

$$R_S = \left(\frac{\pi}{2} \rho g T^2 L_S \gamma_{0S} \right) \times \sum_{m=1}^M \sum_{n=1}^M \{ A_{Sm} A_{Sn} T_{Smn} + B_{Sm} B_{Sn} W_{Smn} \}, \quad (4.13)$$

where T is the maximum thickness and L_S is the length of the strut, respectively, and γ_0 is a dimensionless number related to ship speed. Equations for R_B and R_{SB} have a similar structure and are given by Equations (B.9) through (B.17) in Appendix B.

A computational program has been developed on the basis of those final set of equations. Since the three principal equations for R_S , R_{SB} , and R_B have a similar structure, we shall use the one for R_S as an example for discussing some of the computational aspects of the program. In the above equation for R_S , the Chebyshev coefficients, A_{Sm} and B_{Sm} , are determined solely by strut thickness offsets, while the auxiliary functions, T_{Smn} and W_{Smn} , are determined by the draft-to-length ratio and the speed (or, to be precise, the Froude number); that is, the auxiliary functions do not vary with changes in strut shape. Thus, in case there are several alternate designs to be investigated, the auxiliary functions need to be computed only once provided those designs have the same draft-to-length ratio.

In making the wave resistance computations, the major portion of computer time is taken up by the auxiliary functions, while the Chebyshev coefficients require only a minor amount of effort. Hence, the present development is especially suitable for investigating the effect of hull-form variations on wave resistance. In particular, it would be a straightforward extension to formulate an optimization problem to investigate the theoretical hull form of "minimum" resistance. The

procedure developed in Lin, Webster, and Wehausen (1963) may be easily adapted to the present formulation. The computer program developed on the basis of the present analytical work has been applied to most of the SWATH models investigated at NSRDC. Only the results of two SWATH models will be reported in this paper as typical examples. Since no experiment was conducted to measure wave resistance directly, comparison of theoretical predictions can be made only against residuary resistance. Despite the fact that residuary resistance consists of the so-called "form drag" as well as wave resistance, good qualitative agreement between residuary resistance and theoretical wave resistance was observed.

Schematic diagrams and geometric characteristics of the two SWATH models are given in Figures 1 and 2 and Table 1, respectively. The demihulls of both models have similar cross-sectional shapes, the major difference being that SWATH III has two "straight" (i.e., zero camber) demihulls, while SWATH IV has a slight camber on each demihull intended to minimize the cross-flow effect. Another distinction is in the waterplane shapes, as can be seen from the diagrams.

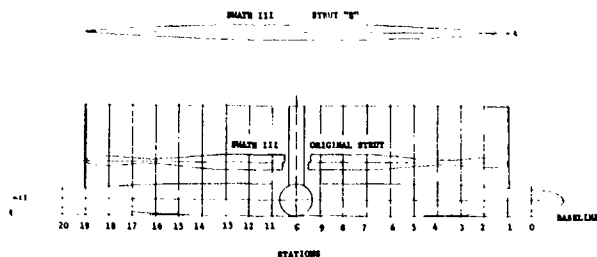


Figure 1 — Reduced Scale Drawing of SWATH III Represented by Model 5276

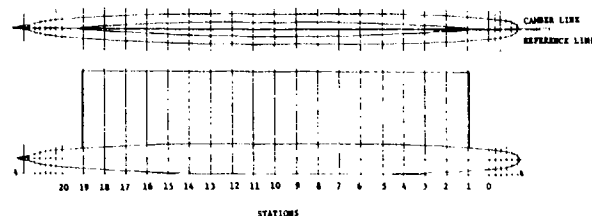


Figure 2 — Reduced Scale Drawing of SWATH IV Represented by Model 5287

A number of test cases have been devised to investigate the merits of this theoretical tool in making resistance predictions. First, to test its ability to reflect the effect of a small change in hull geometry, the demihull of SWATH III with different strut shapes was used. Results of theoretical predictions and the corresponding residuary resistance coefficients are presented in Figure 3. In this figure, the same main body was used for both cases. Although the only difference is in the strut shape, experimental data show marked differences in the residuary-resistance characteristics at lower speeds. This trend is very well predicted by the theory. However, at the higher speed range, the comparison between theory and experiment is not as favorable for this specific example. Although both theory and experiment indicate

TABLE 1 - SHIP DIMENSIONS AND COEFFICIENTS
FOR SWATH DEMIHULLS

	SWATH III	SWATH IV
NSRDC Model Number	5,276	5,287
Length of Body (ft) (L_B)	287	288
Length of Strut (ft) (L_S)	226	227
Diameter of Body (ft) (D)	17.3	18.0
Beam of Strut (ft) (T)	8.0	8.0
Depth of Submergence to \bar{C}_L Body (ft)	19.4	19.0
Total Draft of Demihull (ft)	28.0	28.0
Displacement (tons, s.w.)	3,760.	3,960.
Wetted Surface (sq ft) (S)	17,350	17,540
LCB/LOA	0.479	—
Length/Diameter of Body	16.55	16.02
C_p (Body)	0.758	0.758
C_W (Strut)	0.709	0.740
T/L_S (Strut)	0.035	0.035
(Depth to \bar{C}_L Body)/(Diameter of Body)	1.12	1.06
Design Speed in Knots	32.0	32.0
Scale Ratio	20.4	20.4

NOTE: For a twin hull configuration the separation distance between demihull centerline is 3.68 feet, model scale. This corresponds to a beam/separation distance ratio of 0.106.

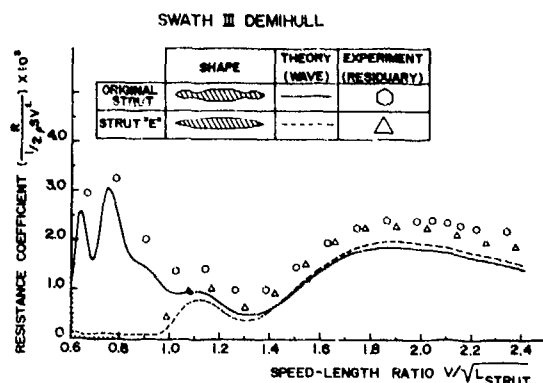


Figure 3 - Effect of Strut Variations—Comparison between Theory and Experiment

that differences in the resistance characteristics will be small at higher speeds, theory predicts a different trend. One thing that may help explain this reversed trend is the fact that the "original" strut possessing a "Coke-bottle" shape may have a higher-than-usual percentage of "form drag" and therefore a higher residuary resistance. The theory, on the other hand, is intended to predict only wave resistance and does not account for the viscous form drag of the Coke-bottle effect.

Figure 4 shows a comparison between single- and twin-hull ships. Since the demihulls of SWATH III are "straight," each is exactly one half of a twin-hull ship. In this figure, the solid- and dotted-line curves show the predicted wave

resistance characteristics of the twin-hull (i.e., SWATH III) form and its demihull, respectively. For most speeds, the twin-hull interference effect amounts to an increase in resistance. However, at certain speed ranges (for example, the speed-length ratio between 1.3 and 1.5), the interference effect becomes favorable. In this case, the twin-hull ship would have less resistance than would two demihulls traveling individually. The experimental data appear to substantiate this predicted trend very well.

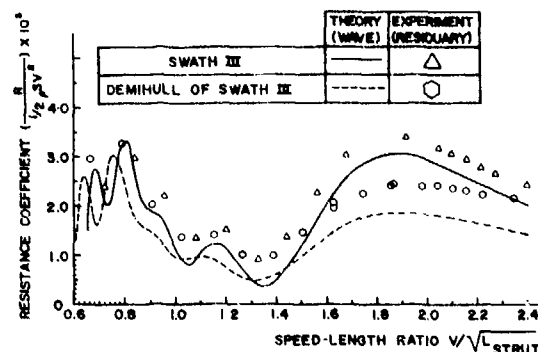


Figure 4 - Effect of Twin-Hull Interference on Resistance Characteristics

Figure 5 shows the theoretical prediction and its comparison with experimental data for SWATH IV. Data from two model-experiment techniques, one with the model captive and the other with the model free to trim and heave, are presented. In contrast with SWATH III, SWATH IV has camber which makes the flow field more closely satisfy the no-cross-flow assumption of the present theory. Thus, the agreement between theory and experiment in this case is the most striking among all the cases investigated. It is also evident from this figure that the theory agrees better with the data from the captive-model experiments.

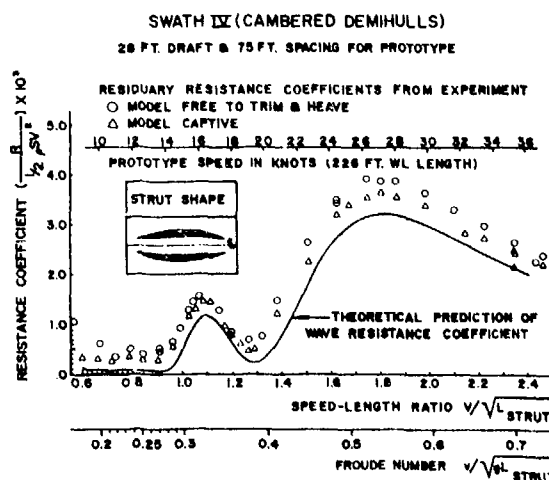


Figure 5 - Comparison between Theoretical Prediction and Data from Two Experimental Techniques

Comparison of the computed and experimental data shows that, for SWATH ships, we may expect generally good correlation between theoretical wave resistance and residuary resistance. A number of reasons which are rather obvious may explain such good agreement. First, the SWATH ships have thin and slender demihulls which well satisfy the assumptions of the theory. Second, the traditional method of estimating viscous drag (i.e., Froude's method) must be quite satisfactory, at least qualitatively, for SWATH ships so that residuary resistance consists mostly of wavemaking resistance. Third, the speeds of interest for SWATH ships fall in a higher Froude number range for which the theory is known to be more reliable. As was previously mentioned, lifting effect seems to be less important to SWATH configurations. For a conventional catamaran, however, lifting effect may become rather significant. In this case, the dipole distributions as well as the source distributions must be considered simultaneously.

ACKNOWLEDGMENTS

The author is indebted to Professors R. Timman and J. N. Newman for many helpful ideas and discussions; to Mr. V. J. Monacella for continued encouragement and guidance through the course of this investigation; and to Miss Claire E. Wright for her expert assistance in editing and preparing the manuscript.

This work was supported under the Naval Ship Research and Development Center's General Hydromechanics Research Program and was funded by the Naval Sea Systems Command under Task Area SR 023 01 01.

REFERENCES

- Abramowitz, M. and I. A. Stegun, "Handbook of Mathematical Functions with Formulas, Graphs, and Mathematical Tables," U. S. Government Printing Office, Washington, D. C. (1964) xiv + 1046 pp.
- Cummins, W. E., "The Force and Moment on a Body in a Time-Varying Potential Flow," *J. Ship Res.*, Vol. 1, No. 1 (1957) pp. 7-18 and 54.
- Eggers, K., "Über Widerstandsverhältnisse von Zweikörperschiffen," *Jahrb. Schiffbautech. Ges.* Band 49 (1955), pp. 516-437; *Erört.* 538-539.
- Gakhov, F. D., "Boundary Value Problems," (1963) English translation by I. N. Sneddon, Pergamon Press.
- Havelock, T. H., "Wave Resistance: The Mutual Action of Two Bodies," *Proc. Roy. Soc., Ser. A*, Vol. 55 (1936), pp. 460-472.
- Hu, P. N., "Forward Speed Effect on Lateral Stability Derivatives of a Ship," Davidson Lab. Report R-829 (Aug 1961), Stevens Inst. of Tech., 38 pp + 2 Figures.
- Kellogg, O. D., "Foundations of Potential Theory," Dover Publications, N. Y. (1929) ix + 384 pp.
- Kochin, N. E., "On the Wave-Making Resistance and Lift of Bodies Submerged in Water," (Russian Orig., 1936) Translated in *Soc. Nav. Archs. and Mar. Engrs. Tech. Res. Bull.* No. 1-8 (1951), 126 pp.
- Landweber, L. and C. S. Yih, "Forces, Moments, and Added Masses for Rankine Bodies," *J. Fluid Mech.* Vol. 1 (Sep 1956), pp. 319-336.
- Landweber, L., "Lagally's Theorem for Multipoles," *Schiffstechnik* Bd. 14 (1967), pp. 19-21.
- Lin, W. C. and W. G. Day, Jr., "The Still-Water Resistance and Propulsion Characteristics of Small-Waterplane-Area Twin-Hull (SWATH) Ships," *AIAA/SNAME Adv. Marine Vehicles Conf.* (1974), San Diego, Calif., 14 pp.
- Lin, Wen-Chin, W. C. Webster, and J. V. Wehausen, "Ships of Minimum Total Resistance," *Int. Sem. Theoret. Wave Resistance*, Ann Arbor (1963), pp. 907-948; disc. 949-953.
- Lunde, J. K., "On the Linearized Theory of Wave Resistance for Displacement Ships in Steady and Accelerated Motion," *Trans. Soc. Nav. Archs. and Mar. Engrs.* Vol. 59 (1951), pp. 25-76; disc. 76-85.
- Magnus, W., F. Oberhettinger, and R. P. Soni, "Formulas and Theorems for the Special Functions of Mathematical Physics," Springer-Verlag, New York, Inc. (1966), VIII + 508 pp.
- Morgan, W. B., "Theory of the Annular Airfoil and Ducted Propeller," *Sym. Nav. Hydrodyn.*, Washington, D. C. (1962), pp. 151-197.
- Muskhelishvili, N. I., "Singular Integral Equations," English translation by J. R. M. Radok, P. Noordhoff N. V.
- Pien, P. C. and C. M. Lee, "Motion and Resistance of Low-Waterplane-Area Catamaran," *Sym. Nav. Hydrodyn.*, Paris (1972).
- Robinson, A. and J. A. Laurmann, "Wing Theory," Cambridge University Press (1956), ix + 569 pp.
- Wehausen, J. V., "The Wave Resistance of Ships," *Advances in Applied Mechanics*, Vol. 13, pp. 93-245, Academic Press, New York (1973).
- Yokoo, K. and R. Tasaki, "On the Twin-Hull Ships," *Rept. Transportation Tech. Res. Inst. of Japan*, No. 1, 20 pp. (1951); No. 2, 9 pp. (1953). Translated in U. of Michigan Dept. of Nav. Arch. and Mar. Eng., Rept. No. 33 and 34 (1969).
- Zucker, R. D., "Lagally's Theorem and the Lifting Body Problem," *J. of Ship Res.* Vol. 14, No. 2 (1970), pp. 135-140.

APPENDIX A

EXPONENTIAL INTEGRAL FUNCTION AND HAVELOCK SOURCE POTENTIAL

The Havelock source potential given in (2.15) may be expressed in terms of the well tabulated exponential integral function. To this end, we first rewrite (2.15) in the following form:

$$\begin{aligned} G(x, y, z; x_0, y_0, z_0) &= \frac{1}{r} + \frac{1}{r_1} \\ &+ \frac{1}{\pi} \int_{-\pi}^{\pi} d\theta \int_0^{\infty} dk k \frac{e^{k\{(z+z_0)+i\tilde{\omega}\}}}{k \cdot \nu} \\ &+ 4 \int_0^{\pi/2} d\theta (k_0 \sec^2 \theta) e^{(k_0 \sec^2 \theta)(z+z_0)} \\ &\times \sin[k_0(x-x_0)\sec\theta] \cdot \cos[k_0(y-y_0)\sin\theta \sec^2 \theta] \\ &= \frac{1}{r} + \frac{1}{r_1} \\ &+ \frac{1}{\pi} \frac{\partial}{\partial a} \int_{-\pi}^{\pi} d\theta \int_0^{\infty} dk \frac{e^{k(a+i\tilde{\omega})}}{k \cdot \nu} \\ &+ 4 \frac{\partial}{\partial a} \int_0^{\pi/2} d\theta e^{\nu a} \cdot \sin[\nu(x-x_0)\cos\theta] \\ &\quad \cdot \cos[\nu(y-y_0)\sin\theta], \end{aligned} \quad (A.1)$$

where $a = z + z_0 < 0$, $\nu = k_0 \sec^2 \theta > 0$, and $\tilde{\omega} = (x - x_0) \cos \theta + (y - y_0) \sin \theta$.

The third term in (A.1) involves a double integration and thus presents the major computational difficulty. Hence, our primary concern is to express the k -integral in terms of a well-known function for which computations may be performed efficiently.

Let us first introduce the following change of variable:

$$t = (k \cdot \nu)(a + i\tilde{\omega}). \quad (A.2)$$

Then, by making use of the definitions of exponential integral functions, the Cauchy integral theorem, and a suitable choice of the paths of integration in a complex plane, the following identity may be established:

$$\begin{aligned} \int_0^{\infty} \frac{e^{k(a+i\tilde{\omega})}}{k \cdot \nu} dk &= \begin{cases} e^{\nu(a+i\tilde{\omega})} \{E_1(\nu(a+i\tilde{\omega})) \pm i\pi\}, & \text{if } \tilde{\omega} \gtrless 0; \\ e^{\nu a} \{-E_1(-\nu a)\}, & \text{if } \tilde{\omega} = 0. \end{cases} \end{aligned} \quad (A.3)$$

The special functions E_1 and E_i in (A.3) are known as exponential integral functions and are defined as follows:

$$\left. \begin{aligned} E_1(w) &= \int_w^{\infty} \frac{e^{-t}}{t} dt, \quad |\arg w| < \pi, \\ E_i(u) &= - \int_u^{\infty} \frac{e^{-t}}{t} dt, \quad u > 0. \end{aligned} \right\} \quad (A.4)$$

Further information concerning these functions may be found in Abramowitz and Stegun (1964, pp. 228-252).

Next, we substitute (A.3) into the double-integral term of (A.1). However, since the θ integral ranges from $-\pi$ to $+\pi$, and variable $\tilde{\omega}$ changes sign in this interval, care is required in making the substitution. Let us introduce the plane polar coordinates ρ and β such that

$$x - x_0 = \rho \cos \beta, \quad y - y_0 = \rho \sin \beta.$$

Then, the variable $\tilde{\omega}$ may be written as

$$\tilde{\omega} = (x - x_0) \cos \theta + (y - y_0) \sin \theta = \rho \cos(\theta - \beta). \quad (A.5)$$

Thus, the double-integral term in (A.1) becomes

$$\begin{aligned} V &= \int_{-\pi}^{\pi} d\theta \int_0^{\infty} dk \frac{e^{k(a+i\tilde{\omega})}}{k \cdot \nu} \\ &= \int_{-\pi}^{\pi} d\theta \int_0^{\infty} dk \frac{e^{k[a+\rho \cos(\theta-\beta)]}}{k \cdot \nu} \\ &= \int_{-\pi}^{\pi} d\theta' \int_0^{\infty} dk \frac{e^{k[a+\rho \cos \theta']}}{k \cdot \nu_1}, \end{aligned} \quad (A.6)$$

where

$$\theta' = \theta - \beta, \text{ and } \nu_1 = k_0 \sec^2(\theta + \beta). \quad (A.7)$$

Since $\rho = \sqrt{(x - x_0)^2 + (y - y_0)^2} > 0$, $\cos \theta' \geq 0$ for $-\pi/2 \leq \theta' \leq \pi/2$, and $\cos \theta' \leq 0$ for $-\pi \leq \theta' \leq -\pi/2$ and $\pi/2 \leq \theta' \leq \pi$, correct substitutions may now be made from (A.3) according to the values of θ' . After a straightforward but somewhat lengthy manipulation involving a change of integration variables, the final result becomes

$$\left. \begin{aligned} E &= \int_{\pi}^{\pi} d\theta \cdot e^{\nu(a+i\tilde{\omega})} \cdot E_1(\nu(a+i\tilde{\omega})) \\ &- 4\pi \int_0^{\pi/2} d\theta \cdot e^{\nu a} \cdot \sin[\nu(x-x_0)\cos\theta] \cdot \cos[\nu(y-y_0)\sin\theta] \\ &4\pi \int_{\pi/2}^{\pi/2+\beta} d\theta \cdot e^{\nu a} \cdot \sin[\nu\rho\cos(\theta-\beta)] \end{aligned} \right\} \quad (A.8)$$

The result obtained in (A.8) is now substituted into (A.1) in place of the double integration. In doing this, we note that the second term on the right side of (A.8) cancels with the last term of (A.1) after the substitution. Thus, the final result gives:

$$\left. \begin{aligned} G(x, y, z; x_0, y_0, z_0) &= \frac{1}{r} + \frac{1}{r_1} \\ &- \frac{1}{\pi} \frac{\partial}{\partial a} \int_{\pi}^{\pi} d\theta \cdot e^{\nu(a+i\tilde{\omega})} \cdot E_1(\nu(a+i\tilde{\omega})) \\ &+ 4 \frac{\partial}{\partial a} \int_{\pi/2}^{\pi/2+\beta} d\theta \cdot e^{\nu a} \cdot \sin[\nu\rho\cos(\theta-\beta)] \end{aligned} \right\} \quad (A.9)$$

where $\beta = \tan^{-1} \{(y-y_0)/(x-x_0)\}$ and $\rho = \sqrt{(x-x_0)^2 + (y-y_0)^2}$, the polar coordinates of the field point (x, y) relative to the singularity point (x_0, y_0) in the plane $z = \text{constant}$. The rest of the variables appearing in (A.9) are defined in (A.1).

Since the double integral has now been reduced to single integrals, (A.9) may provide a more efficient basis for numerical integration. However, we should attempt to reduce (A.9) even further (especially the last integral on the right side of (A.9)) before actually proceeding with numerical evaluations of the function G .

Next, let us investigate a series expansion of G based on the asymptotic expansion of the function E_1 . It is a known property of the exponential integral function (Abramowitz and Stegun, 1964, p. 231) that, for large w ,

$$\left. \begin{aligned} E_1(w) &\sim \frac{e^{-w}}{w} \left\{ 1 - \frac{1}{w} + \frac{2!}{w^2} - \frac{3 \cdot 2 \cdot 1}{w^3} + \dots \right. \\ &\left. + \frac{n!}{(-w)^n} + O(|w|^{-n-1}) \right\} \end{aligned} \right\} \quad (A.10)$$

Note that the argument of E_1 in (A.9) is given by

$$\begin{aligned} w &= \nu(a+i\tilde{\omega}) \\ &= k_0 \sec^2 \theta \{ (z+z_0) + i[(x-x_0)\cos\theta + (y-y_0)\sin\theta] \} , \\ \text{or,} \\ |w| &= k_0 \sec^2 \theta \cdot \sqrt{(z+z_0)^2 + (x-x_0)^2 + (y-y_0)^2} \\ &= \left(\frac{r_1}{L} \right) \cdot \left(\frac{1}{F_n^2} \right) \sec^2 \theta, \end{aligned} \quad (A.11)$$

where $r_1 = \sqrt{(z+z_0)^2 + (x-x_0)^2 + (y-y_0)^2}$; L and F_n are the ship length and the Froude number based on ship length, respectively. Hence, unless r_1 is very small, it may generally be said that $\nu(a+i\tilde{\omega})$ assumes large values for low Froude numbers.

Thus, for low Froude numbers, the first integral on the right side of (A.9) admits the following asymptotic expansion:

$$\begin{aligned} E_1(x-x_0, y-y_0, z+z_0) &= -\frac{1}{\pi} \frac{\partial}{\partial a} \int_{\pi}^{\pi} d\theta \cdot e^{\nu(a+i\tilde{\omega})} \cdot E_1(\nu(a+i\tilde{\omega})) \\ &= -\frac{1}{\pi} \frac{\partial}{\partial a} \int_{\pi}^{\pi} d\theta \left\{ \frac{1}{\nu(a+i\tilde{\omega})} - \frac{1}{\nu^2(a+i\tilde{\omega})^2} + \dots \right\} \\ &= -\frac{1}{\pi} \frac{\partial}{\partial a} \int_{\pi}^{\pi} d\theta \left\{ \sum_{n=1}^N (-1)^n \frac{(n-1)!}{[\nu(a+i\tilde{\omega})]^n} \right. \\ &\quad \left. + O(|\nu(a+i\tilde{\omega})|^{-(N+1)}) \right\} \\ &= G^{(1)} + G^{(2)} + \dots + G^{(N)} + O(|\nu(a+i\tilde{\omega})|^{-(N+1)}). \end{aligned} \quad (A.12)$$

The individual $G^{(n)}$ in (A.2) may be evaluated in closed form by making use of the residue theorem. For example, $G^{(1)}$ may be evaluated as follows:

$$\begin{aligned} G^{(1)} &= -\frac{1}{\pi} \frac{\partial}{\partial a} \int_{\pi}^{\pi} d\theta \cdot \frac{1}{\nu(a+i\tilde{\omega})} \\ &= -\frac{1}{\pi} \frac{\partial}{\partial a} \int_{\pi}^{\pi} d\theta \frac{\cos^2 \theta}{k_0(a+ib\cos\theta+ic\sin\theta)}, \end{aligned} \quad (A.13)$$

where $b = (x-x_0)$ and $c = (y-y_0)$. By making change of variables,

$$\left. \begin{aligned} \zeta &= e^{i\theta} = \cos \theta + i \sin \theta \\ \zeta^{-1} &= e^{-i\theta} = \cos \theta - i \sin \theta \end{aligned} \right\} \quad (\text{A.14})$$

the integration in (A.13) may be transformed into complex integration over a unit circle as follows:

$$\begin{aligned} I_1 &= \int_{-\pi}^{\pi} d\theta \frac{\cos^2 \theta}{k_0 (a + ib \cos \theta + ic \sin \theta)} \\ &= \frac{1}{i 2 k_0} \oint_{|\zeta|=1} \frac{(\zeta^2 + 1)^2 d\zeta}{\zeta^2 \{(c + ib)\zeta^2 + 2a\zeta - (c - ib)\}} \quad (\text{A.15}) \end{aligned}$$

The integrand has two poles within the unit circle. The residues at these poles are found to be

$$\left. \begin{aligned} \delta t_0 &= \frac{-2a}{(c - ib)^2}, \quad \text{at } \zeta = 0; \\ \text{and} \\ \delta t_1 &= \frac{[(r_1 + a)^2 + (c + ib)^2]^2}{2(c + ib)^2 (r_1 + a)^2 + r_1} \\ \text{at } \zeta &= \frac{(a + r_1)}{(c + ib)}. \end{aligned} \right\} \quad (\text{A.16})$$

Hence, by the residue theorem, the integral in (A.15) is equal to

$$\begin{aligned} I_1 &= \frac{1}{i 2 k_0} 2\pi i \{\delta t_0 + \delta t_1\} \\ &= \frac{1}{i 2 k_0} \cdot 2\pi i \left\{ \frac{-1}{r_1} \left[1 + \frac{c^2 - b^2}{(r_1 - a)^2} \right] \right\} \\ &= \frac{\pi}{k_0 r_1} \cdot \left\{ 1 + \frac{c^2 - b^2}{(r_1 - a)^2} \right\}. \quad (\text{A.17}) \end{aligned}$$

Substituting (A.17) into (A.13) and performing the partial differentiation with respect to "a," we finally obtain

$$G^{(1)} = \frac{1}{k_0 r_1^3} \left\{ a + \frac{(2r_1 - a)}{(r_1 - a)^2} \cdot (b^2 - c^2) \right\}. \quad (\text{A.18})$$

Similarly, from (A.12) we may write

$$\left. \begin{aligned} G^{(2)} &= -\frac{1}{\pi} \frac{\partial}{\partial a} \int_{-\pi}^{\pi} d\theta \frac{\cos^4 \theta}{k_0^2 (a + ib \cos \theta + ic \sin \theta)^2} \\ &\dots \dots \dots \\ G^{(N)} &= -\frac{1}{\pi} \frac{\partial}{\partial a} \int_{-\pi}^{\pi} d\theta \frac{(-1)^{N-1} \cdot \cos^{2N} \theta}{k_0^{(N)} (a + ib \cos \theta + ic \sin \theta)^N} \end{aligned} \right\} \quad (\text{A.19})$$

In principle, each $G^{(n)}$ in (A.19) may be integrated in closed form by using the same algebraic operation as that used for evaluating $G^{(1)}$. However, the complexity of the algebra required to find the residues escalates rapidly with the index n . Hence, for $G^{(n)}$'s with higher indices, the algebraic operation may become too complex to be practical. In this case, some other numerical scheme must be developed.

In summary, let us write

$$G(x, y, z; x_0, y_0, z_0) = G^{(0)} + G^{(1)} + G^{(2)} + \dots + G^{(w)}, \quad (\text{A.20})$$

where

$$\left. \begin{aligned} G^{(0)} &= \frac{1}{r} + \frac{1}{r_1}, \\ G^{(w)} &= 4 \frac{\partial}{\partial a} \int_{\pi/2}^{\pi/2 + \beta} d\theta e^{\nu a} \cdot \sin[\nu \rho \cos(\theta - \beta)], \end{aligned} \right\} \quad (\text{A.21})$$

$G^{(1)}, G^{(2)}, \dots, G^{(N)}$ are given in (A.18) and (A.19).

APPENDIX B

EVALUATION OF THE WAVE RESISTANCE INTEGRAL FOR SWATH SHIPS

A typical demihull of a SWATH ship is characterized by having a combination of an elongated main body and a thin strut. The main body is totally submerged and represents the bulk of total ship displacement. The strut extends above the free surface and usually has a uniform thickness vertically. Thus, we shall assume that the relationship between hull geometry and the corresponding source strength, Equation (2.17), may be approximated as follows:

$$\sigma_s = -\left(\frac{U}{2\pi}\right) \frac{dt(x)}{dx} \quad (B.1)$$

$$\sigma_B = -\left(\frac{U}{4\pi}\right) \frac{dA(x)}{dx} \quad (B.2)$$

where $t(x)$ is the half thickness of the strut, $A(x)$ is the cross-sectional area of the main body, and the subscripts "S" and "B" indicate the strut and body, respectively.

In principle, we may substitute Equations (B.1) and (B.2) into Equations (4.5) and (4.2), and then find the wave resistance from (4.9) provided the strut thickness $t(x)$ and the area $A(x)$ of the main body are given analytically. In practice, however, hull geometry is usually given in terms of offset tables.

One way of solving this problem is by representing the hull as a series in some fundamental set of functions. A special form of Chebyshev series has been devised for the present application. This series has been proven to be both effective and efficient in reproducing a faired ship line by making use of its usual offset table.

The Chebyshev series representation of the hull geometry will be developed below. Let

$$x = \sin \theta, \quad -1 \leq x \leq 1 \quad \& \quad -\frac{\pi}{2} \leq \theta \leq \frac{\pi}{2}. \quad (B.3)$$

Define a fundamental set of Chebyshev series as follows:

$$\begin{aligned} U_m(x) &= \cos(2m-1)\theta = \cos[(2m-1)\sin^{-1}x], \\ V_m(x) &= \sin 2m\theta = \sin[2m\sin^{-1}x]. \end{aligned} \quad (B.4)$$

The half-thickness and the sectional area functions will be represented by finite sums of the series in (B.4) as follows:

$$\begin{aligned} t(x) &= \sum_{m=1}^M [A_{Sm} U_m(x) + B_{Sm} V_m(x)] \\ &= \sum_{m=1}^M [A_{Sm} \cos(2m-1)\theta + B_{Sm} \sin 2m\theta], \end{aligned} \quad (B.5)$$

$$\begin{aligned} A(x) &= \sum_{m=1}^M [A_{Bm} U_m(x) + B_{Bm} V_m(x)] \\ &= \sum_{m=1}^M [A_{Bm} \cos(2m-1)\theta + B_{Bm} \sin 2m\theta]. \end{aligned} \quad (B.6)$$

The quantities A_{Sm} , B_{Sm} , and A_{Bm} , B_{Bm} shall be called the Chebyshev coefficients for strut and main body, respectively.

By making use of the orthogonality of the series, the following inversion formulas may be obtained:

$$\begin{aligned} A_{Sm} &= \frac{2}{\pi} \int_{-1}^1 dx \frac{t(x) U_m(x)}{\sqrt{1-x^2}} \\ &= \frac{2}{\pi} \int_{-\pi/2}^{\pi/2} d\theta t(\sin \theta) \cos(2m-1)\theta, \end{aligned} \quad (B.7)$$

$$\begin{aligned} B_{Sm} &= \frac{2}{\pi} \int_{-1}^1 dx \frac{t(x) V_m(x)}{\sqrt{1-x^2}} \\ &= \frac{2}{\pi} \int_{-\pi/2}^{\pi/2} d\theta t(\sin \theta) \sin 2m\theta. \end{aligned} \quad (B.8)$$

If the half-thickness of the strut $t(x)$ is replaced by the area curve $A(x)$ of the main body in Equations (B.7) and (B.8), they become a set of equations for evaluating the main-body Chebyshev coefficients, A_{Bm} and B_{Bm} .

The maximum number of terms required in the series to represent a faired ship line depends on the shape of the specific lines and the degree of accuracy desired. For a typical ship line, twelve to fifteen terms will be able to graphically produce smooth curves with good accuracy. On the other hand, if the primary objective is to evaluate the wave-resistance integrals for a given ship geometry, then a series of six terms seems to give answers with satisfactory accuracy.

Note that in Equations (B.5) through (B.8) the coordinate variables are normalized (i.e., made dimensionless). For example, in Equations (B.5), (B.7), and (B.8), values of x now vary from -1 to $+1$ instead of from $-L/2$ to $+L/2$. The half-thickness $t(x)$ now varies from 0 to 1 instead of from 0 to $(T/2)$, where T is the maximum thickness of the strut.

The final form of the wave resistance integrals suitable for numerical computation may now be developed. Let us first decompose the domain of integration in Equation (4.5) into two parts, one for the strut and one for the main body, and make substitutions from (B.1) and (B.2). Next, in Equation (4.5), we integrate by parts with respect to x once, then substitute the resulting expressions for the P and Q functions into Equations (4.2).

Finally, with substitutions from (B.5) and (B.6), we may write the wave resistance integrals in the following form:

$$R_S = \left(\frac{\pi}{2} \rho g T^2 L_S \gamma_{0S} \right) \times \sum_{m=1}^M \sum_{n=1}^M A_{Sm} A_{Sn} T_{Smn} + B_{Sm} B_{Sn} W_{Smn}, \quad (B.9)$$

$$R_B = \left(\frac{2\pi\rho g A_0^2}{L_S \gamma_{0S}} \right) \sum_{m=1}^M \sum_{n=1}^M \{ A_{Bm} A_{Bn} T_{Bmn} + B_{Bm} B_{Bn} W_{Bmn} \}, \quad (B.10)$$

$$R_{SB} = (2\pi\rho g A_0 T) \sum_{m=1}^M \sum_{n=1}^M \{ A_{Sm} A_{Bn} T_{SBmn} + B_{Sm} B_{Bn} W_{SBmn} \} \quad (B.11)$$

where

$$\left\{ \frac{T_{Smn}}{(2m-1)(2n-1)} \right\} = \int_{\gamma_{0S}}^{\infty} \frac{d\alpha}{\alpha^2 \sqrt{\alpha^2 - \gamma_{0S}^2}} D \left(\alpha; \frac{2b}{L_S}, \gamma_{0S} \right) \times E_S^2(\alpha) \left\{ \frac{J_{2m-1}(\alpha) J_{2n-1}(\alpha)}{J_{2m}(\alpha) J_{2n}(\alpha)} \right\}, \quad (B.12)$$

$$D = 1 + \cos \left[\left(\frac{2b}{L_S} \right) \left(\frac{2}{\gamma_{0S}} \right) \alpha \sqrt{\alpha^2 - \gamma_{0S}^2} \right],$$

$$E_S = 1 - e^{-2(h_S/L_S)(\alpha^2/\gamma_{0S})}, \quad (B.13)$$

$$\gamma_{0S} = \frac{gL_S}{(2U^2)},$$

$$\left\{ \frac{T_{Bmn}}{(2m-1)(2n-1)} \right\} = \int_{\gamma_{0S}}^{\infty} \frac{d\alpha}{\sqrt{\alpha^2 - \gamma_{0S}^2}} D \left(\alpha; \frac{2b}{L_S}, \gamma_{0S} \right) \times E_B^2(\beta) \left\{ \frac{J_{2m-1}(\beta) J_{2n-1}(\beta)}{J_{2m}(\beta) J_{2n}(\beta)} \right\} \quad (B.14)$$

$$E_B = e^{-2(h_B/L_B)(\beta^2/\gamma_{0B})},$$

$$\gamma_{0B} = \frac{gL_B}{(2U^2)}, \quad (B.15)$$

$$\beta = \left(\frac{\gamma_{0B}}{\gamma_{0S}} \right) \alpha,$$

$$\left\{ \frac{T_{SBmn}}{(2m-1)(2n-1)} \right\} = \int_{\gamma_{0S}}^{\infty} \frac{d\alpha}{\sqrt{\alpha^2 - \gamma_{0S}^2}} D \left(\alpha; \frac{2b}{L_S}, \gamma_{0S} \right) \times E_S(\alpha) E_B(\beta) \left\{ \frac{J_{2m-1}(\alpha) J_{2n-1}(\beta)}{J_{2m}(\alpha) J_{2n}(\beta)} \right\}, \quad (B.16)$$

$$J_{2m}(\alpha) = \frac{2}{\pi} \int_0^{\pi/2} \cos(\alpha \sin t) \cos(2mt) dt, \quad (B.17)$$

$$J_{2m-1}(\alpha) = \frac{2}{\pi} \int_0^{\pi/2} \sin(\alpha \sin t) \sin[(2m-1)t] dt.$$

T , L_S , and h_S are the maximum thickness, length, and draft of the strut, respectively; A_0 , L_B , and h_B are the maximum section area, length, and depth of submergence of the axis of the body. The special functions appearing in the above equations, J_{2m} and J_{2m-1} , are Bessel functions of the first kind with integer orders. For further information concerning these functions, one may consult, for example, page 79 of Magnus, Oberhettinger, and Soni.

In the above equations, R_S , R_B , and R_{SB} represent the wave resistance due to one strut, one main body, and the interaction between strut and main body, respectively. Hence, the wave resistance of a SWATH ship becomes:

$$R_w = 2(R_S + R_B + R_{SB}). \quad (B.18)$$

SECOND-ORDER HYDRODYNAMIC FORCES DUE TO STOCHASTIC EXCITATION*

by

Eddie Neal

Naval Ship Research and Development Center
Bethesda, Maryland

ABSTRACT

This paper treats the problems of synthesizing and predicting second-order forces in hydrodynamic systems excited by stochastic forcing functions. Immediate applications are to second-order forces on naval vessels operating in or beneath an irregular wave system. The concept of transfer functions for nonlinear hydrodynamic systems is outlined. An analytical technique is developed for identifying the transfer function from wave and force time histories. The relative merits of the identification technique are discussed, and application to digitally simulated ship-wave systems is shown. The probability density function for hydrodynamic forces is derived to second order under the assumption that the wave excitation is a stationary Gaussian stochastic process. Statistical properties of the resulting hydrodynamic forces are given in terms of physical characteristics of the input wave field. The notions of slowly varying and rapidly varying components of the total second-order hydrodynamic force are introduced and the methodology required for their synthesis and prediction is discussed.

1. INTRODUCTION

Recently, increased attention has been focused on the prediction of the nonlinear response of surface ships and submerged vessels in waves. The present study was undertaken in an effort to develop computational tools for the analysis and prediction of nonlinear ship response to a random or irregular wave system.

The linear statistical theory of a ship's response (motions or force) to an irregular wave system is well known and has had many applications to ship performance prediction and design. The fundamental assumptions that form a basis for the use of linear statistical theory are that: (1) the first-order free-surface wave elevation can be modeled as a stationary normal (Gaussian) function of time, and (2) the ship response to the Gaussian wave system can be modeled as a time-invariant linear dynamical system. These two assumptions imply that the linear ship response will also be a Gaussian random time function which can be easily characterized in terms of its first two moments. The essential features of the linear theory are summarized in Chapter 2 for immediate reference and to motivate the subsequent development.

Some ship responses are inherently nonlinear and cannot be adequately approximated by a linear model. For in-

stance, the added resistance of a ship is related to wave height in a nonlinear manner and has been modeled as a wave-height-squared relation. Also, the rolling motion of ships is strongly nonlinear and has been modeled by a nonlinear Duffing's equation. In general, information sufficient to characterize the nonlinear response cannot be obtained from the linear theory concepts of covariances and energy spectra which are computed in terms of the first two moments of the response. Here, it becomes necessary to introduce higher-order moments, which implies higher-order covariances and higher-order spectra.

The objective of this paper is to treat two aspects of the nonlinear ship response problem. First, the problem of characterizing the nonlinear response in terms of random samples of excitation and response time histories is considered, then the probability structure of the response is investigated. The detailed emphasis is on nonlinearities through second order. This restriction keeps both the exposition and the calculations within manageable bounds. The characterization problem entails the estimation of nonlinear transfer functions, whose application to ship problems was outlined by Hasselmann (1966). His approach is essentially that applied in the present study. However it is shown in Chapter 3 that, by generalizing Hasselmann's Fourier series approach into a continuous energy spectrum wave representation, the resulting form of the response yields a simple and explicit physical interpretation. The fourth chapter addresses the transfer function estimation problem. It is shown that a third-order moment function, the cross-bicovariance, and its Fourier transform, the cross-bispectrum, can be employed to obtain a relation for the second-order transfer function. An efficient algorithm for computing the transfer function is described. Typical computed results are shown in Section 4.2.

Finally, the probability structure of the nonlinear response is considered in Chapter 5. To the author's knowledge, this problem has not received any attention in the ship literature. Thus, application is made of two approximations to the probability density function, and an approach is described for determining the exact probability density function to second order.

2. OVERVIEW OF LINEAR STATISTICAL SHIP RESPONSE THEORY

The statistical theory of linear ship motions and forces in a seaway is well known and has had many applications to ship performance prediction and design. Rudnick (1951) initially

*Read at the Tenth Naval Hydrodynamics Symposium, June 24-28, 1974, Cambridge, Mass. U.S.A.

NOMENCLATURE

$a(t)$	Weighting function defined by (5.7)	$S_X(\omega)$	One-sided spectral density function for process X
$Co(\omega)$	Co-spectrum	$S_{xy}(\omega)$	One-sided cross-spectral density for processes X and Y
C_i	Parameter defined by (5.12)	$S_{xxy}(\omega_1, \omega_2)$	Physically realizable cross-bi-spectral density function defined by (4.7)
E	Expected value	T	Sample length or wave period
$E(\tau)$	Even part of cross-covariance	t	Time
$F^{(n)}$	Term n in functional series	V	Velocity
$f_X(\omega)$	Two-sided spectral density function for process X	$X(t)$	Excitation function
$f_{xy}(\omega)$	Two-sided cross-spectral density for X and Y	$X_i(t)$	Independent Gaussian variate
$f_{xxy}(\omega_1, \omega_2)$	Two-sided cross-bi-spectral density function between X and Y	$X^*(t)$	Least mean square estimator of X
g	Gravitational constant	$Y(t)$	Response function
$H(\omega)$	First-order (linear) transfer function	$Y^{(n)}$	N th order response
$H(\omega_1, \omega_2)$	Second-order transfer function	Γ	Gamma function
h	First-order impulse response function	Δ	Sampling interval
h_n	N th -order impulse response function	δ	Dirac delta function
Im	Imaginary part	δ_{ij}	Kronecker delta function
K	Kernel of integral equation (5.31)	ϵ_n	Phase component of a Fourier series
$M(t)$	Time-varying linear ship response	$\epsilon(\omega)$	Random phase angle
N	Total number of terms	$\eta(t)$	First-order free-surface elevation
$O(\tau)$	Odd part of cross-covariance	λ	Eigenvalue
$Qu(\omega)$	Quadrature spectrum	μ	Mean value
Re	Real part	π	3.14159 ...
$R_X(\tau)$	Covariance function for process X	σ^2	Variance
$R_{xy}(\tau)$	Cross-covariance function for processes X and Y	$\phi(\omega)$	Phase of first-order system
$R_{xxy}(\tau_1, \tau_2)$	Cross-covariance function for processes X and Y	$\phi(\omega_1, \omega_2)$	Phase of second-order system
		$\psi_n(t)$	Time domain eigenfunction
		$\psi_n(\omega)$	Frequency domain eigenfunction
		ω	Radian frequency
		ω_e	Encounter frequency

expressed the idea of modeling the sea surface as a stationary normal (Gaussian) function of time at a fixed point. Birkhoff and Kotig (1952) indicated the potential use of random function (stochastic process) theory in modeling the sea as a Gaussian process, but they expressed concern over the non-linear effects which tended to distort the Gaussian probability distribution function. Pierson (1952) advocated the use of the Gaussian wave surface model despite minor nonlinear effects and treated problems in the analysis of wave records and the propagation of waves. St. Denis and Pierson (1953) used linear system theory to model ship responses to the Gaussian wave system and initiated a new era of ship-response-to-waves research that is still in progress.

2.1 Specification of the Gaussian Seaway and Ship Responses

Many representations of stationary Gaussian processes are possible which probably accounts for the various equations for random ocean surfaces that may be observed in the literature. The earliest Gaussian process representation was through the use of Fourier series expansions with normally distributed coefficients. Such models were used as early as

1910 by Einstein in his investigation of black-body radiation. Also, Fourier series models with deterministic coefficients but uniformly distributed phase angles have been used to obtain periodic Gaussian processes. For real valued processes, this model takes the form

$$\eta(t) = \sum_{n=1}^{\infty} a_n \cos(\omega_n t - \epsilon_n). \quad (2.1)$$

Here the ω_n are related to the period T of oscillation by

$$\omega_n = \frac{2\pi n}{T}, \quad (2.2)$$

where a_n is the deterministic amplitude corresponding to ω_n , and the ϵ_n are independently and uniformly distributed over $(0, 2\pi)$. The Gaussian character of this model is guaranteed by the central limit theorem provided certain general regularity conditions are satisfied. The theory of Fourier series random processes is discussed in detail in a classic paper by Rice (1944-45).

Because of their periodic nature, Fourier series models of random processes may be too restrictive in some instances. The random phase model (Equation 2.1) may be generalized into the Gaussian stochastic integral representation

$$\eta(t) = \int_0^{\infty} \cos(\omega t - \epsilon(\omega)) \sqrt{2 S_{\eta}(\omega)} d\omega. \quad (2.3)$$

This stochastic integral can be well defined as the limit in quadratic mean of a sequence of random partial sums. Here the uniformly distributed phase angles on $(0, 2\pi)$ are indexed over continuous frequency, and the amplitudes are selected from a continuous energy spectral density function, $S_{\eta}(\omega)$, defined over the frequency interval $(0, \infty)$. It should be noted that this model represents an infinite ensemble of sea surface time histories. Each wave surface time history represents but one realization from this infinite collection. This model was used implicitly by Rice (1944) and was formally introduced by Levy (1948). The model's Gaussian structure and related statistical properties were recently derived by Neal and Hurwitz (1974). The model may be viewed as the real Gaussian form of the spectral representation theorem, and it may be written without the square-root symbol as

$$\eta(t) = \operatorname{Re} \int_{-\infty}^{\infty} e^{i\omega t} dZ(\omega), \quad (2.4)$$

where $Z(\omega)$ is a complex valued process with orthogonal increments. The model may be written equivalently as

$$\begin{aligned} \eta(t) = & \int_0^{\infty} \cos(\omega t) dU(\omega) \\ & + \int_0^{\infty} \sin(\omega t) dV(\omega), \end{aligned} \quad (2.5)$$

where $U(\omega)$ and $V(\omega)$ are real processes with orthogonal Gaussian increments. The form (2.3) will be used in the sequel as it admits a straightforward physical interpretation.

St. Denis and Pierson (1953) introduced the random phase model into the ship research field, and they interpreted the model as the time varying, unidirectional wave surface elevation at the origin of a statistically stationary wave field. In their now classic paper, St. Denis and Pierson also extended the random phase model to include a superposition of unidirectional waves in order to model realistic short crested seas. Finally, their paper was highlighted by the introduction of linear system theory to model ship motions in a seaway as a linear, time-invariant dynamical system.

Let $M(t)$ denote any arbitrary ship response at a point fixed in some coordinate system. If the response is related by a linear, time-invariant dynamical system to a wave system, $\eta(t)$, also fixed at some point in the coordinate system, then the relation can be expressed by

$$M(t) = \int_{-\infty}^{\infty} h(\tau) \eta(t - \tau) d\tau, \quad (2.6)$$

If the linear system is causal, the response at any time t will be unaffected by the excitation at any future time $t' > t$. In this case the linear system can be written as

$$M(t) = \int_0^{\infty} h(\tau) \eta(t - \tau) d\tau. \quad (2.7)$$

The question of whether ship-wave systems are causal is unresolved in the literature (see, e.g., Ogilvie, 1964, p. 57), or Dalzell, 1972, p. 32). Therefore (2.6) will be used in what follows. Of course, if a causality assumption applies, $h(\tau)$ will equal zero for $\tau < 0$ and (2.7) will be satisfied automatically. For simplicity we take $\eta(t)$ to be the unidirectional Gaussian wave system (2.3); generalization to short-crested seas is straightforward as indicated by St. Denis and Pierson (1953). For Gaussian excitation, (2.6) must then be interpreted as a stochastic integral and, assuming the existence of the integrals involved, may be written as

$$\begin{aligned} M(t) = & \int_{-\infty}^{\infty} h(\tau) \operatorname{Re} \left\{ \int_0^{\infty} e^{i[\omega(t - \tau) - \epsilon(\omega)]} \right. \\ & \left. \times \sqrt{2 S_{\eta}(\omega)} d\omega \right\} d\tau \\ = & \operatorname{Re} \int_0^{\infty} H(\omega) e^{i[\omega t - \epsilon(\omega)]} \\ & \times \sqrt{2 S_{\eta}(\omega)} d\omega, \end{aligned} \quad (2.8)$$

with

$$H(\omega) = \int_0^{\infty} h(\tau) e^{i\omega\tau} d\tau. \quad (2.9)$$

$H(\omega)$ is a complex valued function called the frequency response function or transfer function of the linear system. The latter term is more commonly used in ship hydrodynamics. If we denote

$$H(\omega) = |H(\omega)| e^{i\phi(\omega)}, \quad (2.10)$$

then (2.6) takes the form

$$M(t) = \int_0^\infty \cos(\omega t - \epsilon(\omega) + \phi(\omega)) \times \sqrt{2|H(\omega)|^2 S_\eta(\omega)} d\omega, \quad (2.11)$$

where $|H(\omega)|$ and $\phi(\omega)$ are the amplitude and phase gain functions of the linear system, respectively. In ship hydrodynamics the function $|H(\omega)|^2$ is called the response amplitude operator (RAO). Equation (2.11) demonstrates the intimate connection between the time-domain linear response and the wave spectrum and transfer function which are both frequency-domain functions.

Because (2.11) is of the same form as (2.3), it follows that the motion process will also have a Gaussian distribution for each t . This fact is extremely important for the study of ship performance in a seaway. It implies that the ship response can be statistically characterized from knowledge of its first two statistical moments, i.e., its mean and variance. Because the mean value of $M(t)$ is zero, the variance of $M(t)$ is

$$\begin{aligned} \sigma_M^2 &= E M^2(t) \\ &= \int_0^\infty |H(\omega)|^2 S_\eta(\omega) d\omega. \end{aligned} \quad (2.12)$$

Thus the response process will be Gaussian, with mean zero and variance determined by the sea spectrum and the response amplitude operator. The time varying motion can be determined from (2.11) and requires knowledge of both the amplitude and phase of the transfer function as well as knowledge of the sea spectrum. The Gaussian structure of the linear ship motion system also simplifies the statistical analysis of extreme values and force or wave amplitudes in a seaway. All of these quantities can be determined as functions of the variance of the response process as treated, for example, by Longuet-Higgins (1952) and Cartwright and Longuet-Higgins (1956).

Upon comparing the spectral representations (2.3) and (2.11) for the Gaussian wave and response processes, and upon recalling that $S_\eta(\omega)$ is the wave energy spectrum (spectral density function), it follows from the uniqueness of the spectral representation that the motion spectrum, $S_M(\omega)$, must be given by

$$S_M(\omega) = |H(\omega)|^2 S_\eta(\omega) \quad (2.13)$$

for each non-negative frequency, ω . Conversely, if the wave and response spectra are known, the response amplitude operator can be obtained as

$$|H(\omega)|^2 = \frac{S_M(\omega)}{S_\eta(\omega)} \quad (2.14)$$

provided $S_\eta(\omega) \neq 0$.

It should be noticed that the above wave system is defined at a fixed point in space. When a ship experiences forward speed the wave process is usually expressed in a moving coordinate system relative to the mean speed, V , of the ship. The frequency in the new coordinate system is called the encounter frequency (ω_e) and is related to the original frequency by

$$\omega_e = \omega + \frac{\omega^2}{g} V. \quad (2.15)$$

The frequency notation, ω , is used throughout this paper with the understanding that encounter frequency will be implied whenever the ship has forward speed.

2.2 Statistical Estimation in Linear Ship Systems

Various theoretical spectral forms are available for modeling the energy spectrum of the seaway. However, these represent idealizations, such as the assumption of a fully developed sea, which may not be realized exactly in a given application. It has therefore been necessary to seek more realistic wave spectra from wave measurements. The determination of the spectral density functions of a stationary stochastic process from a realization (time history) is a problem of statistical spectral analysis. This field has developed a comprehensive literature which was pioneered by Tukey (1949) and Blackman and Tukey (1958). Let $\eta(t)$ be a weakly stationary stochastic process with zero mean value which represents a real valued wave or force system. Here the stationarity assumption is used in the sense that the product moment

$$\begin{aligned} R_\eta(\tau) &= E \{ (\eta(t + \tau) - E \eta(t + \tau)) \\ &\quad \times (\eta(t) - E \eta(t)) \} \end{aligned} \quad (2.16)$$

is a function only of τ . $R_\eta(\tau)$ is defined as the covariance function of the process. For real processes the covariance function is real and symmetric. If $R_\eta(\tau)$ is absolutely integrable, then a continuous non-negative spectral density function $f_\eta(\omega)$ exists and satisfies

$$R_\eta(\tau) = \int_{-\infty}^{\infty} e^{i\omega\tau} f_\eta(\omega) d\omega, \quad (2.17)$$

$$f_\eta(\omega) = \frac{1}{2\pi} \int_{-\infty}^{\infty} e^{-i\omega\tau} R_\eta(\tau) d\tau. \quad (2.18)$$

These are the celebrated Wiener-Khinchine relations. In ship applications it is convenient to express the Wiener-Khinchine relations as real cosine transforms. By using the fact that both $R_\eta(\tau)$ and $f_\eta(\omega)$ are even for real processes, these relations may be written as

$$R_\eta(\tau) = \int_0^\infty \cos(\omega\tau) S_\eta(\omega) d\omega, \quad (2.19)$$

$$S_{\eta}(\omega) = \frac{2}{\pi} \int_0^{\infty} \cos(\omega\tau) R_{\eta}(\tau) d\tau, \quad (2.20)$$

where $S_{\eta}(\omega)$ is the physically realizable spectral density function defined over non-negative frequencies by

$$S_{\eta}(\omega) = \begin{cases} 2 f_{\eta}(\omega) & \text{if } \omega \in [0, \infty) \\ 0 & \text{otherwise.} \end{cases} \quad (2.21)$$

Thus, knowledge of the covariance function is sufficient to determine the energy spectral density exactly by (2.20). In order to determine the covariances from the product moments in (2.16), the indicated averages are evaluated over the process ensemble. However, if the process is ergodic, these mean products can be calculated from a single (infinite) time history as

$$R_{\eta}(\tau) = \lim_{T \rightarrow \infty} \frac{1}{T} \int_0^T \eta(t) \eta(t + |\tau|) dt. \quad (2.22)$$

It is known from stochastic process theory (Doob, 1952, p. 494) that a Gaussian process is ergodic, if its spectral distribution function is everywhere continuous, or, equivalently, if the memory of the process dies out for arbitrarily large time lags. Practically all of the Gaussian processes useful in ship performance studies would seem to have this property.

Since only a finite sample of a process realization can be observed in practice, the limiting operation in (2.22) cannot be performed. Thus as a practical procedure, a sample of length T is observed and the covariance function is approximated by the (biased) estimator

$$R_{\eta}(\tau) = \frac{1}{T} \int_0^{T-|\tau|} \eta(t) \eta(t + |\tau|) dt, \quad (2.23)$$

or by the (unbiased) estimator,

$$R_{\eta}(\tau) = \frac{1}{T - |\tau|} \int_0^{T-|\tau|} \eta(t) \eta(t + |\tau|) dt. \quad (2.24)$$

Parzen (1961, p. 175) has shown that the biased estimator (2.23) generally has a smaller mean square error and thus may be preferable to the unbiased estimator (2.24). The substitution of (2.23) or (2.24) into (2.20) yields an estimate of the spectral density function. The extent of error and bias this estimating procedure may introduce into the resulting spectra, and the means by which these errors may be reduced, are topics that have been studied intensively by researchers during the past two decades. Extensive literature exists (Parzen, 1967) and several textbooks are currently available (see e.g. Jenkins-Watts, 1968). The basic approach involves

smoothing the estimators using time domain "lag windows" or frequency domain "spectral windows" to reduce the variance of the spectral estimators. However, the use of data windows inevitably leads to the introduction of bias so that trade-offs between variance and bias become crucial. These methods have been applied to ocean wave and ship motion problems by many investigators, and reasonably good results have been obtained for wave and motion spectra and for the response amplitude operators (see Yamanouchi, 1974 for a comprehensive review). Alternative estimation methods that have not been widely applied in ship problems include prewhitening (transforming) the data to obtain spectra that are relatively flat and thus reducing the estimation bias (Blackman-Tukey, 1958). Similar procedures may be applied using the autoregressive spectral estimation procedure as given by Parzen (1969) or Akaike (1969).

The response amplitude operator obtained from some method of spectral estimation together with the wave spectrum can be used to compute the motion variance from (2.12) and hence characterize in a probabilistic fashion the Gaussian response process. However, the phase gain function, $\phi(\omega)$, must be determined in order to completely specify the transfer function (2.10). To determine phase information from irregular (random) wave time histories, the cross-spectrum must be used. Consider the time domain stochastic relation between the motion and wave in (2.6) and form the mean product

$$\begin{aligned} E \eta(t) M(t + \alpha) &= \int_{-\infty}^{\infty} h(\tau) E \eta(t) \eta(t + \alpha - \tau) d\tau \\ &= \int_{-\infty}^{\infty} h(\tau) R_{\eta}(\alpha - \tau) d\tau \end{aligned} \quad (2.25)$$

by (2.16) and the fact that the order of expectation and integration can be interchanged in the stochastic integral. The mean product is then a function of α alone and we define

$$R_{\eta M}(\alpha) = E \eta(t) M(t + \alpha) \quad (2.26)$$

as the cross-covariance function between the zero mean processes $\eta(t)$ and $M(t)$. Note that the cross-covariance function is not an even function but satisfies

$$R_{\eta M}(-\alpha) = R_{M \eta}(\alpha). \quad (2.27)$$

If $R_{\eta M}(\alpha)$ admits a Fourier transform, then (2.11) can be written in the frequency domain as

$$f_{\eta M}(\omega) = H(\omega) f_{\eta}(\omega), \quad -\infty < \omega < \infty \quad (2.28)$$

with

$$f_{\eta M}(\omega) = \frac{1}{2\pi} \int_{-\infty}^{\infty} R_{\eta M}(\tau) e^{-i\omega\tau} d\tau. \quad (2.29)$$

In practice (2.28) is usually written over non-negative frequencies as

$$S_{\eta M}(\omega) = H(\omega) S_{\eta}(\omega), \quad (2.30)$$

where $S_{\eta}(\omega)$ is the physically realizable cross-spectrum defined analogously to (2.21) by

$$S_{\eta M}(\omega) = \begin{cases} 2 f_{\eta M}(\omega) & \text{if } \omega \in [0, \infty) \\ 0 & \text{otherwise.} \end{cases} \quad (2.31)$$

Then if $S_{\eta}(\omega) \neq 0$, the complete transfer function is obtained from (2.30) as

$$H(\omega) = \frac{S_{\eta M}(\omega)}{S_{\eta}(\omega)}. \quad (2.32)$$

In applications, it is convenient to express (2.31) as a one-sided Fourier transform. Let us decompose $R_{\eta M}(\tau)$ in (2.29) into the sum of an even and odd function

$$R_{\eta M}(\tau) = E(\tau) + O(\tau), \quad (2.33)$$

with $E(\tau)$ and $O(\tau)$ defined by

$$E(\tau) = \frac{1}{2} (R_{\eta M}(\tau) + R_{\eta M}(-\tau)) \quad (2.34)$$

$$= \frac{1}{2} (R_{\eta M}(\tau) + R_{M\eta}(\tau)),$$

$$O(\tau) = \frac{1}{2} (R_{\eta M}(\tau) - R_{\eta M}(-\tau)) \quad (2.35)$$

$$= \frac{1}{2} (R_{\eta M}(\tau) - R_{M\eta}(\tau)).$$

Then upon substituting (2.34), (2.35) into (2.29) it is seen that (2.31) may be written

$$\begin{aligned} S_{\eta M}(\omega) &= \frac{2}{\pi} \int_0^{\infty} E(\tau) \cos(\omega\tau) d\tau \\ &\quad - \frac{2i}{\pi} \int_0^{\infty} O(\tau) \sin(\omega\tau) d\tau \quad (2.36) \\ &= Co(\omega) - i Qu(\omega). \end{aligned}$$

$Co(\omega)$ and $Qu(\omega)$ are called the cospectrum and quadrature-spectrum, respectively. It then follows from (2.10), (2.32), and (2.36) that $H(\omega)$ can be written as

$$|H(\omega)| = \frac{(Co^2(\omega) + Qu^2(\omega))^{1/2}}{S_{\eta}(\omega)}, \quad (2.37)$$

$$\phi(\omega) = \tan^{-1} (-Qu(\omega)/Co(\omega)). \quad (2.38)$$

As in the case of scalar spectra, the cross-spectral relations must in practice be approximated from finite time histories of the input-output processes; thus the problem of obtaining estimators in (2.37) and (2.38) that have minimal variability and bias remains. In fact, increased bias is introduced into the cross-spectrum estimators due to the phase differences between the input and output signals. Pierson and Dalgzell (1960) discovered that improved cross-spectral estimators could be obtained by shifting the output signal relative to the input such that the effective phase shift would be reduced. This procedure was placed on a rigorous statistical basis by Akaike et al. (1964), and a detailed discussion of the procedure is given by Yamanouchi (1964).

The above methods for estimating the frequency response of linear ship-wave systems are essentially frequency-domain system identification procedures in the terminology of modern control theory. System identification methods may be developed either in the frequency or time domain. In the time domain the impulse response function can be estimated directly from (2.6) by using the sampled-data representation

$$M(t) = \sum_{k=-n}^n h(k\Delta) \eta(t - k\Delta) \cdot \Delta, \quad (2.39)$$

where Δ denotes the constant sampling interval. Then the least squares estimates of the $h(k\Delta)$ satisfy the matrix equation

$$R_{M\eta}(n\Delta) = \sum_{k=-n}^n h(k\Delta) \cdot \Delta R_{\eta\eta}(k - n\Delta). \quad (2.40)$$

Yamanouchi (1964) used this method to obtain the impulse response for ship roll motions.

3. NONLINEAR HYDRODYNAMIC FORCES

Nonlinearities play such a key role in ship hydrodynamics that a linear model of ship response to waves may not be acceptable in many instances. For example, the rolling motion of a ship is often modeled by a Duffing's equation whose nonlinear behavior has been well studied in mechanics. Maruo (1957) investigated the added resistance of a ship due to waves and developed a theory in which the mean added drag is proportional to the square of the wave height. Verhagen (1970) conducted extensive model tests on slow drift oscillations of moored vessels in irregular (random) seas and concluded that the long-period amplitude motion is proportional to the ratio of significant wave height squared and mean wave period.

Various analytical techniques exist for nonlinear dynamical problems. For instance, the method of equivalent linearization and the method of perturbations provide approximate solutions for simple types of nonlinearities but are not easily generalized to more complex systems. Yamanouchi (1964) applied the perturbation method to ship rolling motions, whereas Kaplan (1966) and Vassilopoulos (1970) studied the rolling problem using the equivalent linearization procedure. When the nonlinearity involves displacement and not velocity in the system differential equation, solutions can be obtained via the Fokker-Planck equation provided the excitation has a flat frequency spectrum, i.e., white noise. However, this assumption may be too restrictive for practical ship problems which are subject both to non-white wave excitation and nonlinear damping forces. The Volterra functional series approach to nonlinear system analysis is a very general method that has shown promise for application to realistic ship problems. This method entails expansion of the ship response in a functional Taylor's series relative to the given wave or force excitation. The n th term in such an expansion gives the response component resulting from n th order interactions of the excitation. This makes the method easily adaptable to the physical interpretation associated with the usual perturbation expansion solutions to ship hydrodynamics problems. In addition, the method admits an explicit development of the probability structure of nonlinear ship response in a seaway. Hasselmann (1966) outlined the functional series approach to ship motions and showed that the nonlinear transfer functions were related to higher-order moments of ship motions. Vassilopoulos (1966) outlined essentially the same approach and showed that the formula due to Maruo (1957) for the time averaged added drag on a ship in waves could be derived from nonlinear system theory. Dalzell (1974) formulated the added drag in waves problem as a quadratic functional series and estimated the mean added drag transfer function from irregular wave data.

The theory of functional power series models is briefly summarized in this chapter, and a detailed analysis of second-order hydrodynamic forces in a seaway is given. Computational methods for non-resonant responses are given for the problems of estimating second-order transfer function from irregular wave test data.

3.1 Theory

Let $Y(t)$ denote the nonlinear response of a ship at some fixed point to an excitation $\{X(t) | -\infty < t < \infty\}$. Because $Y(t)$ may respond to the entire time history of $X(t)$, we call $Y(t)$ a functional defined on a class of excitation functions $X(t)$ and we denote

$$Y(t) = F(X(t)). \quad (3.1)$$

If F is a continuous functional of X in the function space sense, then F can be expanded in a functional power series such that

$$\begin{aligned} Y(t) = & g_0 + \int_{-\infty}^{\infty} g_1(t, t_1) X(t_1) dt_1 \\ & + \cdots + \int_{-\infty}^{\infty} \cdots \int_{-\infty}^{\infty} g_n(t, t_1, \dots, t_n) X(t_1) \\ & \cdots X(t_n) dt_1 \cdots dt_n + \cdots \end{aligned} \quad (3.2)$$

The series will have some radius of convergence within which the series will converge uniformly. If the series represents a causal physical system, then the kernel functions satisfy

$$g_n(t, t_1, \dots, t_n) = 0, \text{ if } t_i > t. \quad (3.3)$$

Series satisfying this property were studied by Volterra (1930) early in this century, and series of the form (3.2) that satisfy (3.3) are called Volterra series. Functional series expansions have also been studied by Frechet (1910). Wiener (1942) used an orthogonal series version of (3.2) to study the response of nonlinear devices to Gaussian noise. Barrett (1963) has discussed application of functional series to physical problems.

Let us assume that the nonlinear system is time invariant so that the kernel functions in (3.2) can depend only on time differences. Thus,

$$\begin{aligned} Y(t) = & h_0 + \int_{-\infty}^{\infty} h_1(t - t_1) X(t_1) dt_1 + \cdots \\ & + \int_{-\infty}^{\infty} \cdots \int_{-\infty}^{\infty} h_n(t - t_1, \dots, t - t_n) X(t_1) \\ & \cdots X(t_n) dt_1 \cdots dt_n + \cdots \end{aligned} \quad (3.4)$$

$$\begin{aligned} = & h_0 + \int_{-\infty}^{\infty} h_1(\tau) X(t - \tau) d\tau + \cdots \\ & + \int_{-\infty}^{\infty} \cdots \int_{-\infty}^{\infty} h_n(\tau_1, \dots, \tau_n) X(t - \tau_1) \cdots \\ & X(t - \tau_n) d\tau_1 \cdots d\tau_n + \cdots \end{aligned} \quad (3.5)$$

$$= \sum_{n=0}^{\infty} F^{(n)}(t, x), \quad (3.6)$$

where

$$F^{(0)}(t, x) = h_0 \text{ (a constant)} \quad (3.7)$$

and

$$F^{(n)}(t, x) = \int_{-\infty}^{\infty} \cdots \int_{-\infty}^{\infty} h_n(\tau_1, \dots, \tau_n) X(t - \tau_1) \cdots X(t - \tau_n) d\tau_1 \cdots d\tau_n, \quad n > 0 \quad (3.8)$$

In general, the kernels in (3.8) may not be symmetric functions of their arguments. However, since a permutation of indices in any kernel only affects the order in which the integration is carried out but does not affect the response, the kernels may be symmetrized by defining

$$h'_n(\tau_1, \tau_2, \dots, \tau_n) = \frac{1}{n!} \sum_i h_n(\tau_{i1}, \dots, \tau_{in}), \quad (3.9)$$

where the summation is over all possible permutations of subscripts. Thus, for the purpose of analysis, symmetric kernels may be assumed without loss of generality. In practice, symmetry cannot be assumed a priori, and the operation (3.9) may have to be employed if symmetric kernels are desired. Note also that symmetry of the kernel functions is equivalent to symmetry of their Fourier transforms. In application to physical problems, the question of convergence of the functional power series is not of primary importance. The series is truncated after n terms to yield a functional polynomial, and it is merely assumed that additional terms will provide a more realistic model. Clearly, the resulting response for a finite number of terms will be mathematically meaningful if the input is bounded and each kernel used is absolutely integrable. However, these conditions are not sufficient for convergence of the infinite series (3.6). Here, in addition, it will be necessary that the contribution from terms of order n decrease to zero as $n \rightarrow \infty$.

The continuity assumption of the functional relationship between the excitation and response may also be important. This assumption means that two time histories of the excitation that are arbitrarily close together will yield responses that are arbitrarily close together. Thus, for example, systems containing hysteresis loops would not admit this type of expansion.

We shall limit our analysis to include excitation effects through second order. Thus (3.6) is truncated at $n = 2$ and takes the form

$$Y(t) = h_0 + \int_{-\infty}^{\infty} h_1(\tau) X(t - \tau) d\tau + \int_{-\infty}^{\infty} \int_{-\infty}^{\infty} h_2(\tau_1, \tau_2) X(t - \tau_1) X(t - \tau_2) d\tau_1 d\tau_2, \quad (3.10)$$

where $X(t)$ is identified as the wave excitation. This quadratic

series can then be used to analyze those ship responses that are proportional to either the wave height or the wave height squared. The term h_0 is a constant which denotes the d.c. or steady-state component of the response. If h_0 and h_2 are identically zero, the series reduces to the time-invariant linear system (2.6) with a first-order impulse response function, $h_1(\tau)$. If h_0 and h_1 are identically zero, the series represents the pure second-order response

$$Y^{(2)}(t) = \int_{-\infty}^{\infty} \int_{-\infty}^{\infty} h_2(\tau_1, \tau_2) X(t - \tau_1) X(t - \tau_2) d\tau_1 d\tau_2, \quad (3.11)$$

with the second-order impulse response $h_2(\tau_1, \tau_2)$. Tick (1961) has called (3.10) a time-invariant quadratic system since it includes both a first-order and second-order term. Our main emphasis will be on the second-order term (3.11); however, results will be included for the more general system (3.10).

The excitation $X(t)$ in (3.10) and (3.11) may be either deterministic or stochastic. In the latter case, the integrals are to be interpreted as stochastic integrals which have mean square convergence properties. Assume that $X(t)$ is the Gaussian wave system (2.3); then the pure second-order response (3.11) becomes

$$Y^{(2)}(t) = \frac{1}{2} \operatorname{Re} \int_0^{\infty} \int_0^{\infty} H(\omega_1, \omega_2) \exp[i(\omega_1 + \omega_2)t - i(\epsilon(\omega_1) + \epsilon(\omega_2))] \cdot \sqrt{2 S_{\eta}(\omega_1) 2 S_{\eta}(\omega_2)} d\omega_1 d\omega_2 + \frac{1}{2} \operatorname{Re} \int_0^{\infty} \int_0^{\infty} H(\omega_1, -\omega_2) \exp[i(\omega_1 - \omega_2)t - i(\epsilon(\omega_1) - \epsilon(\omega_2))] \cdot \sqrt{2 S_{\eta}(\omega_1) 2 S_{\eta}(\omega_2)} d\omega_1 d\omega_2, \quad (3.12)$$

where $H(\omega_1, \omega_2)$ is the second-order transfer defined by

$$H(\omega_1, \omega_2) = \int_{-\infty}^{\infty} \int_{-\infty}^{\infty} h(\tau_1, \tau_2) e^{-i[\omega_1 \tau_1 + \omega_2 \tau_2]} d\tau_1 d\tau_2. \quad (3.13)$$

If the transfer function is written in terms of amplitude and phase components as

$$H(\omega_1, \omega_2) = |H(\omega_1, \omega_2)| e^{i\phi(\omega_1, \omega_2)}, \quad (3.14)$$

then the second-order response may be written as

$$\begin{aligned}
Y^{(2)}(t) = & \int_0^\infty \int_0^\infty \cos((\omega_1 + \omega_2)t - (\epsilon(\omega_1) + \epsilon(\omega_2))) \\
& + \phi(\omega_1, \omega_2) \sqrt{|H(\omega_1, \omega_2)|^2 S_\eta(\omega_1) S_\eta(\omega_2)} d\omega_1 d\omega_2 \\
& + \int_0^\infty \int_0^\infty \cos((\omega_1 - \omega_2)t - (\epsilon(\omega_1) - \epsilon(\omega_2))) \\
& + \phi(\omega_1, -\omega_2) \sqrt{|H(\omega_1, -\omega_2)|^2 S_\eta(\omega_1) S_\eta(\omega_2)} d\omega_1 d\omega_2.
\end{aligned} \quad (3.15)$$

The first term in (3.15) represents the contribution of sums of wave frequency pairs to the second-order ship response, whereas the second term gives the contribution of differences of wave frequency pairs. Hasselmann (1966) and Newman (1974) both considered discrete analogues of Equation (3.15), and the latter author defined the second term as the slowly varying second-order force. Continuing this analogy, we will refer to the first term in (3.15) as the rapidly varying second-order response.

Using the fact that the $\epsilon(\omega)$ are statistically independent, it is easy to verify that the expected value (mean) of the rapidly varying sum frequency term is zero. Thus the mean of the second-order response is contributed by the slowly varying difference frequency component which can be computed from (3.15) or from (3.11) together with (2.19) as

$$EY^{(2)}(t) = \int_0^\infty \text{Re} \{ H(\omega, -\omega) \} S_\eta(\omega) d\omega. \quad (3.16)$$

If $H(\omega_1, \omega_2)$ is symmetric then $H(\omega, -\omega)$ will be real and the mean value becomes

$$EY^{(2)}(t) = \int_0^\infty H(\omega, -\omega) S_\eta(\omega) d\omega. \quad (3.17)$$

The form (3.17) is independent of t and matches the form used by Maruo (1957) and Gerritsma et al. (1961) to obtain the mean added resistance in waves. The covariance of the second-order response is given by

$$\begin{aligned}
\text{COV}(Y^{(2)}(t), Y^{(2)}(t+\tau)) = E \left\{ (Y^{(2)}(t+\tau) \right. \\
\left. - EY^{(2)}(t+\tau)) (Y^{(2)}(t) - EY^{(2)}(t)) \right\}.
\end{aligned} \quad (3.18)$$

Then using (3.11) and the factorization relation for higher-order moments of Gaussian processes

$$\begin{aligned}
EX(t_1) X(t_2) X(t_3) X(t_4) = & R_X(t_2 - t_1) \\
& \times R_X(t_4 - t_3) + R_X(t_3 - t_1) \\
& \times R_X(t_4 - t_2) + R_X(t_4 - t_1) R_X(t_3 - t_2),
\end{aligned} \quad (3.19)$$

we obtain

$$\begin{aligned}
\text{COV}(Y^{(2)}(t), Y^{(2)}(t+\tau)) = & \int_0^\infty \int_0^\infty \left\{ |H(\omega_1, \omega_2)|^2 \cos[(\omega_1 \right. \\
& \left. + \omega_2)\tau] + |H(\omega_1, -\omega_2)|^2 \cos[(\omega_1 - \omega_2)\tau] \right\} S_\eta(\omega_1) \\
& S_\eta(\omega_2) d\omega_1 d\omega_2,
\end{aligned} \quad (3.20)$$

which can be written as

$$\text{COV}(Y^{(2)}(t), Y^{(2)}(t+\tau)) = R_{Y^{(2)}}(\tau), \quad (3.21)$$

since the right side of (3.20) is independent of t . In particular, the variance of the second-order response is

$$\begin{aligned}
\sigma_{Y^{(2)}}^2 = & R_{Y^{(2)}}(0) \\
= & \int_0^\infty \int_0^\infty \left\{ |H(\omega_1, \omega_2)|^2 + |H(\omega_1, -\omega_2)|^2 \right\} S_\eta(\omega_1) \\
& S_\eta(\omega_2) d\omega_1 d\omega_2.
\end{aligned} \quad (3.22)$$

The relations (3.20) and (3.16) jointly imply that the second-order force is stationary in the statistical sense. The physically realizable spectral density function of the second-order response is the Fourier transform of $R_{Y^{(2)}}(\tau)$ and is computed from (2.18) and (2.21) as

$$S_{Y^{(2)}}(\omega) = \int_{-\infty}^\infty |H(\omega_1, \omega - \omega_1)|^2 S_\eta(|\omega_1|) S_\eta(|\omega - \omega_1|) d\omega_1. \quad (3.23)$$

3.2 Simulated Second-Order Forces

Digital simulation techniques can be used to illustrate typical characteristics of second-order hydrodynamic forces in a seaway. For convenience, we assume that the stationary seaway is represented by the 30-knot Pierson-Moskowitz (1961) wave energy spectrum shown in Figure 1. Then a digital

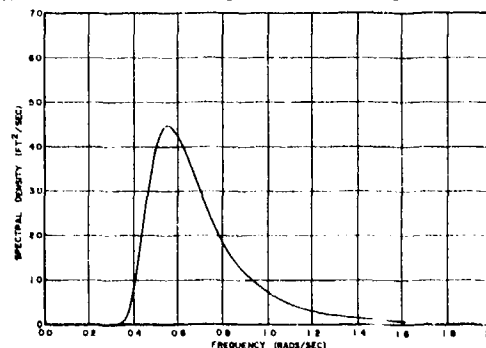


Figure 1 -- 30 Knot Pierson-Moskowitz Wave Spectrum

approximation to the random phase model (2.3) can be used to generate a Gaussian wave surface. For this purpose, n equally spaced subintervals of the frequency interval (0.2, 1.5) radians per second are specified, and a wave frequency component is randomly selected from each subinterval in order to evaluate the Pierson-Moskowitz amplitudes $S(\omega_k)$. The uniformly distributed phase angles $\epsilon(\omega_k)$ are then computed as $2\pi f_k$, where the f_k are obtained from a digital random number generator. This wave generation technique avoids the use of Fourier series models whose periods may be too short. The use of the indicated procedure can be shown to increase the wave period indefinitely. The details of the method are given by Neal and Hurwitz (1974). A segment of a typical wave time history based on the 30-knot Pierson-Moskowitz spectrum is shown in Figure 2a. The curve shown is based on a sampling rate of 1 sample per second and 50 randomly selected frequency components.

Second-order hydrodynamic forces can be simulated from (3.15) provided the second-order transfer function is available. Since very little is known from hydrodynamics theory concerning the actual shapes of nonlinear ship-wave transfer functions, the following transfer function form was assumed for the simulation:

$$|H(\omega_1, \omega_2)| = e^{-6.61 [(|\omega_1| - 0.55)^2 + (|\omega_2| - 0.55)^2]}, \quad (3.24)$$

$$\phi(\omega_1, \omega_2) = -\pi \left(2 - e^{-0.9332 \omega_1^2} - e^{-0.9332 \omega_2^2} \right), \quad (3.25)$$

$$\phi(\omega_1, -\omega_2) = -\pi \left(-e^{-0.9332 \omega_1^2} + e^{-0.9332 \omega_2^2} \right). \quad (3.26)$$

This is a bell-shaped curve centered at bi-frequency (0.55, 0.55). The present form was chosen partially for mathematical convenience. It does seem physically reasonable that the amplitude gain of such a system should peak at some point in the bi-frequency plane and decay in regions far away from the peak. Here the peak is assumed to occur at the bi-frequency point corresponding to the single frequency peak of the wave spectrum. The phase gain function is assumed to be representative of a typical linear ship-wave system in each component and to be zero along the diagonal line $\omega_1 = -\omega_2$. The latter assumption assures that the transfer function will be real in the portion of the bi-frequency plane that contributes to the mean ship response.

The substitution of the assumed transfer function and the Gaussian wave system into (3.15) results in the rapidly varying and slowly varying second-order response shown in Figures 2b and 2c, respectively. The higher frequency oscillators of the rapidly varying response component in 2b as compared to the lower frequency oscillations of the slowly varying response in 2c are noted. The rapidly varying response component is seen to have a zero mean value, while the slowly varying component is non-negative and is asymmetrically distributed about its mean value. If the two second-order response components shown in Figures 2b and 2c are summed, the total second-order response, $Y^{(2)}(t)$, shown in Figure 2d is obtained. Because the transfer function employed is non-negative definite, the total second-order response is everywhere non-negative.

Figures 3a-3d show computed spectral density functions for the four time histories shown in Figures 2a-2d. These spectra were computed using 30-minute segments of the four records and the autoregressive spectral estimation technique discussed in Appendix A. Figure 3a is an approximation to the 30-knot Pierson-Moskowitz spectrum which has peak energy near 0.55 radians per second and tapers off to zero for larger and smaller frequencies. Figure 3b shows the sum frequency effect on the spectral density in that the peak is shifted to approximately twice the frequency of the wave spectrum. The difference frequency effect in the slowly varying response component is shown in Figure 3c where the peak energy occurs near zero frequency and is rapidly attenuated for positive frequencies. Finally, the spectrum of the total second-order response shows the combined effects of the sum and difference frequency contributions. Here, peaks occur both near zero frequency and near twice the peak frequency of the wave spectrum. Verhagen (1970) obtained qualitatively similar bimodal spectra for the slowly varying surge and sway motions of moored vessels in waves; Figure 4 is a spectral density of sway taken from the Verhagen paper. It shows a peak response near zero frequency, representing the dominating slowly varying response and a minor peak at a higher frequency which can be interpreted as a rapidly varying or sum frequency effect.

4. TRANSFER FUNCTION ESTIMATION

In the previous section we have shown that knowledge of the two-dimensional transfer function is required in order to obtain the second-order hydrodynamic response of bodies in waves. Only limited knowledge of this transfer function is available in the literature. Lee (1970) calculated the second-order transfer function for forced oscillations of two-dimensional cylinders floating on the free surface. However, results apparently are not available for the determination of the general second-order transfer function of an arbitrary ship by hydrodynamic theory. Recently, Newman (1974) suggested that the slowly varying transfer function, $H(\omega_n, -\omega_m)$, might be approximated throughout the bi-frequency plane by its diagonal value $H(\omega_n, -\omega_n)$. This diagonal value may then be obtained from model experiments involving monochromatic waves. In general however, the error resulting from this approximation cannot be rigorously established. Further, the approximation applies only to the difference frequency component and does not lead to the identification of the total second-order force.

In this chapter, we discuss a known procedure, the cross-bi-spectrum analysis technique, for estimating (identifying) the second-order transfer function from irregular (random) wave and response time records. Dalzell (1974) applied this method to estimate the mean added resistance in waves. The mean response is determined by the diagonal portion, $H(\omega, -\omega)$, of the second order transfer function which is real for symmetric systems. Dalzell concluded from detailed analysis of simulated and experimental data, that the mean added resistance operator could be identified from irregular wave data but that sample lengths may have to be 10-12 times longer than those required in linear seakeeping problems, in order to obtain comparable accuracy.

In the present work, a prefiltering or prewhitening technique is developed and applied to the cross-bi-spectral estimators in order to improve the quality of estimation and possibly reduce the record length required. The prefiltering technique is

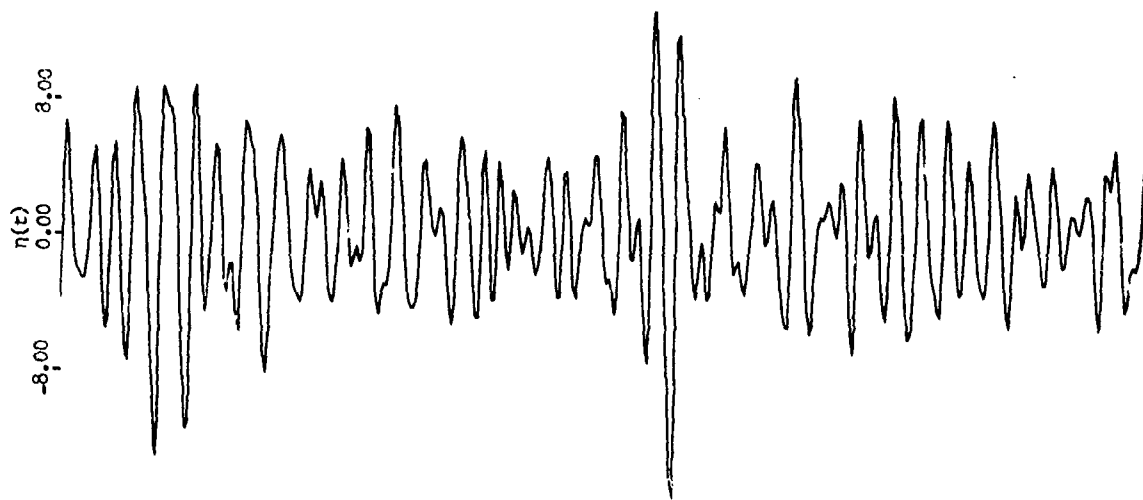


Figure 2a -- First-Order Free-Surface Elevation

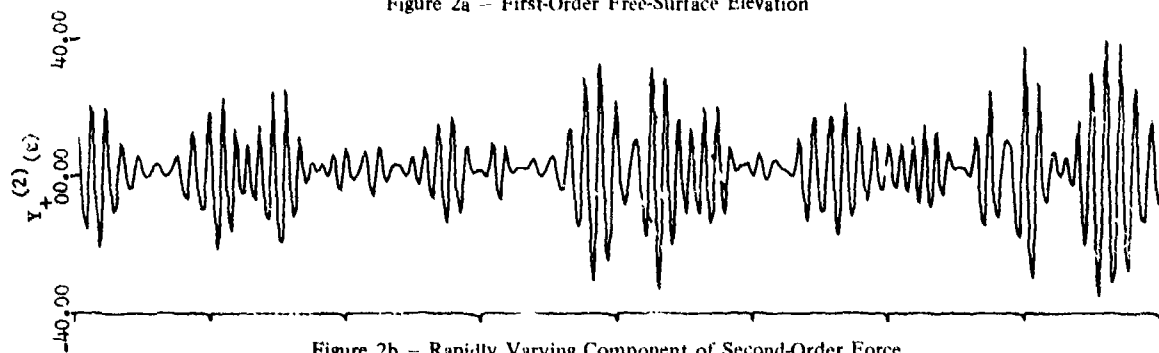


Figure 2b -- Rapidly Varying Component of Second-Order Force

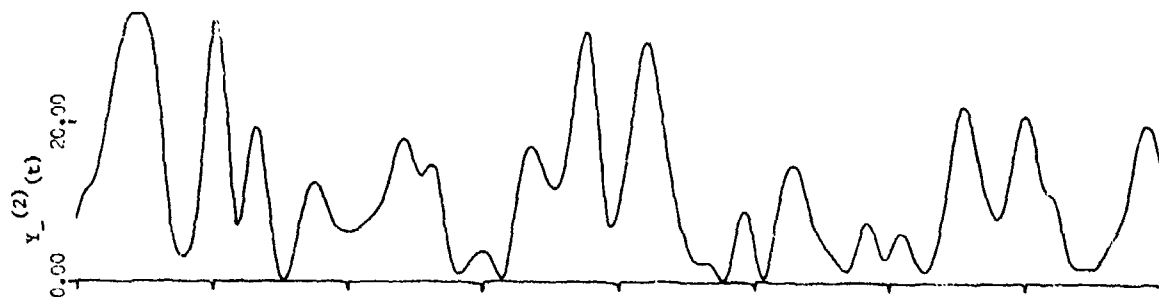


Figure 2c -- Slowly Varying Component of Second-Order Force

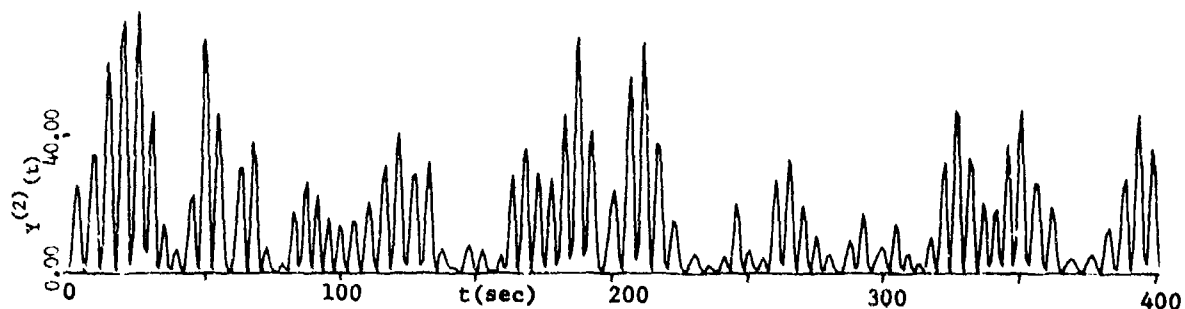


Figure 2d -- Total Second-Order Force

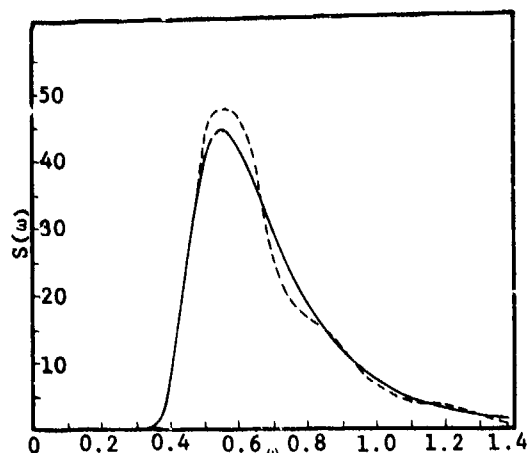


Figure 3a - Computed Wave Spectrum,
30 Minute Record

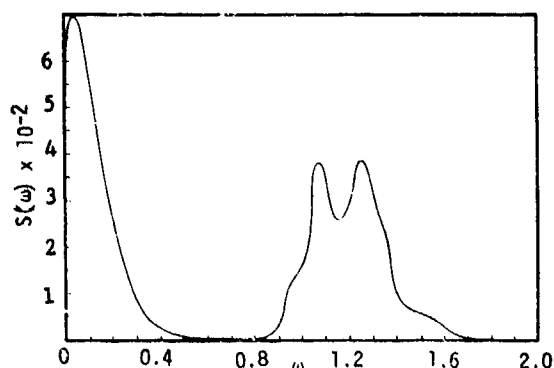


Figure 3d - Computed Spectrum of Total
Second-Order Response,
30 Minute Record

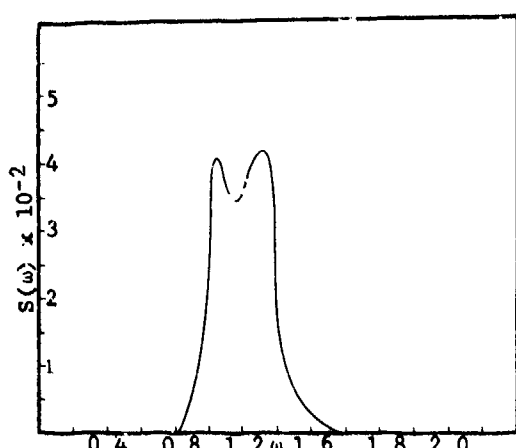


Figure 3b - Computed Spectrum of
Rapidly Varying Response,
30 Minute Record

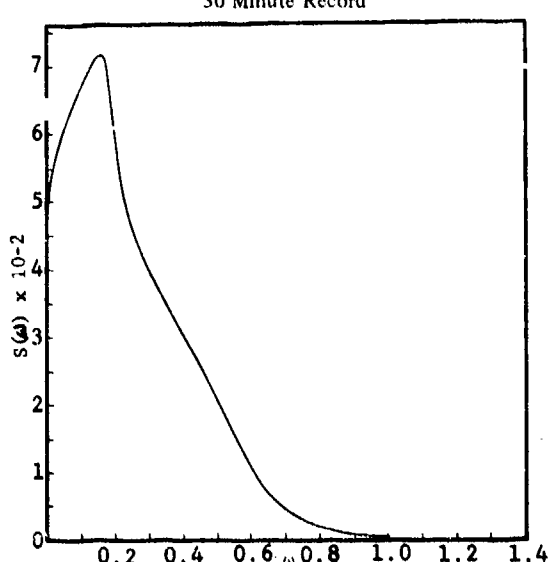


Figure 3c - Computed Spectrum of
Slowly Varying Response,
30 Minute Record

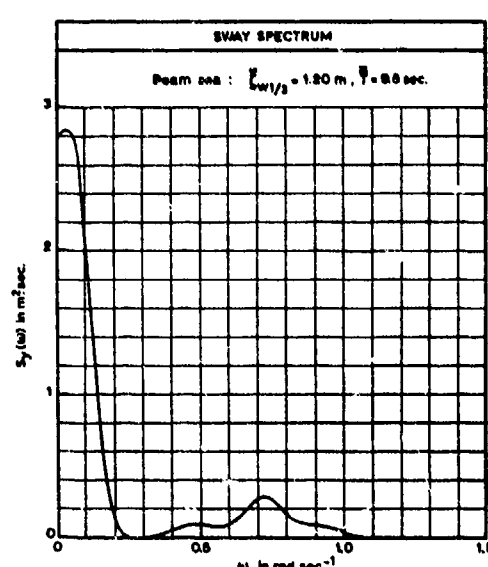


Figure 4 - Sway Spectrum from
Verhugen (1970)

combined with the cross-bi-spectrum analysis technique to form an algorithm to compute transfer functions for the complete second order response. The method is applied to time histories of simulated wave-force systems.

4.1 Cross-Bi-Spectral Analysis

Tick (1961) developed a procedure for estimating the second-order transfer function of a time invariant quadratic system under the excitation of a Gaussian forcing function with zero mean. Specifically, he studied a system of the form

$$Y(t) = \int_{-\infty}^{\infty} h_1(\tau) \eta(t-\tau) d\tau + \int_{-\infty}^{\infty} \int_{-\infty}^{\infty} h_2(\tau_1, \tau_2) \times \eta(t-\tau_1) \eta(t-\tau_2) d\tau_1 d\tau_2, \quad (4.1)$$

which he defined as a quadratic system. He then defined the Fourier transforms of h_1 and h_2 jointly as the quadratic system transfer function. The model (4.1) may be viewed as the functional polynomial (3.10) in which the constant steady-state term h_0 has been subtracted from the total response. Then by invoking the Gaussian process property (3.19) and using the fact that central moments of odd order for a Gaussian process are zero, it follows that a third-moment function about the mean is independent of t and

$$R_{\eta\eta Y}(\tau_1, \tau_2) = E[\eta(t-\tau_1) \eta(t-\tau_2)(Y(t) - EY(t))] \\ = 2 \int_{-\infty}^{\infty} \int_{-\infty}^{\infty} f_{\eta}(\omega_1) f_{\eta}(\omega_2) H_2(\omega_1, \omega_2) \times e^{i(\omega_1 \tau_1 + \omega_2 \tau_2)} d\omega_1 d\omega_2, \quad (4.2)$$

where $f_{\eta}(\omega)$ and $H_2(\omega_1, \omega_2)$ are defined by (2.18) and (3.13), respectively. $R_{\eta\eta Y}(\tau_1, \tau_2)$ is called the cross-bi-covariance function.

Define the Fourier transform of $R_{\eta\eta Y}(\tau_1, \tau_2)$ by

$$f_{\eta\eta Y}(\omega_1, \omega_2) = \frac{1}{(2\pi)^2} \int_{-\infty}^{\infty} \int_{-\infty}^{\infty} R_{\eta\eta Y}(\tau_1, \tau_2) \times e^{-i(\omega_1 \tau_1 + \omega_2 \tau_2)} d\tau_1 d\tau_2. \quad (4.3)$$

Then, if the transform (4.3) exists, we may substitute (4.2) into (4.3) to obtain

$$f_{\eta\eta Y}(\omega_1, \omega_2) = 2 f_{\eta}(\omega_1) f_{\eta}(\omega_2) H(\omega_1, \omega_2), \quad (4.4)$$

where $f_{\eta\eta Y}(\omega_1, \omega_2)$ is defined as the cross-bi-spectrum. The second-order transfer function is obtained from (4.4) as

$$H(\omega_1, \omega_2) = \frac{f_{\eta\eta Y}(\omega_1, \omega_2)}{2 f_{\eta}(\omega_1) f_{\eta}(\omega_2)}, \quad -\infty < \omega_1, \omega_2 < \infty \quad (4.5)$$

provided the denominator is not zero. This is Tick's result. Because of the Gaussian assumption, the second-order transfer function in (4.5) is independent of the first-order transfer function. The first-order function may be obtained exactly as in the linear case.

Note that (4.5) is defined in terms of the two-sided spectral density function, $f_{\eta\eta Y}(\omega_1, \omega_2)$, and that all quantities in the relation are defined over the real frequency axis. Because one-sided wave spectra are usually employed in ship applications, (4.5) may be written as

$$H(\omega_1, \omega_2) = \frac{2 f_{\eta\eta Y}(\omega_1, \omega_2)}{S_{\eta}(|\omega_1|) S_{\eta}(|\omega_2|)}, \quad (4.6)$$

where $S_{\eta}(\omega)$ is the one-sided, physically realizable wave spectrum defined by (2.21). Further, if we define

$$S_{\eta\eta Y}(\omega_1, \omega_2) = 4 f_{\eta\eta Y}(\omega_1, \omega_2), \quad (4.7)$$

Tick's form of the second-order transfer function is obtained in terms of physically realizable spectra as

$$H(\omega_1, \omega_2) = \frac{S_{\eta\eta Y}(\omega_1, \omega_2)}{2 S_{\eta}(|\omega_1|) S_{\eta}(|\omega_2|)}. \quad (4.8)$$

Note that, by its definition, the cross-bi-covariance function, $R_{\eta\eta Y}(\tau_1, \tau_2)$, is a symmetric function of its arguments. Thus, its Fourier transform, the cross-bi-spectrum, will also be symmetric and the transfer function in (4.8) will necessarily satisfy

$$H(\omega_2, \omega_1) = H(\omega_1, \omega_2). \quad (4.9)$$

Therefore, the cross-bi-spectrum analysis technique cannot be directly used to obtain nonsymmetric transfer functions from (4.8).

In practice (4.6) or (4.8) becomes the basis for an identification procedure for estimating symmetric second-order transfer functions. Samples of length T are observed for the excitation and response, and the required spectral functions are then estimated as finite Fourier transforms of moment functions.

To facilitate computations, the cross-bi-spectrum in (4.6) or (4.8) may be expressed in terms of one-dimensional Fourier transforms computed over the interval $(0, \infty)$. Then, well developed computation algorithms used for evaluating the one-variable Fourier transform (2.36) can be adapted to the calculation of cross-bi-spectra. In (4.3) let

$$G(\tau_2, \omega_1) = \frac{1}{\pi} \int_{-\infty}^{\infty} e^{-i\omega_1 \tau_1} R_{\eta\eta Y}(\tau_1, \tau_2) d\tau_1$$

$$= G_R(\tau_2, \omega_1) - i G_I(\tau_2, \omega_1), \quad (4.10)$$

where

$$G_R(\tau_2, \omega_1) = \frac{2}{\pi} \int_0^{\infty} \left\{ \frac{R_{\eta\eta Y}(\tau_1, \tau_2) + R_{\eta\eta Y}(-\tau_1, \tau_2)}{2} \right\}$$

$$\times \cos(\omega_1 \tau_1) d\tau_1, \quad (4.11)$$

$$G_I(\tau_2, \omega_1) = \frac{2}{\pi} \int_0^{\infty} \left\{ \frac{R_{\eta\eta Y}(\tau_1, \tau_2) - R_{\eta\eta Y}(-\tau_1, \tau_2)}{2} \right\}$$

$$\times \sin(\omega_1 \tau_1) d\tau_1. \quad (4.12)$$

Then, the form of cross-bi-spectrum used in (4.8) may be written as

$$S_{\eta\eta Y}(\omega_1, \omega_2) = \int_{-\infty}^{\infty} G(\tau_2, \omega_1) e^{-i\omega_2 \tau_2} d\tau_2. \quad (4.13)$$

Then, by substituting (4.10) into (4.13), we obtain

$$S_{\eta\eta Y}(\omega_1, \omega_2) = \text{Re } S_{\eta\eta Y}(\omega_1, \omega_2) + i \text{Im } S_{\eta\eta Y}(\omega_1, \omega_2), \quad (4.14)$$

where

$$\text{Re } S_{\eta\eta Y}(\omega_1, \omega_2) = \frac{2}{\pi} \int_0^{\infty} \left\{ \frac{G_R(\tau_2, \omega_1) + G_R(-\tau_2, \omega_1)}{2} \right\}$$

$$\cos(\omega_2 \tau_2) d\tau_2 - \frac{2}{\pi} \int_0^{\infty} \left\{ \frac{G_I(\tau_2, \omega_1) - G_I(-\tau_2, \omega_1)}{2} \right\}$$

$$\sin(\omega_2 \tau_2) d\tau_2 \quad (4.15)$$

and

$$\text{Im } S_{\eta\eta Y}(\omega_1, \omega_2) = \frac{-2i}{\pi} \int_0^{\infty} \left\{ \frac{G_I(\tau_2, \omega_1) + G_I(-\tau_2, \omega_1)}{2} \right\}$$

$$\cos(\omega_2 \tau_2) d\tau_2 - \frac{2i}{\pi} \int_0^{\infty} \left\{ \frac{G_R(\tau_2, \omega_1) - G_R(-\tau_2, \omega_1)}{2} \right\}$$

$$\sin(\omega_2 \tau_2) d\tau_2. \quad (4.16)$$

The cross-bi-spectrum is now expressed in terms of one-dimensional Fourier transforms involving even and odd components of the transform (4.10). These one-dimensional transforms may be computed very efficiently using a suitable algorithm. In present work, an algorithm given by Jenkins and Watts (1968, p. 311) was adopted. This method which evaluates the transforms through the solution of a difference equation requires only one cosine-sine pair computation for each transform value, but requires an explicit calculation of the cross-bi-covariances. These covariances were desired in order to gain some insight into their properties.

Unfortunately, moment functions and their Fourier transforms required for estimating the second-order transfer function must be computed from finite records. The estimators will inevitably be subject to variability and bias errors, similar to the situation that occurs in linear spectral analysis. To overcome this problem or, at least to reduce its effect, a prefiltering technique for cross-bi-spectrum estimation is developed in Appendix A.

The usefulness of prefiltering or prewhitening in scalar spectral analysis has become well-known since its introduction by Blackman and Tukey (1958). More recently, Tukey (1967) and Parzen (1969) discussed the use of autoregressive model fitting as a means of improving spectral estimators, and the second author suggested that optimal bias and variance reduction in cross-spectra could also be obtained by this method. Akaike (1969) showed that the autoregressive spectral estimates may be less variable than the usual smoothed covariance estimators in many instances. In Appendix A, we extend Parzen's autoregressive cross-spectrum analysis technique to the estimation of cross-bi-spectra. The resulting estimation procedure may be viewed as a formal approach to prefiltering for cross-bi-spectrum analysis. Essentially, the procedure entails the application of separate time-domain transformations to the excitation and response functions which result in transformed scalar spectra that are flat or nearly flat in the frequency region of interest. Cross-bi-spectra are obtained for the transformed time histories, and the cross-bi-spectrum of the raw data is obtained as an inverse frequency-domain transformation.

4.2 Application to Simulated Second-Order Systems

Simulated wave and second-order response time histories were used to evaluate the described transfer function estimation

procedure. The transfer function (3.24)–(3.26) was used to generate the second-order response function from (3.15), and a 30-knot Pierson-Moskowitz spectrum was used to generate the wave surface excitation as described in Section 3.2. Three 60-minute segments of the wave and second-order response were computed. The three 60-minute record pairs correspond to additional and longer versions of the time histories shown in Figures 2a–2d. The autoregressive fitting procedure was applied and the transformed cross-bi-spectra were computed using the usual lagged covariance approach. The final cross-bi-spectra were then obtained using the inverse relation (A.16).

Figure 5 shows the probability density function for the wave surface computed from a typical 30-minute record. It is seen that the sample record closely approximates the Gaussian distribution, which is required for use of the cross-bi-spectrum approach. The estimated transfer function corresponding to Dalzell's mean response operator is shown in Figure 6 for each of the three time history pairs. It is seen that the results oscillate around the true curve, but that considerable scatter exists in the individual estimators. The mean response operator is real in this case since the transfer function is symmetric in its arguments. Figure 7 shows the average values of the three curves shown in Figure 6. The averages approximate the true curve quite well and show very little effect of variability or bias errors. Figures 8 and 9 show the mean estimated amplitude and phase components respectively, of the transfer function considered along the line $\omega_1 \approx 0.55$ in the bi-frequency plane.

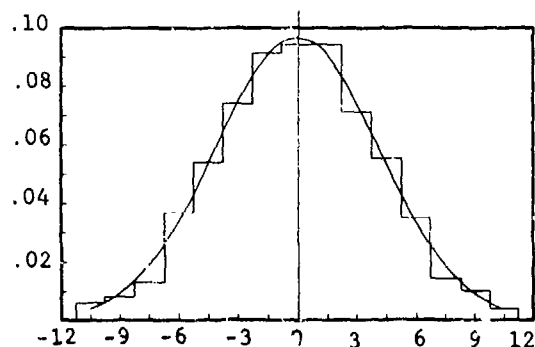


Figure 5 - Sample Probability Density for Wave, 30 Minute Record

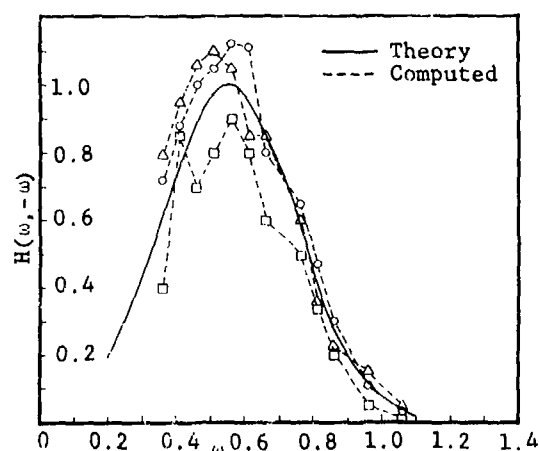


Figure 6 - Computed Transfer Function for Mean Response, 3 Samples

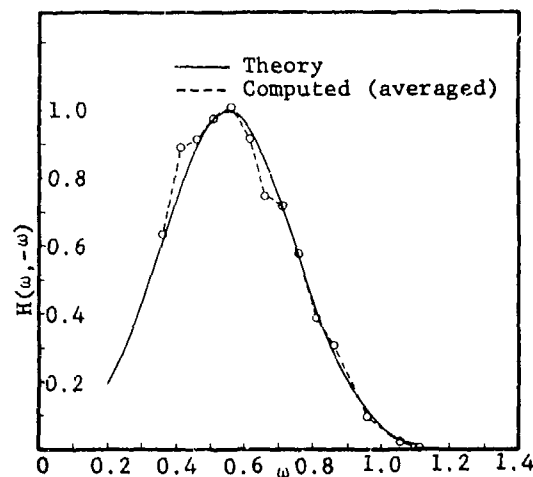


Figure 7 - Estimated Transfer Function for Mean Response, Average of Three Samples

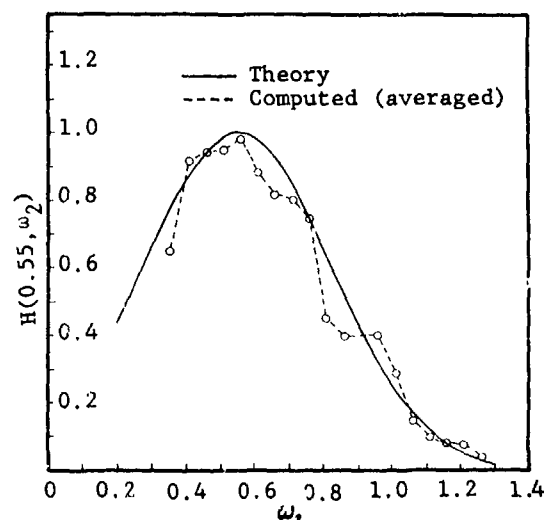


Figure 8 - Estimated Amplitude Gain, Average of Three Samples

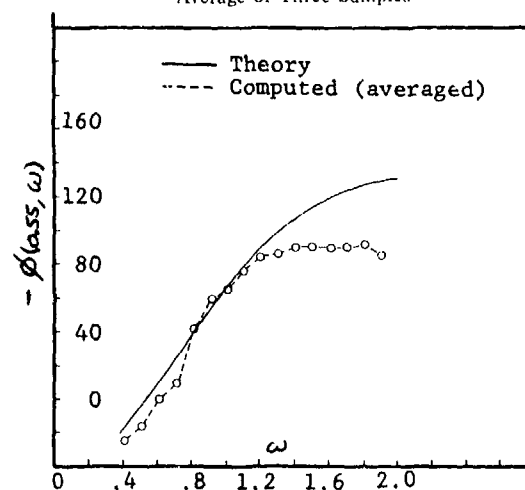


Figure 9a - Estimated Phase Gain, Three Sample Average

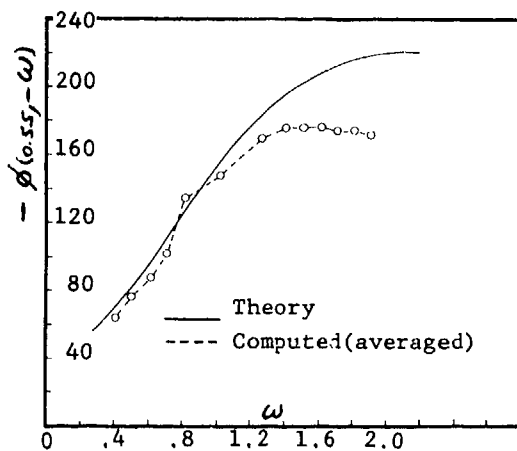


Figure 9b - Estimated Phase Gain,
Three Sample Average

Reasonably good agreement is shown for both the mean amplitudes and phases. The raw amplitudes and phases for the individual runs are not shown, however, considerable run to run variation was also observed in each of the components. The error in the averaged transfer function estimates for the three runs is of the same order of magnitude as was observed for estimates (not shown) of linear transfer functions based on a 30-minute time history. Thus, it would appear that roughly six times as much data as for linear spectral analysis may be sufficient to estimate the second order transfer function. However, more computation experience is required in order to draw strong conclusions concerning the variability of the autoregressive cross-bi-spectrum estimates.

5. PROBABILITY STRUCTURE TO SECOND ORDER OF NONLINEAR SYSTEMS

The probability structure of nonlinear systems is needed in order to extend to the nonlinear domain the various prediction techniques that are widely used in the theory and practice of linear ship performance prediction. In this section, two approaches to the determination of the second-order ship response to a Gaussian seaway are discussed. First, approximations to the probability density function for the second-order response are discussed and comparison with simulated data is shown. Then, the exact form of the probability density function for the general quadratic model (3.10) is derived.

5.1 Approximate Probability Density Functions

An obvious approximation to the second-order response (3.15) is the Gaussian distribution with its mean and variance based on the nonlinear system, according to Equations (3.16) and (3.22). This approximation was applied to the 60-minute samples of the simulated series previously discussed, and the results are shown in Figures 10a through 10c. It is readily seen from these figures that the rapidly varying response component is fairly well represented by the Gaussian density function. However, neither the slowly varying nor the total response are well approximated.

Alternatively, an approximation based on a Type-III distribution was suggested by Rice (1944, p. 92) for non-negative

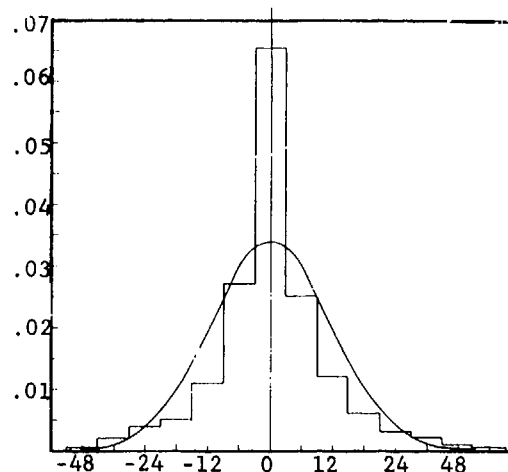


Figure 10a - Gaussian Approximation to
Rapidly Varying Response

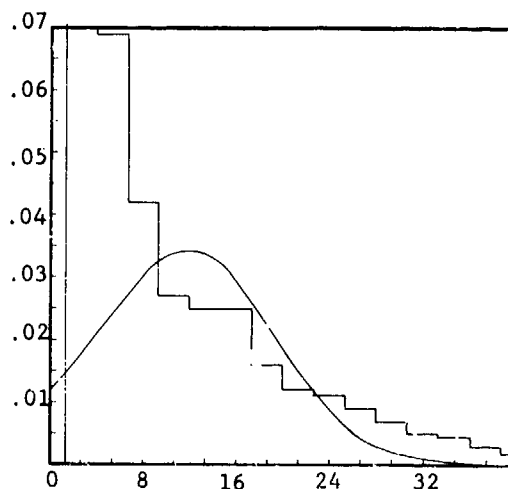


Figure 10b - Gaussian Approximation to
Slowly Varying Response

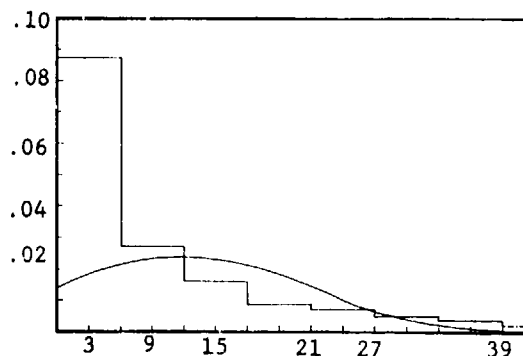


Figure 10c - Gaussian Approximation to
Total Second-Order Response

definite quadratic forms in Gaussian variables. This density function has the form

$$p(y) = \left(\frac{\mu}{\sigma^2}\right)^r \frac{y^{r-1}}{\Gamma(r)} e^{-\mu y/\sigma^2}, \quad (5.1)$$

where μ and σ^2 are the mean and variance of the nonlinear response, respectively. Γ is the gamma function, and

$$r = \mu^2/\sigma^2. \quad (5.2)$$

This approximation was found to better fit the slowly varying and total second-order response data. Typical comparisons for the slowly-varying and total second-order response based on a 60-minute record are shown in Figures 11 and 12, respectively.

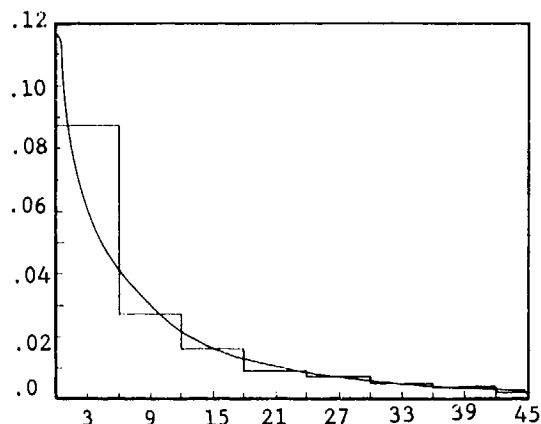


Figure 11 - Type-III Approximation to Total Response

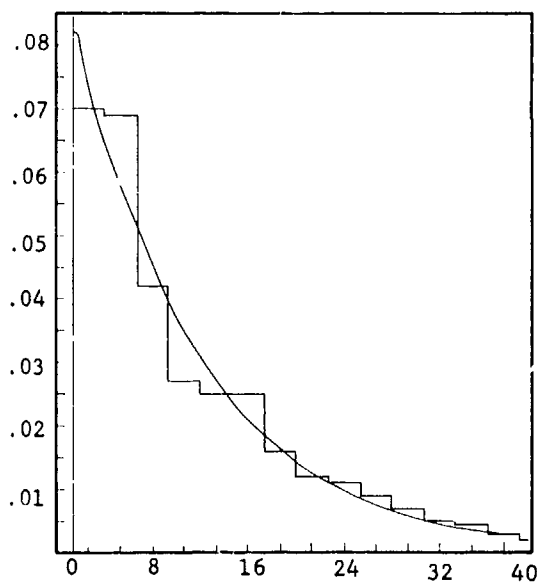


Figure 12 - Type-III Approximation to Slowly Varying Response

5.2 Exact Probability Density Function

We shall consider the distribution of the time-invariant quadratic system (3.10) subject to a stationary Gaussian forcing function, $X(t)$, having zero mean value, covariance function $R_X(\tau)$, and two-sided spectral density function, $f_X(\omega)$. The probability density function of the second-order term (3.11) will then be obtained as a special case of the general result.

We rewrite (3.10) as

$$Y(t) = Y^{(0)} + Y^{(1)}(t) + Y^{(2)}(t), \quad (5.3)$$

where

$$Y^{(0)} = h_0, \quad (5.4)$$

$$Y^{(1)}(t) = \int_{-\infty}^{\infty} h_1(\tau) X(t-\tau) d\tau, \quad (5.5)$$

and

$$Y^{(2)}(t) = \int_{-\infty}^{\infty} \int_{-\infty}^{\infty} h_2(\tau_1, \tau_2) X(t-\tau_1) X(t-\tau_2) d\tau_1 d\tau_2, \quad (5.6)$$

$Y^{(0)}$ is a constant and $Y^{(2)}(t)$ is a linear functional of the Gaussian wave field and hence will have a Gaussian distribution. Therefore, we expect the major task associated with the distribution of (5.3) to be related to the nonlinear term, $Y^{(2)}(t)$. This term is a continuous quadratic form in Gaussian variables which has been studied, principally in the communications field, by several authors. The probability density function of the entire series (5.3) will be obtained by a method first used by Kac and Siegert (1947a, 1947b) to study quadratic forms related to noise in nonlinear receivers, and which is apparently well-known in the communications field. The development given below follows the outline stated by Bedrosian and Rice (1971).

Let $X(t)$ be an equivalent filtered white noise process, or

$$X(t) = \int_{-\infty}^{\infty} a(\tau) N(t-\tau) d\tau, \quad (5.7)$$

where $a(t)$ is the weighting function and $N(t)$ is unit white noise satisfying

$$E N(t) N(t-\tau) = \delta(\tau), \quad (5.8)$$

$\delta(\tau)$ being the Dirac delta function. Then following Kac and Siegert (1947b), we expand the white noise process in a stochastic series of orthonormal functions as

$$N(t-\tau) = \sum_{i=1}^{\infty} X_i(t) \phi_i(\tau), \quad (5.9)$$

with the normalization

$$\int_{-\infty}^{\infty} \phi_i(t) \phi_j(t) dt = \delta_{ij}, \quad (5.10)$$

where the $X_i(t)$ are standardized Gaussian variates that are mutually independent. Then, in terms of the series expansion, the terms in (5.3) become

$$Y^{(1)}(t) = \sum_{i=1}^{\infty} C_i X_i(t), \quad (5.11)$$

with

$$C_i = \int_{-\infty}^{\infty} \int_{-\infty}^{\infty} h_1(\tau) a(\alpha) \phi_i(\tau + \alpha) d\alpha d\tau, \quad (5.12)$$

and

$$Y^{(2)}(t) = \sum_{i,j=1}^{\infty} X_i(t) X_j(t) \int_{-\infty}^{\infty} \int_{-\infty}^{\infty} \phi_i(\alpha) \phi_j(\beta) K(\alpha, \beta) d\alpha d\beta, \quad (5.13)$$

with

$$K(\alpha, \beta) = \int_{-\infty}^{\infty} \int_{-\infty}^{\infty} a(\alpha - \tau_1) a(\beta - \tau_2) h(\tau_1, \tau_2) d\tau_1 d\tau_2. \quad (5.14)$$

Then, since the orthonormal functions in (5.10) have only been arbitrarily specified, we now require them to be the eigenfunctions of the integral equation

$$\int_{-\infty}^{\infty} K(\alpha, \beta) \phi_j(\beta) d\beta = \lambda_j \phi_j(\alpha). \quad (5.15)$$

From the normalization (5.10), it follows that

$$Y^{(2)}(t) = \sum_{i=1}^{\infty} \lambda_i X_i^2(t), \quad (5.16)$$

so that

$$Y(t) = Y^{(0)} + \sum_{i=1}^{\infty} C_i X_i(t) + \sum_{i=1}^{\infty} \lambda_i X_i^2(t), \quad (5.17)$$

with

$$E X_i(t) X_j(t) = \delta_{ij}. \quad (5.18)$$

We can now obtain the probability density $f_Y(y)$ of $Y(t)$ as the inverse Fourier transform of its characteristic function. The characteristic function is

$$\begin{aligned} F(k) &= E e^{iY(t)K} \\ &= \int_{-\infty}^{\infty} f_Y(y) e^{iKy} dy \\ &= \prod_{j=1}^{\infty} E e^{iK(Y^{(0)} + C_j X_j(t) + \lambda_j X_j^2(t))}, \end{aligned} \quad (5.19)$$

where we have used the fact that the $X_j(t)$ are mutually independent. The Gaussian density function of X_j is

$$f_{X_j}(x) = \frac{1}{\sqrt{2\pi}} e^{-\frac{1}{2} x^2} \quad (5.20)$$

This fact, plus the identity (Cramer, 1946, p. 99)

$$\int_{-\infty}^{\infty} e^{iX - \frac{1}{2} hX^2} dX = \sqrt{\frac{2\pi}{h}} e^{-t^2/2h} \quad (5.21)$$

allows the characteristic function to be written as

$$F(k) = \frac{e^{iK Y^{(0)}}}{\prod_{j=1}^{\infty} (1 - 2ik\lambda_j)^{1/2}} e^{-\sum_{j=1}^{\infty} \frac{K^2 C_j^2}{2(1 - 2ik\lambda_j)}} \quad (5.22)$$

The probability density function of $Y(t)$ then becomes

$$f_Y(y) = \frac{1}{2\pi} \int_{-\infty}^{\infty} F(k) e^{-iky} dk, \quad (5.23)$$

with F obtained from (5.22). In general, this integral cannot be obtained in closed form and must therefore be computed numerically. The determination of the parameters in (5.22) requires the solution of the integral Equation (5.15). The kernel $K(\alpha, \beta)$ of this equation depends on the function $a(t)$ which is not uniquely specified by the relation (5.7). Its evaluation can be avoided by defining

$$\psi_n(t) = \int_{-\infty}^{\infty} a(t-u) \phi_n(u) du. \quad (5.24)$$

The integral equation can then be written as

$$\int_{-\infty}^{\infty} K(t,u) \psi_n(u) du = \lambda_n \psi_n(t), \quad (5.25)$$

with

$$\begin{aligned} K(t,u) &= \int_{-\infty}^{\infty} \int_{-\infty}^{\infty} a(v-\tau) a(v-t) h_2(\tau,u) dv d\tau \\ &= \int_{-\infty}^{\infty} h_2(\tau,u) R_X(t-\tau) d\tau, \end{aligned} \quad (5.26)$$

where R_X is the covariance function of X and is computed from (5.7). The normalization relation for the eigenfunctions in (5.25) is obtained from (5.10) and (5.13) as

$$\int_{-\infty}^{\infty} \int_{-\infty}^{\infty} \psi_m(\tau_1) \psi_n(\tau_2) h_2(\tau_1, \tau_2) d\tau_1 d\tau_2 = \lambda_n \delta_{mn}, \quad (5.27)$$

and the parameter C_n in (5.12) becomes

$$C_n = \int_{-\infty}^{\infty} h_1(\tau) \psi_n(\tau) d\tau. \quad (5.28)$$

The integral Equation (5.25) may be solved for eigenvalues and eigenfunctions subject to the normalization (5.27), provided the time domain kernels, $h_1(\tau)$ and $h_2(\tau_1, \tau_2)$ are available. Because these kernels are usually obtained as transfer functions in the frequency domain, it may be convenient to obtain the integral Equation (5.25) in the frequency domain. Let

$$\Psi_n(\omega) = \frac{1}{2\pi} \int_{-\infty}^{\infty} e^{-i\omega t} \psi_n(t) dt. \quad (5.29)$$

Then since the kernel $K(t,u)$ in (5.26) may be written as

$$K(t,u) = \int_{-\infty}^{\infty} f_X(\omega_1) \int_{-\infty}^{\infty} h_2(\tau,u) e^{i\omega_1(t-\tau)} d\tau d\omega_1 \quad (5.30)$$

we obtain from (5.25)

$$\int_{-\infty}^{\infty} \Psi_n(\omega_2) f_X(\omega) H(\omega, -\omega_2) d\omega_2 = \lambda_n \Psi_n(\omega), \quad (5.31)$$

which is a frequency-domain integral equation with kernel

$$K(\omega, \omega') = f_X(\omega) H(\omega, -\omega'). \quad (5.32)$$

$H(\omega, \omega')$ is the transfer function of the second-order response and is defined by (3.13). In terms of the new eigenfunctions $\Psi_n(\omega)$, the orthogonality relation becomes

$$\begin{aligned} \int_{-\infty}^{\infty} \int_{-\infty}^{\infty} \Psi_m(\omega_1) \Psi_n(\omega_2) H(-\omega_1, -\omega_2) d\omega_1 d\omega_2 \\ = \lambda_n \delta_{mn}. \end{aligned} \quad (5.33)$$

Then, using the symmetry of the spectral density function, $f_X(\omega)$, and (5.31), the normalization may be written as

$$\int_{-\infty}^{\infty} \frac{\Psi_m(\omega_1) \Psi_n(-\omega_1)}{f_X(\omega_1)} d\omega_1 = \delta_{mn}. \quad (5.34)$$

Finally, the parameter C_n in (5.28) becomes simply

$$C_n = \int_{-\infty}^{\infty} H_1(\omega) \Psi_n(\omega) d\omega. \quad (5.35)$$

The eigenfunctions in the integral Equations (5.15), (5.25) or (5.31) are needed only for the purpose of evaluating the parameter C_n , which is obtained in terms of the first-order term $Y^{(1)}(t)$ in (5.3). Hence, determination of the eigenfunctions can be avoided if one desires only the second-order component of the total response.

Methods for efficiently evaluating both the eigenvalues and eigenfunctions of the derived integral equations for realistic kernel functions are currently under investigation.

ACKNOWLEDGMENT

The author is appreciative of the assistance provided by several persons during the course of this work. Professor Michael Chi of Catholic University provided an opportunity for several stimulating discussions which enhanced the work. Ms. Rae Hurwitz assisted in some of the numerical work, and Dr. Allen Hansen contributed several ideas during daily coffee breaks. Mr. Alexander Roper and Mr. Willie Fitzpatrick, Jr. provided special support during the preparation of the manuscript, and Ms. Betty Byrne and Ms. Claire Wright provided assistance in typing and editing the final product. Finally, Dr. Wen-Chin Lin provided overall guidance and maintained an atmosphere in which the work could be performed.

The work was performed under the Naval Ship Research and Development Center's General Hydromechanics Research Program and was funded by the Naval Ship Systems Command under Task Area SR 023 0101.

REFERENCES

- Akaike, H. (1969). "Power Spectrum Estimation through Autoregressive Model Fitting," *Annals of the Institute of Statistical Mathematics*, Volume 21, No. 3, 407-419.
- Akaike, H., Y. Yamanouchi et al. (1964). "Studies on the Statistical Estimation of Frequency Response Functions," *Annals of the Institute of Statistical Mathematics*, (Supplement III).
- Barrett, J.F. (1963). "The Use of Functionals in the Analysis of Non-Linear Physical Systems," *Journal of Electronics Control*, Volume 15, No. 6, 567-615.
- Bedrosian, E. and S.O. Rice (1971). "The Output Properties of Volterra Systems (Nonlinear Systems with Memory) Driven by Harmonic and Gaussian Inputs," *Proceedings of the IEEE*, Volume 59, No. 12, 1688-1707.
- Birchhoff, G. and J. K. Tig (1952). "Fourier Analysis of Wave Trains," in *Gravity Waves*, National Bureau of Standards (U.S.) Circ. 521, 221-234.
- Blackman, R.B. and J.W. Tukey (1958). *The Measurement of Power Spectra from the Point of View of Communications Engineering*, Dover Publications, New York.
- Cartwright, D.E. and M.S. Longuet-Higgins (1956). "The Statistical Distribution of the Maximum of a Random Function," *Proceedings of the Royal Society*, Volume 237A, 212-232.
- Cramer, H. (1946). *Mathematical Methods of Statistics*, Princeton University Press.
- Dalzell, J.F. (1972). "Application of Cross-Bi-Spectral Analysis to Ship Resistance in Waves," Report SIT-OL-72-1606, Davidson Laboratory, Stevens Institute of Technology.
- Dalzell, J.F. (1974). "Cross-Bispectral Analysis: Application to Ship Resistance in Waves," *Journal of Ship Research*, Volume 18, No. 1, 62-72.
- Doob, J.L. (1952). *Stochastic Processes*, John Wiley and Sons, New York.
- Efroymson, M.A. (1960). "Multiple Regression Analysis," in *Mathematical Methods for Digital Computers*, Eds. A. Ralston and H. Wilf, Wiley and Sons, New York, 191-203.
- Frechet, M. (1910). "Sur les Fonctions Continues," *Annals de Ecole Normale*, Volume 27, No. 3.
- Gerritsma, J., J.J. Van Den Bosch, and W. Beukelmann (1961). "Propulsion in Regular and Irregular Waves," *International Shipbuilding Progress*, Volume 8, No. 82.
- Hasselmann, K. (1966). "On Nonlinear Ship Motions in Irregular Waves," *Journal of Ship Research*, Volume 10, No. 1, 64-68.
- Jenkins, G.M. and D.G. Watts (1968). *Spectral Analysis and its Applications*, Holden-Day, San Francisco.
- Kac, M. and A.J.F. Siegert (1947a). "On the Theory of Noise in Radio Receivers with Square-Law Detectors," *Journal of Applied Physics*, Volume 18, 383-397.
- Kac, M. and A.J.F. Siegert (1947b). "An Explicit Representation of a Stationary Gaussian Process," *Annals of Mathematical Statistics*, Volume 18, 438-442.
- Kaplan, P. (1966). "Lecture Notes on Nonlinear Theory of Ship Roll Motion in a Random Seaway," *Proceedings of the Eleventh International Towing Tank Conference*, Tokyo, 393-396.
- Lee, C.M. (1970). "The Second-Order Theory for Non-sinusoidal Oscillations of a Cylinder in a Free Surface," *Proceedings of the Eighth Symposium on Naval Hydrodynamics*, ACR-179, U.S. Office of Naval Research, 905-951.
- Levy, Paul (1948). *Processus Stochastiques et Mouvement Brownien*, Monographies Des Probabilities, Fascicule VI, Gauthier-Villars, Ed., Paris.
- Longuet-Higgins, M.S. (1952). "On the Statistical Distribution of the Heights of Sea Waves," *Journal of Marine Research*, Volume XI, No. 3, 245-266.
- Maruo, H. (1957). "The Excess Resistance of a Ship in Rough Seas," *International Shipbuilding Progress*, Volume 4, No. 35, 337-345.
- Masani, P. (1966). "Recent Trends in Multivariate Prediction Theory," in *Multivariate Analysis*, Ed. P.R. Krishnaiah, Academic Press, New York, 351-382.
- Neal, E. and R.B. Hurwitz (1974). "Digital Simulation of a Gaussian Seaway Based on the Random Phase Model," *Naval Ship Research and Development Center Report 4475* (to be published).
- Newman, J.N. (1974). "Second-Order, Slowly-Varying Forces on Vessels in Irregular Waves," *International Symposium on Marine Vehicles and Structures in Waves*, London, 193-197.
- Ogilvie, T.F. (1964). "Recent Progress Toward the Understanding and Prediction of Ship Motions," *Proceedings Fifth Symposium on Naval Hydrodynamics*, ACR-112, U.S. Office of Naval Research, Washington, D.C., 3-128.
- Parzen, Emanuel (1961). "Mathematical Considerations in the Estimation of Spectra," *Technometrics*, Volume 3, No. 2, 167-190.
- Parzen, Emanuel (1967). *Time Series Analysis Papers*, Holden-Day, San Francisco.
- Parzen, Emanuel (1969). "Multiple Time Series Modeling," in *Multivariate Analysis-II*, Ed. P.R. Krishnaiah, Academic Press, 389-409.
- Pierson, W.J., Jr. (1952). "A Unified Mathematical Theory for the Analysis, Propagation and Refraction of Storm Generated Ocean Surface Waves," Parts I and II, *Research Report*, College of Engineering, New York University.
- Pierson, W.J. and J.F. Dalzell (1960). "The Apparent Loss of Coherency in Vector Gaussian Processes Due to Computational Procedures with Application to Ship Motions and Random Seas," *College of Engineering*, New York University.
- Pierson, W.J. and L. Moskowitz (1964). "A Proposed Spectral Form for Fully Developed Wind Seas Based on the Similarity Theory of S.A. Kitaigorodskii," *Journal of Geophysical Research*, Volume 69, No. 24, 5181-5190.
- Rice, S.O. (1944-1945). "Mathematical Analysis of Random Noise," *Bell System Technical Journal*, Volume 23, 282-332, Volume 24, 46-156.

Rudnick, P. (1951). "Correlograms for Pacific Ocean Waves," Proceedings Second Berkeley Symposium on Mathematical Statistics and Probability, University of California, 627-638.

St. Denis, M. and W.J. Pierson, Jr. (1953). "On the Motions of Ships in Confused Seas," Society of Naval Architects and Marine Engineers, Volume 61, 280-357.

Tick, L.J. (1961). "The Estimation of Transfer Functions of Quadratic Systems," Technometrics, Volume 3, No. 4, 563-567.

Tukey, J.W. (1949). "The Sampling Theory of Power Spectrum Estimates," Proc. Symposium on Applications of Autocorrelation Analysis to Physical Problems, Woods Hole, U.S. Office of Naval Research.

Tukey, J.W. (1967). "An Introduction to the Calculation of Numerical Spectrum Analysis," Spectral Analysis of Time Series, Ed., B. Harris, J. Wiley and Sons, New York, 25-40.

Vassilopoulos, L.A. (1967). "The Application of Statistical Theory of Non-Linear Systems to Ship Motion Performance in Random Seas," International Shipbuilding Progress, Volume 14, No. 150, 54-65.

Vassilopoulos, L.A. (1971). "Ship Rolling at Zero Speed in Random Beam Seas with Nonlinear Damping and Restoration," Journal of Ship Research, Volume 15, 289-294.

Verhagen, J.H.G. (1970). "The Drifting Force on a Floating Body in Irregular Waves," Proceedings of the Eighth Symposium on Naval Hydrodynamics, ACR-179, U.S. Office of Naval Research, 955-979.

Volterra, V. (1930). Theory of Functional and of Integral and Integro Differential Equations, Blackie and Sons, Ltd., London.

Wiener, N. (1942). "Response of a Nonlinear Device to Noise," Report No. 129, Radiation Laboratory, Massachusetts Institute of Technology.

Yamanouchi, Y. (1964). "Some Remarks on the Statistical Estimation of Response Functions of a Ship," Proceedings of the Fifth Symposium on Naval Hydrodynamics, ACR 112, U.S. Office of Naval Research, 97-126.

Yamanouchi, Y. (1974). "Ship's Behavior on Ocean Waves as a Stochastic Process," International Symposium of the Dynamics of Marine Vehicles and Structures in Waves, London, 178-192.

APPENDIX A. AUTOREGRESSIVE SPECTRAL ESTIMATION

In this Appendix, we outline the autoregressive series approach to spectral analysis in three parts: first, it is shown how this method leads to a direct estimate of the scalar spectrum of a time series. Then, following Parzen (1969) we show how the autoregressive series approach can be used as a formal approach to prefiltering for cross-spectral estimation. Finally, it is shown how the prefiltering technique can be extended to the estimation of cross-bispectra.

A-1. Scalar Spectrum Estimation

Let $X(t)$ be a real wide sense stationary process that possesses both a covariance function, $R_X(\tau)$, and a (two-sided) spectral density function, $f_X(\omega)$. Without loss of generality, the mean value $EX(t)$, may be taken to be zero. Assume that $\Delta > 0$ and

$$t \in \{0, \pm \Delta, \pm 2\Delta, \dots\}. \quad (A.1)$$

Then, according to Masani (1966, p. 376), it is sufficient that the spectral density function be bounded in order that the process admit a one-sided moving average representation

$$X(t) = \sum_{K=0}^{\infty} [b_K \Delta] \epsilon(t-K\Delta), \quad (A.2)$$

where $\epsilon(t)$ is a sequence of mutually uncorrelated random variables, i.e., white noise. Because linear combinations in the set of random variables, $X(t)$, are equivalent to linear combinations in the set of white noise variables, we can approximate $X(t)$ arbitrarily closely for large N by

$$X(t) = \sum_{K=1}^N [a_K \Delta] X(t-K\Delta) + \epsilon(t) \quad (A.3)$$

$$= X^*(t) + \epsilon(t), \quad (A.4)$$

where $X^*(t)$ is the least mean square estimator of $X(t)$, given a finite number of its past values. The argument leading to (A.3) can be made precise by developing least mean square theory in a geometric (Hilbert space) setting as indicated, for example, by Doob (1952). Then $X^*(t)$ in (A.4) becomes the projection of $X(t)$ on a closed linear manifold.

Note that (A.3) is an autoregressive series of finite order and that

$$\epsilon(t) = X(t) - \sum_{K=1}^N [a_K \Delta] X(t-K\Delta). \quad (A.5)$$

It then follows from the Hilbert space projection theorem that $X^*(t)$ is the projection of $X(t)$ on the subspace generated by its finite past and consequently that $\epsilon(t)$ is an orthogonal

(uncorrelated) sequence, i.e., white noise. We then compute the spectrum of $X(t)$ in terms of the white noise process, which by definition will have a constant (flat) spectrum.

It follows directly from (A.3) that

$$\begin{aligned} R_\epsilon(\tau) = R_X(\tau) - \sum_{j=1}^N [a_j \Delta] R_X(\tau-j\Delta) \\ - \sum_{i=1}^N [a_i \Delta] R_X(\tau+i\Delta) + \sum_{j,k=1}^N [a_k \Delta] [a_j \Delta] \\ R_X(\tau-(j-k)\Delta). \end{aligned} \quad (A.6)$$

Then assuming that the roots of the exponential polynomial in (A.6) do not lie on the unit circle, it follows using Equations (2.18) and (2.17) that

$$\begin{aligned} f_X(\omega) = \frac{\sigma_N^2}{2\pi} \left| 1 - \sum_{j=1}^N [a_j \Delta] e^{i(j\omega\Delta)} \right|^{-2}, \\ -\frac{\pi}{\Delta} < \omega < \frac{\pi}{\Delta}. \end{aligned} \quad (A.7)$$

The white noise variance may be estimated in a least mean square sense from

$$\sigma_N^2 = R_X(0) - \sum_{j=1}^N [a_j \Delta] R_X(j\Delta). \quad (A.8)$$

This is the autoregressive spectral estimation procedure. It gives a continuous frequency representation of the spectrum and avoids the use of the usual spectral or lag windows associated with spectral estimators of the Blackman-Tukey type. The estimator should be bias free if the process under consideration is a N th order autoregressive process. Akaike (1969) has proved that the estimator generally has smaller variability than the classical estimates.

Two important problems in the application of the autoregressive estimation procedure are the determination of the order, N , in (A.3) and the least squares estimation of the coefficients. With respect to the required order, it was found in practical application to wave-ship data that good estimates were obtained by choosing N based on the rate at which the covariance function of the physical process died out. No effort was made to compare this procedure with more rigorous selection procedures. The coefficients in the autoregressive Equation (A.3) are required to satisfy

$$E|X(t) - X^*(t)|^2 = \text{MIN}, \quad (A.9)$$

which results in the matrix equation

$$R_X(n\Delta) = \sum_{j=1}^N [a_j \Delta] R_X((j-n)\Delta), \quad n = 0, 1, \dots, N. \quad (A.10)$$

This equation may be inverted directly to obtain the coefficients. However, in practice N may be quite large due to the long memory of the process. In this case, it may be more efficient to solve Equation (A.10) recursively and obtain only those terms that contribute significantly to the quality of fit in the relation (A.7). For this purpose the step-wise regression procedure of Efroymsen (1960) was employed in the present study.

A.2 Cross-Spectrum Estimation

Let $X(t)$, $Y(t)$ be two processes that satisfy the assumptions stated in the previous section. Let $X^*(t)$ and $Y^*(t)$ be the respective linear least mean square estimators such that

$$X^*(t) = \sum_{j=1}^{N_X} [a_j \Delta] X(t-j\Delta) \quad (A.11)$$

and

$$Y^*(t) = \sum_{k=1}^{N_Y} [b_k \Delta] Y(t-k\Delta). \quad (A.12)$$

Then forming the differences

$$\epsilon_X(t) = X(t) - X^*(t), \quad (A.13)$$

$$\epsilon_Y(t) = Y(t) - Y^*(t) \quad (A.14)$$

and computing cross-spectra analogously to the scalar spectrum computation, we obtain

$$f_{XY}(\omega) = \left(1 - \sum_{j=1}^{N_X} [a_j \Delta] e^{j(j\omega\Delta)} \right)^{-1} \times \left(1 - \sum_{k=1}^{N_Y} [b_k \Delta] e^{j(k\omega\Delta)} \right)^{-1} f_{\epsilon_X \epsilon_Y}(\omega) \quad (A.15)$$

The filtered cross-spectrum on the right side of (A.15) must then be obtained by some method of cross-spectrum estimation. The expression (A.15) may thus be viewed as a prewhitening filter applied to the original process pair.

Parzen (1968) hypothesized that this prefiltering operation should lead to reduced bias and variability in the estimated cross-spectrum. Limited application of the procedure to simulated wave-ship response data in the present study tended to support Parzen's hypothesis. Additional theoretical investigation and practical experience is required in order to more fully evaluate this estimation method.

A.3 Cross-Bi-Spectrum Estimation

By using the same assumptions and procedures as that employed for spectrum and cross-spectrum estimation above, it follows that an autoregressive prefiltering approach to cross-bi-spectrum estimation is

$$f_{XXY}(\omega_1, \omega_2) = \left(1 - \sum_{j=1}^{N_X} [a_j \Delta] e^{ij\omega_1 \Delta} \right)^{-1} \times \left(1 - \sum_{k=1}^{N_X} [a_k \Delta] e^{ik\omega_2 \Delta} \right)^{-1} \times \left(1 - \sum_{l=1}^{N_Y} [b_l \Delta] e^{il(\omega_1 + \omega_2) \Delta} \right)^{-1} f_{\epsilon_X \epsilon_X \epsilon_Y}(\omega_1, \omega_2). \quad (A.16)$$

For the special diagonal case used for mean ship response estimation, the transformation is real and yields

$$f_{XXY}(\omega_1, -\omega_1) = \left(1 - \sum_{l=1}^{N_Y} [b_l \Delta] \right)^{-1} \left| 1 - \sum_{k=1}^{N_X} [a_k \Delta] e^{ik\Delta\omega_1} \right|^{-2} f_{\epsilon_X \epsilon_X \epsilon_Y}(\omega_1, -\omega_1). \quad (A.17)$$

In the results for simulated wave-force systems given in the text of this paper, cross-bi-spectrum for the filtered processes were computed using the usual Blackman-Tukey method with a two-dimensional hanning window. Application of the prefiltering procedure was found to significantly reduce the estimation bias as compared to estimation based on unfiltered series.

FUNDAMENTAL HYDRODYNAMICS

SESSION VI

Thursday, June 27, 1974
9:00 A.M. — 12:10 P.M.

Chairman: Dr. W. E. Cummins
Head, Ship Performance Department
Naval Ship Research and
Development Center
United States

Wave Patterns of Non-Thin or Full-Bodied Ships	543
Joseph B. Keller, Courant Institute of Mathematical Sciences New York University, New York, New York	
Velocity Field Measurements Applied for Analysis of Ship's Wave-Making Singularities	549
T. Kitazawa, Hitachi Shipbuilding & Engineering Co., Ltd. Osaka, Japan and T. Inui and H. Kajitani, The University of Tokyo, Tokyo, Japan	
Note on the Refraction of Head Seas by Long Ships	565
F. Ursell, University of Manchester, England	
Oscillations and Wave Forces in a Man-Made Harbor in the Open Sea	573
H.S. Chen and C.C. Mei, MIT, Cambridge, Massachusetts	
Breaking Waves—in Deep or Shallow Water	597
M.S. Longuet-Higgins, Department of Applied Mathematics and Theoretical Physics, Silver Street, Cambridge, England and Institute of Oceanographic Sciences, Wormley, Surrey, England	

WAVE PATTERNS OF NON-THIN OR FULL-BODIED SHIPS*

Joseph B. Keller
Courant Institute of Mathematical Sciences
New York University
New York, New York 10012

ABSTRACT

A method is presented for determining the wave pattern produced by the motion of a non-thin or full-bodied ship. It is based upon the assumption that the Froude number $F = U^2/gL$ is small, where U is the ship speed, L is the ship length and g is the acceleration of gravity. In this case the wavelength of the resulting waves is small compared to L . Therefore, the waves can be described by a theory like geometrical optics, in which rays, a phase function and an amplitude function play a role. The waves are superposed on the double body flow, which is the potential flow about the ship and its image in the undisturbed free surface. They are produced at the bow and stern, and travel outward and rearward from these points along curved rays, which become straight far from the ship. In addition some waves from the bow travel along the surface at the waterline and leave it tangentially toward the rear along similar rays. Thus the ship wave pattern consists primarily of the waves from two sources, one at the bow and one at the stern. The results are confirmed by comparison with the small F asymptotic evaluation of Michell's solution for thin ships.

1. Introduction

Kelvin initiated the theory of ship waves by determining the wave pattern produced by a point disturbance moving with constant velocity along the surface of water of infinite depth. Michell advanced the theory by obtaining an expression for the wave pattern produced by a thin or slender ship moving with constant velocity. No corresponding result for ships which are not thin or slender has yet been found. The present work is a step toward obtaining such a result.

The basis for our theory is the assumption that the ship motion is slow. In dimensionless terms this means that the Froude number $F = U^2/gL$ is small, where U is the ship speed, L is the ship length and g is the acceleration of gravity. When F is zero, the flow about the ship is the well-known double body flow with potential ϕ . This is the potential flow about the ship and its image in the undisturbed free surface. It does not contain any wave motion. Therefore we assume that for F small, the flow consists of the double body flow plus an oscillatory flow which represents the wave motion.

To determine the oscillatory flow, we first observe that the wave pattern moves with the ship

at speed U . Therefore the waves in it must have phase velocities of order U . Consequently their wavelengths are of order U^2/g . This is small compared to the ship length L since the ratio U^2/gL is just F , which we assume to be small. Because the wavelength is small compared to L , the wave motion can be treated by ray methods, like those of geometrical optics. Therefore we shall develop an appropriate ray theory, and use it to find the ship wave pattern.

We shall begin by considering the phase function s of the wave pattern. In terms of s , the wavefronts are just the curves $s = \text{constant}$. In section 2 we shall derive a first order partial differential equation satisfied by s . In section 3 we shall consider the equation for s in the neighborhoods of the bow and the stern. In section 4 we shall introduce rays, which are the characteristics of this equation, and show how they can be used to solve for s . We have used these methods to illustrate the results by finding s for a point ship and for a thin ship. We shall see that the result for a point ship agrees with that of Kelvin, and the result for a thin ship agrees with Michell's result when his result is evaluated for low Froude number [1]. Results for realistic shapes require similar, but more complicated, calculations.

The next step in the development of the theory is the determination of the amplitude of the wave motion [2]. By using the appropriate conservation law for waves in a narrow tube of rays, it is possible to calculate the amplitude along a ray in terms of its initial value at some point on the ray. The determination of the initial value involves the determination of the flow in the neighborhood of the waterline of the ship, from which the rays originate. The flow in that neighborhood can be found by boundary layer methods, but it has not yet been done in general. Therefore, we shall not deal with the amplitude in this paper.

2. Equation for the Phase Function

In order to determine the phase function s of the waves produced by a ship, we shall first derive a differential equation for s . To do so we recall that in deep water at rest, the frequency ω and the wave vector k of a wave are

related by the dispersion equation $\omega^2 = g|k|$. In water moving with the horizontal velocity $\nabla\phi$, the actual frequency of a wave is $\omega - \nabla\phi \cdot k$, where ω is the apparent frequency. Upon using this frequency instead of ω in the dispersion equation, we get $(\omega - \nabla\phi \cdot k)^2 = g|k|$ as the dispersion equation for waves in moving water.

Now let $s(x, y, t)$ be the phase function of a wave, where x and y are coordinates in the undisturbed free surface $z = 0$. Then the frequency is $\omega = -s_t$ and the wave vector is $k = \nabla s$, where ∇ is the horizontal gradient. We now use these expressions for ω and k in the dispersion equation, and square both sides to avoid writing $|k|$. In this way we obtain

$$(s_t + \nabla\phi \cdot \nabla s)^2 = g^2 (\nabla s)^2. \quad 1.$$

This is a first order partial differential equation for s . In it the velocity $\nabla\phi$ is evaluated on $z = 0$ from the double body potential $\phi(x, y, z, t)$ corresponding to the instantaneous position and velocity of the ship.

For a ship which moves with constant velocity U along the x -axis, it is convenient to introduce coordinates fixed with respect to the ship. In this coordinate system the flow is steady, so both ϕ and s are independent of t . Then (1) becomes

$$(\nabla\phi \cdot \nabla s)^2 = g^2 (\nabla s)^2. \quad 2.$$

The potential ϕ is the solution of the following problem:

$$\Delta\phi = 0, \quad z \leq 0, \quad 3.$$

$$\partial\phi/\partial n = 0, \quad \underline{x} \text{ on } B, \quad 4.$$

$$\phi_z = 0, \quad \text{at } z = 0, \quad 5.$$

$$\phi \rightarrow Ux \text{ as } x \rightarrow \infty. \quad 6.$$

In (4) B denotes the ship surface.

To obtain a boundary condition on s , we note that the horizontal velocity of the water due to the wave motion is proportional to ∇s . If the ship is vertical at the waterline C , the component of horizontal velocity normal to C must vanish. This yields the boundary condition

$$\partial s/\partial n = 0, \quad \underline{x} \text{ on } C. \quad 7.$$

Another condition which s must satisfy is the radiation condition, which requires that the wave energy flow away from the ship. Now the wave energy propagates with the group velocity $\underline{c}_g = (\partial\omega/\partial k_1, \partial\omega/\partial k_2)$ where k_1 and k_2 are the x and y components of the wave vector k . From the first paragraph of this section we see that

$\omega = (g|k|)^{1/2} + \nabla\phi \cdot k$. Differentiation of ω yields

$$\underline{c}_g = \frac{1}{2} \left(\frac{g}{|k|} \right)^{1/2} \frac{k}{|k|} + \nabla\phi = \frac{g^{1/2} \nabla s}{2[(\nabla s)^2]^{3/4}} + \nabla\phi. \quad 8.$$

Thus the radiation condition is that \underline{c}_g , given by (8), be directed away from the ship.

From (4) and (7) we see that the normal components of $\nabla\phi$ and ∇s are zero on C . Then (8) shows that \underline{c}_g is tangent to C , and therefore directed away from it provided that C is convex. However, at the bow and stern there are stagnation points of the flow where $\nabla\phi = 0$, and where ∇s is either zero or infinite. At these points, as (8) shows, \underline{c}_g is also either zero or infinite.

Therefore we must make a more precise calculation of \underline{c}_g near these points in order to impose the radiation condition near them, and we shall now do this.

3. Bow and Stern Stagnation Points

Let us denote by 2α the interior angle made by the waterline C at the stern. (See Fig. 1). We assume that C is symmetric about the x -axis. If the hull is vertical at the stern then the behavior of ϕ there is

$$\phi(r, \theta, 0) \sim hr^v \cos v\theta, \quad v = \pi/(\pi - \alpha). \quad 9.$$

Here r is distance from the stern, θ is the angle measured from the x -axis, and h is a positive constant proportional to the ship speed U . The value of v is the smallest positive number for which $\phi_\theta = 0$ at the hull $\theta = \pi - \alpha$.

We now use (9) in (2) to get

$$(vhr^{v-1} \cos v\theta s_r + vhr^{v-2} \sin v\theta s_\theta)^2 \sim g^2 (s_r^2 + r^{-2} s_\theta^2). \quad 10.$$

We shall seek s in the form

$$s \sim gh^{-2} r^\mu w(\theta). \quad 11.$$

Substitution of (11) into (10) yields the value of μ and an equation for w :

$$\mu = \frac{\pi - 3\alpha}{\pi - \alpha} \quad 12.$$

$$(v\mu w \cos v\theta + v w_\theta \sin v\theta)^2 = \mu^2 w^2 + w_\theta^2 \quad 13.$$

If the ship is symmetric about the x -axis then s must be symmetric also. This yields the boundary condition

$$w_\theta(0) = 0. \quad 14.$$

From (11) and (12) we see that $\mu > 0$ and $s = 0$ at the stern if $\alpha < \pi/3$, while $\mu < 0$ and $s = \infty$ at the stern if $\alpha > \pi/3$. The function $w(\theta)$ must satisfy (13) and (14), but these equations do not determine it uniquely.

We now use (9) and (11) in (8) to calculate \underline{c}_g . We find that the radial component is

$$(\underline{c}_g)_{\text{radial}} \sim \left[\frac{\mu w(\theta)}{2(\mu^2 w^2 + w_\theta^2)^{3/4}} + v \cos v\theta \right] r^{\alpha/(\pi - \alpha)} h. \quad 15.$$

By using (14) in (13) and solving for $w(0)$, we find $w(0) = \pm(v^2\mu)^{-1/2}$. Both solutions make the right side of (15) positive at $\theta = 0$, so this condition does not select a particular solution.

At the bow a similar analysis can be made, with $2\alpha^1$ denoting the interior angle included by C there. Then instead of (9) we have

$$\phi(r, \theta, 0) \sim h^1 r^{v^1} \cos v^1(\pi - \theta), \quad v^1 = \pi/(\pi - \alpha^1) \quad 16.$$

Here r^1 is distance from the bow and h^1 is a negative constant. We again find that s is of the form (11) with h^1 instead of h , with $w^1(\theta)$ instead of w and with $\mu^1 = (\pi - 3\alpha^1)/(\pi - \alpha^1)$. The equation satisfied by w^1 is similar to (13).

4. Rays

To solve (2) for s we introduce the characteristic curves $x(\sigma), y(\sigma)$ where σ is a parameter. We also write $k_1(\sigma) = s_x[x(\sigma), y(\sigma)]$, $k_2(\sigma) = s_y[x(\sigma), y(\sigma)]$, $s(\sigma) = s[x(\sigma), y(\sigma)]$ and we introduce f defined by

$$f(x, y, k_1, k_2) = g^2(k_1^2 + k_2^2) - (k_1\phi_x + k_2\phi_y)^4. \quad 17.$$

Then (2) is just

$$f(x, y, k_1, k_2) = 0 \quad 18.$$

The characteristic equations of (18) are

$$\begin{aligned} \dot{x} &= f_{k_1}, \quad \dot{y} = f_{k_2}, \quad \dot{k}_1 = -f_x, \quad \dot{k}_2 = -f_y, \quad \dot{s} = k_1 f_{k_1} \\ &\quad + k_2 f_{k_2}. \end{aligned} \quad 19.$$

$$\dot{x} = 2g^2 k_1 - 4\phi_x (k_1\phi_x + k_2\phi_y)^3 \quad 20.$$

$$\dot{y} = 2g^2 k_2 - 4\phi_y (k_1\phi_x + k_2\phi_y)^3 \quad 21.$$

$$\dot{k}_1 = 4(k_1\phi_{xx} + k_2\phi_{xy})(k_1\phi_x + k_2\phi_y)^3 \quad 22.$$

$$\dot{k}_2 = 4(k_1\phi_{xy} + k_2\phi_{yy})(k_1\phi_x + k_2\phi_y)^3 \quad 23.$$

$$\dot{s} = -2g^2(k_1^2 + k_2^2). \quad 24.$$

To find a solution s with the behavior (11) near the stern, we introduce rays $x(\sigma, \theta)$, $y(\sigma, \theta)$ which start at the stern in the direction θ . If the stern is at $(L, 0)$, the initial values of x and y are $x(0, \theta) = L$, $y(0, \theta) = 0$ and the initial slope of the ray is $y(0, \theta)/x(0, \theta) = \tan \theta$. If $\alpha < \pi/3$, then $\mu > 0$ and the initial value of $s(0, \theta) = 0$. However, if $\alpha > \pi/3$ then $s = -\infty$ at the stern, so only the asymptotic behavior (11) can be specified. The initial values of k_1 and k_2 can be found by differentiating (11), and they are both infinite at the stern. Therefore only their behavior near the stern can be specified.

REFERENCES

- [1] J.B. Keller and D.S. Ahluwalia, Wave Patterns of Thin Ships. (To be published).
- [2] J.B. Keller, Geometrical Theory of Ship Waves. (To be published).

*This work was supported in part by the Office of Naval Research under Contract No. N00014-67-A-0467-0006 and by the Naval Ship Research and Development Center under Contract No. N00014-67-A-0467-0033.

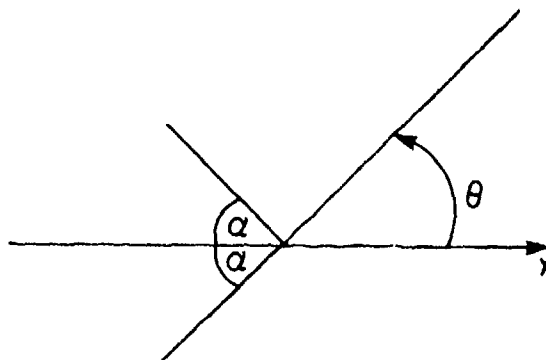


fig. 1

DISCUSSION

T.F. OGILVIE

The naval architect is likely to dismiss short-wave problems as uninteresting because "short waves" implies very low speed, and wave resistance is of little interest under such conditions. Even in problems involving ambient waves, "short waves" implies small motions and small loads — although the latter is perhaps no longer true in the practical problems that involve the so-called "springing" phenomenon.

However, there still remain several important reasons for investigating such problems. I shall mention only those that relate to the steady-motion problem.

1) In most theoretical treatments of ship waves, an assumption is made, either implicitly or explicitly, that all waves of interest have wavelengths that are comparable to ship length. If this assumption is not made, one cannot use thin-ship theory, for example, because one can then not transfer the body boundary condition to the center-plane. This does not seem to be generally recognized by people who work extensively with the thin-ship idealization. One loses all effects caused by hull diffraction of the ship-generated waves unless one considers that the waves are somehow comparable in length to ship beam. We are now learning how to include such things in slender-ship theory, but several major questions remain open. In any case, it is clear that we must consider shorter waves than has been customary.

2) In towing-tank practice, the low-speed tests may have considerable importance in fixing the extrapolator curves, since it is assumed that wave resistance vanishes sufficiently rapidly at low speeds that the remaining measured drag represents only viscous-related effects. However, if wave resistance drops off in some way that is not well-understood, the wrong conclusions may be drawn about the full-scale significance of the tests.

3) Double-body tests or calculations are often used as the starting point for studies of ship-wave phenomena. I would guess that at least 80% of such studies have been fundamentally wrong, because the investigators did not understand that this is a singular perturbation problem.

Professor Keller's approach may be a significant advance toward resolving the third aspect mentioned above. In using "geometrical optics" waves superposed on the nonuniform double-body flow, he obviously understands very well the nature of the singular perturbation problem. The same is true for Professor Timman and Dr. Hermans, as well as for Dr. Dagan and others.

But if Professor Keller believes that he may be able to predict the waves in practical situations involving full-bodied ships, I think that he is mistaken. In such cases, the waves are not nearly short enough to satisfy the conditions of his analysis. He requires explicitly only that the wavelength should be short compared with ship length. However, in order to use his ray techniques, one must have wavelengths short compared with all ship dimensions, including beam, draft, radii of curvature near the bow, An exception to such a requirement can be made only under an opposite extreme condition, namely that the rays emanate from well-defined points. Thus it is not surprising if he can duplicate the waves from Kelvin's fishline or even from Michell's thin ship.

Finally, I should add that I cannot see how Professor Keller can predict the most important practical effect of the shortness of real ship waves, namely, the diffraction of bow waves by a full middle-body. In Professor Ursell's paper, it is shown that there is effectively a "shadow region" along-side a ship, the region growing steadily toward the stern. What does a ray theory say about wave motion in a shadow region?

AUTHOR'S REPLY

Prof. Ogilvie's comments on the reasons for considering short wave problems are very illuminating. I hope they will stimulate interest in such problems. He has also expressed doubts about the possible use of a geometrical optics or ray theory "to predict the waves in practical situations involving full-bodied ships." I can only expect to remove those doubts by using the theory to make such predictions,

and comparing them with observations. This is what I hope to do. However, there is every reason to expect that the theory will work. This is because of the extensive and detailed agreement of the corresponding "geometrical theory of diffraction" with numerical calculations and with observation, in problems involving acoustic waves, electromagnetic waves, surface gravity waves, etc.

VELOCITY FIELD MEASUREMENTS APPLIED FOR ANALYSIS OF SHIP'S WAVE-MAKING SINGULARITIES

T. Kikazawa
Hitachi Shipbuilding
& Engineering Co., Ltd.
Osaka, 554, Japan

T. Inui
The University of Tokyo
Tokyo, 113, Japan

H. Kajitani
The University of Tokyo
Tokyo, 113, Japan

revised 24 August 1974 by H. Kajitani

ABSTRACT

Measurements of the three-dimensional flow velocity components (u , v , w) are carried out around a 2m Inuid Model M21 where a specially developed mini five-hole pitot tube of 6mm diameter is applied satisfactorily.

The velocity components are analyzed (u , v , w - analysis) in a synthetic co-ordination with the corresponding wave analysis (ζ -analysis) which was reported in the Ninth Symposium on the same model (M21).

The study indicates that,
For potential field;

- (1) The two linearized free surface conditions, i.e. the "atmospheric" condition as well as the "kinematical" condition, are both valid either between ζ (measured) and u (measured) or between $\partial\zeta/\partial x$ (measured) and w (measured).
- (2) The behavior of the transverse component $v(y)$ is the most important, because this component alone can give the unique informations for sheltering effects which are not included in the wave-analysis.
- (3) The results analyzed from u or w are almost similar to those already obtained by wave analysis.

For viscous field;

- (4) The flow field analysis is useful also for the refinement of the wake-survey by enabling the quantitative estimation of the disturbance velocity (u_1) which is fictitiously presumed within the wake belt.

NOMENCLATURE

- $A^*(\theta)$ = weighed amplitude function
 $(C_w = 2\pi \int_0^{\pi/2} [A^*(\theta)/L]^2 d\theta)$
- A_i, B_i = coefficients of modified Fourier series expansion
- C_{Fo} = $R_{Fo}/\frac{1}{2}\rho V^2 L^2$ = frictional resistance coefficient for flat plate
- C_v = $R_v/\frac{1}{2}\rho V^2 L^2$ = viscous resistance coefficient
- Fr = Froude number
- g = acceleration of gravity

- G = Green function
- G_1 = double model term of Green function
- H_0, H = total head
- K = form factor
- K_0 = g/U^2 = wave number
- l = $L/2$ = half length of the ship
- $m(\xi, \zeta)$ = distribution function of source density
- p = $P/\frac{1}{2}\rho U^2$ = non-dimensional static pressure
- T = $t \cdot l$ = depth of source distribution
- u, v, w = components of disturbance velocity in x, y, z direction
- u_1, v_1, w_1 = components of disturbance velocity considered fictitiously in the wake zone
- U = velocity of uniform flow
- x, y, z = Cartesian co-ordinates for flow field
- ζ = wave elevation
- Φ = $\tan^{-1}\{\eta/(x-\xi)\}$
- ξ, η, ζ = Cartesian co-ordinates for source distribution
- $\phi(x, y, z)$ = velocity potential
- ω = wake zone

1. WAVE ANALYSIS AND FLOW FIELD ANALYSIS

In model basins during these about ten years the two kinds of microscopic approaches i.e. the wave analysis and the flow field analysis have been carried out together with the traditional macroscopic resistance and propulsion tests which are symbolized as "the force measurement".

Here the wave analysis is based on the scalar data of the surface wave height $\zeta(x, y)$ created by a travelling ship, while the flow field analysis is based on the vector data of flow velocity components which extend three dimensionally around the ship. Therefore when the denseness of both information data is compared, the flow field analysis is evidently superior to the wave analysis. In fact not a few problems which could not be cleared with the wave analysis alone are expected to be clarified with the good co-ordination of this flow field analysis.

The flow field surrounding a ship is divided into two regions. One is inner boundary layer and wake zone where the flow is characterized by viscosity. The other is out of these zones where the potential flow can be assumed. It is considered the wave analysis and the flow field analysis should be carried out in both regions fundamentally. However in the previous works there was a tendency that each analysis was performed in each region exclusively, i.e. the wave analysis in the potential zone and the flow field analysis in the wake zone.

In this paper the flow field analysis is tried in both regions in the sense just mentioned above where a 2m Inuid Model M21 is applied because its precise wave analysis has been already completed not only for the wave profile along the model but also for the whole free wave pattern (Ref. 1).

Of course the measurements of flow velocity components are far elaborate than the records of wave height. Especially at small tanks including the case of the University of Tokyo the usable model is small and hence the absolute value of the testing speed is limited low for a given Froude number comparing with large models at large tanks. It requires not only a very little and yet high accurate five hole pitot tube but also the good cared test equipments and circumstances (for example the cleaning of the water in the tank is essential). Although their details (Ref. 2) are not shown in this paper it may safely be said that the reliable measurements of velocity components by five hole pitot tube are possible even for a 2m small model.

In addition the accuracy of the measured velocity components required is different depending on the type of the analysis. In the usual wake survey this requisition is not so severe as in the analysis of the potential flow field, because the wake survey stands in many cases to evaluate the viscous resistance

which is only enough with the direct summation of the energy component as shown in Eq. (5). Meanwhile in the analysis of the potential flow field measured velocity components are used as initial data to analyze the equivalent source distributions by solving the integral equations (A.2), (A.3) and (A.4) as shown in the later appendix. Such troublesome analysis is awaiting.

2. VALIDITY OF POTENTIAL FLOW ANALYSIS

A lot of new findings are expected by analyzing the actual potential flow field. However the most important finding is so far as the authors' aspect to know the real features of actual flow and wave field, and to make clear the so-called sheltering effect which arises from the condition to be imposed on the initiation and the radiation of ship waves in particular with the surface piercing ship body. By this reason the analysis of the potential field not associated with the wave analysis seems meaningless. Rather with the good co-ordination of the both new findings which have been never obtained before are truly expected.

To this end the following analyses are considered.

2.1 Study on the Linearity of Free Surface Conditions

Both the linearized dynamical and kinematical conditions at the free surface are given under the co-ordinates system shown in Fig. 1,

$$\frac{\zeta}{l} = - \frac{1}{K_0 l} \cdot \frac{u}{U} \Big|_{z=0} \quad (1)$$

$$\frac{\partial}{\partial x} \left(\frac{\zeta}{l} \right) = \frac{w}{U} \Big|_{z=0} \quad (2)$$

If the velocity components u and w are measured just beneath the water surface, although there remains a little trouble with measurements and looking upon as the data of the free surface, it is able to compare the measured wave height ζ with $u(z=0)$ and the measured wave slope $\partial\zeta/\partial x$ with $w(z=0)$ respectively. Through these comparisons it is possible to study quantitatively to what extent the linearized conditions (1) and (2) are valid.

Also the following is worth mentioning. Even if the validity of the linear free surface conditions is found in the actual wave field, this does not imply that the linearized theory without considerations of the sheltering effect can represent the exact actual wave field, since the sheltering effect can not be attributed to the higher order terms of the free surface conditions.

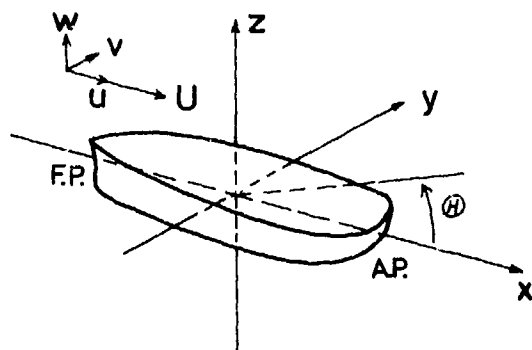


Fig. 1 Coordinates System

2.2 Singularity Distributions Equivalent to Flow Velocity Components

Usable information data in the flow field analysis are quite ample comparing with those in the wave analysis. For example a set of data of wave profile along the ship waterline which was used in the previous wave profile analysis is one dimensional, while in the flow field analysis not only the data on it but also their variations with depth just under this line are given as two dimensional quantities. Furthermore each has three components (u, v, w) instead of u or ζ . Thus prior to the actual flow field analysis, how to treat these ample informations and utilize them in a synthetic analysis becomes itself an important problem, because the three components u, v, w are no longer independent with each other if one assumes the existence of the potential flow in the actual wave field.

However in the present work where the study on this point is inadequate, the velocity components u, v, w are assumed to be independent for each other and the determination of source distributions on the centerplane equivalent to each velocity component is tried to compare with the result from the wave analysis (in the present work the wave profile analysis).

2.3 Draftwise Variation of Source Distribution Equivalent to Flow Velocities

In the wave profile analysis just referred above the source distribution $m(\xi, \zeta)$ equivalent to the wave profile was assumed to be draftwise uniform, and only its lengthwise variation was analyzed corresponding with one-dimensional data of the wave profile $\zeta(\xi)$. However with the application of the flow field analysis where the data at different depth are applicable, the reality of this assumption can be studied.

2.4 Behavior of $v(y)$ and Sheltering Effect

If the two linearized free surface conditions (1) and (2) are found to be valid between the measured ζ, u and w — it is proved practically by the present experiment 1 later on — the importance of each of the data u, v and w for the potential flow analysis becomes different, since u and w are related with ζ closely, and findings derived from the analysis of u or w are guessed more or less similar to those of the wave analysis.

On the contrary quite new findings are indeed expected as for the analysis of v which have never been obtained from the customary wave analysis. Thus the measurements of v in wider range than in the case of u or w is particularly recommended. It might give a possibility to grasp the fundamentals of the sheltering effect and for example to give a reasonable explanation why the measured

wave pattern is shifted outward in usual about ship's half breadth.

2.5 Wake Survey Including the Effect of Potential Flow

The wake-survey is out of the scope of the potential flow analysis. However if the source distribution equivalent to the outer potential flow is known, potential flow component though fictitious can be extrapolated into the wake zone. Thus taking the effect of potential flow component into account, refinements of the wake-survey may be expected.

3. EXPERIMENTS

3.1 Inuid Model M21

Simple hull form such as Wigley model is not suitable for the present analysis because it produces simple large waves and non linear effect happens strongly. Therefore to prevent these effects a complicated less-wave-hull M21 was selected.

The hull geometry of this model was obtained by stream tracing of the following center plane source distribution which is uniform in draftwise direction

$$m(\xi) = 2.17444\xi - 4.11286\xi^3 + 2.25910\xi^5 \quad (3)$$

$$(-1 \leq \xi \leq 1, -0.08 \leq \zeta \leq 0)$$

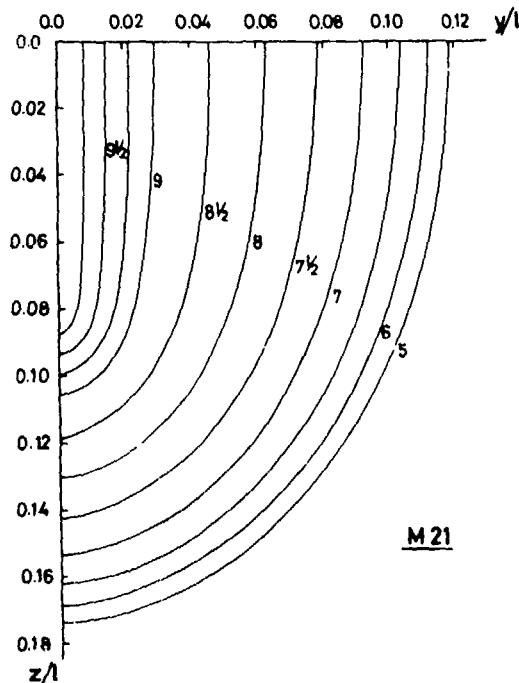


Fig. 2 Body Plan of M21

Principal particulars are listed in Table 1 and its body plan is shown in Fig. 2. All measurements were made at $F_n = 0.289$ according to the optimization Froude number of this model.

3.2 Method of Flow Measurements

To measure the flow velocities a mini five hole pitot tube having the spherical head of 6mm diameter was applied. The out-put was transformed by force balanced pressure transducers and recorded both on a magnetic tape and visigraph. Prior to measurements special cares were paid for leveling of the rail and cleaning of the tank water.

The equipment to calibrate and traverse the pitot tube is so designed that actual measurements may be followed right away after calibration tests without removal of any part of this equipment. Also the setting of angle of pitot tube is important and free surface effect specially acting on w should be carefully calibrated. Analysis was due to Pien's method (Ref. 3).

3.3 Kinds of Experiments

Considering each item of the analyses quoted in the previous section, next three experiments were carried out in these sequences. It should be noted that experiment 2 was planned additionally after new findings were obtained from experiment 1.

Experiment 1. Measurements of three velocity components u, v, w in a wall-sided plane just outside the boundary layer of the model.

Measuring points are shown in Fig. 3 with circular marks (\bullet), which amount in total $25(x) \times 4(z) = 100$ points. Evidently this experiment aims each analysis of (2.1), (2.2) and (2.3). Especially to compare with the known results of the wave profile analysis, the measuring plane was located close to the hull as near as possible.

Table 1 Principal Particulars of M21

Item	M21
L (m)	2.001
B (m)	0.2368
d (m)	0.1724
T (m)	0.08
∇ (m ³)	0.0347
S (m ²)	0.6686
B/L	0.1184
d/L	0.0862

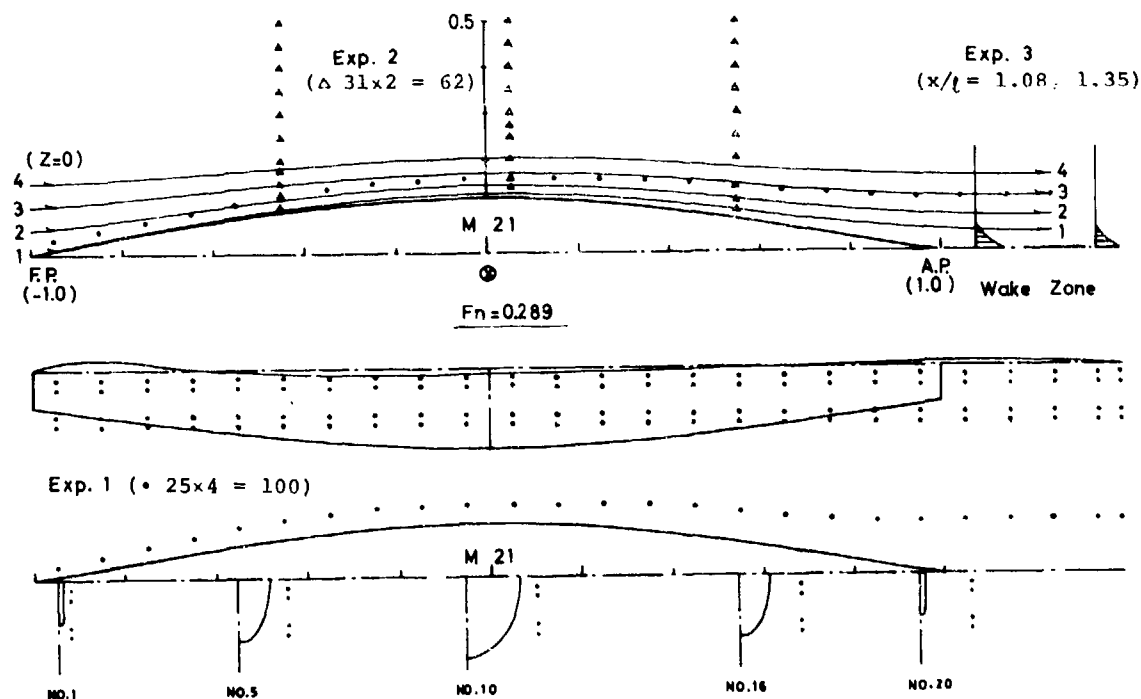


Fig. 3 Measuring Points of Flow Velocity

Experiment 2. Measurements of $v(y, z)$ at three different transverse sections.

As shown in Fig. 3 with triangular marks (Δ), $31(y) \times 2(z) = 62$ points were selected aiming the analysis of (2.4).

Experiment 3. Wake surveys near the stern.

Wake surveys were tried at two sections ($x/l = 1.08, 1.35$) corresponding to (2.5).

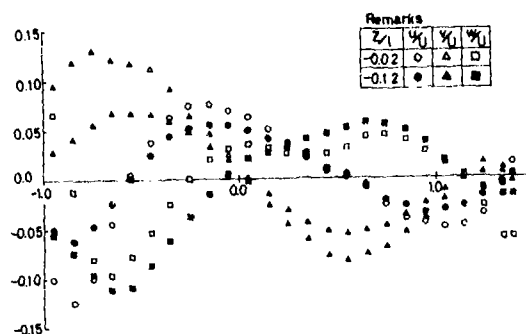


Fig. 4 Measured Velocity Components

4. ANALYSIS FOR EXPERIMENT 1

4.1 Obtained Velocity Components

Velocity components (u, v, w) were measured with good accuracy beyond authors' expectations. Among the data at 100 points which consist from 4 immersed layers with each 25 of x points, results at both, the least immersed layer $z/l = -0.02$ and the most immersed layer $z/l = -0.12$ are shown in Fig. 4. Apparently each measured component forms a fair smooth curve.

4.2 Discussion about Linear Free Surface Conditions

Making use of u, w at least immersion $z/l = -0.02$ and measured wave height ζ with wave slope $\partial\zeta/\partial x$ just on this vertical plane, the linearity of free surface conditions was checked according to the formulas (1) and (2). Results are given in Fig. 5. Upper half figure relates the formula (1) and lower half the formula (2).

With regard to the formula (1), the measured wave elevation ζ is compared first with the R.H.S. of the formula (1) (where u are data at $z/l = -0.02$ not $z = 0$), and second with the following formula (4) which includes the squares of velocities in Bernoulli's equation.

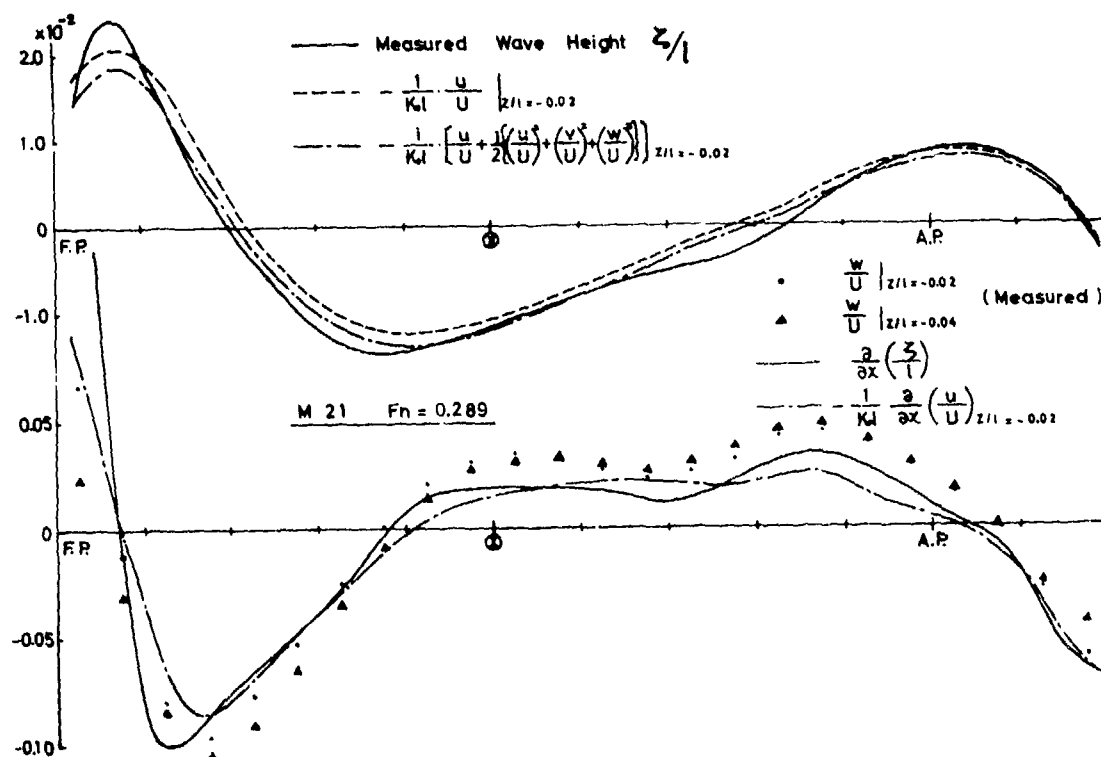


Fig. 5 Comparison of (u, ζ) and $(w, \partial\zeta/\partial x, -\partial u/\partial x)$

$$- \frac{1}{K_0 \ell} \left[\frac{u}{\ell} + \frac{1}{2} \left\{ \left(\frac{u}{\ell} \right)^2 + \left(\frac{v}{\ell} \right)^2 + \left(\frac{w}{\ell} \right)^2 \right\} \right] \quad (4)$$

$z/\ell = -0.02$

With regard to the formula (2), not only the measured w at $z/\ell = -0.02$, but also w at $z/\ell = -0.04$ are plotted for the reference. These are also to be compared first with the wave slope $\partial \zeta / \partial x$ derived from the numerical differentiation of observed wave heights and second with $\partial(-u)/\partial x|_{z/\ell = -0.02}$ derived from the same treatment to the measured velocity components.

Through these comparisons it is found that linear approximations of the both formulas (1) and (2) are well established as a whole in the actual wave field except for the first crest of bow waves. Improvement by non-linear terms seems little with regard to the formula (1), while in the formula (2), $\partial(-u)/\partial x$ at forebody and $\partial \zeta / \partial x$ at aftbody show the better agreement with w both in phase and amplitude.

Two important conclusions are derived from this analysis.

First, the main reasons why the present theory of wave making resistance cannot necessarily give the enough explanation to the actual wave making phenomenon

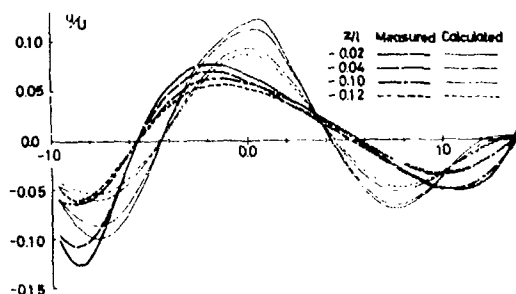


Fig. 6 Comparison of Measured and Calculated Velocity (u) (Use All Terms)

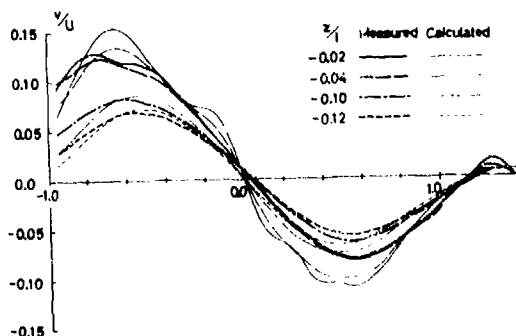


Fig. 7 Comparison of Measured and Calculated Velocity (v) (Use All Terms)

non should not be attributed at least to the linearization of free surface conditions.

Second, the importance of each u , v or w is not equal when each of their analysis is compared with the wave analysis, because u and w are connected with wave and its slope, hence new findings are expected from v which does not appear in the free surface conditions. In order to make this anticipation more effective, the measurement of v should be extended to the whole field.

4.3 Comparison of Velocity Components between Measured and Calculated

About u and v the measured and calculated velocity components are compared in Figs. 6~8. In calculating the velocity component according to the formulas (A.2) and (A.3), (a) the source distribution which was used for stream tracing on the hull therefore the double model source was applied, and (b) Green function consisting from whole terms of the formula (A.6) was used for Figs. 6 and 7, while Fig. 8 is the case where only the double model term G_1 was adopted.

In Figs. 6 and 7 where wave terms of Green function are fully taken, both u and v show fairly large discrepancy between measured and calculated which suggests the existence of the so-called sheltering effect. On the other hand as for v along the hull side it is worth mentioning that rather simple calculations of Fig. 8 based on the double model term of Green function give a better coincidence with the measured. However, the fact that this agreement is confined to the near field of the hull side will be precisely studied in the following section.

4.4 Source Distributions Equivalent to Flow Velocities

As mentioned before three velocity components (u , v , w) are no longer independent with each other in the potential flow field. However in the present analysis it was focused to compare the

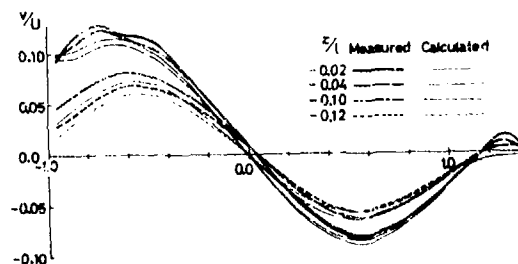


Fig. 8 Comparison of Measured and Calculated Velocity (v) (Use Double Model Term)

measured data with waves rather in the primitive form. Thus the velocity components were taken independent each other and each of the equivalent sources was analyzed as the center plane distribution. The method and formulas to analyze them are summarized in the Appendix.

(4.4.1) Equivalent Sources to u and Their Weighed Amplitude Functions

Three equivalent sources to u are presented in Fig. 9 with the result of wave profile analysis where their variation in draftwise direction was assumed constant. Chain line is obtained from all data of four z/l layers. One dotted line from the nearest layer to the free surface ($z/l = -0.02$), and two dotted line from the deepest layer ($z/l = -0.12$).

From Fig. 9 it is found that equivalent sources to u show the similar tendency as that of the wave analysis, though some differences are observed in the fore part. Source distributions change little with different input data of immersions. It suggests that prescribed assumption of 'draftwise uniform' may be approved. Making use of these sources weighed amplitude functions were calculated and compared including the result of Newman's longitudinal wave analysis (Fig. 10). All of them show the similar movements.

(4.4.2) Equivalent Sources to v or w and Their Weighed Amplitude Functions

Equivalent sources to v or w were also obtained following the case of u . Although their results are not presented for the brevity, three kinds of sources equivalent to each u , v and w look like the same at a glance. However, if their weighed amplitude functions are compared with each other as shown in Fig. 11, one of them which has been derived from v shows a clear difference from the other two. In other words summarizing the results of Fig. 10 and Fig. 11, four kinds of data such as u , w , wave profile along the model and another wave height on a longitudinal cut line applied for Newman's wave analysis give more or less the similar amplitude functions, but the velocity component v supplies a quite different amplitude function.

5. ANALYSIS FOR EXPERIMENT 2

The particular behavior of v is doubtless one of the most noticeable point found out in the analysis of the previous experiment. Evidently the data of v are different in quality because the term v does not appear in the both linearized free surface conditions, where on the contrary u and w are closely related with ζ and its derivative.

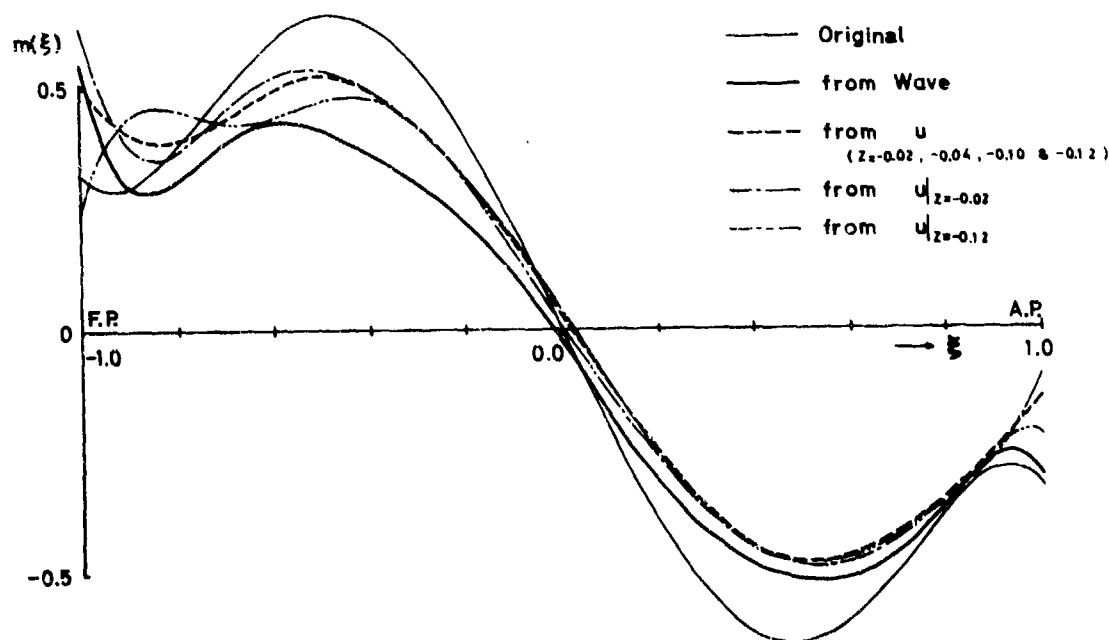


Fig. 9 Source Distributions Analyzed from u and Wave

Accordingly the more detailed investigation about v is desired to learn how the measured v behaves with increasing distance from ship side and how it changes or accords with theoretical calculation. Experiment 2 was thus motivated and objected. Further measurements of v were carried out not confined to the hull surface but spread out widely in y direction.

Measurements were made at three transverse section, i.e. $x/l = -0.45$ where v is enough positive at hull side, $x/l = 0.05$ where v is nearly 0 and $x/l = 0.55$ where v is enough negative. They are measured at two immersed layers $z/l = -0.04$ and -0.06 .

Results for each depth are shown in Figs. 12 and 13 respectively.

5.1 Comparison of v between Measured and Calculated

In each figure four calculated lines are compared with measured points (white marks). Again a) two kinds of source distributions, original source equivalent to hull geometry and analyzed source equivalent to velocity component v , with b) two kinds of Green function, the case that only first term G_1 hence double model term in the right-hand side of (A.6) is used and the other case that all terms are used, make in total four calculated lines.¹

Three conclusions are obtained from Figs. 12 and 13 as follows:

- 1) Near the hull surface, or more exactly saying in the range from hull side to the outer point by half breadth at each ordinate, the calculated lines where double model term G_1 is applied to the double model source as Green function agree quite well with measured.

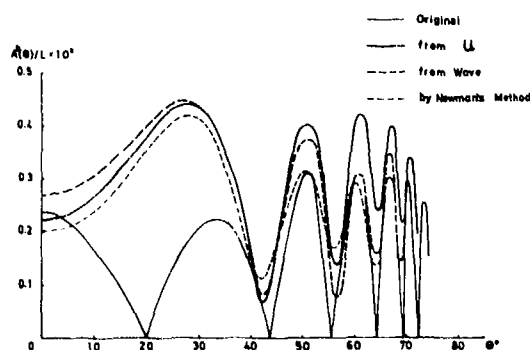


Fig. 10 Weighed Amplitude Function (1)

- 2) At far distance from the hull surface, the calculated line where all terms of Green function are applied to the analyzed source, therefore the free surface effect is taken in both source and Green function, shows a tendentious agreement with measured.
- 3) In the intermediate range of the both, the measured v does not accord with any four lines. However, it seems as if the free surface effect reveals itself gradually outward on the measured v velocities delayed in phase about half breadth at each ordinate.

5.2 Ship Surface Condition and Sheltering Effect Revealed on v (Measured)

When the general behavior of v (measured) is considered synthesizing the result of experiment 2, one finds that the necessary condition for surface piercing ship body is not enough with such a usual ship surface condition that normal velocity must be everywhere zero on its surface.

Because, so far as the discussion is confined on the ship surface, rather double model approximation which gives the rigid water surface shows the better coincidence with measured v than that including the free surface effect, so that the ship surface condition in the usual meaning seems sufficiently satisfied. Problem lies not on the hull surface but on a slightly outgoing region.

Such phenomenon seems quite special and particularly worth noticing that it has never been experienced in the boundary value problem of classical hydrodynamics.

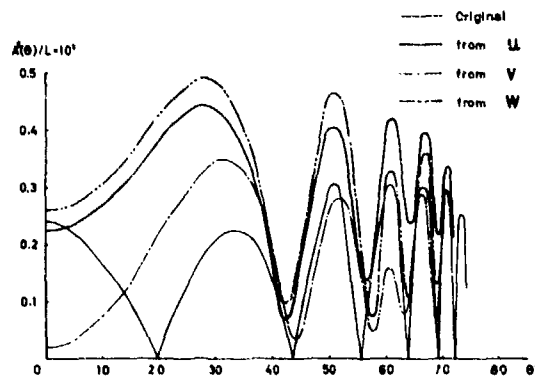


Fig. 11 Weighed Amplitude Function (2)

¹ Note that analyzed source is itself obtained under each Green function. Results are shown in Fig. 14.

Important points are:

- Wave motion is almost completely suppressed in the nearest field to the hull surface.
- Wave component emerges gradually with outgoing from the hull side.
- In this case the phase delay exists evidently of about half breadth.

These are the real features of the sheltering effect, different from usual ship surface condition. Undoubtedly it comes out from free surface piercing by the floating ship itself.

Therefore how and what kind of theoretical model is able to represent this particular flow is raised as an important present task. An analogous model, for example, may be found in the paper by Maruo and Hayasaki (Ref. 4) in which the deformation of waves when waves propagate into uniform wake is studied. The present flow resembles to some extent as if

the fluid interior to the hull surface is completely at rest (i.e. in the wake, $U_2 = 0$) and incoming waves from outside (i.e. out of the wake, $U_1 = U$) is completely dammed at hull's water line, hence the rate of transmission is zero. However according to their conclusions, if the rate of transmission is zero, then the rate of reflection becomes full inversely, and for this reason wave height should be doubled just the same as the perfect reflection at solid wall. This point is extremely different, and the sheltering effect seems to have a character that there is neither transmission nor reflection. It is also interesting to note that the recent work by Mori (Ref. 5) corresponds to the present fact that behavior of v has close relation with the sheltering effect.

Lastly, though it is a short comment as to the double model approximation applied to the stream tracing of Inuid or Pienoid, Wehausen pointed out that it defies the effect of wave term on the hull surface condition (Ref. 6). However

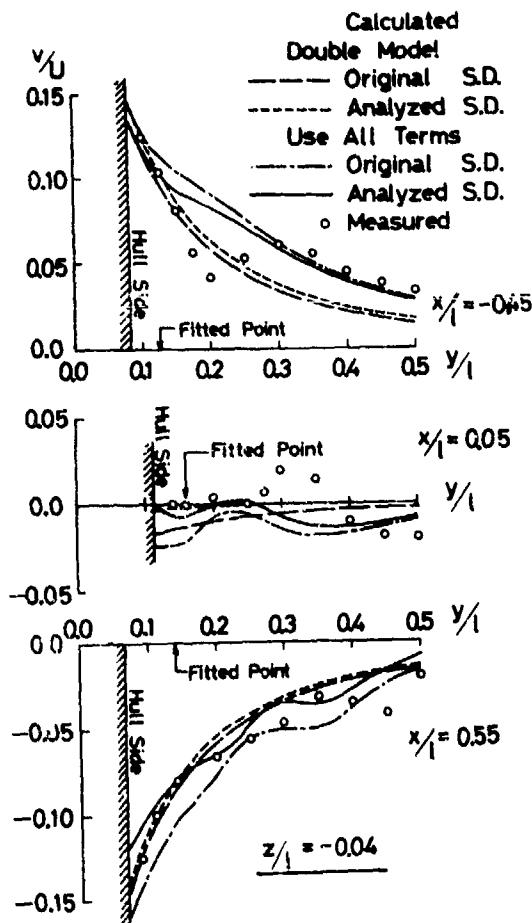


Fig. 12 Comparison of v on Transverse Line (1)

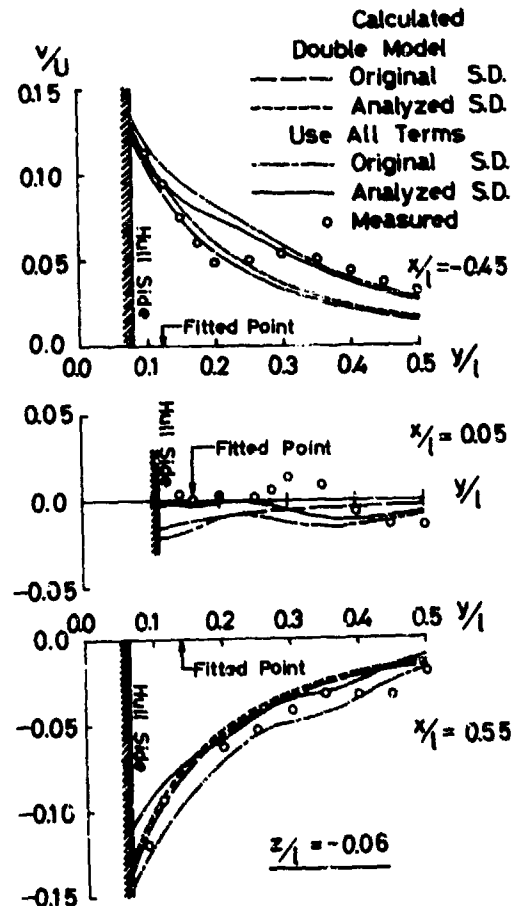


Fig. 13 Comparison of v on Transverse Line (2)

the present experiment shows clearly that the matter is not the dissatisfaction of the ship surface condition but problems lie rather in other points.

5.3 Analysis of v Based on Double Model Approximation

As shown in Fig. 8 since the calculated velocity component v based on rather double model approximation gives the better agreement with the measured near the hull surface, the equivalent source to v was analyzed using double model approximation G_1 where the data of experiment 1 were actually adopted. The analysis of the other equivalent source using all terms of Green function was also tried.

Results are given in Fig. 14 and compared with the original source applied for stream line tracing. The analyzed source by double model approximation coincides well with the original source. It seems that the outer potential field is little affected by the inner boundary layer. However, seeing more in detail,

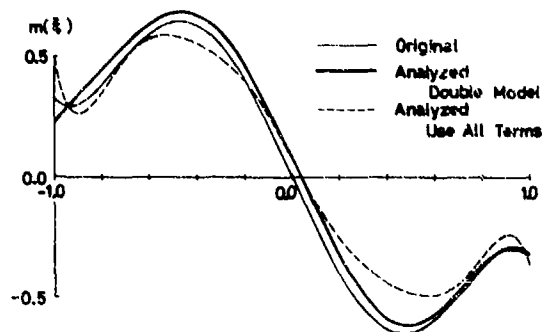


Fig. 14 Source Distributions Analyzed from v

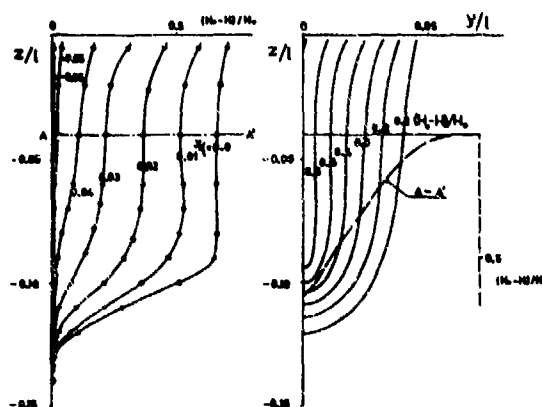


Fig. 15 Wake Contour at $x/\ell = 1.08$

the analyzed source is slightly larger at fore part and smaller in absolute value at aft part than the original source. The transition point from source into sink is shifted 2% of ship length from the midship, it looks like the effect of boundary layer. Using this double model source, some of the stream lines at $z = 0$ were traced for references. On the top of Fig. 3, four stream lines starting from $y = 0.0035, 0.05, 0.1$ and 0.15 respectively at $x/\ell = -1.0$ (F.P. section) are presented numbering from 1 to 4.

6 ANALYSIS OF EXPERIMENT 3

Following to the potential flow analysis, measurements of velocity components in the wake zone were carried out aiming to study the continuation of the wake flow to the outer potential field and to evaluate the viscous resistance. Two measured sections were selected;

- At $x/\ell = 1.08$ where the wave height is still large to know mainly how the wake flow extends to the potential flow field.
- At $x/\ell = 1.35$ where the wave height becomes zero approximately to make the wake survey accurately.

Flow velocities were measured at about 70 points in each survey plane by the same five-hole pitot tube.

Figs. 15 and 16 present the distribution of total head H and disturbance velocity u respectively at $x/\ell = 1.08$. Both contour curves look like the frame line of the model. From Fig. 16 it is seen that even out of the wake u does not disappear, in another words, there remains still potential flow component. In Fig. 17, u and p (static pressure head) were compared between measured and calculated. In calculating the static pressure, the

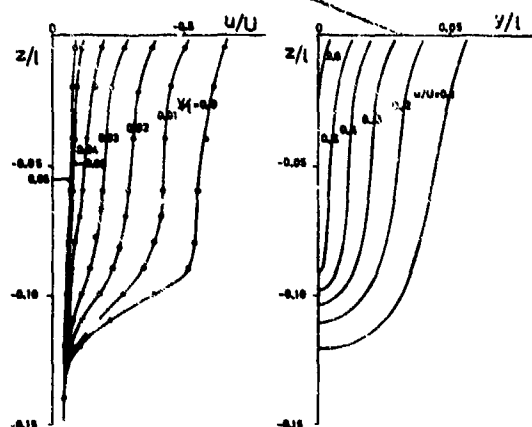


Fig. 16 Distribution of u in Wake at $x/\ell = 1.08$

needed disturbance velocity (u_1, v_1, w_1) was evaluated from the outer potential flow using the equivalent source to u (measured in Experiment 1). The measured static pressure accords well with the calculated even in the wake belt. Also it is clear that disturbance velocity u is gradually merging with the calculated u at out of the wake. The similar results were obtained at $x/l = 1.35$.

Viscous resistance was estimated by the following formula (Ref. 7).

$$R_v = \int_{\omega} (H_0 - H) dS - \frac{\rho}{2} \int_{\omega} u^2 dS + \frac{\rho}{2} \int_{\omega} u_1^2 dS \quad (5)$$

Results are shown in Fig. 18 though the test was made at only one Froude number $F_n = 0.289$. Viscous resistance coefficients C_v non-dimensionalized by U^2 are evaluated,

$$C_v = R / \frac{1}{2} \rho U^2 L^2 = 0.67 \times 10^{-3} \text{ at } x/l = 1.08,$$

$$C_v = 0.74 \times 10^{-3} \text{ at } x/l = 1.35,$$

which accord well with the analysis of the resistance test result,

$$C_{FO}(1 + K) = 0.735 \times 10^{-3}.$$

Especially the evaluation at after section gives a good correspondence to the resistance test result, on the contrary the value at fore section is a little underestimated. Despite the large amount of decrease by the second term of Eq. (5), the contribution of the third term is quite small. Here the integration was made below $z = 0$. If the integration is extended to the wave surface, and extrapolations are appropriate, it might give a more refined estimation.

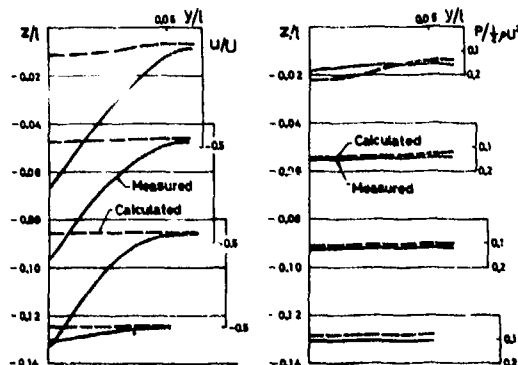


Fig. 17 Distribution of u and P in Wake

7. CONCLUSIONS

The final conclusions will be summarized as follows;

- (1) High accurate velocity components which deserve the quantitative analysis of the potential flow can be measured by a mini five-hole spherical pitot tube even around a $L = 2m$ small model.
- (2) Free surface conditions are satisfactorily linearized in the actual free surface flow not only between u and ζ but also between w and $\partial\zeta/\partial x$ respectively around the ship with least wave resistance.
- (3) The flow field analysis based upon u and w gives nearly the same results as the wave profile analysis.
- (4) No significant differences are observed with regard to the draftwise variation of the analyzed source distributions which are equivalent to the flow velocities. It implies that the assumption of the uniformity is admissible in the draftwise direction which is actually taken in the wave profile analysis.

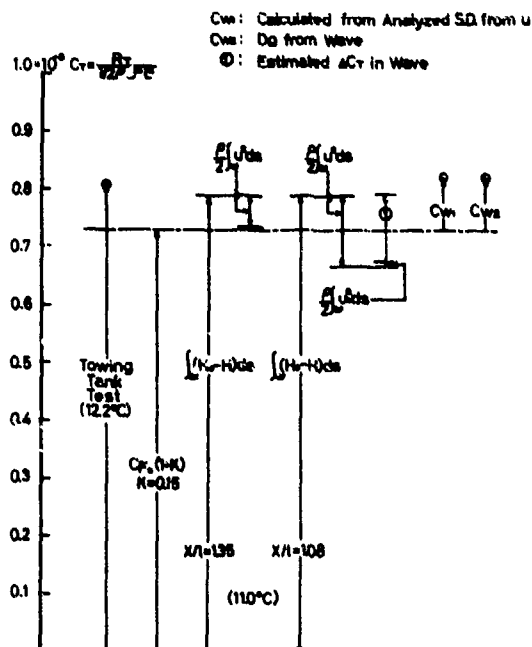


Fig. 18 Component of Viscous Resistance

- (5) The behavior of velocity component v is complicated. In the vicinity of the hull it shows rather good accordance with double model theory. At far points it coincides well with the theoretical value which includes the effect of wave terms. However in the intermediate zone of the both it does not accord with any theoretical calculations. It suggests that the further development of the more exact theory considering the sheltering effect is needed.
- (6) Wake survey is refined with the supplementary analysis of the outer potential flow field which gives the fictitious disturbance velocity in the evaluation of the viscous resistance.

ACKNOWLEDGEMENT

Mr. Shozaburo Ohkoshi (the Experimental Tank of the University of Tokyo) developed the measuring system applied to a mini five-hole pitot tube. Dr. Kazuhiro Mori (the University of Hiroshima) rendered a part of the computing programs. Both are gratefully acknowledged.

REFERENCES

1. Mori, K., Inui, T., and Kajitani, H., "Analysis of Ship-Side Wave Profile, with Special Reference to Hull's Sheltering Effect," presented at 9th Symposium on Naval Hydrodynamics, Paris, Aug. 1972.
2. Inui, T., Ohkoshi, S., Kajitani, H., and Kuzumi, S., "Measurements of Flow Velocities around a 2m Small Model by a Mini Five Hole Spherical Pitot Tube," to be presented at the Spring Meeting of Kansai Society of Naval Architects, Japan, May 1974.
3. Pien, P.C., "Five-Hole Spherical Pitot Tube," Naval Ship Research and Development Center Report 1229, 1958.
4. Maruo, H., and Hayasaki, K., "On the Transfiguration of Water Waves Propagating into a Uniform Wake," Journal of the Society of Naval Architects of Japan, Vol. 132, Dec. 1972, pp. 51-62.
5. Mori, K., "On the Singularity Distribution Representing Surface Ships," (unpublished).
6. Wehausen, J.V., "Wave Resistance of Thin Ships," Proceedings of the 1st Symposium on Naval Hydrodynamics, Washington, 1956, pp. 109-137.
7. Taniguchi, K., and Baba, E., "Study on the Separation of the Resistance Components," Proceedings of the 11th International Towing Tank Conference, Tokyo, 1966, pp. 33-35.

APPENDIX THEORETICAL FORMULAS APPLIED TO THE FLOW FIELD ANALYSIS

Let all quantities in the following equations be non-dimensionalized by $(=L/2)$, half length of the ship, and U , the velocity of the uniform flow. Then, assuming the source strength $m(\xi, \zeta)$ at $Q(\xi, 0, \zeta)$ in the centerplane of the ship as the outcoming of the volume, the disturbance velocity potential $\phi(x, y, z)$ at $P(x, y, z)$ is given by,

$$\phi(x, y, z) = \frac{1}{4\pi} \int_{-1}^1 \int_{-t}^0 m(\xi, \zeta) \cdot G(x, y, z; \xi, \zeta) d\xi d\zeta, \quad (A.1)$$

where $t(=T/l)$ denotes the immersion of the source plane. And each velocity component u, v, w is expressed as;

$$u = \frac{\partial \phi}{\partial x} = \frac{1}{4\pi} \int_{-1}^1 \int_{-t}^0 m(\xi, \zeta) \cdot \frac{\partial G}{\partial x} d\xi d\zeta, \quad (A.2)$$

$$v = \frac{\partial \phi}{\partial y} = \frac{1}{4\pi} \int_{-1}^1 \int_{-t}^0 m(\xi, \zeta) \cdot \frac{\partial G}{\partial y} d\xi d\zeta, \quad (A.3)$$

$$w = \frac{\partial \phi}{\partial z} = \frac{1}{4\pi} \int_{-1}^1 \int_{-t}^0 m(\xi, \zeta) \cdot \frac{\partial G}{\partial z} d\xi d\zeta. \quad (A.4)$$

According to the linearized theory, wave height ζ is given by,

$$\begin{aligned} \zeta &= -\frac{1}{Kol} \cdot \frac{\partial \phi}{\partial x} \Big|_{z=0} \\ &= -\frac{1}{4\pi} \cdot \frac{1}{Kol} \int_{-1}^1 \int_{-t}^0 m(\xi, \zeta) \cdot \frac{\partial G}{\partial x} d\xi d\zeta, \end{aligned} \quad (A.5)$$

where

$$Kol = \frac{gl}{U^2} = \frac{1}{2F_n^2}.$$

In all equations described above, Green function G which satisfies the linearized free surface conditions is represented as follows;

$$G = G_1 + G_2 + G_3, \quad (A.6)$$

$$G_1 = -\frac{1}{r_1} - \frac{1}{r_2}, \quad (A.7)$$

$$G_2 = -4Kol \int_{-\pi/2+\theta}^{\pi/2} \sec^2 \theta \cdot e^{-Kol \sec^2 \theta (z+\zeta)} \cdot \sin(Kol \tan \sec^2 \theta) d\theta, \quad (A.8)$$

$$\begin{aligned} G_3 &= \frac{2Kol}{\pi} \int_{-\pi/2+\theta}^{\pi/2+\theta} d\theta \int_0^\infty k \cdot e^{-kKol|\omega|} \cdot \\ &\quad \cdot \frac{\sec^2 \theta \cdot \cos(kKol \bar{z} + \zeta) - k \cdot \sin(kKol \bar{z} + \zeta)}{k^2 + \sec^4 \theta} dk, \end{aligned} \quad (A.9)$$

with

$$\begin{aligned} r_1^2 &= (x-\xi)^2 + y^2 + (z-\zeta)^2, \\ r_2^2 &= (x-\xi)^2 + y^2 + (z+\zeta)^2, \\ \vartheta &= (x-\xi) \cdot \cos \theta + y \cdot \sin \theta, \\ \Phi &= \tan^{-1}\{y/(x-\xi)\}. \end{aligned} \quad (\text{A.10})$$

Thus we have the fundamental integral equations (A.2)~(A.5) to get singularity distribution which is equivalent to each velocity component or wave height.

For numerical solution of equations (A.2)~(A.5), singularity distribution $m(\xi, \zeta)$ was expressed by the modified Fourier expansions, assuming its draft-wise uniformity:

$$\begin{aligned} m(\xi) &= \sum_{i=1}^n \{A_i \cdot \cos(i\pi \frac{1+\xi}{2}) \\ &\quad + B_i \cdot \sin(i\pi \frac{1+\xi}{2})\} \end{aligned} \quad (\text{A.11})$$

Unknown coefficients A_i and B_i were determined by the least square method.

DISCUSSION

G E GADD

These most interesting experiments certainly demonstrate in fig 5 that the linearized free surface condition is not departed from drastically on the average. However there are considerable discrepancies in some places between the measured w values and those deduced from linearized theory. Is it certain that such discrepancies have little effect on the flow? In principle it would be possible to generate a flow similar to the flow round the ship by means of a double model distribution of Rankine (non-wavemaking) sources above and below the plane $z = 0$ on the hull surface and its image, together with a further distribution of Rankine sources, outside the hull waterline, on the plane $z = 0$. Then the local source density on $z = 0$ would have to be proportional to w . From fig 5 we see that close to the hull the strengths of these imagined $z = 0$ sources could vary over a 2:1 range in certain regions, according as to whether experimental values or deduced values of w were used. Such differences in source strength would make a very considerable difference to the calculated flow over the hull.

K.W.H. EGGERS

The work presented here must be considered essential for any effective assessment of current mathematical models of ship wave flow; the research should be continued and extended under international coordination. I hope that the technique of LASER anemometry may greatly decrease the experimental effort for measuring flow velocities in the future.-

If viscosity can be disregarded, it is customary to blame either non-

linearity of the wave pattern or inaccuracies of the hull singularity system for lack of agreement between theory and experiment. In my opinion, however, neither can give an explanation for the unexpected variation of the sideways velocity v as displayed on figs. 12 and 13. But is the Havelock Green's function (A.6) really pertinent in the vicinity of the ship's water line?

In any case the zero Froude number approximation should be rejected here, as it cannot be considered as a uniform limit. The free surface here never tends to behave like a rigid one near the ship, however small the Froude number may be!

At least from a paper of Wu (Int. Shipb. Progr. 14 (1967) 88-97) and from later investigations by Dagan (JFM 49 1971 171-192) we should know that in the vicinity of the ship inertia-(i.e. displacement-) effects dominate over those of gravity, hence a high Froude number flow model is appropriate.

Expanding (A.6) asymptotically regarding k_0 one may obtain

$$G \sim -1/r_1 + 1/r_2 - 2k_0(z+y)r_2/((z+y)^2+y^2)$$

up to terms of order $O(k_0^{3/2})$.-

(this part of G is just generating that part of the wave elevation which is independent of Froude number once a source distribution depends strictly linear on U).

I sense that such an approach might help to explain the phenomena observed, and I have corresponding computations underway.-

AUTHOR'S REPLY

We sincerely appreciate the deep interest given by Dr. Gadd.

In the lower half of Fig. 5 the measured vertical velocity w is compared not with those deduced from linearized theory but with the measured wave slope $\partial\zeta/\partial x$ or the other variation $\partial u/\partial x$. Both have been obtained from the numerical differentiation of the measured wave height ζ or the disturbance velocity u . The intention of the figure is also to study the linearity of the kinematical condition at the free surface $z = \zeta(x, y)$,

$$w = (U+u) \frac{\partial \zeta}{\partial x} + v \frac{\partial \zeta}{\partial y},$$

$$\text{or } \frac{w}{U} = \frac{\partial \zeta}{\partial x} + \frac{u}{U} \frac{\partial \zeta}{\partial x} + \frac{v}{U} \frac{\partial \zeta}{\partial y}$$

Some differences observed between w and $\partial\zeta/\partial x$ or $\partial u/\partial x$ may be clearly attributed to the non-linear second and third terms of the above equation.

By the way, he points out the effect of the so called "line integral". Although we understand the importance of the effect of free surface singularities outside the hull waterline which are the primitive form of the line integral along the hull water line, we are now convincing that the study of the non-linear propagation of the free waves due to the non-uniform flow should be followed urgently.

We would like also to acknowledge Prof. Eggers' valuable discussions.

At first we expect indeed the development of the technique by Laser-Doppler measurement which can reduce the laborious works of the present experiments. Secondly he has a question whether the Havelock's Green function is (A.6) really appropriate in the vicinity of the ship's waterline to explain the particular behaviour of v revealed in Fig. 12 and 13. Mr. Adachi (Ref. 8) has also the related discussion based on his matched asymptotic expansion method (Ref. 9).

Against this problem we believe now that such particular variation of the sideways velocity v may be well rationalized by considering the outflowing of the free waves. We — including Mr. Okamura who stayed two years in the Institut für Schiffbau under Professor Eggers during his graduate course of the Univ. of Tokyo — found that Prof. Urse's theory in 1960 (Ref. 10) is quite effective. The similar idea has been introduced too by Prof. Keller (Ref. 11) just before.

We assume at first that ship waves from each part may be accumulated to the bow and stern. Then the free waves once generated at bow and stern, they propagate not on the uniform flow but on the affected double model flow which is created by the ship itself. As the result they travel shifting outward on

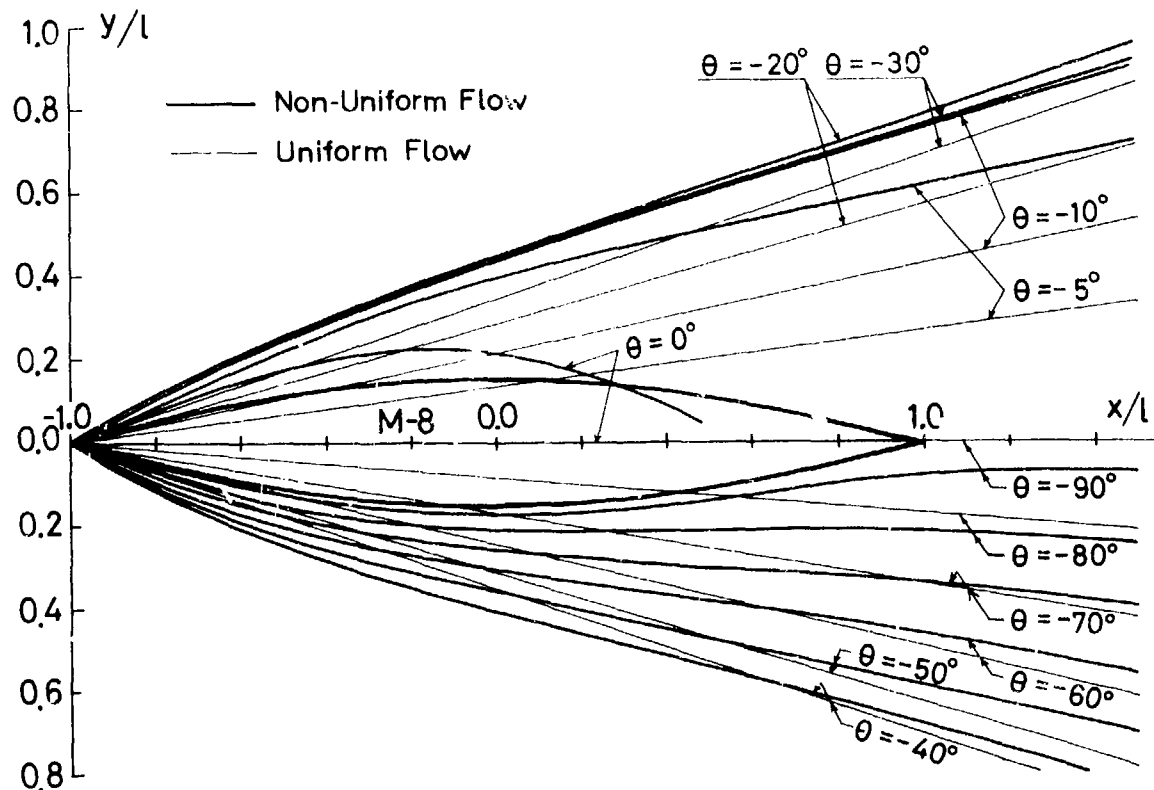


Fig.19 Propagation of Elementary Wave

the curved line near the ship, only in the region far rear the ship they propagate straightforward according to the linear theory.

We would like to show two examples calculated by Okamura (Ref. 12). Fig.19 indicates that each elementary wave having each angle of propagation corresponding to the uniform flow, propagates on a curved line always changing its angle and wavelength. Thus in the non-uniform flow the transfer of wave energy by each elementary wave is not straightforward from the bow.

As well known, the measured wave pattern has, in general, the outward and forward shift comparing with the evaluated wave pattern by linear theory. However, as shown in Fig.20, if we trace the flow of the elementary wave of $\theta = 35^\circ 16'$, for example, which corresponds to the cusp line in the linear theory, we find how it works well on the centre of the measured crest and through points and moreover how the evaluated each crest line directs well with that of the observed waves.

Although our application is few and inadequate at present we believe now that main cause of such particular outward shift of v is due to the deformation of the free waves in the non-uniform

flow. Here we would like to cease further discussions and follow the next opportunity in the near future.

FURTHER REFERENCES

8. Kitazawa, T., Inui, T. and Kajitani, H., "Flow Field Measurement and Analysis around an Inuid Model with Special Reference to Sheltering Effect," *Journal of the Society of Naval Architects of Japan*, Vol.135, June, 1974, pp. 1 - 11.
9. Adachi, H., "Higher-Order Thin-Ship Theory by Means of the Method of Matched Asymptotic Expansions," Report No.137, Dec., 1972, Dept. of Naval Arch. & Marine Eng., University of Michigan.
10. Ursell, F., "Steady Wave Patterns on a Non-Uniform Steady Fluid Flow," *Journal of Fluid Mechanics*, Vol.9, 1960, pp.333 - 346.
11. Keller, J. B., "Wave Patterns of Non-Thin or Full-Bodied Ships," presented at the 10th Naval Hydrodynamics Symposium, Massachusetts Institute of Technology, June, 1974.
12. Okamura, H., "Propagation of Ship Waves on a Non-Uniform Flow," Master's Thesis, Dept. of Naval Arch., the University of Tokyo, March, 1974.

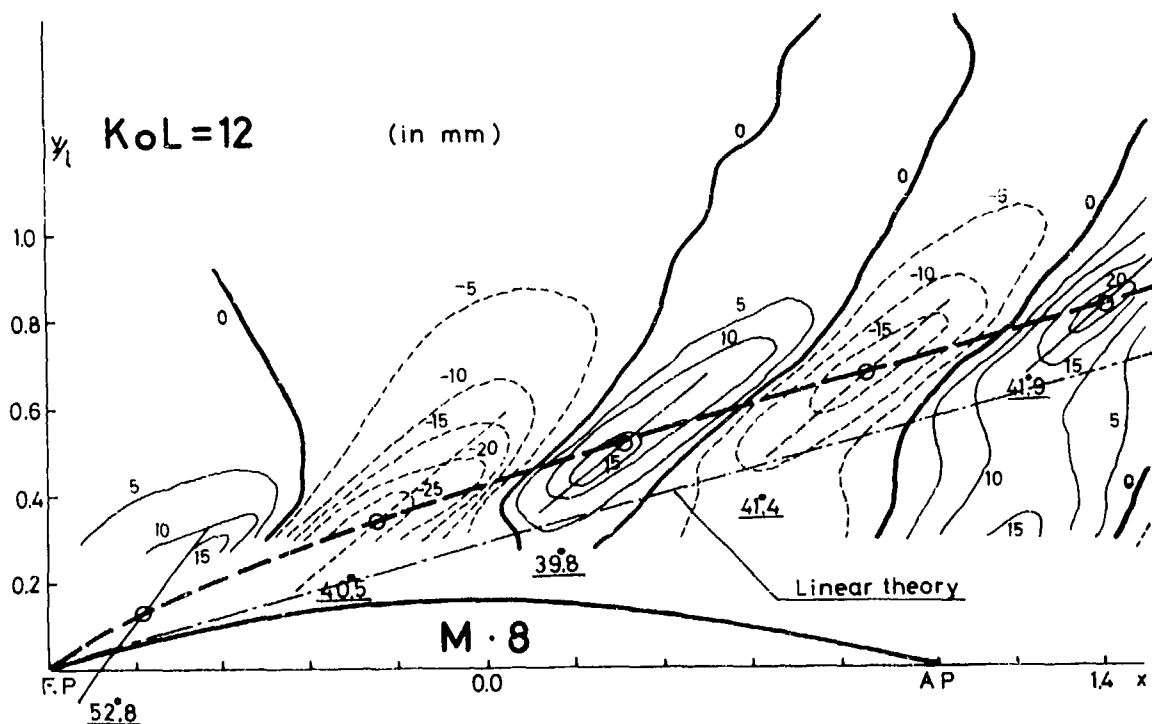


Fig.20 Calculated Cusp Line & the Measured Wave Contour (KoL=12)

NOTE ON THE REFRACTION OF HEAD SEAS BY LONG SHIPS

F. Ursell
University of Manchester, England

1. Introduction

In an earlier paper (Ursell 1968, hereafter referred to as H) it was shown that head seas cannot travel along a long cylindrical ship without deformation. The first attempt to find this deformation was made in that paper where the deformation along a thin wedge-like ship of great but finite length was considered. It was found that the amplitude of the diffracted wave near the wedge ultimately increases like $(Kx)^{1/2}$ where x is the distance from the bow along the ship; this high amplitude is confined to a horizontal layer near the ship which increases in width like $(Kx)^{1/2}$. The total wave amplitude is the sum of the incident head sea and the diffracted wave and depends on their relative phase. Arguments can be given which tend to show that the relative phase in this case depends on the wave motion near the bow, but not on the shape of the cross-section of the wedge.

A long ship of full section was considered by Faltinsen (1973) who used matched asymptotic expansions and slender-body theory. He found that the diffracted wave near the ship is ultimately equal and opposite to the incident head sea, in a layer increasing like $(Kx)^{1/2}$. Thus the total wave amplitude near a ship of full section tends ultimately to zero; we may say that the incident wave is refracted away from the ship. (The effect of forward speed was also considered by Faltinsen, but for the sake of simplicity it will not be considered in Problems 1 and 2 of the present paper.)

The arguments given in these papers were not conclusive, either for the thin ship or for the ship of full section, but they were plausible. The differences between the results in the two cases remain to be reconciled. The present note describes the results of some recent calculations which provide further evidence. In these calculations the ship is replaced by an infinitely long horizontal cylinder of constant cross-section, on which the normal velocity is suitably prescribed. (The same idea is also used to treat the refraction of the steady Kelvin pattern away from a long ship moving with constant forward speed.) For the sake of simplicity the cross-section is taken to be a half-immersed circle which could be treated comparatively simply, but the work can be generalized to an arbitrary constant cross-section.

Three problems will be considered to which the linear theory is applicable. These problems will be described in §2. In each case the

asymptotic form of the potential can be found (when $x \rightarrow +\infty$ while the distance from the axis is kept fixed), and this also will be given in §2. The details of the calculation will be submitted for publication elsewhere, but a brief outline is given in §3.

2. Statement of the problems

Let the x -axis be taken horizontal along the axis of the cylinder, the y -axis horizontal and normal to the x -axis, and the z -axis vertical (z increasing with depth). Also let cylindrical polar coordinates be defined by the equations $y = r \sin \theta$, $z = r \cos \theta$, then on the immersed part of the cylinder we have $r = a$, $-\frac{1}{2}\pi \leq \theta \leq \frac{1}{2}\pi$, $-\infty < x < \infty$.

Problem 1. Zero forward speed is assumed. On the semi-infinite stern section of the cylinder a wave-like pulsating normal velocity is prescribed while on the semi-infinite bow section the normal velocity vanishes. The resulting wave motion near the stern section is to be found; it is reasonable to hope that this motion will resemble the diffracted wave due to head seas incident on a semi-infinite ship.

In mathematical terms, the velocity potential $\phi_1(x, y, z)e^{-i\sigma t}$ of this motion is to satisfy the differential equation

$$\left(\frac{\partial^2}{\partial x^2} + \frac{\partial^2}{\partial y^2} + \frac{\partial^2}{\partial z^2}\right) \phi_1(x, y, z) = 0 \quad (2.1)$$

in the fluid, with the boundary conditions

$$\left(K + \frac{\partial}{\partial z}\right) \phi_1 = 0 \quad \text{on } z = 0, r > a, \quad (2.2)$$

$$\text{and } \frac{\partial \phi_1}{\partial r} = -h(x) \frac{\partial}{\partial r} (e^{-Kz} e^{iKx}) \quad \text{on } r = a, \quad (2.3)$$

where $K = \sigma^2/g$. The function $h(x)$ in (2.3) is such that

$$h(x) = \begin{cases} 0 & \text{when } -\infty < x \leq -l, \\ 1 & \text{when } l \leq x < \infty, \end{cases}$$

and $h(x)$ is infinitely differentiable in the interval $-l \leq x \leq l$. In the range $l \leq x < \infty$ the boundary condition (2.3) corresponds to head seas

$$\phi_{\text{inc}} e^{-i\sigma t} = e^{-Kz} e^{iKx - i\sigma t}$$

incident on a fixed semi-infinite cylinder. There is also a suitable radiation condition at infinity.

When $x \rightarrow +\infty$ while y and z are kept fixed, it is found that the principal wave component of the total wave motion $(\phi_{inc} + \phi_1)e^{-i\omega t}$ is

$$\phi_{1K}(x, y, z)e^{-i\omega t} = -\frac{1}{2\pi^2} e^{-\frac{1}{2}i\pi} \frac{\phi_*(K, y, z)}{(Kx)^{\frac{1}{2}}} e^{iKx-i\omega t},$$

where ϕ_* is the potential defined at the end of §3 below. This result is independent of $h(x)$.

Problem 2. Zero forward speed is again assumed. A pulsating normal velocity is prescribed over a finite part of the cylinder, and the wave motion near the stern section is to be found.

In mathematical terms, the velocity potential $\phi_2(x, y, z)e^{-i\omega t}$ satisfy (2.1) and (2.2), but the boundary condition on the cylinder is now

$$\frac{\partial \phi_2}{\partial r} = v(x, \theta) \quad \text{on } r = a, \quad -\frac{1}{2}\pi \leq \theta \leq \frac{1}{2}\pi, \quad (2.4)$$

where $v(x, \theta)$ is a prescribed function, which is even in θ .

When $x \rightarrow +\infty$ while y and z are kept fixed, it is found that the principal wave component is

$$\phi_{2K}(x, y, z)e^{-i\omega t} = \frac{A_2}{2} \phi_*(\cdot) e^{iKx-i\omega t}$$

where the constant A_2 depends on the details of the prescribed velocity distribution $v(x, \theta)$.

Problem 3. A constant forward speed U in the negative x -direction is assumed, and the motion is steady relative to the cylinder. The normal velocity is prescribed over a finite part of the cylinder, and the refraction of the transverse waves of the Kelvin wave pattern along the stern section is to be found.

In mathematical terms, the velocity potential is $Ux + \phi_3(x, y, z)$, where ϕ_3 satisfies (2.1), with the boundary conditions

$$(U^2 \frac{\partial^2}{\partial x^2} - g \frac{\partial}{\partial z}) \phi_3 = 0 \quad \text{on } z = 0, \quad r > a, \quad (2.5)$$

$$\text{and } \frac{\partial \phi_3}{\partial r} = v(x, \theta) \quad \text{on } r = a, \quad -\frac{1}{2}\pi \leq \theta \leq \frac{1}{2}\pi, \quad (2.6)$$

where $v(x, \theta)$ is a prescribed function, which is even in θ . (It will be observed that (2.5) is the usual free-surface condition of thinship theory but it is not difficult to see that it applies equally to the present problem.)

When $x \rightarrow +\infty$ while y and z are kept fixed, it is found that the principal wave component is

$$\phi_{3K_0}(x, y, z) = \frac{A_3}{x^2} \phi_*(K_0, y, z) \cos(K_0 x + \varepsilon_3),$$

where $K_0 = g/U^2$, and where the constants A_3 and ε_3 depend on the details of the prescribed velocity distribution $v(x, \theta)$.

3. Outline of the mathematical method

The same method of calculation is applicable to all three problems. Only an outline will be

given here, the full details will be published elsewhere. For the sake of definitiveness, let us consider Problem 2. The equation of motion (2.1) and boundary conditions (2.2) and (2.4) have already been given. There is also the radiation condition which states that ϕ_2 represents outward travelling waves at infinity. The suffix 2 and the time-factor $e^{-i\omega t}$ will henceforth be omitted.

It is then not difficult to see that the Fourier transform

$$\phi(k, y, z) = \int_{-\infty}^{\infty} \phi(x, y, z) e^{-ikx} dx$$

satisfies the differential equation

$$\left(\frac{\partial^2}{\partial y^2} + \frac{\partial^2}{\partial z^2} - k^2 \right) \phi(k, y, z) = 0 \quad (3.1)$$

in the fluid, with boundary conditions

$$\left(K + \frac{\partial}{\partial z} \right) \phi = 0 \quad \text{on } z = 0, \quad r > a, \quad (3.2)$$

$$\text{and } \frac{\partial \phi}{\partial r} = \int_{-\infty}^{\infty} v(x, \theta) e^{-ikx} dx = V(k, \theta) \quad \text{on } r = a, \quad (3.3)$$

together with a radiation condition. Thus $\phi(k, y, z)$ is the solution of a two-dimensional boundary value problem in which k is a parameter. The same boundary-value problem (with $|k| < K$) also occurs in the calculation of the diffraction of an oblique sea by a long cylinder; see Bolton and Ursell (1973). It is known that the solution for any real k can be expressed as the sum of a wave-source potential

$$\psi_0(|k|, y, z) = 2 \int_0^{\infty} \frac{|k| \cosh \mu}{|k| \cosh \mu - K} e^{-|k|z \cosh \mu} \cos(|k|y \sinh \mu) d\mu,$$

(with an appropriate path of integration avoiding the pole when $|k| < K$) and of wave-free potentials

$$\begin{aligned} \psi_{2m}(|k|, y, z) = & K_{2m}(|k|r) \cos 2m\theta + \frac{2K}{|k|} K_{2m-1}(|k|r) \cos(2m-1)\theta \\ & + K_{2m-2}(|k|r) \cos(2m-2)\theta, \quad m = 1, 2, 3, \dots \end{aligned}$$

$$\text{Thus } \phi(k, y, z) = p_0(k) \psi_0(|k|, y, z) + \sum_{m=1}^{\infty} p_{2m}(k) \frac{\psi_{2m}(|k|, y, z)}{K_{2m}(|k|a)}. \quad (3.4)$$

The coefficients $p_0(k)$, $p_{2m}(k)$ can be found in principle by applying the boundary condition (3.3) on the semi-circle, but they cannot be found explicitly. It is assumed that Ka is neither large nor small.

We shall also need to consider the corresponding problem for head seas ($|k| = K$) which was treated at length in H. The equation

$$\left(\frac{\partial^2}{\partial x^2} + \frac{\partial^2}{\partial y^2} - K^2 \right) \phi(K, y, z) = 0$$

with the boundary conditions (3.2) and (3.3) can then be solved by means of a similar series, but there is now no radiation condition, and the source function (ψ_{00} , say; cf. H, eqn. A.1.1) is unbounded at infinity. The term (3.4) must then be replaced by the sum of the two terms

$$p_{00} \psi_{00}(K, y, z) + p_{01} e^{-Kz}$$

containing an additional arbitrary constant p_0 . It can then be shown that there is a unique potential $\phi_*(K, y, z)$ satisfying

$$\left(\frac{\partial^2}{\partial y^2} + \frac{\partial^2}{\partial z^2} - K^2\right)\phi_*(K, y, z) = 0$$

in the fluid, with the boundary conditions

$$\frac{\partial \phi_*}{\partial r} = 0 \quad \text{on } r = a, \quad -\frac{1}{2}\pi \leq \theta \leq \frac{1}{2}\pi$$

$$\frac{\partial \phi_*}{\partial z} + K\phi_* = 0 \quad \text{on } z = 0, \quad r > a,$$

and the normalization

$$\phi_*(K, y, z) \sim -2\pi K|y|e^{-Kz} \quad \text{as } |y| \rightarrow \infty.$$

We observe that ϕ_* is unbounded as $|y| \rightarrow \infty$. The potential $\phi_*(K, y, z)$ plays an important part in describing the waves in our problem, in the region where $|y|$ is not large and $x \rightarrow +\infty$.

4. The form of the potential for large x

We have just seen how the Fourier transform $\phi(k, y, z)$ can be determined in principle for all real k . The velocity potential is then given by

$$\phi(x, y, z) = \frac{1}{2\pi} \int_{-\infty}^{\infty} \phi(k, y, z) e^{ikx} dk, \quad (4.1)$$

and is thus also determined in principle but cannot easily be found in practice because $\phi(k, y, z)$ is not known explicitly. We shall however be mainly concerned with the form of the waves near the stern section, i.e., the region where y and z are bounded and $x \rightarrow +\infty$. Asymptotic techniques are then applicable to (4.1). The principal contributions come from values of k at which $\phi(k, y, z)$ or one of its derivatives ceases to be a regular function of k . (cf. Lighthill 1958.) On physical grounds we expect the dominant wave number to be $k = K$, and it can be shown that at this wave number the function $\phi(k, y, z)$ is indeed not regular. It will be assumed that $\phi(k, y, z)$ is regular at all other wave numbers except at $k = 0$. (The contribution from $k = 0$ is evidently not wavelike and will not be considered further.)

The calculation of $\phi(k, y, z)$ near $k = K$ involves a lengthy and detailed consideration of the coefficients $p_0(k)$, $p_{2m}(k)$ defined in (3.4) above, but the result is simple and is here quoted without proof. It is found that, near $k = K$,

$$\begin{aligned} \phi(k, y, z) = & \text{regular function of } k \\ & + \frac{a\Gamma_0}{2\pi} \left(\frac{2}{K}\right)^{\frac{1}{2}} (k-K)^{\frac{1}{2}} \phi_*(K, y, z) \\ & + \text{smaller terms} \end{aligned} \quad (4.2)$$

when $k > K$: when $k < K$, the factor $(k-K)^{\frac{1}{2}}$ must be replaced by $-i(K-k)^{\frac{1}{2}}$. In this expression the function ϕ_* is the potential defined at the end of §3. The multiplier is the coefficient of $\langle a(\partial/\partial r)e^{-Kz} \rangle_{r=a}$ in the expansion

$$\begin{aligned} V(k, \theta) = & \int_{-\infty}^{\infty} v(x, \theta) e^{-iKx} dx \\ = & \Gamma_0 \left\langle a \frac{\partial}{\partial r} e^{-Kz} \right\rangle_{r=a} \\ & + \sum_{m=1}^{\infty} \Gamma_{2m} \frac{1}{K_{2m}'} (Ka) \left\langle a \frac{\partial \psi_{2m}}{\partial r} \right\rangle_{r=a}, \end{aligned}$$

and thus it depends on the details of the prescribed normal velocity distribution $v(x, \theta)$, see eqn. (2.4) above. (If the actual value of Γ_0 is needed it will be necessary to solve an infinite system of equations in an infinite number of unknowns.)

On substituting in (4.1) it is now found that the dominant wave component for large x and bounded y and z is

$$\phi_K(x, y, z) = - (2\pi)^{-\frac{3}{2}} e^{-\frac{1}{2}i\pi} a \Gamma_0 \frac{\phi_*(K, y, z) e^{iKx}}{K^{\frac{1}{2}} x^{\frac{3}{2}}}$$

where $\phi_*(K, y, z)$ is defined at the end of §3 above. The square-root behaviour in (4.2) is due to a square-root singularity in the expansion of the source potential ψ_0 .

5. Discussion and Conclusions

In this note we have been considering the effect of a long cylinder on waves travelling in the axial direction. In our first problem, which correspond to head seas, the amplitude near the stern section decayed like $x^{-\frac{1}{2}}$ whereas head seas travelling along a plane vertical wall do not decay. (Along a wedge they even increase.) In our second problem the waves were generated by a pulsating normal velocity and decayed like $x^{-\frac{3}{2}}$; the corresponding decay along a plane vertical wall is x^{-1} . In our third problem a Kelvin pattern was generated by a prescribed normal velocity travelling with constant velocity and the transverse waves near the cylinder decayed like $x^{-\frac{1}{2}}$, whereas the Kelvin pattern near a plane wall (or in open water) decays like x^{-1} . In each of these three cases the decay is more rapid than near a plane wall, i.e., the wave pattern is refracted away from the cylinder. The width of the comparatively wave-free zone tends to ∞ as x tends to ∞ . These results were obtained for a cylinder of semi-circular cross-section but can be generalized to arbitrary (constant) cross-sections by formulating the problems in terms of integral equations, as in H. The result for our first problem is consistent with the results of Faltinsen (1973) which, as we now see, must represent the asymptotic behaviour of the waves when $x \rightarrow \infty$ in directions close to the axial direction.

We still have to discuss the thin-ship result obtained in H. It has just been noted that in Problem 2 the amplitude decays like $x^{-\frac{1}{2}}$ along a cylinder, like x^{-1} along a plane wall. It is reasonable to suppose that the rate of refraction depends on the wave-length as well as on the cross-section. When Ka is large, it may be conjectured that the refraction is small and only becomes effective at very large distances; when Ka is small or moderate, on the other hand, the effect of the curvature of the cross-section is felt even in the vicinity of the source. (Similar results would be expected in the other two problems.) It would be interesting to extend our calculation to large and to small values of Ka .

Our conclusions in each case depend on the analytical form of $\phi(k, y, z)$ near a critical wave number, e.g. on eqn. (4.2) above. The simplicity of that expression is in contrast with the involved method of derivation, and a simpler derivation would be desirable.

REFERENCES

Bolton, W.E. and Ursell, F. "The wave force on an infinitely long circular cylinder in an oblique sea," J. Fluid Mechs., 57, 1973, 241-256.

Faltinsen, O.M. "Wave forces on a restrained ship in head-sea waves," Oslo, Det Norske Veritas, Publication No. 80, 1973, 42pp.

Lighthill, M.J. "Fourier Analysis and Generalised Functions," Cambridge University Press, 1958.

Ursell, F. "On head seas travelling along a horizontal cylinder," J. Inst. Math. Applicns., 4, 1968, 414-427. (This paper is referred to as H.)

DISCUSSION

T.F. OGILVIE

Professor Ursell started out to provide a better foundation for some important results obtained by Faltinsen several years ago. He not only did what he set out to do, but he has gone much further and provided the most nearly rigorous analysis yet of the way in which a long ship hull diffracts the waves generated by the ship itself in steady forward motion. This is a phenomenon that has been observed frequently over the years: The waves alongside the hull are much smaller near the stern than predicted by linear ideal-fluid theory. This is sometimes called "sheltering effect" by naval architects.

Many years ago, there was an idea that the observed attenuation of waves near the stern is an effect somehow caused by the presence of a boundary layer. More recently, there have been several attempts to describe it as an effect of nonlinearity in the thin-ship model. Now Professor Ursell has shown that the bow-generated waves decay as $x^{-3/2}$ along the length of the parallel middle body, not $x^{-1/2}$, as in thin-ship theory. And he has done this with a completely linear mathematical model.

Two questions now arise: 1) Does his mathematical model agree quantitatively with reality? 2) Does the presence of the boundary layer play any role at all in this phenomenon?

With respect to the first question, the answer is affirmative to a degree. Adachi (Ship Research Institute, Tokyo) measured the ship-generated wave field near a very long, slender model. His model was a 3.5 m. "Inuid," which had been cut in two, with 20 m. of parallel middle-body inserted between the ends. Along a path I, as in the figure, he measured the amplitude of the transverse waves and found that they decayed approximately as $x^{-1.34}$; this observation seemed to be independent of speed. This result does not quite agree with Professor Ursell's prediction ($x^{-1.5}$),

but it is much farther from the thin-ship prediction ($x^{-0.5}$).

Along a path such as II, Adachi found that the amplitude of the transverse waves increased very nearly linearly with distance laterally, and this is just what Professor Ursell predicts.

Adachi found that the transverse waves were shifted forward about 70° with respect to the thin-ship prediction. It is not obvious what Professor Ursell predicts in this aspect, but his result for "Problem 2" suggests that he has a 45° phase shift, which is not in complete agreement with the experiments but is much better than thin-ship theory.

The less-than-perfect agreement between experiments and theory may suggest an answer to my second question, concerning the effect of the boundary layer. Consider that the observed decay rate is *less* than that predicted by the ideal-fluid theory. No one would be surprised if the real-fluid waves decayed more rapidly than predicted, but to have them decay less rapidly is surprising indeed! One must conclude that there is yet another source of waves, and it might be the increasing effective body cross-section in the downstream direction, caused by the displacement thickness of the boundary layer. The underestimate of phase shift might have a similar explanation.

I would like to speculate one step further. Adachi also made measurements with his basic 3.5 m. "Inuid," and he found that the rate of decay of wave amplitude near the track was very sensitive to speed, somewhat as indicated for the "short model" in the figure. The value of the decay power was close to 0.5 for speeds at which there was maximum interference between bow and stern waves, i.e., when transverse waves were smallest. And, conversely, the decay was greatest when the bow/stern interference was constructive. This suggests that the transverse waves can also be diffracted away by a rotational wake, as well as by a solid body.

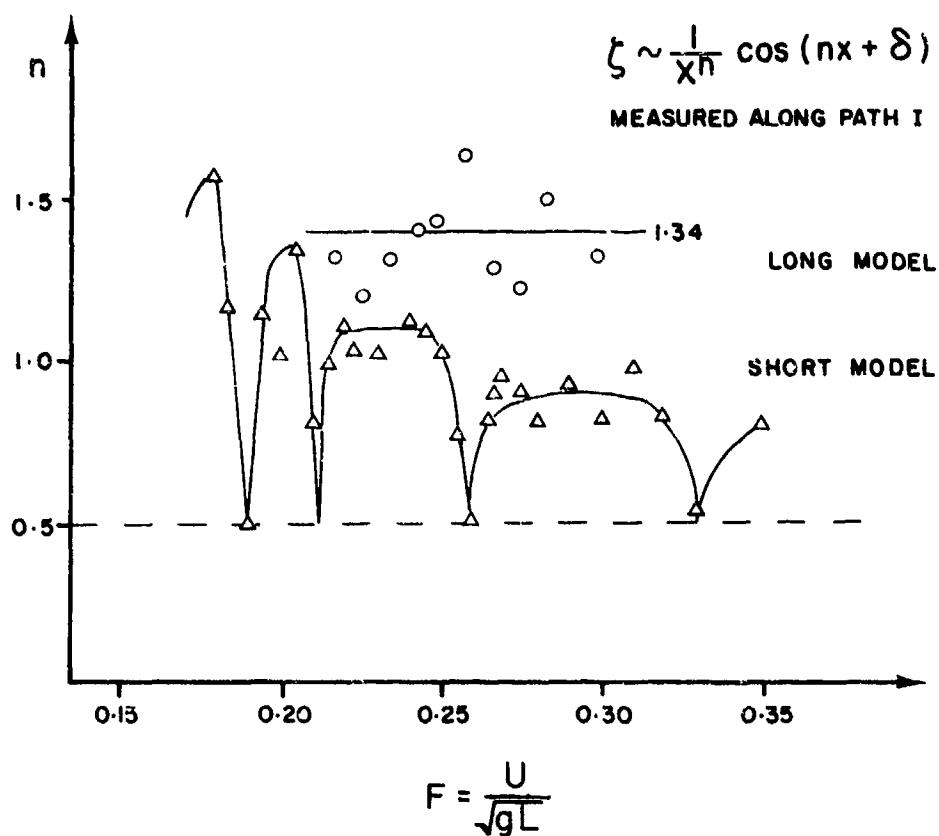
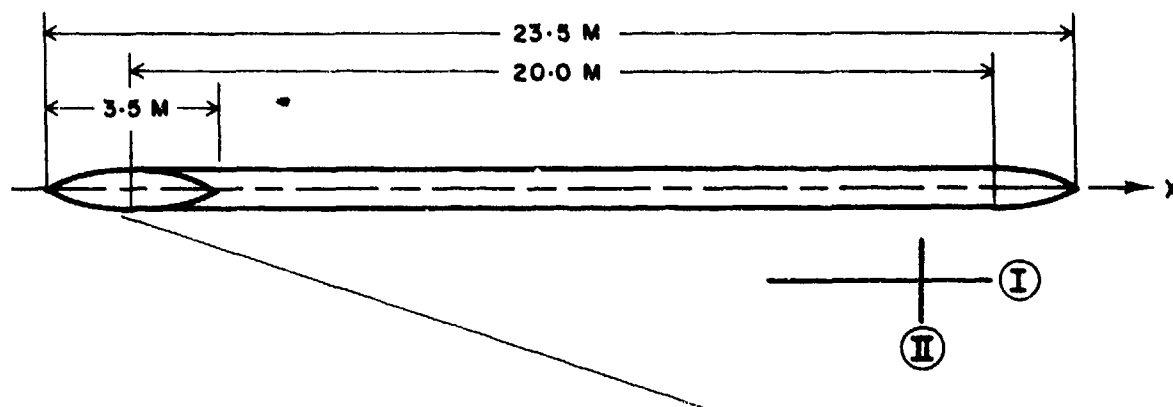


Fig. 1 Data from Adachi's Tests
F is based on length of short model

AUTHOR'S REPLY

I am grateful to Professor Ogilvie for bringing to my attention the measurements of Adachi. Although these show better agreement with the present theory than with thin-ship theory the discre-

pancies are still significant. Professor Ogilvie's remarks point out directions in which improvements to the theory may be sought and will be helpful to theoreticians.

OSCILLATIONS AND WAVE FORCES IN A MAN-MADE HARBOR IN THE OPEN SEA

H. S. Chen
MIT
Cambridge, Massachusetts

C. C. Mei
MIT
Cambridge, Massachusetts

ABSTRACT

Motivated by the Power Plant Project of Public Service Electric and Gas Company of New Jersey, a numerical method using finite elements is developed for computing waves and wave forces inside an offshore harbor in communication with the open sea. A mixed method is used whereby the far field and the neighborhood of the tip of a thin breakwater, if any, are represented analytically, and the remaining fluid region is treated by finite element approximation. A comparison with analytic solutions to problems of simple geometry is used to guide the choice of the element size. Mean harbor response and exciting forces on the platform have been calculated for the case of uniform depth where all solid objects are vertical-walled and bottom-seated, and for the case of shallow water waves using the approximate formulation of John.

This method is an effective tool for diffraction problems involving complex geometry.

NOMENCLATURE

a	radius of a semi-circular harbor
a_0	incident wave amplitude
A	region under the free surface
A	normalized root mean square of harbor response or amplification factor
B	breakwaters or solid bodies
F	region under the stationary platform
F	stationary functional
$\partial A, \partial B, \partial D, \partial F$	boundaries of A, B, D, F
h	still water depth under the free surface
H	vertical clearance underneath the platform
I_1, \dots, I_9	integrals
J_n, K_n, H_n	Bessel functions with $u \equiv H_n^{(1)}$
k	wave number
K, K_I, \dots, K_{IV}	coefficient matrices

F_x, F_y, F_z	amplitude of exciting forces
f_x, f_y, f_z	normalized exciting forces
$ f_x , f_y , f_z $	magnitude of f_x, f_y, f_z
L	length of an arc element on the circle ∂A
ℓ_1, ℓ_2	horizontal dimensions along (x, y) of the platform
M_x, M_y, M_z	amplitudes of exciting moments
P	spatial factor of dynamic pressure
r	radial coordinate
r_A, r_R, r_D	radius of circles $\partial A, \partial R$ and ∂D
t	time
u, v	spatial factor of horizontal velocities
x, y	horizontal coordinates
z	vertical coordinate
α_n, β_n	coefficients of eigenfunctions
ϵ_m	Jacobi symbols
λ	incident wave length
$\underline{\mu}$	vector formed by α_n, β_n
η	free surface displacement
θ	angle variable in polar coordinates
θ_0	angle sustained by harbor entrance
ω	radian frequency
$\underline{\phi}$	vector formed by nodal potentials
$\underline{\psi}$	total unknown vector

Superscripts

$()^I$	of the incident wave
$()^T$	transpose of
$()^*$	of an element

Subscripts

$()_A, ()_D, ()_F, ()_R$	of regions A, D, F, R respectively
\hat{n}_A	unit normal to the boundary of and outward from A
$()_E$	of the even problem (appendix)
$()_O$	of the odd problem (appendix)

INTRODUCTION

This research is a part of the study undertaken for the offshore nuclear power plant project initiated by the Public Service Electric and Gas Company, Newark, New Jersey. To reduce environmental objections, Public Service Company plans to locate two 1150 MWe nuclear power plants on floating platforms at a site 3 miles off the coast near Atlantic City. The floating platforms will be prefabricated by Offshore Power Systems, Jacksonville, Florida. The protecting breakwater system is designed by F.R. Harris Consulting Engineers of New York, and consists of a semi-circular breakwater facing the sea and a straight enclosure breakwater facing the coast. The local depth is averaged at 40 ft. Two openings are designed so that the velocity of the intake water will not exceed 1 fps in order to minimize fish trapping, Fig. 1

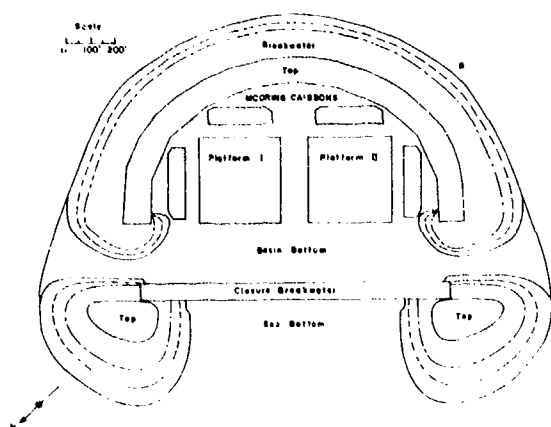


Fig. 1 General Plan of Atlantic Offshore Harbor

Along with several other research groups, the Department of Civil Engineering at M.I.T. is currently involved in studying aspects of thermal discharge (under Professor D.R.F. Harleman) and wave protection problems. In this paper, results of some preliminary theoretical studies are reported. The primary objectives are to study the oscillation in the basin due to incident waves and the associated wave forces on the platforms. The height of the breakwaters is 104 ft., and was chosen based on the estimated storm waves of 16 sec. period and of 40 ft. wave height. Comprehensive laboratory tests modeling the *large amplitude* motions in the storm wave range are now being undertaken at the University of Florida under Professor R.G. Dean. Our effort aims at theoretical predictions for *infinitesimal* waves but for a broad range of wave periods ranging from very long tsunamis to short storm waves so as to provide more information for safety considerations. Special emphasis is on possible resonances in the basin. As is well known in harbor oscillation studies, the cost of a laboratory model which must simulate an infinite ocean increases, while that of numerical modeling decreases, with increasing wave

period. It is therefore hoped that the two approaches complement each other and confirm each other in the regions where both can be employed.

In the storm wave range a mean set-up of 25 feet in the neighborhood of the site has been given as a part of the basic data; the total water depth is such that the ratio of 2π depth to wavelength, i.e., kh , is of the order unity. Furthermore, the clearance under the platforms and the slope of the outside face of the breakwater requires a full three-dimensional treatment without restriction of kh , even in the context of linearized theory. While this is being pursued, the material presented herein is based on the linearized long wave theory, which is a two-dimensional approximation and has been used for ordinary harbors with a straight coast. Although its application to the complex geometry of the platform-harbor system leads to inaccuracy, it is hoped that the results give a useful guide in order-of-magnitude and provide a starting point for the much more complicated three-dimensional computations to be carried out. It is also hoped that our technique provides an efficient alternative to existing numerical methods for harbor analysis in particular [1, 2], and diffraction studies in general.

The technique chosen is the finite element method which is well known in structural mechanics and recently used in essentially two-dimensional water wave diffraction problems by Berkhoff [3] and Bai [4]. These problems include linearized shallow water wave problems, two-dimensional (vertical and horizontal) problems for arbitrary depth or three-dimensional problems involving axial symmetry. Since in most structural problems the physical region is of finite extent while in water waves the region is infinite, for the sake of efficiency, some modification of the usual technique is needed to localize the numerical computation only in the region of direct interest and of complex geometry. For water wave diffraction, Berkhoff applied the finite element discretization within a circular region enclosing the scatterer, while representing analytically the solution outside the circle by a source distribution along the circle. This idea of combining numerical and analytical means is very similar to the mixed approach in elastic crack problem [5] and is also adopted here with some improvement in detail. Related application to other geometries where the analysis is, or can be reduced to, a two-dimensional one involving a vertical coordinate, can be found in [6]. Consideration of singularity near the tips of thin breakwaters and of a coastline is also included so that the present method is easily applicable to very general harbor-coast configuration. Diffractions of long waves by submerged islands, which is an interesting problem because of possible energy trapping [7] and radiation of waves by moving bodies in shallow water, can also be calculated effectively by this technique.

In the appendix, an analytic theory for a harbor bounded by a straight wall and a semi-

circular breakwater is given with a view to providing a comparison with and a guide for the finite element analysis.

FORMULATION

The following simplifying assumptions are made:

- (1) Irrotational flow in an inviscid incompressible fluid
- (2) Infinitesimal amplitude
- (3) Simple harmonic motion with radian frequency ω
- (4) Lateral boundaries (breakwaters, coast, etc.,) are vertical and perfectly reflective
- (5) Constant depth at great distances from the scatterer.

Due to simple harmonic time dependence, the time factor $e^{-i\omega t}$ is assumed for all dependent variables and discussions will be limited to the spatial factor only. For example $\eta(x,y)$ represents the complex amplitude of the free surface displacement, i.e.

$$\text{free surface displacement} = \text{Re } \eta e^{-i\omega t}$$

In the absence of floating bodies, the boundary value problem can be reduced to a two-dimensional one either for a shallow water of variable depth or for an arbitrary but constant depth, as summarized below.

Linearized Long Wave Theory for Variable Depth

Under the free surface denoted by region A, the fluid velocity is approximately horizontal with components $u(x,y)$, $v(x,y)$. The dynamic pressure (total + $\rho g z$) is simply

$$p = \rho g r \quad (1)$$

or

$$P_{\text{total}}(x,y,z,t) = \rho g (\eta e^{-i\omega t} - z) \quad (2)$$

Introducing a velocity potential $\phi(x,y)$

$$u, v = \phi_x, \phi_y \quad (3)$$

it is known that

$$\eta = \frac{i\omega}{g} \phi \quad (4)$$

and ϕ is governed by the following equation

$$\nabla \cdot (h \nabla \phi) + \frac{\omega^2}{g} \phi = 0 \quad x, y \text{ in } A \quad (5)$$

On a solid vertical boundary ∂B extending throughout the water depth

$$\frac{\partial \phi}{\partial n} = 0 \quad x, y \text{ on } \partial B \quad (6)$$

An incident wave is assumed to arrive from infinity where the depth is constant, in the direction which makes an angle α with the x-axis (Fig. 2). In polar coordinates the potential and the free surface displacement are given by

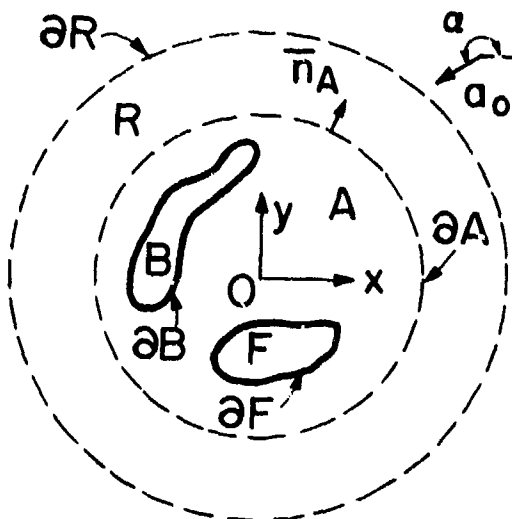


Fig. 2 Definition Sketch

$$\phi^I = -\frac{iga_0}{\omega} e^{ikr} \cos(\theta - \alpha) \quad (7.a)$$

$$\eta^I = a_0 e^{ikr} \cos(\theta - \alpha) \quad (7.b)$$

with

$$k = \omega(gh)^{-1/2} \quad (8)$$

The scattered wave $\phi - \phi^I$ must behave as an outgoing wave at infinity, i.e.,

$$\lim_{kr \rightarrow \infty} \sqrt{r} \left(\frac{\partial}{\partial r} - ik \right) (\phi - \phi^I) = 0 \quad (9)$$

For the purpose of predicting exciting forces we assume the platforms to be stationary. Because of the gap under the bottom of the platforms the local flow should be treated three-dimensionally. For simplicity, we invoke the shallow water approximation due to F. John (see Stoker [8, p. 414 ff] who studied a finite dock in shallow water. It can be shown that under the fixed platforms (denoted by the region F) the two-dimensional velocity potential is governed by

$$\nabla \cdot (H \nabla \phi) = 0 \quad (x, y) \text{ in } F \quad (10)$$

where $H(x,y)$ is the vertical clearance under the platform. The total pressure in the fluid is

$$P_{\text{total}}(x,y,z,t) = i\omega\phi e^{-i\omega t} - \rho g z \quad (11)$$

so that the dynamic pressure, omitting the time factor, is

$$p = i\omega\rho\phi \quad (12)$$

Along the edge of the platform (∂F) we require the continuity of pressure and normal volume flux

$$[\phi]_F = [\phi]_A \quad (13)$$

x, y on ∂F .

$$[h \frac{\partial \phi}{\partial n}]_A = [h \frac{\partial \phi}{\partial n}]_F \quad (14)$$

Linearized Theory for Constant but Arbitrary Depth

In order to avoid three-dimensional analysis we treat the case where all solid bodies rest on the sea bottom. In case of large draft of the platforms, this assumption should be relevant for very short waves (large kh). The three-dimensional velocity potential defined by

$$u, v, w = \phi_x, \phi_y, \phi_z \quad (15)$$

can be related to the free surface displacement by

$$\phi(x, y, z) = -\frac{ig\eta}{\omega} \frac{\cosh k(z+h)}{\cosh kh} \quad (16)$$

The free surface displacement is proportional to the potential at the free surface

$$\phi_0 \equiv \phi(x, y, 0) = -\frac{ig}{\omega} \eta(x, y) \quad (17)$$

which satisfies the Helmholtz equation

$$\nabla^2 \eta + k^2 \eta = \nabla^2 \phi_0 + k^2 \phi_0 = 0, \quad x, y \text{ in } A \quad (18)$$

with

$$\omega^2 = gk \tanh kh \quad (19)$$

Along solid lateral boundaries ∂B we still have

$$\frac{\partial \eta}{\partial n} = \frac{\partial \phi_0}{\partial n} = 0, \quad x, y \text{ on } \partial B \quad (20)$$

At infinity the radiation condition, Eq. (9) is also required. The dynamic pressure in the fluid is

$$p = i\omega\rho\phi = \rho g\eta \frac{\cosh k(z+h)}{\cosh kh} \quad (21)$$

Clearly in the case where all solid bodies rest on the sea bottom and the depth h is constant throughout, the boundary value problems for the long and arbitrary wavelengths are virtually the same (cf (5) and (13)), the dispersion relation (8) being a limiting case of (19).

THE VARIATIONAL PRINCIPLE¹

In most existing examples of finite element methods, the physical region is bounded. In the present case the fluid region is infinite and it is desirable to limit the sub-division into elements only in a finite region of practical interest. This is possible if outside a certain region of large radius, the depth is constant and there is no solid body present, so that the solution for the radiated waves can be easily represented in analytical form. A variational principle will now be derived which enables one to localize the numerical analysis only within this region. The basic idea is similar to that used in fracture mechanics involving cracks, where one treats the neighborhood of a singular point analytically and the remaining region numerically. Let the original domain A be divided into A and R by the circle ∂A as in Figure 2. Along ∂A and outside the depth is constant. We now assume that the formal solution for ϕ in R is already found which satisfies Eq. (5) with $h = \text{constant}$ and the radiation condition along ∂R which is a circle of great radius r_R at infinity. This solution still contains unknowns which must be determined by matching with the potential in A across ∂A , i.e.,

$$(\phi)_A = (\phi)_R, \quad \left(\frac{\partial \phi}{\partial n_A}\right)_A = \left(\frac{\partial \phi}{\partial n_A}\right)_R \quad (22)$$

for (x, y) along ∂A where \vec{n}_A represents the unit normal pointing outward from region A and $(\phi)_A$ and $(\phi)_R$ represent respectively the values of the potential in regions A and R , etc. Note that the radiation condition is now imposed on $(\phi)_R$ instead of $(\phi)_A$.

Case of Long Waves Over Variable Depth

To fix the ideas we first adopt the long wave formulation and assume that all solid bodies rest on the sea bottom and are referred to collectively as B . Let us define the functional

$$\begin{aligned} F\{\phi\} = & \iint_A \frac{1}{2} [h(\nabla\phi)^2 - \frac{\omega^2}{g} \phi^2] \\ & - \iint_R \frac{1}{2} \{h[\nabla(\phi - \phi^I)]^2 - \frac{\omega^2}{g} (\phi - \phi^I)^2\} \\ & - \int_{\partial A} h(\phi - \phi^I)_A \left(\frac{\partial \phi}{\partial n_A}\right)_R \\ & + \int_{\partial R} \frac{1}{2} ikh(\phi - \phi^I)^2 \end{aligned} \quad (23)$$

¹Expert advice from Professor P. Tong has been invaluable to the formulation here.

where for brevity, we omit the symbols dA for the area element in all area integrals and ds for the line element in all line integrals. Note that the third integral contains potentials from both sides of the contour ∂A . We shall now extremize $F(\phi)$ among all trial functions ϕ . Taking the first variation and applying Gauss' theorem, we note that a typical area integral over an area A' can be written in two alternate forms

$$\begin{aligned} \delta \iint_{A'} \frac{h}{2} (\nabla \phi)^2 &= \iint_{A'} h \nabla \phi \cdot \nabla \delta \phi \\ &= \iint_{A'} [\nabla \cdot (h \delta \phi \nabla \phi) - \delta \phi \nabla \cdot (h \nabla \phi)] \\ &= - \iint_{A'} \delta \phi \nabla \cdot (h \nabla \phi) + \int_{\partial A'} \delta \phi h \frac{\partial \phi}{\partial n} \end{aligned} \quad (24.a)$$

or

$$\begin{aligned} &= \iint_{A'} [\nabla \cdot (\phi h \nabla \delta \phi) - \phi \nabla \cdot (h \nabla \delta \phi)] \\ &= - \iint_{A'} \phi \nabla \cdot (h \nabla \delta \phi) + \int_{\partial A'} \phi h \frac{\partial \delta \phi}{\partial n} \end{aligned} \quad (24.b)$$

where A' is any fluid domain with $\partial A'$ as its boundary and \vec{n} as its outward unit normal. In Eq. (23), applying Eq. (24.a) to the area integral over A and Eq. (24.b) to the area integral over R and noting that $\delta \phi^I = 0$, we have

$$\begin{aligned} \delta F &= - \iint_A \delta \phi [\nabla \cdot (h \nabla \phi) + \frac{\omega^2}{g} \phi] \\ &+ \int_{\partial A + \partial R} (\delta \phi)_A \left(h \frac{\partial \phi}{\partial n} \right)_A \\ &+ \iint_R (\phi - \phi^I) \{ \nabla \cdot [h \nabla \delta(\phi - \phi^I)] + \frac{\omega^2}{g} \delta(\phi - \phi^I) \} \\ &- \int_{\partial A + \partial R} (\phi - \phi^I)_R h \left(\frac{\partial \delta(\phi - \phi^I)}{\partial n} \right)_R \\ &- \int_{\partial A} (\phi - \phi^I)_A h \left(\frac{\partial \delta \phi}{\partial n} \right)_R \end{aligned}$$

$$\begin{aligned} &- \int_{\partial A} [\delta(\phi - \phi^I)]_A h \left(\frac{\partial \phi}{\partial n} \right)_R \\ &+ \int_{\partial R} [\delta(\phi - \phi^I)]_R h (\phi - \phi^I)_R. \end{aligned}$$

Using the facts that

- (1) $\partial/\partial n_A = -\partial/\partial n_R$ along ∂A
- (2) $\delta \phi^I = 0$
- (3) $\delta(\phi - \phi^I)_R$ satisfies Eqs. (5) and (9) exactly since $(\phi - \phi^I)_R$ already does

we obtain

$$\begin{aligned} \delta F &= - \iint_A \delta \phi [\nabla \cdot (h \nabla \phi) + \frac{\omega^2}{g} \phi] + \int_{\partial B} \delta \phi \left(h \frac{\partial \phi}{\partial n} \right)_A \\ &+ \int_{\partial A} [\delta \phi]_A \left[\left(h \frac{\partial \phi}{\partial n} \right)_A - \left(h \frac{\partial \phi}{\partial n} \right)_R \right] \\ &+ \int_{\partial A} [(\phi)_R - (\phi)_A] \left(h \frac{\partial \delta \phi}{\partial n} \right)_R \end{aligned} \quad (25)$$

It follows therefore that for $\delta F = 0$, Eq. (5) must be satisfied as the Euler-Lagrange equation, and Eqs. (6) and (22) as the natural boundary conditions.

The more conventional variational principle would involve only the first area integral with A extending to infinity and the last line integral with $\partial R = \partial A$ at infinity, cf. Eq. (23). Our functional, however, has the advantage that after the following transformation, no numerical calculation is needed beyond the circle ∂A . By applying Green's identity to the second integral in (23) and using (9), the area integral over R becomes

$$\begin{aligned} &- \iint_R \frac{1}{2} \{ h [\nabla(\phi - \phi^I)]^2 - \frac{\omega^2}{g} (\phi - \phi^I)^2 \} \\ &= - \int_{\partial A + \partial R} \frac{1}{2} [(\phi - \phi^I)_R h \frac{\partial(\phi - \phi^I)}{\partial n}]_R \end{aligned} \quad (26)$$

By substituting into Eq. (23) and using the radiation condition, the functional may be written as

$$F = I_1 + I_3 + I_4 + I_5 + I_6 + I_7$$

$$= \iint_A \left[\frac{1}{2} [h(\nabla\phi)^2 - \frac{\omega^2}{g} \phi^2] \right] \dots\dots I_1$$

$$+ \int_{\partial A} \left[\frac{h}{2} (\phi - \phi^I) \frac{\partial(\phi - \phi^I)}{\partial n_A} \right]_R \dots\dots I_3$$

$$- \int_{\partial A} h(\phi)_A \left[\frac{\partial(\phi - \phi^I)}{\partial n_A} \right]_R \dots\dots I_4$$

$$- \int_{\partial A} h(\phi)_A \frac{\partial\phi^I}{\partial n_A} \dots\dots I_5$$

$$+ \int_{\partial A} \phi^I \left[h \frac{\partial(\phi - \phi^I)}{\partial n_A} \right]_R \dots\dots I_6$$

$$+ \int_{\partial A} h \phi^I \frac{\partial\phi^I}{\partial n_A} \dots\dots I_7 \quad (27)$$

Since all integrals are evaluated within or along ∂A , the variational principle is a *local* one. We stress again that Eq. (27) is applicable for constant but arbitrary kh when ω^2/g in I_1 is replaced by k^2h and Eq. (8) is used to relate them.

The analytical solution in the region R is easily found. Let us represent the incident waves in terms of partial waves

$$\begin{aligned} \phi^I &= -\frac{iga_0}{\omega} e^{ikr} \cos(\theta - \alpha) \\ &= -\frac{iga_0}{\omega} \sum_{n=0}^{\infty} \epsilon_n(1)^n J_n(kr) \cos n(\theta - \alpha) \\ &= \sum_{n=0}^{\infty} \epsilon_n(1)^n J_n(kr) (\cos n\alpha \cos n\theta \\ &\quad + \sin n\alpha \sin n\theta) \end{aligned} \quad (28)$$

where ϵ_n is the Jacobi symbol

$$\epsilon_0 = 1; \quad \epsilon_n = 2, \quad n = 1, 2, 3, \dots \quad (29)$$

The scattered wave potential which is the total potential less the incident wave potential,

$\phi - \phi^I$, is governed by the Helmholtz equation subjected to the radiation condition. The solution is

$$\begin{aligned} \phi - \phi^I &= \alpha_0 H_0(kr) + \\ &+ \sum_{n=1}^{\infty} H_n(kr) (\alpha_n \cos n\theta + \beta_n \sin n\theta) \end{aligned} \quad (30)$$

which is valid for (r, θ) in R , H_n with $n = 0, 1, 2, \dots$ are Hankel functions of the first kind with the usual superscript $H_n^{(1)}$ omitted. The coefficients α_n and β_n are to be found.

Case of Stationary Floating Platforms

Within the context of the linearized shallow water approximation, the modification is simply to redefine the functional by adding

$$\iint_F \frac{1}{2} H(\nabla\phi)^2 \dots\dots I_2 \quad (31)$$

to the right-hand side of Eqs. (22) and (27) and imposing Eq. (13) as the *essential* boundary condition. In proving the variational principle we find that Eq. (10) is the Euler-Lagrange equation in F while Eq. (14) appears as the *natural* boundary condition.

In order to extend the applicability of the method to other diffraction problems, we add the following two cases.

Case of Thin Tips

In many harbor problems, the thickness of a breakwater is often much smaller than the dominant wave length of interest. A simplification which is often convenient for analytical purposes is to ignore the thickness of the breakwater altogether. In a numerical approach however, such an assumption leads to inconveniences since the neighborhood of a sharp edge is a singular region where fast variations occur; special attention is required. In applying the finite element method to crack problems in plane elasticity, Tong, Pian and Lasry [5] dealt with the singular behaviour near the edge of a crack. Their idea is simply to exclude a small neighborhood encircling the singularity from finite element considerations. Within the neighborhood, an analytical representation (involving unknown coefficients) is sought which accounts for the singular behaviour correctly. The local analytical solution is required to match with the finite element solution from the outside at certain points on the common border. In this way all the unknowns are found. The principle is therefore very similar to the exclusion of the region at infinity where the radiation condition must be satisfied.

Consider the neighborhood of a tip denoted by D , which is enclosed by the circle ∂D of radius r_D centered at the tip. The region A includes all the water space within ∂A excluding D . Within D , the depth will be approximated by a constant and the breakwater by a thin *straight* line. The potential must then satisfy the Helmholtz equation and $\partial\phi/\partial n = 0$ on ∂B .

In addition ϕ_D must be matched with ϕ_A such that

$$(\phi)_A = (\phi)_D \quad \text{and} \quad \left(\frac{\partial \phi}{\partial n}\right)_D = \left(\frac{\partial \phi}{\partial n}\right)_A \quad \text{on } \partial D \quad (32)$$

The appropriate functional is obtained by adding the term

$$- \iint_D \left[\frac{1}{2} (h \nabla \phi)^2 - \frac{\omega^2}{g} \phi \right]_D - \int_{\partial D} h(\phi)_A \left(\frac{\partial \phi}{\partial n} \right)_D \quad (33)$$

to the right-hand side of Eq. (23). The first term can also be changed to a line integral by using the argument leading to Eq. (26), with the result that to the right-hand side of Eq. (27) we must now add

$$I_8 + I_9 = + \int_{\partial D} \frac{1}{2} h(\phi) \left(\frac{\partial \phi}{\partial n} \right)_D \dots I_8 - \int_{\partial D} h(\phi)_A \left(\frac{\partial \phi}{\partial n} \right)_D \dots I_9 \quad (34)$$

If there are several tips, integrals similar to I_8 and I_9 must be added for each tip.

The analytical solution within D is found in terms of local polar coordinates as shown in Fig. 3.

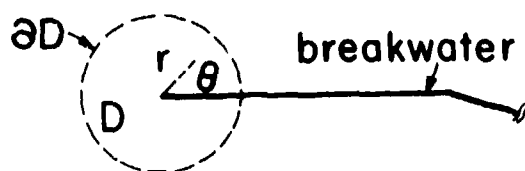


Fig. 3 Neighborhood of the Tip of a Thin Breakwater

$$(\phi)_D = \sum_{n=0}^{\infty} \gamma_n J_{n/2}(kr) \cos \frac{1}{2} n\theta \quad (35)$$

$$0 < r < r_D, \quad 0 < \theta < 2\pi$$

where γ_n , $n = 0, 1, 2, \dots$ are to be found. It should be remarked that for odd n , $J_{n/2}$ may be expressed in elementary functions, e.g.

$$J_{1/2}(kr) = \sqrt{\frac{2}{\pi kr}} \sin kr \quad (36)$$

$$J_{m+1/2}(kr) = \frac{2m-1}{kr} J_{m-1/2}(kr) - J_{m-3/2}(kr) \quad (37)$$

$$m = 0, 1, 2, 3, \dots$$

As will be borne out by numerical evidence, for sufficiently small kr only a few terms in Eq. (35) are needed. Note that $J_{1/2}$ gives the correct singularity in velocity, namely

$$\nabla \phi_D \propto r^{-1/2} \quad \text{as } r \rightarrow 0 \quad (38)$$

Case of a Straight Coast

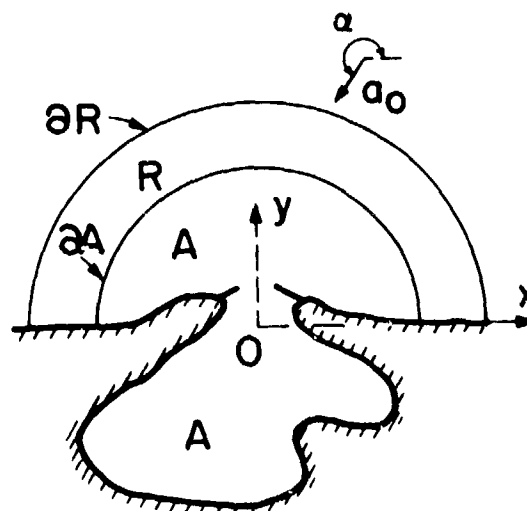


Fig. 4 Harbor with a Straight Coast

Referring to Fig. 4, we draw a semi-circle ∂A sufficiently large so that the depth is constant beyond. The same variational principle applies as in the case without a coast, if the analytical solution outside ∂A in R is modified to satisfy the boundary condition on the coast. For this purpose ϕ^I must be interpreted as the sum of the incident wave and the reflected wave due to the straight coast, i.e.

$$\phi^I = e^{ikr \cos(\theta-\alpha)} + e^{ikr \cos(\theta+\alpha)} = 2 \sum_{n=0}^{\infty} \epsilon_n i^n J_n(kr) \cos n\alpha \cos n\theta \quad (39)$$

The scattered wave $(\phi)_R - \phi^I$ is easily obtained as

$$(\phi)_R - \phi^I = \sum_{n=0}^{\infty} \alpha_n H_n(kr) \cos n\theta \quad (40)$$

It may be remarked that the present modification is particularly useful for a harbor with protruding or detached breakwaters, for one can simply take the semi-circle ∂A large enough to include all of them.

DISCRETE APPROXIMATION

We illustrate the analysis for Eq. (27) only, i.e., a harbor in the open sea without sharp tips and platforms. The principle is to introduce discrete finite elements in A and along ∂A . Within each element the potential is expressed in terms of its unknown nodal values at certain discrete nodal points. The integrals in the functional Eq. (27) become summations involving matrices. On the other hand, the coefficients α_n and β_n for the radiated wave potential are also to be determined (cf. Eq. 20). Thus the functional contains integrals both bilinear (I_1 , I_3 , I_4) and linear (I_5 , I_6) in the unknowns with the inhomogeneous (forcing) terms arising from I_7 and I_8 . Upon extremizing F , I_7 , being a constant, drops out and a matrix equation is obtained which is solved numerically for all the unknowns.

We first evaluate the integrals in Eq. (27).

Line Integrals

Using Eq. (30), the line integral along the circle ∂A of radius r_A can be evaluated by using the orthogonality of trigonometric functions

$$I_3 = \frac{\pi}{2} r_A kh \{ 2\alpha_0^2 H_0' H_0' + \sum_{n=1}^{\infty} H_n H_n' (\alpha_n^2 + \beta_n^2) \} \quad (41)$$

where

$$H_n = H_n^{(1)}(kr_A), \quad H_n' = \left. \frac{d}{dkr} H_n^{(1)}(kr) \right|_{r_A} \quad (42)$$

For computational purposes we truncate the infinite series at the term $n = S$. Define the column vector $\underline{\mu}$ whose transpose is the following row vector which has $M = 2S + 1$ components

$$\underline{\mu}^T = [\alpha_0, \alpha_1, \beta_1, \beta_2, \dots, \alpha_S, \beta_S] \quad (43)$$

and K_{III} as the diagonal matrix of M components:

$$K_{III} = r_R kh \text{diag} [2H_0' H_0', H_1' H_1', \dots, H_S' H_S', H_S' H_S'] \quad (44)$$

We may rewrite Eq. (41) in matrix form

$$I_3 = \frac{1}{2} \underline{\mu}^T K_{III} \underline{\mu} \quad (45)$$

which is bilinear in the unknown $\underline{\mu}$.

Similarly, the line integral I_5 is obtained as

$$I_6 = Q_{VI} \underline{\mu} \quad (46)$$

with Q_{VI} being a $(1 \times M)$ row vector.

$$Q_{VI} = 2\pi r_A kh \cdot \{ J_0' H_0', \dots, i^n J_n' H_n' \cos n\theta, i^n J_n' H_n' \sin n\theta, \dots \} \quad (47)$$

For I_4 and I_5 we divide the circle ∂A into small and equal segments by P nodal points (see Fig. 5) and denote the nodal potential values as a row vector:

$$\underline{\phi}^T = \{\bar{\phi}_1, \bar{\phi}_2, \dots, \bar{\phi}_P\} \quad (48)$$

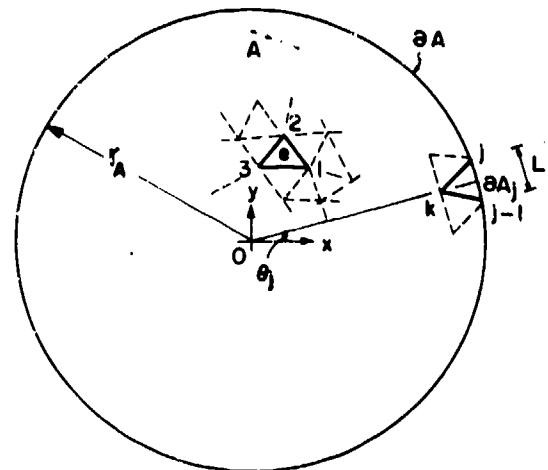


Fig. 5 Typical Boundary and Interior Elements

The length of each segment is

$$L = 2\pi r_A / P \quad (49)$$

Taking L to be very small, for each line element we approximate $(\phi)_A$ by the average of ϕ at two end nodes, replace the integration range by L and the value of θ in $(\phi - \phi^*)_R$ (cf. Eq. (30)) by its value at the mid-point of the element, θ^e , thus we have

$$I_4 = -\frac{1}{2} khL \sum_{e=1}^P (\bar{\phi}_1^e + \bar{\phi}_2^e) [\alpha_0' H_0' + \sum_{n=0}^{\infty} H_n' (\alpha_n \cos n\theta^e + \beta_n \sin n\theta^e)] \quad (50)$$

This can be written in matrix form as

$$I_4 = \frac{1}{2} \underline{\phi}^T K_{IV} \underline{\mu} + \frac{1}{2} \underline{\mu}^T K_{IV}^T \underline{\phi} \quad (51)$$

where K_{IV} is the rectangular matrix :

$$K_{IV} = -\frac{1}{2} Lkh \cdot \begin{pmatrix} 2H'_0 & \dots & H'_n(\cos n\theta_p + \cos n\theta_1) & H'_n(\sin n\theta_p + \sin n\theta_1) & \dots \\ 2H'_0 & \dots & H'_n(\cos n\theta_1 + \cos n\theta_2) & H'_n(\sin n\theta_1 + \sin n\theta_2) & \dots \\ \vdots & & \vdots & \vdots & \\ \vdots & & \vdots & \vdots & \\ 2H'_0 & \dots & H'_n(\cos n\theta_{p-1} + \cos n\theta_p) & H'_n(\sin n\theta_{p-1} + \sin n\theta_p) & \dots \end{pmatrix} \quad (52)$$

(P=M)

in which $n = 1, 2, \dots, S$, and $\theta_1, \theta_2, \dots$ are the values of θ^e for the first, second, line element respectively.

Similarly, the integral I_5 is

$$I_5 = -\sum_{e=1}^P \frac{1}{2} Lkh [i \cos(\theta^e - \alpha) e^{ikr \cos(\theta^e - \alpha)}].$$

$$[\bar{\phi}_1^e + \bar{\phi}_2^e] = Q_V \bar{\phi} \quad (53)$$

where Q_V is a row vector (1xP)

$$Q_V = -\frac{1}{2} khl \{ (q_p + q_1), (q_1 + q_2), \dots, (q_{p-1} + q_p) \} \quad (54)$$

with

$$q_j = i \cos(\theta_j - \alpha) e^{ikr \cos(\theta_j - \alpha)} \quad (55)$$

Finite Element Approximation for the Area Integral

This part is quite standard and detailed description is available in text books [9]. Briefly, we divide the water area A into a network of elements. Within the element, ϕ is approximated by a linear combination of the interpolation functions N_i^e , $i = 1, 2, 3, \dots$ with coefficients being the nodal values ϕ_i^e at the nodal points i . We adopt the simple three-node triangular element so that

$$\phi^e(x, y) = \sum_{i=1}^3 N_i^e \phi_i^e \quad (56)$$

where

$$(\phi^e)^T = (\phi_1^e, \phi_2^e, \phi_3^e) \quad (57)$$

with the subscripts referring to the nodes, and

$$\begin{aligned} N^e &= (N_1^e, N_2^e, N_3^e) \\ N_1^e(x, y) &= (a_1 + b_1 x + c_1 y) / 2\Delta^e; \quad i = 1, 2, 3 \end{aligned} \quad (58)$$

with

$$\begin{aligned} a_1 &= x_2^e y_3^e - x_3^e y_2^e, \quad b_1 = y_2^e - y_3^e \\ c_1 &= x_3^e - x_2^e \end{aligned} \quad (59)$$

Δ^e = area of element e

$$= \frac{1}{2} \begin{vmatrix} 1 & x_1^e & y_1^e \\ 1 & x_2^e & y_2^e \\ 1 & x_3^e & y_3^e \end{vmatrix} \quad (60)$$

Other coefficients $a_2, a_3, b_2, b_3, c_2, c_3$ may be obtained by permutation $1 \rightarrow 2 \rightarrow 3 \rightarrow 1$. Substituting into I_1 we obtain

$$I_1 = \sum_e (\phi^e)^T K_I^e \phi^e \quad (61)$$

where the summation is performed over all elements in A and

$$[K_I^e]_{ij} = \int_A h^e (\nabla N_i^e \cdot \nabla N_j^e - \frac{\omega^2}{gh^e} N_i^e N_j^e) \quad (62)$$

$i, j = 1, 2, 3$

In general the depth h can be a function of x, y within the element; we approximate it, however, by a constant h^e . Carrying out the differentiation and the integration the following result is obtained for K_I^e (see [9])

$$K_I^e = \frac{h^e}{4\Delta^e} [K_{ij}^e] \quad (63)$$

with

$$K_{ii}^e = b_i^2 + c_i^2 - \frac{2}{3} (\Delta^e)^2 \frac{\omega^2}{gh^e}; \quad (64)$$

$$K_{ij}^e = K_{ji}^e = b_i b_j + c_i c_j - \frac{1}{3} (\Delta^e)^2 \frac{\omega^2}{gh^e} \quad (65)$$

$i \neq j$

In general K_I^e is banded and symmetric where the band width depends on the numbering of nodal points.

Assemblage of Matrices

Summarizing all the integrals in the functional we obtain

$$F(\phi) = \frac{1}{2} \sum_e (\phi^e)^T K_I^e \phi^e + \frac{1}{2} \mu^T K_{III}^e \mu^e + \frac{1}{2} (\phi^T K_{IV} \mu + \mu^T K_{IV}^T \phi) + Q_V \phi + Q_{VI} \mu + \text{constant} \quad (66)$$

where K_I^e, K_{III}^e are symmetric and Q_V, Q_{VI} are diagonal matrices. We define a global nodal potential vector which is the union of all ϕ^e , and assemble the matrices K_I^e to a single matrix K_I so that the \sum term above may be written as

$$\frac{1}{2} \phi^T K_I \phi \quad (67)$$

(1×E) (E×E) (E×1)

where E is the total number of nodal points. It should be noted that the union of all boundary nodal potentials ϕ is a subset of ϕ . Let us now assign to ϕ the last P positions in the global vector array ϕ . Next we define the total unknown vector ψ by

$$\psi^T = [\phi^T, \mu^T] = (\phi_1, \phi_2, \dots, \phi_E, \mu_1, \mu_2, \dots, \mu_M) \quad (1 \times N)$$

with

$$N = E + M \quad (68)$$

being the total number of unknowns. It is clear that Eq. (66) can be written as

$$F = \frac{1}{2} \psi^T K \psi + Q \psi + \text{constant} \quad (69)$$

where the total matrix K is

$$K = \begin{bmatrix} K_I & 0 \\ 0 & K_{III} \end{bmatrix} \quad (70)$$

(N×N) E M P M

which is symmetric and the total forcing vector Q is

$$Q^T = \{ 0, Q_V, Q_{VI} \} \quad (71)$$

(1×N) 1×(E-P) (1×P) (1×M)

with the first E-P components being zero.

Finally the stationarity of F implies that

$$\frac{\partial F}{\partial \psi_i} = 0 \quad i = 1, 2, \dots, N \quad (72)$$

or

$$K \psi = Q \quad (73)$$

This is a set of N linear algebraic equations for N unknowns which can be solved by the Gaussian elimination method. It may be remarked that in structural mechanics, K is called the stiffness matrix and Q the load vector.

The potential at all nodal points is thus determined.

COMPUTATIONAL ASPECTS

The symmetric complex coefficient matrix K is in general large, sparse, and banded. In computer programming, its members are stored in a packed form of a rectangular $N \times$ (semi-band width) array. By assigning the last P positions of the vector ϕ to the boundary nodal potential vector ϕ , the semi-band width of K_I is approximately equal to P. The $P \times M$ matrix K_{IV} is full; hence the semi-band width of the $N \times N$ matrix K is $P+M$. The storage required is roughly

$$\text{storage} \sim N(P + M) \quad (74)$$

To solve the corresponding banded system of equations by Gaussian elimination, the needed number of operations is roughly

$$\text{operations} \sim \frac{1}{2} N(P + M)^2 \quad (75)$$

Further economy can be achieved by partitioning the matrix K as follows. Let us enlarge the dimensions of K_{IV} and Q_V by adding zero members so that

$$\begin{bmatrix} K_I & 0 \\ 0 & K_{III} \end{bmatrix} = \begin{bmatrix} 0 & K_{IV} \\ K_{IV}^T & K_{III} \end{bmatrix}; \quad Q_V^T = \{ 0 \quad Q_V \} \quad (76)$$

M×E M×(E-P) M×P (1×E)

We may then write Eq. (70) as

$$K_I \phi + K_{IV} \mu = Q_V \quad (77)$$

$$K_{IV}^T \phi + K_{III} \mu = Q_{VI} \quad (78)$$

Solving μ in terms of ϕ from (78) we have

$$\mu = K_{III}^{-1} (Q_{VI} - K_{IV}^T \phi) \quad (79)$$

which can be substituted into (77) to give

$$(K_I - K_{IV} K_{III}^{-1} K_{IV}^T) \phi = Q_V - K_{IV} K_{III}^{-1} Q_{VI} \quad (80)$$

Since K_{III} is diagonal, $K_{IV} K_{III}^{-1} K_{IV}^T$ is an $E \times E$ symmetric matrix. The semi-band width of $K_I - K_{IV} K_{III}^{-1} K_{IV}^T$ is also approximately equal to P. Now the storage and operation for Gaussian elimination procedure are

$$\begin{aligned} \text{storage} &\sim M + M \times P + E \times P \\ &\sim N \times P, \text{ for } P \gg 1 \end{aligned} \quad (81)$$

which is less than Eq. (74) by $(N+M)$. The number of operations in the Gaussian elimination procedure is

$$\begin{aligned} \text{operations} &= \frac{1}{2} PM^2 \quad (\text{for Eq. (79)}) \\ &+ \frac{1}{2} EP^2 \quad (\text{for Eq. (80)}) \end{aligned} \quad (82)$$

which is less than Eq. (74) by the amount

$$\frac{1}{2} \{ (E+N)PM + M(E(P+M) + M^2) \} \quad (83)$$

For a given total area within $3A$ the number of unknowns (cf. ψ) should be greater for (i) shorter wavelength, i.e. smaller ka where a is the dimension of the scatterer and/or (ii) shorter minimum dimension of the physical boundary. To get an idea of the former, we used as a test, the diffraction by a vertical circular cylinder of radius a . In this case the exact solution is well known:

$$\eta = a \sum_{n=0}^{\infty} \epsilon_n (i)^n \cos n\theta \left[J_n(kr) - \frac{J_n(ka) H_n'(kr)}{H_n'(ka)} \right] \quad (84)$$

We used three concentric circles $r/a = 1, 1.2, 1.4$ and divided the area between them into elements. No advantage is taken of the circular geometry. By comparing results of the finite element method with Eq. (84) it was found that 10 nodes in a wave length were usually adequate, i.e.

$$\ell^*/\lambda \leq 0.1 \quad \text{or} \quad k \ell^* \leq 2\pi/10 \approx 0.628 \quad (85)$$

where ℓ^* is the maximum dimension of an element and λ the incident wave length. For this particular problem it is of course possible to use only one ring $r/a = 1$, i.e. line elements without any area elements. A typical comparison is shown in Table 1 and Figure 6.

Table 1 Comparison on η/a , Between Analytical and Finite Element Calculations for a Vertical Circular Cylinder. Angle of Incidence $\alpha = \pi$ (wave incident from right), $ka = 2$

θ		0°	30°	60°	90°	120°	150°	180°
$r/a = 1$	magnit- tude	1.85853	1.80783	1.56278	1.29659	0.99435	0.42008	0.73185
		1.85536	1.80289	1.55831	1.28780	0.98071	0.41399	0.71600
	phase	-2.15222	-1.91016	-1.19936	-0.05608	1.01750	2.70732	-2.51741
		-2.158	-1.923	-1.222	-0.080	0.982	2.658	-2.557
$r/a = 1.2$	magnit- tude	1.72446	1.71092	1.53601	1.30972	1.02111	0.43010	0.74438
		1.72398	1.71121	1.54090	1.21427	1.01923	0.43037	0.73966
	phase	-2.18380	-1.93511	-1.20573	-0.02799	1.07772	2.77618	-2.43708
		-2.195	-1.949	-1.224	-0.052	1.054	2.745	-2.468

In each space above, the first row is the analytic result and the second row is the finite element result. Phase is in radians between $-\pi, \pi$.

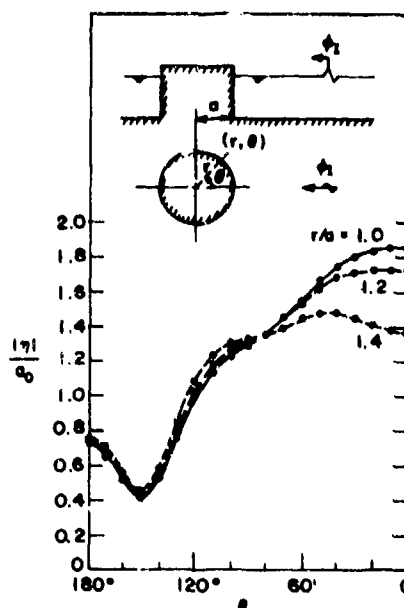


Fig. 6 Comparison of Analytical and Numerical results for a vertical circular cylinder. $ka = 2$, $k\ell \leq 0.63$ by finite elements; —, —, —, analytical

The number of unknown coefficients needed in the series expansion M , also depends on the value of ka and is found by gradually increasing M until the outcome is insensitive to it.

NUMERICAL RESULTS

To demonstrate the application to oscillations in a harbor with thin breakwaters we

first present the case of a semi-circular harbor along a straight coast (or a very long straight breakwater), as shown in Fig. 7. Accurate analytical solution is possible and is given in the

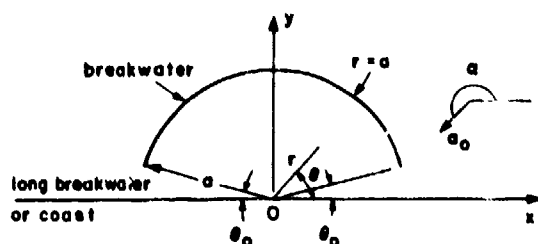


Fig. 7 Definitions for an Idealized Semi-Circular Harbor

Appendix. Only one finite element network is used as is shown in Fig. 8, where the criterion Eq. (85) is satisfied for $0 < ka < 3.5$. Note in particular the circles near the harbor entrances. As a measure of the global response in the harbor we define an amplification factor as the normalized root mean square of the displacement within the harbor:

$$A_{rms} = \frac{1}{2a} \left[\frac{2}{\pi a} \int_0^a r dr \int_0^\pi d\theta |\eta|^2 \right]^{1/2} \quad (86)$$

where $2a$, is the standing wave amplitude at the coast without the harbor. Figure 9 shows the comparison between the analytical and finite element results. It can be seen that noticeable deviation occurs only beyond the intended range of ka

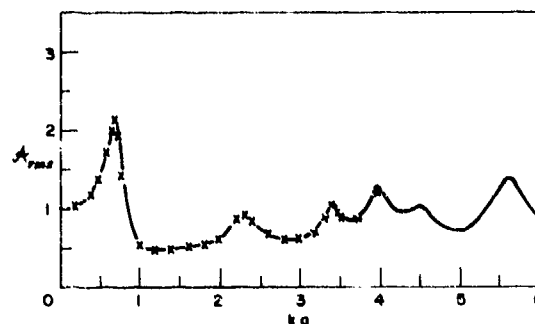


Fig. 9 Comparison between Analytical and Numerical Results for Idealized Semi-Circular Harbor. — analytical, $\times \times$ finite element
 A_{rms} = normalized RMS harbor response

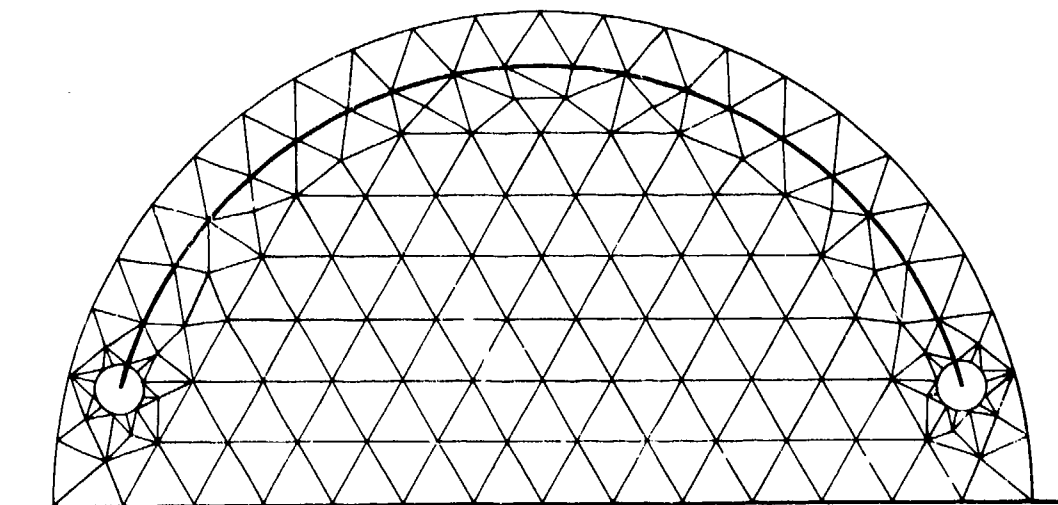


Fig. 8 Network of Finite Elements for Idealized Semi-Circular Harbor

Numerical experience from these two examples is then used as a guide to treat the Atlantic Offshore Harbor. For simplicity, all calculations so far are done for a constant depth of $h = 47$ ft. which is the design depth within the basin. In addition, the sloping outer faces of the breakwaters are replaced by vertical walls (the inside face being already vertical) such that the thickness corresponds to that of the mid-depth, (see Fig. 1 (dashed line)). Three cases have been calculated:

- (i) Harbor without platform
- (ii) Harbor with platforms seated on the sea bottom
- (iii) Harbor with platforms with a clearance of $H = 12$ ft.

In the first two cases the linearised formulation is, of course, exact. In the last case the long wave approximation is used.

For all three cases, we use one finite element network for $0 < ka < 2.5$ where a is the radius of the semi-circular breakwater, taken to be 888 ft., and a finer network for $1.6 < ka < 6$ so that Eq. (88) is satisfied. Results in the overlapping region $1.6 < ka < 2.5$ provide a check for convergence. A typical finite element network is shown in Fig. 10.

In principle, the right angle corners of the platforms should further be treated as singular regions as before. This, however, has not yet been done.

For each case the velocity potential at every nodal point within the circle ∂A is found. Here we define a mean amplification factor A by averaging $|\eta|$ over the free surface area in the harbor, A_H , which lies between the two

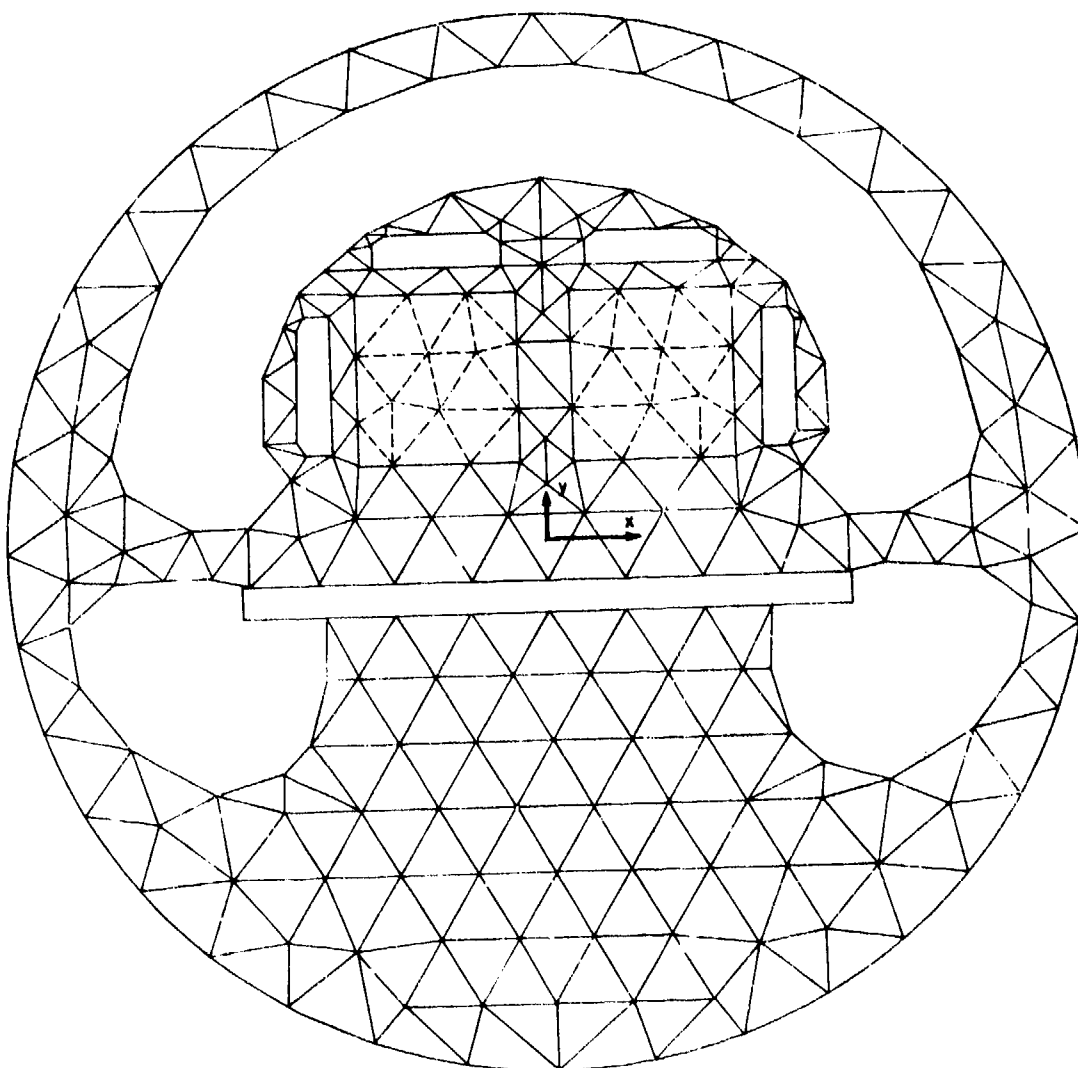


Fig. 10 Network of Finite Elements for Atlantic Offshore Harbor, for $0 < ka < 2.5$.

lines flush with the ends of the straight caisson of the enclosure breakwater:

$$A = \frac{1}{a_0} \frac{1}{A_H} \iint_{A_H} dx dy |\eta| \quad (87)$$

where the normalisation factor is only a_0 (vs. $2a_0$ in Eq. (86)). This is plotted in Fig. 11.

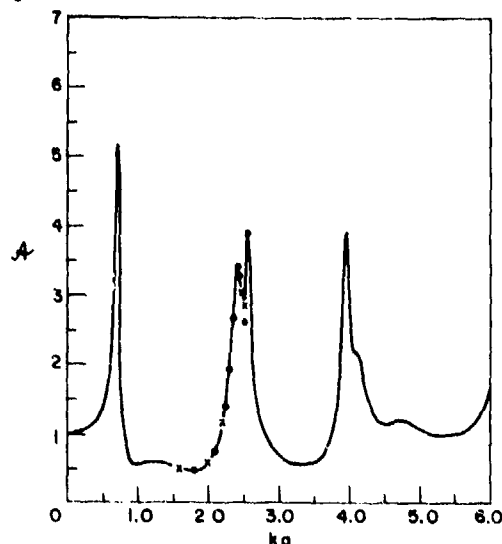


Fig. 11 Mean Harbor Response

For case (iii) we have also calculated the exciting wave forces on the platforms by integrating the dynamic pressure over the bodies, i.e.

$$\vec{F} = (F_x, F_y, F_z) = - \iint_S p \vec{n} dS \quad (88.a)$$

$$\vec{M} = (M_x, M_y, M_z) = - \iint_S (\vec{r} - \vec{r}_c) \times p \vec{n} dS \quad (88.b)$$

where S denotes the wetted area of a platform, \vec{n} the unit normal outward from the body, and \vec{r}_c the position of the moment center. In the present shallow water approximation, the dynamic pressure is independent of depth. As the platforms are rectangular in shape, the forces are simply

$$F_x \equiv f_x \rho g a_0 D l_2 = - \rho g D \int_{\partial F} \eta \cos(n, x) dy \quad (89.a)$$

$$F_y \equiv f_y (\rho g a_0 D l_1) = - \rho g D \int_{\partial F} \eta \cos(n, y) dx \quad (89.b)$$

$$F_z \equiv (f_z \rho g a_0 l_1 l_2) = \rho g \iint_F \eta dx dy \quad (89.c)$$

where l_1, l_2 are the horizontal dimensions and $D = h - H$ the draft of a platform, and f_x, f_y, f_z the normalized forces respectively.

For brevity, only some sample results for case (iii) are shown in Figures 12 - 14, all with the incident angle $\alpha = \pi$ (from $x = +\infty$). It can be seen that in the region $1.6 < ka < 2.5$, agreement between the results from the two finite element meshes (..., coarse mesh; and $\times \times$ fine mesh) is better for smaller ka . To achieve still better agreement, it may be necessary to use finer meshes along the breakwaters and treat the corners of the platforms by the mixed method.

Relevant computational information is summarized in Table 2. It should be pointed out that for the circular cylinder, the band width can be further reduced from 72 to 36 by proper numbering of nodes. The technique of packed storage (cf. Eqs. 79, 80) was applied only to the Atlantic Offshore Harbor. It can be seen that in the same wave number range, $0 < ka < 2.5$, less band-width, storage space and CPU time are needed for the Offshore Harbor despite the greater number of nodes due to the more complicated geometry.

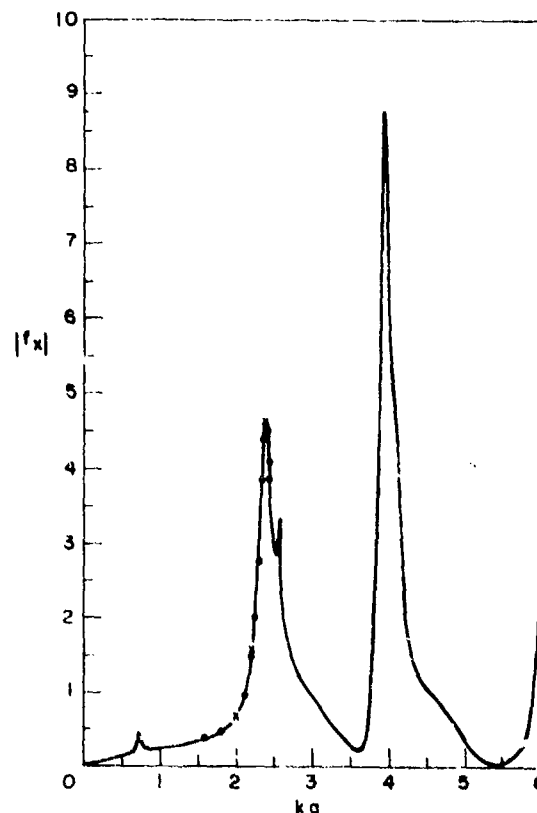


Fig. 12 Exciting Force $|f_x|$ on Platform II

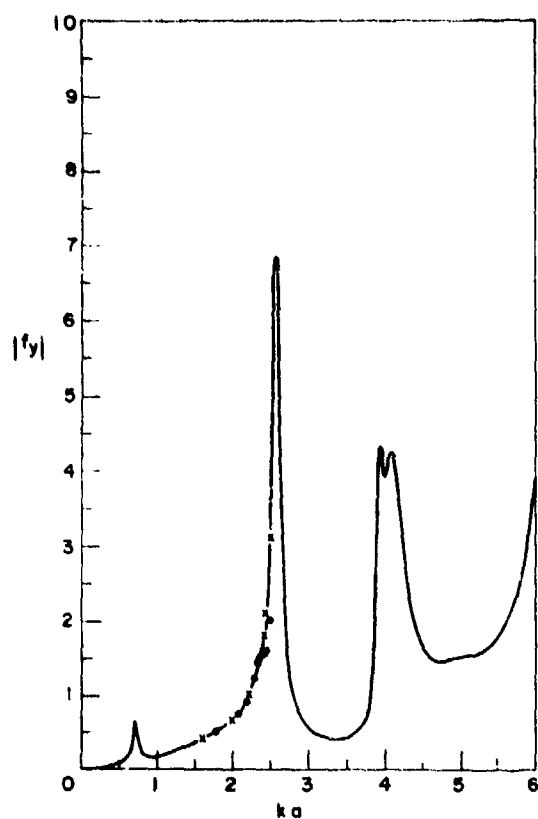


Fig. 13 Exciting Force $|f_y|$ on Platform II

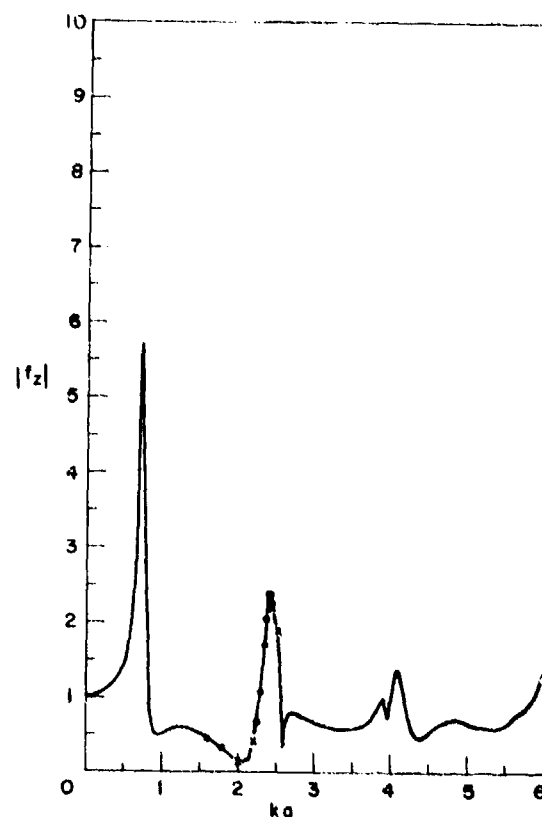


Fig. 14 Heave Exciting Force, $|f_z|$ on Platform II

Table 2 Computational Information

Case	ka	Total no. of elements	E Nodal unknowns	Coefficient unknowns, (M)		Bandwidth	Core Storage	CPU on M165 (min.) for fixed ka
				for R	for D			
circular cylinder (Fig. 6)	2.0	72	72	21	---	72	106K	0.113
Fig. 7	0 ~ 3.5	258	179	12	6	59	194K	0.241
Fig. 1	0 ~ 2.5	359	249	23	---	41	160K	0.206
	0 ~ 6	1013	635	41	---	82	518K	1.84

It is interesting to remark on the physical situation associated with the first few resonant peaks in the Atlantic Offshore Harbor. Referring to Fig. 11, four peaks clearly appear at $ka = 0.7, 2.4, 2.6$ and 3.95 . By examining the instantaneous free surface over a period, we have found that the first ($ka = 0.7$) corresponds to the Helmholtz mode in which the free surface rises and falls more or less in unison, hence f_x is large but f_y and f_z are small. For higher z peaks, waves inside the basin are partially standing with the instantaneous nodal lines yawing about. The magnitudes of the wave forces are associated with the free surface variation at the time when the maximum amplitude is the greatest. In particular for $ka = 2.4$, the free surface tilts about the y -axis, hence $f_x > f_y$. For $ka = 2.6$, it tilts about an axis x^* parallel to the y -axis, hence $f_x > f_y$. For $ka = 3.95$, it has a ridge (or y trough) near the y -axis and is nearly 180° out of phase with the two corners in the directions $\theta = \pi/4$ and $3\pi/4$, hence f_x is very large compared to f_y .

Finally, while a fully three-dimensional theory is being pursued, the results by the two-dimensional long wave theory may be modified to give rough estimates for the short wave range. It is evident from Eqs. (12) and (21) that, when the water depth is everywhere constant, and all the solid walls extend vertically throughout the water depth, we have

$$[p]_{kh} = \sigma [p]_{kh=0}, \quad \sigma = \frac{\cosh k(z+h)}{\cosh kh} \quad (90.a,b)$$

where $[]_{kh}$ stands for the value for arbitrary kh and $[]_{kh=0}$ stands for the value by long wave approximation. Thus the factor σ accounts for the vertical variation of pressure. For a vertical cylinder whose bottom is slightly above the sea bed, i.e. $H \ll h$, Eq. (90) should be approximately valid. We therefore expect to obtain improved results from the long wave theory by multiplying the pressure corresponding to the latter by the correction factor taking the local value of h (and k) if it is variable. Accordingly the vertical force is simply

$$[F_z]_{kh} = [F_z]_{kh=0} \frac{\cosh kh}{\cosh kh}; \quad (91)$$

while the horizontal force is

$$\begin{aligned} \begin{bmatrix} F_x \\ F_y \end{bmatrix}_{kh} &= \begin{bmatrix} F_x \\ F_y \end{bmatrix}_{kh=0} \int_0^{-d} \frac{\cosh k(z+h)}{d \cosh kh} dz \\ &= \begin{bmatrix} F_x \\ F_y \end{bmatrix}_{kh=0} \cdot \frac{1}{kd} \frac{\sinh kh - \sinh kh}{\cosh kh} \quad (92) \end{aligned}$$

with $d = h - H$ being the draft. For the present range ($0 < ka < 6$) the values of kh are small

(< 0.318) and the corrected forces are hardly distinguishable from the values shown in Figures 12, 13 and 14. Nevertheless, for higher values of ka , this correction may well be necessary and *satisfactory*, as is evidenced by Appendix II.

CONCLUDING REMARKS

In this paper, an effective finite element method is applied to two-dimensional diffraction of water waves. Aside from the usual merits of this method, an additional efficiency is gained by mixing analytical and numerical procedures. This idea, which resembles that of Motz [10] for singularities in relaxation methods, essentially regards an analytical region as one single element with many unknown coefficients. In practice, one trades many nodal unknowns for (usually) fewer coefficient unknowns. The strategy is particularly advantageous in dealing with the radiation condition where a very much larger area (hence large number of elements and larger band width of K) would otherwise be involved. Further generalization of this idea is possible. For example, consider a harbor with a very large area of which a considerable part is uniform in depth. One may exclude the largest possible circle (or a rectangle) within this part from subdivision into finite elements and save computation storage and operations.

It is worthwhile to point out the computational difference between water wave problems involving (x,z) and those involving (x,y) coordinates. Although both are two-dimensional problems, the first one (x,z) usually requires less band width in K than the second (x,y) . This is because in the first, the most economical numbering of nodes is to proceed by marking off nodes on a vertical line first, then moving horizontally to the second vertical line, etc. The band-width is controlled by the maximum number of nodes on a vertical line which is usually not large. However, in the second, one should mark off the nodes along one radius, then the next radius, etc., and the band-width is controlled by the number of nodes on the outermost circle, which is usually large.

It is evident that in dealing with practical problems, the ultimate problem is the solution of a large system of algebraic equations. Therefore, efforts to render the coefficient matrix symmetric (which is achieved now by a suitable variational principle), to store the coefficients in properly packed form, and to use external storage on discs or tapes, etc., are important.

Finally, it appears that the finite element method can be applied to many other two-dimensional diffraction problems of technical or scientific interest (e.g. tidal diffraction by topography).

ACKNOWLEDGEMENT

This research is supported by the Public Service Electric and Gas Company, Newark, New Jersey under contract supervised by Professor D.R. Harleman, M.I.T. We are grateful to

Professor P. Tong for his important suggestions

REFERENCES

1. Hwang, L.S. and Tuck, E.O., "On the oscillations of harbours of arbitrary shape", Journal of Fluid Mechanics, Vol. 42, 1970, pp. 447-464.
2. Lee, J.I., "Wave-induced oscillations in harbours of arbitrary geometry", Journal of Fluid Mechanics, Vol. 45, 1971, pp. 375-394.
3. Berkhoff, J.C.W., "Computation of combined refraction-diffraction", Proceedings of the 13th Coastal Engineering Conf., Vol. 1, 1973, pp. 471-490.
4. Bai, K.J., "Diffraction of oblique waves by an infinite cylinder", 1974, submitted to Journal of Fluid Mechanics.
5. Tong, P., Pian, T.H.H. and Lasry, S.J., "A hybrid finite element approach to crack problems in plane elasticity", International Journal of Numerical Methods in Engineering, Vol. 7, 1973, pp. 297-308.
6. Bai, K.J. and Yeung, R., "Numerical solutions of free-surface and flow problems", 10th Symposium in Naval Hydrodynamics, 1974, Office of Naval Research.
7. Longuet-Higgins, M.S., "On the trapping of wave energy round islands", Journal of Fluid Mechanics, Vol. 29, 1967, pp. 781-821.
8. Stoker, J.J., "Water Waves", Interscience, New York: 1957, p. 414 ff.
9. Zienkiewicz, O.C., The Finite Element Method in Engineering Science, McGraw-Hill, New York: 1971, pp. 115-120 and p. 506.
10. Motz, H., "The treatment of singularities of partial differential equations by relaxation methods", Quarterly Appl. Math., Vol. 4, 1966, pp. 371-377.
11. Mei, C.C. & Petroni, R.P., "Waves in a harbor with protruding breakwaters", Journal of Waterways, Harbors & Coastal Engrg. Div., ASCE, May, 1973, pp. 209-229.
12. Black, J.L., Mei, C.C. and Bray, M.C.G., "Radiation and scattering of waterwaves by rigid bodies", Journal of Fluid Mechanics, Vol. 46, 1, 1971, pp. 151-164.
13. Garrett, C.J.R., "Wave forces on a circular dock", Journal of Fluid Mechanics, Vol. 46, 1, 1971, pp. 129-139.
14. Chen, H.S. and Mei, C.C., "Wave Forces on a stationary platform of elliptical shape", Journal of Ship Research, Vol. 17, 2, 1973, pp. 61-71.

APPENDIX 1 ANALYTIC THEORY OF A SEMI-CIRCULAR HARBOR

Description of the Problem

We consider a simple harbor with a straight side or a breakwater and a thin breakwater in the form of an arc of radius a centered at the point O on the straight side. All walls are assumed to be vertical and the depth is con-

stant. This approximates the situation where the straight breakwater is very long. The incident wave has the amplitude a_0 and the angle of incidence α (see Fig. 7). The spatial part of the corresponding displacement is

$$\begin{aligned}\eta_1^I &= a_0 e^{ikr \cos(\theta-\alpha)} \\ &= a_0 \sum_m \epsilon_m i^m J_m(kr) \cos m(\theta - \alpha)\end{aligned}\quad (93)$$

where $\epsilon_m \equiv \sum_{m=0}^{\infty}$. The reflected wave from the straight wall is

$$\begin{aligned}\eta_2^R &= \eta_2^I = a_0 e^{ikr \cos(\theta+\alpha)} \\ &= a_0 \sum_m \epsilon_m i^m J_m(kr) \cos m(\theta + \alpha)\end{aligned}\quad (94)$$

Clearly, by symmetry one may replace the straight wall and the semi-circular basin by a circular harbor with two openings centered at the ends of a diameter and two symmetrically incident waves η_1^I, η_2^I

$$\eta^I = \eta_1^I + \eta_2^I \quad (95)$$

as depicted at the top of Fig. 15.

In view of the fact that the harbor configuration is symmetric with respect to the y -axis, we split the spatial part of the incident waves η_1^I into two parts: namely, even part η_E^I and odd part η_O^I ,

$$\eta^I = \eta_E^I + \eta_O^I \quad (96)$$

as shown in Figure 15, where

$$\begin{aligned}\eta_E^I &= \frac{a_0}{2} [e^{ikr \cos(\theta-\alpha)} + e^{ikr \cos(\theta+\alpha)} \\ &\quad + e^{ikr \cos(\theta-(\pi-\alpha))} + e^{ikr \cos(\theta-(\pi+\alpha))}] \\ &= 2a_0 \sum_{Ev} \epsilon_m i^m \cos m\alpha \cos m\theta J_m(kr)\end{aligned}\quad (97)$$

and

$$\begin{aligned}\eta_O^I &= \frac{a_0}{2} [e^{ikr \cos(\theta-\alpha)} + e^{ikr \cos(\theta+\alpha)} \\ &\quad - e^{ikr \cos(\theta-(\pi-\alpha))} - e^{ikr \cos(\theta-(\pi+\alpha))}] \\ &= 2a_0 \sum_{Odd} \epsilon_m i^m \cos m\alpha \cos m\theta J_m(kr)\end{aligned}\quad (98)$$

with $\epsilon_m = \sum_{m=0,2,4,\dots}^{\infty}$ and $\epsilon_m = \sum_{m=1,3,5,\dots}^{\infty}$. The

sums in (97) and (98) are of the same form except the summation indices are even and odd integers respectively.

In summary, we shall first treat two harbor problems separately; each is circular with two identical openings about $\theta = 0$ and π , but under attack by different incident waves η_E^I and η_E^I . The decomposition is displayed in Fig. 15. Through this treatment, a certain symmetry is achieved and one need only concentrate on one half of the circular harbor, say $-\pi/2 < \theta < \pi/2$, hence only one opening. The results are then added to obtain the solution to the original semi-circular harbor with two openings and one incident wave η_E^I .

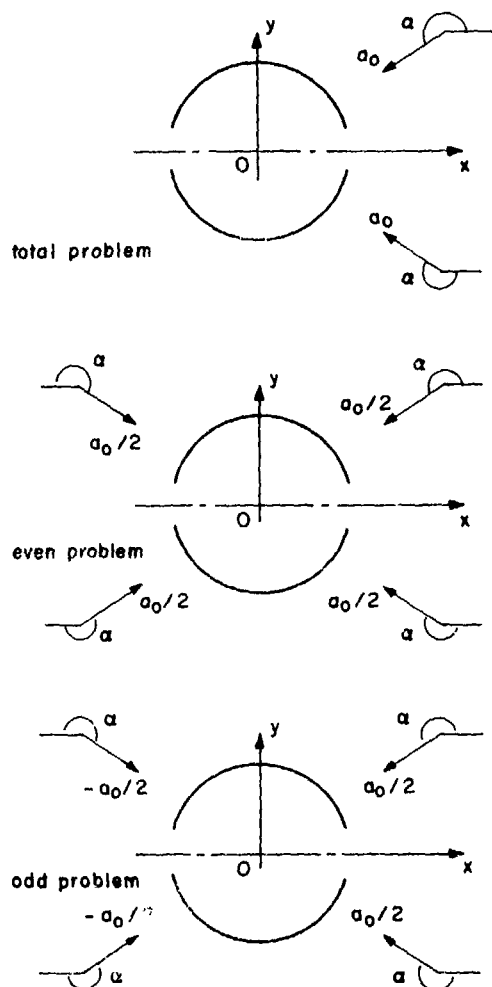


Fig. 15 Decomposition of Diffraction Problem

The Even Problem

First we shall deal with the even problem which has the incident wave η_E^I . Due to the presence of circular-shaped breakwaters, the surface displacement in the open sea can be

represented by

$$\begin{aligned} \eta_E &= \eta_E^I + \eta_E^S + \eta_E^R \\ &= 2a_0 \sum_{m=0}^{\infty} \epsilon_m i^m \cos m\alpha \cos m\theta [J_m(kr) \\ &\quad - \frac{J'_m(ka)}{H'_m(ka)} H_m(kr)] + \sum_{m=0}^{\infty} B_m \cos m\theta \frac{H_m(kr)}{k H'_m(ka)} \end{aligned} \quad (99)$$

In Eq. (99) above, the first term in the bracket is the incident waves (97), the second term represents the wave scattered from the circle of radius a without opening. The last term represents the additional radiated wave due to the presence of the openings. The coefficients B_m are to be determined. The response within the harbor basin can be expressed by

$$\eta_E^< = \sum_{m=0}^{\infty} B_m \cos m\theta \frac{J_m(kr)}{k J'_m(ka)}, \quad r \leq a \quad (100)$$

We note that (99) and (100) satisfy the governing Helmholtz equation and are symmetric about the y -axis as well as the x -axis. Eqs. (99) and (100) also satisfy the continuity of radial velocity at $r = a$

$$\frac{\partial \eta_E^>}{\partial r} = \frac{\partial \eta_E^<}{\partial r} \quad \text{at } r = a \quad (101)$$

However, the fluid velocity at the opening is still unknown.

The solution to be obtained is based on a matching of fluid velocity (or $\partial \eta / \partial r$) and displacement η at the harbor opening in both open sea and harbor basin. We denote

$$\frac{\partial \eta_E^>}{\partial r}(\theta) = \frac{\partial \eta_E^<}{\partial r}(\theta) = F_E(\theta) \quad \text{at } r = a, \quad |\theta| \leq \delta \quad (102)$$

where $F_E(\theta)$ is an unknown function and is proportional to the radial velocity at the opening. θ_0 is the angle sustained by the harbor opening. By the symmetry of the problem, the following properties exist

$$\frac{\partial \eta_E^>}{\partial r}(\pi - \theta) = \frac{\partial \eta_E^>}{\partial r}(-\theta) = \frac{\partial \eta_E^<}{\partial r}(\theta) \quad \text{at } r = a \quad (103)$$

i.e., the fluid velocity is symmetrical about both x - and y -axes. Hence, it is sufficient to consider half the basin, say, $|\theta| \leq \pi/2$, which involves only one opening.

For Eqs. (99) and (100) we have

$$\left. \frac{\partial \eta_E^>}{\partial r} \right|_{r=a} = \left. \frac{\partial \eta_E^<}{\partial r} \right|_{r=a} = \sum_{m=0}^{\infty} B_m \cos m\theta \quad (104)$$

By making use of the orthogonality of $\cos m\theta$ in $[-\pi, \pi]$ and the boundary condition that $\partial \eta_E / \partial r = 0$ on the wall, Eqs. (102) and (103), the Fourier coefficients can be expressed as

$$B_m = \frac{\epsilon_m}{\pi} \int_{-\theta_0}^{\theta_0} d\theta' \cos m\theta' F_E(\theta') \quad (105)$$

Therefore (99) and (100) become

$$\eta_E^> = 2a_0 \sum_{m=E} \epsilon_m i^m \cos m\alpha \cos m\theta [J_m(kr) - \frac{J'_m(ka)}{H'_m(ka)} H_m(kr)] + \sum_{m=E} \int_{-\theta_0}^{\theta_0} \frac{\epsilon_m H_m(kr)}{kH'_m(ka)} \cdot \cos m\theta \cos m\theta' F_E(\theta') d\theta', \quad a \leq r \quad (106)$$

$$\eta_E^< = \sum_{m=E} \int_{-\theta_0}^{\theta_0} \frac{m J'_m(kr)}{k J'_m(ka)} \cos m\theta \cos m\theta' F_E(\theta') d\theta', \quad r \geq a \quad (107)$$

Now matching $\eta_E^> = \eta_E^<$ at the harbor opening $-\theta_0 \leq \theta < \theta_0$

$$2a_0 \sum_{m=E} \epsilon_m i^m \cos m\alpha \cos m\theta [J_m(ka) - \frac{J'_m(ka)}{H'_m(ka)} H_m(ka)] + \sum_{m=E} \int_{-\theta_0}^{\theta_0} \frac{\epsilon_m H_m(ka)}{kH'_m(ka)} \cos m\theta \cos m\theta' F_E(\theta') d\theta' = \sum_{m=E} \int_{-\theta_0}^{\theta_0} \frac{\epsilon_m J'_m(ka)}{\pi k J'_m(ka)} \cos m\theta \cos m\theta' F_E(\theta') d\theta' \quad (108)$$

or

$$\frac{2a_0}{a} \frac{2i}{\pi ka} \sum_{m=E} \frac{\epsilon_m i^m}{H'_m(ka)} \cos m\alpha \cos m\theta - \int_{-\theta_0}^{\theta_0} \frac{2i}{(\pi ka)^2} \sum_{m=E} \frac{\epsilon_m}{J'_m(ka) H'_m(ka)} \cos m\theta \cos m\theta' \cdot F_E(\theta') d\theta' \quad (109)$$

where a Wronskian identity has been used. Eq. (109) can be written in the form of an integral equation

$$\int_{-\theta_0}^{\theta_0} d\theta' F_E(\theta') G_E(\theta, \theta') = \frac{H_E(\theta)}{a} \quad (110)$$

where the kernel $G_E(\theta, \theta')$ is

$$G_E(\theta, \theta') = \frac{2i}{(\pi ka)^2} \sum_{m=E} \frac{m}{J'_m(ka) H'_m(ka)} \cdot \cos m\theta \cos m\theta' \quad (111)$$

$$\text{and } H_E(\theta) = \frac{4ia}{\pi ka} \sum_{m=E} \frac{\epsilon_m i^m}{H'_m(ka)} \cos m\alpha \cos m\theta \quad (112)$$

It is also worth pointing out that the even problem can be applied to the case where the harbor is a 90° sector formed by a circular arc breakwater and two straight coast lines intersecting at a right angle.

Since $G_E(\theta, \theta')$ is a symmetric function of θ and θ' , the integral equation (110) is equivalent to the stationarity of the following functional (see [11])

$$F\{F_E\} = \frac{1}{2} \iint_{-\theta_0}^{\theta_0} d\theta d\theta' F_E(\theta) F_E(\theta') G(\theta, \theta') - \frac{1}{a} \int_{-\theta_0}^{\theta_0} d\theta F_E(\theta) H_E(\theta) \quad (113)$$

Instead of solving the integral equation we employ the stationarity of $F\{F_E\}$ to optimize the choice of an approximate solution, assumed to be of the form

$$F_E(\theta) = f_E f(\theta) \quad (114)$$

where f_E is a multiplicative parameter and $f(\theta)$ prescribed. Substituting (114) into (113) and invoking $dF/df_E = 0$ we obtain

$$f_E = \frac{\frac{1}{a} \int_{-\theta_0}^{\theta_0} d\theta f(\theta) H_E(\theta)}{\iint_{-\theta_0}^{\theta_0} d\theta d\theta' f(\theta) f(\theta') G_E(\theta, \theta')} \quad (115)$$

One reasonable choice for $f(\theta)$ is that

$$f(\theta) = \frac{1}{\pi \sqrt{\theta_o^2 - \theta^2}} \quad (116)$$

which was first suggested by Rayleigh for the acoustical Helmholtz-resonator problem, and would be realized in a two-dimensional potential flow through an opening in a plane barrier.

By making use of the identity

$$\frac{1}{\pi} \int_{-\theta_o}^{\theta_o} \frac{\cos m}{\sqrt{\theta_o^2 - \theta'^2}} d\theta' = J_o(m\theta_o) \quad (117)$$

we have

$$\frac{2a_o}{a} N_E \equiv \frac{1}{a} \int_{-\theta_o}^{\theta_o} d\theta f(\theta) H_E(\theta) \quad (118)$$

$$\frac{2a_o}{a} \frac{21}{ka} \sum_{Ev} \epsilon_m i^m \cos m\alpha \frac{J_o(\theta_o)}{H_m'(ka)} \quad (118)$$

N_E may be interpreted as a measure of excitation to the harbor basin due to the piston action at the openings, since $H_E(\theta)$ is proportional to the pressure due to the waves outside in the absence of openings. Furthermore

$$D_E = \int_{-\theta_o}^{\theta_o} d\theta d\theta' f(\theta) f(\theta') G_E(\theta, \theta') \quad (119)$$

$$= \frac{21}{(\pi ka)^2} \sum_{Ev} \epsilon_m \frac{J_o^2(\theta_o)}{J_m'(ka) H_m'(ka)}$$

where D_E is related to the complex impedance of the harbor basin, it includes the effect of radiation damping. In terms of N_E and D_E we have

$$F_E(\theta) = \frac{2a_o}{a} \frac{N_E}{D_E} \frac{1}{\pi \sqrt{\theta_o^2 - \theta^2}} \quad (120)$$

Hence the harbor response of the even problem is

$$\eta_E^< = \frac{2a_o}{D_E} \sum_{Ev} \frac{\epsilon_m J_o(m\theta_o)}{ka J_m'(ka)} J_m(kr) \cos m\theta \quad (121)$$

$$r \leq a$$

The Odd Problem and the Combined Problem

The odd problem having the incident waves η_0 can be solved by using the same procedures as the even problem. Since in the odd problem the velocity distribution is symmetric with respect to the x-axis and antisymmetric with respect to the y-axis, (102) and (103) should be replaced by

$$\frac{\partial \eta_0^>}{\partial r}(\theta) = \frac{\partial \eta_0^<}{\partial r}(\theta) = F_o(\theta) \quad \text{at } r = a, |\theta| \leq \theta_o \quad (122)$$

$$\frac{\partial \eta_0}{\partial r}(\theta) = \frac{\partial \eta_0}{\partial r}(-\theta) = -\frac{\partial \eta_0}{\partial r}(\pi - \theta) \quad \text{at } r = a \quad (123)$$

Carrying out all the steps, the results are of the same form as the even problem if the subscript E is replaced by "O" (odd), i.e.

$$N_O = \frac{2k}{\pi ka} \sum_{Odd} \epsilon_m i^m \cos m\alpha \frac{J_o(m\theta_o)}{H_m'(ka)} \quad (124)$$

$$D_O = \frac{21}{(\pi ka)^2} \sum_{Odd} \epsilon_m \frac{J_o^2(\theta_o)}{J_m'(ka) H_m'(ka)} \quad (125)$$

$$\eta_O^< = \frac{2a_o}{D_O} \sum_{Odd} \frac{\epsilon_m J_o(m\theta_o)}{ka J_m'(ka)} J_m(kr) \cos m\theta \quad (126)$$

$$r \leq a$$

Summarizing, the total harbor response is

$$\eta^< = \eta_E^< + \eta_O^<$$

$$= \frac{2a_o}{D_O} \sum_{Odd} \frac{\epsilon_m J_o(m\theta_o)}{\pi ka J_m'(ka)} J_m(kr) \cos m\theta$$

$$+ \frac{2a_o}{D_O} \sum_{Odd} \frac{\epsilon_m J_o(m\theta_o)}{ka J_m'(ka)} J_m(kr) \cos m\theta$$

$$= 2a_o \sum_{m=0}^{\infty} A_m \frac{J_m(kr)}{J_m(ka)} \cos m\theta \quad (127)$$

where we define

$$A_m = \begin{cases} \frac{N_E}{D_E} & \text{if } m = \text{even} \\ \frac{\epsilon_m J_o(m\theta_o)}{\pi ka} \frac{J_m(ka)}{J_m'(ka)} & \text{if } m = \text{odd} \end{cases} \quad (128)$$

A_m may be defined as the amplification factor for the mode whose angular pattern is proportional to $\cos m\theta$.

As an overall measure of the response of the harbor basin to an incident wave, the mean-square elevation which is defined by averaging over the entire basin, i.e.

$$(2a_o A_{rms})^2 \equiv \frac{1}{\pi a^2} \int_0^{2\pi} \int_0^a r dr d\theta \eta^< \eta^{<*} = \frac{16a_o^2}{(ka)^2} \sum_{m=0}^{\infty} \frac{A_m^* A_m}{J_m^2(ka)} \sum_{n=0}^{\infty} (m+2n+1) J_{n+2n+1}^2(ka) \quad (129)$$

where the asterisk means complex conjugate. The following identity has been used in reaching (129)

$$\int_0^z t J_{\nu-1}^2(t) dt = 2 \sum_{k=0}^{\infty} (\nu + 2k) J_{\nu+2k}^2(z) \quad (130)$$

Eq. (129) is used for computations. Instead of the variational approximation we have also used the more elaborate Galerkin method of solving the integral equation (110) by representing $F_E(\theta)$ as a series of orthonormal terms. Spotty calculations show that Eq. (129) is sufficiently accurate for the range of parameters studied here.

APPENDIX II COMPARISON OF WAVE FORCES ACCORDING TO CORRECTED LONG WAVE THEORY AND EXACT THEORY FOR A CIRCULAR DOCK

For a dock of circular cross section in our unbounded ocean of constant depth h , the wave forces have been calculated for arbitrary kh by Black, Mei and Bray [12] and by Garrett [13]. In a recent paper on elliptical docks, Chen and Mei [14] applied the long wave approximation similar to the one used herein, and gave as a special case the forces and moment on a circular dock when a plane incident wave attacks from $x \sim -\infty$. The cylinder has a radius a and draft d and the clearance beneath is $H = h - d$. The forces are

$$[F_x]_{kh=0} = [\rho g a_o \pi a^2] \frac{(4/\pi) d/a}{ka H_1'(ka) - \frac{H}{h} H_1(ka)} \quad (131)$$

$$[F_z]_{kh=0} = [\rho g a_o \pi a^2] \frac{2d}{\pi ka H_1'(ka)} \quad (132)$$

The moment about the axis parallel to the y -axis and passing through the point $x = 0, y = 0, z = -h + c$ is

$$[M_y]_{kh=0} = M_y^H + M_y^V \quad (133.a)$$

where M_y^H is due to the horizontal pressure on the side and M_y^V is due to the vertical pressure on the bottom of the dock

$$M_y^H = [\rho g a_o \pi a^2]$$

$$\left\{ \frac{d}{a} \frac{h + H - 2c}{2a} \frac{4/\pi}{ka H_1'(ka) - \frac{H}{h} H_1(ka)} \right\} \quad (133.b)$$

$$M_y^V = \frac{[\rho g a_o \pi a^2]}{\pi [ka H_1'(ka) - \frac{H}{h} H_1(ka)]} \quad (133.c)$$

The normalized F_x, F_z and M_y according to Eqs. (131-133) are plotted in long dashes in Figures

16, 17 and 18 with the moment axis at the bottom of the dock $c = H$. For comparison, the exact results, taken from [13], are plotted in solid lines. It is seen that deviation between the two theories is large for short waves (small ka). After correcting for the vertical variation in accordance with Eqs. (91) and (92), the normalized forces are shown in short dashes. The corresponding corrected moment is given by

$$[M_y]_{kh} \approx M_y^H \left[(ka)^2 \frac{d}{a} \frac{h + H - 2c}{2a} \right]^{-1} [-1 + k(h - c) \tanh kh + k(c - H) \frac{\sinh kh}{\cosh kh} + \frac{\cosh kh}{\cosh kh}] + M_y^V \frac{\cosh kh}{\cosh kh} \quad (134)$$

and is plotted in short dashes in Fig. 18 for $c = H$. The improvement brought about by the heuristic correction is in general remarkable. As the three-dimensional effects due to the edges of the dock should diminish with decreasing h/a it is reasonable to expect still better agreement for larger radius a . Using the same approximation for more general shape, we believe that good results can be obtained if the least principal dimension of the body is not much smaller than the water depth.

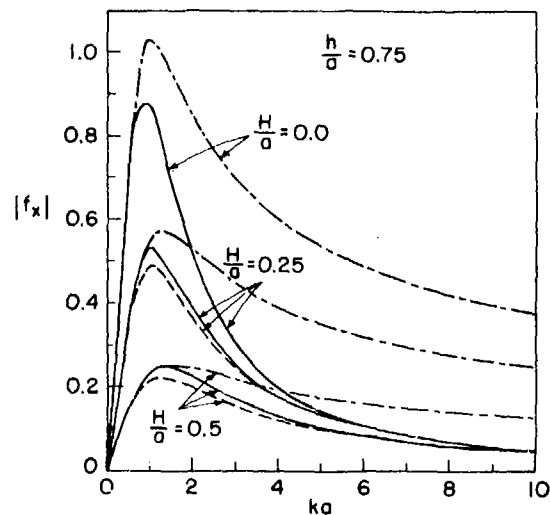


Fig. 16 Normalized horizontal force on a circular dock $f_x = F_x / (\rho g a_o \pi a^2)$ — exact [13], - - - long wave theory, - - - corrected long wave theory.

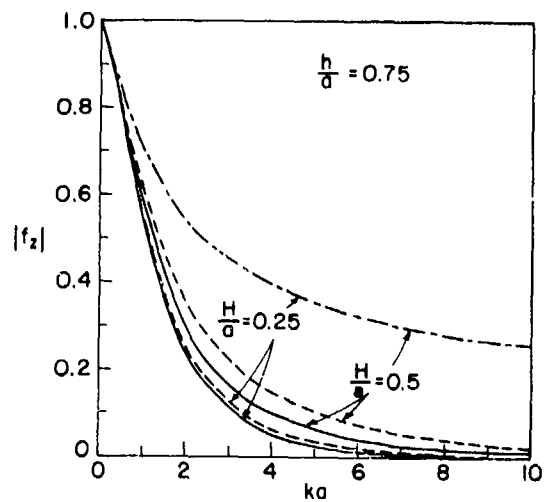


Fig. 17 Normalized vertical force on a circular dock $f_z = F_z (\rho g a_0 \pi a^2)^{-1}$. — exact [13], - - - long wave theory, - · - · - corrected long wave theory

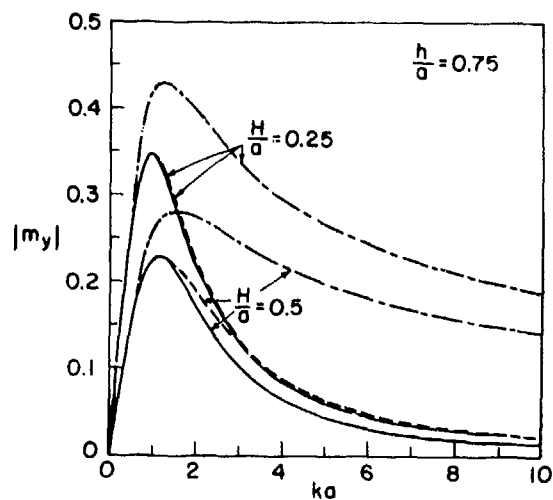


Fig. 18 Normalized moment on a circular dock $m_y = M_y (\rho g a_0 \pi a^3)^{-1}$. — exact [13], - - - long wave theory, - · - · - corrected long wave theory.

DISCUSSION

R. T. HO AND H. BOMZE⁽²⁾

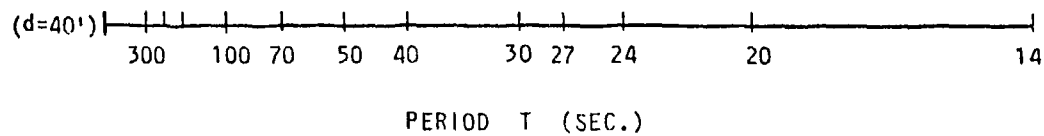
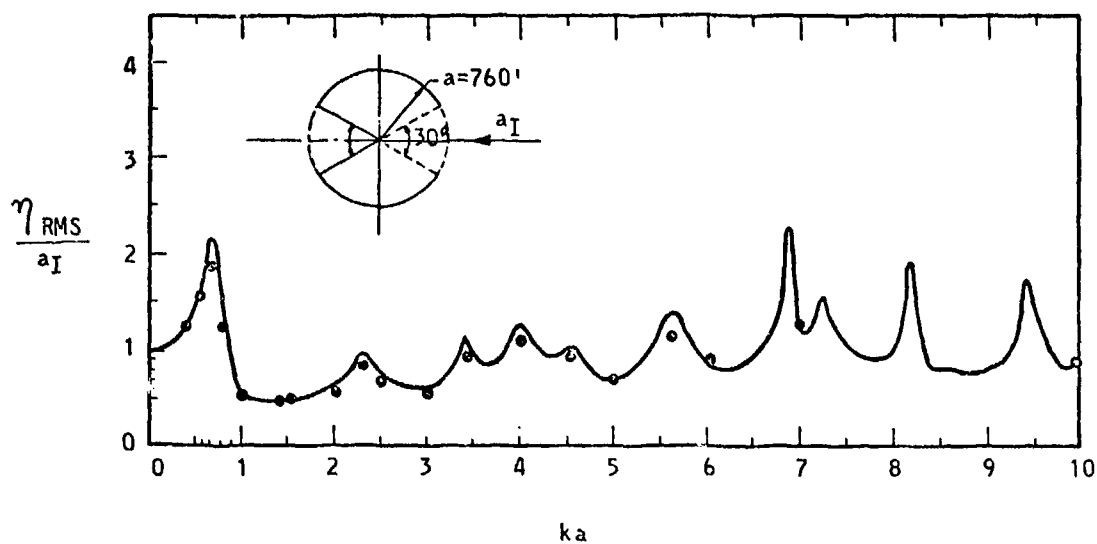
The writers would like to submit a short note about an alternative approach for solving the basin oscillation problem for an offshore harbor, namely, the Green's-function integral equation method — well known to naval architects — which distributes source functions with unknown strength along all solid boundaries where the boundary conditions are not satisfied by the chosen Green's function. For the two-dimensional case in particular, this approach is essentially an extension of Lee and Raichlen's⁽³⁾ method with the difference that both the diffracted wave field outside the breakwater and the radiating wave field through the basin openings are solved together.

Preliminary results for the case of circular harbor with incident waves normal to the basin entrance, shown in Figure 1, are in reasonably good agreement with the analytical solution by Chen & Mei.⁽¹⁾ Further results for the offshore basin are being generated and will be published in the near future. This provides an alternative approach to the

problem and a check to both methods as well.

This work has been sponsored by Public Service Electric and Gas Company of New Jersey in connection with locating floating nuclear power plants in a breakwater enclosure approximately three miles offshore Little Egg Inlet, New Jersey.

- (1) Paper presented by H.S. Chen & C.C. Mei in the tenth symposium on naval hydrodynamics, M.I.T., June 24-28, 1974.
- (2) Frederic R. Harris, Inc., Great Neck, New York.
- (3) Lee, J.J. and Raichlen, F., "Oscillations in Harbors With Connected Basins", ASCE, J. Waterways, Harbors and Coastal Engineering, No. WW3, August 1972.



LEGEND

- CHEN & MEI (1974)
- SWITCH RESULTS (HARRIS)

FIGURE 1

RMS AMPLIFICATION FACTORS IN A CIRCULAR HARBOR
WITH INCIDENT WAVES NORMAL TO THE BASIN OPENING

BREAKING WAVES—IN DEEP OR SHALLOW WATER

M. S. Longuet-Higgins

Department of Applied Mathematics and Theoretical Physics,
Silver Street, Cambridge, England and Institute of
Oceanographic Sciences, Wormley, Surrey, England.

ABSTRACT

Free gravity waves in deep water can be induced to break in a laboratory channel either by decelerating the wave-maker, or by use of the Fresnel envelope at an advancing wave front. The period of breaking is then twice that of the waves. Quasi-steady breakers can be produced by the reflection of a bow-wave from the side of a ship towing tank. Measurements of the mean flow field and the turbulence show a downwards transfer of momentum in the upper part of the wave. A theoretical model of a spilling breaker has been proposed which accounts quantitatively for some features of the whitecap. Some intermittency is observed, which is connected with the rounding of the wave crest due to loss of energy.

INTRODUCTION

Breaking waves are of importance to ship hydrodynamics for several reasons. The breaking of the bow wave near the hull can contribute appreciably to the ship's wave resistance (1,2). Calculations of wave resistance based on the amplitude of the Kelvin wave pattern must also take account of energy lost in breaking. Not least, the impact of heavy seas against the hull or superstructure may cause considerable damage.

Oceanographers have additional reasons for being interested in breaking waves. Breaking is important in the energy budget of wind-generated waves, and in the transfer of momentum from waves to surface currents. It also generates turbulence which mixes the upper layers of the ocean and influences the transfers of heat and momentum between the ocean and atmosphere.

In trying to understand the highly nonlinear phenomenon of a breaking, we encounter the difficulty that as yet there exists no satisfactory theory for any of the various kinds of breaking wave. Moreover, such experimental work has been done, has usually been concerned with waves in shallow water, where the bottom plays an essential role.

It is therefore appropriate to consider possible methods for studying experimentally the breaking of waves in deep water. In the present paper we shall describe several such methods.

In addition we shall discuss a simple model of spilling breakers, which promises to explain some of the observed features of these mixed laminar and turbulent flows.

WAVES IN A LONG CHANNEL

Given a rectangular channel, deep compared to the wavelength to be studied, in which there is a wavemaker at one end and a wave absorber (perhaps in the form of a shoaling beach) at the other (see Figure 1). How is one to induce wave breaking at some intermediate point along the tank?

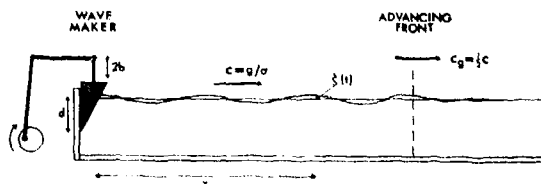


Fig. 1 Schematic drawing of a rectangular wave channel, with wavemaker at one end.

If one increases the amplitude of the wavemaker, keeping the radian frequency σ constant, then two drawbacks appear. In the first place one may get cross-waves, of frequency $\frac{1}{2}\sigma$. Assuming these to be eliminated by technical devices such as parallel baffles, one finds, secondly, that with a steady train of waves the amplitude tends to decay with distance from the wavemaker owing to the progressive loss of energy with horizontal distance x . Hence the waves will break, in deep water, only very close to the wavemaker, where they are possibly distorted by local "transients" due to the wavemaker itself.

To avoid this difficulty we may make use of the dispersive properties of deep-water waves, as follows.

Method 1 : Storm-building. For small-amplitude waves in deep water we know that the group-velocity C' (the propagation velocity for the wave energy) is given by

$$C' = \frac{1}{2} C = \frac{g}{2\sigma} \quad (1)$$

(where C is the phase velocity). The longer waves (with lower σ) are therefore propagated faster than the shorter waves (with higher σ). Suppose that at time t_1 , the wave maker generates a train of waves of frequency σ_1 , and that at time t_2 this is followed by a train of waves of frequency $\sigma_2 > \sigma_1$ (see Figure 2).

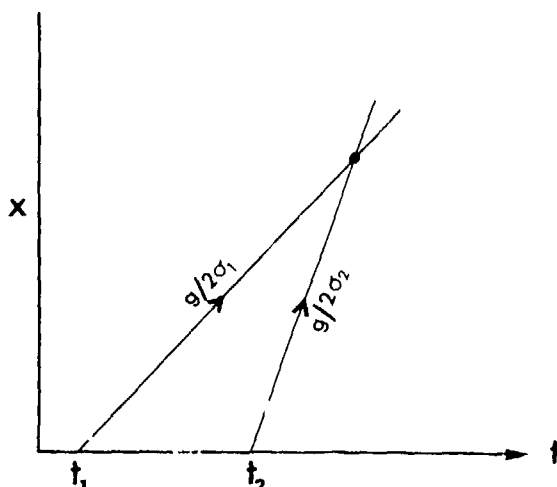


Fig. 2 Propagation diagram for two groups of waves of different frequency.

The second train of waves will overtake the first at time t and at a distance x from the wavemaker, given by

$$\frac{x}{t-t_1} = \frac{g}{2\sigma_1}, \quad \frac{x}{t-t_2} = \frac{g}{2\sigma_2} \quad (2)$$

Eliminating t we have

$$\frac{\sigma_1 - \sigma_2}{t_2 - t_1} = \frac{g}{2x} \quad (3)$$

Clearly if the frequency σ is varied continuously so that

$$\frac{d\sigma}{dt} = -\frac{g}{2x} \quad (4)$$

then the wave energy will tend to converge in the neighbourhood of a single point ∞ , building up a "storm" in which breaking waves can occur. A deep-water breaking wave produced in this manner is shown in Figure 3.



Fig. 3 A breaking wave in relatively deep water produced in a channel 15 m long and 50 cm deep, at a point 7 m from the wavemaker, by decelerating the wavemaker. (Method 1).

(The author suggested this method to Dr. N. Hogben in 1959 at the time of the installation of the wavemaker in the $\frac{1}{4}$ -mile channel at The National Physical Laboratory. It has been used for building wave spectra, but apparently not for studying the process of wave breaking).

Method 2 : Travelling wave fronts.

A second technique depends on the finite bandwidth of frequencies associated with the sudden starting or stopping of the wavemaker.

Suppose that at time $t=0$ the wavemaker is switched on suddenly with constant amplitude b and frequency σ . A train of waves is propagated down the tank, the front moving with approximately the group-velocity $g/2\sigma$. According to linear theory the elevation of the free surface at position x and time t can be shown to be given by

$$\zeta(x,t) \sim i\beta F(\tau) e^{i(\omega t - \sigma^2 x/g)} \quad (5)$$

(the real part being understood) where β is a constant depending on the form of the wavemaker. For a wedge of depth d and angle β we have

$$\beta = 2b(1 - e^{-\sigma^2 d/g}) \sin \beta \quad (6)$$

τ is a dimensionless time variable:

$$\tau = \left(\frac{g}{2\pi x}\right)^{1/2} \left(t - \frac{2\sigma x}{g}\right) \quad (7)$$

which equals zero at the front itself; and $F(\tau)$ describes the wave envelope, in fact

$$F(\tau) = \frac{1}{2} + \frac{1}{(2i)^{1/2}} \int_0^\tau e^{i\pi\lambda^2/2} d\lambda \quad (8)$$

(see for example (2)). This function is related to the Fresnel integral (4). A compressed sketch of the surface elevation ζ is shown in Figure 4.

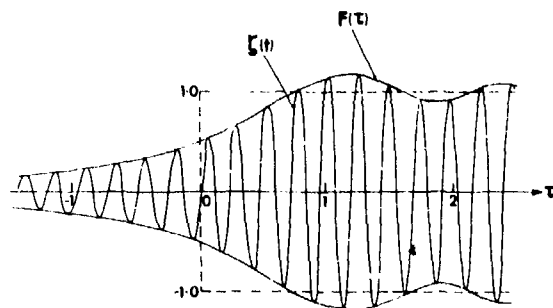


Fig. 4 Sketch of the surface elevation at a fixed point x as a function of the time t . (Method 2).

It can be seen that the envelope function $F(\tau)$ at first increases exponentially, reaches the value $\frac{1}{2}$ at $\tau=0$, then overshoots its final amplitude by about 19% before finally settling down to its final amplitude 1 as $\tau \rightarrow \infty$. This suggests that it may be possible for the waves to attain their breaking amplitude close to the wave front, while not breaking, and so losing energy, in the steady wave train behind.

Figures 5 and 6 show an experimental verification of this idea, which the author carried out in a tank 330 ft long, and 6 ft wide, at the Hydraulics Research Station, Wallingford. The plotted points show the amplitude of successive waves in a record of surface elevation taken at a fixed point 160 ft from the wavemaker. The solid curve is the theoretical amplitude as given by the envelope function $F(\tau)$. The observed wave amplitude follows the theoretical curve fairly well, especially ahead of the front, where the waves are low. The maximum wave amplitude is slightly larger than predicted, and occurs a little sooner. This is probably a nonlinear effect. According to Whitham's theory of nonlinear wave propagation (5) the group velocity (defined as energy flux divided by energy density) is an increasing function of the wave amplitude. The order of magnitude of the discrepancy between observed and theoretical group velocities in Figure 5 is 4%, which is of the same order as would be expected on the basis of nonlinear theory.

Figure 6 shows five records taken at the same point, with different wave amplitudes. As the amplitude is increased, so the arrival of the wave front is advanced. The bottom record, with the largest amplitude shows a sharp-pointed crest typical of a wave of maximum amplitude.

A film record of the advancing wave train shows the occurrence of breaking waves at the head of the wave train.¹ Very striking is the fact that the breakers occur once every two wave cycles. This is due to the relative motion of the waves and their envelope. The waves tend to break when a crest passes the position of a maximum in the wave envelope. But the speed of a crest relative to the envelope is only $\frac{1}{2}c$ (since the envelope itself travels with velocity $\frac{1}{2}c$). If L denotes the wavelength, then the time interval between the occurrence of two successive breakers is

$$\frac{L}{\frac{1}{2}c} = \frac{2L}{c} = 2T, \quad (9)$$

that is to say two wave periods.

It may be mentioned that the same difference between phase and group velocity is responsible for the leap-frogging effect noticed in whitecaps in deep water (6). It was observed from the air that whitecaps tend to occur in sequences, each whitecap being succeeded by the next further downwind, at an interval of about two wave periods.

WAVES FROM A MOVING SHIP

The time-dependence inherent in a breaking wave may be partly eliminated by studying the pattern of waves generated by a body in steady motion through the water. If measuring instruments are attached to the moving body, the waves are then practically "reduced to rest". Some fluctuations of course remain owing to turbulence and possible instabilities in the flow.

With this idea in mind, the present author and Dr. M. Donelar (7) experimented with the production of breakers in the wave pattern following a small motor launch. The venture was only partly successful until we noticed that the wave amplitude was greatly enhanced when the launch was set on a course parallel to an embankment or jetty (see Figure 7). Evidently this was due to the reflection of the waves from the embankment or, to put it another way, to the presence of an

¹ Shown at the Symposium

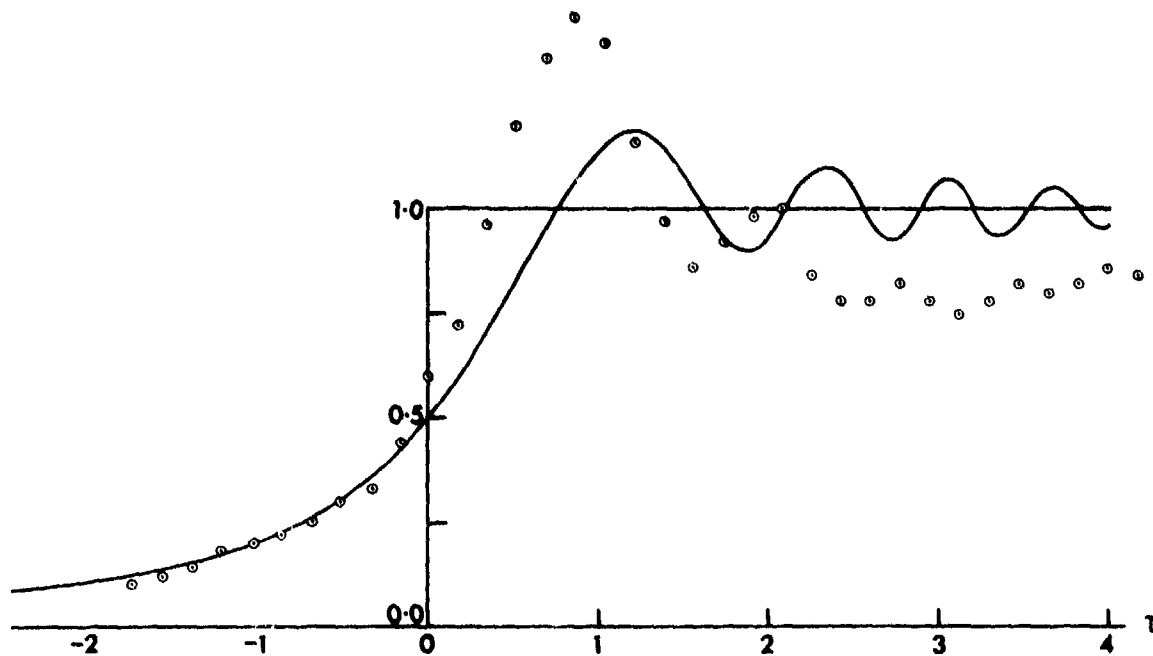


Fig. 5 Comparison of the observed wave amplitude (plotted points) at a point 160 ft from the wavemaker, as a function of the nondimensional time τ . The solid curve represents the envelope function $F(\tau)$ of equation (7). Wave frequency $\sigma = 5.52$ rad/sec.

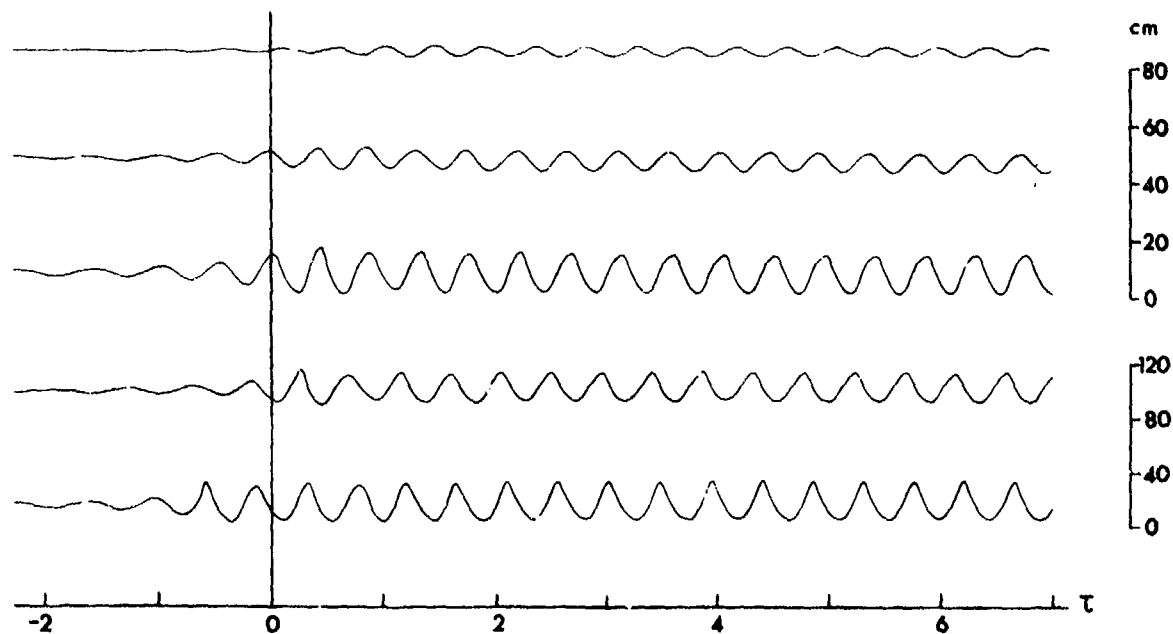


Fig. 6 Records of the wave amplitude at a fixed point $X = 160$ ft, for waves of the same frequency but different amplitude, showing effects of nonlinearity.



Fig. 7 Bow-wave from a moving launch breaking against an embankment.

image ship moving parallel to the first. The wave pattern due to the image ship then reinforced the first so that the wave amplitude near the embankment was easily increased beyond the breaking point. Moreover the wave crests became almost normal to the embankment, making the flow nearly two-dimensional.

For practical reasons, the experiment was transferred to the No. 2 towing tank at the National Physical Laboratory, where moreover the experiment could be repeated under controlled conditions. Figure 8 shows the bow-wave produced by a model ship towed at a speed of 2 m/s parallel to the wall, and at a distance



Fig. 8 The bow wave produced by a model ship towed at a speed of 2.0 m/s in the No. 2 towing tank at the National Physical Laboratory, Teddington.

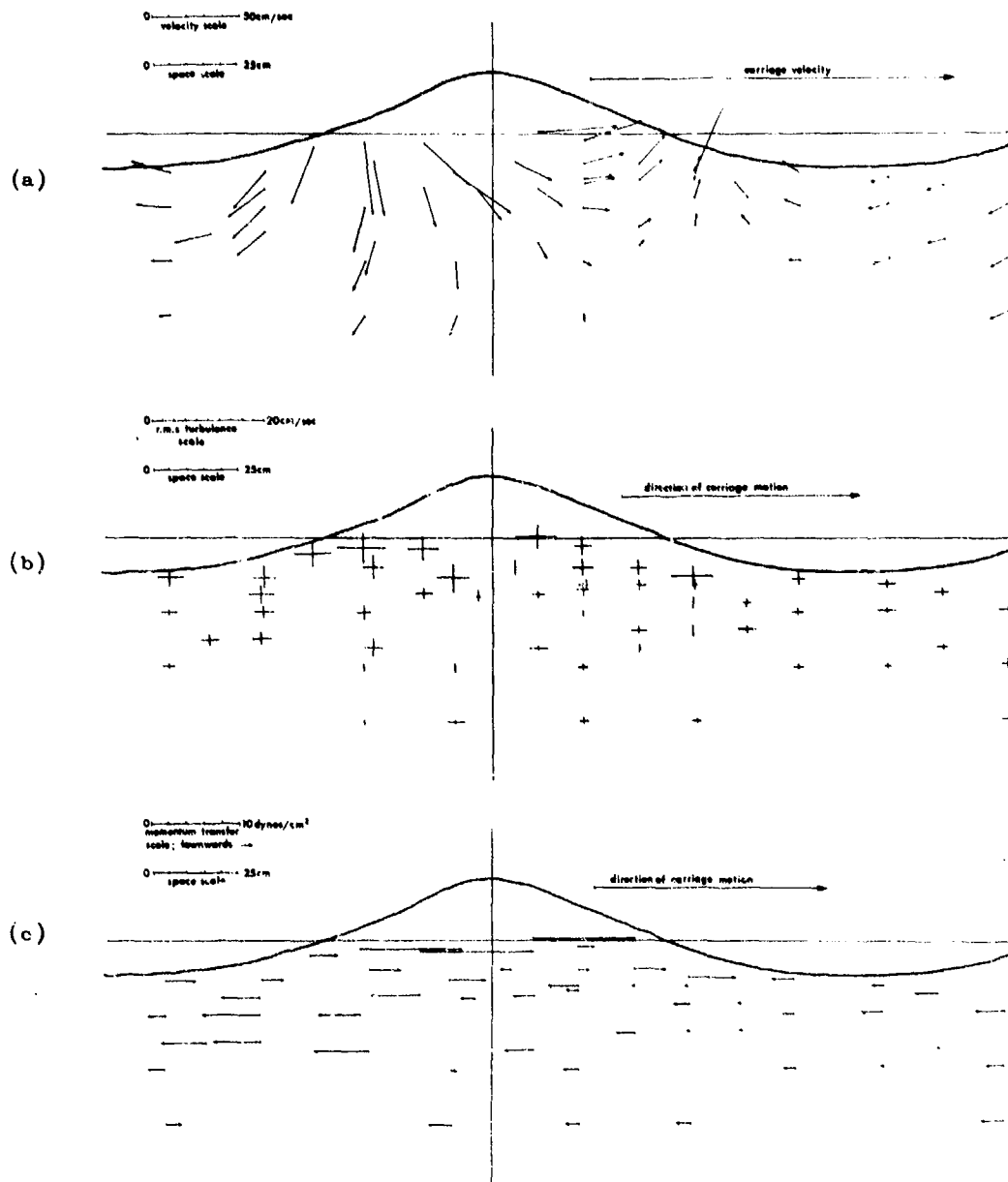


Fig. 9 Velocity measurements in the experiments of Figure 8. (a) mean velocity field, after subtraction of the carriage velocity. (b) r.m.s. levels of turbulence: the horizontal and vertical arms of the crosses represent $(\overline{u'^2})^{1/2}$ and $(\overline{v'^2})^{1/2}$ respectively. (c) the "shear" component of the turbulence: $\overline{u'v'}$. A vector pointing to the right indicates a downward transfer of \mathcal{M} -momentum.

of 1 m from it. The velocity field was measured with an electromagnetic flowmeter capable of recording two components of flow, in this case the vertical component and the horizontal component in the direction of the motion of the carriage. The response time of the flowmeter was of order 0.05 sec so that fluctuations with frequency less than about 20 c/s were measurable. By subtracting out the constant velocity of the carriage it was possible to construct a picture of the mean velocity field (\bar{u}, \bar{v}) relative to a stationary observer and the fluctuating components (u', v') . Because of cavitation round the instrument and its support, it was not possible to measure the velocity very close to the free surface.

The mean velocity field is shown in Figure 9a. Evidently this resembles the particle velocity field in a non-breaking, irrotational wave, that is to say upwards on the forward face and downwards at the rear. These velocities are of course much less than the steady carriage velocity, also shown in Figure 9a.

In Figure 9b can be seen the r.m.s. levels of turbulence in the horizontal and vertical directions: the crosses represent $(\overline{u'^2})^{1/2}$ and $(\overline{v'^2})^{1/2}$. Clearly the highest levels of turbulence begin on the forward face of the wave just below the mean level, where in fact the toe of the whitecap is found. The turbulence is then swept back, with the mean current (in the steady flow referred to axes moving with the wave) towards the rear of the wave. Further to the rear the turbulence starts to decay and also spreads downwards.

Figure 9c shows the turbulent momentum flux $(\overline{u'v'})$. Conventionally the arrows are drawn in the positive x -direction when the flux of x -momentum is downwards. It can be seen that in the upper part of the wave, beneath the crest, the flux is strongly downwards, but below the level of the troughs the flux is, unexpectedly, in the reverse direction, though weaker. This suggests the presence of a jet-like current directed towards the rear, at the level where the momentum transfer changes sign. Such a current may be associated with the injection of air near the toe of the whitecap. On the other hand, in the wave trough at least, the vertical gradient of the steady flow \bar{u} is negative, even in an irrotational wave, so that if turbulence exists, a negative value of $\overline{u'v'}$ is not unreasonable.

SPILLING BREAKERS

To study the flow close to the free surface, photographic methods are clearly the most useful. For this purpose a side

window is essential. Figure 10 shows a

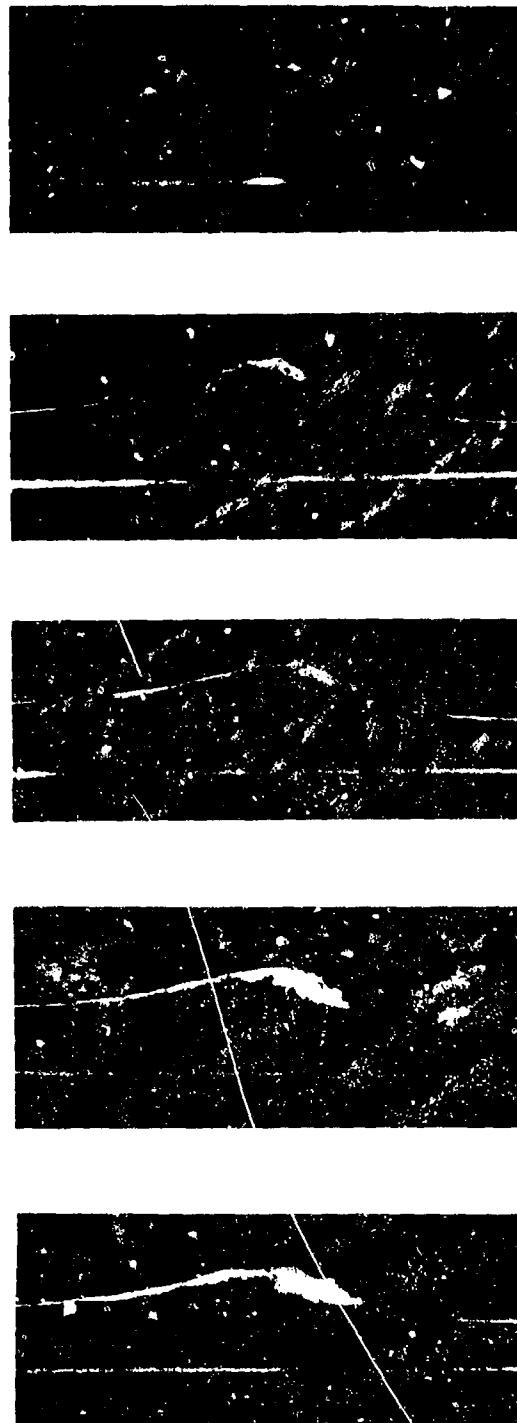


Fig. 10 A sequence showing the development of a spilling breaker (after Kjeldsen and Olsen 1971).

sequence of pictures of breaking waves in shallow water, taken from a recent film by Kjeldsen and Olsen (8). The waves are travelling from right to left in gradually shoaling water, and the breakers are of the spilling type, in which the motion is quasi-steady and the whitecap spreads rather slowly down the forward face of the wave.

A theoretical model of spilling breakers has recently been suggested by Longuet-Higgins and Turner (1973). In this the breaker is regarded as a turbulent gravity current riding down the forward slope of the wave, and retaining its identity because it is lighter than the water below owing to the trapping of air bubbles (Figure 11). It is assumed

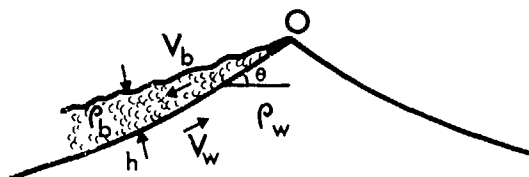


Fig. 11 Model of a spilling breaker.

that across the lower boundary of the gravity current entrainment of heavier fluid takes place, at a rate governed by the overall Richardson number. The entrainment of ass has the effect of increasing the volume of the whitecap and helping to produce an accelerating flow, while the entrainment of momentum gives rise to a drag which reduces the downhill acceleration.

The equations for the conservation of mass and momentum can be shown to be satisfied by a "similarity solution", in which the thickness of the whitecap is proportional to the distance s from the crest of the wave. The down slope velocity is proportional to $s^{1/2}$. (In Eulerian coordinates the velocity is steady; in Lagrangian coordinates each particle undergoes an acceleration parallel to the free surface). Since the velocity in a Stokes 120° angle is also proportional to $s^{1/2}$ this implies that such a flow can start from a small disturbance with zero flux, and propagate with constant acceleration.

Solutions of this kind are possible only when the slope and density difference are sufficiently large; otherwise the upwards drag dominates and a self-sustaining flow cannot form. For a slope of 30° near the crest of the breaking wave, a density difference greater than 8% is required to sustain a steady motion, at which point the downslope velocity is 12% of the opposing velocity at the wave surface. Density differences at least of this order have been observed in hydraulic jumps (9).

The detailed examination of a film sequence of breaking waves has shown a very interesting characteristic of the whitecaps, namely their intermittent behaviour. Figure 12 (10) shows the length of whitecap plotted as a function of time, as given by the frame number in the film record of Kjeldsen and Olsen. What evidently happens is that from time to time the wave crest becomes rounded and part of the whitecap is swept over

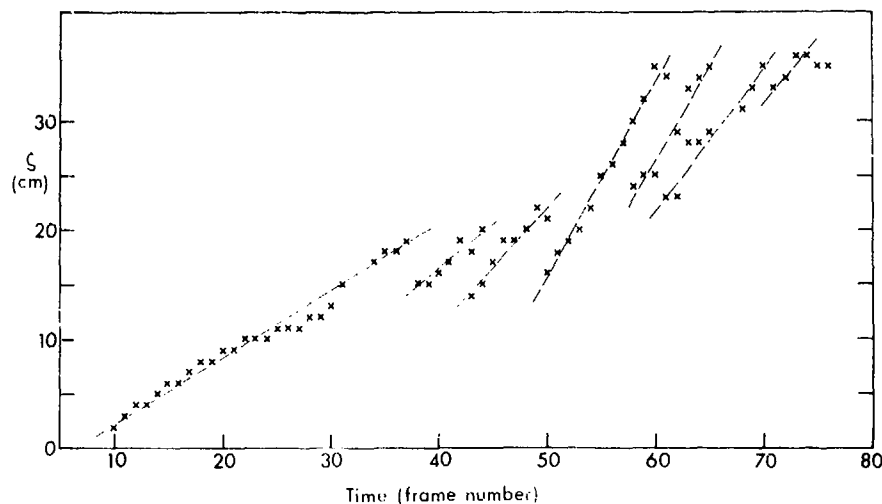


Fig. 12 Measurements of the length of whitecap in a spilling breaker, plotted against frame number, showing intermittency (from Longuet-Higgins and Turner, 1974).

the crest, eventually dissolving on the rear of the wave. This rounding of the whitecap can be attributed to a loss of wave energy resulting from the work done by the wave in supporting the whitecap on its forward face (see Section 8 of reference (10)).

The form of spilling breakers on very gently shelving beaches with gradients of 0.02 or less is known to resemble quite closely that of solitary waves (see (11)). It is therefore relevant to a discussion of this phenomenon that the solitary wave of maximum amplitude (with a crest angle of 120°) has recently been found not to be the most energetic, for a given undisturbed water depth (12). Figure 13 shows the calculated energy and

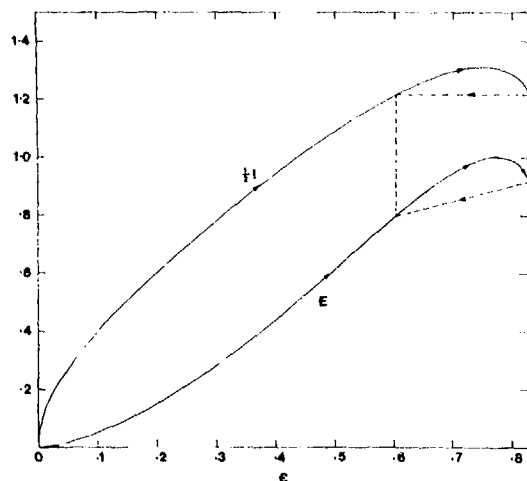


Fig. 13 The dimensionless energy E and momentum I of a solitary wave, as a function of the wave amplitude $\epsilon = a/h$, where h is the undisturbed depth (from Longuet-Higgins and Fenton 1974).

momentum, as a function of wave height. It appears then that a wave on reaching the maximum energy will gain further height only by losing some energy, perhaps by breaking or by instabilities on the forward face. When finally the wave attains its greatest height, any further loss of energy causes it to jump back to a point lower down on the energy curve, possibly to a point where the wave momentum is the same both before and after the jump (as indicated by the arrows to the left in Figure 13). Thus a non-linear property of surface waves may help to produce the observed intermittency.

REFERENCES

1. Baba, E., "Study of separation of ship resistance components," Mitsubishi Technical Bulletin, No. 59, 1969, pp. 1-16.
2. Dagan, G., and Tulin, M., "Two-dimensional free-surface gravity flow past blunt bodies," Journal of Fluid Mechanics, Vol. 51, 1972, pp. 529-543.
3. Miles, J.W., "Transient gravity wave response to an oscillating pressure," Journal of Fluid Mechanics, Vol. 13, 1962, pp. 145-150.
4. Abramowitz, M., and Stegun, I.A., Handbook of Mathematical Functions, Washington, D.C., U.S. Govt. Printing Office, 1964, 1046 pp.
5. Whitham, G.B., "Nonlinear dispersive waves," Proceedings of the Royal Society of London A, Vol. 283, 1965, pp. 238-261.
6. Donelan, M., Longuet-Higgins, M.S., and Turner, J.S., "Periodicity in whitecaps," Nature, London, Vol. 239, 1972, pp. 449-451.
7. Donelan, M., and Longuet-Higgins, M.S., "Some observations of the field of motion in breaking waves in deep water," (in preparation).
8. Kjeldsen, S.P., and Olsen, G.B., "Breaking waves" (16 mm film), Lyngby, Technical University of Denmark, 1972.
9. Rajaratnam, N., "An experimental study of the air entrainment characteristics of hydraulic jump," Journal of the Institution of Engineers of India, Vol. 42, 1962, pp. 247-273.
10. Longuet-Higgins, M.S., and Turner, J.S., "An 'entraining plume' model of a spilling breaker," Journal of Fluid Mechanics, Vol. 63, 1974, pp. 1-20.
11. Ippen, A.T., and Kulin, G., "Shoaling and breaking characteristics of the solitary wave," Massachusetts Institute of Technology, Hydrodynamics Laboratory Technical Report No. 15, 1955.
12. Longuet-Higgins, M.S. and Fenton, J.D., "On the mass, momentum, energy and circulation of a solitary wave II," Proceedings of the Royal Society of London A, (in press).

FUNDAMENTAL HYDRODYNAMICS

SESSION VII

Friday, June 28, 1974
9:00 A.M. — 12:10 P.M.

Chairman: Prof. Dr. K. Wieghardt
Director, Institute for Shipbuilding
Germany

Numerical Solutions to Free-Surface Flow Problems	609
K.J. Bai and R.W. Yeung, MIT, Cambridge, Massachusetts	
Numerical Solutions of Two-Dimensional Nonlinear Wave Problems	649
C.H. vonKerczek and N. Salvesen, NSRDC, Bethesda, Maryland	
Two-Dimensional Calculations of the Motion of Floating Bodies	667
R.K.C. Chan and C.W. Hirt, Science Applications, Inc., La Jolla, California	
Three-Dimensional Turbulent Boundary Layers	685
J. Kux, Institut für Schiffbau der Universität Hamburg, Hamburg, Germany	
The Prediction of Transition from Laminar to Turbulent Flow in Boundary Layers on Bodies of Revolution	705
P.S. Granville, NSRDC, Bethesda, Maryland	

NUMERICAL SOLUTIONS TO FREE-SURFACE FLOW PROBLEMS

K. J. Bai
M.I.T.
Cambridge, Massachusetts

R. W. Yeung
M.I.T.
Cambridge, Massachusetts

Two numerical methods for solving boundary-value problems related to potential flows with a free surface are introduced in this paper. Only forced motion and diffraction problems are considered here, although these schemes are equally applicable to any first order time-harmonic problem of similar nature.

The first method, termed finite-element variational method, applies the conventional variational form for this type of boundary value problems. A modified variational method utilizing eigenfunctions expansions is also described. This latter scheme proves to be much more efficient.

The second method, termed fundamental-singularity distribution method, works with the fluid boundary only. Green's theorem is applied using merely the source function for an unbounded fluid. This results in an integral equation with the unknown function being the potential along the entire fluid boundary. An alternative scheme to deal with the case of an infinitely deep fluid is also presented.

Both methods place no restrictions on the geometry of the body nor the bottom topography and are valid for either two- or three-dimensional problems. Test results obtained by the present methods for the case of a heaving circular cylinder in water of finite or infinite depth agree well with those obtained by others, except for the behavior of the added-mass coefficient at low frequency in water of finite depth. For three-dimensional problems, test computations for a sphere in heave and sway motion by both methods agree well with others. Results obtained by the second method for an ellipsoid also agree very well with existing results.

1. INTRODUCTION

Small oscillatory motions of an inviscid, incompressible fluid with a free surface are described by a boundary-value problem governed by Laplace's equation with a mixed boundary condition on the free surface, a homogeneous Neumann condition on the bottom of the fluid, and appropriate radiation conditions at infinity. Forced-motion or diffraction problems of a floating or submerged body require an additional boundary condition on the body surface as well, generally stating that the normal velocity of the body and fluid are equal.

An exhaustive list of literature on this subject may be found in Wehausen (1972). Here it suffices to say that, in the past, problems of this type were generally solved by distributing sources (and/or dipoles) on the body boundary and using Green's theorem to obtain an integral equation for the strength of these boundary singularities or, alternatively, by using sources and higher order multipole expansions at an interior point within the body, the strengths of these singularities being determined so as to satisfy the body boundary condition. In all cases it is conventional

to utilize the singularities which are solutions of the boundary-value problem stated above, except the body boundary condition which is invoked separately to determine the singularity distribution. For two- and three-dimensional motions with a fluid of infinite depth, or of finite but constant depth, the required singularities are well known, although of rather complicated analytical form, so that the approach described above corresponds to solving a Fredholm integral equation over the body surface, with a rather complicated kernel function.

In this paper two numerically oriented as well as more versatile methods are introduced as alternative approaches to the solution of the problem. The first alternative is based on a variational principle which is utilized to determine the velocity potential throughout the fluid domain. In this procedure (Bai, 1972), the radiation condition is first applied at a finite distance. By subdividing the fluid domain into a number of finite elements, we may approximate the potential within each element by a set of polynomial trial functions. Thus, in effect, an integral equation over the body boundary with a complicated kernel is replaced by a system of

equations over a much larger fluid domain, but a much simpler kernel. This approach, which is described in more detail by Bai (1972) for two-dimensional and axis-symmetric three-dimensional problems and also by Bai (1975) for diffraction problems of oblique waves by an infinite cylinder, will be described very briefly here for completeness. We present, in more detail instead, a modified scheme which makes use of certain analytic solutions in the outer flow field. In this modified variational approach, the radiation condition is replaced by appropriate junction conditions. Two new functionals are obtained and shown to be much more efficient for numerical computations. With this modification the fluid domain to be dealt with using finite-element method reduces to a much smaller one than that without the modification. Application of this modified variational method to the diffraction problem of a two-dimensional (and axis-symmetric-three-dimensional) bottomless oil reservoir tank will be reported in a separate paper in the near future.

The other alternative method of solution that we will be discussing is an integral equation method (Yeung, 1973). Here, Green's second identity is applied to the unknown potential using merely the source function for an unbounded fluid. The fluid domain is truncated by a radiation boundary taken at a finite distance as mentioned earlier. For the problem at hand, the normal derivative of the potential along the boundary is either known or expressible in terms of the potential itself since the boundary condition is of either a Neumann or Mixed type. The net result is that one gets an integral equation for the potential along the entire fluid boundary, but with a relatively simple kernel. It is of interest to point out that if a certain part of the boundary had a Dirichlet type condition, the normal velocity could then be regarded as unknown along this part of the boundary and then one would proceed along the same line as before. The integral equation is solved by the method of discretization. It is evident here that a compromise is made: we have traded away the much more complicated Green function in return for a larger boundary and also traded away a much larger domain of the straightforward variational approach (not the modified variational method mentioned earlier) in return for non-polynomial and singular kernel functions as well as a full coefficient matrix. This approach stands somewhat in between the conventional Green's function method and the variational method without modification.

Previous studies of the variational method applied to water-wave problems have been made, besides by the first

author, by Berkhoff (1972), by coupling the variational method and source distribution along the outer boundary, for the problem of refraction and diffraction of the water waves, in the scope of the shallow water theory. Several other references along this approach are given in Section 3.

Previous studies of the method of fundamental sources and dipole distributions have been done by Hess and Smith (1967) for an unbounded fluid, in which the fundamental source is just the Green function of the problem. This particular case actually belongs to the category of the method of Green's functions. There exist no previous studies on water-wave problems in an infinite domain using the method of fundamental sources and dipole distributions.

Since both methods described are fairly new, we concentrate in this paper on establishing their validity by presenting test results for both two- and three-dimensional problems and by comparing them with those obtained by other authors.

2. MATHEMATICAL FORMULATION

We consider here the wave-body interaction of a three- (or two) dimensional body floating or submerged in the free surface of a fluid (Fig. 2.1). Such interaction may occur either as a forced oscillation problem or as a diffraction problem. In the former case, wave motion is generated by some prescribed motion of the body; in the latter, the body is held fixed but subject to the excitation of an incoming wave system. It is well known that mathematically, these two problems are essentially identical, the only difference being that the boundary condition on the body takes on different functional specifications.

We assume that the body has no forward velocity, the fluid is incompressible and inviscid, and the flow irrotational. No assumptions on the geometry of the body and the bottom are necessary.

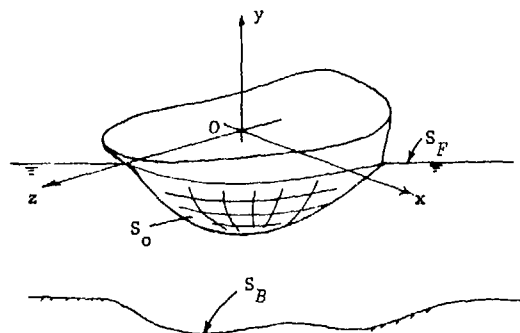


Fig. 2.1 Coordinate System.

2.1 Governing Equations

We choose the coordinate system $Oxyz$ (not shown) to be mounted on the body which, if in motion, oscillates harmonically about an inertial system $Oxyz$, with the y -axis pointing vertically upwards and the Oxy -plane being the undisturbed water surface. The two systems coincide when the body is at rest. At the onset, we assume the motion is small, so that the boundary conditions on the body can be satisfied at its equilibrium position instead of its instantaneous position. With such an assumption we can henceforth dispense with the $Oxyz$ system and seek the solution of the boundary value problem posed below in a domain of definition which does not change with time. For the diffraction case, the body is held fixed and we need, of course, only one set of coordinate system.

Let $\phi(x, y, z, t)$ be the velocity potential describing the flow field. The continuity equation requires ϕ to satisfy Laplace's equation. Let σ be the angular frequency of the time-harmonic solution, then introducing the usual time and spatial decomposition, we have:

$$\phi(x, y, z, t) = \operatorname{Re} \left[\phi^{(m)}(x, y, z) \dot{a}^{(m)}(t) \right], \quad m = 1, \dots, 7 \quad (2.1)$$

where

$$\phi^{(m)} = \phi_1^{(m)} + i\phi_2^{(m)} \quad (2.2)$$

is the complex-valued spatial potential, and $a^{(m)}(t)$ the complex time-harmonic motion amplitude of the body corresponding to the m -th mode, i.e.

$$a_m(t) = \operatorname{Re} \left[a^{(m)}(t) \right] = \operatorname{Re} \left[\left(a_1^{(m)} + i a_2^{(m)} \right) e^{-i\sigma t} \right], \quad (2.3)$$

where $a_m(t)$ is the body motion amplitude. For $m = 7$, the diffraction problem corresponding to an incoming wave system of unity amplitude, one simply sets $a_1 = 0$ and $a_2 = 1/\sigma$ in (2.3). The potential functions $\phi(x, y, z)$ must satisfy:

$$\left(\frac{\partial^2}{\partial x^2} + \frac{\partial^2}{\partial y^2} + \frac{\partial^2}{\partial z^2} \right) \phi(x, y, z) = 0 \quad (2.4)$$

in the fluid,

$$\phi_y - v\phi \Big|_{S_F} = 0, \quad (2.5a)$$

$$\phi_n \Big|_{S_B} = 0, \quad (2.5b)$$

$$\phi_n \Big|_{S_0} = v_n = f(s), \quad (2.5c)$$

where $v = \sigma^2/g$, g being the acceleration of gravity, S_F is the undisturbed free surface, $y=0$, outside of the body, S_B the bottom surface, and S_0 the wetted surface of the body at its equilibrium position. $f(s)$, the only non-homogeneous boundary condition, depends on the mode index m . For $m = 1, 2, \dots, 6$, corresponding to the sway, heave, surge, pitch, yaw and roll modes of motion respectively, $f(s)$ is given by

$$f^{(i)}(s) = n_i,$$

with

$$\begin{aligned} (n_1, n_2, n_3) &= (n_x, n_y, n_z) \\ (n_4, n_5, n_6) &= (\vec{r} - \vec{r}_0) \times \vec{n} \end{aligned} \quad (2.6)$$

where \vec{n} is the unit inward normal of the body with components (n_x, n_y, n_z) , \vec{r}_0 the location of the center of rotation, and

$$\vec{r} = (x, y, z).$$

For $m = 7$,

$$f(s) = \frac{-\partial \phi_I}{\partial n} \quad (2.7)$$

where ϕ_I is the spatial potential associated with the incoming wave system.

Finally, in order to have an unique solution for the problem, we must impose a radiation condition at infinity, which states that the forced waves or diffracted waves must be outgoing. To derive this condition, we let R be the radial horizontal distance, i.e.

$$R = (x^2 + z^2)^{1/2},$$

and θ be the polar angle in the (x, z) -plane. Let also the bottom geometry,

$$y = h(x, z) = h(R, \theta)$$

be a constant beyond some minimal value of R . Then a set of elementary solutions satisfying Laplace's equation, the free surface and bottom conditions can be obtained by the method of separation of variables (see Wehausen, 1960, pp. 472-475). With little difficulty, it may be shown that only the following combinations in the set will give a solution corresponding to waves propagating outwards to infinity:

$$\begin{aligned} \phi(x, y, z) &\propto \cosh m_0(y+h) \\ &\times H_n^{(1)}(m_0 R) \cdot \cos(n\theta + \delta), \end{aligned} \quad (2.8)$$

where $H_n^{(1)}$ is the Hankel function of the first kind and of order n . m_0 , a separation constant, is the root of the following equation:

$$m_0 \tanh m_0 h = \sigma^2/g. \quad (2.9)$$

The function $H_n^{(1)}(m_0 R)$ has an asymptotic expansion of the following form for large values of R (Watson, 1966, p. 212).

$$H_n^{(1)}(m_0 R) = \left(\frac{2}{\pi m_0 R}\right)^{1/2} \exp\left[i\left(m_0 R - \frac{n\pi}{2} - \frac{\pi}{4}\right)\right] \times \left[1 - i\frac{n+1/4}{2m_0 R}\right] + O[(m_0 R)^{-5/2}] \quad (2.10)$$

Using (2.1), one can see that

$$\phi(x, y, z, t) \sim \text{Re}[\phi(x, y, z) e^{-i\sigma t}] \sim \cosh m_0(y+h) \cdot \left(\frac{2}{\pi m_0 R}\right)^{1/2} \cdot \text{Re}\left[\exp i\left\{(m_0 R - \sigma t) - \frac{2n+1}{4}\pi\right\}\right] f(\theta) \quad (2.11)$$

does represent an outgoing wave-system. A few algebraic steps then yield the following information on the behavior of ϕ :

$$\frac{\partial \phi}{\partial R} = \left(\frac{-1}{2R} + im_0\right)\phi + O(R^{-5/2}) \quad (2.12)$$

Equation (2.12) is the radiation condition we shall use. It is based on the assumption that the 'local disturbance', which is the difference between the total potential and the propagating-wave potential, dies out fast enough to be negligible at the place where (2.12) is applied. Condition (2.12) is consistent with the classical form:

$$R \rightarrow \infty \quad \left(\frac{\partial \phi}{\partial R} - im_0 \phi\right) = 0.$$

given, for instance, by John (1950, p. 54).

For the case of a two-dimensional problem, the radiation conditions reduce to:

$$\frac{\partial \phi}{\partial x}(x_R, y) = im_0^R \phi, \quad x_R \gg 0, \quad (2.13a)$$

$$\frac{\partial \phi}{\partial x}(x_L, y) = -im_0^L \phi, \quad x_L \ll 0, \quad (2.13b)$$

where m_0^R, m_0^L are the wave numbers corresponding to fluid depths on the right and left sides of the body respectively.

2.2 Forces, Moments and Wave-Heights

The linearized forces and moments about 0 acting on the body are given by:

$$F_j(t) = \iint_{S_0} p \cdot n_j dS, \quad (2.14)$$

$$M_j(t) = \iint_{S_0} p(\vec{r} \times \vec{n})_j dS, \quad (2.15)$$

where dS is an infinitesimal surface element and the pressure p can be obtained from the linearized version of Bernoulli's equation:

$$p(x, y, z, t) = -\rho \phi_t - \rho g y \quad (2.16)$$

ρ being the density of the fluid. Of primary interest is the hydrodynamic component, which comes from the $-\rho \phi_t$ term. Introducing the notation

$$(F_4, F_5, F_6) = (M_1, M_2, M_3),$$

we may write the hydrodynamic forces and moments for the case of forced motion as follows:

$$F_j = -\mu_{ji} \ddot{a}_i(t) - \lambda_{ji} \dot{a}_i(t), \quad (2.17)$$

Here, repeated indices are summed from 1 to 6. μ_{ji} and λ_{ji} are the added-mass and damping coefficients respectively. They are defined by the integrals:

$$\mu_{ji} + i\frac{\lambda_{ji}}{\sigma} = \rho \iint_{S_0} \phi^{(i)} n_j dS = \rho \iint_{S_0} \phi^{(i)} \frac{\partial \phi^{(j)}}{\partial n} dS, \quad (2.18)$$

which depend on the body and bottom geometry as well as the angular frequency σ . The diffraction forces may be obtained by solving the boundary value problem of $\phi^{(j)}$ defined in §2.1 and by using (2.14) and (2.15), or, alternatively, by the application of Haskind's relation [see Newman (1962)] utilizing the solutions of the forced motions. In the latter case the forces are given simply by

$$F_j = -i\sigma \rho \iint_{S_0} \phi^{(j)} \frac{\partial \phi^{(j)}}{\partial n} dS. \quad (2.19)$$

Finally, the free-surface elevation $\eta(x, z, t)$ can be obtained from the dynamic boundary condition used in arriving at (2.5a), and is given by

$$\eta(x, z, t) = -g^{-1} \phi_t(x, 0, z, t) = \sigma^2/g \text{Re}[\phi^{(m)}(x, 0, z) a^{(m)}(t)], \quad (2.20)$$

Whence, by (2.3) one can define a spatial free-surface function $\eta^{(m)}(x, z)$ corresponding to the m -th mode as:

$$\eta^{(m)}(x, z) = \eta \phi^{(m)}(x, 0, z) \cdot [a_1^{(m)} + ia_2^{(m)}] \quad (2.21)$$

with

$$\eta(x, z, t) = \text{Re}[\eta^{(m)}(x, z) e^{-i\sigma t}]. \quad (2.22)$$

3. SOLUTION BY THE VARIATIONAL METHOD

We present in this section a method of solution based on the variational formulation common in many other fields of engineering mechanics. In §3.1 the application of the classical variational method is described very briefly since

one can find more details in Bai (1972, 1975). In §3.2 a modification to this method is made in order to use two different classes of trial functions: polynomial trial functions, and a set of eigenfunctions. In §3.3, the two classes of trial functions (also known as interpolation functions) are discussed in greater detail, and the admissibility of the polynomial trial functions is considered. Throughout this section, the superscript m the potential defined in §2 is omitted with the understanding that ϕ will always depend on m .

3.1 Classical Variational Method

Let us consider a well-posed boundary value problem described for a complex-valued function $\phi(x, y)$ as

$$\nabla^2 \phi(x, y) = 0 \quad \text{in } R \quad (3.1)$$

with the mixed-type boundary condition on the boundary S .

$$\phi_n + \alpha\phi = \beta \quad \text{on } S \quad (3.2)$$

where $\alpha(S)$ and $\beta(S)$ are known complex functions. In the theory of the calculus of variations, we can solve an alternative problem, one that requires the determination of a function ϕ which makes the associated functional stationary, instead of solving directly the above partial differential equation with the given boundary condition. In order to construct the associated functional for the above problem, we introduce a complex variation $\delta\phi(x, y)$ and integrate (3.1) in the domain R and (3.2) on the boundary S after multiplying both equations by $\delta\phi$. Then we obtain

$$-\iint_R \nabla\phi\delta\phi dx dy + \int_S (\phi_n + \alpha\phi - \beta)\delta\phi ds = 0. \quad (3.3)$$

If we make use of Green's theorem, which holds also for complex functions, in the first integral in (3.3) and of the relation $\nabla\delta\phi = \delta\nabla\phi$, the left-hand side of (3.3) becomes

$$\begin{aligned} & \iint_R \nabla\phi\delta\phi dx dy + \int_S (\alpha\phi - \beta)\delta\phi ds \\ &= \delta \left[\iint_R \frac{1}{2} \nabla\phi \cdot \nabla\phi dx dy + \int_S \left(\frac{1}{2} \alpha\phi^2 - \beta\phi \right) ds \right]. \end{aligned} \quad (3.4)$$

Now we shall define the associated functional F for the above problem, (3.1) and (3.2) as

$$F\{\phi\} \equiv \iint_R \frac{1}{2} \nabla\phi \cdot \nabla\phi dx dy + \int_S \left(\frac{1}{2} \alpha\phi^2 - \beta\phi \right) ds \quad (3.5)$$

Then by (3.3) we have

$$\delta F\{\phi\} = 0. \quad (3.6)$$

Since (3.6) is equivalent to (3.1) and (3.2), we will take this alternative

as mentioned earlier.

Consider now the two-dimensional problem of forced motion or diffraction as formulated in §2. The boundary conditions given by (2.5) and (2.13) correspond merely to certain specific choices of values of $\alpha(S)$ and $\beta(S)$ in (3.2). Let S be $S_F \cup S_{FU} \cup S_{RU} \cup S_L \cup S_B$ as shown in Fig. 3.1. Then the functional associated with the problems at hand is simply:

$$\begin{aligned} F\{\phi\} = & \iint_R \frac{1}{2} \nabla\phi \cdot \nabla\phi dx dy - \frac{\nu}{2} \int_{S_F} \phi^2 ds \\ & - \frac{i m_0}{2} \int_{S_L} \phi^2 ds - \frac{i m_0}{2} \int_{S_R} \phi^2 ds - \int_{S_0} f(s) \phi ds. \end{aligned} \quad (3.7)$$

In the case of the three-dimensions the analogous functional is:

$$\begin{aligned} F\{\phi\} = & \iiint_R \frac{1}{2} \nabla\phi \cdot \nabla\phi dx dy dz - \frac{\nu}{2} \iint_{S_F} \phi^2 dS \\ & - \frac{i m_0}{2} \iint_{\Sigma_R} \phi^2 dS + \frac{1}{4} \iint_{\Sigma_R} \frac{1}{R} \phi^2 dS - \iint_{S_0} f(s) \phi dS, \end{aligned} \quad (3.8)$$

where the radiation boundary Σ_R is chosen to be a vertical circular cylinder of sufficiently large radius, R , which includes the body and the variation of the bottom topography.

When we have an axi-symmetric body in three dimensions, it is convenient to express the potential defined in (2.1) in polar coordinates as

$$\phi(R, \theta, y, t) = \text{Re} [\phi(R, y) \cos(n\theta + \delta) \dot{a}(t)] \quad (3.9)$$

Then the Laplace equation (2.4) reduces to

$$\frac{\partial}{\partial R}(R\phi_R) - \frac{n^2}{R}\phi + R\phi_{yy} = 0. \quad (3.10)$$

It is understood in (3.10) that a proper value of n is taken for the individual problem; for example, $n=0$ for the case of heave motion and $n=1$ for the case of surge and pitch motions. In diffraction problems, the incident wave potential ϕ_I can be written as

$$\phi_I = \frac{gA}{\omega} \frac{\cosh m_0(y+h)}{\cosh m_0 h} e^{i m_0 x} \quad (3.11)$$

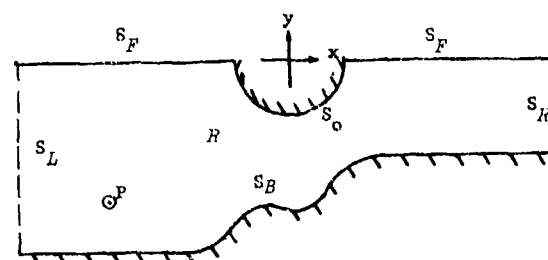


Fig. 3.1 Configuration of Boundary Geometry.

where A is the amplitude of the incident wave. For a body geometry with an axisymmetry, it is convenient to express $\exp(imx)$ in the above equation in terms of Bessel functions:

$$\exp(im_0 x) = \sum_{n=0}^{\infty} \epsilon_n i^n J_n(m_0 R) \cos(n\theta), \quad (3.12)$$

where $\epsilon_n = 1$ for $n=0$
 $\epsilon_n = 2$ for $n \geq 1$.

Then the body boundary condition (2.17) can be expressed as a sum of all the values of n by substituting (3.12) into (3.11). The diffraction problem of an axis-symmetric body in three dimensions therefore reduces to the two-dimensional problem given by (3.10) which we have to solve for all n ($n=0, 1, \dots, \infty$). In practice, only a finite number of terms is necessary. In a procedure similar to that in obtaining (3.7), we may find that the associated functional for this problem is

$$F(\phi) = \iint_R \frac{1}{2} R \cdot (\phi_R^2 + \phi_y^2) dR dy - \frac{1}{2} \int_{S_F} R \phi^2 ds - \frac{im_0}{2} \int_{\Sigma_R} R \phi^2 ds + \frac{1}{4} \int_{\Sigma_R} \phi^2 ds - \int_{S_0} R f(\theta) \phi ds, \quad (3.13)$$

where Σ_R is reduced to a line boundary due to the axis-symmetry.

In the method described above and the method of fundamental source and dipole distribution to be described in §4, the construction of the 'numerical radiation boundary', which reduces the exact problem defined in the infinite domain to an approximating problem in a finite domain, is very important. In order to truncate the original infinite boundary into a finite domain, one should examine the behavior of the local disturbance, for example, how fast it decays along the free surface. The decaying behavior of the local disturbance of each problem is a function of the wave frequency, the characteristic length of the body and the fluid depth. A more detail discussion on this can be found in Bai (1972) and Yeung (1973).

3.2 A Modified Variational Method

The main disadvantage of the variational method discussed in §3.1, for our problem, is that the finite domain obtained by truncating the original infinite domain is still too large for solving the problem economically. For example, as shown in Fig. 3.1, the radiation boundaries have to be located at a couple of wave lengths away from the body. As a consequence, there is still a substantial amount of fluid region to deal

with. In order to overcome this disadvantage, a modification is made to further reduce the fluid domain by utilizing known analytic solutions in certain sub-domain which will be defined later.

For simplicity, we shall consider in detail only the problem shown in Fig. 3.2.

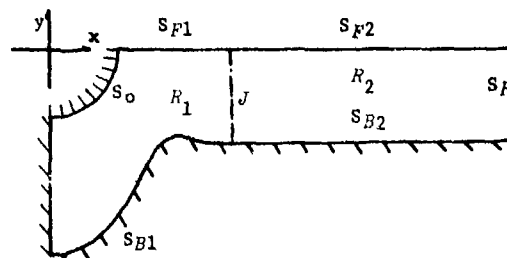


Fig. 3.2 Inner and Outer Regions of the Modified Variational Method.

Let us draw an imaginary line J (or a vertical circular cylinder in three dimensions) which separates the fluid into a region R_1 of irregular bottom and the body and a region R_2 of uniform depth as shown in Fig. 3.2. Then the original fluid domain R is divided into two subdomains, i.e., R_1 and R_2 with the common interface boundary J . The boundary of y the subregion is denoted $S_1 = S_{F1} \cup S_{B1} \cup J \cup S_0$ and the boundary of R_2 is denoted $S_2 = J \cup S_{F2} \cup S_R \cup S_{B2}$. Let ϕ_1 and ϕ_2 denote the potentials in these regions, respectively, then we have

$$\begin{aligned} \nabla^2 \phi_1 &= 0 & \text{in } R_1, \\ \phi_{1y} - \nu \phi_1 &= 0 & \text{on } S_{F1}, \\ \phi_{1n} &= \nu_n & \text{on } S_0, \\ \phi_{1n} &= 0 & \text{on } S_{B1}, \end{aligned} \quad (3.14)$$

and

$$\begin{aligned} \nabla^2 \phi_2 &= 0 & \text{in } R_2, \\ \phi_{2y} - \nu \phi_2 &= 0 & \text{on } S_{F2}, \\ \phi_{2n} &= 0 & \text{on } S_{B2}, \\ \lim_{x \rightarrow \infty} (\phi_{2x} - im_0^R \phi_2) &= 0 & \text{on } S_R. \end{aligned} \quad (3.15)$$

In addition, we have

$$\begin{aligned} \phi_1 &= \phi_2, \\ \phi_{1n} &= -\phi_{2n} & \text{both on } J, \end{aligned} \quad (3.16)$$

where the normal vector is taken outwards from the fluid domain, for instance,

$$\phi_{1n} = \phi_{1x}, \quad \phi_{2n} = -\phi_{2x} \quad \text{on } J.$$

By the juncture conditions (3.16), the potentials ϕ_1 and ϕ_2 can have unique

solutions.

Let us assume that the most general solutions of (3.15) are known and that $\phi_2(x, y)$ can be expressed in terms of them with coefficients to be determined later.

We shall skip the procedures of the construction of the associated functionals for the above problem and simply present the results below:

$$F_1(\phi_1, \phi_2) = \iint_{R_1} \frac{1}{2} (\nabla \phi_1)^2 dx dy - \frac{1}{2} \int_{S_{F1}} \phi_1^2 ds$$

$$- \int_{S_0} V_n \phi_1 ds + \int_J (\phi_1 - \frac{1}{2} \phi_2) \phi_{2n} ds, \quad (3.17)$$

$$F_2(\phi_1, \phi_2) = \iint_{R_1} \frac{1}{2} (\nabla \phi_1)^2 dx dy - \frac{1}{2} \int_{S_{F1}} \phi_1^2 ds$$

$$- \int_{S_0} V_n \phi_1 ds + \int_J [(\phi_2 - \phi_1) \phi_{1n} + \frac{1}{2} \phi_2 \phi_{2n}] ds. \quad (3.18)$$

Then setting either

$$\delta F_1(\phi_1, \phi_2) = 0, \quad (3.19a)$$

or

$$\delta F_2(\phi_1, \phi_2) = 0 \quad (3.19b)$$

is the same as solving Equations (3.14), (3.15) and (3.16). To see this, we note that

$$\delta F_1(\phi_1, \phi_2) = \iint_{R_1} -\nabla^2 \phi_1 \delta \phi_1 dx dy + \int_{S_{F1}} (\phi_{1n} - V_n \phi_1) \delta \phi_1 ds + \int_{S_0} (\phi_{1n} - V_n) \delta \phi_1 ds + \int_J [\delta \phi_1 (\phi_{1n} + \phi_{2n}) + \phi_1 \delta \phi_{2n} - \frac{1}{2} (\phi_2 \delta \phi_{2n} + \phi_{2n} \delta \phi_2)] ds, \quad (3.20)$$

$$\delta F_2(\phi_1, \phi_2) = \iint_{R_1} -\nabla^2 \phi_1 \delta \phi_1 dx dy + \int_{S_{F1}} (\phi_{1n} - V_n \phi_1) \delta \phi_1 ds + \int_{S_0} (\phi_{1n} - V_n) \delta \phi_1 ds + \int_J [(\phi_2 - \phi_1) \delta \phi_{1n} + \phi_{1n} \delta \phi_2 + \frac{1}{2} (\phi_2 \delta \phi_{2n} + \phi_{2n} \delta \phi_2)] ds. \quad (3.21)$$

By making use of Green's theorem to the functions ϕ_2 and $\delta \phi_2$ in the region R_2 , we obtain

$$\iint_{R_2} [\delta \phi_2 \nabla^2 \phi_2 - \phi_2 \nabla^2 (\delta \phi_2)] dx dy =$$

$$= \oint_{S_2} (\phi_{2n} \delta \phi_2 - \phi_2 \delta \phi_{2n}) ds. \quad (3.22)$$

From the assumptions we stated on the function ϕ_2 , Equation (3.22) reduces to

$$\int_J (\phi_{2n} \delta \phi_2 - \phi_2 \delta \phi_{2n}) ds = 0. \quad (3.23)$$

If we use the relation (3.23) in (3.20) and (3.21), we obtain

$$\delta F_1 = \iint_{R_1} -\nabla^2 \phi_1 \delta \phi_1 dx dy + \int_{S_{F1}} (\phi_{1n} - V_n \phi_1) \delta \phi_1 ds + \int_{S_0} (\phi_{1n} - V_n) \delta \phi_1 ds + \int_J (\phi_{1n} + \phi_{2n}) \delta \phi_1 ds + \int_J (\phi_1 - \phi_2) \delta \phi_{2n} ds = 0, \quad (3.24)$$

$$\delta F_2 = \iint_{R_1} -\nabla^2 \phi_1 \delta \phi_1 dx dy + \int_{S_{F1}} (\phi_{1n} - V_n \phi_1) \delta \phi_1 ds + \int_{S_0} (\phi_{1n} - V_n) \delta \phi_1 ds + \int_J (\phi_2 - \phi_1) \delta \phi_{1n} ds + \int_J (\phi_{1n} + \phi_{2n}) \delta \phi_2 ds = 0. \quad (3.25)$$

Since the variations $\delta \phi_1, \delta \phi_2, \delta \phi_{1n}, \delta \phi_{2n}$ in (3.24) and (3.25) are arbitrary, we obtain Equations (3.14) and (3.16). Due to the assumption on the function ϕ_2 stated earlier, ϕ_1 and ϕ_2 obtained from the above functional method are the solutions of the equations (3.14), (3.15) and (3.16) (note that this solution satisfies the exact radiation condition). The integral expressions of the functionals involve only with the sub-region R_1 which we shall call 'the localized-finite-element region'.

As shown above, the new functionals F_1 and F_2 were obtained by making a modification to the functional F in (3.7) in §3.1. Similarly, the analogous functionals F_1 and F_2 for three-dimensional problems in general can be obtained simply by replacing the radiation boundary integrals in (3.8) by

$$\iint_J (\phi_1 - \frac{1}{2} \phi_2) \phi_{2n} ds \quad (3.26a)$$

for F_1 , or by

$$\iint_J [(\phi_2 - \phi_1) \phi_{1n} + \frac{1}{2} \phi_2 \phi_{2n}] ds \quad (3.26b)$$

for F_2 . For the special case of axisymmetric geometry, F_1 and F_2 can be obtained by replacing the radiation-boundary integrals in (3.13) by

$$\int_J R(\phi_1 - \frac{1}{2}\phi_2)\phi_{2n} ds \quad (3.27a)$$

for F_1 , or by

$$\int_J R[(\phi_2 - \phi_1)\phi_{1n} + \frac{1}{2}\phi_2\phi_{2n}] ds \quad (3.27b)$$

for F_2 . Here obviously ϕ in (3.8) or (3.13) is to be replaced by ϕ_1 , and ϕ_2 is understood to be the most general solution in the outer region R_2 .

It is of interest to note that the stationary value of both functionals in two or three dimensions are:

$$F_1(\phi_1, \phi_2) = -\frac{1}{2} \int_{S_0} V_n \phi_1 ds, \quad (3.28)$$

$$F_2(\phi_1, \phi_2) = -\frac{1}{2} \int_{S_0} V_n \phi_1 ds, \quad (3.29)$$

if ϕ_1 and ϕ_2 are the exact solutions.

This stationary value is simply $(-1/2\rho)$ times the added-mass and damping coefficients integrals defined in (2.18).

If the most general solution for ϕ_2 in the sub-domain R_2 contains a constant, the functional F_1 defined in (3.17) can not be used since its first derivative is identically zero (see the last integral in (3.24)) and we have

$$\delta(3C/\partial n) = 0. \quad (3.30)$$

Therefore the functional F_2 defined in (3.18) should be used in this case. Fortunately in our problem we do not have a constant in the general solution for ϕ_2 in R_2 if $0 < \sigma < \infty$.

Two limiting cases should be noted: Let us assume that the most general solution for ϕ_2 in (3.15) can be expressed as a series of eigenfunctions as given in (3.36) and (3.37). If the localized-finite-element region R_2 is taken very large, in other words, if the boundary J is taken at a large distance from the body (and the irregular bottom topography), then ϕ_2 can be represented very well just by one term in the series [the first term in (3.36)]. In such case, the present functional method reduces to that treated in the previous sub-section. In the opposite limit, if a wave-maker problem is considered with a uniform depth, then the localized-finite-element region R_1 can be taken as zero and as a consequence, we have only the boundary J . Then both functionals F_1 and F_2 reduce to

$$F_1(\phi_2) = F_2(\phi_2) = -\frac{1}{2} \int_J \phi_2 \phi_{2n} ds, \quad (3.31)$$

which was obtained earlier by Bessho (1970), and was basis of the numerical computations by Sao, Maeda and Hwang

(1971), who used the source distributions to represent ϕ_2 .

From these two limiting cases one can readily see that the functionals defined in (3.17) and (3.18) are a much more general formulation compared with (3.7) or (3.31). For example, if one takes the localized-finite-element region to be small, then as a consequence, the domain of the area integrals in the functionals will also be small, while on the other hand, one has to take many terms (eigenfunctions) to represent ϕ_2 in the computation for the approximate solutions, and vice versa.

The method of eigenfunction expansion in both inner and outer regions has been used by Black and Mei (1970) in conjunction with the Schwinger-type variational form. Applications were made to several vertical-walled bodies in two and three dimensions. Isshiki and Hwang (1973) considered the axis-symmetric three-dimensional body in water of finite depth and computation was made based on the functional (3.31), by utilizing eigenfunctions in the both regions. Chen and Mei* (1974) also considered a diffraction and radiation problem within the scope of the shallow-water theory by a similar approach to ours.

3.3 Construction of Trial Functions and Approximate Solutions

We shall describe briefly here the numerical procedure by which the functional form (3.19a) can be reduced into an operational form for finding the approximate solutions, in conjunction with the functional defined (3.17). The other functionals discussed earlier can be treated in a similar way. There are two important steps in this procedure. The first step is to discretize the fluid domain in region R_1 into a number of finite elements, within each one of which ϕ_1 is approximated by a polynomial trial function. The second step is to represent the solution of ϕ_2 by a finite number of the eigenfunctions in R_2 , where the most general solution (i.e., infinite series of the eigenfunctions) of ϕ_2 is known. Once these two approximations are made, the rest of the numerical procedure is rather straightforward.

Before we discuss the construction of the trial functions we shall discuss the admissibility of the trial functions in the region R_1 . As mentioned earlier, because of the equivalence of differential equations and variational problems either can be the basis of various computational schemes. One significant difference between the functional method and the differential equation is the fact that the expressions for the associated functionals involve no second derivatives, because integration by parts have been

*The first author owes thanks to Professor C. C. Mei for his valuable comments in the way of developing this localized-finite-element method.

used to construct these functionals (more specifically, Goursat's theorem is used here). These functionals will be well defined if the integrals in the domain and on its boundary (only ϕ and $\nabla\phi$ are involved) are finite in value. Therefore the class of the admissible functions in the problem to find the stationary point is enlarged to a space bigger than the one for the original differential equations. We now have the advantage, while searching for the stationary point of the functional, of being able to try functions which were outside of the original class of admissible function space. In practice, this means that we can now try continuous functions whose first derivatives are only piecewise continuous, that is, the first derivatives can have finite discontinuities at the juncture points between adjacent elements. It is very easy to construct functions which satisfy the above requirements and we shall discuss this point in this section.

Let the region R_1 occupied by fluid, up to the boundary J , be subdivided by lines into a (not necessarily rectangular) grid system. Each connected piece within the subdivision will be called an 'element'. Let us introduce a set of trial functions $N_i^e(x, y)$, $i=1, \dots, n$, associated with each element and of such a character that $\phi_1(x, y)$ can be approximated as a sum of these functions, each multiplied by the value of ϕ_1 at, say, a node of the grid associated with the element (ϕ_{1i} at the i -th node). However, these values of ϕ_{1i} need not be nodal values of ϕ_1 but may be other values (parameters) characterizing ϕ_1 in the element, for our numerical scheme requires finding the stationary point of a functional which is represented in integral form rather than finding directly the values of the function itself. Let us write the set of trial functions as a row vector

$$[N]^e = [N_1^e, N_2^e, \dots, N_n^e] \quad (3.32)$$

and the set of nodal values as a column vector

$$\{\phi_1\}^e = [\phi_{11}^e, \phi_{12}^e, \dots, \phi_{1n}^e]^T \quad (3.33)$$

in an n -node element. The superscript e in the above equations means that these values are considered in an individual element. We may then approximate ϕ_1 in each element by the sum:

$$\phi_1 = [N]^e \{\phi_1\}^e. \quad (3.34)$$

When we further define the trial functions $[N]^e$ to be identically zero outside the associated element, then we can represent the approximate solution ϕ_1 in the entire fluid by a sum of the repre-

sentation (3.34) as follows:

$$\begin{aligned} \phi_1 &= \sum_{e=1}^E [N]^e \{\phi_1\}^e \\ &= \sum_{i=1}^N \phi_{1i} N_i(x, y) \end{aligned} \quad (3.35)$$

where E is the total number of elements and N is the total number of nodes in the entire fluid.

In our numerical computations, an eight-node quadrilateral element was used in the finite-element discretization. The trial functions for an eight-node square element are constructed in Appendix A. A very extensive and detailed exposition about this procedure can be found in Zienkiewicz (1971).

There are several choices for the trial functions for $\phi_2(x, y)$ in the sub-region R_2 which satisfy condition (3.15). A set of properly chosen eigenfunctions will be used in the following procedure even though some other representation for the admissible trial functions can be employed as mentioned earlier.

Let us represent the function $\phi_2(x, y)$ in terms of the eigenfunctions $\psi_i(x, y)$ ($i=0, \dots, M-1$) with unknown coefficients ϕ_{2i} ($i=0, \dots, M-1$) to be determined as part of the solution later:

$$\phi_2(x, y) = \sum_{i=0}^{M-1} \phi_{2i} \psi_i(x, y), \quad (3.36)$$

$$\begin{aligned} \psi_0(x, y) &= e^{im_0 x} \cosh m_0(y+h) / \cosh m_0 h, \\ \psi_1(x, y) &= e^{-m_1 x} \cos m_1(y+h), \\ &\vdots \\ \psi_{M-1}(x, y) &= e^{-m_{M-1} x} \cos m_{M-1}(y+h), \end{aligned} \quad (3.37)$$

$$\begin{aligned} \text{where} \quad m_0 \tanh m_0 h &= \frac{\sigma^2}{g}, \\ m_i \tan m_i h &= -\frac{\sigma^2}{g}, \end{aligned} \quad (3.38)$$

In three dimensions $\phi_2(R, \theta, y)$ can be represented by

$$\phi_2(R, \theta, y) = \sum_{k=0}^{K-1} \sum_{l=0}^{L-1} \phi_{kl} \psi_{kl}, \quad (3.39)$$

where

$$\begin{aligned} \psi_{0l} &= H_l^{(1)}(m_0 R) \cosh(m_0 R) \cos(l\theta + \delta), \\ \psi_{1l} &= K_l(m_1 R) \cos m_1(y+h) \cos(l\theta + \delta), \\ &\vdots \\ \psi_{kl} &= K_l(m_k R) \cos m_k(y+h) \cos(l\theta + \delta); \end{aligned} \quad (3.40)$$

($k \geq 1$).

Here, ϕ_{kl} are unknown constants and K_l is the modified Bessel function of the

second kind.

Once we set up all the trial functions, polynomial trial functions for the function $\phi_1(x,y)$ in R_1 and the eigenfunction trial functions for $\phi_2(x,y)$ in R_2 [actually, in (3.17) computation of $\phi_2(x,y)$ occurs only along the interface boundary J] we can find the stationary point of the functional $F_1\{\phi_1, \phi_2\}$ numerically by the following equations:

$$\frac{\partial F_1\{\phi_1, \phi_2\}}{\partial \phi_{1i}} = 0 \quad i=1, \dots, N, \quad (3.41a)$$

$$\frac{\partial F_1\{\phi_1, \phi_2\}}{\partial \phi_{2i}} = 0 \quad i=0, \dots, M-1. \quad (3.41b)$$

Substituting (3.35) and (3.36) into (3.41), we obtain:

$$\begin{aligned} \frac{\partial F_1}{\partial \phi_{1i}} = & \iint_{R_1} (\phi_{1x} \cdot \frac{\partial \phi_{1x}}{\partial \phi_{1i}} + \phi_{1y} \cdot \frac{\partial \phi_{1y}}{\partial \phi_{1i}}) dx dy \\ & - \nu \iint_{S_{F_1}} \phi_1 \cdot \frac{\partial \phi_1}{\partial \phi_{1i}} dS - \int_{S_0} v_n \cdot \frac{\partial \phi_1}{\partial \phi_{1i}} dS \\ & - \int_J \phi_{2x} \cdot \frac{\partial \phi_1}{\partial \phi_{1i}} dS, \end{aligned} \quad (3.42a)$$

$$\begin{aligned} \frac{\partial F_1}{\partial \phi_{2i}} = & \int_J \left[\frac{1}{2} (\phi_2 \cdot \frac{\partial \phi_{2x}}{\partial \phi_{2i}} + \phi_{2x} \cdot \frac{\partial \phi_2}{\partial \phi_{2i}}) \right. \\ & \left. - \phi_1 \cdot \frac{\partial \phi_{2x}}{\partial \phi_{2i}} \right] dS. \end{aligned} \quad (3.42b)$$

When we make use of the relations

$$\begin{aligned} \frac{\partial \phi_1}{\partial x} &= \left[\frac{\partial N_1}{\partial x}, \frac{\partial N_2}{\partial x}, \dots \right] \{\phi_1\}, \\ \frac{\partial}{\partial \phi_{1i}} \left(\frac{\partial \phi_1}{\partial x} \right) &= \frac{\partial N_i}{\partial x}, \\ \frac{\partial \phi_1}{\partial \phi_{1i}} &= N_i, \\ \frac{\partial \phi_{2x}}{\partial \phi_{20}} &= i m_0 \cdot \psi_0(x, y), \quad \frac{\partial \phi_2}{\partial \phi_{2i}} = \psi_i, \\ \frac{\partial \phi_{2x}}{\partial \phi_{2i}} &= (-m_i) \cdot \psi_i(x, y) \quad i \geq 1, \end{aligned} \quad (3.43)$$

then (3.42) reduces to the following set of $(M+N)$ algebraic equations:

$$\begin{bmatrix} A_{11} & A_{12} \\ A_{21} & A_{22} \end{bmatrix} \begin{bmatrix} \phi_1 \\ \phi_2 \end{bmatrix} = \begin{bmatrix} Q_1 \\ Q_2 \end{bmatrix} \quad (3.44)$$

where

$$\begin{aligned} A_{11} &= [a_{ij}]_{N \times N}, \\ A_{22} &= [b_{ij}]_{M \times M}, \end{aligned} \quad (3.45)$$

$$\begin{aligned} A_{12} &= [c_{ij}]_{N \times M}, \\ A_{21} &= [d_{ij}]_{M \times N}, \\ Q_1 &= \{f_i\}, \\ Q_2 &= \{0\}. \end{aligned} \quad (3.45)$$

The elements of the above matrix are defined as follows:

$$\begin{aligned} a_{ij} &= \iint_R (N_{ix} N_{jx} + N_{iy} N_{jy}) \cdot dx dy \\ &\quad - \nu \int_{S_{F_1}} N_i N_j \cdot dS, \\ b_{ij} &= \int_J \frac{1}{2} (\psi_{ix} \psi_{jx} + \psi_{iy} \psi_{jy}) \cdot dS \\ c_{ij} &= d_{ji} = - \int_J N_i \psi_{jx} \cdot dS \\ f_i &= \int_{S_0} v_n N_i \cdot dS \end{aligned} \quad (3.46)$$

The problem has now been reduced to the set of algebraic equations (3.44). The coefficient matrix is symmetric complex, as one sees readily from the expressions in (3.46), and is banded if the nodes are numbered in proper sequence. The actual numerical computations of the integrals in (3.42) for general eight-node quadrilateral elements are made by Gaussian numerical quadrature after a coordinate transformation into a square.

There exist rigorous mathematical treatments on the convergence and error estimates of a convex functional which is positive definite, but the convergence proof for the complex functional $F\{\phi\}$ in (3.5) is more difficult. It is beyond the scope of the present paper to give a rigorous mathematical proof for convergence in the case of this particular functional $F\{\phi\}$. One can find it in Strang and Fix (1973).

A typical subdivision of meshes to solve, by the localized-finite-element-method, a forced motion problem of a rectangular cylinder (half-beam/draft = 1.0) in water of finite depth ($h/\text{half-beam} = 2.0$) is shown by the solid lines in Fig. 3.3, and this subdivision was

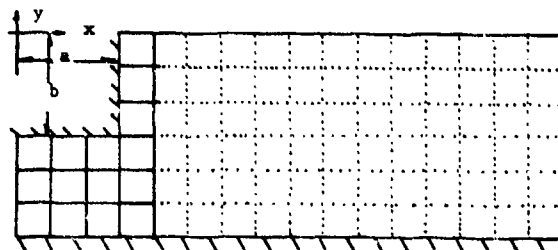


Fig. 3.3 A Typical Subdivision of Meshes in the Fluid.

used for all the frequency ranges $0.0025 < \nu a < 6$ where the computations were made. As a comparison, another typical subdivision of meshes to solve the same problem, by the variational method without the modification, is also shown in the extra region as dotted lines in Fig. 3.3 for the case $\nu a = 1$.

4. SOLUTION BY THE METHOD OF FUNDAMENTAL SOURCE AND NORMAL-DIPOLE DISTRIBUTION

An alternative approach to solving the boundary value problems formulated earlier is by the method of integral equation. This permits us to deal only with the fluid boundaries. Here we avoid working with the complicated kernel associated with the usual wave source by introducing merely the fundamental source function, $1/r$, or $\log 1/r$ in the case of two dimensions. This novel approach to free-surface flow problems is made possible here by: (1) that the normal derivative of ϕ is either known or expressible in terms of ϕ itself [see Eqn. (2.5)], and; (2) that the originally external boundary value problems can be converted to internal ones by the application of the radiation condition at a finite distance.

4.1 Application of Green's Theorem

We illustrate the basic idea behind the method by considering first the two-dimensional problem. Referring to Fig. 3.1, we let P be a field point inside the fluid. We assume that ϕ is a continuous function everywhere in the fluid and apply Green's second identity to the functions ϕ and $\log 1/r$, in a fluid domain enclosed by the boundary S defined by $S_0 \cup S_F \cup S_B \cup S_R \cup S_L$. This results in the following expression of $\phi(P)$ in terms of its boundary values and its normal derivative on the boundary:

$$2\pi\phi^{(m)}(P) = \oint_S \frac{\partial\phi^{(m)}(Q)}{\partial n} \log(1/r) ds(Q) - \oint_S \phi^{(m)} \frac{\partial}{\partial n} [\log(1/r)] ds(Q) \quad (4.1)$$

where

$$r = \overline{PQ}, \quad \frac{\partial}{\partial n} = \vec{n} \cdot \left(\frac{\partial}{\partial \xi}, \frac{\partial}{\partial \eta} \right),$$

ξ, η being variables of integration on S . In order that we may apply the radiation conditions (2.15), as in the case of the variational method, S_R and S_L should be located where the potential is essentially that of propagating waves. We observe that (4.1) consists of a simple distribution of strength $\phi^{(m)}$ and a double distribution of strength $\frac{\partial\phi^{(m)}}{\partial n}$. The potential contributed by the first distribution is continuous throughout space, and $\phi^{(m)}$ is continuous on S itself if $\phi^{(m)}$ is piecewise continuous (Kellogg, 1929). Hence, a discontinuous normal-

derivative boundary condition does not contradict our original assumption on the continuity of ϕ .

Next we make use of the boundary conditions (2.5) and (2.15) to rewrite (4.1) in terms of $\phi^{(m)}$ only. Then, letting the observation point P approach S , we obtain the following integral equation for $\phi^{(m)}$ on S :

$$\begin{aligned} \pi\phi^{(m)}(P) = & \int_{S_0} \phi^{(m)}(Q) \frac{\partial}{\partial n} \log r ds(Q) \\ & + \int_{S_F} \phi^{(m)} \left[\frac{\partial}{\partial n} \log r - \nu \log r \right] ds \\ & + \int_{S_B} \phi^{(m)} \frac{\partial}{\partial n} \log r ds \\ & + \int_{S_R} \phi^{(m)} \left[\frac{\partial}{\partial n} \log r - i m_0^R \log r \right] ds \\ & + \int_{S_L} \phi^{(m)} \left[\frac{\partial}{\partial n} \log r - i m_0^L \log r \right] ds \\ & - \int_{S_0} f^{(m)}(s) \log r ds, \quad P \in S \end{aligned} \quad (4.2)$$

Solution of this integral equation yields the value of $\phi^{(m)}$ along S without further calculations. The kernel here consists of a linear combination of the fairly simple functions, $\log r$ and $\frac{\partial}{\partial n} \log r$.

Evidently, the approach here can be extended to the more trivial case of a fluid domain of finite extent, for example, a canal or a basin. The radiation condition is simply replaced by $\phi_n = 0$ and no outgoing waves occur. For this case, Chang (1972) started with an unknown distribution, $\sigma(s)$, of $\log(1/r)$ along the boundary of the fluid, and had shown rigorously that the resulting integral equation for $\sigma(s)$ has a unique solution if the forcing frequency does not coincide with the natural frequencies of the basin.

4.2 Discretization of the Integral Equation

By the method of discretization, the integral equation (4.2) for $\phi^{(m)}$ can be reduced to a set of linear algebraic equations with the unknowns being the

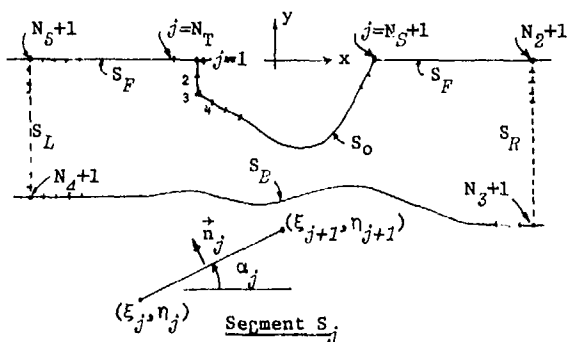


Fig. 4.1 Subdivision of the Contour S .

values of the potential,

$$\phi_j^{(m)} = \phi^{(m)}(x_j, y_j), \quad i=1, \dots, N_T$$

at a discrete set of control points along the boundary. Using the notation defined in Fig. 4.1, Eqn. (4.2) can be written in the following discretized form:

$$\sum_{j=1}^{N_T} [-\pi \delta_{ij} + c_{ij}] \phi_j^{(m)} = K_i, \quad (4.3)$$

$$i = 1, 2, \dots, N_T$$

where δ_{ij} is the Kronecker delta,

$$c_{ij} = \begin{cases} Q_{ij}, & \text{for } j=1, \dots, N_S; \\ & j=N_S+1, \dots, N_T; \\ Q_{ij} - v P_{ij}, & \text{for } j=N_S+1, \dots, N_T; \\ & j=N_S+1, \dots, N_T; \\ Q_{ij} - i \left(\frac{m_R}{m_0} \right) P_{ij}, & \text{for } j=N_S+1, \dots, N_T; \\ & j=N_S+1, \dots, N_T, \end{cases} \quad (4.4)$$

and

$$K_i = \sum_{j=1}^{N_S} f_j^{(m)}(x_j, y_j) P_{ij}. \quad (4.5)$$

Here, we have used a constant distribution (or interpolation) function for ϕ between each pair of consecutive grid points. The kernel integrals or influence coefficients, P_{ij} , and Q_{ij} are defined by line integrals over a small segment S_j as follows:

$$P_{ij}(\xi_j, \eta_j; \xi_{j+1}, \eta_{j+1}) = \int_{S_j} \log[(x_i - \xi)^2 + (y_i - \eta)^2]^{1/2} ds, \quad (4.6a)$$

$$Q_{ij}(\xi_j, \eta_j; \xi_{j+1}, \eta_{j+1}) = \int_{S_j} \frac{\partial}{\partial n_j} [\log(x_i - \xi)^2 + (y_i - \eta)^2]^{1/2} ds, \quad (4.6b)$$

and can be evaluated analytically. It should be pointed out that the matrix $[-\pi \delta_{ij} + c_{ij}]$ is neither symmetric nor diagonally dominant. The matrix is, however, predominantly real, except for columns associated with control points on S_R and S_L , the radiation boundaries. Evidently, a unique solution for $\phi_j^{(m)}$ exists if the determinant of the matrix does not vanish.

If the geometry of both body and bottom is symmetric with respect to $x=0$, and if $x_c=0$, $\phi^{(m)}(x, y)$ will be an even function of x , for $m=2$, and an odd function of x for $m=1$ or 6 . Such symmetry (or anti-symmetry) allows us to deal with, say, just the right side of the fluid. More specifically, the influence coefficients P_{ij} and Q_{ij} may be interpreted as the sum of two integrals:

$$P_{ij} = P_{ij}^R(\xi_j, \eta_j; \xi_{j+1}, \eta_{j+1}) + q(m) \cdot P_{ij}^R(-\xi_j, \eta_j; -\xi_{j+1}, \eta_{j+1}), \quad \xi \geq 0 \quad (4.7)$$

$$Q_{ij} = Q_{ij}^R(\xi_j, \eta_j; \xi_{j+1}, \eta_{j+1}) - q(m) \cdot Q_{ij}^R(-\xi_j, \eta_j; -\xi_{j+1}, \eta_{j+1}), \quad \xi \geq 0$$

where P_{ij}^R and Q_{ij}^R are defined by Eqns. (4.6a) and (4.6b). Here, $q(m)$ takes on the value of 1 or -1 according to the relation:

$$\phi^{(m)}(-x, y) = q(m) \phi^{(m)}(x, y).$$

With such a modification, it is then only necessary to solve for $\phi_j^{(m)}$ on the right side of the fluid.

4.3 The Infinite-depth Case

The technique discussed earlier appears to be impractical if we want to consider the case of an infinitely deep fluid, especially when the wave length is long. This difficulty may be circumvented by noting that for an infinitely deep fluid, the third integral in (4.2) can be discarded, and that for the boundary integrals associated with S_R , for instance, we may replace the unknown function $\phi(\xi_R, \eta)$ by $\phi(\xi_R, 0)e^{v\eta}$, $\phi(\xi_R, 0)$ being unknown. In other words, an exponentially decaying distribution is assumed. Note that this assumed behavior of ϕ at ξ_R is valid to the same extent that the radiation condition is valid. The resulting integrals associated with S_R now become:

$$\int_{S_R} \phi^{(m)}(\xi_R, \eta) \left[\frac{\partial}{\partial n} \log r - i v \log r \right] ds$$

$$= \phi^{(m)}(\xi_R, 0) \int_{-\infty}^0 e^{v\eta} \left[\frac{\partial}{\partial \xi} \log r - i v \log r \right] d\eta$$

$$= \phi^{(m)}(\xi_R, 0) [F^R(v, \xi_R, x, y) - i G^R(v, \xi_R, x, y)] \quad (4.8)$$

Again, the integrals F^R and G^R may be evaluated rather expediently [see Yeung (1973)].

Similar considerations may be applied to the finite-depth case: Using a $\cosh m_0(y+h)/\cosh m_0h$ distribution function instead of $e^{v\eta}$, we can reduce a sequence of unknowns on S_R or S_L to a single unknown, $\phi(\xi_R, 0)$ or $\phi(\xi_L, 0)$, on the free-surface. It is worthwhile to point out that one further simplification occurs in the fluid is of constant depth. By distributing a positive image system about the line $y=-h$, we can eliminate the sequence of unknowns on the bottom surface. In other words:

$$\begin{aligned}
P_{ij} &= P_{ij}^T(\xi_j, \eta_j; \xi_{j+1}, \eta_{j+1}) \\
&+ P_{ij}^T[\xi_j, -(2h+\eta_j); \xi_{j+1}, -(2h+\eta_{j+1})] \\
Q_{ij} &= Q_{ij}^T(\xi_j, \eta_j; \xi_{j+1}, \eta_{j+1}) \\
&- Q_{ij}^T[\xi_j, -(2h+\eta_j); \xi_{j+1}, -(2h+\eta_{j+1})]
\end{aligned}$$

where P_{ij}^T and Q_{ij}^T are expressions resulted from evaluating (4.6a) and (4.6b) analytically. Combined with the $\cosh m_0(y+h)$ distribution on S_R and S_L as discussed earlier, it will only be necessary to solve for $\phi_j^{(m)}$ on $S_{OU}S_F$.

4.4 The Three-dimensional Problem

It is rather straight forward to extend the above scheme to three-dimensional bodies, at least in principle, although the complexity of the computer program increases manifold. Here, due to practical limitations, we consider only body shape with two planes of symmetry (symmetry about the Oxy and Oyz planes) in infinitely deep water. The radiation condition (2.12) is now appropriate. Applying Green's theorem in three-dimension and making use of the boundary conditions (2.5), we may write:

$$\begin{aligned}
\Omega \phi^{(m)}(P) &+ \iint_{S_O} \phi^{(m)}(Q) \frac{\partial}{\partial n} \left(\frac{1}{r} \right) dS(Q) \\
&+ \iint_{S_F} \phi^{(m)}(Q) \left[\frac{\partial}{\partial n} \left(\frac{1}{r} \right) - v \left(\frac{1}{r} \right) \right] dS(Q) \\
&+ \iint_{\Sigma_R} \phi^{(m)}(R, 0, \theta) e^{v\eta} \left[\frac{\partial}{\partial n} \left(\frac{1}{r} \right) + \left(\frac{1}{2R} - im_0 \right) \frac{1}{r} \right] R d\theta d\eta \\
&= \iint_{S_O} f^{(m)}(s) \frac{1}{r} dS, \quad P \in S \quad (4.9)
\end{aligned}$$

where Σ_R corresponds to the surface of a vertical cylinder of radius R enclosing

the body. $\Omega(>0)$, in general, takes a value of 2π if P is on a planar surface, but otherwise is the solid angle inside the fluid in the neighborhood of point P if P happens to be a vertex point. $f^{(m)}(s)$ and m_0 are given by (2.6) and (2.9), respectively. Note that we have made use of the distribution function:

$$\phi^{(m)}(R, y, \theta) = \phi^{(m)}(R, 0, \theta) e^{vy}, \quad y \leq 0 \quad (4.10)$$

and as a result we are required to determine ϕ of Eqn. (4.9) on the body and free surface S_F only.

To solve Eqn. (4.9) numerically, we will discretize the integral equation as follows. The surface $S_{OU}S_F$ is first subdivided by a grid system as shown in Fig. 4.2: the body by transverse sections and waterline sections as commonly used by naval architects, the free surface by quasi-radial lines and circumferential lines. To each grid point we assign an index i , $[i=1, \dots, N_T]$ and $\phi_i^{(m)}$ thus denotes the potential of the m -th mode at grid point i . For simplicity of notation, we discard the superscript (m) in this section with the understanding that ϕ obviously depends on m . Each surface element can be characterized by the double indices (k, j) corresponding to the sector number and the element count from the keel upwards, respectively. We have chosen to use triangular elements with linear distributions to approximate the potential. This type of element has the advantage that when joined edge to edge, the elements form a closed surface and the potential across these edges is continuous. On Σ_R , we shall use a special element, one which is infinite in length and has an exponential-decaying distribution in the vertical direction, but a linear distribution in the horizontal direction.

Let S_{kj} be the surface area of the (k, j) element, $N(k)$ be the number of elements in the k -th sector, and M be the

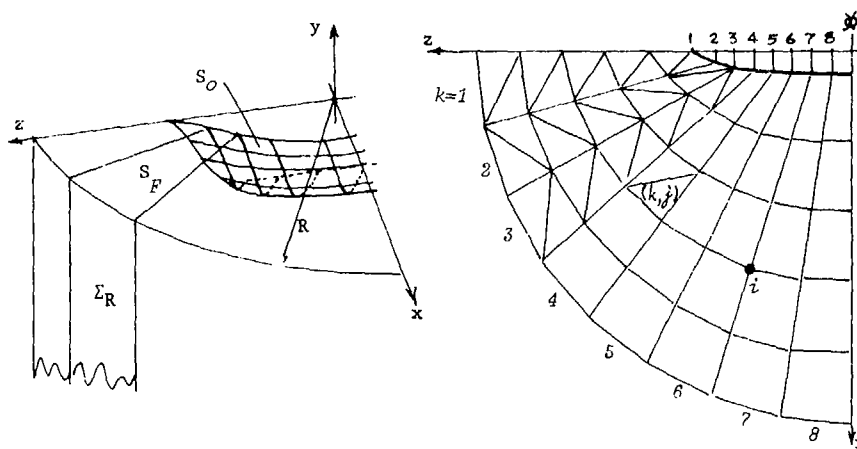


Fig. 4.2 Schematic showing the Subdivision of Surfaces S_O, S_F, Σ_R .

number of sectors in one quadrant of the x-z plane, then

$$\iint_{S_0} + \iint_{S_F} + \iint_{\Sigma_R} dS = \sum_{k=1}^M \sum_{j=1}^{N(k)} \iint_{S_{kj}} () dS \quad (4.11)$$

The integrands of these integrals depend evidently on whether j corresponds to an element lying on S_0 , S_F , or Σ_R . Also, since we are only integrating one quadrant in the x-z plane, mirror images of the integrals over S_{kj} in the other three quadrants must be accounted for. Note that $\phi_j^{(m)}$ will assume either an odd or even behavior about the Oxy and Oyz planes depending on the mode that is under consideration.

If $N_0(k)$ denotes the index of the last element lying on S_0 in the k -th sector, and $N_F(k)$ denotes the corresponding index of the element lying on S_F , then Eqn. (4.9) may be written as:

$$\begin{aligned} \Omega\phi(P) = & \sum_{k=1}^M \sum_{j=1}^{N_0(k)} \left[\iint_{S_{kj}} f(s) \frac{1}{r} ds \right. \\ & \left. - \iint_{S_{kj}} \phi(Q) \frac{\partial}{\partial n} \left(\frac{1}{r} \right) ds(Q) \right] \\ & + \sum_{k=1}^M \sum_{j=N_0(k)+1}^{N_F(k)} \left[\iint_{S_{kj}} \phi \frac{1}{r} ds \right. \\ & \left. - \iint_{S_{kj}} \phi \frac{\partial}{\partial n} \left(\frac{1}{r} \right) ds(Q) \right] \\ & + \sum_{k=1}^M \sum_{j=N_F(k)+1}^{N_F+1} \left[\left(-\frac{1}{2R} + iv \right) \iint_{S_{kj}} \phi \frac{1}{r} ds \right. \\ & \left. - \iint_{S_{kj}} \phi \frac{\partial}{\partial n} \left(\frac{1}{r} \right) ds \right] \quad (4.12) \end{aligned}$$

Now the function ϕ within each patch is approximated by some convenient distribution function \tilde{g} (linear, in the present case), as follows:

$$\begin{aligned} \phi(\xi, \eta, \zeta) \Big|_{S_{kj}} &= [g_1(\xi, \eta, \zeta), g_2, g_3] \begin{Bmatrix} \phi_{\beta_1} \\ \phi_{\beta_2} \\ \phi_{\beta_3} \end{Bmatrix}, \\ &= \tilde{g} \cdot \vec{\phi}_{\beta}(k, j), \quad \zeta = \zeta(\xi, \eta). \quad (4.13) \end{aligned}$$

The integers β_i 's evidently depend on (k, j) and $\vec{\phi}_{\beta}$ is a vector of three components. Combining (4.12) and (4.13), we obtain:

$$\begin{aligned} \Omega\phi(P) + & \sum_{k=1}^M \sum_{j=1}^{N_0(k)} \vec{Q}_{kj} \cdot \vec{\phi}_{\beta}(k, j) \\ & + \sum_{k=1}^M \sum_{j=1}^{N_F(k)} (\vec{Q} - v\vec{P})_{kj} \cdot \vec{\phi}_{\beta}(k, j) \end{aligned}$$

$$\begin{aligned} & + \sum_{k=1}^M \left[\vec{Q} + \left(\frac{1}{2R} - iv \right) \vec{P} \right]_{k, N_F+1} \cdot \vec{\phi}_{\beta}(k, N_F+1) \\ & = \sum_{k=1}^M \sum_{j=1}^{N_0(k)} \vec{P}_{kj} \cdot \vec{\phi}_{\beta}(k, j), \quad (4.14) \end{aligned}$$

where \vec{P} and \vec{Q} are source and normal-dipole distribution integrals over element S_{kj} and are defined as follows:

$$\vec{P} = \iint_{S_{kj}} (g_1, g_2, g_3) \frac{1}{r} dS, \quad (4.15)$$

$$\vec{Q} = \iint_{S_{kj}} (g_1, g_2, g_3) \frac{\partial}{\partial n} \left(\frac{1}{r} \right) dS. \quad (4.16)$$

It should be emphasized that (4.15) and (4.16) actually represent four different integrals, one in each quadrant, taking into account the oddness and evenness of the function $\phi(x, y, z)$ [see Ref. (31)]. For this method to be successful, we must be able to evaluate these integrations fairly expeditiously, preferably analytically. The \vec{Q} integral, corresponding essentially to the negative of the normal velocity induced by a linear distribution of sources over a general triangular planar element, has been considered by Webster (1974). Appendix B provides the details concerning the evaluation of the \vec{P} integral. Certain aspects related to the numerical instability of the final expression are also discussed. For the evaluation of integrals over Σ_R , we refer the reader to Reference (31).

So far, we have left the observation point P in Eqn. (4.14) undecided. If we choose P to be the grid points, then $\Omega\phi(P) \rightarrow \Omega_i\phi_i$, ($i=1, \dots, N_T$), and we have a system of linear equations with an equal number of unknowns and equations. In practice, it is numerically more stable to evaluate the coefficients given in (4.15) and (4.16) at a small distance from the vertex (or corner) of the element rather than right at the vertex. Equation (4.14) is the three-dimensional analog of (4.3) for two-dimensional problems. Again, elements of the matrix are predominantly real except for columns associated with the last free-surface variable on each radial line. This advantage is fully exploited in storing as well as in solving the matrix.

5. RESULTS AND DISCUSSIONS

Because of the relative newness of the present two methods of solution, we concentrate on validating our approaches by comparing our results with existing solutions obtained by other authors. Also, since our methods of solutions do not depend on any particular choice of body geometry, mathematically simple shapes, such as a circular cylinder or a sphere, are in fact, as general as any

other shapes to our methods. We begin in §5.1 with some standard added-mass and damping coefficients computations for circular and rectangular cylinders. Next, diffraction and pressure distribution problems in two dimensions are considered. Finally, test computations in three dimensions are presented for comparison with existing solutions.

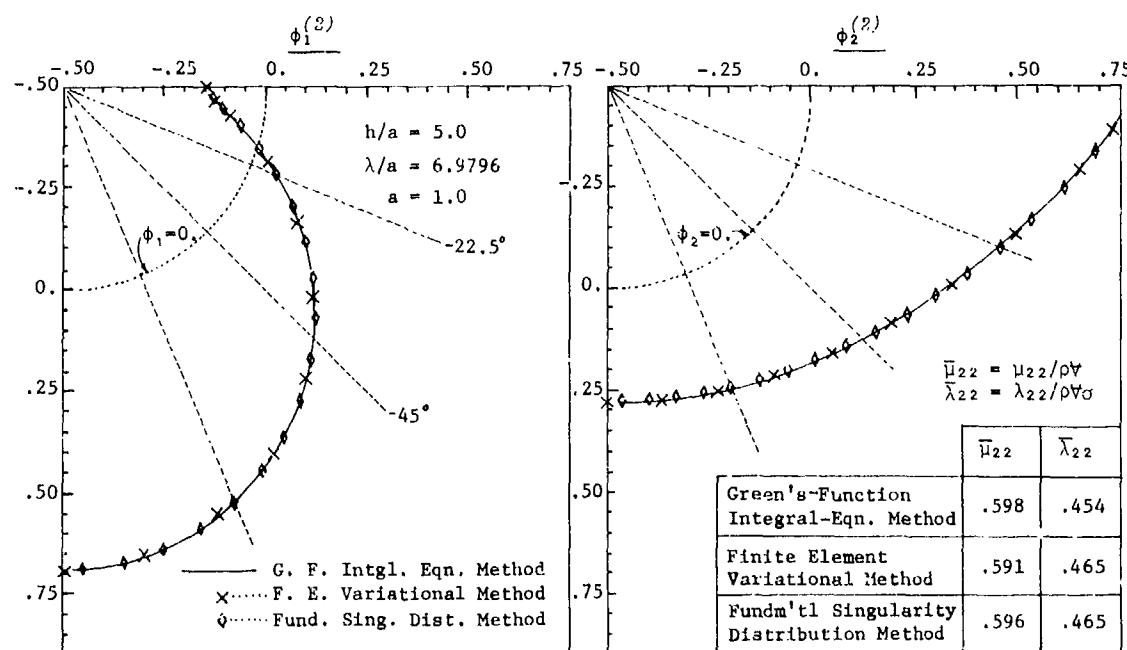
5.1 Force Coefficients of Cylinder in Finite or Infinite Depth

As a test case, the two numerical methods discussed in this paper (§3.1 and §4.1) were first applied to solve the classic problem of a semi-submerged circular cylinder heaving in a deep fluid, a problem which was first solved by Ursell (1949). Fig. 5.1 shows a comparison of the values of potentials on the cylinder's surface for the case $K\sigma a = 0.9$, a being the radius of the cylinder. Here the dotted circle corresponds to values of ϕ that are identically zero; the radial distance from the reference circle represents the value of ϕ_1 or ϕ_2 . The comparison is made with results obtained using the Green-function integral-equation method ($h=\infty$). Our results are based on a h/a ratio of 5.0, which corresponds to a depth-to-wavelength ratio of 0.72 at this frequency. The fluid could be considered as infinitely deep in such a case. It can be seen that the agreement is very good.

Fig. 5.2 shows the added-mass coefficient for the same cylinder over a

range of frequency for two depths, $h/a=\infty$ and $h/a=2.0$. Results obtained by the second method using the infinite-depth formulation described in §4.3 is shown here to be compared with the dash-dot line, which is obtained from Kim's (1969) work using Ursell's multipole expansion method. Results obtained by the variational method is based on the formulation given in §3.2. The agreement, as can be seen, is good. Similar agreement, though not shown, also applies to the case of damping coefficients.

Added-mass and damping coefficients for cylinders in water of finite depth have been computed in the past by Yu and Ursell (1961), Lebreton and Margnac (1966), and C. H. Kim (1969). Yu and Kim both used the multipole expansion method whereas Lebreton and Margnac used the Green's-function integral-equation method. In cases where common results are available for comparison, agreement has been poor especially in the low frequency range. We furnish here some fresh calculations using the two new methods and hope to be able to shed some light on the subject. Figs. 5.2 and 5.3 contain, for $h/a=2.0$, curves of added-mass coefficients and amplitude ratio based on a number of past works together with results by the present methods. Our results for the added-mass coefficients do not agree with those by Yu and Ursell (1961), or by Kim (1969). Our calculations seem to indicate that this coefficient approaches a constant value as the frequency parameter $K\rightarrow 0$, whereas



(Circular Cylinder in Heave, $K\sigma^2 a/g=0.9$)

Fig. 5.1 Comparison of Potentials on Body Surface as Obtained by Three Methods.

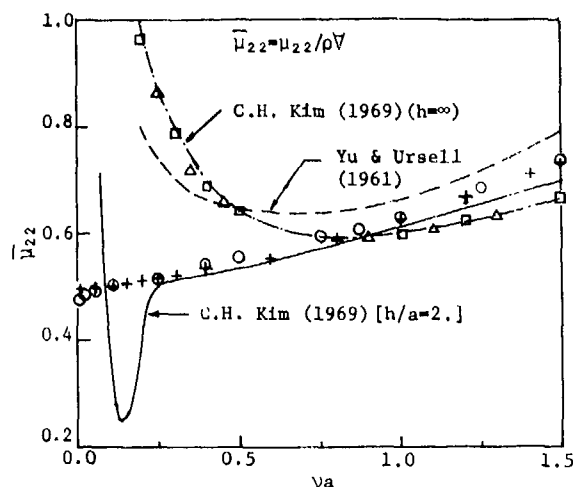


Fig. 5.2 Added-Mass Coefficient of a Circular Cylinder in Heave.

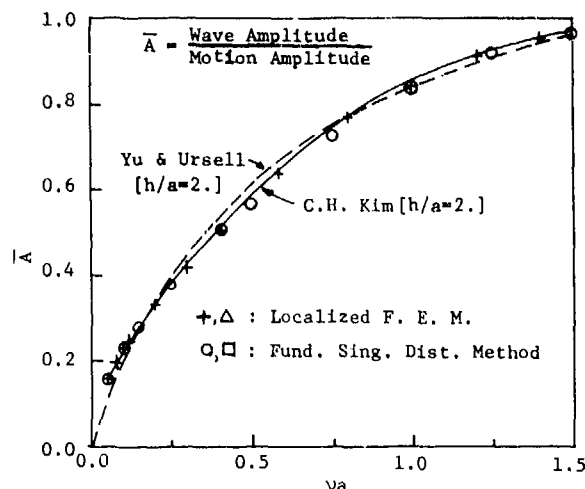


Fig. 5.3 Amplitude Ratio of a Circular Cylinder in Heave.

those of other authors tend to infinity in the limit. Note that, however, the agreement on the damping coefficient (or the amplitude ratio) for all authors are excellent.

The present findings of the low-frequency behavior of the heave added-mass do not contradict those obtained by Lebreton and Margnac (1966), who have computed $\bar{\mu}_{22}$ and $\bar{\lambda}_{22}$ for rectangular sections in various depths. We reproduce here in Figs. 5.4 and 5.5 results by Lebreton and Margnac, as well as those by C. H. Kim from their publications. Strictly speaking, Kim's section, corresponding to his values of $H=1$ and $B=1$, is not absolutely rectangular. We see, however, for the added-mass curve,

oscillation similar to the case of a circular cylinder occurs at the low-frequency end whereas our results, by both methods, agree well with Lebreton and Margnac.

In performing these computations at low frequency, it was found that numerical instability occurs in the fundamental singularity distribution method when $K < 0.02$. For such low values of ν , it is suspected that the smallness of the ratio $\nu P_{ij}/Q_{ij}$ in Eqn. (4.4) when combined with round-off error in solving the large matrix makes the free-surface condition numerically undetectable. Also, added-mass coefficients computed by the localized finite-element method increase abruptly as K approaches zero

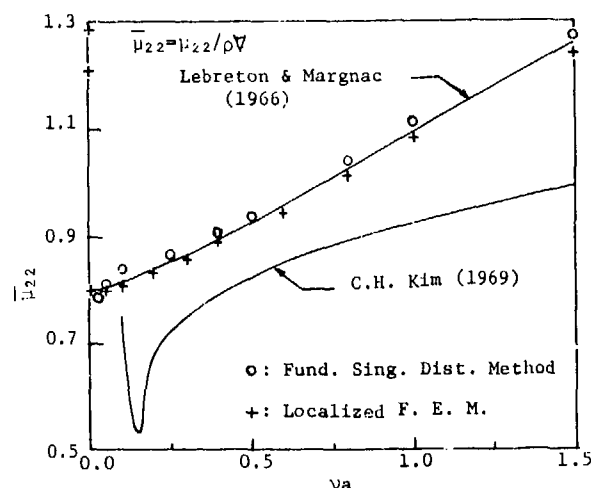


Fig. 5.4 Added-Mass Coefficient of a Rectangular Cylinder in Heave.

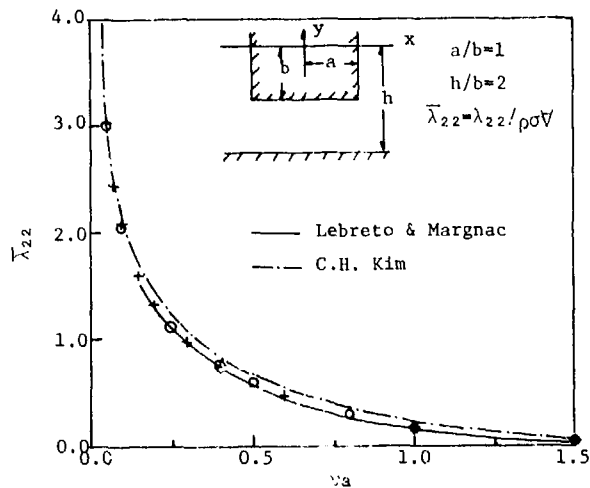


Fig. 5.5 Damping Coefficient of a Rectangular Cylinder in Heave.

Table 1. Approximate Computational Costs for Various Methods on IBM Computer.

Various Numerical Methods	Approx. CPU Time in Seconds	Approx. Total Cost
Finite-Element Variational Method (F.E.M.) ($h=\infty$)	29	\$13.38
Finite-Element Variational Method (F.E.M.) ($h\neq\infty$)	13.3	\$ 3.68
Localized Finite-Element Method (L.F.E.M.)	2.6	\$ 0.51
Fund. Singularity Dist. Method ($h\neq\infty$)	14.0	\$ 1.85
Fund. Singularity Dist. Method ($h=\infty$)	6.5	\$ 0.88
Green-Function Integral-Eqn. Method ($h=\infty$)	2.7	\$ 0.41

in the interval of $0 < K < .001$. It is possible that this behavior is also caused by numerical instability.

It is of interest to compare the computation costs for various methods involved. We tabulate in Table 1 the approximate CPU execution time as well as the total dollar cost required for a typical case of computation of a single frequency, all based on the MIT IBM-370 machine. The total cost is given here because in some of the methods, extensive use of peripheral devices leads to additional charges. It should be pointed out that the Green-function integral-equation method for the case of finite depth will require at least three times as much computation time as the case of infinite depth. Figures given for the fundamental-singularity distribution method are based on double-precision arithmetic. If the number of unknowns is less than 100, single precision will be sufficient, which leads to a 50% reduction in CPU time.

Table 2. Computation Time and Convergence of the Localized Finite-Element Method.

M	N	\bar{u}_{22}	$\bar{\lambda}_{22}$	C.P.U. in secs.
1	93	0.6279	0.4580	2.42
5	97	0.6298	0.4140	2.47
10	102	0.6065	0.4074	2.63
20	112	0.6060	0.4000	2.78
30	122	0.5985	0.4068	2.80
F.E.M.	492	0.5990	0.4048	28.96
Porter (1960)		0.60	0.40	

M - Number of Eigenfunctions taken.

N - Number of Complex Algebraic Equations

A more detailed comparison of the computational efficiency of the classical variational method versus the modified method is given in Table 2. The computations are carried out for a circular cylinder in heave motion in water of infinite depth and $K=1.0$. Also shown are the convergence characteristics of the localized finite-element method as a function of the number of eigenfunctions taken.

5.2 Diffraction and Pressure-Distribution Problems in Two dimensions

The variational method described in §3.1 has been applied to a variety of diffraction problems: a submerged circular cylinder in water of infinite depth; a rectangular cylinder on the free surface or on the bottom in water of finite depth; a triangular and a sinusoidally shaped obstruction on the bottom in water of finite depth; and two vertical flat plates piercing the free surface in water of finite depth. However, we present here only results of the diffraction problem for a sinusoidal hump on the bottom; one can find other results in Bai (1972).

The geometry of the obstruction is shown in Fig. 5.6. The incident wave

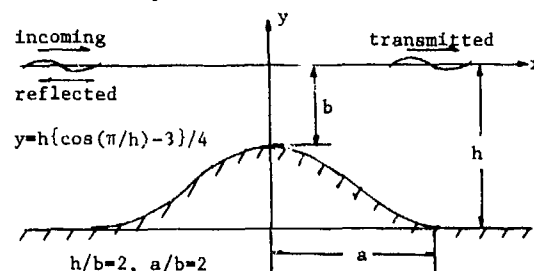


Fig. 5.6 Configuration of a Sinusoidal Hump on the Bottom.

amplitude defined in Eqn. (3.11) was chosen to be unity. Referring to Eqn. (2.21) the complex wave function $\psi(x)$ of the diffracted waves can be written as:

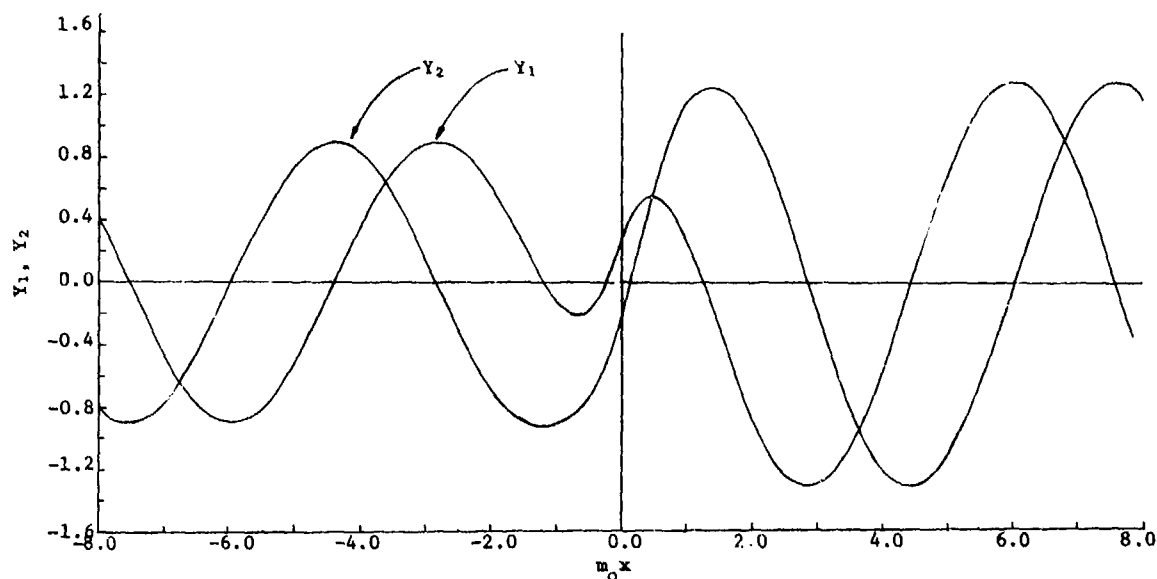


Fig. 5.7 Diffracted Waves due to a Sinusoidal Hump on the Bottom ($m_0 h = 0.5$).

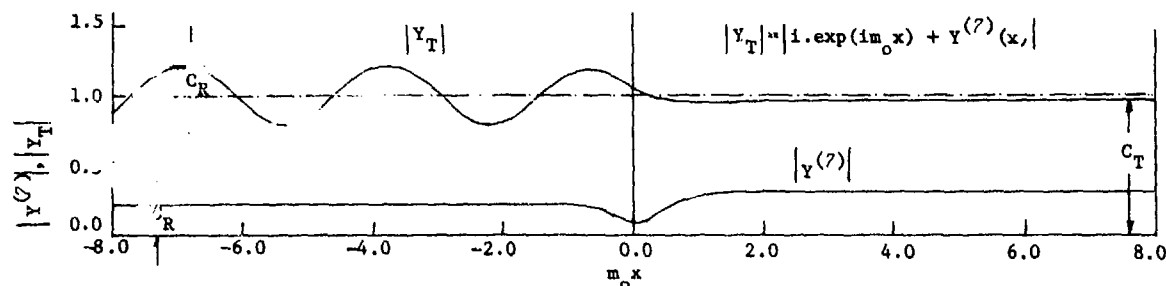


Fig. 5.8 Maximum Wave Amplitudes of the Diffracted Waves and the Total Waves.

$$Y^{(?)}(x) = Y_1(x) + iY_2(x) \quad (5.1)$$

Figs. 5.6 and 5.7 show the real and imaginary components of $Y^{(?)}(x)$ and $|Y^{(?)}|$, respectively. For $x < 0$, $|Y^{(?)}|$ as shown is simply the reflection coefficient, C_R . Also plotted in Fig. 5.7, is the total wave amplitude, Y_T , which is the sum of the incident wave and the diffracted waves. The transmission coefficient C_T is therefore given by $|Y_T|$ for $x > 0$.

It is straightforward to extend our methods to problems with a pressure distribution on the free surface. In the absence of any physical body, Eqn. (2.5c) can be discarded and if a denotes the

half-length of the distribution Equation (2.5a) becomes:

$$\phi_y(x, 0) - v\phi = \begin{cases} \sigma p(x)/\rho g, & |x| \leq a, \\ 0, & |x| > a, \end{cases} \quad (5.2)$$

where $p(x)$ is the pressure distribution function; presently, we will choose it to be a constant. In terms of the usual Green-function, G , the solution for ϕ is simply:

$$\phi(x, y) = c \int_{-a}^a G(x, y; \xi, 0) d\xi, \quad c = \sigma p / \rho g, \quad (5.3)$$

where G is available from Wehausen and Laitone (1960, p. 483). In Fig. 5.9 we compare results obtained by

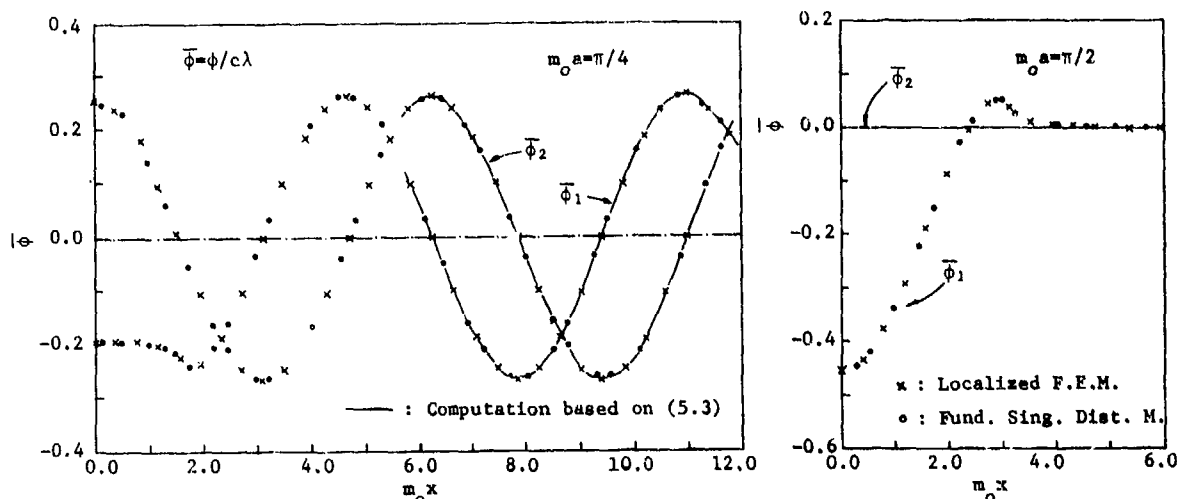


Fig. 5.9 Potentials on the Free Surface due to an oscillating Pressure Distribution.

both new methods with those computed using (5.3). As indicated by Stoker (1957), there exists a set of values of a such that when $m_0 a = n\pi$, n being an integer, there are no outgoing waves. Our results agree well with this phenomenon.

5.3 Three-Dimensional Bodies

Past investigations in hydrodynamic forces acting on three-dimensional bodies have been quite restricted in scope, mostly confined to mathematically well-defined shapes. Lebreton and Margnac (1968), however, have completed some calculations for two barge shapes using the Green-function integral-equation method.

The computer program using the variational methods given in §3.1 & §3.2 can deal with any axis-symmetric body with axis-symmetric or non-axis-symmetric fluid motion. The computer program for three-dimensional bodies using the fundamental-singularities distribution method (§4.4) was developed to handle all six degrees of motion for bodies with center plane and midship symmetry. Also, the capability of calculating diffraction forces in oblique waves can be easily incorporated since this would only involve evaluating the integral (2.19). In another paper [Bai (1975)] the quasi-three-dimensional problem of the diffraction of oblique waves by an infinitely long cylinder was solved by the finite-element method and comparisons with other authors were made.

We present here some test computations for three-dimensional bodies and compare them with existing results. A sphere has been chosen since results are available from a number of sources [Havelock (1955), Wang (1966), and W. D. Kim (1965)]. The heaving motion case, in particular, provides an excellent check on the computer program using the singularity-distribution method, for here the sphere is treated merely as a

Table 3. Comparison of Results by Various Methods for a Sphere and an Ellipsoid.

Body	$K=va$	Mode	$\bar{\mu}_{ii}$	$\bar{\lambda}_{ii}$	Method
Sphere	0.4	Heave	1.350	0.713	Wang, S.
			1.357	0.719	B(L.F.E.M.)
			1.183	0.663	Y
			1.318	0.710	Y(M=9)
		Surge	1.28	0.106	Kim, W.D.
			1.280	0.115	B(L.F.E.M.)
			1.203	0.100	Y(Surge)
			1.17	0.099	Y(Sway)
	0.5	Heave	1.226	0.709	Wang, S.
			1.232	0.726	B(L.F.E.M.)
			1.131	0.681	Y
		Surge	1.33	0.207	Kim, W.D.
			1.388	0.205	B(L.F.E.M.)
			1.244	0.196	Y(Surge)
			1.218	0.195	Y(Sway)
	1.0	Heave	0.897	0.519	Wang, S.
			0.856	0.514	B(F.E.M.)
			0.896	0.526	B(L.F.E.M.)
			0.837	0.530	Y
		Surge	1.21	0.71	Kim, W.D.
			1.190	0.71	B(L.F.E.M.)
			1.11	0.648	Y
1:1/4 Ellipsoid	1.0	Heave	0.172	0.115	Kim, W.D.
			0.164	0.109	Y
		Surge	0.0137	0.0024	Kim, W.D.
			0.0132	0.0024	Y
		Pitch	0.029	0.0047	Kim, W.D.
			0.0265	0.0043	Y
		Sway	0.137	0.0114	Y

$$\bar{\mu}_{ii} = \mu_{ii}/\rho a^3, \quad \bar{\lambda}_{ii} = \lambda_{ii}/\sigma \rho a^3, \quad i=1,2,3$$

$$\bar{\mu}_{ii} = \mu_{ii}/\rho a^5, \quad \bar{\lambda}_{ii} = \lambda_{ii}/\sigma \rho a^5, \quad i=4,5,6$$

body with two planes of symmetry. Table 3 tabulates the computed results for the purpose of comparison. Here, 'B'

signifies values obtained by the finite-element method, which assumes axis-symmetry; 'Y' indicates the values obtained by the fundamental-singularity distribution method, which used, in the present case, only 4 sectors per quadrant to represent the body. Such representation is, of course, crude, but serves the purpose of testing the program of the second method. However, one test computation using 9 sectors was made for $K=0.4$ to check the convergence of the result. "a" here denotes the radius of the sphere. Results for a 1:1/4:1/4 ellipsoid at one frequency is also given and compared with W. D. Kim (1966). Here, a is the half-length of the ellipsoid. The agreement is generally very good.

The localized finite-element method has also been applied to compute the sway added-mass and damping coefficients of a vertical circular cylinder in water of finite depth. Here $h/a=6$ and $a/b=2.0$, a and b being the radius and the draft of the cylinder, respectively. As mentioned in §3.2, this problem was considered earlier by Isshiki and Hwang (1973). In our computations, thirty terms in the k-series and one term in the l-series (l=1 only) of Eqn. (3.39) were taken. Our results are shown and compared with the results obtained by

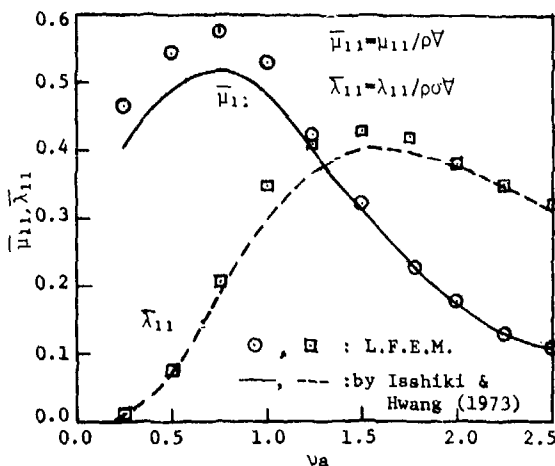


Fig. 5.10 Sway Added-Mass and Damping Coefficients of a Circular Dock.

Isshiki and Hwang (1973) in Fig. 5.10. Agreement is not good in certain range of va . In view of the good agreement between our results and those computed by many others for other configurations, and in view of the number of eigenfunctions taken in the computation, (Isshiki and Hwang had taken only seven terms) we are inclined to favor our results in this particular case.

More refined computations were carried out at three frequencies for an 1:1/8:1/8 ellipsoid using the fundamen-

tal-singularity distribution computer program. The body was defined by off-sets given at eight stations with seven points per station. The blunt end of the body, of course, could not be perfectly represented. Solutions were obtained for all six modes of motion. The roll motion gives vanishingly small results since this is a body of revolution. Results for the other five modes are shown in Table 4 and compared with Kim's whenever available. The agreement is very good. In the present program, if one makes use of the same grid geometry per three frequencies, the average CPU time on a CDC6400 machine is approximately 130 secs/mode/frequency.

Table 4. Added-Mass and Damping Coefficients of a 1:1/8:1/8 Ellipsoid at three Frequencies.

K=va	Mode	$\bar{\mu}_{ii}$	$\bar{\lambda}_{ii}$
0.15	Heave	.00915 (.00796)*	.0106 (.0093)
	Surge	.00104 (.00099)	0. (0.0)
	Pitch	.00996 (.0100)	0. (0.0)
	Sway	.0346	0.
	Yaw	.00615	0.
1.0	Heave	.0629 (.0637)	.0392 (.0400)
	Surge	.00121 (.00125)	.000168 (.00018)
	Pitch	.0115 (.0120)	.00139 (.00141)
	Sway	.0361	.000935
	Yaw	.00614	0.
2.0	Heave	.0415 (.0407)	.0420 (.0433)
	Surge	.00114 (.00118)	.000579 (.00064)
	Pitch	.0110 (.0116)	.00476 (.00513)
	Sway	.0412	.00652
	Yaw	.00689	.000211

* All numbers in parenthesis are based on W. D. Kim's (1966) paper.

6. REMARKS AND CONCLUSIONS

In this paper, we have presented two numerical-oriented methods of solution that are applicable to a variety of time-harmonic free-surface flow problems and have investigated the validity of these methods by applying them to a number of test problems with relatively simple geometry. In every case, we

obtained very satisfactory agreement.

The obvious advantage of the new methods is that they are capable of dealing with arbitrary boundary-geometry. Another advantage is that they do not suffer from a phenomenon known as John's frequencies (John, 1950), in the neighborhood of which, Frank (1967) and others have found that the traditional Green's-function integral-equation method yields inaccurate results. Of all the methods available in the past, the Green's-function method is the most versatile. It can be applied to problems with varying bottom topography, provided, for the case of two dimensions, that the depths on the right and left sides are the same. The more general situation of unequal depths, of course, offers little conceptual difficulty to the methods described herein. As for simple bottom geometry in two dimensions, it appears that, from the viewpoint of computational efficiency, the Green's-function method is unsurpassable in fluid of infinite depth, whereas the localized finite-element method and the fundamental-singularity distribution method are highly competitive with the Green's-function method for the case of finite depth.

Among the methods introduced, the fundamental singularity-distribution method, in general, is superior to the classical variational method described in §3.1. On the other hand, since the latter method involves only a banded matrix and the former a full matrix, the variational approach can be more efficient if the bottom topography is highly complicated and if the fluid domain is small. Of all approaches, the localized finite-element method, which preserves the versatility of the finite-element formulation in the inner flow field and concomitantly eliminates excessive computations in the outer flow field, is the most efficient. It would be worthwhile to examine whether or not an equally beneficial modification can be applied to the fundamental-singularity distribution method, which currently appears to be efficient mostly in the intermediate frequency-range.

For the localized finite-element method, it should be pointed out that in §3.3 we have taken a set of eigenfunctions to represent the solution in the outer flow-field. However, we could have used, instead, the Green function for the problem. In such a case, the interface boundary 'J' can be any arbitrary contour enclosing the body rather than a vertical line.

For three-dimensional problems, the current computer program using the singularity-distribution method can accommodate any body-shape that has two planes of symmetry. It is possible to relax this restriction to the case of one plane of symmetry. This would result in a linear increase of matrix generation

costs and a cubic increase of matrix solution time. It would be interesting to compare the computational efficiency between this method and the Green's-function method in three dimensions. The major obstacle in applying the latter method had been the development of efficient means of evaluation of integrals of the complicated kernel function over some small element (Hess and Wilcox, 1969), but was apparently first overcome by Lebreton and Margnac (1968) although no specific details were given of its treatment therein.

Work on extension of the localized finite-element method to the case of general three-dimensional bodies is presently under progress.

ACKNOWLEDGEMENT

The authors would like to express their gratitude to Professors J. V. Wehausen, J. R. Paulling, Jr., and W. C. Webster of the University of California for their guidance and enthusiasm during the development of the methods described in §3.1 and §4. Thanks are also due to Professors J. N. Newman and G. Strang of the Massachusetts Institute of Technology for various discussions on the subject. Acknowledgement is made for support from the Office of Naval Research, GHR Grant Contract No. N00014-69-A0200-1048 and N00014-67-A-0204-0023 for the variational method and Contract No. N00014-69-A-0200-1023 for the fundamental-singularity distribution method.

REFERENCES

1. Bai, K. J., "A Variational Method in Potential Flows with a Free Surface," Univ. of Calif. Berkeley, College of Engineering, Rep. NA 72-2, Sept. 1972, vi + 137 pp.
2. Bai, K. J., "Diffraction of Oblique Waves by an Infinite Cylinder," 1975, to be published.
3. Berkhoff, J. C. W., "Computation of Combined Refraction - Diffraction," *Proceedings of the 13th Coastal Engineering Conference*, vol. 2, 1972, pp. 471-490, A.S.C.E.
4. Bessho, Masatoshi, "Variational Approach to Steady Ship Wave Problem," *8th Sym. Naval Hydrodynamics*, Pasadena, Calif., 1970, 36 pp.
5. Black, J. L. and Mei, C. C., "Scattering and Radiation of Water Waves," Mass. Inst. of Tech., Dept. of Civil Engineering, Report No. 121, 248pp.
6. Chang, S. C., "On Surface Wave in a Canal of Arbitrary Shape," Research Report, Univ. of Alabama, Huntsville, 1972.
7. Chen, H. S. and Mei, C. C., "Oscillations and Wave Forces in a Man-made Harbor in the Open Sea," *10th Symposium on Naval Hydrodynamics*, Cambridge, Mass, 1974.
8. Frank, W., "Oscillation of

Cylinders in or Below the Free Surface of Deep Fluids," Naval Ship Research and Development Center, Report 2375, 1967, vi + 40 pp.

9. Havelock, T., "Waves Due to a Floating Sphere Making Periodic Heaving Oscillations," *Proc. Roy. Soc. London, Ser. A*, vol. 231, 1955, pp. 1-7 = *Collected Papers*, pp. 602-608.

10. Hess, J. L. and Smith, A. M. O., "Calculation of Potential Flow about Arbitrary Bodies," *Progress in Aeronautical Sciences*, vol. 3, 1967, pp. 1-137.

11. Hess, J. L. and Wilcox, D. C., "Progress in the Solution of the Problem of a Three-Dimensional Body Oscillating in the Presence of a Free Surface," McDonnell Douglas Report No. DAC 67647, Mar. 1967, 95 pp.

12. Isshiki, H. and Hwang, J. H., "An Axi-symmetric Dock in Waves," Seoul National Univ., Korea, College of Engineering, Dept. of Naval Architecture, Report No. 73-1, Jan., 1973, 38 pp.

13. John, F., "On the Motion of Floating Bodies. II. Simple Harmonic Motions," *Comm. Pure Appl. Math.*, vol. 3, 1950, pp. 45-101.

14. Kellogg, O. D., *Foundations of Potential Theory*, J. Springer, Berlin, 1929, Also Dover Publications, ix + 384 pp.

15. Kim, C. H., "Calculation of Hydrodynamic Forces for Cylinders Oscillating in Shallow Water," Chalmers Univ. of Tech., Gothenburg, Sweden, Div. of Ship Hydromechanics Report No. 36, Feb., 1967, 34 pp., also *J. Ship Res.*, vol. 13, 1969, pp. 137-154.

16. Kim, W. D., "Oscillations of a Rigid Body in a Free Surface," *J. Fluid Mech.*, vol. 21, 1965, pp. 427-451.

17. Kim, W. D., "On a Free-Floating Ship in Waves," *J. Ship Res.*, vol. 10, 1966, pp. 182-200.

18. Lebreton, J. C. and Margnac, M. A., "Traitement sur Ordinateur de Quelques Problèmes Concernant l'Action de la Houle sur Corps Flottants en Théorie Bidimensionnelle," *Bulletin du Centre de Recherches et d'Essais de Chatou*, No. 18, 1966.

19. Lebreton, J. C. and Margnac, M. A., "Calcul des Mouvements d'un Navire ou d'une Plateforme Amarrée dans la Houle," *La Houille Blanche*, Nov. 5, 1968.

20. Newman, J. N., "Exciting Forces on Fixed Bodies in Waves," *J. Ship Res.*, vol. 6, no. 3, 1962, pp. 10-19.

21. Porter, W. R., "Pressure Distributions, Added Mass, and Damping Coefficients for Cylinders Oscillating in a Free Surface," Univ. of Calif Berkeley, Inst. Engineering Res. Report 8216, July, 1960, x + 181 pp.

22. Sao, Kunihisa, Maeda, Hisaaki, and Hwang, J. H., "On the Heaving Oscillation of a Circular Dock," *J. Soc. Naval Arch.*, Japan, 130, 1971, 121-130.

23. Stoker, J. J., *Surface Waves*, Interscience Publishers, New York, 1957, xxviii + 567 pp.

24. Strang, G. and Fix, G., *An Analysis of the Finite Element Method*, Prentice-Hall, 1973, xiv + 306 pp.

25. Ursell, F., "On the Heaving Motion of a Circular Cylinder in the Free Surface of a Fluid," *Quart. J. Mech. Appl. Math.*, vol. 2, 1949, pp. 218-231.

26. Wang, S., *The Hydrodynamic Forces and Pressure Distributions for an Oscillating Sphere in a Fluid of Finite Depth*, Dissertation, Mass. Inst. of Tech., Dept. of Naval Arch. and Marine Engineering, June, 1966, xiv + 87 pp.

27. Watson, G. H., *Theory of Bessel Functions*, 2nd ed., Cambridge Univ. Press, 1966, vi + 804 pp.

28. Webster, W. C., "The Flow about Three-dimensional Bodies," paper under preparation, to be submitted to the *Journal of Ship Research*, 1974.

29. Wehausen, J. V., "The Motion of Floating Bodies," *Annual Review of Fluid Mechanics*, vol. 3, 1971, pp. 237-268.

30. Wehausen, J. V. and Laitone, E. V., "Surface Waves," *Handbuch der Physik*, vol. 9, pp. 446-778, Springer-Verlag, Berlin, 1960.

31. Yeung, R. W., "A Singularity-Distribution Method for Free-Surface Flow Problems with an Oscillating Body," Univ. of Calif. Berkeley, College of Engineering, Report NA 73-6, Aug., 1973, vi + 124 pp.

32. Yu, Y. S. and Ursell, F., "Surface Waves Generated by an Oscillating Circular Cylinder on Water of Finite Depth" Theory and Experiment, *Journal of Fluid Mech.*, vol. 11, 1961, pp. 529-551.

33. Zienkiewicz, O. Z., *The Finite Element Method in Engineering Science*, McGraw-Hill, London, 1971, xiv + 521 pp.

APPENDIX A

Interpolation Functions for an Eight-Node Square Element

Although in our actual computations an eight-node quadrilateral element was used, we shall give for the purpose of illustration the example of an eight-node square element. Let us consider a square element with one node at each vertex and one node at the mid-point of each side, as shown in Fig. A.1.

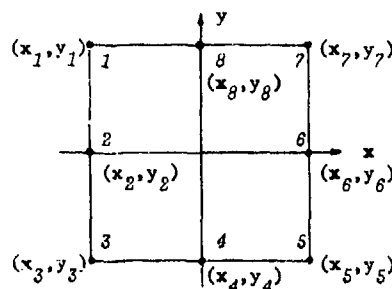


Fig. A.1 An Eight-node Square Element.

The coordinates of each node and nodal numbers are shown also in Fig. A.1. If we want to interpolate a function $\phi(x,y)$ in this element and if the function $\phi(x,y)$ is known at the eight nodes, we can assume that the function $\phi(x,y)$ can be expressed as

$$\phi(x,y) = C_1 + C_2x + C_3y + C_4x^2 + C_5y^2 + C_6xy + C_7x^2y + C_8xy^2 \quad (A.1)$$

where C_i ($i=1, \dots, 8$) are the coefficients to be determined. These eight coefficients can be determined if we use the eight conditions:

$$\phi(x,y) \Big|_{\substack{x=x_i \\ y=y_i}} = \phi_i \quad (i=1,8) \quad (A.2)$$

where (x_i, y_i) is the coordinate of the i -th node. From (A.1) and (A.2) we obtain:

$$\phi(x,y) = \sum_{i=1}^8 \phi_i N_i(x,y), \quad (A.3)$$

where

$$N_1(x,y) = \frac{1}{4} \{ (1-x)(1+y) - (1-x^2)(1+y) - (1-x)(1-y^2) \}$$

$$N_2(x,y) = \frac{1}{2} (1-x)(1-y^2)$$

$$N_3(x,y) = \frac{1}{4} \{ (1-x)(1-y) - (1-x^2)(1-y) - (1-x)(1-y^2) \}$$

$$N_4(x,y) = \frac{1}{2} (1-x^2)(1-y)$$

$$N_5(x,y) = \frac{1}{4} \{ (1+x)(1-y) - (1-x^2)(1-y) - (1+x)(1-y^2) \}$$

$$N_6(x,y) = \frac{1}{2} (1+x)(1-y^2)$$

$$N_7(x,y) = \frac{1}{4} \{ (1+x)(1+y) - (1-x^2)(1+y) - (1+x)(1-y^2) \}$$

$$N_8(x,y) = \frac{1}{2} (1-x^2)(1+y)$$

APPENDIX B

The Potential and Normal Derivative Integrals of a Triangular Patch Element

We would like to evaluate the potential integral I , and the normal-derivative integral J over a triangular patch (see Fig. B.1) as defined below:

$$\begin{pmatrix} I \\ J \end{pmatrix} = \iint_S \phi(\xi, \eta) \begin{pmatrix} 1/r \\ \frac{\partial}{\partial n} \frac{1}{r} \end{pmatrix} dS, \quad (B.1)$$

$$r = [(x-\xi)^2 + (y-\eta)^2 + (z-\zeta)^2]^{1/2}; \quad \frac{\partial}{\partial n} = \frac{\partial}{\partial \zeta}$$

where (x,y,z) are coordinates of an observation point in the coordinate sys-

tem of the element, (ξ, η) are variables of integration, and S , the surface element, is in the plane $\zeta=0$. We assume that $\phi(\xi, \eta)$ is a linear function of (ξ, η) :

$$\phi(\xi, \eta) = \alpha + \beta\xi + \gamma\eta. \quad (B.2)$$

The J -integral has been successfully performed by Webster (1974) and only the results will be reproduced here. We will, however, evaluate the I -integral here following essentially the same notation and analysis.

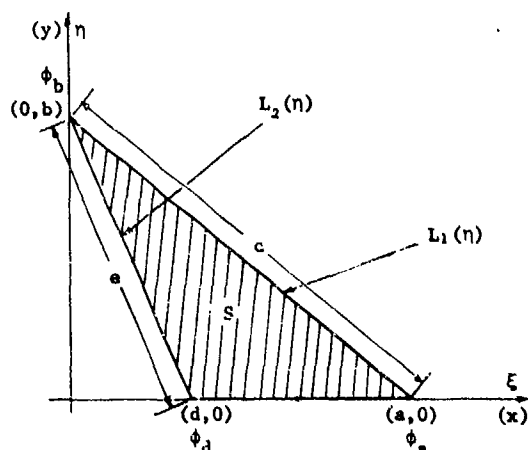


Fig. B.1 A Triangular Patch Element.

In Eqn. (B.2)

$$\alpha = (d\phi_a - a\phi_d) / (d-a),$$

$$\beta = (\phi_d - \phi_a) / (d-a),$$

$$\gamma = [\phi_b(d-a) - d\phi_a + a\phi_d] / [b(d-a)],$$

where ϕ_a , ϕ_b , and ϕ_d are potentials at points A, B, and D, respectively. The distribution functions ϕ discussed in Eqn. (4.12) are simply the coefficients of ϕ_a , ϕ_d and ϕ_b when (α, β, γ) are substituted into (B.2). If we regard $\phi(\xi, \eta)$ as the density of a distribution, I and J are respectively the potential and the negative of the normal velocity induced by a simple layer of density $\phi(\xi, \eta)$ varying linearly over a triangular patch. We want to express both I and J as a linear combination of ϕ_a , ϕ_d , and ϕ_b ; the coefficients in front of them correspond to the P_i and Q_i , $i=1,2,3$, defined in Eqns. (4.15) and (4.16) (of course, without the image elements!).

Exact Solution

Consider the potential integral, $I(\phi_a, \phi_d, \phi_b)$, we write:

$$I = \int_0^b d\eta \int_{L_2(\eta)}^{L_1(\eta)} \frac{(\alpha + \beta\xi + \gamma\eta) d\xi}{[(x-\xi)^2 + (y-\eta)^2 + z^2]^{1/2}}$$

$$= (\alpha + \beta x + \gamma y) I_1 + \beta I_2 + \gamma I_3, \quad (B.3)$$

where

$$I_1 = \iint_S \frac{1}{r}, \quad I_2 = \iint_S \frac{-(x-\xi)}{r} ds,$$

$$I_3 = \iint_S \frac{-(y-\eta)}{r} ds.$$

We introduce the following notations, which will facilitate evaluating these integrals:

$$\begin{aligned} r_a &= \sqrt{(x-a)^2 + y^2 + z^2}, \\ r_b &= \sqrt{x^2 + (y-b)^2 + z^2}, \\ r_d &= \sqrt{(x-d)^2 + y^2 + z^2}, \end{aligned} \quad (B.4)$$

and

$$\begin{aligned} \rho &= bx + ay - ab, & \bar{\rho} &= bx + dy - db, \\ \rho_a &= ax - by - a^2, & \bar{\rho}_d &= dx - by - d^2, \\ \rho_b &= ax - by + b^2, & \bar{\rho}_b &= dx - by + b^2. \end{aligned}$$

The integral I_1 can be integrated analytically, and after a substantial amount of algebraic manipulations, one may obtain the following result:

$$\begin{aligned} I_1 &= y \cdot \log \left[\frac{r_a - (x-a)}{r_d - (x-d)} \right] + \frac{\rho}{c} \log \left[\frac{cr_a + \rho_a}{cr_b + \rho_b} \right] \\ &\quad - \frac{\rho}{e} \log \left[\frac{er_d + \bar{\rho}_d}{er_b + \bar{\rho}_b} \right] + z\hat{T} \end{aligned} \quad (B.5)$$

where

$$\begin{aligned} \hat{T} &= -\tan^{-1} \left[\frac{ar_b^2 - x\rho_b}{zbr_b} \right] + \tan^{-1} \left[\frac{ar_a^2 - (x-a)\rho_a}{zbr_a} \right] \\ &\quad + \tan^{-1} \left[\frac{dr_b^2 - x\bar{\rho}_b}{zbr_b} \right] - \tan^{-1} \left[\frac{dr_d^2 - (x-d)\bar{\rho}_d}{zbr_d} \right]. \end{aligned}$$

Efforts required for the evaluation of I_2 and I_3 are less strenuous. The results are:

$$\begin{aligned} I_2 &= \frac{b}{2c} \cdot \left[\frac{\rho_b r_b - \rho_a r_a}{c} + \left(z^2 + \frac{\rho^2}{c^2} \right) \right. \\ &\quad \times \log \left[\frac{cr_b + \rho_b}{cr_a + \rho_a} \right] \Bigg] \\ &\quad - \frac{b}{2c} \cdot \left[\frac{\bar{\rho}_b r_b - \bar{\rho}_d r_d}{e} + \left(z^2 + \frac{\bar{\rho}^2}{e^2} \right) \right. \\ &\quad \times \log \left[\frac{er_b + \bar{\rho}_b}{er_d + \bar{\rho}_d} \right] \Bigg] \end{aligned} \quad (B.6)$$

and

$$I_3 = \frac{a}{2c} \cdot \left[\frac{\rho_b r_b - \rho_a r_a}{c} + \left(z^2 + \frac{\rho^2}{c^2} \right) \right]$$

$$\begin{aligned} &\times \log \left[\frac{cr_a - \rho_a}{cr_b - \rho_b} \right] \\ &\quad - \frac{d}{2e} \cdot \left[\frac{\bar{\rho}_b r_b - \bar{\rho}_d r_d}{e} + \left(z^2 + \frac{\bar{\rho}^2}{e^2} \right) \right. \\ &\quad \times \log \left[\frac{er_d - \rho_d}{er_b - \rho_b} \right] \Bigg] \\ &\quad - \frac{1}{2} \cdot \left[r_d(x-d) - r_a(x-a) + (y^2 + z^2) \right. \\ &\quad \times \log \left[\frac{r_a - (x-a)}{r_d - (x-d)} \right] \Bigg]. \end{aligned} \quad (B.7)$$

Next, we abbreviate the logarithmic terms as follows:

$$\begin{aligned} I_{ad}^{\pm} &= \log [r_a \pm (x-a)] / [r_d \pm (x-d)], \\ I_{ab}^{\pm} &= \log [(cr_a \pm \rho_a) / (cr_b \pm \rho_b)], \\ I_{db}^{\pm} &= \log [(er_b \pm \bar{\rho}_d) / (er_b \pm \bar{\rho}_b)]. \end{aligned} \quad (B.8)$$

and define:

$$\begin{aligned} R_{ad} &= r_a(x-a) - r_d(x-d), \\ F_{ab} &= \rho_b r_b - \rho_a r_a, \\ F_{db} &= \bar{\rho}_b r_b - \bar{\rho}_d r_d. \end{aligned} \quad (B.9)$$

The expressions for I_1 , I_2 , and I_3 are now substituted into (B.3). After using the definitions of α , β , and γ and grouping terms according to ϕ_a , ϕ_d , and ϕ_b , we obtain the following final expression for the integral I :

$$\begin{aligned} I(\phi_a, \phi_d, \phi_b) &= \\ &\frac{\phi_a}{2b(a-d)} \left\{ 2\bar{\rho}z\hat{T} + dR_{ad} + (b^2+ad)F_{ab}/c^2 \right. \\ &\quad - F_{db} + [2\rho\bar{\rho} - (b^2+ad)(z^2 + \frac{\rho^2}{c^2})]I_{ab}^+/c \\ &\quad \left. + e(z^2 - \frac{\bar{\rho}^2}{e^2})I_{db}^+ + [2y\rho - d(y^2+z^2)]I_{ad}^+ \right\} \\ &+ \frac{\phi_d}{2b(a-d)} \left\{ -2\rho z\hat{T} - aR_{ad} + (b^2+ad)F_{db}/e^2 \right. \\ &\quad - F_{ab} + [2\rho\bar{\rho} - (b^2+ad)(z^2 + \frac{\bar{\rho}^2}{e^2})]I_{db}^+/e \\ &\quad \left. + c(z^2 - \frac{\rho^2}{c^2})I_{ab}^+ - [2y\rho - a(y^2+z^2)]I_{ad}^+ \right\} \\ &+ \frac{\phi_b}{2b} \left\{ 2yz\hat{T} + aR_{ad} + aF_{ab}/c^2 - dF_{db}/e^2 \right. \\ &\quad + [2y\rho - a(z^2 + \frac{\rho^2}{c^2})]I_{ab}^+/c + (y^2 - z^2)I_{ad}^+ \\ &\quad \left. - [2y\bar{\rho} - d(z^2 + \frac{\bar{\rho}^2}{e^2})]I_{db}^+/e \right\}. \end{aligned} \quad (B.10)$$

In writing down (B.10), we have used the

identities $I_{db}^+ = -I_{db}^-$ and $I_{ab}^+ = -I_{ab}^-$. The expressions in the curly brackets are the quantities P_1 , P_2 , and P_3 defined in Eqn. (4.15). Note that the contribution due to the arc tangent term, \hat{T} , vanishes when the observation point is in the same plane as the patch.

For the normal-derivative integral, J , the corresponding expression is:

$$J(\phi_a, \phi_d, \phi_b) = \frac{-\phi_a}{b(a-d)} \left[\hat{\rho}\hat{T} - (ad+ab^2)zI_{ab} + ezI_{db} - dzI_{ad} \right] + \frac{\phi_d}{b(a-d)} \left[\hat{\rho}\hat{T} - (ad+ab^2)zI_{bd} - czI_{ab} - azI_{ad} \right] + \frac{\phi_b}{b} \left[-y\hat{T} + \frac{az}{c}I_{ab} - \frac{dz}{e}I_{db} + zI_{ad} \right]. \quad (B.11)$$

Here, omission of the sign superscript in I_{ab} , I_{db} , or I_{ad} implies the "plus" case. The log terms in this expression vanish when $z=0$; what is left then is just the \hat{T} term, which contributes the well-known $\pm 2\pi$ factor*, depending on whether $z=0^+$ or 0^- inside the patch. To see this point, we recall the following facts:

$$\begin{aligned} ar_b^2 - x\rho_b &= (y-b)[a(y-b)+bx] + az^2, \\ ar_a^2 - (x-a)\rho_a &= y[a(y-b)+bx] + az^2, \\ dr_b^2 - x\rho_b &= (y-b)[d(y-b)+bx] + dz^2, \\ dr_d^2 - (x-d)\rho_d &= y[d(y-b)+bx] + dz^2, \end{aligned} \quad (B.12)$$

where one can easily recognize that $[a(y-b)+bx] < 0$ corresponds to a region below a line joining points A and B, $[d(y-b)+bx] > 0$ corresponds to a region above a line joining D and B. As z approaches zero, the denominator of the arc tangent terms in Eqn. (B.5) vanishes, each providing a value of $\pi/2$ but with different signs, depending on which region (x,y) is in. Full cancellation occurs unless the three inequalities $0 < y < b$, $[a(y-b)+bx] < 0$ and $[d(y-b)+bx] > 0$ are satisfied, i.e., when (x,y) lies inside the patch, in which case, the four terms combine to give a value of $-\text{sgn}(z) \cdot 2\pi$ for \hat{T} .

We also want to remark that the log terms are numerically unstable if the observation point (x,y,z) lies on the "inappropriate" side of the extension of the edges of the element. To illustrate this point, take I_{ad} for example; if $x > a > d$, and y, z are both very small, the argument of the log function becomes

$$\frac{r_a - (x-a)}{r_d - (x-d)} = \frac{|x-a| - (x-a)}{|x-d| - (x-d)},$$

where an "=" sign, instead of an ">"

*See, for example, Kellogg (1929), p. 167.

sign is used because the value of (y^2+z^2) is simply 'lost' when added to a large value of $(x-a)$. The difficulty may be resolved if we replace I_{ad} with $(-I_{ad})$. On the other hand, this does not solve the problem completely, if $d < x < a$ when (y,z) are both small. It was found that replacing the top and bottom terms separately by

$$\begin{aligned} r_a - (x-a) &\approx \frac{1}{2}(y^2+z^2)/|x-a|, \\ r_d - (x-d) &\approx \frac{1}{2}(y^2+z^2)/|x-d|, \end{aligned} \quad (B.13)$$

whenever each by itself is small, is a more versatile solution. Similar observations apply to I_{db} and I_{ab} also.

Discrete-sources Approximation

For a large distance from the patch, it will be more economical to represent the potential integral, I , and normal-derivative integral, J , by discrete sources. This can be done by expanding the function $1/r$ in a Taylor series about (ξ, η) . Some fairly straight-forward calculations then yield:

$$I = \frac{\bar{A}}{3} \left[\phi_a \frac{1}{r_{o1}} + \phi_d \frac{1}{r_{o2}} + \phi_b \frac{1}{r_{o3}} \right] \quad (B.14)$$

with

$$r_{oi} = [(x-\xi_i)^2 + (y-\eta_i)^2 + (z-\zeta_i)^2]^{1/2},$$

where (ξ_i, η_i, ζ_i) are the coordinates of the centroid of the i -th right pyramid projected on the plane of the patch. The i -th pyramid has an apex of unit height located at the i -th vertex. The expression corresponding to J is:

$$J = \frac{\bar{A}}{3} \left\{ \left[\frac{n_x(x-\xi_1) + n_y(y-\eta_1) + n_z(z-\zeta_1)}{r_{o1}^3} \right] \phi_a + \left[\frac{n_x(x-\xi_2) + n_y(y-\eta_2) + n_z(z-\zeta_2)}{r_{o2}^3} \right] \phi_d + \left[\frac{n_x(x-\xi_3) + n_y(y-\eta_3) + n_z(z-\zeta_3)}{r_{o3}^3} \right] \phi_b \right\} \quad (B.15)$$

where (n_x, n_y, n_z) are components of the outward normal of the triangle. In these expressions, \bar{A} is the area of the triangle.

DISCUSSION

NILS SALVESEN

The authors should be congratulated for their pioneering work. They are the first to apply the finite element method and the fundamental singularity method to free-surface problems where the free surface extends to infinity. They have shown that for the two-dimensional problems of a cylinder oscillating in the free surface, their numerical methods give results which agree well with results obtained by conventional analytical methods. For the infinite-depth case, they have found that their methods are considerably slower than the Green's function method, while it is extremely interesting to note that for the finite-depth case, their computer time seems to be about the same as for the Green's function method.

The great significance of this work is not that they just have developed another method for solving two-dimensional linearized free-surface problems. For such problems, we already have workable computational tools which are well-established. The real importance of their contribution is that they have developed new numerical methods which clearly have the potentials to solve a large class of free-surface problems which we have not been able to solve without conventional analytical methods. They have already demonstrated that their singularity method successfully can predict the added mass and damping for three-dimensional bodies with any general shape and bottom configuration. This is quite an accomplishment considering that we have not been able to solve any three-dimensional body wave problems for general body shaped with the conventional analytical methods.

It seems to me that the most significant application of their methods may be in solving nonlinear body-wave problems. Both methods can easily be used with a perturbation scheme to obtain higher-order solutions and due to their very general formulation, it should take approximately the same computer time to obtain second- and third-order solutions as the linear solution; while using the Green's function approach, it takes up to ten times as much time to compute the second-order solutions as the linearized solutions.

On the other hand, it seems that the extension of their method to the case of creating the complete nonlinear free-surface condition is far from trivial. Therefore, I would very much like to hear the authors' view on the potential use of their methods to nonlinear ship-wave problems in general.

H. KEIL

First I want to congratulate the authors on their success in developing methods for calculating hydrody-

namic forces on two-dimensional as well as three-dimensional bodies in shallow water.

I would like to comment on the results for the two-dimensional case given in the paper. In (1) I extended Grim's multipole expansions to finite water depths and showed that for any prismatic body with Lewis-form section heaving in shallow water the added mass remains finite as frequency tends to zero. As to the circular cylinder the results of the authors are in full agreement with my own. (Fig. 1)

The fact that the added mass remains finite is shown also by Ursell (2).

Asking for a physical interpretation of this result, the cause has to be sought in the fact that at zero frequency the outgoing wave in deep water travels with infinite velocity, while in shallow water wave velocity cannot exceed the limiting critical value.

In the case of the rectangular cylinder there exists a difference of about 8 percent which may be caused by the fact that the equivalent Lewis-form is a bit different from a rectangular section. (Fig. 2).

The results given by Yu-Ursell and C.H. Kim are not quite correct due to an error in the numerical evaluation of the integral $G_1(v)$ in the papers cited.

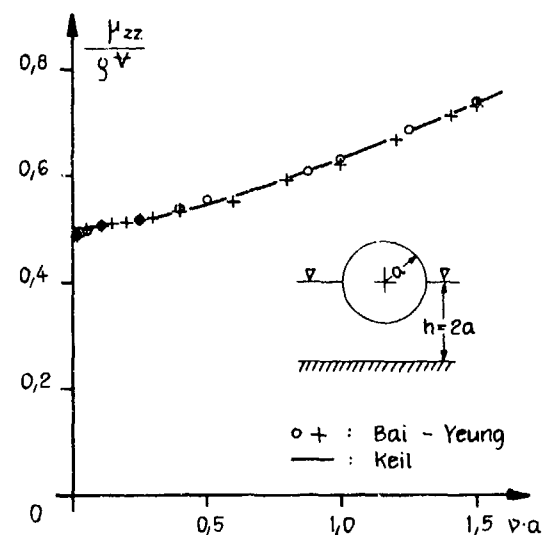


Fig 1

(1) Keil, H.: Die hydrodynamischen Kräfte bei der periodischen Bewegung zweidimensionaler Körper an der Oberfläche flacher Gewässer. Institut für Schiffbau Hamburg Rep. 305, Febr. 1974.

(2) Ursell, F.: Note on the Virtual Mass and Damping Coefficients in Water of Finite Depth. University Manchester, Dept. Mathematics, May 1974.

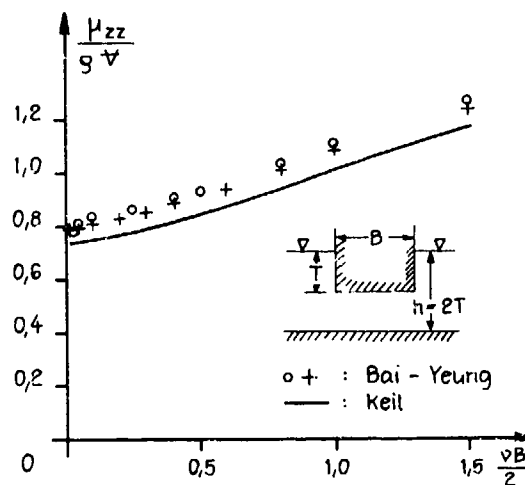


Fig. 2

Y.K. CHUNG, H. BOMZE and M. COLEMAN

Considering that the Frank's program (Ref. 1) for deep water is simple to use and requires little computer time, the authors have recently extended Frank's program to shallow water. The extension has been accomplished by replacing the deep water Green's function in Frank's formulation by the shallow water function. Results of the shallow

water integral equation method are compared with other methods (Ref. 2, 3) on Figures 1, 2, 3 and 4. In general, the program has a tendency to give slightly higher values than others. This is also indicated in the Table for a bulbous bow case as given by Yeung.

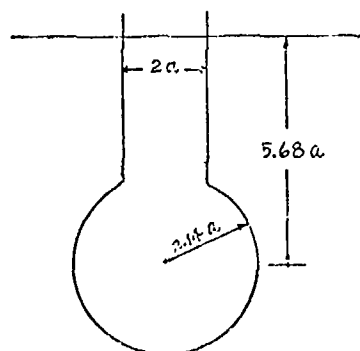
Figure 3 was supplied to the authors by C.H. Kim.

Table
Added-Mass and Damping Coefficients
for a Bulbous Section in Heave, by
Three Methods

K	$\bar{\mu}_{22}$			$\bar{\lambda}_{22}$		
	B(13)	Y(21)	L(28)	B(13)	Y(21)	L(28)
.01	.4349	.461	.474	.1172	.138	.147
.02	.4153	.422	.432	.0973	.101	.107
.03	.4045	.408	.417	.0716	.073	.077
.05	.4003	.405	.414	.0347	.035	.038
.07	.4090	.413	.422	.0140	.014	.016
.10	.4242	.428	.438	.0002	.002	.002
.15	.4396	.442	.454	.0017	.001	.001
.20	.4433	.446	.459	.0063	.005	.006
.30	.4403	.444	.457	.0091	.008	.009

Notes

- 1) B, Y, L represent finite-element method, present method, and Frank's method, respectively.
- 2) Parenthetical numbers indicate the number of points used to represent the body. Quadratic element was used in finite-element method; the others, constant potentials assumed within each segment.



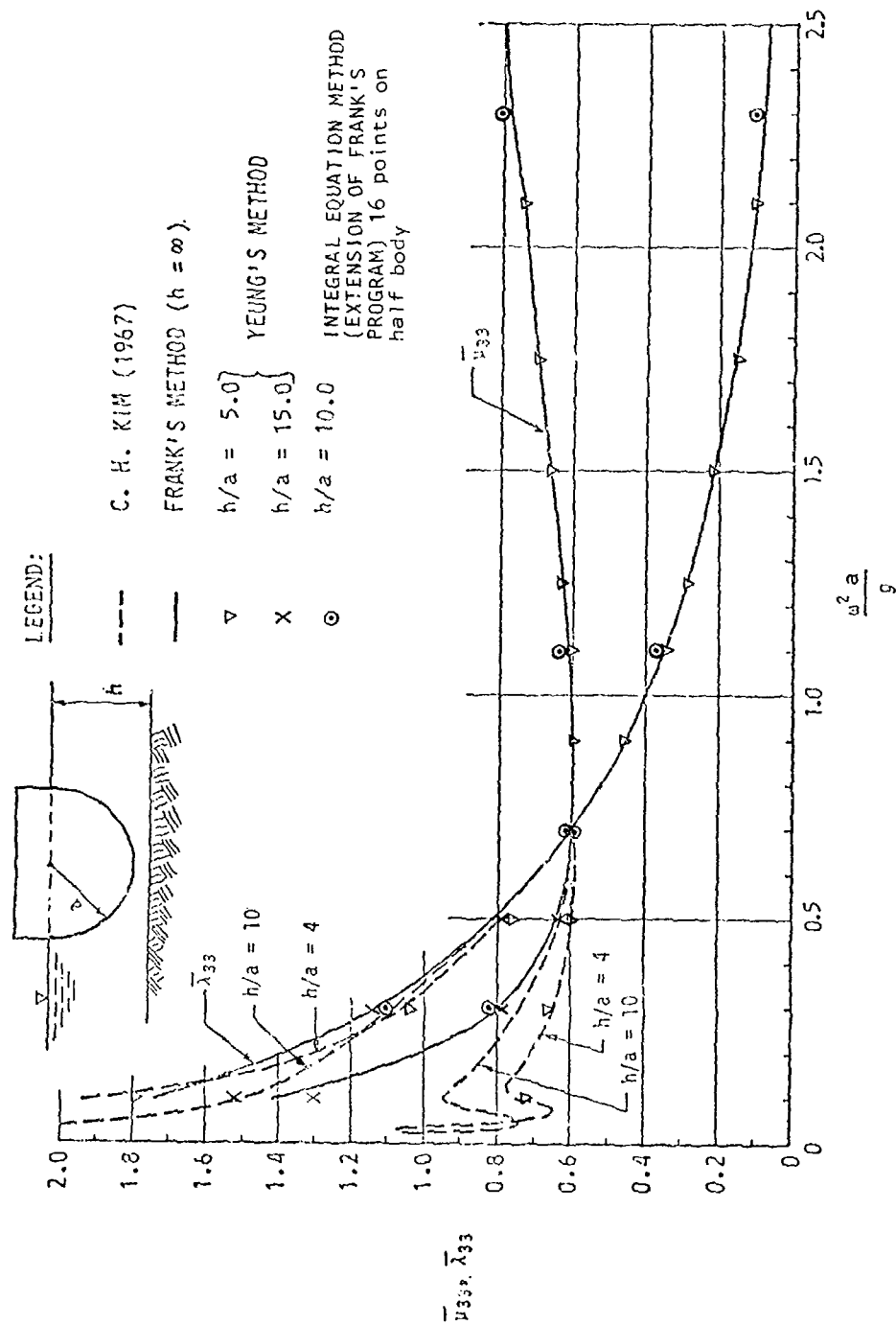
$$K = \frac{\sigma^2}{g} a$$

$$V = 20.23 a^2$$

$$\bar{\mu}_{22} = \mu_{22} / \rho V$$

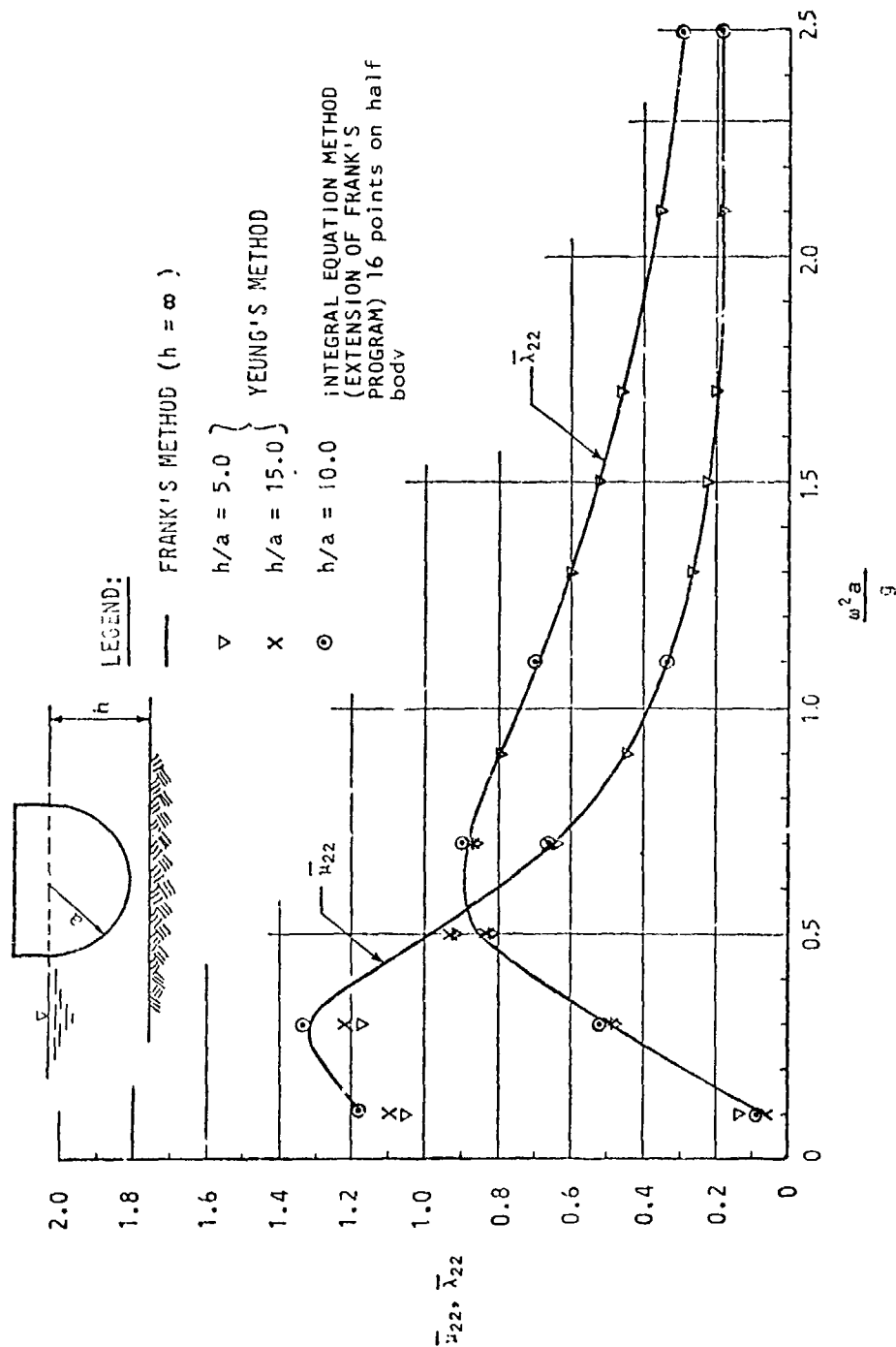
$$\bar{\lambda}_{22} = \lambda_{22} / \rho \sigma V$$

From: A Singularity-Distribution Method for Free-Surface Flow Problems with an Oscillating Body by Ronald W. C. Yeung September 1973.



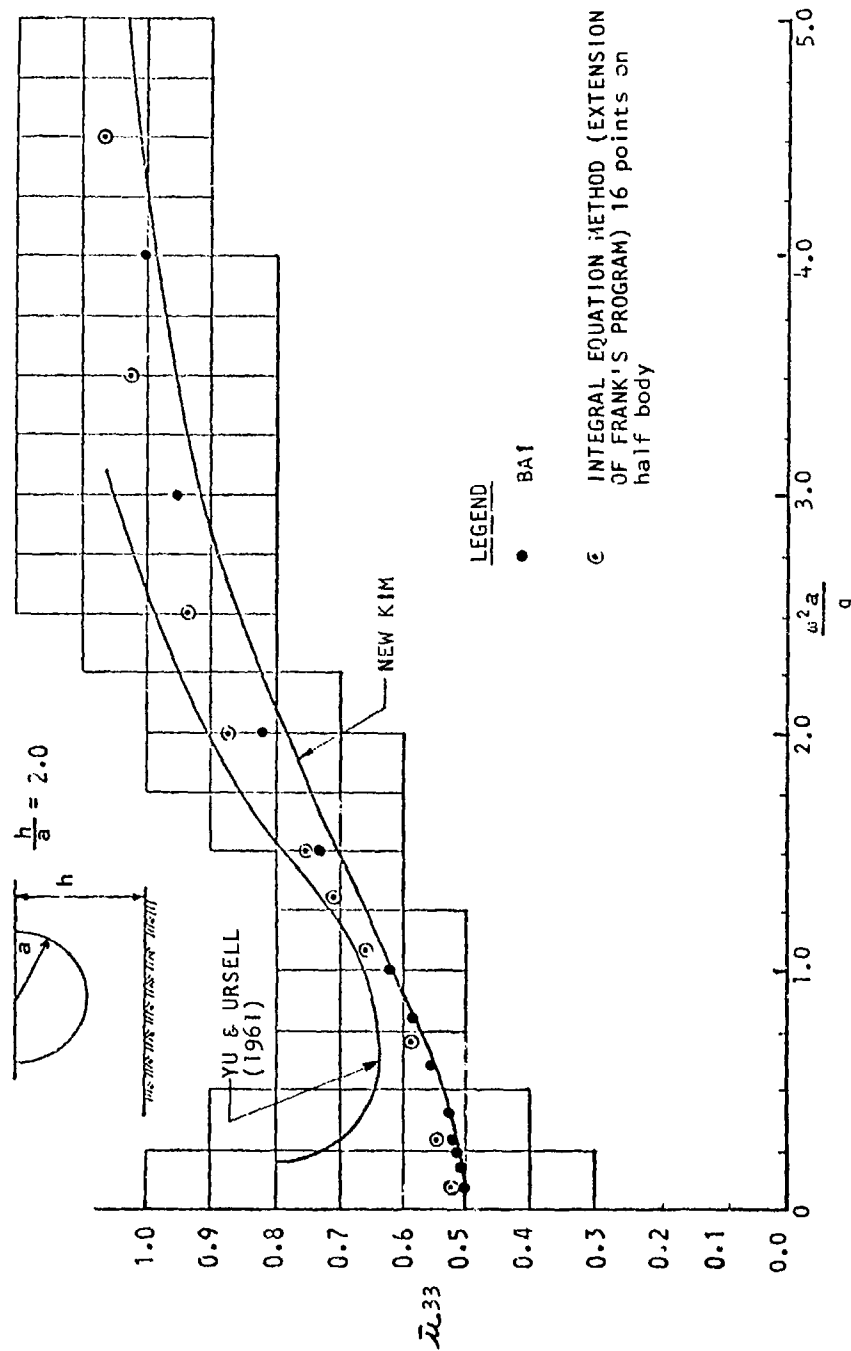
ADDED MASS AND DAMPING COEFFICIENTS FOR SEMI-CIRCLE IN HEAVE

FIGURE 1



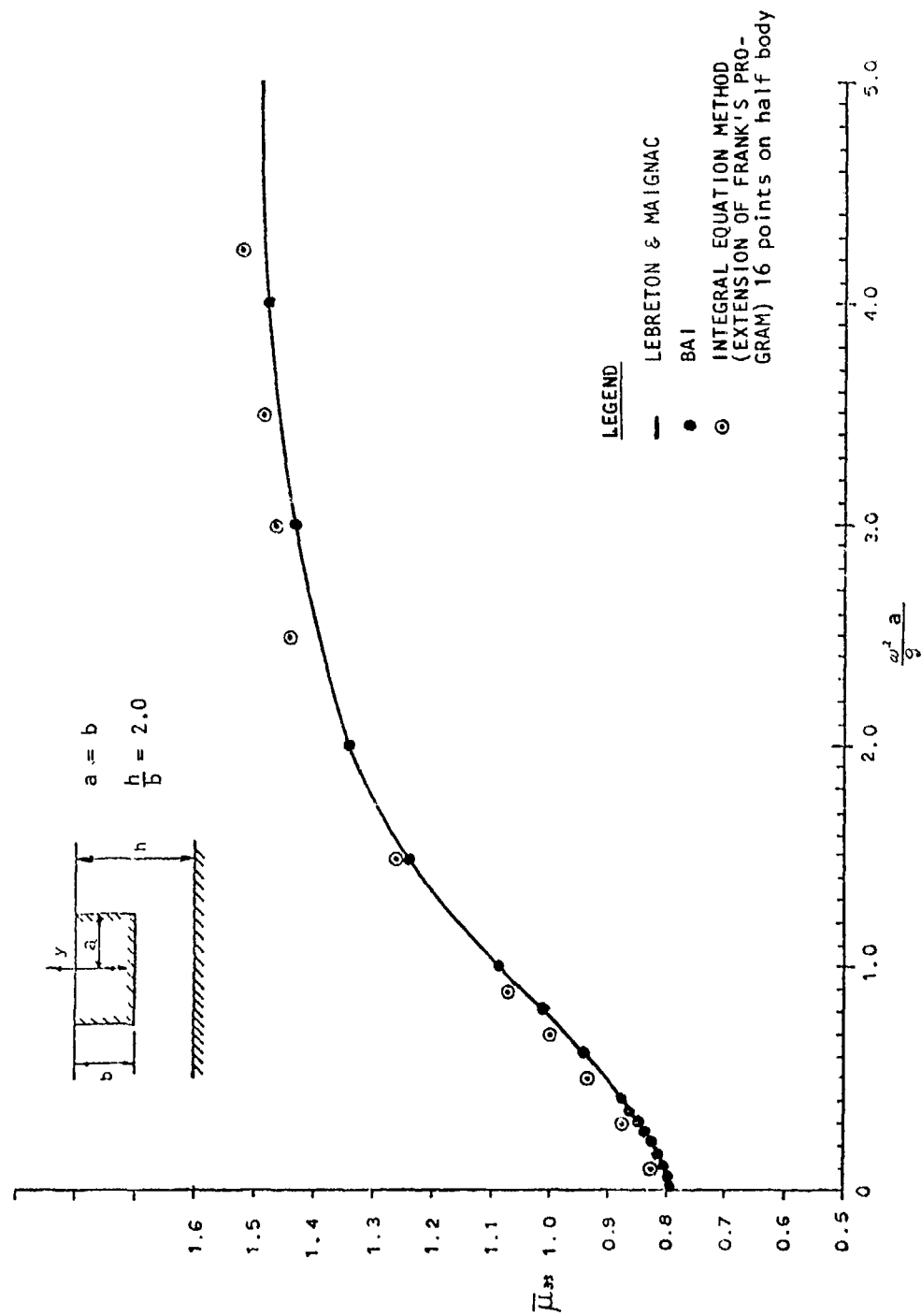
ADDED MASS AND DAMPING COEFFICIENTS FOR SEMI-CIRCLE IN SWAY

FIGURE 2



ADDED MASS COEFFICIENT FOR SEMI-CIRCLE IN HEAVE

FIGURE 3



ADDED MASS COEFFICIENT FOR RECTANGULAR CYLINDER IN HEAVE, non-dimensionalized by mass

FIGURE 4

REFERENCES

1. Frank, W., "Oscillation of Cylinders in or below the Free Surface of Deep Water", Naval Research Center Report No. 2375
2. Kim, Cheung H., "Hydrodynamic Forces and Moments for Heaving, Swaying and Rolling Cylinder on Water of Finite Depth", Journal of Ship Research, June 1969.
3. Yeung, Ronald W.C., "A Singularity-Distribution Method for Free-Surface Flow Problems with an Oscillating Body", Ph.D Dissertation, University of California, Berkeley, California, September 1973.

F. URSELL

The computations by Bai and Yeung for the semi-circle disagree with earlier computations which moreover differ among themselves. The disagreement is most striking in the long-wave region (wave-length \gg depth) where they find that the virtual-mass coefficient remains finite as the wave-length tends to infinity, whereas it becomes infinite in the computations of Yu and Ursell (1961; this paper will hereafter be referred to as Y) and in other later computations. It has been known for some time that the virtual-mass coefficients given in Y contain errors; thus Rhodes-Robinson found in his analytical treatment of the short-wave limit that at high frequencies his results were in agreement with unpublished computations by W.R. Porter but not with those in Y.

I have made a theoretical calculation dealing with the question whether the virtual-mass coefficient remains finite or becomes infinite as the wave-length tends to infinity, i.e. as the frequency tends to zero. This can be settled by analytical methods, and it is found that the virtual-mass coefficient does indeed remain finite, whereas for infinite depth it becomes infinite. As in Y, a half-immersed circular cylinder was treated, and the potential was expanded in terms of a complete set of harmonic functions. (In the case of infinite depth this becomes the well-known expansion in terms of a wave source and wave-free potentials.) The behaviour of these harmonic functions was investigated in the limit as the frequency tends to 0. It was found that one of these tends to infinity while the others tend to finite limits. (The coefficients in the expansion also tend to finite limits.) The most important step in the investigation was the determination of the finite limits where they exist. The principal result was as follows: Let 2 denote the amplitude of oscillation, a the radius of the cylinder, and σ the angular frequency, and let $\langle \phi(a \sin \theta, a \cos \theta) \rangle$ denote the value of the potential on the circle. It is found that for both finite and infinite depth the quotient $\langle \phi \rangle / 2\sigma a$ becomes infinite as the wave-length tends to infinity, but that for finite depth it is ultimately in phase with the velocity of the cylinder, whereas for infinite depth it is ultimately in quadrature. The virtual-mass coefficient for finite depth tends to a finite limit, whereas for infinite depth it tends to infinity.

The virtual-mass coefficient involves the harmonic function $\hat{B}(x, y)$ which is a solution of the limiting boundary-value problem. This

function satisfies

$$a \frac{\partial \hat{B}}{\partial r} = \cos \theta \quad \text{on the circle,}$$

$$\frac{\partial \hat{B}}{\partial y} = 0 \quad \text{on the bottom,}$$

but it satisfies the limiting boundary condition

$$\frac{\partial \hat{B}}{\partial y} = 0 \quad \text{on the free surface}$$

instead of the usual free-surface condition. We note that if $\hat{B}(x, y)$ is any solution of this problem then $\hat{B}^* + (\text{an arbitrary constant})$ is another solution. The theoretical calculation shows that the particular solution $\hat{B}(x, y)$ which we require is uniquely defined. We may describe $\hat{B}(x, y)$ as being that solution of the limiting boundary value problem which satisfies $\hat{B}(x, y) - |x|/h \rightarrow 0$ as $|x| \rightarrow \infty$. It is found that the virtual-mass coefficient tends to the finite limit

$$\frac{4}{\pi} \int_0^{\frac{1}{2}\pi} (\hat{B}(a \sin \theta, a \cos \theta) - \frac{a}{h}) \cos \theta \, d\theta,$$

where h is the depth of fluid. Note that this expression involves the combination $\hat{B}(x, y) - \frac{a}{h}$. It would be interesting to make a numerical comparison of this result with the computations of Bai and Yeung.

The limiting behaviour of the amplitude ratio can be found fairly easily and agrees with the computations of Bai and Yeung both for the semi-circle and the rectangle. At present all these results should be regarded as provisional, but I trust that analytical calculations of this kind, for both low and high frequencies will provide useful checks on computations.

C. J. GARRISON

The authors have presented two new methods for the solution of harmonic free surface flow problems. Although the methods appear to be considerably more cumbersome in application than the Green's function method using wave-type sources, they have the advantage of being applicable to cases involving irregular bottom topography and, in addition, do not break down at certain "John's frequencies".

The authors compare their three-dimensional results obtained by the localized finite element method with the results of Isshiki and Hwang (1973) for the case of a vertical circular cylinder floating at a draft of one-half

the radius in water of 6.0 radii depth. The writer has also presented calculations (Garrison 1975) using the Green's function method (Garrison 1974) for the added mass and damping coefficients for this configuration. These results are plotted on the author's Fig. 5.10 which is reproduced as Fig. 1 herein. The agreement appears to be reasonable and the approximately 3.0 percent difference is no doubt within the expected accuracy of either the authors' or the writer's method.

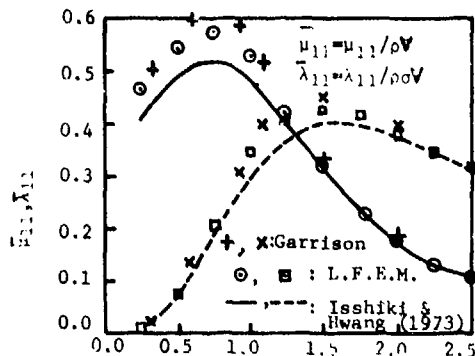


Fig. 1 Sway Added-Mass and Damping Coefficients of a Circular Dock.

The present paper as well as several previous papers have pointed out discrepancies between the results of various authors. In this connection I believe it is important that more consideration be given to the validation of numerical results by comparison with asymptotic, analytical results where they exist and, particularly, to making self-checks and balances. For example, recognizing that the damping coefficient may be calculated by two different methods supplies one such self-check. The obvious method of evaluating this parameter is to carry out an integration of the pressure over the immersed surface, thereby utilizing the near field solution. In view of energy considerations, the damping coefficient may also be expressed in terms of the wave generated at a large distance from the body and compared with that obtained from the pressure distributor. Accordingly, for the two-dimensional case,

$$N_{11} = \left(\frac{A_1}{a} \right)^2 \frac{2ah + \sinh(2ah)}{2 \sinh^2(ah)} \quad (1)$$

where A_1 denotes the dimensionless amplitude at infinity and N_{11} denotes the damping coefficient. In the case of three-dimensional bodies this result becomes

$$N_{11} = \frac{\tanh(ah)}{2} \left[1 + \frac{2ah}{\sinh(2ah)} \right] r \cdot \int_0^{2\pi} \frac{|\phi_j(r, \theta, 0)|^2}{\sigma^2 a^4 x_j^2} d\theta \quad (2)$$

where the integration is to be carried out around a large circle of radius r . In the case of the Green's function method the limit for $r \rightarrow \infty$ may be taken analytically, the equation resulting from which is given by Garrison (1974). In application of Eq. (2) to the present finite element method, r and ϕ_j would be evaluated at the edge of the truncated region.

Similar results commonly known as Haskind's relations which involve wave force coefficients can also be applied as a self-check on numerical results. For the two-dimensional case this takes the form

$$C_1 = \frac{1}{2} \frac{A_1}{a} \frac{\sinh(2ah) + 2ah}{\sinh(ah) \cosh(ah)} \quad (3)$$

where C_1 denotes the i -th component of the wave force (or moment) coefficient associated with wave action on the fixed cylinder and A_1 denotes the dimensionless wave amplitude at a large distance from the cylinder caused by the i -th component oscillation of the cylinder in otherwise still water. The three-dimensional counterpart of Eq. (3) is given by

$$C_1 = \frac{(2\pi a)^{1/2}}{\cosh^2 ah} \left[\frac{\sinh(2ah)}{2a} + h \right] \sqrt{r} \cdot \frac{1}{\sigma \pi^2 x_j^2} |\phi_j(r, \pi, 0)| \quad (4)$$

where $\phi_j(r, \pi, 0)$ denotes the velocity potential evaluated at $\theta = \pi$ at some large value of r . The subscript $j = 1, 2$ and 6 denote the surge, heave, and pitch modes of oscillation, respectively. In addition, the derivation of Eq. (4) requires midplane symmetry of the body. In the case of the Green's function method, Garrison (1974) gives the appropriate form of Eq. (4) involving a surface integration of the source strength since the limit for $r \rightarrow \infty$ is taken analytically.

The wave force coefficients given by Eqs. (3-4) depend on the solution to the radiation problem. They may also be obtained by a straightforward integration of the pressure obtained from a solution of the diffraction problem and a comparison of the results makes a good indicator of the validity of the solutions.

Clearly, this is a necessary condition for a valid solution even though it cannot be shown to be mathematically sufficient. In practice the writer has found this method of checking the validity of the results to be very useful.

References

Garrison, C.J., "Hydrodynamics of Large Objects in the Sea, Part I-Hydrodynamic Analysis", *Journal of Hydronautics*, Vol. 8, No. 1, Jan. 1974, pp 5-12.

Garrison, C.J., "Hydrodynamics of Large Objects in the Sea, Part II-Motion of Free-Floating Bodies", 1975 (to be published)

Nomenclature

\bar{a} = characteristic body dimension
 A_1 = amp. of wave at infinity/ $X_1^0 \bar{a}$
 a = $2\pi\bar{a}/L$
 C_1 = max. wave force (or moment)/ $\rho g \bar{a}^3$ (or $\rho g \bar{a}^4$)
 g = acceleration of gravity
 h = water depth/ \bar{a}
 \bar{L} = wave length
 N_{ii} = damping coef. (linear damping/ $\rho g \bar{a}^3$), (angular damping/ $\rho g \bar{a}^5$)
 r = radius/ \bar{a}
 T = period
 X_1^0 = amp. of body motion (linear disp./ \bar{a}), (angular disp., rad.)
 ρ = density
 σ = $2\pi/T$
 ϕ = velocity potential

D.C. TOLEFSON

This discussion concerns the eigenfunction expansion (3.36) associated with the "outer" region R_2 in Fig. 3.2. Noticing that each term of the expansion with the exception of the first is oscillatory with respect to the vertical coordinate y , it is apparent that the number of terms retained in the expansion should bear some relationship to the grading or fineness of the element spacing along the J boundary. Perhaps a reasonable estimate of this relationship can be made if one applies the rule-of-thumb that a minimum of ten elements of the isoparametric type (with three nodes along an edge) is generally required per wavelength on the free-surface.

The authors' example of a circular cylinder heaving on the free-surface offers the opportunity to make some rough calculations in this regard. First, the data from section 5.1 of the paper, namely $h/\bar{a} = 5.0$ and $K = \sigma^2 \bar{a}/g = 1.0$ yields the following values of m_1 (see 3.38) if a , the radius of the cylinder, is taken to be unity:

$$m_1 = .388, m_2 = 1.11, m_3 = 1.78, \text{ etc.}$$

From these values ψ_1 , ψ_2 , and ψ_3 are determined to have "wavelengths" of 16.2, 5.66, and 3.53 units, etc. while the depth, corresponding to unit radius of the cylinder, is five units. Thus, corresponding to each of these "wavelengths" one would expect, if the rule-of-thumb has any merit, that the number of elements (of the type mentioned previously) along the J boundary should be approximately three, nine, fourteen, etc. As best as can be ascertained from information in the paper (Fig. 3.3 and Table 2) about six elements were actually used, which would imply that inclusion of any eigenfunctions beyond, say, ψ_2 , in (3.36) would be redundant. The writer would be interested in the authors' comments on this point and also what the authors might recom-

mend with regard to an alternate choice for the trial functions ϕ_2 in R_2 .

E.O. TUCK

My discussion centers upon the authors' Table 1, which indicates some aspects of the comparison between various methods on a basis of their cost, or computer time taken. In the first place I should like to commend the authors for their attempt to provide this very difficult type of comparison. Economy in computing is not always taken seriously enough. As relative computing costs decrease, an argument sometimes heard is that efficiency is less important than ease of programming. However, the kind of program being discussed here is seldom an end in itself, and is often used over and over as a sub-unit in a major program such as a strip-theory program for ship motions.

Efficiency comparisons such as this are notoriously hard to make. To what extent can one divorce a method, from a particular programmer's realization of it? Also, usually time increases as accuracy improves, so that one must be very careful to compare only programs which do achieve the same accuracy. But then how does one measure accuracy?

It seems to me a fascinating paradox that it is precisely in this particular area of use of the computer, where the efficiency and power of the machine are being stretched to its limits, that maximum demands are also being made upon the intuition of the human programmer. In all of the methods used or discussed by the authors the programmer must make largely-subjective pre-computation decisions (e.g. choice of his finite element mesh, or of an appropriate accuracy of evaluation of Green's function integrals) which vitally affect the efficiency of the computation, as measured by accuracy/second of C.P.U. time.

This is however an area where the principle of maximum ease of programming and of data preparation is worth some weight, as against efficiency. To a certain extent the "best" method will always be that which appeals most to the person programming it, and hence that which gives him the greatest chance of writing a successful program, irrespective of efficiency. There is no less efficient program than one which doesn't work at all.

To a limited extent I believe that computation obeys the principle of the cussedness of nature, i.e. that you can't win. This means that, all else being equal (which it never is), all rational numerical methods should be as good as each other. As an example, inversion of dense $N \times N$ matrices (as result from boundary methods) takes times like N^3 , whereas much more efficient procedures are available for sparse matrices (as result from finite element methods). A problem which requires N boundary elements will probably require N^2 interior nodes to achieve the same accuracy, and hence the sparse matrix will be $N^2 \times N^2$. Thus the times taken can easily end up comparable, e.g. in the present example if the sparse matrix routine takes times like $N^{3/2}$.

Another mystic principle of computing is that of spreading the required computing effort uniformly throughout a computation. For the reason I personally favor the "Green's function-integral-equation" method, in which the most complicated Green's function which can reasonably be calculated is used. The use of such a Green's function, e.g.

the Havelock source potential in water-wave problems, removes certain boundaries (e.g. the free surface) from the domain of unknowns in the integral equation, and hence enables us to work with a matrix of smaller order N . There is thus a trade-off between the greater labor of evaluating the integrals in the Green's function, and the lesser effort required to invert a smaller matrix. It seems to me that every problem has an intrinsic amount of difficulty and that it is an illusion to think that use of a simpler Green's function removes this difficulty - it simply shifts it elsewhere. I should guess that any computing problem involving inversion of a dense matrix is optimized by making the

time taken to invert the matrix about equal to that required to evaluate its elements.

The above remarks reflect a certain personal philosophy of computing, at least for problems of the nature of those treated in this paper. I consider that in some ways the results of the present paper support this philosophy, e.g. in indicating that the Green's-function-integral-equation method is apparently best, at the present time, even if only by a small margin. I commend the authors for a very interesting contribution.

AUTHOR'S REPLY

First of all, we would like to thank all the discussers for their comments on our paper.

Dr. Salvesen's observation that both methods can be easily extended to solve second-order problems is quite correct. If a perturbation scheme is used, only minor modifications in our formulation are necessary. However, if the exact free-surface condition is directly employed, for the finite element method for example, a system of nonlinear algebraic equations will result since the position of the free surface is not known initially. Conceptually, these equations may be solved by some iterative scheme, although the process may be quite time-consuming. We welcome this question and believe it is an interesting problem for investigation.

We thank Dr. Keil and Dr. Chung (et. al) for presenting results of their recent computations for the added-mass and damping coefficients of a cylinder in water of finite depth. It is particularly gratifying to see results of Dr. Keil's Fig. 1 agree well with ours. Discrepancies of results between his and ours in Fig. 2 can rightfully be attributed to the fact that the shape of the equivalent Lewis form is not absolutely rectangular and that, as pointed out by Lebreton & Margnac (1966), the solution of the potential is quite sensitive to the sharpness of the corners. Chung's computations using the Green's function method (Fig. 4) are consistent with ours given in Fig. 5.4. That his results are generally higher in Figs. 1 through 3 is most likely caused by the fact that the number of points taken on the body are fewer than those used by other authors. Hence the comparison quoted in Table A is irrelevant in the present context. We presume that Dr. Chung had used the Green function for water of finite depth as Lebreton & Margnac did in 1966, since a "shallow-water Green function" will involve the additional assumption that the water-depth to wave-length ratio is small. In summary, concerning the low-frequency behavior of the added-mass coefficient of a cylinder in water of finite depth, we find that these recent computations by the discussers confirm our findings presented in §5.1 of this paper.

Professor Ursell's explanation of the limiting behavior of this coefficient from the view point of finding the solution of the limiting boundary value problem is very enlightening and much appreciated.

We concur with Dr. Garrison's comment that for extensive numerical calculations such as ours, consistency checks should be performed. For example, in

the case of a general three-dimensional body oscillating in water with an asymptotic depth h , the damping coefficient λ_{kl} , as shown in Wehausen (1970), is related to the asymptotic wave amplitude by

$$\alpha_k \bar{\alpha}_l \lambda_{kl} = \frac{\rho g^2 R}{2\sigma^3} D \cdot \int_0^{2\pi} Y^{(k)}(R, \theta) \bar{Y}^{(l)}(\theta) d\theta \quad (C.1)$$

where α_k, α_l are the complex amplitude of the k -th and l -th modes of motion, and

$$D(m_0 h) = \tanh(m_0 h) + m_0 h [1 - \tanh^2(m_0 h)] \quad (C.2)$$

It can be seen that $D(m_0 h)$ approaches $2m_0 h$ as $h \rightarrow 0$ and approaches 1 as $h \rightarrow \infty$. For the present methods of solution, the quantities $Y^{(k)}$ and $Y^{(l)}$ were available easily without additional computations, hence provisions have been made in the computer programs to compare and cross check the value of λ_{kl} as obtained by (2.18) vs. that by (C.1). For the case of a cylinder oscillating in water with depths h_R and h_L on the right and left, respectively, the following relation can be shown to be valid [Yeung (1973)]:

$$|\alpha_k|^2 \lambda_{kk} = \frac{\rho g^2}{2\sigma^3} [Y_R^2 D(m_0^R h_R) + Y_L^2 D(m_0^L h_L)] \quad (C.3)$$

Turning now to Dr. Tolefson's question on the fineness of finite element mesh near the boundary J , we would like to add that the potential ϕ , which is a linear combination of the eigenfunctions, is not highly oscillatory although each individual eigenfunction itself is. Therefore, integration of the coupling term along J can be approximated by

$$\begin{aligned} & \int_{S_i} \phi(x, y) \cos m_i(y+h) dy \\ & \approx \int_{S_i} (ay^2 + by + c) \cos m_i(y+h) dy \end{aligned} \quad (C.4)$$

where S_i is the element boundary along J , and the integral on the right can be evaluated analytically. Hence, no refinement in mesh size is necessary even when m_i is large.

Finally, concerning the remark by Dr. Tuck on Table 1, we would like to emphasize that the purpose of this paper is to present new alternatives for solving free-surface flow problems that have complicated boundary-geometry. It should be quite obvious that efficiency of each type of method will depend on the programmer and his motivation. Thus, Table 1 should be regarded only as a qualitative rather than an absolute comparison.

AUTHOR'S REPLY

First of all, we would like to thank all the discussers for their comments on our paper.

Dr. Salvesen's observation that both methods can be easily extended to solve second-order problems is quite correct. If a perturbation scheme is used, only minor modifications in our formulation are necessary. However, if the exact free-surface condition is directly employed, for the finite element method for example, a system of non-linear algebraic equations will result since the position of the free surface is not known initially. Conceptually, these equations may be solved by some iterative scheme, although the process may be quite time-consuming. We welcome this question and believe it is an interesting problem for investigation.

We thank Dr. Keil and Dr. Chung (et. al) for presenting results of their recent computations for the added-mass and damping coefficients of a cylinder in water of finite depth. It is particularly gratifying to see results of Dr. Keil's Fig. 1 agree well with ours. Discrepancies of results between his and ours in Fig. 2 can rightfully be attributed to the fact that the shape of the equivalent Lewis form is not absolutely rectangular and that, as pointed out by Lebreton & Margnac (1966), the solution of the potential is quite sensitive to the sharpness of the corners. Chung's computations using the Green's function method (Fig. 4) are consistent with ours given in Fig. 5.4. That his results are generally higher in Figs. 1 through 3 is most likely caused by the fact that the number of points taken on the body are fewer than those used by other authors. Hence the comparison quoted in Table A is irrelevant in the present context. We presume that Dr. Chung had used the Green function for water of finite depth as Lebreton & Margnac did in 1966, since a "shallow-water Green function" will involve the additional assumption that the water-depth to wave-length ratio is small. In summary, concerning the low-frequency behavior of the added-mass coefficient of a cylinder in water of finite depth, we find that these recent computations by the discussers confirm our findings presented in §5.1 of this paper.

Professor Ursell's explanation of the limiting behavior of this coefficient from the view point of finding the solution of the limiting boundary value problem is very enlightening and much appreciated.

We concur with Dr. Garrison's comment that for extensive numerical calculations such as ours, consistency checks should be performed. For example, in

the case of a general three-dimensional body oscillating in water with an asymptotic depth h , the damping coefficient λ_{kl} , as shown in Wehausen (1970), is related to the asymptotic wave amplitude by

$$\alpha_k \bar{\alpha}_l \lambda_{kl} = \frac{\rho g^2 R}{2\sigma^3} D \cdot \int_0^{2\pi} Y^{(k)}(R, \theta) \bar{Y}^{(l)} d\theta \quad (C.1)$$

where α_k, α_l are the complex amplitude of the k -th and l -th modes of motion, and

$$D(m_0 h) = \tanh(m_0 h) + m_0 h [1 - \tanh^2(m_0 h)] \quad (C.2)$$

It can be seen that $D(m_0 h)$ approaches $2m_0 h$ as $h \rightarrow 0$ and approaches 1 as $h \rightarrow \infty$. For the present methods of solution, the quantities $Y^{(k)}$ and $Y^{(l)}$ were available easily without additional computations, hence provisions have been made in the computer programs to compare and cross check the value of λ_{kl} as obtained by (2.18) vs. that by (C.1). For the case of a cylinder oscillating in water with depths h_R and h_L on the right and left, respectively, the following relation can be shown to be valid [Yeung (1973)]:

$$|\alpha_k|^2 \lambda_{kk} = \frac{\rho g^2}{2\sigma^3} [Y_R^2 D(m_0^R h_R) + Y_L^2 D(m_0^L h_L)] \quad (C.3)$$

Turning now to Dr. Tolefson's question on the fineness of finite element mesh near the boundary, we would like to add that the potential ϕ , which is a linear combination of the eigenfunctions, is not highly oscillatory although each individual eigenfunction itself is. Therefore, integration of the coupling term along J can be approximated by

$$\begin{aligned} & \int_{S_i} \phi(x, y) \cos m_i(y+h) dy \\ & \approx \int_{S_i} (ay^2 + by + c) \cos m_i(y+h) dy \end{aligned} \quad (C.4)$$

where S_i is the element boundary along J , and the integral on the right can be evaluated analytically. Hence, no refinement in mesh size is necessary even when m_i is large.

Finally, concerning the remark by Dr. Tuck on Table 1, we would like to emphasize that the purpose of this paper is to present new alternatives for solving free-surface flow problems that have complicated boundary-geometry. It should be quite obvious that efficiency of each type of method will depend on the programmer and his motivation. Thus, Table 1 should be regarded only as a qualitative rather than an absolute comparison.

As has been stated in our conclusion, the Green-function-integral-equation method, because of its compactness, generally tends to be superior to others, but not in every case. For instance, the Green function method, or other existing methods, for that matter, fails if one is faced with the two-dimensional problem of a cylinder in water with different depths on the left and the right.

We disagree with Dr. Tuck's statement that all else being equal, any rational numerical method should be as good as another. Take, for instance, the example used by Dr. Tuck: the finite-element method with the sparse matrix routine will be comparable to the singularity-distribution method if it takes $N^{3/2}$ steps for solution of the sparse matrix. However, in reality, the sparse matrix will have a bandwidth of approximately N . Furthermore, it is well known that the number of operation steps required for solving a banded matrix is proportional to $N^2 \cdot M$, where M is

the dimension of matrix. Therefore, solution of the "sparse" matrix will require, for this particular example, N^4 steps, in contrast to N^3 steps for a dense matrix of dimension N . This explains why the finite element variational method is considerably slower than the localized finite element method and the fundamental singularity distribution method.

In conclusion, we would like to add that it has been proven worthwhile to investigate into new methods, even though they may at most be of comparable efficiency to existing ones. The reason is that there is no such thing as a super method; some methods may be more versatile than others while some may suffer inherent disadvantages of some kind, and others do not. New approaches for solving problems very often uncover old mistakes which may not be apparent in the absence of any new means of computation or analytical predictions.

NUMERICAL SOLUTIONS OF TWO-DIMENSIONAL NONLINEAR WAVE PROBLEMS

C. H. vonKerczek
NSRDC
Bethesda, Maryland

N. Salvesen
NSRDC
Bethesda, Maryland

ABSTRACT

The nonlinear free-surface effects on the two-dimensional potential flow past a disturbance is examined by a direct numerical procedure and a perturbation technique. The numerical procedure used to solve the complete nonlinear problem is an iterative one in which the Laplace equation is solved by finite differences in a field bounded by an assumed free-surface shape which is systematically corrected until it satisfies the nonlinear free-surface boundary condition. Wave resistances and free-surface profiles are computed using first- and second-order perturbation solutions. These are compared to the results obtained from the direct numerical solution of the nonlinear problem.

1. INTRODUCTION

The main objective of this work is to determine whether the nonlinear body-wave problem can be solved directly by use of numerical methods. Numerical methods have previously been applied to solve the problem of free-running waves and also to the linear waves generated by disturbances; however, there presently exist no numerical solutions to the nonlinear waves generated by a disturbance. This investigation is restricted to two-dimensional problems.

The two-dimensional nonlinear wave problem of the steady flow past a disturbance has previously been solved only approximately. The approximation requires that wave height be small compared to wave length. The problem can then be linearized and solutions readily obtained. Higher-order improvements of the linearized solutions may then be obtained in the context of the method of perturbation series expansions. A fairly complete account of the method as applied to the two-dimensional free-surface problem is given by Salvesen (1969). The basic requirement in this type of procedure is that the body or other obstruction in the flow be a "small disturber" in a certain sense. In problems where the disturber is not small perturbation methods may not suffice. The nonlinearities at the free surface may be severe and other methods may have to be developed to cope with such problems. One possibility for solving nonlinear free-surface problems is direct numerical solution. It is in this area that the present work makes an initial attempt.

There are primarily two approaches to the nonlinear body-wave problem. One is a time-dependent initial-value problem approach and the other is direct solution of the steady-state problem. In the time-dependent problem the steady state is obtained approximately by considering a large interval of time from the initial instant.

The advantage of the time-dependent problem is that the extrapolation of the free-surface shape from one time step to the next is carried out naturally by numerically solving the differential equation that represents the dynamic boundary condition at the free surface. No guesswork or trial and error procedure is required to find the free-surface shape. However, some disadvantages of the time-dependent problem approach are that rapid numerical methods may be prone to numerical instability and lifting cylinders leave behind a trailing vortex sheet during the transient part of the motion. The location of the trailing vortex sheet is not known a priori and thus it constitutes a second free surface which must be found in the course of the solution of the problem.

The main difficulty in the steady-state problem is that the free-surface shape is not known in advance and it must be determined as part of the solution of the problem. Thus most numerical procedures for solving this problem will entail some kind of iteration procedure in which a trial free surface is assumed and then systematically modified until the correct free-surface shape, i.e., the one that satisfies the free-surface boundary condition, is obtained.

In this paper a numerical method is described which solves two-dimensional, steady-state, nonlinear body-wave problem. A procedure for generating the free surface in a systematic way is presented. Each time the free surface is modified in the procedure the linear two-dimensional potential problem in a well defined region must be solved. This step can be carried out by several standard techniques such as source-sink distributions (integral equation methods), finite element methods or finite difference methods. The last of these is used in the present method simply because it is very easy to program and is very reliable.

The numerical method described in this paper, particularly the systematic generation of the free surface, was developed by

Prof. Allan J. Malvick* during the years 1962-1964 while at the University of Notre Dame. Malvick used this method to generate progressive waves on a stream of uniform depth, but did not carry his investigation to completion and did not publish the method or any of his results. Subsequently von Kerczek (1965) modified Malvick's program (but not his method for generating the free surface) and made some preliminary investigations of the flow past a vortex-like disturbance. This investigation was not carried very far, but did indicate that the numerical method held some promise for investigating the nonlinear problem because agreement with linear theory, for small disturbances, was obtained.

In the present paper, we describe our attempt to investigate this numerical method more completely. Our aim is to make systematic comparisons between analytical perturbation theory results of first and second order with Malvick's numerical method. For this two specific cases are chosen. The first is that of the flow past a line vortex and the second is the flow disturbed by a finite-length pressure distribution on the free surface. The degree of nonlinearity in the free surface flow is controlled by the strength of the circulation induced by the vortex or by the amplitude of the pressure disturbances at the free surface.

Since the flow field must be finite in the numerical problem only finite depth streams are considered. However, in order to facilitate the comparison of numerical results with perturbation theory results for infinite depth, the numerical results correspond to deep water, i.e., stream depth is at least one half the wavelength of the waves following the disturbance.

*Presently at the Civil Engineering Department, University of Arizona.

The present two-dimensional problem serves as a convenient test case for direct numerical solution because much is known about it from perturbation solutions and experiment (Salvesen 1966). Although the numerical method is probably not suitable for three-dimensional problems, it is useful for gaining experience in numerically solving nonlinear wave problems. However, some of the results might be directly useful, in a restricted sense, in some realistic problems. For example, the local flow under an air cushion vehicle with rigid side walls may be analyzed by the two-dimensional methods presented here.

2. EXACT MATHEMATICAL FORMULATION

The following two classes of two-dimensional problems are treated: (i) an infinitely long cylinder (or a line singularity distribution with uniform strength) which is moving at constant velocity U in a direction perpendicular to its axis and at a fixed distance below the undisturbed free surface, and (ii) an infinitely wide pressure distribution on the free surface which is moving at constant velocity U and has finite length in the direction of motion. The problem is to determine the surface waves and the wave resistance, as well as to obtain a description of the total flow field.

The flow is steady in a coordinate system moving with the cylinder or the pressure disturbance. A two-dimensional coordinate system is used with the y -axis pointing upwards, and the x -axis located in the undisturbed free surface with x positive in the direction of motion. It is assumed that the fluid is inviscid, incompressible and without surface tension, and that the flow is irrotational.

NOMENCLATURE

(Additional nomenclature are defined as they appear in the text)

D = Depth of water
 E_i = Error in free-surface condition
 \vec{F} = Force on vortex
 I = Complex function defined by (4.15)
 N = Maximum value of j
 R = Wave resistance
 U = Uniform stream velocity
 \vec{V}_{FS} = Free-surface velocity
 a, b = x and y location of vortex
 c = Location of vortex, complex
 f = Function defined by (4.7)
 g = Gravitational acceleration
 i, j = x and y indices for nodes
 \vec{i}, \vec{j} = Unit vector in x - and y -direction

λh = Extrapolation length
 p = Pressure
 $u^{(i)}$ = Perturbation velocity defined by (4.3)
 x, y = Two-dimensional coordinate system
 Ψ = Stream function defined by (3.1)
 α = First-order wave amplitude far downstream
 η = Free-surface elevation
 θ = Angle defined in (3.15)
 λ = Wave length
 ρ = Mass density of water
 τ = Circulation strength
 ψ = Stream function
 ψ' = Stream function defined by (3.1)

Formulating these two-dimensional, steady-state, potential-flow problems in terms of the stream function $\psi(x, y)$, one has that ψ must be a solution of the Laplace equation

$$\nabla^2 \psi = \psi_{xx} + \psi_{yy} = 0, \quad (2.1)$$

and satisfy the following boundary conditions. On the unknown free surface, $y = \eta(x)$ two conditions are to be satisfied: (1) The kinematic condition states that any particle which is on the surface remains there, thus at the free surface the stream function must be a constant, here set equal to zero

$$\psi = 0 \quad \text{on} \quad y = \eta(x). \quad (2.2)$$

(2) The dynamic condition requires that the pressure above the free surface is everywhere constant (also set equal to zero) except over a specified region where an external pressure disturbance, $p(x)$ may be applied; hence, by the Bernoulli equation it follows that

$$\frac{1}{2} |\nabla \psi|^2 + gy + \frac{p(x)}{\rho} = \frac{1}{2} U^2 \quad \text{on} \quad y = \eta(x), \quad (2.3)$$

where g is the gravitational acceleration.

Far upstream the flow is uniform with no waves and hence

$$\lim_{x \rightarrow -\infty} \vec{k} \times \nabla \psi = -U \vec{i} \quad (2.4)$$

where \vec{i} is the unit vector in the x -direction, $\vec{k} = \vec{i} \times \vec{j}$, and \vec{j} is the unit vector in the y -direction. Far downstream it is assumed that there is a train of periodic outgoing waves with unknown wave length, λ ; hence

$$\psi(x, y) = \psi(x + \lambda, y) \quad \text{as} \quad x \rightarrow -\infty. \quad (2.5)$$

In the case of infinite depth

$$\lim_{y \rightarrow -\infty} \vec{k} \times \nabla \psi = -U \vec{i}, \quad (2.6)$$

and for finite uniform depth the bottom condition is

$$\psi = U D \quad \text{at} \quad y = -D. \quad (2.7)$$

For finite depth it is also necessary to specify that the Froude number with respect to depth is less than unity, $Fr = U/\sqrt{gD} < 1.0$, so that it can be assumed that no waves exist upstream of the disturbance.

The two separate classes of problems which are treated here, the submerged cylinder case and the free-surface pressure case, must both satisfy the above stated conditions. For the cylinder case an additional condition must be satisfied on the cylinder surface:

$$\psi = \text{constant}, \quad (2.8)$$

where the constant is determined by specifying the circulation around the cylinder. For the pressure case one has that the pressure disturbance is given by some function $p = p(x)$ on $\eta = \eta(x)$. This completes the exact mathematical formulation of the specified two-dimensional potential-flow problems.

The main objective of this work is to explore the intrinsic difficulty of solving nonlinear free-surface problems by a direct numerical method so that complications posed by an actual submerged body are disposed of by considering only simple disturbances. Two specific problems are solved here: (i) a submerged vortex with constant strength in a uniform stream and (ii) a sinusoidal pressure disturbance applied to the free surface of a uniform stream. The exact mathematical formulation for these potential flow problems are given by equations (2.1) through (2.7). In the next section Laplace's equation and the exact boundary conditions for these problems are replaced by their finite difference approximations and then direct numerical solutions of the problems are obtained. In Section 4 of the paper the exact problem is reformulated in terms of a perturbation scheme and the first- and second-order solutions are derived.

3. FINITE DIFFERENCE METHOD

In this Section, the exact potential problems as stated in the previous Section, are replaced by their finite difference approximations and then direct numerical solutions of the nonlinear problems are obtained.

It is most convenient for numerical purposes to divide the stream-function ψ into two parts

$$\psi(x, y) = \Psi(x, y) + \psi'(x, y) \quad (3.1)$$

where $\Psi(x, y)$ is the stream function for a two-dimensional singularity in a stationary infinite fluid domain. Thus for a vortex at (a, b) with circulation τ , Ψ is given by

$$\Psi(x, y) = \frac{\tau}{2\pi} \ln \left(\sqrt{(x-a)^2 + (y-b)^2} \right) \quad (3.2)$$

When considering the problem of a pressure distribution on the free surface as the sole disturbance Ψ is identically zero and $\psi' \equiv \psi$.

The boundary value problem to be solved for ψ' is then obtained from (2.1) through (2.7), where ψ' satisfies the field equation,

$$\nabla^2 \psi' = 0 \quad (3.3)$$

in the entire field, and the boundary conditions

$$\psi'(x, \eta) = -\Psi(x, \eta) \quad (3.4)$$

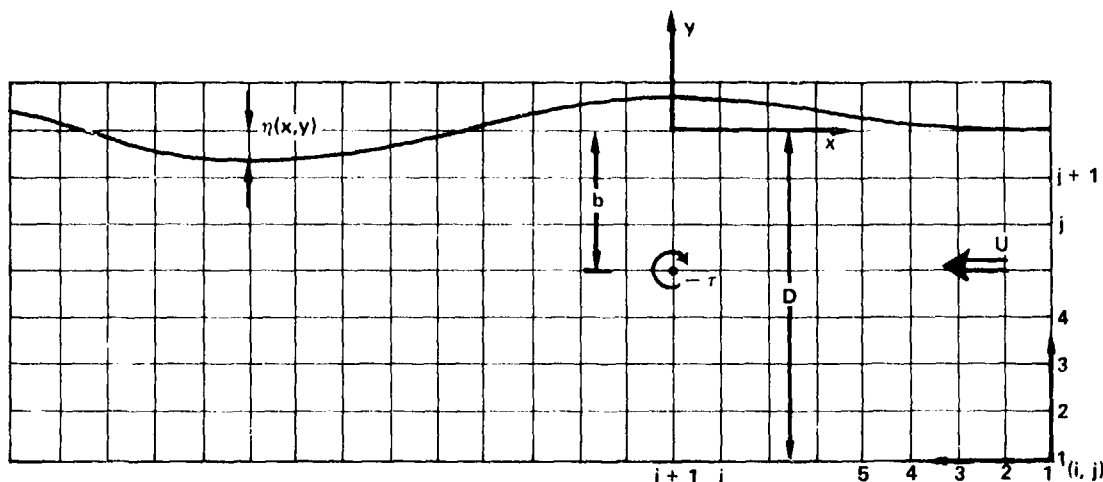


Figure 1. Finite Difference Grid

and

$$\frac{1}{2} |\nabla \psi'|^2 + \nabla \psi' \cdot \nabla \psi + g\eta + \frac{P(x)}{\rho} = \frac{1}{2} U^2 - \frac{1}{2} |\nabla \psi|^2 \quad (3.5)$$

on the free surface $y = \eta(x)$,

$$\text{Limit}_{x \rightarrow \infty} \vec{k} \times \nabla \psi' = -U \vec{i} - \vec{k} \times \nabla \psi \quad (3.6)$$

and

$$\psi' = U D - \psi(x, -D) \text{ at } y = -D. \quad (3.7)$$

Only finite depth cases are considered in the numerical problem.

3.1 Numerical Formulation

The problem is formulated numerically by first overlaying the entire flow field with a uniform grid (or mesh) as shown in Figure 1. The intersections of the horizontal and vertical lines of this grid are called the nodes. The stream-function $\psi'(x, y)$ is to be determined at each node of the grid. These nodes are labeled by pairs of indices i, j referring to their coordinate values (x_i, y_j) . The nodes are numbered so that the bottom corresponds to nodes $(i, 1)$ with i increasing downstream. Some distance upstream of the origin of the coordinate system is the vertical line of nodes labeled $(1, j)$ with j increasing from bottom to top. The selection of the upstream location of the nodal line $(1, j)$ is discussed later. The intersection of the free surface and vertical lines of the grid are boundary nodes which must be determined in the problem. The first interior node below the free surface on a vertical line of the grid is usually (for a wavy free surface) connected by unequal length grid-line segments to its four neighbors. Such a node and its connecting line segments is referred to as an "irregular star." All nodes except those immediately adjacent to the free surface belong to "regular stars."

The value of the stream function ψ' at each node (x_i, y_j) is designated as $\psi'_{i,j}$ that is

$$\psi'(x_i, y_j) = \psi'_{i,j}. \quad (3.8)$$

The boundary value problem (3.3) to (3.7) is then replaced by a standard finite-difference problem. Laplace's equation (3.3) is replaced by the finite-difference equations (Forsythe and Wasow, 1960)

$$\psi'_{i,j} = \frac{1}{4} (\psi'_{i+1,j} + \psi'_{i-1,j} + \psi'_{i,j+1} + \psi'_{i,j-1}) \quad (3.9)$$

when node (i, j) is a regular star, and by

$$\psi'_{i,j} = \frac{\alpha\beta\gamma\delta}{(\gamma\delta + \alpha\beta)} \left[\frac{\gamma\psi'_{i,j-1} + \delta\psi'_{i,j+1}}{(\gamma + \delta)\gamma\delta} + \frac{\beta\psi'_{i-1,j} + \alpha\psi'_{i+1,j}}{(\alpha + \beta)\alpha\beta} \right] \quad (3.10)$$

when (i, j) is an irregular star with grid-line segments of lengths α, β, γ and δ respectively as shown in Figure 2.

The kinematic boundary condition (3.4) at the free surface is replaced by

$$\psi'(x_i, \eta_i) = \psi'_{FS_i} \equiv -\frac{1}{2\pi} \ln \left(\sqrt{(x_i - a)^2 + (\eta_i - b)^2} \right) \quad (3.11)$$

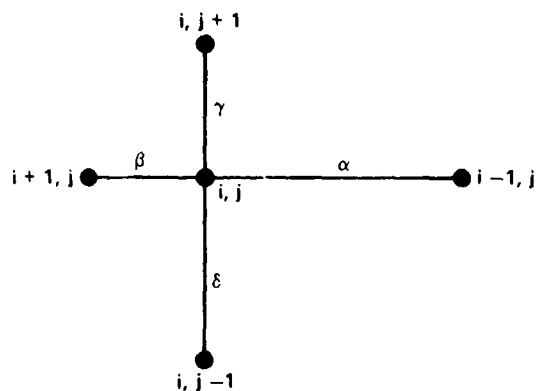


Figure 2. An Irregular Star

and at the bottom by

$$\psi'(x_i, -D) = \psi_{B_i} \equiv U D - \frac{\tau}{2\pi} \ln \left(\sqrt{(x_i - a)^2 + (-D - b)^2} \right). \quad (3.12)$$

The dynamic boundary condition (2.3) at the free surface is calculated by using a direct finite-difference approximation for the velocity, \vec{v}_{FS_i} , at the free surface, given by

$$g\eta_i + \frac{p(x_i)}{\rho} = \frac{1}{2} U^2 - \frac{1}{2} \vec{v}_{FS_i} \cdot \vec{v}_{FS_i} \quad (3.13)$$

The velocity \vec{v}_{FS_i} is given by

$$\vec{v}_{FS_i} = (\vec{k} \times \nabla \psi)_{i,y=\eta}. \quad (3.14)$$

Since the velocity \vec{v}_{FS_i} is tangential to the free surface, it is seen from (3.14) that only the gradient of ψ in the direction normal to the free surface must be determined. With reference to Figure 3, it is easy to see that

$$(\nabla \psi)_{i,\eta} = \left(\frac{1}{\cos \theta} \frac{\partial \psi}{\partial y} \right)_{i,\eta} \quad (3.15)$$

where θ is the angle between the vertical and the unit normal to the free surface. The total stream function, ψ , used in formulas (3.14) and (3.15), is easily obtained at each node using formulas (3.1), once ψ' is known there.

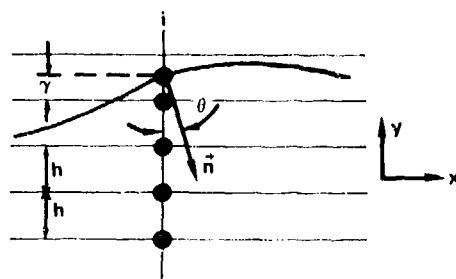


Figure 3. The Free Surface and Its Normal

The y-derivative of ψ , at the free surface, is obtained numerically using the five point Lagrange differentiation formula (Abramowitz and Stegun, Chapter 25, 1964)

$$\begin{aligned} \left(\frac{\partial \psi}{\partial y} \right)_{i,\eta} &\approx \frac{(\gamma + h)(\gamma + 2h)(\gamma + 3h)}{6\gamma h^3} \psi_{i,j} \\ &- \frac{\gamma(\gamma + 2h)(\gamma + 3h)}{2h^3(\gamma + h)} \psi_{i,j-1} \\ &+ \frac{\gamma(\gamma + h)(\gamma + 3h)}{2h^3(\gamma + 2h)} \psi_{i,j-2} \\ &+ \frac{\gamma(\gamma + h)(\gamma + 2h)}{6h^3(\gamma + 3h)} \psi_{i,j-3}. \end{aligned} \quad (3.16)$$

Since

$$\tan \theta_i = \left(\frac{d\eta}{dx} \right)_i \quad (3.17)$$

one has

$$\cos \theta_i = \frac{1}{\left(1 + \left(\frac{d\eta}{dx} \right)_i^2 \right)^{1/2}}. \quad (3.18)$$

Formula (3.18) is evaluated by approximating $\left(\frac{d\eta}{dx} \right)_i$ by the 5 point finite difference formula (Abramowitz and Stegun, Chapter 25, 1964)

$$\left(\frac{d\eta}{dx} \right)_i = \frac{2}{3} (\eta_{i+1} - \eta_{i-1}) - \frac{1}{12} (\eta_{i+2} - \eta_{i-2}). \quad (3.19)$$

In a finite difference calculation the infinite field of problems (3.3) to (3.7) must be truncated to a finite field. The condition (3.6) for the far upstream flow is applied in an approximate manner at $i = 1$ which is chosen far enough upstream where the disturbance is not felt. An upstream distance of about $2\pi \sqrt{U^2/g}$ (a wave length in linear theory with infinite depth) was found to be more than adequate in all cases. At $i = 1$, the flow is assumed to be parallel with uniform velocity $-U\hat{i}$. Hence at

$i = 1$, the free surface is assumed to be horizontal with $\eta = 0$. In the cases of the submerged vortex and surface pressure disturbance, the $\psi'_{i,j}$ are respectively given by

$$\psi'_{i,j} = U y_j - \frac{\tau}{2\pi} \ln \left(\sqrt{(x_1 - a)^2 + (y_j - b)^2} \right) \quad (3.20)$$

and

$$\psi'_{i,j} = U y_j.$$

In the numerical problem, the truncation of the field at a finite distance downstream requires that a boundary condition be specified on the last column of grid points. Since the form of the downstream wave train is unknown in the nonlinear problem, an artificial boundary condition is imposed. The effect of this condition is then checked a posteriori by simply locating the downstream boundary at various distances behind the disturbance and checking the solutions to see whether the effect of the downstream boundary is *localized*. The following downstream boundary condition is applied at $j = N$, where N is such that there will be on the order of five or six waves between the disturbance and the downstream end of the field:

$$\psi'_{N,j} = \psi'_{N-3,j} + 3(\psi'_{N-1,j} - \psi'_{N-2,j}). \quad (3.21)$$

This is simply the Lagrange three-point interpolation formula (Abramowitz and Stegun, Chapter 25, 1964) used to extrapolate the value $\psi'_{N,j}$ from the three previous values of ψ' at the same level j . This simple closure condition appears to work quite well in all of the calculations. Its erroneous effect (i.e., $\psi'_{N,j}$ does not satisfy the field equation 3.3) only seems to significantly affect the flow field over a distance of about 1/4 of a wavelength upstream.

3.2 Numerical Solution

If the free surface is *known*, then equations 3.9 (or 3.10), 3.11, 3.12, 3.20, and 3.21 suffice to determine the field quantity $\psi'_{i,j}$ at every interior point of the grid. The solution method is that of standard overrelaxation (Forsythe and Wasow, 1960) with an overrelaxation constant of 4/3, which yields the convenient recurrence formula (at regular stars only)

$$\psi'_{i,j}(n) = \frac{1}{3} \left(\psi'_{i,j+1}(n) + \psi'_{i-1,j}(n) + \psi'_{i,j-1}(n-1) + \psi'_{i+1,j}(n-1) - \psi'_{i,j}(n-1) \right) \quad (3.22)$$

where the superscript n refers to the latest value of the quantity in the present relaxation cycle and $n-1$ refers to the value of the quantity from the previous relaxation cycle. Each

relaxation cycle is carried out sequentially along vertical grid lines.

The remaining, and central problem of the numerical method, is the generation of the free surface shape. The basic idea behind Malvick's method for systematically guessing a part of the free surface is that any perturbation of the free surface shape at a point results in a limited and monotonically decaying effect in front of the perturbation. Behind the perturbation it is expected that the effect is propagated downstream as waves with wave length nearly equal to $2\pi \sqrt{g}/g$.

Let the error in the free surface pressure condition (3.13) at any station i , be defined as

$$E_i \equiv g\eta_i + \frac{1}{\rho} p(x) - \left[\frac{1}{2} U^2 - \frac{1}{2} \vec{v}_{FS_i} \cdot \vec{v}_{FS_i} \right] \quad (3.23)$$

where \vec{v}_{FS_i} is computed using formulae (3.14-

3.19). Let E be the maximum error allowed at the free surface. One may approximate the initial free surface by the linear-theory free-surface elevation or something of similar character or simply as the undisturbed plane. In any case far enough upstream the free surface elevation is $\eta_i = 0$ and $|E_i| < E$ for $i = 1, 2$ and 3. Suppose that for the assumed free surface, the error $|E_i| > E$ occurs for the first time at $i = i^*$, whereas $|E_i| < E$ for all $i < i^*$.

Then the free surface elevation at $i^* + 1$ is modified by an amount $\Delta\eta_{i^*+1}$ (the amount is explained below). This modification of the free surface elevation is smoothed into the existing free surface a distance of about one half a wave length *downstream* of $i^* + 1$. The free surface upstream of $i^* + 1$ remains fixed. With the new free surface, Laplace's Equation (finite difference formulae 3.9 and 3.10) is solved subject to the boundary conditions 3.11, 3.12, 3.20 and 3.21. Then E_{i^*} is recalculated (using formulae 3.14-3.19 and 3.23). If the current E_{i^*} does not satisfy $|E_{i^*}| < E$, then a new value of $\Delta\eta_{i^*+1}$ is interpolated or extrapolated using the previous two pairs of values of $(E_{i^*}, \Delta\eta_{i^*+1})$. On the first calculation of E_{i^*} , $\Delta\eta_{i^*+1} = 0$. The second time, $\Delta\eta_{i^*+1} = 0.1h$ (where h is the basic mesh spacing) is chosen. Once the value of $\Delta\eta_{i^*+1}$ is found such that $|E_{i^*}| < E$, the process proceeds to the next station. It is to be noted that the modification of the free surface elevation at station $i^* + 1$, which reduces the error in the free surface condition (3.5) at i^* to within specified tolerance, has the effect of destroying the satisfaction of the free surface condition (3.5) further upstream, particularly at stations $i^* - 1$ and $i^* - 2$. A complete pass over the entire length of the field reduces $|E_i|$ below E at each free surface node at least temporarily.

Repeated iterations over the field, correcting the free surface at each station, eventually brings $|E_i| < E$ at every station except at $N - 1$ and N , which are ignored.

The process of smoothing the free surface modification at $i^* + 1$ into the remaining free surface is carried out using an interpolation polynomial. The procedure has two forms. The first is the *prediction* phase and is used in the initial pass when the initial free surface is assumed to be a plane. After the initial prediction phase or if the first guess for the free surface is the linear free surface or any other good guess of a similar character, a free surface *correction* procedure is used only. The two procedures are similar and are explained as follows:

In the prediction pass, the values η_{i^*-2} , η_{i^*-1} , η_{i^*} and $\eta_{i^*+1} + \Delta\eta_{i^*+1}$ determine the height, slope and curvature of the free surface at station $i^* + 1$. These quantities plus zero height and slope (to conform to the existing plane free surface) at a distance lh (called the *extrapolation length*) downstream of station $i^* + 1$ determine an interpolation polynomial of fourth degree. This interpolation polynomial replaces the existing free surface η between stations $i^* + 1$ and $i^* + 1 + l$ (l is taken to be an integer so that lh is about one half the wave length of linear theory). The formula for this free surface prediction polynomial is (where $s \in [0, 1]$, $s = 0 \Rightarrow x = x_{i^*+1}$ and $s = 1 \Rightarrow x = x_{i^*+1+l}$)

$$\begin{aligned} \eta(s) = & \eta(x_{i^*+1}) + \eta'(x_{i^*+1})s + \frac{1}{2}\eta''(x_{i^*+1})s^2 \\ & - \frac{1}{(lh)^3} [4\eta(x_{i^*+1}) + 3\eta'(x_{i^*+1})lh \\ & + \eta''(x_{i^*+1})(lh)^3]s^3 \\ & + \frac{1}{(lh)^4} [3\eta(x_{i^*+1}) + 2\eta'(x_{i^*+1})lh \\ & + \frac{1}{2}\eta''(x_{i^*+1})(lh)^3]s^4. \end{aligned} \quad (3.24)$$

The derivatives of $\eta(x)$ in formula (3.24) are evaluated using the finite difference approximations

$$\begin{aligned} \eta'(x_{i^*+1}) = & \frac{1}{6} [11\eta(x_{i^*+1}) - 18\eta(x_{i^*}) \\ & + 9\eta(x_{i^*-1}) - 2\eta(x_{i^*-2})] \end{aligned} \quad (3.25)$$

$$\eta''(x_{i^*+1}) = \eta(x_{i^*+1}) + \eta(x_{i^*-1}) - 2\eta(x_{i^*})$$

where

$$\eta(x_{i^*+1}) = \eta^{(n-1)}(x_{i^*+1}) + \Delta\eta_{i^*+1}.$$

The sequence of sketches in Figure 4 illustrates the *prediction* process. In this figure the dotted line is the free surface which is being replaced by the prediction polynomial between station $i^* + 1$ and $i^* + 1 + l$. The solid line is the prediction polynomial (3.24).

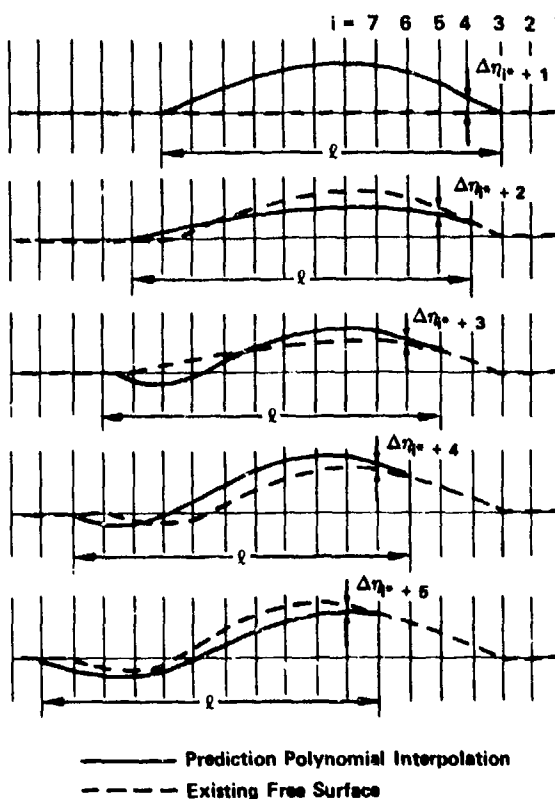


Figure 4. Free-Surface Prediction Starting at $i^* = 3$

When the prediction pass is completed or if a good approximation of the free surface is used at the outset, then only free-surface *corrections* are made. The correction polynomial is again formula (3.24), but now the derivatives of η appearing in the polynomial are simply taken as

$$\eta'(x_{i^*+1}) = \frac{3}{2}\Delta\eta_{i^*+1} \quad (3.26)$$

$$\eta''(x_{i^*+1}) = \Delta\eta_{i^*+1}$$

and the resulting polynomial (3.24) is added to the existing free surfaces. One step in the correction process is shown in Figure 5.

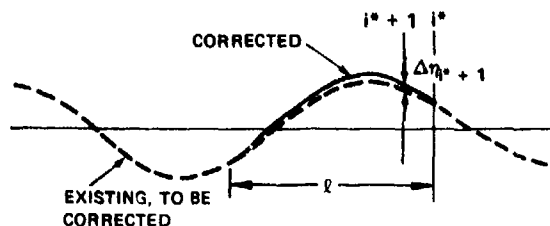


Figure 5. Free-Surface Correction

The free-surface correction passes are repeated until $|E_i| < E$ at every station i . This may involve up to ten or more passes.

It was found that the process is most efficiently carried out over small sections of the field of about one to two wave lengths. That is, the free surface is predicted and corrected in a section of about two wavelengths until $|E_i| < E$ for all i in this section. Then the process is continued in the next section (of the same length) downstream, but overlapping the previous section by about half a wavelength.

When the process is completed over the entire finite difference field, the problem is essentially completed. If the disturbance is a submerged singularity, such as a vortex, the force on it can be found by using Lagally's theorem. The force on the vortex is given by

$$\vec{F} = \rho \tau \vec{k} \times \vec{V}' \quad (3.27)$$

where

$$\vec{V}' = \vec{k} \times \nabla \psi' \quad (3.28)$$

The derivatives of ψ' are obtained using the five point difference formula

$$\begin{aligned} (\psi'_x)_{i,j} &= \frac{1}{12} \psi'_{i-2,j} - \frac{2}{3} \psi'_{i-1,j} \\ &+ \frac{2}{3} \psi'_{i+1,j} - \frac{1}{12} \psi'_{i+2,j} \end{aligned} \quad (3.29)$$

and a similar formula for ψ'_y (Abramowitz and Stegun, Chapter 25, 1964).

4. PERTURBATION METHOD

In this Section, the exact potential flow problems as stated in Section 2, are reformulated in terms of a perturbation scheme and then the first- and second-order solutions are derived.

4.1 Perturbation Formulation

It is assumed that the submerged singularity and the free-surface pressure distribution are "weak" disturbances so that in the neighborhood of the free surface, the perturbations about the uniform flow are everywhere "small." Note that in the neighborhood of the submerged singularity, the perturbations about the uniform flow are not necessarily "small"

and hence, in the case of the submerged singularity, it must be assumed, in order to have "small" free-surface disturbances, that the submergence is "large." "Large" here means that if, for example, the submerged singularity is a doublet, the submergence must be "large" relative to the radius of the cylinder generated by such a doublet in a uniform stream without a free surface.

Furthermore, it is assumed that the stream function, $\psi(x, y)$ has the following expansion in terms of a perturbation parameter ϵ :

$$\psi(x, y) = -Uy + \psi^{(1)} + \psi^{(2)} + \dots \quad (4.1)$$

where $\psi^{(n)}$ is of $O(\epsilon^n)$. It should be noted that for the submerged singularity case, this expansion is not valid in the neighborhood of the singularity, but only at the free surface and in the far field. However, since there is no body boundary condition to be satisfied in the problems treated here, it is not necessary to introduce an additional expansion valid in the near field as used by Salvesen (1969) in solving the problem of a submerged body.

In the same way it is assumed that the free-surface elevation $\eta(x)$ has the expansion

$$\eta(x) = \eta^{(1)} + \eta^{(2)} + \dots \quad (4.2)$$

and that the uniform-stream velocity U is an unknown of the problem with the expansion

$$U = u + u^{(1)} + u^{(2)} + \dots \quad (4.3)$$

where $\eta^{(n)}$ and $u^{(n)}$ are both of $O(\epsilon^n)$. The uniform-stream velocity is chosen here as an unknown, in the manner of Wehausen and Laitone (1960, p. 655). This simplifies the derivation; but it is probably physically more attractive to let the wavelength (as in the previous Section) or the wave-number be unknown, and expand these quantities. The two alternative expansion methods are equivalent.

By substituting the expansion for the stream function (4.1) into Laplace's equation (2.1), it follows that each of the functions $\psi^{(n)}$ must be harmonic functions. Furthermore, substitution of the expansions (4.1), (4.2), and (4.3) into the exact free-surface conditions (2.2) and (2.3) gives the linearized free-surface conditions for the submerged singularity case

$$\psi_y^{(1)} - v \psi^{(1)} = 0 \text{ on } y = 0 \quad (4.4)$$

and for the free-surface pressure case

$$\psi_y^{(1)} - v \psi^{(1)} = \frac{1}{\rho u} p(x) \text{ on } y = 0 \quad (4.5)$$

and the second-order free-surface condition to be satisfied for both cases is

$$\psi_y^{(2)} - v \psi^{(2)} = f(x) \text{ on } y = 0 \quad (4.6)$$

where the right-hand side is a function of the first-order solution,

$$f(x) = \frac{1}{2u} (\psi_y^{(1)2} + \psi_x^{(1)2}) + \eta^{(1)} [v \psi_y^{(1)} - \psi_{yy}^{(1)}] - 2vu^{(1)} \eta^{(1)} \quad (4.7)$$

and $v = g/u^2$ is the wave number. From the upstream and downstream conditions at infinity (2.4) and (2.5), it follows that

$$\lim_{x \rightarrow -\infty} \nabla \psi^{(n)} = 0 \quad (4.8)$$

and

$$\psi^{(n)}(x, y) = \psi^{(n)}(x + \lambda, y) \text{ as } x \rightarrow -\infty \quad (4.9)$$

Similarly, from the infinite depth condition one has that

$$\lim_{y \rightarrow -\infty} \nabla \psi^{(n)} = 0 \quad (4.10)$$

and from the finite depth condition

$$\psi^{(n)} = 0 \text{ at } y = -D. \quad (4.11)$$

The first- and second-order free-surface elevations are given by

$$\eta^{(1)} = \frac{1}{u} \psi^{(1)}(x, 0) \quad (4.12)$$

and

$$\eta^{(2)} = \frac{1}{u} [\psi^{(2)} + \eta^{(1)} \psi_y^{(1)} - u^{(1)} \eta^{(1)}]_y = 0 \quad (4.13)$$

This completes the formulation of the first- and second-order problems.

It should be pointed out that in deriving the free-surface conditions (4.4) and (4.5) it is assumed that the nondimensional wave number, $bv = gb/u^2$, is of order 1 (i.e. the Froude number, $Fr = u/\sqrt{gb}$ is also of order 1). Here b refers to the submergence depth of the singularity or the length of the pressure distribution. Strictly speaking, therefore, this scheme is applicable only when the wavelength, $\lambda = 2\pi/v$, is of the same order as b . Salvesen (1969) has shown how the perturbation solution breaks down as the Froude number, $Fr \rightarrow 0$ and that in fact, the expansion is singular for $Fr = 0$.

4.2 Perturbation Solutions

Perturbation solutions for the submerged vortex and the free-surface pressure distribution are given only for the infinite-depth case.

(i) First-order solution

Considering a vortex of constant strength, τ located at c ($c = a + ib$) it follows from Wehausen and Laitone (1960, p. 489) that the first-order solution is

$$\psi^{(1)} = \frac{\tau}{2\pi} \text{Im} \left[-i \ln(z - c) + i \ln(z - c^*) + 2e^{-ivz} \int_{-\infty}^z \frac{e^{ivu}}{u - c^*} du \right] \quad (4.14)$$

Here $z = x + iy$ is the complex variable and Im stands for the imaginary part. Defining the complex function

$$I(\zeta) = e^{-\zeta} E_1(-\zeta) = e^{-\zeta} \int_{-\zeta}^{\infty} \frac{e^{-u}}{u} du, \quad (4.15)$$

where the notation of the exponential integral E_1 is that of Abramowitz and Stegun (1964).

Then (4.15) can be written as

$$\psi^{(1)} = \frac{\tau}{2\pi} \text{Re} [-\ln(z - c) + \ln(z - c^*) + 2I\{iv(z - c^*)\}] \quad (4.16)$$

Introducing known expansions for E_1 it can easily be shown that the complex function (4.15) has the series expansion

$$I(\zeta) = e^{-\zeta} \left(-\gamma - \ln \zeta + i\pi - \sum_{n=1}^{\infty} \frac{\zeta^n}{n \cdot n!} \right) \quad (4.17)$$

and the asymptotic expansion

$$I(\zeta) \sim \left\{ \frac{1}{\zeta} + \frac{1}{\zeta^2} + \frac{2!}{\zeta^3} + \frac{3!}{\zeta^4} + \dots \right\} + (1 \pm i) i\pi e^{-\zeta}, \quad (4.18)$$

with plus sign for $\text{Im } \zeta \rightarrow -\infty$ and minus sign for $\text{Im } \zeta \rightarrow +\infty$.

For the free-surface pressure case, the first-order solution can be expressed in terms of the convolution integral (see Wehausen and Laitone, 1960, p. 601)

$$\psi^{(1)} = \frac{1}{\pi} \int_{-\infty}^{\infty} ds \frac{1}{\rho u} p(x) \text{Re } I\{i v(z - s)\}. \quad (4.19)$$

Note that $\text{Re } I \{i v (z - s)\} / \pi u$ is the stream function for a pressure p , concentrated on an infinitely narrow band of the free surface at $x = s$.

(ii) Second-order solution

The second-order problem is essentially the same as the first-order free-surface pressure problem. Comparing the free-surface condition for the first-order pressure problem (4.5) with the second-order free-surface condition (4.6) it is seen that they are the same inhomogeneous boundary conditions with the right-hand sides being known functions in the variable x . The infinity conditions are also the same for the two problems as stated in equations (4.8), (4.9) and (4.10). Hence, the solution to the second-order problem is of the same form as the solution to the first-order pressure problem (4.19), namely

$$\psi^{(2)} = \frac{1}{\pi} \int_{-\infty}^{\infty} ds f(s) \text{Re } I \{i v (z - s)\} \quad (4.20)$$

where the function, $f(x)$ is given by equation (4.7). Applying the first-order free-surface conditions (4.4) and (4.5) and also using the equation

$$\frac{d}{dz} I \{i v z\} = -\frac{1}{2} - i v I \{i v z\} \quad (4.21)$$

it can be shown that the function, $f(x)$ reduces to

$$f(x) = \frac{u}{2} v^2 \eta^{(1)2} + \frac{1}{2u} \psi_x^{(1)2} - \eta^{(1)} T(x) - 2 v u^{(1)} \eta^{(1)} \quad (4.22)$$

where, for the submerged vortex case,

$$T(x) = \frac{\tau}{\pi} \left[\frac{v b}{(x - a)^2 + b^2} - \frac{(x - a)^2 - b^2}{\{(x - a)^2 + b^2\}^2} \right]$$

and

$$\psi_x^{(1)} = \frac{\tau}{\pi} \left[\frac{-(x - a)}{(x - a)^2 + b^2} + v \text{Im } I \{i v (x - c)\} \right]$$

and for the free-surface pressure case

$$T(x) = \frac{1}{\pi} \int_{-\infty}^{\infty} ds \frac{1}{\rho u} p(s) \left\{ \frac{-1}{(x - s)^2} \right\}$$

and

$$\psi_x^{(1)} = \frac{1}{\pi} \int_{-\infty}^{\infty} ds \frac{1}{\rho u} p(s) \left[\frac{-1}{(x - s)} + v \text{Im } I \{i v (x - s + i0)\} \right]$$

The solution (4.20) is bounded only if the functions $f(x)$ given by (4.22) are nonoscillatory for large negative values of x . Applying the asymptotic expansion (4.18) to (4.22), one obtains

$$\lim_{x \rightarrow -\infty} f(x) = \text{const.} - 2 v u^{(1)} \eta^{(1)}(x), \quad (4.23)$$

where $\eta^{(1)}(x)$ is a regular outgoing sinusoidal wave. Hence, the downstream infinity condition is only satisfied if

$$u^{(1)} = 0. \quad (4.24)$$

The uniform-stream velocity, U has been considered an unknown with the expansion (4.3), $U = u + u^{(1)} + u^{(2)} + \dots$, but (4.24) shows that there is no "correction" resulting from the second-order solution to the uniform-stream velocity used with the first-order solution. However, completing the third-order solution Salvesen (1969) has shown that

$$u^{(2)} = \frac{1}{2} v^2 \alpha^2 u \quad (4.25)$$

where α is the first-order wave amplitude far downstream. Hence, within the third-order theory the uniform-stream velocity is

$$U = u \left(1 + \frac{1}{2} v^2 \alpha^2 \right) \quad (4.26)$$

which is recognized as the result originally obtained by Stokes (1847) for the third-order Stokes wave. This implies that the wavelength according to the third-order theory is

$$\lambda = \frac{2\pi}{v} = \frac{2\pi}{g} U^2 (1 - v^2 \alpha^2), \quad (4.27)$$

while the wave length given by both the linear and second-order theory is $\lambda = (2\pi/g) U^2$.

(iii) Wave elevation and wave resistance

Using the first-order potentials for the submerged vortex (4.16) and for the free-surface pressure disturbance (4.19), the first order wave elevation (4.12) can be expressed in the following form for the vortex

$$\eta^{(1)} = \frac{\tau}{\pi u} \text{Re } I \{i v (x - a - i b)\} \quad (4.28)$$

and for the pressure disturbance

$$\eta^{(1)} = \frac{1}{\pi u} \int_{-\infty}^{\infty} ds \frac{1}{\rho u} p(s) \text{Re } \{i v (x - s + i0)\}. \quad (4.29)$$

Similarly, using the second-order potential (4.20), the second-order wave elevation (4.13), for both cases is

$$\eta^{(2)} = \frac{1}{\pi i} \int_{-\infty}^{\infty} ds f(s) \\ \text{Re } I \{ i v (x - s + i0) \} + v \eta^{(1)2} \quad (4.30)$$

The "exact" formula for the wave resistance as derived by energy considerations in John (1949) or by the momentum theorem in Salvesen (1966) is

$$R = \frac{-\rho}{2} \int_{-\infty}^{\eta(x_0)} \left[\psi_y^2 + \psi_x^2 \right]_{x=x_0} dy \\ + \frac{\rho g}{2} \eta^2(x_0) \quad (4.31)$$

where ψ is the "exact" stream function, $\eta(x)$ is the "exact" wave elevation, x_0 denotes any transverse vertical plane behind the disturbance, and ρ is the mass density of the fluid. Salvesen (1966) has shown that by applying (4.31) in a plane far downstream, the wave resistance, R , can be expressed in terms of the trough-to-crest wave height, H , as

$$R = \frac{1}{4} \rho g \left(\frac{1}{2} H \right)^2 + O(\epsilon^4) \quad (4.32)$$

As first pointed out by Salvesen (1966), equation (4.32) gives the wave resistance correct to $O(\epsilon^3)$ even when the waves are not exactly sinusoidal.

5. RESULTS

In this section numerical results for the case of free-surface flow past a submerged vortex and past a free-surface sinusoidal pressure distribution are compared with first- and second-order analytical results. Before presenting the results it should be pointed out that it has been demonstrated previously (Salvesen, 1966 and 1969) that results obtained from perturbation schemes agree reasonably well with experimental results for a submerged cylinder at Froude number = $O(1)$. In particular, it was shown that for the downstream waves of wave height near the breaking point, wave heights predicted by second-order theory agree very well with experimental values; third-order effects make a negligible change to the wave height. However for steep waves there can be as much as a 6 percent shortening of the wave length due to third-order effects. It should be noted that this nonlinear effect on the wave length can be determined according to equation

(4.27) from the first-order wave amplitude. Hence, it is felt that it is sufficient to compare the numerical results with first- and second-order theory in order to determine whether the numerical method predicts nonlinear effects which have the same trend as predicted by the perturbation scheme.

Many cases of the vortex and pressure distribution problems were calculated, but only cases for which numerical results for finite depth can be compared to infinite-depth perturbation theory are presented here. If the depth of the stream is greater than about half a wave length, then the stream is comparable to one of infinite depth. For example, the present cases all have the far upstream speed, $U = 10$ feet per second. In this case deep water waves have the approximate wave length of 20 feet. The numerical results presented are for depths slightly greater than 9 feet. According to linear theory the difference between the wave lengths for a 9 foot depth and an infinite depth stream, both with a wave phase velocity of 10 feet per second, is less than one half of one percent.

In all cases a free-stream speed of $U = 10$ feet per second is maintained. The finite difference grid was selected to have a uniform spacing of one foot. This corresponds to about twenty grid points per wavelength. The field length was selected to be about 120 feet (or grid points), with 25 feet upstream of the disturbance and 95 feet (about five complete waves) downstream.

The free surface error tolerance E was selected to be $0.001 U^2$ and it was found by numerical experiments that this required that the convergence criteria in the relaxation procedure for solving Laplace's equation,

$$|\psi_{i,j}^{(n)} - \psi_{i,j}^{(n-1)}| < e$$

at all nodes (i, j) , satisfy $e < 0.001$. Several cases were computed with both E and e reduced by a factor of 10, but this made essentially no difference in the final results. No numerical experiments in which the mesh length h was varied were carried out.

Computer execution time varies strongly with the following parameters; depth D , tolerance E and strength of the disturbance. For the results presented here (with $D = 9$ feet and $E = 0.001 U^2$) each case required about 10 minutes of execution time on a CDC 6600. There are many improvements that can be made in the program and numerical method which would ultimately lead to a significant reduction in computer execution time. However, at this time our primary concern is the testing of the numerical method, not its optimization with respect to execution time.

As a starting condition a planar free surface was taken when the disturbance is weak, i.e., circulation $|\Gamma| \lesssim 0.8 \text{ ft/sec}^2$ or magnitude of free surface pressure is less than about

*"Exact" in quotation marks refers to exact within potential-flow theory.

6.0 lb/ft². For disturbances whose strengths were greater than these values the free surface corresponding to one previously obtained at a different value of disturbance strength was simply scaled linearly to that corresponding to the desired disturbance strength and used as the initial free surface guess. This was done, instead of simply using linear or second order free-surface shapes as initial guess, so as to minimize any bias towards the perturbation solutions.

As long as the disturbance strength is small ($|\tau| < 0.8$ ft/sec² or p_0 , the pressure

amplitude, < 6 lb/ft²) the numerical results are in very close agreement with second order perturbation theory and thus need not be shown. In Figure 6, the numerically computed wave resistance of the vortex is compared with that of first- and second-order perturbation theory results. These examples are for a 4.1 foot vortex depth of submergence beneath the mean free surface level. The stream depth is 9.1

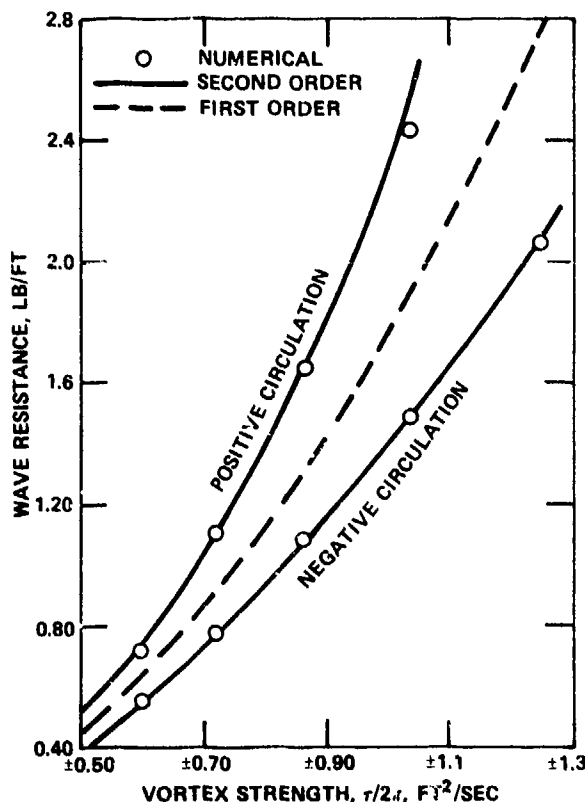


Figure 6. Wave Resistance as a Function of Vortex Strength

(Uniform stream velocity is 10 ft/sec, vortex submergence is 4.1 feet and the depth is 9.1 feet for the numerical results and infinite for the analytical results.)

feet. The wave height and nonlinear effects are controlled by the magnitude of the vortex circulation τ . Note the excellent agreement between the numerical and second order theory except for large values of circulation.

It was found that even when the numerically computed downstream waves were not in good agreement with the second-order theory waves, the numerically computed wave resistance of the vortex is still in good agreement with second-order theory results. This is because only the local flow in the vicinity of the vortex is used in the numerical calculation of force.

Figures 7 and 8 show the free surface, obtained by the numerical method and first- and second-order perturbation theory respectively, for the vortex with circulation $\tau = 1.4\pi$ feet²/sec, 1.15π feet²/sec and the pressure distribution with amplitude $p_0 = 8.6$ lb/ft². These three cases correspond to fairly large disturbances. Note that the numerically-calculated free-surface shapes agree with the second-order theory somewhat better than with first-order theory for the vortex cases, Figures 7 and 8. The main differences between the numerically-calculated and second-order theory waves are that the numerical wave peaks are lower whereas the troughs are deeper for the negative circulation case and shallower for the positive circulation case. Some of this effect might be due to the finite bottom in the numerical method. The finite bottom tends to reduce the amplitude of the wave. This can be roughly explained for the vortex case by modeling the bottom as an infinite-depth stream with an additional vortex of equal strength but opposite circulation placed at the image point, with respect to the bottom, of the disturbance vortex. Then the wave elevation according to linear theory is the superposition of the waves due to each vortex individually. The image vortex produces a wave having the same wave length but 180° out of phase and of much smaller amplitude than the disturbance vortex waves. The superposition of these waves then tends to reduce the wave amplitude of the disturbance wave alone in infinite depth. However, one must note that this approximation for the bottom effect does not alter the wavelengths in the same way as the actual bottom does. Also the mean level of the free surface behind the disturbance is slightly lowered when the stream has finite depth.

The results for the pressure distribution seem to agree more closely with linear theory than second-order theory. Again this may be, at least partially, due to the finite bottom in the numerical calculation. Note also that there is considerable difference in the first free-surface hump underneath the pressure distribution between that found by the numerical method and that found by either first- or second-order theory.

Finally it should be mentioned that for the cases computed to date, the disturbances are not strong enough to produce nonlinearities that significantly alter the wave length from

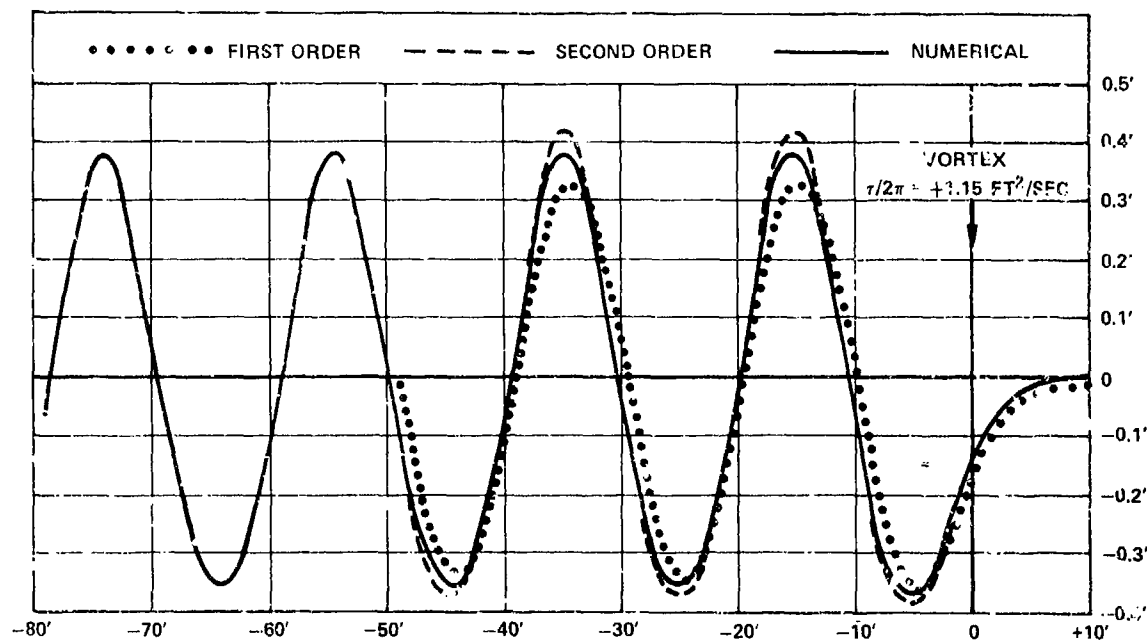
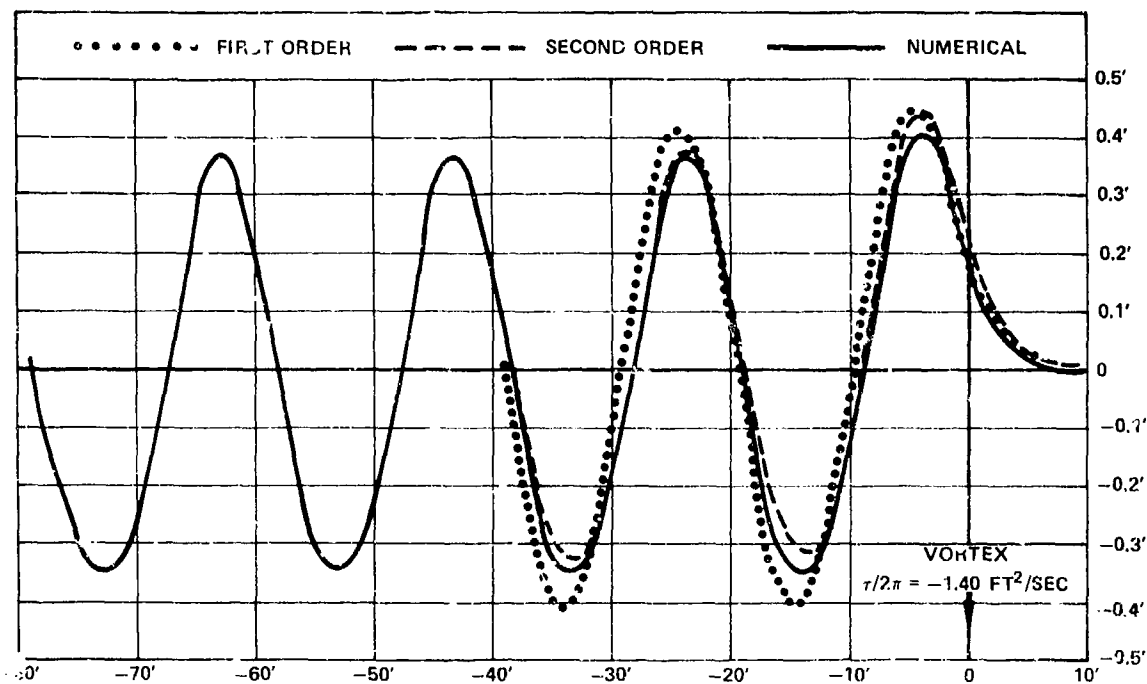


Figure 7. Wave Elevations Generated by a Submerged Vortex ($b = 4.5 \text{ Ft}$) in Uniform Stream ($U = 10 \text{ FT/SEC}$)

(Predicted numerically and by first- and second-order theory. Depth is 9.5 feet for numerical results and infinite for theoretical results.)

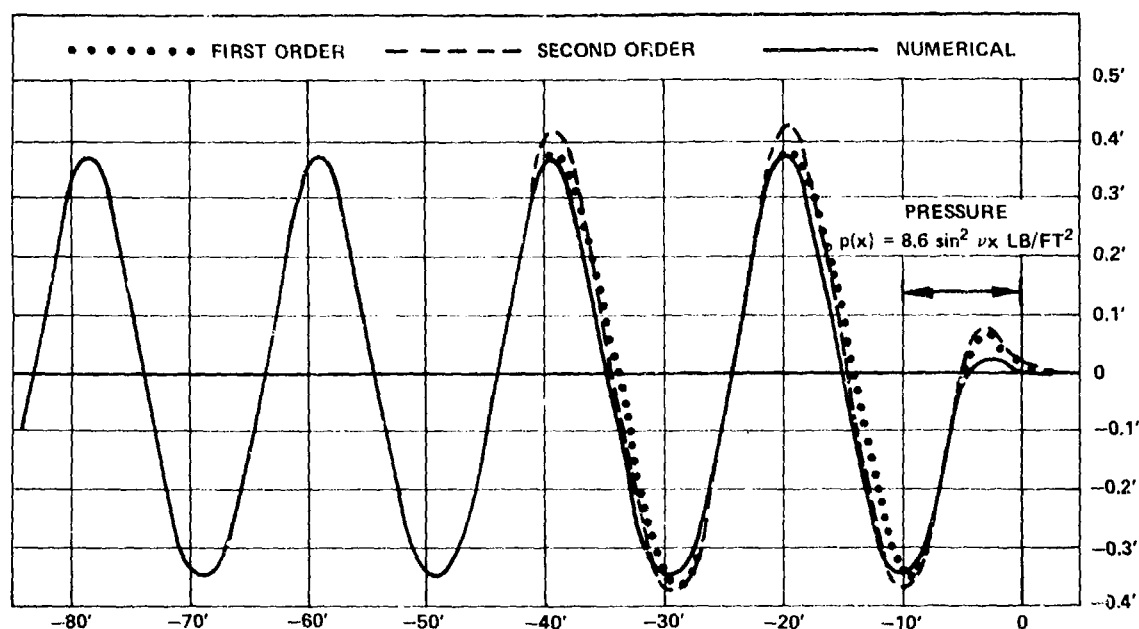


Figure 8. Wave Elevations Generated by a Pressure Distribution on the Free Surface

(Predicted numerically and by first- and second-order theory. Uniform stream velocity is 10 ft/sec and depth is 9.5 feet for numerical results and infinite for theoretical results.)

that predicted by second order theory. In particular, no systematic change in wave length, as predicted at third order from equation (4.27), has as yet been detected. Applying (4.27) to the present results shows that for the wave heights indicated the change in wavelength due to nonlinear effects is a shortening of less than one percent. The numerical results are for finite depth which in the present case would tend to lengthen the waves by about one half of one percent which offsets the shortening of the waves. Thus, the resulting wave lengths of the finite-depth numerical results are essentially the same as the second-order theory results for infinite depth. Further work is required to handle more severe disturbances in deep water.

6. CONCLUDING REMARKS

The numerical solutions obtained are accurate for small and moderate disturbances. These results are very close to second order theory. However, as the strength of the disturbance gets larger the numerical solutions begin to depart from second-order theory. Part of the difference in wave height may be explained by a finite bottom effect.

Further refinements of the numerical method would probably improve the results and enable one to calculate the flow for more severe disturbances. A more sophisticated treatment of the problem of the finite difference field truncation may be helpful and improve accuracy. Part of the difference between the numerical results and perturbation-theory results might be due to limitation of accuracy

within mesh size used. One can easily refine the mesh but this incurs severe penalties in computer time required. The best thing to do would be to work out the perturbation theory for finite depth so that a comparison can be made with finite-depth numerical results. Then fairly shallow-depth streams, say of the order of 1/3 of a wave length, can be used. This makes a considerable difference in computer execution time so that a finer mesh can be used with an overall small increase in execution time.

The main conclusion to be drawn is that the present numerical scheme is a very promising approach to solving nonlinear free-surface problems. Further refinements should enable consideration of more severe disturbances which give rise to more severe nonlinear free-surface effects. Furthermore, a variety of disturbers, i.e., almost any kind of two-dimensional submerged foil or system of foils, can be handled with only minor modification of the basic methodology developed to date.

7. REFERENCES

1. Abramowitz, M. and Stegun, I. A., "Handbook of Mathematical Functions," National Bureau of Standards, Applied Mathematics Series, No. 55 (1964).
2. Forsythe, G. E. and Wasow, W. R., "Finite-Difference Methods for Partial Differential Equations," Chapter 3, John Wiley and Sons, Inc., New York (1960).

3. John, F., "On the Motion of Floating Bodies, I," Comm. Pure Applied Mathematics 2, pp. 13-57 (1949).

4. von Kerczek, C. H., "The Force and Moment on Bodies Submerged in a Uniform Stream of Finite Depth," Master of Science Thesis, University of Notre Dame, Indiana (1965).

5. Salvesen, Nils, "On Higher-Order Wave Theory for Submerged Two-Dimensional Bodies," Journal of Fluid Mechanics Vol. 38, Part 2, pp. 415-432 (1969).

6. Salvesen, Nils, "Second-Order Wave Theory for Submerged Two-Dimensional Bodies," ONR 6th Naval Hydrodynamics Symposium, pp. 595-636 (1966).

7. Stokes, G. C., "On the Theory of Oscillatory Waves," Trans. Camb. Phil. Soc., 8, pp. 441-455 (1847).

8. Wehausen, J. V. and Laitone, E. V., "Surface Waves," Hand. Phys. 9, Berlin: Springer (1960).

DISCUSSION

H.J. HAUSSLING

As mentioned by the authors, initial-value techniques offer an alternative approach to solving steady-state problems. Such methods can yield full transient solutions, although they usually are not the fastest methods for obtaining steady-state results. However, another alternative to the iterative scheme presented by the authors might be obtained by starting with an initial-value technique, but using large time steps, relaxation, or other methods for reducing computer time.

Other techniques also exist for solving the Laplace equation. For some problems, such as that of the moving surface pressure disturbance, the expansion of the dependent variable in a finite series of functions, each of which satisfies the governing equation and certain of the boundary conditions, can be effective. The avoidance of the use of a grid eliminates the problems associated with following the moving boundary through a fixed mesh.

We have recently obtained transient potential flow results with a numerical method which employs the functional-expansion approach in space and finite differencing in time. A sequence showing a free-surface time development for the surface pressure distribution problem is presented in Fig. 1. The disturbance is accelerated impulsively from rest in initially calm water. More general accelerations can easily be handled. The flow near the disturbance achieves almost steady-state conditions quite rapidly, but thereafter the approach to steady state is slower. Numerical results have been obtained for both the linear and nonlinear equations and a comparison is given in Fig. 2. The waves shown in this figure are considerably steeper than those shown in the paper. Waves with about twice the steepness of those in Fig. 2 would break. Our linear numerical results agree with

the linear theory. Our nonlinear results for almost steady state agree quite well with the steady-state perturbation theory, including the third-order wavelength correction. Thus, it seems that these numerical schemes can yield good results, even for waves which are close to breaking conditions. Further studies in this area should add to the contribution of Drs. von Kerczek and Salvesen and help to determine the effectiveness of numerical methods in solving nonlinear ship-wave problems.

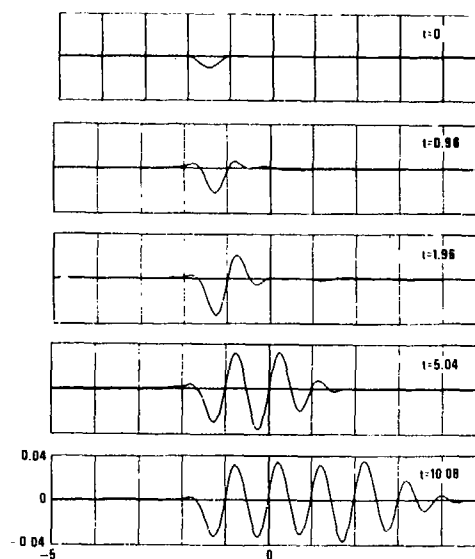


Fig. 1 Development of Surface Elevation for Abruptly Accelerated Surface Pressure Distribution.

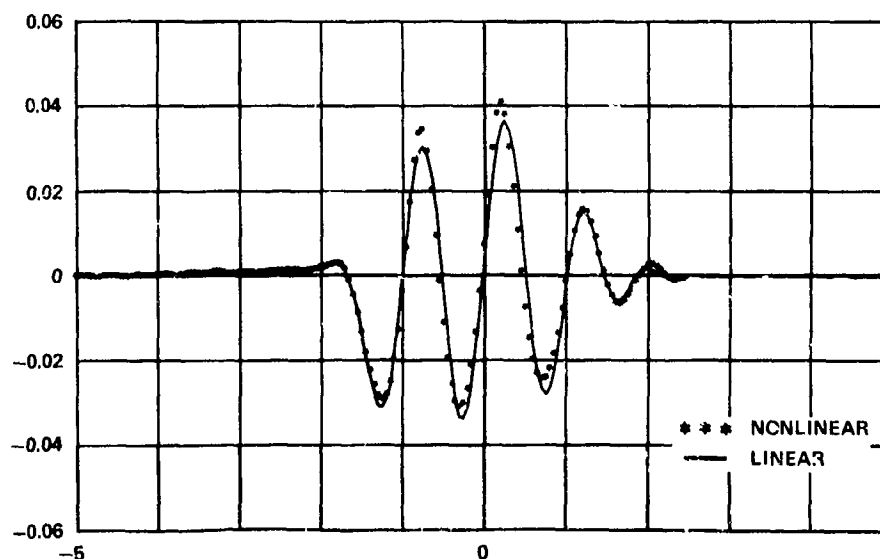


Fig. 2 Comparison of Surface Elevations at $t=5.76$ Generated by Linear and Nonlinear Numerical Schemes.

C. M. LEE

This is a valuable piece of work which demonstrates an encouraging sign of validity of perturbation analysis of a free-surface problem.

I would like to comment on the following points:

One of the main purposes of the paper was to check whether higher-order analysis of a perturbed free-surface flow by a singularity converges to an exact solution. If the check was made for more severe free-surface disturbances, the effect of the

Benjamin and Feir, "The Disintegration of Wave Trains on Deep Water, Part I," JFM, Vol. 27, Part 3, 1967.

convergence of the higher-order analysis could have been demonstrated more rigorously. A shallower depth of submergence of the vortex or an increased vortex strength would generate larger free surface disturbances.

It will be of great interest to many of us to use the numerical scheme introduced in this work to check the phenomenon of a disintegration of wave trains on deep water, shown by Benjamin and Feir.¹ They have shown by their theory that two progressive plane waves having slightly different wave numbers can be disintegrated after traveling some distance. The present numerical scheme may adopt two submerged pulsating sources of slightly different frequencies, compute wave profiles, and check if the disintegration phenomenon do exist.

AUTHOR'S REPLY

We find the results of the transient solution to the two-dimensional pressure problem, discussed by Dr. Haussling, extremely interesting. The initial value technique has the advantage of being a much more general technique applicable to the steady-state problems as well as the transient problems. Furthermore, the initial value technique does not require the "guess work" involved in our iterative scheme. However, it may take unreasonably long time to obtain a completely steady-state solution by the transient approach. On the other hand, we note that "the flow near the disturbance achieves almost steady-state conditions quite rapidly", so that in predicting steady-state forces such as wave resistance and lift on a body, relatively short

time may be used with reasonable accuracy. It is very encouraging to observe that the numerical scheme used by Dr. Haussling seems to predict accurately the expected nonlinear effects including the third-order wavelength correction.

We agree with Dr. Lee that it is unfortunate that we at this time only have nonlinear numerical solutions for moderately steep waves. The objective of this work has been to demonstrate that the complete nonlinear wave-disturbance problem could be solved numerically and with stable solutions for moderate disturbances. The next phase of our work will include steeper waves and we also plan in the near future to investigate the Benjamin and Feir disintegration phenomena.

TWO-DIMENSIONAL CALCULATIONS OF THE MOTION OF FLOATING BODIES

R. K. C. Chan
Science Applications, Inc.
La Jolla, California

C. W. Hint
Science Applications, Inc.
La Jolla, California

ABSTRACT

In this paper the attention is focused on the feasibility, the advantages, and the limitations of using numerical simulation techniques in the study of floating-body motions. Two simulation techniques, the Generalized Arbitrary Lagrangian-Eulerian (GALE) method and the Transient Potential Flow (TPF) method, have been considered. To assess their accuracy and practicality, both methods have been used to calculate the heaving of a semi-submerged circular cylinder in the free surface. The computed hydrodynamic forces, the added masses, and the damping coefficients are in good agreement with linear analytic theory and measurements. The first-order and the second-order TPF methods have also been applied to the forced motions of a rectangular cylinder and some nonlinear effects have been obtained. It has been found that the second-order TPF method is much easier and more economical to use and it can be easily extended to three dimensions.

NOMENCLATURE

- | | |
|--|---|
| <p>A Mean submerged area of a two-dimensional floating body.</p> <p>a A Lagrangian coordinate in the GALE method; the amplitude of the displacement of a heaving cylinder.</p> <p>B Beam width of a two-dimensional floating body.</p> <p>b A Lagrangian coordinate in the GALE method.</p> <p>F_2 Total vertical hydrodynamic force in heaving.</p> <p>\bar{F}_2 Normalized F_2.</p> <p>g Absolute value of the gravitational acceleration.</p> <p>g_x The x-component of the gravitational acceleration.</p> | <p>g_y The y-component of the gravitational acceleration.</p> <p>h Depth of the fluid.</p> <p>i The first suffix in a two-dimensional finite difference system.</p> <p>j The second suffix in a two-dimensional finite difference system.</p> <p>n A superscript denoting the time step in a numerical simulation.</p> <p>\vec{n} A unit normal vector.</p> <p>p Pressure.</p> <p>s A subscript denoting the free surface.</p> <p>T The draft of a floating body.</p> <p>t Time.</p> <p>u The x-component of the velocity.</p> <p>V The volume of a computational cell.</p> <p>v The y-component of the velocity.</p> <p>\vec{v} Velocity vector.</p> <p>x The abscissa of a rectangular cartesian coordinate system.</p> <p>y The ordinate of a rectangular cartesian coordinate system.</p> <p>ω_2 The vertical displacement from the mean position of a heaving cylinder.</p> <p>$\dot{\omega}_2$ The vertical velocity of a heaving cylinder.</p> <p>$\ddot{\omega}_2$ The vertical acceleration of a heaving cylinder.</p> <p>Δt Time increment.</p> |
|--|---|

Δx	Spatial increment in the x-direction.
Δy	Spatial increment in the y-direction.
η	Free surface displacement from its mean position.
λ_∞	The asymptotic wave length.
λ_{22}	Damping coefficient in heave.
$\bar{\lambda}_{22}$	Normalized λ_{22} .
μ_{22}	Added mass in heave.
$\bar{\mu}_{22}$	Normalized μ_{22} .
π	3.14159 ...
ρ	Fluid density.
ϕ	Velocity potential.
ω	Angular frequency of forced oscillations.
∇^2	Laplacian operator.

INTRODUCTION

Since Ursell's (1) work in 1949 on a semi-submerged circular cylinder heaving in the free surface, the problem of forced harmonic oscillations of a rigid body in a fluid with a free surface has received considerable attention by research workers in naval hydrodynamics. The subsequent development of the linearized theory and validation by experiments have been summarized in detail by Wehausen(2). As pointed out by Yeung(3), most of the analytic treatments revolve around two methods of solution: the method of multipole expansions and the method of integral equations. The trend toward obtaining solutions for bodies of arbitrary shape makes the integral-equation method superior to the multipole-expansion method. A successful application of the integral-equation method, however, depends on the availability of a suitable Green's function, which is in general complicated and may not be found easily for arbitrary-shaped bottom of the fluid. In a new approach advanced by Yeung(3), the complicated Green function is replaced by an integral equation for the velocity potential ϕ over the entire fluid boundary. This method has produced results in very good agreement with earlier theories. In addition, this method can be used to calculate the oscillatory motions of a three-dimensional floating body with an arbitrary shape.

Except for the simplest geometry, all analytical approaches must ultimately resort to numerical evaluation of certain series or

integrals and, in some cases, the integral equations can be solved only by solving a large system of linear algebraic equations. In short, even in analytic methods a fair amount of computation is involved. The question then arises whether for some problems it is feasible or even more attractive to construct numerical simulation techniques capable of handling complicated geometries, transients, and non-linear effects. Modern computer systems have been continuously increased in speed while reducing cost, making direct numerical simulations economically reasonable. Furthermore, rapid advancement in numerical techniques, developed in connection with almost every branch of physics, has brought increasing confidence in the accuracy of these methods. Thus it appears that time has come for taking a fresh look at the possibility of developing an efficient and reliable technique which will lead to the solution of the three-dimensional free-surface flows about an arbitrary-shaped floating body.

There are differences between a numerical simulation approach and an analytical one, besides the ease of treating more complex geometric shapes. First, all existing theories formulate the problem in a state of equilibrium oscillation. Thus the correct formulation of an appropriate radiation boundary condition is of vital importance. Although within the realm of linear theory fairly general time variation in the forcing function can be achieved by superposition, non-periodic oscillations can not be easily treated. In a numerical simulation, an initial-boundary-value problem is formulated, with no assumptions regarding the asymptotic behavior of the fluid motion either in time or in space. Consequently, the time variation of the forcing function can be completely general. Second, nonlinear effects, especially those related to the free surface, are much more easily included in numerical simulations(4, 5). Valuable insight can therefore be obtained to assess the limits of linear theories in various problems. Third, additional physics, such as energy dissipation through breaking waves and the effects of the thermocline, can be handled in a straightforward manner in numerical simulations.

In this paper, the attention is focused on the feasibility, the advantages, and the limitations of numerical simulation techniques when applied to the study of floating-body motions. Two simulation methods have been considered: the Generalized Arbitrary Lagrangian-Eulerian (GALE) method(6) and the Transient Potential Flow (TPF) method of Chan and Stuhmiller(7). In the former method, the fluid domain is represented by Lagrangian cells which can follow the fluid motion, while the rigid-body boundaries and the free surface coincide with

the computational mesh lines. In the latter method, a potential flow is assumed and boundary conditions are expanded in Taylor series about the mean position of the boundaries. To assess the accuracy of the simulations, both methods have been used to calculate the heaving of a semi-submerged circular cylinder in the free surface. The TPF method has also been applied to the motions of a rectangular cylinder with the specific objective of analyzing the nonlinear effects. However, no attempt has been made to calculate all possible modes of motion, this being beyond the scope of the present investigation.

NUMERICAL SIMULATION TECHNIQUES

As mentioned above, we have considered two different numerical simulation methods in our present effort to explore the feasibility of such approaches to floating-body problems. The first method is the Generalized Arbitrary Lagrangian-Eulerian (GALE) method (6). Generally, the computation region is divided into a number of quadrilaterals or cells (Figure 1). The cells are set up in such a way that physical boundaries, e.g., the free surface and the boundary between the fluid and a rigid body, coincide with the cell boundaries. The vertices of these cells are designated by the (i, j) suffix system (Figure 2). Associated with

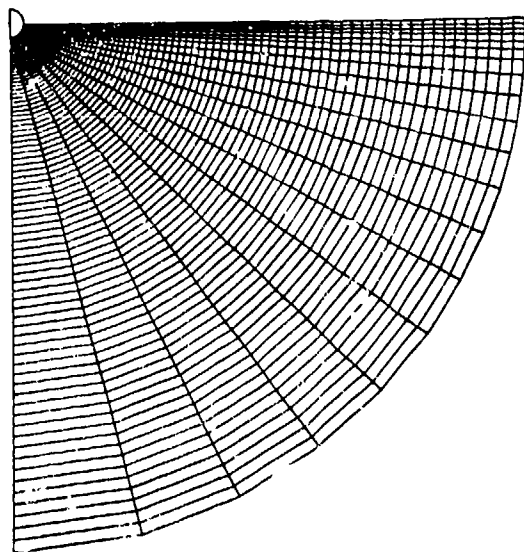


Fig. 1 An Example of Computational Mesh Used in the GALE Method

each vertex are its rectangular cartesian spatial coordinates (x, y) and velocity components (u, v).

At some initial time $t = 0$, a set of initial conditions on the values of (u, v) and (x, y) at

each vertex is needed to begin the calculation. Then the vertices are moved to their new positions according to their instantaneous velocities through a small but finite increment in time Δt . That is,

$$\begin{aligned} x_{i,j}^{n+1} &= x_{i,j}^n + \Delta t \cdot u_{i,j}^{n+\frac{1}{2}} \\ y_{i,j}^{n+1} &= y_{i,j}^n + \Delta t \cdot v_{i,j}^{n+\frac{1}{2}} \end{aligned} \quad (1)$$

where the superscript n refers to the (n)th increment in the time. This is the Lagrangian phase of the motion since the discretized computational elements follow the fluid motion.

The time-centered average velocities $(u_{i,j}^{n+\frac{1}{2}}, v_{i,j}^{n+\frac{1}{2}})$ are defined as

$$\begin{aligned} u_{i,j}^{n+\frac{1}{2}} &= \frac{1}{2} (u_{i,j}^{n+1} + u_{i,j}^n) \\ v_{i,j}^{n+\frac{1}{2}} &= \frac{1}{2} (v_{i,j}^{n+1} + v_{i,j}^n) \end{aligned} \quad (2)$$

To calculate $(x_{i,j}^{n+1}, y_{i,j}^{n+1})$ through the use of Equation (1), the still undetermined advanced time velocities $(u_{i,j}^{n+1}, v_{i,j}^{n+1})$ must be obtained by applying a set of cell equations and appropriate boundary conditions. One of the two governing equations, shown for a typical cell in Figure 2, requires that the volume V of the cell remains unchanged as the calculation proceeds from the (n)th step to the (n+1)th step, that is, the fluid is assumed to be incompressible. In the present problem, the flow is

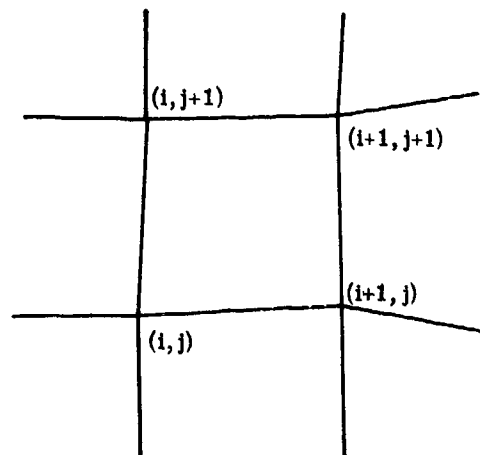


Fig. 2 A Typical Quadrilateral Cell Used in the GALE Method

taken to be inviscid and irrotational, therefore the velocity circulation Γ around any fluid element should vanish at all times. By requiring $\Gamma_{i,j}^{n+1} = 0$ for each cell, one obtains the second cell equation. On rigid boundaries the condition

$$(\vec{v} - \vec{v}_{\text{rigid body}}) \cdot \vec{n} = 0, \quad (3)$$

where \vec{v} is the fluid velocity and \vec{n} is the unit vector normal to the boundary, is applied. Following Brennen and Whitney(8) the Lagrangian equation of motion

$$\left(\frac{Du}{Dt} - g_x \right) \frac{\partial x}{\partial a} + \left(\frac{Dv}{Dt} - g_y \right) \frac{\partial y}{\partial a} + \frac{1}{\rho} \frac{\partial p}{\partial a} = 0 \quad (4)$$

is imposed at a free surface. Here a is a Lagrangian coordinate axis conformed to the free surface (Figure 3); p is the known surface pressure ($\frac{\partial p}{\partial a} = 0$ in the present application) and ρ is the fluid density; g_x and g_y are the x- and y-components of the gravitational accelerations, respectively.

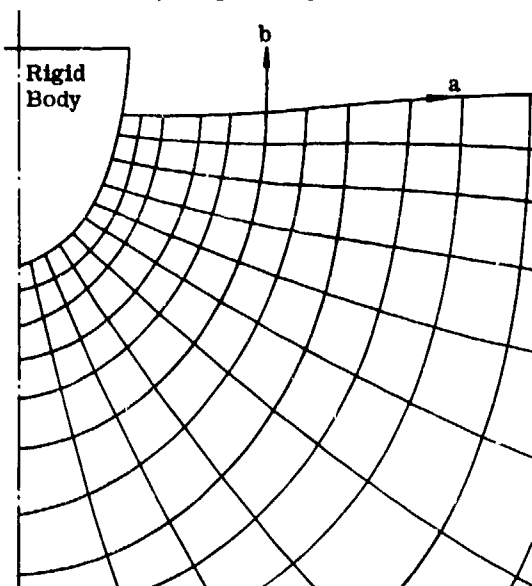


Fig. 3 Lagrangian Coordinate Lines

When written in finite-difference form, Equations (3), (4) and the two cell equations form a system of nonlinear algebraic equations with the set of variables $(u_{i,j}^{n+1}, v_{i,j}^{n+1})$ as the unknowns. The solution can be obtained by employing a Successive Over-Relaxation procedure. The interested readers should refer to Reference (6) for greater details. The procedure outlined above employs the

Lagrangian description of fluid motion.

Theoretically, the process of finding $(u_{i,j}^{n+1}, v_{i,j}^{n+1})$ and $(x_{i,j}^{n+1}, y_{i,j}^{n+1})$ can be repeated for as long as one wishes. In practice, however, the computational cells will be badly distorted or even inverted in regions of highly strained motions. This will severely limit the usefulness of a pure Lagrangian method. To remove this difficulty an automatic rezoning procedure, such as used by Hirt(9), can be employed. The basic idea behind the rezoning technique is to redefine the mesh coordinate system by adjusting the position of vertices at the end of each time increment, so that a nearly optimum shape is always maintained for each cell. In making such adjustment, due consideration is given to the amount of flux that results from moving the mesh lines relative to the fluid. This rezoning capability has the character of an Eulerian mesh system, except that it is more general and flexible. In the present application, the rezoning feature is rarely needed.

The use of circulation and the relatively complicated finite-difference equations will probably limit the use of the GALE method to two-dimensional problems, for in full three-dimensional time-dependent calculations the complexity of difference equations tends to increase appreciably the computing time as well as the computer storage. Consequently, we have considered an alternative approach which has the potential of extension to three dimensions much more easily.

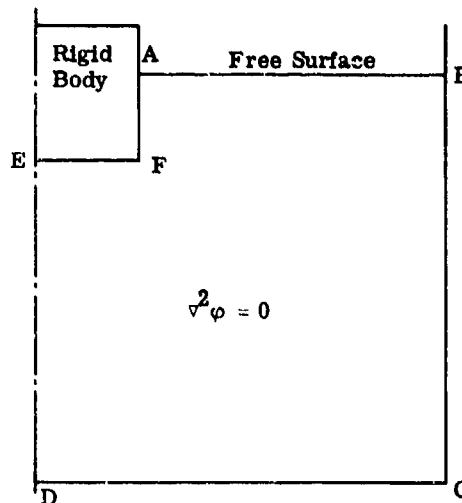


Fig. 4 Formulation of a Potential Flow

The second numerical simulation technique for the problem under consideration is the Transient Potential Flow (TPF) method. As the name implies, in this method we consider the evolution of a potential flow in a region bounded by the free surface, the rigid body or bodies, and the basin that contains the fluid (Figure 4). In the fluid region the Laplace equation

$$\nabla^2 \phi = 0 \quad (5)$$

must be satisfied, and the normal derivative ϕ_n should vanish on all fixed rigid walls. At the free surface and the boundary of the floating rigid body, we assume the displacement of the boundaries from their mean positions is always small but finite. This assumption allows us to apply perturbation expansions of the pertinent boundary conditions about the mean boundary positions. The result is a set of modified boundary conditions to be imposed at the mean position of these boundaries. Consequently, the region in which Equation (5) is to be solved does not change with time; the boundary conditions do change, of course. Aside from the simplicity in geometry, which expedites the numerical solution of Equation (5), the TPF method offers the advantage of calculating the flow in various orders of approximation. For example, if one keeps only the lowest-order terms in the perturbation expansion of the boundary conditions, the classical linearized boundary conditions for the free surface and the rigid-body boundary are obtained. One would then expect a single-frequency sinusoidal forcing function to excite surface waves that are sinusoidal, and the results can be rigorously compared to linear analytic theories. If one carries terms one order higher in the perturbation expansion, then the lowest-order nonlinearity should manifest itself in the solutions.

The TPF method has been described and validated in detail by Chan and Stuhmiller(7). In what follows for the sake of simplicity, we illustrate the general computational procedure involved by using only the first-order, i.e., linearized, boundary conditions. Computational results for both the first-order and the second-order approximations are compared in the next section.

Referring to Figure 4, the appropriate boundary conditions for the forced heave of a rectangular cylinder are

$$\overline{AB} \text{ (free surface): } \frac{\partial \eta}{\partial t} = \frac{\partial \phi}{\partial y} \quad (6)$$

$$\frac{\partial \phi}{\partial t} = -g\eta \quad (7)$$

$$\overline{BC} \text{ (fixed wall): } \frac{\partial \phi}{\partial x} = 0 \quad (8)$$

$$\overline{CD} \text{ (fixed bottom): } \frac{\partial \phi}{\partial y} = 0 \quad (9)$$

$$\overline{DE} \text{ (line of symmetry): } \frac{\partial \phi}{\partial x} = 0 \quad (10)$$

$$\overline{EF} \text{ (bottom of cylinder): } \frac{\partial \phi}{\partial y} = \dot{\alpha}_2(t) \quad (11)$$

$$\overline{FA} \text{ (side of cylinder): } \frac{\partial \phi}{\partial x} = 0 \quad (12)$$

where $\eta(x, t)$ is the displacement of the free surface from its mean level, g is the absolute value of the gravitational acceleration, and $\dot{\alpha}_2(t)$ is defined in Equation (19).

To translate Equations (5)-(12) into a finite-difference scheme, we first divide the computational region into a number of rectangular cells (Figure 5). These cells, unlike those used in the GALE method, remain unchanged in position throughout the entire calculation. The spacing of the mesh lines, both in the x - and the y -directions can be chosen so as to optimize the spatial resolutions. A reasonable choice would be using closely spaced lines near the rigid body while increasing the spacing toward the bottom of the fluid as well as toward the far end of the tank (Figure 5). Of course one should provide adequate resolution for the length of wave under study. For simplicity in this illustration, let us assume that all the cells are rectangles with

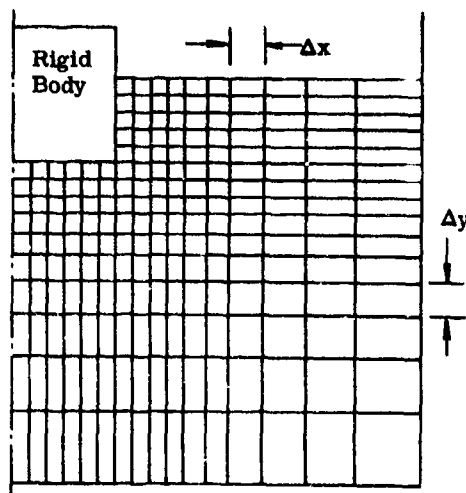


Fig. 5 A Mesh with Variable Spacings

the constant spacings Δx and Δy . Then Equation (5) has the finite-difference representation (Figure 6)

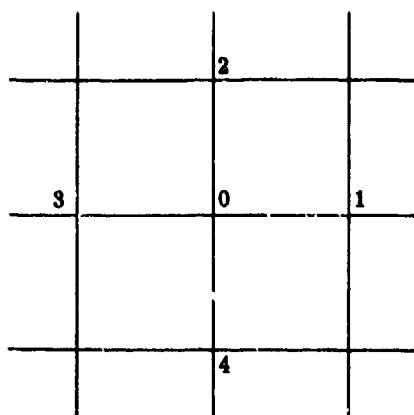


Fig. 6 Typical Cell Setup in the TPF Method

$$\frac{\varphi_1^{n+1} - 2\varphi_0^{n+1} + \varphi_3^{n+1}}{\Delta x^2} + \frac{\varphi_2^{n+1} - 2\varphi_0^{n+1} + \varphi_4^{n+1}}{\Delta y^2} = 0 \quad (13)$$

and Equations (6) and (7) become

$$\eta^{n+1} = \eta^n + \Delta t \left(\frac{\partial \varphi}{\partial y} \right)_s^{n+1} \quad (14)$$

$$\varphi_s^{n+1} = \varphi_s^n - \Delta t g \eta^{n+1} \quad (15)$$

with Δt defined as the time increment and the subscript s denoting the free surface. The right-hand sides of Equations (14) and (15) have been so written to insure numerical stability. A general solution procedure is the following.

First, a provisional value for η^{n+1} is calculated by the explicit formula

$$\eta^{n+1} = \eta^n + \Delta t \left(\frac{\partial \varphi}{\partial y} \right)_s^n \quad (16)$$

Then the value of φ^{n+1} along the free surface is computed by Equation (15). With finite-difference representation of the boundary conditions (8)-(12) on φ^{n+1} , we can now solve Equation (13) by the well-known method of Successive Over-Relaxation(10). This gives us

the entire distribution of φ^{n+1} , from which

$\left(\frac{\partial \varphi}{\partial y} \right)_s^{n+1}$ can be evaluated. Equation (14) is then used to calculate the final value for η^{n+1} . The procedure just described can be repeated to update the flow field from one time step to the

next, for as long as one wishes. At the very beginning of the calculation, one should of course assign a set of initial conditions on φ and η . When the dynamic pressure at the surface of the rigid body is desired, one simply has to evaluate

$$p_{\text{dynamic}}^n = - \left(\frac{\partial \varphi}{\partial t} \right)^n = - \left(\frac{\varphi^{n+1} - \varphi^{n-1}}{2\Delta t} \right) \quad (17)$$

and integrate it along the boundary of interest to obtain the resultant force on the body.

When second-order boundary conditions are included, the numerical integration procedure outlined above remains the same, except that nonlinear terms will appear in Equations (6) and (7). It is then important to write these additional terms in appropriate conservational forms. These derivations are lengthy and the reader is referred to Reference (7).

SAMPLE RESULTS AND DISCUSSIONS

To test the validity of the two numerical simulation methods used in this study, the problem of two-dimensional cylinders oscillating in the free surface has been selected. The calculation on the roll has not been completed at the time of this writing, so that only the results on forced heave of a circular cylinder and the forced heave and sway of a rectangular cylinder are presented here. The comparisons will be based on the amplitude of the dynamic pressure force exerted by the fluid on the hull and the so-called added mass and damping coefficient. Finally, some nonlinear effects will be noted and discussed.

First, the GALE method has been used to calculate the forced heave of a semi-submerged circular cylinder. The vertical displacement of the cylinder from its mean position is given by

$$\alpha_2(t) = a \cos \omega t \quad (18)$$

where a is the amplitude and we used $a = 0.1 \left(\frac{B}{2} \right)$, B being the beam of cylinder.

The frequency of oscillation $\omega \sqrt{\frac{B}{2g}}$ took on the values 0.5, 0.6, 1.253, and 2.0 in a series of computations. Figure 1 shows a typical computational mesh system. Note that this is a set of Lagrangian cells which differs from the usual polar coordinate system in that the mesh lines are not necessarily orthogonal to each other. After the cylinder has undergone four complete oscillations the mesh system appears as shown in Figure 7, in which the

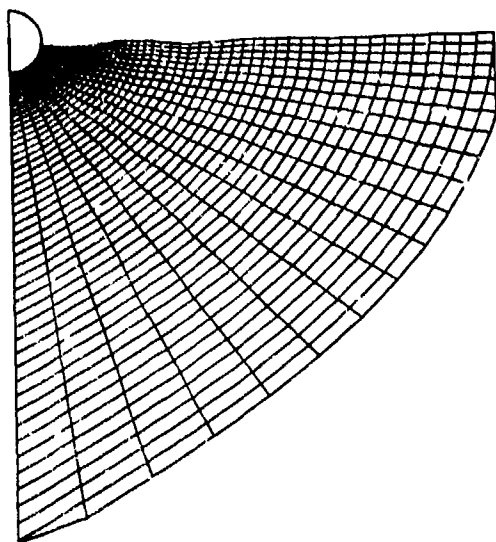


Fig. 7 Mesh Configuration After Four Vertical Oscillations of a Circular Cylinder

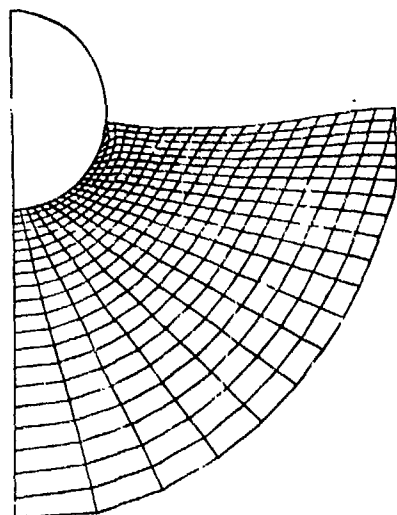


Fig. 8 Close-up of the Mesh System near the Circular Cylinder

disturbances at the free surface can be easily seen. Figure 9 is a close-up of the mesh configuration in the vicinity of the cylinder after three oscillations. The corresponding velocity vectors, drawn at each mesh point, are shown in Figure 9. In this plot the flow field can be visualized at a glance. Figure 10 shows the time history of free surface profiles with the vertical scale exaggerated by a factor of 50. In Figures 7-10 we have used $a = 0.1 \cdot \left(\frac{B}{Z}\right)$ and $\omega \sqrt{\frac{B}{2g}} = 1.253$.

Following the notations used by Yeung (3) and other workers in the field, the total dynamic pressure force in the upward vertical direction is written as

$$F_2(t) = -\mu_{22}\ddot{y}_2(t) - \lambda_{22}\dot{y}_2(t) \quad (19)$$

where the dots denote time differentiation. The added mass μ_{22} and the damping coefficient λ_{22} can be normalized as follows:

$$\bar{\mu}_{22} = \mu_{22}/(\rho A) \quad (20)$$

$$\bar{\lambda}_{22} = \lambda_{22}/(\rho A \omega) \quad (21)$$

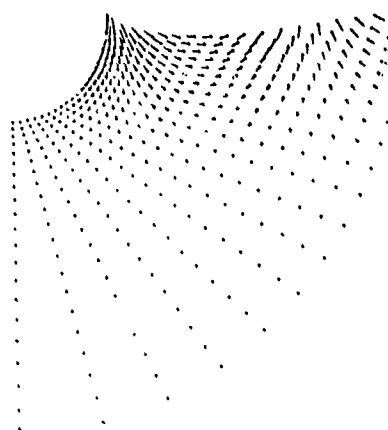


Fig. 9 Velocity Vector Field Corresponding to Fig. 8

Here A is the mean submerged area. The computed added mass and damping coefficient are compared in Figures 11 and 12 with the linear theory of Porter (11) and Frank (12). It is seen that the GALE method, which is a fully nonlinear model, yields added mass in very good agreement with the linear theory in the frequency range considered. The present GALE calculation, however, yields higher values for the damping coefficient.

Let us now consider some applications of the TPF method. This technique has also been used to calculate the problem of heaving circular cylinder for the frequencies $\omega \sqrt{\frac{B}{2g}} = 0.5$, 0.8, and 1.253. In these runs only the first-order TPF method was used and the results on the added mass and the damping coefficient are compared with the linear theory and the GALE results in Figures 11 and 12. The agreement with the linear theory is excellent. The development of the free surface profile as the number of oscillations increases is shown in Figure 13 for the case $\omega \sqrt{\frac{B}{2g}} = 1.253$. It is

interesting to note the establishment of a standing wave pattern near the body and that the asymptotic wave length $\frac{\lambda_\infty}{(B/2)} = \frac{2\pi}{(\omega^2/g)} = 4.0$

is very quickly reached after a few oscillations. The asymptotic amplitude of the outgoing waves, however, is not yet reached at the end of six oscillations. The vertical dynamic pressure force F_2 can be normalized as

$$\bar{F}_2 = \frac{F_2}{\rho g \left(\frac{B}{2}\right)^2} \quad (22)$$

In Figure 14, \bar{F}_2 is shown as a function of time for the heaving circular cylinder. It is quite clear from this plot that $\bar{F}_2(t)$ reaches its asymptotic state only after one oscillation and that $\bar{F}_2(t)$ is indeed a sinusoidal function, which is expected for a first-order method. The amplitude of \bar{F}_2 is 0.18 which is the same as Ursell's theory (1) predicted.

Next, we examine the effect of non-linearity using the problem of a rectangular cylinder heaving in the free surface. Again, $\omega\sqrt{\frac{B}{2g}} = 1.253$ so that $\lambda_\infty/\left(\frac{B}{2}\right) = 4.0$, and the

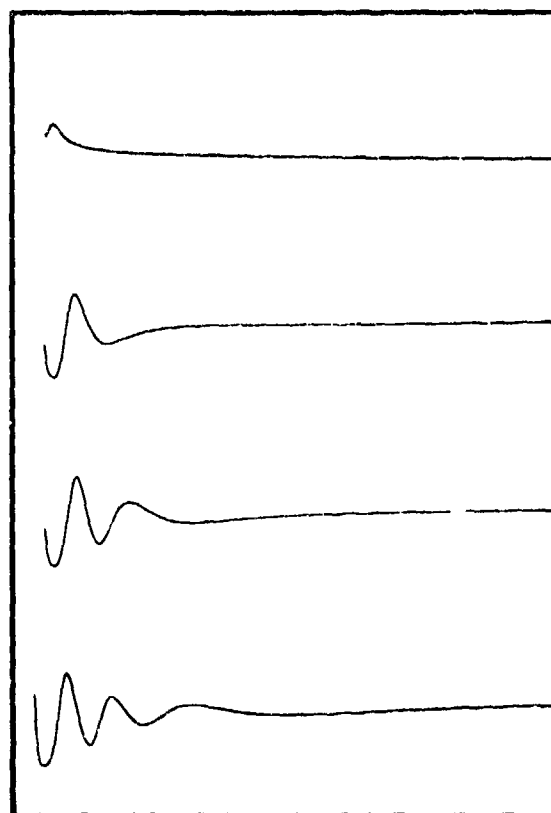


Fig. 10 Computer Output of the Development of the Free Surface Profile

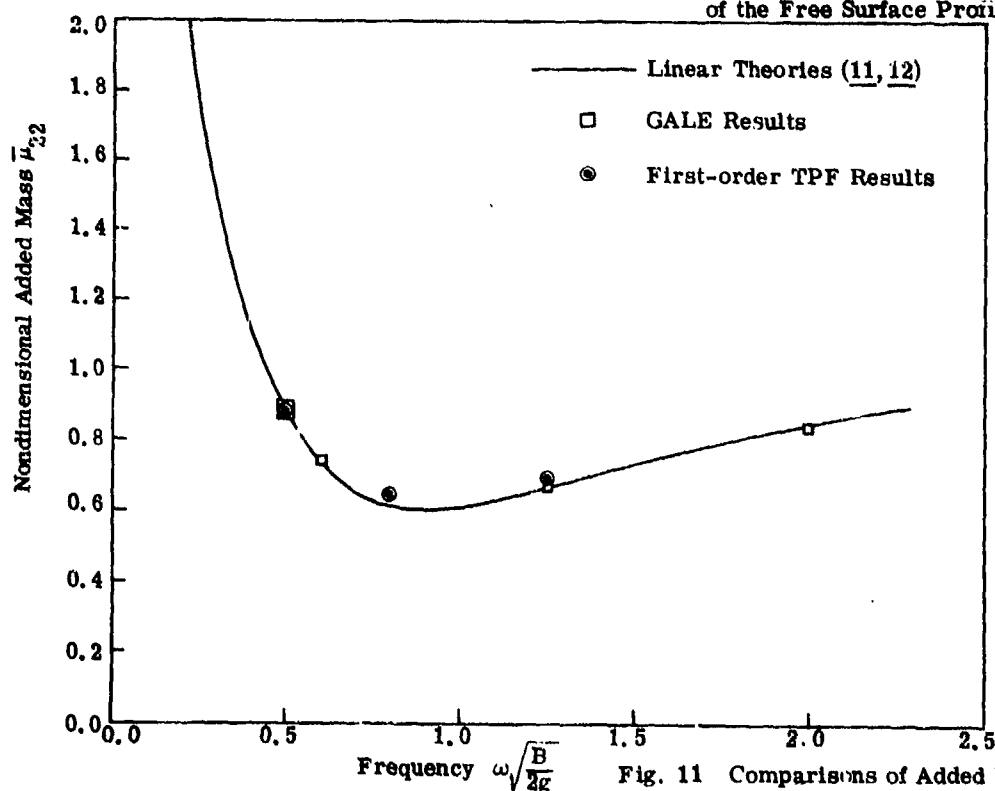


Fig. 11 Comparisons of Added Mass

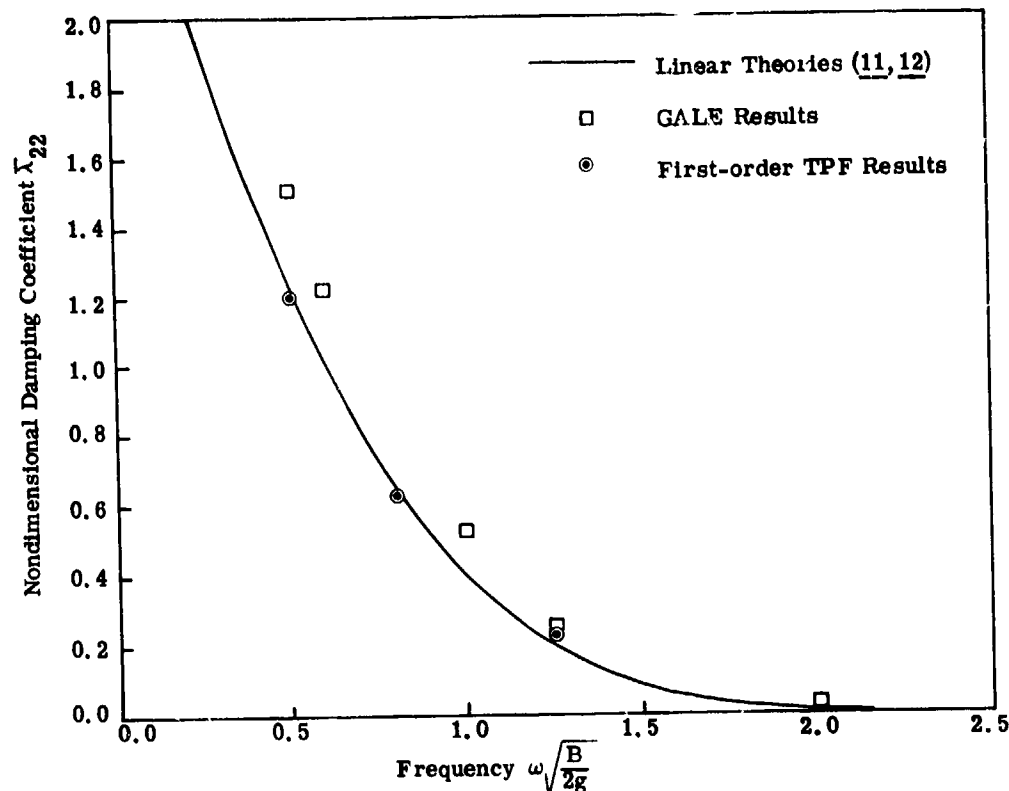


Fig. 12 Comparisons of Damping Coefficients

depth of the fluid is $h/(\frac{B}{2}) = 7.15$. The beam-to-draft ratio is $B/T = 2.0$. Two amplitudes have been considered: $a/(\frac{B}{2}) = 0.1$ and 0.2 .

Both the first-order TPF and the second-order TPF methods have been used so that the nonlinear effects can be studied. Figure 15 compares the free surface profiles between the first-order TPF and the second-order TPF methods at the time when the body has executed three complete oscillations with the amplitude $a/(\frac{B}{2}) = 0.2$. It is seen that there is a substantial difference between the two solutions for waves in the vicinity of the cylinder. This does not seem unreasonable because of the nonlinearity associated with the large amplitude of the body displacement. The discrepancy between the two solutions is expected to decrease for waves radiated far from the body, where the flow is fairly linear. In Figure 16 the time history of $\bar{F}_2(t)$ is compared between the first-order and the second-order TPF calculation for the amplitude $a/(\frac{B}{2}) = 0.1$. Notice first the pure sinusoidal variation of $\bar{F}_2(t)$ obtained from the first-order simulation. The second-order result differs from the first-order in a slight shift in the phase and some skewness in the $\bar{F}_2(t)$ profile. These nonlinear effects become

quite pronounced for the larger-amplitude case, $a/(\frac{B}{2}) = 0.2$, as shown in Figure 17.

Obviously, for non-sinusoidal $F_2(t)$ the decomposition of $F_2(t)$ into components in phase with $\dot{\alpha}(t)$ and $\ddot{\alpha}(t)$ becomes incomplete and meaningless. Nevertheless, for the case $a/(\frac{B}{2}) = 0.1$, the second-order $\bar{F}_2(t)$ does not differ too much from a sinusoidal function so that we may still speak of the added mass and the damping coefficient. For this case, Vugts (13) obtained $\bar{\mu}_{22} = 1.15$ from his experiment and $\bar{\mu}_{22} = 1.01$ from his calculation using Ursell's (1) method. As a comparison, the present second-order TPF calculation yields $\bar{\mu}_{22} = 1.06$ and the first-order TPF gives $\bar{\mu}_{22} = 1.03$. It seems that the second-order TPF method produces results in better agreement with the experiment. As to the damping coefficient, Vugts' experiment gives $\bar{\lambda}_{22} = 0.1$ which is about the same as that obtained by both TPF methods. Of course, at this relatively high frequency ($\omega\sqrt{\frac{B}{2g}} = 1.253$) accurate experimental measurement of $\bar{\lambda}_{22}$ becomes difficult because $F_2(t)$ is almost completely out of phase

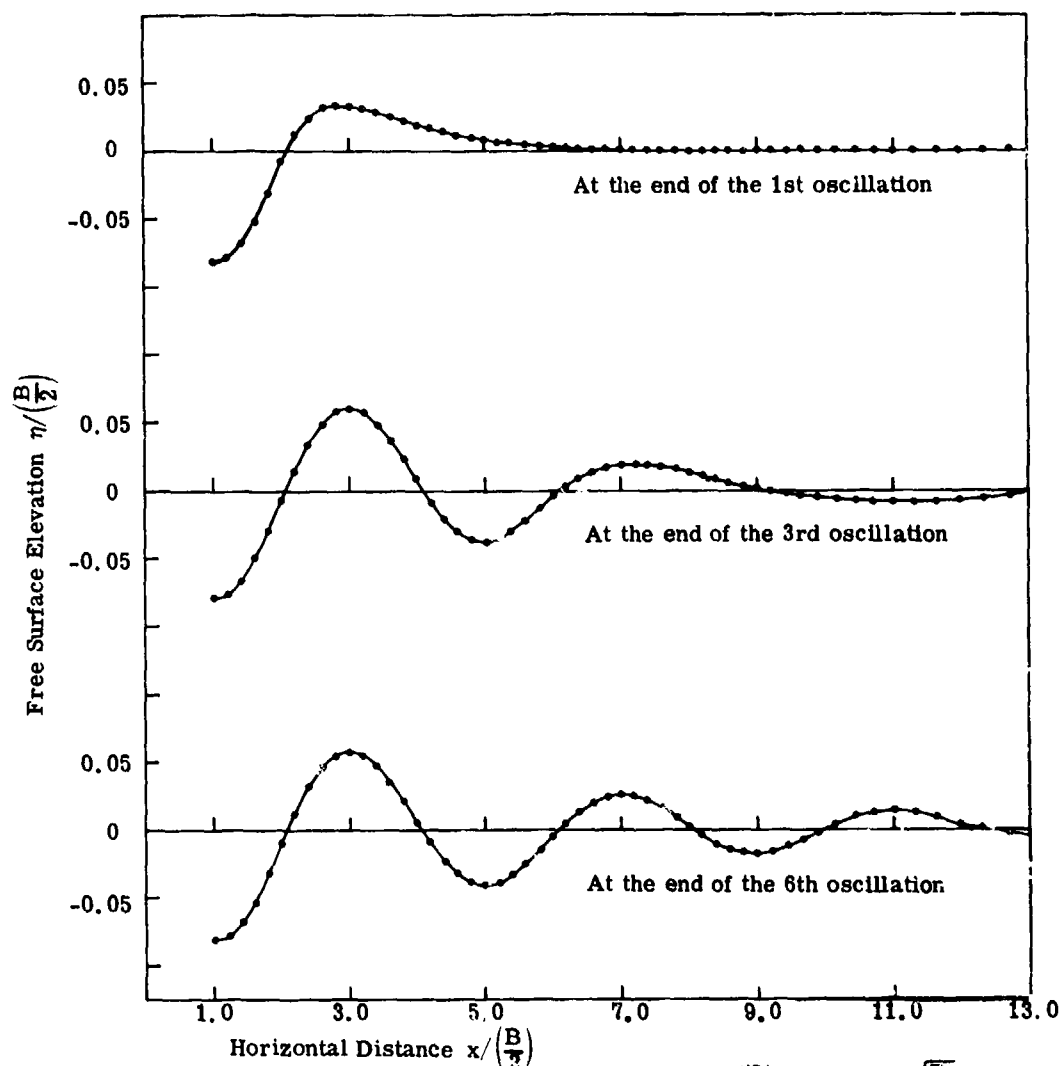


Fig. 13 Free-surface Profiles for a Heaving Circular Cylinder with $a/(B/2) = 0.1$ and $\omega\sqrt{B/2g} = 1.253$

with $\dot{\alpha}_2(t)$ and $\bar{\lambda}_{22}$ is a small quantity.

Finally, we used the first-order TPF method to calculate the flow field of a rectangular cylinder swaying in the free surface, with $\omega\sqrt{B/2g} = 1.253$, $B/T = 2.0$ and the amplitude of the horizontal displacement equals $0.1(B/2)$.

Figure 18 shows the wave profiles, both to the left and to the right of the cylinder, after four oscillations. The reflective tank walls are placed at $x/(B/2) = \pm 14.0$ and the vertical sides of the cylinder are located at $x/(B/2) = \pm 1.0$, but only the waves near the cylinder are shown here. Note that these two wave trains are anti-symmetric to each other about the cylinder, as a linear theory should predict. Furthermore, unlike the heaving motions, the asymptotic amplitude of the wave train is very quickly estab-

lished in this case. The computed wave amplitude ratio, defined as the asymptotic wave amplitude divided by the displacement amplitude, is 1.7, the same as measured by Vugts. The normalized horizontal dynamic force $\bar{F}_{11}(t)$ on the cylinder as a function of time is presented in Figure 19. Similar to the treatment in Equations (19)-(21), we obtain the normalized added mass $\bar{\mu}_{11} = 0.063$, which is close to

Vugts' calculation and measurement. Again, it is difficult to measure this quantity because $\bar{F}_{11}(t)$ is almost completely out of phase with the horizontal acceleration of the cylinder. On the other hand, the damping coefficient $\bar{\lambda}_{11}$ can be determined to greater accuracy. We obtained $\bar{\lambda}_{11} = 0.67$ which agrees with Vugts' calculation using linear theory. Vugts' measurement shows $\bar{\lambda}_{11} = 0.75$. This may be due to some

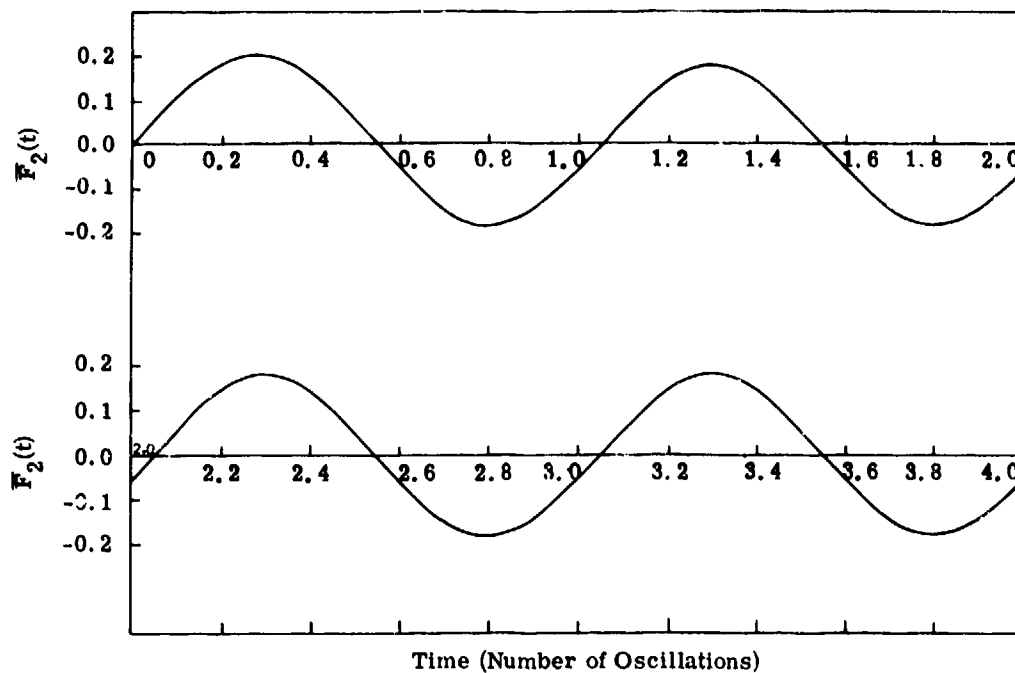


Fig. 14 Time History of the Dynamic Pressure Force for a Heaving Circular Cylinder (First-Order TPF Method)

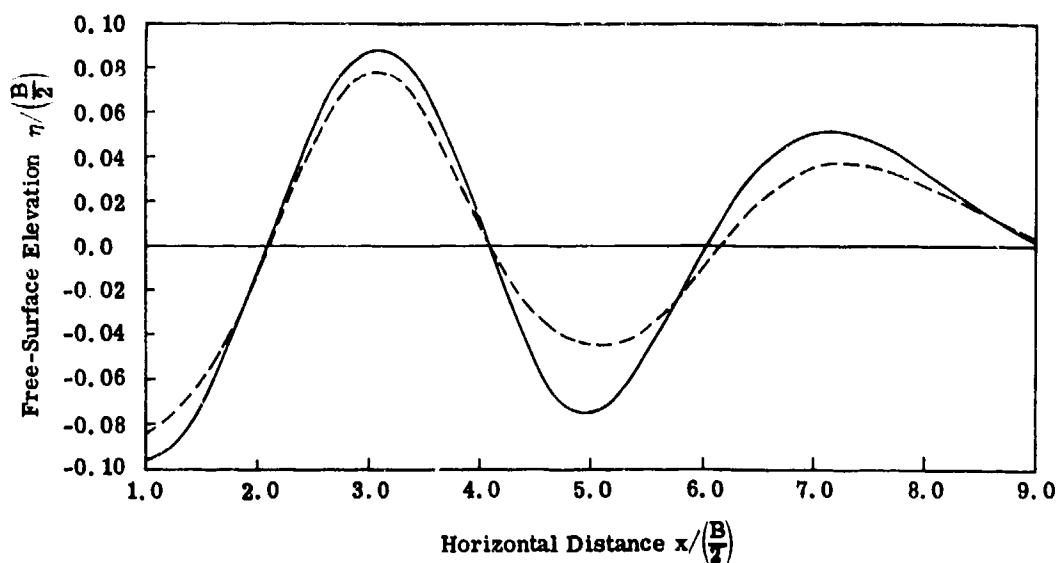


Fig. 15. Comparison of Wave Profiles for a Heaving Rectangular Cylinder at the End of Three Oscillations. (Solid Line: First-Order TPF Method; Dotted Line: Second-Order TPF Method.)

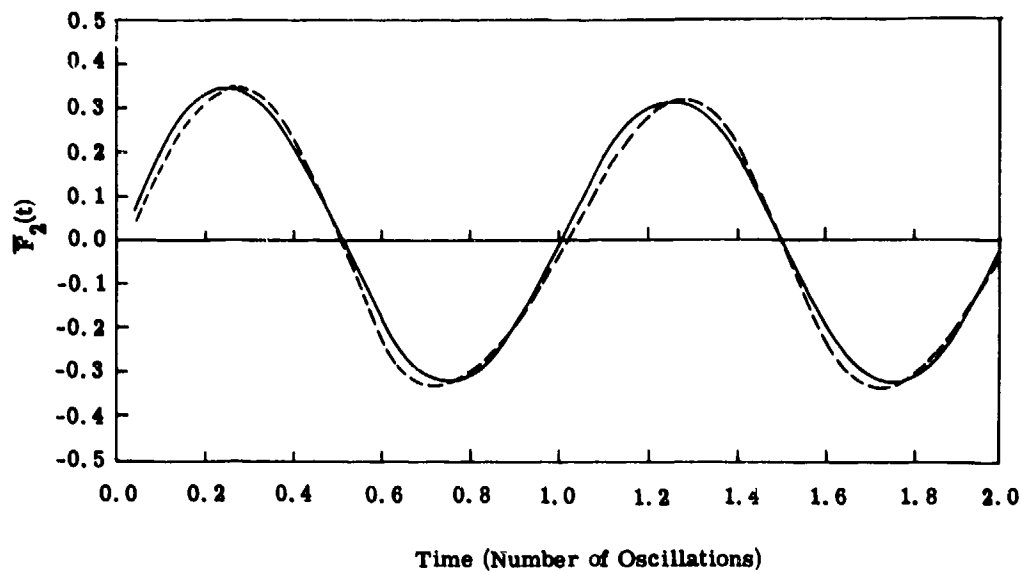


Fig. 16. Comparison of Dynamic Pressure Force for a Heaving Rectangular Cylinder with $a/\left(\frac{B}{2}\right) = 0.1$ and $\omega \sqrt{\frac{B}{2g}} = 1.253$. (Solid Line: First-Order TPF Method; Dotted Line: Second-Order TPF Method.)

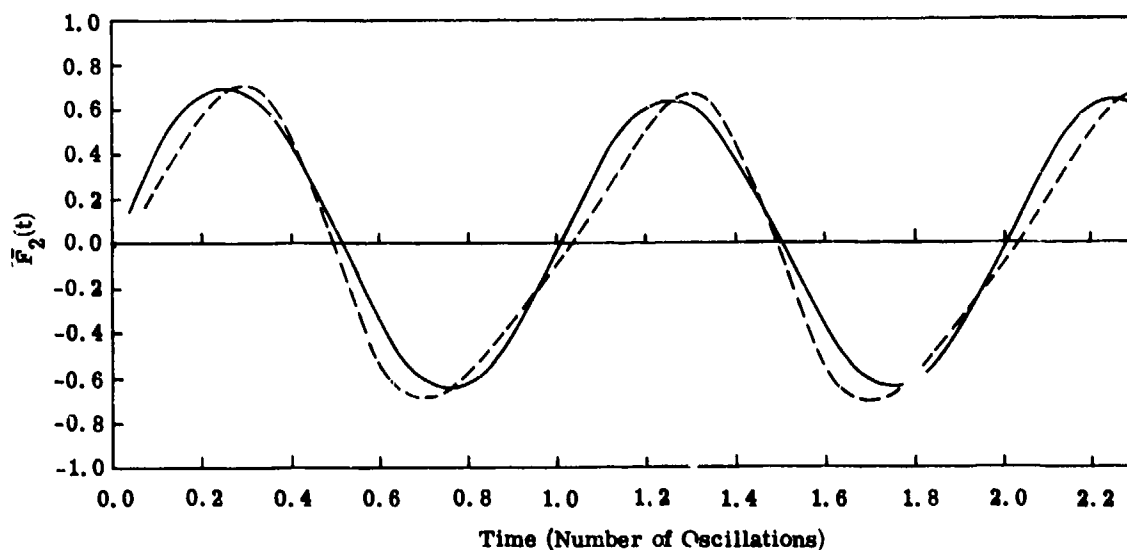


Fig. 17. Comparison of Dynamic Pressure Force for a Heaving Rectangular Cylinder with $a/\left(\frac{B}{2}\right) = 0.2$ and $\omega \sqrt{\frac{B}{2g}} = 1.253$. (Solid Line: First-Order TPF Method; Dotted Line: Second-Order TPF Method.)

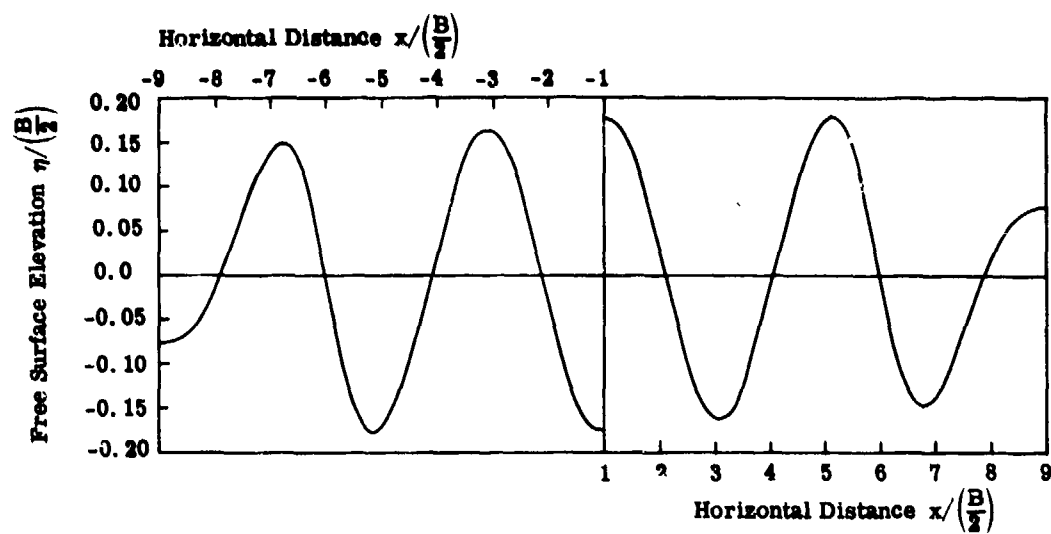


Fig. 18. Wave Profile for a Swaying Rectangular Cylinder After Four Oscillations.

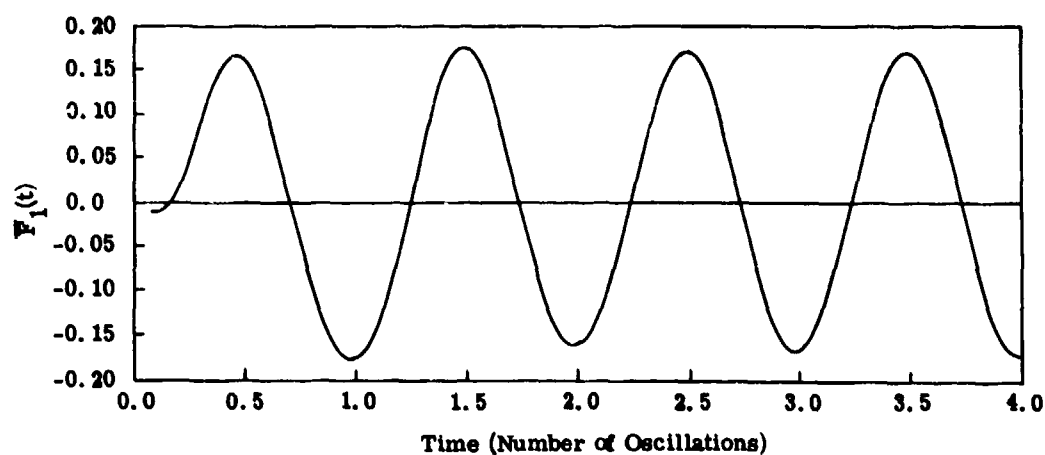


Fig. 19. Horizontal Dynamic Force for a Swaying Rectangular Cylinder.

nonlinearity in the vicinity of the cylinder. However, we defer judgment until we use the second-order TPF method to see if nonlinearity is important in this case.

CONCLUSIONS AND FUTURE EXTENSIONS

In view of the results and discussions presented in the last section, we conclude that

1. Both the GALE and the TPF numerical simulation methods have been successfully used to obtain solutions that are in good agreement with experimental measurements and linearized analytical theory.

2. For small but finite oscillations, the second-order TPF method provides correct nonlinear effects. In general, the TPF method is much easier to use and more economical than the GALE method in studying the motion of two-dimensional floating bodies when viscous effects are neglected. For very large amplitude motions, however, the GALE method is more appropriate.

3. Since the simulation techniques described in this paper are formulated as initial-boundary-value problems, they will have wide applications. For example, the motion of the body can be any prescribed function of time, or the body can be allowed to undergo free oscillations in complicated situations. Furthermore, the geometry of the body and that of the fluid bottom can be quite general; in particular, motion of realistic ship hull sections can be easily simulated.

4. The TPF method, both first-order and second-order, possesses a great potential in studying the motion of three-dimensional floating vessels of complicated shape. The motion is not restricted to the oscillatory type considered in this paper, but it can also be used to calculate the forward motion of ships and related wave resistance.

5. The cost of computation is also quite reasonable. A typical calculation (using the TPF method) to determine the added mass and the damping coefficient for a given frequency requires about one minute of execution in the CDC 7600 system. Of course, it will be more expensive for more complicated body shapes and for general three-dimensional simulations. It should be pointed out that, although the cost of time-dependent simulations appears to be higher than that required for the linear analytic theories in general, we do gain the complete generality in the geometry and the type of motion to be studied, as explained in the last paragraph. Furthermore, once a general computer program is set up, very little effort is required to modify it to apply to various types of problems related to the ship motion.

ACKNOWLEDGMENTS

This work has been supported by the Office of Naval Research under contract N00014-73-C-0128. Appreciation is due Ms. Ellen J. Fredricksen for her assistance in the development of TPF computer codes.

REFERENCES

1. Ursell, F., "On the Heaving Motion of a Circular Cylinder on the Free Surface of a Fluid," Quarterly Journal of Mechanics and Applied Mathematics, Vol. 2, 1949, pp. 218-231.

2. Wehausen, J. V., "The Motion of Floating Bodies," Annual Review of Fluid Mechanics, Vol. 3, 1971, pp. 237-268.

3. Yeung, R. W.-C., "A Singularity-Distribution Method for Free-Surface Flow Problems with an Oscillating Body," Report No. NA 73-6, 1973, College of Engineering, University of California, Berkeley.

4. Chan, R. K.-C. and Street, R. L., "A Computer Study of Finite-Amplitude Water Waves," Journal of Computational Physics, Vol. 6, No. 1, 1970, pp. 68-84.

5. Street, R. L., Chan, R. K.-C., and Fromm, J. E., "Two Methods for the Computation of the Motion of Long Water Waves - A Review and Applications," Proceedings of the 8th Symposium on Naval Hydrodynamics, Pasadena, California, ACR-179, Office of Naval Research, Department of the Navy, 1970, pp. 147-187.

6. Chan, R. K.-C., "A Generalized Arbitrary Lagrangian-Eulerian (GALE) Method for Incompressible Flows with Sharp Interfaces," SAI-73-575-LJ, November 1973, Science Applications, Inc., La Jolla, California, to be submitted to the Journal of Computational Physics.

7. Chan, R. K.-C. and Stuhmiller, J. H., "Transient Potential-Flow Calculations of Free Surface Flows," SAI-74-548-LJ, May 1974, Science Applications, Inc., La Jolla, California, to be submitted to the Journal of Ship Research.

8. Brennen, C. B. and Whitney, A. K., "Unsteady, Free Surface Flows: Solutions Employing the Lagrangian Description of the Motion," Proceedings of the 8th Symposium on Naval Hydrodynamics, Pasadena, California, ACR-179, Office of Naval Research, Department of the Navy, 1970, pp. 117-145.

9. Hirt, C. W., "An Arbitrary Lagrangian-Eulerian Computing Technique," Proceedings of the Second International Conference on Numerical Methods in Fluid Dynamics, Berkeley, 1970; Lecture Notes in Physics, Springer-Verlag, Berlin, 1971.

10. Forsythe, G. E. and Wasow, W. R., Finite Difference Methods for Partial Differential Equations, John Wiley and Sons, Inc., New York, 1960

11. Porter, W. R., "Pressure Distributions, Added Mass, and Damping Coefficients for Cylinders Oscillating in a Free Surface," Report No. 82-16, 1960, Institute of Engineering Research, University of California, Berkeley.

12. Frank, W., "Oscillation of Cylinders In or Below the Free Surface of Deep Fluids," Report No. 2375, 1967, Naval Ship Research and Development Center, Department of the Navy.

13. Vugts, J. H., "The Hydrodynamic Coefficients for Swaying, Heaving and Rolling Cylinders in a Free Surface," International Shipbuilding Progress, Vol. 15, 1968, pp. 251-276.

DISCUSSION

NILS SALVESEN

The authors have developed two new numerical methods for solving the two-dimensional problem of a cylinder oscillating in the free surface. The GALE method treats the complete nonlinear free-surface condition, while the TPF method is a perturbation scheme carried out to the second-order.

It is shown that the second-order perturbation method agrees in the linear range with linearized methods and that for steeper waves, the results have the characteristic features of second-order solutions; however, no comparisons have been performed with other nonlinear results. Particularly, it is unfortunate that the two methods presented here have been applied to two different problems, so that no comparison between the complete nonlinear method and the perturbation

method can be made. It is impossible therefore to make any judgment at this time with regard to how accurately the nonlinear effects can be predicted by these methods.

For example, it is seen in Figure 12 that for a case with rather small disturbances the damping coefficient obtained by the complete nonlinear method, the GALE method, is as much as 25% larger than predicted by linear theory. It is questionable whether this large difference between the nonlinear and linear results is actually caused by nonlinear free-surface effects or if it is due to numerical inaccuracies. I would welcome the authors' view on this point.

I would also like to use this opportunity to congratulate the authors with their valuable contribution and I hope they will have the opportunity in the near future to evaluate more precisely these new promising methods for solving nonlinear free-surface problems.

AUTHOR'S REPLY

We appreciate Dr. Salvesen's careful review of our paper which reveals a few questions that we did not look into because of the scope of the study when this paper was written. We agree with Dr. Salvesen in that comparisons with other nonlinear results are essential to validate the numerical models proposed here.

In answering the question on the 25% difference in the damping coefficient between the calculations using the GALE method and the linear theory, we should say that, since cross-checks with higher-order perturbation methods have not been made, there is no simple way of ascertaining its accuracy. There are, however, two considerations which seem to indicate that the use of damping coefficient as a basis for comparison can be misleading. First, for even a weakly nonlinear problem the decomposition of the

dynamic pressure on the body into a component in phase with the acceleration (the added mass) and another in phase with the velocity (the damping coefficient) is not complete, because higher frequency components are also present. Second, we found a slight phase shift in the dynamic pressure, as a function of time, of the nonlinear GALE calculation as compared to the linear result. This phase shift is primarily responsible for the difference in the damping coefficient, which, in other words, is a fairly sensitive quantity. If we use the dynamic pressure as a basis for comparison, then the GALE calculation shows an amplitude approximately 10% larger than that of the

linear theory for $\omega \sqrt{\frac{B}{2g}} = 1.0$. This difference is consistent with $ka = \frac{\omega^2}{g} a = 0.1$.

THREE-DIMENSIONAL TURBULENT BOUNDARY LAYERS

J. Kux

Institut für Schiffbau der Universität Hamburg
2 Hamburg 60, Lammersbeth 90, Germany

ABSTRACT

There are now a series of methods for calculation of three-dimensional boundary layers applicable to the flow over ship hull surfaces. The formulation of the equations in general coordinate systems on curved surfaces implies the use of differential geometric relations. The question of geometry and general coordinate systems are reviewed. A short discussion of semi-empirical modeling in order to achieve closure of the equations is included considering the generalization to the three-dimensional case. The importance of integral methods and the definition of integral parameters for these methods is stressed. The velocity profiles generally assumed in order to obtain a relation between the integral parameters are presented. No numerical methods or schemes are discussed.

NOMENCLATURE

a	= constant	ℓ_s	= dissipation length
$a^{\alpha\beta}, a_{\alpha\beta}$	= surface metric tensor	n	= constant
a^{α}, a_{α}	= base vectors of surface coordinate system	Q	= magnitude of the velocity vector
$b_{\alpha\beta}, b_{\beta\alpha}$	= surface curvature tensor	\bar{p}^2	= square of length of superimposed turbulent velocity vector
C	= constant	Re_τ	= turbulent Reynolds number
g	= function describing cross flow	u^{α}, u^{β}	= turbulent velocity
g_{ij}, g^{ij}	= metric tensor in general surface induced coordinate system	v^{α}	= general vectorial quantity
g^{α}, g_{α}	= base vectors in general coordinate system	U^{α}, U^{β}	= mean velocity
G, H', H''	= empirical functions	\bar{x}^i	= cartesian coordinates defining surface
\mathcal{H}	= mean curvature of surface	x^{α}	= coordinates on surface
h_{α}, h_{β}	= metrical coefficients (orthogonal coordinates)	x^{β}	= coordinate normal to the surface
\mathcal{F}	= geometrical function	β	= angle between outer flow direction and limiting streamline
\mathcal{K}	= Gaussian curvature of surface	δ	= boundary layer thickness
k, k', k''	= constants	$\delta^*, \delta^+, \delta^-$	= displacement thickness in three-dimensional boundary layer
l_m	= mixing length	$\delta_m, \delta_u, \delta_v, \delta_t$	= momentum-loss thickness in three-dimensional boundary layer
		δ_{α}^{β}	= Kronecker symbol
		$\epsilon, \epsilon_1, \epsilon_2$	= eddy viscosity
		κ	= v. Kármán constant
		μ	= viscosity
		ν	= kinematic viscosity
		τ	= magnitude of shear stress
		τ_{ij}	= shear stress tensor
		τ_1, τ_2	= components of shear stress vector
		φ	= dissipation
		<u>Suffixes</u>	
		D	= diffusion
		e	= outer edge of boundary
		w	= wall

INTRODUCTION

Boundary Layers in Naval Hydrodynamics

A review of the present status of our knowledge on three-dimensional turbulent boundary layers is impossible to be given in a talk of half an hour. Considering this, it shall be given a synopsis of methods and tendencies of development as they appeared in the last years.

From the broad spectrum on which three-dimensional turbulent boundary layer research work is being done, three rather narrow domains will be treated here: 1. basic facts about geometry and curvature, 2. the extension of the modeling methods used in two-dimensional problems, and 3. integral methods.

The numerical methods of solution applied in differential and in integral methods will not be discussed. Out of scope there will remain some special new methods were relationships for the development of a length scale are searched for and also all those rather important questions as transition, separation and compressibility. Compressibility may not be discarded any more, since water containing a certain percentage of air-bubbles is far from incompressibility.

For those that have to apply boundary layer calculation methods, it is of the most outstanding importance, to be provided with methods of easy and broad applicability. A method to be tailored to fit the needs of every hull to be investigated, is not a satisfactory solution. Notwithstanding we are almost at this stage and not further. Many methods for boundary layer calculation use the flow lines of the outer inviscid flow, or the curvature lines on the body, or at least orthogonal coordinates.

The naval architect has been provided with excellent and powerful methods for the calculation of the inviscid outer flow field. These panel methods, pioneered by the work of A.H.O. Smith et al. (1), work with no more than a point array on the wall surfaces as input. Any coordinate lines are obsolete. The methods are, as pointed out by Argyris (2), finite element methods; in fact they were the first finite element methods to appear and they happened to appear in hydrodynamics, not in structural analysis. So it would not be too immodest to ask for a finite element boundary layer method. There is none, as far as I know, though I am sure it will come soon, probably along lines similar to those in a paper by Oden and Wellford Jr. (3).

Considering that once the inviscid flow problem is solved for two directions of the incident flow, by the principle of superposition the flow field for every angle of attack may be constructed, it seems by far too expensive if for the boundary layer calculation it would be necessary to construct a special coordinate system for each case. Coordinates fixed to the body seem therefore desirable, although, in special cases, streamline coordinates may present considerable advantages.

If the same body is to be investigated under different conditions of trim and draft, again the coordinate system should be one fixed to the body.

There are modern books, even on hydrodynamics (4), that provide a great deal of the formalism of differential geometry necessary to work with non-orthogonal curvilinear coordinates on curved surfaces. And that is exactly what is required. The point array, as prepared as input for the inviscid flow calculation program should be enough. The points of the array considered as points of intersection of the coordinate lines provide a system of wall-coordinates. In addition, the formulae of differential geometry, given in tensor notation are well suited for programming. I am afraid that there is a kind of reluctance against the use of this notation, what implies that scientists and engineers are not too familiar with this nomenclature. Through appropriated polynomial approximations of the surface, like the bicubic spline (5) approximation, the metric tensor (6), curvature parameters and related magnitudes may easily be computed. They are to be kept in storage, the same than coordinates or the pressure gradient, at disposition of the boundary layer program running in the computer.

This pleading for general coordinates must be appended by a short warning. Of course it has to be taken care, not to start with input data leading to ambiguous coordinates, intersecting coordinate lines of the same family, etc. It should be kept in mind also, that the question of the dimensional character of the magnitudes, of how to define natural or physical components of tensorial magnitudes is not a trivial one (7) in nonorthogonal coordinates.

Classification of boundary layer methods

As there is a profusion of calculation methods a principle of classification would be welcome. There are various, and it is a matter of taste according to which aspect to classify. The methods may be classified according to

1. whence the turbulent shear stresses are put in relation to the mean flow or are determined

through an approximation of a suitable transport equation

2. which equations are considered (e.g. the energy equation is included or not)
3. whence the differential equations are attacked directly with a numerical algorithm (differential methods) or this is performed after a previous integration process (integral methods)
4. Simplifying assumptions, approximations or empirical relationships used (e.g. eddy viscosity model)
5. the order of approximation

The third aspect is the one generally considered first. It was indeed an almost revolutionary idea to integrate the boundary layer equations along the coordinate normal to the surface. A new kind of quantities describing the layer, the so called integral parameters arose. Information on the details of the flow like profiles of velocity and shear stresses, is lost. In fact the engineer is generally not interested in the detailed description of the flow in the domain occupied by the layer, but wants information about forces to be expected, about wall friction, or about the displacement of flow due to the presence of the boundary layer. Integral methods yield this information as well as differential methods. The reduction of the number of independent variables by one is a decisive advantage, though not as striking as in the two-dimensional case, where the resulting equations become ordinary differential equations.

GEOMETRY, COORDINATES, BASIC EQUATIONS

Basic Facts on Nonorthogonal Coordinates

Let us consider a curved surface to be given in our three-dimensional physical space. The latter one is, at least for our purposes, perfectly euclidean, flat. The surface given is on the contrary a two dimensional curved space, which will impose its crooked nature to the flow on its vicinity. In an over all cartesian coordinate system, the surface is given by

$$\vec{x}^i = \vec{x}^i(x^1, x^2);$$

capital latin indices (referring always to this system) will run from 1 through 3. These coordinates are functions of x^1 and x^2 , the wall-coordinates. The base vectors on the surface, defined as

$$\vec{a}_i = \frac{\partial \vec{x}^i}{\partial x^i}$$

are, generally speaking, functions of the

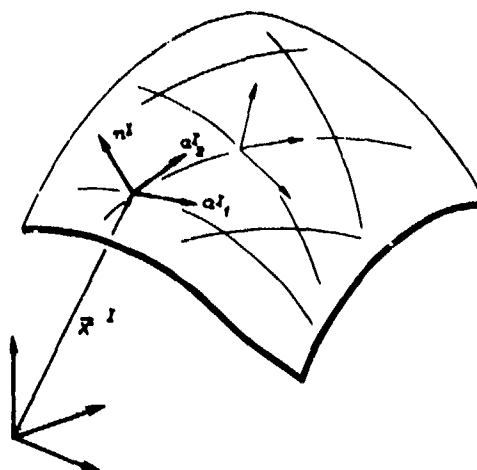


Fig. 1 Coordinate Systems

coordinates again, their direction in three-dimensional space changes under translation. Greek indices have values of 1 or 2. The surface metric tensor is obtained through

$$a_{ij} = \vec{a}_i \cdot \vec{a}_j = \left(\sum_k \frac{\partial \vec{x}^k}{\partial x^i} \frac{\partial \vec{x}^k}{\partial x^j} \right) \quad i, j = 1, 2$$

We make the convention that the appearance of two identical indices in a product implies summation over their value-range.

With the help of

$$a^{ij} a_{jk} = \delta^i_k = \begin{cases} 1 & \text{if } i=k \\ 0 & \text{if } i \neq k \end{cases}$$

a tensor a^{ij} is defined. It is the contravariant surface metric tensor. Every vector v^i on the surface is expressible as

$$v^i = a^i_j v^j$$

In nonorthogonal coordinates one has to distinguish the covariant components v_i (index in the lower position) and the contravariant components v^i (index in the upper position) of a given vector; the two forms of the metric tensor giving the connection between them

$$v^i = a^{ij} v_j, \quad v_i = a_{ij} v^j$$

i.e. the metric tensor may be used to raise or lower indices. In order to formulate differential equations in this twodimensional system, we need a rule for obtaining derivatives in curvilinear coordinates. This is no problem with a scalar, but vectors and tensors suffer a twofold change due to an infinitesimal displacement. They eventually variate as

functions in relation to the local base vectors and in addition these base vectors may have suffered a change in direction. In order to compensate for the latter effect, the so called covariant derivative is introduced. In the case of a vector it reads

$$v^{\alpha}_{;\beta} = v^{\alpha}_{,\beta} + \Gamma^{\alpha}_{\beta\gamma} v^{\gamma}$$

the symbols in brackets being called "Christoffel-symbols" of the second kind. They are essentially the components of the rate of change of the base vectors projected onto these same base vectors.

If we project these alterations of the base vectors, due to an infinitesimal translation, onto the surface normal, we get a tensor b^{α}_{β} which we will term the curvature tensor. Clearly, if the surface is plane, even with extremely curved lines on it, the base vectors will never change in such a way as to render a component out of the plane. b^{α}_{β} is by this means a measure for the degree of curvature of the surface, not in an invariant form, not intrinsic to the surface, but depends on the coordinates chosen. The trace and the determinant of b^{α}_{β} , known as mean curvature \mathcal{H} and as Gaussian curvature \mathcal{K} , provide us with invariant curvature measures. It is clear that the metric and the Christoffel-symbols are always dependent on the system and do not reflect explicitly intrinsic surface characteristics. (A celebrated theorem by Gauss shows their connection with curvature.)

If we now look for an appropriate wall oriented three-dimensional coordinate system, it is obviously practical to choose the normal to the wall surface as third coordinate axis, the third coordinate x^3 being zero on the surface. In this new general three-dimensional coordinate system a metric tensor $g_{\alpha\beta}$, $g^{\alpha\beta}$ and a covariant differentiation $v^{\alpha}_{;\beta}$ are defined in a similar way than on the surface. Lower case latin indices refer to this three-dimensional system, running from 1 to 3. On the surface the base vectors g^{α}_{β} of the new system coincide with the base vectors a^{α}_{β} , but the base vectors for different points on the same normal, in general will not be parallel any more.

Through the construction of this coordinate system a connection is given between its metric and the metric and curvature tensors of the surface. This relation is carried over to the covariant derivatives. A differential equation, formulated in the three-dimensional system may be split into its surface components and its normal component. In the equations there will only appear metrical quantities referring to the surface. In this way one becomes able to apply an

order of magnitude analysis to the different terms of the equations considering the geometrical peculiarities of the surface.

Certain research activity in the past has been inverted into the development of transformations comparable to the well known Mangler-transformation. This transformation takes an axially symmetric problem over into a plane one. In the light of differential geometry this reduces to the problem of determining geodesic coordinates on the surface. We are taught, that locally this is always possible.

There is another way to treat three-dimensional vector fields, starting with the concept of the (vector-) field-line. Vector fields in three dimensions have been analyzed under the special consideration of their intrinsic description by Marris and Marris and Passman (9). Their contribution to the understanding of the geometry of vector fields may raise new methods.

The normal and geodesic curvature of a streamline on a surface may be evaluated, if the surface or its spline approximation are given (9).

The basic equations

Turbulence still remains one of the problems to be solved. It is usual to split the motion of the flow into a mean component and a superimposed turbulent motion $V^{\alpha} + u^{\alpha}$. With this construction equations are derived both, for the mean flow field and for turbulent quantities. These equations are not independent. The turbulent motion appears as Reynolds shear stresses in the momentum equation of the mean flow. If a transport or rate equation for the shear stresses is added, one is faced with the fact that now triple correlations appear, and so on. This is the well known problem of closure. It lead to the physical modeling of expressions for the unknown terms, promoting the development of a variety of calculation methods. This modeling is of course empirical.

In terms of the notation developed we obtain as basic equations:

the equation of continuity

$$V^{\alpha}_{;\alpha} + \frac{1}{\mathcal{H}} (\mathcal{H} V^3)_{,3} = 0$$

and the equations of momentum for the mean flow

$$\begin{aligned} \rho (V^{\alpha}_{;\beta} V^{\beta} - b^{\alpha}_{\beta} V^{\beta} V^{\beta} + V^{\alpha}_{,3} V^3) \\ = -\mathcal{H}_{,\alpha} \tau^{\alpha} + \frac{1}{\mathcal{H}} (\mathcal{H} \tau^{\alpha})_{,\alpha} + \tau^{\alpha}_{,3} - b^{\alpha}_{\beta} \tau^{\beta} \end{aligned}$$

$$\begin{aligned} g(V^i_j V^j + b_{ij} V^i V^j + V^i_{,i} V^j) \\ = -\mathcal{P}_{,i} + \frac{1}{\mathcal{F}} (\mathcal{F} \tau^{ij})_{,i} + b_{ij} \tau^{ij} + \tau^{ij}_{,i} \end{aligned}$$

$$\text{with } \tau^{ij} = \mathcal{K} (V^i_{,i} g^{ij} + V^j_{,i} g^{ij}) - \mathcal{F} \overline{u^i u^j}$$

$$\text{and } \mathcal{F} = 1 - 2\mathcal{H}x^3 + \mathcal{H}(x^3)^2$$

These equations apply to the stationary flow of an incompressible Newtonian fluid, external body forces assumed to be zero, but are otherwise quite general. In order to apply the covariant differentiation on the surface and to perform integrations through the layer, we should shift vectorial and tensorial quantities down to the surface. In the equations given, the mentioned quantities are to be considered as shifted to the surface. We do not make any difference in notation here between a magnitude before and after the shifting.

For the sake brevity only the rate or transport equation for the kinetic energy of the turbulent motion will be given:

$$\begin{aligned} V^j (-\frac{\overline{q^2}}{2})_{,j} + V^j (\frac{\overline{q^2}}{2})_{,i} &= \\ \text{convection} \\ -(\overline{u^i} [\frac{\overline{q^2}}{2} + \frac{\overline{q^2}}{2}])_{,i} - \frac{1}{\mathcal{F}} (\mathcal{F} \overline{u^i} [\frac{\overline{q^2}}{2} + \frac{\overline{q^2}}{2}])_{,i} &= \\ \text{diffusion} \\ + \overline{u^i u^j} V_{i,j} - \overline{u^i u^j} b_{ij} V^j - \overline{u^i u^j} b_{ij} V^i - \overline{u^i u^j} V_{i,i} &= \\ \text{production} &- \overline{u^i u^j} U_{i,j} - \overline{u^i u^j} U_{i,i} \\ + \varphi &= \\ \text{dissipation} \end{aligned}$$

with $\overline{q^2} = \overline{u^i u^i}$ and \mathcal{P}' as the turbulent variation of pressure superimposed to \mathcal{P} . The dissipation φ has not been written down explicitly in order to keep the equations presented down to a reasonable length.

The equations for the transport of the Reynolds stresses have a similar structure, though the tensorial character of the stresses implies the appearance of additional terms. The equation for the energy is the most simple in structure because the energy is a scalar, the covariant derivative reducing to the usual derivative and the dependence on curvature disappearing. We distinguish the terms describing convection, production, diffusion and dissipation.

To derive the boundary layer equations, an order of magnitude analysis of the different terms in the basic equations is performed and the simplification achieved by discarding the terms

of lower order of magnitude. In general coordinates there are now terms present in the equations which reflect the peculiarities of these coordinates. If one wants to conserve generality, nothing can be said concerning their order of magnitude.

On curved surfaces it is easy to find local characteristic lengths of the problem: the radii of curvature. Therefore a good reference quantity for an order of magnitude analysis will be the product of mean curvature \mathcal{H} and boundary-layer thickness δ . This product is assumed to be small as compared to one and in a first order theory all the terms of an order of magnitude equal to $\mathcal{H}\delta$ and smaller are discarded. In a second order theory (10) (11), terms with an order of magnitude not smaller than $\mathcal{H}\delta$ will be retained. This is the usual procedure. There is a certain difficulty in assigning the exact order of magnitude to the terms of the transport or rate equations. The order of magnitude of the shear stresses is assumed to be at most $\mathcal{H}\delta$ (12).

The equations obtained for the boundary layer as the momentum equations for the mean motion (to a first order of approximation) are:

$$\begin{aligned} g(V^i_j V^j + V^i_{,i} V^j) &= -\mathcal{P}_{,i} a^{ij} + \tau^{ij}_{,i} \\ 0 &= -\mathcal{P}_{,i} + \tau^{ij}_{,i} \end{aligned}$$

The rate equation for the turbulent kinetic energy is

$$\begin{aligned} V^j (-\frac{\overline{q^2}}{2})_{,j} &= -\frac{1}{\mathcal{F}} (\mathcal{F} \overline{u^i} [\frac{\overline{q^2}}{2} + \frac{\overline{q^2}}{2}])_{,i} + \overline{u^i u^j} U_{i,j} \\ &+ \varphi \end{aligned}$$

An interesting feature is, that in the rate equations for the shear stresses not given here, in a first order theory, only production and dissipation terms would be present, leading to a local equilibrium model for the turbulence. As this is in fact misleading, one should ask if boundary layer theories of the first order are an appropriate description at all, once one has accepted to take into account the history of turbulent motion through a rate equation.

MODELS AND DIFFERENTIAL METHODS

Semiempirical Modeling

It has early been attempted to circumvent the lack of closure of the disposable equations by modeling. Modeling is not new. As there is no exact molecular theory for the viscosity, Newton's law of friction also is an empirical model. We have almost forgotten this, because of the wide range

of applicability of that law.

Modeling can be done at different levels: at the mean flow level or at the level of the rate equations. It can be done in integral equations as well as in differential equations.

Some methods have tried to introduce an empirical relation between Reynolds stresses and mean flow. More recent methods using the kinetic energy equation for the turbulence, postulate a relation between the shear-stresses and this kinetic energy. Those models, which promise to be of some success also in three-dimensional boundary layers, will be reviewed shortly.

Eddy viscosity model. Here a relation similar to that of Newton in laminar flow is sought:

$$-\overline{u'u'} = \epsilon_1 \nabla^2 u,$$

$$-\overline{u'u'} = \epsilon_2 \nabla^2 u,$$

Good results have been obtained though the hypothesis is questionable: in the turbulent case the momentum transfer should be performed by fluctuating motions with a length scale small as compared with the scale of spatial variation of $\nabla^2 u$. Sometimes the eddy viscosity is considered as a scalar ($\epsilon_1 = \epsilon_2 = \epsilon$).

Mixing-length hypothesis. It assumes

$$\epsilon = \ell_m \nabla \quad \nabla = \{(\nabla^2 u)^2 + (\nabla^2 v)^2\}^{1/2}$$

i.e. the magnitude of the rate of strain vector with ℓ_m , the mixing length, equal to .09 times the boundary layer thickness δ in the outer part of the layer and proportional to the normal coordinate near the wall. (Fig. 3).

The whole tensor of turbulent shear stresses may not be represented by means of an eddy viscosity, the normal stresses requiring a separate treatment. This has been pointed out by Hinze (13).

The experiment by So and Mellor (14) has shown, that as the influence of curvature (at least convex curvature) increases, the eddy viscosity assumption loses its validity.

Relationship between shear stress and turbulent kinetic energy

This relationship has been searched for along two different lines: one expressing the eddy viscosity, assumed to be scalar, as a function of the turbulent kinetic energy, and another one as a direct relationship.

The first assumption is realized through

$$\epsilon = \epsilon_0 H'(R_T) \quad \text{with} \quad R_T = \frac{\sqrt{\overline{q^2}} \cdot \ell}{\nu}$$

as turbulent Reynolds number.

ℓ may be the dissipation length and H' is an empirical function (15).

The alternative direct relation would be of the form

$$-\overline{u'u'} = \alpha \overline{q^2} \nabla^2 u / \nabla$$

$$-\overline{u'u'} = \alpha \overline{q^2} \nabla^2 u / \nabla$$

using the magnitude of the rate of strain vector

Modeling of the turbulent kinetic energy equation

The diffusion and the dissipation terms have to be modeled. The energy diffusion takes place through two processes: transport by the convective motion of the turbulence and transport by the action of pressure fluctuations.

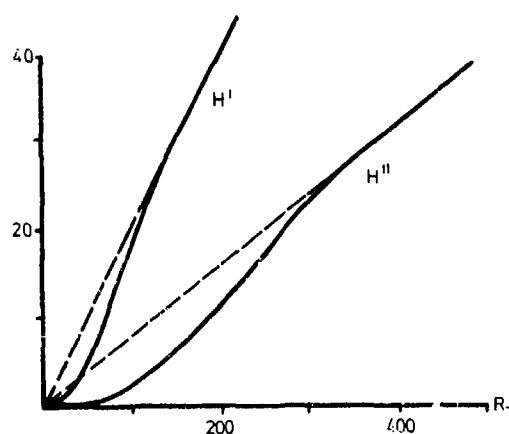


Fig. 2 Empirical Functions

We differentiate between two models which have been proposed: The gradient diffusion, where it is assumed that (15)

$$\frac{\overline{u'u'}}{2} + \frac{\overline{u'u'}}{\rho} = \nu (1 + H'(R_T)) \left(\frac{\overline{q^2}}{2} \right),$$

with another empirical function H'' , and the bulk diffusion, where

$$\frac{\overline{u'u'}}{2} + \frac{\overline{u'u'}}{\rho} = \left\{ \begin{array}{l} A \cdot (\overline{q^2})^{1/2} \cdot \sin[(\overline{q^2})^{1/2}] \\ G \cdot (\overline{q^2}) \cdot (\overline{q^2}_{max})^{1/2} \end{array} \right.$$

The latter model needs the empirical function G . q_{max} is the maximum value in the outer three quarters of the layer

at the particular station.

These models, derived for two-dimensional mean flow, should extend to three-dimensional flows because turbulence as an instantaneous phenomenon is perfectly three-dimensional.

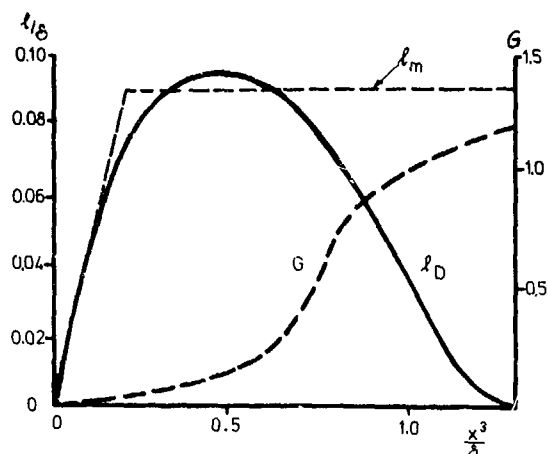


Fig. 3 Empirical Functions

The dissipation is modeled with the aid of a dissipation length (16)

$$\psi = (\bar{q}^2)^{1/2} / l_D$$

or through the aid of the same empirical function H^* used in the diffusion term:

$$\psi = \nu \cdot C (1 + H^*(R_+)) \cdot \bar{q}^2 / \ell$$

C being a constant and ℓ an equivalent to l_D .

Modeling of the Reynolds-stress equations.

These equations are now included more and more into calculation procedures, though about the individual terms much less is known than about the corresponding terms in the turbulent kinetic energy equation. Though questionable, it is usual to neglect the second order production terms. The pressure-strain terms are those describing the principal mechanism of shear stress reduction. Models proposed are of the form

$$k \overline{u^2 u^2} (\bar{q}^2)^{1/2} / l_D$$

or

$$k' \overline{u^2 u^2} \psi_{11} - k'' \overline{u^2 u^2} (\bar{q}^2)^{1/2} / l_D$$

Differential Methods

Many different methods have been developed using certain combinations of the basic equations just discussed. The application of the turbulent kinetic energy equation has been favoured first but the information provided by the shear-stress transport equations seems to be estimated higher. Some methods (17), (18), allow for control of the sensitivity of the alignment of the shear stress direction in response to a change of the main strain-rate vector.

One of the main difficulties to day, if one wants to assign figures of merit to different methods, is the lack of experimental data. So nothing decisive may be said in favour or against determined approaches.

INTEGRAL CALCULATION METHODS

On the Definition of Integral Parameters

The development of these methods progressed along lines which are to be considered as extrapolations or extensions of two-dimensional concepts. Two almost astonishing points happened to be accepted without criticism, both referring to the definition of integral parameters, as displacement thickness, momentum-loss thickness, etc. Their definition for plane flow is

$$\delta^* = \int (1 - \frac{U'}{U_e}) dx$$

$$\delta^* = \int \frac{U'}{U_e} (1 - \frac{U'}{U_e}) dx$$

where the coordinate x' is the one perpendicular to the wall and the subscript e refers to the edge of the boundary layer. For axially symmetric flows along bodies of revolution they should be defined as

$$\delta^* = \int (1 - \frac{U'}{U_e}) (1 + \frac{x^2}{x_0^2}) dx$$

$$\delta^* = \int \frac{U'}{U_e} (1 - \frac{U'}{U_e}) (1 + \frac{x^2}{x_0^2}) dx$$

neglecting longitudinal curvature and with $x_0 = x_0(x)$ as the local radius of the rotationally symmetric body. The additional factor takes into account the increase in broadness of the space between two adjacent normals as one proceeds in outward direction. There is more space available for the outer parts of the layer than there is for the parts adjacent to the wall. Nevertheless, as far as I know, such additional factors have never been introduced in the definitions for the integral parameters in three dimensions. They are generally given as:

$$\delta_1 = \frac{1}{Q_e} \int_0^{\infty} (V_e^1 - V^1) dx^1 \quad \delta_2 = \frac{1}{Q_e} \int_0^{\infty} (V_e^2 - V^2) dx^2$$

$$\delta_{12} = \frac{1}{(Q_e)^2} \int_0^{\infty} \int_0^{\infty} V^1 (V_e^1 - V^1) dx^1 dx^2 \quad \delta_{21} = \frac{1}{(Q_e)^2} \int_0^{\infty} \int_0^{\infty} V^2 (V_e^2 - V^2) dx^2 dx^1$$

$$\delta_{12} = \frac{1}{(Q_e)^2} \int_0^{\infty} \int_0^{\infty} V^1 (V_e^1 - V^1) dx^1 dx^2 \quad \delta_{21} = \frac{1}{(Q_e)^2} \int_0^{\infty} \int_0^{\infty} V^2 (V_e^2 - V^2) dx^2 dx^1$$

$$\text{with } Q_e = \{ (V_e^1)^2 + (V_e^2)^2 \}^{1/2}$$

In the three dimensional case, the factor omitted would read

$$\gamma = 1 - 2 \cdot \mathcal{H}(x^1) + \mathcal{K}(x^1)^2 \approx 1 - 2 \cdot \mathcal{H} \cdot x^1$$

with mean curvature \mathcal{H} and Gaussian curvature \mathcal{K} . The discussion might be of academic interest if first order approximations are considered to be allowable; it will become important as the second order is considered.

The second objection relates to the question of the physical meaning of the integral parameters. Displacement along the normal to the wall is just one thing, and it is surprising to find two displacement thicknesses. Momentum in a boundary layer which has been reduced by integration to a two dimensional skin without a dimension perpendicular to the wall, is expected to be a vectorial quantity with two components. We are faced with four momentum-loss thicknesses.

Applying a thorough analysis to the procedure used in the two-dimensional case, Moore (19) and Lighthill (20) derived what may really be called the three-dimensional displacement-thickness. Similarly there has been made a proposition for the definition of a two-component momentum-loss thickness and a scalar energy-loss thickness with a sound physical meaning (21).

Integral thicknesses have usually been defined in close analogy to the two-dimensional case. Admittedly it is not surprising, that curvature effects were neglected in the definitions in first order theories. On the other side it is worthwhile to reflect on the way these thicknesses may be defined. Lighthill (20) gives four alternative theoretical treatments for the real displacement thickness. This emerges as one magnitude which is the distance the inviscid outer flow is displaced. He gives the expression:

$$\delta = \delta_1 + \frac{1}{Q_e} \int_0^{\infty} \delta_2 dx^2$$

showing the connection with the integral parameters as usually defined. The question has been taken up by Gersten (22) recently including higher order curvature and compressibility effects. Expansions in powers of the displacement thickness are given leading to more involved equations. The generalization to other thicknesses has been given in (21).

One possibility to define these is comparing different flow magnitudes as massflow, momentum flow, energy flow in the boundary layer through a nearly cylindrical or prismatic control surface perpendicularly intersecting the boundary layer. Suitably this surface is taken to be a developable surface formed by the normals to the wall surface through the points of a closed curve on the wall bounding an

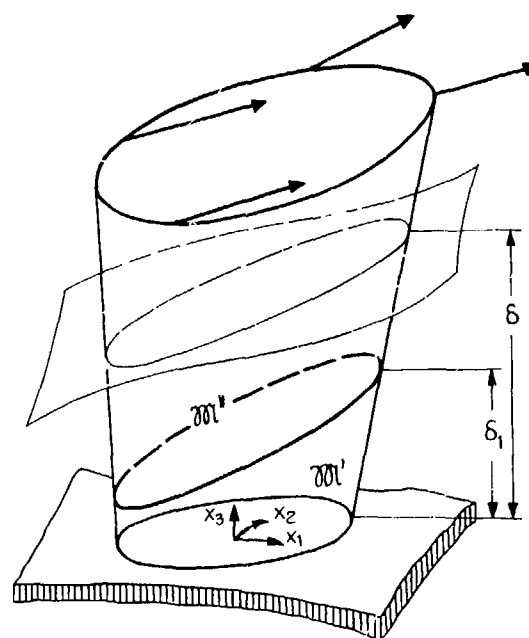


Fig. 4 Control surface for the definition of integral boundary layer parameters

infinitesimal domain there. Due to the curvature of the wall, the control surface will depart more or less from a prismatic or cylindrical shape. In the case of momentum flow $\rho V^1 V^2$ one may define the momentum loss thickness by equating the net flow of the real fluid through the whole surface with the net flow of the inviscid fluid taken over a portion m' of the control surface alone, down to a certain limit, precisely the thickness one is searching for

$$\iint_{\sigma} \rho V_e^* U_e^* V_n d\sigma = \iint_{\sigma} \rho V^* U^* V_n d\sigma$$

$$\sigma = \sigma_1 + \sigma_2$$

$$\beta = 1, 2$$

V_n is the normal on the control surface.

This thickness appears as the lower limit of integration over the normal coordinate in the lefthand side in this equation and depending on the order of the curvature may be extracted with more or less exactitude from there.

With $\delta \approx 1$ the defining equation for δ , the momentum-loss thickness, may be written (not to be summed over α)

$$[V_e^* U_e^* \delta]_{\eta\beta} = \int (V_e^* U_e^* - V^* U^*) dx', \eta\beta$$

Again the connection between the two kinds of integral parameters is readily established. From this point of view it will be indifferent, which kind of definition to choose as starting point of a calculation method. On the other side there are two advantages: 1) The fewer integral parameters appearing, the fewer empirical relations are needed to complete the set of equations (the closure problem in integral methods). 2) If a second iteration step is to be performed, the subsequent calculation of the inviscid outer flow has to be done with the body thickened by the real displacement thickness.

The equations for the second kind integral parameters seem to be less involved than those for the first kind, even for curved surfaces. A calculation procedure in terms of this second kind of parameters is not yet available. The equations for the integral parameters of the first kind read for orthogonal curvilinear coordinates:

$$V_e^* \delta_{111} + \frac{1}{\delta_1} \delta_{112} + (2\delta_{11} + \delta_1) V_e^{*1} + (\delta_{11} - \delta_{12}) V_e^{*2} \frac{\delta_{11}}{\delta_1} = \frac{\tau_{1w}}{\rho(V_e^*)^2}$$

$$V_e^* \delta_{111} + \frac{1}{\delta_1} \delta_{112} + 2\delta_{11} V_e^{*1} + (\delta_{11} + \delta_{12} + \delta_1) \frac{1}{\delta_1} \frac{V_e^{*1}}{V_e^*} + 2\delta_{11} V_e^{*2} \frac{\delta_{11}}{\delta_1} = \frac{\tau_{1w}}{\rho(V_e^*)^2}$$

Where a series of assumptions has been made:

The x^* coordinate has been taken in the direction of the projection of the streamlines of the external flow on the surface of the body and identified with the velocity potential leading to $\delta_1 = 1/V_e^*$. δ_1 and δ_2 are the geometrical coefficients. They are the remaining diagonal components of $a_{\alpha\beta}$ in the orthogonal case being considered. Thus the equations given are the momentum equations in the "streamwise" and "cross-flow" directions. In these streamline coordinates also

$$V_e^{*2} \equiv 0 \quad \text{and} \quad \delta_{12} = \delta_{21} - \delta_2$$

a reduction of the number of unknowns by one. (Compare (12)).

The relationships between the integral parameters are generally derived assuming a definite form for the velocity profiles in both directions. Having a definite formula for the profile form, the integral parameters are easy to be related, the parameters of the profile formulae remaining as variables to be determined.

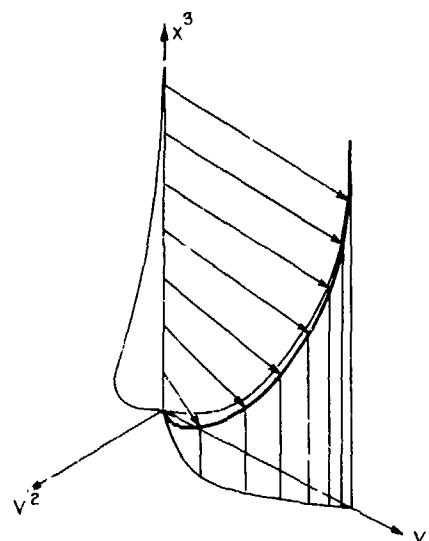


Fig. 5 Three-dimensional Mean Velocity Profile

Generally streamline orientations are chosen. Then $V_e^{*2} \equiv 0$ and V^* becomes the so called cross flow, the flow at right angles to the mean flow direction at the outer boundary-layer edge.

This method of assuming determinate velocity profiles, even with some parameters to adjust, is not very comforting. The idea in integral methods is precisely not to make any assumption about the profiles. Nevertheless, as far as other questionable empirical laws are avoided through this, it must be accepted.

Velocity Profiles

The following profiles deserve mention:

Streamwise velocity profiles. There are first the one parameter profiles. The best known is the power law profile

$$\frac{v'}{v_e} = \left(\frac{x'}{\delta}\right)^{1/n}$$

where in two-dimensional problems the exponent n varies from about 7 at zero pressure gradient to 2 near separation.

Further there is a series of two parameter profiles. Among these also profiles are classified which are made up from the law of the wall and the wake law:

$$\frac{v'}{v_e} = \frac{v_\tau}{v_e} \left[f(x'^{+}) + \frac{v_\tau}{v_e} w\left(\frac{x'}{\delta}\right) \right]$$

with $v_\tau = (\tau_w/\rho)^{1/2}$, the friction velocity, $x'^{+} = \frac{v_\tau x'}{\nu}$,

and the two laws mentioned are approximated through

$$f(x'^{+}) = \frac{1}{\kappa} (\ln(x'^{+}) + C)$$

$$\kappa = .41(\theta), \quad C = 2.3$$

$$w\left(\frac{x'}{\delta}\right) = 1 - \cos\left(\frac{\pi x'}{\delta}\right)$$

It must be stressed, that this is the more in error, the larger the wall cross flow angle becomes. Indeed the value v_τ should be regarded as a free parameter since it is neither related to the resultant wall shear stress nor its component in streamwise direction. It is generally accepted, that the logarithmic law of the wall holds for the velocity component in wall shear stress direction and not for the streamwise direction. A measured streamwise profile is not appropriate to give information about the skin friction by means of a Clauser plot, if there is any cross flow.

Notwithstanding this objections, the profile has been applied, assuming v_τ as equal to the friction velocity. Further it must be pointed out, that κ and C are constants, with values empirically found, and these values are not beyond any discussion. Including these "constants", the profile would emerge as a four parameter profile.

Cross flow profiles. The model of Prandtl:

$$\frac{v'}{v_e} = g\left(\frac{x'}{\delta}\right) \tan \beta$$

with an universal function g satisfying $g(0) = 1$, $g(1) = 0$ and β as the angle between outer edge flow direction

and limiting wall stream line, i.e. wall shear stress direction.

The proposal of Mager (23) for g is

$$g = \left(1 - \frac{x'}{\delta}\right)^2$$

The triangular cross flow profile of Johnston (24) deserves mention:

$$\frac{v'}{v_e} = \left\{ \frac{v_\tau}{v_e} \tan \beta \right. \left. \left(1 - \frac{v_\tau}{v_e}\right) \tan \alpha \right\} \text{ whence } \frac{v'}{v_e} \left\{ \begin{array}{l} < \\ > \end{array} \right\} \left(\frac{v'}{v_e} \right)_p$$

The index p referring to the apex of the triangle:

$$\left(\frac{v'}{v_e} \right)_p = \left\{ 1 + \frac{\tan \beta}{\tan \alpha} \right\}^{-1}$$

The proposition of Coles (25) is:

$$\frac{v'}{v_e} = \frac{v_\tau}{v_e} \left[\cos \alpha w f(x'^{+}) + \frac{v_\tau}{v_e} w\left(\frac{x'}{\delta}\right) \right]$$

$$\frac{v'}{v_e} = \frac{v_\tau}{v_e} \left[\sin \alpha w f(x'^{+}) + \frac{v_\tau}{v_e} w\left(\frac{x'}{\delta}\right) \right]$$

with f and w as already defined and with α_w as the angle between wall shear stress direction and the first coordinate base vector and v_τ , v_τ as two constants or components of a vectorial

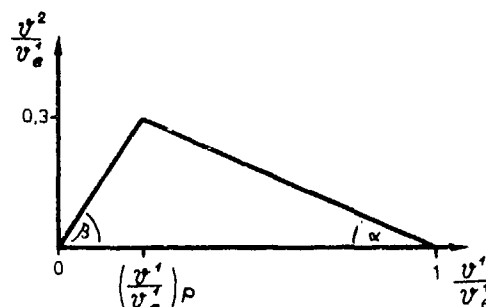


Fig. 6 Johnston Polar Plot

quantity to be adjusted in a relation as to ensure that for $x' = 1.5$ the free stream direction is obtained.

Remarks on existing methods

Myring (26) has presented an integral calculation method with application of the power-law profile for the component in mean flow direction and the Mager and Johnston cross-flow-profiles. The assumption of orthogonal streamwise oriented coordinates is abandoned and the equations are formulated for a general coordinate system.

The numerical calculation schemes that are applied to the equations may be of different forms. They will not be discussed in detail, but it should be kept in mind, that the numerical solution is by no means a trivial side of the problem and the convergence of iterations and the stability conditions pose severe restrictions on the methods, the mesh-sizes, etc.

Himeno and Tanaka (27) applied the vectorial model of Coles for the velocity profile to ship hull surfaces in an integral method using the moment of momentum equation in the direction of the coordinate along the water lines on the hull. The shearing stresses are represented with a scalar eddy viscosity

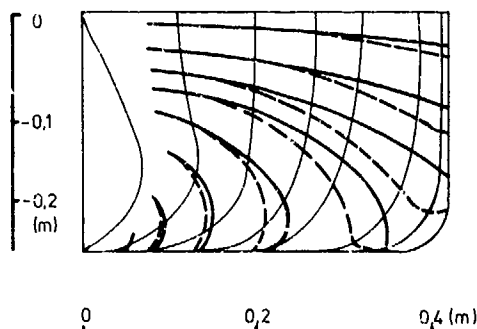


Fig. 7 Streamlines on Ship Hull Surface (Model)

taken to be a polynomial in x' as distribution function. The results are interesting and encouraging. The figures show qualitatively the limiting streamlines found and the distribution of boundary layer parameters along a determined potential line. The limiting

streamline direction compares favourably with model measurements.

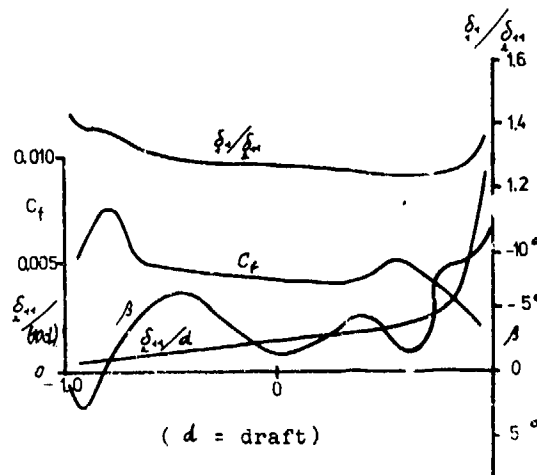


Fig. 8 Parameters of Boundary Layer along Potential Streamline

CONCLUDING REMARKS

The state of the art is, that research work on the theoretical side has rendered a number of quite different methods for a thorough treatment of three-dimensional boundary layers, some of them well developed, some just appearing on the scene. It is not possible at the moment to evaluate their merits at all, and because of the empirical assumptions involved, comparison with the experiment will decide. Experimental data is needed covering a broad domain of interesting geometrical forms. In his review on the boundary layer research in the decade from 1960 to 1970, A.M.O. Smith (28) was able to state that the maturity of the computer was the event believed to be of greatest importance on the field. Looking forward experimental data, possibly the laser anemometer may prove to be a comparable progress.

REFERENCES

1. Hess, J.L. and Smith, A.M.O., "Calculation of Potential Flow About Arbitrary Bodies", *Progress in Aeronautical Sciences*, Vol. 8, D. Kuchemann, ed., 1967, pp. 1-138.
2. Argyris, J.H. and Scharpf, D.W., "Two- and Three-Dimensional Flow by the Method of Singularities", Twelfth Lanchester Memorial Lecture, "The Impact of the Digital Computer on Engineering

Sciences", Part I, The Aeronautical Journal of the Royal Aeronautical Society, January 1970, Vol. 74, pp. 13-41.

3. Oden, J.T. and Wellford Jr., L.C., "Analysis of Viscous Fluids by the Finite-Element Method", American Institute of Aeronautics and Astronautics Journal, Vol. 10, No. 12, December 1972, pp. 1590-1599.

4. Aris, R., "Vectors, Tensors and the Basic Equations of Fluid Mechanics", Prentice Hall, Inc., Englewood Cliffs, N.J., 1962.

5. de Boor, C., "Bicubic Spline Interpolation", Journal of Mathematics and Physics, Vol. 41, 1962.

6. Smith, P.D. and Gaffney, P.L., "Approximation of the Surface Metric Tensor by Means of Bicubic Spline Interpolation", Royal Aircraft Establishment, Technical Report 72185, September 1972.

7. Truesdell, C., "The Physical Components of Vectors and Tensors", Zeitschrift für Angewandte Mathematik und Mechanik, Vol. 33, 1953, pp. 345-356.

8. Marris, A.W., "Vector Fields of Solenoidal Vector-Line Rotation", Arch. Rat. Mech. Anal. 27, 1967, pp. 195-232.

Marris, A.W. and Passman, S.L., "Vector fields and flow on developable surfaces", Arch. Rat. Mech. Anal. 32, 1969, pp. 29-86.
Marris, A.W., "On steady three-dimensional motions", Arch. Rat. Mech. Anal. 35, 1969, pp. 122-168.

9. Miloh, T. and Patel, V.C., "Orthogonal Coordinates for Three-Dimensional Turbulent Boundary Layers, with Particular Reference to Ship Forms", Journal of Ship Research, Vol. 17, No. 1, 1973, pp. 50-58.

10. van Dyke, M., "Higher Approximations in Boundary Layer Theory", Journal of Fluid Mechanics, Vol. 14, 1962, pp. 161-177.

11. Rotta, J.C., "Grenzschichttheorie zweiter Ordnung für ebene und achsensymmetrische Hyperschallströmung", Zeitschrift für Flugwissenschaft, Vol. 15, No. 8/9, 1967, pp. 329-334.

12. Nash, J.F. and Patel, V.C., "Three-Dimensional Turbulent Boundary Layers", SBC Technical Books 1972, Scientific and Business Consultants, Inc., Atlanta.

13. Hinze, J.O., "Turbulence", McGraw Hill Book Company, New York, 1959.

14. So, M.C. and Mellor, G.L., "Experiment on Convex Curvature Effects in Turbulent Boundary Layers", Journal of Fluid Mechanics, Vol. 60, 1973, pp. 43-62.

15. Glushko, G.S., "Turbulent Boundary Layer on a Flat Plate in an Incompressible Fluid" Izv. Akad. Nauk SSSR, Mekhanika, Vol. 4, 1965, p. 13. (Transl. NASA TT F-10, 080).

16. Bradshaw, P., Ferriss, D.H. and Atwell, N.P., "Calculation of Boundary-Layer Development Using the Turbulent Energy Equation", Journal of Fluid Mechanics, Vol. 28, part 3, 1967, p. 593.

17. Nash, J.F., "An Explicit Scheme for the Calculation of Three-Dimensional Turbulent Boundary Layers", Journal of Basic Engineering, Series D, Vol. 94, 1972, pp. 131-141, (ASME Paper 71-PE-19).

18. Nash, J.F. and Patel, V.C., "A Generalized Method for the Calculation of Three-Dimensional Turbulent Boundary Layers", Proceedings of a Workshop held at the Georgia Institute of Technology, June 1971 (Project SQUID).

19. Moore, F.K., "Displacement Effect of a Three-Dimensional Boundary Layer", NACA, Technical Note 2722, 1952.

20. Lighthill, M.J., "On displacement thickness", Journal of Fluid Mechanics, Vol. 4, 1958, pp. 383-392.

21. Kux, J., "Über dreidimensionale Grenzschichten an gekrümmten Wänden", Institut für Schiffbau der Universität Hamburg, Bericht Nr. 273, 1971.

22. Gersten, K., "Die Verdrängungsdicke bei Grenzschichten höherer Ordnung", Zeitschrift für Angewandte Mathematik und Mechanik, Vol. 54, 1974, pp. 165-171.

23. Mager, A., "Generalization of Boundary Layer Momentum-Integral Equations to Three-Dimensional Flows Including Those of a Rotating System", NACA Techn. Note 2310.

24. Johnston, J.P., "On the Three-Dimensional Turbulent Boundary Layer Generated by Secondary Flow", Journal of Basic Engineering, Series D, Trans. ASME, Vol. 82, 1960, pp. 233-250.

25. Coles, D., "The law of the Wake in the Turbulent Boundary Layer", Journal of Fluid Mech., Vol. 1, part. 2, p. 191.

26. Myring, D.F., "An Integral Prediction Method for Three Dimensional Turbulent Boundary Layers in Incompressible Flow", Royal Aircraft Establishment, Technical Report 70147, 1970.

27. Himeno, Y., Tanaka, J., "An Integral Method for Predicting the Behaviors of Three-Dimensional Turbulent-Boundary Layers on Ship Hull Surfaces", Technology Reports of the Osaka University, Vol. 23, No. 1146, 1973, pp. 617-647.

28. Smith, A.M.O., "A Decade of Boundary Layer Research", Applied Mechanics Reviews, 1970, No. 1, p. 1.

DISCUSSION

V.C. PATEL

The author has reviewed, but not critically, some of the well-known results of three-dimensional turbulent boundary-layers. His principal suggestions concern the use of non-orthogonal coordinates and the inclusion of surface curvature terms in the definitions of the integral thicknesses. The various empirical models for closure and methods of calculation listed by the author have been described and, to some extent, evaluated elsewhere (e.g. 12). In this connection, it is not fair to say, as the author implies, that the methods have not been compared with experimental data. The differential methods of Nash and Patel (18), Bradshaw (29, 30)¹, and Pierce and Klinkiek (31) have indeed been compared with available data on three-dimensional turbulent boundary-layers, and found to perform quite adequately. In order to increase the confidence in such methods, however, it is necessary to perform experiments in boundary layers over bodies of more complex geometry, such as ship forms. The author and his colleagues at Hamburg have made an admirable start in this direction and we look forward to their results.

Apart from these general observations, I would like to make some specific comments on the problems associated with three-dimensional turbulent boundary-layers.

Coordinates and Equations: The geometry of non-orthogonal surface coordinate systems, and the Reynolds and boundary-layer equations in such coordinates, have also been discussed by Bradshaw (32). Such generalized coordinates will be useful when efficient numerical procedures for the solution of the appropriate boundary-layer equations have been developed. The author's suggestion that finite-element methods rather than finite-difference methods may be more suitable for this purpose is a good one and merits further investigation. Some caution is, however, required in the development of sophisticated numerical techniques so that the physics of the problem is kept abreast with the numerics. (Note that there is no such fear in the solution of potential-flow problems.) Secondly, the possibilities of using somewhat specialised coordinates for a particular class of problems, such as the suggestion in (9) for boundary layers on ship forms, should not be overlooked in the effort to develop more generally applicable methods. The present-day use of streamline coordinates with integral methods, and simple orthogonal ones with differential methods, has been dictated not only by simplicity but also by the nature of the empirical information which is introduced to effect the closure of the equations.

¹Additional references are listed at the end of the discussion.

Integral Thicknesses and Curvature: The exclusion of surface curvature terms from the definitions of the integral thicknesses as well as the boundary-layer equations does not seem very surprising since in all previous treatments of three-dimensional boundary layers it has been assumed that the boundary layer is thin in comparison with the principal radii of curvature of the surface. There have been a number of studies in two-dimensional laminar and turbulent boundary-layers where "thick" boundary layers (i.e. surfaces of large longitudinal or transverse curvature) have been considered, and it is found that integral thicknesses have been defined appropriately in such studies. In three dimensions the retention of surface curvature terms in the "second-order" boundary layer equations is not a very fruitful exercise since then the equations do not differ much from the parent Navier-Stokes (or Reynolds) equations (see 12). As pointed out at some length by Bradshaw (31) in a recent monograph, the direct influence of streamline curvature on the turbulence (and therefore on the closure models such as mixing-length, eddy viscosity, etc.) is much more important than the surface curvature terms in the equations themselves. A thorough investigation of such direct curvature effects, as they apply in three-dimensional turbulent boundary-layers, is therefore necessary before the problem of "thick" boundary layers can be considered. In any case, the solution of the second-order equations will be a much more formidable problem since they are elliptic while the first-order equations are either parabolic or hyperbolic.

Practical Computations: Some thought has to be given to the effort and expense involved in the calculation of three-dimensional boundary layers on forms of practical interest. Although the older integral methods are simpler to use, they are now being abandoned in favor of methods based on the differential equations, the primary justification being that the differential equations can contain greater amount of physical information on the turbulence and that such information can be introduced at a more fundamental level. The differential methods, however, have so far been tested only against three-dimensional flows observed in typical laboratory situations. Experience with both explicit (12) and implicit (unpublished on-going work at The University of Iowa) numerical schemes has suggested that such methods become prohibitively expensive in terms of computer time when one wishes to perform calculations on shapes of practical interest, such as airplane wings or ship forms. With about 2000 streamwise steps, each of the order of one boundary layer thickness, and about 20 points in the cross-stream direction, a typical explicit scheme requires two to three hours on a modern computer, while implicit methods take somewhat longer. To this must be added the time required to calculate the potential flow and establish the necessary coordinate system. Herein lies a considerable incentive to develop more efficient numerical procedures. Whether

this will lead to a finite-element approach or a resurgence of interest in developing better integral methods remains to be seen.

Boundary layers on Ship Forms: Three-dimensional boundary layers on ship forms present a number of challenges in addition to those which are common with other, primarily aerodynamic, situations. The formation of bilge vortices, the influence of the free surface, and the possibilities of the boundary layer becoming thick in comparison with the local surface curvatures near the keel, bow and stern, all remain to be examined in detail. Some of these phenomena can best be explained through well conceived experiments, and "calibration" of the physical models and calculation procedures against the data.

ADDITIONAL REFERENCES:

(29) Bradshaw, P. "Calculation of Boundary layer Development Using the Turbulent Energy Equation: Three-Dimensional Flow," Journal of Fluid Mechanics, Vol. 46, 1971, p. 417.

(30) Johnston, J.P. "Measurements in a Three-Dimensional Turbulent Boundary Layer Induced by a Swept, Forward Facing Step", Journal of Fluid Mechanics, Vol. 42, 1970, p. 623.

(31) Pierce, F.J. and Klinkaiek, W.F. "An Implicit Numerical Solution of the Turbulent Three-Dimensional Incompressible Boundary layer Equations," Virginia Polytechnic Inst. & State Uni., Report VPI-E-71-14, 1971.

(32) Bradshaw, P. "Effects of Streamline Curvature on Turbulent Flow", Agard Report, AGARD-AG-169, 1973.

T.T. HUANG

It is rather difficult to discuss three-dimensional turbulent boundary layers critically without considering relevant data. The author mainly devotes his paper to the formulation of the boundary-layer equations on curved surfaces which has been developed in the literature.

Some important problems related to ship-hull boundary-layer computations not discussed by the authors are:

1. Estimation of the initial conditions, especially for fuller form ships.
2. Large cross flow for flow around the bilge region.
3. Thick boundary layers on ship stems where the ordinary boundary-layer assumptions are no longer valid.
4. Accurate outer flow computations.

These problems ought to be answered before fruitful applications of 3-D turbulent boundary layer computations can be made to ship hulls.

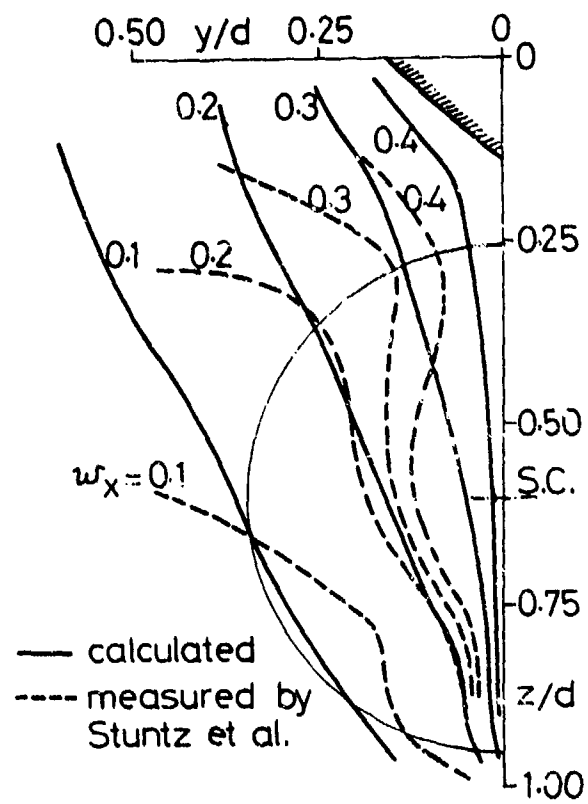
The numerical results given in Figure 8 are incomplete and do not address the problem fully.

I. TANAKA

I congratulate the author for his comprehensively presented paper on the three-dimensional turbulent boundary layer.

I notice that two figures of my work, Ref. (27), are quoted in this paper as Figs. 7 and 8. I wish to add some comments on them. In Fig. 7, potential stream lines are shown in solid lines and viscous limiting ones in dotted. In parallel body, which is not seen in the figure, tendency is reversed. About Fig. 9, description is not given in detail in the paper, but it should be noted that the result is for a particular potential stream line, the fifth from the top in Fig. 7. Waviness in β seems to be ascribable to a change encountered when the line passes the bilge. So, for stream lines which do not pass there, the variation in β is small.

Second, let me show you a slightly further work done after Ref. 27, which was published in September 1973 in the "Journal of the Kansai Society of Naval Architects, Japan" (in Japanese). We can apply the method of calculation of the three-dimensional boundary layer theory to calculate the viscous portion of inflow velocity to propeller. Potential port is obtained from Hess-Smith method. Calculated results (see Fig.) for ship forms of Series 60 show that, if the fullness of ships is not large, we can estimate inflow velocity in practically allowable order.



G. E. GADD

The author cites the work of Myring (26). It may be of interest to note that Sachdeva (33, 34) has applied this method for calculating the flow over a double model of a tanker hull, and has compared the results with measurements made both in a flume and a wind tunnel. The calculated streamwise velocity profile parameters (momentum and displacement thicknesses and skin friction) agree quite well with experiment even in the stern region. Similar results are obtained by the cruder theory of Gadd (35), suggesting that the dominant three-dimensional effect on the flow is the one taken account of in the latter theory, namely the effect of convergence or divergence of the external flow streamlines. Neither theory however predicts the flow directions at the wall very accurately in the stern region, presumably due to inadequacy of the assumed Mager crossflow profiles here.

REFERENCES

33. Sachdeva, R.C. "The development of three-dimensional incompressible turbulent boundary layers"
Ph.D. Thesis, Liverpool University, 1973
34. Sachdeva, R.C., and Preston, J.H.
"Investigation of turbulent boundary layers on a tanker model"
Paper submitted to Roy.Inst.Naval Architects, 1974
35. Gadd, G.E. "The approximate calculation of turbulent boundary layer development on ship hulls"
Trans.Roy.Inst.Naval Architects, Vol. 113, 1971, pp.59-71

AUTHOR'S REPLY

The discussion by Dr. Patel is a very valuable contribution. It must be stressed again as pointed out in the introduction, not results were reviewed but methods of calculation. They indeed were not reviewed critically because, and this was also stressed, to my opinion not enough experimental data is at disposition covering different geometrical possibilities to assign figures of merit to those methods. This is also pointed out by the discussor. It was not my intention to imply, that there has been no comparison with experiment. I have to apologize if this impression has been rised.

I can not agree with the remark, that generalized coordinates will become useful once efficient numerical procedures for the treatment of the equations will be available. The coordinates suggested should increase the applicability of the methods, avoiding the previous construction of a coordinate system subjected to special requirements. Though this might go at the expense of more terms in the equations the basic character of the numerical procedures needed should not be different.

The question of the finite element methods that possibly will once become of importance may require some clarification. Two approaches seem feasible: The substitution of finite-difference methods as applied to the differential equations of the boundary layer by finite-element methods is one possibility. The application of the finite-element method to the integral equations is the second one. The problem reduced to a two-dimensional one may be well suited for a finite-element treatment. Work on the finite-element methods as applied to fluid flow problems is just beginning (36), (37).

Of course, the direct influence of the curvature on the turbulent motion is of outmost importance and there is no discussion about the necessity of more intense investigation of these effects.

Concerning the question of practical computation, it is precisely the prohibitive expensiveness in terms of computer time which possibly will ensure the come-back of old fashioned integral methods. Specially practical interest will rise if they are formulated in a manner independent of the streamlines of outer inviscid flow.

The discussion by Mr. Huang stresses four problems which in fact did not obtain the attention they deserve but as was stated in the introduction only a few problems were to be treated to a certain degree.

Initial conditions are of paramount importance in differential methods. Integral methods seem to present advantages as to initial conditions. Large cross-flow is a concept of importance as long as one proceeds along coordinate lines oriented along (outer) streamlines. In general coordinates or the method works even with large turning angles of the velocity vector inside the boundary layer or it does not work at all. It may well once be demonstrated, that integral methods will not work with a large cross-flow, but results are still encouraging to my opinion.

Thick boundary layers require higher order equations. The basic equations in the geometrical frame as given in the paper presented are specially well suited for the derivation of such extended boundary-layer equations.

Accurate outer flow computations present problems only because of the presence of the free surface and because of boundary-layer separation.

I thank Dr. Gadd for his interesting remarks and the references given.

It is Prof. I. Tanaka that must be congratulated for his fine work. His discussion provides some very interesting pictures demonstrating that with integral methods even the calculation of wake contours seems to be feasible. The figures selected from his paper were reproduced without detailed discussion. The idea was just to give an impression of what integral methods may yield. The calculations of Prof. Tanaka are outstanding examples for this.

I have finally to thank to those discussors whose contribution were not presented in written form, which nevertheless were as valuable as those appearing in these pages.

ACKNOWLEDGEMENTS

My grateful acknowledgement is due to Mr. Cooper and the Office of Naval Research for the kind invitation to the symposium. Some of the ideas presented

in the paper were partly result of the work done at the Sonderforschungsbereich 98, Schiffstechnik und Schiffbau.

ADDITIONAL REFERENCES

36. Argyris, J.H., Mareczek, G., "Potential Flow Analysis by Finite Elements", Ingenieur Archiv, Vol.42, 1972, pp. 1-25

37. Argyris, J.H., Mareczek, G., "Finite Element Analysis of Slow Incompressible Viscous Fluid Motion", Ingenieur Archiv, Vol.43, 1974, pp. 92-109

THE PREDICTION OF TRANSITION FROM LAMINAR TO TURBULENT FLOW IN BOUNDARY LAYERS ON BODIES OF REVOLUTION

P. S. Gnanville
NSRDC
Bethesda, Maryland

ABSTRACT

A new correlation of experimental data is developed for predicting transition from laminar to turbulent flow in boundary layers on smooth bodies of revolution immersed in axisymmetric flows with very low background turbulence. The correlation incorporates not only the usual effect of pressure gradients but the effect of axisymmetric spreading of the boundary layer on the location of transition. Existing methods are also examined critically.

NOMENCLATURE

C_p	Pressure coefficient on body surface
D	Maximum diameter of body
H	Boundary-layer shape parameter, $H = \delta^*/\theta$
H^*	Boundary-layer energy shape parameter, $H = \theta^*/\theta$
x	Axial distance from nose of body
L	Overall length of body
L	Arbitrary length in Mangler's transformation
r_w	Local radius of body of revolution
R_L	Reynolds number given by $U_\infty L/\nu$
R_s	Reynolds number given by U_s/ν
R_θ	Reynolds number given by $U\theta/\nu$
s	Arc length along body starting from stagnation point
t	Time
T	Nondimensional wall shearing stress $T = \left[\frac{\partial(u/U)}{\partial(y/\delta^*)} \right]_{y=0}$
(Tr)	Transition criterion of van Driest and Blumer
u	Streamwise component of boundary-layer velocity

U	Velocity at edge of boundary layer
U_∞	Incoming velocity of flow to body
y	Normal distance from body surface
α	Angle between body surface tangent and axial direction
β	Wedge angle
β_i	Amplification factor in stability
δ	Boundary-layer thickness
δ^*	Boundary-layer displacement thickness
ν	Kinematic viscosity of fluid
θ	Boundary-layer momentum thickness
θ^*	Boundary-layer energy thickness

Subscripts

n	Indicating conditions at neutral stability point
t	Indicating transition

INTRODUCTION

The extent of laminar or turbulent flow in the boundary layer surrounding a body moving in a fluid is of critical importance in many hydrodynamic applications. The regular motion of a fluid in the laminar regime results in a frictional or viscous resistance which may be an order of magnitude less than that due to the chaotic motion of fluid in the turbulent regime. The flow in the boundary layer on a moving body usually begins at the nose or leading edge as laminar flow, and at sufficiently high Reynolds number undergoes transition to turbulent flow downstream at some point (line) or over small region. The higher the Reynolds number, the lesser is the extent of the laminar boundary layer. The position of transition is also very sensitive to other factors: the roughness of the surface, the level and frequency distribution of turbulence in the incoming flow, and the pressure gradient along the body surface, among others.

The problem to be considered here is the prediction of the position of transition on smooth bodies of revolution in axisymmetric flow where the incoming flow contains a very low level of turbulence; under this condition transition is said to be natural or self-excited. Such a low level of turbulence may be found in the depths of the ocean and upper reaches of the atmosphere. Presumably it is also found in specially constructed wind and water tunnels with appropriate contraction ratios and damping screens which reduce the freestream turbulence.

The transition from laminar to turbulent flow involves some of the most intricate and complex phenomena in fluid mechanics. The non-linear characteristics have so far defied analytical solution (1).¹ Transition and turbulence have been described (2) as probably the greatest unsolved problems in the physical sciences. To make matters worse, the experimental data exhibit large scatter due to the extreme sensitivity of the transition process to hard-to-control environmental factors.

Since theory is insufficiently developed to provide a method for predicting the location of transition on arbitrary bodies, recourse must be made to correlation of experimental data in a manner conducive to such prediction. Parameters used for correlation should conform as much as possible to physical observation and relevant theory.

For the transition under discussion, turbulence results from the amplification of infinitesimal disturbances downstream of the neutral stability point. The neutral stability point is the point where all disturbances no matter what the frequency are neither damped or amplified. Downstream of this point there exist some disturbances which are amplified. The positions of both the neutral stability point and the transition point are influenced by pressure gradients. For axisymmetric flow, there seems to be an added effect due to the radial spreading or contracting of the boundary layer flow which is not present in two-dimensional flow. Hence, a correlation of axisymmetric transition data should incorporate both the effect of pressure gradient and radial spreading. Since the neutral stability point is theoretically predictable and physically meaningful, it should also be included in any correlation. In general, a criterion for transition is usually given in terms of some type of Reynolds number.

Two-dimensional transition of airfoils has been investigated experimentally quite thoroughly. Various correlations have been proposed. Granville (3) was the first to incorporate the neutral stability point and the pressure gradient directly in a transition correlation. Smith and Gamberoni (4) also included the maximum rate of amplification of disturbances in arriving at a correlation. Unfortunately, the linear stability theory used only applies to the early stage

of the transition process and not to the later stages which produce turbulent flow.

Eichelbrenner and Michel (29) were the first to develop a correction for axisymmetric spreading without, however, explicitly recognizing the need. This was done by Groth (5) in his studies of transition on bodies of revolution. However, the correction proposed by Groth shows excessive experimental scatter.

It is the purpose of this paper to develop a correlation for transition in axisymmetric boundary layers over bodies of revolution which fits experimental data to a satisfactory degree. First, the physical aspects of the transition process are briefly described. Existing procedures for locating the neutral stability point are summarized.

Existing two-dimensional and axisymmetric methods for locating transition are briefly described and critically evaluated. There is much room for improvement, especially for the axisymmetric methods.

In an effort to develop an improved correlation for transition on bodies of revolution at zero angle of attack (axisymmetric flow) a special set of tests is examined. These tests were conducted by Groth (5) on an ellipsoid of revolution in unbounded flow and two different bounded flows. The purpose here is to separate the effects of pressure gradient and geometric spreading since, in unbounded flow, the geometry of the body determines the pressure distribution. An analysis of the data shows that the effect of pressure gradient seems to be confined mostly to locating the neutral stability point. This leaves the region from the neutral stability point to the transition point as mostly a function of geometrical spreading. Further analysis of data for other bodies suggests a specific parameter to accommodate geometrical spreading. Finally, a large collection of data from bodies without parallel middle body is satisfactorily correlated with this parameter. The correlation can only be applied to bodies of revolution without parallel middle bodies since on a parallel middle body the controlling effect is solely pressure gradient; no geometrical spreading is present.

PROCESS OF TRANSITION

As summarized by Dryden, (6) natural or self-excited transition occurs when the freestream turbulence is less than about 0.1 percent. In this case the existing infinitesimal disturbances are sufficient to lead to transition after sufficient amplification within the laminar boundary layer. On a body, there is a point (line) termed the neutral stability point, upstream of which disturbances of all frequencies are damped out. Downstream, however, disturbances are amplified at different rates according to their frequency. Regular wave-like patterns follow which are named Tollmien-Schlichting waves after the investigators most responsible for developing the stability concept of transition. Owing to cross disturbances the Tollmien-Schlichting waves develop three-dimensional

¹ References are listed on page 11.

characteristics with a transverse wave structure. Turbulence originates locally further downstream as turbulent bursts in the regions of maximum wave amplitude. The appearance of turbulent bursts is usually considered the beginning of transition. Still further downstream the turbulent bursts occur more frequently and are of longer duration until finally the whole flow appears turbulent and the transition process is complete. A detailed description of the transition process is given by Tani (7, 8).

In two-dimensional flows, pressure gradients have a marked effect on the transition process; positive or adverse pressure gradients hasten transition while negative or favorable gradients delay transition.

For axisymmetric flows on bodies of revolution, there seems to be an added factor affecting transition, the radial stretching on the nose and the contraction of the boundary layer on the tail. The stretching hastens while the contraction delays transition. As indicated by Kuethe, (9, 10) the amplification of disturbances is increased on the nose by axisymmetric stretching of the boundary layer.

NEUTRAL STABILITY POINT

The location of the neutral stability point is required for some methods of predicting the location of transition. This is determined by solving the classical Orr-Sommerfeld equation for the stability of two-dimensional parallel flows for a particular velocity profile. The effect of pressure gradient on the neutral stability point enters indirectly by specifying the shape of the velocity profile, especially its curvature. A one-parameter velocity profile then gives a neutral stability point determined by a single parameter.

The one-parameter Pohlhausen-type velocity profile which is a polynomial governed by end conditions was used by Schlichting and Ulrich (11) to calculate the neutral stability point. The results are a Reynolds number $(U\delta^*/\nu)_n$ as a

function of Pohlhausen parameter $(\delta^2/\nu)(dU/ds)$ (Figure 17.3 of Reference (11)).

Here U = streamwise velocity outside the boundary layer

δ^* = displacement thickness

ν = kinematic viscosity of fluid

s = streamwise length from stagnation point

n = subscript denoting neutral stability

The Pohlhausen parameter specifying the shape of the velocity profile is also a pressure-gradient parameter. This simplifies matters since only a solution of the boundary-layer momentum equation is required to determine the Pohlhausen parameter. Mangler (12) converted these results into the more convenient parameters of momentum-thickness Reynolds number $(U\theta/\nu)_n$ as a function

of $(\theta^2/\nu)(dU/ds)$ which is reproduced as Figure 1. Here θ = momentum thickness.

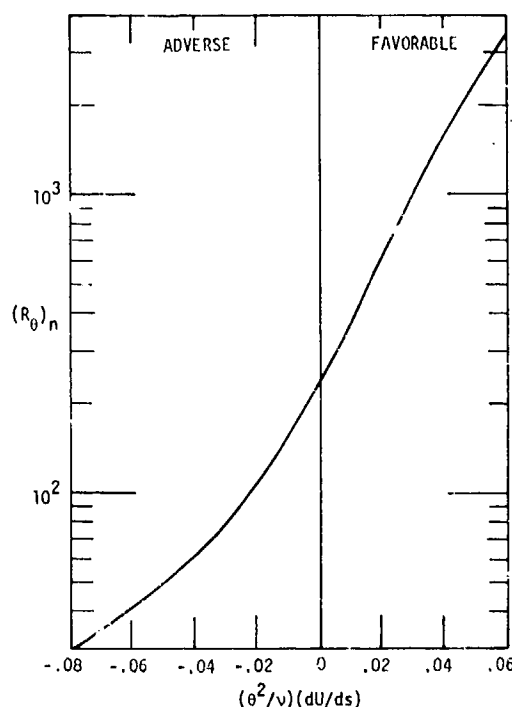


Fig. 1 Neutral Stability Point as Function of Pressure Gradient (Mangler (12))

Wieghardt (13) developed a method for solving laminar boundary layers involving both momentum and energy equations. Since the results included values for shape parameter $H = \delta^*/\theta$, Wieghardt prepared a chart for neutral stability where $(U\theta/\nu)_n$ is a function of H . The velocity profiles correspond to a one-parameter system of flows over wedges, also called Hartree profiles, which are solutions of the Falkner-Skan equation for similarity solutions of the laminar boundary layer equation. A fit is given by Wieghardt as

$$(U\theta/\nu)_n = \exp [26.3 - 8 H] \quad (1)$$

Stuart (14) presents the results of various neutral stability-point calculations in two graphs, $(U\theta/\nu)_n$ as a function of $(\theta^2/\nu)(dU/ds)$ and $(U\delta^*/\nu)$ as a function of H . (Figures 1X.14 and 1Y reference (14)).

Thiede (15) compares the results of Schlichting and Ulrich (Pohlhausen profile) and those of Pretsch (Hartree profile) in terms of $(U\theta/\nu)_n$ as a function of H^* . Here H^* is the energy shape parameter, $H^* = \theta^*/\theta$ where θ^* is the energy thickness.

As stated by Schlichting, (11) the stability of a laminar boundary layer on a body of revolution was investigated by Pretsch. When the boundary layer is thin compared with the body's transverse radius, which is the case on most bodies forward of their tails, the resulting stability equation becomes identical to that for two-dimensional flow. Hence, it is

concluded that the neutral stability charts for two-dimensional flows are also applicable to axisymmetric flows over bodies of revolution.

EXISTING TWO-DIMENSIONAL METHODS²

Michel 1951 (17)

For two-dimensional flows over airfoils in a wind tunnel, Michel correlated the values of two Reynolds numbers at transition: $U\theta/\nu$ and Us/ν , where s is distance along the airfoil, and obtained a mean line which may be fitted by

$$(U\theta/\nu)_t = 1.535 (Us/\nu)^{0.444} \quad (2)$$

Here t is a subscript denoting transition.

Michel's correlation shows little scatter. However, this is a case where the locus line of prediction intersects the correlation line at a very acute angle and consequently produces a prediction with a large possible error. To demonstrate this consider the slope of Equation (2) which is

$$\frac{d \ln (U\theta/\nu)_t}{d \ln (Us/\nu)} = 0.444 \quad (3)$$

Now an approximate solution to two-dimensional laminar boundary layers may be written (3) as

$$U\theta/\nu = 0.664 \sqrt{Us/\nu} \times \left[\frac{1}{(U/U_\infty)^5} \int_0^{s/L} (U/U_\infty)^5 d(s/L) \right]^{1/2} \quad (4)$$

Here U_∞ is the velocity of the incoming flow and U/U_∞ is a function of s/L ; L is a reference length such as airfoil chord.

This equation is the locus of prediction whose slope is very closely approximated by

$$\frac{d \ln (U\theta/\nu)}{d \ln (Us/\nu)} = 0.5 \quad (5)$$

where the variation of the term within the brackets with Us/ν is small. The difference in slopes 0.056 is quite small and on this basis Michel's method may be considered a poor prediction method.

Granville 1953 (3)

Granville developed a correlation for two-dimensional transition data to fit the physical processes involved. Since transition occurs after amplification of disturbances past the neutral stability point, it was decided to use the difference in Reynolds numbers from the neutral stability point to the transition point as a parameter $(U\theta/\nu)_t - (U\theta/\nu)_n$. The values of $(U\theta/\nu)_n$ are obtained from Mangler's chart for

Pohlhausen-type velocity profiles as given in Figure 1. It was also observed that the amplification of disturbances leading to transition depends on the cumulative effect of pressure gradient. Hence, an average pressure-gradient parameter $(\theta^2/\nu)(dU/ds)$ was chosen as a correlating parameter where the averaging is done from the neutral stability point to the transition point.

$U\theta/\nu$ is calculated from Equation (4) while $(\theta^2/\nu)(dU/ds)$ is calculated from a closed-form solution

$$(\theta^2/\nu)(dU/ds) = 4/45 - 1/5 \times \left[\frac{(U\theta^2/\nu)_t - (U\theta^2/\nu)_n}{s_t - s_n} \right] \quad (6)$$

Existing data for transition on airfoils in low-turbulence wind tunnels and on wings in flight tests correlated well. This correlation is reproduced by Schlichting (11) as Figure 17.11.

Smith and Gamberoni 1956 (4)

Smith and Gamberoni developed a prediction method for transition based on the amplification rates of infinitesimal disturbances β_i . Frequencies are selected to provide maximum amplification and are integrated starting at neutral stability to give an amplification factor $\exp \int \beta_i dt$. Use is made of solutions of the Orr-Sommerfeld equation obtained by Pretsch for Hartree velocity profiles (wedge flows). Comparison with measured transition points led to selection of a value of e^9 for amplification factor $\exp \int \beta_i dt$ as providing good correlation.

The transition method is given in terms of Michel parameters, $(U\theta/\nu)_t$ versus Us/ν , as a

correlation for the e^9 -calculations:

$$(U\theta/\nu)_t = 1.174 (Us/\nu)^{0.46} \quad (7)$$

This is quite close to Michel's correlation of test data. As previously stated, the Michel parameters give good correlation but poor predictions.

Further insight into this method may be obtained if the results are stated in terms of Crabtree parameters $(U\theta/\nu)_t$ versus $(\theta^2/\nu)(dU/ds)$.

Figure 3 of Reference (4) shows the results of Smith and Gamberoni in terms of $U\delta^*/\nu$ and H versus wedge angle β for various maximum amplification ratios $\exp \int \beta_i dt$ obtained from

Pretsch's calculations for wedge flows (Hartree velocity profiles). $U\theta/\nu$ is readily obtained since, by definition of H , $\theta = \delta^*/H$. To

obtain $(\theta^2/\nu)(dU/ds)$ from β use can be made of a convenient table by Hall and Gibbings (18) (Table 1). The results for several amplification factors are plotted in Figure 2. It is quite evident from the curves that the choice

² See also survey by Hairston (16).

Table 1 Transition Data of Bodies of Revolution

Body	L/D	Length in.	Test Facility	Method of Locating Transition	Reference
Ellipsoid	9	96	Northrop Low Speed Wind Tunnel	Surface Microphone	5
			Flight Tests	Evaporation of Fluorene in Petrol Ether	
Modified Sears-Haack Body	9	96	Northrop Low Speed Wind Tunnel	Total Head Tubes	
			Flight Tests		
Modified Paraboloid	9	96	Northrop Low Speed Wind Tunnel	Total Head Tubes	
			Flight Tests		
Ellipsoid	9 7.5	96 96	Ames Wind Tunnel	Surface Microphone	30

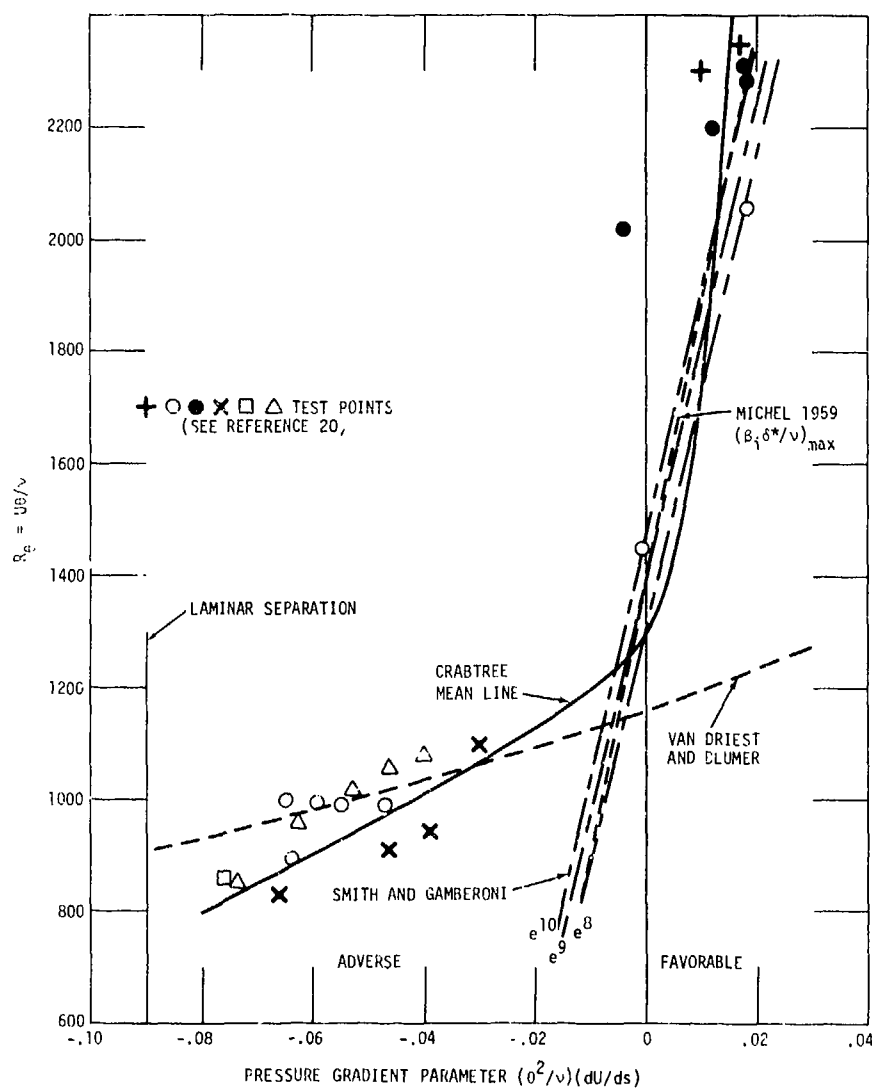


Fig. 2 Crabtree's Correlation for Transition on Two-Dimensional Bodies

of an amplification factor to represent transition is empirical and that prediction is good for favorable pressure gradients and poor for adverse pressure gradients.

The main objection to the method of Smith and Gamberoni is that it does not conform to the physical facts. Transition to turbulent flow is the result of nonlinear behavior which is not closely modeled by the linear Orr-Sommerfeld equation.

It should be mentioned that van Ingen (19) independently worked out a similar analysis to Smith and Gamberoni using amplification factors.

Crabtree 1957 (20)

Crabtree decided, for the sake of computational simplicity, to correlate transition data using the same parameters as those for the neutral stability point: $U\theta/\nu$ and $(\theta^2/\nu)(dU/ds)$. As seen in Figure 2, the Crabtree "mean line" fit is not too bad. There is large scatter but the trend is quite definite. Favorable pressure gradients or positive values of $(\theta^2/\nu)(dU/ds)$ delay transition while adverse pressure gradients hasten transition.

Michel 1959 (21)

Michel reconsidered his earlier (1951) correlation, $(U\theta/\nu)_t$ versus U_s/ν , for transition on airfoils, and replotted the test data for a combination of these parameters:

$$\left[\frac{(U\theta/\nu)^2}{(U_s/\nu)} \right]^{1/2}_t$$
 versus U_s/ν . This seemed to make the experimental scatter more evident. It is clear that the prediction precision remains the same as for Michel's original correlation.

Michel also considered the application of stability theory to the prediction of transition. Instead of $\int \beta_i dt = 9$ used by Smith and

Gamberoni, Michel advocated use of the maximum value of $(\beta_i \delta^*/U)_{\max}$ to represent conditions at transition. Using the results of Pretsch for Hartree velocity profiles, Michel correlated $U\delta^*/\nu$ at $(\beta_i \delta^*/U)_{\max}$ against the shear-stress

factor $T = \left[\frac{\partial(u/U)}{\partial(y/\delta^*)} \right]_{y=0}$ with transition test

data. However, Michel's curve can be converted into Crabtree parameters $U\theta/\nu$ and $(\theta^2/\nu)(dU/ds)$ as follows. Pretsch (22) relates T to wedge angle β (Table of Reference 22). Also H is a function of β (Figure 3 of Reference 4) which converts δ^* to H . Finally $(\theta^2/\nu)(dU/ds)$ is a function of β (Table 1 of Reference 18). The resulting Michel curve is shown plotted on the Crabtree diagram in Figure 2. It is evident that agreement with experimental data is good for favorable pressure gradients and poor for adverse pressure gradients, as is the case for the Smith and Gamberoni correlation.

van Driest and Blumer 1963 (23)

Van Driest and Blumer (see also van Driest (24)) developed a criterion for transition based on the ratio of local inertial stress to local viscous stress within the boundary layer, $0 \leq y \leq \delta$, which is written as

$$(Tr) = \left[(y^2/\nu)(du/dy) \right]_{\max} \quad (8)$$

where (Tr) is a transition criterion

y is the normal distance from the wall and

u is the streamwise velocity component within the boundary layer.

The value of (Tr) increases downstream from the stagnation point and, after comparison with data, transition is considered to occur at $(Tr) = 1690$. As a matter of interest, Equation (8) is also a stability criterion stated by Rouse (25) for laminar flow.

For low freestream turbulence, van Driest and Blumer evaluate Equation (8) for Pohlhausen velocity profiles, obtaining:

$$\frac{9860}{(U\theta/\nu)_t} = 1 - 0.0485 (\delta^2/\nu)(dU/ds) \quad (9)$$

This is the correlation line for predicting transition.

For purposes of comparison momentum thickness θ may be substituted (11) for boundary-layer thickness δ for Pohlhausen velocity profiles by the expression

$$\frac{\theta}{\delta} = \frac{1}{63} \left[\frac{37}{5} - \frac{1}{15} \frac{\delta^2}{\nu} \frac{dU}{ds} - \frac{1}{44} \left(\frac{\delta^2}{\nu} \frac{dU}{ds} \right)^2 \right] \quad (10)$$

to give the Crabtree parameters $U\theta/\nu$ and $(\theta^2/\nu)(dU/ds)$. The result is plotted in Figure 2. Here, it is evident that agreement is good for adverse pressure gradients and very poor for favorable pressure gradients.

Eppler 1969 (26)

Eppler correlated experimental data in a manner similar to Crabtree except that the energy shape parameter H^* is substituted for pressure gradient parameter $(\theta^2/\nu)(dU/ds)$. The use of $(U\theta/\nu)_t$ is retained. An empirical fit is given by Eppler as

$$\ln (U\theta/\nu)_t = 18.4 H^* - 21.74 \quad H^* \leq 1.585 \quad (11)$$

$$\ln (U\theta/\nu)_t = 34.2 H^* - 46.78 \quad H^* \geq 1.585 \quad (12)$$

Since for one parameter velocity profiles H^* is a function of $(\theta^2/\nu)(dU/ds)$, the Eppler correlation is mostly a modified Crabtree correlation.

Jaffe, Okamura and Smith 1970 (27)

Jaffe, Okamura and Smith developed further the method of Smith and Gamberoni. Instead of using Hartree velocity profiles, exact velocity profiles calculated from numerical solutions of the boundary-layer equations are used to solve the Orr-Sommerfeld stability equation. Here, the amplification factors are more correctly evaluated on a spatial basis. A comparison with test data using e^{10} as the amplification factor for transition gave on an average 8.27-percent deviation from experimental data for two-dimensional cases and 16.5 percent for axisymmetric cases.

Thiede 1970 (28)

Thiede prefers the use of the energy shape parameter H^* instead of the pressure-gradient parameter $\theta^2/\nu \, dU/ds$ for correlation purposes as a consequence of using the energy equation to solve the laminar boundary-layer equations. For one-parameter velocity profiles H^* is a function of $(\theta^2/\nu)(dU/ds)$.

The neutral stability point is then obtained from $U\theta/\nu$ as a function of H^*

$$\log_{10} \left(\frac{U\theta}{\nu} \right)_n = 4.556 - 76.87 (1.670 - H^*)^{1.542} \quad (13)$$

For transition an average \bar{H}^* is used instead of the $\nu(dU/ds)$ of Granville. The correlation is fitted by

$$\log_{10} \left[\left(\frac{U\theta}{\nu} \right)_t - \left(\frac{U\theta}{\nu} \right)_n \right] = 1.6435 - 24.20 (1.5150 - \bar{H}^*), 1.515 \leq \bar{H}^* \leq 1.560 \quad (14)$$

and

$$\log_{10} \left[\left(\frac{U\theta}{\nu} \right)_t - \left(\frac{U\theta}{\nu} \right)_n \right] = 3.312 - 967.5 (1.6250 - \bar{H}^*)^{2.715}, 1.560 \leq \bar{H}^* \leq 1.625 \quad (15)$$

where

$$\bar{H}^* = \frac{\int_{s_n}^s H^* ds}{s_t - s_n} \quad (16)$$

Since for one-parameter velocity profiles, H^* is a function of $(\theta^2/\nu)(dU/ds)$, the Thiede correlation is a modified Granville correlation.

Thiede 1972 (15)

In later work, Thiede accommodates both two-dimensional and axisymmetric transition data by correlating $(Us/\nu)_t - (Us/\nu)_n$ with \bar{H}^* . An empirical fit is given as

$$\log_{10} \left[\left(\frac{Us}{\nu} \right)_t - \left(\frac{Us}{\nu} \right)_n \right] = 4.27 + 39.42 (\bar{H}^* - 1.515), 1.55 \leq \bar{H}^* \leq 1.60 \quad (17)$$

For two-dimensional flows, this correlation is the same as that of Thiede 1970. For axisymmetric flow, this correlation implicitly incorporates a Mangler correlation for axisymmetric conditions.

EXISTING AXISYMMETRIC METHODS

Granville 1953 (3)

Granville (3) considered the application of his two-dimensional correlation to axisymmetric conditions, $(U\theta/\nu)_t - (U\theta/\nu)_n$ against $(\theta^2/\nu)(dU/ds)$. Application of Mangler's transformation showed no change in $(\theta^2/\nu)(dU/ds)$ but produced an arbitrary constant for $U\theta/\nu$. A tentative decision based on existing experimental data was to keep $U\theta/\nu$ the same or an arbitrary constant of one. Later more extensive measurements showed the need of an axisymmetric correction or a change in the arbitrary constant.

Eichelbrenner and Michel 1958 (29)

To apply the two-dimensional correlation expressed in Michel parameters $U\theta/\nu$ and Us/ν to axisymmetric conditions on bodies of revolution, Eichelbrenner and Michel made use of Mangler's transformations. U remains unchanged, but the two-dimensional equivalent s is given by

$$s = \frac{1}{L^2} \int_0^{\tilde{s}} r_w^2 d\tilde{s} \quad (18)$$

and the equivalent two-dimensional θ by

$$\theta = \frac{r_w}{L} \tilde{\theta} \quad (19)$$

Here the tilde represents the axisymmetric condition, r_w is the local transverse radius of a body of revolution, and L is an arbitrary length to be considered. Eichelbrenner and Michel decided to keep Us/ν the same for both two-dimensional and axisymmetric conditions, so that $s = \tilde{s}$; then

$$L = \left(\frac{\int_0^s r_w^2 ds}{s} \right)^{1/2} \quad (20)$$

and

$$\frac{U\theta}{v} = r_w \left(\frac{s}{\int_0^s r_w^2 ds} \right)^{1/2} \left(\frac{U\theta}{v} \right)_t \quad (21)$$

Comparison of the above correlation with experimental data on bodies of revolution showed a much improved agreement but still not as good as that for two-dimensional data.

Groth 1957 (5)

Groth analyzed a very extensive set of experimental data for transition on bodies of revolution obtained under low-turbulence conditions in wind tunnels and in flight. Comparing a criterion for two-dimensional $(U\theta/v)_t$ at transition with the experimental axisymmetric $(U\theta/v)_t$ at the same value of pressure-gradient parameter $(\theta^2/v)(dU/ds)$, and noting a consistently large deviation in these, led Groth to the conclusion that axisymmetric spreading or contraction of the boundary layer on a body of revolution strongly affects the position of transition. To accommodate this effect Groth plotted the ratio of $(U\theta/v)_t$ to $(U\theta/v)$, at the same

$(\theta^2/v)(dU/ds)$, against a spreading parameter $(L/r_w)(dr_w/dL)$. Here L is the axial distance from the nose and L is the length of the body. Despite the very extensive experimental scatter, a consistent correlation was realized.

Thiede 1970 (28)

The axisymmetric correction of Eichelbrenner and Michel was modified by Thiede so that the Mangler's transformation is used only to determine the distance from the neutral stability point to the transition point. Then

$$\left(\frac{U\theta}{v} \right)_t = r_w \left(\frac{s_t - s_n}{\int_{s_n}^{s_t} r_w^2 ds} \right)^{1/2} \left(\frac{U\theta}{v} \right)_t \quad (22)$$

This appears more reasonable since the axisymmetric effect seems confined to the region from the neutral stability point to the transition point.

TRANSITION DATA FOR NORTHROP ELLIPSOID

General

A unique set of transition data was obtained by Groth (5) for an ellipsoid of revolution whose pressure distribution was varied by situating the body at various axial locations inside the contraction cone of the Northrop

Low-Speed Wind Tunnel. Data for three conditions are available over a range of length Reynolds numbers from 3×10^6 to 8×10^6 :

- Body in normal position in test section of wind tunnel
- Nose of body 16 inches inside of contraction cone
- Nose of body 40 inches inside of contraction cone

The body tested was an ellipsoid of revolution with a fineness ratio of 9 and a maximum diameter of 10 1/2 inches faired into a cylindrical supporting sting. Transition was indicated by pressure measurements from taps in the surface of the body. The criterion for the beginning of transition was one burst of turbulence per second. The pressure distributions and positions of transition for the three test conditions are given in Figures 3 and 4.

The purpose of using the same body with different pressure distributions to study transition was to isolate the effect of pressure gradient on transition. In the usual test section, representing unbounded flow, the pressure coefficient distribution calculated from potential theory is solely a function of body geometry.

Correlation by Some Existing Methods

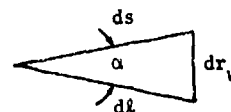
The required boundary-layer parameters for analyzing transition data are calculated from the approximate solution of the laminar boundary layer given in Reference 3.

$$\frac{R_\theta^2}{R_L} = \frac{(0.664)^2}{\left(\frac{U}{U_\infty} \right)^4 \left(\frac{r_w}{L} \right)^2} \int_0^{L/L} \left(\frac{U}{U_\infty} \right)^5 \times \left(\frac{r_w}{L} \right)^2 \sec \alpha d \left(\frac{L}{L} \right) \quad (23)$$

and

$$\frac{\theta^2}{v} \frac{dU}{ds} = \left(\frac{R_\theta^2}{R_L} \right) \frac{1}{\left(\frac{U}{U_\infty} \right)^2} \frac{d \left(\frac{U}{U_\infty} \right)}{d \left(\frac{L}{L} \right)} \cos \alpha \quad (24)$$

Here $R_\theta \equiv \frac{U\theta}{v}$, $R_L \equiv \frac{U_\infty L}{v}$ is the length Reynolds number, and α is the angle between the surface tangent and the axial direction.



Equation (23) is an alternate form of Equation (4). This approximate solution is sufficiently accurate for analyzing transition data. It is identical to Thwaites' solution for two-dimensional flow, as transformed to a body of

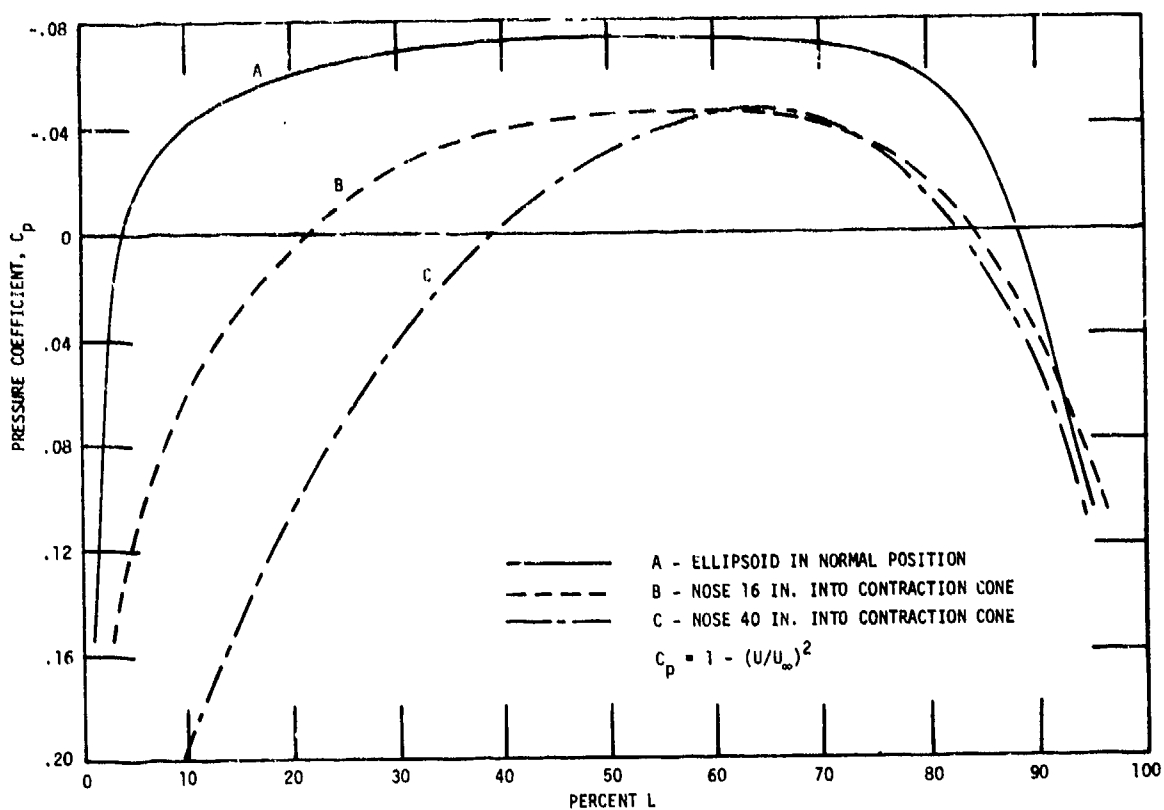


Fig. 3 Pressure Distributions of Northrop Ellipsoid

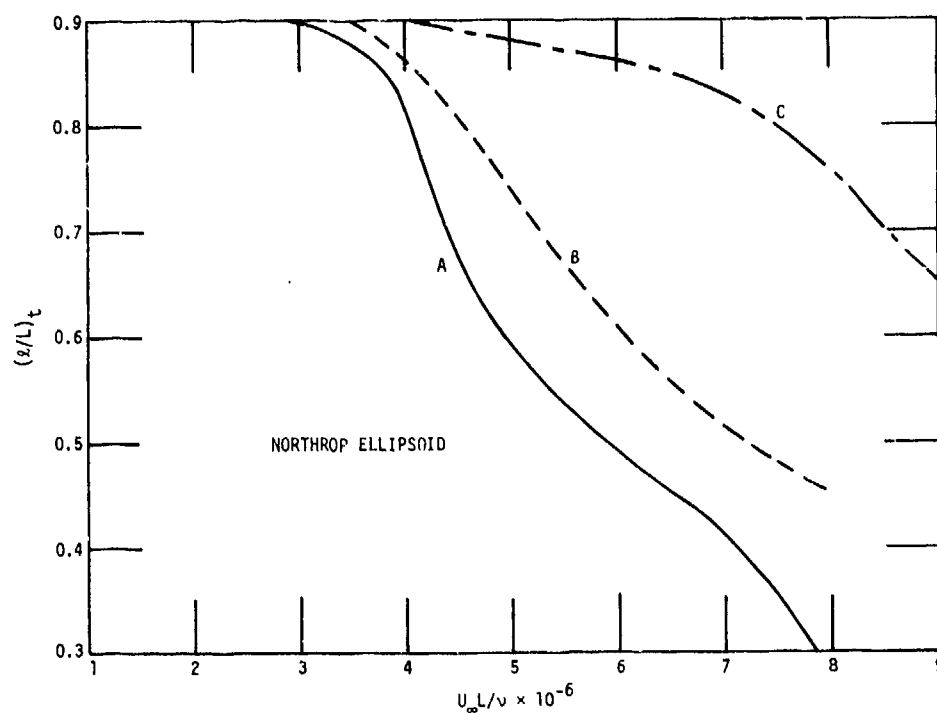


Fig. 4 Transition Data of Northrop Ellipsoid

revolution, except for a small change in the constant. The value of 0.664 is chosen to agree with the exact Blasius solution for a flat plate. The neutral stability point is determined from Figure 2.

Groth's correlation of the test data for these cases is quite poor.

To illustrate the axisymmetric spreading effect on transition, the data for the three conditions are plotted in the Crabtree manner of $(R_\theta)_t$ against $(\theta^2/\nu)(dU/ds)$ in Figure 5, and the Granville manner of $(R_\theta)_t - (R_\theta)_n$ against $(\theta^2/\nu)(dU/ds)$ in Figure 6.

It is evident from Figures 5 and 6 that two-dimensional correlation does not apply in the slightest degree.

If the same data are adjusted to axisymmetric conditions by the method of Eichelbrenner and Michel, Equation (21), and plotted in the Michel parameters of R_θ and R_s in Figure 7, it is also evident that the correlation is poor.

A NEW CORRELATION

The positions of the neutral stability points for the Northrop ellipsoid in pressure conditions A, B, and C are calculated and plotted in Figure 8. The positions are obtained from intersections of locus lines representing the body boundary-layer parameters with the neutral stability line of Figure 1. The required R_θ and $(\theta^2/\nu)(dU/ds)$ values for the locus lines are obtained from the pressure distribution in Figure 4 using Equations (23) and (24) for the calculations of the laminar boundary layer.

Comparison with the positions of transition also plotted in Figure 8 show the large distance between neutral stability and transition. If perchance the corresponding differences in momentum-thickness Reynolds number, $(R_\theta)_t - (R_\theta)_n$, are plotted against relative position $(L/L)_t$ in Figure 9, it is seen that there is excellent correlation. This is a happy accident. The curves for conditions A and B practically coalesce and the curve for condition C is very close. Since only pressure gradient and not geometry was varied in the Groth experiments, it may be inferred that the effect of pressure gradient on the position of transition has been sufficiently accommodated in this case by the effect of pressure gradient on the position of the neutral stability point as indicated by $(R_\theta)_n$.

For the effect of geometry on $(R_\theta)_t - (R_\theta)_n$, the NACA test data (30) for two ellipsoids of fineness ratios 9 and 7.5 are examined in Figure 10. Here $(R_\theta)_t - (R_\theta)_n$ is plotted against $(L/L)_t$. The correlation is surprisingly good. It is of interest to consider now the effect of

axisymmetric spreading and contracting, which is a purely geometrical effect. Groth (5) introduced a parameter $L/r_w dr_w/dL$, which represents the relative change in cross section parameter $2\pi r_w$ in the axial direction, since

$$\frac{L}{r_w} \frac{dr_w}{dL} = \left[\frac{d(2\pi r_w)}{dL} \right] / (2\pi r_w/L) \quad (25)$$

The length of the body L is added to provide a nondimensional ratio. It is now proposed to try a correlation, $(D/r_w)(dr_w/dL)$, nondimensionalized on the maximum diameter D instead of L . In Figure 11, $(R_\theta)_t - (R_\theta)_n$ for two ellipsoids is plotted against $[(D/r_w)(dr_w/dL)]_t$. It is seen that overall the correlation is improved over $(L/L)_t$ with the greatest discrepancy at the ends.

It is now proposed to correlate transition data on bodies of revolution in axisymmetric flow with

$$(R_\theta)_t - (R_\theta)_n = f \left[\left(\frac{D}{r_w} \frac{dr_w}{dL} \right)_t \right] \quad (26)$$

where

$$(R_\theta)_n = f \left[\frac{\theta^2}{\nu} \frac{dU}{ds} \right] \quad (27)$$

The test data to be correlated are assembled in Table 1. The shapes of the bodies are shown in Figure 12 and the measured pressure distributions, in terms of velocity at the edge of the boundary layer, are shown in Figure 13. The positions of the neutral stability points, calculated from Equations (23) and (24) and Figure 2, are shown in Figure 14 as functions of Reynolds number.

Transition data from wind tunnel tests and flight tests, presented in terms of $(R_\theta)_t - (R_\theta)_n$ against $[(D/r_w)(dr_w/dL)]_t$, are compared in Figure 15. Close observation reveals two principal trends. The data from flight tests and the low-turbulence Ames tunnel (0.02 percent free-stream turbulence) seem to correlate reasonably well. However, the data from the Northrop wind tunnel, which has a somewhat higher free-stream turbulence (~ 0.1 percent) seem to correlate along a different line.

For the purpose of predicting transition in a low-turbulence free stream, the data from the flight tests and from the Ames wind tunnel are correlated by a mean line shown in Figure 16. This is the line of correlation to be used in making predictions by means of an intersection with a locus line representing an arbitrary body in a flow with an arbitrary Reynolds number.

For example, for transition to occur at the abscissa $[(D/r_w)(dr_w/dx)]_t$, the locus line obtained by varying the overall Reynolds number $U_\infty L/\nu$ is parallel to the ordinate. It is evident that the angles of intersection are not too acute.

CONCLUSIONS

It should be evident that predicting transition on bodies of revolution in axisymmetric flow is in not too satisfactory a state. There is definitely need for more experimental work under carefully controlled conditions to elucidate the physical processes involved, especially the stretching effect due to geometry which seems peculiar to axisymmetric flow.

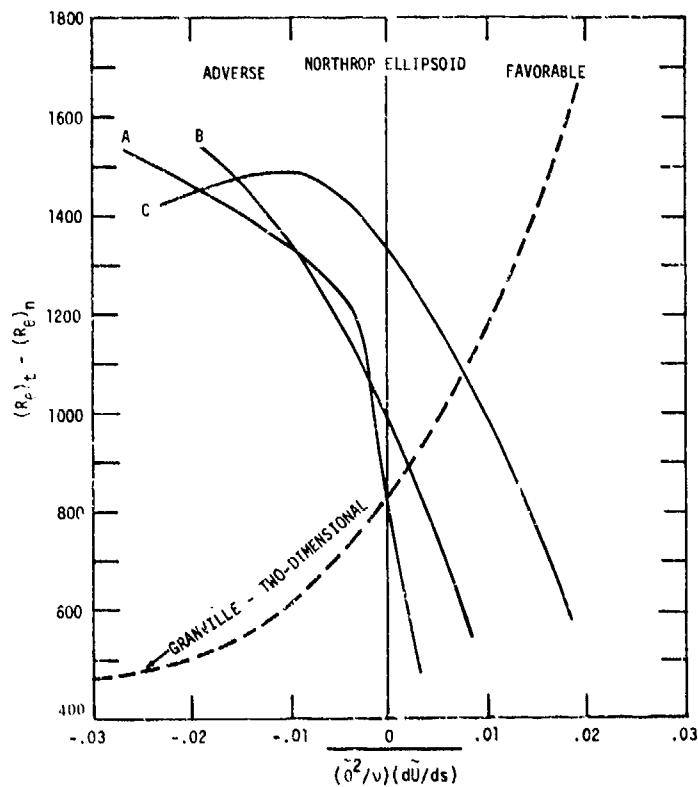
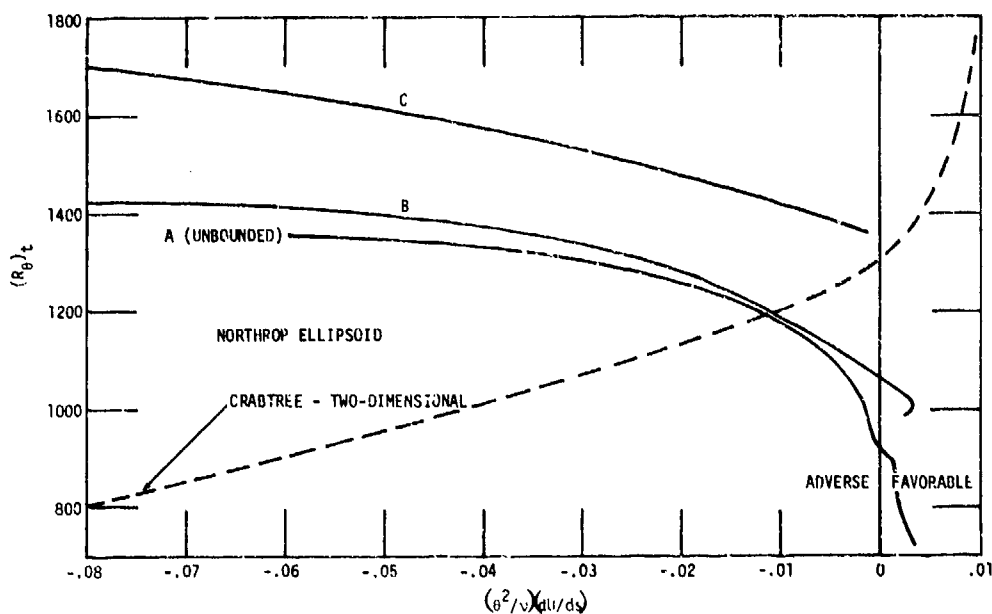
The proposed correlation is recommended for predicting transition on bodies whose geometries are similar to the test bodies. Obviously bodies with parallel middle body represent conditions not investigated.

REFERENCES

1. Reshotko, E., "Stability Theory as a Guide to the Evaluation of Transition Data," AIAA Journal, Vol. 7, No. 6, June 1969, pp. 1086-1091.
2. Griffith, W.C., "Is Fluid Mechanics Becoming Extinct as a Branch of Science?," Applied Mechanics Reviews, Vol. 17, No. 8, Aug. 1964.
3. Granville, P.S., "The Calculation of the Viscous Drag of Bodies of Revolution," David Taylor Model Basin Report 849, July 1953.
4. Smith, A.M.O. and Gamberoni, N., "Transition, Pressure Gradient and Stability Theory," Douglas Aircraft Co. Report ES26388, Aug. 1956.
5. Groth, E.E., "Boundary Layer Transition on Bodies of Revolution," Northrop Aircraft Co. Report NAI-57-1162 (BLC-100), July 1957.
6. Dryden, H.L., "Transition from Laminar to Turbulent Flow," Turbulent Flows and Heat Transfer, edited by C.C. Lin, Princeton University Press, Princeton, N. J., 1959.
7. Tani, I., "Review of Some Experimental Results on Boundary Layer Transition," Boundary Layers and Turbulence, K.F. Bowden et al. eds., The Physics of Fluids Supplement 1967, American Institute of Physics, New York, 1967.
8. Tani, I., "Boundary Layer Transition," Annual Review of Fluid Mechanics, Vol. 1, W.R. Sears and M. van Dyke, eds., Annual Reviews Inc., Palo Alto, California, 1969.
9. Kuethe, A.M., "On the Stability of Flow in the Boundary Layer Near the Nose," Rand Corporation RM 1972, Aug. 1957, (AD-150687).
10. Kuethe, A.M., "On the Character of the Instability of the Laminar Boundary Layer Near the Nose of a Blunt Body," Journal of Aeronautical Sciences, Vol. 25, No. 5, May 1958, pp. 338-339.
11. Schlichting, H., Boundary Layer Theory, 6th Ed., McGraw-Hill, New York, 1968.
12. Mangler, W., "Boundary Layers on Bodies of Revolution in Symmetric Flow," BIGS 13, June 1946.
13. Wieghardt, K.E.G., "On a Simple Method for Calculating Laminar Boundary Layers," Aeronautical Quarterly, Vol. 5, May 1954, pp. 25-38.
14. Stuart, J.T., "Hydrodynamic Stability," Laminar Boundary Layers, L. Rosenhead, ed., Clarendon Press, Oxford, 1963.
15. Thiede, P., "Kriterien zur Vorausbestimmung des laminar-turbulenten Grenzschichtumschlags in umströmten Körperkonturen," Fortschritt-Berichte der VDI Zeitschriften, Series 7, No. 31, Dec. 1972.
16. Hairston, D. E., "Survey and Evaluation of Current Boundary Layer Transition Prediction Techniques," Paper 71-985, AIAA 8th Annual Meeting, Oct. 1971.
17. Michel, R., "Détermination du Point de Transition of Calcul de la Trainée des Profils d'Ailes en Incompressible," La Recherche Aéronautique, No. 24, 1951.
18. Hall, D.J. and Gibbings, J.C., "Influence of Stream Turbulence and Pressure Gradient Upon Boundary Layer Transition," Journal of Mechanical Engineering Science, Vol. 14, No. 2, Apr. 1972, pp. 134-136.
19. van Ingen, J.L., "A Suggested Semi-Empirical Method for the Calculation of the Boundary Layer Transition Region," Delft Technische Hogeschool, Dept. of Aero. Eng. Report V.T.H. 74, Sep. 1956.
20. Crabtree, L.F., "Prediction of Transition in the Boundary Layer on an Aerofoil," Royal Aircraft Establishment (Farnborough) Technical Note Aero 2491, Jan. 1957; also Journal of Royal Aeronautical Society, Vol. 62, 1958, p. 525.
21. Michel, R., "Critère de Transition et Amplification des Ondes d'Instabilité Laminaire," La Recherche Aéronautique, No. 70, May-June 1959, pp. 25-27.
22. Pretsch, J., "Calculation of the Limit of Stability of Boundary Layer Profiles and of the Amplification of Disturbances," AVA Monographs, R&T 1004, Mar. 1948.
23. van Driest, E.R. and Blumer, C.B., "Boundary Layer Transition Freestream and Pressure Gradient Effects," AIAA Journal, Vol. 1, No. 6, June 1963.
24. van Driest, E.R., "Recent Studies in Boundary Layer Transition," International Journal of Engineering Science, Vol. 3, 1965, pp. 341-353.
25. Rouse, H., Engineering Hydraulics, John Wiley and Sons, New York, 1950, p. 84.
26. Eppler, R., "Laminar profile für Reynolds-Zahlen grösser als 4×10^6 ," Ingenieur-Archiv, Vol. 38, 1969, pp. 232-240.
27. Jaffe, N.A., Okamura, T.T., and Smith, A.M.O., "Determination of Spatial Amplification Factors and Their Application to Predicting Transition," AIAA Journal, Vol. 8, No. 2, Feb. 1970, pp. 301-308.
28. Thiede, P., "Theoretische Untersuchungen zur Laminarhaltung der Grenzschicht in Rotationskörpern durch Absaugeschlitze bei inkompressible Strömung," Fortschritt-Berichte der VDI Zeitschriften, Series 7, No. 27, Nov. 1970.

29. Eichelbrenner, E.A. and Michel, R.,
"Observations sur la Transition Laminair-
Turbulent on Trois Dimensions," La Recherche
Aéronautique, No. 65, 1958.

30. Bolt, F.W., Kenyon, G.C., and Allen,
C.Q., "Measurements of Boundary Layer Transition
at Low Speeds on Two Bodies of Revolution in a
Low-Turbulence Wind Tunnel," NACA Research Memo
A56G17, Sep. 1956.



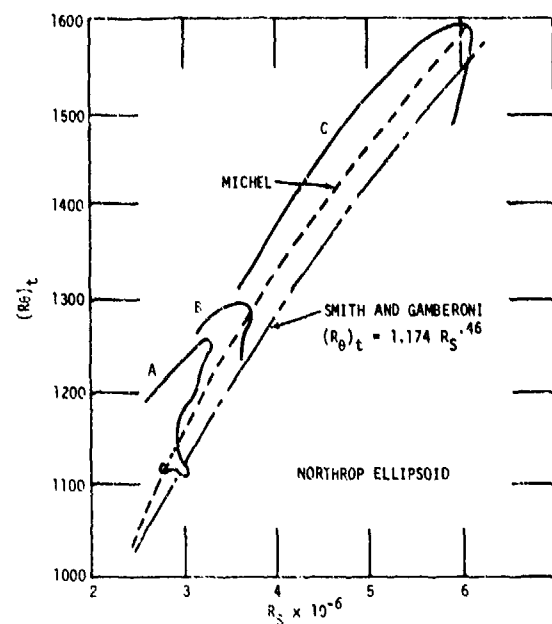


Fig. 7 Transition Data on Michel-Type Plot

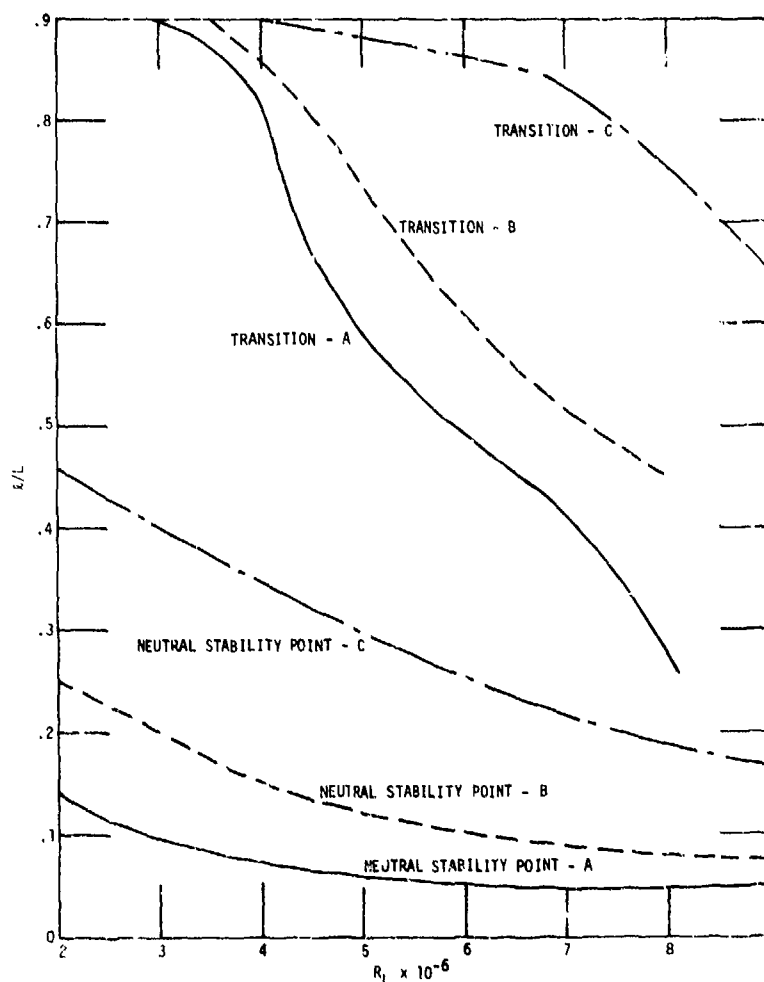


Fig. 8 Location of Transition and Neutral Stability Points for Northrop Ellipsoid

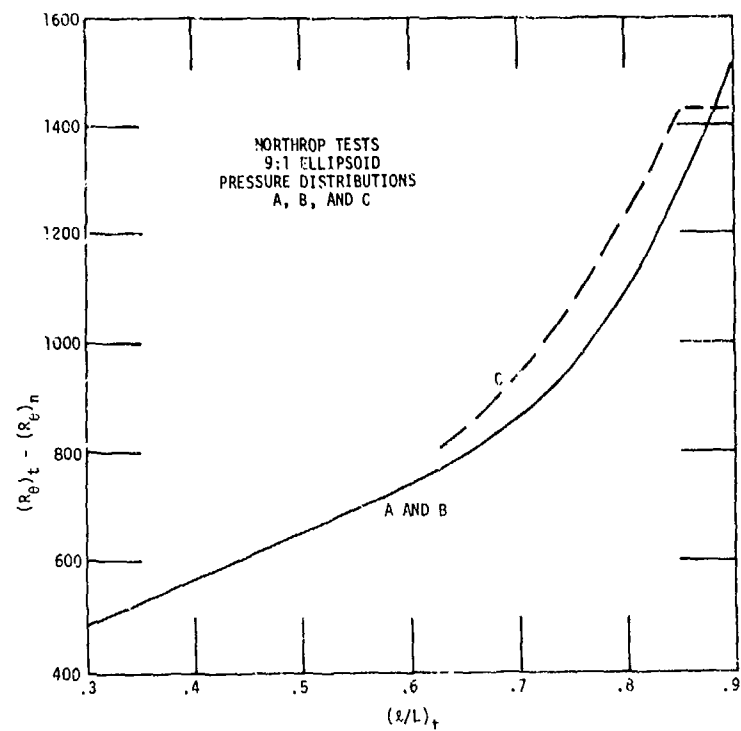


Fig. 9 Correlation of Transition Data for Northrop Ellipsoid

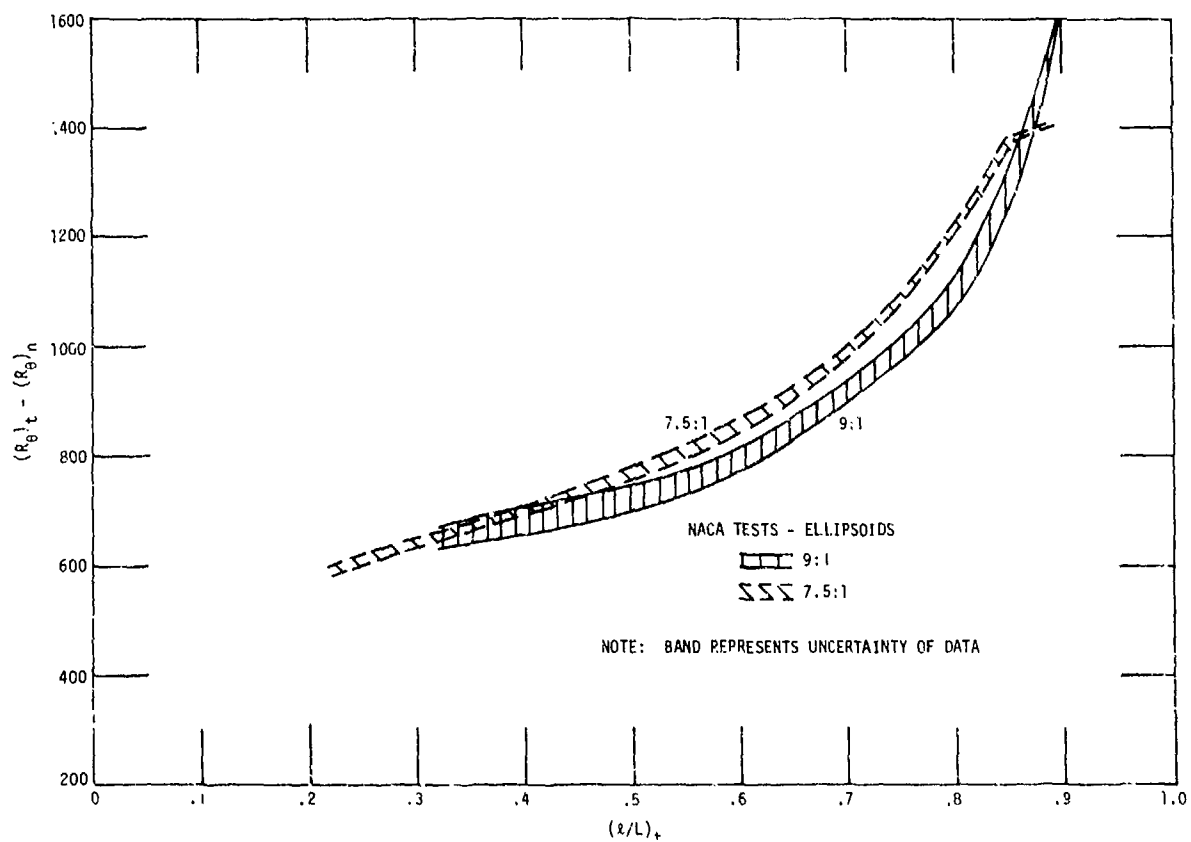


Fig. 10 Correlation of Transition Data for NACA Ellipsoids

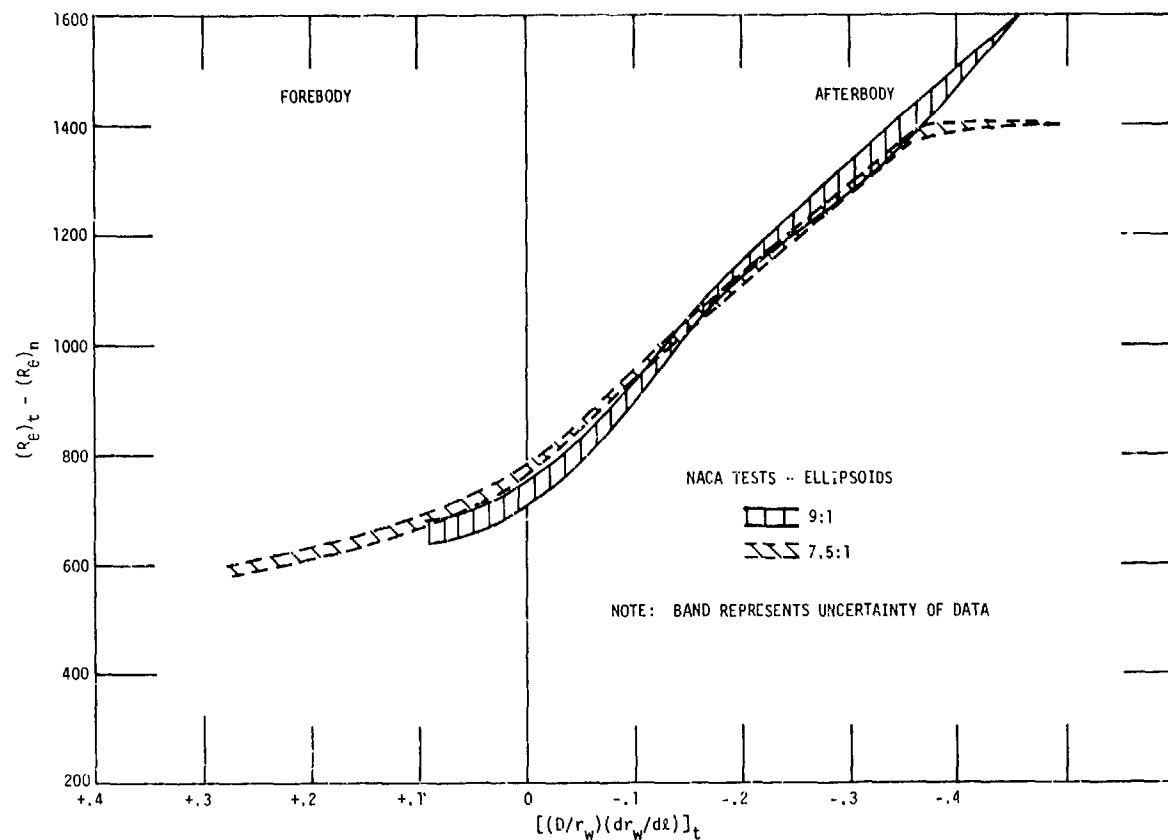


Fig. 11 Additional Correlation of Transition Data for NACA Ellipsoids

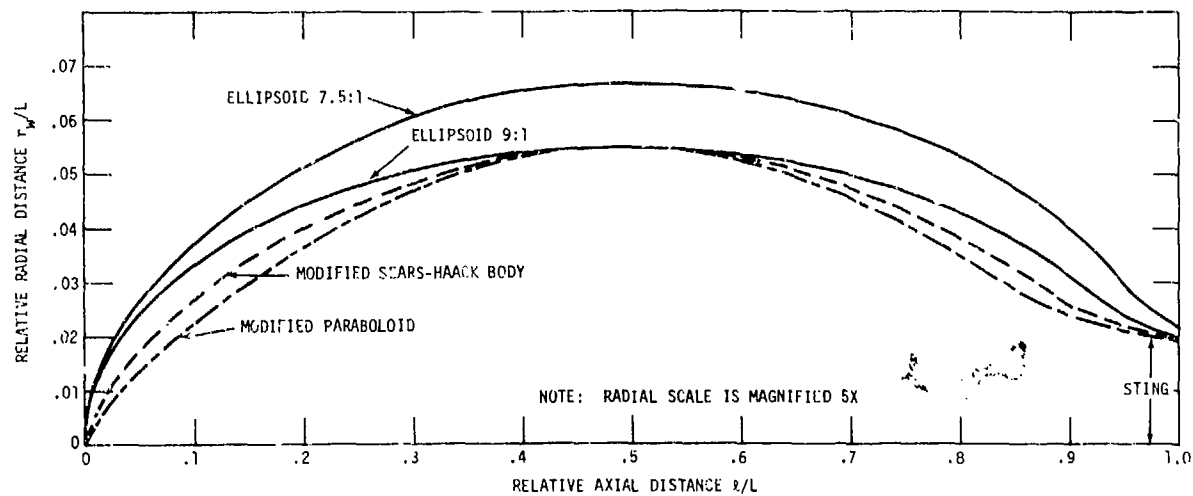


Fig. 12 Comparative Shapes of Bodies

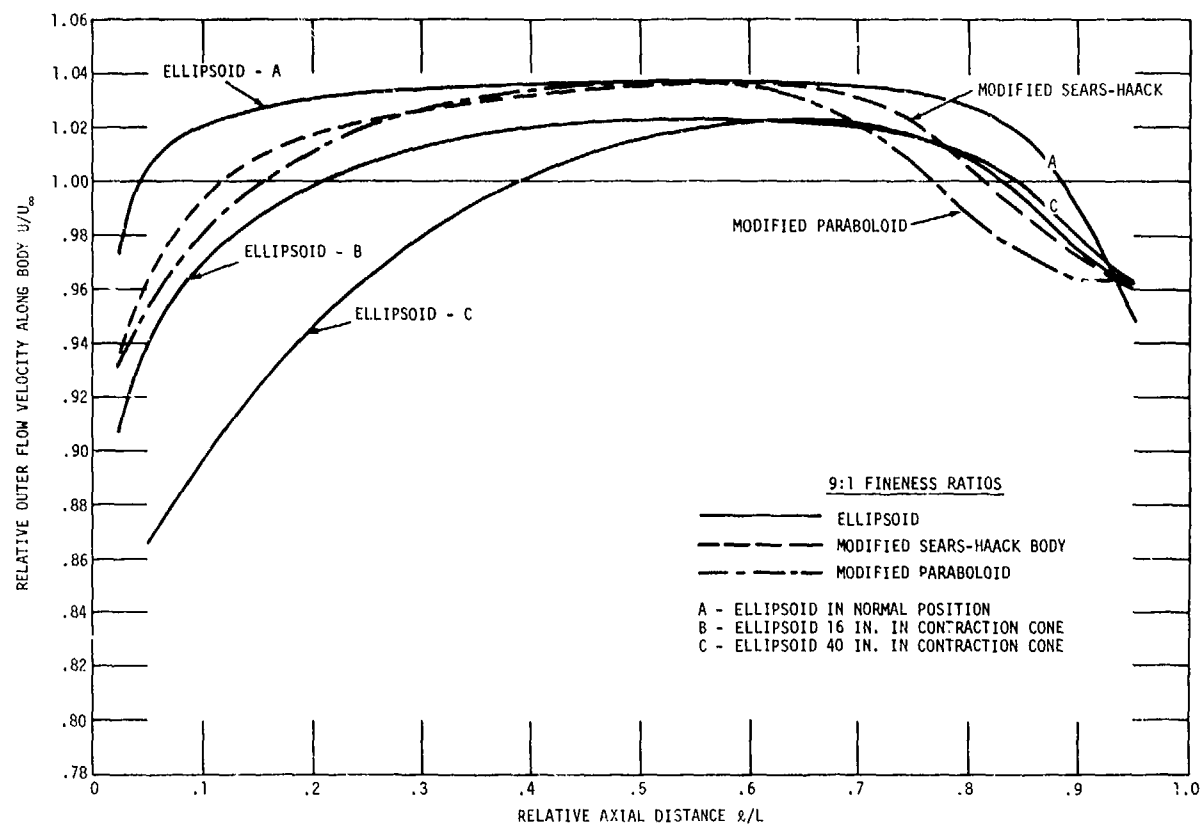


Fig. 13 Pressure Distributions (Outer Flow)

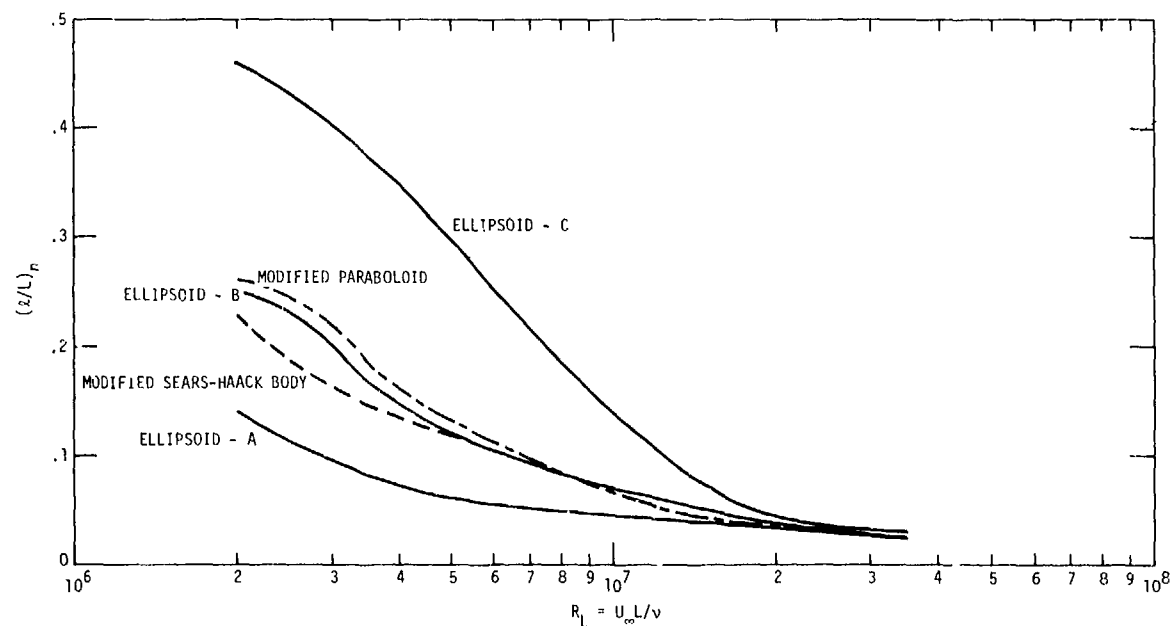


Fig. 14 Calculated Locations of Neutral Stability Point

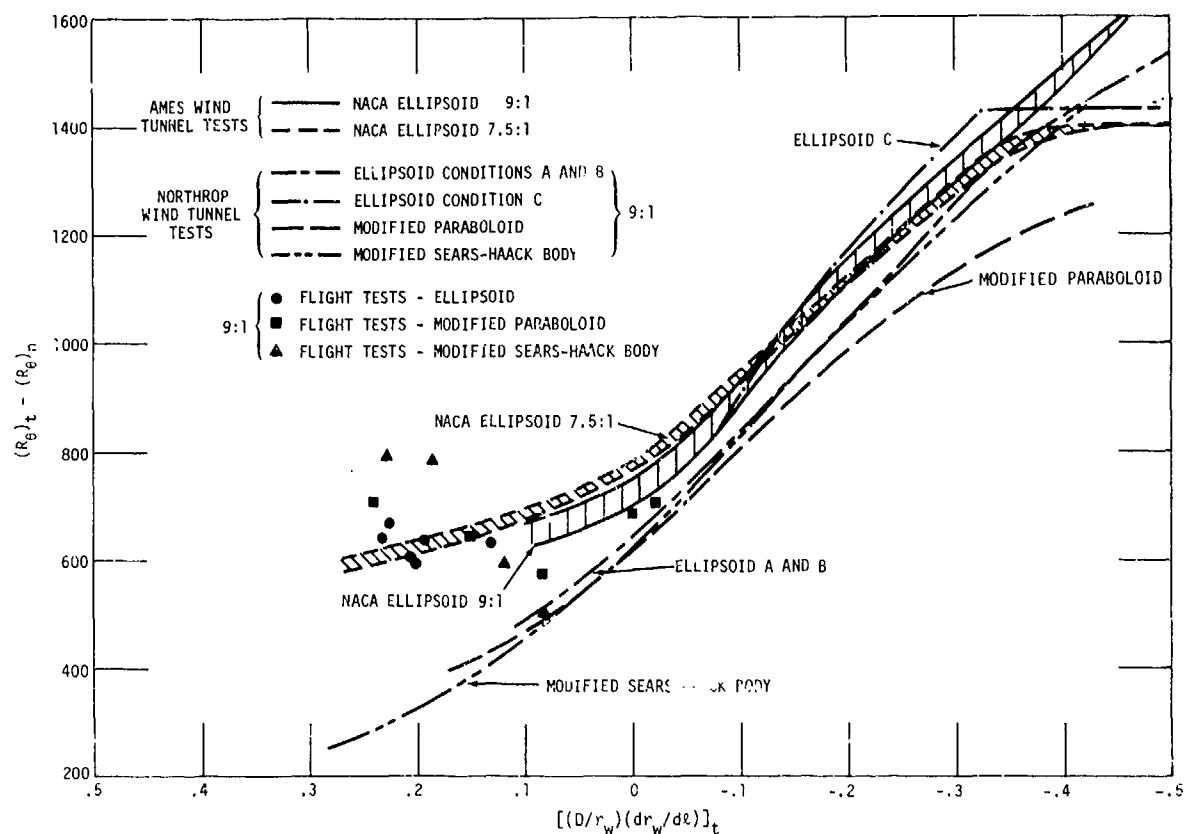


Fig. 15 Correlation of Transition Data for Bodies of Revolution

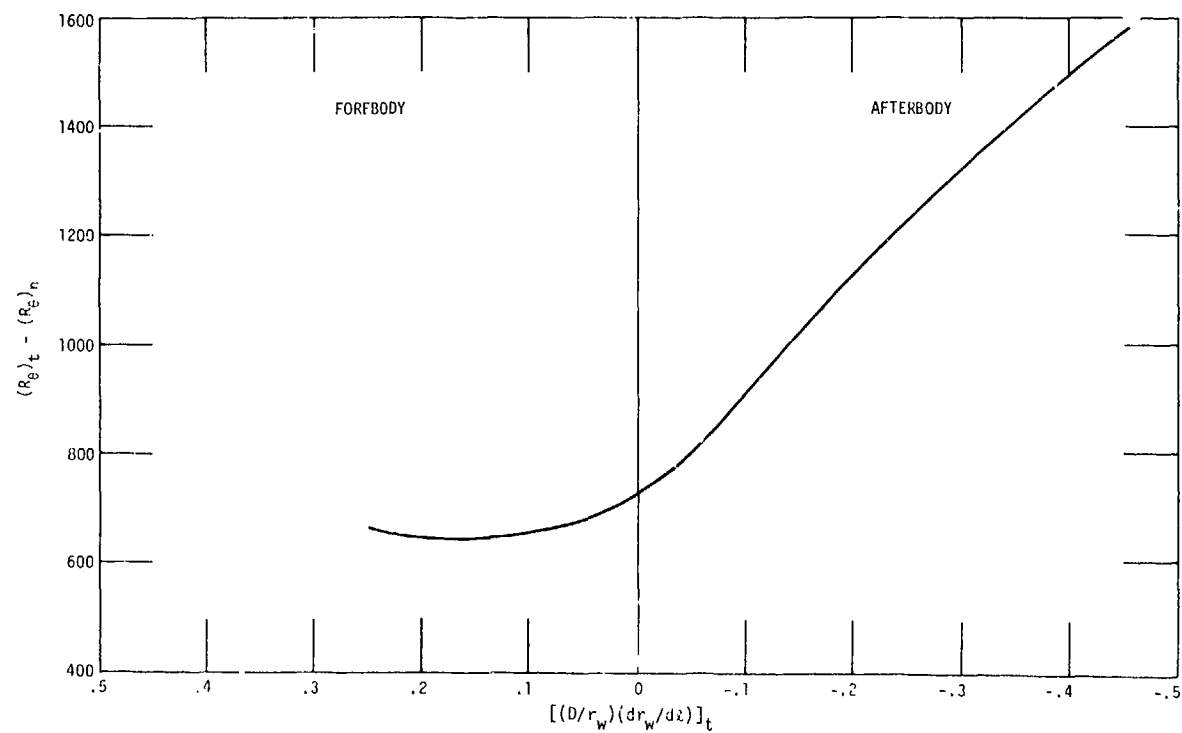


Fig. 16 Correlation Line for Prediction of Transition on Bodies of Revolution in Flow with Low Background Turbulence

DISCUSSION

A. M. O. SMITH and K. KAUPS

Mr. Granville has made a very useful survey of the various methods. Whether his new correlation is indeed an improvement still remains to be seen. A larger variety of test data is needed to establish the method with finality. In Granville's original method, he had a correlation based on a mean Pohlhausen parameter. In the new work he dispenses with that and uses a geometry parameter $(d/r)(dr/dx)$. The basic boundary-layer equations for axisymmetric flow involve two variable constants $(x/u_e)(du_e/dx)$ and $(x/r)(dr/dx)$. Mr. Granville is substituting the second for essentially the first. But according to the equation of motion, both are needed. Only if $(x/u_e)(du_e/dx)$ — as supplied by the inviscid solution — showed a close relation to $(x/r)(dr/dx)$ would we obtain a universal correlation. We doubt that there is this close relation. For instance, the entrance flow in a long round tube has a strong favorable gradient and extreme laminar runs — of 40,000,000 or so. But $(x/r)(dr/dx)$ for this case would be zero. Perhaps though, on ordinary convex bodies the correlation will indeed be proven better by additional test data.

On one point we would like to set the record straight: In reference (4) the two-dimensional transition correlation of Michel was applied to axisymmetric bodies via the Mangler transformation with $L = r_{max}$, and not with the transformation implied in reference (29), and also repeated here. The origin of this misunderstanding is not known. Unfortunately, the error has also appeared in a paper (28) which aims at improving the correlation.

C. S. Wells, Jr.

This paper represents a substantial contribution to the empirical correlation of boundary layer transition data, based on a general knowledge of the physical process leading to transition. Mr. Granville's proposed new correlation technique makes good use of existing data to account for the significant effects of axisymmetric spreading on bodies of revolution. However, the correlation is based on limited data and further evaluation of the technique must await the results of experiments over a wider range of the geometric parameters.

I would like to join the author in emphasizing the need for more experimental work under carefully controlled conditions, and especially for testing at low freestream turbulence levels typical of the atmosphere and oceans.

F.R. GOLDSCHMIED

The author is to be congratulated for making a start in the consideration of body geometry for the prediction of axisymmetric transition and for a careful historical review of the problem. A few minor points, however, require discussion:

1. The author deals only with slender bodies ($L/D = 7.5$ and 9.0) and he ignores the 1966 Carmichael⁽¹⁾ data of a "fat" body ($L/D = 3.3$) just as he ignored it before in his 1968 report⁽²⁾ on the comparison of several transition methods. There data show that the Mangler transform cannot be applied, either with length or with maximum radius reference, if the drag is to be predicted correctly, as it is evident from Figure A.
2. The author states that radial flow stretching (by increasing body diameter) hastens transition, while conversely contraction (decreasing body diameter) delays transition. I believe that this should be clarified as follows:

If the diameter of the body is increasing, two conflicting effects are felt. In the first, an increase of diameter means that the boundary-layer must be spread over an ever widening area, promoting thinning and altering the boundary-layer profile much as suction would do. It might be expected that this would delay instability beyond the point to which it is already delayed by the favorable pressure-gradient usually present on the forebody. In the second, cross-stream vorticity is being stretched, which, due to the associated increase in intensity, should result in an earlier occurrence of instability and transition. This suggests that there well may be a Reynolds Number range where the first effect predominates and another domain where the second effect predominates, leading to the visualization of some characteristic relationship between longitudinal curvature and transverse curvature which would define the boundary between the two ranges.

3. Although the explanation can be found in the text, Figure 2 could be highly misleading and create the impression that the Michel/Smith criterion is directly related to that group of transition methods based on the Pohlhausen parameter. A clarification should be added to the figure.
4. The author does not show how predictions made on the basis of the correlation curve of Figure 16 compare with the actual experimental results and what the prediction error may be, in terms of length or drag.
5. The author recognizes only one axisymmetric transition mechanism over the entire Reynolds Number range and attempts to make all experimental data fit one correlation mode. From Figure 15 it is apparent that the flight-test data envelope has a decreasing slope opposite to the increasing trend of the wind-tunnel data envelope. The actual test data of the 3 bodies considered by the author are shown in Figures B, C and D; it is quite apparent that in all three cases there must be two different

transition mechanisms at work and that a "switchover" point can be defined without undue difficulty in terms of location X and Reynolds Number Re . Thus, it is not surprising to see the conflicting slopes of Figure 15.

In conclusion, I am postulating a Tollmien-Schlichting two-dimensional transition mechanism up to the "switchover" point; the Jaffe/Okamura/Smith⁽³⁾ method will be valid up to this point. At the higher Reynolds Numbers, I am postulating a Gortler-type longitudinal-vortex transition mechanism. Finally, I am proposing that this "switchover" point can be correlated by a characteristic relationship between body longitudinal curvature and transverse curvature as shown in Figure E.

REFERENCES

1. Carmichael, B.H., "Underwater Vehicle Drag Reduction Through Choice of Shape", AIAA Paper 66-657, June 1966.
2. Granville, P.S., "Comparison of Existing Methods for Predicting Transition From Laminar to Turbulent

Flow on Bodies of Revolution", U.S. Navy NSRDC Hydromechanics TN 111, August 1968.

3. Jaffe, N.A., T.T. Okamura, and A.M.O. Smith, "The Determination of Spatial Amplification Factors and Their Application to Predicting Transition", AIAA Paper 69-10, January 1969.

LIST OF SYMBOLS

- D Maximum body diameter
- L Body length
- R Body radius at location X
- Re Reynolds number based on length $V^{1/3}$
- V Body volume
- X Axial coordinate
- X_t Axial transition location

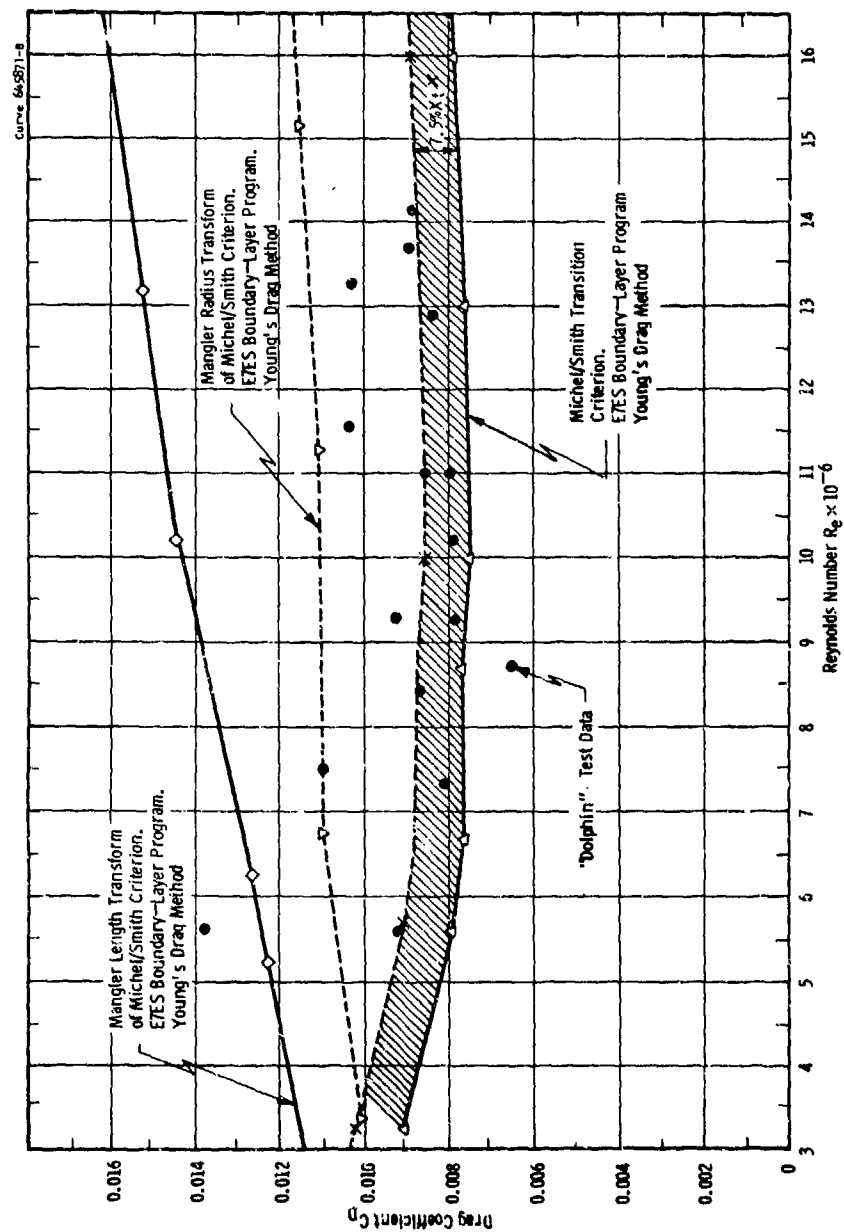


Fig. A—Experimental verification of Michel/Smith transition criterion for drag computation of Dolphin

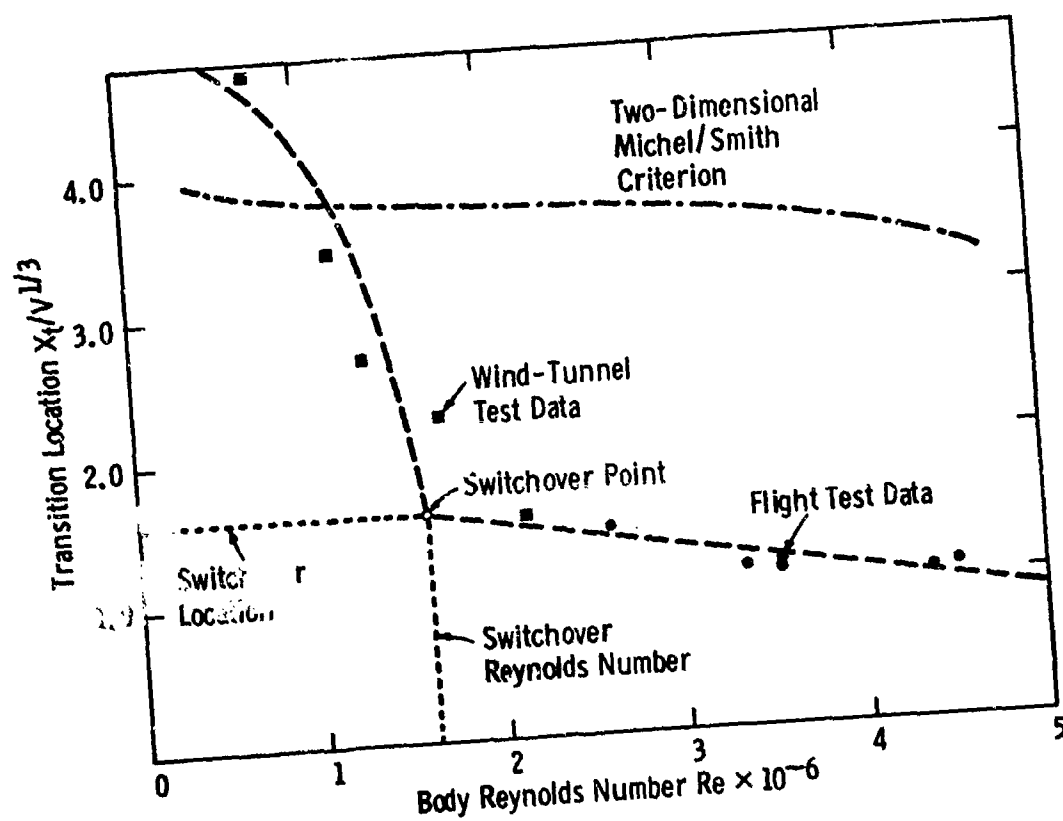


Fig. B—Experimental transition plot for 9:1 Elliptic body

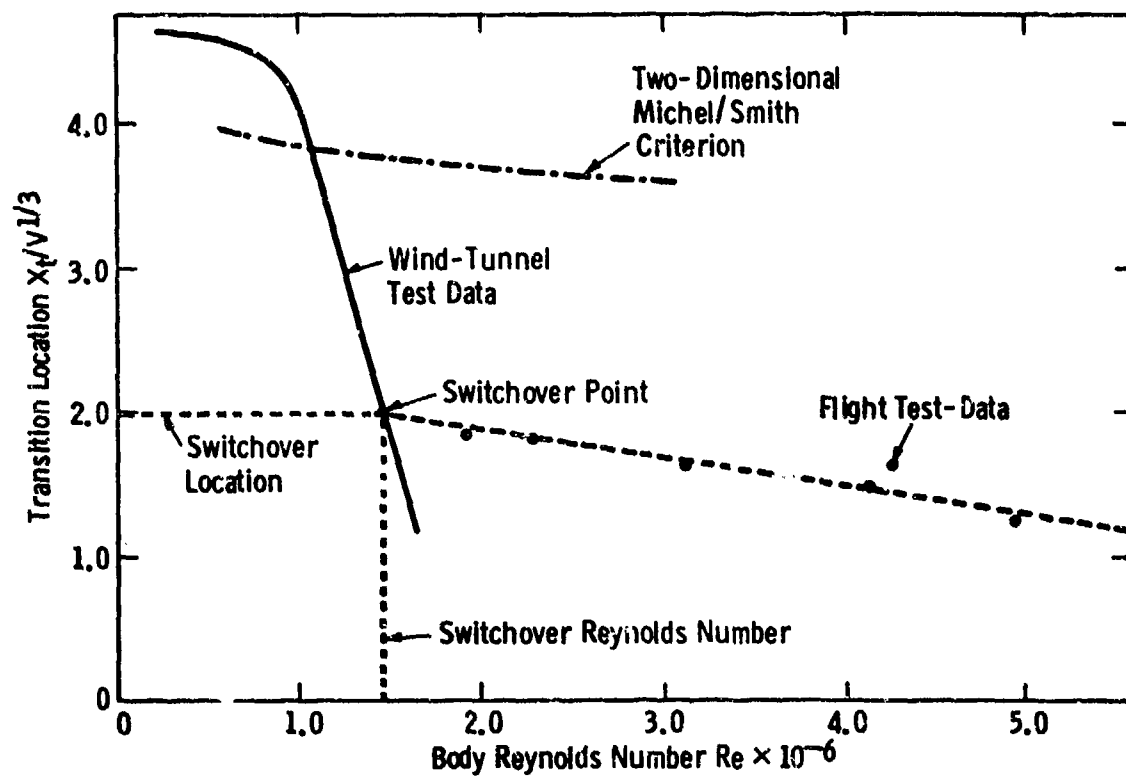


Fig. C--Experimental transition plot for Sears/Haack body

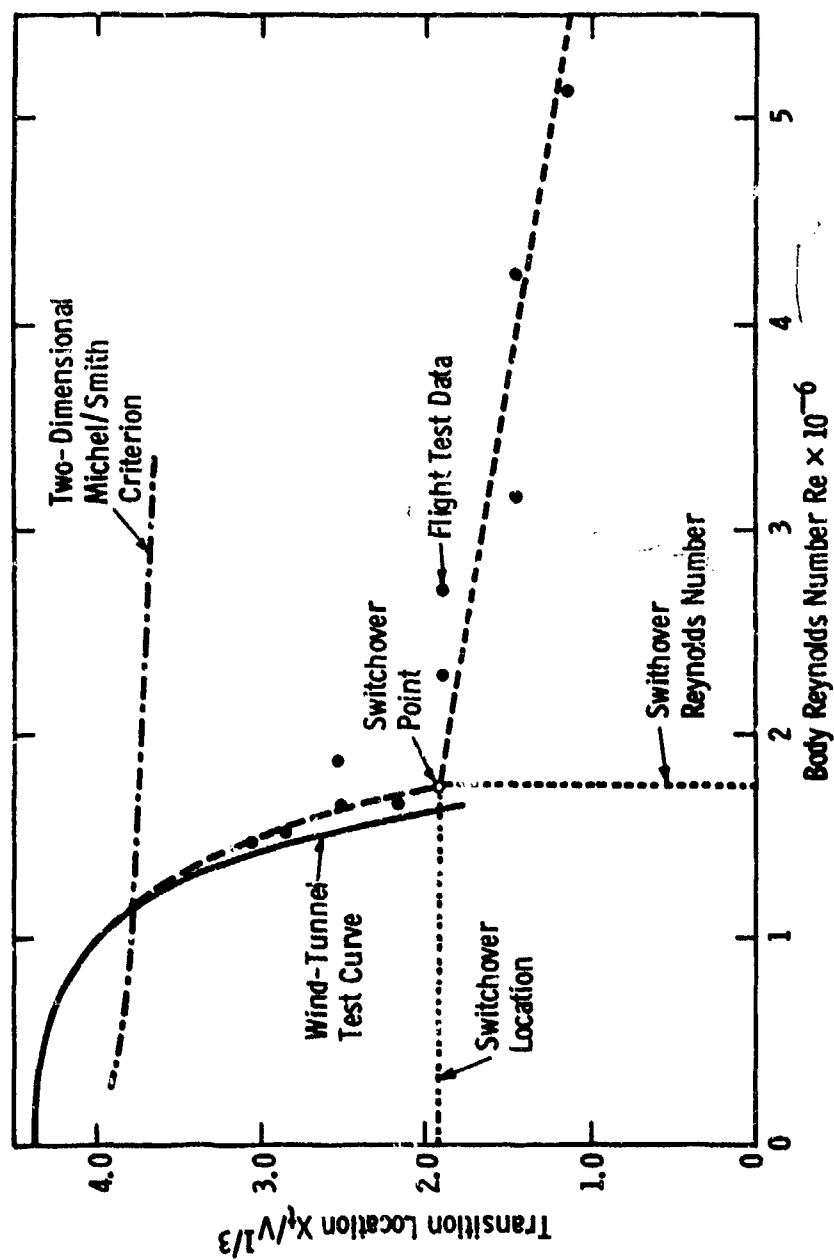


Fig. D—Experimental transition plot for Parabolic body

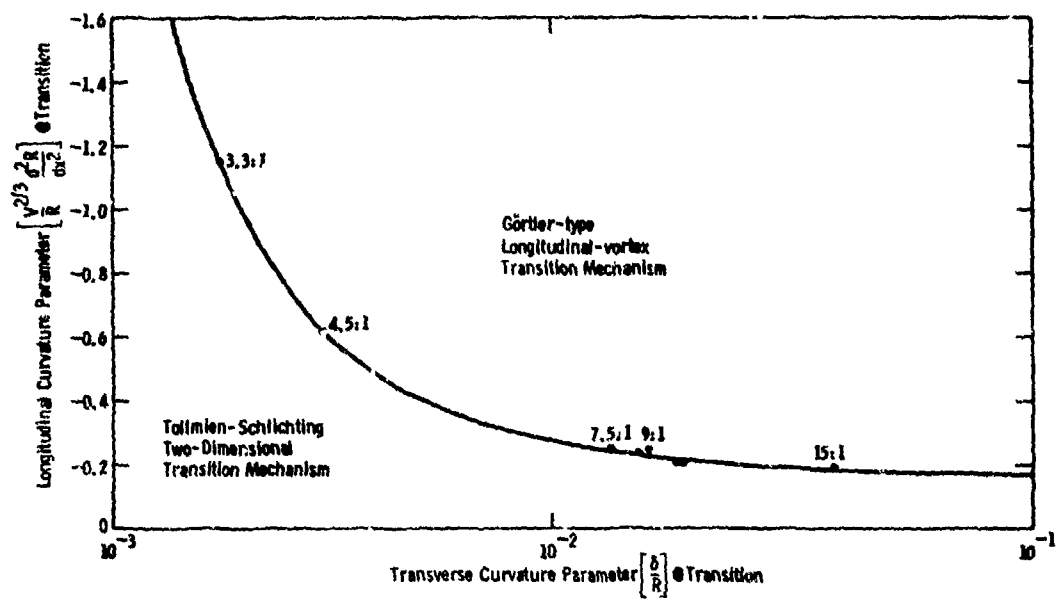


Fig. E--Axisymmetric correlation plot: transition switchover from Tollmien-Schlichting to Görtler mechanism

AUTHOR'S REPLY

As indicated in the text, the correlation of transition data applies only to curved bodies of the same general shape as the test bodies. A more universal correlation remains to be developed. The axisymmetric adjustment by Mangler's transformation was ascribed to Smith and Gamberoni by Eichelbrenner and Michel. Since Mr. Smith disclaims responsibility, the name of the method has been accordingly changed to Eichelbrenner and Michel in the revised text.

I agree with Dr. Wells that more experimental work is needed for bodies of revolution.

In reply to item 1 of Mr. Goldschmied's discussion: Carmichael's thick body was not considered in the correlation since there were no actual measurements of the position of transition. In item 2 the question of the effect of the axisymmetric spreading or contracting of the boundary layer in transition is raised. As considered in the text, this effect is more than that accounted for

by the change in the velocity profile as it develops under axisymmetric conditions. As stated in the text, the effect does not directly apply to the neutral stability point but only in the region from instability to transition. In item 3, the original results of Smith and Gamberoni were plotted in Figure 2 in terms of Crabtree parameters. Smith and Gamberoni used these same results for a Michel-type correlation. In item 4, future experience will show the validity of Figure 16 in making predictions of transition. In item 5, the "switchover" point referred to seems to be no more than that of the maximum width of the body where the forebody becomes the afterbody. This confirms the thesis of this paper that forebody stretching tends to hasten transition while afterbody contraction tends to delay transition. However, there seems to be here an additional mechanism than that associated with the usual two-dimensional Tollmien-Schlichting transition process. I do not understand the applicability of the Görtler-type transition process here.

FUNDAMENTAL HYDRODYNAMICS

SESSION VIII

Friday, June 28, 1974
2:00 P.M. - 5:10 P.M.

Chairman: Dr. T. F. Ogilvie
Chairman, Department of Naval Architecture
and Marine Engineering
University of Michigan
United States

Rayleigh-Taylor Instability of Surface Layers as the Mechanism for Bioconvection	733
Milton S. Plesset, Christopher G. Whipple, and Howard Winet, California Institute of Technology, Pasadena, California	
Hydrodynamics of the Containment of Oil Slicks	743
J.H. Milgram and R.J. VanHouten, M.I.T., Cambridge, Massachusetts	
The Maneuverability of Fish, With Possible Implications for Man-Made Vessels	763
D. Weihs, Technion-Israel Institute of Technology, Haifa, Israel	
Laser-Doppler Measurements of Trailing Vortices in a Water Tunnel	771
S.J. Barker, California Institute of Technology, Pasadena, California	
The Influence of Fences on Surface Piercing Struts and Foils	779
R.C. McGregor, J.L. Foster, R.S. Rothbium, and P.D. Swales, The University, Leeds, England	

RAYLEIGH-TAYLOR INSTABILITY OF SURFACE LAYERS AS THE MECHANISM FOR BIOCONVECTION

Milton S. Flesset, Christopher G. Whipple, and Howard Winet
California Institute of Technology, Pasadena, California

ABSTRACT

Swimming micro-organisms which show negative geotaxis, that is, which swim upward against gravity, develop characteristic bioconvection patterns; similar bioconvection patterns are found in swimming micro-organisms which are phototropic. This bioconvection is explained here as the consequence of Rayleigh-Taylor instability. The instability analysis is based on a treatment of the liquid with contained micro-organisms as a continuous fluid, and a justification of this treatment is given. In a well-developed culture which has a sufficiently high density of micro-organisms a steady state circulation can occur, and this condition is analyzed here. The quantitative experimental data obtained by Winet and Jahn for an organism with negative geotaxis, *T. pyriformis*, make possible detailed comparison with the theoretical analysis. It is also shown that the highly organized swimming of the micro-organisms in the upward direction rules out the applicability of ideas of random walk and diffusion. As a final subject the effect of a distributed unstable density distribution is analyzed and compared with the effect of a step discontinuity in density.

1. INTRODUCTION

A large class of swimming micro-organisms exhibit negative geotaxis; that is, they swim upward against gravity in their liquid medium. When a sufficiently large concentration of micro-organisms has developed in a surface layer, a characteristic bioconvection pattern forms. The pattern has fingers of fluid falling downward from the top layer in a rather regular array (see Figs. 1 and 2). Similar patterns are also observed with swimming phototropic micro-organisms; that is, micro-organisms which are attracted to regions of increased light intensity. The swimming, or self-propelling, capability of the micro-organisms is essential since the organisms of concern are heavier than the fluid medium.

Bioconvective patterns have been known since 1848, and have been observed in bacterial, flagellate, plankton, and ciliate cultures. Many attempts have been made to explain the formation of the patterns. In particular, it has been suggested that the patterns are driven by thermal instability. This mechanism was put forward because the bioconvective

patterns show some resemblance with Bénard cells. This idea was disproved by the experiments of R. Donnelly [1] who showed that bioconvective patterns persisted even when a stabilizing temperature gradient was imposed on the medium.

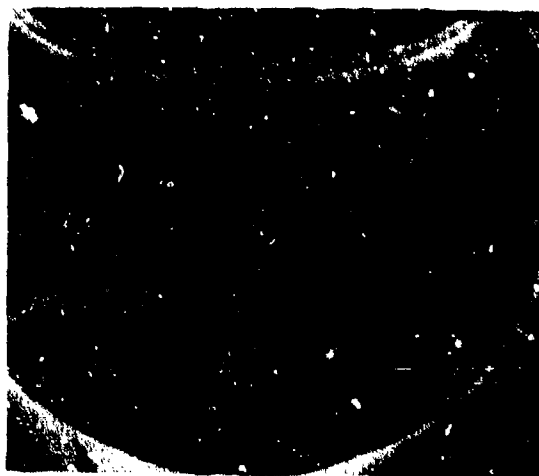


Fig. 1. *Tetrahymena pyriformis* culture - side view (pattern distorted by walls).

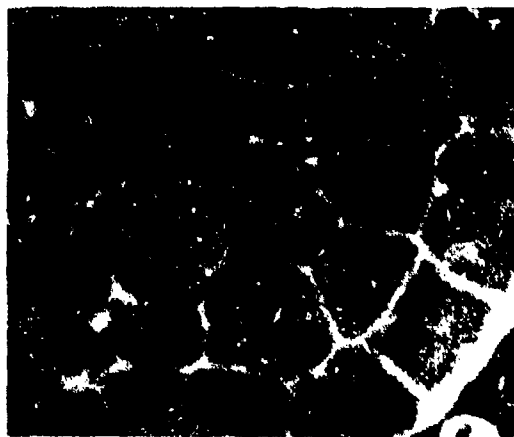


Fig. 2. *Tetrahymena pyriformis* culture - top view.

It has recently been proposed [2, 3] that a quantitative description of bioconvection patterns is given in terms of Rayleigh-Taylor instability. A quantitative comparison of a theoretical analysis with experiment is possible because of the extensive measurements by Winet and Jahn [4] on cultures of *Tetrahymena pyriformis*. It is observed that the surface layer represents a rather sharp rise in cell concentration when compared with the underlying culture. One makes the approximation that this upper layer is a homogeneous liquid which differs from the liquid below only by being somewhat heavier. If one is given the thickness of the upper layer, its density, and the density of the underlying liquid, then the Rayleigh-Taylor instability analysis predicts a preferred wavelength, or distance between fingers falling out of the upper layer. While the predictions of this homogeneous, continuum model agree very well with observations [2], it is certainly instructive to provide justification for the use of this continuum model. This justification is a primary consideration of the present paper. Consideration will also be given to the possibility of a steady state micro-organism circulation.

2. VALIDITY OF THE CONTINUUM MODEL

The justification of the continuum model will be given specifically in terms of the micro-organism *Tetrahymena pyriformis* since, as has been indicated, detailed measurements are available for this organism. The discussion should apply to micro-organisms both in fresh and salt water. *Tetrahymena pyriformis* is a ciliate which is about 5×10^{-3} cm in length and about 3×10^{-3} cm in width, and which has a swim speed U of approximately 4.5×10^{-2} cm/sec. The density of *T. pyriformis* is 1.076 gm/cm³ and the medium in which it lives is water with a relatively small amount of nutrient additives. If a culture has initially a uniform concentration of cells, C_0 , the swimming of the micro-organisms produces a net upward flux. Since the cells do not all swim precisely in the vertical direction, one may take the mean upward velocity to be αU . It will be seen from the discussion of the so-called steady state that α has a value only slightly less than unity. Experimental observations [4] show that, when the cells approach the surface, 17% stay in a well-defined layer on the surface. This layer has a thickness h which ranges from 0.1 cm to 0.5 cm. The remaining 83% of the approaching cells are "reflected" from the surface layer, or from the abrupt increased cell concentration in that layer. These reflected cells fall downward for a distance which is many times the surface thickness h . It appears that a considerable amount of time is required before a cell turns around and resumes its normal upward ascent. If the culture has the uniform initial concentration C_0 , the upper layer concentration, C_u , will grow linearly with time provided that the layer thickness remains constant. This thickness appears to remain essentially constant; it does depend on the age of the culture but this dependence is measured on a time

scale which is much longer than the time of pattern formation. When C_u has reached a minimum value, patterns begin to develop in the surface (see Fig. 2) which correspond to regions of higher cell concentration separated by regions of lower concentration. At the intersections of these lines, or clusters, of high concentration falling "fingers" form which attain a terminal fall velocity of about 0.1 cm/sec. This terminal velocity from the nodal intersections is already reached as soon as the fingers are discernible below the lower boundary of the surface layer. It may be remarked that this fall velocity is more than twice the swim velocity of the organisms and is much greater than the Stokes fall velocity of a single cell under gravity ($\approx 6.6 \times 10^{-3}$ cm/sec). Clearly the patterns and the finger fall velocity cannot be generated by any action of an individual cell. This behavior must arise from a cooperative macroscopic effect.

When a swimming micro-organism is moving with constant velocity, there can be no net force acting on it. The self propulsion of the cell balances both the drag and the gravitational force. If V_T is the volume of a cell, ρ_T its density, then the gravitational force is $V_T \rho_T g$ where g is the acceleration of gravity. This gravitational force is partially balanced by the buoyancy force $V_T \rho_0 g$ where ρ_0 is the density of the medium. A nonaccelerating cell must therefore exert a net downward force given by

$$V_T(\rho_T - \rho_0)g = V_T \Delta \rho_T g.$$

This force is the only significant effect of a cell on the fluid. A possible additional effect could come from accelerations in cell motion. As an extreme acceleration case, the acceleration force of a cell may be estimated under the assumption that the swim speed U is acquired from rest in one body length. The swim speed $U = 4.5 \times 10^{-2}$ cm/sec, the body length $l = 5 \times 10^{-3}$ cm so that the acceleration is $a \approx 0.2$ cm/sec², the ratio of the acceleration force, F_a , to the gravity force, F_g , is therefore

$$\frac{F_a}{F_g} = \frac{\rho_T V_T a}{\Delta \rho_T V_T g} = \frac{\rho_T a}{\Delta \rho_T g}.$$

With $\rho_T = 1.076$ gm/cm³, $\Delta \rho_T = 0.076$ gm/cm³, $g \approx 10^3$ cm/sec², one has

$$\frac{F_a}{F_g} \approx 3.2 \times 10^{-3}.$$

It is evident that acceleration forces are unimportant compared with the gravity force. A similar argument shows also that the arrest of the upward motion of a cell at the surface of the medium gives rise to forces small compared with gravity. This acceleration and the corresponding locomotive force is in agreement with the general results presented by Brennen [5].

There is a momentum flux from cells entering the upper layer of the medium. This flux exerts a force per unit volume of the

upper layer. As might be expected, this force per unit volume is quite small compared with the gravity force per unit volume of the upper layer. The net horizontal momentum flux is zero, and the vertical momentum flux is estimated as follows. The upper layer, which has cell concentration C_u , overlays the lower fluid which has cell concentration C_L . The lower fluid region has a depth large compared with h . The cells swim upward with a mean speed aU and of those coming up to the lower boundary of the upper layer, the number entering per unit area per unit time is $0.17 C_L aU$ where we use Winet's figure for the fraction of incident cells which enter the upper layer. These cells bring a vertical momentum $\rho_T V_T aU$ so that their contribution of vertical momentum flux per unit area per unit time has the value $0.17 C_L \rho_T V_T a^2 U^2$, or a force per unit volume of the upper layer of magnitude

$$\frac{0.17 C_L \rho_T V_T a^2 U^2}{h}.$$

The number of cells "reflected" from the lower boundary of the upper layer per unit area per unit time is $0.83 C_L aU$, and the vertical momentum imparted to the upper layer is at most $2\rho_T V_T aU$ so that the vertical force per unit volume from these cells is

$$\frac{1.66 C_L \rho_T V_T a^2 U^2}{h}.$$

The ratio of the total force per unit volume from cells coming up from the lower medium to the gravity force per unit volume of the upper layer is, therefore,

$$\frac{f_m}{f_g} = \frac{1.83 C_L \rho_T V_T a^2 U^2}{h C_u \Delta \rho_T V_T g} = 1.83 \frac{C_L \rho_T a^2 U^2}{C_u \Delta \rho_T h g}$$

we have $C_L/C_u < 1$, $\rho_L/\Delta \rho_T < 15$, $aU \approx 4 \times 10^{-2}$ cm/sec, $h > 0.1$ cm, and $g \approx 10^3$ cm/sec² so that

$$\frac{f_m}{f_g} < 4 \times 10^{-4}.$$

Clearly this cell momentum flux effect is negligible.

In a very young culture bioconvection is not observed until the concentration of cells in the upper layer is greater than about 4×10^4 cells/cm³. The corresponding distance between cell centers is 3×10^{-2} cm. The minimum observed wavelength, or distance between the falling jets is about 0.5 cm so that the effect of individual cells and their separation is not too important. Even for the thinnest observed upper layer, 0.1 cm, and for the minimum cell concentration there are 4×10^3 cells per cm² of the layer. The granular nature of the increased density in the upper layer is not too significant, and one can conclude that to a reasonable approximation one has a uniform upper layer with a density increment over the underlying medium. Any

effects arising from individual cell motions must be of very short wavelengths of the order of the nearest neighbor distance and therefore are not significant when compared with the internodal distance. That there should be a minimum density increment, or cell concentration, in the upper layer is not surprising. The finger, or jet, fall velocity decreases as $\Delta \rho$ decreases, and for a sufficiently small value of $\Delta \rho$ this fall velocity will not exceed the upward swim velocity of the micro-organisms. It follows that falling jets will not develop until the cell concentration has risen above a minimum value.

The theoretical solution which has been used to deduce the internodal distance [3] assumes a discontinuous jump in the density at the lower boundary of the upper layer. One does not expect that this mathematical prescription is exactly satisfied in the bioconvective problem; however, photographs of *T. pyriformis* cultures with side illumination with collimated light indicate that the cell concentration jump appears to take place in a distance which is usually less than 0.05 cm. It may be remarked that this distance is only twice the nearest neighbor distance just calculated, but it may be pointed out that most of the experimental conditions of interest correspond to cell concentrations at least an order of magnitude greater than this concentration used for that nearest neighbor estimate. Yet it must be admitted that with upper layer thicknesses of 0.10 cm to 0.15 cm some error is introduced by the assumption of a step density change. While the error introduced for the thinner layers by a finite density transition region could be estimated along the lines to be described later, it is believed that the error is unimportant.

The physical view of the bioconvection process is that one has a well-defined layer of thickness h which has density ρ' which exceeds the density ρ of the underlying medium by $\Delta \rho$. This situation is one familiar in fluid mechanics as Rayleigh-Taylor instability, but a somewhat unusual feature here is that the gravity force is so small that viscosity becomes quite important. Measurements have been made which show that the presence of the micro-organisms do not affect the viscosity of the medium appreciably. It seems reasonable to assume that the surface tension is also not affected. The only important physical difference, then, between the upper layer and the underlying medium is in the density. The Rayleigh-Taylor problem here has an upper liquid layer of thickness h and of density ρ' with its upper boundary a free surface with surface tension T . The lower medium is of thickness large compared with h and of density ρ .

The surface tension, T , is taken to be continuous across the interface. The kinematic viscosities of both regions are supposed to have the same value ν . Both T and ν are taken to have the values appropriate for water. A rigorous solution has been carried out for this problem in which the kinematic viscosities are allowed to be different [3] and it may be shown that a small difference in kinematic viscosity gives only a second order effect. It is also found from the exact solution that the surface

tension at the free surface does not make an important contribution.

The growth of an interfacial instability may be determined in a straightforward way so long as its amplitude is small; that is, so long as the linearized hydrodynamic equations may be used. The amplitude referred to here is $a_k(t)$, where the displacement of the interface is taken to be of the form

$$\eta_k(x, t) = a_k(t) \sin kx,$$

and where $k = 2\pi/\lambda$ is the wave number. The amplitude, $a_k(t)$, within the range of validity of the linearized theory grows exponentially,

$$a_k(t) = a_k(0)e^{nt},$$

and the analysis leads to a relationship between n and k . It has been shown [3] that a rather simple approximation with a straightforward physical basis leads to an approximation to this relationship from the solution of this equation:

$$n^2 + 2\nu k^2 n - \frac{gk(\rho' - \rho)}{\rho' + \rho \coth kh} = 0. \quad (1)$$

From this relation it is easy to see that n as a function of k , or λ , has a maximum. Figure 3 shows n as a function of λ both as determined by Eqn. (1) and as determined from the precise linearized theory. The approximate theory gives a result which is in fairly good agreement with the exact theory and has the considerable advantage of giving

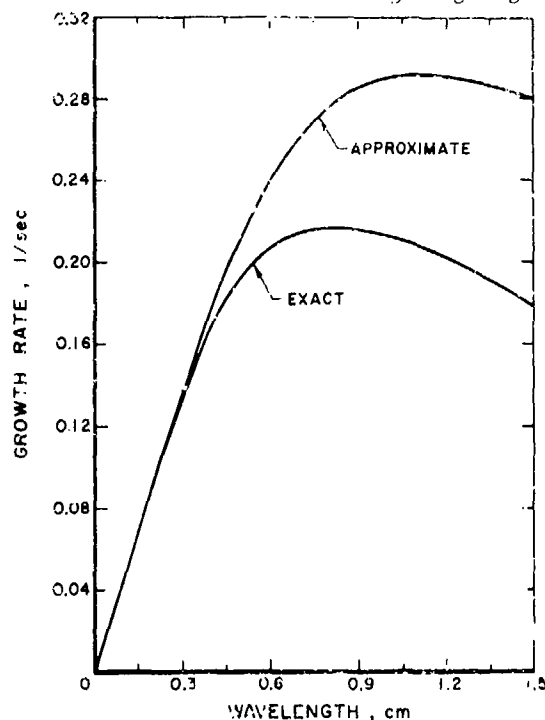


Fig. 3. Growth rate versus wavelength for the small density difference case with a free surface at $z = h$; $\Delta\rho = 1.21 \times 10^{-4}$ gm/cm³.

approximate numerical values very readily. Figure 4 shows how the "preferred" wavelength, or the wavelength which gives maximum n , varies with the thickness h of the upper layer. As would be expected, the approximate theory gives poorer values for decreasing h .

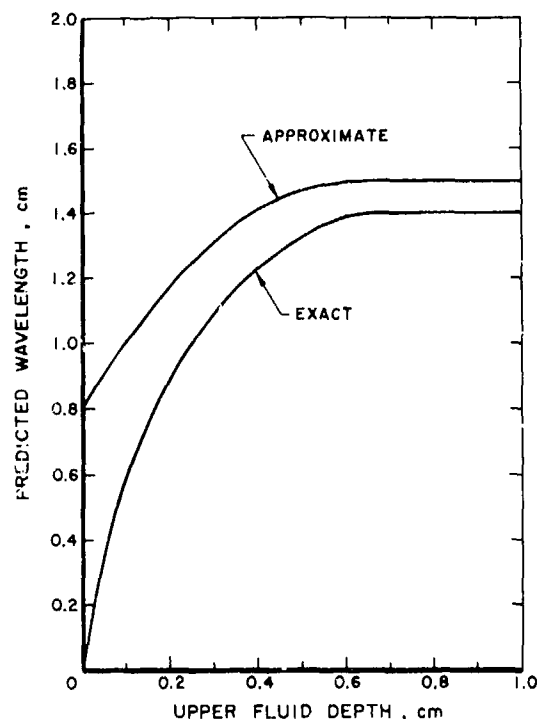


Fig. 4. Preferred wavelength versus depth for small density difference, free surface case; $\Delta\rho = 1.21 \times 10^{-4}$ gm/cm³.

In the application of the results of the instability theory to the bioconvection problem, it is expected that the wavelength for which n is a maximum, λ_m , would correspond to the most frequently observed separation distance between the fingers. While the theory is limited to small amplitudes, the wavelength which leads in growth may be expected to continue to lead. On this basis some comparisons of the theoretical results with experiment are given in Table 1 which is taken from Ref. 2. The agreement between theory and experiment may be seen to be good.

TABLE 1 Measured and theoretical values for two *Tetrahymena* cultures

C_0 (cells cm ⁻³)	3×10^4	2.71×10^4
h (cm)	0.13	0.13
C_1 (cells cm ⁻³)	0	5.6×10^4
C_2 (cells cm ⁻³)	7.1×10^4	1.4×10^4
$\Delta\rho$ (g cm ⁻³)	1.21×10^{-4}	1.08×10^{-4}
$\lambda_{max}(cm)$	~ 1.0	0.655
$\lambda_{theo}(cm)$ (exact theory)	0.80	0.525
$\lambda_{theo}(cm)$ (approximate theory)	1.1	0.65

The range of parameters shown is characteristic of *T. pyriformis* culture systems and although stated values of C_0 are exceeded in both directions no modes appear at values below the smaller figure and cultures at values above the larger figure were not analysed. The symbols are defined in the text.

A remark may be interposed at this point regarding nonlinear effects on the preferred wavelength. If \vec{u} is the fluid velocity, the term neglected in the momentum equation

$$\frac{\partial \vec{u}}{\partial t} + \vec{u} \cdot \nabla \vec{u} = -\frac{1}{\rho} \nabla p + \nu \nabla^2 \vec{u} \quad (2)$$

in the linearized theory is $\vec{u} \cdot \nabla \vec{u}$. In the range of validity of the linearized theory $a(t) = a_0 e^{nt}$, and the velocity \vec{u} varies like $\vec{u} \approx n a_0 e^{nt}$, and the acceleration behaves like $\ddot{u} \approx n^2 a_0 e^{nt}$. The first term on the left hand side of Eqn. (2) varies like un , and the omitted term like $u^2 k$ so that one may expect the linearized theory to be valid so long as

$$\frac{u^2 k}{un} \ll \epsilon$$

where ϵ is a small quantity. This inequality is equivalent to

$$k a_0 e^{nt} \ll \epsilon \quad (3)$$

This last inequality indicates that, for comparable small initial amplitudes, a_0 , the disturbance with the longer wavelength follows the exponential growth described by linear theory for a longer time. There is then the possibility that disturbances with longer wavelengths could overtake the disturbance with the preferred wavelength. If one now looks at the experimental situation, it is immediately evident that the falling instability fingers in a very short time and after a very short distance below the initial level of the interface attain terminal velocity. This terminal velocity of fall is about 0.1 cm/sec and, if one extrapolates the linear solutions to this stage of the motion, one finds that the amplitude of the preferred disturbance exceeds that of a long wavelength disturbance by more than an order of magnitude. It seems reasonable to suppose that the nature of the subsequent fall of the heavier fluid, and the rise of the lighter fluid, has been fairly well determined. This subsequent motion leads to the narrowing of the falling heavier fluid into a narrow jet and the flattening of the interface at the top of the rising lighter fluid. The separation distance between the jets, or fingers, should not change significantly.

3. STEADY STATE CIRCULATION

In a young culture of swimming micro-organisms such as *T. pyriformis*, after the cells have accumulated sufficiently in the surface layer, the bioconvection pattern forms and the fingers fall from this layer until the concentration of cells is depleted. A new bioconvection pattern will form again but only after the micro-organisms have swum back up to the surface. Typically a new pattern will form in a laboratory culture but only after a time interval of the order of 20 to 40 seconds. In this culture state the appearances of the bioconvection patterns are a separated, distinct sequence of transient events. As the number of cells increases with culture age, the cell concentration in the region underlying

the surface layer is large enough to sustain the cell concentration of the surface layer. Then the bioconvection pattern goes into a fairly steady state which will now be considered. The preferred wavelength, or separation, of the falling jets for the steady state will still be determined in the same way as is appropriate for a transient state. This procedure is readily justified for the steady state since, as will be made apparent, the return flow is quite small and, will therefore produce negligible disturbance in the dynamics of the surface layer. It will be evident that the return fluid velocity in the medium is about 0.002 cm/sec. This flow velocity is small enough to be ignored, for it means that the bulk of the fluid has had a negligible displacement in the time required for the micro-organisms to fall in the jets and then to return to the surface. This return time is less than one or two minutes since the falling jets are fairly well depleted of their micro-organisms in 2 or 3 centimeters. Here we see a fundamental difference between the present flow problem and the flow problem in Bénard convection. In the Bénard pattern formation the entire fluid medium partakes of the transport motion. In bioconvection the transport consists primarily of micro-organisms with negligible transport of the medium.

The formation of the jets in the upper layer produces the polygonal patterns in the surface (see Fig. 2) with lines of greater concentration of cells forming the borders of the polygons. The micro-organisms are carried along these lines into the jets which occur at the intersection of these lines. The irregular polygon shapes may be easily accounted for. This effect is not due either to the steady state or to nonlinearities. The linearized theory predicts the preferred wavelength, but it is determined from a two-dimensional calculation. This theory predicts the distance between parallel wave crests in the interface. Since no direction is preferred, lines of waves can develop in arbitrary directions, and the intersections of these families of lines form the polygons. In the two-dimensional theory, the greatest growth occurs at the wave crests; in the three-dimensional theory the maximum growth occurs at the intersections ("nodal") points of the two independent families of crests.

The jets which form at the nodal points grow into narrow fingers with separations determined essentially by the wavelength for which the growth parameter n is a maximum. A typical experimental observation gives a jet fall velocity $u = 0.10$ cm/sec, with a jet radius $b \approx 0.06$ cm when the jet length l has a value of about 0.26 cm. Only an approximate value for the density jump in the upper layer, $\Delta\rho$, is available in these measurements of jet fall, but it is estimated $\Delta\rho$ is approximately 10^{-3} gm/cm³. Such a density difference is entirely consistent with the observed internodal distance $\lambda \approx 0.70$ cm.

The density difference may be inferred in another way from the observed terminal velocity. The drag force on a slender cylindrical rod of length l and radius b is [6]

$$f_a = \frac{2\pi\mu l u}{\ln l/b - 0.8069} \quad (4)$$

where u is its velocity and μ is the coefficient of viscosity. The gravity force is

$$f_g = \pi b^2 / g \Delta \rho. \quad (5)$$

At terminal velocity these forces are equal so that one has

$$\frac{2\pi u \ell u}{\ln \ell/b - 0.8069} = \pi b^2 / g \Delta \rho, \quad (6)$$

or

$$\Delta \rho = \frac{2\mu u}{b^2 g (\ln \ell/b - 0.8069)}. \quad (7)$$

For the present typical case, one has $u \approx 0.10$ cm/sec, $\ell \approx 0.26$ cm, $b = 0.06$ cm, $\mu = 0.01$ poise, and $g = 980$ cm/sec² which gives

$$\Delta \rho \approx 9 \times 10^{-4} \text{ gm/cm}^3. \quad (8)$$

We now consider the possibility of a balance in cell distributions in a steady state model with continuous circulation of microorganisms. For our typical example, the surface, or upper layer has a cell concentration $C_u = 1.4 \times 10^6$ cells/cm³ and the region just beneath the upper layer has a concentration $C_m = 5.6 \times 10^5$ cells/cm³. The mean concentration over the whole culture is $C_o = 2.7 \times 10^5$ cells/cm³.

For an area A of the interface between the upper layer and the underlying region, the flux out of the upper layer is

$$F_u^o = C_u u \Delta A$$

where u is the speed of the falling jets and ΔA is the area taken up by the jets out of the total area A . If we recall that 17% of the cells incident on the upper layer from below actually enter the upper layer, the flux into the upper layer is

$$F_k^i = 0.17 C_m u_o (A - \Delta A)$$

where $u_o = aU$ is the mean vertical projection of the swim speed U , and $A - \Delta A$ is the area available for the inflow. The area of a single jet is $\pi b^2 = 0.011$ cm² and, if λ is the average distance between the falling jets, then A/λ^2 jets are present in A . Thus, we have

$$\Delta A = \frac{\pi b^2}{\lambda^2} A.$$

For these cell concentrations, $\lambda = 0.7$ cm which is an average separation. The ratio of fluxes for the upper layer is

$$\frac{F_u^i}{F_u^o} = \frac{0.17 C_m a U (A - \Delta A)}{C_u u \Delta A},$$

and with $A/\Delta A = 43$, $U = 0.045$ cm/sec,

$$\frac{F_u^i}{F_u^o} = 1.29 a \quad (9)$$

For a flux ratio of unity we are led to

$$a \approx 0.78 \quad (10)$$

If the upper layer has thickness h , and if the region with concentration C_m has thickness h' , the concentration of cells in the lowest region of the culture may be computed in terms of the total depth, d , of the culture. The total number of cells is $N = C_o A d$. If C_l denotes the concentration in the lowest region,

$$\frac{N}{A} = C_o d = h C_u + h' C_m + (d - h - h') C_l.$$

For the experimental case under consideration we have $h \approx 0.1$ cm, $h' = 0.5$ cm, and $d = 2.0$ cm. These values give $C_l = 8.6 \times 10^4$ cells/cm³. It should be remarked that a density step does not exist between the middle layer and the lowest region. A rather mild continuous gradient in concentration is observed. The effect of such a gradient is considered in the last section of this paper.

For the fluxes into and out of the middle layer, one has $F_m^o = 0.17 a U C_m$ and $F_m^i = a U C_l$. The flux ratio is

$$\frac{F_m^i}{F_m^o} = \frac{C_l}{0.17 C_m} = 0.935, \quad (11)$$

which is indeed close to unity. Finally, the ratio of the fluxes into and out of the lowest region is

$$\frac{F_l^i}{F_l^o} = \frac{C_u u \Delta A}{C_l a U (A - \Delta A)}. \quad (12)$$

With $a = 0.78$, this ratio is

$$\frac{F_l^i}{F_l^o} = 1.10 \quad (13)$$

which again is near unity. In view of the approximations which are made in the calculations, the present model for steady state convection seems quite acceptable.

While there are obvious approximations in the calculations just presented, the general conclusions seem very well supported. It is evident that the upward swimming velocities are quite highly organized in the vertical direction. Further, the return upward liquid velocity, which is $(A/\Delta A - 1)u$, is so small that it may be ignored so far as any effect on the surface pattern, or λ_m , is concerned. With $A/\Delta A = 43$ and $u = 0.1$ cm/sec, this return flow velocity is 0.002 cm/sec.

4. EFFECTS OF MICRO-ORGANISM DIFFUSION - RANDOM WALK

Some workers in the study of micro-organisms have proposed to apply random walk theory or diffusion theory to the distribution of micro-organisms in a medium. From the discussion just presented here it seems clear that these notions are inapplicable to swimming organisms which exhibit a taxis such as the negative geotaxis of *T. pyriformis*. The motion of these micro-organisms is highly organized in the vertical direction.

We now determine the possible effects of diffusion which would operate for organisms with nondirected motions. The appropriate mean free path which determines the diffusion coefficient is the Clausius mean free path since the micro-organisms may be supposed to all have the same swim speed. This mean free path is

$$\lambda = \frac{0.75}{C\sigma}$$

where C is the number of organisms per unit volume and σ is their collision cross section. For *T. pyriformis* we have a micro-organism with the approximate radius $r \approx 2 \times 10^{-3}$ cm. The cross section then is

$$\sigma = 4\pi r^2 \approx 5 \times 10^{-5} \text{ cm}^2,$$

and the mean free path, for randomly directed motion, is

$$\lambda \approx \frac{10^4}{C}$$

in cm if C is the concentration of cells per cm^3 . The mean free path for $C = 10^6/\text{cm}^3$ has the value $\lambda \approx 10^{-2}$ cm and for $C = 10^5/\text{cm}^3$, $\lambda \approx 10^{-1}$ cm. The diffusion coefficient, or the diffusivity, is

$$D = \frac{1}{3} \lambda u$$

where u is the swim speed. For $C = 10^6$, $D \approx 1.5 \times 10^{-4} \text{ cm}^2/\text{sec}$, and for $C = 10^5$, $D \approx 1.5 \times 10^{-3} \text{ cm}^2/\text{sec}$. The time required to diffuse 1 cm is given numerically by $1/D$, and for $C = 10^6$, this diffusion time is 6×10^3 sec and for $C = 10^5$ it is 6×10^2 sec. These times are very long compared with times which characterize the cultures of *T. pyriformis*. The time for a falling jet to traverse 1 cm is 10 seconds; the time for organisms to swim 1 cm is about 20 seconds. It would seem clear that, not only is the motion highly organized in a culture with taxis, but also that diffusion times are not pertinent.

5. RAYLEIGH-TAYLOR INSTABILITY IN A FLUID WITH VARIABLE DENSITY

We consider the following problem: for $z < 0$, we have a fluid of density ρ_1 ; for $z > 0$ the fluid has density ρ_2 ; and for $0 \leq z \leq d$, the density is $\rho = \rho_1 e^{\beta z}$ so that $\rho_2 = \rho_1 e^{\beta d}$. We suppose also that the unperturbed pressure field gives a constant acceleration g in the $-z$ direction. This problem has been considered by Rayleigh [7] in the so-called Boussinesq approximation; that is, while density variations may be large, compressibility effects are small. The problem is a stability problem, and as is usual it is treated by linearization. It may be remarked that the elementary instability case is the one in which the density change is a step-function of z , say. It might very well be expected that the situation in which the density changes over a finite distance would occur quite often. Such a situation occurs in the transition from C_m to C_l described above. The only such transition case which has been successfully treated is the one in which the density transition is given by an exponential function.

The solution of the problem is straightforward and the procedure may be given here since it can be formulated and solved in a rather brief way. While the density varies, the particle density is supposed not to change in accord with our assumption of incompressibility. Thus

$$\frac{D\rho}{Dt} = \frac{\partial \rho}{\partial t} + u \frac{\partial \rho}{\partial x} + w \frac{\partial \rho}{\partial z} = 0 \quad (14)$$

where we are making the "plane-assumption" that in the direction perpendicular to g the field quantities vary only with x . The velocity in the x -direction is u and in the z -direction it is w . The equation of continuity is

$$\frac{\partial \rho}{\partial t} + \frac{\partial}{\partial x} (\rho u) + \frac{\partial}{\partial z} (\rho w) = 0, \quad (15)$$

which because of Eqn. (14) gives

$$\frac{\partial u}{\partial x} + \frac{\partial w}{\partial z} = 0. \quad (16)$$

The velocities u, w are supposed to be small quantities in accordance with the perturbation approach. The pressure is $p^* = p + p'$, and the density is $\rho^* = \rho + \rho'$ where p is the unperturbed pressure, and p' is a small quantity. The density ρ is the unperturbed density with a dependence only on z as described above and ρ' is a small quantity. The equations of motion in the x - and z -directions

$$\begin{aligned} \rho^* \frac{\partial u}{\partial t} &= - \frac{\partial p^*}{\partial x}, \\ \rho^* \frac{\partial w}{\partial t} &= - \frac{\partial p^*}{\partial z} - g\rho^* \end{aligned} \quad (17)$$

in the linearized approximation become

$$\rho \frac{\partial u}{\partial t} = - \frac{\partial p'}{\partial x} \quad (18)$$

$$\rho \frac{\partial w}{\partial t} = - \frac{\partial p'}{\partial z} - g\rho' \quad (19)$$

Equation (14) may be written

$$\frac{\partial \rho'}{\partial t} + w \frac{\partial \rho}{\partial z} = 0, \quad (14')$$

We now take the x and t dependence of ρ' , p' , u , w to be of the form $e^{nt + ikx}$ so that Eqns. (14'), (16), (18), and (19) give

$$n\rho' + w \frac{d\rho}{dz} = 0; \quad (20)$$

$$iku + w_z = 0; \quad (21)$$

$$n\rho u + ikp' = 0; \quad (22)$$

$$n\rho w + p'_z + g\rho' = 0. \quad (23)$$

In these equations $w_z = dw/dz$, $p'_z = dp'/dz$, and ρ is a given function of z . These equations apply in the region $0 \leq z \leq d$. The equation for $w(z)$ in this region is easily obtained as follows. From Eqns. (21) and (22) one gets upon elimination of u

$$-p' = \frac{n\rho w_z}{k^2}.$$

From Eqns. (20) and (23) upon elimination of p' one gets

$$-p'_z = n\rho w - \frac{g}{n} \rho_z w.$$

The function p' may then be eliminated using these last two equations to get the equation for w :

$$w_{zz} + \beta w_z - wk^2 \left(1 - \frac{g\beta}{n^2}\right) = 0, \quad 0 \leq z \leq d. \quad (24)$$

The quantity β is ρ_z/ρ . In the regions $z < 0$ and $z > d$ we have $\beta = 0$ so that the vertical velocity w satisfies the equation

$$w_{zz} - k^2 w = 0, \quad (25)$$

in both of these regions.

It is a straightforward matter to find n as a function of k , g , and β . If m_1 and m_2 are the roots of

$$m^2 + \beta m - k^2 \left(1 - \frac{g\beta}{n^2}\right) = 0,$$

the solution for the region $0 \leq z \leq d$ is

$$w = Ae^{m_1 z} + Be^{m_2 z}. \quad (26)$$

In the region $z > d$, the appropriate velocity solution of Eqn. (25) must behave like e^{-kz} since the disturbance must approach zero as $z \rightarrow \infty$. It follows that we have

$$\frac{dw/dz}{w} = -k$$

as $z \rightarrow d$ from above. For continuity we must have for the solution in the inner region, as given by Eqn. (26),

$$\frac{m_1 A e^{m_1 d} + m_2 B e^{m_2 d}}{A e^{m_1 d} + B e^{m_2 d}} = -k. \quad (27)$$

Similarly the velocity in region $z < 0$ must behave like e^{kz} so that continuity of the solutions at $z = 0$ requires

$$\frac{m_1 A + m_2 B}{A + B} = k. \quad (28)$$

Elimination of A and B from these two equations leads to the relation

$$(m_1 + k)(m_2 - k)e^{m_1 d} = (m_1 - k)(m_2 + k)e^{m_2 d} \quad (29)$$

which is readily put in the form

$$\frac{(m_2 - m_1)k}{m_1 m_2 - k^2} = \tanh \frac{(m_2 - m_1)d}{2} \quad (30)$$

If one defines

$$\theta = (m_2 - m_1)d,$$

then Eqn. (30) may be written as

$$\frac{kd\theta}{(\beta^2 d^2/4) - k^2 d^2 - (\theta^2/4)} = \tanh \frac{\theta}{2}. \quad (31)$$

Equation (31) is a transcendental equation which determines θ . Then from the definition of θ :

$$\theta^2 = d^2(m_2 - m_1)^2 = \beta^2 d^2 + 4k^2 d^2 \left(1 - \frac{g\beta}{n^2}\right), \quad (32)$$

one finds n .

One can see how the solution behaves in the limiting case of a discontinuous jump in density by letting $d \rightarrow 0$ while βd is kept finite. It is evident that θ then has the approximate value βd . If we use this approximate value on the right hand side of Eqn. (31), we can get an improved value as

$$\frac{1}{4} \beta^2 d^2 - \frac{1}{4} \theta^2 = k\beta d \coth \frac{\beta d}{2},$$

and, if this value is used in Eqn. (32), one finds

$$n^2 = gk \frac{\rho_2 - \rho_1}{\rho_2 + \rho_1}$$

so that one has the usual instability if $\rho_2 > \rho_1$.

For the finite transition region, the practical approach appears to be to find the roots for θ of Eqn. (31) by a numerical method. Then given a solution for θ of this equation, the value of n is then determined from Eqn. (19). One obvious root of Eqn. (31) is $\theta = 0$ which gives

$$n^2 = \frac{4g\beta k^2}{\beta^2 + 4k^2} \quad (33)$$

which goes to zero as $k \rightarrow 0$, and as $k \rightarrow \infty$, n approaches the value

$$n^2 = \frac{1}{2}\beta. \quad (34)$$

A numerical solution of Eqns. (31) and (32) is shown in Fig. 5 where the dependence of $n' = n/(g\beta)^{1/2}$ on $k' = k/d$ is shown for the case in which $d = 1$ cm, $\beta = 5.9 \times 10^{-4}$ /cm with $g = 10^3$ cm/sec² and $\nu = 0.01$ cm²/sec. This figure shows that n' is a maximum for $k' = 4$ /cm. This k' corresponds to $\lambda = 1.6$ cm a value which is similar in magnitude to those obtained for the density step calculations although somewhat larger.

If one uses the numerical values appropriate for the density transition from the middle concentration C_m to the lowest region C_1 in the example considered in detail above, one finds a preferred wavelength but it does not have significance for experimental observations. The growth rate n for this disturbance is appreciably less than the growth rate of the disturbance at the step density change of the surface layer. The instability in continuous density change is for the present case much the weaker one, and one would not expect to observe it.

REFERENCES

- [1] Platt, J. R., Science, **133**, 1766 (1961).
- [2] Plesset, M. S. and Winet, H., Nature, **248**, 441 (1974).
- [3] Plesset, M. S. and Whipple, C. G., Physics of Fluids, **17**, 1 (1974).
- [4] Winet, H. and Jahn, T. L., Biorheology, **9**, 87 (1972).
- [5] Brennen, C., J. of Fluid Mechanics, in press.
- [6] Cox, R.G., J. of Fluid Mechanics, **44**, 791 (1970).
- [7] Rayleigh, Proc. Lond. Math. Soc., **14**, 170 (1883).

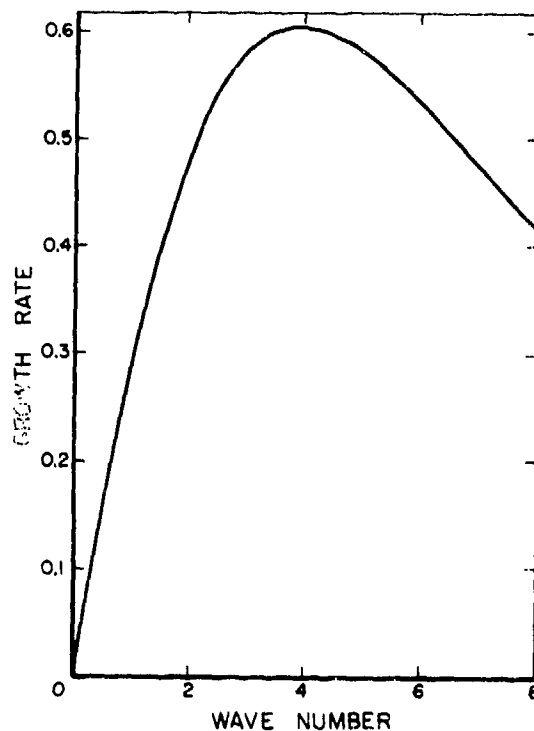


Fig. 5. Nondimensional curve of growth rate versus wave number for exponential density gradient.

HYDRODYNAMICS OF THE CONTAINMENT OF OIL SLICKS

J. H. Milgram
M.I.T.
Cambridge, Massachusetts

R. J. VanHouten
M.I.T.
Cambridge, Massachusetts

ABSTRACT

Many basic hydrodynamic problems become of practical interest when one attempts to clean up an oil spill by physical means. Three of these problems are studied in this paper. The first is the mass transport of oil by water waves and includes a determination of the types of waves that can propagate through a system comprised of an oil layer above deep water. The second problem is the stability of the oil-water interface between a motionless oil layer and flowing water. This is a simplified model of the situation when oil pollution is contained by a containment barrier in a current. The third problem examined is the determination of the equilibrium thickness distribution of an oil pool being contained by a barrier in a current.

NOMENCLATURE

$A = U^2/gd$, square of Froude Number
 $B = \rho_1/\rho_2$, density ratio
 $C = kd$, non-dimensional wavenumber
 $D = T/\rho_2gd^2$, non-dimensional surface tension
 $E = \omega/d/g$, reduced frequency
 g =acceleration due to gravity
 k =circular wavenumber
 m =depth of oil below waterline
 M =rate of mass transport of oil
 P =pressure
 t =time or oil thickness
 T =surface tension
 U =current speed
 V_g =group velocity
 V_p =phase velocity
 x, y =cartesian coordinates
 y is vertically upwards
 δ =oil layer thickness
 $\Delta = (\rho_2 - \rho_1)/\rho_2$, density difference ratio
 ϵ =small parameter
 η =free surface displacement
 ζ =interface displacement
 ω =radian frequency

ϕ =velocity potential

ρ =density

Subscripts and Superscripts

$()_1$ =quantity in oil

$()_2$ =quantity in water

$()^{(n)}$ =perturbation quantity of order n

$()'$ =dimensionless quantity

1. INTRODUCTION

A physical barrier for containing oil spills is basically a floating fence whose draft exceeds the depth of the oil slick, which is intended to prevent the passage of oil from one of its sides to the other. The way in which a physical barrier is used to contain oil depends upon whether or not a current exists. In the absence of a current relative to the barrier, an oil slick must be encircled; whereas, in the presence of a current, a physical barrier in a U-shaped configuration, as viewed from above, can be used to hold the oil against the current. In calm water, oil can be held in such a barrier configuration by towing the barrier. When substantial water waves are present, in order for a physical barrier to work, it must respond to the waves, especially in heave, so that the oil does not pass over or under the barrier. This is due to the fact that it is impractical to make a barrier whose height exceeds that of ocean waves.

Although some use of physical barriers has been made for a considerable period of time in calm water, it is only within the past six or seven years that the use of containment barriers in the presence of waves or currents has been attempted. As can be expected, the barriers that were first used were far too weak and inevitably broke up due to wave or current forces. In the instances where physical integrity was maintained, the smallest waves were found to carry oil over or under barriers. However, as the development of barriers has gone on, barriers have been developed which have sufficient strength for maintaining physical integrity even in moderate storms and which have a seakeeping ability, which allows them to follow waves sufficiently well so that oil does not pass directly over the barrier and so that oil does not pass beneath the barrier by the skirt of the barrier temporarily moving higher than the bottom of the oil pool. With the solution of these relatively straight-forward problems of adequate strength and adequate seakeeping ability, more intricate causes for failure to contain oil have been found. A number of basic hydrodynamic problems are associated with this containment failure and with the logistics of the use of spill cleanup equipment and procedures. It is impossible to cover all of these problems in a paper of this type. Hence, three of the more important problems will be covered. None of these problems is yet completely understood although much has been learned, and active research in these areas is presently ongoing.

The first problem considered is the nature of travelling waves in the presence of an oil slick including the mass transport of oil by the waves. This has two indirect influences on oil containment. First of all, water waves at sea transport oil so that when a spill occurs in the presence of waves, the mass transport of the slick must be known so the future location of the slick can be predicted in order to be able to intercept the slick with pollution control equipment at the time it is deployed. Also, skimming devices are frequently put into an oil pool being contained by a barrier. In the presence of waves, the skimming devices move in the waves and under some conditions, the relative motion between a device and the oil is such that the oil is driven away from the device so that the oil slick thickness is so small that effective collection is impossible.

The second problem deals with the stability of an oil-water interface in the presence of a current. Instabilities on this interface lead to interfacial waves which can cause leakage by two means. One is the case where the interfacial wave hits the oil bar-

rier and oil passes beneath the barrier either due to its increased depth in the wave or to the breaking of the wave against the barrier. The other is the situation where the interfacial waves break, and the agitation results in small bubbles of oil in the water deep enough to be carried beneath the barrier by the current.

The third problem deals with the hydrodynamics of the equilibrium thickness of the oil pool as a function of distance from the leading edge of the slick when oil is being held by a barrier in a current. When the thickness of the oil at the barrier exceeds the barrier draft, oil simply passes beneath the barrier. However, a much more troublesome problem is the fact that for current speeds on the order of 0.6 knots or higher, the equilibrium thickness distribution has a pronounced lump near the leading edge (edge farthest from the barrier) of the oil slick, and small droplets of oil are torn off this lump by the current. Some of these droplets rise up to the slick, and some initially move to depths large enough for them to be carried beneath the barrier by the current. Some of the droplets that rise up to the slick rejoin it, but some do not and seem to bounce or roll along the oil-water interface and eventually move deeply enough to pass beneath the barrier. These droplets may be oil covered water droplets with so little buoyancy that they are easily driven to relatively large depths. However, the failure of these droplets to rejoin the slick in spite of the presence of surface tension energy for the rejoining reaction is not presently understood. This problem forms one of the most interesting areas for future research in the oil pollution field.

Figure 1.1 shows an aerial photograph of a barrier containing dyed soybean oil being towed at a speed of 0.7 knots in a calm sea. The dye in the oil makes it easily visible. No oil is passing over the barrier, and the barrier depth of 27 inches greatly exceeds the slick thickness of a few inches. Nevertheless, substantial leakage can be observed, and this is completely due to small oil droplets passing beneath the barrier.

2. THE MOVEMENT OF OIL SLICKS BY WATER WAVES

2.1 Introduction

It has been observed that when water waves pass through an oil slick, sometimes there is substantial mass transport of the oil. When there is a solid object in the sea, the relative motion between the object and the waves often drives the oil away from the object. If the solid object is an oil collector, the effect is detrimental



FIGURE 1.1 AERIAL PHOTOGRAPH OF DYED SOYBEAN OIL IN A BARRIER BEING TOWED AT 0.7 KNOTS. Note the leakage under the barrier, especially the subsurface oil visible as faint streaks. The leakage is due to droplet entrainment.

to the collection of oil since the collection rate of such devices increases with increases in oil depth. The movement of a slick by waves must be known in order to be able to plan the logistics of dealing with a slick. For example, in the case of most spills at sea, it takes several hours for pollution control equipment to arrive on the scene and be deployed after notification of the spill is made. Therefore, if the location of a slick is known at a given time, it will be essential to be able to immediately predict its location several hours after this time from knowledge of climatic conditions in order to dispatch equipment to the deployment location.

The first step in learning how waves move oil is a study of the simplified problem of the mean velocity imparted to an oil slick of uniform thickness by two-dimensional periodic water waves. This problem is formulated here as a regular perturbation

expansion in powers of wave slope and the first- and second-order problems are then solved.

2.2 Formulation of the problem

The situation considered here is that of infinitely deep water having density ρ_2 beneath an oil layer having density ρ_1 of thickness δ when undisturbed (Figure 2.1). The problem is set in an (x,y) coordinate system with x horizontal and y vertically upwards with the origin on the undisturbed free surface. A two-dimensional water wave of radian frequency ω and length λ is propagating in the $+x$ direction, and the inviscid solution for the flow is sought. The displacement of the air-oil interface is called η , and the displacement of the oil-water interface is called ζ . The velocity potential in the oil is called ϕ_1 , and the velocity potential in the water is called ϕ_2 . Both potentials are to satisfy the Laplace equation.

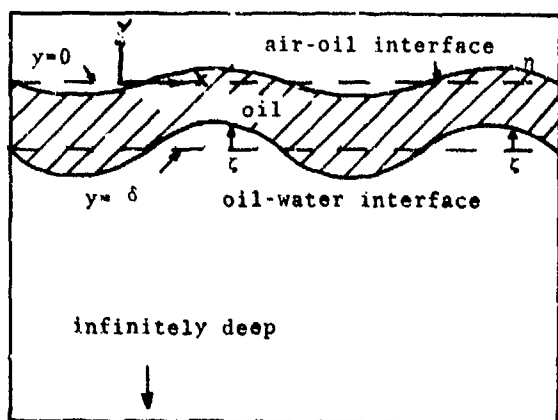


FIGURE 2.1 GEOMETRY CONSIDERED FOR THE PROBLEM OF THE MOVEMENT OF OIL SLICKS BY WATER WAVES.

The free surface boundary conditions are:

1) Kinematic

$$[\phi_y - \eta_t - \phi_{xx} \eta_x]_{y=\eta} = 0 \quad (2.1)$$

2) Dynamic

$$[\phi_{tt} + \frac{1}{2}(\phi_{xx}^2 + \phi_{yy}^2) + g\eta]_{y=\eta} = 0 \quad (2.2)$$

The interfacial boundary conditions are:

1) Kinematic

$$[\phi_y - \phi_{xx} \zeta_x - \phi_{xy} + \phi_{xx} \zeta_x]_{y=-\delta+\zeta} = 0 \quad (2.3)$$

2) Dynamic pressure matching across the oil-water interface:

$$\rho_1 [\phi_{tt} + \frac{1}{2}(\phi_{xx}^2 + \phi_{yy}^2) + g\zeta]_{y=-\delta+\zeta} = \quad (2.4)$$

$$\rho_2 [\phi_{tt} + \frac{1}{2}(\phi_{xx}^2 + \phi_{yy}^2) + g\zeta]_{y=-\delta+\zeta}$$

The following perturbation expansions will be used:

$$\phi_1 = \epsilon \phi_1^{(1)} + \epsilon^2 \phi_1^{(2)} + \epsilon^3 \phi_1^{(3)} + \dots \quad (2.5)$$

$$\eta = \epsilon \eta^{(1)} + \epsilon^2 \eta^{(2)} + \dots \quad (2.6)$$

$$\phi_2 = \epsilon \phi_2^{(1)} + \epsilon^2 \phi_2^{(2)} + \dots \quad (2.7)$$

$$\zeta = \epsilon \zeta^{(1)} + \epsilon^2 \zeta^{(2)} + \dots \quad (2.8)$$

ϵ is a dimensionless parameter that is small when the waves are small; for example, the wave slope. Using (2.5) and (2.6) and writing free surface quantities as Maclaurin Series in y , and separating into powers of ϵ up to order 2 gives, for the free surface conditions:

$$[\eta_t^{(1)} - \phi_{1y}^{(1)}]_{y=0} = 0 \quad (2.9)$$

$$[\eta_t^{(2)} - \eta_{xx}^{(2)} \phi_{1y}^{(1)} - \phi_{1y}^{(2)} - \eta^{(1)} \phi_{1yy}^{(1)}]_{y=0} = 0 \quad (2.10)$$

$$[\phi_{1t}^{(2)} + g\eta^{(2)}]_{y=0} = 0 \quad (2.11)$$

$$[\phi_{1t}^{(2)} + \eta^{(2)} \phi_{1yy}^{(1)} + \frac{1}{2}(\phi_{1xx}^{(2)} + \phi_{1yy}^{(2)}) + g\eta^{(2)}]_{y=0} = 0 \quad (2.12)$$

Combining the first-order free surface conditions gives:

$$[\phi_{1tt}^{(1)} + g\phi_{1y}^{(1)}]_{y=0} = 0 \quad (2.13)$$

and combining the second-order free surface conditions gives:

$$[\phi_{1tt}^{(2)} + g\phi_{1y}^{(2)}]_{y=0} = \quad (2.14)$$

$$[2g\phi_{1xx}^{(1)} \eta^{(1)} - g\phi_{1yy}^{(1)} \eta^{(1)} - 2\phi_{1xy}^{(1)} \eta^{(1)} - \phi_{1xx}^{(1)} \eta^{(2)}]_{y=0}$$

The first- and second-order boundary conditions at the oil-water interface are:

$$[\phi_{1y}^{(1)} - \phi_{2y}^{(1)}]_{y=-\delta} = 0 \quad (2.15)$$

$$[\phi_{1y}^{(2)} - \phi_{2y}^{(2)}]_{y=-\delta} = [\zeta^{(2)} (\phi_{2yy}^{(1)} - \phi_{1yy}^{(1)}) - \eta_{xx}^{(1)} (\phi_{2x}^{(1)} - \phi_{1x}^{(1)})]_{y=-\delta} \quad (2.16)$$

$$[\rho_1 \phi_{1t}^{(2)} - \rho_1 g \zeta^{(2)}]_{y=-\delta} = [\rho_2 \phi_{2t}^{(2)} - \rho_2 g \zeta^{(2)}]_{y=-\delta} \quad (2.17)$$

$$[\rho_1 \phi_{1t}^{(2)} - \rho_2 \phi_{2t}^{(2)} - g(\rho_1 - \rho_2) \zeta^{(2)}]_{y=-\delta} = \quad (2.18)$$

$$[\zeta^{(2)} (\rho_2 \phi_{2yy}^{(1)} - \rho_1 \phi_{1yy}^{(1)}) + \frac{1}{2}(\rho_2 \phi_{2xx}^{(1)} + \rho_2 \phi_{2yy}^{(1)} - \rho_1 \phi_{1xx}^{(1)} - \rho_1 \phi_{1yy}^{(1)})]_{y=-\delta} = \quad (2.19)$$

$$\phi_{1t}^{(2)} = [\phi_{1y}^{(2)} - \phi_{1xx}^{(2)} \eta^{(1)} + \zeta^{(2)} \phi_{1yy}^{(1)}]_{y=-\delta} \quad (2.20)$$

$$[\rho_1 \phi_{1t}^{(2)} - \rho_2 \phi_{2t}^{(2)} + g(\rho_1 - \rho_2) \zeta^{(2)}]_{y=-\delta} = 0 \quad (2.21)$$

2.3 Solution of the First Order

Problem

Solutions are sought which are periodic in time and space, which satisfy the boundary conditions (2.13) through (2.21) and which satisfy:

$$\nabla^2 \phi^{(i)} = 0 \quad i=1,2 \quad (2.22)$$

The first order solution is:

$$\phi_1 = e^{i(kx - \omega t)} [ae^{ky} + be^{-ky}] \quad (2.23)$$

$$\phi_2 = e^{i(kx - \omega t)} ce^{ky} \quad (2.24)$$

From (2.13)

$$-\omega^2(a+b) + kg(a-b) = 0 \quad (2.25)$$

From (2.21)

$$-\rho_1 \omega (ae^{-k\delta} + be^{k\delta}) + \rho_2 \omega^2 ce^{-k\delta} + gk(\rho_1 - \rho_2)(ae^{-k\delta} - be^{k\delta}) = 0 \quad (2.26)$$

and from (2.15)

$$c = a - be^{2k\delta} \quad (2.27)$$

Eq. (2.25) yields the relationship between a and b as:

$$a = -b \frac{\omega^2 + gk}{\omega^2 - gk} \quad (2.28)$$

We define

$$\Delta \equiv \frac{B - \rho_1}{\rho_2} \quad (2.29)$$

and

$$g' \equiv g\Delta \quad (2.30)$$

Eqs. (2.26), (2.27) and (2.28) give the dispersion relation:

$$(\omega^2 + gk)(\Delta\omega^2 - g'k)e^{-k\delta} + (\omega^2 - gk)[\omega^2(2 - \Delta) - g'k]e^{k\delta} = 0 \quad (2.31)$$

The dispersion relation (2.31) shows that for each value of k, there are two solutions for ω^2 . Although any wave moves both interfaces, the wave associated with the higher frequency is called the surface wave, and its radian frequency is called ω_s . For this wave, eq. (2.31) has the ω_s^2 solution.

$$\omega_s^2 = gk \quad (2.32)$$

The phase velocity of this wave is called V_{ps} and is given by:

$$V_{ps} = \omega_s/k = \sqrt{g}/\sqrt{k} \quad (2.33)$$

The group velocity, V_{gs} , is given by $d\omega_s/dk$ and is:

$$V_{gs} = \frac{1}{2} \sqrt{g}/\sqrt{k} \quad (2.34)$$

The other wave is called the interfacial wave and has radian frequency ω_i and (2.31) gives:

$$\omega_i^2 = gk\Delta \frac{e^{k\delta} - e^{-k\delta}}{(2 - \Delta)e^{k\delta} + \Delta e^{-k\delta}} \quad (2.35)$$

Its phase velocity is:

$$V_{pi} = \sqrt{g\Delta/k} \left[\frac{e^{k\delta} - e^{-k\delta}}{(2 - \Delta)e^{k\delta} + \Delta e^{-k\delta}} \right]^{1/2} \quad (2.36)$$

and its group velocity is:

$$V_{gi} = \omega_i/2k + \frac{gk\Delta\delta e^{-2k\delta}}{\omega_i(2 - \Delta + \Delta e^{-2k\delta})} \left[1 + \frac{\Delta(1 - e^{-2k\delta})}{2 - \Delta + \Delta e^{-2k\delta}} \right] \quad (2.37)$$

From (2.11);

$$\eta^{(w)} = \frac{i\omega}{g}(a+b)e^{i(kx - \omega t)} \quad (2.38)$$

and from (2.19):

$$\varphi^{(w)} = \frac{ikc}{\omega} e^{-k\delta} e^{i(kx - \omega t)} \quad (2.39)$$

The first order rate of mass transport of oil, $M_1^{(w)}$, is:

$$M_1^{(w)} = \lim_{T \rightarrow \infty} \frac{1}{T} \int_{-T}^T \left\{ \int_{-i}^0 \phi_1^{(w)} dy \right\} dt = 0 \quad (2.40)$$

2.4 Solution of the Second Order Problem

To solve the second-order problem, the origin of the time scale will be chosen such that:

$$\phi_1^{(w)} = [ae^{ky} + be^{-ky}] \cos(kx - \omega t) \quad (2.41)$$

$$\phi_2^{(w)} = ce^{ky} \cos(kx - \omega t) \quad (2.42)$$

$$\eta^{(w)} = -(a+b) \frac{g}{\omega} \sin(kx - \omega t) \quad (2.43)$$

$$\eta'' = -\frac{k\epsilon}{\omega} e^{-k\delta} \sin(kx - \omega t) \quad (2.44)$$

Then (2.14) gives:

$$\begin{aligned} [\phi_{11}^{(2)} + g \phi_{1y}^{(2)}]_{y=0} = \\ 6 \left[k^2 \omega (a+b)^2 - \frac{\omega^2 k}{g} (a^2 - b^2) \right] \sin 2(kx - \omega t) \end{aligned} \quad (2.45)$$

Define

$$a' = a \exp(-k\delta) \quad (2.46)$$

$$b' = b \exp(k\delta) \quad (2.47)$$

$$c' = c \exp(-k\delta) \quad (2.48)$$

Then (2.18) and (2.20) give:

$$\begin{aligned} [\rho_1 \phi_{11}^{(2)} - \rho_2 \phi_{21}^{(2)} + g(\rho_1 - \rho_2) \phi_{1y}^{(2)}]_{y=0} = \\ 2 \left[2g \frac{k^2 c'}{\omega} (\rho_1 - \rho_2) (a' + b') + \rho_2 k^2 \omega c'^2 \right. \\ \left. - \rho_1 k^2 \omega c' (a' - b') \right] \sin 2(kx - \omega t) \end{aligned} \quad (2.49)$$

Eqs. (2.45) and (2.49) show that $\phi_1^{(2)}$, $\zeta^{(2)}$ and $\eta^{(2)}$ have a dependence on x and t of the form $\exp\{\gamma^2(kx - \omega t)\}$. Therefore, the second-order rate of mass transport, $M_1^{(2)}$, depends only on first-order quantities and is given by:

$$\begin{aligned} M_1^{(2)} = \\ \lim_{T \rightarrow \infty} \frac{1}{2T} \int_{-T}^T \int_{-\delta}^{\eta} \phi_{1x}^{(2)} dy dt + O(\epsilon^3) \end{aligned} \quad (2.50)$$

Using the form for $\phi_1^{(2)}$ from eq. (2.41), the integration in y can be carried out analytically. This gives:

$$\begin{aligned} M_1^{(2)} = \lim_{T \rightarrow \infty} \frac{1}{2T} \int_{-T}^T \left\{ -[ae^{ky} - be^{-ky}]_{-\delta - \frac{k\epsilon}{\omega}}^{-(a+b)\frac{\omega}{g}} \sin(kx - \omega t) \right. \\ \left. - \delta - \frac{k\epsilon}{\omega} \sin(kx - \omega t) \right\} dt + O(\epsilon^3) \end{aligned} \quad (2.51)$$

Because of the periodicity of the integrand, the time average over an infinite interval can be replaced by a time average over one period whose time interval is $2\pi/\omega$. Also, since x is arbitrary, we can let x equal zero. This gives the second-order rate of mass transport of oil as:

$$\begin{aligned} M_1^{(2)} = \frac{\omega}{2\pi} \int_0^{2\pi/\omega} \left\{ a \cdot \exp \left[(a+b) \frac{k\omega}{g} \sin \omega t \right] \right. \\ - a \cdot \exp \left[k(-\delta + \frac{k\epsilon}{\omega} e^{-k\delta} \sin \omega t) \right] \\ - b \cdot \exp \left[-(a+b) \frac{k\omega}{g} \sin \omega t \right] \\ \left. + b \cdot \exp \left[-k(-\delta + \frac{k\epsilon}{\omega} e^{k\delta} \sin \omega t) \right] \right\} \sin \omega t dt \end{aligned} \quad (2.52)$$

The part of eq. (2.52) defined by the integral is not exactly proportional to the wave amplitude squared. By expanding eq. (2.52) in powers of a and b and retaining only the lowest order terms gives $M_1^{(2)}$ in a form correct to order 2 in ϵ that has a quadratic dependence on the wave amplitude for a fixed wave length. This is:

$$M_1^{(2)} = \frac{1}{2} \left[(a+b)^2 \frac{k\omega}{g} - \frac{gck^2}{\omega} e^{-2k\delta} - \frac{bck^2}{\omega} \right] \quad (2.53)$$

2.5 Calculations

The independent variables for the physical situation of two-dimensional periodic waves moving through deep water with a layer of oil on it are:

The oil thickness in calm water, δ ;
The water density, ρ_1 ;
The oil density, ρ_2 ;
The gravitational acceleration, g ;
The wave radian frequency ω ; and
The wave amplitude on the free surface, η . (Alternatively, the interfacial wave elevation, ζ , could have been chosen.)

A dimensional analysis shows that any dimensionless dependent variable is functionally dependent on any three independent dimensionless quantities of the problem. Primed symbols will be used where necessary for dimensionless quantities. Three independent dimensionless quantities are:

The density ratio, $(\rho_2/\rho_1)/\rho_2 \equiv \Delta$;
The reduced frequency, $\omega \sqrt{\delta/g} \equiv \omega'$;
The amplitude parameter
 $\zeta'/\delta \equiv \zeta'$ or $\frac{\eta^{(2)}}{\delta} \equiv \eta'$.

By virtue of the perturbation expansions used in the theoretical development, the various quantities to be calculated depend on the amplitude parameter to the zeroth, first or second power in an obvious way. Therefore, calculations have been carried out only for the variations in density ratio and reduced frequency. The dimensionless quantities that were calculated are:

The amplitude ratio $R = \zeta'/\eta'$

The dimensionless rates of mass transport of oil

$$M_1^{(2)'} = \begin{cases} M_1^{(2)}/\eta'^2 \omega & , \text{ for the surface wave} \\ M_1^{(2)}/\zeta'^2 \omega & , \text{ for the interfacial wave} \end{cases}$$

The normalized wavenumber:

$$k' = kg/\omega^2$$

The normalized phase velocity:

$$V_p' = V_p \omega / g$$

The normalized group velocity:

$$V_g' = V_g \omega / g$$

For the surface waves, all the characteristics, except for the rate of mass transport of oil, are very well known (see section 2.6). The surface wave oil transport rate and all the characteristics of the interfacial waves are given in figures 2.2 through 2.4.

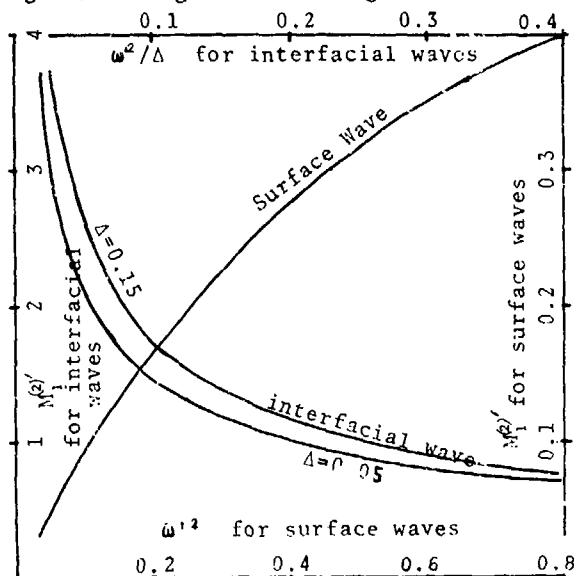


FIGURE 2.2. DIMENSIONLESS MASS TRANSFER RATES FOR THE SURFACE AND INTERFACIAL WAVES.

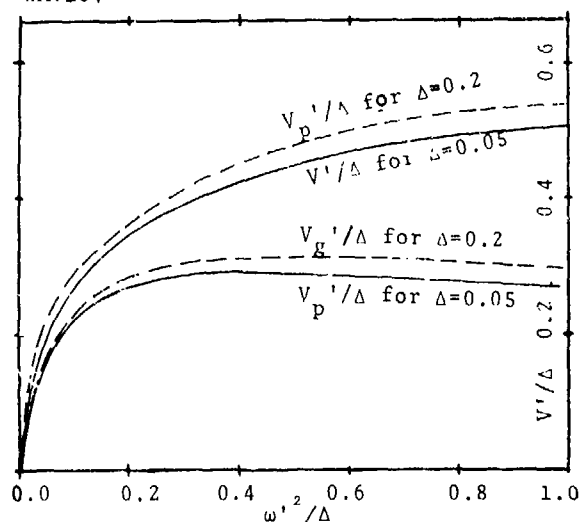


FIGURE 2.3. GROUP AND PHASE VELOCITIES FOR INTERFACIAL WAVES

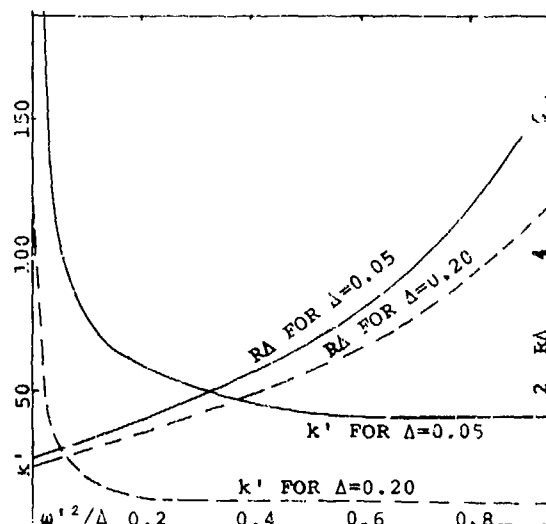


FIGURE 2.4. AMPLITUDE RATIO AND DISPERSION RELATION FOR INTERFACIAL WAVES

It is of interest to calculate the dimensional mass transfer rate for specific dimensional conditions to provide a physical feeling of the situation. The surface wave will be considered as this is the wave that will usually exist when there is unconfined oil on the sea and accounts for mass transport of oil under such a circumstance.

We shall consider a surface wave 60 feet long and 4 feet high (amplitude of 2 feet). Δ will be taken as 0.1 and δ as 0.1 feet. For this wave, $k = 2\pi/60 = 0.1 \text{ ft}^{-1}$ and from eq. (2.32) $\omega = 1.8 \text{ sec}^{-1}$. From Figure 2.2, $M_1^2 = 0.01$ so that $M_1^2 = 0.01 \times 1.8 \times (2)^2 \text{ ft}^2/\text{sec} = 0.072 \text{ ft}^2/\text{sec}$. Since the mean slick thickness is 0.1 feet, the flow speed associated with the mass transport is 0.72 ft./sec.

2.6 Conclusions about the movement of oil by waves

The fluid mechanics of the surface wave with the dispersion relation given by eq. (2.32) are identical to those of ordinary deep water waves in the absence of oil. In short, the wave is the same whether or not there is oil present. The only aspect of the surface waves that has not been well known before is its mass transport of oil. At very low reduced frequencies, the two interfaces move up and down together so that the oil transport rate is very small. At high reduced frequencies, the oil-water interface is nearly motionless, and the mass transport of oil is identical to that which would be associated with the Stokes drift caused by waves in a single fluid.

The interfacial wave is more interesting. As shown in Figure 2.4, the air-oil interface has a very small vertical motion in comparison to that of the oil-water interface. At large wavenumbers, the motion at the water-

oil interface decays rapidly as distance away from the interface is increased upwards or downwards. At small wavenumbers, the waves in the oil layer have the same properties as "upside-down" shallow water waves. As the wavenumber approaches zero, the interfacial waves approach the non-dispersive condition with both group and phase velocity approaching the limit $(g\Delta\delta)^{1/2}$. As is the case with ordinary shallow water waves, the mass transport rate of oil by an interfacial wave of small wavenumber is far larger than that of a surface wave of the same amplitude and wavenumber.

For a given wavenumber, the frequency, group velocity and phase velocity of the interfacial wave are much smaller than the corresponding quantities associated with the surface wave. This effect is accentuated at small wavenumbers, and it can be used to explain one of the more troublesome problems encountered when attempts are made to collect an oil slick in rough seas. If an oil pool is relatively thick (several inches) such as is often the case when oil is contained in a barrier; a collecting device, usually called a skimmer, is often put into the pool to pick up the oil and pump it through a hose to a container (such as a ship or a barge). In rough conditions, some skimmers drive all the oil away from themselves and can be observed centered on a small region of the surface completely devoid of oil although there is oil completely surrounding this region.

Skimmers whose motion follows the motion of the fluid particles in the ocean waves will tend to avoid this problem of driving oil away from themselves; whereas, skimmers that do not follow the waves well do not. When a skimmer does not follow the motion of fluid particles in an ocean wave, the skimmer is moving with respect to the fluid. As a region of the skimmer surface advances into the fluid, the oil layer thickens so that the interfacial waves generated by the relative motion can move as fast as the skimmer surface. When the relative motion of the skimmer reverses and the surface moves away from the fluid, the flow around the skimmer separates since skimmers have bluff shapes. The interfacial waves keep advancing and move the oil away from the skimmer. Eventually, pressure forces generate interfacial waves which move the oil toward the skimmer again. However, the part of the oil layer nearest the skimmer is then quite thin so the wave group velocity is limited to $(g\Delta\delta)^{1/2}$ which is small for the existing small values of δ and Δ . Thus it is possible for a skimmer to drive enough oil away from itself in rough seas so that it cannot collect an oil spill.

For the dimensional numerical example given in the last section, the mass flow speed was 0.72 ft./sec. in a wave 60 feet long and 4 feet high. This flow velocity is typical of mass transport speed in moderate conditions so that wave effects on the mass transport of slicks cannot be neglected.

3. THE INTERFACIAL WAVE PROBLEM

3.1 Introduction to the Stability Problem

When an oil slick is contained by a barrier in a current, under most conditions waves that are generated on the oil-water interface are observed. These waves can reduce containment efficiency in a number of ways. When the interfacial waves impinge on the barrier, oil sometimes passes beneath the barrier either by the lowest part of the wave simply being deeper than the barrier or by oil bubbles being formed by the breaking of the wave, with some of the bubbles passing beneath the barrier.

The viscous shear force of the flowing water on the oil will be larger if the interface is rough than if it is smooth. The shear force is the major factor in the pile-up of oil against a barrier in a current (see § 4). If the shear force is increased due to the roughness of the interfacial waves, the oil depth at the barrier will increase so the waves can reduce the holding capacity of a barrier in this way.

Waves on the interface between a relatively motionless oil slick and the moving water beneath it are intimately connected with the stability of the interface to small disturbances. A slick at sea is subjected to many small unsteady disturbances, and a very small disturbance will result in a substantial interfacial wave only if the interface is unstable.

To study the basic elements of the interfacial stability a simplified physical and mathematical model will be considered (Figure 3.1). Viscous effects will be neglected and initially, an infinite layer of oil of constant thickness and at rest will be considered above water of infinite depth flowing with a constant horizontal velocity. In this simplified model, the total shear between the water and the oil is concentrated at the interface. The air layer above the oil has such a small density compared to oil or water that the usual surface wave assumption of vacuum above the liquid surface will be made. The physical configuration is identical to that of § 2 except for the steady motion of the lower fluid in this case. In § 2 the characteristics of waves generated by an external means and passing through the oil slick were studied.

Here, we are concerned with the possibility that tiny waves may grow in size along the interface. In stability problems of this sort, the procedure utilized is to assume a wave form such as:

$$\phi = \text{Re} \phi(y) e^{i(kx - \omega t + \delta)} \quad (3.1)$$

where ϕ is a wave-like velocity potential which obeys Laplace's equation. The boundary restraints on ϕ are then used to determine $\phi(y)$ and the dispersion relationship $\omega = \omega(k)$, where k is a real quantity and ω is in general complex. Those values of k which result in positive imaginary parts of ω are considered unstable wavenumbers, as they result in infinitesimal waves whose amplitudes are increasing with time. This was carried out by W. T. Jones (1972) for the present problem, and he found that for any given set of physical variables there is a value of flow speed under which there are no unstable wavenumbers.

Observers of the waves in question, however, have noted that wave amplitudes increase with distance downstream and not with time. This type of growth corresponds to a negative imaginary part to k (assuming x is positive downstream). The most relevant stability analysis is therefore one which assumes that wavenumbers are complex in general and that temporal variations are harmonic only and do not contain growth terms. This is the type of analysis given here.

3.2 Derivation of Dispersion Relationship

Since infinitesimal waves are being considered, linearized water wave theory will be used. The free surface boundary conditions are identical to those of §2. The interfacial boundary conditions here not only have all the terms of the interfacial conditions in §2, but also have additional terms to account for the effects of the streaming flow of the water.

The configuration considered is shown in Figure 3.1. The potentials in the oil and water, called ϕ_1 and ϕ_2 respectively must satisfy the Laplace equation, and they will be sought in the form:

$$\phi_1 = (ae^{ky} + be^{-ky}) e^{i(kx - \omega t)} \quad (3.2)$$

$$\phi_2 = Ux + ce^{ky} e^{i(kx - \omega t)} \quad (3.3)$$

Physical quantities are the real parts of corresponding complex quantities. These assumed potentials automatically satisfy the boundary condition $\phi_2(-\infty) = 0$ only if $\text{Re}(k)$ is positive. If we allow ω to take on both positive and negative values, we can consider waves moving to the right and to the left.

Boundary conditions on the flow are as follows:

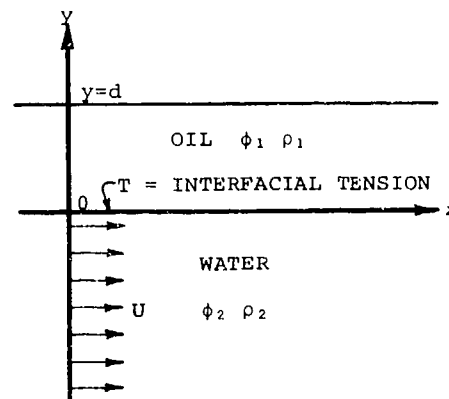


FIGURE 3.1. SITUATION CONSIDERED FOR EXAMINATION OF INTERFACIAL STABILITY

$$[\phi_{tt} + g\phi]_{y=0} = 0 \quad (3.4)$$

This is the usual linearized boundary condition at a free surface. At $y=-\delta$, the kinematic condition of continuity of the interface is:

$$[\phi_y]_{y=-\delta} = [\phi_x]_{y=-\delta} - U \frac{\partial \zeta}{\partial x} = \zeta_t \quad (3.5)$$

where ζ is the elevation of the interface. This can be rewritten as:

$$[\phi_{yt}]_{y=-\delta} = [\phi_{yt} - U\phi_{yx}]_{y=-\delta} \quad (3.6)$$

At $y=-\delta$, the requirement of pressure continuity yields:

$$\rho_1 [\phi_{tt} + g\phi_y]_{y=-\delta} = \rho_2 \{ \phi_{xxt} + U\phi_{xxt} + g\phi_y \} - T\phi_{yxx} \}_{y=-\delta} \quad (3.7)$$

If the boundary conditions Eqs. (3.4) and (3.6) are used to fix two of the constants (a , b , c) in relation to the third, eq. (3.7) can then be used to determine the dispersion relationship $k = k(\omega)$ just as was done in §2.

In order to simplify the analysis, nondimensional quantities will be used to reduce the number of variables:

- $A = \frac{U^2}{gd}$ - the square of a Froude number based on slick depth.
- $B = \frac{\rho_1}{\rho_2}$ - the specific gravity of the oil in relation to water.
- $C = kd$ - wave number non-dimensionalized on slick depth.

$D = \frac{T}{\rho_2 g d^2}$ - non-dimensionalized surface tension

$E = \omega \frac{d}{g}$ - reduced frequency

The dispersion relationship obtained is:

$$DE^2 - AE^2C^2 + (E^2 + 2\sqrt{A}E^3)C - E^4 + (-DC^4 + AC^3 + (B-1-2\sqrt{A}E)C^2 + E^2C - BE^4) \tanh C = 0 \quad (3.8)$$

This transcendental expression reduces to a polynomial for those roots large enough for $\tanh C$ to be considered to be unity. These roots correspond to short waves on one of the interfaces which are not affected by the presence of the other interface. That polynomial, in factored form, is:

$$(C-E^2)(DC^3 + AC^2 + (B-1-2\sqrt{A}E)C + (B+1)E^2) = 0 \quad (3.9)$$

The first root, $C = E^2$, is that corresponding to a normal water wave, but which in this case exists on the oil-air interface. There are three roots to the second expression, but only those which have positive real parts correspond to waves on the oil-water interface since only these waves satisfy the condition of boundedness at great depth. Waves moving in the negative x direction can be obtained by letting E be negative, and solving for positive $R_1(C)$.

3.3 Solutions to the Dispersion Relation

To determine the stability of waves having a reduced frequency E , eq. (3.8) must be solved for those values of C which satisfy the equation. This is equivalent to finding the zeros (values of C for which $F=0$) of the equation

$$F(C) = DE^2C^3 - AE^2C^2 + (E^2 + 2\sqrt{A}E^3)C - E^4 + (-DC^4 + AC^3 + (B-1-2\sqrt{A}E)C^2 + E^2C - BE^4) \tanh C \quad (3.10)$$

Consider non-negative E ; since $F(C)$ is real for real values of C , all complex zeros of F must occur in conjugate pairs. The existence of complex zeros then is associated with an instability.

The zeros of F for which $\tanh C \approx 1$ correspond to solutions of eq. (3.9). The solution $C = E^2$ is stable. Therefore, the existence of instabilities for $\tanh C \approx 1$ ($C \gg 3$) can be determined by examining the solutions of

$$-DC^5 + AC^2 + (B-1-2\sqrt{A}E)C + (B+1)E^2 = G(C) = 0 \quad (3.11)$$

Eq. (3.11) will be considered first. dG/dC is given by:

$$\frac{dG}{dC} = 3DC^2 + 2AC + (B-1-2\sqrt{A}E) \quad (3.12)$$

dG/dC has either two real zeros or a conjugate pair of zeros. Call the zeros C_1 and C_2 . If dG/dC has a conjugate pair of zeros, dG/dC is not zero for any real value of C and G will have the form shown in Figure 3.2. Note that the coefficient of C^3 is negative. In this case, G has only one real zero so it must have a conjugate pair of zeros and unstable waves exist for the values of A , B , D and E under consideration. If dG/dC has two real zeros, the values of G at these values of C can be determined. Eq. (3.12) shows that these values of C must be positive so that G must have one of the three forms shown in Figure 3.2. Instability corresponds to only one real zero of G . This occurs if $G(C_1)$ has the same sign as $G(C_2)$ which is an easy condition to test. Neutral stability corresponds to a double zero of G , in which case both G and dG/dC are zero at either C_1 or C_2 .

For a given set of values of A , B , D and E , the above procedure can be used to determine if there are any complex zeros for the range of C for which $\tanh C \approx 1$. If any such complex zeros exist, the situation is unstable. If no such complex zeros exist, $F(C)$ must be examined for complex zeros over the range of C for which $\tanh C$ cannot be well approximated by unity. This is essentially the range $-3 < C < 3$.

The solutions of Eq. (3.11) can be found by the usual method of solving cubic equations. The values of C which solve the equation will have $\tanh C \approx 1$ for some range of values of A , B , D and E . The first step is to find a point within the range and find the three solutions to eq. (3.11). A fourth solution is $C = E^2$. The location of the zeros of F in the complex C plane are regular functions of A , B , D and E , except at the singularities of $\tanh C$. Once a set of solutions has been found as described above, the solutions for other values of A and E are found as described below (B and D are constants, depending only on the type of oil).

First A or E is changed slightly. The solutions are approximated by those found before A or E were changed. Then Newton's Method is used as an iterative scheme to find the values of C corresponding to the new values of A and E . Then A or E is again changed and the process is repeated to obtain the appropriate values of C . The process is repeated until the stability is determined for all the values of A and E of interest. The process would have to be curtailed if C approached a singularity of $\tanh C$, but this did not happen in our analysis.

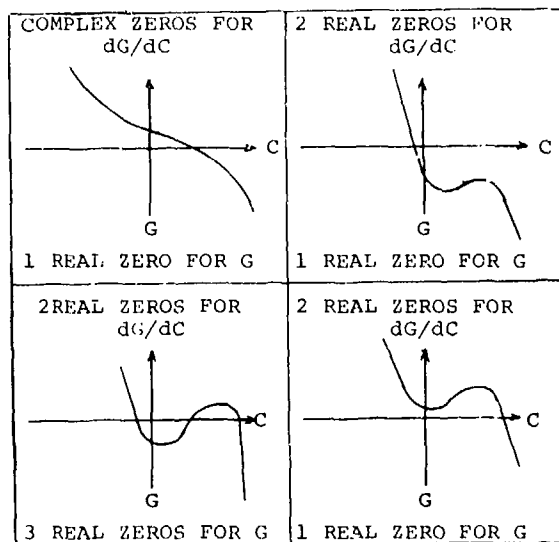


FIGURE 3.2 FORMS OF $G(C)$. NOTE THAT ONLY ONE FORM HAS THREE REAL ZEROS.

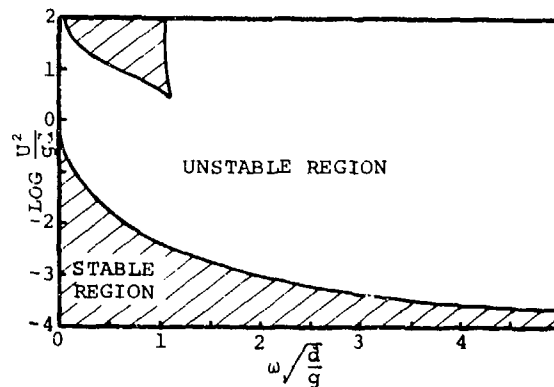


FIGURE 3.3 CURVES OF MARGINAL STABILITY FOR WAVES OF POSITIVE PHASE VELOCITY FOR $B=0.95$ AND $D=0$. ONLY WAVES FOR POSITIVE ω MOVING IN SAME DIRECTION AS CURRENT ARE SHOWN HERE.

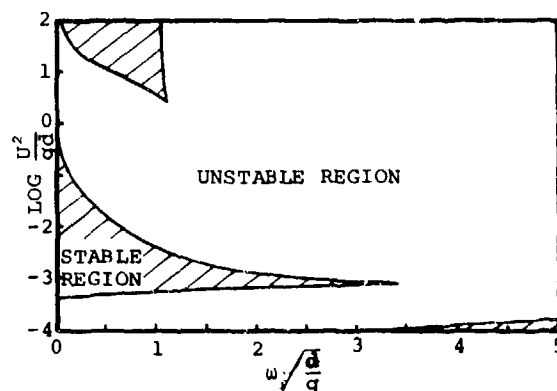


FIGURE 3.4. CURVE OF MARGINAL STABILITY FOR $B=0.95$ AND $D=10^{-6}$. LOWERMOST CURVE CORRESPONDS TO $\text{Re}(k)=0$. BELOW THIS CURVE ANY WAVE WOULD GROW WITH DEPTH AND VIOLATE THE LOWER BOUNDARY CONDITION; THEREFORE, THE REGION IS STABLE.

Figures 3.3 through 3.5 show results for oil with $B=0.95$ and varying amounts of surface tension. Jones (1972) gives results for waves that grow in time, with real wavenumbers for $B=0.86$ and values of D equal to 2.72×10^{-4} , 4.7×10^{-4} , and 1.07×10^{-3} . For purposes of comparison of Jones' results with ours, we show his results for $D=4.7 \times 10^{-4}$ in Figure 3.6 and ours for $B=0.86$ and $D=4.7 \times 10^{-4}$ in Figure 3.7.

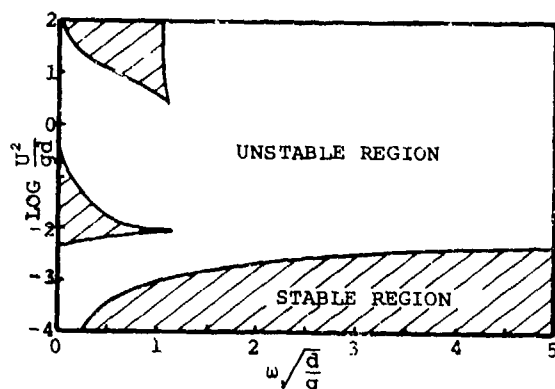


FIGURE 3.5. CURVE OF MARGINAL STABILITY FOR $B=0.95$ AND $D=10^{-4}$.

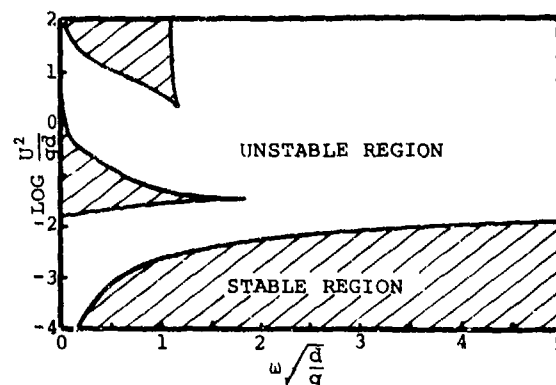


FIGURE 3.7. CURVE OF MARGINAL STABILITY FOR WAVES GROWING IN SPACE WITH POSITIVE PHASE VELOCITY FOR $B=0.86$ AND $D=4.74 \cdot 10^{-4}$.

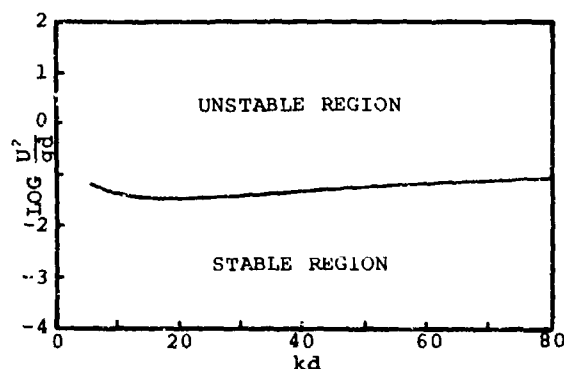


FIGURE 3.6. CURVE OF MARGINAL STABILITY FOR JONES (1972) FOR $B=0.86$ AND $D=4.74 \cdot 10^{-4}$. HERE, THE WAVENUMBER, k , IS REAL AND UNSTABLE WAVES ARE THOSE WHICH GROW IN TIME.

4. THE STEADY STATE CONFIGURATION OF A CONTAINED OIL SLICK IN A CURRENT

4.1 Introduction and Historical Background

The thickness distribution of an oil slick contained by a barrier in a current is of paramount importance. If the amount of oil contained by a barrier in a fixed current is slowly increased, eventually the oil pool thickness at the barrier will be very nearly equal to the barrier depth. If any more oil is added to the pool, an equal amount of oil will pass beneath the barrier. The volume of oil contained by the barrier in this condition is called the holding capacity of the barrier. The holding capacity depends on the current speed since the current speed affects the thickness distribution.

Under most conditions, the observed thickness distribution of oil contained by a barrier in a current has a pronounced "lump" near the leading edge of the slick as shown in Figure 4.1. For current speeds in excess of 0.8 feet per second, oil droplets are usually observed being torn off this "lump", called a "headwave". With increasing current speed, the rate of oil droplet formation rapidly increases. If the slick is very long compared to its thickness, for current speeds between 0.8 and 1.1 feet per second, the droplets usually rejoin the oil slick downstream from the headwave. At higher current speeds, however, many of the droplets are driven deeply enough to pass beneath the barrier and result in oil leakage. Because of this, it has been impossible to contain oil in currents without substantial leakage.

In practice, the situation is complicated by ocean waves and interfacial instabilities. However, the salient

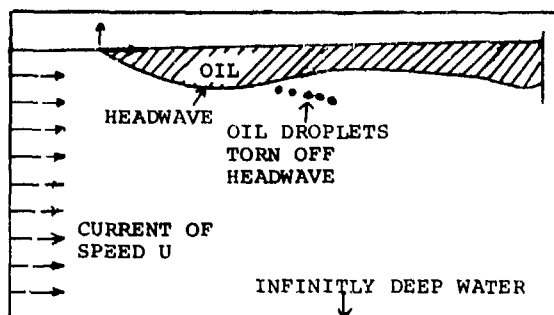


FIGURE 4.1 SCHEMATIC VIEW OF FORM OF OIL THICKNESS DISTRIBUTION WHEN AN OIL POOL IS CONTAINED BY A BARRIER IN A CURRENT

features of the problem are revealed by a study of the steady problem in which these effects are ignored except possibly for the increase in steady frictional force on the oil by the water due to an increase in interfacial roughness. Most of the important features of the problem exist in the simplified two-dimensional problem of an infinitely wide barrier transverse to a current. This is the problem that will be considered here.

If we momentarily adopt a reference frame moving with the water, we can readily see that the present problem is related to, or perhaps included in, a class of problems called density, or gravity currents. The classic example of this type of current is the intrusion of a heavy fluid beneath a lighter one of infinite extent, such as an atmospheric cold front or the intrusion of salt water into fresh. One of the first analytical works in this field was by von Karman (1940), who assumed an infinitely long intruding layer (called a gravity current) which eventually reached a constant height downstream. To determine the speed of propagation U of a gravity current whose height downstream asymptotically approached a constant, H , or conversely the downstream depth of a current travelling at velocity U , von Karman assumed that the pressure in the heavy fluid was hydrostatic, and that the lighter fluid was inviscid. Matching the pressure of the two fluids at the interface, and writing Bernoulli's equation along the upper side of the interface, he obtained:

$$\frac{1}{2} V^2 = \Delta g y \quad (4.1)$$

where V is the local velocity of the upper fluid and y is the height of the interface. This yields:

$$U = \sqrt{2\Delta g H} \quad (4.2)$$

He further noted that a headwave must exist, using an argument that appears to be related to the fact that the drag on any semi-infinite half-body in potential flow must be zero. Von Karman then considered the flow near the leading edge. By looking for a "corner flow" where the velocity squared is proportional to the distance from the stagnation point, he ascertained that the slope of the interface at the leading edge is 60° . From the above reasoning, he gave a sketch like that shown here in Figure 4.2, which agrees with observed gravity currents and resembles an "upside down" oil slick with a headwave except for the fact that the after portion of an oil pool does not have constant thickness.

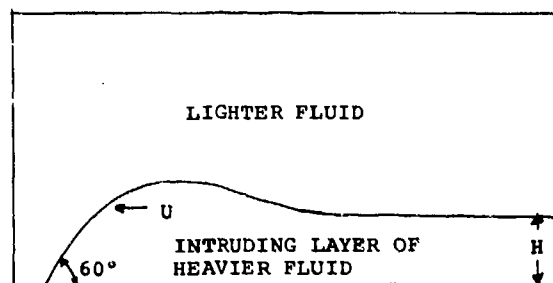


FIGURE 4.2 GRAVITY CURRENT TREATED BY VON KARMAN

The existence of a headwave similar to that predicted by von Karman has been reported by numerous investigators, notably Keulegan (1958) and Middleton (1966). Benjamin (1968), however, argued that one could not use Bernoulli's equation from the leading edge to a point far downstream, due to the fact that in purely irrotational flow, there is 1) no frictional drag, and 2) no hydrodynamic drag on a semi-infinite half-body. There is, however, a net hydrostatic force in the direction of propagation of the heavy fluid equal to $\frac{\rho_{lower} - \rho_{upper}}{2} g H^2$. The momentum deficiency in the wake of a breaking headwave was seen as essential for equilibrium. It remained unclear from Benjamin's analysis, however, why frictional forces in a relatively thin boundary layer could not provide the balancing force. If this were the case, the existence of the headwave could still be investigated using irrotational flow theory.

There are some essential differences between the problem of an oil slick on the surface of a body of water and that considered by von Karman and Benjamin. One is that the oil is limited in horizontal extent, and cannot in general be

approximated as a semi-infinite half-body. This can be seen in particular if there is a barrier present at the slick's trailing edge. Secondly, and perhaps the most important, is the fact that since the slick exists on a free surface, the hydrostatic motive force behind a density current need not be present: the free-surface height can adjust itself to provide horizontal equilibrium. Therefore, it seems that Benjamin's arguments cannot apply to the present case.

Previous work has been done on the slick thickness distribution problem by Wicks (1969), Hoult (1970), and Lindenmuth, Miller & Hsu (1970). All developed equilibrium equations which ignored completely the dynamic pressure in the water. Essentially, they balanced viscous shear and hydrostatic pressure. When the shear stress is assumed to be constant (as Hoult found to be the case experimentally), this analysis results in a thickness distribution proportional to the square root of the distance from the leading edge. Wicks (1969) and Lindenmuth (et al) (1970), however, reported the results of experiments with contained oil slicks which indicated the existence of a headwave at practically all flow speeds, the downstream side of which was unstable. To account for this in some way, both authors applied the viscosity-gravity equilibrium equation only to the portion of the slick downstream of the headwave (and in Wick's case, upstream of the region affected by the barrier).

In later studies (1972), Hoult looked at the free spreading of oil on calm water. He found that three phases of spreading exist. In the first, gravitational forces are balanced by inertial forces; in the second, gravitational and viscous forces are balanced; in the third, surface tension balances viscous effects. He presented both analytical and experimental results, including a picture of a spreading oil slick in the first phase (where viscous and surface tension effects were assumed to be negligible) which was remarkably similar to experimentally derived configurations of restrained oil slicks. This demonstrates the importance of inertial forces in the present problem. Hoult's analytical results for the same case failed to show this configuration, but the equations developed did not include dynamic pressures in the water.

Buckmaster (1973) solved the problem of the viscous-gravity spreading of an oil pool by considering the pressure in the oil to be hydrostatic and using the boundary layer equations in the water. Some of the details of the fluid mechanics at the leading edge are identical in the oil spreading problem and the problem of a contained pool in a current. This makes the work of Buckmaster of interest for the contained pool problem because knowledge of the distribution of skin

friction is necessary. One of Buckmaster's theoretical results is that the oil thickness distribution is blunt at the leading edge. This shows that his underlying boundary layer theory cannot be correct near the leading edge since the theory is accurate only when the thickness distribution has small slope. One of the factors which must be considered is the pressure force in the water owing to streamline curvature, and this is the factor that is to be studied here.

4.2 Water Dynamics

If we assume the water to be inviscid, Bernoulli's equation can be written along the interface to give:

$$p_2 = -\rho_2 g y - \frac{\rho_2}{2} [V^2 - U^2] \quad (4.3)$$

where V is the velocity of the fluid, U is the velocity at infinity, and the pressure of the atmosphere is taken to be zero. If V is broken up into the free-stream velocity and perturbation velocities, we get

$$p_2 = -\rho_2 g y - \rho_2 U u - \frac{\rho_2}{2} (u^2 + v^2) \quad (4.4)$$

where u and v are the horizontal and vertical perturbation velocities, respectively. If the slope of the interface is assumed to be small, u and v will be small, and the pressure, to first order in interfacial slope, is

$$p_2 = -\rho_2 g y - \rho_2 U u \quad (4.5)$$

4.3 Oil Dynamics

In the oil, the Navier-Stokes equations are:

$$u \frac{\partial u}{\partial x} + v \frac{\partial u}{\partial y} = -\frac{1}{\rho} \frac{\partial p}{\partial x} + \nu \left(\frac{\partial^2 u}{\partial x^2} + \frac{\partial^2 u}{\partial y^2} \right) \quad (4.6)$$

$$u \frac{\partial v}{\partial x} + v \frac{\partial v}{\partial y} = -\frac{1}{\rho} \frac{\partial p}{\partial y} + \nu \left(\frac{\partial^2 v}{\partial x^2} + \frac{\partial^2 v}{\partial y^2} \right) \quad (4.7)$$

The order of magnitude of the terms in Eqs. (4.6) and (4.7) can be determined and only the largest order terms retained to obtain a simplified approximation to these equations.

Define:

$$\gamma = \frac{\partial t}{\partial x} \quad (4.8)$$

where t is the thickness of the slick.

Due to the requirement of continuity,

$$u \sim O(\tau u) \quad (4.9)$$

$$\frac{\partial u}{\partial y} \sim O\left(\frac{\tau u}{t}\right) \quad (4.10)$$

$$\frac{\partial u}{\partial x} \sim O\left(\frac{\tau u}{t}\right) \quad (4.11)$$

$$\frac{\partial^2 u}{\partial y^2} \sim O\left(\frac{u}{t^2}\right) \quad (4.12)$$

Thus the viscous terms will dominate the convective terms in Eq. (4.6) if $u\tau u/\nu$ is small. If this is the case,

$$\frac{\partial R}{\partial x} = \mu_1 \frac{\partial^2 u}{\partial y^2} \sim \frac{\mu_1 \tau u}{t^2} \quad (4.13)$$

Similar argument shows that $\frac{\partial R}{\partial y} \sim O(\tau \frac{\partial R}{\partial x})$. Hence, if τ and $u\tau/t$ are small compared to unity, the flow in the oil will have the same character as couette flow. To determine u , Eq. (4.13) must be integrated twice. The result, simplified by use of the requirement of continuity, is:

$$u = \frac{1}{\mu_1} \left(\frac{\tau_0 t^2}{2} - \tau_0 y + \frac{\tau_0 y^2}{2t} \right) \sim O\left(\frac{\tau_0 t^2}{\mu_1}\right) \quad (4.14)$$

where

$$\tau_0 = \frac{\partial R}{\partial x} t \quad (4.15)$$

therefore

$$\frac{u \tau t}{\nu_1} \sim \frac{\tau_0 t^2}{\mu_1} \sim \frac{\tau_0 t^3}{\mu_1 l} \equiv Q \quad (4.16)$$

where l is the length of the slick. If, in addition to small slope, Q is small, inertial forces in the oil can be neglected, and the pressure in the oil will be hydrostatic. At the interface then,

$$p_1 = \rho_1 g t \quad (4.17)$$

To determine the typical magnitude of Q , consider a typical contained slick, 100 feet long and one foot thick. Suppose $\Delta = 0.1$ and $\mu_1 = 0.1$ slugs/foot-sec. Then

$$\tau_0 \sim O\left(\frac{\Delta g \Delta t^2}{l}\right) \sim O(.06)$$

$$Q \sim O(.12)$$

Hence, for typical slick densities and sizes, the assumption of hydrostatic pressure in the oil is expected to be quite accurate. An exception possibly exists near the leading edge of the slick where the interfacial slope may be large enough to make the assumption invalid.

For the study presented here, we shall assume the pressure in the oil is hydrostatic.

4.4 Equilibrium Equation

Figure 4.3 shows the forces acting on a differential element of the slick.

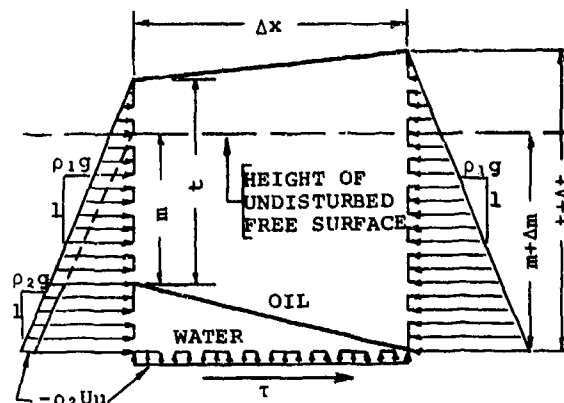


FIGURE 4.3 DIFFERENTIAL ELEMENT OF OIL SLICK, AND FORCES ACTING UPON IT

Summing the forces in the x-direction, we get:

$$\frac{1}{2} \rho_1 g t^2 + (m + \frac{1}{2} \Delta m) \Delta m \rho_2 g - \Delta m \rho_2 U u + \frac{1}{2} C_f U^2 \Delta x = \frac{1}{2} \rho_1 g (t + \Delta t)^2 \quad (4.18)$$

where C_f is a non-dimensional friction coefficient which in general depends on position. As we let Δx become arbitrarily small, Δm and Δt go to zero, and this equation becomes:

$$\rho_1 g m \frac{dt}{dx} - \rho_2 U u \frac{dm}{dx} + \frac{1}{2} C_f U^2 = \rho_1 g t \frac{dt}{dx} \quad (4.19)$$

Summing forces in the y-direction, we get:

$$t = \frac{\rho_2 m - \rho_1 U u}{\rho_1 g} \quad (4.20)$$

$$\frac{dt}{dx} = \frac{\rho_2}{\rho_1} \frac{dm}{dx} - \frac{U}{g} \frac{du}{dx} \quad (4.21)$$

Substituting in the x-equation, and letting $\Delta = \frac{\rho_2 - \rho_1}{\rho_1}$, we get:

$$-\left(\frac{\Delta}{1-\Delta}\right) g m \frac{dm}{dx} + \left(\frac{1-\Delta}{1-\Delta}\right) U u \frac{dm}{dx} + \left(\frac{1-\Delta}{1-\Delta}\right) U m \frac{du}{dx} - \left(\frac{1-\Delta}{1-\Delta}\right) \frac{U^2}{g} u \frac{du}{dx} = -\frac{C_f}{2} U^2 \quad (4.22)$$

4.5 Simplification of the Equation

Eq. (4.22) contains two unknown functions of position: m , the depth of the interface below the waterline; and u , the x -component of the perturbation velocity. The problem can be recast as an equation in a single variable by exploiting the fact that the slick is thin and has a small slope. The method used is similar to that used in thin airfoil theory. In particular, it is assumed that the perturbation flow in the water can be represented by that generated by a source distribution of strength $q(x)$ lying on the free surface over the region occupied by the oil slick. The interfacial slope and the perturbation velocity are given by the following functionals of the source sheet distribution.

$$\frac{dm}{dx} = \frac{q(x)}{2U} \chi = \frac{q}{2} (1 - \cos \theta) \quad (4.23)$$

$$u(x) = \frac{1}{2\pi} \int_{-\infty}^{\infty} \frac{q(\xi)}{x - \xi} d\xi \quad (4.24)$$

where in Eq. (4.24) the integral is the principle value type.

If we then define

$$I \equiv \int_{-\infty}^{\infty} \frac{q(\xi)}{x - \xi} d\xi \quad (4.25)$$

the equilibrium equation can be written as:

$$\begin{aligned} -\Delta m \frac{dm}{dx} + \frac{\Delta U^2}{g\pi} I \frac{dm}{dx} + \frac{U^2}{g\pi} m \frac{dI}{dx} \\ - \frac{U^4}{g^2\pi^2} I \frac{dI}{dx} = -\frac{(1-\Delta)C_F U^2}{2g} \end{aligned} \quad (4.26)$$

If the barrier extends below the bottom of the slick, it can be represented as a concentrated source, an impulse in the source sheet distribution.

In principle, the integral defining I is taken over the entire free surface where dm/dx outside of the oil slick is the free surface slope. However, we will solve the simpler problem here in which the free surface slope is zero upstream from the leading edge of the slick. Setting the "source strength" q equal to zero also downstream from the barrier simulates separation from the bottom of the barrier. Thus, the water flow is quite akin to the flow over a two-dimensional semi-infinite body.

4.6 Discretization

Due to the non-linear character of Eq. (4.26), an analytic solution cannot be obtained. Instead, a solution with a finite number of degrees of freedom

can be sought, where either the depth or slope of the interface is assumed to have the form of a sum of arbitrarily selected functions:

$$\left. \frac{dm}{dx} \right\} = \sum_{n=0}^N A_n \phi_n \quad (4.27)$$

The most obvious set of functions ϕ is a train of impulsive sources Q_n . In this case, the following approximations can be used:

$$m = \frac{1}{2U} \left\{ \sum_{i=0}^{N-1} Q_i + \frac{Q_N}{2} \right\} \quad (4.28)$$

$$\frac{dm}{dx} = \frac{Q_n}{U(x_{n+1} - x_{n-1})} \quad (4.29)$$

$$I = \frac{1}{2U} \left\{ \sum_{i=0}^{N-1} \frac{Q_i}{x_n - x_i} + \sum_{i=N+1}^N \frac{Q_i}{x_n - x_i} \right\} \quad (4.30)$$

where all quantities are measured at x_n , the location of source Q_n . This approximation to the Cauchy integral, however, is fairly crude. A superior approach would be one where this integral can be evaluated exactly for each function ϕ . If we make the well-known change of variables $\chi = \frac{1}{2}(1 - \cos \theta)$, we find that there are two reasonable Fourier-type expansions which allow this exact evaluation.

One method is to expand slick depth in terms of sines and cosines:

$$\begin{aligned} \frac{m}{L} = \\ \sum_{n=0}^{N/2} A_n \cos n\theta + \sum_{n=1}^{N/2} A_{n+1/2} \sin n\theta \end{aligned} \quad (4.31)$$

Glauert (1947) derived the contribution to I from the sine modes:

$$I_s = 2\pi \sum_{n=1}^{N/2} A_{n+1/2} \frac{n \sin n\theta}{\sin \theta} \quad (4.32)$$

The cosine modes are not so simple and must be computed recursively from the relation:

$$I_c = -2 \sum_{n=0}^{N/2} n A_n I_n \quad (4.33)$$

where

$$I_n = 2 \cos \theta I_{n-1} - I_{n-2} + \begin{cases} 0, & n \text{ odd} \\ \frac{4}{n^2-1}, & n \text{ even} \end{cases} \quad (4.34)$$

$$I_0 = 0 ; I_1 = \ln \left[\frac{1 - \cos \theta}{1 + \cos \theta} \right] \quad (4.35)$$

If only the cosine terms were used, the expansion would be equivalent to a series of Chebyshev polynomials. These polynomials can be shown to be a complete set of functions for the representation of an arbitrary, infinitely differentiable function on a finite domain. Furthermore, they have the advantage of converging exponentially rapidly as N goes to infinity. In our problem, however, we can expect an infinite slope at the leading edge (at least in the zero-Froude number limit), so the sine terms, which have infinite slopes at $\theta=0$ and at $\theta=\pi$, must be included.

Another approach which results in the analytic solution of the Cauchy integrals is to expand interfacial slope in terms of sines, with a cotangent term to allow an infinite slope at the leading edge:

$$\frac{dm}{dx} = A_0 \cot \frac{\theta}{2} + \sum_{n=1}^N A_n \sin n\theta \quad (4.36)$$

This is identical to Glauert's representation of the circulation along the chord of a two-dimensional airfoil. It can be shown that the cotangent term gives the uniform value $I = \pi A_0$, while the sine terms yield $I = \pi \sum_{n=1}^N A_n \cos n\theta$. This representation allows either infinite or zero slope at the leading edge (depending on whether A_0 is non-zero or zero, respectively) and requires a zero slope at the trailing edge.

If the terms multiplied by the unknown coefficients are called where $i=1, 2, 3, 4$ represent the series for m , $\frac{dm}{dx}$, I , and $\frac{dI}{dx}$ respectively, Eq. (4.26) can be written as:

$$\sum_n \sum_l A_n A_l \left\{ \frac{\Delta}{2F} Q_n'(\theta) Q_l'(\theta) - \Delta Q_n''(\theta) Q_l'(\theta) - Q_n'(\theta) Q_l''(\theta) + 2F Q_n''(\theta) Q_l'(\theta) \right\} - \frac{(1-\Delta) C_F(\theta)}{8} = 0 \quad (4.37)$$

or

$$\sum_n \sum_l A_n A_l Q_{nl}(\theta) - \frac{(1-\Delta) C_F(\theta)}{8} = 0 \quad (4.38)$$

where $F = \frac{U^2}{gZ}$ is a form of Froude number. If a barrier is included, the above equations will include linear terms in A_n and another term independent of A_n .

4.7 Solving for the Coefficients

The coefficients A_n may be obtained by any of a number of techniques. The relative complexity of the equation makes the simplest technique--that of collocation--particularly attractive. To collocate, one merely satisfies the equation exactly at $N+1$ points along the slick, or in a least-squares sense at more than

$N+1$ points. Unfortunately, there is no guarantee that the error will remain small between collocation points.

An alternative technique is that of Galerkin in which the criterion for selecting the best set of coefficients is that the resulting error be orthogonal (with respect to a weighting function) to each of the functions ϕ_j .

If the Galerkin method is used, Eq. (4.38) becomes:

$$\sum_n \sum_l A_n A_l \int_0^\pi Q_{nl}(\theta) \phi_j(\theta) d\theta - \frac{(1-\Delta)}{8} \int_0^\pi C_F(\theta) \phi_j(\theta) d\theta = 0 \quad j=0,1,\dots,N \quad (4.39)$$

Thus, regardless of our procedure, we obtain at least $N+1$ equations of the form

$$\sum_n \sum_l A_n A_l G_{nl}^j - H^j = 0 \quad j=0,1,2,\dots,J \quad (4.40)$$

These equations can best be solved by a vector extension of Newton's method. An initial guess for the vector A_n is made, and the error in the Eq. (4.40) is found from:

$$E^j = -\sum_n \sum_l A_n A_l G_{nl}^j + H^j \quad (4.41)$$

The derivative of the terms on the left-hand side of Eq. (4.40) with respect to each of the coefficients is then computed as follows:

$$\alpha_n^j = \frac{d}{dA_n} \left| \sum_l A_n A_l G_{nl}^j - H^j \right| = \sum_l A_l |G_{nl}^j + G_{ln}^j| \quad (4.42)$$

We now construct the matrix equation:

$$\begin{bmatrix} \alpha_0^0 & \alpha_0^1 & \alpha_0^2 & \dots & \alpha_0^N \\ \alpha_1^0 & \alpha_1^1 & & & \\ \alpha_2^0 & & & & \\ \vdots & & & & \\ \alpha_J^0 & & & & \end{bmatrix} \begin{bmatrix} \Delta A_0 \\ \Delta A_1 \\ \vdots \\ \Delta A_N \end{bmatrix} = \begin{bmatrix} E^0 \\ E^1 \\ \vdots \\ E^J \end{bmatrix} \quad (4.43)$$

Solving Eq. (4.43), we find the vector ΔA_n . The procedure is iterated, using $A_n = A_n + \Delta A_n$ for the second approximation to A_n , recomputing and solving for ΔA_n . This is continued until the coefficients converge to a solution

--i.e., until the vector ΔA_n is acceptably small.

Like the scalar form of Newton's method, the vector form converges rapidly to the desired solution only if the initial guess is good. Otherwise, solutions which do not satisfy the physical problem will be encountered--such as those leading to negative oil thickness. To avoid this difficulty, the solution can be obtained for small Froude numbers first, and then for successively higher values. In the small Froude number limit, the first term of Eq. (4.26) dominates the solution, and can be integrated directly to give as an initial approximation:

$$\frac{m}{l} = \sqrt{\frac{l-\Delta}{\Delta}} f C_f \frac{x}{l} \quad (4.44)$$

If a non-zero barrier projection is present, it must be introduced gradually at low Froude numbers so as to avoid convergence to an undesirable solution.

4.8 Preliminary Results

Due to its relative simplicity, collocation has been used in the initial attempts to solve Eq. (4.38). Errors in the equation were then checked at many points along the slick. It was found that the Glauert-type representation led to large errors between collocation points, whereas the representation of depth as sines and cosines did not. The errors in the latter case were quite small over the region between the first and last collocation points, at least in the cases where the end collocation points are not taken closer to the leading or trailing edges than half the distance between collocation points. This was true for points equally spaced in θ as well as in x , so that the region interior to the end collocation points extended (for the 13 term expansion) over 99% of the slick length. An elementary error analysis (wherein it is postulated that all the error occurs in the first term of Eq. (4.26)) showed that the error in depth caused by errors in the equation in the interior region was of the order of 1%. However, when one case was run with two different sets of collocation points, the results at high Froude numbers would vary significantly as can be seen in Figure 4.4. Surprisingly, the results would converge quite well for low Froude number cases, even for those representations which showed relatively large errors. This was evidently due to the oscillatory nature of the errors, but indicates that whatever errors are present at the leading and trailing edges which prevent the solutions from converging increase with Froude number.

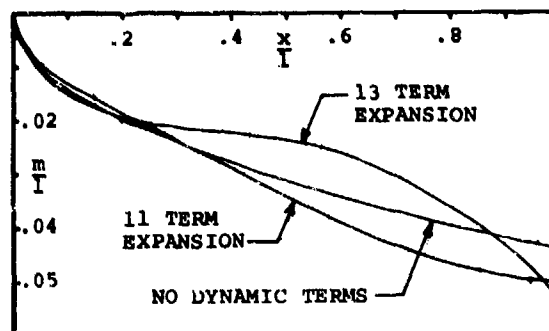


FIGURE 4.4. TWO "SOLUTIONS" TO EQUATION 4.37 ($F=0.316$, $\Delta=0.14$, $C_f=0.01$), EACH OF WHICH HAS SMALL ERROR IN INTERIOR. (VERTICAL SCALE EXAGGERATED)

5. CONCLUDING REMARKS

Theoretical studies of three phenomena related to the physical containment of spilled oil have been described. The first is the movement of oil slicks by water waves. Although a unified theory is presented here, from the operational standpoint of dealing with an oil spill, there are two mass transport problems. These are the global mass transport problem and the local mass transport problem. The global problem relates to the bulk movement of an uncontained slick by waves. A generally held belief is that wind moves an oil slick, and a commonly used rule of thumb is that the slick moves at $3\frac{1}{2}$ of the wind speed. In actuality, it seems likely that the slick movement is only slightly related to the shear force of the wind on the oil, and that most of the global mass transport of the slick is related to the effect of the wind-generated ocean waves. The direct effect of waves passing through a slick on the mass transport of oil is analyzed in this paper. A "back-of-the-envelope" calculation shows that for the size and length of typical wind-generated waves and for typical slick depths, the order-of-magnitude of the direct wave-related mass transport velocity is the same as the order-of-magnitude of $3\frac{1}{2}$ of the wind speed. There is another wave-related source of mass transport of oil that is not considered in this paper. This is the fact that a water wave passing through a slick loses some of its momentum due to free boundary layer effects at the oil-water interface. This results in a force on the oil that increases the rate of mass transport in the direction of wave propagation. This problem has just begun to receive analytical study.

The "local mass transport" is an effect related to what is called the interfacial wave in § 2. This effect is related to the fact that the group and phase velocities of interfacial waves

are very low and depend on the depth of the oil layer. As a result, when an object in a slick is moving in waves, the relative motion between the object and the oil can result in the object's keeping the oil away from itself most of the time. If the object is an oil skimmer, it cannot efficiently collect oil if the oil is kept away from it. To prevent this effect, a skimmer must follow the wave particle motion closely.

Experimental confirmation of the theory for the mass transport of oil by waves does not yet exist. The experiments for this are the next step in research in this area.

The second phenomenon analyzed is the stability of the oil-water interface when a slick is contained by a barrier. In practice, small interfacial waves are almost always seen, and there has been a question among scientists as to whether these waves are due to interfacial instabilities or due to the response of the interface to turbulent fluctuations in the pressure. Our analysis shows that the interface is unstable to spatially growing waves at all flow speeds. However, at some speeds, the unstable waves have wavelengths that are so long that the waves would have little effect, and at some speeds the unstable waves are so short that the viscous damping of the waves, which was neglected in the analysis, must be of importance.

The interfacial stability problem really needs extensive experimental study at this time. The experiments have to be done in a carefully controlled environment. In particular, the basic flow in the water must have turbulent static and total pressure fluctuations that are small in comparison with the pressure differences associated with the waves being studied. These pressures themselves are small because of the similar densities of oil and water so that the turbulent fluctuations in the flowing water must be extremely small indeed. We do not know of any flow channel existing at this time with the required smooth flow. Some attempts have been made at studying the problem in a towing tank by towing a barrier containing oil. The difficulty encountered is that it typically takes several minutes for the slick to attain its equilibrium mean configuration. During this time, very slow moving waves can be seen moving back and forth in the slick with each wave passage changing the thickness distribution. Typical tank lengths are too small to be able to have the slick attain its equilibrium configuration. Because of this, a precision flow channel needs to be built to carry out these experiments.

The third problem analyzed is the determination of the equilibrium thickness distribution of an oil slick contained by a barrier in a current. The equation obtained for the oil thickness distribution is quite different from

the one commonly found in the literature. Our equation is a non-linear singular integro-differential equation which we believe can only be solved by numerical means. In attempting to carry out the numerical solution, we found that it was possible to find rather different solutions with each having very small error over 99% of the slick length. This raises the question of whether or not a unique numerical solution can be found.

Although there are many problems and questions about the solution of our slick thickness equation, these questions are only a small "subset" of the total group of questions about the thickness distribution. The analysis leading to our equation neglects the effects of bluntness at the leading edge on dynamic pressure in the water, viscous effects, dynamic effects in the oil and possible head loss in the flowing water associated with the breaking of the headwave.

Although numerous experiments on the slick thickness distribution have been carried out, none seem aimed at revealing the physics of just what is going on. For example, no one has measured the dynamic head of the water upstream and downstream from the headwave to see if there is a reduction in dynamic head. Also, no one seems to have measured the details of both water and oil flow in the immediate vicinity of the leading edge of the slick. These details are essential in gaining an understanding of the flow. One of the problems in carrying out the needed experiments is that the same level of precision and low water turbulence is needed here as is needed in experiments on interfacial stability.

At the present time, oil cannot be contained without leakage occurring when the current speed is larger than 0.7 knots. The problem in affecting containment is the entrainment of oil droplets, principally from the headwave. This problem is a portion of the slick thickness distribution problem and because of its importance, the needed analysis and experiments should receive high priority.

The reader will have noticed at this point that more experimental research on the problems of containing oil is the needed ingredient for obtaining solutions and understanding. When research on oil containment was begun a few years ago, initial experiments were carried out to obtain rough measures of the conditions affecting oil containment. After this work was done, analytical studies, such as those described in this paper, received research interest. Although some experimental work has continued, it has been on a similar basis to the initial work. More refined experiments aimed at obtaining a quantitative physical understanding of the fluid mechanics have not received the emphasis they need, and we strongly believe that this lack of emphasis should immediately be changed

for the better.

(Following the time of initial printing, an error was discovered in the computer program for calculating the slick thickness distribution (§4). The complexities of its correction have not been resolved at the time of final printing.)

REFERENCES

- BENJAMIN, T.B., 1968 Gravity Currents and Related Phenomena. *Jl. Fluid Mech.*, 31, 209
- BUCKMASTER, J., 1973 Viscous-Gravity Spreading of an Oil Slick. *Jl. Fluid Mech.*, 59, 481
- HOULT, D.P., 1970 The Containment of Oil Spills by Physical and Air Barriers. Fluid Mechanics Laboratory Report, Massachusetts Institute of Technology
- HOULT, D.P., 1972 Oil Spreading on the Sea. *Annual Review of Fluid Mechanics*, Vol. 4, Annual Reviews, Inc.
- JONES, W.T., 1972 Instability at an Interface Between Oil and Flowing Water. *Jl. of Basic Engineering*, ASME, December 1972, 374
- KARMAN, T. VON, 1940 The Engineer Grapples with Non-Linear Problems. *Bull. of Amer. Math. Soc.* 46, 615
- KEULEGAN, G.H., 1958 The Motion of Saline Fronts in Still Water. *Natl. Bureau of Stds. Rept.* 5831
- LINDENMUTH, W.T., MILLER, E.R., and Hsu, C.C., 1970 Studies of Oil Retention Boom Hydrodynamics. Hydronautics, Inc. Tech. Rept. No. 7013-2
- MIDDLETON, G.U., 1966 Experiments on Density and Turbidity Currents. I. Motion of the Head. *Canadian Jl. of Earth Sci.* 3, 523
- WICKS, M., 1969 Fluid Dynamics of Floating Oil Containment by Mechanical Barriers in the Presence of Water Currents. Joint Conf. on the Prevention and Control of Oil Spills (Am. Petroleum Institute and U.S. Federal Water Pollution Control Adm.)

THE MANEUVERABILITY OF FISH, WITH POSSIBLE IMPLICATIONS FOR MAN-MADE VESSELS

D. Weihs
Technion - Israel Institute of Technology
Haifa, Israel

ABSTRACT

An analytical and experimental study of the maneuvering of fish is presented. Slender body theory adapted to deal with unsteady curvilinear large amplitude motions of elongated finned bodies is applied to turning and acceleration of fish. The contribution of non-slender fins is represented by the vorticity shed, obtained with the aid of indicial theory.

Analysis of experimental observations of fish performing these maneuvers shows that very efficient use is made of body and fin motions. In the case of rapid starting, a theoretically obtained optimal mode was observed.

The forces and moments on the fish calculated by the present theory are in good agreement with observations.

Some possible implications of the techniques analysed, to low speed maneuvering of man made vessels are discussed.

NOMENCLATURE

- a - curvilinear coordinate along the fish longitudinal centerline, origin at rear end.
- C_L - lift coefficient.
- \bar{c} - depth of fish cross section.
- $\frac{E}{T}$ - rate of energy expenditure.
- F - instantaneous force.
- l - length of fish (when stretched out).
- m - added mass per unit length, of fish cross section.
- \vec{n} - coordinate normal to longitudinal centerline.
- \vec{r} - radius of turn.
- s - coordinate tangential to longitudinal centerline.
- t - time.
- T - thrust force.
- u, v - velocity components in \vec{s}, \vec{n} directions, respectively.
- x, y - inertial Cartesian coordinates parallel and normal to initial fish heading.
- α - angle of attack.
- δ - displacement thickness of boundary layer.
- ϵ - defined in (7).
- ρ - density.

Subscripts

- b - body only (without fins).
- c - center of mass.
- i - index.
- q - defined in (4).

INTRODUCTION

The hydrodynamical aspects of fish locomotion started attracting interest in recent years after observations of the surprising performance of various aquatic creatures.

The propulsion mechanism of fishes has been studied intensively and two different theories for motion at high Reynolds numbers have been developed. One treats fish by means of a slender body analysis (1,2) based on the fact that most species of fish with good swimming performance have an elongated cylindrical shape. A different approach (3) treats fish as two dimensional flapping surfaces.

Such swimming analyses are of possible relevance to naval architecture in two ways. First, the oscillating foil (fish tail) has been considered as an alternative propulsor for boats, especially of shallow draft (4). Also submarines and yachts (when including a mirror-image above the free surface) among others, have shapes comparable to fish bodies (5).

As a result of these studies, it now appears that the constant velocity motion of aquatic animals is well understood. However, the maneuvering capabilities of fish have received less attention. Here also it is possible that the naval architect may be able to profit from comparisons with the techniques employed by fish for turning, starting etc.

It has been recently shown by the author that fish have learnt to make use of hydro-mechanics in saving energy by schooling (6) and in increasing range by alternate gliding and swimming (7) so that one can expect the maneuvers mentioned above to be carried out efficiently.

In the present paper maneuvers such as turning and accelerating of fish are examined from two points of view. First, a theoretical approach which allows the calculation of forces on a finned fish in unsteady curvilinear motion is presented. This is based upon a generalization of Lighthill's theory of large-amplitude motions of a slender body (8). Some further correction for viscous effects, which are neglected in all the theoretical work previously described is also included.

In parallel some observations of fish actually performing the maneuvers mentioned above are analysed and compared to the calculations. Good agreement between theoretically derived motions and observations, as well as between measured and calculated forces is obtained. Finally some possibilities of applying the ideas obtained from observation of fish motion to maneuvering are raised.

SLENDER FINNED BODY THEORY

Slender-body theory, in its usual form is the result of a perturbation scheme for situations in which one length dimension is much larger than the other typical dimensions associated with the problem. This framework has been applied (1) to the case of unsteady small amplitude motions perpendicular to the large length coordinate by means of a transformation causing the undulating body to become a fixed surface. This allowed the use of the slender-body technique to study fish locomotion and has since been generalized to include the effects of fins (2,5) and body thickness (5,9).

Almost all of the work mentioned above is limited to the linear case of small lateral undulations of the slender fish. This can be applied to analysis of steady swimming of fish at a constant velocity. However, when one attempts to study the maneuverability of fishes this limitation becomes too restrictive as acceleration turning, stopping and other processes of interest are achieved by means of large lateral motions of sections of the fish's body.

The small lateral amplitude theories are therefore not applicable, and we follow Lighthill's (8) generalization of his elongated body theory to include large lateral motions. The main result of the slenderness of the fish here is that the momentum imparted to the water near a given longitudinal section of the fish depends only upon the lateral virtual mass and lateral velocity of that section. The application to large amplitude motions is achieved by considering coordinates parallel, and perpendicular to the instantaneous orientation of the fish backbone.

Consider a frame of reference in which the velocity of the water far from the fish is zero. Dealing now with neutrally buoyant fish swimming in a horizontal plane described by Cartesian coordinates. The directions x and y can be chosen arbitrarily, and a practical choice is the x direction for the original orientation of the "stretched straight" fish.

Still following (8) we define an arc coordinate a along the fish backbone (longitudinal axis of symmetry), a takes values from 0 to l (see Fig. 1). From observations one finds that the velocity component perpendicular to the backbone is usually small, even if lateral motions are large.

Neglecting now any extensibility of the fish spine the position of any point along the fish at a time t can be regarded as functions $x(a,t)$ and $y(a,t)$.

The velocity in the horizontal plane can be separated into components tangential and normal to the curved backbone.

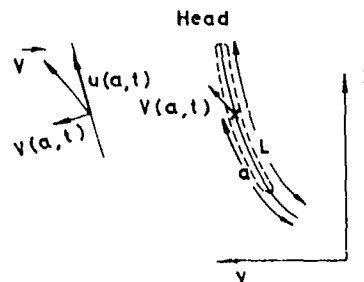


Fig. 1 The Coordinate System

$$u = \frac{\partial x}{\partial t} \frac{\partial x}{\partial a} + \frac{\partial y}{\partial t} \frac{\partial y}{\partial a} \quad (1a)$$

$$v = \frac{\partial y}{\partial t} \frac{\partial x}{\partial a} - \frac{\partial x}{\partial t} \frac{\partial y}{\partial a} \quad (1b)$$

The reactive forces on an elongated body in an inviscid fluid result almost completely from movements in the normal \vec{n} direction as the disturbances in the \vec{s} (tangential) direction are negligibly small. As suggested before, the momentum per unit length of fish produced by these normal movements is equal to $m\vec{v}\vec{n}$ where m is the lateral virtual mass and $\vec{n} = (-\partial y/\partial a, \partial x/\partial a)$ is a unit vector in the \vec{n} direction.

The momentum changes in the wake can be obtained by considering the half space bounded by a vertical plane π intersecting the tip of the caudal fin at a right angle to the longitudinal axis of symmetry, and moving along with its point of intersection in the x,y plane.

Using this approach Lighthill (8) obtained an expression for the net force upon a slender body performing large amplitude undulations

$$\vec{F} = - \frac{d}{dt} \int_0^l m \vec{v} \vec{n} da - \left[\frac{1}{2} m \vec{v}^2 + m \vec{v} \vec{u} \right]_{a=0} \quad (2)$$

The first term in the square brackets describes the resultant of the pressures arising from the lateral motions on the plane separating the fish from its wake. The second shows the rate of change of momentum due to convection (arising from the motion of the plane π). Only translation of π causes a convective momentum change, as fish cross-sections have lateral symmetry and rotation of π will not cause a change of momentum in either half space.

A characteristic feature of slender body theory appears in (2). The momentum shedding effects are all concentrated at the rear end of the body, and depend in magnitude on the dimensions of this rear end. In classical slender wing theory, it is well established (10) that only the parts of wings in which the span increases contribute to the lift forces, and regions of lessening span are "shadowed" and do not add or detract from the lift.

Many species of fish typically have their maximum span at the middle of their stretched-out length, so that according to the theory, forces are produced only along the front part of the fish. In his analysis of rectilinear swimming at constant speed, Lighthill (2) took the effect partially into account (see his Eq. 27) by adding a term equivalent to the momentum shed from the dorsal fin, again evaluated at the rear end of the tail fin.

This type of analysis as well as that of (5) is permissible when the curvature of the body is small and the quantities studied are total thrust forces. In this case the exact point of application of the resultant is of no great importance. Alternatively it is assumed that the vortex wakes from the dorsal and anal fins are partially or completely absorbed into the flow around the tail fin.

The present analysis attempts the study of maneuvers with time-dependent speed and direction of motion of the center of mass. As a result, one has to know, in addition to the net thrust force the actual instantaneous forces on different parts of the fish and the point of application of these forces. Also, wakes of the fins may be separate due to different sections of fish following non-identical paths.

Recalling that we are still dealing at present with an inviscid flow we assume that vortex-wakes, producing lift forces are shed only from sharp edged surfaces. The model fish consists of a smooth elongated body with discrete fins having sharp trailing edges¹. The instantaneous momentum shed into the wake can now be obtained by equating it to the changes in circulation around the assorted fins, plus the elongated body contribution.

Equation (2) can now be rewritten in the form

$$\vec{F} = - \frac{\partial}{\partial t} \int_0^l m_D \vec{v} \cdot \vec{n} da - \sum_{i=1}^k \vec{L}_i - \left[\frac{1}{2} m_D v^2 \vec{s} + m_D \vec{v} \cdot \vec{u} \vec{n} \right]_{a=0} \quad (3)$$

The advantage of the formulation in (3) is that when calculating the lift forces \vec{L}_i , one has the actual point of application, and orientation of the fin forces. On the other hand some complications arise when actual fish motions are analysed. In (2) all quantities are measurable, while here the lift forces \vec{L}_i have to be

1 Some species of fish have series of finlets along the rear half of their bodies, which makes this division into categories more difficult. However these finlets are probably mechanisms for delaying separation rather than lifting surfaces, and are therefore less relevant in this connection.

calculated separately from measurables. Also, the definition of m_D in sections which are composed of fin and body combinations can be difficult.

The general analysis of unsteady lift generation on an airfoil performing arbitrary motions is extremely complex and has to be treated numerically. However, recalling that the velocities perpendicular to the backbone $v(a,t)$ are small, the general motions may be separated approximately into a series of indicial motions (11). This allows the calculation of the lift coefficient of each fin by means of straight-forward steady state methods (12), and correcting for the unsteady motion by calculating the reduction in lift due to the incomplete buildup in circulation, obtained by the indicial method. The lift and moment on a wing during arbitrary maneuvers can then be found with the aid of Duhamel's integral. For the lift coefficient of a pitching and plunging airfoil, for example, this is written

$$C_L(t) = \frac{d}{dt} \int_0^t [C_{L_\alpha}(t-t_1)\alpha(t_1) + C_{L_q}(t-t_1)q(t_1)] dt \quad (4)$$

where $q \equiv \dot{\theta} c/U$. The indicial method is useful here as maneuvers such as turning, or lunging consist of a sequence of one-time phases with no periodic motions involved usually. There is an obvious inconsistency in applying decomposition and subsequent superposition techniques to an inherently non-linear situation. However observation of actual fish maneuvers show that these can be separated into distinct phases, in which the lifting surfaces perform different motions, sustained during each phase.

The analysis presented up to now assumed the fluid to be inviscid. In rapid maneuvering this is not too bad an assumption, and the errors may be roughly estimated from constant speed calculations, where it is clear that the average net force found by inviscid methods is equal and opposite to the net drag on the fish.

Some viscous effects can be estimated directly. Returning to (2) or (3) we see that the last term in the square brackets results from the tangential velocity of the fish. However, in real flow, some water will be dragged along due to the no-slip condition. The mass per unit length of fluid dragged along with the fish is $2\rho\delta^*$ where the factor 2 results from the two sides of the tail fin. Equation (2) now takes the form

$$\vec{F} = - \frac{d}{dt} \int_0^l m_D \vec{v} \cdot \vec{n} da - \left[\frac{1}{2} m_D v^2 \vec{s} + (m - 2\rho\delta^*) \vec{v} \cdot \vec{u} \vec{n} \right] \quad (5)$$

recalling that the lateral added mass of elliptical sections (including the circle and flat plate as limiting cases) is

$$m = \frac{\pi}{4} \rho d^2 \quad (6)$$

equation (5) can be written as

$$\vec{F} = - \frac{d}{dt} \int_0^l m_D \vec{v} \cdot \vec{n} da - \left[\frac{1}{2} m_D v^2 \vec{s} + m(1-\epsilon) \vec{v} \cdot \vec{u} \vec{n} \right] \quad (7)$$

where $\epsilon = \frac{8\delta^*}{\pi d}$.

The same type of correction can be made to (4). Rough estimates of the magnitude of ϵ can be made assuming laminar flat plate flow.

This is based on the fact that fish cross sections are usually highly elliptical, while the fins are approximately flat plates too. Such estimates show that ϵ is of the order of a few percents.

However, the lateral motions of the fish cross sections cause both longitudinal and lateral separation on the body. These effects are being studied at present. The effect of longitudinal separation can be shown to increase ϵ . The boundary layer thickness is proportional to the length of the body raised to a fractional power depending on the flow regime. Assume now that whenever a longitudinal boundary layer separates, a new one starts and the separated layer remains as a distinct momentum defect passing out of the control volume due to the fish motion.

For demonstration, let us now assume laminar flow and one separation exactly halfway along the fish

$$\epsilon = (\text{const}) \times (\delta_1^* + \delta_2^*) = (\text{const}) \times \left[\left(\frac{l}{2} \right)^{\frac{1}{2}} + \left(\frac{l}{2} \right)^{\frac{1}{2}} \right] \quad (8)$$

while for unseparated flow $\epsilon = (\text{const}) l^{\frac{1}{2}}$. The ratio of ϵ with and without separation is therefore

$$\frac{(\frac{l}{2})^{\frac{1}{2}} + (\frac{l}{2})^{\frac{1}{2}}}{(\frac{l}{2})^{\frac{1}{2}}} = \frac{\frac{l}{2} + \frac{l}{2} + 2(\frac{l}{2})^{\frac{1}{2}}}{l} > 1 \quad (9)$$

FISH TURNING

The first type of maneuver we study in detail is the process of changing direction. The analysis of turning was carried out by examination of filmed sequences of fish moving in tanks with an accurately scaled background.

The sequences chosen for analysis included horizontal turns only, of neutral buoyant fish so that the two dimensional approach, neglecting body forces is permissible. Also in the cases selected surface waves were negligible.

Preliminary observations of fish performing turns of up to 180° (13) lead to the conclusion that there exists a "unit turn" of approximately 90° . When changes in direction of over 90° are required, the fish breaks these into a 90° turn and one of whatever further deflection required. Turns of less than a right angle were accomplished in one step. As a result, it seems that the most useful conclusions can be obtained from analysis of 90° turns. Two different cases will be described in detail now, that of a turn at right angles while moving at cruising speeds, and a standing turn. The turns chosen were horizontal so that most of the data required for calculations were obtained by following the movements of the longitudinal centerline $a(x,y,t)$ and plotting its position as a function of time (Figs. 2, 3). This was done by tracing the centerline position from enlarged projections of successive frames of the filmed sequence.

First, the trajectory of the instantaneous center of mass (see Fig. 3) for cases with finite mean initial velocity was plotted. Three stages can then be discerned, characterized by different motions of the center of mass (c.m. from here on). In the first stage the c.m.

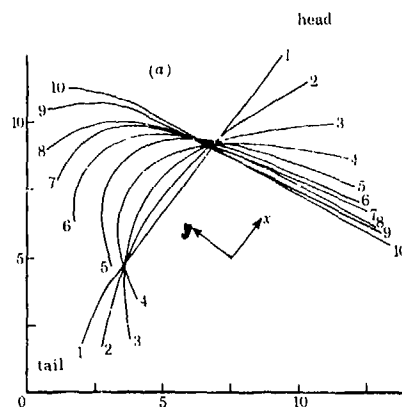


Fig. 2 Tracings of Position of Backbone of Goldfish during Turning Process. Numbers Refer to Film Frames. Distances are in cm, and Time Interval Between Frames 0.04 sec.

moves along a straight line in the direction of motion, in the second it travels along a curve and in the last phase, the c.m.'s motion is in a straight line again, in the new mean direction of movement of the fish. These three phases are approximately of equal duration, and can be roughly described as the preparatory, active and concluding stages of the turning process.

We now go into an analysis of the motions during each phase, looking initially at the goldfish of Fig. 2 performing a standing turn. At the beginning of the preparatory stage the head starts rotating in the direction of turn. This results in a force acting on the fish, opposing the rotation, causing a countering couple on the fish. Meanwhile, the tail is rotating in the opposite sense, and the reaction here produces a couple opposing that of the head (see Fig. 4). The balance of forces is completed by the reactions on the central part of the body (from "shoulder" to tail). This part moves slightly due to the requirement of the centerline (backbone) being a continuous curve. The added mass of this part of the fish is relatively large so that even these rather smaller motions produce forces large enough to balance the head and tail forces so that no sideways motion of the c.m. is observed. For simplicity, the discussion here deals with lumped forces on three parts of the goldfish while the actual forces are distributed along the whole length of the fish (see Fig. 4). During the preparatory stage therefore we see that the fish curves and has brought its head close to the final orientation and rotating rather rapidly. No net unnecessary forces or couples caused which would cause superfluous motions of the c.m. and reduce efficiency are produced.

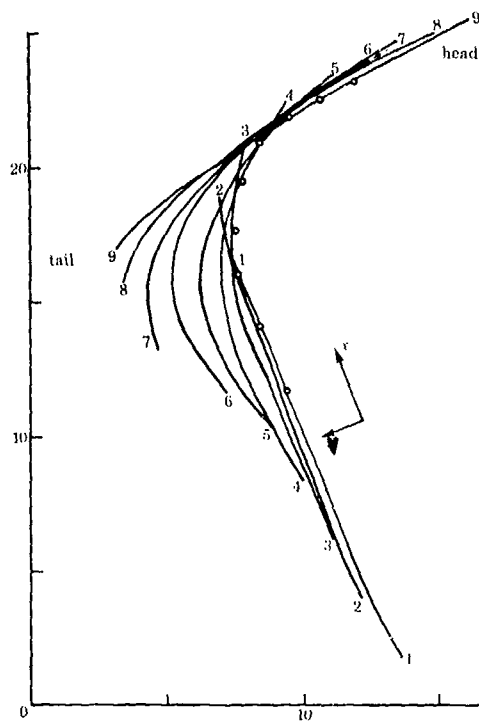


Fig. 3 Tracing of Backbone of Rudd During Turning Process. Hollow Dots Show Position of Center of Mass. Rest of Symbols as in Fig. 2.

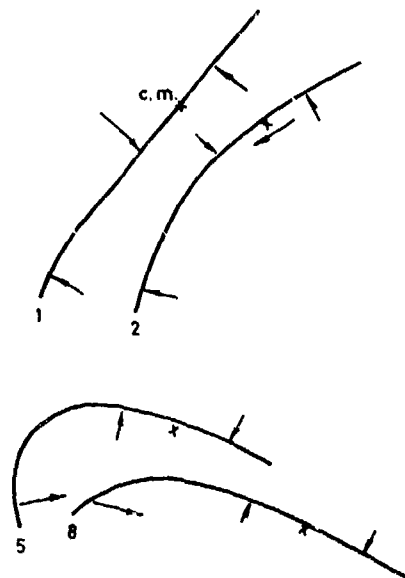


Fig. 4 Lumped Forces During the Various Stages of Turning (from Fig. 2).

The active turning stage starts off with the fish strongly arching its central section. The tail now changes direction and moves ahead at a small angle of attack, while the head, which has reached its final orientation by frames 5-6 is slowing down. The force picture has drastically changed, with a large force in the direction of the center of turn, caused mainly by the lift on the tail fin, but also at the beginning of this stage due to the large lateral motions of the central body.

Meanwhile the turning moment, which started growing at the end of the preparatory stage and caused the angular velocity of the c.m., has changed direction. During the latter part of the active stage the large lift forces on the tail cause a countering moment. The angular velocity is rapidly reduced and vanishes at the beginning of the concluding stage.

During the first calculations based upon this description according to the slender-body theory presented before a discrepancy in the balance of angular momentum was obtained. According to these the restoring moment was appreciably larger than the initial turning moment. Further study of the experimental results showed that the beginning of the active stage was accompanied by asymmetric deployment of the pectoral fins. The fin closer to the center of turn was placed vertically and stretched out, while the other pectoral was horizontal. This causes a retarding force, and a couple tending to rotate the c.m. in the direction of required turn, which settled the difference in moments mentioned above. The retarding force obtained apparently as a side-effect plays an important role in reducing the tangential velocity of the fish before actual rotation of the c.m. starts. Recalling that the centripetal force required for a turn at constant radius is

$$F_c = \frac{mu^2}{r} \quad (10)$$

we see that this helps reduce the turning radius for given force the fish can exert, and given initial forward speed.

In the concluding stage the fish straightens out in its chosen new direction of swimming. The tail is rapidly flicked into line, while lessening the angle of attack. The tail is moved so that the lift forces are almost parallel to the new direction of movement and accelerating the fish back to close to the initial speed. At the same time, the couple produced by the eccentricity of these lift forces serves to bring the rotation to zero.

Turns at different initial and final speeds all have the same characteristics with modifications in the detailed behaviour. The sideways motions of the tail in the preparatory stage are much less pronounced at cruising speeds as the lift forces are produced by simply placing the tail at an incidence to the direction of motion, the active and concluding stages again are similar to the case described before. The existence of a forward velocity while turning enables the fish to perform the turn with less vigorous bodily movements, as both the inertial (added mass) and lifting forces are dependent on the absolute velocity component perpendicular to the backbone. However the energy required for these sideways motions at higher speed

is larger. Also, the turning radius is increased both because of the dependence of the centripetal force on the tangential velocity and the fact that the fish keeps moving ahead during the finite time required for each stage.

Having obtained an understanding of the mechanism of turning, the theory described before was used to obtain quantitative results. The actual procedure went the other way, with the calculations showing the way to the three stage approach and lumping of forces, as well as the importance of the pectoral fins in producing the required turning moment. Details of the calculations have appeared elsewhere, (14) and will therefore not be repeated here, except to mention that there was only a 12% discrepancy between the calculated and observed turning radius. Such results are amazingly good in view of the fact that two numerical differentiations of photographic data, as well as other simplifying assumptions, were employed. The two numerical differentiations were required for the integral term in Eqs. (2) and (3). The data points were obtained (for displacements) from Figs. 2 and 3 and the velocities appearing in Fig. 5 by means of a 3-point Lagrangian scheme. This was used again for the time differentiation required in Eqs. (2) and (3).

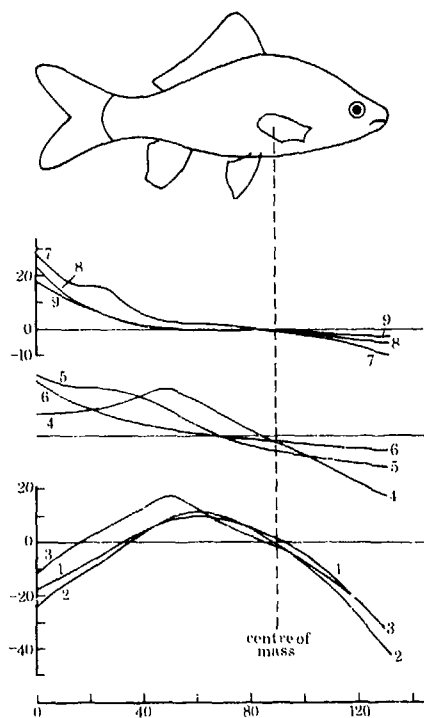


Fig. 5 Local Perpendicular Component of the Velocity During Turning. The Three Stages are Separated to Emphasize the Different Behaviour. Numbers along the Curves Refer to Frames in Fig. 2.

ACCELERATION

Theoretical Analysis

Another interesting and potentially useful facet of fish locomotion is the method employed for rapid acceleration. Most species of fish which have developed good lunging abilities are elongated, and therefore the theory of slender fish is applicable in this case also.

This theory can be used to obtained trends in optimal motions for rapid acceleration. Obviously the results will be approximate and very generalized as actual fish have a great variety of body and fin configurations. The optimal sequences of motion will be defined as those producing a maximum average thrust force for given bounded energy expenditure. The premise here is that when the fish has strong enough motivation (such as extreme danger, or hunger) it will use its available energy at the highest possible short-term rate which is a measurable constant.

Take for simplicity the case of a smooth elongated fish for which Eq. (2) is suitable, the thrust can be written as

$$T = \frac{d}{dt} \int_0^l mv \frac{\partial v}{\partial a} da + [um(1-\epsilon) v \frac{\partial y}{\partial a} + \frac{1}{2} mv^2 \frac{\partial x}{\partial a}]_{a=0} \quad (11)$$

The kinetic energy associated with movements normal to the longitudinal axis is $1/2mv^2$ per unit length. This energy leaves the semi-infinite control volume by convection, so that the rate of working is

$$\dot{E} = T u_c + \frac{1}{2} mv^2 u(1-\epsilon^*) \Big|_{a=0} + \frac{d}{dt} \int_0^l mv^2 \frac{\partial y}{\partial a} da \quad (12)$$

The last term in (12) vanishes for processes which are periodic or start and end in the same configuration. In any case, both the second and third terms in (12) are proportional to v squared, so that a first conclusion is that the perpendicular velocities v should be small for good efficiency, especially close to the tail.

The thrust can be rewritten as (8)

$$T = [mv \frac{\partial y}{\partial t} - \frac{1}{2} mv^2 \frac{\partial x}{\partial a} - mv\epsilon^* u \frac{\partial y}{\partial a}]_{a=0} + \frac{d}{dt} \int_0^l mv \frac{\partial y}{\partial a} da \quad (13)$$

Small v is advantageous here too, as the positive contributions are dependent on the first power of v . Also for the thrust to be large $\partial y/\partial t$ should be large. This implies that the tail should move in a line as close as possible to the perpendicular to the direction of motion, at a large velocity. The former condition of v being small now means that the tail should be moving rapidly at a small positive angle of incidence. The thrust force consists mainly therefore of the lift force on the tail. The first term can then be identified as the pressure difference in steady motion while the second term represents the leading edge suction. The vectorial sum of these two acts in the direction of motion of the fish c.m.

The head and front part of the fish are seen to play a secondary role in thrust production. Therefore it should be kept as rigid as possible and more straight forwards. This conclusion stems from viscosity as any average sideways motion of the bluff body would cause flow separation and useless side forces.

Actual Fish Motions

As in the turning case, fish with good acceleration capability were chosen for observation, and checking the validity of the theory. The fish were chosen from a variety of unpublished filmed sequences of fish rapid starting, taken by Sir James Gray in Cambridge, England. The sequences finally selected were of trout (Fig. 6) and pike, for which extreme accelerations of 40 and 50 $\text{m} \cdot \text{sec}^{-2}$ have been measured.

The analysis is similar to the process described for turning. Tracings of the position of the longitudinal centerline as a function of time provide the data on velocities and accelerations. The rapid start can be separated into stages distinguished by different motions.

- a) The preparatory stage, in which the fish changes from a stretched-out initial resting position into an L shape. This was sometimes carried out as a precautionary measure, when the fish sensed danger.
- b) The propulsive stroke, in which the tail is moved perpendicularly to the fish orientation, ending with the fish in an L shape again with the tail pointing the other way. This stage was sometimes repeated several times.
- c) The final stage. The fish returns to a stretched straight configuration gliding slowly to a halt, or starts a normal propulsive cycle. Both steady swimming and gliding is usually at an acute angle to the original heading. The magnitude of this angle is roughly proportional to the average acceleration during the start.

For a more detailed analysis, we take the trout of Fig. 6. The initial motions, intended to bring the fish into the efficient L-shape are at the base of the caudal fin which is rapidly moved diagonally forward. The moment produced by this motion is countered, as in the case of turning, by rotation of the head. The tail fin itself moves forward at an angle of incidence, producing lift forces approximately in the original heading and starting the acceleration.

The rotation of the head, which is a side product of the preparatory stage stops at the end of this phase (frame 3). The angular deflection of the head is thus related to the time in which the preparatory stage is completed. If this stage is performed slowly (not the present case) pectoral fin motions are usually sufficient to balance the couples and no rotation of the head is observed.

The main propulsive phase begins with the tail pointed at approximately right angles to the front part of the body. Here (frame 3) the tail is moved in a curve approximately perpendicular to the instantaneous radius-vector between it and the c.m. The c.m. is moving in the direction the head is pointing in. The motion of the caudal fin is the closest approach to the theoretical requirement of linear motion at right angles to the direction

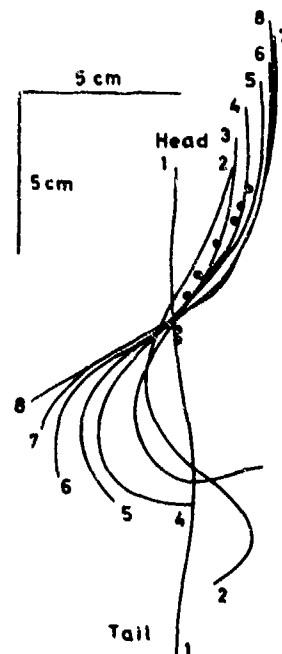


Fig. 6 Tracings of Position of Backbone of Trout during Rapid Starting. Numbers Refer to Frames. Time Interval Between Successive Frames was 0.025 sec. Dots show instantaneous position of center of mass.

of advance, because of the constant length, and minimum radius of curvature of the backbone. This stage ends with the fish in a mirror-image configuration from the beginning (frame 8).

The trout illustrated in Fig. 6 displayed rather unusual behaviour using the paired fins (not shown) to return to the initial heading.

The final stage starts with the fish in an inverse L-shape (frame 8). The momentum gained up to this point carried the fish forward, causing the tail to be pulled back in line. Several variations in behaviour were observed from here on. In some cases, the propulsive stage was repeated twice or more (see also 15, Fig. 204). In others, a regular swimming rhythm was now initiated. Still others (including the trout of Fig. 6) just went on gliding idly.

The slender body theory was again used for the calculation of forces during lunging, and again good agreement was achieved. Calculated and measured average accelerations were 2.4g and 2.1g respectively for the trout and discrepancies of no more than 35% were obtained for some other examples.

The main conclusion from this analysis is that the efficient sequence for rapid starting, predicted by large amplitude slender body theory is closely approached in nature. The theory predicted the propulsive stage, as could be expected.

CONCLUDING REMARKS

The techniques employed by fish for rapid maneuvering were shown to be highly effective, with good use made of a variety of control surfaces, as well as the body flexibility. While it is hard to imagine man made vessels of such high degree of flexibility, it seems that some ideas may still be taken from the observation and understanding of fish motions, especially for low speed maneuvering.

Thus, by combinations of active rudders, and ducted thrusters, a rigid elongated vessel can still simulate a curving flexible fish to some extent. One interesting result of the turning study is the relative importance of bow controls for efficient change of direction. Also, if the oscillating vane propulsor (4) is used, further improvement of maneuverability, not realized in the original studies on this alternative to the propeller, may be achieved by asymmetric vane action, as in the concluding stages of turning and starting.

ACKNOWLEDGEMENTS.

The author wishes to thank Sir James Lighthill for numerous fruitful discussions, and Sir James Gray for permission to use his facilities and unpublished data.

REFERENCES

1. Lighthill, M.J., "Note on the Swimming of Slender Fish", Journal of Fluid Mechanics, Vol. 9, 1960, pp.305-317.
2. Lighthill, M.J., "Aquatic Animal Propulsion of High Hydromechanical Efficiency", Journal of Fluid Mechanics, Vol.44, 1970, pp. 265-301.
3. Wu, T.Y., "Swimming of a Waving Plate", Journal of Fluid Mechanics, Vol. 10, 1960, pp.321-344.
4. Scherer, J.O., "Experimental and Theoretical Investigation of Large Amplitude Oscillating Foil Propulsion Systems", Hydro-nautics Inc. Rep. presented to SNAME (Chesapeake Section), Dec. 1968.
5. Newman, J.N. and Wu, T.Y., "A Generalized Slender-Body Theory for Fishlike Forms", Journal of Fluid Mechanics, Vol. 57, 1973, pp.673-693.
6. Weihs, D., "Hydrodynamics of Fish Schooling", Nature, Vol. 241, No. 5387, Jan. 1973, pp.290-291.
7. Weihs, D., "Mechanically Efficient Swimming Techniques for Fish with Negative Buoyancy", Journal of Marine Research, Vol. 31, No. 3, Sept. 1973, pp.194-209.
8. Lighthill, M.J., "Large-Amplitude Elongated-Body Theory of Fish Locomotion", Proceedings of the Royal Society Ser. B, Vol. 179, 1971, pp.125-138.
9. Newman, J.N., "The Force on a Slender Fish-like Body", Journal of Fluid Mechanics, Vol. 58, No. 4, 1973, pp.689-702.
10. Thwaites, B., Ed. "Incompressible Aerodynamics", Oxford, 1960, pp.385-404.
11. Jones, W.P. ed. "AGARD Manual on Aeroelasticity", Vol. 2, Ch.6, AGARD, 1960.
12. Robinson, A. and Laurmann, J.A. "Wing Theory", Cambridge University Press, 1956.
13. Gray, Sir James., "Animal Locomotion", Weidenfeld and Nicolson, London, 1968, pp.34-37.
14. Weihs, D., "A Hydrodynamical Analysis of Fish Turning Maneuvres", Proceedings of the Royal Society, Ser. B, Vol. 182, 1972, pp.59-72.
15. Hertel, H. "Structure-Form-Movement" Reinhold, New York, 1966, pp.160-162.

LASER-DOPPLER MEASUREMENTS OF TRAILING VORTICES IN A WATER TUNNEL

S. J. Barker
California Institute of Technology
Pasadena, California 91109

ABSTRACT

Recent measurements of trailing vortex wakes behind hydrofoil models in a water tunnel are described. These measurements were made in the Caltech Free-Surface Water Tunnel, using a laser-doppler velocimeter. Both axial and tangential velocity components in the vortices were measured. Various model planform shapes were tested, and each model was run at several values of angle of attack and free stream velocity. The distance downstream of the model was varied from five to sixty chord lengths.

The effects of the random motion of the vortices are shown to be very important in steady state measurements. The influence of this "vortex wandering" upon the measurements has been roughly calculated, and the corrected results are shown to be in reasonable agreement with existing trailing vortex theory.

INTRODUCTION

The problem of aircraft wake turbulence has stimulated many recent measurements of velocities in trailing vortex wakes. In spite of the great interest in this problem, experiments have not yet established the details of the roll up and decay of vortex wakes as functions of wing shape. Several types of measurements have been attempted so far. Free flight measurements such as Caiger and Gould(1), or Chevalier(2), have not yet produced satisfactory results because of the difficulty in locating the vortex cores behind a full scale aircraft. Wind tunnel measurements using total pressure probes(3) are subject to doubt because of probe interference effects, which will be discussed below. There have also been some measurements of vortex wakes in towing basins(4,5), but in these cases the flow is time dependent rather than stationary, and the details of the velocity profiles are difficult to measure.

The only velocity measuring instrument presently available which cannot disturb the model flow and has high spatial resolution is the laser-doppler velocimeter(LDV). Because of the excel-

lent results obtained with an LDV in hydrodynamic flows, it was decided to use this technique in Caltech's Free-Surface Water Tunnel to measure trailing vortex wakes. The water tunnel also has the advantages of producing high Reynolds numbers at relatively low speeds, and the ease of flow visualization in water which makes it possible to measure photographically the position of the vortex. In addition, there are sufficient small light-scattering particles in the water tunnel to allow continuous operation of the LDV without adding foreign particles to the flow. Laser-doppler measurements of trailing vortices in a wind tunnel have been recently reported by Orloff and Grant(6).

EXPERIMENTS

Flow Facility

The Caltech Free-Surface Water Tunnel has a maximum velocity of 24 feet per second through a test section which is eight feet long and twenty inches on each side. The free stream turbulence level of the tunnel was measured at the beginning of this program and found to be about 0.7%. Since that time, a new honeycomb flow straightener has been installed upstream of the test section and the turbulence level has been reduced to about 0.4%. Free stream turbulence has been found to be extremely important in the measurement of vortex wakes, so further efforts are presently being made to reduce the turbulence level. For a complete description of the water tunnel, see Knapp and Levy(7).

Four hydrofoil models have been studied to date. Two of these have a rectangular planform with a span of six inches and a chord of one inch. Both have a symmetric semicircular arc section profile, with a ten percent thickness and a 0.030 inch leading edge radius. The difference between these two models is that one has square wingtips while the other has semicircular ones. The second two models are delta shapes, one having a 30 degree nose angle and the other a 60 degree nose angle. The delta models are flat on the bottom with sharp, beveled edges. All models are supported

horizontally in the water tunnel by a thin vertical strut attached to the center of span of the model. This strut is attached to a mechanism above the water surface which controls the depth and angle of attack of the model. The model is located at the upstream end of the test section, and measurements can be made at distances of up to sixty chord lengths downstream (fig. 1).

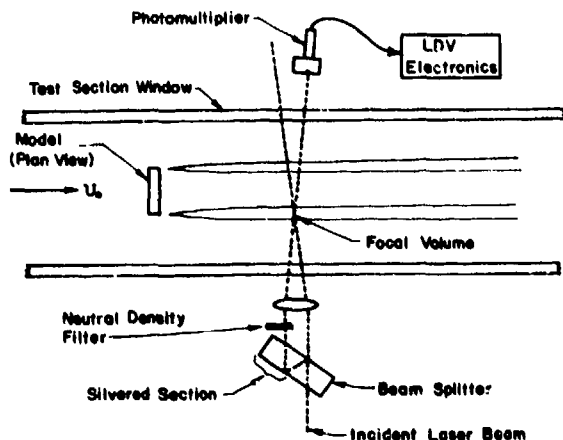


Fig. 1 Experimental Geometry

Instrumentation

The LDV used for this experiment is mounted on a traversing system which moves the laser and all of the optics with respect to the water tunnel. The traverse is capable of locating the center of the LDV focal volume to within 0.002 inch of a desired position. The LDV operates in the so-called "local oscillator" mode, which will be described briefly.

The beam from a five milliwatt helium-neon laser ($\lambda = 6328 \text{ \AA}$) is split into two parallel beams by a glass prism beam splitter which uses partial internal reflection of the incident beam. One of the beams from this splitter is about ten times weaker than the other, and this beam is further attenuated by a factor of 100 by a neutral density filter. The two parallel beams, separated by about one inch, then pass through a single biconvex lens of focal length 12 inches. The beams pass through the side window of the tunnel test section and cross at a point within the fluid flow. Since the two beams were collimated as well as parallel when they entered the lens, they are also focussed at the same point at which they cross. The volume in which they intersect is about 1 mm in length and 0.1 X 0.1 mm in cross section.

The two laser beams leave the tunnel test section through the window on the opposite side, and the weaker one passes through a 1 mm aperture into a photo-

multiplier tube. In the photomultiplier, the light from this weak "reference beam" is mixed with light from the brighter beam which has been scattered from the volume in which the two beams intersect. The scattered light has been doppler shifted by the motion of the scattering particles, and thus has a slightly different frequency from that of the reference beam. The combination of these two different light frequencies in the photomultiplier produces a beat frequency which is proportional to one component of the fluid velocity, assuming that the scattering particles follow the instantaneous velocity of the fluid. For a more detailed discussion of the optical principles of the LDV, see references 8, 9 and 10.

The signal from the photomultiplier tube is amplified, band-pass filtered, and then clipped to remove some of the random amplitude modulations of the beat frequency signal. This clipped doppler signal is then fed into a phase-locked loop, which produces a continuous square wave whose frequency tracks that of the doppler signal. The phase-locked loop will accurately track the fluctuations in the doppler frequency as long as the turbulence level of the flow does not exceed about twelve percent. For higher turbulence levels, the phase-locked loop cannot follow the larger fluctuations in frequency.

The square wave from the phase-locked loop is fed into a digital counter which averages the doppler frequency over a ten second period. The counter frequency is then converted to a velocity simply by multiplying it by a known scalar constant. The square wave signal is also fed into a frequency to voltage converter, which produces an analog signal proportional to the doppler frequency. This signal then represents the instantaneous velocity, with a bandwidth of from 0 Hertz to about 1/50 of the doppler frequency. The R.M.S. value of this signal divided by its DC average is equal to the local turbulence level.

The ability of an LDV system to measure fluctuations in velocity is limited by the doppler "ambiguity noise" (11). This is a noise on the demodulated velocity signal (it has no effect upon the mean) which is caused by: 1) the finite transit time of scattering particles passing through the focal volume, 2) mean velocity gradients across the focal volume, and 3) turbulent fluctuations within the focal volume. The ambiguity noise produced by 3) is negligible in the present case, but the noise produced by 2) may be significant near the core of the vortex. In this region the mean velocity gradients are extremely high. The noise from 1) is constant for a given focal volume and scattering particle density,

and has been measured in the laboratory for laminar flows. This component of the ambiguity noise is equivalent to a background turbulence level of about 0.25%.

The LDV system has several significant advantages over conventional measurement techniques in the present experiment. The most important of these is the fact that with the LDV there is no material probe in the flow, and no flow interference is possible. Flow visualization studies suggest that model trailing vortices of sizes that can be generated in the laboratory are very sensitive to disturbances created by the smallest probes. This fact alone makes it essential to use the LDV or some other non-interfering technique in these measurements. Other advantages of the LDV are its linear response to velocity, high spatial resolution, and its sensitivity to only one velocity component.

Procedure

The measurements made to this date include axial and tangential velocity profiles in vortex wakes behind four different hydrofoil models, as described above. The axial velocity component was measured directly by aligning the axis of the LDV with the direction of the free stream flow. The tangential component was found indirectly by measuring the velocity component at a 45 degree angle to the free stream and using this together with the axial component to calculate the tangential component. The tangential component could not be measured directly in this case because the mean tangential velocity passes through zero in the center of the vortex. The LDV measures the magnitude but not the sign of the velocity, so that velocity profiles which pass through zero are difficult to measure (unless frequency biasing techniques, which will not be discussed here, are used). However, the velocity component at 45 degrees to the free stream is always positive in sign, and can be easily measured with the LDV.

Velocity surveys at each downstream station were made in a horizontal plane, starting well out in the free stream and proceeding inward past the center of span of the model. Each mean velocity measured was averaged over a thirty second period, and the results were found to be very repeatable.

RESULTS AND CONCLUSIONS

Vortex Wandering

One of the first observations made in this model flow is that the trailing vortex wakes do not remain stationary in space. Flow visualization in the core of the vortex shows that the center of the vortex is displaced about its mean location in a random manner. This vortex wandering phenomenon is apparently caused

by free stream turbulence in the water tunnel, since the same degree of wandering is observed in a dye streak released from the model in a zero lift configuration. This implies that the measured mean velocity profiles are actually weighted averages of the instantaneous profiles in the vortices.

By photographing dye streaks injected into the vortex cores, it is possible to measure the standard deviation of the position of the vortex wake. If we assume that the wandering motion is Gaussian, we can represent the vortex motion by a turbulent eddy diffusivity K . Then the center of the vortex will fluctuate about its mean position at a given downstream distance x with a probability density

$$p(\eta, \zeta) = (1/2\pi\sigma^2) \exp[-(\eta^2 + \zeta^2)/2\sigma^2],$$

where $\sigma^2 = 2Kx/U_\infty$. We can measure the eddy diffusivity K from the dye streak photographs, and we find that the turbulent Prandtl number ν/K lies in the range 0.2 - 0.4.

Using this expression for the wandering motion of the vortex, we can write an integral equation which relates the measured average velocity profiles to the instantaneous profiles. From this equation we calculate the effects of the wandering upon the following quantities: 1) the vortex core radius, defined as the distance from the peak in tangential velocity to the vortex center, 2) the maximum tangential velocity in the vortex, and 3) the maximum axial velocity defect in the core. These calculations were performed by P. Saffman and G. Baker, and are described in more detail in ref. 12. The predicted effects of wandering upon the three parameters of the vortex are shown in figure 2. In this figure,

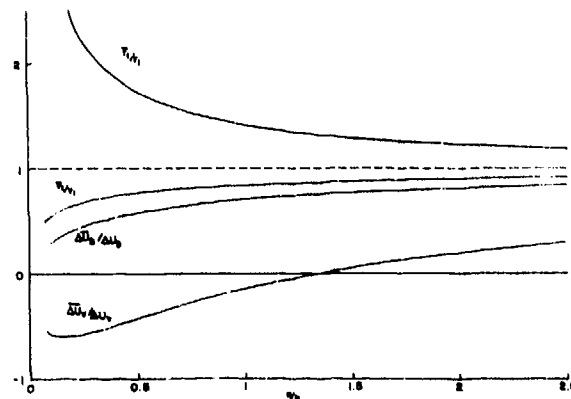


Fig. 2 Effect of Vortex Wandering on Core Radius, Maximum Tangential Velocity, and Axial Velocity on Mean Axis

F_1/r_1 is the relative change in core radius and ∇_1/v_1 is the relative change in the maximum tangential velocity. The other two curves on this figure represent the contributions to the axial velocity defect due to the pressure field induced by the vortex roll up ($\Delta U_v/\Delta U_v$), and the retardation in the boundary layer on the model ($\Delta U_b/\Delta U_b$). The abscissa of this figure, v/K , is the ratio of the kinematic viscosity to the turbulent eddy diffusivity for the wandering motion. Thus the wandering decreases as x increases on this plot.

Experimental Results

Typical velocity profiles for a rectangular planform model are shown on the left side of figure 3. The axial and tangential velocities are normalized by the free stream velocity, and profiles for two different values of x/c (where c is wing chord) are shown. The spanwise coordinate y is normalized by the wing span b . Note that as distance downstream is increased, the maximum tangential velocity and axial velocity defect both decrease. These data were obtained for an angle of attack of ten degrees and a free stream velocity of 100 cm/sec.

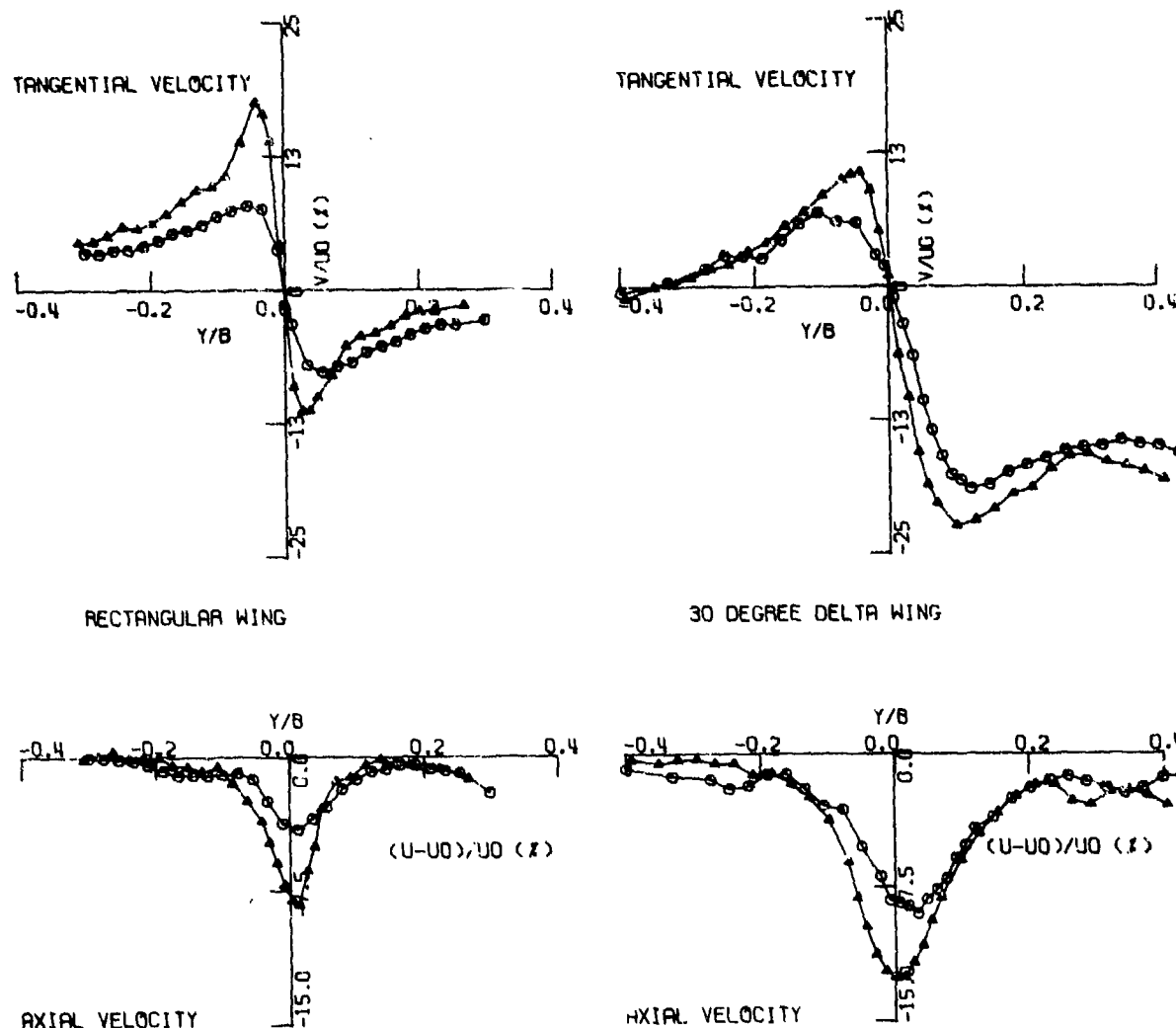


Fig. 3 Typical trailing vortex velocity profiles. Left side (rectangular wing) - Δ : $x/c = 10$, O : $x/c = 60$. Right side (30 degree delta) - Δ : $x/c = 7$, O : $x/c = 15$.

Velocity profiles for the thirty degree delta wing model are shown on the right side of figure 3. In this case also, the angle of attack is ten degrees and the free stream velocity is 100 cm/sec. Qualitative comparison of these two sets of velocity profiles shows some interesting similarities and differences. The tangential profiles for both models have a region near the center of the vortex in which the velocity is proportional to r , the distance from the center. This region of solid body rotation is generally referred to as the core of the vortex wake, and the core radius \bar{r}_c is defined as half the distance between the two tangential velocity maxima.

Note that for the rectangular model the tangential velocity profiles are roughly antisymmetric, with the velocity outside of the core varying approximately as $1/r$ on both sides. For all of the data shown here the second trailing vortex from the other side of the wing is to the right of the plotted profile, so that the data points to the right of the plot origin are from the region between the two vortices. In the case of the rectangular model this second trailing vortex appears to have little effect upon the one in the plot at these values of x/c . For the delta wing, however, the tangential profiles are not antisymmetric. A strong downwash velocity is observed in the region between the two vortices, indicating that the vortices interact with one another. This downwash velocity, observed in all of the delta wing data, is more than 15% of the free stream velocity in the case shown here.

The axial velocity profiles shown in the lower half of figure 3 have a velocity defect in the center of the core in all cases. This defect decreases with increasing distance downstream. In the analysis of Moore and Saffman (13), the axial defect is represented as the sum of two terms. The first term, u_v , is due to the pressure field induced by the roll up and decay of the trailing vortex. The second term, u_r , is the velocity defect caused by the retardation in the boundary layer of the wing. (The effects of vortex wandering upon these two terms are shown in figure 2.) For a rectangular high aspect ratio wing both terms are negative; that is, they both predict an axial defect such as the one observed in the data. For the delta wing, however, the u_v term is positive and predicts an axial velocity excess in the core. Apparently the boundary layer retardation term overcomes this, since a velocity defect has been observed in all of the delta wing data.

Three parameters which can be measured from the velocity profiles are the core radius, the maximum tangential vel-

ocity, and the maximum axial velocity defect. The laminar trailing vortex theory of Moore and Saffman (13) has been applied to the rectangular wing to predict these quantities. In figure 4 the theoretical predictions of the core radius can be compared with the present experimental results. Here the core radius \bar{r}_c is normalized by the chord Reynolds number R_c and the chord length c . The normalized core radius is plotted as a function of the downstream distance x . Two theoretical curves are shown: the core radius based on the instantaneous velocity profile (dashed line), and the core radius as modified by the vortex wandering effect (solid line). The open data points on this plot are for the two rectangular models. Model 1 has the square wingtips and model 2 has the rounded ones. The solid data points are for the two delta planforms. Model 3 is the sixty degree delta and model 4 is the thirty degree delta. The data points for the rectangular models lie reasonably close to their theoretical predictions. The core radii for the delta models are considerably larger, but this is not unexpected since the delta wing vortex begins to roll up at the leading edge of the wing.

Figure 5 is a plot of the maximum tangential velocity \bar{V}_t versus downstream distance. The quantities used to normalize \bar{V}_t are the chord Reynolds number R_c , the free stream velocity U_∞ , and the angle of attack in degrees α° . As in figure 4, the theoretical predictions for the rectangular wing are shown for both the instantaneous and vortex wandered profiles. The data points for the rectangular models again fall reasonably close to the theoretical line. The data from the two delta wings exhibit a lower value of maximum tangential velocity, which is consistent with the fact that the delta wing wakes have larger core radii.

The axial velocity measurements for the rectangular models have also been compared with the laminar theory, with roughly the same agreement (see reference 12). For the delta models at higher angles of attack (up to 20°) the axial velocity defect in the center of the core is as high as 30%.

The agreement of these experimental results with the laminar theory of Moore and Saffman is encouraging in view of the difficulty of making the measurements. The most serious experimental problem is that caused by the vortex wandering phenomenon, whose effects must be accounted for in some way. The present technique of measuring the wandering photographically and calculating its effect on the instantaneous velocity profiles is a good first approximation, but does not solve the problem. Probably the best solution is a reduction of the free

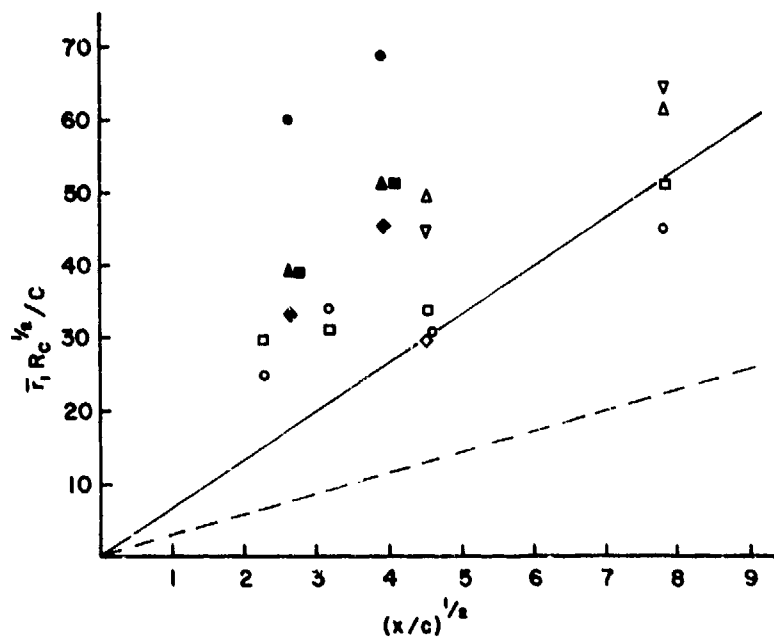


Fig. 4. Dimensionless core radius as function of downstream distance. Theoretical predictions: ---- instantaneous value, — vortex wandered value.

SYMBOL	○, △	▽	□, ◇	●	▲	■	◆
MODEL	1	1	2	3	3	4	4
ALPHA	10	5	10	10	15	10	15

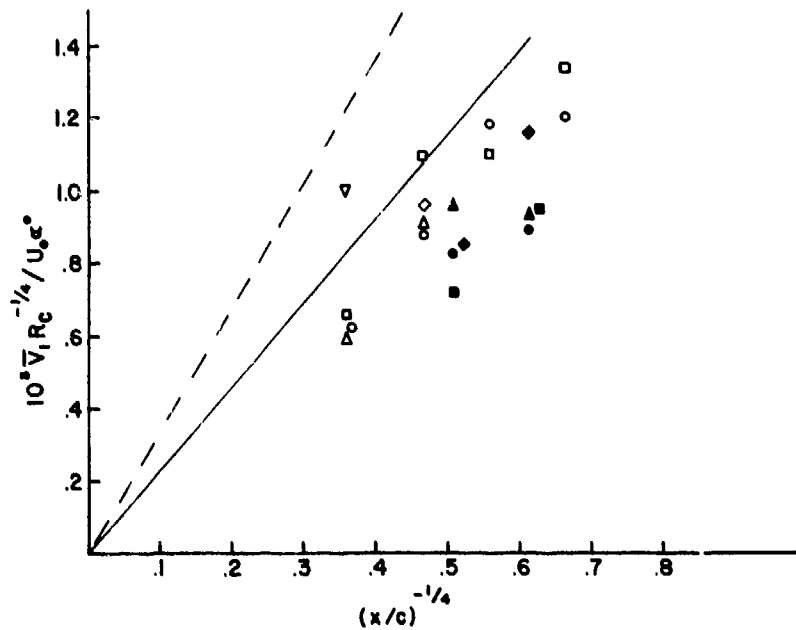


Fig. 5. Dimensionless maximum tangential velocity versus downstream distance. Symbols have same meaning as in Fig. 4.

stream turbulence in the tunnel to the point that the wandering can be ignored. This would also allow us to answer another question about the vortex cores: whether they are laminar or turbulent. The theory with which we have compared the present data is for laminar cores, and the vortex cores produced in the water tunnel do appear to be laminar when visualized with dye. The present LDV measurements cannot determine whether the core flow is laminar or turbulent, because the wandering produces an artificial turbulence in any region where there is a velocity gradient.

ACKNOWLEDGMENTS

I would like to thank Professor Philip Saffman and graduate student Kete Bofah for their assistance in analyzing the experimental data.

REFERENCES

1. Caiger, B., and Gould, D., "An Analysis of Flight Measurements in the Wake of a Jet Transport Aircraft," Aircraft Wake Turbulence and its Detection, Plenum Press, 1971, pp. 125-136.
2. Chevalier, H., "Flight Test Studies of the Formation and Dissipation of Trailing Vortices," Journal of Aircraft, 10, no. 1, January, 1973, p. 14.
3. Mason, H., and Marchman, J., "The Farfield Structure of Aircraft Wake Turbulence," AIAA paper no. 72-40, 1972.
4. Miller, E., and Brown, C., "An Experimental Study of Trailing Vortex Wakes Using a Large Towing Tank," HYDRO-NAUTICS Technical Report no. 7105-1, 1971.
5. Olsen, J. H., "Results of Trailing Vortex Studies in a Towing Tank," Aircraft Wake Turbulence and its Detection, Plenum Press, 1971, pp. 455-472.
6. Orloff, K., and Grant, G., "The Application of a Scanning Laser-Doppler Velocimeter to Trailing Vortex Definition and Alleviation," AIAA paper no. 73-680, 1973.
7. Knapp, R., and Levy, J., "The Hydrodynamics Laboratory of the California Institute of Technology," Transactions ASME, July 1948, p. 437.
8. Adrian, R., "Statistics of Laser-Doppler Velocimeter Signals: Frequency Measurement," Journal of Physics E: Scientific Instruments, vol. 5, 1972, pp. 91-95.
9. Goldstein, R., "Turbulent Flow Measurements Utilizing the Doppler Shift of Scattered Laser Radiation," Physics of Fluids, vol. 10, no. 6, 1967, p. 1349.
10. Wang, C. P., "A Unified Analysis on Laser Doppler Velocimeters," Journal of Physics E: Scientific Instruments, vol. 5, 1972, pp. 763-766.
11. George, W. K., "The Laser Doppler Velocimeter and its Application to the Measurement of Turbulence," Journal of Fluid Mechanics, vol. 60 part 2,

1973, pp. 321-362.

12. Baker, G. R., Barker, S. J., Bofah, K. K., and Saffman, P. G., "Laser Anemometer Measurements of Trailing Vortices in Water," Journal of Fluid Mechanics, Vol. 66, August 1974, p. 525.

13. Moore, D. W., and Saffman, P. G., "Axial Flow in Laminar Trailing Vortices," Proc. Roy. Soc. London A, vol. 333, 1973, pp. 491-508.

THE INFLUENCE OF FENCES ON SURFACE PIERCING STRUTS AND FOILS

R. C. McGregor
The University
Leeds, LS2 9JT
England

J. L. Foster
The University
Leeds, LS2 9JT
England

R. S. Rothblum
The University
Leeds, LS2 9JT
England

P. D. Swales
The University
Leeds, LS2 9JT
England

ABSTRACT

This paper describes the mechanisms by which ventilation of surface piercing struts occurs, and explains why fences on the strut inhibit ventilation. It was found experimentally that, providing the fence around the leading edge of a strut is above a minimum size, the type of surface rupture known as nose ventilation was prevented. At the other end of the scale, very wide fences enhanced the probability of tail ventilation. After consideration of force changes an optimum nose fence size is suggested.

It was found difficult to prevent tail ventilation but a fence inclined at 20° to the horizontal increased the useful incidence range by several degrees. The same configuration had a marked effect on washout angle, because of the sealing action of the water sheet which was shed from the downstream edge of the fence. Parameters controlling this sealing action are discussed. Lift and drag forces associated with specific fences are presented and a recommendation made.

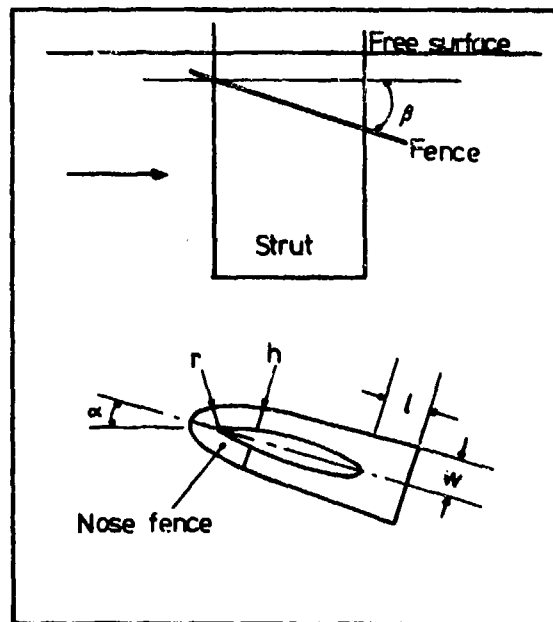
NOMENCLATURE

- A aspect ratio defined as ratio of submerged span, relative to undisturbed water surface, to chord.
- C_D drag coefficient, non-dimensionalised by the submerged area of the strut in undisturbed water and the dynamic head of the stream.
- C_L lift coefficient, non-dimensionalised by the submerged area of the strut in undisturbed water and the dynamic head of the stream.
- h width of 25% chord nose fence at fence's trailing edge.
- l overhang length of fence.
- m, n functions of fence's nose geometry and inclination.
- r nose radius of fence.
- w fence width at its own trailing

edge, or the strut's trailing edge whichever is further aft, on the low pressure side.

- α strut incidence angle.
- α_v ventilation inception angle for strut.
- α_w angle of washout from the tip of the strut.
- β fence inclination angle relative to the horizontal.

The following diagrams show the geometric features of the strut-fence configuration



INTRODUCTION

BACKGROUND

According to Janes(1) fences are small partitions, attached in the direction of flow, placed at short intervals down the upper and lower surfaces of a hydrofoil to prevent air ventilation passing down to destroy the lift. This

definition is rather over-simplified and some of its aspects will be questioned in the course of this paper.

Fences have been used by hydrofoil designers from the first craft and are employed almost universally on today's boats. Generally they have been considered a necessary evil, producing some deterioration in overall performance for the sake of avoiding the disastrous sudden loss of lift caused by ventilation. Apart from ventilation prevention, fences have been required to double as stiffeners for hollow struts for ducting water to a water jet propulsion system. In these cases comparatively large fences may prove acceptable.

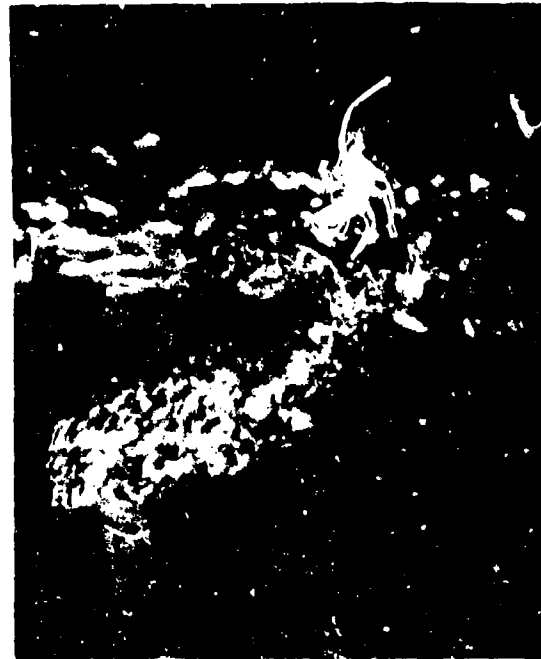
To date there have been no reported parametric studies of fences. The development of fence design has been largely on the basis of ad hoc modifications to eliminate a prototype problem. Such methods do not lead to an optimum design or satisfactory understanding of the mechanisms by which fences suppress ventilation.

MECHANISM OF VENTILATION

It is essential, in order to understand the role of fences, to have a clear grasp of the situation in the unfenced case. Recent work at Leeds(2,3,4,5) has led to a good understanding of the physics of ventilation on surface piercing struts under a wide variety of conditions. Three distinct modes of ventilation inception have been identified. They may be distinguished by the point at which the air, which subsequently implodes to become the ventilated cavity, first breaks into a low pressure, separated region on the strut. One of these modes, that of inception via the tip vortex, is not considered here because of the unsuitability of fences for its suppression. The other two modes relate to breaches of the unseparated layer of water nearest the air-water interface. This layer, known as the surface seal, isolates the atmospheric air from the separated regions of flow further below the water surface.

Nose Ventilation

In the first of the modes considered here, nose ventilation, the air breaches the surface seal near the leading edge (or nose) of the strut and spreads very rapidly until it engulfs the entire low pressure face. This mode of inception is preceded by a bubble of low pressure separated flow which sometimes exists behind the nose of a fairly sharp strut. A free stream disturbance, or a local flow deformation caused by the nose of the strut itself, opens up a path to the bubble that allows enough air through to blow off



(a) With this sharp nosed biogival foil at 9° incidence, the surface has been breached at the nose, and air is traveling down and across the foil. Flow is from left to right, at 5 fts $^{-1}$.



(b) Appearance of underside of free water surface showing growth of perturbations just before ventilation inception. Flow was from left to right at 10 fts $^{-1}$ and the foil was an NACA 16-021 at 20° incidence angle.

Fig. 1. Mechanisms of Ventilation

the remaining attached liquid flow (Fig. 1a).

Tail Ventilation

In the second mode considered, tail ventilation, the air leaks into a low pressure separated region in the neighbourhood the trailing edge (or tail) of the strut. The air entrainment is caused by the downwards acceleration of the surface seal which results from the large pressure gradient across it. This accelerating field stimulates the growth of surface perturbations to such an extent that by the time they reach the trailing edge they are grossly distorted globular waves (Fig. 1b). These perturbations eventually break in the trough behind the strut, introducing a small amount of air into the tail separated region where it lingers until it is either washed away down-stream or reinforced from subsequent perturbations. With increasing incidence angle, the separated region grows larger and the rate of air entrainment becomes greater, until a completely ventilated cavity is suddenly formed with unrestricted access to the atmosphere. The transition to fully ventilated flow takes rather longer than in the case of nose ventilation.

Influence of Strut Geometry

In general terms, nose ventilation is associated with struts of small nose radius. The pressure field about such struts has a sharp negative peak which encourages the formation of a small separated region at the nose. In contrast, tail ventilation will occur on any strut at a sufficiently high incidence to create extensive separation. It is seen in its purest form on struts with a moderately flat pressure profile and extensive separation which extends into, or from, the region of the tail.

Influence of Vapour Cavitation

As speed is increased, the introduction of vapour cavitation may alter the modes of ventilation somewhat. In the presence of a nose cavitation bubble, the surface seal may be breached after the manner of nose ventilation with the cavitation region replacing the separation bubble. If extensive face cavitation exists, it is possible for air to be drawn down by the instability mechanism of tail ventilation. In this case, air enters the cavity and causes ventilation at a lower incidence angle than in non-cavitating conditions. With increasing speed, the point at which the surface seal breaks down moves towards the nose until there is little to distinguish between the nose and tail modes of inception.

A mixed mode may occur when there is a small nose cavity with a large, well aerated, tail separation zone close behind it. The pulsing nose cavity may

be breached below the surface at about mid-span by air entrained in the tail separation region. The contact between the two regions and resulting introduction of air into the vapour cavity precipitates a full scale breach of the surface seal and a fully ventilated cavity springs from the nose at mid-span.

THE INFLUENCE OF FENCES

It is well known that the ventilation inception angle can be increased by the presence of fences. Almost invariably, ventilation occurs first on the portion of the strut above the fence, and a significant increase in incidence angle is required before the ventilated cavity jumps the fence to give complete ventilation. It has usually been assumed that the fence acts as a physical barrier to the passage of air. The mechanism of tail ventilation just described throws doubt on the validity of this explanation, as the air path to the separated regions is often downstream of the path blocked by fences. Some preliminary experiments were carried out to clarify the situation(7,8).

These experiments showed that horizontal fences, extending completely around the foil (envelope fences), did indeed prevent nose ventilation by denying air to the low pressure separated region or vaporous cavity below the fence. This was confirmed by the fact that a small hole in the fence in the vicinity of the nose separation bubble rendered the fence inoperative. Conversely, a half fence covering only the downstream 50% chord was completely ineffective in preventing ventilation. Eames(9) reached similar conclusions.

Even with a full envelope fence, the mechanism producing tail ventilation was still present. High speed photography and observation under stroboscopic lighting showed the characteristic perturbation growth in the accelerating water surface. Ventilation on struts with full envelope fences was invariably observed to be from the tail. As nose ventilation is more random than tail ventilation, and occurs at lower incidence angles, the present success of fences clearly depends on changing the mode from nose to tail ventilation. It was established that the presence of the fence could hasten tail ventilation, causing it to occur at incidence angles a degree or so smaller than in the unfenced case. When fences shorter than full chord were used, this tendency was reduced. Increased depth of submergence of the fence was found to have little effect on ventilation angle.

Attempts were made to inhibit tail ventilation by using a variety of fence shapes. Within practical limits the overhang, h , of the fence or its width or the trailing edge, w , had little effect but a significant improvement was obtained by inclining the fence to

the horizontal. Somewhat surprisingly, this produced a marked change in washout angle. Another approach preliminarily explored was to try to reinforce the surface seal by locally accelerating the fluid using streams of water externally fed through horizontal or vertical slots in the foil(14). This procedure proved complex and is still being studied.

OBJECTIVES

The preliminary experiments indicated some fruitful areas for further study, which formed the basis of the work reported here. The first aim of the present study was to determine the smallest fence which would successfully eliminate nose ventilation, and to assess the associated effects in terms of drag and lift force. The second purpose was to study effects of inclination angle and fence geometry on tail ventilation and washout angles, again evaluating lift and drag.

NOSE FENCES

EXPERIMENT

The preliminary experiments previously described(8) established that nose ventilation did not occur on unfenced struts which had a nose separation bubble length in excess of 25% of chord. A fence length of 25% chord was therefore fixed and the width was taken to be the dimension to be varied.

The strut used throughout the tests was a brass biogive with a blunt trailing edge and a 4" chord. Previous experience(2) had shown that this strut would exhibit nose ventilation at 15fts⁻¹. This was chosen as the test speed. The tests were carried out in both a high speed channel and a recirculating water channel(10,11) with the strut at a submergence aspect ratio of 1.9.

The fences were attached to the strut one half chord length below the undisturbed water surface. Any gaps between the fence and the strut were carefully sealed because even a small hole was found to render the fence ineffective.

In the high speed channel, a foil rotator was used to obtain a steady rate of turn of 2.6 sec/deg (0.385 deg/sec), making the tests conditions absolutely self consistent(12). In the recirculating water channel a dynamometer was used to measure lift (side force) and drag and the angle was changed at a similar rate to that in the other channel.

A set of ten 25% chord fences of different widths ranging from 1" (25% of chord) down to 0.015" (0.4% of chord) were fixed to the strut in turn. For each, the ventilation and washout angles were recorded for six angle traverses in both channels. In the recirculating

channel the forces were also recorded at two degree intervals for increasing and decreasing incidence angles.

RESULTS

Differences in the flow conditions in different facilities have been shown to influence the ventilation phenomenon. For these two channels, differences in the condition of the water surface, turbulence level upstream water aeration and speed fluctuations all occurred. It is therefore desirable to consider the results from the two facilities separately.

High Speed Channel

The values of ventilation and washout angles for each fence width are presented in tabular form (Table 1) with the ventilation angle being plotted against fence width on a logarithmic scale in Fig. 2.

Table 1. Nose fences at 15 fts⁻¹ (H.S. channel; each result mean of six)

Fence width h"	Ventilation angle α_v		Washout angle α_w°	
	To Fence	Complete	To Fence	Complete
No. Fence		4.6		3.4
0.015	4.3	5.5	3.5	2.5
0.026	4.0	6.0	3.3	2.5
0.030	4.1	10.0	3.6	2.6
0.070	4.5	12.1	3.4	2.7
0.12	4.3	14.4	3.5	2.6
0.20	4.3	14.5	3.6	3.0
0.30	3.9	14.5	3.5	2.5
0.40	4.4	11.1	3.5	2.8
0.50	4.0	10.4	2.9	2.5
1.00	4.0	10.7	3.1	2.8

As the fence width was reduced the angle for ventilation to the fence remained constant, but the angle at which complete ventilation occurred showed a maximum when the fence width was 0.2", corresponding to one half of maximum strut thickness, or 5% of chord. For this width, the ventilation inception angle was three times the unfenced value and 50% greater than the angle for the widest fence.

Stroboscopic illumination showed that first nose ventilation occurred down to the fence. Aft of the fence, perturbations at the new interface grew until they precipitated tail ventilation.

Recirculating Channel

For the same fence width the ventilation angles were a maximum in both channels. However, the ventilation angle, for the unfenced strut, was so much higher in the recirculating channel that the fence's influence was less dramatic. These results are shown in Fig. 2.

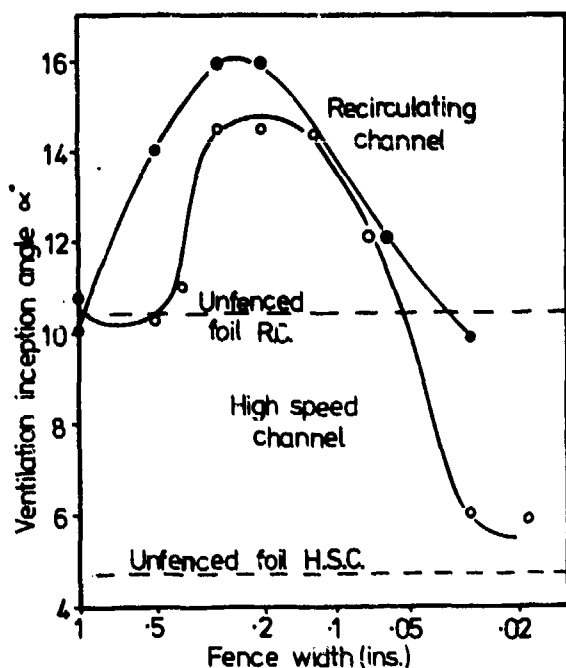


Fig. 2. Nose fences: ventilation angles with varying fence width.

Figs. 3, 4 and 5 show drag, lift and lift/drag ratio plotted non-dimensionally against fence width. The drag was a minimum at a fence size of about 0.6" where the fence seemed to create no drag penalty at all. There was a maximum at a width of 0.25" where the fence increased the drag by about 40% relative to the unfenced case. As the width decreased further, the drag approached the unfenced value.

The lift changed more dramatically with width. The widest fence corresponded to the highest lift force. With decreasing width, the lift dropped to a minimum at 0.5" and then rose to a sharp peak at 0.4" where only a small percentage of the unfenced lift was lost. After another minimum at 0.2" the lift rose to the unfenced value, provided that the angle was sufficiently small that ventilation had not already occurred down to the fence. This partial ventilation explains the change of shape and non-asymptotic behaviour for the higher angles.

The lift/drag ratio was high for widths greater than 0.4", then fell with decreasing width to a low between 0.3" and 0.18" before returning to its best value at 0.1". The agreement of the small fences with the unfenced case was not very good.

DISCUSSION

It was reassuring to observe that the high speed and the recirculating channels gave the same general shape for

the ventilation angle curve in Fig. 2., in spite of the appreciable differences between the two facilities and the necessary changes in the experimental method. These differences, (e.g. condition of water surface, turbulence level and speed fluctuations) adequately explain the discrepancies in absolute values.

If it is assumed that nose ventilation cannot occur around a fence whose width is greater than the thickness of the associated separation bubble, then from the high speed channel data shown in Fig. 1. it is possible to deduce that the thickness of the nose separated region is about 0.03"; rather less than 1% of chord.

The existence of maxima in Fig. 2 was somewhat surprising but an explanation was suggested from the observations with stroboscopic illumination. Above a certain width, all the fences prevented nose ventilation below the fence. The wider the fence, however, the greater the vorticity which was shed into the flow near the new interface. This vorticity enhanced the curvature normal to the chord and consequently assisted ventilation.

The plots of force versus fence width show undulations which can not yet be explained. The consistency of these curves for different incidence angles indicates that they describe real phenomena. Even so, it would be unwise to assume that the same relationships will hold at higher Reynold's numbers, since the extent of the separated region may well change.

Choosing the optimum nose fence width must be a compromise arrived at by weighing the relative importance of ventilation angle, drag, lift and lift/drag ratio in specific cases. The best values of the ventilation angles are for widths in the range 0.2" to 0.25" which correspond to the poorest values of the lift/drag ratio. The comparative figures are shown in Table 2.

INCLINED FENCES

EXPERIMENT

From the preliminary experimental work(8) it was clear that tail ventilation could be influenced by fences inclined to the horizontal and also that washout angles could be increased quite markedly. In an attempt to determine the mode of action of an inclined fence, half envelope fences (Fig. 6a), which were later modified to include a nose fence (Fig. 6b), were tested on both the high pressure and the low pressure faces. The results obtained from the initial experiments, suggested an optimum inclination, $\beta=30^\circ$, but this angle is too large to be practicable on low aspect ratio struts and therefore a compromise angle of 20° was taken for the design of

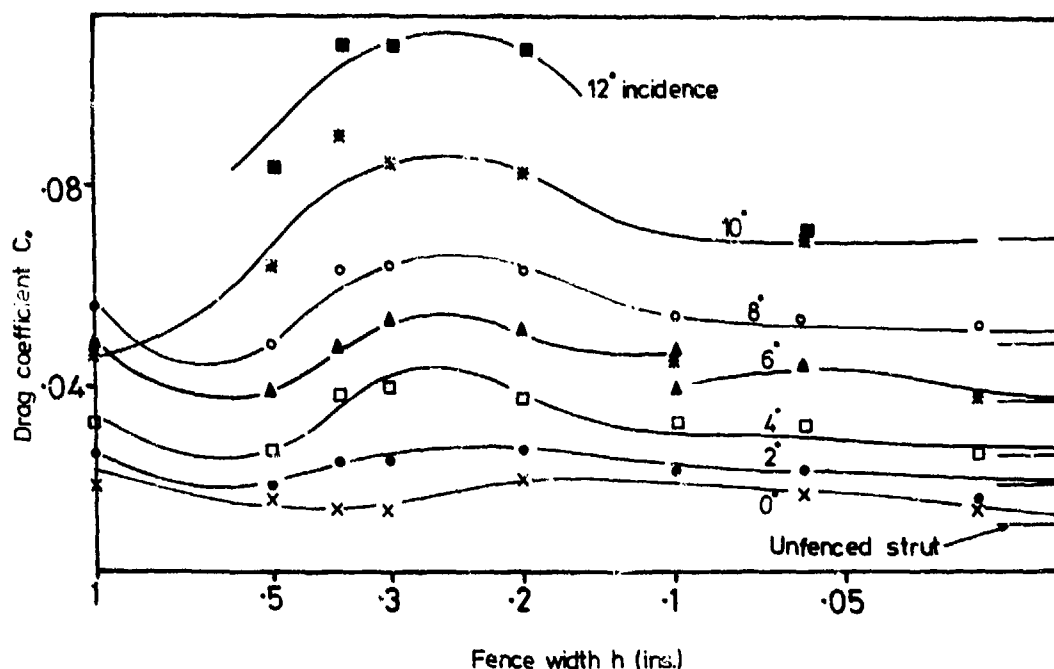


Fig. 3. Nose fences: drag coefficients

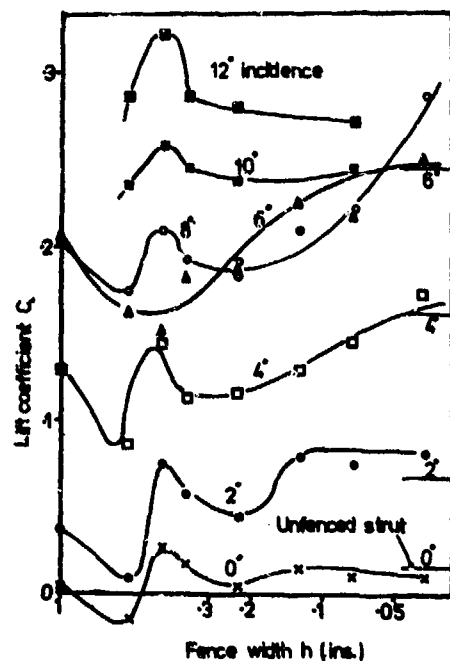


Fig. 4. Nose fences: lift coefficients

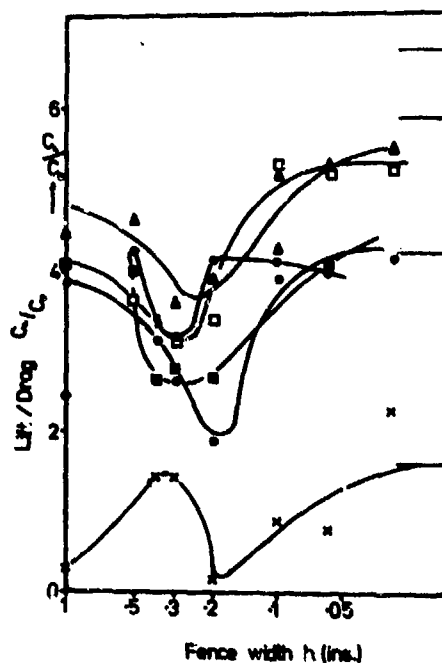


Fig. 5. Nose fences: lift/drag ratios

further fences. These experiments, and the lack of influence on washout of nose fences (shown in Table 1), indicated that tail geometry had the most effect on washout angle. To test this, a series of fences of differing trailing edge

widths and a one half chord overhang were designed (Figs. 6c, d and e) and tested at an inclination of 20° in the recirculating channel. The speed was 15 ft sec^{-1} in all cases. Ventilation and washout angles were found from the mean

Table 2: Comparison of four nose fences with unfenced case (forces from RWC)

Fence Width h (inches)	α_v° in RWC	α_v° in HSC	Force Coefficients at $\alpha=4^\circ$			Force Coefficients at $\alpha=8^\circ$		
			C_D	C_L	C_L/C_D	C_D	C_L	C_L/C_D
Unfenced	10.5	4.5	0.023	0.162	7.04	0.046	0.331	7.20
0.5	14.0	10.5	0.024	0.086	7.75	0.045	0.180	4.00
0.4	15.5	11.5	0.031	0.146	4.71	0.055	0.205	3.73
0.25	16.2	14.9	0.040	0.111	2.78	0.067	0.194	2.90
0.1	14.2	14.0	0.030	0.147	4.90	0.053	0.212	4.00

RWC Recirculating Water Channel
HSC High Speed Channel

of four traverses of incidence angle. The overhang, z , was cut down by $\frac{1}{4}$ " steps and the runs repeated until the fences were flush with strut's trailing edge. One of the fences was cut down in three further stages as shown in Fig. 6c to provide additional values of w . A $\frac{1}{4}$ " envelope fence (Fig. 6f) was also tested to determine the influence of changing the dimensions of the fence in the vicinity of the nose.

On completion of the angle surveys, four fences were selected on the grounds of interesting ventilation or washout characteristics. For these fences the force coefficients were recorded for comparison with the plain strut.

RESULTS

Inclination Angle

The effect of the inclination angle, δ , on ventilation and washout angles for the fences 6a and 6b on both sides is shown in Fig. 7. These show the high pressure face fence to be much less efficient than the low pressure fence with respect to both ventilation and washout. The incidence angle for tail ventilation inception can be increased by 4 to 5 degrees by inclining a full chord fence.

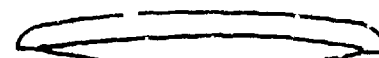
The maximum washout angle observed corresponded to the largest inclination angle tested, 30° .

Variable Tail Geometry

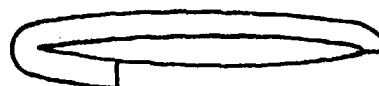
The results (Fig. 8 and Table 3) showed that ventilation and washout angles were insensitive to the overhang, z , except in the case of the widest fence (Fig. 6e) where the width, w , also changed significantly. The influence of width on ventilation angle was rather complicated but it was clear that values above $\frac{1}{4}$ " were not desirable as may be seen in Table 3. When considering washout, however, all the data for a given nose geometry are seen to collapse onto a straight line which may be expressed by

$$\alpha_w = mw + n.$$

The results from the $\frac{1}{4}$ " fence (Fig. 6f) suggest that in this case a different



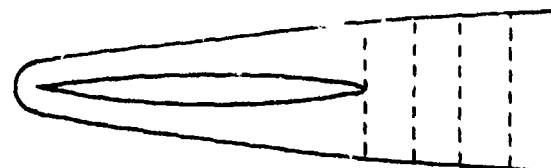
a. Asymmetric fence



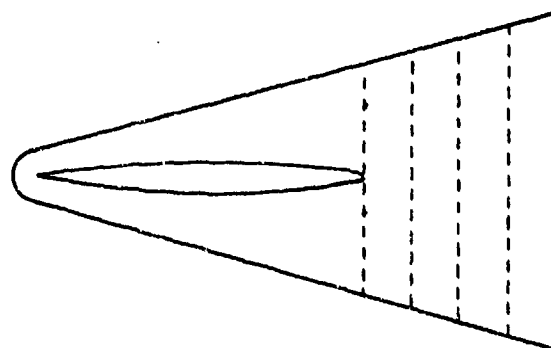
b. Modified asymmetric fence



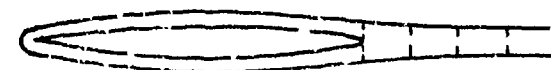
c. Envelope, $r=0.5$ ", $w=0.5$ "



d. Envelope, $r=0.5$ ", $w=1.0$ "



e. Envelope, $r=0.5$ ", $w=2.0$ "



f. Envelope, $r=0.25$ ", $w=0.125$ "

Fig. 6. Experimental tail fences

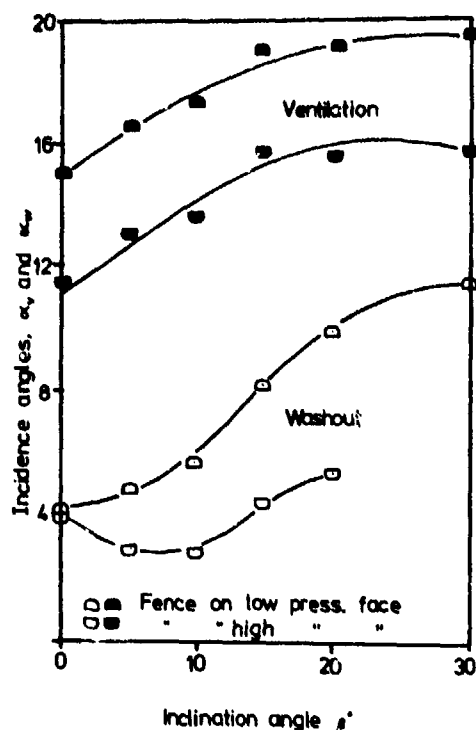


Fig. 7. Effect of inclination angle on ventilation and washout (fence type as shown in Fig. 6b).

relationship would be required corresponding to the different nose geometry. This, and the change in washout angle with incidence imply that in general m and n are functions of the nose geometry and the inclination angle. The preliminary experiments (8) on an asymmetrical delta fence showed the importance of the width of the fence on the low pressure face.

The force coefficients are shown in Figs. 9 and 10. In the absence of full ventilation the lift coefficient (Fig. 9) was not very much altered by the existence of the fence, the maximum penalty being of the order of 10%. It may be noted that the fence of 2" width (Fig. 6d) always had a higher lift coefficient than the unfenced strut since it washed out at an angle higher than the bare strut ventilated. The 4" wide fence (Fig. 6e) also showed high lift characteristics with the smaller fences causing a small loss. The drag curves (Fig. 10) suggested that form drag was the major contributor to the fence drag penalty. The small fences increased the strut drag by about 30% at small incidence with the change reducing to almost nothing at higher angles. The larger fences doubled or trebled the form drag and were responsible for a drag coefficient penalty of

0.03 or 0.04 over the whole angle range (assuming that the unfenced results may be extrapolated).

Table 3: Ventilation and Washout Characteristics of Fences (all angles are the average of four readings in recirculating water channel).

Fence profile (see F Fig 6)	w (ins)	l (ins)	α_v°	α_w°
a	0.5	0.5	18.5	8.5
b	0.5	0.5	18.7	9.5
c	0.5	1.5	18.2	9.9
	0.5	1.0	17.9	9.8
	0.5	0.5	17.9	9.8
	0.5	0	17.6	9.2
c1	0	0	18.0	7.9
c2	0	0	18.4	7.3
c3	0.3	0	18.8	8.5
d	1.0	2.0	19.7	10.0
	0.95	1.0	19.6	9.9
	0.92	1.0	19.6	9.9
	0.92	0.5	18.9	10.4
	0.9	0.125	18.0	10.0
	0.9	0	17.8	10.3
e	2.0	2.5	17.4	11.3
	1.8	1.5	17.3	13.1
	1.7	1.0	17.1	12.4
	1.6	0.5	17.3	12.0
	1.5	0	17.4	11.0
skew delta	2.5	2.0	19.9	14.7
f	0.15	2.0	17.2	6.4
	0.2	1.5	17.1	6.1
	0.25	1.0	16.8	6.0
	0.3	0.5	16.3	5.9
	0.35	0.125	16.5	6.0

DISCUSSION

Inception and Washout Angles

Normally, the aim of ventilation fences is to increase the incidence angle of inception. However, no matter how much care is taken to prevent ventilation, an unfortunate transient situation may result in its occurrence. It may thus be considered desirable to maximise the washout angle so that with the passing of the transient the strut will return to its normal wetted flow condition with the minimum of delay.

Inclining the fences increases the ventilation inception angle by a few degrees and changes the washout angle by a surprisingly large amount. The maximum washout angle observed, 15° for a 2½" wide fence, compared with 4° for the unfenced strut. This improvement carries little penalty in terms of lift (side force) but adversely affects the drag. For a given nose geometry and inclination, the washout angle is a linear function of fence width. Too much reliance should not be placed in the force measurements for the reasons given earlier. Larger scale experiments

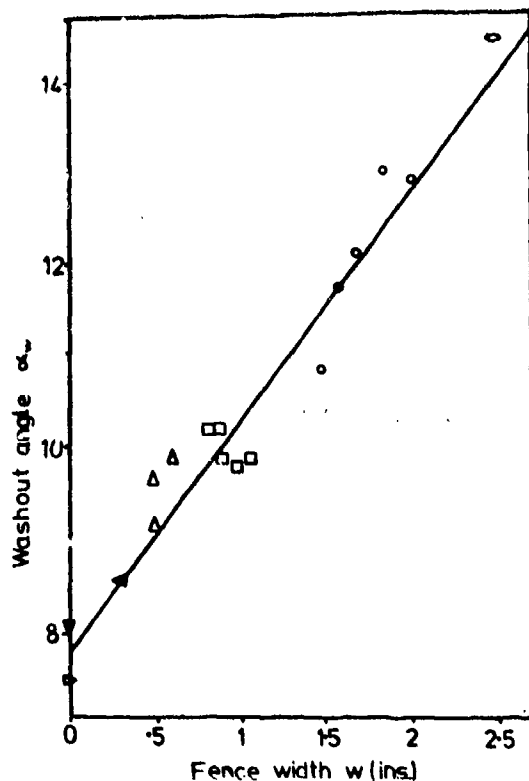


Fig. 8. Influence of fence width, w , on washout angles.

would be required to determine the drag penalty on a hydrofoil craft.

Delayed Ventilation Inception

The suggested mechanism by which the inclined fence improves the ventilation inception point is as follows. Initially an atypical ventilation occurs down to the fence. Even at very low or zero incidences the fence is ventilated in a manner analogous to the ventilation of a fully submerged foil in the proximity of the surface. That is, the upper surface is fully aerated but the air path is not directly down the strut, which in this case may be wetted, but from a point above the strut's wake. This leaves a relatively stable air-water interface streaming from the under face of the fence. This interface is less vulnerable to Taylor instability than the upstream water surface because it does not experience the finite amplitude disturbances inherent in the flow and because the fence itself eliminates the vertical accelerations caused by the strut pressure field. Thus tail ventilation is delayed. Also, the surface cannot be breached at the nose because of the physical presence of the fence.

When ventilation does occur, the mechanism is different from the unfenced case. The subambient strut pressures

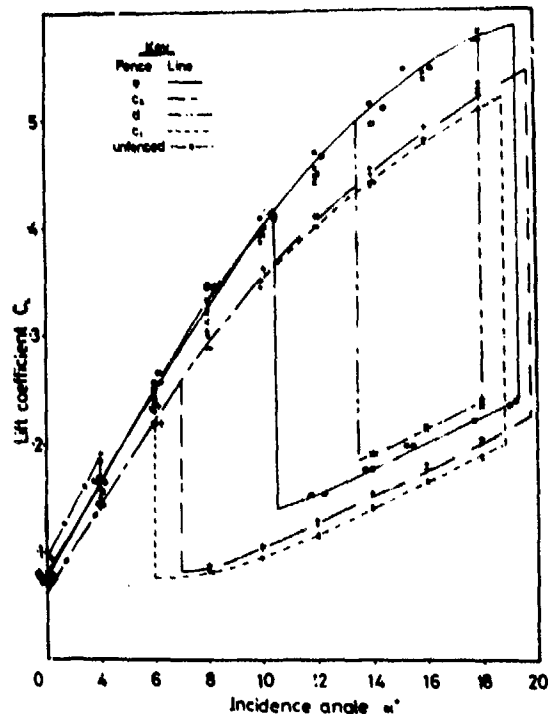


Fig. 9. Inclined fences: lift coefficients

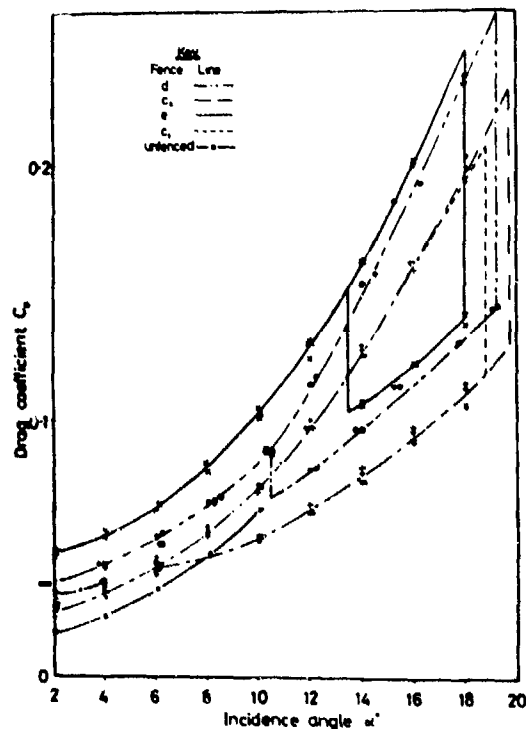


Fig. 10. Inclined fences: drag coefficients.

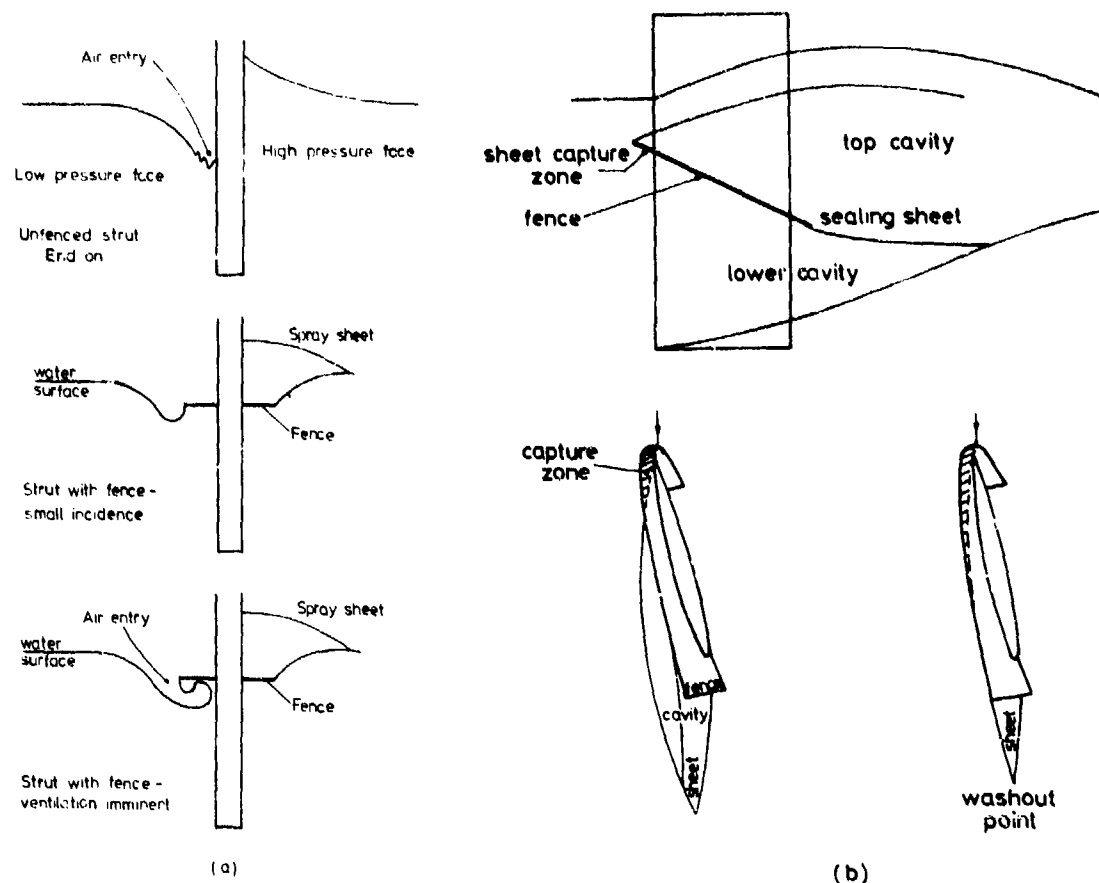


Fig. 11. Mechanism of (a) ventilation, (b) washout with an inclined fence.

which exist beneath the fence distort the surface beyond the boundaries of the fence. Under the influence of these pressures the surface wraps over the side of the fence and when the distortion is sufficient, as shown in Fig. 11a, air penetrates below the fence.

Enhanced Washout

The change in washout angle appears to be the result of the sealing action of a water sheet which is shed from the underside of the downstream edge of the fence. Because of the confused flow pattern and its three dimensional nature, the sheet is extremely difficult to photograph, but an examination under stroboscopic light has shown it to be continuous and glasslike for some distance downstream. A schematic drawing of the sheet is shown in Fig. 11b. Since there are no large pressure gradients tending to rupture the sheet, which leaves the fence well aft of the strut's low pressure zone, its action is simply to restrict the passage of air to the lower cavity. In the ventilated

state the major part of the underside of the fence is within the cavity and consequently is not wetted directly by the mainstream flow. Only the nose section of the fence has contact with the mainstream and it is the flow impinging on this part which forms the sealing sheet. Thus fences with smaller nose sections, like the $\frac{1}{2}$ " fence (Fig. 6f), capture less water so producing less effective sealing sheets. Since the amount of water captured is proportional to $\cos \theta$ it is possible to see why a monotonic increase of washout angle with incidence occurs (Fig. 7). The width of the trailing edge is critical in determining the lateral extent of the sheet. The effectiveness of the physical barrier and the restriction of the air supply by the water sheet are both reduced with decreasing fence width.

CONCLUSIONS

OPTIMUM FENCE CONFIGURATIONS

It was found for the conditions

studied that all nose fences wider than 1% of chord prevent nose ventilation. Of the 25% chord fences tested the one whose width was approximately 6% of chord was most effective at suppressing ventilation. This fence carried the biggest drag penalty, though this would be small compared with the total craft drag. If, however, drag is a severe constraint, these tests indicate that fence widths of 10% or 2½% of chord provide nearly the same protection against nose ventilation but with a smaller drag penalty.

Tail ventilation is much harder to influence. Inclined fences up to 30° were tried with appreciable success. Although this inclination produced the greatest delay it is impracticable on struts of submergence aspect ratio of less than unity, and an inclination of 20° may be more acceptable. Fairly large drag penalties were measured for the larger inclined fences, but one fence (Fig. 6c-2) produced good results with respect to both ventilation and force criteria and may be recommended.

Washout occurred at large incidence angles with inclined fences. Greater width at the fence trailing edge also increased washout angle, provided the underside of the fence had sufficient wetted area at the nose in the post ventilated flow state.

Explanations of the mechanisms by which the various types of fences act have been suggested in each case.

SCALING CONSIDERATIONS

In view of the uncertainty about the mode of ventilation on prototype craft it is essential to retain a clear idea of the context and limitations of this programme. With all tests carried out at the same Reynold's number, the same Froude number and the same cavitation number, there can be no justification for attempting to scale the values to a full-sized craft. Nevertheless physical parallels with larger scale struts and higher speeds may be anticipated. It has been shown(6) that high speed ventilation is increasingly associated with the tail mechanism but the position of surface rupture moves upstream with increasing speed. Thus a nose fence such as that considered in the first part of the work might be more efficient at higher speeds.

FUTURE WORK

It can not be claimed that the work presented in this paper represents the last word on fences. Within the limitations of mechanical fences there is scope for improvement of washout angles now the mechanism is understood, and the problems of higher speeds with associated cavitation are still unexplored. Some of these situations may be better

tackled by boundary layer control and liquid fences. It has been shown(14) that blowing water from suitably positioned vertical slots can appreciably retard tail ventilation on a NACA section and nose suction in the region below the surface can also prevent nose ventilation. The role of a sealing sheet of liquid in the observed washout mechanism indicates that blowing liquid from horizontal slots may be useful. It is possible that the use of liquid blowing may suppress cavitation as well as separation. Such techniques successfully applied could enhance lift and extend the possible speed range of craft using sub-cavitating foils and struts.

ACKNOWLEDGEMENT

The authors are indebted to the Defence Research Establishment Atlantic, Halifax, Nova Scotia, Canada for funding this research programme and also to the United States' Government for funding Mr. R.S. Rothblum as a research fellow at Leeds.

REFERENCES

1. McLeavy, R., ed., Jane's Surface Skimmers Hovercraft and Hydrofoils, 7th ed., St. Giles House, London, 1974.
2. Swales, P.D., McGregor, R.C., Rothblum, R.S., and Wright, A.J., "The Mechanism of Ventilation Inception on Surface Piercing Foils", to be published in Journal of Mechanical Science, Institution of Mechanical Engineers, March 1974.
3. Wright, A.J., Swales, P.D., and McGregor, R.C., "Inception of Ventilation on Surface Piercing Structures", Nature, Vol. 240, Dec. 1972, No. 5382, pp.465-6.
4. Swales, P.D., Wright, A.J., McGregor, R.C., and Cole, B.N., "Separation and Ventilation Interaction Studies", Hovering Craft and Hydrofoils, Vol. 13, No. 1, Oct. 1973, pp 11-15.
5. McGregor, R.C., Wright, A.J., Swales, P.D., and Crapper, G.D., "An Examination of the Influence of Waves and Ventilation Inception", Journal of Fluid Mechanics, Vol. 61, No. 1, Oct. 1973, pp. 85-97.
6. Rothblum, R.S., McGregor, R.C., and Swales, P.D., "A Photographic Study of Speed and Roughness Effects on Ventilation", Proceedings of International Hovering Craft, Hydrofoil and Advanced Transit Systems Conference, May 1974, Brighton, England.
7. McGregor, R.C., and Wright, A.J., "Exploratory Investigation into The Role of Fences", Appendix D, TP/DREA/7, March 1973, Dept. of Mech. Eng., Univ. of Leeds.
8. Vick, S.M., and Foster, J.L., "The Effect of Fences on Surface Piercing Hydrofoil Strut Ventilation", Research Report, June 1973, Dept. of

studied that all nose fences wider than 1% of chord prevent nose ventilation. Of the 25% chord fences tested the one whose width was approximately 6% of chord was most effective at suppressing ventilation. This fence carried the biggest drag penalty, though this would be small compared with the total craft drag. If, however, drag is a severe constraint, these tests indicate that fence widths of 10% or 2½% of chord provide nearly the same protection against nose ventilation but with a smaller drag penalty.

Tail ventilation is much harder to influence. Inclined fences up to 30° were tried with appreciable success. Although this inclination produced the greatest delay it is impracticable on struts of submergence aspect ratio of less than unity, and an inclination of 20° may be more acceptable. Fairly large drag penalties were measured for the larger inclined fences, but one fence (Fig. 6c-2) produced good results with respect to both ventilation and force criteria and may be recommended.

Washout occurred at large incidence angles with inclined fences. Greater width at the fence trailing edge also increased washout angle, provided the underside of the fence had sufficient wetted area at the nose in the post ventilated flow state.

Explanations of the mechanisms by which the various types of fences act have been suggested in each case.

SCALING CONSIDERATIONS

In view of the uncertainty about the mode of ventilation on prototype craft it is essential to retain a clear idea of the context and limitations of this programme. With all tests carried out at the same Reynold's number, the same Froude number and the same cavitation number, there can be no justification for attempting to scale the values to a full-sized craft. Nevertheless physical parallels with larger scale struts and higher speeds may be anticipated. It has been shown(6) that high speed ventilation is increasingly associated with the tail mechanism but the position of surface rupture moves upstream with increasing speed. Thus a nose fence such as that considered in the first part of the work might be more efficient at higher speeds.

FUTURE WORK

It can not be claimed that the work presented in this paper represents the last word on fences. Within the limitations of mechanical fences there is scope for improvement of washout angles now the mechanism is understood, and the problems of higher speeds with associated cavitation are still unexplored. Some of these situations may be better

tackled by boundary layer control and liquid fences. It has been shown(14) that blowing water from suitably positioned vertical slots can appreciably retard tail ventilation on a NACA section and nose suction in the region below the surface can also prevent nose ventilation. The role of a sealing sheet of liquid in the observed washout mechanism indicates that blowing liquid from horizontal slots may be useful. It is possible that the use of liquid blowing may suppress cavitation as well as separation. Such techniques successfully applied could enhance lift and extend the possible speed range of craft using sub-cavitating foils and struts.

ACKNOWLEDGEMENT

The authors are indebted to the Defence Research Establishment Atlantic, Halifax, Nova Scotia, Canada for funding this research programme and also to the United States' Government for funding Mr. R.S. Rothblum as a research fellow at Leeds.

REFERENCES

1. McLeavy, R., ed., Jane's Surface Skimmers Hovercraft and Hydrofoils, 7th ed., St. Giles House, London, 1974.
2. Swales, P.D., McGregor, R.C., Rothblum, R.S., and Wright, A.J., "The Mechanism of Ventilation Inception on Surface Piercing Foils", to be published in Journal of Mechanical Science, Institution of Mechanical Engineers, March 1974.
3. Wright, A.J., Swales, P.D., and McGregor, R.C., "Inception of Ventilation on Surface Piercing Structures", Nature, Vol. 240, Dec. 1972, No. 5382, pp. 465-6.
4. Swales, P.D., Wright, A.J., McGregor, R.C., and Cole, B.N., "Separation and Ventilation Interaction Studies", Hovering Craft and Hydrofoils, Vol. 13, No. 1, Oct. 1973, pp. 11-15.
5. McGregor, R.C., Wright, A.J., Swales, P.D., and Crapper, G.D., "An Examination of the Influence of Waves and Ventilation Inception", Journal of Fluid Mechanics, Vol. 61, No. 1, Oct. 1973, pp. 85-97.
6. Rothblum, R.S., McGregor, R.C., and Swales, P.D., "A Photographic Study of Speed and Roughness Effects on Ventilation", Proceedings of International Hovering Craft, Hydrofoil and Advanced Transit Systems Conference, May 1974, Brighton, England.
7. McGregor, R.C., and Wright, A.J., "Exploratory Investigation into The Role of Fences", Appendix D, TP/DREA/7, March 1973, Dept. of Mech. Eng., Univ. of Leeds.
8. Vick, S.M., and Foster, J.L., "The Effect of Fences on Surface Piercing Hydrofoil Strut Ventilation", Research Report, June 1973, Dept. of

Mech. Eng., Univ. of Leeds.

9. Eames, M.C., Contribution to Discussion, Proceedings of the 2nd Naval Hydrodynamics Symposium, Office of Naval Research, 1958, pp 444-5.

10. Hunter, B., Swales P.D., and Cole, B.W., "A High Speed Short Duration Water Channel", Journal of Physics E: Scientific Instruments. Vol. 6, 1973, pp 145-146.

11. Hunter, B., Swales, R.D., and Cole, B.W., "Variable Pressure Recirculating Water Channel", The Engineer, Vol. 225, March 1968, pp 515-9.

12. Wright, A.J., McGregor, R.C., and Swales, P.D., "Ventilation Inception on Surface Piercing Foils", Hovering Craft and Hydrofoils, Vol. 12, No. 9, April 1973, pp. 9-12.

13. Swales, P.D., Wright, A.J., and Jones, E.A., "Two force measurement balance using hydrostatic principles", to be published in Bulletin of Mechanical Engineering Education, 1974.

14. Rothblum, R.S., "Liquid Ventilation Fence-Suppression by Boundary Layer Control", Section F, TP/DREA/11, March 1974, Dept. of Mech. Eng., Univ. of Leeds.

DISCUSSION

E. A. JONES AND R. T. SCHMITKE

As the authors acknowledge, the Defence Research Establishment Atlantic has funded the Leeds ventilation research programme from its initial stages. Our comments therefore relate to how we view this work in the context of full scale design.

The original objectives of the project were to first develop a thorough understanding of the physical mechanisms of ventilation and then to identify the best methods of avoiding or delaying it. The strength of the studies has lain chiefly in the very fine photographic techniques developed by the team, culminating in this paper's clear exposition of ventilation mechanisms. The chief limitation has been the small scale at which experiments were performed, and the authors quite correctly warn against directly applying their results to full scale design.

Of particular importance is the explanation of how fences prevent the nose type of ventilation. In support of the Leeds results, we note that partial chord fences have worked well on hydrofoil research craft at DREA. They were not used on the 200 ton Canadian hydrofoil ship BRAS D'OR simply because of the intuitive feeling that since partial chord fences worked well, full chord fences would work better. The Leeds work shows that this is not necessarily so and gives firm grounds for using partial chord fences in future full scale designs.

Drag of fences is by no means insignificant and the optimum size is therefore of considerable practical interest. The fact that fence width for maximum ventilation delay coincides with fence width for maximum drag is certainly worth studying further. Also worthy of further investigation is optimum fence shape, bearing in mind the mechanical difficulties in attaching fences to the main foil structure.

The practical usefulness of the work on fences to control tail ventilation is not clear, particularly when one considers the wide range of submergence depths and incidence angles that occur during operation in a seaway. Nevertheless the experiments have shown that an inclined fence significantly improves washout angles and is therefore the first device to overcome the primary limitation of conventional fences, the fact that they do little to suppress ventilation once started.

A. BARR

Having proposed a method, based on airfoil separation data, for predicting ventilation inception on submerged and surface piercing foils and struts, I have found the work at Leeds in this area most interesting. The present paper is particularly useful in its systematic treatment of the problem.

I would like, however, to raise a question about the applicability of the author's conclusions to thin (say, 12 percent or less thickness — chord ratio) airfoil type sections operating at full scale Reynolds numbers. NACA and RAE data for such cases indicate that at Reynolds numbers above about 10^7 , the initial separation bubble does not grow steadily in chordwise extent, but "explodes"

suddenly to a length comparable to the chord length. It seems highly probable that in such cases ventilation inception can occur with the long bubble and that a 25 percent of chord length fence will be ineffective. Studies such as those of this paper are needed for airfoil sections of typical section thickness chord ratios (say six to 15 percent) at Reynolds numbers above 10^7 .

B. MORGAN AND E. P. KOOD

This paper presents an extensive parametric experimental investigation on the use of fences on streamlined surface-piercing struts. The discussion of the types of ventilation and the mechanism of ventilation is especially important for the understanding of this phenomenon. My remarks will generally be restricted to discussion of scaling the data presented to full scale.

The data presented in Figure 2 show a significant difference in the ventilation inception angle between the recirculating channel and the high speed channel. In general, the data obtained in the two facilities are quite different. The paper states that the differences between the two facilities and experimental methods adequately explain the discrepancies. However, I do not find this explanation satisfactory because it gives no indication of which results would be most applicable to full scale nor the physical differences causing the discrepancies. For instance, how should model experiments, or can they, be performed in either of these two facilities to predict what will happen full scale?

The paper gives considerable data on the effect of nose fence size on ventilation. According to the paper, this type of ventilation is related to separated flow near the nose. Since the length and thickness of this separated region is highly Reynolds number dependent, how should the data be scaled? The paper indicates that the fence width relative to the thickness of the separation bubble might be an important parameter? If it is, full scale fences should be relatively different in size than the model fences. This could be important since the fence width should be as small as possible. Would the authors comment on the relative size of full-scale and model nose fences?

The relative importance of nose and tail ventilation for full scale craft is not clear to me. Would the authors please comment on the relative importance of the two types of ventilation for full scale craft?

The authors' description of the model states that the strut trailing edge was blunt. Was the base in fact vented? If so, it would explain why the side ventilation angles are lower than those reported by the authors for a streamlined NACA section. What effect would the absence of a base vent have on the ventilation mechanism for fenced struts? If the biogive strut was wetted at the trailing edge, the implication is that strut section may influence the effects of forces.

AUTHOR'S REPLY

Reply To Jones And Schmitke

Thank you for your comments on the practicality of this work. It is gratifying to find that sponsors are keen to examine their previous practices in the light of new material and to see model research developed along applicable lines.

Reply T. Barr

The classical aeronautical 'short' bubble was not seen in the course of this project although some behavioural similarities were observed on the NACA struts (4). When ventilation occurs with an extended separation zone it is initiated from the tail; a nose fence would not be effective and a tail fence would be required.

The authors agree that further systematic studies are required for practicable struts at high Reynolds' numbers. It must be noted that if such an increase is produced by speed changes then the separation bubbles, whether 'long' or 'short', will be replaced by a pulsating cavity.

Reply To Morgan And Rood

From the results obtained in this work no attempt at scaling to full scale is justified. This is a parametric survey of fence dimensions carried out at one Reynolds' number and as such does not indicate a trend for behaviour at higher speed. Physical differences in the roughness of the water surface, the turbulence level and channel size can change ventilation inception angles markedly. One of the difficulties of ventilation research is that of comparing results from different facilities. In the circumstances Fig. 2 shows good agreement when fences are present. Experiments can be carried out in the recirculating water channel which scale cavitation correctly but, as Morgan and Rood indicate, Reynolds' number effects are important and extreme caution is required before applying model scale results to full scale, particularly in the absence of any confirmatory full scale data. A comprehensive discussion of scaling, and the applicability of model tests may be found in Rothblum (15).

We are not in a position to be dogmatic about dimensions of fences at full scale as stated above. In the absence of better data we hope our report will provide a useful guide.

The role of the two ventilation modes at high speed was discussed fully in Rothblum et al (6). It was found that as the speed is increased the point of ingress from tail ventilation moved progressively forward suggesting that ventilation at prototype speeds will occur from a point reasonably near the nose.

Finally, the strut model had a rounded trailing edge of radius 1% of chord. It was not base ventilated.

REFERENCE

15. Rothblum, R.S., "Control of Ventilation in Surface-Piercing Struts", Ph. D. Thesis, The University of Leeds, Leeds, England, to be submitted.